

spacing are dependent on relative rates of formation (requiring ATP hydrolysis) and dissociation from the DNA (limited lifetime of the protein-DNA interaction). Linear DNA fragments may be expected to support fewer of these structures if they dissociate upon reaching an end. At present, the composition and stoichiometry of subunits in these structures is not clear, nor is the mechanism, rate, and directionality of translocation. Both of these questions are currently under study.³

1. Nossal, N.G. and Alberts, B.M. (1983) in *Bacteriophage T4* (C.K. Mathews, ed.) Amer. Soc. Microbiol., p. 71.
2. Gogol, E.P., Young, M.C., Kubasek, W.L., Jarvis, T.C. and von Hippel, P.H. (1990) *Proc. XIIth Intl. Cong. Elect. Mic.*, San Francisco Press, p. 264.
3. This work has been supported by an institutional grant from the Lucille B. Markey Caritable Trust and the NIH grants GM29158 and GM15792 to P.H. v. H. and AI07568 to M.C.Y.

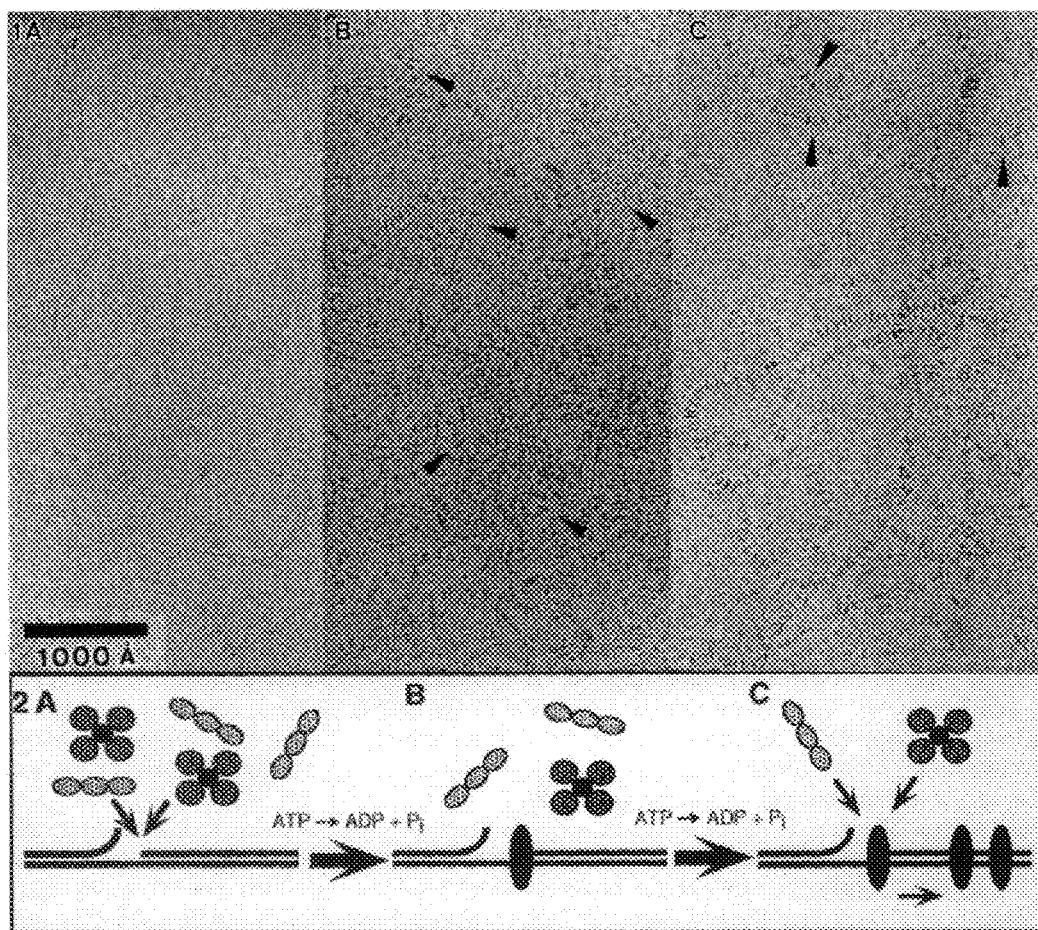


FIG. 1.— Cryo-electron micrographs of T4 replication protein complexes and plasmid DNA cofactors in the presence of Mg-ATP : A, intact supercoiled plasmid; B, plasmid relaxed by nicking at a single site per molecule; C, plasmid with a single ~300 base single-stranded gap. Clusters of the bar-like structures are readily visible. Arrowheads point out some isolated (i.e., unclustered) complexes.

FIG. 2.— Schematic model for formation of the bar-like complexes of replication proteins with DNA cofactors, starting with association at nick/gap sites (A to B, with site shown as a frayed DNA end), and leading to clusters formed by translocation from the site of formation (C).

DNA COMPLEXED WITH RECA PROTEIN

Edward H. Egelman and Xiong Yu

Department of Cell Biology and Neuroanatomy, University of Minnesota Medical School,
Minneapolis, MN 55455

We have been using electron microscopy and computed image analysis to understand the structure of the helical polymer that the RecA protein from *E. coli* forms on DNA. Recent work has addressed the following points:

1) RecA binds an ATP analog, ATP- γ -S, and hydrolyzes this analog several thousand times more slowly than ATP is hydrolyzed by RecA. We have shown¹ that structural transitions may be seen within RecA filaments on the same time scale (several hours) on which ATP- γ -S is being hydrolyzed, and several lines of evidence suggest that these conformational changes are due to the RecA ATPase. We have therefore been able to directly visualize these motions, using image analysis of bundles of RecA filaments.

2) RecA forms two different filamentous structures: a compact form, that has no known activity, and an extended, active form that can cleave the LexA repressor, catalyze a DNA strand exchange reaction, and hydrolyze ATP. The compact state can form on DNA, but can also form as a self-polymer, and can form with no nucleotide but can also bind ADP. The extended form requires DNA as a substrate and an ATP cofactor. We have used Scanning Transmission Electron Microscopy (STEM), cryo-EM of frozen-hydrated specimens, and conventional negative stain microscopy to look at both of these states. Chang *et al.* (1988)² found that there was a shrinkage of the pitch in both states of the RecA filament between frozen-hydrated EM and negative stain. We find the same shrinkage that they described for the compact state in negative stain as well as in freeze-dried specimens, but do not see any shrinkage for the extended state. Rather, we see that the extended filaments can be easily stretched in frozen-hydrated specimens by fluid flow during blotting.

3) We have been able to analyze images of frozen-hydrated RecA-DNA filaments in the compact, inactive state, and show that there are about 6.1 subunits per turn of a 76Å pitch helix in this state. This value has been confirmed with STEM measurements. From analyzing RecA-covered circular DNA molecules, we have been able to determine that the DNA is not stretched in this state, the way that it is in the active RecA filament, and that the binding stoichiometry of DNA bases:RecA is about 5:1. This contrasts with the 3:1 stoichiometry in the active state, which strongly suggests that these two states are not interconvertible, as has already been established on kinetic grounds.³

4) The crystal structure of the RecA protein has been solved,⁴ and RecA forms a helix in the crystal, in the absence of DNA and ATP, with 6.0 subunits per turn of an 82Å pitch helix. Since this is close to the active RecA filament, with 6.2 subunits per turn of a 95Å pitch helix,⁵ it has been thought that the two states are closely related. However, we can now show that the crystal structure is closer, both biochemically and structurally, to the inactive filament, which is not interconvertible with the active RecA filament. Thus, information from electron microscopy will be very important in understanding the conformational changes that occur between the crystal structure and the active RecA-DNA filament.

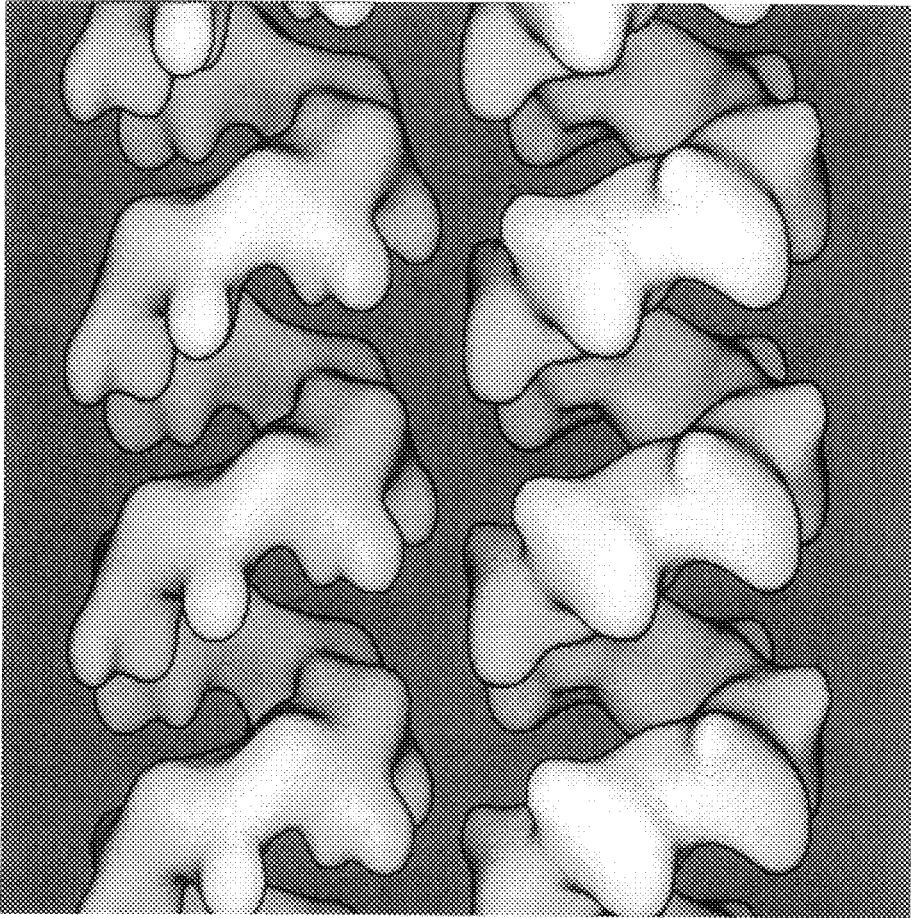


FIG. 1.-- Surface view of reconstruction of compact, inactive RecA-DNA filament (right) from frozen-hydrated specimens. Three filaments were averaged together for this reconstruction. For comparison, a surface view of the RecA crystal⁴ has been generated (left) using a Gaussian filter with a 30Å standard deviation to match the EM resolution.⁶

References

1. X. Yu and E. Egelman, *J. Molecular Biology* (1992) **224**, in press.
2. C-F. Chang *et al.*, *J. Ultrastructure and Mol. Structure Research* (1988) **100**, 166-172.
3. J.W. Lee and M.M. Cox, *Biochemistry* (1990) **29**, 7666-7676.
4. R.M. Story *et al.*, *Nature* (1992) **355**, 318-325.
5. X. Yu and E.H. Egelman, *Biophysical Journal* (1990) **57**, 555-566.
6. This research supported by N.I.H. grant GM35269

TRANSCRIPTION FACTOR/DNA INTERACTIONS VISUALIZED BY ELECTRON SPECTROSCOPIC IMAGING

David P. Bazett-Jones, Mark L. Brown

Departments of Anatomy and Medical Biochemistry, The University of Calgary, Calgary, Alberta, Canada T2N 4N1

A multisubunit RNA polymerase enzyme is ultimately responsible for transcription initiation and elongation of RNA, but recognition of the proper start site by the enzyme is regulated by general, temporal and gene-specific trans-factors interacting at promoter and enhancer DNA sequences. To understand the molecular mechanisms which precisely regulate the transcription initiation event, it is crucial to elucidate the structure of the transcription factor/DNA complexes involved. Electron spectroscopic imaging (ESI) provides the opportunity to visualize individual DNA molecules. Enhancement of DNA contrast with ESI is accomplished by imaging with electrons that have interacted with inner shell electrons of phosphorus in the DNA backbone. Phosphorus detection at this intermediately high level of resolution ($\approx 1\text{nm}$) permits selective imaging of the DNA, to determine whether the protein factors compact, bend or wrap the DNA. Simultaneously, mass analysis and phosphorus content can be measured quantitatively, using adjacent DNA or tobacco mosaic virus (TMV) as mass and phosphorus standards. These two parameters provide stoichiometric information relating the ratios of protein:DNA content.

We are studying the structure and function of transcription complexes which are involved in regulating the 5S rRNA genes of *Xenopus*, genes transcribed by RNA polymerase III. We have shown by ESI that TFIID, a factor required for accurate transcription initiation, compacts the DNA and is able to create a hairpin-shaped bend in the backbone of the DNA double helix (1) (Figure 1). That TFIID can bend DNA is further supported by more recent solution DNA bending assays (2). Complexes formed on a mutant gene, $\Delta 66$, which lacks the 5' portion of the TFIID binding site called the A box, is required for TFIID-induced bending. Without the A box, the DNA is not compacted by TFIID but is nearly fully extended (Figure 2). Alternatively, the control mutant, $\Delta 47$, which has an intact TFIID binding site, is bent by TFIID (Figure 1). We have substantiated these results with assays which measure DNA bending in solution. Whereas the A box is required for TFIID-induced DNA bending, the C-terminal domain of TFIID, which is required for transcription, is not required for DNA bending. Complexes with DNA of the smaller, C-terminal-deleted, 33 kD form of TFIID are indistinguishable from the native form (Figures 3-6).

References

1. D.P. Bazett-Jones, M.L. Brown, *Mol. Cell. Biol.* (1989) 9,336.
2. G.P. Schroth et al., *Nature* (1989) 340,487.
3. This work was supported by a grant from the Medical Research Council of Canada.

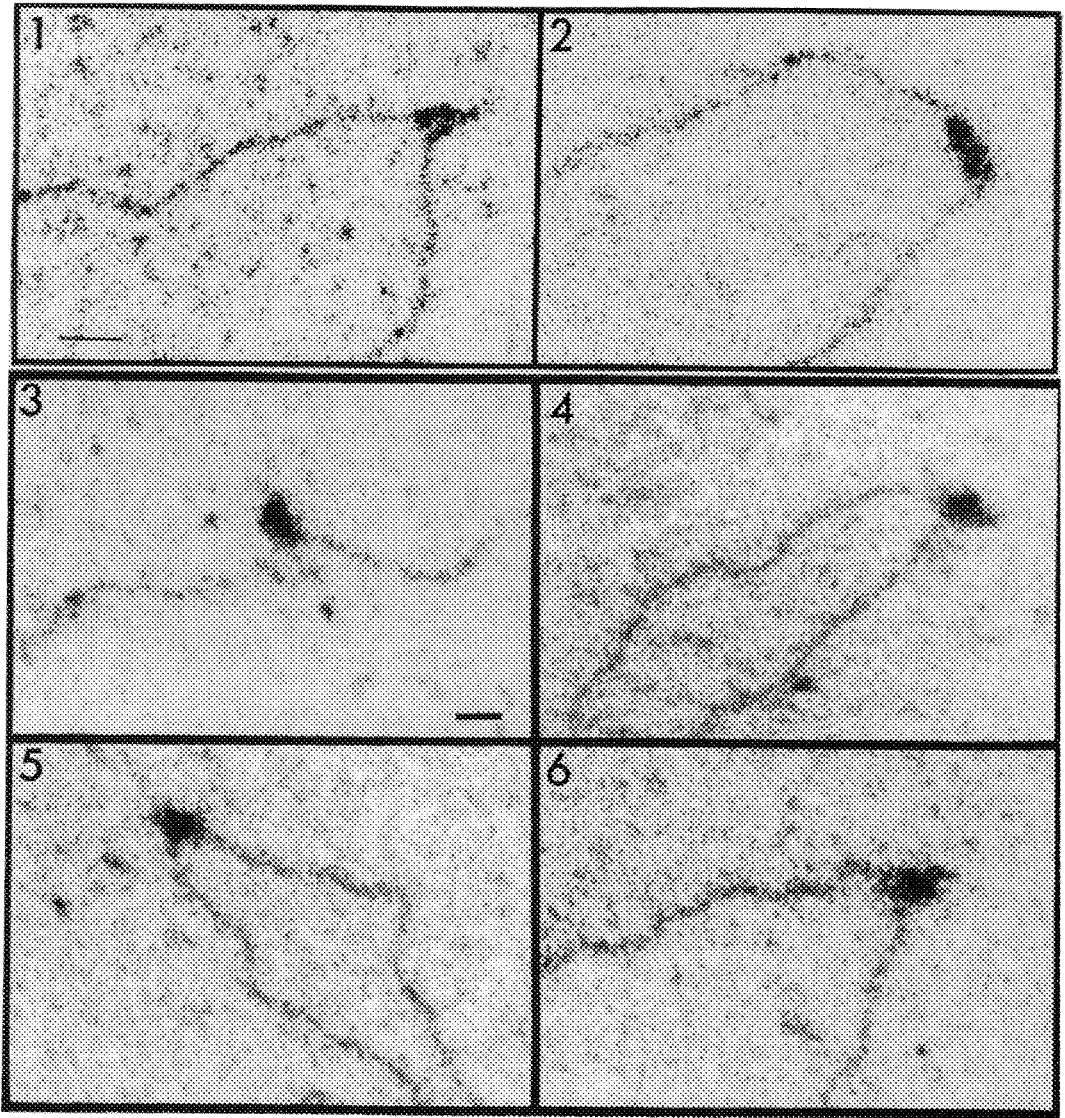


Figure 1 - Electron spectroscopic image of TFIIIA complexed with $\Delta 47$ deletion mutant of the 5S rRNA gene. The micrograph was recorded at 160 eV in the energy loss spectrum. Bar=13nm.

Figure 2 - Electron spectroscopic image of TFIIIA complexed with $\Delta 66$ deletion mutant of the 5S rRNA gene. Unlike the $\Delta 47$ mutant, $\Delta 66$ lacks the 5' portion of the TFIIIA binding site. The imaging conditions were identical to those used to obtain Figure 1.

Figures 3-6 - Electron spectroscopic images of the 33 kD protease digested fragment of TFIIIA complexed to the native 5S rRNA gene. The images were recorded at an energy loss of 60 eV. Bar=12.4nm.

ORGANIZATION OF dsDNA IN ICOSAHEDRAL VIRUS CAPSIDS

Frank P. Booy^{*}, Benes L. Trus^{**}, William W. Newcomb^{***}, Jay C. Brown^{***}, Philip Serwer^{****} and Alasdair C. Steven^{*}

^{*} Laboratory of Structural Biology, NIAMS; and ^{**} Computer Systems Laboratory, DCRT, NIH, Bethesda, MD 20892; ^{***} Department of Microbiology and Cancer Center, University of Virginia Health Sciences Center, Charlottesville, VA 22908; ^{****} Department of Biochemistry, The University of Texas Health Science Center, San Antonio, TX 78284

Condensation/decondensation reactions which effect the packaging of viral genomes into their capsids and their subsequent release constitute one of the basic phenomena which structural biology seeks to explain. The appropriate nucleic acid molecule(s) must be selected; then packaged at a high density to allow efficient utilization of the available space; the mutual electrostatic repulsion of DNA strands must somehow be overcome; and the arrangement of the DNA must allow for its ready release upon initiation of infection. Cryo-electron microscopy has emerged as an incisive tool for visualizing the internal organization of packaged DNA inside viral capsids^{1,2}. We illustrate its effectiveness with observations relating to bacteriophages T4, T7, and herpes simplex virus, type 1 (HSV-1).

Phage T4D was grown in *E. coli* B40 and purified on sucrose gradients. T7 was purified from infected *E. coli* lysates on cesium chloride density gradients. HSV-1 C-capsids were purified from infected BHK cells by sucrose gradient centrifugation. After extensive dialysis into PBS, samples at 1-3 mg/ml protein were freeze-vitrified in liquid ethane for cryo-electron microscopy, and visualized in a Gatan 626 cryo-holder in a Philips EM400T, using low-dose techniques. Micrographs were recorded relatively close to focus, with the first zero of the phase contrast transfer function at about $(2\text{ nm})^{-1}$.

T4D virions are shown in Fig 1; a close-packed array of T7 virions in Fig 2; and a field of HSV-1 C-capsids in Fig. 3. All three images clearly show striking features that have strong contributions in the spatial frequency range of $\sim (2.6\text{ nm})^{-1}$, which relate to the side-by-side packing of DNA duplexes in locally ordered, parallel (or antiparallel), bundles. In Fig 1, one sees predominantly lateral views of these bundles, i.e. linear striations. Other aspects include quasi-hexagonal punctate formations in which the DNA bundles are viewed end-on (Fig. 2, 3), as well as other interference patterns generated when the bundles are viewed from other directions (*, Fig. 2). Because these images are dominated by the center-to-center spacing between duplexes, they are most clearly visualized in micrographs recorded at defocus values that do not accentuate the protein shell (whose capsomers tend to be dominated by lower frequencies). Nevertheless, computational removal of the protein shell after three-dimensional reconstruction further enhances the DNA images in the case of HSV-1, whose shell is relatively thick $(15\text{ nm})^2$.

The configuration of encapsidated DNA in these viruses closely resembles liquid crystals of DNA formed in vitro under appropriate ionic conditions³. Other than being confined within the cavity defined by the inner surface of the capsid shell, these observations do not indicate any icosahedral ordering to the DNA: rather, its packing seems to be dominated by DNA-DNA interactions. The absence of an attraction between the DNA and this surface would certainly facilitate exit of the DNA upon infection. These observations suggest that a common structural solution has been adopted by all three viruses to organize their condensed DNA, and it seems likely to apply to many other comparable viruses, i.e. with double-stranded genomes, and few internal capsid proteins. This mode of packing appears to be fundamentally different from those of icosahedral ssDNA viruses, whose genomes often interact with positively charged domains of their capsid proteins; and those of dsDNA viruses whose genomes are packaged with stoichiometric amounts of internal proteins.

REFERENCES

1. J. Lepault et al., EMBO J. (1987)6, 1507.
2. F. P. Booy et al., Cell (1991)64, 1007.
3. K. Richter & J. Dubochet, Proc. XIIth Int. Cong. EM (1990) Vol 1, 488.

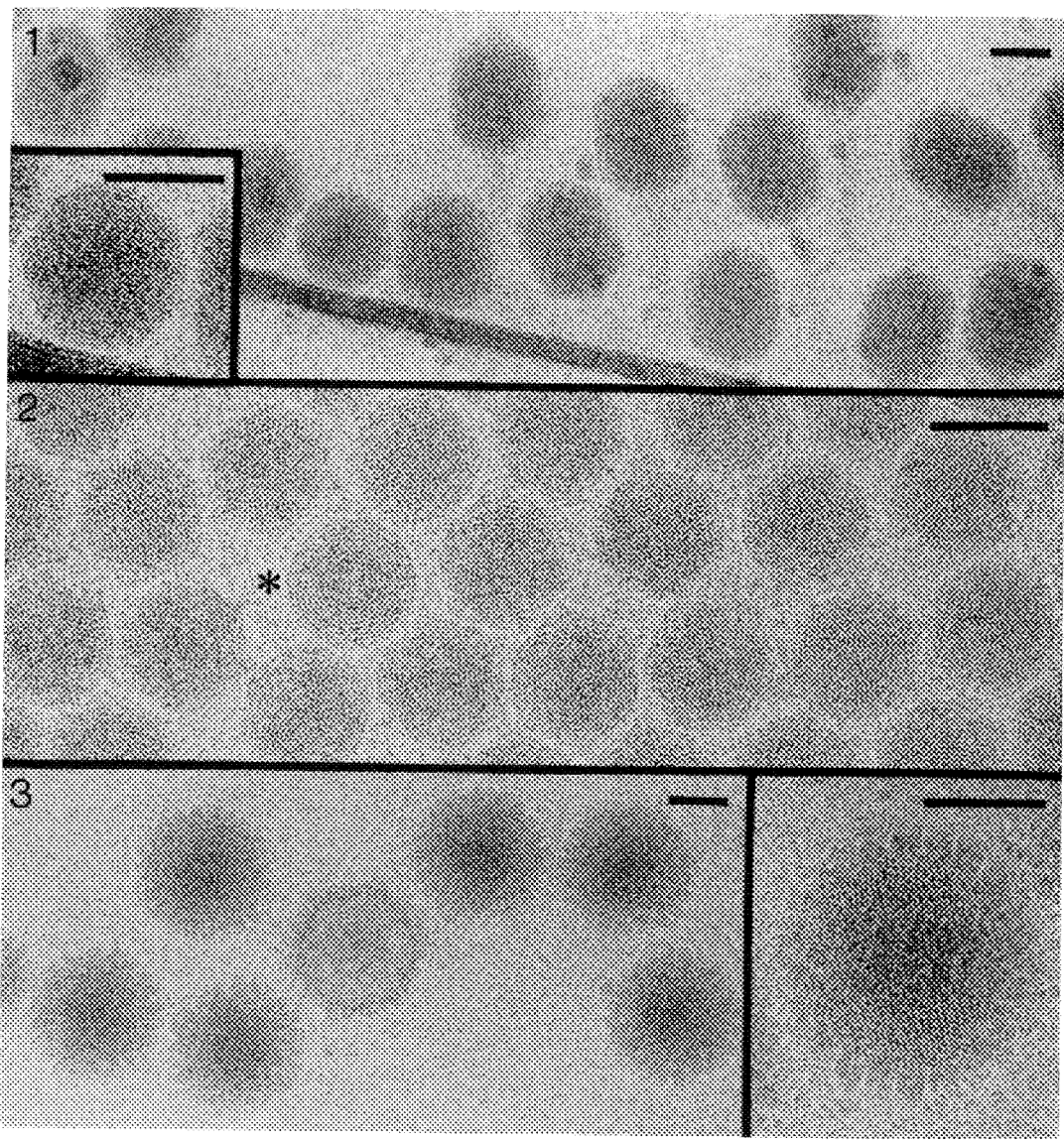


Fig. 1 : Cryo-electron micrograph of bacteriophage T4 virions, showing motif of encapsidated DNA duplexes. Bar = 50 nm.

Fig. 2 : Cryo-electron micrograph of closely packed field of bacteriophage T7 virions, showing various aspects of packaged DNA motif. Bar = 50 nm.

Fig. 3 : Cryo-electron micrograph of purified HSV-1 capsids. The DNA-containing C-capsids have dense interiors that exhibit essentially the same DNA motif as phages T4 and T7. Bar = 50 nm.

ORGANIZED PACKING OF RNA INSIDE VIRUSES AS REVEALED BY CRYO-ELECTRON MICROSCOPY AND X-RAY DIFFRACTION ANALYSIS

T. S. Baker, R. H. Cheng, J. E. Johnson, N. H. Olson, G. J. Wang, and T. J. Schmidt

Department of Biological Sciences, Purdue University, West Lafayette, IN 47907

The development of modern electron microscopy techniques to visualize the hydrated structures of biological macromolecules has stimulated many new studies¹, especially with viruses² and virus-macromolecule complexes^{3,4} that are too large to study with current x-ray crystallographic methods. Cryo-electron microscopy (cryoEM) in conjunction with three-dimensional reconstruction procedures is capable of revealing both external and internal features of these structures.¹

Until recently there was little evidence for icosahedrally arranged nucleic acid components contained inside the capsids of spherical viruses. X-ray crystallographic studies of beanpod mottle virus (BPMV)⁵ and canine parvovirus⁶ have revealed regions of ordered ssRNA and ssDNA, respectively. The nucleic acid portion of most viruses typically scatters x-rays at low angle (>2nm resolution) which is generally not recorded or is not available for crystallographic analysis. Thus, the typical 2-3nm resolution achieved by cryoEM is ideally suited for examining potential nucleic acid organization in viruses.

We have studied the organization of the ssRNA in cowpea mosaic virus (CPMV), a virus closely related to BPMV. The capsid structure of each of these viruses has been determined to atomic resolution^{7,5} and each virus separates into three components on cesium chloride gradients on the basis of their different nucleic acid contents. The CPMV top component (CPMV-T) is devoid of RNA, whereas middle (CPMV-M) and bottom (CPMV-B) components contain different RNA molecules ($M_r = 1.22 \times 10^6$ for RNA-M, and 2.02×10^6 for RNA-B). Both RNA species must be present for successful infection and replication of progeny virus.

Despite the remarkable similarities in the capsid structures of BPMV and CPMV, only the BPMV-M component showed the presence of icosahedrally ordered regions of RNA in contact with the protein shell.⁵ We have recorded low-irradiation images of vitreous samples of all three CPMV components and have computed three-dimensional reconstructions to ~2.5nm resolution for each (Fig. 1A,B,C). Each reconstruction was scaled (magnification and contrast) to best fit the x-ray model (Fig. 1D)^{7,8}, and difference maps were then computed to view the RNA-M (Fig. 1E) and RNA-B (Fig. 1F) distributions. The densities in both difference maps are similarly distributed between radii of 8-10nm, suggesting that the capsid may strongly influence a common packing arrangement of the separate RNA molecules. The "RNA" features are primarily confined within cylindrical volumes directed between adjacent icosahedral three-fold axes of symmetry and within a disk-like volume beneath the capsid inner surface on the five-fold axes. A difference map between CPMV-B and CPMV-M (data not shown) revealed net positive "RNA" density as expected.

The nucleic acid organization inside CPMV differs from that observed in BPMV-M.⁵ In CPMV the "RNA" density crosses the two-fold axes whereas in BPMV the well-ordered portion is directed between adjacent three-fold and five-fold axes. Also, the CPMV "RNA" density is displaced ~0.5nm to lower radii than in BPMV-M, which might in part explain why ordered RNA was not observed in the crystallographic analysis of CPMV.⁷ BPMV-B is more similar to CPMV than BPMV-M, which shows RNA in close van der Waals contact with the capsid subunits. Finally, the location of the "RNA" density in CPMV puts it in close proximity with those (amino-terminal) portions of the 60 CPMV large subunits that are directed tangentially near the two-fold axes. Low resolution (>2nm) x-ray crystallographic data are being collected from all three CPMV components to confirm and correlate with our cryoEM results.⁹

References:

1. M. Stewart and G. Vigers, *Nature* **319**(1986)631.
2. M. Adrian, *et al.*, *Nature* **308**(1984)32.
3. B. V. V. Prasad *et al.*, *Nature* **343**(1990)476.
4. G. J. Wang, *et al.*, *Nature* **355**(1992)275.
5. Z. Chen, *et al.*, *Science* **245**(1989)154.
6. J. Tsao, *et al.*, *Science* **251**(1991)1456.
7. Z. Chen, *et al.*, *Sem. Virol.* **1**(1990)453.
8. R. H. Cheng, (1992), these proceedings.
9. We thank M. Love and Y. Li for providing purified samples of CPMV, and C. Tsai and J. B. Dai for helping generate the x-ray model. Research supported by NSF grant DMB-8905062 (TSB), NIH grant AI-18764 (JEJ), and a grant from the Lucille P. Markey Charitable Trust for the development of structural studies at Purdue.

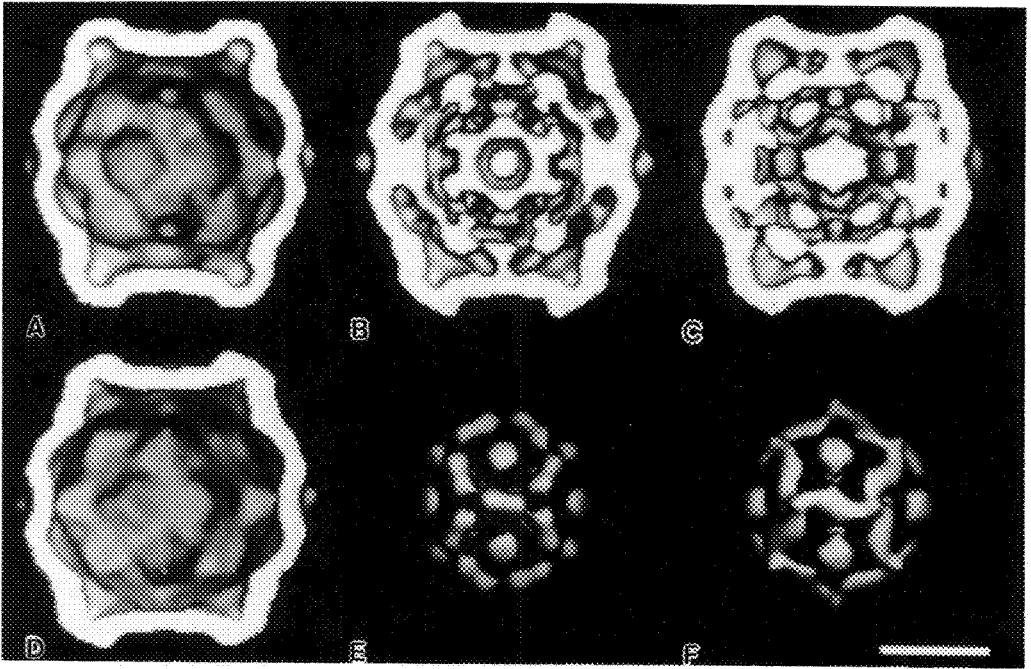


FIG 1. Surface-shaded representations of three CPMV reconstructions (A,B,C), x-ray model (D), and difference maps between two reconstructions and x-ray model ($E = B - D$; $F = C - D$), all at ~ 2.5 nm resolution. Reconstructions (A,B,C) were corrected for effects of microscope contrast transfer function⁸, scaled to x-ray model (D), and contoured to give corresponding solvent-excluded volume for 60 copies of large and small subunits in the capsid shell. Bar $\simeq 10$ nm.

- A. Back-half of CPMV-T reconstruction (from 15 separate particle images).
- B. Back-half of CPMV-M reconstruction (20 particle images).
- C. Back-half of CPMV-B reconstruction (15 particle images).
- D. Back-half of CPMV capsid x-ray model, computed to 2.5nm resolution from coordinates of all non-hydrogen atoms.
- E. Front portion (40%) of difference map between CPMV-M (B) and x-ray model (D).
- F. Front portion (40%) of difference map between CPMV-B (C) and x-ray model (D).

Helical Polymers of the REV Protein of Human Immunodeficiency Virus 1

Manoj Misra*, Benes L. Trus**, Paul Wingfield*** and Alasdair C. Steven*

* Laboratory of Structural Biology, NIAMS, and ** Computer Systems Laboratory, DCRT, National Institutes of Health, Bethesda, MD 20892; *** Pfizer Central Research Division, Eastpoint Road, Groton, CT 06340

The pattern of viral gene expression in cells infected with HIV-1 is orchestrated by several regulatory proteins. One such viral gene product is **Rev** (regulator of expression of virus), a 13 kDa basic protein that plays a crucial role in determining whether full-length transcripts coding for the major structural proteins of HIV-1 are exported intact from the nucleus into the cytoplasm, so that active proliferation of the virus can ensue¹. Purified **Rev** has been shown to polymerize in vitro into long filamentous polymers². Based on this and other observations, it has been hypothesized that **Rev** functions rather like the nucleocapsid protein of a filamentous RNA virus, and that coating of the transcripts in question by **Rev** is the mechanism whereby they are protected from splicing². To explore this hypothesis further, we have studied the structure of these **Rev** polymers in greater detail.

Rev was purified from a bacterial expression system, shown to retain biological activity by the criterion of specifically recognizing RRE (**Rev** Responsive Element) RNA, and polymerized as described². The polymers were imaged after negative staining, or in the frozen, hydrated state, in Philips EM400T and Zeiss EM902 electron microscopes. Digitized filaments were computationally straightened³, and subjected to Fourier analysis and other image processing using the PIC system⁴. STEM micrographs of freeze-dried specimens were kindly provided from the Brookhaven STEM facility by Drs M. Simon and J. Wall.

Rev filaments negatively stained with uranyl acetate are (Fig. 1a) are compared with unstained, dehydrated, filaments imaged in STEM dark field (Fig. 1b), and unstained, hydrated filaments imaged by phase contrast (CTEM bright field) in Fig. 1c. These data concur that the filaments are of uniform in width, and are hollow. The outer diameter measured in negative stain (16 - 18 nm) is somewhat higher than that determined from the unstained specimens, which in both cases, was 14 - 15 nm, probably on account of flattening of the stained specimens upon air-drying. The freeze-dried representation (Fig. 1c) seems to underestimate the extent of the axial channel. The most convincing dimensions are those from the frozen-hydrated specimens, which indicate a lumen diameter of ~ 4 nm, and thus, a wall thickness of 5 - 6 nm. Strong evidence of helical symmetry was obtained by negative staining with PTA (Fig. 2), whereby oblique striations were clearly visualized. The corresponding diffraction patterns (e.g. Fig. 3) show a strong layer-line at an axial spacing of (5.1 nm)⁻¹. Preliminary Fourier analysis suggests that this represents a six-stranded family of helices with a pitch-angle of 40° and an inter-strand spacing of ~ 4.1 nm. STEM measurements of mass-per-unit-length (Fig. 4) indicate a homogeneous population of filaments that average 70 kDa/nm.

Our observations to date reveal certain structural parameters of the polymers. Although the general morphology of these filaments approximates that of tobacco mosaic virus coat protein, it is evident that their helical symmetry is distinctly different. Moreover, well ordered co-polymerization of **Rev** with RNA has not yet been achieved.

REFERENCES

1. C. A. Rosen & G. N. Pavlakis, AIDS 1990 (1990)4, 499.
2. P. T. Wingfield et al., Biochemistry (1991)30, 7527.
3. A. C. Steven et al., Proc. 43rd Ann. Mtg. EMSA (1985) p.738.
4. B. L. Trus & A. C. Steven, Ultramicroscopy (1981)6, 383.

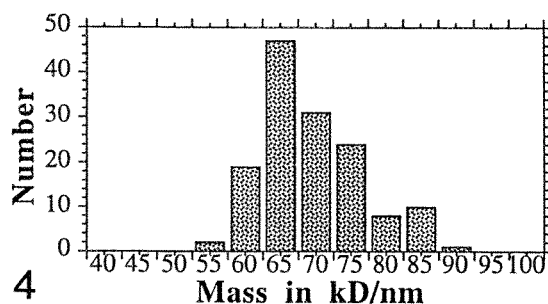
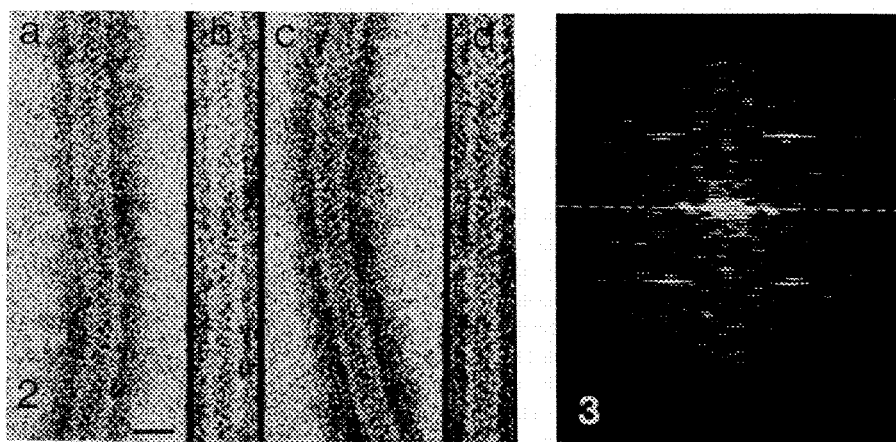
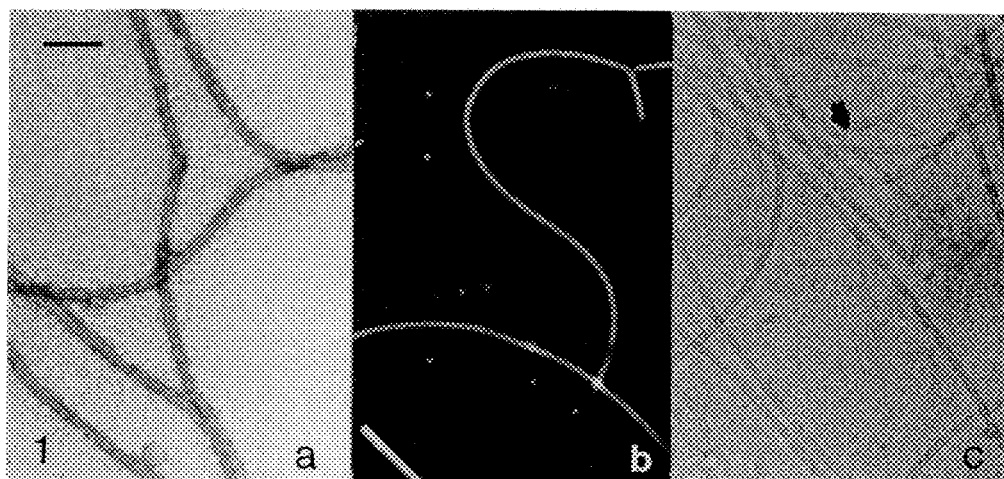


Fig. 1 : **Rev** filaments imaged in (a) negative stain (uranyl acetate) - bright-field CTEM; (b) unstained, frozen, dried - dark-field STEM; (c) unstained, frozen, hydrated - bright-field CTEM. Bar = 100 nm.
 Fig. 2 : **Rev** filaments negatively stained in PTA, before (a, c) and after (b, d) computational straightening. Bar = 20 nm.
 Fig. 3 : Computer diffraction pattern of straightened **Rev** filament.
 Fig. 4 : Distribution of mass-per-unit-length measurements made from STEM micrographs.

IMMUNOLocalIZATION OF VAULT PARTICLES IN CULTURED CELLS

Nancy L. Kedersha* and Leonard H. Rome

Department of Biological Chemistry and the Mental Retardation Research Center, UCLA School of Medicine, Los Angeles, CA 90024-1737. *present address is ImmunoGen Inc. Cambridge, MA 02139

We first reported on the existence of vault ribonucleoprotein particles in 1986¹, and since this study we have demonstrated that these unusual RNPs are ubiquitously expressed and highly conserved among diverse eukaryotes². These particles are quite large (65 x 35 nm) and distinctly regular in shape and dimensions. The polypeptide composition of vaults is also similar between species, dominated by a ~100 Kd protein which makes up >70% of the particles mass. The RNA component of vaults, which has been sequenced and characterized from both rat and bullfrog³, does not appear to serve a structural role⁴, and due to the strong conservation of its secondary structure could serve a functional role.

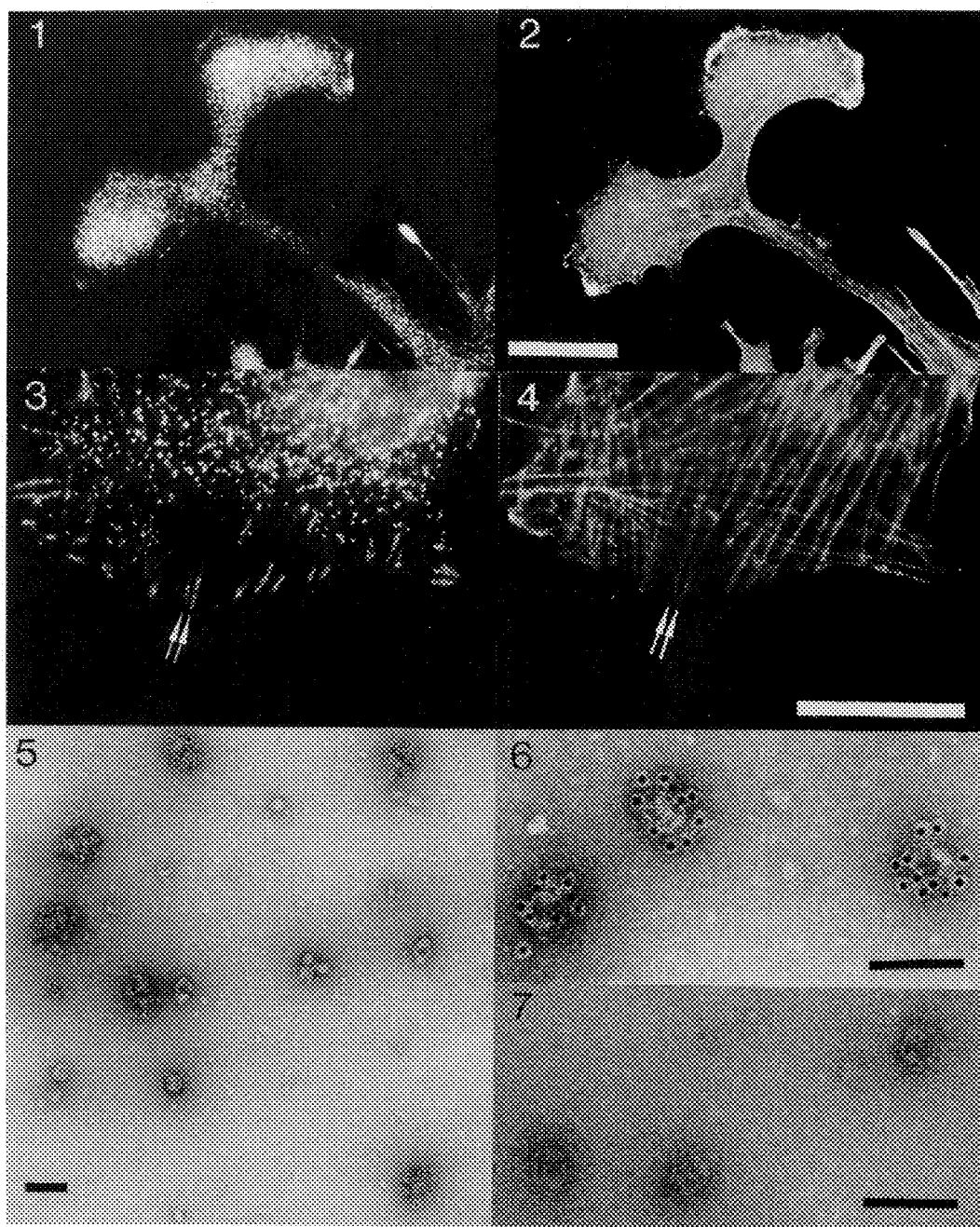
Immunofluorescence has been used to localize vaults in cultured cells⁵. Staining by reaction with affinity-purified anti-vault antibodies (primarily directed against the major vault polypeptide) and fluorochrome-conjugated secondary antibodies reveals a punctate cytoplasmic pattern with some cells containing thousands of punctate sites. Localized concentrations of vaults are often seen in spreading lamellipodia localized into discrete zones largely devoid of filamentous actin but bounded by actin-rich ruffling edges (Figs. 1-2). While the majority of the vaults appear to be randomly distributed in the perinuclear region of most spread cells, a significant subpopulation appear to associate with the termini of actin stress fibers (Fig. 3-4, arrows).

Purified vaults exist in two forms; the closed, intact form which predominate in rat liver preparations, and open or half vaults which are the major form seen in *Dictyostelium* preparations. When "closed" vaults from rat liver were adhered to coverslips and stained with affinity-purified polyclonal anti-vault sera, punctate staining was observed; however, both methanol-fixed and formaldehyde-fixed cells displayed much brighter individual loci than did the isolated, closed vaults. The brighter loci observed *in situ* could represent either "open" vaults, in which the exposure of the radial petals would allow more antibody access and hence binding, or clusters of individual vault particles. The uniformity of the loci suggests open vaults rather than clusters. This is supported by EM studies using immunogold secondary antibodies on intact vaults, where each vault maximally binds 8-14 gold particles. Vaults fixed with paraformaldehyde prior to staining show similar maximum binding, however, many vaults remain completely unstained using this procedure (Figs. 5-6), suggesting that a closed/locked conformation may prevent antibody binding altogether.

We have been unable to "open" rat vaults *in vitro* to directly compare the staining of the two forms. *Dictyostelium* (open and half) vaults bound to coverslips and stained with an anti-*Dictyostelium* antibody displayed larger and brighter loci than did purified rat vaults stained with excess anti-rat vault antibody. The stained *Dictyostelium* vaults are very heterogeneous, consistent with their mixed morphology² and they do not exhibit clumping under EM. We conclude that the vault-specific loci seen in stained cells represent individual vault particles rather than clusters. Furthermore, variation in staining intensity may reflect differences in vault morphology *in situ*, e.g. open versus closed.⁶

References

1. N.L. Kedersha and L.H. Rome. *J. Cell Biol.* (1986) **103**, 699.
2. N.L. Kedersha, et al., *J. Cell Biol.* (1990) **110**, 895.
3. V.A. Kickhoefer, et al., (Submitted).
4. N.L. Kedersha, et al., *J. Cell Biol.* (1991) **112**, 225.
5. N.L. Kedersha and L.H. Rome. *Molec. Biol. Reports* (1990) **14**, 121.
6. This research was supported by NIH Grant GM 38097.



FIGS. 1-4. Immunofluorescence of fixed rat fibroblasts stained for vaults and visualized with rhodamine (1 & 3), and stained for actin and visualized with FITC (2 & 4). Bar represents 10 μ m. FIGS. 5-7. TEM of pure rat liver vaults incubated with anti-vault IgG and 10 nm gold-conjugated secondary antibodies (5-6) or with pre-immune primary antibody + gold (7) Bars represents 100 nm.

STRUCTURE OF SPICEOSOMAL UsnRNPs.

Reinhard Lührmann, Sven-Erik Behrens and Berthold Kastner

Institut für Molekularbiologie und Tumorforschung, Philipps-Universität
Marburg, D-3550 Marburg, GERMANY

The major snRNPs, U1, U2, U4/U6 and U5, are essential *trans*-acting factors in the pre-mRNA splicing process. They assemble with a pre-mRNA and a number of other non-snRNP splicing factors prior to the splicing reaction to form an active spliceosome¹. We are interested in investigating the biochemical composition of UsnRNPs and their ultrastructure as well as their function in splicing. In HeLa cell nuclear extracts the spliceosomal UsnRNPs exhibit differential association behaviour depending on the salt concentration. Thus, at high salt (420 mM) the majority of the U1, U2, U4/U6 snRNPs migrates on sucrose gradients at 10-12S, while U5 snRNP sediments at 20S. Under *in vitro* splicing conditions (i.e. at about 100 mM salt), U5 and U4/U6 snRNPs form a 25 S [U4/U6.U5]tri-snRNP-complex and U2 snRNPs sediment at about 17 S. We have isolated the various types of UsnRNPs under native conditions using mainly immunoaffinity chromatography procedures. Today we can distinguish more than 35 distinct snRNP proteins. They can be grouped into two classes. The first class comprises eight common snRNP proteins which are present in each of the spliceosomal UsnRNPs. In addition, the individual snRNPs contain snRNP-specific proteins. These include three (70k, A, C) for the 12 S U1 snRNP, two (A', B'') for the 12 S U2 snRNP, an additional eight for the 17 S U2 snRNP and eight for the 20 S U5 snRNP. The 25 S [U4/U6.U5]tri-snRNP-complex contains, in addition to the common proteins and the U5-specific proteins, a third group of six proteins which are essential for the stable formation of the tri-snRNP-complex. Thus, the different S-values of a particular snRNP particle result from differences in the population of snRNP-specific proteins associated with that particle².

We have investigated the various types of native snRNPs at the ultrastructural level using electron microscopy. Purified snRNPs were negatively stained with uranyl formate employing the double carbon film technique. In addition, individual snRNP components have been localized at the surface of native snRNPs using either immunoelectron microscopy or DNA oligonucleotide hybridization EM^{3,4}. These studies revealed a common structure determining principle for the spliceosomal UsnRNPs. That is, the spliceosomal snRNP species share a core RNP domain, round in shape which consists of the common proteins. The characteristic dimensions and morphology of each snRNP species is, however, mainly determined by the number of snRNP-specific proteins and the manner in which they are attached to the cognate core RNP domain⁵.

¹ T. Maniatis and R. Reed, *Nature* (1987)325, 673.

² R. Lührmann, B. Kastner and M. Bach, *Biochim. Biophys. Acta* (1990)1087, 2650.

³ B. Kastner, M. Bach and R. Lührmann, *Proc.Natl.Acad.Sci. USA* (1990)87, 1710.

⁴ B. Kastner, U. Kornstädt, M. Bach and R. Lührmann, *J. Cell. Biol.* (1992)116, 839.

⁵ This research was supported by a grant from the Deutsche Forschungsgemeinschaft (SFB 272/A3).

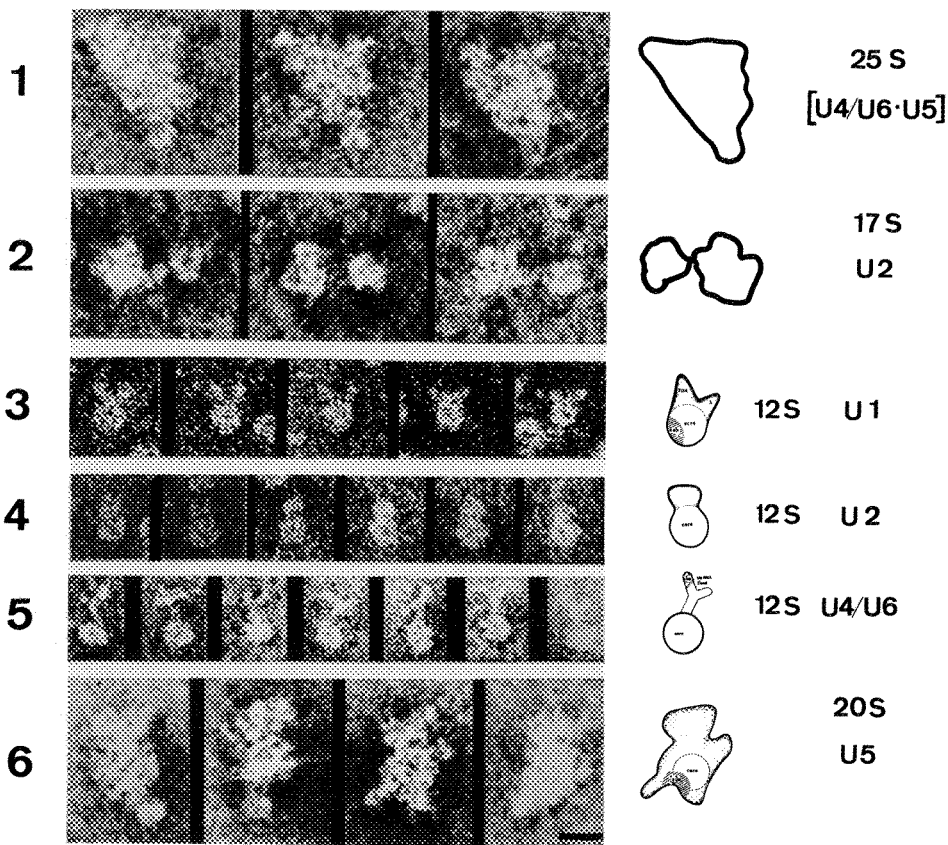


Fig. 1 25S [U4/U6·U5]tri-snRNPs negatively stained with uranyl formate.

Fig. 2 17S U2 snRNPs.

Fig. 3 12S U1 snRNPs. The globular domain contains the common snRNP proteins. The two main protuberances have been identified with the U1-specific proteins A and 70k.

Fig. 4 12S U2 snRNPs. The globular domain contains the common snRNP proteins. The additional domain contains the U2-specific proteins A' and B".

Fig. 5 12 U4/U6 snRNPs purified by Mono Q chromatography. The globular domain represents the core RNP domain of U4 RNP; the Y-shaped filamentous domain represents the 5'half of U4 and the 3'half of U6 RNA comprising the Y-shaped U4-U6 interaction domains.

Fig. 6 20S U5 snRNPs. (Bar = 10 nm).

STRUCTURE OF rRNA IN THE RIBOSOME

M. Boublik* and J. S. Wall**

*Roche Institute of Molecular Biology, Roche Research Center, Nutley NJ 07110
USA

**Department of Biology, Brookhaven National Laboratory, Upton NY 11973

Ribosomes are complex subcellular organelles playing a central role in protein biosynthesis. They are composed of more than fifty different proteins and three or four ribonucleic acids (rRNA) unevenly distributed (with no symmetry) between the large and small ribosomal subunit. It has been well established that ribosomal proteins and rRNAs are both involved in formation of the internal architecture of the ribosome as well as its function in protein synthesis. Understanding the fundamental relationship between structure and function requires establishment of the 3-D structure of the ribosome and its components at a molecular level.

The structure of rRNAs has been studied to much greater extent than that of the ribosomal proteins. Combination of *in situ* rRNA-rRNA and rRNA-protein crosslinking and application of chemical and enzymatic probing techniques lead to proposal of rRNA 2-D secondary structure, deduction of rRNA intramolecular pairing and tertiary folding and ultimately to a proposal of a 3-D model of rRNA *in situ* (in the case of the simplest known ribosome of *E. coli*).¹ However, evidence for the proposed 3-D folding of rRNA is rather indirect. A direct approach to the solution of rRNA conformation can be provided by high resolution (dedicated BNL) scanning transmission electron microscopy (STEM).^{2,3} We have developed a procedure that can resolve the conformation of rRNA under various ionic conditions (Fig. 1), monitor conformational transitions and mass changes induced in rRNA by interactions with ribosomal proteins during the assembly steps of ribosomal particles from their components (Fig. 2) and correlate the structure of partly and/or completely reconstituted ribosomal particles with their biological activity. These results can shed light upon the involvement of individual ribosomal proteins in the rRNA folding into the compact ribosomal particle but not on the distribution of the rRNA-protein moiety. *In situ* location of the rRNA molecules within the ribosomal subunits can be obtained from the difference image from the large and small angle annular detectors (Fig. 3) or from low dose electron energy loss imaging (in progress).

References:

1. Hill, W.E. *et al.* (eds.) in *The Ribosome: Structure, Function and Evolution* (1990) Amer. Soc. for Microbiol., Washington DC
2. Wall, J.S. in *Introduction to Analytical Electron Microscopy* (Hren, J.J. *et al.*, eds.) (1979), pp. 333-342, Plenum Press, New York NY
3. Boublik, M. *et al.* (1988) in *Methods in Enzymology* **164**, 49-63
4. We wish to acknowledge the contribution of Dr. S.J. Tumminia to this study and to thank W. Hellmann, F.E. Kito, B. Lin and Dr. M. Simon for excellent technical assistance. This work was partially supported by U.S.D.O.E. and N.I.H. RR01777 grant to J.S.W.

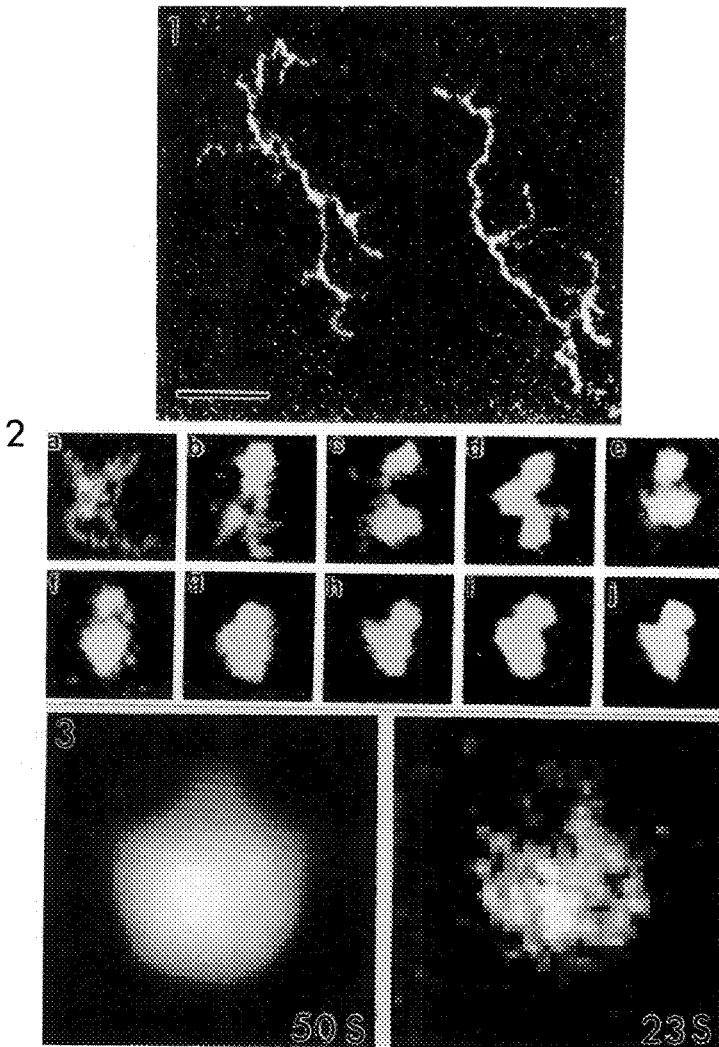


Fig 1 STEM image of 28S rRNA from eukaryotic large ribosomal subunit, unstained and freeze-dried. Bar = 50 nm

Fig 2 Gallery of STEM images illustrating conformational stages in the process of total reconstitution of 30S *E. coli* subunit from 16S rRNA (a) and 21 individual ribosomal proteins (b-i). Control 30S subunit (j).

Fig 3 Conceivable *in situ* location of 23S rRNA molecule within the 50S subunit of *E. coli* obtained from the difference image from the large and small angle annular detectors from BNL STEM.

DENSITY-BASED DISCRIMINATION OF PROTEIN AND RNA IN THE RIBOSOME

Joachim Frank

Wadsworth Center for Laboratories and Research, New York State Department of Health,
Albany, New York 12201-0509 and Department of Biomedical Sciences, State University of
New York at Albany, Albany, New York 12222

Cryo-electron microscopy combined with single-particle reconstruction techniques¹ has allowed us to form a three-dimensional image of the *Escherichia coli* ribosome.² In the interior, we observe strong density variations which may be attributed to the difference in scattering density between ribosomal RNA (rRNA) and protein. This identification can only be tentative, and lacks quantitation at this stage, because of the nature of image formation by bright field phase contrast. Apart from limiting the resolution, the contrast transfer function acts as a high-pass filter which produces edge enhancement effects that can explain at least part of the observed variations. As a step toward a more quantitative analysis, it is necessary to correct the transfer function in the low-spatial-frequency range. Unfortunately, it is in that range where Fourier components unrelated to elastic bright-field imaging are found, and a Wiener-filter type restoration would lead to incorrect results. Depending upon the thickness of the ice layer, a varying contribution to the Fourier components in the low-spatial-frequency range originates from an "inelastic dark field" image. The only prospect to obtain quantitatively interpretable images (i.e., which would allow discrimination between rRNA and protein by application of a density threshold set to the average RNA scattering density^{3,4}) may therefore lie in the use of energy-filtering microscopes.

In the absence of such an instrument, the only "hard" information to go by is the volume ratio rRNA:protein which may be inferred from Wittmann's⁵ published molecular weights and mass densities of the two components as approximately 0.85:1. This ratio has some uncertainty, however, because of an unaccounted portion of the total ribosomal molecular weight, and so the boundary rRNA:protein deduced from the volume ratio is subject to some error. An additional uncertainty is introduced by the likelihood that rRNA and protein are strongly intermeshed, so that a low-resolution study (currently at 40 Å) can only yield the spatial distribution of higher versus lower concentrations of rRNA ("RNA-rich" versus "RNA-poor"; see ref. 2).

Despite these uncertainties, the rRNA mass identified in the *E. coli* ribosome (Fig. 1) appears to be consistent with a number of observations from other experiments and with expectations on the basis of cross-linking information. Especially intriguing is the suggestion of a "bridge" along which the putative 16S and 23S RNA masses are connected ("b" in Fig. 1a).⁶

1) P. Penczek et al., Ultramicroscopy, in press.

2) J. Frank et al., J. Cell Biol. (1991)115, 597.

3) W. Kuhlbrandt, Ultramicroscopy (1982)7, 221

4) W. Kuhlbrandt and P. N. T. Unwin, J. Mol. Biol. (1982)156, 431.

5) H. G. Wittmann, Annu. Rev. Biochem. (1982)51, 155.

6) Supported, in part, by NIH R01 GM29169.

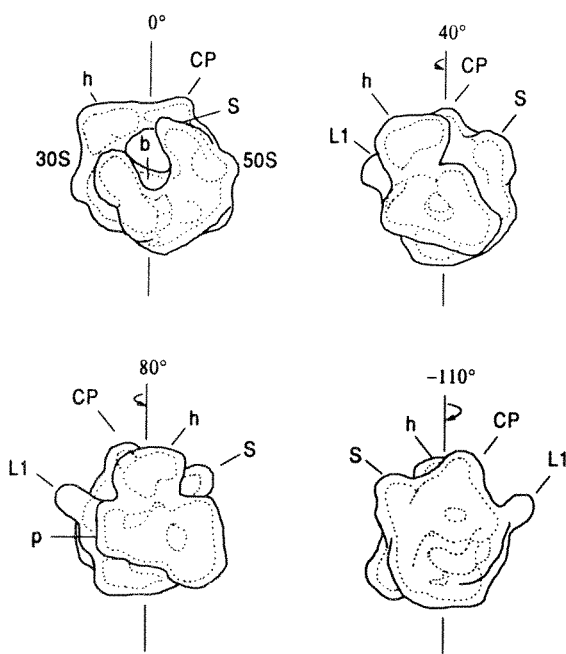


FIG. 1.—Sketches of the *E. coli* ribosome² in different orientations, related by rotation around the vertical axis by the angle indicated. The outline of the particle (protein:water interface) is drawn in a solid line, the putative rRNA boundary is indicated in a broken line. Meaning of symbols: h = head, p = platform of small (30S) subunit; L1 = L1 arm, S = stalk base, CP = central protuberance of large (50S) subunit; b = bridge connecting 16S-23S rRNAs. (Partially reproduced from ref. 2, by permission of The Rockefeller University Press).

VISUALISATION OF *E. coli* RIBOSOMAL RNA *in situ* BY ELECTRON SPECTROSCOPIC IMAGING AND IMAGE AVERAGING

Daniel Beniac and George Harauz

Molecular Biology and Genetics, University of Guelph, Guelph, Ontario, N1G 2W1, Canada

The structures of *E. coli* ribosomes have been extensively probed by electron microscopy of negatively stained and frozen hydrated preparations. Coupled with quantitative image analysis and three dimensional reconstruction, such approaches are worthwhile in defining size, shape, and quaternary organisation.^{1,2} The important question of how the nucleic acid and protein components are arranged with respect to each other remains difficult to answer, however. A microscopical technique that has been proposed to answer this query is electron spectroscopic imaging (ESI), in which scattered electrons with energy losses characteristic of inner shell ionisations are used to form specific elemental maps.³ Here, we report the use of image sorting and averaging techniques to determine the extent to which a phosphorus map of isolated ribosomal subunits can define the ribosomal RNA (rRNA) distribution within them.⁴

E. coli ribosomal subunits were purified by sucrose density gradient centrifugation and prepared for electron microscopy as described by Korn *et al.*⁴, except that staining with uranyl acetate was omitted since uranium has an energy loss peak at 112 eV which would interfere in the calculation of the net phosphorus distribution. Micrographs were taken at 100, 120 and 150 eV losses in a Zeiss EM 902, thus bracketing the phosphorus L_{2,3} ionisation edge at 132 eV. The micrographs were digitised and used to calculate the net phosphorus distribution as described by Locklear *et al.*⁵ A total of 163 phosphorus maps of the large ribosomal subunit were generated and analysed in the framework of the IMAGIC image processing system¹. Averages of the characteristic crown and kidney views are shown in Fig. 1.

The present results show a high concentration of rRNA below the L1 shoulder that extends to the base region of the 50S subunit; this area is proximal to the 30S-50S subunit interface.² As well, the 5S rRNA appears to be localised in the central protuberance. These images were compared with projections of a theoretical model of the *E. coli* rRNA phosphate backbone based on studies by other (mainly biochemical) approaches (Fig. 2).⁶ There is a good correspondence between the averaged phosphorus maps of the crown view (Figs. 1 a-c) with the corresponding projection of the phosphate backbone (Figs. 2 a,b), in regions of high phosphorus density. The correlation between the respective kidney views (Figs. 1 d-f, Fig. 2 c) is only partial. The ESI map shows a high phosphorus density in the base of the subunit, whereas the phosphate backbone appears more broadly distributed in this region in the model. Weaker (especially peripheral) elemental signals appear to be less reliably distinguishable.

Further improvement in the (originally very low) signal to noise ratio is achievable by averaging images grouped with the assistance of multivariate statistical analysis of much larger populations of isolated particles.¹ This strategy is currently being pursued on the basis of the favourable results yielded so far, in order to extract larger and more homogeneous subpopulations of images of individual ribosomal subunits.

References

1. G. Harauz *et al.* Meth. Enzymol. 164 (1988) 35.
2. J. Frank *et al.* J. Cell Biol. 115 (1991) 597.
3. F.P. Ottensmeyer. J. Ultrastruct. Res. 88 (1984) 121.
4. A.P. Korn *et al.* Eur. J. Cell Biol. 31 (1983) 334.
5. L. Locklear *et al.* Nucl. Acids Res. 18 (1990) 7015.
6. K. Nagano *et al.* J. Theor. Biol. 31 (1988) 199.
7. This work was supported by NSERC of Canada.

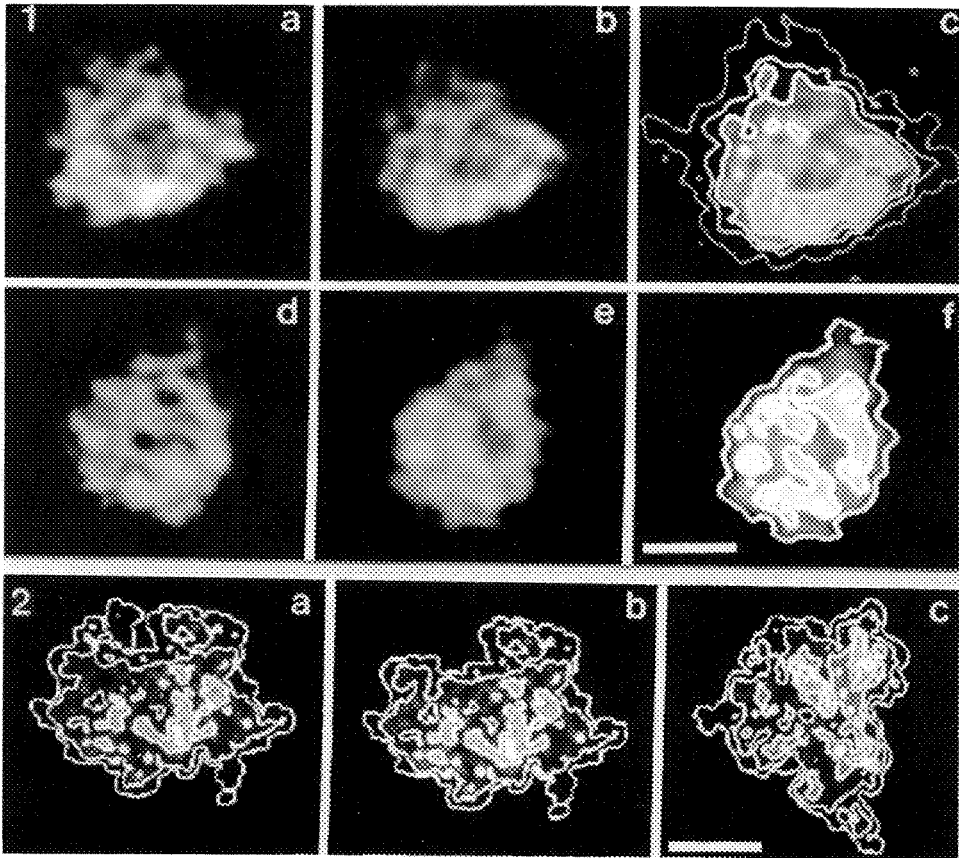


Figure 1. Computed averages of unstained, air-dried, and glutaraldehyde fixed 50S *E. coli* large ribosomal subunits in the (a,b,c) crown (15 subunits), and (d,e,f) kidney (11 subunits) orientations. (a,d) 150 eV loss images; (b,e) net phosphorus images; (c,f) net phosphorus images with isodensity contour lines superimposed. Scale bar represents 10 nm.

Figure 2. Computer generated rRNA projections based on the model of Nagano *et al.*⁶ of the (a) 23S and 5S rRNA in the crown orientation; (b) 23S rRNA only in the crown view; (c) 23S and 5S rRNA in the kidney orientation. Scale bar represents 10 nm.

NEURONAL TRANSPLANTATION IN THE CENTRAL NERVOUS SYSTEM: PRECLINICAL AND CLINICAL STUDIES

Alan Fine

**Neuroscience Institute and Department of Physiology and Biophysics, Faculty of Medicine,
Dalhousie University, Halifax, Nova Scotia, CANADA B3H 4H7**

Embryonic central nervous system neurons can survive transplantation to the adult brain and spinal cord in diverse mammalian species. Such transplanted cells can differentiate anatomically, neurochemically and physiologically, extending processes, establishing synaptic connections with host CNS neurons, and influencing host behavior. Neuronal grafts can thus serve as useful tools for the study of factors influencing aspects of differentiation, for the analysis of function of particular brain pathways, and for the development of new therapeutic strategies for the treatment of traumatic or neurodegenerative disorders.

Two neural pathways with relevance to particular neurodegenerative diseases will serve as illustrations of these applications of neuronal transplantation. Acetylcholine-secreting neurons of the basal forebrain project widely to the neocortex, hippocampus and other regions; these cells are known to degenerate in Alzheimer's disease. Grafts of embryonic basal forebrain cells to the acetylcholine-depleted neocortex and hippocampus are able to correct profound learning and memory impairments resulting from experimental cholinergic depletion of these structures, in rodents and monkeys. The dependence of cell survival and fiber outgrowth from these grafts upon the site of implantation provides clues to the nature of trophic influences on developing and mature cholinergic basal forebrain neurons.

Dopamine-secreting neurons of the ventral mesencephalon substantia nigra project to the forebrain striatum, where they participate in control of movement. These cells degenerate in Parkinson's disease. Available drug therapy for Parkinson's disease is frequently limited by progressive degeneration. Embryonic ventral mesencephalic cells can restore dopamine levels in the striatum following experimental depletion, and can correct the depletion-induced movement disorders in rodents and monkeys. On the basis of these observations, clinical trials of human fetal dopaminergic neuronal transplantation for treatment of Parkinson's disease have begun in Sweden, Mexico, the United States, England, Canada, and a number of other countries.

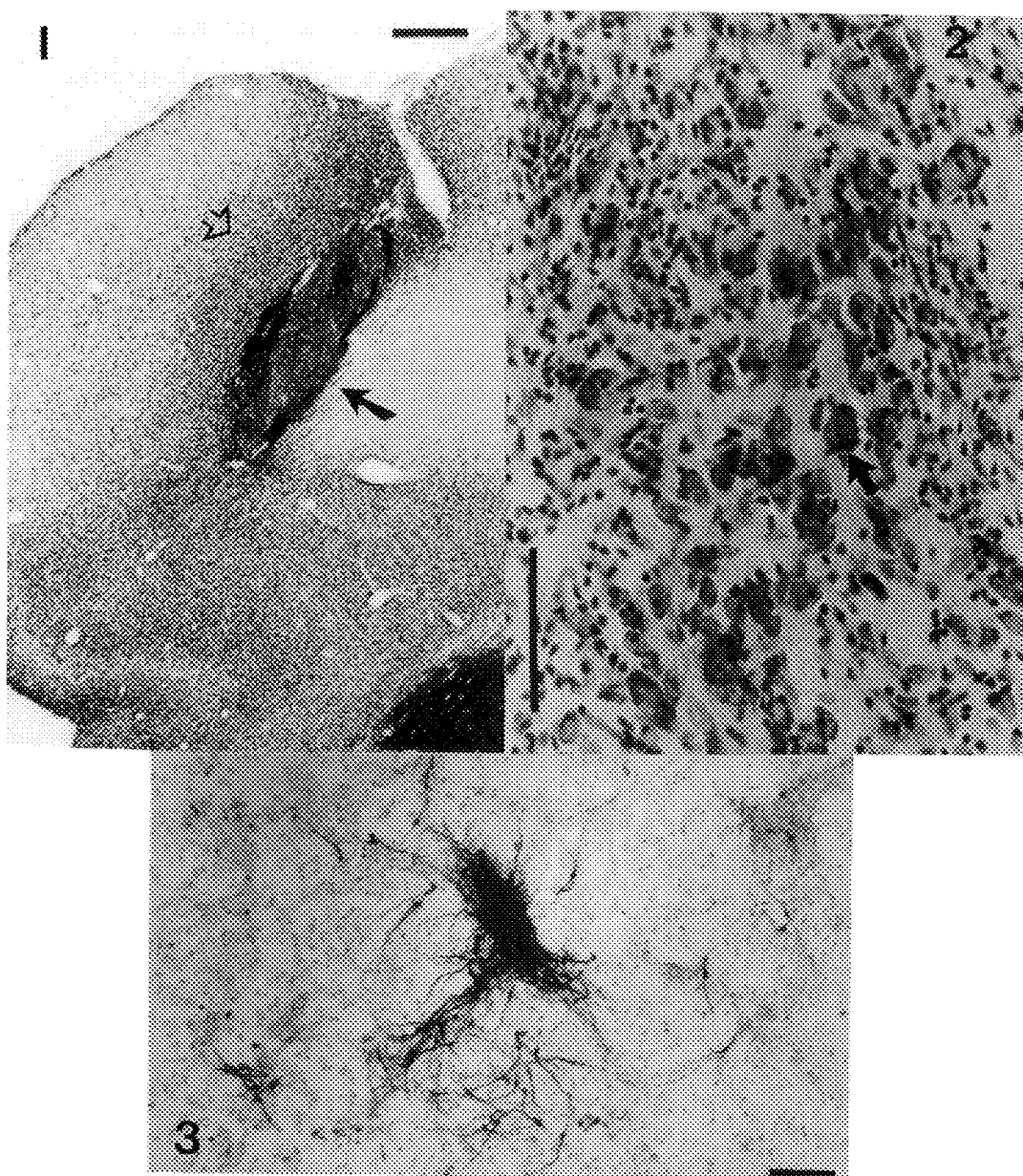


FIG. 1.--LM of rat neocortex containing graft of fetal basal forebrain cells 6 months after implantation (arrow). Acetylcholinesterase-positive graft-derived fibers (arrowhead) grow into the surrounding cortex, depleted of acetylcholine by prior lesion. Bar = 500 μ m.

FIG. 2.--LM of graft as in Fig. 1, stained with toluidine blue, showing large perikarya of grafted nucleus basalis cells (arrow), with minimal gliosis. Bar = 100 μ m.

FIG. 3.--LM of human fetal dopaminergic substantia nigra neurons in tissue culture, stained with antiserum to tyrosine hydroxylase. Bar = 200 μ m.

TRACT TRACING, NEURONAL MORPHOLOGY AND ULTRASTRUCTURAL STUDIES IN HUMAN POSTMORTEM BRAIN

Rosalinda C. Roberts*, Michael W. Vogel*, Maarten de Rijk*, Frank J. Peretti**, Robert R. Conley*, and Sarah M.N. Francis*

*Maryland Psychiatric Research Center, University of Maryland School of Medicine, Baltimore, MD 21228. **Assistant Medical Examiner, Office of the Chief Medical Examiner, State of Maryland, Baltimore, MD 21201

Classical and modern neuroanatomical techniques are applied to an analysis of the neuroanatomical basis of schizophrenia using postmortem brain tissue from the Maryland Brain Collection. Techniques for Golgi staining of cell bodies and dendritic arbors, axonal tract tracing with the carbocyanine dye, DiI,² and ultrastructural analyses will be used to study brain tissue with postmortem times of less than 6 hours. Although these techniques are routinely used in animal models, they are rarely used for studying human brain tissue. These techniques will allow us to characterize neuronal architecture in normal and diseased brains.

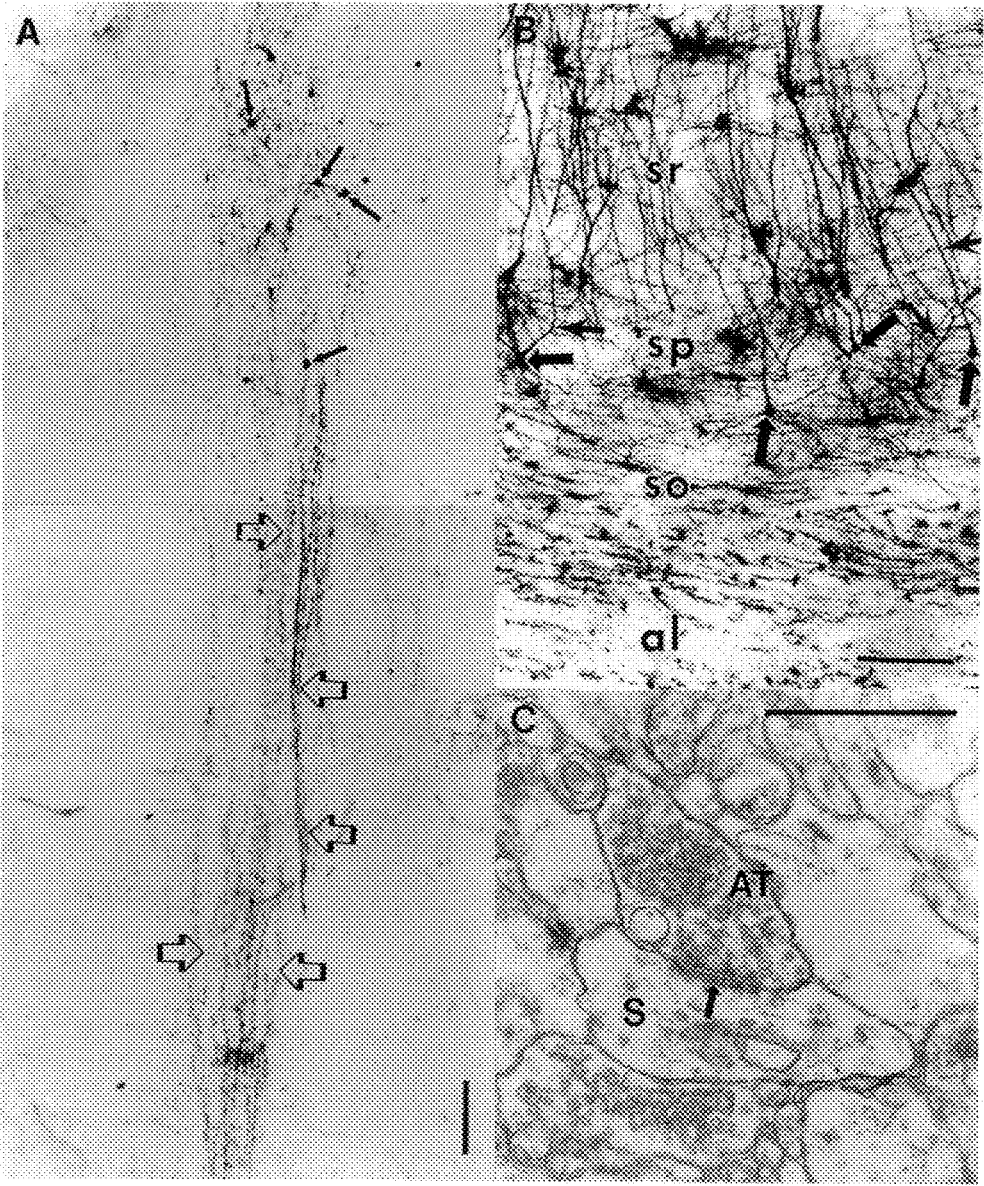
Tract tracing: Glass shards are immersed in a solution of DiI and alcohol, dried¹ and inserted into the granule cell area of the dentate gyrus, the pyramidal cell layer of CA₃ or the parahippocampal gyrus. Tissue is placed in 4% paraformaldehyde for up to 1 year, and then sectioned with a vibratome (100 μ m) and viewed with a fluorescent microscope for labeled fibers. Selected sections are photographed and/or photooxidized.¹ The advantage of photooxidation is that it provides a permanent preparation and can be combined with EM. Briefly, selected sections that display optimal fluorescent staining are incubated in a 0.15% diaminobenzidine solution under rhodamine fluorescence with a 4X objective for approximately 2 hours (for 20 minutes after the last fluorescence disappears). Preliminary results show dye transport in axons within the hippocampus at a rate of approximately 1mm/month (Figure 1A).

Golgi studies: Fresh (unfixed) brain is immersed in Golgi Cox solutions (10 parts of solution A [5mg potassium dichromate + 5mg mercuric chloride in 450ml water] and 1 part of solution B [5% solution of potassium chromate]) and stored in the dark for 6-8 weeks.³ Tissue is then dehydrated, embedded in celloidin and cut 100 μ m thick in the coronal plane.

Ultrastructure: Tissue collected from brains with post mortem intervals less than 3 hours (sudden death only) yields excellent EM preservation (Figure 1C). Briefly, tissue is put into a solution of 4% paraformaldehyde and 2% glutaraldehyde in 0.1M phosphate buffer (4°C) for one week. The solution is changed twice during that time. The tissue is then prepared for standard electron microscopic analysis.⁴

References:

1. P.G. Bhide and D.O. Frost, *J. Neurosci.* (1991) 11:485-504.
2. E.J. Mufson et al., *Neurobio. Aging* (1990) 11:649-653.
3. D.A. Sholl, *J. Anat.* (1953) 87:387-406.
4. Acknowledgements to Maryland Brain Collection for brains. Supported by MH44211.



A. Photooxidized human hippocampus 3 months after injection with DiI illustrating labeled somata (arrows) at the injection site and labeled fibers emanating from it in the typical laminar pattern of this area of the brain (open arrows). Scale bar=100 μ m.
B. Golgi impregnated human hippocampus (Ammon's horn) illustrating labeled somata (bold arrows) and dendrites (arrows). al=alveus, so=stratum oriens, sp=stratum pyramidale, sr=stratum radiatum. Scale bar=200 μ m.
C. Electron micrograph of human putamen (postmortem interval of 3 hours). AT=axon terminal. S=spine. Asymmetric synapse (arrow). Scale bar=0.5 μ m.

LIVING AND FIXED NEURONS OBSERVED IN BRAIN SLICES BY LASER-SCANNED CONFOCAL LIGHT MICROSCOPY

James N. Turner^{†‡}, Donald H. Szarowski[†], Karen L. Smith[†] and John W Swann^{†‡}

[†] Wadsworth Center for Laboratories and Research, Albany, New York 12201-0509; [‡] Department of Biomedical Sciences, School of Public Health, University at Albany, Albany, New York 12201

Thick slices of brain tissue are studied *in vitro* because neurons deep in the slice maintain physiologic contact with large numbers of other neurons, and are thought to function in a manner similar to that of in tact brain.¹ The three-dimensional (3-D) morphology and electrophysiology of these cells can be studied and correlated.² The confocal light microscope with its z-direction discrimination forms optical sections through the entire thickness of the slice, and stereo pairs or full 3-D reconstructions can be displayed using the optical sections as data sets. Individual neurons injected with fluorescent dyes or peroxidase based stains are imaged in either the fluorescent or reflection modes.^{2,3}

Rat hippocampal slices 500 μ m thick were maintained in oxygenated cerebral spinal fluid. Individual neurons were impaled with microelectrodes, electrophysiologically characterized, injected with either lucifer yellow, biocytin, or peroxidase, and imaged.^{2,3} Live observations were made in slices cultured at 37°C in 5% CO₂.⁴ DiI was applied as a small crystal and confocal images collected over the course of hours or days. Multiple slices were co-cultured to monitor axonal growth as a function of anatomic juxtaposition. Images were reconstructed using Analyze™ run on an IBM RISC 6000.

Figure 1 is a 3-D volume rendering of two dye-coupled hippocampal neurons contrasted with lucifer yellow. The larger cell (lower) is a typical pyramidal neuron with extensive basilar and apical dendrites. The initial axon segment projects into the middle of the basilar dendritic field (lower center) where it branches. One branch projects up and to the left through the cell body layer. The other is a collateral projection to the right. The second cell (arrows) is near the first branch point of the first cell's apical dendrites. It has large apical (upper arrow) but only a few small basilar dendrites. Dye-coupled cells are frequently observed in these slices.^{2,3}

Figure 2 is a 3-D reconstruction of an interneuron filled with biocytin via coupling to a pyramidal cell (not shown). Primary dendrites project from each corner of the triangular soma, and three potential contact points with dendrites of the injected pyramidal neuron are indicated (arrows). This image was recorded using the reflection mode.

Figure 3 is two fields of three live slices co-cultured for two weeks, and imaged 18 hrs. after DiI was applied to the pyramidal cell layer of a mini-slice (CA₃ region). The left micrograph shows the large number of projections stained in the mini-slice in stratum radiatum. The right micrograph shows the other two slices in contact with each other and with the mini-slice (to the left). The upper slice has a number of axons that have projected from the mini-slice and stained a number of neurons. The lower slice has only one stained neuron. This system is under investigation as a model of axonal growth and projection into juxtaposed brain regions.

1. P.A. Schwartzkroin, Brain Res. (1975)85, 423; J.W. Swann and R.J. Brady Devel. Brain Res.(1984)12,243.
2. J.N. Turner, D.H. Szarowski, K.L. Smith, M. Marko, A. Leith, J.W. Swann, J. Elec. Microsc. Tech.(1991)18,11.

3. J.S. Deitch, K.L. Smith, J.W. Swann, and J.N. Turner, *J. Elec. Microsc. Tech.*(1991)18,82; J.S. Deitch, K.L. Smith, C.L. Lee, J.W. Swann, and J.N. Turner, *J. Neurosci. Methods*(1990)33,6; J.S. Deitch, K.L. Smith, J.W. Swann, and J.N. Turner, *J. Microsc.*(1990) 160,265.
4. L. Stoppini, P.A. Buchs, D. Muller, *J. Neurosci. Methods*(1991) 37, 173.
5. Grant support is acknowledged from: NIH R55RR06904, NS18309, and NSF DIR 9108492.

FIG. 1 Projection of dye coupled neurons imaged with a 20X oil objective NA=0.8. Depth of field is 156 μm and the width is 300 μm .

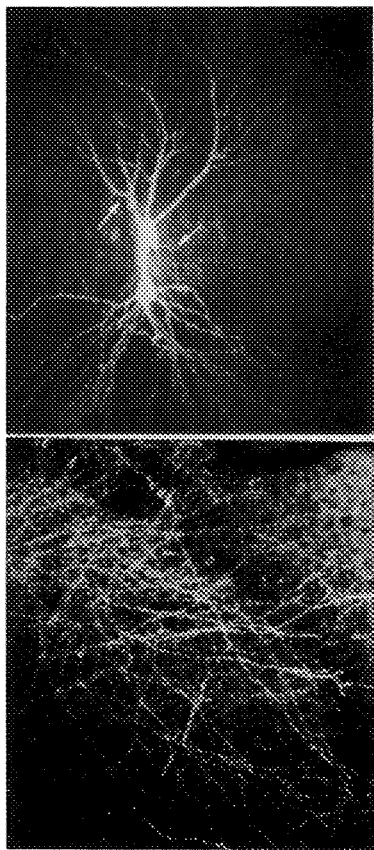


FIG. 2 Projection of an interneuron imaged with a 40X oil objective NA=1.0. Depth of field is 30 μm and the width is 150 μm .

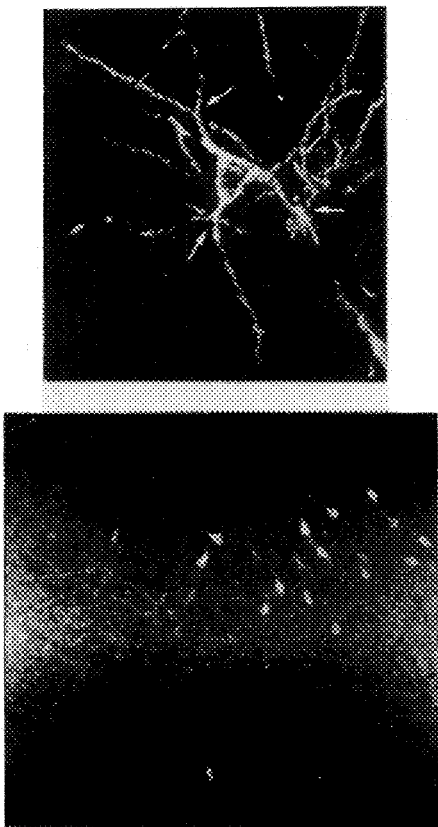


Fig. 3 Projection of Dil labelled axons and neurons in live slices imaged with a 10 X objective NA=0.3. Depth of field is 80 μm and the width is 1,200 μm .

Cellular and Molecular Mechanisms of Proliferating and Migrating Neurons

Gord Fishell and Mary E. Hatten

Center for Neurobiology and Behavior, Dept. Pathology, College of Physicians and Surgeons of Columbia University, New York, NY 10032

In the developing CNS, neurogenesis is restricted to discrete zones, the ventricular zones and the External Germinal Layer (EGL) of the cerebellar cortex. At early postnatal periods, in the mouse, the cerebellar EGL contains two discrete zones, a superficial layer, one-two cells thick containing mitotic figures and an underlying zone of postmitotic cells. It is in this lower zone where the first visible evidence of neural differentiation can be seen (Ramon y Cajal, 1911), the extension of granule cell axons, the parallel fibers, and the inward migration of the cell soma of immature granule cells along the radially aligned processes of the Bergmann glial cells (Rakic, 1971). To provide an experimental analysis of the molecular components of granule cell neurogenesis and migration, we have developed *in vitro* model system using purified EGL precursor cells.

In vitro studies in our laboratory have followed the migration of postmitotic granule neurons along astroglial fibers in real time, providing a dynamic view of the neuron-glia apposition and mode of movement of granule cells along glial fibers (reviewed in Hatten, 1990). To analyze the molecular components of migration, we have used a series of *in vitro* assays to identify a novel immune activity, **astrotactin**, which mediates neuron-glia binding, and to determine the contribution of neural cell adhesion molecules, cadherins and integrins to neuron-glia interactions. Those studies indicate that glial-guided neuronal migration occurs by a different molecular mechanism than does growth cone locomotion on glial substrates. Whereas the latter apparently involves neural cell adhesion molecules, cadherins and integrins, granule cell binding to astroglia utilizes the neuronal antigen **astrotactin** (Stitt and Hatten, 1990; Fishell and Hatten, 1991). During cerebellar development, these different molecules are expressed in a specific spatiotemporal pattern, consistent with their functions, with astrotactin being restricted to the soma and leading process of migrating granule cells.

To examine earlier steps in CNS neural patterning, in particular, the dispersion of premigratory cells within ventricular zones, we have developed an *in situ* whole mount preparation. Embryonic cortex was removed intact by dissection of the lateral wall of the lateral ventricle of mouse embryos on the fifteenth embryonic day (E15), and a random subset of ventricular cells was labeled with a dilute solution of the lipophilic dye, DiI. Movement of labeled cells within the ventricular zone was then monitored using a computer assist video system, with a light-intensified CCD camera. Individual cells were identified as neural precursors by incorporation of BrdU and by expression of the neural marker nestin. Neuronal precursors were observed to rapidly undergo apparently undirected dispersion within the cortical ventricular explant. Cells were observed to move at a rate of 10mm/hr and maintained this rate during the entire observation periods (from 8 to 36 hrs). Initially adjacent cells (in some case daughters) were observed to move independently, often leading to them being separated by as much as 150mm in an eight hour period. Cells were however never observed to cross from the cortical ventricular zone to the lateral ganglionic eminence (the area of ventricular area thought to give rise to the striatum). This early restriction of cells across the cortical/ ganglionic eminence border is similar to restrictions observed at the boundaries between rhombomeres in the hindbrain (Fraser, Keynes and Lumsden)

These findings suggest widespread movement of progenitor cells within ventricular zones of developing brain. Movement is restricted by boundaries apparently present between the ventricular zones of cortex and subcortical structures. In vitro studies suggest that the migration of postmitotic, partially differentiated young neurons is supported by the glial fiber system, where a specialized neuron-glia apposition and expression of the neuron-glia ligand astrotactin are required for cell movement. The relatively large movement of cells in the proliferative zone suggests that clones of neural progenitors spread extensively during early cycles of cell division in the proliferative zone, prior to their radial migrations along the glial fiber system.

References

1. Ramon y Cajal (1911) *Histologie du Systeme Nerveux de l'Homme et des Vertebres*.
2. Rakic, P. (1971) *J. Comp. Neurol.* 145: 425-427.
3. Hatten, M.E. (1990) *Trends Neurosci.* 13: 179-184.
4. Stitt, T.N. and M.E. Hatten (1990) *Neuron* 5: 639-649.
5. Fishell, G. and M.E. Hatten (1991) *Development*, 113, 755-765.
6. Fishell, G., Mason, C.A. and M.E. Hatten, submitted.
7. Fraser, S., Keynes, R. and A. Lumsden (1990) *Nature* 344, 424.
8. This work was supported by NS 15429 (MEH) and a MRC fellowship (GF)

OBSERVATION OF NEURONAL ACTIVITY USING REAL-TIME VOLTAGE-SENSITIVE DYE IMAGING

John S. Kauer, Angel Cinelli, David Wellis, Joel White

Section of Neuroscience, Depts. of Neurosurgery and Anatomy & Cell Biology, Tufts Medical School and New England Medical Center, Boston, MA

Sensory systems are confronted with the problem of taking "information" in the outside world and encoding and manipulating it in forms that can be used in the neuronal world. A major challenge is to document how the transition between these worlds takes place (transduction) and, once it has taken place, how the data are manipulated by neural circuits (integration). Since the brain is an intrinsically parallel device, carrying out many functions simultaneously, it would appear as important to record brain activity in a similarly parallel manner, as to record events in single cells and membranes. Optical recording of neuronal events offers a first step toward trying to observe events that are distributed among the cells and processes of a neuronal network^{4,5}.

In the sense of smell odors appear to be encoded by activity distributed across many neurons at each level of the system studied so far, from the sensory cells in the nose to the pyramidal cells in prepyriform cortex (for review see ²). Thus, to elucidate how the molecular properties of odorants are represented by neurons it is probably necessary to observe the patterns of distributed activation. The distribution of activity across many neuronal elements, in contrast to representing odor molecules by dedicated "labelled lines", confers redundancy and fault tolerance on a system that is crucial for complex behaviors that underly survival for many animal species, as well as providing flexibility for being sensitive to large numbers of compounds.

We have developed a animal model system, the tiger salamander, in which to try to investigate how odors are encoded. This animal affords advantages for gathering anatomical, physiological, and behavioral data on the olfactory system in a single experimental species. It permits the use of odorants that can be controlled precisely in time and space for physiological experiments, and is it amenable to operant conditioning using odor stimuli ³. Recently it has been found that the salamander also has major advantages for voltage-sensitive dye recording ^{1,4}. The present paper presents the methods used for recording neuronal activity using this technique and an interpretation of the results in the context of how odor information might be encoded by the nervous system.

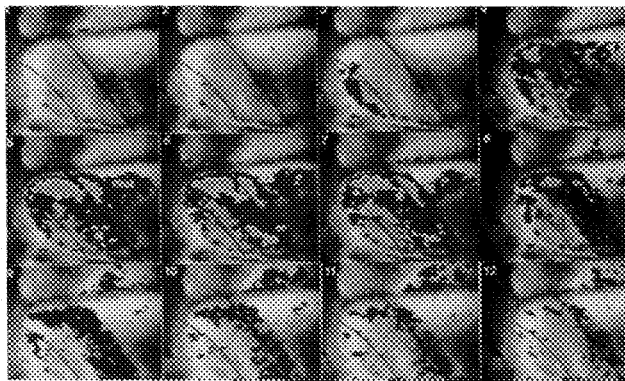
The voltage-sensitive dye RH414 (1 mg/ml) (kindly provided by A. Grinvald) was topically applied to the exposed olfactory bulb of the anaesthetized tiger salamander. In a variety of different experiments we have imaged responses using Newvicon and CCD video cameras after electrical stimulation of the olfactory nerve (inputs) or medial olfactory tract (outputs) or after precisely controlled odor stimulation of the olfactory epithelium (sensory receptors). The output frames of the video camera at 30 frames/sec are digitized to 8 bits (256 gray levels) and sequentially stored in computer memory. These frames can then be analyzed by a number of image processing algorithms and played back as a short "movie", displaying the dynamics of the responses in both time and space. In these experiments we have applied a number of pharmacological agents to manipulate the known synaptic circuits in the bulb (e.g. GABA blocker bicuculline; glutamate antagonists CNQX, and AP5) to examine the changes in the response patterns when various components of the circuit are inactivated. These results are interpreted in correlation with intracellular and whole cell patch recordings from the major output neuron, the mitral/tufted cell.

The results of these studies have allowed us to formulate a model ⁶ of how the olfactory bulb may function as a neuronal parallel processor. The model is constrained by the anatomical and

physiological characteristics of the real system, yet it generates responses, in the form of changes in membrane and action potentials, that are strikingly similar to those found in the real circuit.

References

1. Kauer, J.S. *Nature* (1988) **331**, 166-168
2. Kauer, J.S. *TINS* (1991) **14**, 79-85
3. Mason, J.R., Meredith, M. & Stevens, D.A. *Physiol.Behav.* (1981) **27**, 125-132
4. Orbach, H.S. & Cohen, L.B. *J.Neurosci.* (1983) **3**, 2251-2262
5. Tasaki, I., Watanabe, A., Sandlin, R. & Carnay, L. *Proc.Natl.Acad.Sci.* (1968) **61**, 883-888
6. White, J., Hamilton, K.A., Neff, S.R. & Kauer, J.S. *J.Neurosci.* (1992) (In Press)



Sequential 33 ms frames from voltage-sensitive dye recording of responses elicited across the olfactory bulb by electrical stimulation of the olfactory nerve (from ¹). This view is down onto the tope of the the planar, bulbar layers from a living, intact animal. The bulb is about one mm across. Anterior is to the left. The midline of the brain is seen near the top of each frame. The colors represent degrees of depolarization; green one S.D. above background, red two S.D.'s. "mot" = medial olfactory tract.

THE NORMAL HUMAN HIPPOCAMPUS AND THAT OF ALZHEIMER'S PATIENTS CONTAIN FILOPODIA LIKE THOSE OF OCTOPUS NEUROPILS AND NERVE GROWTH CONES

Robertson, J. David and Psyche Lee

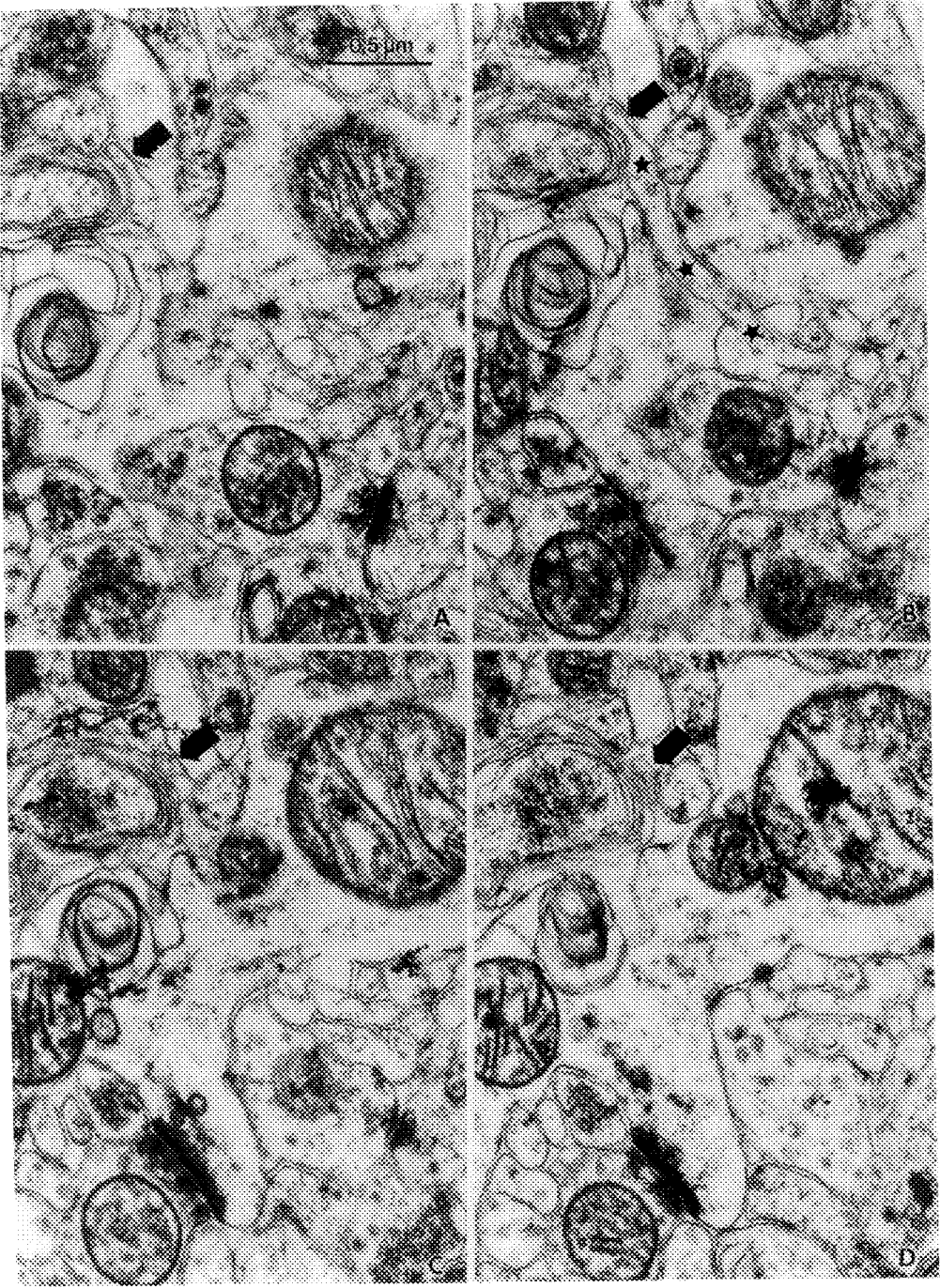
Dept. of Neurobiology, Duke Medical School, P.O. Box 3554, Durham, N.C. 27710

New synapses are generally formed in long-term learning [See (3) for references], but it is believed that short-term learning involves only alterations in synaptic efficacy with activity (1). We have studied this problem extensively in *Octopus vulgaris* (2-5). Electron Microscopic (EM) studies of serial sections reveal that filopodia like those in nerve growth cones occur in its touch learning neuropils (2). They increase in numbers transiently during learning and some form new synapses, while others retract. Calcium influx into neurites during activity triggers actin polymerization and related filopodial extension. This, by interpolation of new membranes, results in separation of interactive membranes, formerly in contact. An alteration in the total electrochemical interactions of the membranes results that alters the summation of interactions between all the membranes and changes the overall integrated output. This can be defined as learning and one of us has advanced a filopodial theory of learning based on these ideas (5). Accordingly, there is a localized reactivation of growth processes normally only operating during development to bring about structural alterations beginning with short-term learning. If correct, learning should be blocked by cytochalasins B (CB) and D (CD) that interfere with actin polymerization and it should be stimulated by nerve growth factor (NGF). We have good evidence that CB and CD block touch learning reversibly in *Octopus* (2-5) and recently that NGF stimulates touch learning.

Alzheimer's disease is characterized by a deficiency in learning and memory. We asked whether or not the above theory can be applied to the adult human brain. The first question we addressed was: Are filopodia present in the human brain? We prepared hippocampal specimens from human rapid autopsies for EM serial section study. We define filopodia as indefinitely long cylindrical extensions of a neurite 0.3 μm or less in diameter containing no clearly defined organelles except putative actin filaments. Figs. A-D show four serial sections of the neuropil around pyramidal cells in the hippocampus of an aged human brain used as a control in Alzheimer's studies. The sections include a structure we define as a filopodium denoted by the black arrow. It is cylindrical, $\sim 0.25 \mu\text{m}$ long by 50-80 nm in diameter; it contains no well defined organelles. It tapers from an $\sim 0.15 \mu\text{m}$ diameter cylindrical process $\sim 1.5 \mu\text{m}$ long (B-stars) that is probably also a filopodium. We conclude that filopodia are present and that many of the structures of this kind seen in cross section throughout the neuropil probably are filopodia. We then looked at the hippocampus of Alzheimer's patients, expecting to find reduced filopodia. Instead, we saw even more abundant filopodia containing more actin. If correct, there may be too many filopodia in the Alzheimer's brain. This suggests a deficiency of actin depolymerization mechanisms for retraction of filopodia with consequent clogging of the system. Our Alzheimer's brain material is, however, so far, not well enough preserved to permit us to draw definite conclusions. Supported by grants NSF-BNS-90-12628; BNS-88-20409; NIH-1R01-NS-26853-01A2; NIH-2P50-AG-05128007-Sub #17.

REFERENCES:

1. Bear, M.F., L.N. Cooper and F. Ebner. 1987. *Science* **237**: 42-48.
2. Robertson, J. David and Psyche Lee. 1989. *Proc. Electron Microscopy Society of America. 47th Annual meeting*. Ed. G.W. Bailey. San Francisco Press. San Francisco, CA. pp. 954-955.
3. Robertson, J. David and Psyche Lee. 1990. *Progress in Cell Research* Ed. J.M. Ritchie, P.J. Magistretti and L. Bolis. Elsevier Press B.V. (Biomed. Div.), N. Y. **1**: 287-306.
4. Robertson, J. David, Owen Schwartz and Psyche Lee. 1991. *J. Cell Biol.* **115**: 465a.
5. Robertson, J. David. 1992. *Anat. Rec.* **232(4)**: 74A-75A.



THE PHOTORECEPTOR CYTOSKELETON VISUALIZED

Beth Burnside

Department of Molecular and Cell Biology, 335 LSA, University of California, Berkeley, CA 94720

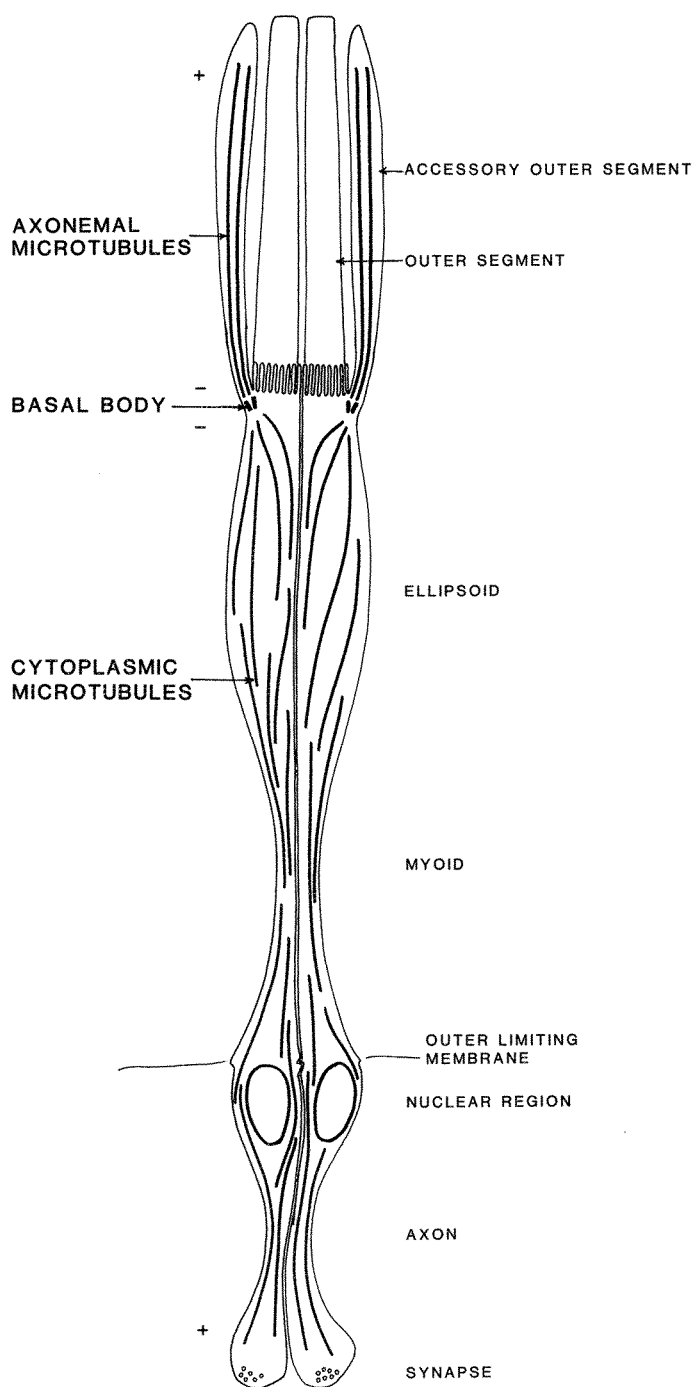
The vertebrate photoreceptor provides a dramatic example of cell polarization. Specialized to carry out phototransduction at its distal end and to synapse with retinal interneurons at its proximal end, this long slender cell has a uniquely polarized morphology which is reflected in a similarly polarized cytoskeleton. Membranes bearing photopigment are localized in the outer segment, a modified sensory cilium. Sodium pumps which maintain the dark current critical to photosensory transduction are anchored along the inner segment plasma membrane between the outer segment and the nucleus.¹ Proximal to the nucleus is a slender axon terminating in specialized invaginating synapses with other neurons of the retina. Though photoreceptor diameter is only 3-8 μ , its length from the tip of the outer segment to the synapse may be as great as 200 μ . This peculiar linear cell morphology poses special logistical problems and has evoked interesting solutions for numerous cell functions. For example, the outer segment membranes turn over by means of a unique mechanism in which new disks are continuously added at the proximal base of the outer segment, while effete disks are discarded at the tip and phagocytosed by the retinal pigment epithelium.² Outer segment proteins are synthesized in the Golgi near the nucleus and must be transported north through the inner segment to their sites of assembly into the outer segment, while synaptic proteins must be transported south through the axon to the synapse.³ The role of the cytoskeleton in photoreceptor motile processes is being intensely investigated in several laboratories.¹⁻³

In addition to carrying out numerous motile maintenance activities, some photoreceptors are also athletes. In fish, amphibians and birds, photoreceptors undergo length changes in response to changing light conditions: in the light, cones contract and rods elongate; whereas in the dark these movements are reversed. These movements are mediated by paraxially aligned microtubules and actin filaments. Cone elongation is microtubule-dependent, whereas cone contraction, rod elongation, and rod contraction are all actin-dependent. Our lab has been studying the mechanisms of regulation and force production for these "retinomotor" movements.^{4,5}

To understand the role of the cytoskeleton in photoreceptor motile processes, we and others have examined the distributions of cytoskeletal components in photoreceptors by a variety of morphological approaches. Photoreceptor actin and microtubule cytoskeletons have been visualized in situ and in isolated cells and cell fragments by thin section TEM, immunolocalization of cytoskeletal proteins at light and EM level, 3-D reconstruction of serial sections, and whole mount microscopy using the intermediate voltage EM. Recent observations from these studies will be presented with emphasis on their implications for cytoskeletal function in photoreceptor motile processes.⁶

1. S. A. Madreperla, M. Edidin, and R. Adler, *J. Cell Biol.* (1989)109, 1483.
2. J. C. Besharse, *Prog. Retinal Res.* (1982)1, 81.
3. D. K. Vaughan, et al., *J. Cell Biol.* (1989)109, 3053.
4. L. L. Truett and B. Burnside, *J. Neurosci.* (1988) 8, 2371.
5. K. Pagh-Roehl, J. Brandenburger, E. Wang, and B. Burnside, *Cell Motility Cytoskel.* (in press)
6. This work supported by NIH grant #R37-EY03575.

Figure: Microtubule distribution in teleost retinal twin cones. Axonemal microtubules are oriented with minus ends toward the basal body and plus ends distal; cytoplasmic microtubules are all oriented with their minus ends toward the outer segment and plus ends toward the synapse. Actin filaments in inner segment bundles are also highly polarized, with barbed ends toward the outer segment and pointed ends toward the outer limiting membrane (not shown in this figure).



THE PHOTORECEPTOR CYTOSKELETON AND DISK TURNOVER

Dorothy J. Roof, Annmarie Hayes, Michael Adamian

Berman-Gund Laboratory, Harvard Medical School, 243 Charles Street, Boston, MA 02114

The light sensitive part of the rod photoreceptor, the outer segment, is continually renewed within the retinas of adult vertebrates. This process of membrane renewal consists of two distinct components, disk addition and disk shedding, which are maintained in a constant dynamic balance throughout adult life. Thus, although each rod outer segment loses approximately 10% of its length each day due to shedding and phagocytosis of rod tips by the adjacent pigment epithelial layer, the total length of the outer segment remains constant due to assembly of new disks at the base of the outer segment. The mechanisms of disk shedding and disk addition are, as yet, undefined although it appears that each phase of the overall disk renewal cycle may involve some cytoskeletal components.^{1,2}

We have recently characterized two different types of cytoskeletal components within the rod photoreceptor, each of which may be related to disk membrane renewal. One component is a collection of microtubule-like structures that are concentrated near the extreme tip of the rod outer segment in amphibian rods. The total number of these tubules in each rod outer segment tip varies with the light/dark status of the photoreceptor. This variation in number of tubules coincides with light onset and is abolished by detaching the retina from the adjacent layer of pigment epithelial cells. This suggests that the tubules might be modulated by light-induced interactions between the photoreceptors and pigment epithelium, such as those that occur during the disk shedding phase of membrane turnover. We have also characterized a quite different cytoskeletal protein from the apical inner segment of mouse rod photoreceptors. This protein, which we have termed RET52 because of its retinal localization and 52 kDa mobility on SDS polyacrylamide gels, possesses some of the properties appropriate for a protein that might be involved in disk addition. Further characterization of each of these types of elements is described below.

The microtubule-like structures present within the tips of rod outer segments from the toad, *Bufo marinus*, are oriented longitudinally along the length of the rod outer segment (ROS), immediately beneath the plasma membrane. In amphibian rods, each disk membrane in the stack of 2000 or more disks is penetrated by several deep incisures that divide the disk into multiple lobes. The lobes of all the disks within a single rod outer segment are aligned with each other along the length of the disk stack. The microtubule-like structures are localized in clusters that lie along the shallow grooves formed by the alignment of the disk incisures. The cross-sectional dimensions of the tubules, 25-30 nm with a 15 nm central clear space, resemble those of microtubules. However, the distal ROS tubules are distinct from the previously described "ciliary" microtubules of the rod photoreceptor, do not cross react with a number of microtubule-specific antibodies, and are not affected by a battery of microtubule-disrupting drugs. Thus, although the composition of the tubules is not yet known, they are probably not composed of conventional forms of tubulin.

The function of the "distal ROS tubules" is difficult to approach in the absence of a well-defined molecular identity. However, the light/dark behavior of the tubules may provide a clue to the potential physiological significance of these unusual structural elements. We quantitated the number of tubules within each ROS at a specified distance from the extreme tip under two different lighting conditions. We compared the total number of tubules in each outer segment within retinas from dark-adapted animals that were sacrificed one hour before light onset vs. one hour after light onset. We found that the median number of tubules per ROS was three- to fourfold higher one hour after light onset. Further, this increase in tubule number did not occur if the retinas were separated from the adjacent pigment epithelial layer before the lights were turned on. These results may suggest that tubule accumulation depends on the association of photoreceptor tips with the adjacent retinal pigment epithelium and that tubule accumulation is triggered by disk shedding rather than by light onset alone.

We also initiated a separate line of experimentation to identify photoreceptor cytoskeletal elements that might be involved in the disk addition phase of membrane turnover. Using a preparation of neonatal mouse retinas as an immunization mixture, we generated a set of monoclonal antibodies that recognize a novel retinal antigen in unfixed tissue sections. The antigen, which we term RET52, is localized to the apical inner segment of rod photoreceptors, near the site at which membranes are translocated into the outer segment to form new disks. RET52 is also present within the layer of photoreceptor synapses, the outer plexiform layer.

Biochemical characterization of RET52 suggests that this 52 kDa polypeptide is a cytoskeletal antigen related to the 52 kDa subunit of a previously characterized protein from the red cell membrane skeleton. Dematin (protein 4.9),^{3,4} the red cell homolog of RET52, is known to be an actin-bundling protein, with bundling activity regulated via its phosphorylation state.⁵ Both dematin and RET52 are substrates for cAMP dependent kinase *in vitro*. A physiological function has not yet been defined for either dematin or RET52. However, the biochemical properties and location of RET52 within the rod photoreceptor suggest that RET52 could act as a potential modulator of actin networks within the inner segment. This, in turn, could profoundly affect the dynamics of protein translocation from the site of synthesis to the site of disk assembly at the base of the outer segment.⁶

References

1. J.C. Besharse and D.A. Dunis, in J.G. Hollyfield, Ed., *The Structure of the Eye*, North Holland: Elsevier (1982)85.
2. D. S. Williams et al., *J. Comp. Neurol.* (1988)272, 161.
3. D.L. Siegel and D. Branton, *J. Cell Biol.* (1985)100, 775.
4. A. Husain-Chishti, et al., *Nature* (1988)334, 718.
5. W.C. Horne, et al., *J. Biol. Chem.* (1985)260, 9073.
6. This research was supported by grants from the National Eye Institute (EY 06514), the National Retinitis Pigmentosa Foundation, and the Massachusetts Lions Research Fund.

CELL ADHESION AND CYTOSKELETON IN THE RETINAL PIGMENTED EPITHELIUM

Michal Opas

Department of Anatomy and Cell Biology, University of Toronto, Toronto, Ont., M5S 1A8 Canada

The development and differentiation of tissues depend on the ability of cells to move and control their shape. In cell movement, a force generated by the contractile cytoplasmic machinery which includes the cytoskeletal microfilaments (MF) is, through cell-substratum adhesion, translated into traction. The chick embryonic retinal pigmented epithelium (RPE) differentiates in vitro, it can also be persuaded to transdifferentiate, and it displays differentiation dependent organization of the cytoskeleton, adhesiveness and ECM production.

Since its introduction by Curtis¹, the technique of interference reflection microscopy (IRM) has been used frequently to study the topography of the cell surface adherent to a glass substratum. IRM takes advantage of the interference of wavefronts reflected at the phase boundaries created by the thin layer of culture medium which separates a cell and the glass substratum to which that cell adheres. The resultant fringe image can be interpreted in terms of the distance of separation between the cell and the substratum and directly related to the adhesive properties of the cell. Three major types of cell-substratum adhesions can be distinguished: a) - *focal contacts* - strongly adhesive structures appearing black by IRM microscopy; and b) - *close contacts* - large and labile areas, appearing dark grey in IRM microscopy. Focal contacts are invariably associated with the termini of MF bundles. Several proteins such as vinculin, talin and tensin, localized almost exclusively in focal cell-substratum contacts.² Both vinculin (Vn) and talin (Tn) are instrumental in anchoring MF bundles to the plasma membrane in those contact regions. A newly discovered class of proteins, integrins, play a pivotal role in linking the cytoskeletal complex to the proteins of extracellular matrix (ECM) in the focal contacts.³ Interestingly, it has been shown that myosin and tropomyosin are excluded from the termini of stress fibres, suggesting that while more proximal parts of stress fibres are contractile, their termini are specialized for attachment.^{4,5} Thus, it is conceivable that focal contacts with their associated proteins act as organizing centres for the surrounding cytoplasm. A role of integrin in contact formation and its relation to the focal contact-associated stress fibres in spreading cells is unknown. A spreading cell generates centripetal tension by an isometric contraction which promotes formation of MF bundles which in turn are contractile. The contraction of MF bundles breaks down the circumferential arrangement of adhesions and a spread cell becomes irregularly stretched between the few strongest points of attachment to the substratum. In this simplified, mechanistic model, arrangement of stress fibres in a fully spread cell has been proposed to partly reflect the lines of a tension field generated by cellular contractile activity and spatially restricted by adhesions to the substratum.⁶

Embryonic chick RPE cells grown on glass form colonies in which cells in the central part are differentiated, that is cuboidal, pigmented and tightly packed, whereas cells towards the edge of the colony become progressively less pigmented and display features of undifferentiated, motile cells. This gradient in cell morphology is paralleled by a redistribution of MF from a linear arrangement in the edge cells to a circumferential one in the differentiated cells in the colony centre.^{7,8} The proteins of the circumferential rings of MF in the differentiated cells are spatially segregated across the width of the F-actin ring, with Vn concentrated on its outer, membrane-facing side, while myosin and tropomyosin predominate on its cytoplasmic side.⁹ This suggests the specialization of the outside of the ring for membrane attachment and the inside for contraction. This arrangement thus is similar to the one in stress fibres in the cells near the edge of the colony where the same proteins are spatially segregated along the length of the fibre in such a manner that the "attachment" proteins predominate

in their distal parts, while the "contractile" proteins predominate in the proximal parts of the fibre.⁵ Also, while peripheral RPE cells display predominantly cell-substratum adhesiveness, cells towards the colony centre shift progressively to predominantly cell-cell adhesiveness.⁸ Studies on adhesive interactions of RPE cells with removable or immobilized protein carpets have shown that RPE cells spread on a removable protein carpets without focal contacts, then for the next several hours cells contract, and then they respread this time forming definite focal contacts.¹⁰ The contracted cells remove large areas of the carpet and the respreading occurs only on *carpet-free regions*. Therefore: a) if only a single observation is made, cells may be spread or not, motile or not, remove carpet or not, depending on the time of observation, and the composition and method of carpet preparation; b) cells quickly remove weakly adsorbed protein carpets; c) in agreement with Grinnell¹¹ carpet removal is a mechanical process; and d) spread morphology with stress fibres and focal contacts occurs when the substratum is mechanically resistant enough. When the RPE cells are plated out onto the malleable substratum such as ECM gel, they aggregate and do not spread, and they contract and tear the gel into compact balls connected by the stretched gel strands. In these aggregates only the cells which are pulling the gel strands develop Vn- and Tn-containing focal contacts. These focal contacts, together with MF bundles are always aligned with the tension lines, running along the gel strands.¹² These observations give support to a mechanistic hypothesis that the organization of the cytoskeleton in RPE cells in vitro is a function of cell adhesiveness and substratum deformability where both linear and circumferential arrangements of microfilaments are proposed to reflect lines of a tension field generated by the cell's contractile activity and spatially restricted by the sites of adhesion.¹³ This is based on the assumption that cell tractional forces are in mechanical equilibrium with the elastic forces operating within the substratum.¹⁵ Consequently, the stress fibres and focal contacts of cultured cells are not artifacts of an in vitro growth, but a natural cellular response to the nondeformability of commonly used tissue culture substrata.

From the effects of various substrata on the adhesion of RPE cells the following conclusions can be drawn: a) cytoskeleton-ECM linkage complexes in RPE cells grown on different substrata show variability with respect to the presence or absence of extracellular components, whereas their cytoskeletal parts are the same; b) the proteins of the basement membrane promote expression of the differentiated phenotype by RPE cells in vitro, but their promotional effects are greatly enhanced if cell spreading is prevented by the mechanical properties of the substratum; and c) in general, cell reaction to the mechanical properties of a substratum involves an attempt to spread, the extent of which is determined by the substratum resilience. Thus, elastic forces operating within the substratum determine the maximal cell traction allowable and, indirectly, the cytoskeletal organization. Consequently, the organization of the cytoskeleton in RPE cells during growth and differentiation in vitro is a function of cell adhesiveness and substratum deformability.¹⁵

REFERENCES

1. Curtis, A.S.G. (1964) J. Cell Biol. 20, 199.
2. Burridge, K. et al. (1988) Ann. Rev. Cell Biol. 4, 487.
3. Albelda, S.M. and Buck, C.A. (1990) FASEB J. 4, 2868.
4. Geiger, B. et al. (1984) J. Cell Biol. 99, 83s.
5. Opas, M. and Kalnins, V.I. (1986) Invest. Ophthalmol. Vis. Sci. 27, 1622.
6. Greenspan, H.P. and Folkman, J. (1977) J. Theor. Biol. 54, 397.
7. Turksen, K. et al. (1983) Exp. Cell Res. 147, 379.
8. Opas, M. et al. (1985) Dev. Biol. 107, 269.
9. Opas, M. and Kalnins, V.I. (1985) Cell. Tiss. Res. 239, 451.
10. Opas, M. and Dziak, E. (1991) In Vitro Cell. Dev. Biol. 27A, 878.
11. Grinnell, F. (1986) J. Cell Biol. 103, 2697.
12. Opas, M. (1989) Dev. Biol. 131, 281.
13. Opas, M. in J. Bereiter-Hahn et al. Eds., Cytomechanics, Heidelberg, Springer Verlag (1987) 273.
14. Oster, G.F. et al. (1983) J. Embryol. Exp. Morphol. 78, 83.
15. Supported by the MRC and the RP ERF of Canada.

HIGH-VOLTAGE ELECTRON MICROSCOPY OF SUBRETINAL SCAR FORMATION

G. E. Korte*, M. Marko** and G. Hageman***

*Depts. of Ophthalmology and Anatomy, Albert Einstein College of Medicine, Bronx, NY. ** NY State Dept. of Health, Albany, NY.

*** Bethesda Eye Inst., St. Louis Univ. St. Louis, MO

Sodium iodate iv. damages the retinal pigment epithelium (RPE) in rabbits. Where RPE does not regenerate (e.g., 1,2) Muller glial cells (MC) forma subretinal scar that replaces RPE. The MC response was studied by HVEM in 3D computer reconstructions of serial thick sections, made using the STEREOCON program (3), and the HVEM at the NYS Dept. of Health in Albany, NY. Tissue was processed for HVEM or immunofluorescence localization of a monoclonal antibody recognizing MC microvilli (4).

At sites of scar formation the junctions between MC and photoreceptors that form the external limiting membrane (elm) break down and MC processes enter the subretinal space. This is apparent in 2um sections (Fig. 1) and sections stained with antibody to MC microvilli (Fig. 2), which are lost where scars form (c.f., arrows, Figs. 1,2). In routine thin sections MC processes extend up to the remnant RPE basement membrane (bm), where they form attachment sites (Fig. 3). Computer reconstructions of serial thick sections through these processes reveal: i) processes in younger scars are more complex than in older, more mature scars (c.f., Figs. 4,5). ii) Remnant microvilli and elm junctions stud the surface of the scar processes (Fig. 6). iii) When scar processes contact the RPE bm their contour becomes regular, e.g., left panel of Fig. 7, a section stack through the part of a process contacting the bm, and the right panel, from the same process but where not in contact. These features were not apparent in single sections.

References

1. G. Korte and M. Song. Proc. Intl. Cong. Electron Microsc. (1990) p.408.
2. G. Korte and M. Song. Proc. Electron Microsc. Soc. Am. (1991)p.250
3. M. Marko et al. J. Electron Microsc. Techn. (1988)9,395.
4. D. Pratt et al. Invest. Ophthalmol. Suppl. (1987)28,258.
5. Supported by grants from NIH (EY08284 to GK; EY06463 to GH; RR01219 supporting the NY State HVEM) and Research to Prevent Blindness, Inc. to the Dept. of Ophthalmology, Albert Einstein College of Medicine and the Bethesda Eye Inst., St. Louis Univ.

FIG. 1. Light micrograph of scar (s) above some intact elm. Arrow corresponds to arrow in Fig. 2. Bar=10um.

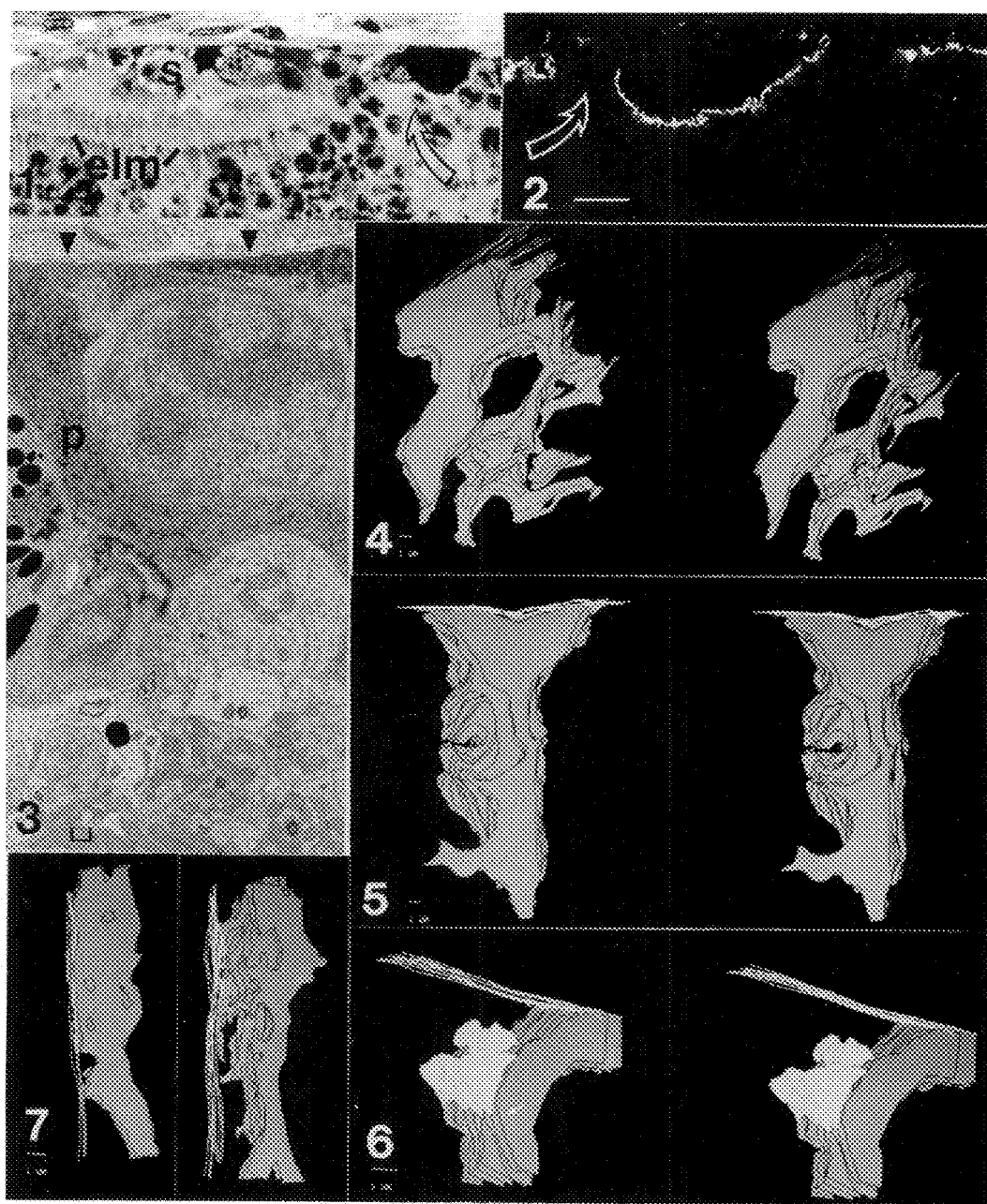
FIG. 2. Immunofluorescence of antibody to MC microvilli. Note intensely stained elm. Arrow corresponds to arrow area in Fig. 1. Bar=30um

FIG. 3. Thin section of MC process (p) at bm of RPE (arrowheads). Bar=1um.

FIGS. 4,5. 3D reconstructions of immature (Fig. 4) and mature (Fig.5) scar processes. RPE bm denoted by lines in all 3D pictures.

FIG. 6. 3D reconstruction of scar processes showing remnant microvilli (white zones) and elm junctions (arrow).

FIG. 7. Scar process contacting bm of RPE (left) and not in contact (right).



VISIONS OF VISION: STUDIES OF THE HORSESHOE CRAB COMPOUND EYE

Steven C. Chamberlain

Department of Bioengineering & Institute for Sensory Research, Syracuse University, Syracuse, NY 13244-5290

The lateral eye of the horseshoe crab, *Limulus polyphemus*, is an important model system for studies of visual processes such as phototransduction, lateral inhibition, and light adaptation. It has also been the system of choice for pioneering studies of the role of circadian efferent input from the brain to the eye. For example, light and efferent input interact in controlling the daily shedding of photosensitive membrane and photomechanical movements. Most recently, modeling efforts have begun to relate anatomy, physiology and visually guided behavior using parallel computing. My laboratory has pursued collaborative morphological studies of the compound eye for the past 15 years. Some of this research has been correlated structure/function studies; the rest has been studies of basic morphology and morphological process.

An adult horseshoe crab has 800 to 1000 facets in its eye. To determine how these individual cuticular cones map to the visual field, a two-circle goniometer was constructed and mounted on the stage of a compound light microscope equipped for epifluorescence. A new technique was developed for measuring the orientation of each cuticular lens. Fixation in formaldehyde induces rhodamine-band fluorescence of the internal surface of each cone. Ultraviolet illumination from the external surface produces a red fluorescence pattern which resembles the petals of a zinnia blossom. Alignment of concentric light and dark circles gives the orientation of the optic axis. The diameter of the display gives the interlens angle, and any departure from circularity indicates the degree of difference in the interlens angle between the vertical and horizontal directions. Examination of the inner surface of the array of cuticular cones with the scanning electron microscope gives a correlated picture of the lens arrangement and reveals the goodness of packing across the array. Adult animals see much of a lateral visual hemisphere with each eye with little binocular overlap. The region of highest resolution is directed anteriorly and slightly below the horizon.¹

The structure of the cuticular cones is a matter of interest because these elegant dioptric structures focus incoming parallel light out the exit aperture by internal refraction, i.e. each cone is a cylinder lens. Examination with transmitted light of sections cut normal to the optic axis shows that one region of the cone is organized as a single outward spiral whereas another region is organized as a pair of outward spirals. The normal interpretation of such spirals is that of an optical effect caused by the alignment of microscopic filaments in transparent cuticle. Correlated LM/SEM observation of individual sections, however, revealed that the spiral structures are physically present and not an optical effect. Development of the cones preceding each episode of ecdysis must be a complex process.

Under each cuticular cone is a group of about 12 photoreceptors arranged around the central dendrite of a second-order neuron, the eccentric cell. The photoreceptors have arrays of microvilli centrally fused in each ommatidium to form the light sensitive rhabdom. Each photoreceptor is divided into two segments, the rhabdomeral segment and the arhabdomeral segment, which are analogous to the outer and inner segments of a rod or cone. Between the photoreceptors and the cone is an aperture formed by lucent cone cells surrounded by opaque pigment cells. Both the dimensions of the aperture and the arrangement of the rhabdom is modulated by circadian neural input from the brain and by light. At night the aperture is wide open and the rhabdom is in a position to capture as much light as possible. During the day, the aperture closes to reduce the light

entering the rhabdom and the rhabdom lengthens away from the incoming light to reduce its light catch. These morphological changes occur as a result of neural input from a circadian clock in the brain even in total darkness; however, light enhances the daytime changes.² Each day at first light onset, the microvillar array of the rhabdom is transiently disorganized as photosensitive membrane is shed. Thereafter shed membrane is progressively degraded over the next 24 hours, moving away from the rhabdom into the A-segment.³ Both photomechanical movements and the daily shedding of rhabdom are driven by light, but require preceding circadian efferent input before light is effective. A combination of LM and TEM is used to assay these changes.

Studies with cytoskeletal inhibitors suggest that actin and microtubules are both involved in various ways in photomechanical movements and rhabdom shedding. We have used fluorescence immunocytochemistry and phalloidin labeling to visualize the location of microtubules and actin with the light microscope.⁴ The abundance of actin in the rhabdom suggests a role in membrane shedding. The selective distribution of actin and microtubules in the aperture, pigment cells, photoreceptors, and eccentric cell suggests complex possible roles for these cytoskeletal elements.

Lateral inhibition between ommatidia serves to enhance edges in the visual image. Lateral inhibition is mediated by a neural plexus of eccentric cell collaterals that spans the retina under the clusters of photoreceptors. Our recent efforts to discover what neurotransmitters are involved in efferent neurotransmission and afferent neurotransmission yielded a convenient way to selectively stain and visualize this neural plexus. Modern techniques to demonstrate acetylcholine esterase selectively stain the fine processes of the neural plexus.⁵ This both reveals the structure of the plexus and suggests that acetylcholine must be evaluated as a possible neurotransmitter candidate.

Currently we are involved in a collaborative effort to dissociate the lateral eye to obtain isolated photoreceptors in organ culture for use in whole-cell and excised-patch patch-clamp recordings.⁶ We have used a combination of stereomicroscopy, Hoffman contrast modulation microscopy, TEM and SEM to evaluate the results of our procedures. Freshly excised compound eyes can be dissected in such a way that all the ancillary cells are removed in one piece leaving only the photoreceptors and cone cells attached to the cuticular cones. SEM examination of this preparation clearly shows the naked membranes of the photoreceptor A-segments on the surface of the "desheathed" ommatidia. When the desheathed preparation is treated with collagenase, trypsin, and papain and gently disrupted mechanically, isolated ommatidia and single photoreceptors can be observed with Hoffman optics. In isolated ommatidia, the A-segment membrane is easily approached for patch-clamp recording. In single photoreceptors the membrane of both the R-segment and A-segment is accessible. TEM studies show that photoreceptor ultrastructure is essentially normal after dissociation.⁷

1. W.W. Weiner & S.C. Chamberlain, *Invest. Ophthalmol. Vis. Sci. Suppl.* 32(1991)1128.
2. S.C. Chamberlain & R.B. Barlow, Jr., *J. Neurosci.* 7(1987)2135.
3. S.C. Chamberlain & R.B. Barlow, Jr., *Science* 206(1979)361.
4. B.G. Calman & S.C. Chamberlain, *Vis. Neurosci.* (1992) in press.
5. E.P. Hornstein et al., *Invest. Ophthalmol. Vis. Sci. Suppl.* 32(1991)1127.
6. R.N. Jinks, S.C. Chamberlain, W.B. Hanna & G.H. Renninger, *Vis. Neurosci.* (in prep).
7. This research was supported by NIH EY03446 and the Department of Bioengineering.

STRUCTURE, ASSEMBLY AND INTERACTIONS OF THE NUCLEAR LAMINA AND THE NUCLEAR PORE COMPLEX

N. Panté, M. Jarnik*, E. Heitlinger, and U. Aebi

M.E. Müller-Institute at the Biocenter, University of Basel, Switzerland; *present address: Montreal General Hospital Research Institute, Quebec, Canada

The nuclear pore complex (NPC) is a ~120 MD supramolecular machine implicated in nucleocytoplasmic transport, that is embedded in the double-membraned nuclear envelope (NE).^{1,2} The basic framework of the ~120 nm diameter NPC consists of a 32 MD cytoplasmic ring, a 66 MD 'plug-spoke' assembly, and a 21 MD nuclear ring.^{2,3} The 'central plug' seen in en face views of the NPC reveals a rather variable appearance indicating that it is a dynamic structure.² Projecting from the cytoplasmic ring are 8 short, twisted filaments (Fig. 1a), whereas the nuclear ring is topped with a 'fishtrap' made of 8 thin filaments that join distally to form a fragile, 30-50 nm distal diameter ring centered above the NPC proper (Fig. 1b).^{2,4} While the cytoplasmic filaments are sensitive to proteases, they as well as the nuclear fishtraps are resistant to RNase treatment.² Removal of divalent cations destabilizes the distal rings and thereby opens the fishtraps, addition causes them to reform.² Protruding from the tips of the radial spokes into perinuclear space are 'knobs' that might represent the large luminal domain of gp210, a membrane-spanning glycoprotein.^{2,5} (Fig. 1c) which, in turn, may play a topogenic role in membrane folding and/or act as a membrane-anchoring site for the NPC. The lectin wheat germ agglutinin (WGA) which is known to recognize the 'nucleoporins', a family of glycoproteins having O-linked N-acetyl-glucosamine,⁶ is found in two locations on the NPC (Fig. 1, d-f): (i) whereas the cytoplasmic filaments appear unlabelled (Fig. 1d&e), WGA-gold labels sites between the central plug and the cytoplasmic ring (Fig. 1e; i.e., at a radius of 25-35 nm), and (ii) it decorates the distal ring of the nuclear fishtraps (Fig. 1, d&f; arrowheads). Concerning the lamins, the major building blocks of the nuclear lamina,⁷ we are exploring (i) their quaternary structures and phosphorylation-dependent assembly properties, and (ii) their interaction with specific components of the NPC. For this purpose, *in situ* analyses are combined with *in vitro* studies using a battery of bacterially expressed normal and site-specifically altered lamins.^{8,9,10}

References

- 1) C.W. Akey, Curr. Opin. Struct. Biol. (1992), in press.
- 2) M. Jarnik and U. Aebi, J. Struct. Biol. (1991), **107**, 291.
- 3) R. Reichelt et al., J. Cell Biol. (1990), **110**, 883.
- 4) H. Ris, EMSA Bull. (1991), **21**, 54.
- 5) U.F. Greber et al., EMBO J. (1990), **9**, 1495.
- 6) G.D. Holt et al., J. Cell Biol. (1987), **104**, 1157.
- 7) Aebi et al., Nature (1986), **323**, 560.
- 8) Heitlinger et al., J. Cell Biol. (1991), **113**, 485.
- 9) Peter et al., EMBO J. (1991), **10**, 1535.
- 10) Heitlinger et al., J. Struct. Biol. (1992), **108**, 74.

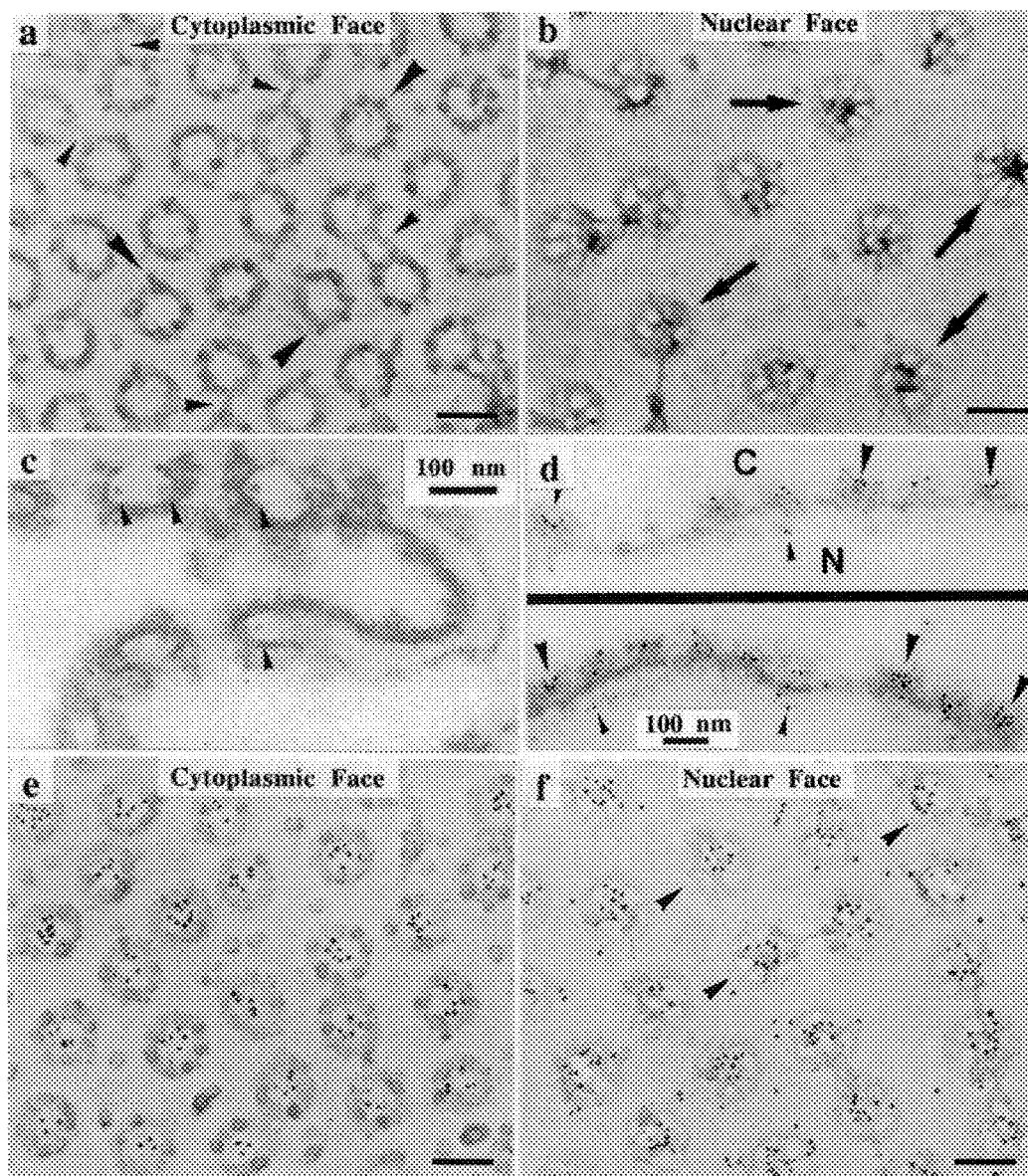


Fig. 1: (a,b) Cytoplasmic (a) and nuclear (b) faces of quick-frozen/freeze-dried/rotary metal-shadowed intact spread *Xenopus* oocyte NEs after chemical fixation with 2% glutaraldehyde/1% OsO₄. (c) Cross-section of cryofixed/cryosubstituted/Epon-embedded/thin-sectioned *Xenopus* oocyte NE. Arrowheads mark distinct knobs depicted in the lumen of the double-membrane that are probably associated with the peripheral part of the NPC proper. (d) Cross-sections of Epon-embedded/thin-sectioned *Xenopus* oocyte NEs revealing WGA-gold labelled NPCs. (e,f) Cytoplasmic (e) and nuclear (f) faces of quick-frozen/freeze-dried/rotary metal-shadowed spread *Xenopus* oocyte NEs revealing WGA-gold labelled NPCs. Scale bars, 100 nm (a-f).

HIGH-RESOLUTION SCANNING ELECTRON MICROSCOPY (HRSEM) OF THE NUCLEAR ENVELOPE (NE): NUCLEAR PORE SUBSTRUCTURE; BASKETS AND FIBROUS COMPONENTS OF THE INNER NE

Martin W. Goldberg and Terence D. Allen

CRC Department of Structural Cell Biology, Paterson Institute for Cancer Research, Christie Hospital NHS Trust, Wilmslow Road, Manchester, M20 9BX, U.K.

The nuclear envelope (NE) of eukaryotic cells has been studied for many years by a variety of em techniques yielding a three dimensional model of the nuclear pore complex (NPC) consisting of two rings (~120nm diameter), one at the outer NE and one at the inner NE. Between the rings are eight spoke structures and a central plug. The cytoplasmic ring may be decorated with up to eight particles¹. The NPCs are embedded in a proteinaceous network: the nuclear lamina. Recently, low voltage HRSEM was used to show the existence of a basket-like structure attached to the nucleoplasmic ring². SEM is an ideal technique for the study of membrane surfaces. High resolution can be achieved in SEMs by the use of a field emission source which produces a high brightness probe of less than 1nm diameter and a specimen stage within the objective lens, reducing chromatic aberrations and production of SEIII electrons. Resolution of biological specimens can be further enhanced by coating with thin, continuous films of refractory metals such as chromium or tantalum which allows the use of higher accelerating voltages and magnifications³. The NEs of *Xenopus* oocyte germinal vesicles have been prepared as previously described for HRSEM² without detergent except they have been coated nominally with 3nm of tantalum by magnetron sputtering instead of ion beam sputtered platinum. NEs have then been examined at 30kV. The ring, plug/spoke complex and particles can all be seen at the cytoplasmic surface as well as details of the outer membrane structure and particles associated with it (Fig. 1). On the nucleoplasmic surface (Fig. 2) the inner ring is observed. It has a subunit appearance with eight filaments extending from between the subunits to a third ring structure: these make up the basket-like structure. When 'baskets' are close together they are joined by fibres at the 'basket ring' (Fig. 2). When several baskets are in close proximity these fibres form a network like a canopy over the baskets (Fig. 3). Other fibres are present on the inner membrane surface which may be membrane associated fibres or canopy fibres that have collapsed⁴. It is uncertain which, if any, of these fibres are lamins as a further level of fibres is observed at the level of the nucleoplasmic ring when the membrane is removed with detergent (Fig. 4). These fibres are consistent with previously described lamina⁵.

References

1. P.N.T. Unwin and R.A. Milligan, *J. Cell Biol.* (1982) 93, 63.
2. H. Ris, *EMSA Bulletin* (1991) 21, 54.
3. K.R. Peters, *Scan. Electron. Microsc.* (1985) 4, 1519.
4. M. Stewart and S. Whytock, *J. Cell Sci.* (1988) 90, 409.
5. U. Aebi *et al.* *Nature* (1986) 323, 560.
6. This research was supported by the Cancer Research Campaign.

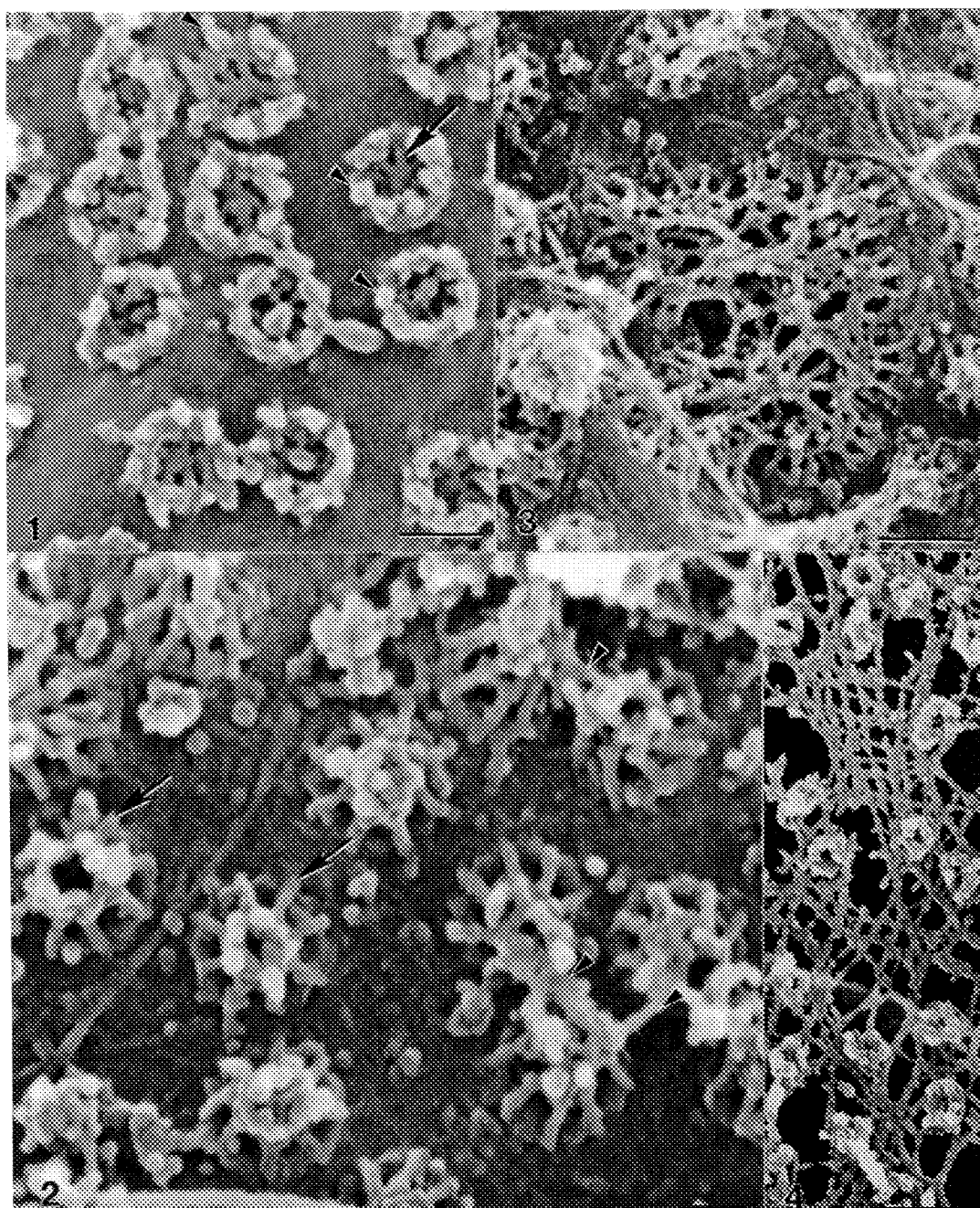


FIG. 1.--Cytoplasmic surface of NE, showing plug/spoke complex (arrow) and particles (arrowhead). Bar = 100 nm. FIG. 2.--Nucleoplasmic surface showing basket structures (arrows) and connecting fibres (arrowheads). Bar = 50 nm. FIG. 3.--Cluster of baskets with canopy of fibres. Bar = 150 nm. FIG. 4.--NE treated with 1% CHAPS to expose putative lamina. Bar = 300 nm.

VARIATIONS IN SIGNAL-MEDIATED TRANSPORT THROUGH THE NUCLEAR PORES AS A FUNCTION OF CELLULAR ACTIVITY

C.M. Feldherr and D. Akin

Department of Anatomy and Cell Biology, University of Florida, Gainesville, Florida

Previously, we utilized colloidal gold particles coated with nucleoplasmin, which contains well characterized nuclear localization signals (NLS), to study signal-mediated nuclear transport in proliferating and quiescent BALB/c 3T3 cells¹. The particles were injected into the cytoplasm, and nuclear uptake (N/C gold ratios) was later determined by TEM. The functional size of the transport channels was also analyzed by measuring the particles that entered the nucleoplasm. When large gold particles (110 to 270 Å in diameter) were injected, nuclear uptake was significantly greater in proliferating as compared to quiescent cells. The average functional pore diameter was approximately 230 Å during proliferation, and 140 Å or less in quiescent populations.

In this study, possible causes of the observed permeability changes were investigated. Initially, we wished to determine if the differences are due to variations in the availability of soluble cytoplasmic factors, such as ATP or NLS receptors², or to changes in the pores themselves. Proliferating and serum starved cells (4 days in 0.5% calf serum) were fused, and signal-mediated nuclear transport was analyzed after 1 hour (Fig. 1a and b). The N/C gold ratios for proliferating and starved nuclei (1.32 and 0.29, respectively) remained significantly different following fusion. Since the nuclei shared a common cytoplasm, these results indicate that the permeability differences are due to modifications of the pores. To establish the effect of growth factors on nuclear import, serum starved cells were treated with EGF and IGF-1, and recovery of nuclear transport capacity was analyzed for up to 18 h, i.e., the approximate time required for normal recovery in 10% calf serum. As seen in Table 1, partial recovery was achieved by adding the growth factors individually; however, both factors were necessary for complete recovery. Treatment with cycloheximide inhibited the recovery process. The effect of cell shape on signal-mediated transport was also examined. Using the procedure of Ireland et al., different size palladium domains were deposited on a non-adhesive poly (HEMA) substrate³. Cells plated on this surface only attached to the palladium, and their shapes varied from extended to spherical, depending on the size of the domain that they occupied. The N/C ratios obtained following the injection of large gold particles were significantly greater in extended versus rounded cells (1.48 and 0.58, respectively). However, the ratios were not significantly different when small particles (50 to 80 Å in diameter) were used, demonstrating that the permeability changes were size dependent.

References

1. C.M. Feldherr and D. Akin, *J. Cell Biol.* (1991)115, 933.
2. S.A. Adam and L. Gerace, *Cell* (1991)66, 837.
3. G.W. Ireland et al., *J. Cell Sci.* (1987) Suppl.8, 19.

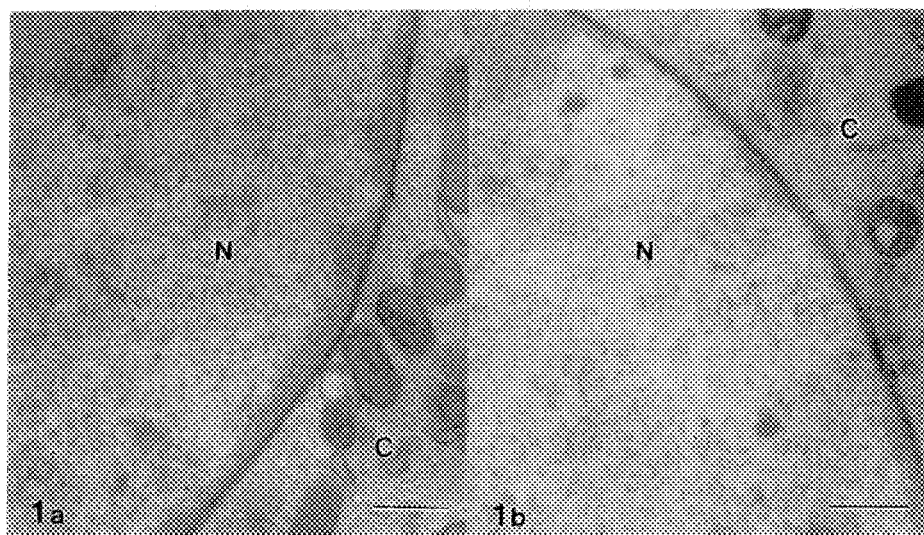


Figure 1a and b. Electron micrographs of a heterokaryon obtained by fusing a serum starved BALB/c 3T3 cell and a proliferating cell. Following fusion, the heterokaryon was injected with a 110 to 270 Å gold fraction and fixed for EM after 30 minutes. Gold uptake was greater in the proliferating (a) than in the serum starved nucleus (b). N, nucleus; C, cytoplasm; Bar = 0.5µm.

Table 1 - Effect of growth factors on transport recovery

<u>Experiment*</u>	N/C Gold Ratios***		
	<u>6 hr</u>	<u>12 hr</u>	<u>18 hr</u>
Starved controls	0.16 (50)*	0.16 (5)	0.16 (21)
Recovery controls	0.89 (47)	1.37 (7)	1.57 (18)
EGF (10 ng)**	0.42 (8)	---	0.62 (10)
EGF (50 ng)	0.73 (35)	0.56 (18)	1.47 (12)
IGF-1 (10 ng)	0.69 (11)	---	0.67 (11)
EGF (10 ng) + IGF-1 (10 ng)	---	---	1.73 (29)

* The serum concentration was 0.5% in all experiments except the recovery controls, in which case the serum content of the medium was increased to 10%.

** Concentration in ng/ml.

*** The injected gold fraction contained particles ranging from 110 to 270 Å in diameter, including the protein coat.

* Number of cells examined.

DNA SEQUENCE MAPPING IN INTERPHASE AND METAPHASE CHROMOSOMES BY FLUORESCENCE *IN SITU* HYBRIDIZATION

Barbara Trask¹, Susan Allen¹, Anne Bergmann¹, Mari Christensen¹, Anne Fertitta¹, Hillary Massa¹, Rainer Sachs² and Ger van den Engh¹

¹Biomedical Sciences Division, Lawrence Livermore National Laboratory, Livermore CA;

²Department of Mathematics, University of California, Berkeley, CA

Using fluorescence *in situ* hybridization (FISH), the positions of DNA sequences can be discretely marked with a fluorescent spot. The efficiency of marking DNA sequences of the size cloned in cosmids is 90-95%, and the fluorescent spots produced after FISH are $\approx 0.3 \mu\text{m}$ in diameter. Sites of two sequences can be distinguished using two-color FISH. Different reporter molecules, such as biotin or digoxigenin, are incorporated into DNA sequence probes by nick translation. These reporter molecules are labeled after hybridization with different fluorochromes, e.g., FITC and Texas Red. The development of dual band pass filters (Chromatechnology) allows these fluorochromes to be photographed simultaneously without registration shift.

We have chosen cosmid probes from several test chromosome regions for which restriction maps are available. The genomic distance between selected cosmids is known. Various pairs of probes were hybridized to interphase nuclei (G1 nuclei from fibroblast cell cultures) or to metaphase chromosomes. The physical distance between the resulting fluorescent spots in the microscope preparations was then compared to the known genomic distance. To obtain a large number (>100) of distance measurements for each probe pair hybridized to interphase cells, color photographic slides were made of randomly selected nuclei. These slides then enlarged by projection onto a wall where the measurements were made. In metaphase, the ability to resolve and correctly order sequences was scored along ≥ 50 chromatids.

Several conclusions can be drawn from the experiments.

- 1) The sites of DNA sequences can be consistently resolved in interphase into two fluorescent spots if the sequences are >100 kbp apart¹.
- 2) Mean interphase distance increases with genomic distance in the range from 50 kbp to 1-2 Mbp. This relationship was observed in several different human chromosomal regions, Xq28 (color vision and factor 8)², 6p21 (MHC)³, 4p16.3 (Huntington disease region)³, and in the DHFR region on Chinese hamster chromosome 2¹.
- 3) The frequency distribution of measured distance and the relationship between mean interphase distance and genomic distance can be described by random walk models, which view the chromatin fiber after hybridization as a polymer⁴.

4) The relative distance between markers and the periphery of the flat fibroblast nuclei can be studied to determine whether sequenced distribution is random or nonrandom.

5) Chromosome abnormalities such as translocations can be diagnosed in interphase cells by hybridizing probes that flank the breakpoint on the normal chromosome. The sequences become well separated in interphase when they are separated by translocation onto different chromosomes. Conversely, sequences normally on separate chromosomes may be brought into close juxtaposition in interphase by a translocation event⁵.

6) As expected, metaphase chromatin is considerably more condensed than is interphase chromatin. Sequences can be consistently resolved and oriented correctly determined along chromosomes only if the sequences are >500-1000 kbp apart ^{2,3}.

6) Using interphase distance and metaphase order derived from FISH experiments, detailed maps of DNA sequences can be established along chromosomes. To this end, we have mapped over 500 DNA sequences to chromosomal bands on chromosome 19⁶. Over 60 of these have been ordered with respect to each other using two-color interphase and metaphase FISH mapping. The resulting map has on average one marker every 1 Mbp along the chromosome⁷. It is technically feasible to make chromosome maps with 100 kbp average density using this approach⁴.

¹ Trask, B.J., et al., *Genomics* 5 (1989) 710.

² Trask, B.J., et al., *Am. J. Hum. Genet.* 48 (1991)1.

³ Trask, B.J., manuscript in preparation.

⁴ van den Engh, G.J., et al, submitted.

⁵ Tkachuk, D.C., et al., *Science* 250 (1990) 559.

⁶ Trask, B.J., et al., submitted.

⁷ Trask, B.J., et al. manuscript in preparation.

Work performed at LLNL under the auspices of the U.S. Department of Energy under contract number W-7405-Eng-48 with support from NIH grant HG00256.

THREE-DIMENSIONAL ORGANIZATION OF CHROMATIN FIBERS *IN SITU* EXAMINED BY EM TOMOGRAPHY

C.L. Woodcock*, R.A. Horowitz*, and D.A. Agard**

*Department of Zoology, University of Massachusetts, Amherst, MA 01003

**Department of Biochemistry and Biophysics, U.C.S.F., San Francisco, CA 94143

Electron tomography is being used to understand the 3D organization of chromatin *in situ*. As demonstrated previously, the nuclei of *Patiria miniata* (starfish) sperm contain particularly well-defined chromatin fibers¹. These studies are being extended through the analysis of 3D reconstructions of material embedded at low temperature in Lowicryl K11M and contrasted with osmium ammine-B, which preferentially stains nucleic acids². Tilt series of sections were recorded at 150KV, over an angular range of $\pm 75^\circ$ and tilt increment of 2.5° using a Philips EM430. Image data were collected directly using a 1024x1024 CCD array with 2x2 binning to give a final pixel size of 1.3nm. Gold beads deposited on the sections were used for alignment, and reconstruction was by weighted back projection³. Six volumes totalling 0.48 μm^3 and containing numerous chromatin fibers have been examined utilizing VoxelView (Vital Images, Fairfield Iowa) software running on a Silicon Graphics Iris 4D workstation.

Fig 1a shows a projection of a reconstruction traversed by a number of chromatin fibers (stain appears light in all micrographs). Their complex trajectory is illustrated by the stereo pair (Fig 1a) in which the paths of a few fibers have been traced in 3D within the transparently rendered volume. Central slices extracted from the reconstruction (thickness = 1.3nm) of fiber segments lying parallel to the plane of the section are shown in Fig 2. The stain distribution is evidently related to nucleosome location and is non-random, although a variety of staining patterns are seen. There is little evidence for the type of long-range order predicted by any of the helical models of chromatin fiber structure.

Diameter measurements taken from the 3D data as well as from stereo pairs show that the fibers have considerable short range heterogeneity. In many cases this heterogeneity arises from a ribbon-like morphology in which the orientation of the major and minor axes varies continuously along the fiber length. Ribbon structures are illustrated in Fig 2e,f, and in stereo views of a fiber segment rendered transparently (Fig 3a) and as an extracted solid (Fig 3b).

Examination of individual stain deposits shows a variety of 3D motifs, some of which have a size and shape corresponding to nucleosomes (Fig 4).⁴

References

1. C.L. Woodcock et al., Proc. XII Int. Cong. Elec. Microscop. (1990)116.
2. R.A. Horowitz and C.L. Woodcock, J. Histochem. Cytochem. (1992)40,123.
3. A.S. Belmont et al., J. Cell Biol. (1987)105,77.
4. Supported by NIH GM-43786 to CLW and GM-31267 to DAA.

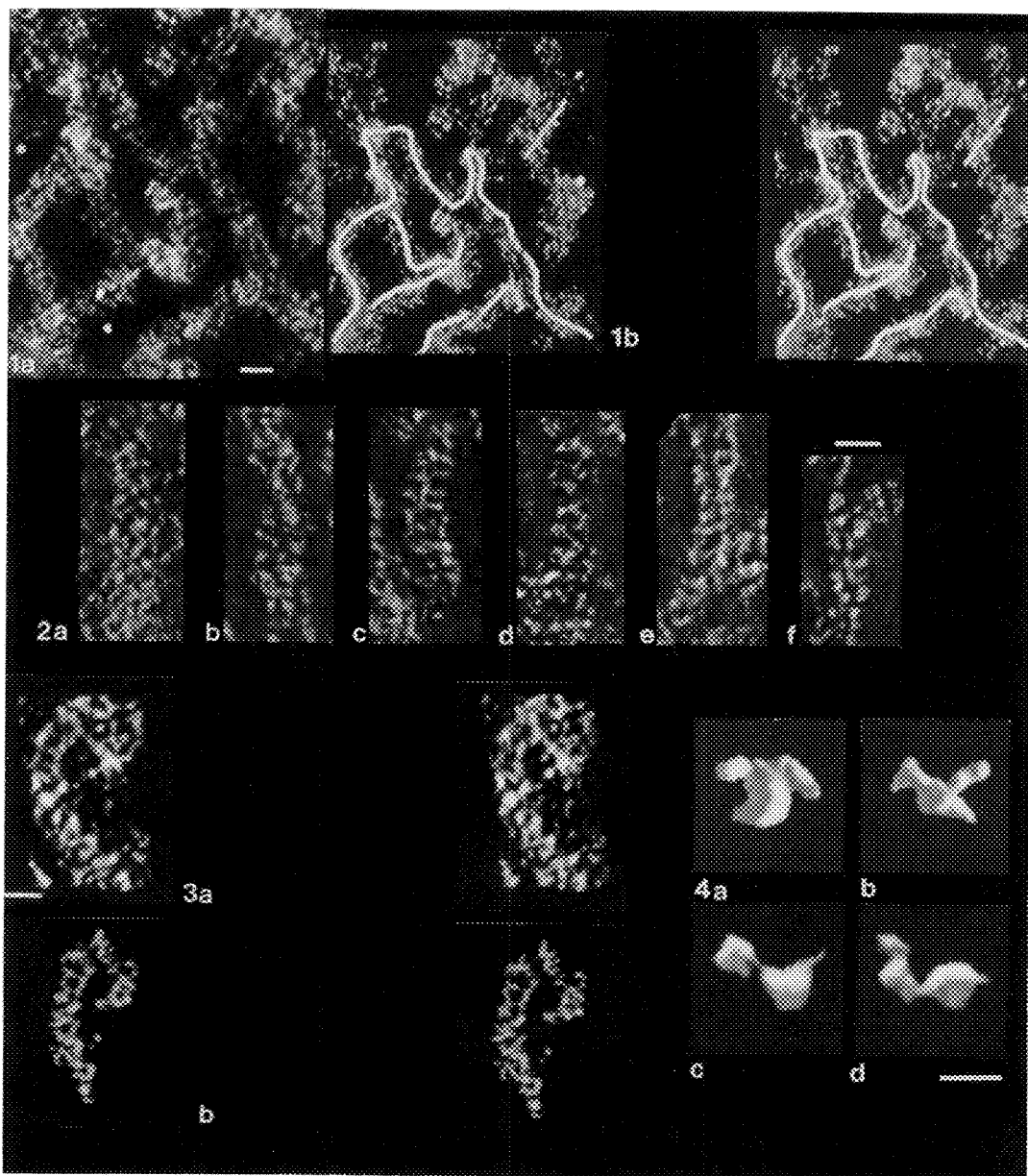


Fig 1. Projection of a complete reconstruction (a), and stereo pair of the reconstructed volume of the same area with the paths of a few fibers traced in 3D (b).

Fig 2. Single slices of reconstruction showing variety of staining patterns.

Fig 3. Stereo pairs of a fiber showing ribbon-like morphology viewed in situ in a transparent rendering of the reconstructed volume,(a) and an extracted subvolume viewed as a solid (b).

Fig 4. Shaded surface representations of individual stain deposits.

Scale markers are 30nm for Figures 1-3, 10nm for Figure 4.

THREE-DIMENSIONAL LOCALIZATION OF POLY(A) RNA AND SPLICING COMPONENTS IN THE NUCLEUS

Kenneth C. Carter*, Douglas Bowman#, Walter Carrington#, Kevin Fogarty#, John A. McNeil*, Fredric S. Fay#, and Jeanne Bentley Lawrence*

Depts. of *Cell Biology and #Physiology and the #Biomedical Imaging Group
University of Massachusetts Medical Center, Worcester, MA 01655

The physical distribution of active genes has long been a subject of interest and speculation, however technical limitations have necessitated that it be addressed only by indirect approaches with sometimes contradictory results.^{1,2} However, developments in fluorescence in situ hybridization methodologies allow the position of specific genes and RNAs to be visualized directly within intact cells, thus providing a more direct means to study such questions.^{3,4} To address whether compartmentalization occurs during the production and processing of pre-mRNA in mammalian somatic cells we have recently investigated the distribution of nuclear polyadenylated transcripts which represent approximately 90% of all pre-mRNA. We found that poly(A) RNA forms discrete nuclear "transcript domains" which are specifically positioned with respect to the underlying genome and contain snRNP antigens of the pre-mRNA splicing class.⁵ Several lines of evidence indicate a close spatial and temporal linkage between transcription and processing of pol II RNAs (reviewed in 5), therefore, it is possible that poly(A) RNA transcript domains reflect a clustering of active genes at these sites.

Recent improvements in high resolution 3D digital imaging and light microscopy have now allowed us to approach several fundamental questions about the structure and possible function of these regions at a level not feasible by standard approaches. We have addressed long-standing questions concerning the subnuclear location of pol II transcript metabolism using digital imaging microscopy combined with algorithms which reverse the blurring introduced by the fluorescence microscope, thus "restoring" the true distribution of the imaged molecules. As compared with standard confocal microscopy, such restored images give the highest possible 3D spatial resolution at the light microscope level.⁶

In cultured fibroblasts, myoblasts, and HeLa cells we found that individual transcript domains were internally localized and did not come in contact with nuclear envelope or with each other. Generally, all domains were positioned along the ventral or cytoplasmic half of the nucleus. Standard fluorescence microscopy indicates that snRNP splicing components^{7,8} and the non-snRNP splicing factor SC-35^{9,10} form a clustered pattern, which we found overlaps substantially with that of poly(A) RNA⁵. Our 3D analysis indicates that within individual transcript domains there is a differential placement of poly(A) RNA and splicing components. Distinct from these relatively large, brightly-staining transcript domains, which measured up to several microns in diameter, there were less intense filamentous regions of signal seen throughout the nucleus.

These data provide evidence that pre-mRNA splicing may occur in discrete non-randomly positioned domains within the nuclear interior. Further, these regions may themselves be functionally partitioned.

REFERENCES

1. S. Fakan and E. Puvion, *Int. Rev. Cytol.* (1980) 65, 255.
2. N. Hutchinson and H. Weintraub, *Cell* (1985) 43, 471.
3. J.B. Lawrence, C.A. Villnave and R.H. Singer, *Cell* (1988) 52, 51.
4. J.B. Lawrence, R.H. Singer and L.M. Marseille. *Cell* (1989) 57, 493.
5. K.C. Carter, K.L. Taneja and J.B. Lawrence, *J. Cell Biol.* (1991) 115, 1191.
6. W.A. Carrington et al., in *Confocal Microscopy Handbook*. 151-161.
7. D.L. Spector, W.H. Schrier and H. Busch, *Biol. Cell* (1983) 49, 1.
8. U. Nyman et al., *J. Cell Biol.* (1986) 102, 137.
9. X.-D. Fu and T. Maniatis, *Nature (Lond.)* (1990) 343, 437.
10. D.L. Spector, X.-D. Fu and T. Maniatis. *EMBO J.* (1991) 10, 3467.

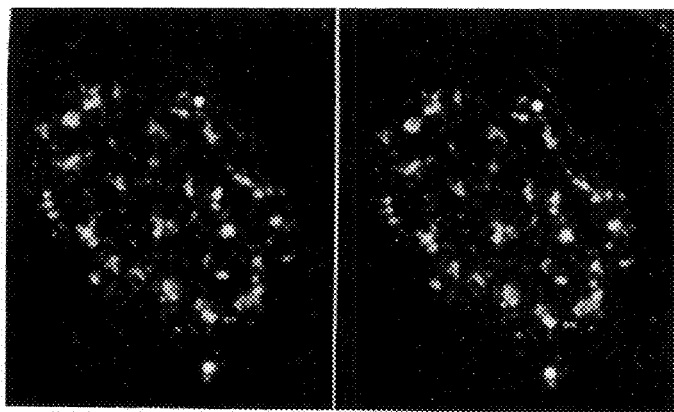


FIG. 1. Stereo pair view of total poly(A) RNA in a human diploid fibroblast nucleus labeled by fluorescent in situ hybridization.

PRE-mRNA SPLICING AND NUCLEAR ORGANIZATION

David L. Spector, Gayle Lark and Sui Huang

Cold Spring Harbor Laboratory, Cold Spring Harbor, New York 11724

Several major classes of small nuclear ribonucleoprotein particles (snRNPs) (U1, U2, U4/U6, U5) as well as other splicing factors have been shown to be involved in the processing of pre-mRNA molecules¹⁻². For most RNA polymerase II transcripts, such processing includes the addition of a 7-methylguanosine cap structure at the 5' end of the nascent RNA transcripts, hnRNP assembly, splicing, polyadenylation, and the exchange of hnRNP proteins for mRNP proteins¹⁻³. Splicing of nuclear pre-mRNA molecules occurs in spliceosomes, macromolecular complexes composed of a pre-mRNA, snRNPs and other splicing factors¹⁻². Since RNA processing is essential to cellular function, we and others have been interested in identifying the organization of splicing factors in cell nuclei. We have examined the localization of snRNPs in a variety of mammalian cells and have observed differences in the organization of these factors in transformed cells, immortal cells, and cells of defined passage number. Cells of defined passage number exhibit a speckled staining pattern after immunolabeling with anti-Sm, anti-B", or anti-m₃G antibodies. Furthermore, 2 to 3% of the cells, in a given population, exhibit 1 to 2 round "foci" in addition to the speckled labeling pattern. However, transformed cells exhibited 1 to 4 intensely stained round foci, in 81 to 99% of the cells, in addition to the speckled labeling pattern. Immortal cells exhibited 1 to 4 intensely stained smaller foci in 4 to 40% of the cells, in addition to the speckled labeling pattern. When immortal cells (REF-52) which had been transformed by adenovirus (REF-52 Ad5.4) were examined, these cells exhibited an increase in the percentage of cells containing 1 to 2 intensely stained foci, in addition to the speckled labeling, from 24% to 99%. We have identified these intensely stained foci as coiled bodies which can be visualized in the nucleoplasm of cells with or without antibody labeling. This study is the first to directly correlate an increase in the number of cells containing coiled bodies in a given cell population with the transformed phenotype. Based on this study, we conclude that the organization of snRNPs within the mammalian cell nucleus is a reflection of the physiology of the cell which may change upon transformation or immortalization.

References

1. Bindereif, A. and Green, M. (1990) In: Genetic Engineering, J. Setlow, ed. 12:201-224.
2. Krainer, A.R. and Maniatis, T. (1988) In: Frontiers in Molecular Biology: Transcription and Splicing. B. D. Hames and D. M. Glover, eds. (Oxford and Washington D C: IRL press), pp131-296.
3. Steitz, J.A., Black, D.L., Gerke, V., Parker, K.A., Kramer, A., Frendewey, D., and Keller, W. (1988) In: Structure and Function of Major and Minor Small Nuclear Ribonucleoprotein Particles. M.L. Birnstiel ed. (Springer Verlag, Berlin and Heidelberg), pp115-154.
4. This research was supported in part by grants to D.L.S. from the American Cancer Society (NP-619B) and the N.I.H. (GM42694). The Cold Spring Harbor Electron Microscopy Facility is supported by a grant from N.I.H. (5P30 CA45508).

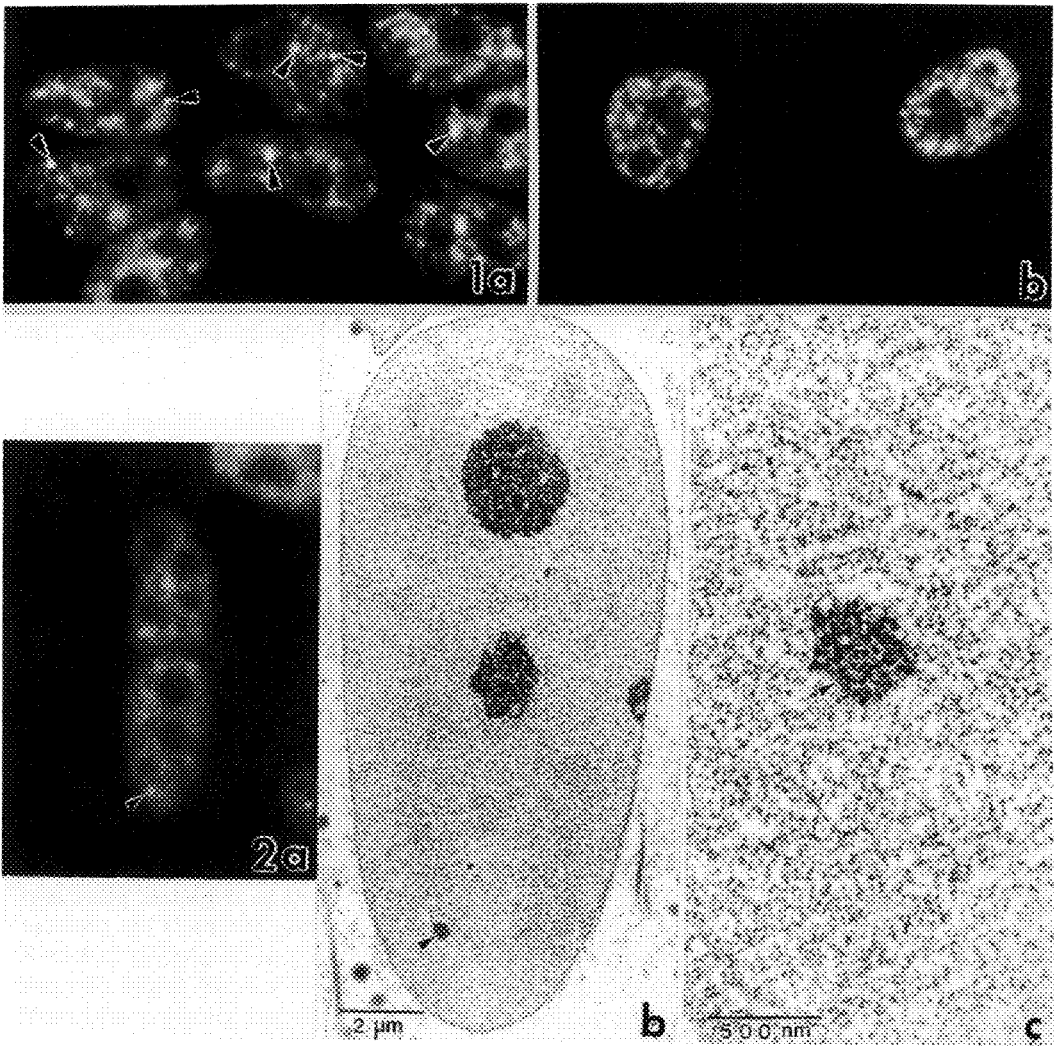


FIG. 1.--293 cells immunolabeled with anti- m_3G antibodies (a) exhibit speckles and diffuse nuclear staining. 1 to 4 large foci were observed in 90% of the cells examined. Normal human diploid fibroblasts (MRC-5 cells) immunolabeled with m_3G antibodies (b) exhibit speckles and diffuse nuclear staining. Foci are rarely observed (3%) in MRC-5 cells.

FIG. 2.--Foci are coiled bodies. HeLa cells were immunolabeled with anti-Sm monoclonal antibody, photographed and then prepared for electron microscopy. The focus shown in panel (a) by immunofluorescence microscopy is identified as a coiled body in the same nucleus (panels b,c arrowheads) by electron microscopy.

THE 3-D SUBSTRUCTURE OF RNA IN NASCENT RNP GRANULES: A NOVEL APPLICATION OF OSMIUM AMMINE-B STAINING AND ELECTRON SPECTROSCOPIC IMAGING

Ada L. Olins*, Donald E. Olins*, Manesh B. Shah*, Henri A. Levy* and David P. Bazett-Jones†

* The University of Tennessee-Oak Ridge Graduate School of Biomedical Sciences, Biology Division, Oak Ridge, Tennessee 37831-8077, and † Department of Medical Biochemistry, The University of Calgary, Calgary, Alberta, Canada T2N 4N1

RNA has a particulate substructure when visualized *in situ* with the nucleic acid specific stain osmium ammine-B (OA-B).^{1,2,3} In this study energy spectroscopic imaging (ESI) was used to enhance the contrast and collect the data for tomographic reconstructions.

The Balbiani ring (BR) in the salivary gland polytene chromosomes of *Chironomus tentans* larvae furnishes a well known model for the structure of nascent m-RNA. This gland produces copious amounts of silk-like secretory proteins which are very large (10^6 daltons). The site of transcription, the BR, is easily recognized in the EM by its characteristic "puff" structure and electron-dense granular transcripts. Mature BR granules are 45-50 nm in diameter and can be easily observed within the nucleus and passing through nuclear pores.

Tomographic reconstructions of conventionally stained (uranyl, lead) sections of BR transcription axes have been previously reported.^{4,5} These studies could not differentiate between protein and nucleic acid. Employing a new nucleic acid specific stain, (OA-B) on Lowicryl sections containing BR granules, we demonstrate a RNA-rich particulate substructure (~10 nm particle diameter; 10-12 particles per BR granule). The contrast is weak due to the low, local concentrations of RNA. ESI was used to enhance "structure-sensitive contrast," minimizing the contribution of carbon and strengthening the osmium signal, by forming the final image with 250 ± 10 eV loss electrons, just before the carbon K edge ($\Delta E = 284$ eV) of the energy loss spectrum. An example of the enhanced contrast observed is shown in FIG. 1. Note that only nucleic acid is imaged; proteins and most cellular structures have become transparent.

Tomographic reconstructions of mature BR granules in the nucleoplasm, arrow in FIG. 1, indicate that the 37Kb m-RNA forms a reproducible higher-order substructure. The ~10 nm diameter particles have a distinct arrangement in 3-D space which is unfolded and appears as a string of particles when the BR granule passes through nuclear pores. At present we are unable to visualize the connection between particles and assume that an extended single strand of RNA is below the sensitivity of the method. Calculations of the size and the low number of particles per 37Kb m-RNA make it unlikely that they are ribonucleosomes. Clusters of ribonucleosomes or unique RNP structures are possible candidates for the BR granule particles.

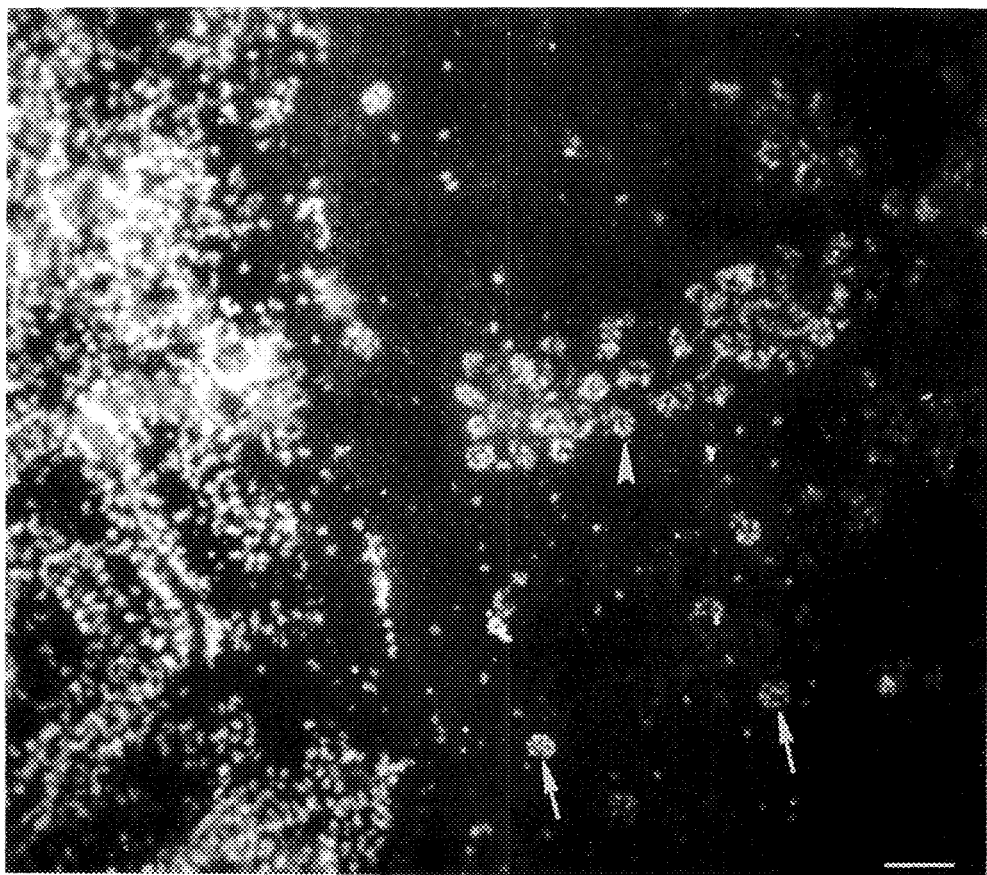


FIG. 1. Nucleic acid specific stain, OA-B, on a Lowicryl section^{2,3} of *Chironomus tentans* salivary gland. Imaging with 250 ± 10 eV loss electrons, Zeiss 902. Notice ribosomes in cytoplasm on left, where RNA is uniform and has central distribution within the ribosome. In mature BR granules (arrows) and nascent BR granules (arrowhead) the particulate nature of the m-RNA is apparent. Bar = 100 nm

References

1. A. L. Olins, et al., J. Histochem. Cytochem. (1989) 37, 395.
2. M. Derenzini and F. Farabegoli. J. Histochem. Cytochem. (1990) 38, 1495.
3. A. L. Olins, et al. J. Cell Biol. (1992) 117, No. 3 (in press).
3. D. E. Olins, et al., Science (Wash. DC). (1983) 220, 498.
4. U. Sköglund, et al., Nature (Lond.). (1986) 319, 560.
5. This study was supported by research grant National Science Foundation DIR 90 15886 to D. E. Olins and A. L. Olins, by Dept. of Energy under contract DE-AC05-84OR21400 with Martin Marietta Energy Systems, Inc., to D. E. Olins and by an operating grant from the Medical Research Council of Canada to D. P. Bazett-Jones.

USE OF HUMAN AUTOANTIBODIES AND IMMUNOELECTRON MICROSCOPY TO STUDY STRUCTURE AND FUNCTION OF THE NUCLEOLUS AND NUCLEAR BODIES

Robert L. Ochs

Autoimmune Disease Center, Department of Molecular and Experimental Medicine, The Scripps Research Institute, 10666 N. Torrey Pines Rd., La Jolla, California 92037

By conventional electron microscopy, the formed elements of the nuclear interior include the nucleolus, chromatin, interchromatin granules, perichromatin granules, perichromatin fibrils, and various types of nuclear bodies (Figs. 1a-c).¹ Of these structures, all have been reasonably well characterized structurally and functionally except for nuclear bodies. The most common types of nuclear bodies are simple nuclear bodies and coiled bodies (Figs. 1a,c). Since nuclear bodies are small in size (0.2-1.0 μm in diameter) and infrequent in number, they are often overlooked or simply not observed in any random thin section. The rat liver hepatocyte in Fig. 1b is a case in point. Historically, nuclear bodies are more prominent in hyperactive cells, they often occur in proximity to nucleoli (Fig. 1c), and sometimes they are observed to "bud off" from the nucleolar surface.²

Because of the lack of specific probes, information regarding nuclear bodies has been confined to purely ultrastructural studies. Using human autoantibodies as probes, we have identified an 80 kD protein (p80-coilin) which is specific for the nuclear coiled body, a type of round nuclear body composed of coiled fibers containing RNA and protein.^{3,4} Depending upon the cell type, the average number of coiled bodies per nucleus is 0-7 (Fig. 2a-d) but this number is variable, even within the same culture flask.^{3,4} By cryo-immunoelectron microscopy (Fig. 4a,b), coiled bodies were the only structures labeled with the human autoantibody to p80-coilin and at no time were coiled bodies found within the nucleolus. Using double label immunofluorescence, coiled bodies have been shown to contain the nucleolar proteins fibrillarin, topoisomerase I, and the NOR silver staining protein, as well as a number of snRNP-related proteins.^{2,3} Cell synchronization studies indicated that coiled bodies varied in number throughout the cell cycle, with a peak occurring at late G₁ or S-phase. No intact coiled bodies were observed during M-phase. Western blotting indicated that p80-coilin was constant in amount throughout all phases of the cell cycle. Physiologically, the expression of coiled bodies could be modulated by growth conditions or hormone stimulation.

In summary, coiled bodies contain nucleolus-related components, pre-mRNA splicing components, and they vary in size, number, and distribution throughout the cell cycle. Furthermore, coiled bodies are inducible by hormonal stimulation and growth conditions. Although the function(s) of nuclear coiled bodies is not yet known, based upon their content of nucleolar proteins and pre-mRNA splicing components, we propose that they are related to either ribosomal RNA transport or to events of pre-mRNA splicing and transport.⁵

References

1. I. Raska et al., *Electron Microsc. Rev.* 3(1990)301.
2. I. Raska et al., *J. Struct. Biol.* 104(1990)120.
3. I. Raska et al., *Exp. Cell Res.* 195(1991)27.
4. L.E.C. Andrade et al., *J. Exp. Med.* 173(1991)1407.
5. The author gratefully acknowledges the contributions of Drs. Raska, Andrade, Chan, Brasch, and Tan.

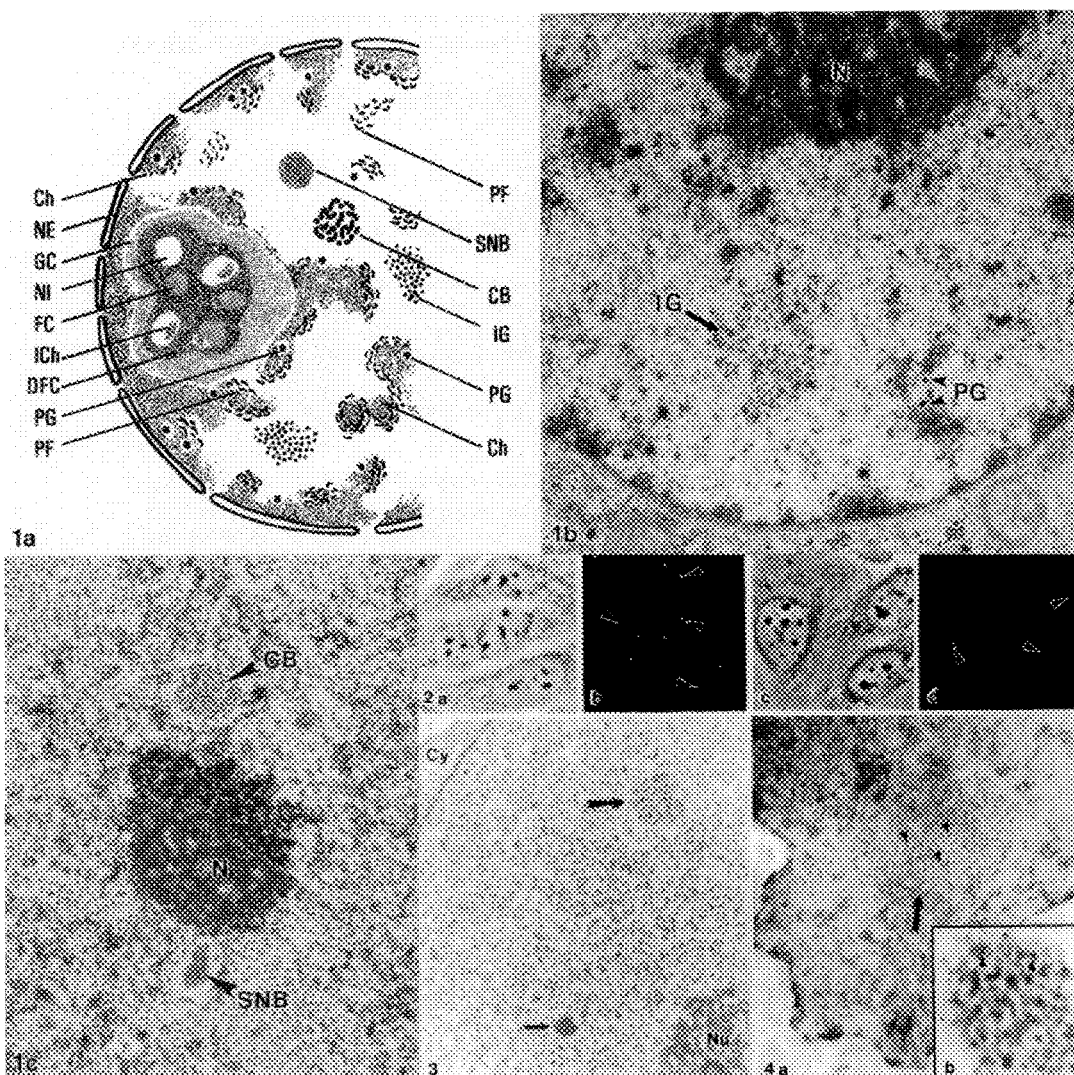


Fig 1a. Schematic diagram illustrating the formed elements of the nucleus: Ch, chromatin; NE, nuclear envelope; GC, nucleolar granular component; NI, nucleolar interstices; FC, nucleolar fibrillar center; ICh, interstitial chromatin; DFC, nucleolar dense fibrillar component; PG, perichromatin granule; PF, perichromatin fibril; SNB, simple nuclear body; CB, coiled body; IG, interchromatin granules.

Fig 1b. TEM of rat liver hepatocyte illustrating many of the formed elements of the nucleus.

Fig 1c. TEM of a WI-38 fibroblast cell nucleus showing the nucleolus (N), coiled body (CB), and simple nuclear body (SNB).

Fig 2-4. Labeling of nuclear coiled bodies (arrowheads) by indirect immunofluorescence (Fig. 2a-d) and cryo-immunoelectron microscopy (Fig. 4a,b) using a human autoantibody specific for p80-coilin. For reference, a TEM is included (Fig. 3) showing a simple nuclear body (small arrow) and a coiled body (large arrow).

PROGRESS IN ULTRASTRUCTURAL AND MOLECULAR ANALYSIS OF THE NUCLEAR MATRIX

Edward G. Fey

Dept. of Cell Biology, U. of Mass. Medical School, Worcester, MA, 01655

In the past few years, considerable advances have been made regarding the structure and function of the nuclear matrix. In the first half of this presentation, the field of nuclear matrix research will be summarized. Emphasis will be placed on those studies where molecular interactions are demonstrated *in situ* utilizing high resolution light and/or electron microscopy. Studies demonstrating the role of the nuclear matrix in DNA synthesis and replication, RNA transcription and processing, and the binding of matrix attachment regions to specific nuclear matrix proteins will be summarized.

Recent progress in the molecular characterization of the nuclear matrix (NM) will be presented. The NM is operationally defined as a ribonucleoprotein structure which remains after detergent extraction and removal of most of the chromatin from cells. The NM retains many morphological characteristics of the intact nucleus, including the nuclear pore-lamina complex at the nuclear periphery, residual nucleoli, and a complex, fibrillogranular network in the nuclear interior. In addition, structures and activities essential to genome maintenance and expression have been shown to reside in the NM, including RNA splicing activity, DNA replication origins, and binding sites for DNA matrix attachment regions which anchor the loops of active chromatin in interphase cells. When resolved by 2D PAGE, the proteins of the NM appear as a complex mixture of low abundance proteins, the precise composition of which varies dramatically with cell type and differentiation state as well as with transformation.

We have been working to characterize these proteins at the molecular and structural level. Antibodies to NM proteins, raised by immunizing animals with total NM from human carcinoma cell lines, have been used to initiate several lines of investigation. By screening cDNA expression libraries, we have obtained clones for several novel proteins of the interior NM and one which is part of nuclear pore complex. Database searches for the open reading frames obtained from the cDNA sequences reveal no significant homologies to known proteins. We have named one of the interior NM proteins MT-1. MT-1 has a molecular weight of 71 kD and a pI of 5.4. Computer analysis suggests an unusual structure which consists of two proline-rich globular termini joined by an extended region of alpha helix.

Immunofluorescence studies performed with a number of antibodies to NM proteins reveal some striking staining patterns. MT-1 (Figure 1A), as well as several other interior NM proteins, are present as hundreds of punctate foci throughout much of the nuclear interior, but are absent from the nucleolus and from regions rich in poly-A RNA. At mitosis, these proteins are seen to associate with the mitotic spindle apparatus. Antibody 203.37 (Figure 1C & D) detects a nuclear pore protein and produces discontinuous peripheral nuclear fluorescence. This pattern is visibly quite distinct from the smooth peripheral pattern obtained with antibody to lamin B (Figure 1B).

We expect that many of the structural and functional roles observed to reside in the NM will soon be assigned to specific NM components. In addition, progress in these areas should also contribute to our understanding of the molecular events accompanying the establishment of nuclear ultrastructure during differentiation and malignant transformation.

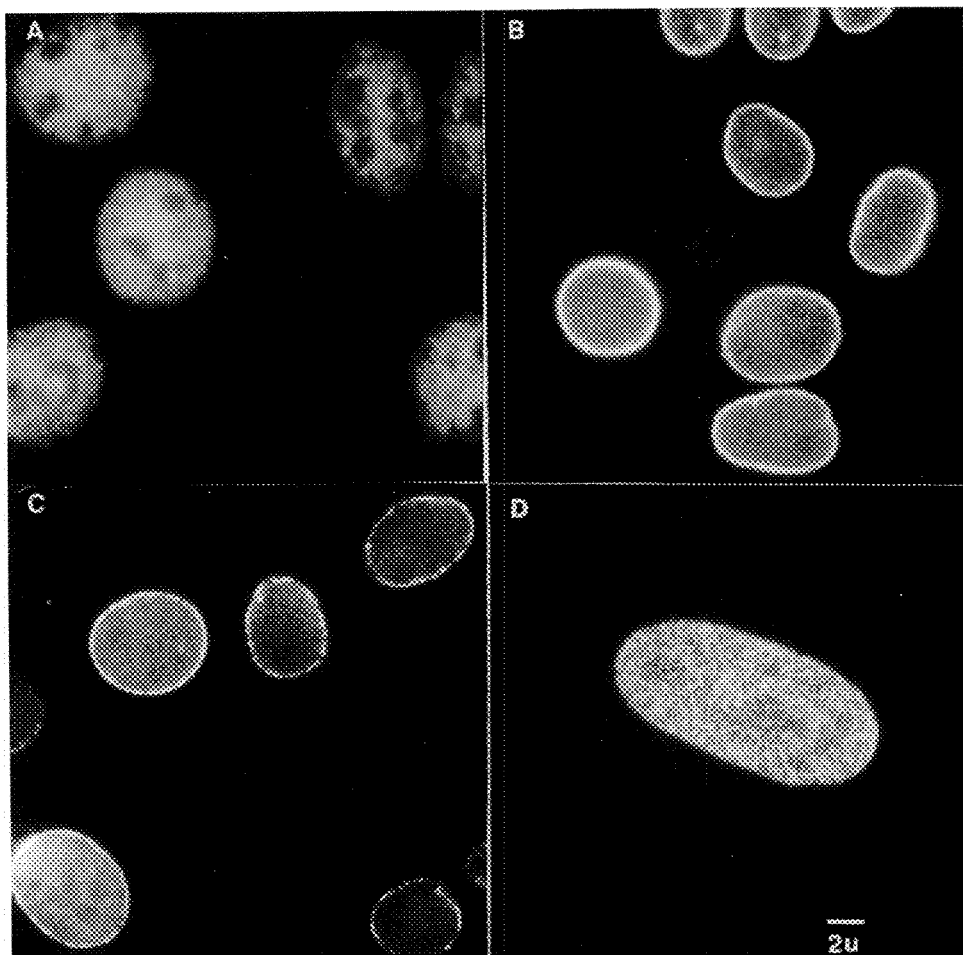


Figure 1. Immunofluorescence staining of cervical carcinoma cell line ME-180 (A., B., and C.) and fibroblast line WI-38 (D.) with monoclonal antibodies to nuclear matrix proteins (produced by Matritech, Inc., Cambridge, MA). Cells are extracted with Triton X-100 and fixed in 4% paraformaldehyde prior to incubation with antibodies. A. MT-1 is distributed as hundreds of small punctate foci throughout most of the nuclear interior, but is excluded from nucleoli and from smaller areas thought to be poly-A rich regions. B. A markedly different pattern of distribution is seen with antibody to lamin B, which localizes to the nuclear periphery and appears as a continuous circumferential ring when the plane of focus bisects the nucleus. C. & D. Antibody 203.37 detects a component of the nuclear pore complex. In C., most cells are seen in mid-focus, and as with anti-lamin B, the staining pattern is peripheral; however, 203.37 forms a discontinuous punctate ring, indicative of discrete pore complexes. D. In a plane of focus tangent to the upper surface of the fibroblast nucleus, hundreds of pore complexes can be seen studding the nuclear surface.

ELECTRON MICROSCOPY AND IMAGE RECONSTRUCTION REVEAL THE STRUCTURAL BASIS FOR SPECTRIN'S ELASTIC PROPERTIES

Amy M. McGough† and Robert Josephs*

† Rosenstiel Basic Medical Sciences Research Center, Brandeis University, Waltham, MA 02254

* Department of Molecular Genetics and Cell Biology, The University of Chicago, Chicago, IL 60637

The remarkable deformability of the erythrocyte derives in large part from the elastic properties of spectrin, the major component of the membrane skeleton. It is generally accepted that spectrin's elasticity arises from marked conformational changes which include variations in its overall length (1). In this work the structure of spectrin in partially expanded membrane skeletons was studied by electron microscopy to determine the molecular basis for spectrin's elastic properties. Spectrin molecules were analysed with respect to three features: length, conformation, and quaternary structure. The results of these studies lead to a model of how spectrin mediates the elastic deformation of the erythrocyte.

Membrane skeletons were isolated from erythrocyte membrane ghosts, negatively stained, and examined by transmission electron microscopy (2). Particle lengths and end-to-end distances were measured from enlarged prints using the computer program MACMEASURE. Spectrin conformation (straightness) was assessed by calculating the particles' correlation length by iterative approximation (3). Digitised spectrin images were correlation averaged or Fourier filtered to improve their signal-to-noise ratios. Three-dimensional reconstructions were performed using a suite of programs which were based on the filtered back-projection algorithm and executed on a cluster of Microvax 3200 workstations (4).

Analysis of electron micrographs of partially expanded skeletons shows that spectrin's length can vary in the absence of significant particle curvature. Three-dimensional reconstructions demonstrate that spectrin possesses a helical structure formed by the regular twisting of the α and β subunits about a common axis. The pitch of the helix can vary from particle to particle (83 Å - 166 Å). Increases in pitch are accompanied by decreases in particle diameter and produce changes in the overall length of the molecule. Axial views of the reconstructions show how variations in particle diameter are produced by alterations in the radial separation of the subunits (Fig. 1). The relationship between pitch and diameter mirrors the behavior expected from the extension of a helical spring.

References

1. B. G. Vertessy and T. L. Steck, *Biophys. J.* (1989) 55, 255.
2. A. M. McGough and R. Josephs, *PNAS (USA)* (1990) 87, 5208.
3. T. R. Coleman et al., *Cell Motil. Cytoskel.* (1989) 12, 248.
4. B. Carragher et al., *J. Mol. Biol.* (1988) 199, 315.

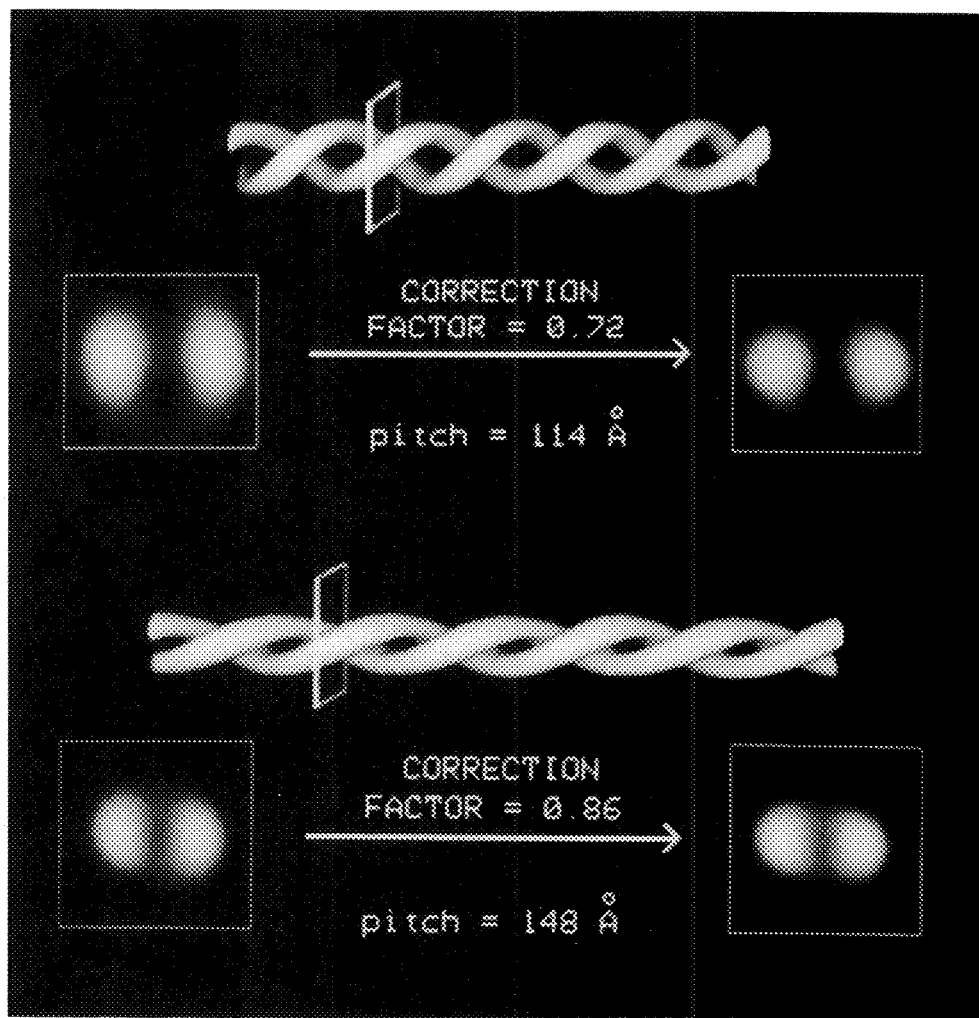


Figure 1. Three-dimensional reconstructions of spectrin particles with different pitches. The reconstructions are presented as lateral surface views and axial projections. The space-filling renderings (surface views) were contoured at the same molecular volume. Boxes on the surface views indicate the projection planes to which the axial views (left) correspond. Because the sectioning plane is normal to the helix axis, the subunits are sectioned at an angle and their shape is elongated. When the effect of sectioning the strands at an angle is accounted for, the resulting axial views (right) show that the spectrin subunits are actually circular in cross-section. In addition to varying in pitch (top particle, 114 Å; bottom particle, 148 Å), the diameters of the particles also vary.

HIGH RESOLUTION SPOT SCAN IMAGING OF FROZEN, HYDRATED ACTIN BUNDLES WITH 400KV ELECTRONS

J.Jakana, M.F.Schmid, P.Matsudaira*,and W.Chiu

Verna and Marrs McLean Dept. of Biochemistry and W.M.Keck Center for Computational Biology, Baylor College of Medicine, One Baylor Plaza, Houston,TX 77030; and *Whitehead Inst. for Biomedical Research and Dept. of Biology, Massachusetts Inst. of Technology,Cambridge, MA 02142

Actin is a protein found in all eukaryotic cells. In its polymerized form, the cells use it for motility, cytokinesis and for cytoskeletal support. An example of this latter class is the actin bundle in the acrosomal process from the *Limulus* sperm. The different functions actin performs seem to arise from its interaction with the actin binding proteins. A 3-dimensional structure of this macromolecular assembly is essential to provide a structural basis for understanding this interaction in relationship to its development and functions.

Under low dose conditions ($<10\text{e}/\text{\AA}^2$), electron images of frozen hydrated actin bundles were recorded with a spot scan computer controlled procedure in our JEOL4000 electron cryo-microscope¹. The specimen temperature was maintained at -168°C ; ice contamination on the specimen was minimized by using three JEOL anti-contaminators at -180°C situated about the specimen. Figure 1 is an example of a spot scan image at 30,000 magnification; this is an *h0l* view where the filaments are well separated and have a 2_1 symmetry which we used to evaluate the crystallinity of the bundle². Figure 2 is the optical diffraction pattern showing the crystallinity of the actin bundle with an isotropic resolution beyond 11\AA . Even though the specimen was on unsupported holey carbon films, the contrast transfer function (CTF) effect is visible in the pattern; it was therefore possible to correct for the microscope defocus and astigmatism in subsequent data processing. Computer analysis of these images reveal structural data exceeding twice the background to beyond 6\AA resolution. Figures 3 and 4 are CTF corrected 2 D projection maps of the image in Figure 1 and a merged map with two other spot scan images respectively. The projection map shows the mass densities of this protein complex which may be interpreted in terms of actin and bundling protein. This crystallographic analysis has led us to propose that the formation and stability of this bundle is governed by crystallographic packing of the actin and the bundling protein into a slowly twisting assembly that displays varying projections along the bundle axis².

In order to obtain an initial 3D structure, we have recorded tilt series of actin bundle and this 3-dimensional data set is being analyzed to provide a complete visualization of this macromolecular assembly.

Acknowledgement: Research supported by NIH grants and W.M.Keck Foundation.

References:

- 1) Brink, J. and Chiu, W., manuscript in preparation.
- 2) Schmid, M.F., et al., J.Mol. Biol. 221:711-725, 1991.

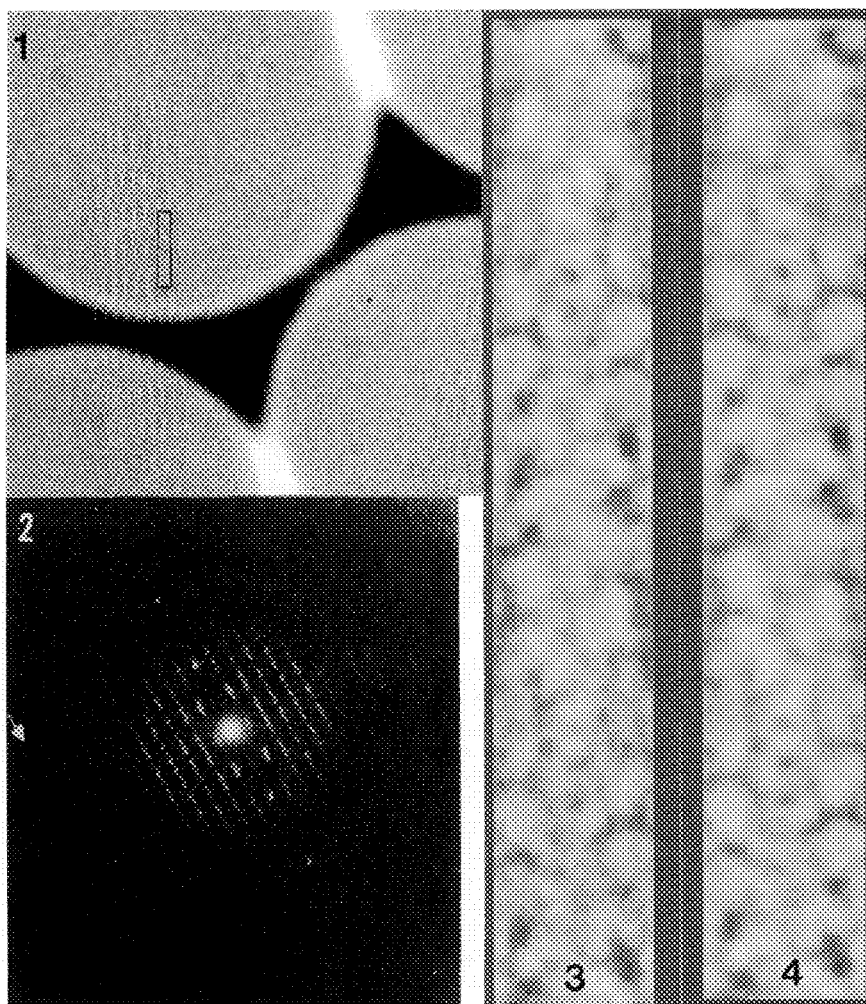


FIG.1 Electron spot scan image of frozen, hydrated actin bundle at 30,000 magnification imaged with 400 kV electrons. Defocus is 1.7 μ . Box indicates one unit cell; 127x762Å. The protein is dark.

FIG.2 An optical diffraction pattern of the image above; the CTF is visible. The arrow points to the 11th order in h (<11.5Å resolution).

FIG.3 A 6Å CTF corrected 2-D projection map of the image in Figure 1. The map was generated with reflections that were better than twice the background (IQ 4 or better). The protein is light.

FIG.4 A composite CTF corrected 2-D reconstruction of the image above and two other spot scan images; reflections used were IQ 4's or better. The map includes data out to 4Å. Actin helix is in center and the bundling protein sometimes appears near the edge.

THREE-DIMENSIONAL RECONSTRUCTION OF THE BACTERIAL BASAL BODY/SWITCH COMPLEX BY ELECTRON CRYOMICROSCOPY

Noreen R. Francis, Gina E. Sosinsky, Dennis Thomas, and David J. DeRosier

Rosenstiel Basic Medical Sciences Research Center, Brandeis University, Waltham, MA 02254-9110

The bacterial flagellum is unique among Nature's motors in that it possesses a reversible, rotary motor and a propeller that converts torque into thrust. The basal body, that part of the flagellum isolated from cells in attempts to purify the motor, contains eight different structural proteins. In *Salmonella typhimurium*, the basal body consists of four rings (denoted M, S, L, and P) threaded on a coaxial rod. The M-S, L and P rings are each composed of a different protein, FliF, FlgH, and FlgI, each of which is present in ~26 copies. The rod contains four different proteins, FlgB, FlgC, FlgF, and FlgG. Also present is FliE. These all are present in ~6 copies except for FlgG present in ~26 copies^{1,2}. The proteins important for motor rotation, however, are missing in standard basal body preparations. These missing proteins include the three "switch" proteins, FliG, FliM, and FliN, which control motor reversal (clockwise and counter-clockwise rotation) and may correspond to the rotor and gearbox of the motor. FliG has recently been shown to be localized at the M ring³.

We have developed a preparative procedure from which we obtain basal bodies containing additional structures. The new structures form an extra component we have termed the C (for cytoplasmic) ring. These preparations react positively against anti-FliG and anti-FliN antibodies on immunoblots suggesting that at least two of the three switch proteins are present. We have not yet tested for the presence of FliM or for other basal body proteins, for example, the proteins involved in the flagellar specific export apparatus. Mass measurements by scanning transmission electron microscopy (STEM) have shown that the extra components contribute an additional ~2000 kDa to the basal body (molecular mass ~4400 kDa). If the C ring contains only the three switch proteins, each present in equal amounts, its mass is consistent with ~26 copies of each of the switch proteins. From electron micrographs of these extended basal bodies in vitreous ice, we obtained an averaged image and a three-dimensional reconstruction of the cylindrically averaged structure. The M ring, relative to that in the absence of the C ring, has undergone a large conformational change with the insertion of extra material between the M ring and the rod. The C ring appears to show some subunit structure. We are presently applying correspondence analysis to sort our images of the C ring to determine its subunit symmetry.

1. Sosinsky, G., Francis, N., DeRosier, D., Wall, J., Simon, M., and Hainfeld, J., (1992), Proc.Natl.Acad.Sci., in press.
2. Jones, C., Macnab, R., Okino, H., and Aizawa, S.-I., (1990). J.Mol.Biol. 212, 377-387.
3. Francis, N. Irikura, V., Yamaguichi, S., DeRosier, D., and Macnab, R., (1992), Proc.Natl.Acad.Sci., in press.

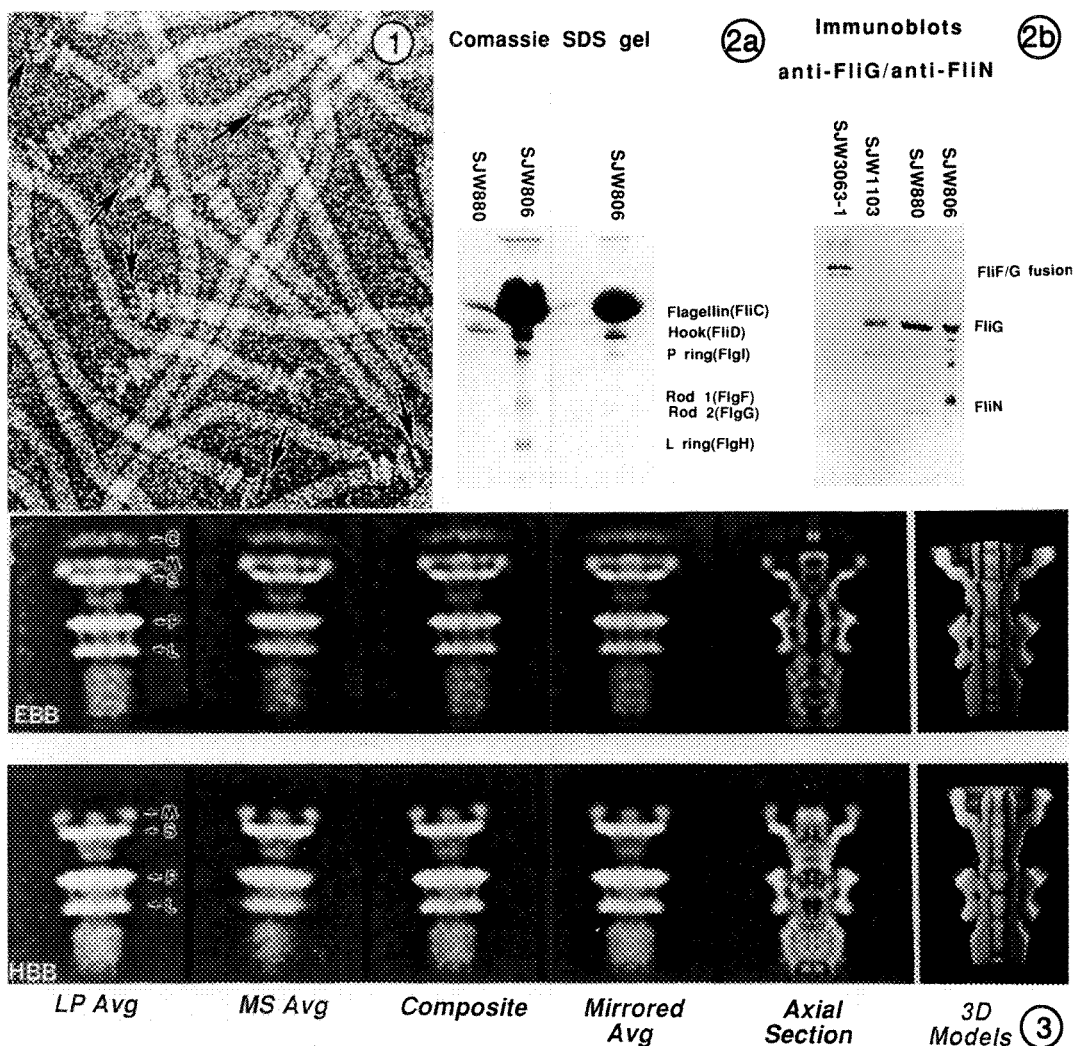


Figure 1. Field of Frozen-Hydrated Extended Basal Bodies from *S. typhimurium* (SJW 880). This *Salmonella* strain is a mutant which lacks hook length regulation. The cells have a long hook or polyhook but no flagellar filaments. Arrows point to the new features which extend into the cytoplasm of the bacteria.

Figure 2. (A) Coomassie stained SDS-PAGE of SJW 880 (polyhook mutant) and SJW 806 strains of *S. typhimurium* with intact C-ring proteins as determined by EM. Switch proteins are not visible on the

stained gel. Major proteins visible are flagellin (FliC) and hook (FlgE). (B) Double immunoblots of SJW 806 and SJW 880 with primary antibodies against two different switch proteins (FliG and FliN) (lanes 3 and 4). Lane 2 is a control SJW 1103 without C ring proteins. Lane 1 is SJW 3063-1 a positive control for anti-FliG activity. These basal bodies contain a mutant FliF/FliG fusion protein.

Figure 3. Three-dimensional reconstruction of the cylindrically averaged extended basal body (EBB) and the standard hook-basal body complexes (HBB). In addition to the M, S, L, and P rings, the EBB complex contains an additional ring of structures, the C ring. The C ring is not cylindrically symmetric and appears blurred by the averaging process.

**NEW METHODS FOR THE ANALYSIS OF HELICAL OBJECTS:
APPLICATION OF CROSS-CORRELATION TECHNIQUES**

D.G. Morgan, C. Owen, L. Melanson and D.J. DeRosier
Rosenstiel Basic Medical Sciences Research Center
Brandeis University, Waltham, MA 02254

Electron microscopy coupled with image analysis has recently been used to solve the structure of several membrane proteins to near atomic resolution (1,2). Helical objects have also been examined using similar techniques, but in general, the resulting structures have been limited to relatively low resolution. A major factor contributing to this limitation is that helical structures are inherently weak diffractors compared to the same amount of material arranged in a planar crystal. The diffracting power of a helical object may be two orders of magnitude weaker. It is possible to compensate for this effect by averaging the data from many identical particles. However, it has been impractical to analyze sufficiently large data sets to recover reliable weak diffraction data at high resolution. We have recently developed image processing programs which will make the analysis of such large data sets possible.

A number of distinct steps are involved in the analysis of helical objects. If the object has significant curvature, it must either be straightened or discarded. Layer line positions in the Fourier transform must be determined and the Fourier data extracted along these lines. After several sets of Fourier data have been brought to a common phase origin, the data are averaged. Using the averaged data, a three-dimensional reconstruction is performed using Fourier Bessel inversion techniques. We have automated the first three steps by implementing cross-correlation techniques (3). The helical axis of each particle is located using the peaks in a cross-correlation map of short segments of the particle and a reference data set, and the particle is straightened along this axis using a spline algorithm (4). The cross-correlation maxima are also used to determine the layer line positions for each particle. Systematic deviations between the positions of the maxima and the positions predicted by the symmetry of the reference data are used to refine the helical symmetry of each particle. From the helical symmetry, the exact layer line positions for each particle are determined. The alignment of Fourier data sets is performed by cross-correlating each individual data set with a reference data set. By automating these procedures, it is possible to analyze hundreds of images in a short amount of time. This represents at least an order of magnitude improvement in the numbers of images which can be aligned and averaged and results in a significant improvement in the signal-to-noise ratio of the final data set.

The filament protein from *Salmonella typhimurium* flagella forms a structure which appears ordered to at least 5 Å (5). Images recorded from glucose and PTA embedded samples show evidence of significant information at modest resolution (Fig. 1a and b). The programs mentioned above have been used to extract and merge data from 150 such images and result in significant data at a nominal resolution of 10 Å (Fig. 2). We are currently attempting to correct these data for the effect of the CTF and to combine the Fourier phases extracted from the images with amplitudes obtained by electron diffraction.

1. R. Henderson, J.M. Baldwin, T.A. Ceska, F. Zemlin, E. Beckmann, and K. Downing, *J. Mol. Biol.* (1990) 213, 899-929.
2. B.K. Jap, P.J. Walian and K. Gehring *Nature* (1991) 350, 167-170.
3. D.G. Morgan and D.J. DeRosier *Ultramicroscopy*, in press.
4. E.H. Egelman *Ultramicroscopy* (1986) 19, 367-374.
5. W. Astbury and C. Weibull *Nature* (1949) 163, 280-282.

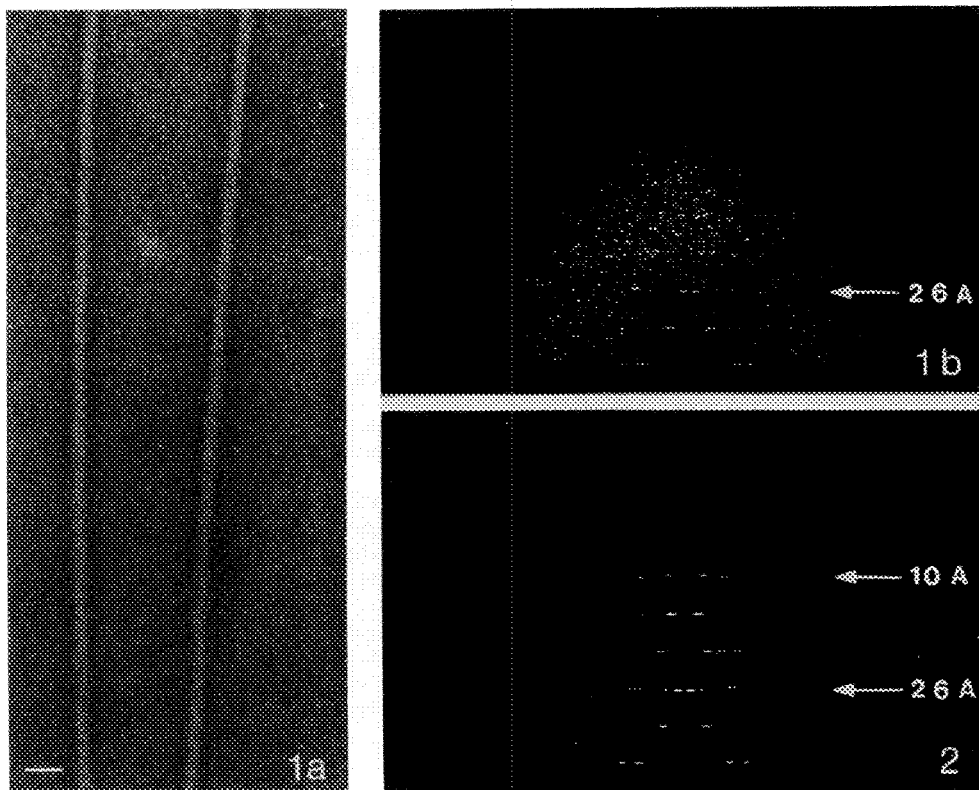


Figure 1a: Flagellar filaments from *Salmonella typhimurium* embedded in glucose and PTA. The scale bar in the lower left corner represents 500 Å.

Figure 1b: Layer line data from a single filament. The 1/26 Å resolution layer line (corresponding to the 1st Bessel order) is marked with an arrow and represents the highest resolution information which is visible in this data set.

Figure 2: Averaged layer line data set. Both the 1/26 Å layer line marked in Fig. 1b and a layer line at 1/10 Å (corresponding to the -3 Bessel order) are marked with arrows.

ELECTRON DIFFRACTION OF HELICAL STRUCTURES

Ruiz, T., Diaz, R., Ranck, J-L., Caspar, D.L.D. and DeRosier, D.J.

Rosenstiel Basic Medical Sciences Research Center, Brandeis University, Waltham MA 02154

Electron microscopy has advantages over X-ray diffraction for the study of helical structures. For X-ray studies, one needs large well oriented samples which are difficult to obtain. Only one helical structure, TMV, has been solved by conventional X-ray analysis using multiple isomorphous replacement. In contrast, one requires single particles or small rafts for studies by electron microscopy. We are attempting to use a combination of imaging and electron diffraction data to analyze helical structures at 9-10 Å resolution in order to visualize α -helices. To obtain electron diffraction patterns we produced well-ordered domains ($\sim 1-3 \mu\text{m}$ in diameter) for diffraction work. Several methods succeeded in aligning helical particles: the lipid monolayer technique^{1,2}, mica sandwiching³ and unidirectional blotting. The lipid monolayer technique proved to be the best for high resolution work. The three samples under study (flagellar filaments from *Salmonella typhimurium*, TMV and TMV stacked disk protein aggregate) gave electron diffraction patterns out to ~ 10 Å resolution.

Electron diffraction patterns from arrays (diam. 2-3 μm) of well-oriented straight bacterial flagella filaments stained with 2% PTA (pH 7.0) showed layer-lines out to $\sim 9-10$ Å resolution. These arrays consistently formed by applying either the unidirectional blotting or the lipid monolayer technique, although a larger the number of well-ordered regions was obtained by the latter method. Because of the better order in our arrays compared to those used in X-ray studies we can separate layer-lines that were overlapping in the X-ray patterns.

Depending on the concentration, ionic strength or pH, the TMV particles show a remarkable self-organization properties. This is an ideal model system for checking alignment procedures. With each technique we have been able to obtain well-ordered domains and in some cases ordered three dimensional domains. The resolution currently observed is limited to ~ 11 Å.

Well ordered domains $\sim 0.25 \mu\text{m}$ wide were obtained by blotting for the stacked disk aggregate of TMV protein. The sandwiching technique however produced ordered arrays at least twice as big, but these were still too small to give ideal conditions for diffraction. The lipid monolayer method has not been successful yet, probably due to the high negative charge of the protein (pI ~ 3.7).

References

1. Fromhertz, P. (1971) Electron microscopic studies of lipid protein films. *Nature*, 23:267
2. Uzgiris, E.E. (1986) Supported phospholipid bilayers for two-dimensional protein crystallization. *Biochem. Biophys. Res. Commun.*, 134:819
3. Horne, R.W., and Pasquali Ronchetti, I. (1974) A negative staining-carbon film technique for studying viruses in the electron microscope. *J. Ultrastruct. Res.*, 47:361

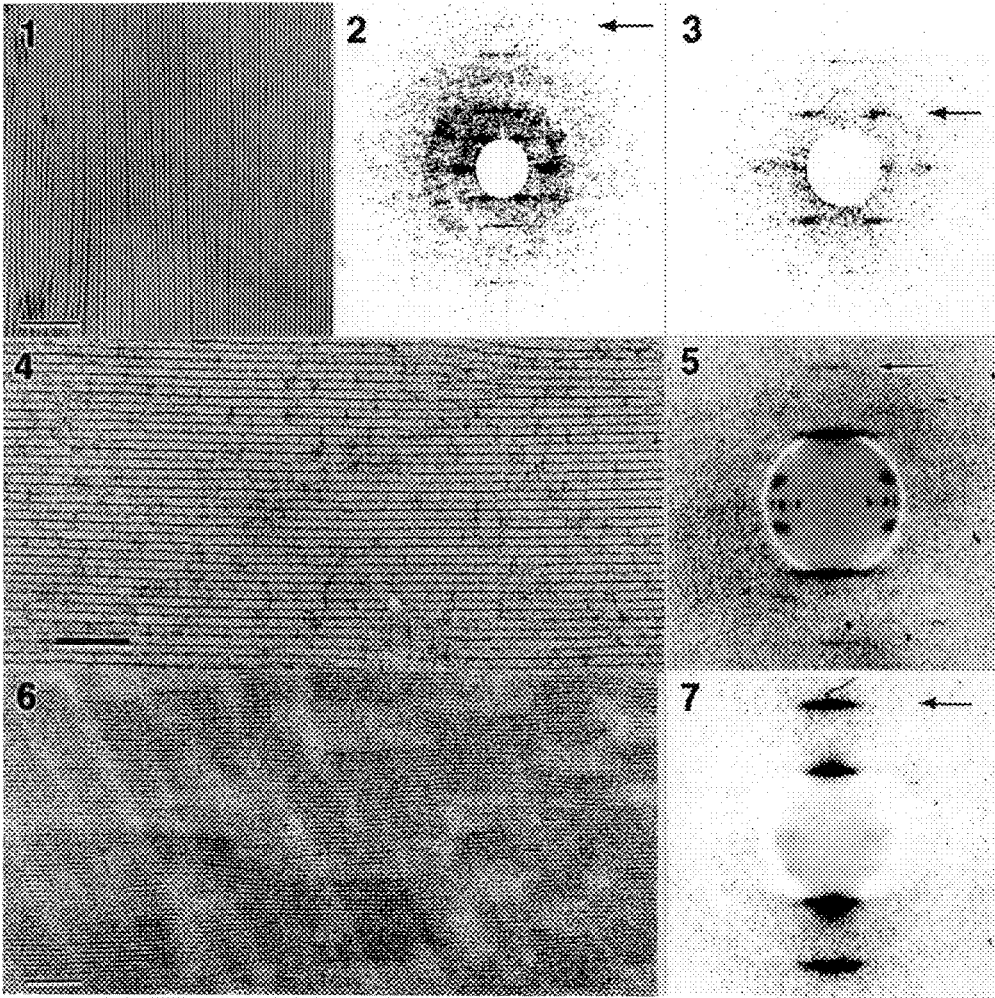


Figure 1. Raft of flagella filaments from the SJW1660 mutant of *Salmonella typhimurium* formed using the lipid monolayer technique. Bar = 0.5 μm

Figure 2. Electron diffraction pattern from a raft of flagella filaments, showing a resolution of 10 \AA .

Figure 3. Electron diffraction pattern from a raft of flagella filaments, showing a resolution of 52 \AA and the separation between layerlines with resolution of 50 \AA and 54 \AA .

Figure 4. Raft of TMV formed using the mica sandwiching technique. Bar = 0.2 μm

Figure 5. Electron diffraction pattern from a raft of TMV, obtained by the lipid monolayer technique, showing a resolution of 11.5 \AA .

Figure 6. Raft of TMV stacked disk protein aggregate formed using the sandwiching technique. Bar = 0.1 μm

Figure 7. Electron diffraction pattern from a raft of TMV stacked disk protein aggregate, showing a resolution of 12.5 \AA .

Cooling-Induced Wrinkling of Thin Crystals of Biological Macromolecules Can Be Prevented by Using Molybdenum Grids

Robert M. Glaeser

Department of Molecular and Cell Biology, University of California, Berkeley, CA 94720

It is an important requirement of high resolution electron diffraction and electron microscopy of thin crystals of biological macromolecules that the specimen be flat (i.e. planar) to one degree or less over distances of one micrometer or more. This high degree of specimen flatness is required in order to collect diffraction patterns and images at high tilt angles and high resolution.¹ Imperfect flatness causes the diffraction spots which are perpendicular to the tilt axis to become streaked or blurred, while the spots parallel to the tilt axis remain sharp. If the specimen wrinkling, or mosaic angular spread, is too severe, the diffraction spots overlap one another to make a continuum, and data retrieval becomes impossible (see Figure 3, for an example). Even before that point is reached, the broadening of the diffraction spots makes it increasingly difficult to obtain accurate background-subtracted diffraction intensities, and the signal-to-noise ratio in the computed Fourier transform of high resolution images is severely decreased. In some preparations of thin protein crystals the stringent requirements for specimen flatness can be met with a reasonable rate of success. In the case of bacteriorhodopsin, prepared as large single-crystal sheets by detergent-induced fusion² of the native purple membrane of *Halobacterium halobium*, the frequency of success is normally very low.

Although we have been able to overcome the problem of preparing flat specimens of glucose-embedded bacteriorhodopsin at room temperature, as judged by electron diffraction patterns, it has been especially frustrating to find that such specimens become badly wrinkled when cooled to a temperature of -120°C .³ It is important to be able to work with samples that are cooled to low temperature because of the 5 to 7-fold improvement in the resistance of the specimen to radiation damage that occurs at low temperature.

It is reasonable to suspect that cooling-induced wrinkling, when it does occur, is due to a difference in the thermal coefficients of two or more components which are strongly bonded ("welded") together, as in a bimetal foil. Thus, the problem might lie in the difference in the amount of thermal contraction of the carbon film relative to the metal EM grid, a difference in contraction of the protein crystal relative to the carbon film, or both. Cooling-induced buckling of carbon films mounted on copper grids, on a length scale of micrometers, has recently been reported by Booy.⁴ Most importantly, however, these authors have found that the carbon films show little or no buckling on molybdenum grids, which have a far smaller thermal coefficient than does copper. The implication is that the thermal coefficient of evaporated carbon films, which is not known from other work, must be smaller than that of copper, but larger than or equal to that of molybdenum.

We have now found that the cooling-induced wrinkling which we encountered previously with copper grids can be largely prevented by using molybdenum grids. Using the same techniques of optimal specimen preparation on 400 mesh copper grids which we reported previously, specimens can be tilted to high angle and diffraction patterns can be found routinely which are well resolved in the direction perpendicular to the tilt axis.³ An example is shown in Figure 1. When these specimens are cooled to -120°C and examined without tilting, the diffraction patterns still look extremely good (Figure 2). However, when tilted to high angle, severe wrinkling has evidently occurred as the result of cooling, for the diffraction spots are now badly blurred in the direction perpendicular to the tilt axis (Figure 3). When the same experiment is performed with molybdenum grids rather than copper, however, the diffraction patterns that are obtained at high tilt angle often remain as sharp at low temperature as they were at room temperature, as is shown in Figure 4.⁵

References

1. R.M. Glaeser *et al.*, J. Microscopy (1991)161, 21.
2. J.M. Baldwin and R. Henderson, Ultramicroscopy (1984)14, 319.
3. R.M. Glaeser and K.H. Downing, Proc. 12 Intl. Cong. EM (1990)98.
4. F. Booy, private communication, (1991) work in preparation.
5. This work was supported by the Office of Health and Environmental Research, US Department of Energy, under contract no. DE-AC03-76SF00098, and by the National Institutes of Health Program Project Grant GM36884.

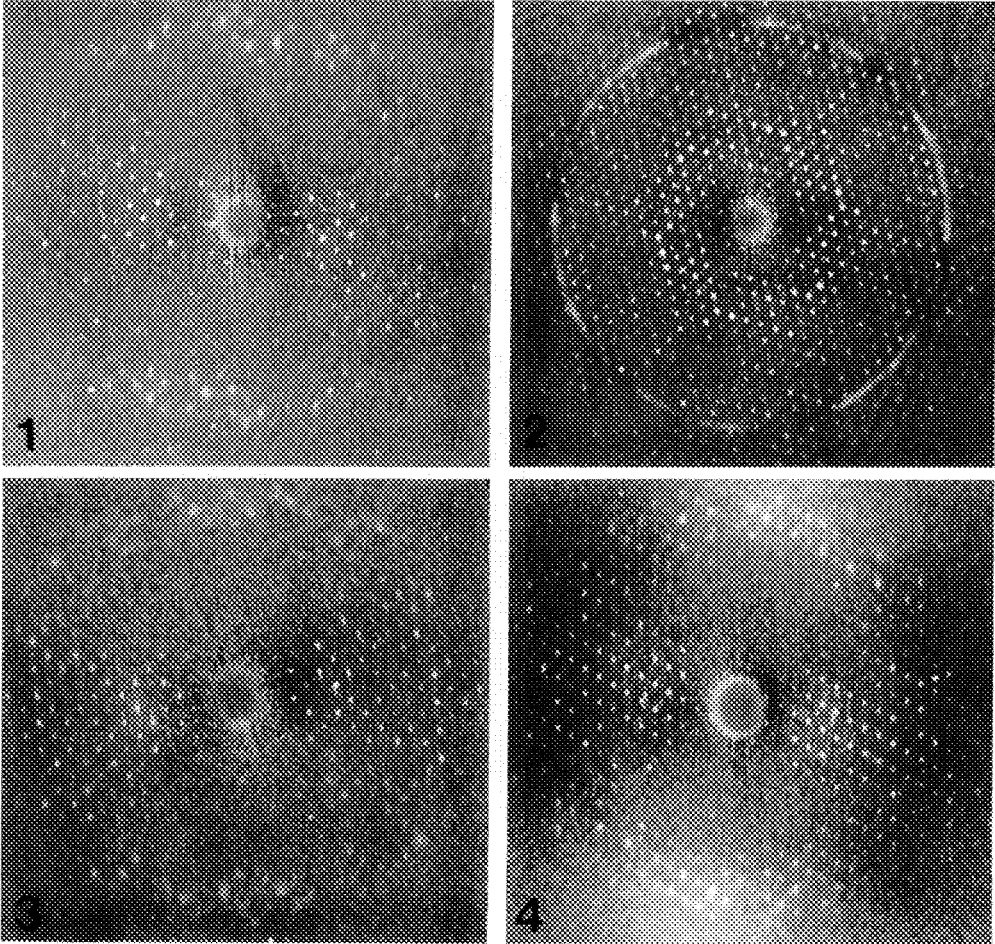


Fig. 1--Electron diffraction pattern of glucose-embedded purple membrane, tilted to 52 degrees; specimen at room temperature. 400 mesh copper grid.

Fig. 2--Electron diffraction pattern of glucose-embedded purple membrane, untilted; specimen temperature -120° C. 400 mesh copper grid.

Fig. 3--Electron diffraction pattern of glucose-embedded purple membrane, tilted to 52 degrees; specimen temperature -120° C. 400 mesh copper grid.

Fig. 4--Electron diffraction pattern of glucose-embedded purple membrane, tilted to 52 degrees; specimen temperature -120° C. 400 mesh molybdenum grid.

IMMUNO-ELECTRON MICROSCOPY AT SUB-NANOMETER RESOLUTION

Alasdair C. Steven^{*}, William W. Newcomb^{**}, Frank P. Booy^{*}, Jay C. Brown^{**}, and Benes L. Trus^{***}

^{*} Laboratory of Structural Biology, NIAMS; and ^{***} Computer Systems Laboratory, DCRT, NIH, Bethesda, MD 20892; and ^{**} Department of Microbiology and Cancer Center, University of Virginia Health Sciences Center, Charlottesville, VA 22908

We have been studying the structure and assembly properties of the capsid of herpes simplex virus, type 1 (HSV-1), whose icosahedral shell ($T=16$) is ~ 125 nm in diameter, has a mass of ~ 200 MDa, and is composed of at least six protein species, ranging from 12 kDa to 149 kDa per monomer. To this end, the structures of empty and full purified capsids have been visualized in three-dimensional reconstructions from cryo-electron micrographs, at a resolution of ~ 3.5 nm^{1,2}. With the intent of identifying specific structural features of the capsid in terms of particular proteins, or particular segments of these proteins, we have begun to explore the potentialities of cryo-reconstructions of capsids decorated with monoclonal antibodies.

B-capsids were purified from BHK cells infected with the MP strain of HSV-1. Some material was analyzed directly by cryo-electron microscopy and image reconstruction as described^{1,2}. Other samples were incubated with approximately equimolar amounts of a monoclonal antibody (8F5) raised against purified VP5 (the major capsid protein, 149 kDa). The resulting precipitate was then washed with buffer to flush out unbound antibodies, and then analyzed in the same way, i.e. by observation in a Philips EM400T equipped with a Gatan 626 cryo-holder. The specificity of Mab.8F5 for VP5 was confirmed by an ELISA with purified VP5.

Cryo-electron micrographs of the immuno-precipitate and control B-capsids are compared in Fig. 1. The reconstructions demonstrate that this antibody binds to the external tips of hexons (the capsomers located at local six-fold symmetric sites), but not to pentons (Fig. 2). Measurement of the antibody density in the reconstructed density map yielded an average binding stoichiometry of 0.65 - 0.70 Mabs per VP5 monomer. This figure was confirmed by quantitative SDS-PAGE of the immuno-precipitate. To localize the epitope as precisely as possible on the hexon, we examined tangential sections through the density maps, close to the tips of the hexon protrusions. In this way, and by comparing corresponding sections from the labelled and unlabelled reconstructions, the points at which the Fab arm of the antibody makes contact with the hexon can be mapped very precisely within the defined frame of reference of the icosahedral surface lattice (Fig. 4). On the basis of repeated trials, we estimate the uncertainty to be less than one pixel, i.e. < 0.8 nm, even though the nominal resolution of our reconstructions is about 3.5 nm. This remarkably precise localization of the epitope is not strictly a reflection of resolution *per se*: it relates primarily to the statistical reproducibility with which the centroid of a visualized feature may be defined within a specific frame of reference; it also relies on *a priori* knowledge of the high resolution structure of Fab fragments³. These, and other recent results⁴, hold out encouraging prospects for mapping specific epitopes on the surfaces of macromolecular complexes at unexpectedly high resolution. We are currently attempting to use this approach to determine whether Mab.8F5's failure to label pentons indicates that the pentons are not made of VP5, or whether it is a consequence of quasi-equivalence.

REFERENCES

1. T. S. Baker et al., *J. Virol.* (1990)64, 563.
2. F. P. Booy et al., *Cell* (1991)64, 1007.
3. D. R. Davies et al., *Ann. Rev. Biochem.* (1990)59, 439.
3. G. J. Wang et al., *Nature* (1992)355, 275.

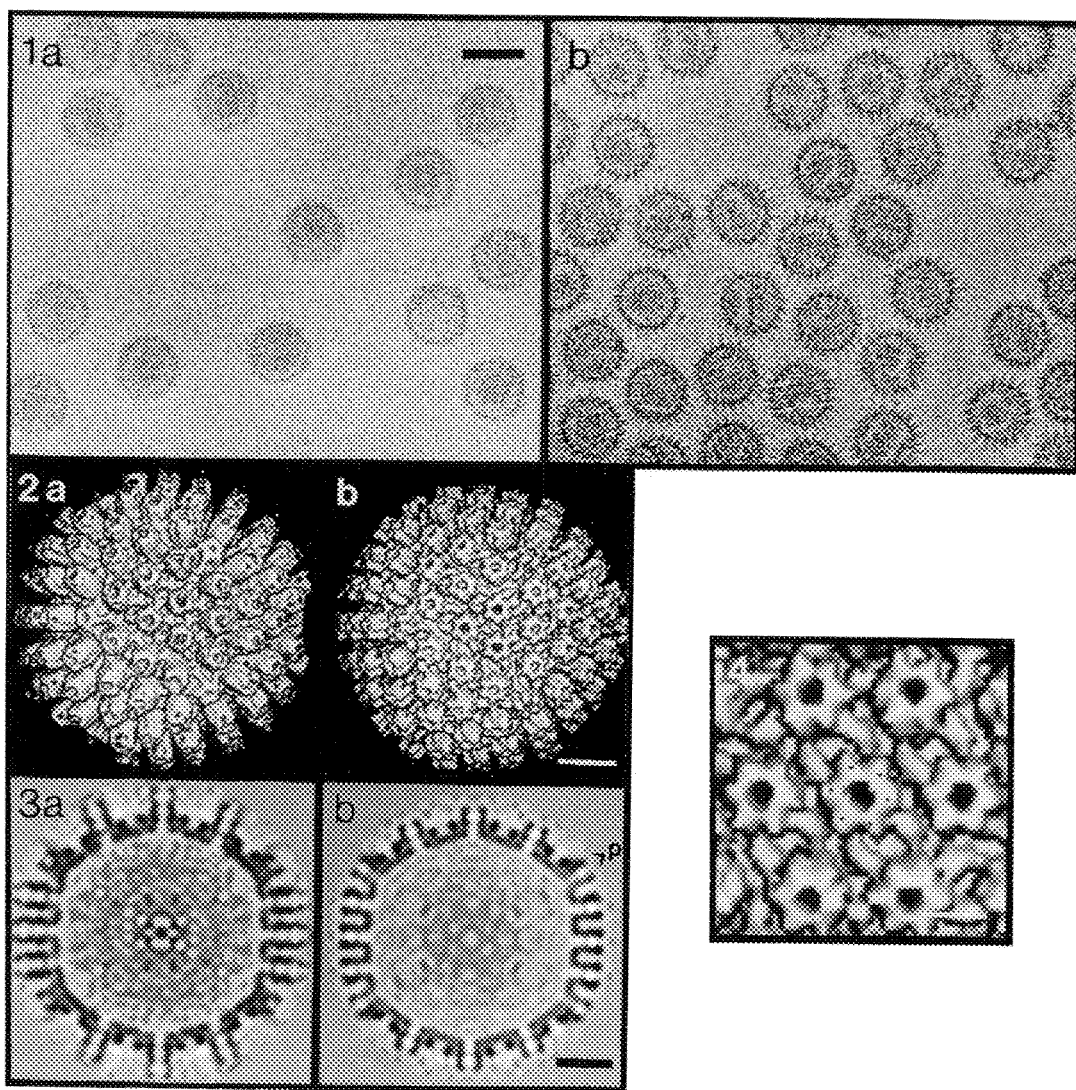


FIG. 1 : Cryo-electron micrographs of (a) purified B-capsids (a DNA-free precursor form) of HSV-1; (b) immuno-precipitate of B-capsids with an anti-VP5 monoclonal antibody. Bar = 100 nm.

FIG. 2 : Cryo-reconstructions of (a) HSV-1 B-capsids labelled with Mab.8F5, and (b) control B-capsids, viewed along a 3-fold axis of symmetry. Bar = 25 nm.

FIG. 3 : Central thin sections (0.8nm) through the reconstructions of (a) Mab-labelled B-capsids, and (b) unlabelled B-capsids, as viewed along a 2-fold symmetry axis. "p" marks a penton (unlabelled). Bar = 25 nm.

FIG. 4 : Blow-up of 3-fold view of hexons on outer surface of HSV-1 capsid, marking locations of epitope for Mab.8F5 (crosses). Bar = 10 nm.

CRYOELECTRON MICROSCOPY OF COMPLEXES OF HUMAN RHINOVIRUS WITH A MONOCLONAL F_{AB} AND THE VIRAL CELLULAR RECEPTOR

Norman H. Olson, Thomas J. Smith, Prasanna R. Kolatkar, Marcos A. Oliveira, Roland R. Rueckert,*
Jeffrey M. Greve,** Michael G. Rossmann, and Timothy S. Baker

Department of Biological Sciences, Purdue University, West Lafayette, IN 47907; *Institute for Molecular Virology and Department of Biochemistry, University of Wisconsin, Madison, WI 53706; **Molecular Therapeutics, Inc., Miles Research Center, 400 Morgan Lane, West Haven, CT 06516

Cryoelectron microscopy and image analysis techniques make it possible to study structural and functional relationships of macromolecular complexes that currently are not easily examined with crystallographic techniques. We have recorded images of frozen-hydrated human rhinovirus serotype-14 (HRV-14) complexed with a neutralizing, monoclonal, antibody fragment (F_{ab}-171a; Fig. 1A); and HRV-16 complexed with the amino-terminal, two-domain fragment (D1D2) of its cellular receptor (intercellular adhesion molecule-1, ICAM-1; Fig. 1B). Three-dimensional reconstructions (Figs. 2A,B) were calculated to ~3nm resolution from 35 and 44 images of each complex, respectively. The HRV-14/F_{ab} structure clearly identified the footprint of the F_{ab} on the surface of the virion. The HRV-16/D1D2 reconstruction presents, for the first time, the three-dimensional structure of a complete virus complexed with its cellular receptor.

Human rhinovirus is the major cause of the common cold. The icosahedral virus consists of 60 copies each of four proteins (VP1-VP4) and a single copy of a single-stranded RNA genome¹. Four areas on the surface of the virion have been identified as neutralizing immunogenic sites (NIm-Ia, NIm-Ib, NIm-II and NIm-III)². A surface depression, or canyon, that is 2nm deep and 1.2-1.5nm wide encircles each of the twelve, fivefold vertices and lies approximately half-way between the fivefold and threefold icosahedral axes. This canyon was initially identified as the site of cellular recognition with structural, mutational, and drug-binding studies². ICAM-1 normally functions as a cell surface ligand for the lymphocyte function-associated antigen-1 adhesion receptor and in leukocyte adhesion during inflammation. The extracellular portion of ICAM-1 consists of five, immunoglobulin-like domains³. The N-terminal portion of the ICAM-1 molecule is narrow enough to fit into the canyon and bind to viral residues on the canyon floor, however a F_{ab}, which has twofold-related heavy and light chains, is thought to be too large to fit inside the canyon¹.

Comparisons of the two reconstructions (Fig. 2) confirmed key hypotheses about structural and functional aspects of HRV which were based on previous studies. Both the F_{ab} and D1D2 molecules fully saturated HRV (~60 copies/virion). The F_{ab} molecule is narrow at its base and widens into a globular head (Fig. 2A). A central depression in the head corresponds to the switch region between the constant and variable domains. The F_{abs} surrounding adjoining vertices are twofold related and lie in position as expected for the formation of a (F_{ab})₂ structure⁴. The D1D2 molecule is approximately 7.5nm long and is bilobed as expected for the two-domain ICAM-1 fragment (Fig. 2B). Mutational analysis indicated that F_{ab}-171a is bound to NIm-Ia on VP1⁵ which is located about one-third the distance from the fivefold vertex along a line connecting the icosahedral fivefold and threefold axes. This location is confirmed in the reconstruction; however, the F_{ab} footprint also straddles the canyon. The footprint of D1D2 is centered over the canyon, as expected, but it also contacts both rims of the canyon. Consequently, binding of F_{ab}-171a to the virion precludes binding of the cellular receptor, as was previously suggested⁶, since the two footprints overlap.

These reconstructions, in conjunction with model building experiments based on known atomic structures, are currently being used to investigate the precise interactions of the HRV virion to the bound molecules⁷.

References

1. M. G. Rossmann *et al.*, *Nature (London)* (1985)317, 145.
2. M. G. Rossmann and J. E. Johnson *Annu. Rev. Biochem.* (1989)58, 533.
3. J. M. Greve *et al.*, *Cell* (1989)56, 839.

4. A. G. Mosser *et al.*, in B. L. Semler and E. Ehrenfeld, Eds., *Molecular Aspects of Picornavirus Infection and Detection*, Washington, D.C.:Amer. Soc. Microbiol. (1989)155.
5. B. Sherry *et al.*, *J. Virol.* (1986)57, 246.
6. R. J. Colonno *et al.*, *J. Virol.* (1989)63, 36.
7. We thank Cindy L. Music for photographic assistance. This work was primarily supported by NIH grants to TSB, TJS, and MGR, and a Lucille P. Markey Foundation award.

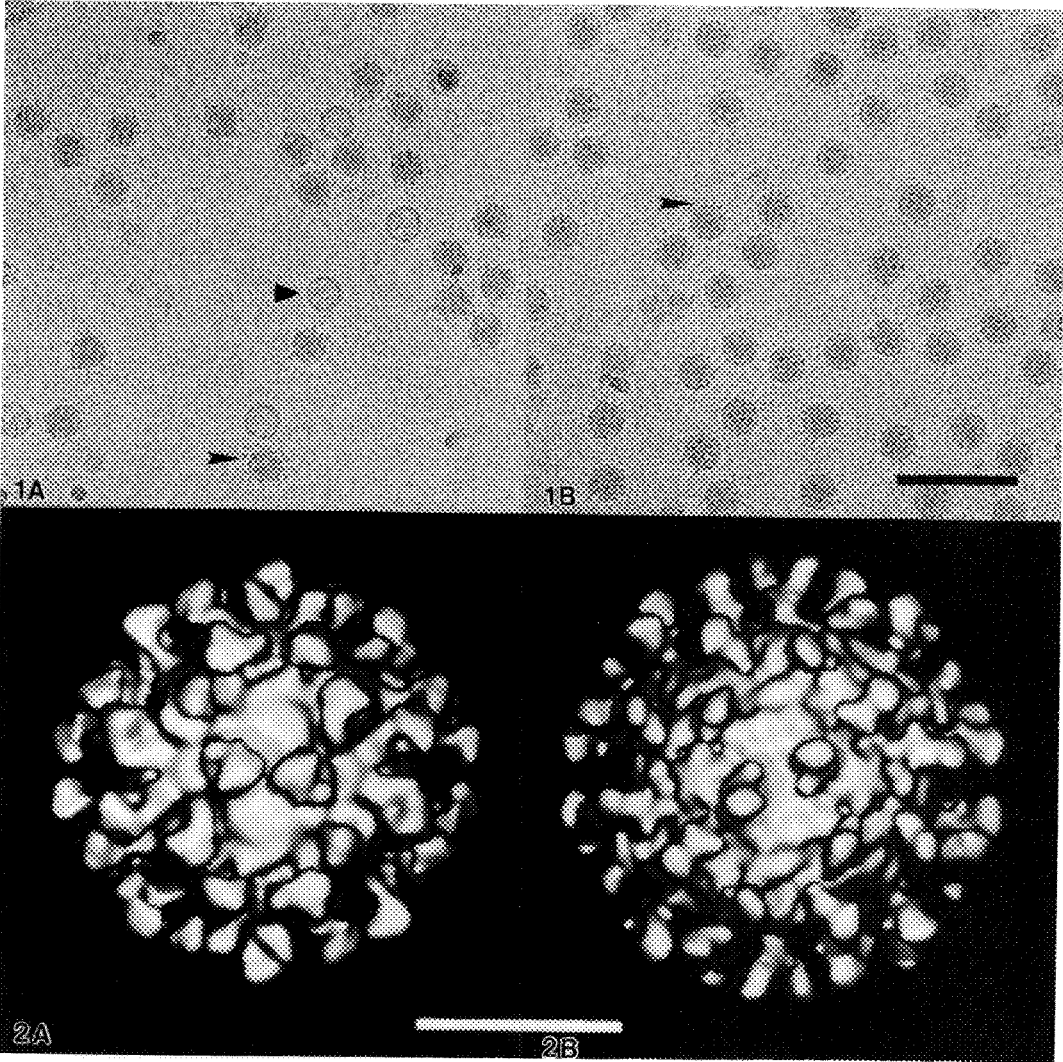


FIG. 1. Frozen-hydrated HRV-14/F_{ab}-17Ia (A), and HRV-16/D1D2 complexes (B). Arrows in each indicate F_{ab} or D1D2 molecules, respectively. Native virions have a smooth profile. Triangle (A) indicates an uncomplexed virion that has lost its ssRNA. Bar = 100 nm.

FIG. 2. Shaded, surface representations of three-dimensional reconstructions of HRV-14/F_{ab}-17Ia (A), and HRV-16/D1D2 complexes (B). Bar = 20 nm.

1.4NM GOLD CLUSTER LABELING OF tRNA AND PYRUVATE DEHYDROGENASE COMPLEX

James F. Hainfeld, Frederic R. Furuya, and Kyra Carbone

Biology Department, Brookhaven National Laboratory, Upton, N.Y., 11973

A new 1.4 nm gold cluster¹ that is stable, water soluble, and can be covalently linked to specific sites has recently been described.^{2,3} Previous applications have coupled this gold to Fab' fragments to make one of the smallest EM immunolabels yet developed. This gold differs from colloidal gold significantly: it does not aggregate proteins by non-specific binding; binding is covalent and to a specific residue (e.g., thiol, amine, or carboxyl); it is very uniform in size; its small size makes it a high resolution marker.

Previously we reported labeling of thiol bases on tRNA with undecagold clusters.^{4,5} This report focuses on the use of the 1.4nm gold cluster. *E. coli* tRNA^{Val} has a free carboxyl group at position 34 on the naturally occurring modified RNA base, uridine 5-oxyacetic acid. This was reacted with EDC (1-ethyl-3-(3-dimethylaminopropyl)carbodiimide)^{6,7} and SNHS (N-hydroxysulfosuccinimide) which produced an activated ester (N-hydroxysuccinimide ester) which then was reacted with monoamino-1.4 nm gold cluster (Fig. 1). The final reaction was chromatographed on a gel filtration column to separate unbound gold. This produced virtually 100% labeling of all tRNA molecules (Fig. 3). These were visualized in the high resolution Brookhaven STEM in unstained samples freeze dried on thin carbon films. The tRNA is only 27,000 MW and appears as a small grey mass next to the dense gold particle. tRNA content was verified by UV-visible spectra and the sample ran similarly to a native tRNA sample on a gel filtration column well separated from unbound gold clusters. Controls of tRNA alone also verified the tRNA identification by STEM mass measurement⁸. This result indicates that RNA can be labeled in high yield at a specific base with a high resolution EM label. We are investigating the further use of the labeled tRNA in higher order complexes with ribosomes.

Pyruvate dehydrogenase complex (PDC) is composed of 3 enzymes: 24 copies of dihydrolipoyl transacetylase (E2), 24 copies of pyruvate dehydrogenase (E1), and 12 copies of dihydrolipoyl dehydrogenase (E3)⁹. The normal enzyme substrate is attached to a lipoyl moiety thiol on the E2 and it is postulated the 1.4 nm long lipoyl chain acts as an arm to shuttle the substrate between enzymes. In order to locate the position of these lipoyl groups in the complex, the lipoyl thiols were reacted with the monomaleimido-1.4 nm gold cluster (Fig. 2). The product was isolated on a gel filtration column to separate unreacted gold. This produced complexes with multiple gold particles (Fig. 4). The radial position and extent of flexibility of the lipoyl arms may be largely deduced from this direct evidence.

The 1.4 nm gold cluster thus provides a high resolution site specific marker useful in obtaining submolecular structural details by electron microscopy.¹⁰

References

1. 1.4 nm gold cluster is "Nanogold", available from Nanoprobes, Inc. or E.F. Fullam.
2. J. F. Hainfeld, F. R. Furuya, and R. D. Powell, EMSA Proceedings (1991) 284.
3. J. F. Hainfeld and F. R. Furuya, J. Histochem. Cytochem. (1992)40, 177.
4. J. F. Hainfeld et al. EMSA Proceedings (1991) 44.

5. J. F. Hainfeld et al. *J. Struct. Biol.* (1991)107, 1.
6. J. V. Staros et al. *Anal. Biochem* (1986)156, 220.
7. J. Offengand et al. *Meth. Enzomol.* (1988)164, 372.
8. J. S. Wall and J. F. Hainfeld, *Annu. Rev. Biophys. Biophys. Chem.* (1986)15, 355.
9. L. J. Reed and R. M. Oliver, in *Structure, Function, and Evolution in Proteins*, Brookhaven Symposia in Biology (1968)21, 397.
10. The authors thank the BNL STEM staff: J.S. Wall, B. Lin, M. N. Simon, F. E. Kito. PDC was a gift from P. Frey. This research was supported by the Office of Health, Education, and Research of the U.S. Department of Energy.

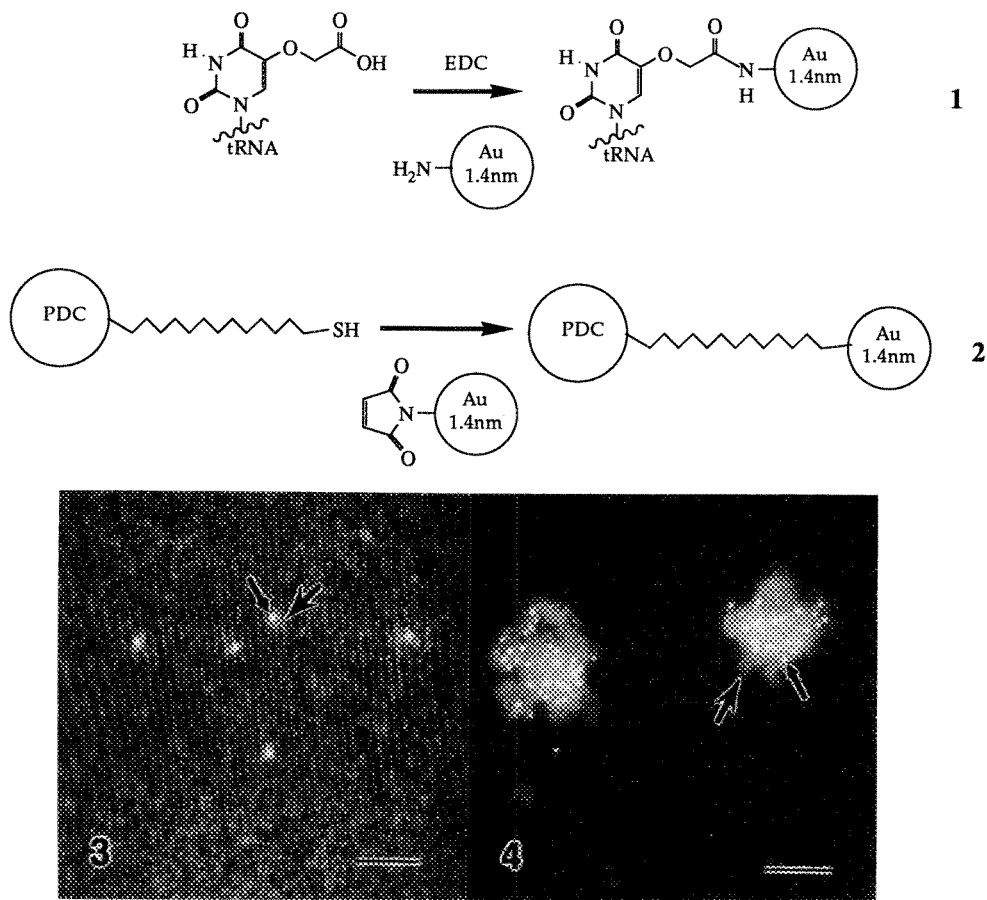


Fig. 1.--Coupling reaction of Au1.4nm to tRNA base.

Fig. 2.--Coupling reaction of Au1.4nm to pyruvate dehydrogenase complex.

Fig. 3.--STEM darkfield micrograph of tRNA (thick arrow) labeled at position 34 with the Au1.4nm cluster (thin arrow). 128 nm full width. Bar=20 nm.

Fig. 4.--STEM darkfield micrograph of PDC (thick arrow) labeled at lipoyl moieties with the Au1.4nm cluster (thin arrow). 128 nm full width. Bar=20 nm.

VISUALISATION OF THE INTERACTION OF A SPECIFIC MONOCLONAL ANTIBODY WITH THE GROEL-LIKE PROTEIN FROM *Bordetella pertussis*

M. Kessel^{*,†}, J.L. Gould-Kostka[#] and D.L. Burns[#]

^{*}Hebrew University-Hadassah Medical School P.O.B. 1172, Jerusalem 91010, Israel, [†]The Dept. of Microbiology, University of Maryland, College Park, Md. 20742 and [#]Division of Bacterial Products, FDA, Bethesda, Md. 20892

We have characterised a protein from *Bordetella pertussis*, the whooping cough agent, and found it to be almost identical with the heat shock protein from *E.coli*, GroEL.¹ These molecules, also termed chaperonins, are oligomeric proteins of approximately MW800,000 comprised of 14 subunits arranged in two rings of 7 subunits each, with a diameter of 15nm. When negatively stained, the GroEL-like molecules, examined in the electron microscope, are seen mainly in the top view clearly displaying the sevenfold symmetry, or as the less common side view with three characteristic electron dense striations separating four stain excluding regions (Fig. 1).

We have examined the effect of three different monoclonal antibodies Mab54G8, Mab47D5 and Mab45C2 on the GroEL-like protein. Only one of the antibodies, Mab54G8, showed a specific interaction with the GroEL-like protein, abolishing the ability of GroES to inhibit the ATPase activity of both GroEL from *E. coli* and the GroEL-like protein of *B. pertussis*. For electron microscopy, antibodies were mixed with GroEL-like protein at ratios of 14, 2.8 and 0.5 antibody molecules per molecule of protein. 3.0µl of the protein-antibody mixture were applied to carbon coated, collodion covered grids for 30secs and negatively stained with 1% aqueous uranyl acetate (Fig. 2). GroEL-like protein-antibody complexes were clearly seen at ratios of 2.8:1 and 0.5:1 with the expected quantitative differences between these two ratios. At the ratio of 14:1 no protein molecules were seen on the grid, and we assume that the protein-antibody complex precipitated.

Those molecules of GroEL-like protein interacting with the antibody are seen mainly in side view as chains connected end to end by the antibody. In most cases there appears to be only a single antibody attached to the GroEL-like protein at the external surface of either one of the two rings of seven subunits. In some cases (Fig. 2 inset) two antibody molecules appear to link the GroEL-like proteins. This would imply more than a single antibody attachment site per GroEL-like molecule. In a number of cases a single antibody molecule appears to connect two GroEL-like protein molecules possibly via its V-shaped Fab fragments (Fig. 3a-e). From a close examination of the antibody-GroEL-like protein pairs the location of the antibody binding site appears to be closer to the outer circumference of the molecule as if viewed from the top. Interactions of the antibody with the GroEL-like protein in top view alone are difficult to visualise however it was possible to find interactions between antibody and one molecule in top view and the other in side view (Fig. 3f-g).

Examination of the morphology of the Mab-GroEL-like protein interaction leads us to suggest that the antibody binding site(s) is apparently equivalent on the external surface of either of the two seven-fold rings.

References

1. Burns, D.L., Gould-Kostka, J.L., Kessel, M. and Arciniega, J.L. Infection and Immunity (1991) 59:1417

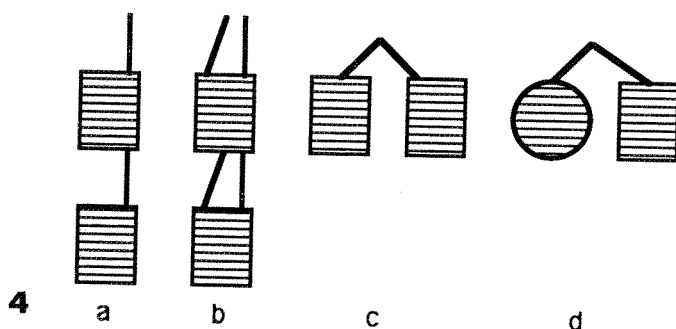
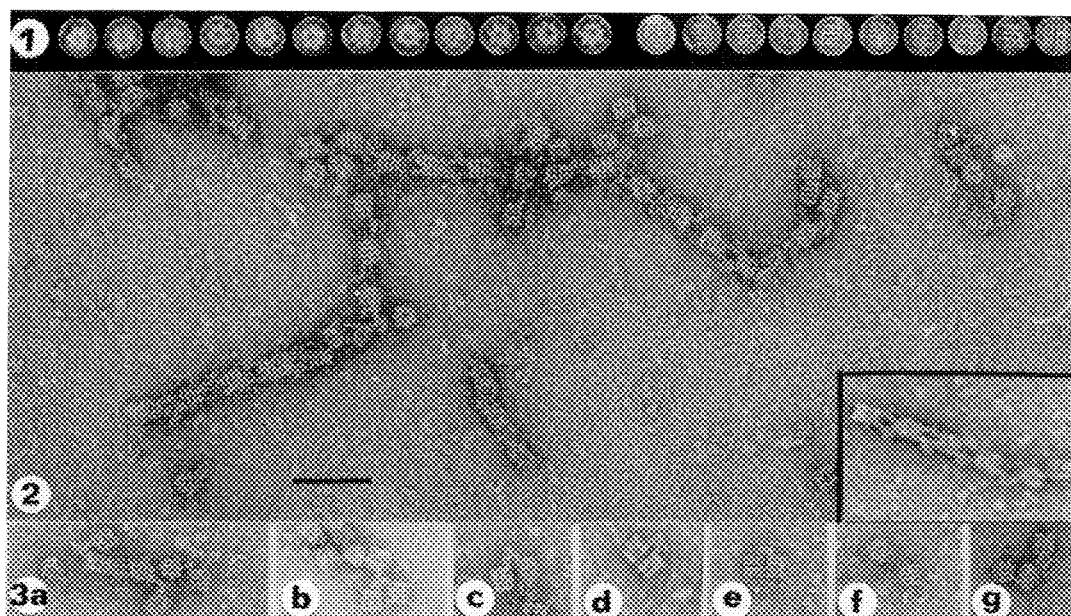


FIG. 1 -- Molecules of the GroEL-like protein from *Bordetella pertussis* seen (left) in top view showing the sevenfold symmetry, and (right) in side view showing the striated appearance.

FIG. 2 -- A field of GroEL-like protein molecules after being mixed with the monoclonal antibody Mab54G8. The GroEL-like proteins predominantly in the side orientation, are seen bound head to tail mainly by a single antibody molecule. Inset shows a chain of GroEL-like proteins linked to each other by two antibody molecules.

FIG. 3 -- (a-e) Side-views of pairs of GroEL-like protein molecules linked by the Fab fragments of a single antibody molecule. (f-g) Pairs of GroEL-like protein molecules linked by antibody with one of the pair in top view and other in side view.

All micrographs are at the same magnification. Bar equals 50nm

FIG. 4 -- Schematic of GroEL-like protein interactions with Mab54G8
(a) Fig. 2 (b) Fig. 2 Inset (c) Fig. 3a-e (d) Fig. 3f-g

CRYO-ELECTRON MICROSCOPY OF TWO-DIMENSIONAL CRYSTALS OF REDUCED TYPE B BOTULINUM NEUROTOXIN

P. F. Flicker, V.S. Kulkarni, J. P. Robinson, G. Stubbs and B. R. DasGupta*

Department of Molecular Biology, Vanderbilt University, Nashville, TN 37235

*Food Research Institute, University of Wisconsin, Madison, WI 53706

Botulinum toxin is a potent neurotoxin produced by *Clostridium botulinum*. The toxin inhibits release of neurotransmitter, causing muscle paralysis. There are several serotypes, A to G, all of molecular weight about 150,000. The protein exists as a single chain or as two chains, with two disulfide linkages. In a recent investigation on intracellular action of neurotoxins it was reported that type B neurotoxin can inhibit the release of Ca^{++} -activated [3H] norepinephrine only if the disulfide bonds are reduced¹. In order to investigate possible structural changes in the toxin upon reduction of the disulfide bonds, we have prepared two-dimensional crystals of reduced type B neurotoxin. These two-dimensional crystals will be compared with those of the native (unreduced) type B toxin².

Type B neurotoxin was reduced in sodium phosphate buffer, pH 7.3, 0.1 M NaCl, by making the solution 50 mM in dithiothreitol (DTT) and incubating for one hour at room temperature. It was then dialyzed against citrate-phosphate buffer, pH 5.6, 5 mM DTT, at 40°C.

Two-dimensional crystals were prepared by a similar method to one reported earlier³, using the ganglioside-binding property of the toxin. Crystallization of the toxin was set up in a specially designed teflon trough. The reduced toxin solution is placed in the V-shaped central compartment of the teflon trough. Electron microscope grids coated with holey carbon support film are placed along the groove of the trough in the toxin solution. About 5 μl of a solution of egg lecithin and ganglioside GT1b (5% ganglioside; total concentration 2 mg/ml) is spread on the surface of the toxin solution. The trough is sealed with a glass plate and incubated at 40°C for 15-18 hours. After incubation, the level of the toxin solution is carefully lowered using a syringe, so that crystals which have formed at the solution/air interface adhere to the grids. The grids are then frozen and observed by cryo-electron microscopy using a Philips CM-20 electron microscope equipped with a Gatan 626 cryo-transfer holder.

Images of the reduced neurotoxin show that it has formed tubes 60 to 73 nm in diameter and 0.5 to 5 μm in length (Fig. 1). An optical diffraction pattern from a typical tube (insert) shows layer lines characteristic of helical symmetry. The layer lines extend to about 20 Å resolution in the meridional direction. The spacing between layer lines corresponds to a repeat distance of 167 Å⁴.

REFERENCES

1. R. Lomneth et al., J. Neurochem. 57 (1991) 1413
2. M.F. Schmid et al., Proc. XII Int. Cong. Electron Microscopy 1 (1990) 496
3. D.G. Morgan et al., Proc. Ann. Meeting EMSA 47(1989) 1034
4. Supported by NIH grants GM25020 (GS) and NS17742 (BRD)



Figure 1: Frozen-hydrated reduced type B botulinum neurotoxin tubes suspended over a hole in the carbon support film. The protein is dark in this image. Bar = 100 Å. Insert: an optical diffraction pattern from a typical tube of reduced type B botulinum neurotoxin shows layer lines characteristic of helical symmetry.

EFFECTS OF RADIATION DAMAGE ON FROZEN HYDRATED CAPSIDS OF HSV-1

James F. Conway,* Benes L. Trus,** Frank P. Booy,* William W. Newcomb,** Jay C. Brown*** and Alasdair C. Steven*

*Laboratory of Structural Biology Research, NIAMS, and **Computer Systems Laboratory, DCRT, National Institutes of Health, Bethesda, Maryland 20892, USA. ***Department of Microbiology and Cancer Center, University of Virginia Health Sciences Center, Charlottesville, Virginia 22908

Radiation damage imposes severe limitations on the information content of frozen hydrated specimens.¹ In this context we have investigated the effects of electron radiation damage on three dimensional density maps calculated from cryo-electron micrographs, using capsids of herpes simplex virus type-1 (HSV-1) as a model system. These studies investigated the "moderate" dose regime, ie prior to the onset of severe and conspicuous structural defects such as "bubbling".

Highly purified B-capsids (DNA-free precursor capsids) were imaged by cryo-electron microscopy using a Philips EM 400T operating at 100 kV. Multiple exposures were recorded of the same field, each exposure corresponding to a dose of $\sim 6\text{ e}/\text{\AA}^2$. The first ($6\text{ e}/\text{\AA}^2$) and fifth ($30\text{ e}/\text{\AA}^2$) images were analyzed further. Corresponding portions of these images are shown in Figs. 1A and 1B respectively. The orientations of 39 particles were determined from the first image and these data were subsequently reconstructed using Fourier-Bessel techniques to generate the three dimensional structure of the capsid (for experimental procedures, see [2]). The same set of particles from the fifth exposure were also reconstructed with a uniform (small) adjustment applied to the orientations to compensate for a relative rotational offset introduced during digitization. The capsids' outer surfaces viewed down a two-fold axis of symmetry, as represented in the two reconstructions, are shown in Figs. 2A and 2B respectively. The effects of the higher cumulative dose are readily visible in both the micrographs and the reconstructions. Differences between the micrographs are most apparent at the particles' edges, where the capsomer protrusions are viewed side-on: sharp edges in the first image (Fig. 1A) become blurred in the cumulative dose image (Fig. 1B) indicating that some structural detail has been degraded. In the reconstructions, the changes are evident in the capsomers as a loss of fine detail - the prominent lobes of the single-dose capsomers (Fig. 2A) have become smoother after multiple exposures (Fig. 2B). A change is also apparent at the density features located at the sites of local three-fold symmetry ("triplexes"). In the low-dose reconstruction the triplexes show departures from three-fold symmetry (which is not imposed by the reconstruction procedure). But in Fig. 2B they are visibly rounder, and more closely approximate three-fold symmetry. However, we wish to stress that it is not yet possible to make a conclusive statement about triplex morphology.

To quantify the changes in the capsid between $6\text{ e}/\text{\AA}^2$ and $30\text{ e}/\text{\AA}^2$, phase residual functions were calculated in each case. Prior to this procedure, the interiors of the reconstructions were set to the background solvent level since the organization of the internal proteins does not exhibit icosahedral symmetry. The "emptied" reconstructions were reprojected into the orientations corresponding to each of the 39 constituent particles and then each reprojection was scaled to match the total power of the original particle. Fourier transforms were calculated for both reprojection and particle, and amplitude weighted phase differences between them were calculated as a function of Fourier spacing. These phase residual functions for all 39 such pairs were averaged for each reconstruction. Both averages are shown in Fig. 3. At low Fourier spacings, the two residuals functions are superimposable, indicating that the low resolution structure is essentially unaffected by radiation doses up to $30\text{ e}/\text{\AA}^2$. Differences are confined to spacings beginning at about 14 nm and continuing to the resolution limit of the reconstruction. A resolution estimate for each reconstruction was calculated based on the onset of the asymptotic value of the phase residual: this corresponded to $\sim 3.6\text{ nm}$ for the $6\text{ e}/\text{\AA}^2$ reconstruction and $\sim 4.6\text{ nm}$ for the $30\text{ e}/\text{\AA}^2$ reconstruction. These results demonstrate that significant structural changes are induced in protein complexes, even at moderate resolutions, in the regime of electron dose which is sufficiently low that no gross effects such as bubbling are visible in the micrographs.

References

1. M. F. Schmid *et al.*, J. Struct. Biol. 108 (1992) 62
2. F. P. Booy *et al.*, Cell 64 (1991) 1007

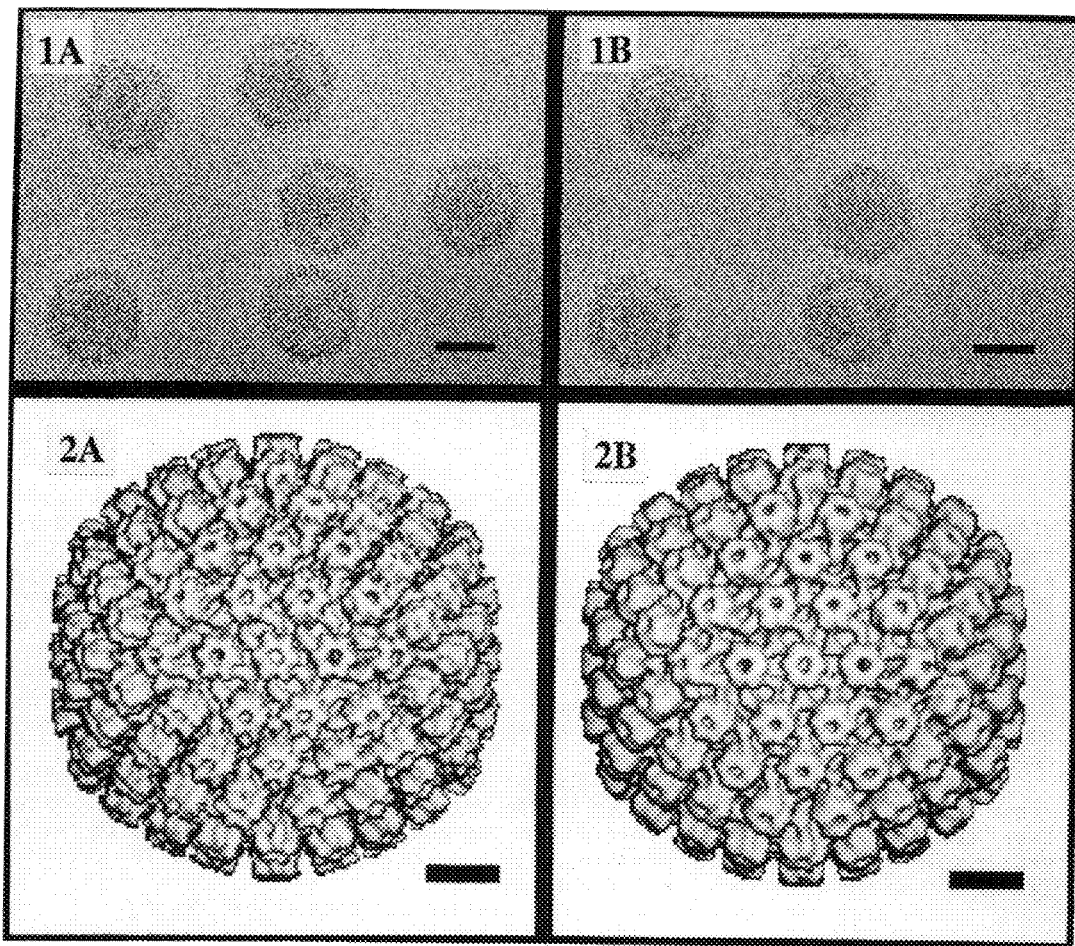
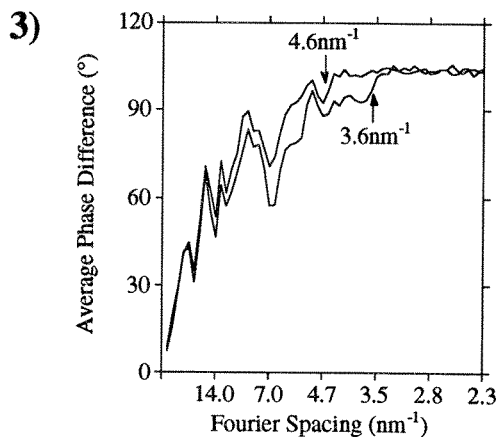


FIG. 1. Corresponding regions showing HSV-1 particles from A) single dose (6 \AA^2) micrograph, and B) multiple dose (30 \AA^2) micrograph. Bar = 100 nm.

FIG. 2. Outer surfaces of reconstructions calculated from A) single dose image, and B) multiple dose image. Bar = 20 nm.

FIG. 3. Average phase differences calculated for the reconstructions based on comparisons between particles and the corresponding reprojections. Arrows indicate estimated resolution limits of 3.6 nm^{-1} and 4.6 nm^{-1} for single dose and multiple dose reconstructions respectively.



LINEAR AND RADIAL MASS DENSITY OF VITRIFIED HELICAL SPECIMENS DETERMINED BY SCANNING TRANSMISSION ELECTRON MICROSCOPY

S. Trachtenberg¹, K.R. Leonard² and W. Tichelaar²

¹The Hebrew University-Hadassah Medical School, Jerusalem 91010, Israel; and

²EMBL, Postfach 102209, Heidelberg D-6900, Germany

We determined the linear and radial mass densities of vitrified bacterial flagella (*Salmonella typhimurium*), pili (*Escherichia coli*), Tobacco mosaic virus (TMV) and its RNA free coat protein (TMV-P) using STEM dark field images. Apart from their inherent importance and usefulness in the analysis of spherical particles, radial density functions may be potential substitutes for equatorial data in three-dimensional image reconstructions of helical particles. We explored this suitability, in terms of similarity between TMV STEM generated mass density functions and equators derived from X-ray diffraction¹.

The equator represents an axial projection of the helical particles' density much like the directly determined STEM radial density functions². Equatorial data originating from TEM images are usually considered unreliable and are either omitted or replaced by model data. The unreliability of the equator stems from its origin, due to density differences between the structure studied and the unhomogeneous environment in which it is embedded. The consequence is a misrepresentation of the relative strength of the densities in the reconstruction: overestimation at the periphery and underestimation at the center of the density map. In vitrified specimens, additional difficulties arise from uncertainties regarding the mechanism of image formation and contrast transfer characteristics of the TEM.

The cryo-STEM provides some distinct advantages in overcoming these problems: (a) specimens can be studied in the vitrified state. In fact, the very same specimen can be studied both in the TEM and the STEM. (b) The STEM has a very simple contrast transfer function; and (c) its dark field signal is proportional to the mass thickness of the specimen.

Linear mass density was found to be similar for both freeze-dried (10.3 ± 0.7 kD/A)³ and vitrified (10.2 ± 1.3 kD/A) flagellar filaments, provided that the specimens and mass standard (TMV) are close in diameter and embedded in a flat and uniform ice layer ~10 nm thicker. The linear mass density of vitrified pili, having a smaller diameter than TMV, is grossly underestimated (2.4 ± 0.7 kD/A) compared to freeze-dried ones (3.4 ± 0.4 kD/A)⁴. The signal-to-noise and contrast in vitrified specimens is lower than that of freeze dried ones.

The resolution of radial mass density profiles of freeze-dried TMV² and bacterial flagella⁵ is too low to be compatible with the higher resolution of the non-equatorial layer lines. In the radial mass density profiles of vitrified TMV, density peaks resolved in the X-ray equator¹ can be identified at radii of ~40, ~67, ~78. The relative height of the peaks is maintained as well. The inner peak, at 24 Å cannot be resolved as it is embedded in noise. We consider the data at radii smaller than 30 Å inherently too noisy to be reliable. The maximal density difference between TMV and TMV-P profiles is at a radius of ~40 Å corresponding to that of the X-ray data¹.

In the density profiles of bacterial flagella density peaks are resolved at radii of ~42, ~60, ~85, ~100 Å.

REFERENCES

1. Franklin, R.E. & Holmes, K.C. Acta Crystallog. 11:213-220. 1958
2. Steven et al. Proc. Natl. Acad. Sci. USA 81:6363-6367. 1984

3. Trachtenberg et al. J. Mol. Biol. 190:569-576. 1986
4. Freeman, R. & Leonard, K.R. J. Microsc. 122:275-286. 1981
5. Trachtenberg, S. & DeRosier, D.J. J. Molec Biol. 220:66-77. 1991
6. Lepault, J. J. Microsc. 140:73-80. 1985

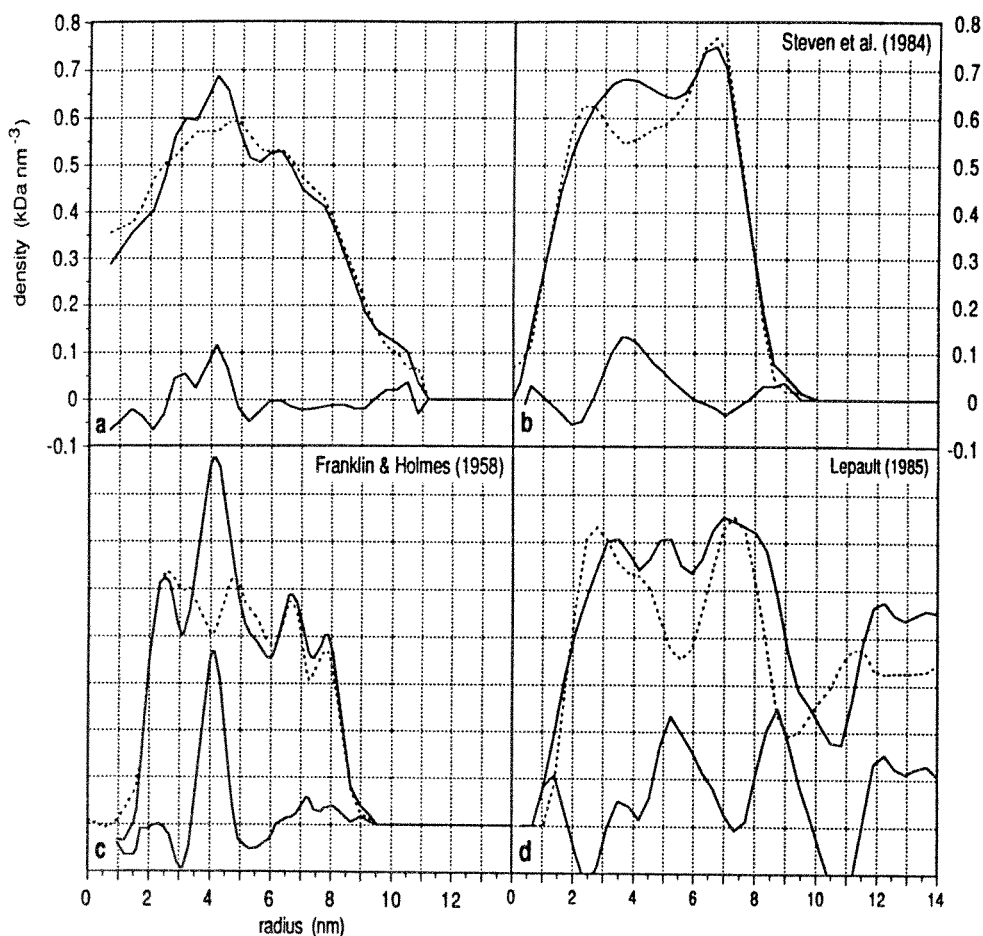


Figure 1. Radial mass density profiles of TMV and TMV-P obtained by STEM dark field of vitrified TMV particles (a) and freeze-dried ones (b)², X-ray diffraction of hydrated sols (c)¹, and TEM bright field (d)⁶ of vitrified specimens. The difference curves for the density profiles of TMV and TMV-P are added.

CORRECTION OF THE CONTRAST TRANSFER FUNCTION TO DETERMINE THE RADIAL DENSITY DISTRIBUTION OF FROZEN-HYDRATED TOBACCO MOSAIC VIRUS

Michael F. Smith and John P. Langmore

Biophysics Research Division, The University of Michigan, Ann Arbor, MI 48109-2099

The purpose of image reconstruction is to determine the mass densities within molecules by analysis of the intensities within images. Cryo-EM offers this possibility by virtue of the excellent preservation of internal structure without heavy atom staining. Cryo-EM images, however, have low contrast because of the similarity between the density of biological material and the density of vitreous ice. The images also contain a high background of inelastic scattering. To overcome the low signal and high background, cryo-images are typically recorded 1-3 μm underfocus to maximize phase contrast. Under those conditions the image intensities bear little resemblance to the object, due to the dependence of the contrast transfer function (CTF) upon spatial frequency. Compensation (*i.e.*, correction) for the CTF is theoretically possible, but implementation has been rare.^{1,2} Despite numerous studies of molecules in ice, there has never been a quantitative evaluation of compensated images of biological molecules of known structure.

We have used TMV to verify the accuracy of using electron image intensities to determine the absolute mass, mass per unit length and mass density of biological molecules. In order to test the accuracy of the results, a computer model of TMV was built from the atomic coordinates assuming uniform solvent density. The validity of the model was confirmed by comparison of x-ray scattering and predictions of the model (R -factor = 0.05). For calculation of the electron image model, elastic scattering amplitudes and intensities were used from the tables of Schaeffer *et al.*,³ and inelastic cross sections were used from experiments on biological molecules and ice. The energy filter was virtually 100% efficient in removal of inelastically scattered electrons from 150 nm-thick layers of ice (Fig. 1). The empirical mean free path for inelastic scattering in ice was measured to be 180 nm.

Energy-filtered TMV images (at defocus values of 780 nm and 4620 nm) were collected using a Zeiss EM902 operated at 80 Kev, 30,000 X magnification, 600 electrons/nm². The image resolution was determined to be 1.9 nm by the criterion of 45° phase error in the equatorial data at that spatial frequency. A radial density distribution at 1.9 nm resolution was calculated from the compensated electron images using the algorithm of Steven *et al.*⁴ and compared to that calculated from the model. First-order corrections for the CTF were necessary and sufficient for conversion of the cryo-EM images into accurate representations of the mass density. The empirical ratio of the scattering contrast to phase contrast, Q , was determined from two images of the same molecules taken at different defocus.² For TMV in 150 nm of vitreous ice the optimum value of Q was 0.14 (Fig. 2). At 1.9 nm resolution the compensated reconstruction and model had density peaks of similar magnitude at 2.4, 4.2, 6.0, and 7.8 nm radius and a central hole of 2 nm radius (Fig. 3). Equatorial Fourier transforms of the corrected electron images were in excellent agreement with predictions of the model (R factor = 0.12). Thus the uniform solvent approximation was adequate at 1.9 nm resolution to quantitatively describe x-ray scattering in liquid water and electron imaging in vitreous ice.

The absolute magnitude of electron scattering from TMV was within 3.0% of that predicted, with inelastic scattering accounting for ~ 80% of the scattering contrast. The absolute values of

contrast from RNA and protein, and the total amount of elastic and inelastic scattering agreed well with the predictions. Thus, cryo-EM can accurately determine the absolute mass, mass per unit length, and mass density of biological molecules in much the same manner as STEM, except cryo-EM can achieve appreciably higher resolution.

References

1. H. Erickson, and A. Klug, *Phil. Trans. Roy. Soc. Lond.* B261(1971)105.
2. C. Toyoshima and N. Unwin, *Ultramicroscopy* 25(1988)279.
3. L. Schafer, et al., *J. Chem. Phys.* 55(1071)3055.
4. A. Steven, et al., *Proc. Nat. Acad. Sci. U.S.A.* 81(1984)6363.

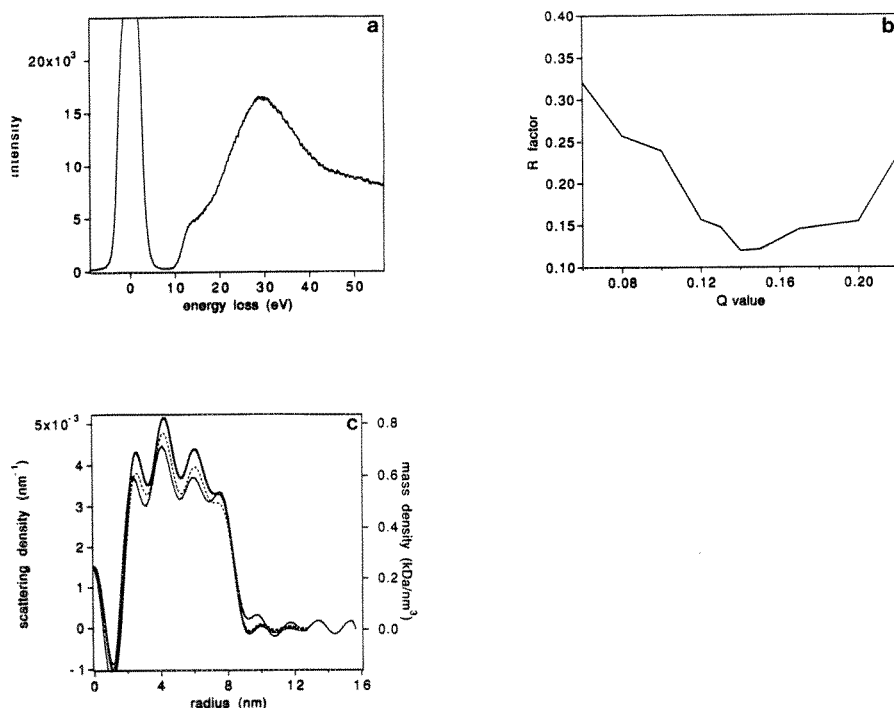


FIG. 1 Energy loss spectrum of electrons transmitted by a layer of vitreous ice about 140 nm thick through an objective aperture of $\alpha_0 = 4.12 \text{ nm}^{-1}$. For recording energy-filtered images, the spectrometer slit transmits electrons of energy loss 0 - 10 eV at the center of the image area and 0 - 2 eV at the edge of the image area. Even at the center of the images more than 99% of the energy-loss electrons are intercepted.

FIG. 2. Sensitivity of image compensation to choice of Q as measured by the crystallographic R factor. Fourier amplitudes were normalized to unity at zero spatial frequency. 1.9 nm resolution.

FIG. 3. Comparison of predicted mass densities with experimental and predicted scattering densities of TMV at 1.9 nm resolution. Predicted radial mass densities (—). Predicted radial scattering densities (---). CTF-compensated radial scattering densities (—).

CONFORMATIONAL SWITCHING IN THE FLAGELLAR FILAMENT OF SALMONELLA TYPHIMURIUM

S. Trachtenberg¹ and D.J. DeRosier²

¹The Hebrew University-Hadassah Medical School, Jerusalem 91010, Israel and

²Rosenstiel Center, Brandeis University, Waltham, MA 02254

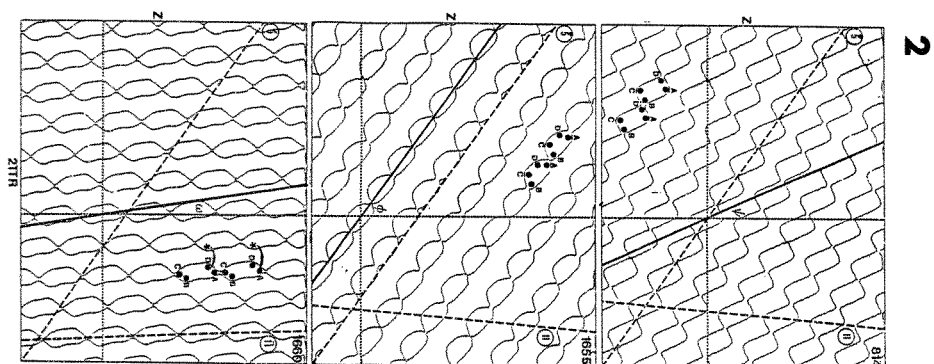
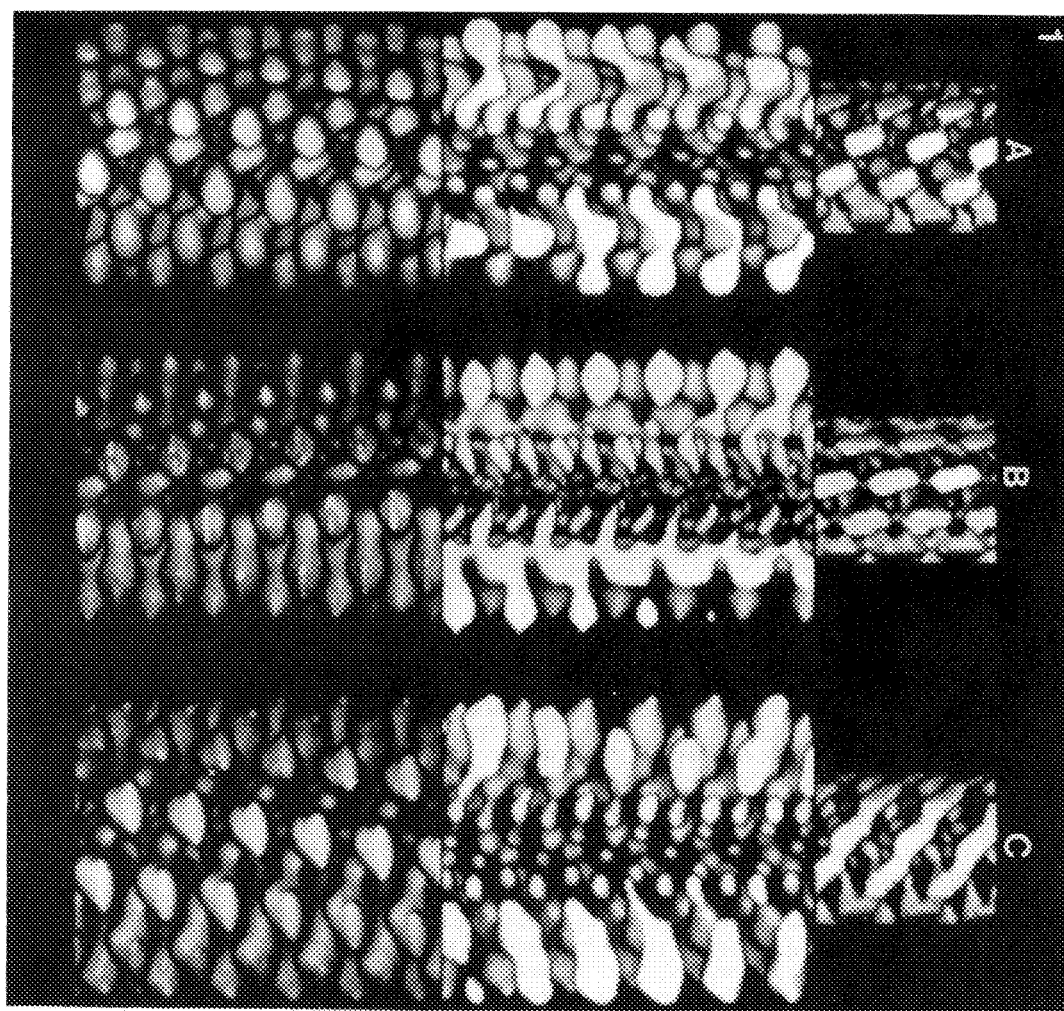
The flagellum is the bacterial organelle of motility. It is constructed from a basal body (rotary motor) a hook (universal joint), and a filament (propeller). The filament is a self-assembling helical structure usually composed of one protein species - flagellin. Flagellins from different species differ in their molecular weight and amino acid composition. However, the amino and carboxy termini of all flagellin are highly homologous ¹. The outer flagellin domain, comprising the central part of the primary sequence, is variable and not obligatory for motility ². To function as a propeller, the straight helical flagellin assembly, in which all subunits are equivalent, needs to supercoil into a corkscrew-shaped rigid structure in which the subunits are quasiequivalent. The filament can be viewed as an assembly of 11 helical protofilaments or subunit strands. Supercoiling is believed to be possible due to the coexistence of flagellin subunits in two stable and switchable conformations. Switching is cooperative and each protofilament acts as a unit. Switched protofilaments differ in length from unswitched ones, the result of which is an introduction of twisting and bending forces which can be relieved by deformation or supercoiling of the filament. If all subunits are either in the R- or L- conformation, the filament is straight and either right-handed or left-handed, respectively. Progressive switching of protofilaments results in a total of 12 polymorphic states.

Using the combined techniques of cryoelectron microscopy and image analysis, we generated three-dimensional reconstructions of straight right-handed (SJW 1655 and SJW 814) and left-handed (SJW 1660) S. typhimurium filaments. The differences between the R- and L- density maps reveal the changes accompanying conformational switching of flagellin subunits. In the case of SJW 1655 and 1660, which are derived from the same wild-type-parent SJW 1103, the switch involves a 30° rotation clockwise about a radial axis, a 38° rotation clockwise about a vertical axis, and a 50 bend of the outer domain. The intersubunit spacing changes from 51.6 Å to 52.1 Å. The 0.5 Å shortening occurs at a radius of 30 Å among the inner domains. In the middle domain, at a radius of ~65 Å, the connectivity along the 5-start direction is replaced by strong connectivity along the 11-start direction. We believe that these changes are the switch that forces changes in the inner domains ³. SJW 814, unlike SJW 1655 and 1660, can be un-locked from its straight conformation and induced to supercoil by pH and ionic strength changes. The orientation of its subunits is intermediate to that of the latter ones.

Figure 1 represents the three-dimensional reconstructions (bottom), the interior of the filaments (middle) and the density shell at 62 Å (top), exposing the middle domains for the three filaments. A-814; B-1660; C-1655.

Figure 2 shows subunit connectivity using cylindrical sections at a radius of 62 Å. The 5- and 11- start lines are indicated; the solid line indicates the axis of the middle domain and its inclination off the Z-axis or rotation about a radial axis. The subunits' binding sites are indicated by A, B, C, and D. The 1660-1655 switch (C=A to B=A) requires a larger rotation than the 1660-814 (C=A to B=D) switch.

1. Hyman, H.C. and Trachtenberg, S., J. Mol. Biol. 220:79-88. 1991
2. Trachtenberg, S. and DeRosier, D.J., J. Mol. Biol. 202:787-808. 1988
3. Trachtenberg, S. and DeRosier, D.J., J. Mol. Biol. 220:67-77. 1991



THE MICROTUBULE ASSOCIATED PROTEIN (MAP) TAU FORMS A NEW CLASS OF TRIPLE-STRANDED LEFT-HAND HELICAL FIBROUS PROTEIN POLYMER

G. C. Ruben*, K. Iqbal°, I. Grundke-Iqbal°, H. Wisniewski°, T. L. Ciardelli@, & J. E. Johnson, Jr.†

*Dept. Biology, Dartmouth College, Hanover, NH 03755; ° Instit. for Basic Res. in Develop. Disabilities, Staten Island, NY 10314; @ Dept. Pharm., Dartmouth Med. Sch., Hanover, NH, 03756; †Dept. of Integr. Biol., UC, Berkeley, CA 94720 and Dept. of Neurosci., SRI, Menlo Park, CA

In neurons, the microtubule associated protein, tau, is found in the axons.¹ Tau stabilizes the microtubules required for neurotransmitter transport to the axonal terminal. Since tau has been found in both Alzheimer neurofibrillary tangles (NFT) and in paired helical filaments (PHF),^{2,3} the study of tau's normal structure had to precede TEM studies of NFT and PHF. The structure of tau was first studied by ultracentrifugation.⁴ This work suggested that it was a rod shaped molecule with an axial ratio of 20:1. More recently, paracrystals of phosphorylated and nonphosphorylated tau have been reported. Phosphorylated tau was 90-95 nm in length and 3-6 nm in diameter where as nonphosphorylated tau was 69-75 nm in length. A shorter length of 30 nm was reported for undamaged tau indicating that it is an extremely flexible molecule.⁵ Tau was also studied in relation to microtubules, and its length was found to be 56.1 ± 14.1 nm.⁶

High resolution TEM has shown that bovine tau are 2.1 ± 0.2 nm diameter filaments which are triple-stranded left-hand helical structures composed of three 1.0 ± 0.2 nm strands [Fig. 2a & d].^{7, 8} The reported amino acid sequence of human and bovine tau have been computer processed to predict secondary structure of ~38% β -turns, ~22% alpha helix, and ~40% coil. Within the constraints imposed by the images, the secondary structure models and other structural information have been used to calculate tau's maximum and minimum length [95.8 nm and 27.8 nm].⁷ The length calculations and secondary structure form the basis for image interpretation. This work indicates that each ~1.0 nm strand is a tau polypeptide chain and that the ~2.1 nm filament is composed of three separate tau chains ($\tau\alpha_3$). Bovine tau length measurements indicate that tau trimer filaments are generally longer than a fully extended tau monomer [Fig. 1]. These measurements indicate that each trimer, $\tau\alpha_3$, is joined with other trimers to form long tau polymers, $(\tau\alpha_3)_n$. An inverse temperature transition has been found in the circular dichroism spectrum of tau indicating that its structure is less ordered below 20°C and more ordered at 37°C. The implications of this phenomenon with respect to tau's temperature dependent ability to reconstitute microtubules has been discussed and a mechanism for the possible abnormal aggregation of tau into neurofibrillary tangles in Alzheimers disease has been proposed.⁷

Since $(\tau\alpha_3)_n$ appears to be a continuous ~2.1 nm filament [Fig. 1], the ends of one $\tau\alpha_3$ smoothly intermesh with each consecutive $\tau\alpha_3$ unit. It has been suggested that the N-terminals are at one end and the C-terminals at the other end of each $\tau\alpha_3$. This should align the two cysteines in each tau sequence to form a disulfide bond with an adjacent tau monomer. Joining the tau trimers, N-terminal to C-terminal would orient the $\tau\alpha_3$ within the $(\tau\alpha_3)_n$ with the same chain polarity and equidistant spacing between microtubule binding domains. In addition the C-terminal domains are predominantly positively charged and the N-terminal domains are negatively charged so that opposite charge attraction could drive the polymerization process.⁷ Each tau monomer strand has a complex secondary structure, has little tertiary structure and assembles with a triple-stranded left hand helical quaternary structure [Fig. 2a]. This kind of protein structure is new and is quite different from the 1.5 nm triple-stranded right-handed helix of collagen [Fig. 2b] and a 2-2.5 nm triple-stranded alpha helix coiled coil suggested for alpha keratin and T3 tail fibers [Fig. 2c].^{9,10} Neither of these structures is consistent with the secondary structure predicted from tau's primary sequence, with the tau images or with circular dichroism results. Evidence for a triple-stranded left-hand helical fibrous protein like tau has not been reported before. Although the model of tau is presented as a regular structure to facilitate the calculation of its length, all of the tau samples frozen from an initial temperature of 18-20°C were only partially regular [Fig. 2d].

References

1. L.I. Binder et al., J. Cell Biol. 101 (1985) 1371.
2. I. Grundke-Iqbal et al, J Biol.Chem. 261(1986) 6084; Proc. Natl. Acad. Sci. USA. 83 (1986) 4913.
3. V. M.-Y. Lee et al., Science 251(1991) 675.
4. D.W. Cleveland et al., J. Mol. Biol. 116 (1977) 227.
5. T. Hagestedt et al., J. Cell Biol. 109 (1989)1643.
6. N. Hirokawa et al., J. Cell. Biol. 107 (1988) 1449.
7. G. C. Ruben et al., J. Biol. Chem. 266 (1991) 22019.
8. G. C. Ruben, J. Electr. Microsc. Tech. 13 (1989) 335.
9. F.H.C. Crick, Acta Crystallogr.6 (1953) 689; R.D.B. Fraser et al., Nature 193 (1962) 1052.

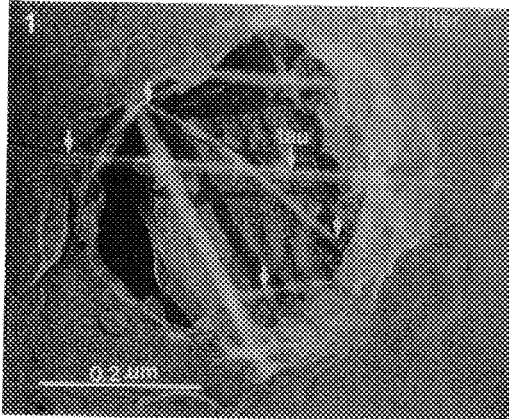
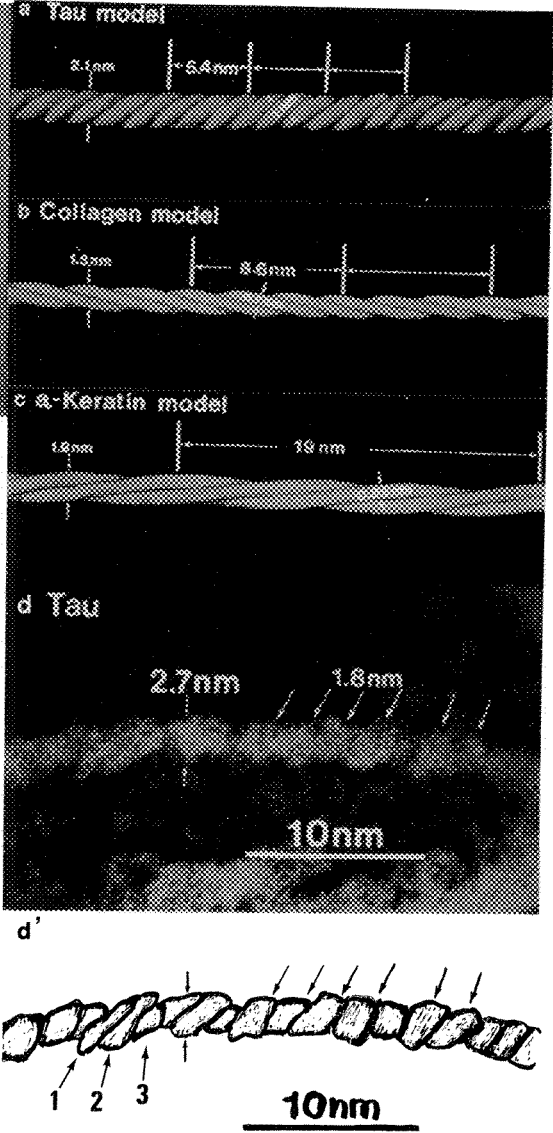


FIG. 1. Isolated Bovine Tau on a 0.1μm Millipore filter was washed with distilled water (18°-20°C) before freezing. This sample was freeze-dried and vertically replicated with 1.04 nm Pt/C and backed with 13.8 nm of evaporated carbon.⁸ The arrows point to long thin 2.1±2 nm filaments [2.7 nm with 0.6 nm Pt-C coating]⁸ which are identified as tau. The larger filaments are 10±1 nm and 13±1nm in width. Filters without tau did not contain long thin ~2.1 nm or larger filaments extending across the filter holes. The longest tau filament is ~800 nm.

FIG. 2a. This tau model idealizes the structural features of tau that have been observed in FIG. 2d. The diameter of 2.1 nm is composed of three ~1.0 nm strands which cross the filament axis at ~1.8 nm intervals with a pitch of ~5.4 nm. FIG. 2b The model for collagen is shown with a 1.5 nm diameter. Three 0.7 nm strands cross the axis at ~2.9 nm intervals along the axis with a pitch of 8.6 nm. The collagen strands also contain a triplet repeat motive, (gly-X-Y)_n where X and Y are frequently proline and hydroxy proline. These residues form a left-handed helix with a pitch of 0.87-0.90 nm with each amino acid extending 0.295-0.30 nm axially. This is very near the fully extended amino acid distance of 0.35 nm (~17% longer than 0.3 nm) found in B sheet and probably explains why rat tail collagen can only extend about 1.5-17% before it ruptures.⁷

FIG. 2c. The model for alpha keratin is shown with a 1.9 nm diameter. Three 0.95 nm strands cross the axis at ~6.3 nm intervals along the axis with a pitch of 19 nm. The coiled coil of three alpha helices has a diameter of 1.9-2.5 nm and is composed of three helices each 0.95-1.0 nm in diameter which left-hand twist around each other with a pitch of 18.6-20 nm.⁹ FIG. 2d Isolated freeze-dried vertically replicated (1.04 nm Pt-C) bovine tau prepared as in FIG.1. The 2.1 nm diameter has been enlarged by 0.6 nm of Pt-C to 2.7 nm and the ~1.0 nm strands, enlarged to 1.6 nm by 0.6 nm Pt-C, cross the axis at ~1.8 nm intervals in a partially regular region.⁸ An optical diffraction pattern of this filament was attempted and was unsuccessful. The traced tau filament is recorded below the half tone image. The edges of the strands are black and the strand widths are not perfectly regular. The arrows labeled 1, 2, and 3 point to separate strands in the triple-stranded left-handed tau helix. The coil structure or β spiral structure in the strands of tau monomer can in theory be stretched as thin as the backbone amino acid chain.



THREE-DIMENSIONAL RECONSTRUCTION OF A MAMMALIAN Z-BAND FROM SKELETAL MUSCLE

J. P. Schroeter, M. A. Goldstein, J. P. Bretaudiere, and R. L. Sass

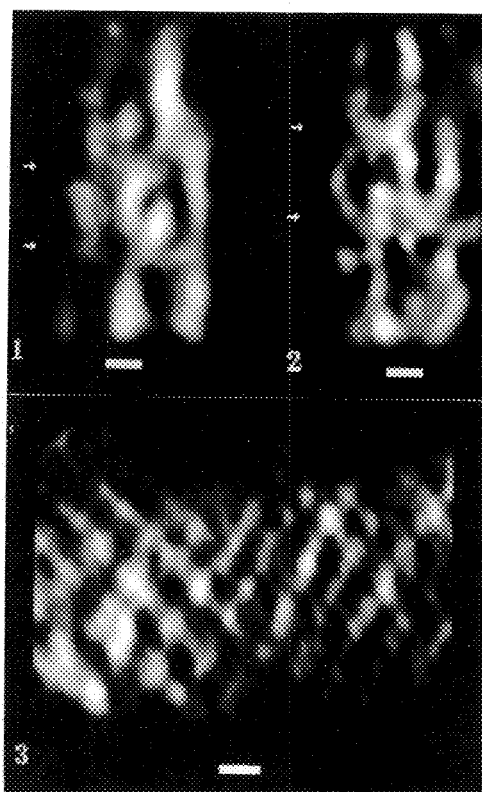
Baylor College of Medicine, University of Texas Health Science Center at Houston, and Rice University, Houston, TX

We have completed 3-d reconstructions of several regions of the Z-band in relaxed rat soleus muscle using the method of weighted back projection on a tilt series from two different longitudinal sections. Various displays of the reconstructions were interpreted after corrections for section shrinkage and comparisons to three dimensional models. Examination of cross-sections of the reconstructed Z-bands reveal that the lattice is in the small square form. We have previously shown that this form of the Z-band lattice is predominate in relaxed skeletal muscle¹. The reconstructions reveal that cross-connecting Z-filaments are arranged in opposing pairs along the axial filament. Successive pairs of filaments are rotated by ninety degrees about the axial filament, thus generating the four-fold appearance seen in the projected small square lattice.

The symmetry of the lattice, the interfilament distances, and the angle of attachment of cross-connecting Z-filaments are all affected by beam-induced section shrinkage. Shrinkage ranges from about 10% in-plane to 30-50% uniform collapse parallel to the electron beam². The thickness of the reconstructed Z-band was measured as approximately 0.6 times the thickness of the original longitudinal section before exposure to the electron beam. This is consistent with the shrinkage reported by other workers². However, the Z-band lattice spacing was measured as 18 nm, close to the 20 nm average spacing seen in 2-d analysis of Z-bands cut as cross-sections¹. Furthermore, the reconstructed cross-section showed little evidence of the difference in dimensions perpendicular and parallel to the beam expected from a uniform collapse of the section. Our data suggest that section shrinkage in the Z-band does not occur solely by means of a uniform collapse parallel to the beam.

References

1. M. A. Goldstein, et al., *Electr. Microsc. Rev.* (1990)3, 227.
2. P. K. Luther, in *Electron Tomography: Three-dimensional imaging with the transmission electron microscope*, Plenum (1991)39.



- FIG. 1--A longitudinal projection of part of one of the Z-band reconstructions, in the "chevron orientation." Two layers of cross-connecting Z-filaments are visible (arrows). In this and the other two figures, protein appears light against a dark background. Bar = 10 nm.
- FIG. 2--A longitudinal projection of the same part of the Z-band as in Figure 1, rotated ~ 90 degrees about the vertical axis. The cross-connecting Z-filaments (arrows) appear vertically offset from those of Figure 1. Bar = 10 nm.
- FIG. 3--A cross-sectional projection of a Z-band reconstruction, showing the small square form of the Z-lattice. There is little evidence of uniform section collapse parallel to the electron beam (vertical axis). Bar = 10 nm.

Z-BAND CROSS SECTIONS IN RIGOR SKELETAL MUSCLE HAVE SIMILAR DETAILED STRUCTURES AS IN TETANIZED MUSCLE

M. A. Goldstein, J. P. Schroeter, and R. J. Edwards

Department of Medicine, Baylor College of Medicine, Houston, TX 77030-3498

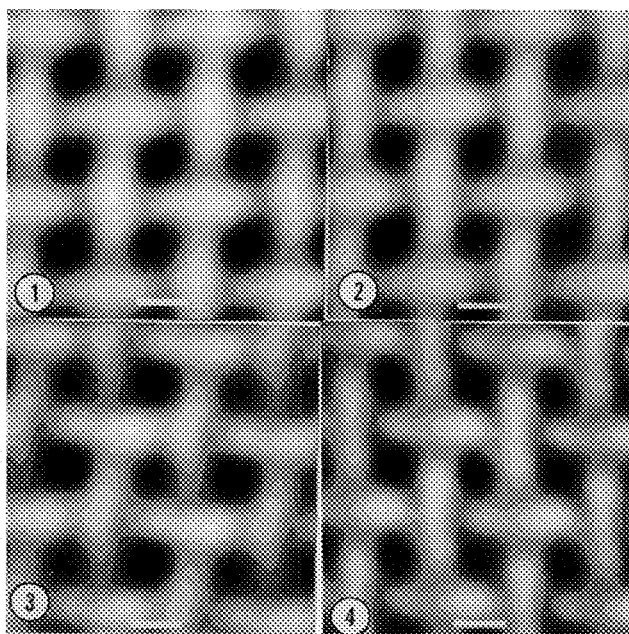
We have previously shown that two structural states of the Z-band in muscle cross-sections are related to the contractile state of the muscle¹. In skeletal muscle at rest, the Z-band is in the small square (ss) form, but tetanized muscle exhibits the basket weave (bw) form. Recently, we have shown that skeletal muscle in rigor also exhibits the bw form and dimensions².

We have used two dimensional computer enhancement techniques on digitized electron micrographs to compare the detailed structure of the tetanized and rigor Z-band lattices. Both lattice averaging and Fourier filtering techniques were used, with enhanced images displayed as grey-scale projections, as contour maps, and in false color. There is only a slight difference between the lattices produced by the two different enhancement techniques. Thus, information in the enhanced images is not likely to be an artifact of the enhancement algorithm.

The enhanced images from the tetanized and rigor muscles showed the basket weave form of the Z lattice, with four cross-connecting filaments which appear to connect each axial filament to its four nearest neighbors. Each image showed a difference in the appearance of nearest neighbor axial filaments, as previously observed. Additionally, the large diameter of the axial filaments seen in these basket weave images is consistent with previous comparative studies of the small square and basket weave lattices³. Observed differences between the rigor and tetanized enhanced images were comparable to differences seen in different regions of tetanized or rigor Z-bands. Thus, image enhancement provides no evidence for difference in the detailed structure of cross-sections of rigor and tetanized Z-bands.

References

1. M. A. Goldstein, et al., FASEB J. (1987)1, 133.
2. R. J. Edwards, et al., J. Ultrastr. Molec. Struc. Res. (1989)102, 59.
3. J. P. Schroeter, et al., JEM Tech. (1991)18, 296.



- FIG. 1.--Lattice averaged enhanced image of a Z-band cross section in rigor in rat soleus muscle. Protein is dark against a white background. Bar = 10 nm.
- FIG. 2.--Fourier filtered enhanced image of the same region as Fig. 1.
- FIG. 3.--Lattice averaged enhanced image of a Z-band cross section from tetanized rat soleus muscle. Again, protein appears dark against a white background. Bar = 10 nm.
- FIG. 4.--Fourier filtered enhanced image of the same region as Fig. 3.

WHAT HAPPENS TO THE NORMAL CYTOPLASMIC FEATURES OF FISH ERYTHROPHORES WHEN, UNDER IDENTICAL CONDITIONS OF CULTURE, THE ERYTHROPHORES ARE FUSED WITH NORMAL RAT KIDNEY CELLS?

Keith R. Porter and Karen L. Anderson

Department of Biology, University of Pennsylvania, Philadelphia PA 19104-6018

We have shown that a small population of normal cells can be cultured from the scales of the squirrel fish, Holocentrus rufus. They can be grown directly on Formvar-carbon-coated gold grids and, while still on the grids they can be fixed, stained and dehydrated for high voltage electron microscopy. One of the cell types (epidermal) spreads out on the carbon-coated surface and is thin enough in most parts for conventional (100kV) electron microscopy. The aspect of wholeness represented in these cells should not be overlooked for it provides information that might be missed in a series of thin sections where the sample is obviously smaller. Furthermore, if experimental studies are contemplated, they can be made while the cells are still alive and available for light microscopy.

These advantages of the system along with others encouraged us to attempt hybridization by fusion of two radically different cells such as the fish erythrocyte (with an abundance of pigment granules and an associated wealth of microtubules and a mechanism for bringing them into parallel array) and a normal rat kidney cell (without pigment and associated microtubules but an abundance of free ribosomes as well as ER and associated ribosomes). Both of these cell types were found to tolerate culture conditions and to fuse in small numbers under these conditions. The results of the fusions observed were nothing if not surprising. The NRK cell has a much larger nucleus and this is retained in the hybrid. The cell center of the hybrid is larger than that of the erythrocyte and spreads to dominate a larger portion of the cytoplasm. The fusion is a fusion of two cytoplasts; the larger one is associated with the NRK nucleus and a smaller one with the erythrocyte. The pigment granules in the erythrocyte vary in size from 20 to 25 μ m. They lack a typical cell membrane and have instead a cortex that is osmophilic and measures about 20nm. The hybrid cytoplasts (cells) are loaded with pigment granules and what is seemingly odd, they are all of one size, 45nm. They are extremely numerous. Unlike the pigment in the erythrocyte they are not distributed in files; instead they seem to be randomly arranged, which is also true of the microtubules. These latter in the erythrocytes are arranged parallel to radii from the cell center whereas in the hybrid and in the NRK's their orientation is essentially random. A judgemental decision on the microtubules would describe them as numerous in the erythrocyte and arranged mostly parallel; they appear to be tied to one another by short bridges. In the NRKs they are present, and frequently oriented parallel to the surface of ER membranes to which they seem attached by short bridges.¹

1. Supported by National Institutes of Health Resource Grant RR-2483.

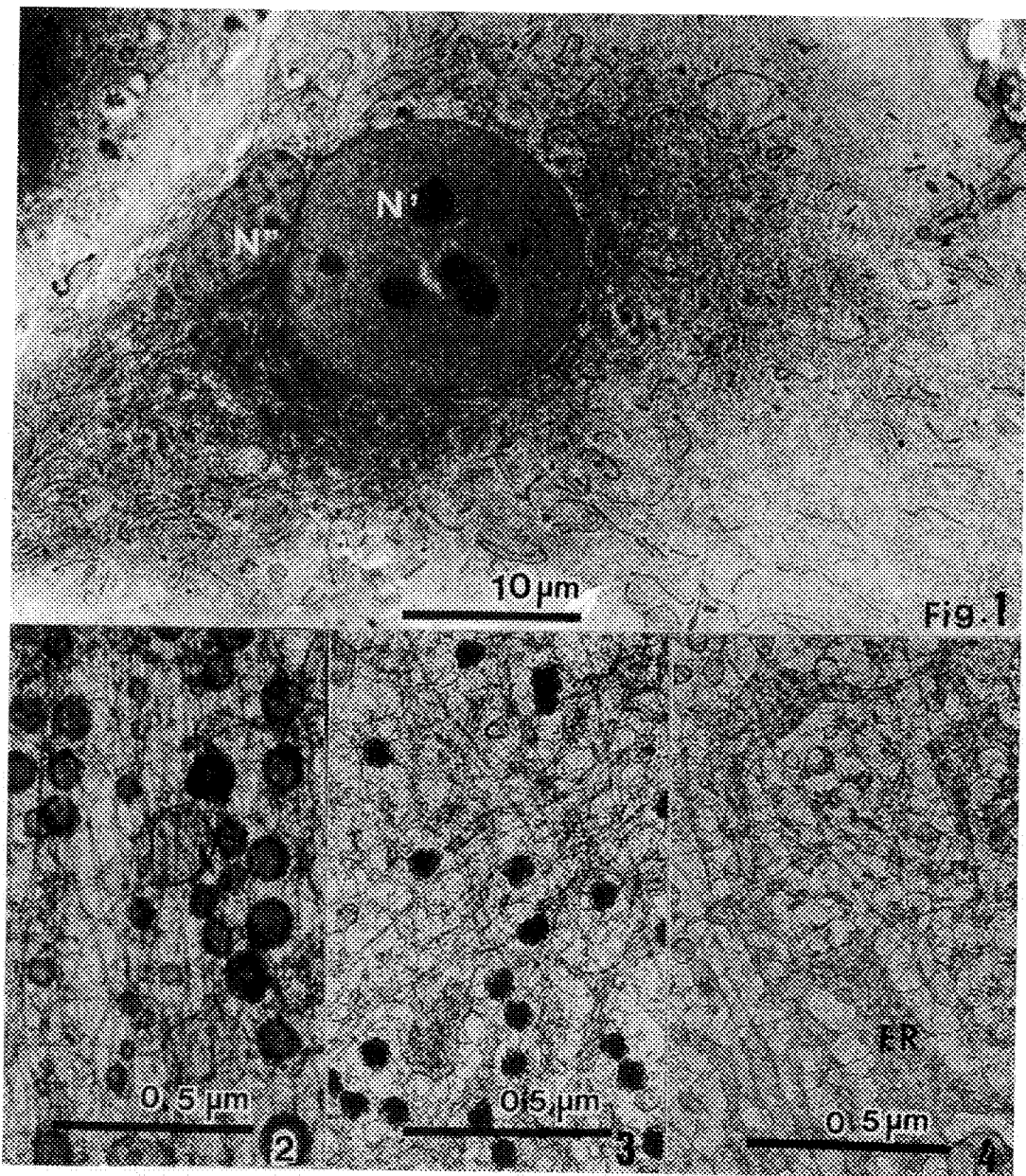


FIG. 1.--Low power micrograph of hybrid cell. Large nucleus (N') is from the NRK cell; small nucleus (N'') is from the erythrocyte.
 FIG. 2.--Cytoplasm from erythrocyte shows parallel array of microtubules with large numbers of pigment granules.
 FIG. 3.--Cytoplasm from hybrid shows randomly oriented array of microtubules; pigment granules of uniform size.
 FIG. 4.--Cytoplasm from NRK cell shows no pigment granules but an abundance of ER, free and attached ribosomes.

AN ULTRASTRUCTURAL STUDY OF SERTOLI CELLS IN TWO
GEOGRAPHICALLY ISOLATED POPULATIONS OF *Aphanius dispar*

Taher A. Ba-Omar* and Philip F. Prentis#

*Department of Biology, College of Science, Sultan Qaboos University PO Box 32486,
Al Khoud, Muscat, Sultanate of Oman. #Electron Microscopy Unit, College of Medicine
PO Box 32485, Al Khoud, Muscat, Sultanate of Oman

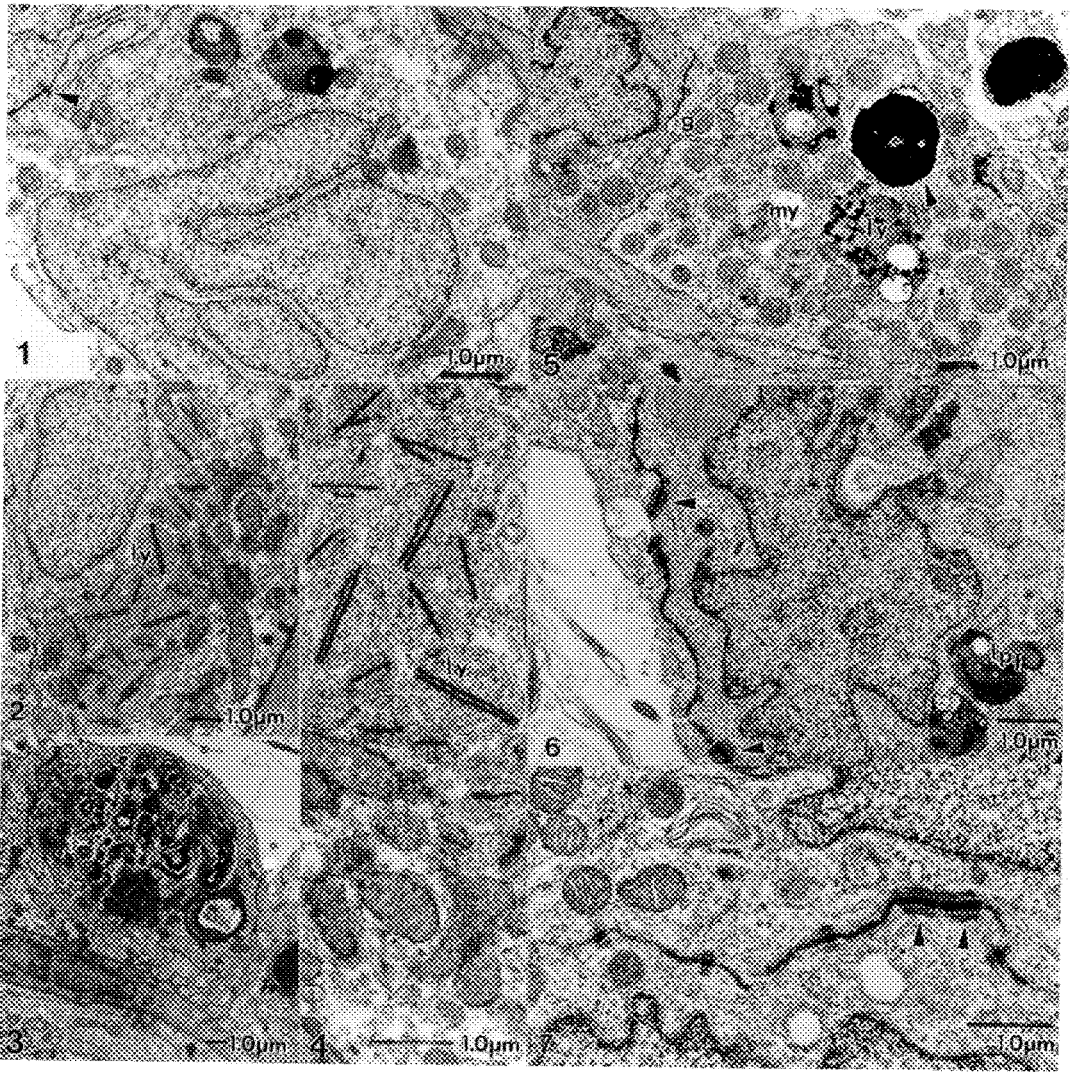
We have recently carried out a study of spermiogenic differentiation in two geographically isolated populations of *Aphanius dispar* (freshwater teleost), with a view to ascertaining variation at the ultrastructural level. The sampling areas were the Jebel Al Akhdar in the north (Group A) and the Dhofar region (Group B) in the south. Specimens from each group were collected, the testes removed, fixed in Karnovsky solution, post fixed in OsO₄, en bloc stained with uranyl acetate and then routinely processed to Agar 100 resin, semi and ultrathin sections were prepared for study.

Figs. 1-4 depict Sertoli cells of Group A, and Figs. 5-7 are of Group B. Sertoli cells of (A) are quite polymorphic in terms of size and shape of both the cell in general and the nuclei in particular, the latter being observed as rounded or even very elongated and with deep invaginations. Chromatin is finely granular and in most cells, homogenous. Few nucleoli were seen in this Group. SER, RER, ribosomes, polysomes and bundles of cytoplasmic filaments and mitochondria were abundant. The latter were generally elongated with tubular cristae and cloudy matrix. Sertoli cells adjacent to cysts containing spermatids or free spermatozoa contained in addition to those organelles aforementioned, structures containing one or several crystalline-like bodies. The structures were membrane bound and were generally observed as rounded or slightly oval. The crystal-like bodies spanned the organelle from membrane to membrane across the diameter or along the long axis. These were found exclusively in the Sertoli cells of Group (A). Lipofuchsin bodies and also many myelin figures were also noted. Cells of Group (B) closely resembled those of Group (A) in most respects with the major exception of the crystal-containing body. Additionally, myelinated figures were present in much greater abundance than in the cells of Group (A), there being large groups of Sertoli cells containing little else but myelin figures, lipofuchsin bodies and other clear evidence of lysosomal activity. The intercellular junctional complexes of both groups were extensive and comprised mainly of macula adherens desmosomes, tight junctions and in the case of Group (B) cells continuous junctions also. The desmosomes in Group (B) were in the main larger than those in Group (A), in neither group was RER found in conjunction with the junctional complexes.

We think it likely that the crystal-containing structures in Group (A) represent some form of lysosome, but in a quiescent state, as lysosomal activity appeared to be much less than in Group (B), the crystals could be a means of storing enzymic proteins - future studies using EDX spectrometry is planned. Our source references 1, 2, 3. revealed no similar organelles reported in Sertoli cells of other species.

References:

1. D.W. Fawcett, in: The Cell, 2nd Edition (1981)
2. W.S.B. Yeung, et al Cell Tissue Res. (1985)
3. L. Weiss, in: Cell and Tissue Biology (1988)



1. Typical Sertoli Cell of Group (A), note invaginated nucleus, small desmosome.
2. Sertoli cell containing many membrane-bound crystalline bodies (ly) lysosome.
3. Large quantities of myelin figures are found in some Sertoli cells Group (A).
4. High magnification of crystal-containing bodies. Note single membrane.
5. Typical Sertoli cells of Group (B), note lysosomes, myelin figure and a phagocytosed spermatid (arrowhead).
6. Group (B) cell containing lipofuscin granules and extensive intercellular junctional complexes.
7. Higher magnification electron micrograph of intercellular junctional complexes

FLUORESCENCE MICROSCOPY OF MOLECULAR ORGANIZATION AND DYNAMICS IN CULTURED CELLS

Yu-li Wang

Cell Biology Group, Worcester Foundation for Experimental Biology, Shrewsbury, MA 01545

Over the past ten years various technical advances have allowed the direct study of molecular activities in cultured cells under a fluorescence microscope. Fluorescent probes are well known for their high sensitivity, specificity and amenability to various spectroscopic analyses. When used in conjunction with low-light-level detectors and image processing computers, high resolution images of weak signals from single cells can be successfully acquired. In addition, the availability of digitized images has greatly facilitated the extraction of photometric and morphometric information.

We use Zeiss inverted microscopes equipped with epi-illuminators and Dage-MTI ISIT video cameras or Photometrics cooled CCD cameras. Custom incubator systems built on the microscope stages allow the maintenance of live cells for up to several days. The signals are processed with image processing systems (Imaging Technologies) interfaced with graphics workstations (Silicon Graphics, Model 3130 or 4D/20) or personal computers (386/33). All images are acquired by frame averaging/signal integration, followed by subtraction of the dark noise, and storage as computer files. A variation of this simple processing strategy has allowed the detection of extremely weak signals that are essentially invisible on unprocessed ISIT images. Computer programs are then used to display sequences of images as motion pictures, to measure the linear dimension and angular orientation, and to integrate intensities over defined areas.

Several types of probes have been used successfully to reveal activities in living cells. First, cellular protein components have been fluorescently labeled and microinjected into living cells¹. This has allowed the direct visualization of the redistribution of cytoskeletal structures during cell locomotion and cell division. Recently this approach was extended to RNA molecules². We (with the collaboration of Dr. T. Pederson) have demonstrated the association of fluorescent pre-mRNA molecules with putative splicing sites following the microinjection into nucleus. A closely related approach involves the use of fluorescent phalloidin, an agent known to bind specifically and tightly to actin filaments³. Furthermore, the microinjection of fragments of phalloidin-labeled actin filaments allowed the direct observation of the movement of actin filaments inside living cells⁴. Small polystyrene beads, conjugated with specific protein molecules, have also been used to study the movement of molecules on the cell surface and inside the cytoplasm.

While the above approaches rely on the direct resolution of structures, a number of methods have been used successfully to obtain information on molecular dynamics and organization beyond the resolution of the light microscope. Photobleaching of cells containing fluorescent probes can be performed with a circular or linear laser microbeam^{5,6}. Information on random movement and directional flow of molecules are obtained based on the recovery and translocation of the bleached region. A complementary approach uses "caged" fluorescent compounds, which remain non-fluorescent until the photolysis with an UV microbeam⁷. Recently, we have used fluorescence polarization microscopy to examine the organization of molecules in the cytoskeleton. Even though the structures may appear homogeneous and isotropic in direct fluorescent images, additional details can be revealed under polarized optics. Current studies using this approach indicate that it may be possible to detect very early stages of the assembly and dynamic reorganization of contractile structures in living cells.

References

1. Y.-L. Wang, *Method Cell Biol.* (1989)29, 1.
2. J. Wang, L.-G. Cao, Y.-L. Wang and T. Pederson, *Proc. Natl. Acad. Sci. USA* (1991)88, 7391.
3. L.-G. Cao and Y.-L. Wang, *J. Cell Biol.* (1990)110, 1089.
4. L.-G. Cao and Y.-L. Wang, *J. Cell Biol.* (1990)111, 1905.
5. Y.-L. Wang, *J. Cell Biol.* (1985)101, 597.
6. S.K. Stickel and Y.-L. Wang, *J. Cell Biol.* (1987)104, 1521.
7. J.A. Theriot and T.J. Mitchison, *Nature* (1991)352, 126.

ULTRASTRUCTURAL ANALYSIS OF THE SPATIAL DISTRIBUTION OF MRNA

Gary Bassell and Robert H. Singer

Dept. of Cell Biology, Univ. of Mass. Medical School, Worcester MA 01655

We have been investigating the spatial distribution of nucleic acids intracellularly using *in situ* hybridization. The use of non-isotopic nucleotide analogs incorporated into the DNA probe allows the detection of the probe at its site of hybridization within the cell. This approach therefore is compatible with the high resolution available by electron microscopy. Biotinated or digoxigenated probe can be detected by antibodies conjugated to colloidal gold. Because mRNA serves as a template for the probe fragments, the colloidal gold particles are detected as arrays which allow it to be unequivocally distinguished from background.

Because of the high magnifications required to visualize individual colloidal gold particles, it was difficult to obtain an overview of the cell and the distribution of particular mRNA sequences. In addition it was not possible to optimize this approach for the ultrastructural analysis without tedious quantitation of the gold. Therefore we developed an approach using silver enhancement of colloidal gold to observe the distribution of mRNA throughout the cell using a poly(dT) probe to the poly(A) mRNA. The probe was synthetically labelled with a single biotin or digoxigenin. Due to the high abundance of poly(A) mRNA within the cell, a strong signal was observed in single cells with minimal background obtained using a control poly(dA) probe. The same cells could be viewed either by light microscopy or EM and revealed the spatial distribution of mRNA in the cell.

MRNA has been previously shown to be cytoskeletal associated. Triton extraction of the chicken or human fibroblasts, fixation by glutaraldehyde and hybridization to poly(dT) showed that the signal was substantially the same as with unextracted cells. This afforded the opportunity to investigate the disposition of poly(A) mRNA with respect to the cytoskeleton in order to define the nature of this association, and perhaps the cytoskeletal-associated molecules involved. It was apparent that the mRNA was located predominately at intersections of cytoskeletal filaments. In order to ascertain which of the three major cytoskeletal filaments were involved; actin, vimentin or tubulin, a double labelling procedure was employed using 5nm gold for protein and 10nm gold for mRNA. It was found that approximately 70% of the vertices were composed of actin filaments and 30% were vimentin filaments. The site of mRNA at the intersections of actin filaments suggests that actin-binding proteins may be involved in the construction of the actin-mRNA complex. Several actin-binding proteins were assessed for their colocalization with mRNA by double-labelling and the protein filamin (ABP 280) was found to coincide with the mRNA signal. This protein is a homodimer responsible for actin crosslinking.

In order to determine how many poly(A) molecules exist per vertex, two poly(dT) probes each labelled with a different hapten were hybridized simultaneously and each detected with a separate antibody with its respective colloidal gold size. The majority of vertices contained a single colloidal gold size, suggesting that few molecules, most likely only one, exist at each vertex. Nonetheless a significant number of vertices contained at least two molecules of poly(A).

This work suggests that functional domains exist within the cytoskeleton which anchor mRNA. These domains are the sites of active protein synthesis, as evidenced by the presence of polysomes at these vertices. Presumably other translation factors can be concentrated here. The presence of a subcompartment within the cytoskeleton provides a structural basis for mRNA segregation within the cell. The assembly of macromolecular structures within the cell may be facilitated by the sorting of the functionally related mRNAs to these sites. To this end, one might expect mRNAs sequestered within the same vertex or in nearby vertices to be functionally related. It is known that actin mRNA is located at the lamellipodia of motile cells where G-actin is actively polymerizing into F-actin. Therefore a relationship exists between the site of synthesis of a protein and its site of function. The mechanism by which this occurs is unknown, but the vertex may represent an addressing system, perhaps distinguished by different actin-binding proteins, which can provide for mRNA sorting and anchoring.

References

- Lawrence JB and Singer RH. Intracellular Localization of Messenger RNAs for Cytoskeletal Proteins. Cell 45:407-415, 1986.
- Singer RH, Langevin GL, and Lawrence JB. Ultrastructural Visualization of Cytoskeletal mRNAs and their Associated Proteins Using Double-Label in situ Hybridization. J Cell Biol 108:2343-2353, 1989.
- Singer RH, Lawrence JB, Silva F, Langevin GL, Pomeroy M and Billings-Gagliardi S. Strategies for Ultrastructural Visualization of Biotinated Probes Hybridized to Messenger RNA in situ. Current Topics Microbiol Immunol 143:55-69, 1989.
- Silva F, Lawrence JB, and Singer RH. Progress Toward Ultrastructural Identification of Individual mRNAs in Thin Section: Myosin heavy-chain mRNA in Developing Myotubes. Techniques in Immunocytochemistry 4:147-164, 1989.
- Pomeroy M, Lawrence J, Singer R and Billings-Gagliardi S. Electron microscopic localization of myosin heavy chain mRNA in embryonic muscle tissue. Dev Biol 143:56-67, 1991.
- Bassell G and Singer R. Ultrastructural in situ hybridization using immunogold. In: Immunoelectron microscopy in virus diagnosis and research, A.D. Hyatt and B.T. Eaton, CRC Press, 1992.
- Sundell C and Singer R. Requirement of microfilaments for actin mRNA sorting. Science 253:1275-1278, 1991.

ULTRASTRUCTURAL ANALYSIS OF EARLY PRE-MESSENGER RNA PROCESSING EVENTS USING THE MILLER CHROMATIN SPREADING METHOD

Ann Beyer and Yvonne Osheim

Dept of Microbiology, University of Virginia, Charlottesville, VA 22901, 804-924-5611

We use the Miller chromatin spreading technique for electron microscopic visualization of transcriptionally active genes.¹ In this method, cells are hypotonically disrupted and cellular contents are diluted into water at pH 8-9 and fixed with formaldehyde. The dispersed cellular contents are centrifuged onto a carbon-coated EM grid; the majority of the material that is deposited on the grid consists of entangled masses of dispersed chromatin, some regions of which are transcriptionally active (Fig 1). Our interests lie in ultrastructural analysis of co-transcriptional RNA processing events on pre-mRNA transcripts, which we analyze by mapping structural features on successive nascent transcripts on a given gene.² The two processing events that we have been able to study by this approach are the removal of introns by splicing³ and generation of the 3' end of the transcript.

We have found that the determinative step in splicing, i.e., splice site selection by deposition of the splicing machinery, typically occurs within seconds of 3' splice site synthesis for a given intron and is independent of intron length. This phenomenon has been examined in *Drosophila* tissues, in *Xenopus* oocytes and in virally infected Hela cells. The actual splicing step may or may not occur rapidly after splice site selection. That is, in *Drosophila* and Hela cells, splicing typically is complete within about 3 min of synthesis of the intron, or within about 2 min of deposition of the spliceosome. However, in late stage 6 *Xenopus* oocytes, the removal of the intron frequently is delayed until 10 min or longer after spliceosome deposition. Because of this lag in actual intron removal, most splicing occurs post-transcriptionally in *Xenopus* oocytes, although some splicing is co-transcriptional, as is the rule in *Drosophila* and Hela cells. Thus, we observe no evidence for obligatory transport of pre-mRNA transcripts from their site of synthesis for splicing in nuclear domains enriched in splicing components. Furthermore, by dispersing cells at pH 7 instead of pH 9, we have found that the bulk of the spliceosome appears to be deposited as a single unit, making contacts at both 5' and 3' splice junctions and concomitantly looping out the intron. There does not appear to be stepwise assembly of snRNPs on the nascent transcripts, with the exception of a small particle that is deposited at the 5' splice site, is independent of the presence of the 3' splice site, and may correspond to U1 snRNP. We have also examined transcript patterns at the 3' ends of genes with the goal of understanding the temporal and spatial relationships between cleavage at the poly(A) site and transcription termination. The termination process is poorly understood for eukaryotic Polymerase II genes, but has been shown in several cases to be dependent on a functional poly(A) site.⁴ It typically is assumed that cleavage at the poly(A) is the event that releases the transcripts from the template. However, our observations of specific genes in both *Drosophila* and *Xenopus* oocytes suggest that transcription termination is more frequently responsible for transcript release and that cleavage at the poly(A) site is post-transcriptional.

References

1. O. L. Miller, Jr and B. R. Beatty, *Science* (1969)164, 955.
2. Y. N. Osheim and A. L. Beyer, *Meth. Enzymol.* (1989)180, 481.
3. A. L. Beyer and Y. N. Osheim, *Genes & Dev.* (1988)2, 754.
4. N. J. Proudfoot, *Trends Biochem. Sci.* (1989)14, 105.



FIG. 1.--TEM of *Drosophila* embryo chromatin showing 5 active genes (curved arrows). The two genes at the upper left are transcribed in opposite directions from the same chromatin strand; the 2 long genes at the bottom are identical genes on sister chromatid strands. Arrowheads indicate splicing complexes at the base of intron loops. Bar = 1 μ m

DISTRIBUTION AND FUNCTION OF NON-HISTONE PROTEINS IN HUMAN CHROMOSOMES

W.C. Earnshaw & C.A. Cooke

Dept. of Cell Biology and Anatomy, Johns Hopkins School of Medicine, Baltimore, MD 21205

The role of non-histone proteins in the structure and movements of mitotic chromosomes remains poorly understood. We describe here experiments aimed at characterization of the distribution of two very different classes of these proteins. The first is composed of integral components of the centromere (or primary constriction). The second class consists of proteins that we have termed "chromosome passenger proteins". These proteins are chromosomal during most of the cell cycle, but appear to be associated with the cytoskeleton during anaphase and telophase.

The centromere regions of chromosomes perform three essential functions in mitosis. (1) They form the site of attachment of the chromosomes to the mitotic spindle. (2) They contain the mechanochromal motor molecules that are responsible for the movements of the chromosomes along microtubules. (3) They regulate the pairing of sister chromatids during mitosis. The first two of these mitotic functions are properties of a disk-shaped structural specialization, the kinetochore, which is located at the surface of the centromeric heterochromatin.

We have begun to identify and characterize centromeric proteins primarily through the use of sera from autoimmune patients with scleroderma spectrum disease. We showed that these sera recognize a group of centromere protein (CENP) antigens. Here we describe experiments characterizing CENP-B (80 kDa) and CENP-C (140 kDa) in greater detail.

cDNA cloning experiments reveal CENP-B to be a multi-domain protein of MW 65,000 whose most notable structural features are two large highly acidic regions in its carboxy-terminal region. Anti-CENP-B monoclonal antibodies show great variability in their binding to different chromosomes, suggesting that the binding of CENP-B to the centromere might involve recognition of specific DNA sequences. This has been confirmed by Okazaki and coworkers, who demonstrated that CENP-B recognizes a specific 17 base pair "box" present in a subset of α -satellite DNA monomers. In studies to be presented here, we have used immunoelectron microscopy to demonstrate that CENP-B is distributed throughout the heterochromatin beneath the kinetochore (Fig. 2). We now believe that CENP-B binding may cause profound changes in the chromatin structure of centromeres.

CENP-C is a basic (pI - 9.4) protein of MW 107,000 that is located in the region immediately beneath the outer kinetochore plate. Thus CENP-C may be a component of the inner kinetochore plate (Figs. 1,3). CENP-C is therefore the first component of either kinetochore plate to be identified. CENP-C also binds DNA *in vitro*, and it is tempting to speculate that this DNA may represent the human homologue of yeast CEN DNA.

The INCENPs (two polypeptides of 135 and 150 kDa) enter mitosis as tightly bound chromosomal proteins. We have used confocal microscopy and immunoelectron microscopy to provide a detailed picture of the intracellular location of these proteins during mitosis. In early metaphase, the INCENPs gradually become concentrated at the centromeres, forming a ring at the center of the metaphase plate. They then separate from the chromosomes, so that by late metaphase they lie between the chromosomes in streaks that traverse the plate parallel to the spindle axis. During anaphase and telophase the INCENPs are associated with the central spindle and cell cortex at the contractile ring (Figs. 4, 5). Together, these results suggest that the INCENPs may represent a new class of "chromosomal passenger" proteins that are carried to the spindle equator by the chromosomes and subsequently perform a cytoskeletal role following their release from the chromosomes. This model is supported by recent cloning experiments that reveal regions of significant sequence similarity between INCENPs and myosin.

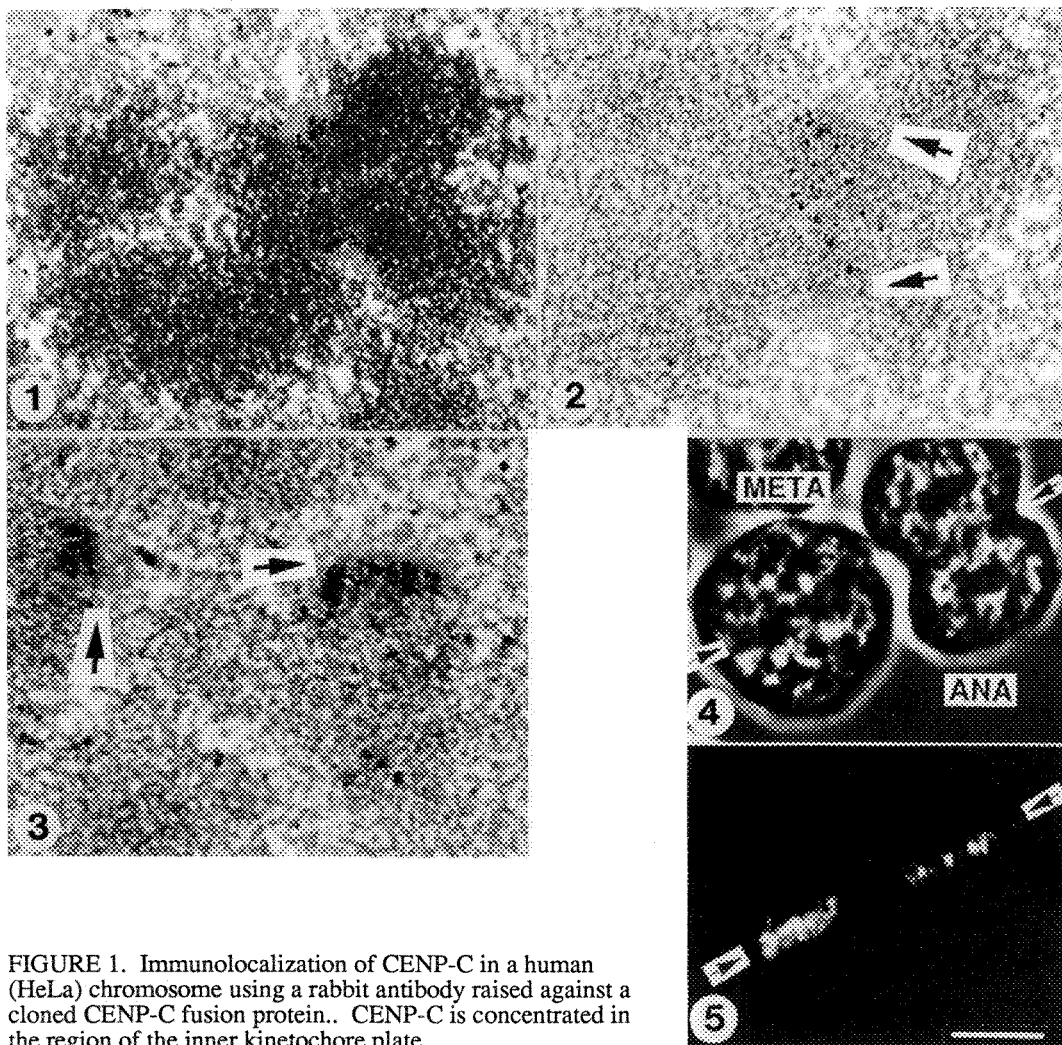


FIGURE 1. Immunolocalization of CENP-C in a human (HeLa) chromosome using a rabbit antibody raised against a cloned CENP-C fusion protein.. CENP-C is concentrated in the region of the inner kinetochore plate.

FIGURE 2. Immunolocalization of CENP-B on a human chromosome using a rabbit antibody raised against a cloned CENP-B fusion protein.. This experiment was performed in parallel with that shown in Fig. 3. CENP-B is distributed through the interior of the centromere in an area extending between the two sister kinetochores (arrowed).

FIGURE 3. Higher magnification of the CENP-B localization. Note that the outer kinetochore plate (arrowed) is not labeled.

FIGURE 4. Phase contrast micrograph of two chicken cells in metaphase (META) and anaphase (ANA) of mitosis.

FIGURE 5. Localization of the INCENP antigens (using a rabbit antibody raised against a cloned INCENP fusion protein.) in these two cells as observed by laser scanning confocal microscopy.

FLUORESCENCE IN SITU HYBRIDIZATION: INVESTIGATING THE FUNCTIONAL ORGANIZATION OF GENES AND RNAS

Jeanne Bentley Lawrence, Kenneth C. Carter, John R. Coleman,
Michael Gerdes, Carol V. Johnson and Yigong Xing

Dept. of Cell Biol., U. of Mass. Med. Center, Worcester MA 01655

Developments in fluorescence in situ hybridization accrued over recent years now make it possible to detect and precisely localize nucleic acid sequences with a sensitivity sufficient to detect single copy genes or their primary transcripts (Reviewed in Ref.1). These advances have essentially revolutionized the field of molecular cytogenetics, providing not only a powerful approach to gene mapping and genetic diagnosis, but a new way to probe the higher level organization of the nucleus and chromosome. The methodology we and others primarily utilize is based on non-isotopic labelling of DNA probes with moieties such as biotin or digoxigenin, which are detected by fluorochrome-conjugated avidin or anti-digoxigenin antibodies. Alternatively, probes directly labeled with fluorochromes have recently become available. Appropriate modifications of protocols allow either cellular DNA or RNA to be targeted, and hybridization can be to intact cells, nuclei, or chromosomes.

Our laboratory has been developing and applying in situ hybridization procedures for two major areas of related interests: human gene mapping and genome/nuclear organization. Fluorescence in situ hybridization provides a very high-resolution and rapid approach to map genes on banded or unbanded chromosomes and has made an important contribution to the current world-wide effort to map the entire human genome in terms of the linear arrangements of genes and DNA segments on chromosomes. In addition, far greater resolution is provided by hybridization to decondensed interphase chromatin, where DNA segments separated by as little as 50 kilobases are visually resolvable by light microscopy. In addition to large scale mapping of chromosomes, these techniques can greatly aid the search for specific disease genes because they provide a straightforward rapid approach for screening clones close to a chromosomal marker for a disease.

A major effort of the lab is also directed at understanding the organization of the genome in its functional state, in terms of the three dimensional organization of different classes of DNA within the interphase nucleus. Because RNA metabolism is critical to the function of the genome, our work on nuclear organization takes an integrative approach in which localization of specific DNAs, RNAs, and proteins are analyzed in relation to one another. The intranuclear location of specific classes of RNA is of particular interest in that this provides insight into sites of transcription, processing, and transport of RNAs. Nuclear poly(A) RNA, which represents approximately 90% of pre-mRNA, is localized within discrete nuclear "transcript domains" which also contain concentrations of pre-mRNA splicing components². These transcript domains are non-randomly positioned with respect to the underlying genome, are most likely regions of pre-mRNA processing and, possibly, also transcription. Three dimensional analyses indicate that these domains are interiorly located, with much less concentrated sites of poly(A) RNA observed throughout the nucleoplasm. Individual species of pre-mRNA can be visualized by fluorescent in situ hybridization as discrete accumulations of transcripts which often form curvilinear "tracks".

While first observed for specific viral transcripts¹, we have now investigated the distribution of several endogenous RNAs. Generally, when using gene-specific genomic probes, one or two discrete RNA foci or tracks are seen surrounded by weaker diffuse signal throughout the nucleus. The morphology of these tracks varies considerably from cell to cell. Double label experiments show that both introns and exons are present within these foci, but that introns are not present throughout the full length of more elongated tracks defined by an exon probe. In addition to the foci, intron probes give a readily apparent punctate signal throughout the nucleus, whereas exon probes label primarily the nuclear foci or tracks and the cytoplasm. These results provide direct evidence that these tracks are sites of primary transcripts undergoing processing, and further indicate that exon sequences remain localized while introns may be free to diffuse after splicing. Double-label experiments also show that genes and their cognate RNA foci are coincident, providing the first direct evidence that these RNA accumulations reflect sites of transcription.

Another of our major areas of interest is how the spatial organization of DNAs and RNAs within nuclei is established and maintained. A potentially powerful approach to such questions is provided by coupling in situ hybridization with now well-established biochemical fractionation techniques used in defining the nuclear matrix. Using such an approach we have shown that tracks of specific viral RNAs are completely preserved both quantitatively and morphologically throughout fractionation procedures which remove 95% of nuclear protein, phospholipid and DNA³. We have also, more recently, developed methods to directly examine the positions of individual genes on loops of DNA which are anchored to the matrix. This approach has allowed us to demonstrate a differential packaging of specific genes during the cell cycle by examining in S-, non S-phase, and mitotic cells, genes for NGFR, myosin heavy chain, RPG-6, U, snRNA, dystrophin, and histone. Additionally, there is a clear difference in the packaging of these genes correlated with their transcriptional activity. (Supported by NIH grant HG00251)

References

1. JA McNeil et al. (1991) Genet. Anal. Techniq. Applic. 8:41.
2. KC Carter, K. Taneja, JB Lawrence (1991) J. Cell Biol. 115:1191
3. Y Xing and JB Lawrence (1991) J. Cell Biol. 112:1055.

NEW VIEWS INSIDE CELLS WITH THE DIGITAL IMAGING MICROSCOPE

F.S. Fay,* E.D.W. Moore,* D. Elliot,** M. Rosbash,** K. Carter,*** J. Lawrence,**
R. Lynch,**** L. Lifshitz* and K. Fogarty*

* Biomedical Imaging Group, Univ. of Mass. Medical School, Worcester, Mass

** Dept. of Biology, Brandeis University, Waltham, Massachusetts

*** Dept. of Cell Biology, Univ. of Mass. Medical School, Worcester, Mass

**** Dept. of Physiology, U. of Arizona Health Sciences Center, Tucson, Arizona

The digital imaging microscope has been developed as a tool for understanding changes in molecular distribution underlying changes in cell function. It has evolved principally to meet the needs and opportunities afforded cell biologists to analyze molecular distribution in single cells with an ever increasing range of bright fluorescent indicators having a high degree of molecular specificity. The operation of the digital imaging microscope usually involves four basic steps: 1. image acquisition; 2) image restoration, to reverse the distortion introduced by the optics; 3) image feature extraction, to identify and isolate important characteristic features of an image, and; 4) visualization and interactive analysis of the image. These procedures differ depending on the nature of the specimen and the questions being asked. It is this malleability of the digital imaging microscope that makes it such a powerful and versatile tool.

A number of problems have recently been investigated with the digital imaging microscope, all of which have in common that they involve the analysis of distribution of two or more molecular species with respect to one another inside a cell. Such information is vital in understanding the organization of the nucleus for production and export of RNA, the coupling of glycolytic and oxidative metabolism, and the coupling of pumps and exchangers involved in regulating $[Na^+]$ and $[Ca^{2+}]$ inside the cell. These processes are thought to come about because groups of key proteins are organized, often in a dynamic manner, into characteristic clusters that subserve one or several steps in a multi-step process that give rise to a specific cell function. It has therefore become increasingly important to understand how proteins or other molecules in cells are organized with respect to one another.

Specific hardware and algorithms have therefore been developed in order to obtain such information from cells. As a first step in this process, images at multiple focal planes are obtained with a unique wide field microscope capable of obtaining images of molecular distribution in as brief as 1 msec. and in collecting a series of such images at multiple focal planes in as short as 20 msec. The information contained in this series of optical sections is then used in conjunction with information about the microscope's 3D blurring function to obtain a highly accurate estimate of the 3D molecular distribution in that cell. The algorithm used to reverse the distortion introduced by the optics is based on the theory of ill-posed problems. It is fast and runs effectively on inexpensive workstations. The resulting 3D images have considerably higher resolution than even those available from commercial confocal microscopes. Multi-fluorophore 0.2 μ m diameter fluorescent beads are added to the specimen to facilitate the 3D registration of images obtained at multiple wavelengths. In order to analyze relative patterns of distribution of two or more molecules in a cell the 3D images are further processed

using *a priori* information to restrict the analysis of co-localization to specific signals within the cell. For example, in analyzing the relative distribution of proteins involved in transmembrane ion movements algorithms have been developed to identify the components of the signal that are most likely in the plane of the membrane. Following this segmentation process the distribution of two or more molecules may be compared visually utilizing a unique 3D visualization scheme that allows the investigator to assess which voxels contain one or both of the molecules of interest. Further analytical software allows for a calculation of the percentage of the signal due to each molecule that coexists with that of another molecular species. Finally, statistical procedures have been developed to assess the likelihood that a given level of co-localization of two molecules in a cell might be due simply to chance. This procedure has now been applied to a range of biological problems.

It has been used to investigate how molecules involved in mRNA production are distributed within the nucleus of cells ranging from yeast to human fibroblasts. It has revealed that factors responsible for mRNA splicing are organized in discrete regions at some distance from the nuclear envelope in all cells studied to date. mRNA itself is clustered in these islands of splicing activity. In yeast it appears that the splicing factors are localized to specific domains due to the presence of unique binding sites in the nucleus. These results indicate that the chemistry for mRNA production and possibly export is highly organized within the nucleus.

The techniques have also been applied to understand how molecules involved in Na^+ and Ca^{2+} homeostasis at the surface membranes and the membrane surrounding internal Ca^{2+} stores are distributed in the smooth muscle cell. The results reveal that the Na^+/K^+ pump and $\text{Na}^+/\text{Ca}^{2+}$ exchanger are co-localized to the same region of the plasma membrane. This domain is complementary to the region where the contractile elements are attached to the cell surface. Finally, we found that elements of the sarcoplasmic reticulum enriched in the Ca^{2+} storage protein calsequestrin are closely apposed to and in register with the domains of the surface membrane containing the Na^+/K^+ pumps and $\text{Na}^+/\text{Ca}^{2+}$ exchangers. This pattern of organization appears to facilitate the coupling of the activities of the Na^+/K^+ pump and $\text{Na}^+/\text{Ca}^{2+}$ exchanger as well as to provide a means for coupling Ca^{2+} extrusion activity at the surface membrane with Ca^{2+} storage in the sarcoplasmic reticulum.

While the foregoing analyses have all been carried out on fixed cells, these general methods have also been applied to living cells as well. We have recently used this approach to analyze the dynamics of association of hexokinase with the mitochondrial surface in a variety of cell types. Binding of hexokinase to mitochondrial membranes has been shown *in vitro* to enhance its catalytic activity, and hence the dynamics of this binding *in vivo* are likely to have a profound influence on cellular metabolism. In order to study this process *in vivo* a functionally competent fluorescence analog of hexokinase was micro-injected into single cells and its association with individual mitochondria analyzed. The results indicate that the binding of hexokinase to the mitochondrial surface is affected by both the level of glycolytic metabolism of the cell as well as the energetic state of the mitochondria. The results suggest that cytoplasmic and mitochondrial energy metabolism may be highly coordinated by translocation of important elements in glycolytic metabolism to the mitochondrial surface.

These general approaches provide a powerful means for analyzing a broad range of problems at the molecular level in the context of the intact cell.

DYNAMIC ASPECTS OF NEURONAL INTERPHASE NUCLEI: VISUALIZATION OF SUBNUCLEAR DOMAINS
BY PHASE CONTRAST MICROSCOPY, CONFOCAL MICROSCOPY & ULTRASTRUCTURAL CYTOCHEMISTRY

Umberto De Boni, Kosta Milankov, Kwame S. Amankwah and Paul C. Park

Depts. of Physiology and Anatomy, University of Toronto, Toronto M5S 1A8, CANADA

Neuronal chromatin moves, in a saltatory and periodic manner, within the 3-dimensional (3-D) space of interphase nuclei in vitro. This is generally known as nuclear rotation (NR) which has been proposed to function, during differentiation, in the transposition of specific chromatin domains into a cytotypic chromosome pattern, a pattern which, in part, may also be related to the functional state of the cell. Exposure of neurons in vitro to nerve growth factor or to neurotransmitters results in altered gene expression, in altered rates of NR, as well as in a reorganization of chromosome patterns. Moreover, long term potentiation, induced in neurons in hippocampal slices, reduces the number of detectable satellite DNA signals, possibly by increased clustering.

It had been controversial whether NR represents motion of nuclei in toto or represents independent motion of individual subnuclear domains. Quantification of motion of individual nucleoli in multi-nucleolate neurons in vitro shows that motion of nucleoli is spatially restricted to subnuclear regions, that the rate of motion exhibits power spectra with resonance, typical of forced harmonic motion, suggestive of multiple levels of control and that individual nucleoli may move independently, suggesting multiple motors. Nucleolar fusion is associated with transient increases in NR rates, suggesting a link between NR and nucleolar fusion.

The number of nucleoli in multi-nucleolate neurons decrease progressively as a function of in vitro age, related to nucleolar fusion and differentiation. In a test of the hypothesis that specific chromatin domains in addition to nucleoli undergo rearrangements during differentiation, the spatial distribution of kinetochores was compared in mono-, bi- and tri-nucleolate nuclei, by use of autoimmune sera. Numbers of kinetochore signals per nucleus decrease as cells change from tri- to bi- to mono-nucleolate states, with corresponding increases in signal size. This, together with results of immunodetection of kinetochores at the ultrastructural level, shows that centromeric regions undergo clustering as cells differentiate and that NR represents independent motion of chromatin domains rather than motion of the nucleus in toto. Thus, NR may function in chromatin rearrangement during differentiation.

While the motor driving NR remains enigmatic, myosin and a specific actin isoform have been shown to be constituents of interphase nuclei. Actin aggregates have been detected in neuronal nuclei by immunocytochemistry with confocal microscopy and by ultrastructural immunogold labeling. Actin aggregates are decorated by antibodies to alpha-sarcomeric actin, but not by antisera to alpha-smooth muscle actin. Several aggregates are localized to each nucleolus which suggests that these aggregates may represent the separate "motors" predicted above. Labeling with FITC-phalloidin or with heavy meromyosin indicates that some intranuclear aggregates contain f-actin. We postulate that NR and motion of nucleoli during fusion are driven by intranuclear acto-myosin motors.

The results suggest that interphase nuclei represent a dynamic mechanical system and that acto-myosin complexes may play a role in the placement of specific chromatin domains into the cytotypic, 3-D pattern observed in interphase nuclei.

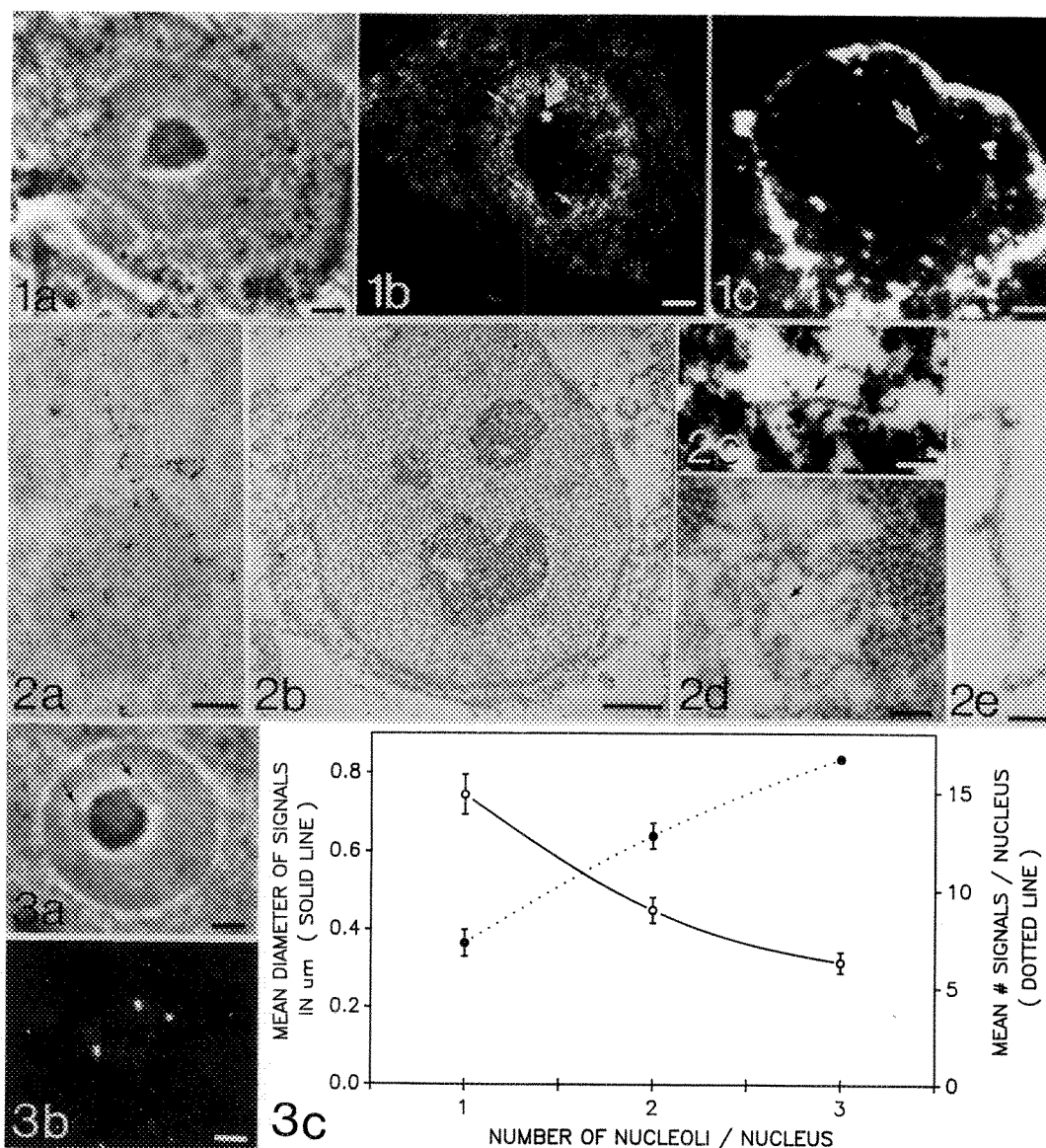


Fig.1: Phase contrast image (1a) and corresponding confocal, optical section (1b) showing nucleolar (curved arrow) and nucleoplasmic (small arrows) actin aggregates labeled with anti-actin antibody. Fig.1c: FITC-phalloidin labeled actin aggregate (arrow) in a different neuron. Fig.2: Ultrastructural detection of nuclear actin by immunogold (2a) and decoration by heavy meromyosin (2c,d) in a glycerol extracted neuron (2b). Note the typical "arrowhead" pattern (arrows) comparable to that observed in neuronal cytoplasm (2e). Fig.3: Detection of kinetochores (KC) by autoimmune serum. Note association of KC (Fig.3b) with nucleolar satellites in corresponding phase contrast image (arrows, 3a). Fig.3c: Relationship between number of KC signals and the mean signal size as a function of number of nucleoli. Mag: 1a,1b,1c,2b,3a,3b Bar=2 μm . 2a Bar=0.5 μm . 2c,2d Bar=0.1 μm . 2e Bar=0.05 μm .

CORRELATIVE CONFOCAL LIGHT MICROSCOPY AND HIGH-VOLTAGE ELECTRON MICROSCOPY OF NEURONS

J.N. Turner, D.H. Szarowski, D. Decker, K.L. Smith, M. Fejtl, J.W. Swann and D.O. Carpenter

Wadsworth Center for Laboratories and Research, New York State Department of Health, and School of Public Health, The University at Albany, Albany, NY 12201-0509

Neurons are cells with extensive dendritic and axonal arborizations extending from the cell body hundreds of micrometers or more in all three-dimensions. These structures have specializations, such as dendritic spines, that are at or just below the level of resolution of the light microscope (LM), and others, such as synapses, that can be resolved only in the electron microscope. Thus, it can be essential to correlate light and electron microscopic images from the same specimen. Due to its discrimination along the z-dimension (optic axis), the confocal light microscope is ideal for investigating neurons and correlating their structure and function.¹ At the ultrastructural level, we use the high-voltage electron microscope (HVEM) to collect three-dimensional data, because it images thick objects.² We are studying neurons in culture, and in thick acute and long term cultured brain slices.³ LM observations are made either after fixation or live by LM, and these images are correlated with HVEM ultrastructural observations.^{1,2}

Neurons are contrasted with either fluorescent dyes or peroxidase based stains. The latter are imaged in the reflection mode.¹ The cultured neurons shown here were isolated from the major ganglia of juvenile *Aplysia californica*, cultured in modified L-15 media containing 20% *Aplysia* hemolymph, and stained with DiI in artificial sea water with Pluronic F-127 and DMSO. Confocal images were recorded using a Bio-Rad MRC 600 mounted on an Olympus microscope, and were reconstructed using Analyze™⁴ run on an IBM RISC 6000.

The electrical properties (resting membrane potential, input resistance, capacitance, and size, shape and onset of action potentials) of these cultured neurons are being correlated with their 3-D morphology and ion transport. Changes in cell volume, as expected, alter these properties. However the expected direction of variation in input resistance is often opposite to that observed. The discrepancies, e.g. an increase in conductance caused by cell shrinkage, may be the result of additional ionic conductances and/or presently uncharacterized metabolic responses. There is also a complication of degenerating glial cells which may be adherent to the membrane, and might affect cell volume and electrical measurements. Figure 1 is a volume-rendered image of two neurons with processes growing on the substrate, and a convoluted cell surface which changes reversibly with osmolarity. The convolutions in the upper left of the larger cell are also shown in Figure 2 which is an optical section 30 μm above the substrate. The smaller cell shows an unstained center. Figure 3 is an HVEM image of the larger cell in the region of Figure 2, and shows cell debris adhered to the neuron's surface, apparently from deteriorating glial cells. Figure 4 is an HVEM image of the smaller cell below the level of Figure 2 showing a clean neuronal surface. The center region is the nucleus corresponding to the unstained region in Figures 1 & 2.

1. J.N. Turner, D.H. Szarowski, K.L. Smith, M. Marko, A. Leith, J.W. Swann, J. Elec. Microsc. Tech.(1991)18, 11; J.S. Deitch, K.L. Smith, C.L. Lee, J.W. Swann, and J.N. Turner, J. Neurosci. Methods(1990)33, 6.
2. J.S. Deitch, K.L. Smith, J.W. Swann, and J.N. Turner, J. Elec. Microsc. Tech.(1991)18, 82; J.N. Turner and D.N. Collins, J. Histotechnology (1990)13, 93.
3. P.A. Schwartzkroin, Brain Res. (1975)85, 423; J.W. Swann and R.J. Brady, Devel. Brain Res.(1984)12, 243; L. Stoppini, P.A. Buchs, D. Muller, J. Neurosci. Methods(1991)37, 173.
4. R.A. Robb, and C. Barillot, IEEE Trans. Med. Imaging(1989)8, 217.
5. Grant support is acknowledged from: NIH R55RR06904, NS18309, NS 23807, and NSF DIR 9108492.

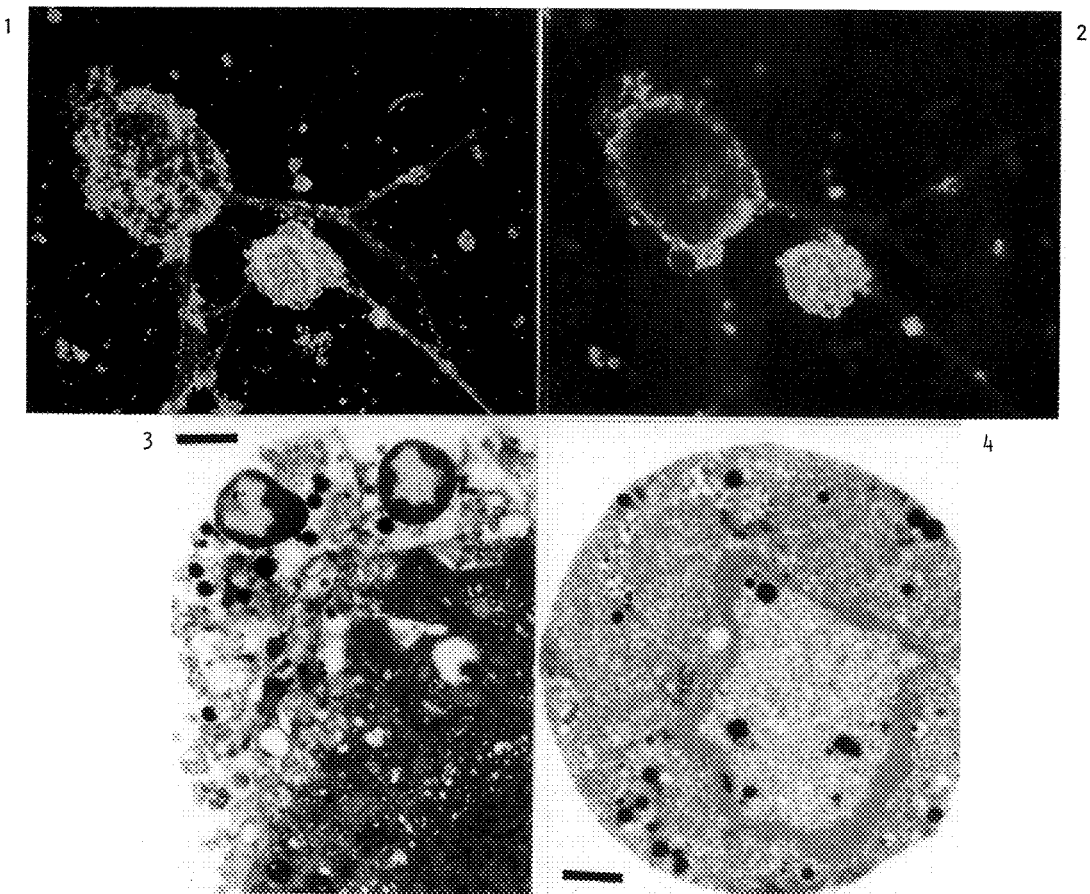


FIG. 1.—Volume rendered image corresponding to 75 μm in the z direction and a field width of 450 μm .

FIG. 2.—Optical section 30 μm above substrate.

FIG. 3.—HVEM image of a 0.25 μm -thick section; bar = 1 μm .

FIG. 4.—HVEM image of a 0.25 μm -thick section; bar = 5 μm .

LIGHT MICROSCOPY OF LIVING CELLS CORRELATIVE TO HIGH-VOLTAGE ELECTRON MICROSCOPY AND LOW-VOLTAGE SCANNING ELECTRON MICROSCOPY OF CELL CRYO-WHOLE-MOUNTS

Marek Malecki

Integrated Microscopy Resource, National Institutes of Health Biotechnology Resource and Laboratory of Molecular Biology, University of Wisconsin, Madison, WI 53705

Analysis of motility phenomena in a living cell observed with light microscopy can be significantly enriched by preparing a whole-mount of this cell for high voltage electron microscopy (to reveal the intracellular organization) and for low voltage scanning electron microscopy (to reveal the surface topography). In earlier studies, cell whole-mount preparation by chemical fixation and drying was adequate for studies of slow cellular motions at the subcellular level (e.g. receptor movements).¹ Fast cellular motions analysed at the supramolecular level (e.g. transmitter release, cytoskeleton reorganization) required development of much faster cryo-immobilization methods.^{2,3} However, in studies of cells grown on grids, these freezing methods involved time consuming transfer of these cells, from an incubator to a freezer,⁴ making impossible fine correlations between images of a living cell and its cryo-whole-mount. To overcome this constraint for correlative microscopical studies of neoplastic cell motility, I designed an instrument consisting of a freezer attached to a light microscope and allowing cryoimmobilization within milliseconds after recording.⁵ The main objective of the current project was refinement of an instrument and improvement of appropriate specimen cryo-preparation techniques.

The key elements of the instrument design are illustrated in Figure 1. A light microscope located on an antivibration frame has a horizontal optical path. A container with melting ethane is located beneath the microscope and is closed with a shutter. A micromanipulator mounted on a vertical rod allows x,y shifts in a plane perpendicular to the optical axis. Human adenocarcinoma cells were grown on the polystyrene film supported by a gold grid mounted into a frame. This frame, held with forceps, was clamped to the micromanipulator.⁶ The whole instrument was covered with a plastic bag inflated with carbogen and water vapors. Immediately after recording and closing of the Polaroid camera shutter, the container shutter was opened and the grid plunged into melting ethane. Within milliseconds after recording the cells were cryoimmobilized. Then cells were freeze-substituted,⁴ rehydrated, conductively stained,⁷ and critical point dried.⁸ Cell cryo-whole-mounts were observed in the AEI MarkII high voltage electron microscope at 1MeV (HVEM) and the Hitachi S-900 low voltage scanning electron microscope at 2.5kV (LVSEM).

The cells previously observed in the living state with the light microscope (Fig.2) were afterwards seen in the HVEM (Fig.3-5) and the LVSEM (Fig.6-8). Only a thin edge of a spreading cell was transparent to electrons at the HVEM (Fig. 3,4). At the higher magnification a dense, regular network of filaments indicated absence of ice segregation patterns. Conductive staining introduced adequate contrast. Furthermore, uniform thickness of filaments and absence of fusions between these filaments indicated good drying (Fig.5). Cellular filopodia standing straight up and having uniform thickness provided evidence, in the LVSEM, for appropriate handling of cells prior to freezing (Fig. 6,7). At 100000x magnification, the preserved integrity of cell membranes allowed recognition of fine microdomains (Fig.8). In conclusion, the new instrument design and improved cryo-procedures for electron microscopy offer opportunities for ultrastructural analysis of fast cellular motility phenomena with significantly enhanced temporal resolution at the supramolecular level.

References. 1. Wetzel B & Albrecht RM 1989. *Scan. Microscopy Sup.* 3: 1-6. 2. Heuser JE & Kirschner MW 1980. *J. Cell Biol.* 86: 212-234. 3. Malecki M & Ris H 1992. *Scanning* 14(2):10-20. 4. Bridgman PC & Reese TS 1984. *J.Cell Biol.* 99:1655-1668. 5. Malecki M 1991. In: *The Science of Spec. Prep. for Electr. Micr.* (Johari O & Roomans G eds.) 53-73. 6. Malecki M 1992. *Scan.Mic.*(in press). 7. Kelley RO Dekker RA Bluemink JG 1973. *J.Ultr.Res.* 45: 254-258. 8. Ris H 1985. *J.Cell Biol.* 100: 1474-1487.

Acknowledgments. I acknowledge with thanks discussions with Drs. Hans Ris and J.Victor Small, photography by Mr. Eric Landmark, drawing and type-writing by Mrs. Nina Malecki and manuscript correction suggestions by Dr. Joyce Sexton. This work was supported by the NIH Grant DRR-570 to the Integrated Microscopy Resource.

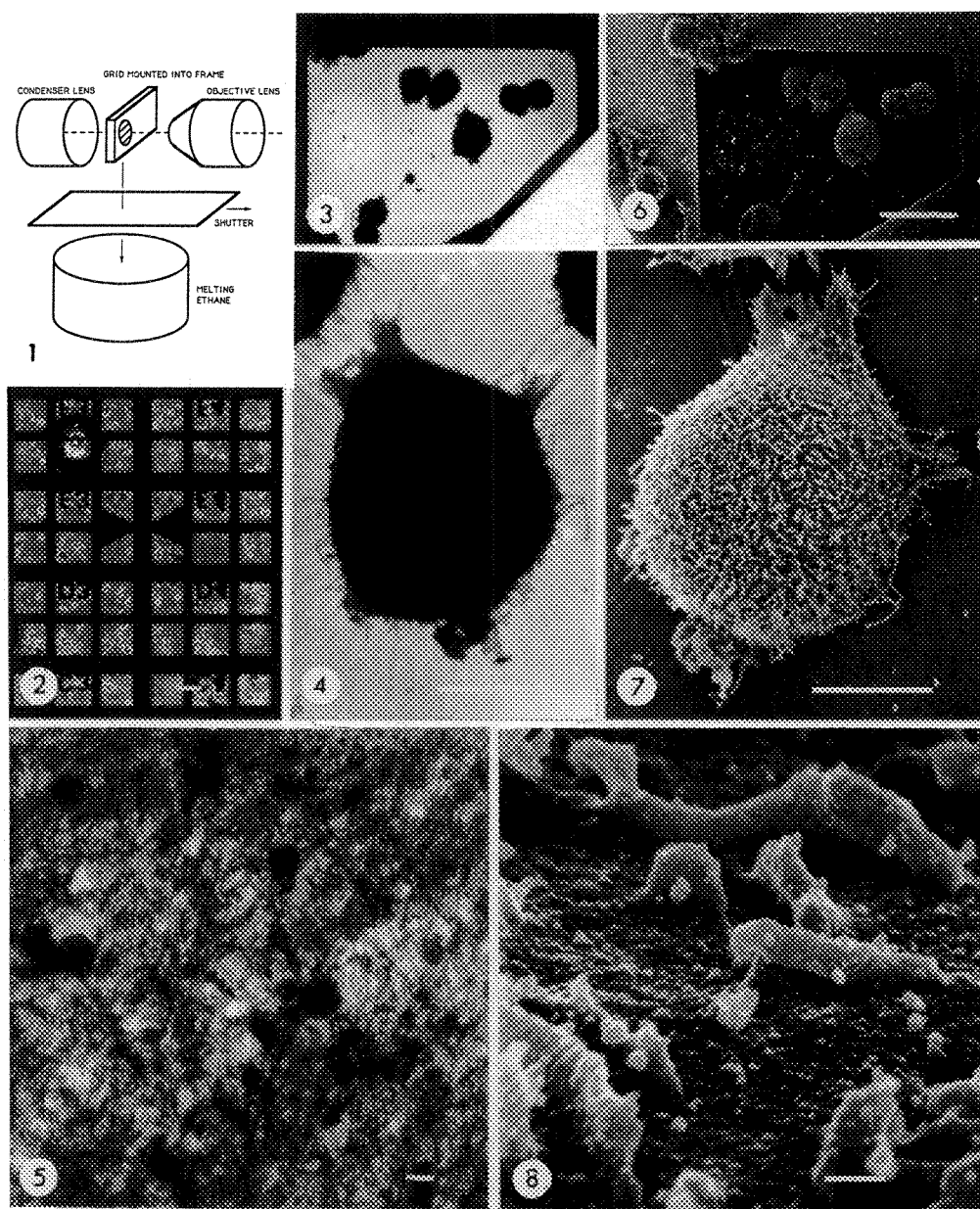


Figure Legends. Fig.1. Diagram of the instrument design. Fig.2. Phase-contrast light microscopical (LM) image of adenocarcinoma cells spreading on the polystyrene film supported by a finder grid. Bar 50 μ m. Fig.3. HVEM. Selected area of the sample observed previously (Fig.2). Bar 20 μ m. Fig. 4. HVEM. Cell selected from the sample observed in Fig.2. Only a thin cell edge is transparent to electrons. Bar 5 μ m. Fig.5. HVEM. Filamentous network at the thin cell edge. Absence of ice segregation patterns. Filaments have uniform thickness. Bar 200nm. Fig.6. LVSEM. The same area as in Fig.3. Bar 20 μ m. Fig.7. The same cell as in Fig.4. Cellular filopodia are straight up and have uniform thickness. Bar 5 μ m. Fig.8. Peripheral region of the same cell. Membrane integrity well preserved. Note membrane protrusions. Bar 100nm.

SELF-ORGANIZING CYTOPLASMIC MICROTUBULE NETWORKS IN FORAMINIFERAN PSEUDOPODIA

Elizabeth Patterer Welnhöfer*, Donald Orokos*, Gerald Rupp** and Jeffrey L. Travis*

*Department of Biological Sciences, State University of New York at Albany, Albany, NY 12222; and **Department of Anatomical Sciences, State University of New York at Buffalo, Buffalo, NY 14124

The foraminifera (i.e. "forams"), like all Granuloreticulose protists, produce extensive networks of pseudopodia that are supported and powered by an elaborate cytoskeleton of motile microtubules (MT). These pseudopodia may reach lengths nearly 100X the diameter of the cell body, which is the synthetic center of the cell, and the network is continuously remodelled as pseudopodia form, extend, retract, branch and fuse. The fact that these morphogenetic processes occur in even the most remotely located regions of the network suggests there is considerable local autonomy in the assembly, disassembly, and organization of the MT cytoskeleton.

We have used video-enhanced contrast differential interference contrast light microscopy, immunocytochemistry and correlative light and electron microscopy to study the behavior and organization of MT in control and experimentally treated forams. The assembly state of foram MT can be controlled by either physical or chemical methods. Rapid cold shock, as well as treatment with antimicrotubule drugs or high external $[Mg^{2+}]$ induces the pseudopodial MT to rapidly "disassemble" into 5 nm helical filaments (HF), which are an inactive storage or pre-assembly form of MT-protein polymer.¹⁻³ This transformation results in loss of all pseudopodial motility, presumably because the HF lack the MT protofilament lattice required by MT-based mechanoenzymes.

When the disassembly stimulus is removed, the HF transform back into functional MT and motility is restored. High resolution video enhanced contrast light microscopy shows that MT reform simultaneously at numerous sites in the network, and suggests that they are subsequently organized by transport-mediated MT-MT interactions. For example a particle attached to one MT may contact and be transported along a second MT, resulting in the realignment of both MT relative to each other. Reiteration of this process could account for the subsequent integration of randomly assembled MT into a typical pseudopodial cytoskeleton of extensively branched and anastomosed MT bundles.⁴

Pseudopodial satellites,^{5,6} which form when portions of the pseudopodia are microsurgically severed from the cell body, provide additional insight into the self-organizing ability of the MT cytoskeleton. These enucleate cell fragments resemble miniature foraminifera, and consist of a relatively large cytoplasmic mass centralized in a radially arrayed pseudopod network (Fig. 1). The metabolic poison 2,4-dinitrophenol (DNP) prevents intracellular

transport and thus inhibits the cytoplasmic and cytoskeletal reorganizations that lead to satellite formation. However, DNP does not effect the assembly state of foram MT, indicating that the MT organization and assembly are separate processes. We suggest that coding for the microtubule pattern in forams is built into the motile pseudopodial MT network and is independent of MT nucleating or organizing instructions originating from the cell body.

References

- 1.J.L. Travis and S.S. Bowser. Cell Motil. Cytoskel.(1986)6, 1.
- 2.G. Rupp et al. Cell Motil. Cytoskel.(1986)6, 363.
- 3.R. Golz and M. Hauser. Eur. J. Cell Biol.(1986)40, 124.
- 4.J.L. Travis et al. J. Cell Biol. (1983)97, 1668.
- 5.T.L. Jahn and R.A. Rinaldi. Biol. Bull.(1959)117, 100.
- 6.J.L. Travis and S.S. Bowser. Cell Motil. Cytoskel.(1986)6, 146.

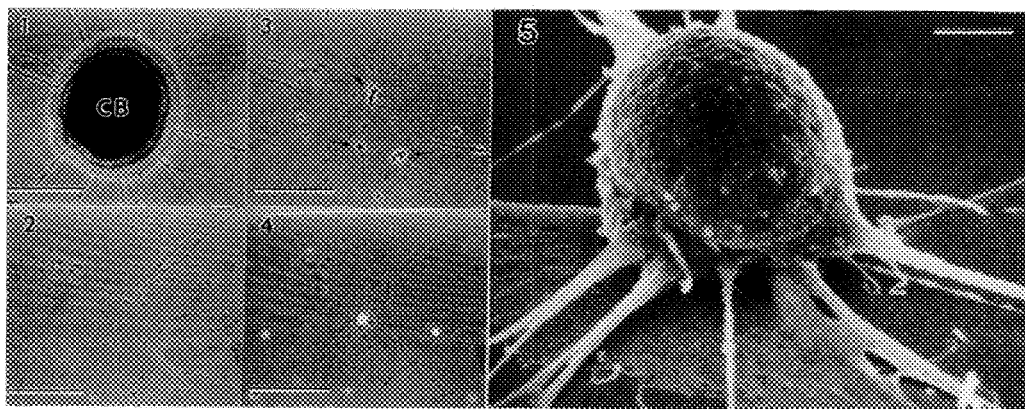


FIG. 1.--Phase contrast light micrograph (PC) of a living foram (*Allogromia*) showing a typical pseudopodial network radiating from the cell body (CB). Bar = 250 μ m.

FIG. 2.--PC of the same network shown in Fig. 1, but taken 5 sec after microsurgical removal of cell body. Bar= 250 μ m.

FIG. 3.--PC of the network 3 min after the cell body has been removed. Organization of satellites (arrows) has begun. Bar= 250 μ m.

FIG. 4.--After 9 min, the cytoplasmic rearrangements have been completed, resulting in the formation of a single satellite. Bar= 250 μ m.

FIG. 5.--SEM of the same satellite shown in Fig.4. Bar = 10 μ m.

CILIARY COORDINATION IN NEWT LUNG CELLS REQUIRES MICROTUBULE-BASED LINKAGES BETWEEN BASAL BODIES: A CORRELATIVE LIGHT AND ELECTRON MICROSCOPIC STUDY

Robert Hard, Gerald Rupp, Matthew L. Withiam-Leitch, and Lisa Cardamone

Department of Anatomical Sciences, School of Medicine, SUNY at Buffalo, Buffalo, NY 14214

In a coordinated field of beating cilia, the direction of the power stroke is correlated with the orientation of basal body appendages, called basal feet. In newt lung ciliated cells, adjacent basal feet are interconnected by cold-stable microtubules (basal MTs).¹ In the present study, we investigate the hypothesis that these basal MTs stabilize ciliary distribution and alignment. To accomplish this, newt lung primary cultures were treated with the microtubule disrupting agent, Colcemid. In newt lung cultures, cilia normally disperse in a characteristic fashion as the mucociliary epithelium migrates from the tissue explant.² Four arbitrary, but progressive stages of dispersion were defined and used to monitor this redistribution process. Ciliary beat frequency, coordination, and dispersion were assessed for 91 hrs in untreated (control) and treated cultures. When compared to controls, cilia dispersed more rapidly and ciliary coordination decreased markedly in cultures treated with Colcemid (2 mM). Correlative LM/EM was used to assess whether these effects of Colcemid were coupled to ultrastructural changes. Living cells were defined as having coordinated or uncoordinated cilia and then were processed for transmission EM.³

Correlative LM/EM of uncoordinated tufts demonstrated that basal feet were randomly oriented and that MT-based linkages between adjacent basal feet were absent following Colcemid treatment. Coordinated beating and basal feet realignment could not be restored upon Colcemid reversal, even though MTs were reestablished on basal feet and were stable to subsequent cold treatment. Our data demonstrate that the interconnecting MTs appear to maintain the uniform basal body orientation and order prerequisite for coordinated, unidirectional beating. In addition, we show that the stability of basal MTs is intermediate to that of ciliary axonemes/basal bodies and cytoplasmic MTs.

What is the cause of this stability? Post-translational modifications of tubulin, such as detyrosination and acetylation of α -tubulin, are known to be related to (although not necessarily the basis of) MT stability. Therefore we also characterized the distribution of detyrosinated and acetylated tubulins in the newt lung ciliary apparatus, with special emphasis on the MT-based cross-linkages. To test for antibody specificity, we first performed western blots using extracts of isolated sheets of newt lung mucociliary epithelium and antibodies directed against detyrosinated or acetylated forms of α -tubulin. Our results demonstrate that both detyrosinated and acetylated tubulins are present in this tissue and that no other newt lung proteins are labelled by these antibodies. Immunocytochemical localization of tubulin antigens was performed at the LM level using either newt lung primary cultures or demembranated and reactivated ciliary tufts. For EM immunolocalization, either cultured cells or intact newt lungs were used. At the LM level, immunofluorescence results clearly demonstrated that antibodies directed against detyrosinated tubulin were bound along the entire ciliary length. Photomicrographs of isolated ciliary tufts viewed from the side showed that some label also was localized in the basal apparatus. EM immunolocalization using secondary antibodies conjugated to 10 nm gold beads confirmed that detyrosinated antigens were present along the entire lengths of both axonemes and the MTs that cross-link adjacent basal feet. At the LM level, antibodies directed against acetylated tubulin were

1. Hard, R. and C.L. Rieder, *Tissue and Cell* (1983)15, 227.
2. Hard, R. and A. Weaver, *Tissue and Cell* (1983)15, 217.
3. Rieder, C.L. and R. Hard, *Int. Rev. Cytol.* (1990)122, 153.

bound only to the distal tips (as much as 1/3) of ciliary axonemes. Diffuse staining also was observed in the region of the basal apparatus. EM immunocytochemistry confirmed that acetylated tubulin was localized in the distal axoneme, but on no occasion were antibodies found localized to the basal MTs. Our evidence demonstrates that the MTs cross-linking adjacent basal feet in newt lung ciliary arrays are detyrosinated but not acetylated. Further work will be necessary to determine the role of detyrosination in conferring stability to this important class of MTs.

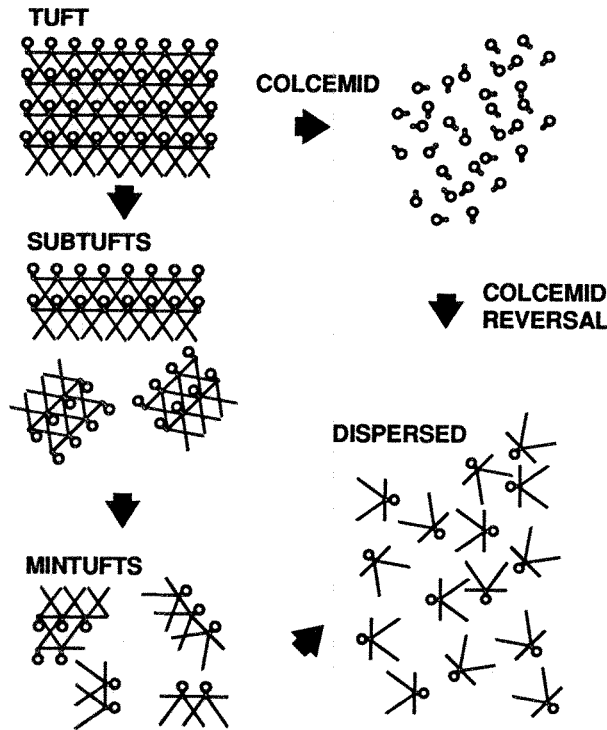


Figure 1: Diagrammatic representations of the basal apparatus of newt lung cilia, which summarize the results found for control, Colcemid treated, and Colcemid reversed cultures. In control cultures, ciliated cells nearest the explant bear single tufts whose basal bodies are aligned and interconnected by a set of cold stable MTs via their basal feet. As cells flatten, single tufts progressively disperse by breaking up into smaller, but coordinated units (subtufts and minitufts), whose basal feet still are oriented and interconnected by basal MTs. Eventually, complete dispersion occurs in the most highly flattened cells. Long term Colcemid treatment causes depolymerization of the basal MTs with subsequent randomization of basal foot orientation and a loss of coordination. The unconstrained basal bodies disperse at a more rapid rate than in control cells. In Colcemid reversed cells, cold stable basal MTs are found to emanate from basal feet, but few interconnections are found and basal foot reorientation is for the most part lacking. A uniform numbers of basal MTs, basal MT cross links, and ordered basal feet have been drawn for simplicity and are not truly representative.

CORRELATIVE LIGHT AND ELECTRON MICROSCOPY OF PRIMARY (9+0) CILIA: RESPONSE OF CILIARY VARICOSITIES TO HYPOTONIC TREATMENT IN KIDNEY EPITHELIAL CELLS

Samuel S. Bowser, Karen E. Roth, and Conly L. Rieder

Wadsworth Center for Laboratories & Research, P.O. Box 509, Albany, NY 12201 and Department of Biomedical Sciences, State University of New York, Albany, NY 12222

Primary cilia are centrosomal appendages which in kidney epithelia extend several micrometers from the apical cell surface into the lumen of the kidney tubule. Although considered by some to be "rudimentary appendages" because they are nonmotile, their intimate structural association with the Golgi apparatus and nucleus suggests to others that they mediate interactions between the cell and its environment.¹ Such a sensory role is not without precedence since various photo- and chemoreceptors are highly modified primary cilia. Despite the near-ubiquitous distribution of primary cilia few studies have addressed their function experimentally, and little detailed information is available regarding their behavior *in vivo*.

We have previously shown that primary cilia can be easily visualized in live cells by digitally-enhanced video light microscopy when the cells are viewed on edge using a novel "flexible substrate" technique.^{2,3} Briefly, the cells are grown on Formvar films which are then folded in half (cell-side out) and mounted in simple coverslip chambers. In confluent cultures scores of primary cilia can be easily imaged along the folded edge of a single preparation and their response to various treatments assayed in real time, or time-lapse recordings, by simply perfusing an experimental solution through the chamber. Cells can also be fixed and embedded in the chamber for fully correlative light and electron microscopic analyses.⁴

Many of the primary cilia in various segments of the nephron possess one or more swellings or varicosities along their shaft *in situ*.^{5,6} We have previously shown that up to 20% of the primary cilia expressed by various kidney cell lines (e.g., PtK₁, see Fig. 1) also possess such swellings.² Here we report that primary cilia with swellings are differentially sensitive to hypotonic media. Within one minute of perfusing hypotonic (100-200 mOsm/kg H₂O) L-15 medium through the culture cilia containing swellings rapidly and dramatically shorten until only the swelling projects from the cell surface (cf. Figs. 1a,b). This phenomenon was never observed in response to flow alone or *hypertonic* treatment, nor were any length or shape changes observed in those cilia lacking swellings. When the plasma membrane of cells containing hypotonically-shortened cilia was extracted with 0.15% Triton X-100 in PHEM buffer⁷ the ciliary axoneme "unfurled" (Fig. 1c). Thus, shrinkage in response to hypotonic media is not due to axoneme disassembly, but correlates with a coiling of the axoneme within the ciliary swelling. Computer-assisted 3D ultrastructural reconstructions of cells fixed 30 seconds after hypotonic treatment confirm the coiled arrangement of the axoneme within the swelling (Fig. 2).

Our findings clearly demonstrate that the two primary cilia phenotypes present in cultured kidney cells respond differently to physiologically-relevant hypotonic media, and underscores the dynamic nature of these enigmatic organelles. Although the relevance of this finding to primary cilia function is currently unknown, it is tempting to speculate that their differential response to hypotonic media is part of an intricate biological "feedback" mechanism for monitoring the flow rate and tonicity of kidney ultrafiltrate as it passes through the tubules.⁸

References

1. D.N. Wheatley, The Centriole: A Central Enigma of Cell Biology, New York: Elsevier

(1982)147.

2. K.E. Roth *et al.*, J. Cell Sci. 89(1988)457.
3. C.L. Rieder *et al.*, J. Tissue Culture Meth. 11(1988)185.
4. K.E. Roth *et al.*, Proc. Ann. EMSA Meeting 45(1987)828.
5. P.M. Andrews and K.R. Porter. Am. J. Anat. 140(1974)81.
6. H. Hucker and H. Frenzel. Virchows Arch. B, Zellpath. 18(1975)157.
7. M. Schliwa and J. van Blerkom. J. Cell Biol. 90(1981)222.
8. This research was supported by grants from the American Heart Association, New York State Affiliate, No. 89-029G (to S.S.B.), the National Institutes of Health GMS RO1 40198 (to C.L.R.) and PHS-01219 to support the Wadsworth Center's Biological Microscopy and Image Reconstruction Facility as a National Biotechnological Resource.

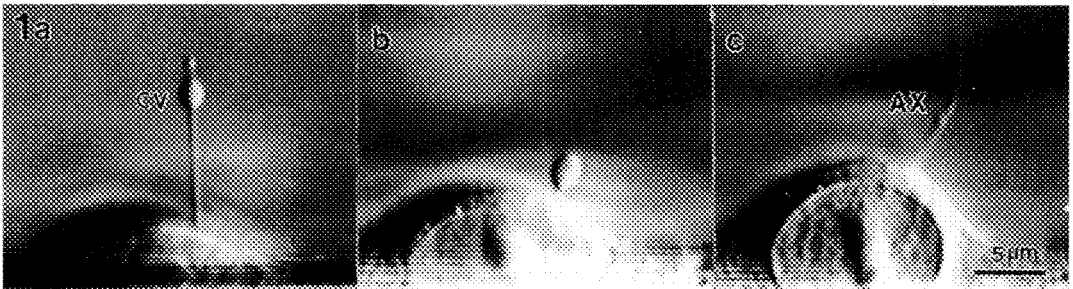


Fig 1. Sequential video light micrographs of primary cilium before (a) and 2 min after (b) hypotonic treatment, and subsequent Triton X-100 extraction (c). CV = ciliary varicosity; AX = axoneme.

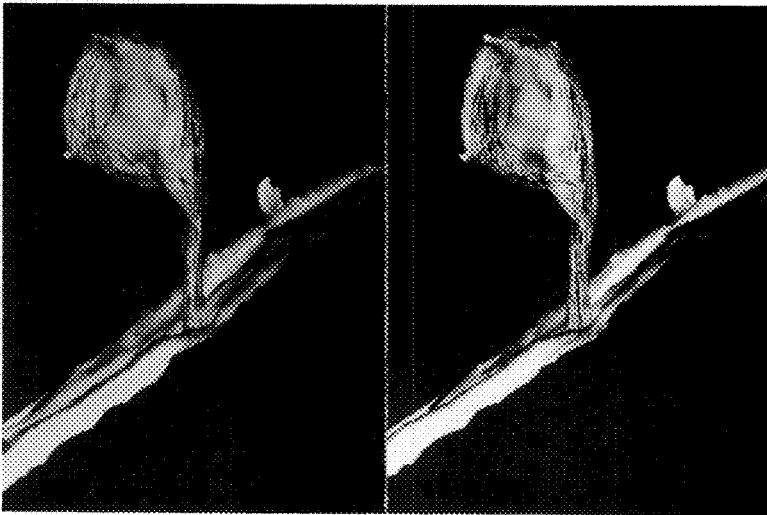


Fig. 2. Stereoscopic view of a hypotonically-shortened primary cilium reconstructed from serial 100-nm sections. Note that the axonemal microtubules (black lines) are coiled within the shortened swollen cilium.

THE DYNAMICS OF LIPOPROTEIN BINDING AND ENDOCYTOSIS IN MACROPHAGES: A CORRELATIVE ULTRASTRUCTURAL AND LIGHT MICROSCOPIC APPROACH

Nancy L. Jones, Stephen C. Landers, Nina S. Allen* and Jon C. Lewis

Pathology and *Biology Departments, Bowman Gray School of Medicine, Wake Forest University, Medical Center Blvd., Winston-Salem, NC 27157-1092

The dynamics of lipoprotein binding and endosome formation on pigeon monocyte-derived macrophages have been studied using Allen video-enhanced contrast, differential interference-contrast microscopy (AVEC-DIC) and nanovid (video-enhanced brightfield) microscopy. Subsequent to video-microscopy the ultrastructural (3-D) organization was examined by correlative Intermediate Voltage Electron Microscopy (IVEM). The use of gold "finder" grids mounted on glass coverslips provided the mechanism by which cells after being observed in the video system were located in the electron microscope. The lipoprotein, beta migrating low density lipoprotein (β VLDL), was conjugated to gold colloids (15-40 nm) to enhance visibility in both video-microscopy and IVEM. Subsequent to video microscopy, the cells were fixed with glutaraldehyde, dehydrated through ethanol and dried from CO₂ by the critical point method for whole-mount EM.¹ Such a correlative approach allowed static ultrastructural features to be associated with cellular dynamics as observed and recorded by video.

Receptors for β VLDL were localized to two ligand-induced regions of pigeon monocyte-derived macrophages by correlative microscopy. These regions were microvilli (retraction fibers) and membrane ruffles.² Previously, β VLDL was shown to internalize by both clathrin-coated and non-coated portions of the plasma membrane.³ More recently, quantitation of β VLDL to microvilli and membrane ruffles by thin section TEM and 3-D reconstruction of serial thin sections demonstrated an association of clathrin-coated membranes with microvilli and membrane ruffles.⁴ This present study, examines by AVEC-DIC living cells incubated with β VLDL and documents vesicle formation at the base of microvilli. These vesicles translocated linearly towards the cell center (centripetally) with rates of movement of 0.02 to 0.04 μ m per second.

Correlative microscopy was used to determine whether vesicles formed at the base of microvilli were clathrin-coated. Macrophages were initially observed by AVEC-DIC during β VLDL incubation (50 μ g/ml, gold conjugates) for 5-20 minutes at 37°C. Subsequent to AVEC-DIC, the cells were permeabilized with either Brij 58 or methanol (-20°C), and coated vesicles were immunolocalized using antibodies to either clathrin (Polysciences #18458) or α -adaptin (AC1-M11, provided by Dr. M.S. Robinson). After immunochemistry, the cells were prepared for whole-mount EM. Immunogold localization documented that the vesicles which form at the base of microvilli are clathrin-coated. These data support our hypothesis that β VLDL internalization near microvilli involves primarily clathrin-coated vesicles.⁵

1. JC Lewis et al., *Cell Motility* (1983) 3, 589.
2. NL Jones, NS Allen, JC Lewis, *Cell Motil. Cytoskel.* (1991) 19, 139.
3. DA Henson, R St.Clair, JC Lewis, *Exp Mol. Path.* (1989) 51, 243.
4. SC Landers, NL Jones, JC Lewis, *FASEB J* (1991) 5, A1253.
5. This work was supported by NIH grants HL-41990, RR-02722 (National Resource for IVEM), and HL-14164 (SCOR in atherosclerosis).

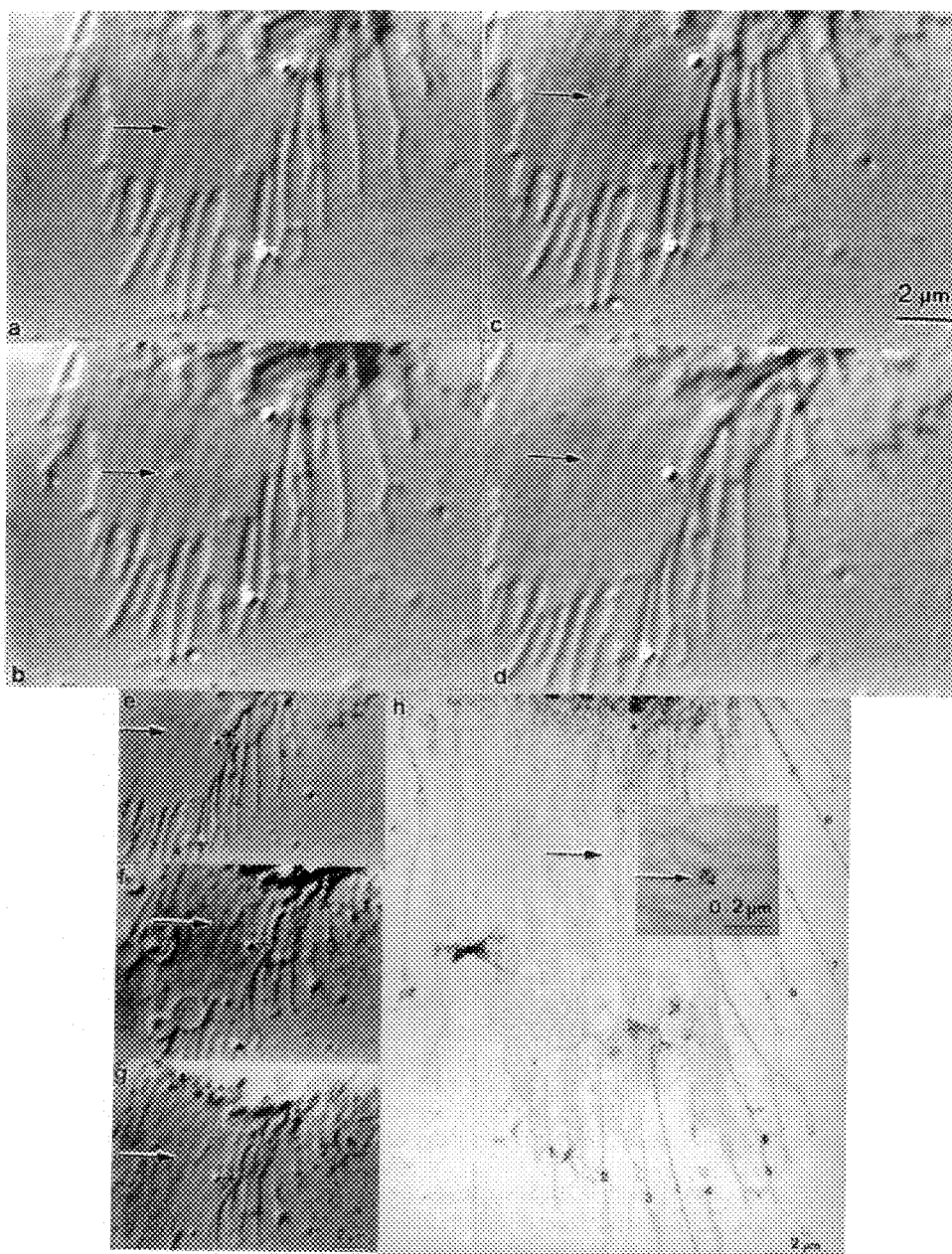


Figure: Transcytoplasmic movement of vesicle and immunolocalization for clathrin. Cells grown on formvar-coated "finder" grids were observed during BVLDL incubation by AVEC-DIC. A vesicle (arrow), formed near the base of a microvillus, was observed during translocation into the cell cytoplasm (a-d). The cell was then permeabilized with Brij 58 (f-g) and immuno-labeled for clathrin. h. The resulting IVEM whole mount of this cell is seen. The microvilli are numerically labeled (1-8) in the video-micrograph (e) and IVEM (h). The inset is a higher magnification of the vesicle showing the clathrin label.

THREE-DIMENSIONAL ORGANIZATION AND FUNCTIONAL RELATIONSHIPS OF ENDOCYTOTIC COMPARTMENTS IN PIG INTESTINAL EPITHELIAL CELLS

Julian P. Heath, Buford L. Nichols and László G. Kömüves

Department of Pediatrics, Children's Nutrition Research Center, Baylor College of Medicine, Houston, TX 77030

The newborn pig intestine is adapted for the rapid and efficient absorption of nutrients from colostrum. In enterocytes, colostral proteins are taken up into an apical endocytotic complex of channels that transports them to target organelles or to the basal surface for release into the circulation. The apical endocytotic complex of tubules and vesicles clearly is a major intersection in the routes taken by vesicles trafficking to and from the Golgi, lysosomes, and the apical and basolateral cell surfaces.

Jejunal tissues were taken from piglets suckled for up to 6 hours and prepared for electron microscopy and immunocytochemistry as previously described.^{1,2}

The apical complex of pig enterocytes comprises deep invaginations of the apical surface, vacuoles 1 to 3 μm in diameter, and numerous tubules about 50 to 100 nm in diameter. Within 40 minutes of suckling, electron dense material is found in small vesicles and in large granules (Figure 1). We have previously shown that these structures contain colostral immunoglobulin presumably en route to the basal cell surface.¹ We injected horseradish peroxidase into the intestinal lumen of unsuckled animals. After 2 minutes the marker entered the invaginations and was found in all of the vacuoles but only a few of the tubules (Figure 2). At 10 minutes, the vacuoles and almost all the tubules were labelled. Some sub-nuclear vesicles were also labelled indicating traffic between the apical complex and the basal regions (Figure 3). Stereo views of 200 nm thick sections (Figure 4) show that tubules run between the terminal web and small granules.

Why are so many tubules present in the ATVS and what is their role in endocytosis? We found that not all the tubules contain colostrum as judged by the absence of electron dense material and immunogold labeling for immunoglobulins. The tubules often pass into the terminal web but direct connections between tubules and the apical surface were rarely seen perhaps because such interactions are of low frequency and transient. We consider two roles for the tubules: as a vehicle for the recycling of membrane and receptors from the granules back to the apical cell surface, and/or as a primary endosomal structure that fuses with the plasma membrane and develops into an invagination. Further experiments to examine the nature of the tubules and their association with endocytosis and the trans-golgi biosynthetic pathway are in progress.³

(1) Kömüves, L.G. et al. (1990) Proc. XII Cong. Elect. Microsc. 3:922-923

(2) Kömüves, L.G., Nichols, B.L. and Heath, J.P. (1992) Histochem. J. (Submitted)

(3) Supported by USDA/ARS Cooperative agreement 50-6250-1-003

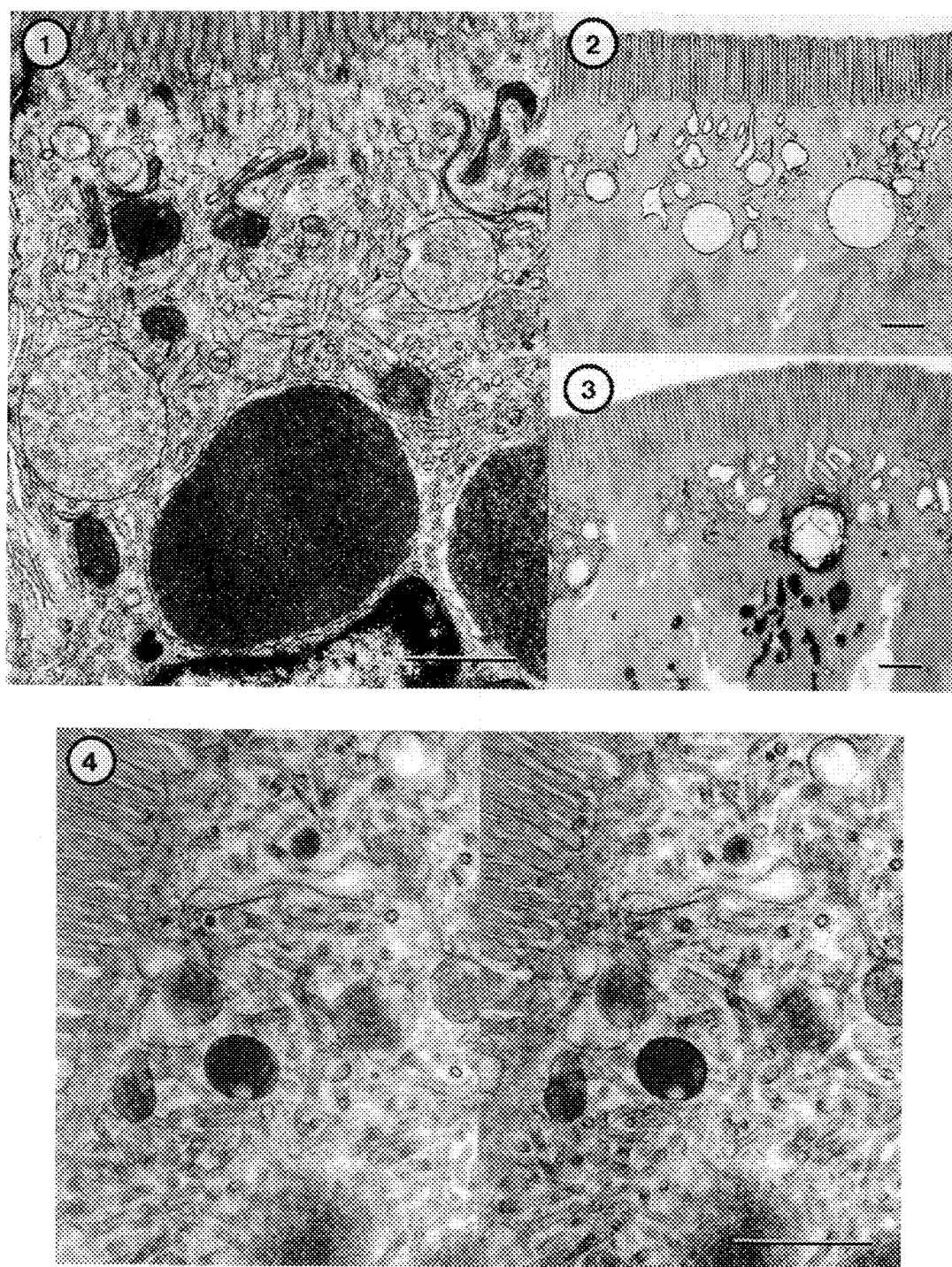
Fig. 1. Apical tubulo-vesicular system (ATVS) in jejunal enterocyte of a neonatal suckling piglet

Fig. 2. Endocytosis of HRP after 2 minutes incubation. Invaginations and vacuoles are labelled, but no label is seen in tubules.

Fig. 3. Endocytosis and transport of HRP to basal regions after 10 minutes incubation.

Fig. 4. Stereo pair showing interconnections of tubules and small granules.

All scale bars = 1 μm



3-D RECONSTRUCTION AND ANALYSIS OF MAMMALIAN MITOTIC SPINDLE STRUCTURE

Kent McDonald, David Mastronarde, Rubai Ding, Eileen O'Toole and J. Richard McIntosh

Laboratory for Three-Dimensional Fine Structure, MCD Biology,
University of Colorado, Boulder, CO 80309

Mammalian spindles are generally large and may contain over a thousand microtubules (MTs). For this reason they are difficult to reconstruct in three dimensions and many researchers have chosen to study the smaller and simpler spindles of lower eukaryotes. Nevertheless, the mammalian spindle is used for many experimental studies and it would be useful to know its detailed structure.

We have been using serial cross sections and computer reconstruction methods to analyze MT distributions in mitotic spindles of PtK cells, a mammalian tissue culture line. Images from EM negatives are digitized on a light box by a Dage MTI video camera containing a black and white Saticon tube. The signal is digitized by a Parallax 1280 graphics device in a MicroVax III computer. Microtubules are digitized at a magnification such that each is 10-12 pixels in diameter. All the section images are aligned, the MTs detected by an automatic MT recognition routine, models are built and edited, then analyzed quantitatively¹.

One of our interests is the structure of the spindle interzone or region of overlap between half spindles. We find that at metaphase the MTs from each pole show considerable overlap and that the extent of overlap diminishes during spindle elongation. By late anaphase or telophase there is relatively little overlap (Fig. 1). A cross-section through the region of overlap in a late spindle (Fig. 2) shows mixing of MTs from opposite poles, and an analysis of near neighbors for each MT indicates a specific interaction between MTs of opposite polarity.

Analysis of the kinetochore fiber² reveals that it is a hybrid of true kinetochore MTs, i.e., those attached to the kinetochore region of the chromosome, and non-kinetochore MTs. As with the spindle interzone MTs, there is considerable mixing of the two classes, but unlike the interzone, there is no specific near neighbor interaction. Length distribution measurements of the kinetochore MTs shows that they are somewhat longer than previously thought³.

References

1. K. McDonald, D. Mastronarde, E. O'Toole, R. Ding & J.R. McIntosh. (1991). EMSA Bull. 21:47-53.
2. K. McDonald, E.O'Toole, D. Mastronarde & J.R. McIntosh (1992). J. Cell Biol. (in press).
3. Rieder, C. (1981) Chromosoma 84:145-158.

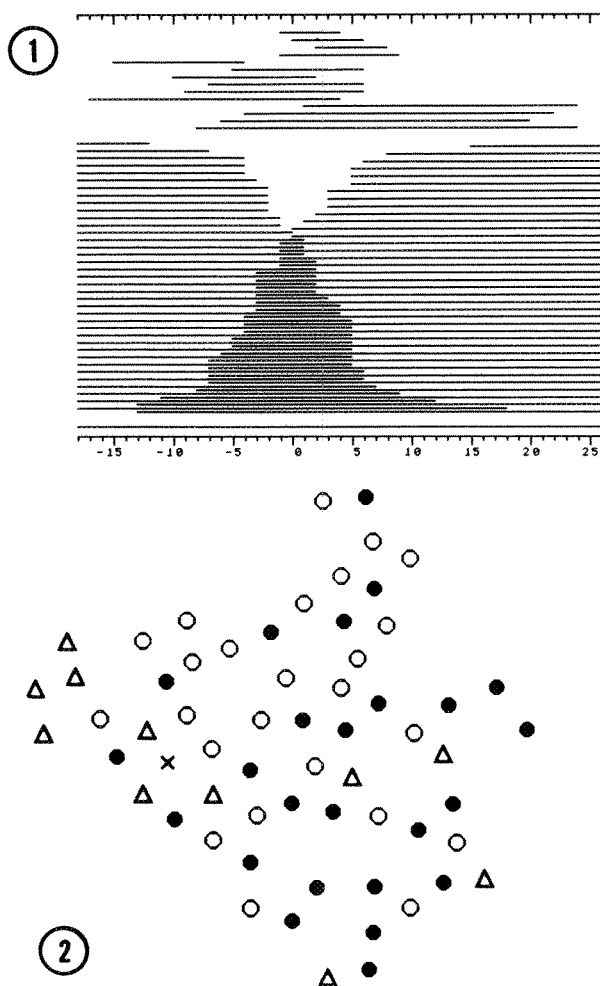


Fig. 1. Each line represents an individual MT: its ends depict the section in which it began and ended. The MTs from each half spindle are arranged top to bottom in order of increasing length in order to show the extent of possible MT overlap. Those MTs which have both ends within the area sampled are laid out at the top. The one MT which traversed the whole length sampled is shown at the bottom.

Fig. 2. Cross-section through the center of the interzonal region from a telophase zone of overlap. MTs from either pole are represented as filled and open circles. The cross is the MT which traverses the whole region, the triangles are MTs with both ends free or which passed out of the region sampled.

THREE-DIMENSIONAL RECONSTRUCTION BY HVEM TOMOGRAPHY

Bruce F. McEwen¹ and Joachim Frank^{1,2}

1) Wadsworth Center for Laboratories and Research, New York State Department of Health,
P.O. Box 509, Albany, NY 12201-0509

2) Department of Biomedical Sciences, State University of New York at Albany, Albany, NY 12222

Electron Tomography has recently emerged as an effective tool for three-dimensional (3D) ultrastructural analysis, particularly when combined with Intermediate or High Voltage Electron Microscopy (IVEM and HVEM) (reviewed in 1-3). In this approach a tilt series is recorded over a large angular range, up to 180°, typically with an angular interval of 2-5°. The individual images are digitized, rotationally and translationally aligned, the image density normalized,^{1,4} and finally the 3D reconstruction computed. After low pass filtration to the limiting resolution,¹ the reconstruction volume can be examined by a growing number of computer graphic tools.⁵ The chief advantages of tomography are that: 1) the reconstruction is an objectively determined, uninterrupted 3D density map of the specimen, as seen in the electron microscope; and 2) the method is generally applicable to any sample which is sufficiently contrasted or isolated from its surrounding environment.

Because of its generality tomography has been applied to a diverse group of biological preparations including: positively stained cilia, Balbiani rings, RNP particles, chromosomes and mammalian kinetochores in 0.10 - 0.25 μm thick sections; negatively stained 30 nm chromatin fibers; stained and unstained preparations of mineralizing turkey tendon in 0.50 μm thick sections; selectively stained dendrites and Golgi apparatuses in 2 - 3.0 μm thick sections; critical point dried chromosomes; freeze dried patch-clamped membranes in glass micropipettes; and puffball spores mounted on glass micropipettes. These studies are reviewed in refs. 2 and 3. More recently the method has been applied to: mitochondria;⁶ the tubular network of lipid engorged foam cells;⁷ and chick bone calcification.⁸

Analysis of the computed 3D reconstructions has been the limiting step in the application of HVEM tomography.⁵ Relatively large 3D volumes, typically on the order of 256 X 256 X 128 voxels, are required to represent the more intricate structures adequately. Such volumes present the investigator with a confusing amount of information from which the relevant features must be extracted. At present this is accomplished principally with density thresholds, an approach that works well in cases such as tendon mineralization where the major structural components have distinct image densities.² However, in determining the distribution of crystals between different collagen zones, a 3D masking operation (i.e. feature extraction based upon spatial criteria) had to be employed⁹ because crystals in the two zones have virtually the same image density. For the mammalian kinetochore (Fig. 1) key structural components, such as the outer plate, are embedded in a larger domain with approximately the same image density. Hence it is necessary to mask (Fig. 2) before informative views like those in Fig. 3 and 4 can be obtained. From these and similar views it was found that the plate: 1) fragments at its peripheral edges; 2) is constructed from a cross-striated or "quilted" pattern of fibrous elements; and 3) is bipartite.

Efforts to improve the quality of the computed reconstructions, and the efficiency and structural continuity of the 3D masking operation,⁵ promise to greatly enhance the effectiveness of HVEM and IVEM tomography. These developments, along with the continued increase in power and storage space of modern computers, make tomography an extremely powerful tool for ultrastructural analysis.¹⁰

References

1. J. Frank in *Electron Tomography*, ed. J. Frank, Plenum 1992, p. 1.
2. B. F. McEwen in *Electron Tomography*, ed. J. Frank, Plenum 1992, p. 281.
3. C. L. F. Woodcock in *Electron Tomography*, ed. J. Frank, Plenum 1992, p. 313.
4. B. F. McEwen et al., *Proc. Natl. Acad. Sci. USA* (1986)83, 9040.
5. J. Frank and B. F. McEwen, these Proceedings.
6. M. Marko et al., these Proceedings.
7. W. G. Jerome et al., these Proceedings.
8. J. Arena et al., these Proceedings.
9. B. F. McEwen et al., *Proc. Ann. EMSA Meeting* 49(1991)190.
10. Supported by NIH R01 GM40165 (to J.F.) and RR01219 (Wadsworth Center's Biological and Image Reconstruction Facility, a National Biotechnological Resource).

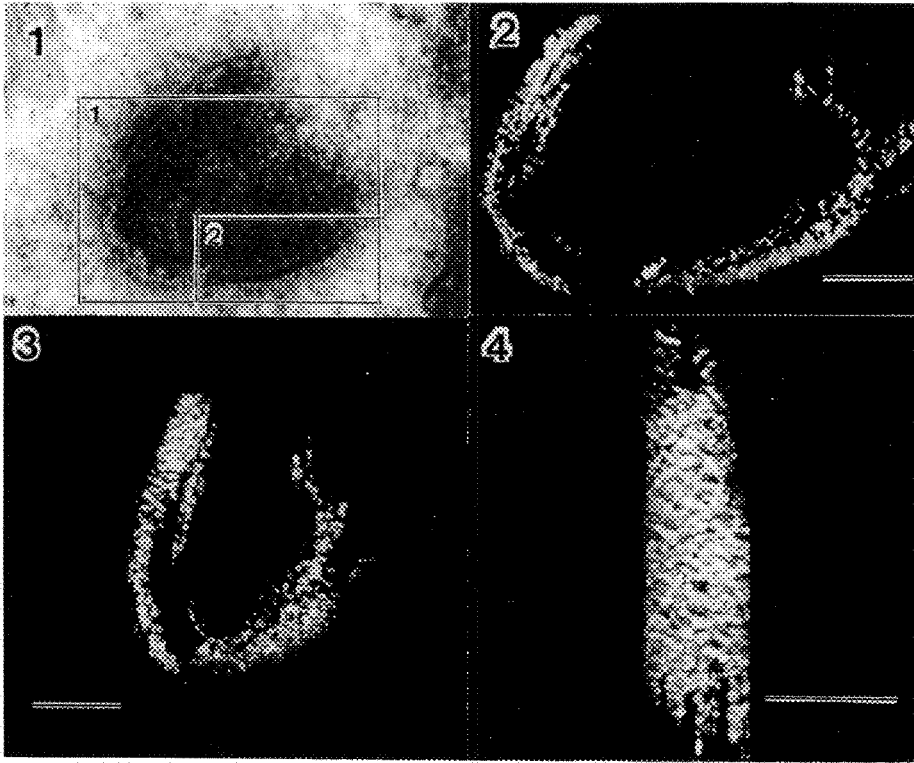


FIG. 1.--Electron micrograph of sister kinetochores from colcemid treated Ptk cells. Bar = 250 nm.
 FIG. 2.--Volume rendering of a 3D tomographic reconstruction from area #1 in Fig. 1. Densities corresponding to the chromosome and corona material have been removed using a 3D masking operation. Bar = 250 nm.
 FIG. 3.--Same as Fig. 2 but viewed at a 60° angle. Bar = 250 nm.
 FIG. 4.--En face view of the outer plate. A volume rendering of a 3D reconstruction of area 2 in Fig. 1. The reconstruction was masked similar to Fig. 2, but is viewed from a direction orthogonal to Figs. 1-3. Bar = 250 nm.

A STUDY OF THE MINERALIZATION OF BONE BY HIGH VOLTAGE ELECTRON MICROSCOPIC TOMOGRAPHY

James Arena,* Bruce F. McEwen,* Min Ja Song,* and William J. Landis**

*Wadsworth Center for Laboratories and Research, New York State Department of Health, Albany, NY 12201-0509; **Department of Orthopedic Surgery, Harvard Medical School and Children's Hospital, Boston, MA 02115

Complete characterization of the inorganic and organic interaction in calcifying tissues is fundamental to understanding their structure-function relations. In this context, high resolution tomographic three-dimensional (3D) reconstruction of normally calcifying avian tendon imaged by high voltage electron microscopy has recently been used to determine specific structural features of hydroxyapatite crystals associated with collagen fibrils in this vertebrate model of biological mineralization.¹⁻³ The present work is an extension of these previous investigations, now applied to bone for the first time.

The tibiae from normal 17-day-old embryonic chicks (Spafas, Inc., Norwalk, CT) were rapidly dissected and treated by anhydrous means with 100% ethylene glycol as detailed by Landis et al.⁴ The methodology is documented to maintain mineral constituents of the tissue which may be artifactually changed by alternative preparative methods.⁴ Newly mineralizing periosteal regions from the midshaft of the tibiae were embedded in Spurr resin, trimmed, and cut first into 0.25 μm thick sections and then into 80 nm thin sections, the latter, after uranyl acetate and lead citrate staining, serving as an aid to ultrastructural identification on conventional (100 kV) electron microscopy in a JEOL 100C instrument. Thick sections were examined unstained in the Albany (NY) high voltage electron microscope and a 5° tilt series of micrographs over a minimum range of $\pm 60^\circ$ were recorded at 1.0 MV.¹ The resulting images were digitized using an EIKONIX EC 78/99 digital camera with a pixel size of 1.3 nm. Rotational alignment was accomplished with fiducial markers and a least squares-based matrix operation.⁵ Translational alignment and computation of the weighted back-projection reconstruction were carried out as previously described.⁶ The 3D reconstruction was low pass filtered⁷ and examined on a PIXAR graphics display using volume rendering algorithms.

One of the sites of early bone mineralization in the embryonic chick tibia is illustrated by high voltage microscopy in Figure 1. The mineral crystals of hydroxyapatite are associated with a few thin collagen fibrils located in the relatively unmineralized osteoid region of the tissue. Figure 2 shows a stereopair of the mineral-collagen interaction in the reconstructed volume of this site. The results of tomographic reconstruction demonstrate that the early crystals are thin platelets of irregular shape and variable length (<90 nm) and width (<15 nm). Their thickness is generally uniform, approximately 4 nm. Crystal habit and size resemble the features of hydroxyapatite of tendon.¹ Bone crystals, also like those of tendon,¹ are aligned parallel to one another in simultaneous fashion. This characteristic is observed as well in neighboring but spatially separate collagen fibrils. Finally, at the stage of mineral development analyzed here, crystals are located in both collagen hole and overlap zones as found in tendon¹ and other calcifying vertebrate tissues studied by conventional microscopy.^{8,9} More extensive structural characterization of the association between crystals and collagen in bone is continuing in order to elaborate the mechanism for vertebrate mineralization. High voltage electron microscopic tomography is presently one of the most powerful approaches in this direction.¹⁰

References

1. W. J. Landis et al., *J. Cell Biol.* (1990)111, 24a.
2. W. J. Landis and M. J. Song, *J. Struct. Biol.* (1991)107, 116.
3. B. F. McEwen et al., *Proc. Ann. EMSA Meetg.* (1991)49, 190.
4. W. J. Landis et al., *J. Ultrastruct. Res.* (1977)59, 1.
5. M. C. Lawrence, in *Electron Tomography*, J. Frank (Ed.), Plenum Press, Inc., New York, In press.
6. B. F. McEwen et al., *Proc. Natl. Acad. Sci. USA*, (1986)83, 9040.
7. R. A. Crowther et al., *Proc. Roy. Soc. Lond.* (1970)A317, 319.
8. A. J. Hodge and J. A. Petruska, in *Aspects of Protein Structure*, G. N. Ramachandran (Ed.), Academic Press, London (1963)289.
9. M. J. Glimcher and S. M. Krane, in *A Treatise on Collagen. Biology of Collagen*, G. N. Ramachandran and B. S. Gould (Eds.), Academic Press, New York (1968)IIB, 68.
10. This work was supported by NIH grants AR34078, AR34081, RR01219, GM40165, and NASA grant NAG-2-538.

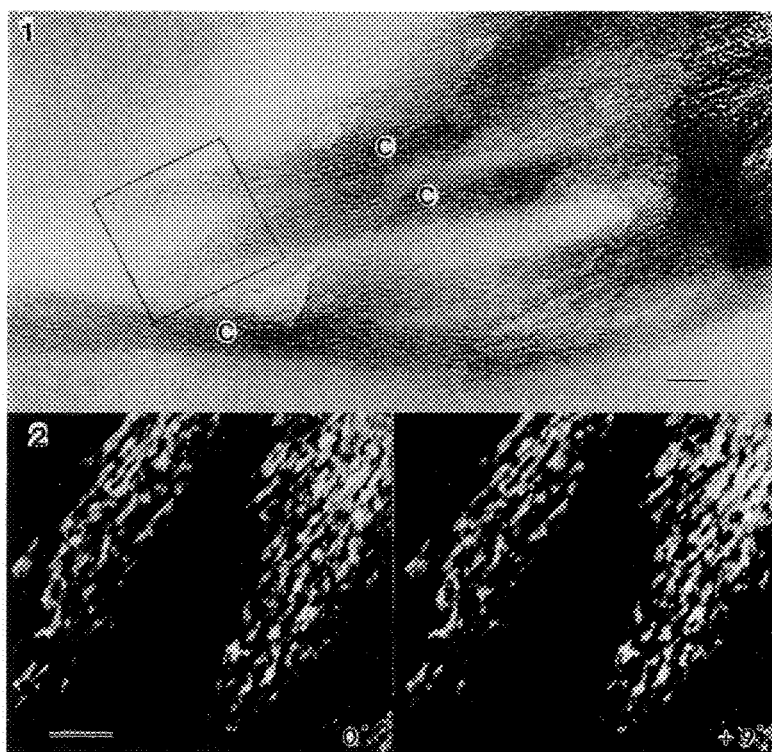


FIG. 1.--A region of the extracellular matrix along the periosteum of the midshaft in an embryonic chick tibia, illustrating a number of thin, newly mineralizing collagen fibrils (C). Unmineralized fibrils present elsewhere in the zone are not visible in this unstained section. The narrow ends of two fibrils containing early mineral crystals and outlined in the box were examined by tomographic reconstruction. Bar = 0.1 μ m.

FIG. 2.--A stereopair of the reconstructed volume of Fig. 1 showing newly deposited mineral crystals in association with collagen fibrils. Bar = 0.05 μ m.

3D X-RAY MICROSCOPY WITH A STORAGE PHOSPHOR PLATE DETECTOR

Roger H. Johnson, Robert M. Fisher* and Alan C. Nelson

Center for Bioengineering, WD-12 and *Department of Materials Science, FB-10
 University of Washington, Seattle, Washington 98195

X-ray microscopy provides the ability to obtain transmission, micron-order spatial resolution images of thick, wet objects at atmospheric pressure, e.g. to image some living specimens under dynamic conditions.¹ Past excitement in the field was dulled by difficulties in extracting desirable information from the vast amount of data which gets superimposed on an integrating planar detector such as film. Tomographic techniques such as backprojection reconstruction and laminography can solve the detail superimposition problem. Recent advances in solid state detectors facilitate the timely acquisition of multiple images required for tomographic imaging. We report here on our x-ray source and detector characteristics as well as initial planar microscopy and 3D imaging results from our ongoing development of a low-cost x-ray microtomograph.²

Our instrument, based on a modified JSM-U3 SEM, is illustrated in Figure 1. The 5-50keV electron beam is focused, with the aid of the secondary-electron image, onto a foil target conductively adhered to a grounded beryllium window terminating the vacuum. X-ray filters may be inserted into the emergent cone-beam to tailor the spectrum. Marked contrast enhancement may be achieved by dual-energy imaging or by the proper choice of foil target, beam filter, and specimen labeling or stain combinations. The sample is supported within millimeters of the source by a three-axis stage. Geometric magnification of up to 200X is achieved by placing the detector eleven centimeters from the source. The useful detected area is 10x10cm providing a 25° cone half angle. For backprojection microtomography or stereography, the sample is glued to the tip of a precision rotating shaft (Figure 2). Figure 3 shows a micrograph of an osteoporotic trabecular bone section from an iliac crest biopsy.

For a given specimen, image quality, as measured by photometric accuracy and spatial resolution, depends primarily upon the number of detected photons, the noise of the detection process, the x-ray source size and the detector's spatial resolution referred to object space. For a semithin-transmission-target x-ray source such as ours, the number of photons emitted into a cone of half-angle β is given by:

$$\sum_{E_v=E}^{E_v=E} \left[\frac{K}{1.602 * 10^{-19} \left(\frac{C}{e} \right)} * \frac{(E-E_v)}{E_v} * Z * I * \frac{1-\cos\beta}{2} * \exp(-R(E_v)_{\text{filter}} * T_{\text{filter}}) \right] \frac{\text{photons}}{\text{second}}$$

where $K = 2.2 * 10^{-6}$ is a constant, Z is the foil target Z number,

E (keV) and I (amps) are the electron beam accelerating voltage and current,

E_v is the photon energy interval in kilovolts,

and $R(E_v)_{\text{filter}}$ (cm^2/gm) and T_{filter} (gm/cm^2) are the filter cross section and thickness.^{3,4}

As examples, for a platinum target and 25° cone half angle, the total photon flux at 5keV with 10nA beam current and 10 microns aluminum filtration is $5 * 10^5$ photons/second and for 45kV with 100nA and 25 microns aluminum it is $6 * 10^8$ photons/second. Due to the small beam currents available in a one-micron probe, images acquired with reasonable exposure times (<5minutes) will always be photon-starved, making low noise in the detection process a critical requirement.

Table 1 compares the three major classes of imaging x-ray detectors. The solid state detectors offer improvement over film in every technical aspect except spatial resolution. To intercept as many x-rays as possible the detector must subtend a large cone angle. To avoid the detector pixel size (Table 1) imposing the limit on spatial resolution, the source-to-detector distance must be large enough to achieve adequate direct, point-projection magnification. These requirements favor a large-format detector. Their availability in large size at reasonable cost (8x10 inches for \$500) is the main advantage of stimulable phosphor plates over charge-coupled devices (CCD's). The laser-stimulated luminescence apparatus for phosphor plate readout, which presently limits both the photometric accuracy and the spatial resolution of these detectors, is undergoing improvement at a rapid pace.

For tomography, CCD's and phosphor plates share the advantage over film that images are available directly in digital form for mathematical processing. CCD's have additional advantages: The views in a tomographic tilt series are automatically spatially registered. With both phosphor plates and film there is a significant time lapse between image acquisition and image viewing, whereas CCD images are available almost in real time, easing the

crucial and nontrivial process of correct specimen positioning. Our future goals include comparison of phosphor plate with cooled CCD data as input to conebeam volume reconstruction algorithms.⁸

References:

1. T.A. Hall et al., Eds., X-ray Microscopy in Clinical and Exp. Med., Springfield, Ill.: Charles Thomas (1972).
2. R.H. Johnson et al., Proc. XIIth ICEM (1990)518.
3. H.A. Kramers, Phil. Mag. 46 (1923)836.
4. T.S. Rao-Sahib and D.B. Wittry, J. Applied Physics 45 (1974)5060.
5. L.K. Wagner et al., in J. Sturge et al., Eds., Imaging Processes and Materials, NY: Van Nostrand (1989)497.
6. M.M. Blouke et al., Proc. SPIE 290 (1981)6.
7. Y. Amemiya et al., Rev. Sci. Instrum. 60 (1989)1552.
8. Research supported by the W.M. Keck Foundation.



FIG. 3.--X-ray micrograph of 800-micron section of osteoporotic cancellous bone. Bar=100µm.

TABLE 1.--Comparison of three major classes of x-ray detectors for imaging.

	FILM		COOLED CCD		STORAGE PHOSPHOR
	alone	w/ screen	1:1*	5:1*	
PHOTON SENSITIVITY	very poor	fair to good	good	fair	excellent
DYNAMIC RANGE	<100 ⁵		10,000 ⁶		100,000 ⁷
NOISE	poor	very poor	good	fair	good to excellent
PIXEL SIZE	<1µm		25µm		88µm
SPATIAL RESOLUTION	<<1µm		5.0µm (20X#)	1.0µm (100X#)	0.8µm (100X#)
TOMOGRAPHY POTENTIAL	very poor		excellent		fair
COST	low		\$50,000		\$1,000

*Minification from a 100µm-thick conversion phosphor screen to a 2/3" diagonal, thermoelectrically-cooled CCD.
 #Direct magnification at detector (maximum attainable for the CCD) for a 1mm sample and cone half angle of 25°.

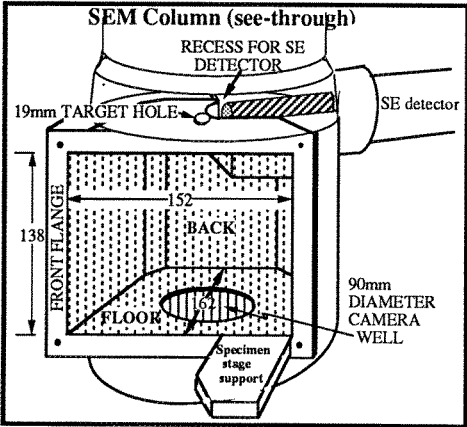


FIG. 1.--Sample chamber of microtomograph. Specimen stage not shown.

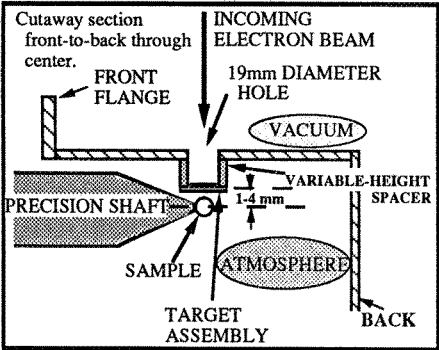


FIG. 2.--Side view of x-ray source/sample arrangement for microtomography.

THREE -DIMENSIONAL VISUALIZATION OF THE EYE

Barry R. Masters

Department of Anatomy and Cell Biology, Uniformed Services University of the Health Sciences, Bethesda, Maryland 20814-4799

The structure of the in situ rabbit cornea can be observed at high resolution and contrast with reflected light confocal microscopy¹⁻⁵. This paper describes the three dimensional reconstruction of the in situ cornea from an enucleated rabbit eye with confocal reflected light microscopy and volume rendering computer techniques. This paper shows the 3-D reconstruction of the full thickness of the cornea based on cubic voxels.

A laser scanning confocal microscope (BioRad MRC 600) was used in the reflected light mode to obtain the two-dimensional image stack from the cornea of a freshly enucleated rabbit eye. The eye was maintained in a physiological state with aerated Ringer's solution. The light source was an argon ion laser with a 488 nm wavelength. The microscope objective was a Leitz X50, NA 1.0 water immersion lens. The 400 micron thick cornea was optically sectioned into 1200, 0.33 micron sections. The optical sectioning was performed perpendicular to the optical axis of the eye globe. The voxels are cubic.

The structures observed in the two dimensional reflected light images of the cornea include the following: superficial epithelial cells and their nuclei (Fig. 1), basal epithelial cells, basal lamina, nerve plexus, nerve fibers, nuclei of stromal keratocytes, Descemet's membrane and endothelial cells. Fig. 2. shows the branching nerve fibers in the anterior stroma. The contrast of these structures as seen in reflected light cofocal microscopic images is similar to that observed in stained, sectioned sections. The 3-D volume reconstructions were performed on a Silicon Graphics work station with Vital Images, Voxel View software. This software uses the volume rendering technique to visualize the cornea^{6,7}. The full thickness volume rendering of the cornea reconstructed from the two dimensional data stack is shown (Fig.3).

References

1. M.A. Lemp, P.N. Dilly, & A. Boyde, *Cornea* (1985/86) 4, pp. 205-209.
 2. B.R. Masters and S. Paddock, *J. Microscopy* (1990) 158, 267-274.
 3. G.Q. Xiao, G.S. Kino, & B.R. Masters, *Scanning* (1990), 12, pp. 161-166.
 4. B.R. Masters and G.S. Kino, in B.R. Masters, Ed. **Noninvasive Diagnostic Techniques in Ophthalmology**, (1990), New York, Springer-Verlag, pp. 152-171.
 5. B.R. Masters, in T. Wilson, Ed. **Confocal Microscopy**, London, Academic Press, (1990), pp. 305-337.
 6. B.R. Masters, S.W. Paddock, *Applied Optics*, (1990) 29, pp. 3816-3822.
 7. A. Kriete, and B.R. Masters, *Transactions of the Royal Microscopical Society*, (1990) Volume 1: MICRO 90, pp. 401-404.
- Support from N.I.H, National Eye Institute, Grant EY-06958.

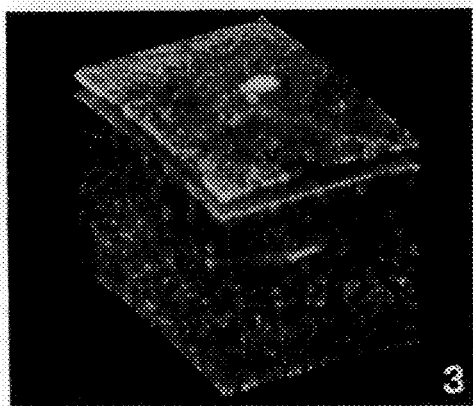
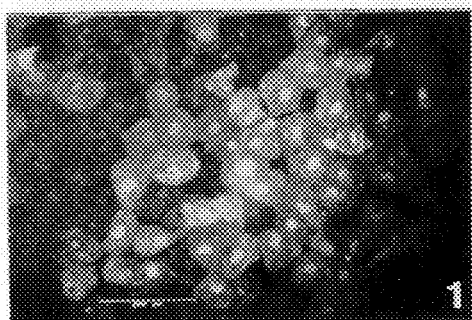


Fig. 1. Confocal reflected light image of epithelial cells in *ex vivo* rabbit eye. Bright nuclei are shown in center of epithelial cells.

Fig. 2. Confocal reflected light image of cornea in *ex vivo* rabbit eye. Nerve fiber and branches in anterior stroma. Nuclei of keratocytes are shown.

Fig. 3. Three-dimensional confocal reflected light image cornea in *ex vivo* rabbit eye. Top of figure is epithelium; nerve is shown on face of reconstruction; lower surface is corneal endothelium.

CHROMOSOME STRUCTURE AND DYNAMICS AS REVEALED BY 3-D AND 4-D IMAGING

David A. Agard, Jason R. Swedlow*, Yasushi Hiraoka, Michael R. Paddy, and John W. Sedat

Graduate Group in Biophysics* and Dept. of Biochemistry and Biophysics and Howard Hughes Medical Institute, University of California, San Francisco, San Francisco, CA 94143

Cellular DNA is packaged into chromosomes through complex processes whereby the DNA becomes compacted up to 10,000-fold by assembly into higher-order structures. In spite of many decades of intense study, the details of this process are not known. In addition, there is little information describing the dynamics of these higher-order structures during DNA replication, transcription, and mitosis. The goal of our laboratory is to use state-of-the-art 3-D imaging methods to understand how DNA is arranged into chromosomes and how chromosomes are spatially and temporally organized in the nucleus.

Towards this end, we have developed a digital fluorescence microscope workstation optimized for collecting three-dimensional multi-wavelength data from fixed and living specimens¹. The multiple-wavelength capability of this system allows us to simultaneously examine the spatial relationships of different chromosomal components in 3-D. Fixed samples can be labelled with up to three different fluorophore-conjugated antibodies and a fluorescent DNA binding dye, DAPI. Three-dimensional multi-wavelength data collection proceeds by sequentially recording images of each color, changing the focus, and then repeating the process as many times as necessary. The out-of-focus information in these images is removed by an iterative, three-dimensional deconvolution algorithm with a positivity constraint². To collect data from living samples, fluorescently labelled proteins are microinjected into cells and subsequently become incorporated into cellular structures. Three-dimensional images are then collected as a function of time. The time-lapse data can be processed using either the full 3-D deconvolution method or using an approach called synthetic projection imaging where out-of-focus information is removed from stereo pair projections of each data set at each time point by a two-dimensional deconvolution algorithm^{2,3}. The result is either a time-lapse 3-D or stereo, multi-wavelength movie.

The juxtaposition of three-dimensional data from fixed and living samples has proven essential to fully appreciate the organization and dynamics of chromosomal structures within *Drosophila* diploid nuclei. A comparison of data from fixed and living specimens has demonstrated an ordered arrangement of mitotic chromosomes and the spatial and temporal coordination of chromosome condensation, prometaphase congression, nuclear envelope breakdown, and mitotic spindle formation⁴. At the end of interphase, we have discovered that chromosome condensation initiates at a very few chromosomal sites adjacent to the nuclear envelope. Condensation then proceeds bidirectionally from these specific sites. At prophase, chromosomes have a geometrically polarized arrangement with centromeres localized on the side of the nucleus closest to the embryo surface and the telomeres on the opposite side. During prometaphase, a number of spatially polarized events begin in a concerted fashion. The nuclear envelope begins to break down where the centromeres are positioned. The mitotic spindle also begins to form at the position of the partial breakdown of the nuclear envelope. Prometaphase chromosome congression occurs as a wave moving from one side of the nucleus to the other; again beginning at the centromeres and ending at the telomeres. By metaphase, the nuclear envelope has broken down completely. After telophase, the chromosomes decondense and the last sites to decondense appear to be the same nuclear envelope-attached sites as where condensation will start at the next prophase. Throughout mitosis, chromosomes occupy separate domains within the nucleus: individual chromosomal arms never invade a neighboring chromosome's space.

We are also analyzing the molecular basis for chromosome architecture by determining the localization and dynamics of the important chromosomal protein, topoisomerase II. Although this protein has been proposed to play a general structural role in organizing chromosomes^{5,6}, there is

very little information to support this contention. What is necessary is to show a direct correlation between distribution, activity, and chromosome structure and dynamics. Therefore, we have analyzed the distribution of topoisomerase II in both fixed and living *Drosophila* embryonic nuclei. Topoisomerase II was detected in fixed samples by indirect immunofluorescence and three-dimensional dual-wavelength microscopy. From these studies, it is clear that topoisomerase II is associated with chromosomes but its distribution along each chromosome is quite heterogeneous; suggesting that the enzyme is concentrated at specific sites along the chromosome. The optical analysis has sufficient resolution for us to conclude that while some of these sites are coincident with the chromosome arm as might be expected, other sites are clearly adjacent to the chromosome. Similar results were obtained from 3-D immunofluorescence studies of *Drosophila* tissue culture cells. We do not yet know whether the observed chromosomal distribution of topoisomerase II is static or dynamic. To address this, we have injected *Drosophila* embryos with rhodamine-conjugated purified *Drosophila* topoisomerase II. In the living embryo, topo II appears to concentrate in the nucleus in interphase; a densely-labeled spot is also quite apparent. By late interphase it is clear that there are two pools of topo: chromosomal and soluble within the nucleus. The soluble pool leaves during nuclear envelope breakdown. Topoisomerase II levels vary with the cell cycle and are a minimum at telephase. These results suggest that the distribution of topoisomerase is quite dynamic during mitosis. We are currently examining the behavior of the enzyme at higher resolution.

It is clear that the application of three- and four-dimensional microscopy to the study of chromosomes has allowed a new appreciation of their organization and complexity. The approaches developed for these studies are quite general and thus should allow the detailed study of temporal and spatial organization of many different molecules and cellular structures.

References:

1. Y. Hiraoka et al., *Sem. in Cell Biol.* (1991), 2:153-165.
2. D. A. Agard et al., *Meth. Cell Biol.* (1989) 30:353.
3. Y. Hiraoka et al., *Nature* (1989) 342: 293.
4. Y. Hiraoka et al., *J. Cell Bio.* (1990) 111: 2815.
5. W. C. Earnshaw and M. M. S. Heck, *J. Cell Biol.* (1985) 100: 1716.
6. S. M. Gasser et al., *J. Mol. Biol.* (1986) 188:613.

CRYO-ELECTRON MICROSCOPY: THE METHOD OF CHOICE FOR DIRECT STUDY OF 3D-SHAPE OF INDIVIDUAL DNA MOLECULES IN A SOLUTION

Jan Bednar, Patrick Furrer, Andrzej Stasiak and Jacques Dubochet

Laboratoire D'Analyse Ultrastructurale, Université de Lausanne, CH-1015 Lausanne, Switzerland

3-D reconstruction of the trajectory of individual DNA molecules freely suspended in vitrified buffer^{1,2} opens new ways to study DNA. We showed that tightly supercoiled regions appearing as one thick filament can be reconstructed from their two projections². We present here use of this technique to trace normal double-stranded DNA regions to study the effect of DNA supercoiling on the overall shape of circular DNA molecules.

Method: Specimens were prepared as described previously^{1,3}. A 3µl drop of DNA solution (~50µg/ml in Tris-EDTA (pH 7.5)), was put on perforated carbon-platinum film. An automatic system⁴ blotted most of the drop in ca. 1 sec. and immediately released the plunger. After 0.1 sec. free fall, the specimen was immersed into the liquid ethane cooled close to its freezing point. The thin liquid layer of the solution, spanning the holes of the supporting film is then vitrified in ca. 10⁻⁴ sec. The vitrified specimen was mounted into a Gatan 626 cryo-specimen holder and transferred, without rewarming, into a Philips CM 12 electron microscope equipped for cryo-work. Stereo-pairs of micrographs were taken with a tilt angle of ± 15° at minimum dose exposure. For the 3-D reconstruction a system of coordinates was chosen so that x,y plane corresponds to the plane of the first micrograph and y axis is parallel to the tilt axis. The micrographs were mutually aligned along the Oy direction on the basis of a reference point, which is a well defined feature, clearly visible on both micrographs. This reference point is taken as the origin of the system of coordinates. The projection of the object results in the set of x',y' values for each point in the first tilted image and in x'', y'' in the second one. As the y is parallel to the tilt axis, y_i'=y_i'' for "i-th" point. A simple calculation then gives the z coordinate for this point : $z'_i = (x'_i \cos q - x''_i) / \sin q$, where q is the tilt angle between the two micrographs.

The determination of the path of the DNA molecules is made by clicking with the mouse along the center of the DNA filaments displayed on the screen of a computer. Clicking of individual points on the first image defines their coordinates (x_i', y_i'). This also defines the y_i'' coordinate for the corresponding points on the second image. The movement of the pointer is then restricted to the x direction at y_i' = y_i'' = y_i'''. The distance between successive points typically corresponds to 6 nm on the molecule. Bi-cubic spline interpolation based on these chosen points results in a smooth path overlapping each displayed projection of the molecule. The reconstructed molecules are visualized as flexible cylinders, obtained by attributing an arbitrary thickness to the 1-D curve.

Results: 3-D reconstructions of naturally supercoiled DNA molecules (Fig. 1) reveal that interwound segments do not contact each other, but they appear as continuously wrapped on the surface of an imaginary, irregular cylinder having a mean diameter of about 12 nm. Diameter of the superhelix is a result of counteracting torsional pressure, bringing the segments together, and repulsive interactions and entropic effects, tending to keep interwound segments separated in space. By varying the supercoiling density of analysed molecules and ionic strength of the solution (determining the repulsive forces) one should be able to quantify the entropic and repulsive effect in determining the shape of supercoiled DNA molecules in solution. 3-D reconstructions of supercoiled DNA molecules allow the first direct measurements of such topological parameters of DNA like writhe. In the shown case of this naturally supercoiled DNA molecule the writhe amounts to -3.36. Conventional EM preparations based on the adsorption of DNA on a surface are unable to provide this type of structural information.

1. M. Adrian et al., EMBO J. (1990)9,4551.
2. I. Dustin et al., J. Struct. Biol. (1991)107,15
3. J. Dubochet et al., Q. Rev. Biophys. (1988)21,129
4. M. Cyrklaff, M. Adrian and J. Dubochet, J. Electron Microsc. Tech. (1990)16,351
5. This research was supported in part by Swiss National Fund Grants 31-25694.88 and 31-27146.89.

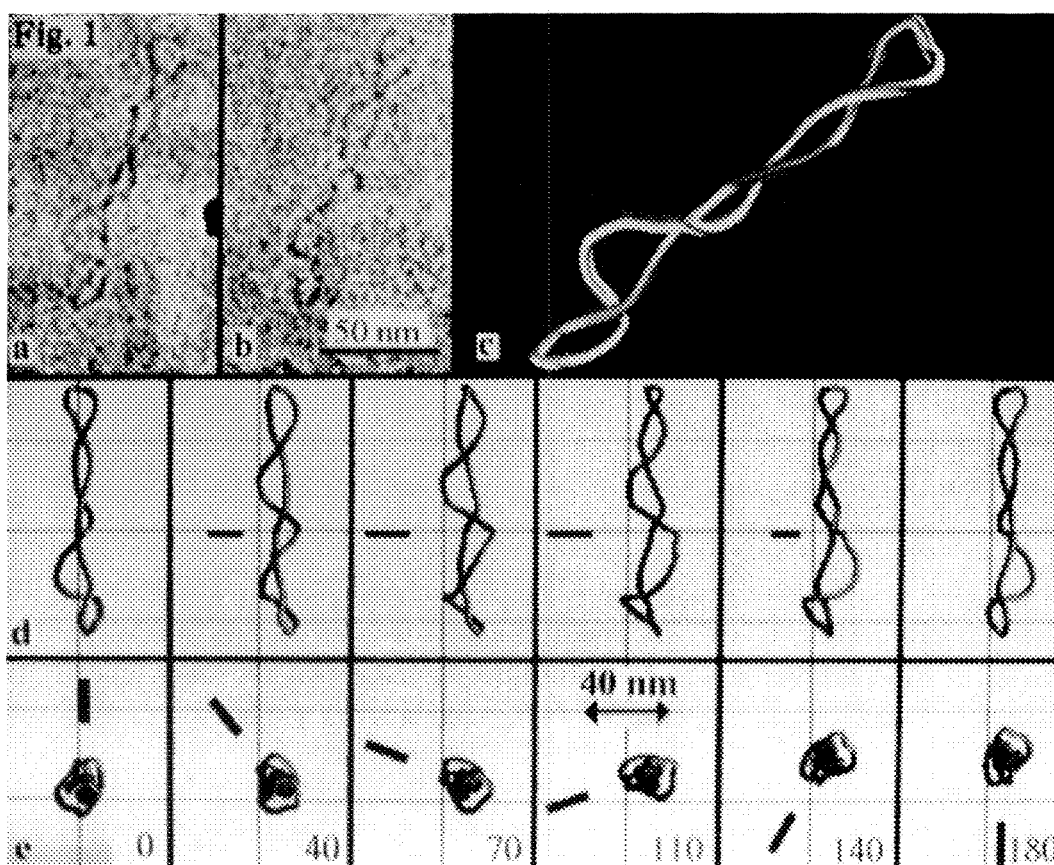


Fig. 1: 3D-reconstruction of naturally supercoiled DNA molecule (plasmid 995 base-paires).

a,b - stereo-pair of the micrographs of unstained DNA molecule freely suspended in the thin layer of vitrified buffer. Tilt axis is parallel to the vertical direction

c - 3D representation of the molecule as formed by the reconstruction. The orientation corresponds to the micrograph a, except it is rotated along z-axis perpendicular to the picture plane.

d,e - side-view (d), and end-view (e) of the molecule subsequently rotated 180 degrees along direction parallel to its geometrical axis. The value of the rotation relatively to the starting position is marked for each picture. Thick bar shows the orientation of the molecule. The side view allows to visualise and measure the superhelical diameter as varying value. The mean diameter of the superhelix was calculated as a statistical mean of the maximal diameter of every loop for every projection. The end-loops were excluded. The diameter of the loop was taken as a maximal distance between the filaments measured perpendicularly to the projection of superhelical axis. Superhelical axis in its projection goes through all crossing points and is equally distant from both filaments.

ULTRASTRUCTURAL THREE-DIMENSIONAL RECONSTRUCTION OF A T LYMPHOCYTE

Karen K. Bovard and Joseph N. Marcus

Department of Pathology, Creighton University School of Medicine, Omaha, NE 68178

There have been many electron microscopy studies of normal and neoplastic lymphocyte microanatomy. However, only a few use three-dimensional analysis techniques to visualize organelle relationships, such as nuclear shape and chromatin distribution¹, nucleolar organizing regions², and, by high voltage electron microscopy, the microtubular networks over a limited depth though the cell.³ To date, there has been no three-dimensional serial reconstruction of a T Lymphocyte and its organelles.

In this study, we serially reconstruct a complete T lymphocyte in 79 sections, using PC-based software (HVEM-3D, Laboratory for High Voltage Electron Microscopy, U. Colorado, Boulder). Peripheral blood lymphocytes were isolated by sequential Ficoll-hypaque and Sepracell-MN density gradients. Gall bodies, a marker of T lymphocytes, were visible by phase microscopy in 30% of the purified lymphocytes.⁴ The cells were fixed in 3% glutaraldehyde, postfixed in 1% OsO₄, dehydrated in a graded series of ethanol, and embedded in Poly/Bed 812 resin. One cell was chosen for serial sectioning due to the presence of Gall bodies and clustered dense bodies, also a morphological marker for T cell lymphocytes.^{5,6,7} Serial ultrathin (80 nm) sections were collected onto Formvar-coated slot grids, stained with uranyl acetate and lead citrate, and photographed at a constant magnification on a Phillips 201 TEM. Section contours were entered into a PC using a digitizing tablet using the HVEM-3D software program. A hard copy output was achieved by using Grafplus (Jewel Technologies, Inc.), a screen capture program, to capture a PCX format graphic file. The image file was translated to a PICT format graphic file using an Apple Mackintosh IIci computer and Adobe Photoshop software program (Adobe Systems, Inc.) which could be used by the video film recorder (Lasergraphics) for a high resolution picture image.

The reconstruction was successful with satisfactory registration (Fig. 1,2). Two Gall bodies were observed, one near clustered dense bodies, a spatial association previously described.⁸ The majority of organelles (Golgi apparatus, Gall bodies, centriole, clustered dense bodies, mitochondria, and vesicular bodies), were clustered in a wide crescent spanning 150° (Fig. 3). The endoplasmic reticulum was not well developed, indicative of a resting lymphocyte.

Among other applications, the techniques used in this first full 3-D reconstruction of a lymphocyte could be used in adjunct with immunoelectron-microscopy to better characterize the production, intracellular localization, and trafficking of T cell receptor-associated molecules.⁹

References

1. I. Dardick et al., *Human Pathol.* 16 (1985) 1187-1199.
2. P. Hozak et al., *Biol. Cell* 66 (1989) 225-233.
3. J.C. Guatelli et al., *Biol. Cell* 42 (1982) 69-80.
4. E.A. Gall, *Am. J. Med. Sci.* 191 (1934) 380-387.
5. Y. Watanabe et al., *Acta Haem. Jap.* 87 (1974) 655-666.
6. Y. Kanayama et al., *Acta Haem.* 70 (1983) 220-228.
7. J.N. Marcus et al., *Lab. Invest.* 44 (1981) 41A.
8. J.N. Marcus, *Lab. Invest.* 46 (1982) 52A.
9. J.J. Peters et al., *Nature* 349 (1991) 669-676.

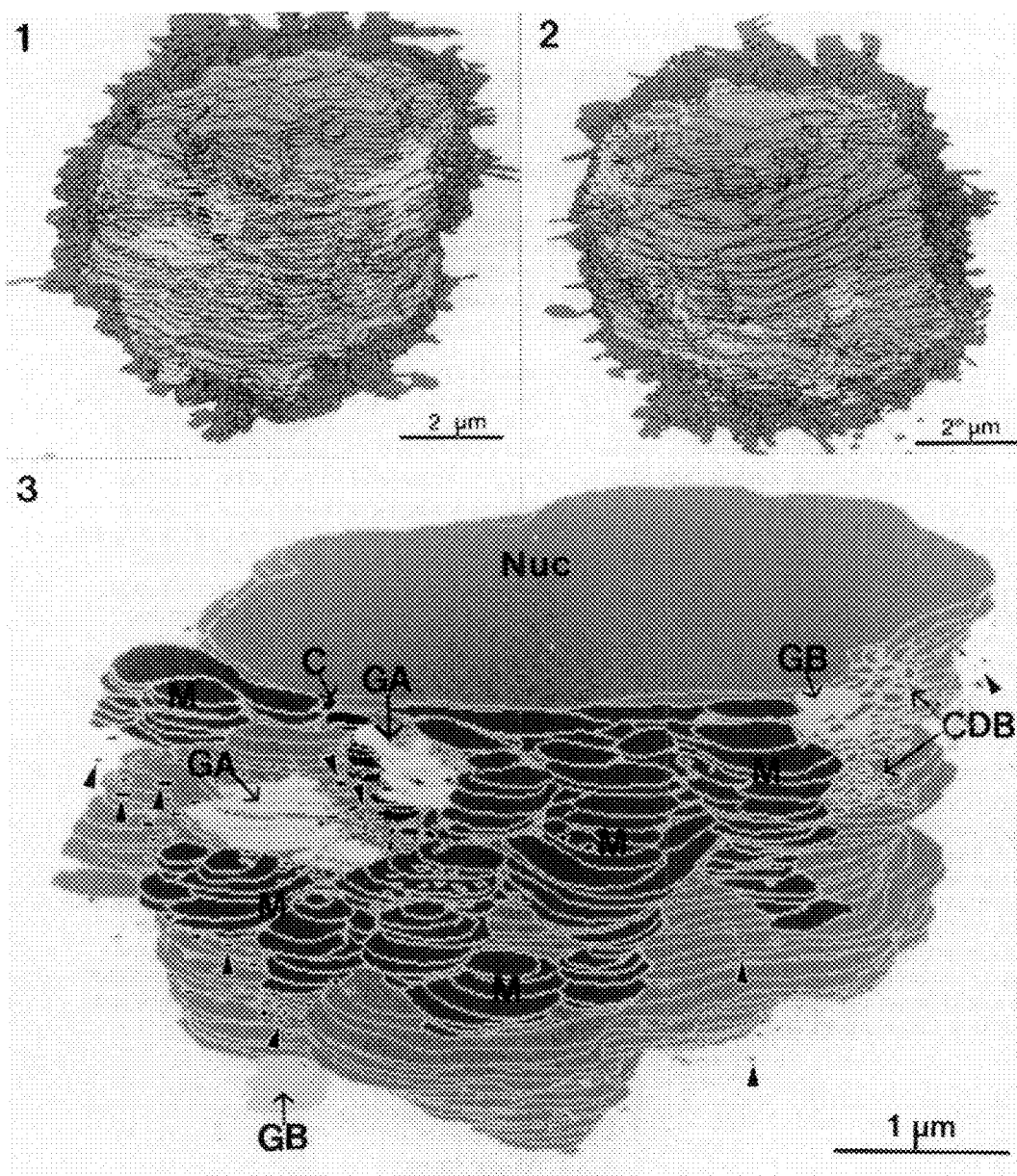


Fig. 1 Whole cell view.

Fig. 2 Whole cell view, opposite side of cell in Fig. 1.

Fig. 3 2-D/3-D, half-cell view of cell organelles with plasma membrane extracted. Nucleus (Nuc), Gall body (GB), Centriole (C), Mitochondria (M), Golgi apparatus (GA), Vesicular bodies (arrowhead), Clustered dense bodies (CDB)

The Effect of Cytoskeletal Protein Mutations on Cell Motility and Morphogenesis

David A. Knecht

Department of Molecular and Cell Biology, University of Connecticut, Storrs, CT 06269

The cortical cytoskeleton of eukaryotic cells is composed of actin filaments and a variety of associated proteins. The polymerization, depolymerization, cross-linking and bundling of these filaments, are presumed to be intimately involved in such processes as cell motility, cell adhesion and cell shape. In developing systems, all of these processes are involved in the morphogenetic mechanisms that shape tissues, organs and organisms.

We are investigating the complex interactions among cytoskeletal proteins using the simple eukaryotic amoebae, *Dictyostelium discoideum*. Our approach is to determine the function of the components of the cytoskeleton by creating mutants lacking particular proteins, or containing specific alterations in these proteins. Mutants lacking myosin heavy chain have been created using antisense RNA and homologous gene targeting.^{1,2} These cells have alterations in their shape and movement, and are incapable of accomplishing normal morphogenesis.³ Another cytoskeletal protein is ABP-120, which is capable of cross-linking actin filaments into orthogonal arrays, leading to the formation of an actin gel *in vitro*. ABP-120 is found in newly formed pseudopods extended during the chemotactic response to extracellular cAMP.⁴ Mutants lacking this protein have been created by disruption of the chromosomal gene with a transformation vector. These cells are not as dramatically affected as the myosin mutants, but have clear alterations in their motility and in the pathway of responses in the cytoskeleton that correlate with the expected function of this protein.⁶ Mutations in several other cytoskeletal genes are currently being constructed.

Several recently developed microscopic techniques are being applied to the analysis of the movement of these mutant cells. DMS⁵ (dynamic morphology system) is being used for computer assisted quantification of the parameters of movement in mutant and wild-type cells. With this system, the specific alterations in the process of movement that occur in mutant cells can be pinpointed. Confocal microscopy is also being used to analyze wild-type and mutant cells. The relative 3-dimensional localization of cytoskeletal proteins is being determined in mutant and wild-type cells by immunofluorescence. Second, the microscope is being used to track the movements of individual cells in the multicellular organism to determine how movement and shape changes correlate with morphogenetic alterations. This should allow us to determine how the modelling of the organism as a whole is determined by the behavior of individual cells, and how specific mutations affect this process.

1. D. Knecht and W. Loomis, Science (1987)236, 1081.
2. D. Manstein, et al., EMBO J (1989)8, 923.
3. D. Wessels, et al., Dev Biol (1988)128, 164.
4. J. Condeelis, et al., Cell Motil Cytoskeleton (1988)10, 77.
5. D. R. Soll, et al., J. Cell. Biochem. (1988)37, 177.
6. D. Cox, et al., J. Cell Biol. (1992)116,943.

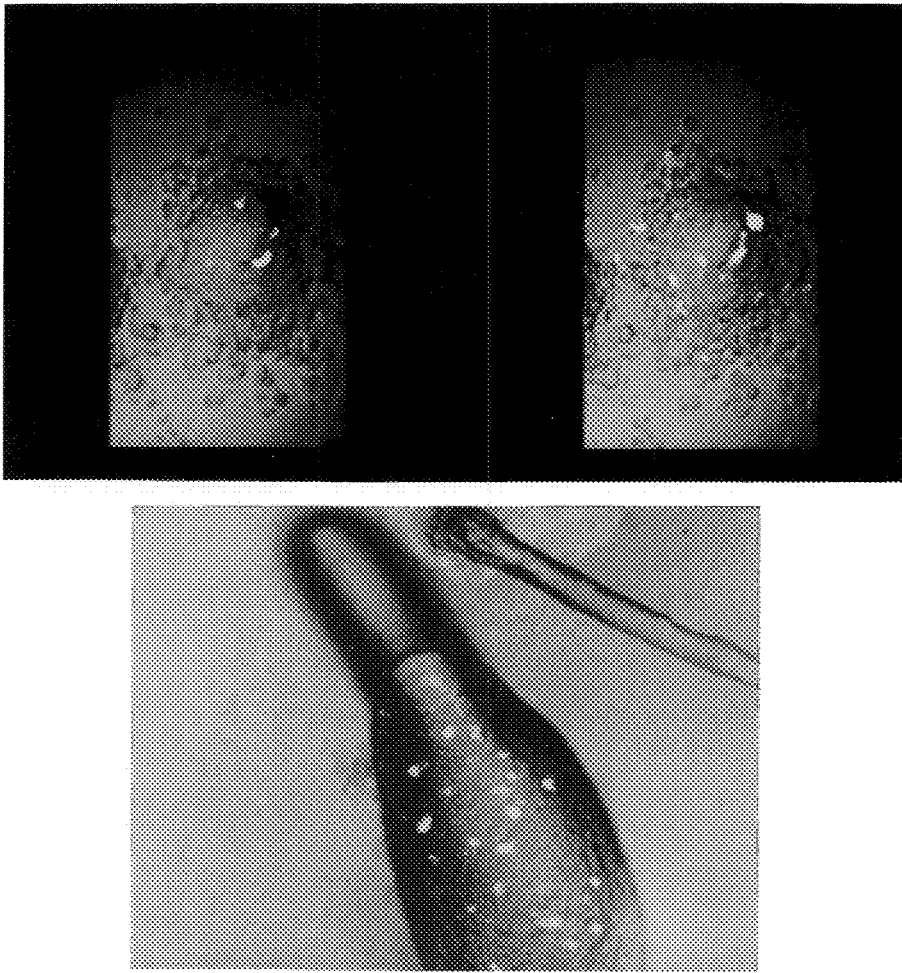


Fig. 1.-- (Top) Optical sections through an aggregate in two different focal planes visualizing the location of fluorescently labeled amoebae within the aggregate.
(Bottom) Optical section through a migrating slug showing location of labeled amoebae.

PRONUCLEAR MIGRATION, MATURATION AND FUSION: A CONFOCAL LIGHT MICROSCOPY STUDY OF FERTILIZATION IN *DROSOPHILA*

Timothy L. Karr

Department of Biochemistry and The Beckman Institute for Advanced Science and Technology,
University of Illinois, Urbana IL 61801

Most of what we know about fertilization in animals comes from studies of the interactions at the surface, or near the surface of sperm and egg. Examples include the acrosome reaction, cortical exocytosis and the formation of the fertilization envelope. One area in particular where our knowledge is limited are those events that occur inside the egg following sperm penetration. These include pronuclear maturation, pronuclear migration and pronuclear fusion. Molecular studies have also suffered from the lack of a genetically tractable system that would allow function to be assigned to the individual molecules associated with fertilization.

Fertilization in *Drosophila*, and in insects in general, have numerous fundamental differences compared to fertilization in mammals and marine invertebrates. I will compare and contrast these differences by examining fertilization and early embryonic development in the fruit fly, *Drosophila melanogaster*. These differences probably reflect differences in reproductive strategies that have evolved in insects. The study of fertilization in *Drosophila* may be particularly useful in the study of sperm-egg interactions as they occur inside the egg following sperm penetration. *Drosophila* also has the advantage of genetics which we are currently exploring.

Figure 1 is a diagrammatic depiction of fertilization starting with sperm penetration and completion of meiosis II (1A), pronuclear maturation and migration (1B), completion of migration and the juxtaposition of the fully mature pronuclei (1C), followed by the early nuclear divisions (1D). Two outstanding features of *Drosophila* fertilization distinguish insect from mammalian fertilization: 1. the lack of sperm-egg membrane fusion (originally described by Perotti¹), and 2. the presence of the entire 1.8 mm long sperm tail in the egg². We are currently investigating the three-dimensional structure of the sperm in the egg with particular emphasis on the maternal factors responsible for the exclusive anterior localization, and apparent stereotypic folding, of the sperm in the egg. A video tape describing the 3D structure will be presented to illustrate these phenomena. 3D structures were generated using the real-time volume rendering programs Viewit and Lathe running on a Connection Machine 2 (developed by R. Brady, P. Moran and C. Potter, National Center for Supercomputer Applications, University of Illinois).

Evidence for possible sperm function(s) post-fertilization is presented in Figure 2. The embryo shown has been stained with a polyclonal anti-sperm antisera and a monoclonal antibody that stains interphase nuclei. Both low (Fig. 2A) and high (Fig. 2B) reveal an unusual and unexpected association of the sperm tail with a single zygotic nucleus. The functional significance of this association is at present unclear. However, the position of the nucleus attached to the sperm is consistently observed at the anterior boundary of the early cleavage nuclei, and may indicate a role in marking or otherwise positioning nuclei during these early stages of development³.

References

1. Perotti, M. E. (1975) pp. 57-68. In: Afzelius Ba, ed. The functional anatomy of the spermatozoon. New York, Pergamon Press.
2. Karr, T.L. (1991) Mech. Dev. 34: 101-112.
3. This research was supported by the NSF and the Beckman Institute, University of Illinois. Special thanks to Nick Kisseberth for computer programming and data analysis.

FIGURE 1

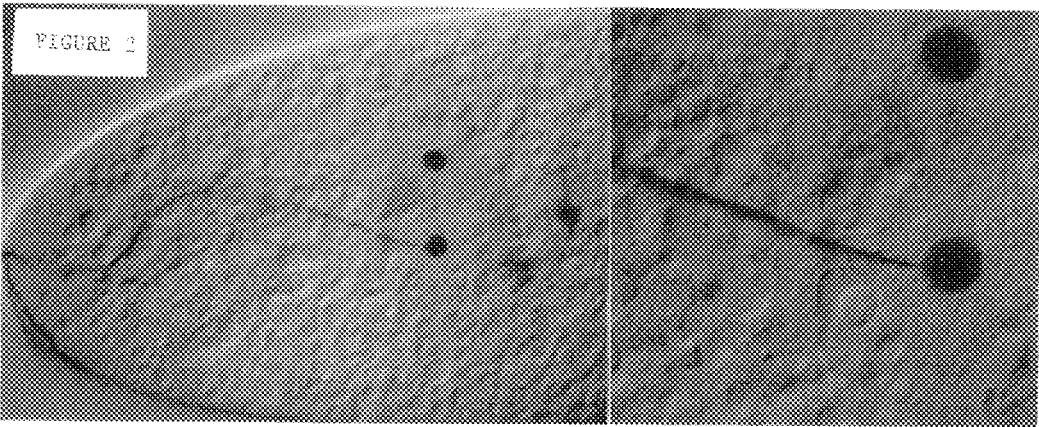
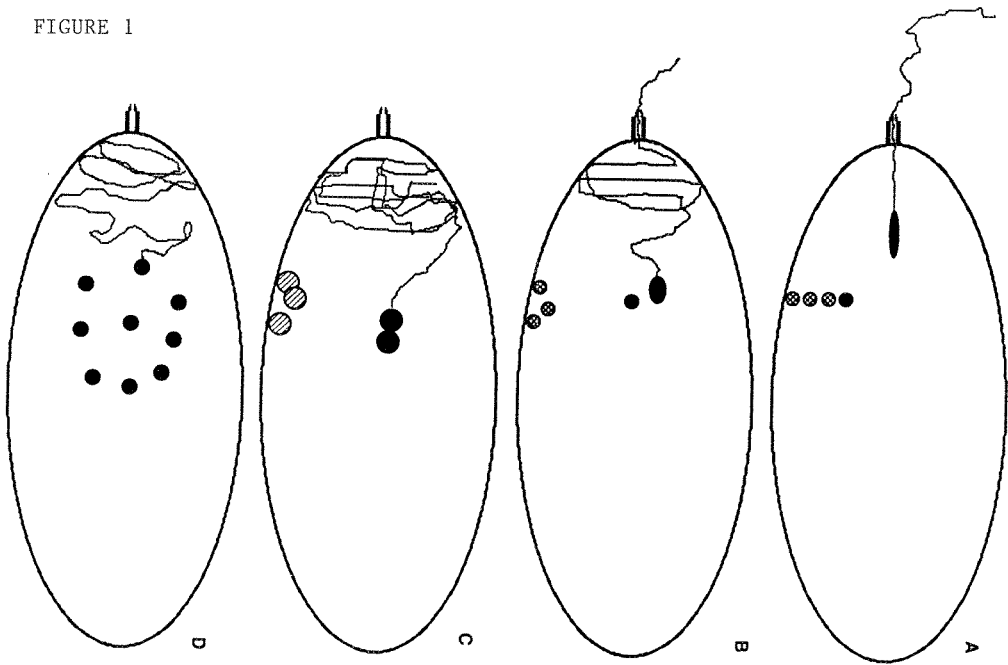


Figure 1. Schematic depiction of fertilization in *D. melanogaster*. (A), sperm entry and initiation of meiosis II; (B), pronuclear migration; (C), pronuclear fusion; (D), early cleavage divisions.

Figure 2. Persistence of sperm in the egg following fertilization. Both a low (left) and high (right) magnification view of a fertilized egg fixed during nuclear division cycle 3. This egg was stained with a polyclonal antisera against the sperm and a mouse monoclonal that recognizes interphase nuclei. Note the unique nucleus/sperm attachment site.

SPATIAL AND TEMPORAL EXPRESSION OF FIBRONECTINS AND INTEGRINS DURING *XENOPUS* DEVELOPMENT

Douglas W. DeSimone, M. Susan Dalton, Mark D. Hens, Bethanne Hill, Joe W. Ramos, David G. Ransom and Charles A. Whittaker

Department of Anatomy and Cell Biology and the Molecular Biology Institute,
University of Virginia Health Sciences Center, Charlottesville, VA 22908

A central challenge in biology is to understand the cellular processes that direct morphogenesis and the formation of the basic body plan during development. These events are controlled to large extent, by adhesive interactions of cells with one another and with their extracellular environments. Specifically, we are investigating the structure, function and expression of two groups of molecules thought to play important roles in promoting cell adhesion and migration in the embryo: fibronectins (FNs), which are large extracellular matrix (ECM) glycoproteins with many adhesion related functions; and integrins, which are the cellular transmembrane-receptors for FNs and several other components of the ECM.

In the amphibian *Xenopus laevis*, FN is first synthesized in all regions of the early embryo but becomes localized to the inner roof of the blastocoel where it is presumed to support the migration of mesodermal cells during gastrulation¹. We have shown that activation of mesoderm adhesion to FN is one of the first responses made by these cells as a consequence of embryonic induction^{2,3}. Evidence suggests that proper expression of the cellular receptors for FN is essential, not only for cell adhesion, but also for localized assembly of FN into the ECM. A major focus of our research, therefore, is to define and characterize integrins that are expressed in the embryo.

The integrin family includes several receptors that can account for most, if not all, FN-mediated cell adhesion. All integrins are heterodimers of distinct α and β subunits. Different $\alpha\beta$ combinations differ in their ligand binding specificities. We have used degenerate oligodeoxynucleotide primers and polymerase chain reaction methods to amplify and clone *Xenopus* integrin subunits β_1 , β_2 , β_3 , α_2 , α_3 , α_4 , α_5 , α_6 , α_{IIb} and a novel subunit β_X . Full-length cDNAs for several of these subunits have been obtained and bacterial fusion proteins prepared for use as immunogens in order to produce integrin subunit-specific antibodies. The spatial (Figs. A-G) and temporal patterns of expression for integrins β_1 , β_3 and α_3 have been determined using these antibodies. We are also currently using "reverse genetic" approaches to analyze integrin and FN structure/function relationships during development⁴.

References

1. D.W. DeSimone and K.E. Johnson, Meth. Cell Biol. (1991) 36, 527.
2. J.C. Smith et al., Development (1990) 108, 229.
3. D.W. DeSimone et al., in R. Keller et al., Eds., Gastrulation, New York: Plenum (1991) 185.
4. This research is supported by USPHS grant R01-HD26402 and by an Pew Scholars Award in the Biomedical Sciences and an American Cancer Society Junior Faculty Research Award (to DWD).

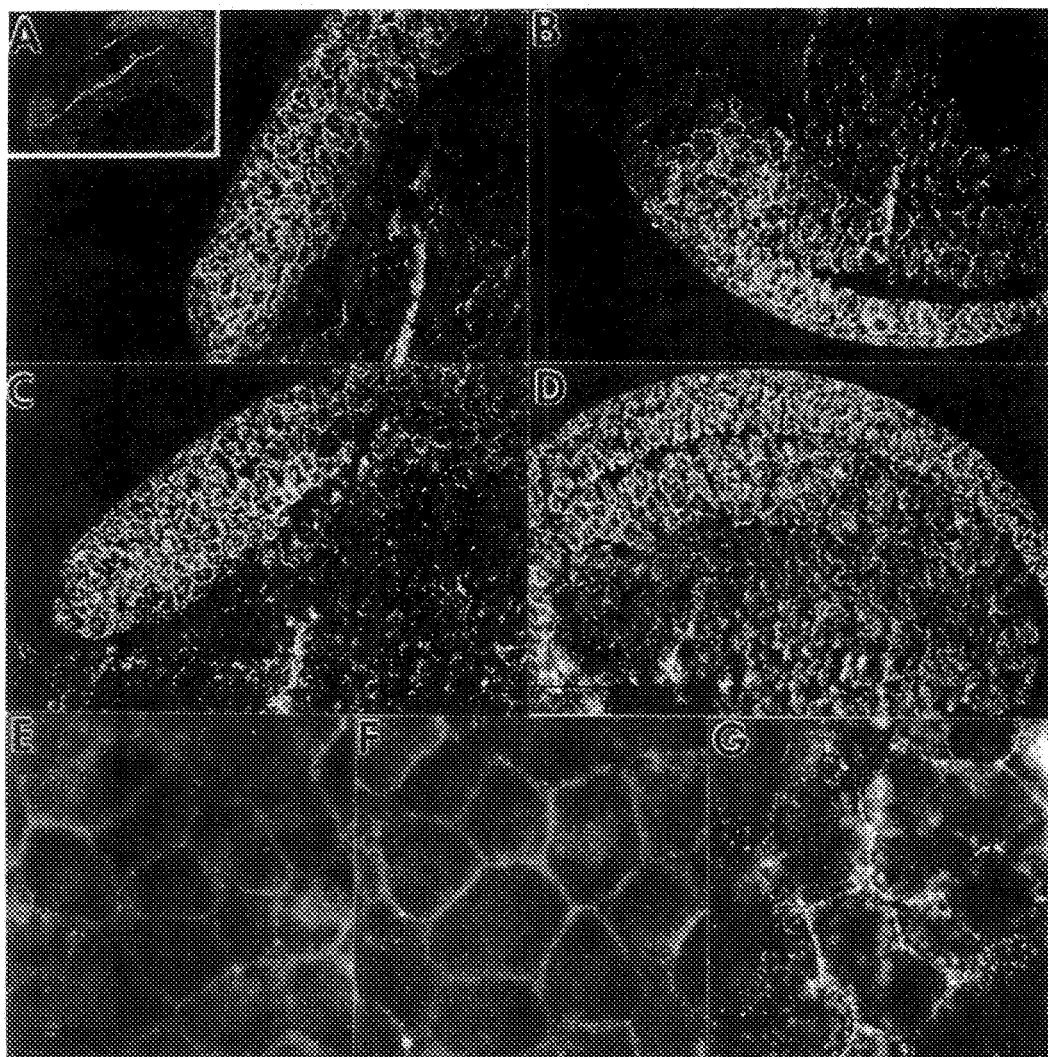


FIG. A.--Immunofluorescence analysis of β_1 integrins expressed in a mid-gastrula stage embryo sectioned along the animal-vegetal axis. Inset shows lower magnification of same embryo. β_1 staining is noted on all cells but is most pronounced on involuting and non-involuting cells of the dorsal lip, marginal zone and the blastocoel roof.

FIG. B.--Same embryo as in Fig. A. showing ventral lip, blastocoel roof and involuting mesoderm.

FIG. C.--Mid-gastrula embryo stained with anti- β_3 antibody shows similar pattern of expression as with the β_1 (Figs. A and B).

FIG. D.--Anti- α_3 antibody stains the cells of the blastocoel roof and the layer of mesodermal cells in contact with the overlying roof. Lighter cell-surface staining is noted on endodermal cells.

FIGS. E,F,G.--Whole mount blastocoel roof preparations stained with the β_1 , β_3 and α_3 fusion protein antisera, respectively. Note that each antibody stains sites of cell-cell contact.

CELL-MATRIX INTERACTIONS IN THE EARLY MOUSE EMBRYO

A.E. Sutherland*, P.G. Calarco and C.H. Damsky*

Departments of Anatomy and *Stomatology, University of California, San Francisco, San Francisco, CA 94143

Cell-extracellular matrix (ECM) interactions mediated by the integrin family of receptors are critical for morphogenesis and may also play a regulatory role in differentiation during early development. We have examined the onset of expression of individual integrin subunit proteins in the early mouse embryo, and their roles in early morphogenetic events. As detected by immunoprecipitation, the $\alpha 6$, αV , $\beta 1$, and $\beta 3$ subunits are detected as early as the 4-cell stage, $\alpha 5$ at the hatched blastocyst stage and $\alpha 1$ and $\alpha 3$ following blastocyst attachment. We tested the role of these integrins in the attachment and migratory activity of two cell populations of the early mouse embryo: the trophoblast giant cells, which invade the uterine stroma and ultimately contribute to the chorio-allantoic placenta, and the parietal endoderm, which migrates over the inner surface of the trophoblast and ultimately forms Reichert's membrane and the parietal yolk sac. Experiments were done in serum-free medium on substrates coated with laminin (Ln) and fibronectin (Fn). Trophoblast outgrowth occurs on Ln and its E8 fragment (long arm), but not on the E1' fragment (cross region) (Figs. 1, 2). This outgrowth is inhibited by anti-E8, anti-Ln, and by the anti- $\beta 1$ family antiserum anti-ECMR, but not by anti- αV or the function-perturbing GoH3 antibody that recognizes the $\alpha 6/\beta 1$ integrin, a major Ln (E8) receptor. This suggests that trophoblast outgrowth on Ln or E8 is mediated by a different $\beta 1$ integrin such as $\alpha 3/\beta 1$. Early stages of trophoblast outgrowth (up to 48 hours) on Fn are inhibited by anti-Fn and by function-perturbing anti- αV antibodies, whereas at later times outgrowth becomes insensitive to anti- αV but remains sensitive to the anti- $\beta 1$ family antiserum anti-ECMr, indicating that trophoblast cells modulate their interaction with Fn during outgrowth. Trophoblast outgrowth on vitronectin (Vn) is sensitive to anti- αV antibodies throughout the 5-day period examined.

Parietal endoderm cells (PE), which migrate out onto the culture dish after 3-5 days of blastocyst outgrowth, also recognize Fn and the E8 fragment of Ln. Unlike trophoblast outgrowth, migration of PE on Fn is not affected by anti- αV antibodies, but migration on Ln is inhibited by the GoH3 antibody, indicating that $\alpha 6/\beta 1$ is the major Ln receptor for these cells (Figs. 3, 4). Indirect immunofluorescence shows that, consistent with the functional data, $\alpha 6/\beta 1$ is expressed strongly in cells of the primitive endoderm in hatched blastocysts and parietal endoderm cells in embryo outgrowths, but that there is little detectable $\alpha 6/\beta 1$ in trophoblast cells (Fig. 5).

These studies demonstrate that significant diversification and modulation of integrin-mediated events accompany the development of migratory behavior in the early mouse embryo. (supported by HD26732 and CA42032).

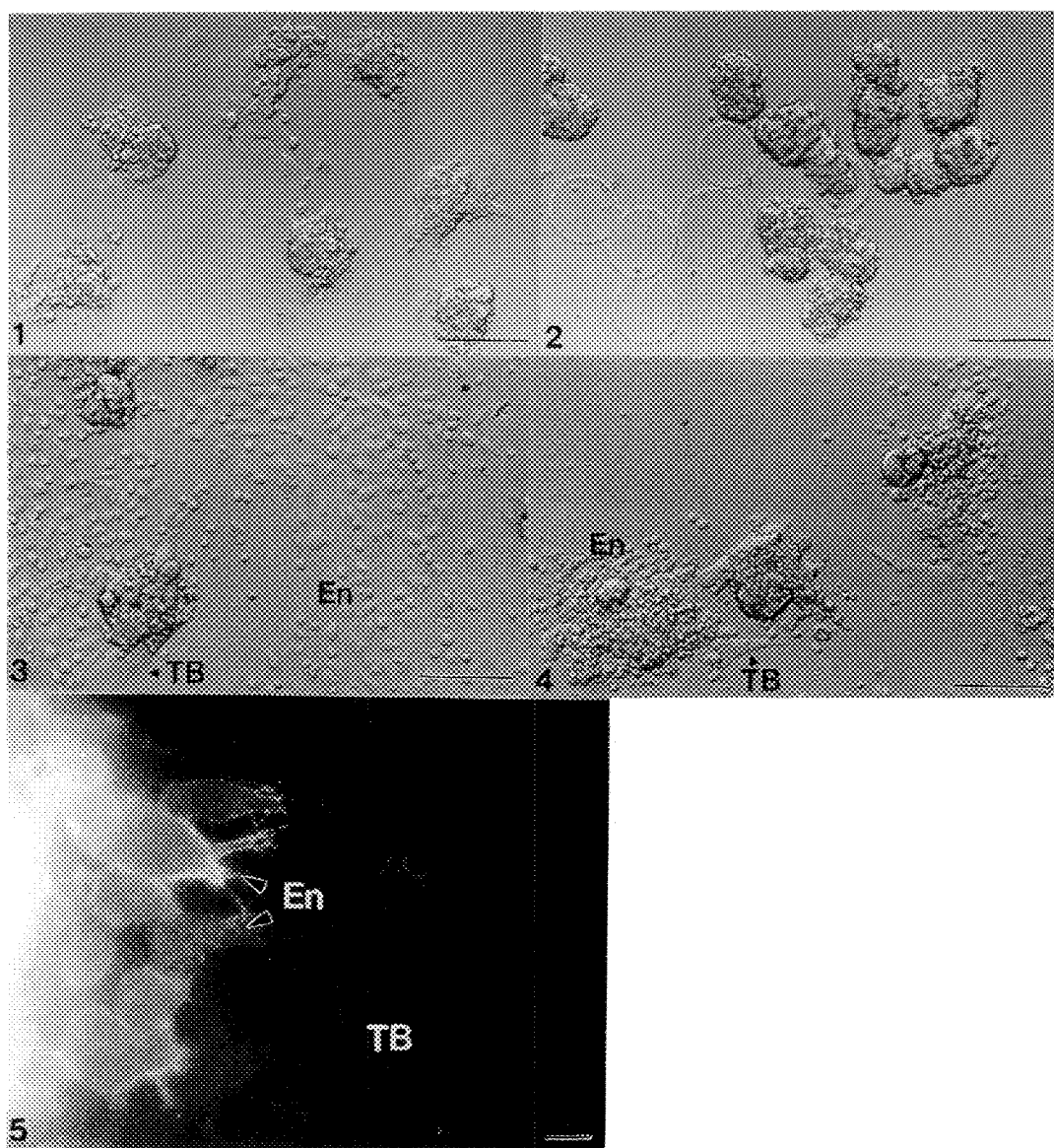


FIG 1.--Embryo outgrowths on the E8 fragment of Ln. Bar = 50 μ m.

FIG 2.--Embryo outgrowths on the E1' fragment of Ln. Bar = 50 μ m.

FIG 3.--Outgrowths with endoderm on a substrate of whole Ln; control conditions. En, endoderm, TB, trophoblast. Bar = 50 μ m.

FIG 4.--Outgrowths with endoderm on a substrate of whole Ln; the antibody GoH3 against $\alpha 6$ has been added to the medium. Bar = 50 μ m.

FIG 5.--Embryo outgrowths stained with the antibody GoH3 against $\alpha 6$. Bar = 5 μ m.

USE OF F9 TERATOCARCINOMA STEM CELLS TO STUDY CELL-MATRIX INTERACTIONS IN THE EARLY MOUSE EMBRYO

Marc Lenburg, Rulang Jiang, Lengya Cheng and Laura Gabel

Department of Biology, Wesleyan University, Middletown, CT 06459

We are interested in defining the cell-cell and cell-matrix interactions that help direct the differentiation of extraembryonic endoderm in the peri-implantation mouse embryo. At the blastocyst stage the mouse embryo consists of an outer layer of trophoctoderm surrounding the fluid-filled blastocoel cavity and an eccentrically located inner cell mass. On the free surface of the inner cell mass, facing the blastocoel cavity, a layer of primitive endoderm forms. Primitive endoderm then generates two distinct cell types; parietal endoderm (PE) which migrates along the inner surface of the trophoctoderm and secretes large amounts of basement membrane components as well as tissue-type plasminogen activator (tPA), and visceral endoderm (VE), a columnar epithelial layer characterized by tight junctions, microvilli, and the synthesis and secretion of α -fetoprotein. As these events occur after implantation, we have turned to the F9 teratocarcinoma system as an *in vitro* model for examining the differentiation of these cell types. When F9 cells are treated in monolayer with retinoic acid plus cyclic-AMP, they differentiate into PE. In contrast, when F9 cells are treated in suspension with retinoic acid, they form embryoid bodies (EBs) which consist of an outer layer of VE and an inner core of undifferentiated stem cells. In addition, we have established that when VE containing embryoid bodies are plated on a fibronectin coated substrate, PE migrates onto the matrix and this interaction is inhibited by RGDS as well as antibodies directed against the $\beta 1$ integrin subunit.¹ This transition is accompanied by a significant increase in the level of tPA in the PE cells.² Thus, the outgrowth system provides a spatially appropriate model for studying the differentiation and migration of PE from a VE precursor.

Recent work has focused on examining the role of the membrane bound heparan sulfate proteoglycan syndecan and tPA in the VE to PE transition and the subsequent migration of PE cells. Using indirect immunofluorescence (monoclonal 281-2 is a antibody generous gift of M. Bernfield) we observed that syndecan is localized between all cells in young or undifferentiated EBs and becomes localized beneath the VE layer as differentiation occurs. This localization is consistent with a role for syndecan in attaching VE to the basal lamina. In outgrowth cultures, no immunologically detectable syndecan structure is associated with the PE, although significant levels of syndecan are still localized to the basal lamina of the VE in the EB. Northern analysis for syndecan message indicates that although PE express no immunologically detectable syndecan protein, significant levels of syndecan message are present in these cells. In order to explain this discrepancy and to provide a mechanism for the VE to PE transition, we propose the following hypothesis. The model is based on several observations: the presence of a potential serine protease cleavage site in syndecan just outside of the cell in the extracellular domain, the increase in tPA associated with the VE to PE transition, and treatment of differentiating PE cells with anti- $\beta 1$ integrin antibodies promotes tPA accumulation. We propose that an interaction between fibronectin

and an appropriate integrin receptor stimulates tPA accumulation, and tPA, in turn, directly, or indirectly via a plasmin intermediate, cleaves syndecan, releasing its ectodomain into the medium. This facilitates the release of VE from the EB and promotes the close substrate attachment critical to the PE transition. Experiments are underway to assess the accuracy of the model.

We have also recently investigated the role played by tPA in promoting PE migration based presumably on its ability to directly or indirectly digest the fibronectin substrate. Antibodies directed against tPA, but not antibodies directed against a cell surface protein ($\beta 2$ microglobulin), inhibit PE outgrowth in a dose dependent manner. Certain serine protease inhibitors have similar inhibitory activity. Future studies are aimed at determining if PE secreted tPA can degrade the fibronectin substrate.

We have also used the F9 monolayer system to investigate the developmentally regulated acquisition of focal contacts.³ Undifferentiated stem cells express actin, vinculin, $\beta 1$ integrin, and fibronectin but are unable to organize them into a focal contact. Following retinoic acid treatment, these components are localized to form substrate adhesion sites. We have previously described that coincident with this transition, $\beta 1$ integrin becomes dramatically less phosphorylated, and that the phosphorylation is predominantly on serine residues.⁴ We now demonstrate that $\alpha 3$ and $\alpha 5$ integrin subunits are present at essentially equivalent levels in undifferentiated and differentiated F9 cells and that these subunits also undergo developmentally programmed desphosphorylation. Interpretation of these results as well as plans for future studies will be discussed.

References

1. L. Grabel and J. Casanova. *Differentiation* (1986) 32, 67.
2. L. Grabel and T. Watts. *J. Cell Biol.* (1987) 105, 441.
3. S. Dahl and L. Grabel. *J. Cell Biol.* (1989) 108, 183.
4. K. Sabbag et al. *Development* (1989) 106, 195.

HUMAN MAST CELLS BUT NOT HUMAN BASOPHILS COCULTURE WITH MOUSE 3T3 FIBROBLASTS

J. P. Goff¹, A. S. Kirshenbaum^{2,4}, J. P. Albert¹, S. W. Kessler³ and D. D. Metcalfe⁴

¹ Division of Molecular Virology and Immunology, Georgetown University Medical Center Rockville, MD 20852

² Allergy Division, Department of Medicine, Homewood Hospital Baltimore, MD 21211

³ Immunobiology and Transplantation Dept, Naval Medical Research Institute Bethesda, MD 20889

⁴ Mast Cell Physiology Section, NIAID NIH Bethesda, MD 20892

Human mast cells and basophils have been shown to arise from CD34+ pluripotent progenitor cells in the presence of rhIL-3 (1). Two different culture systems using CD34+ cells, the agarose interphase culture and 3T3 fibroblast/CD34+ coculture, give rise to mast cells and basophils but with markedly different results. (1,2). By 3 weeks in interphase agarose cultures, CD34+ cells give rise to approximately 25-45% basophils and 1-5% tryptase positive mast cells. These mast cells have homogeneous granule patterns that resemble immature mast cells. With the addition of stem cell factor (rhSCF) (3) to rhIL-3, total cell number increases and mast cell maturation is promoted without altering the percentages of mast cells and basophils (4). These mast cells have tryptase-positive granules, with characteristic patterns seen in mature mast cells. In contrast, CD34+ cells cocultured with mouse 3T3 fibroblasts give rise by 6 weeks to approximately 50% tryptase positive mast cells which adhere to the monolayer and possess granule scroll patterns. No basophils are ever identified by six weeks in cocultures.

To determine whether human basophils would survive, or phenotypically change and become mast cells when cocultured with 3T3 fibroblasts, IgE receptor positive cells consisting of 92-94% basophils were enriched by immunomagnetic cell selection from 3 week old cultures of IL-3 dependent CD34+ cells and placed on 3T3 fibroblasts. Cultures were sampled at 2 days, 1, 2, and 6 weeks and examined by histochemical staining and electron microscopy for the presence of basophils.

Basophils decreased markedly by 1 week and were absent from cocultures by 2 weeks. In contrast, basophils re-cultured over agarose surfaces gradually decreased over 6 weeks. Ultrastructural examination of cocultures revealed that basophils could be observed being phagocytosed intact at 2 days. Disrupted basophil membranes and granules were phagocytized by 1 week, giving fibroblasts the appearance of mast cells by toluidine blue staining. Fibroblasts with basophilic granules were easily discerned from human mast cells by electron microscopy. Ultrastructural examination after immunogold labelling of cocultures revealed tryptase negative basophilic granules within fibroblasts.

It has been suggested that mast cells and basophils share a common progenitor, and that depending on culture conditions may be phenotypically altered to mast cells. 3T3 fibroblasts provide the appropriate environment to allow survival of human mast cells in vitro, when cells are obtained from CD34+ human stem cells. Long term survival and maturation of human mast cells and not basophils may be due to the presence of SCF (1,4). Our data show that IgE receptor-positive basophils do not survive coculturing conditions that favor the growth and maturation of mast cells from progenitor cells. The differences in culture conditions also suggest, but not prove, that basophils and mast cells may arise from two distinct progenitors arising from CD34+ pluripotent progenitor cells.

Highly enriched basophils derived from CD34+ pluripotent progenitor cells, unlike mast cells do not survive coculturing with 3T3 fibroblasts and are not altered phenotypically into mast cells.

References

1. Kirshenbaum, AS, SW Kessler, JP Goff and DD Metcalfe. *J Immunol* 146:1410, 1991.
2. Kirshenbaum, AS, JP Goff, SA Dreskin, AM Irani, LB Schwartz, and DD Metcalfe. *J Immunol* 142:2424, 1989..
3. Zsebo KM, DA Williams, et al. *Cell* 63:213, 1990.
4. Kirshenbaum, AS, JP Goff, SW Kessler, JM Mican, KM Zsebo and DD Metcalfe. *J Immunol* 148:772, 1992

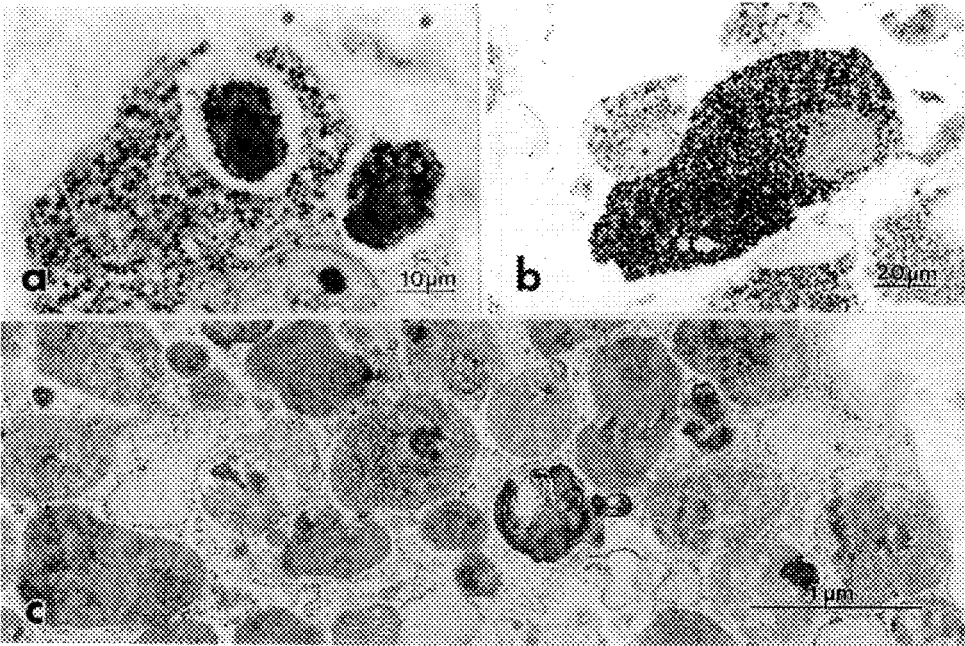


Figure 1. (a) LM of basophils being phagocytosed intact by 3T3 fibroblasts at 2 days. (b) LM of basophil / 3T3 coculture at 1 week. Disrupted basophil membranes and granules fill the cytoplasm, giving fibroblasts the appearance of mast cells by toluidine blue staining. (c) EM of fibroblast cytoplasm with phagocytized granules at 14 days. Immunogold labelling revealed tryptase-negative basophilic granules within the fibroblasts.

IN VIVO TARGETING OF ERYTHROCYTES TO CIRCULATING T-CELLS

Laura Chiarantini,** Robert E. Droleskey,* and John R. DeLoach*

*USDA-ARS, Food Animal Protection Research Laboratory, Route 5, Box 810, College Station, TX 77845 and **Institute di Chimica Biologica, Università degli Studi, Via Saffi, 2, 61029 Urbino, Italy

The use of carrier erythrocytes to specifically deliver toxic drugs to cancer cells has been a continuing effort in many laboratories. Carrier erythrocytes offer the advantages of having a large volume, are biodegradable, are easily obtained and prepared, and have the capability of circulating as well as normal erythrocytes. The selective *in vivo* targeting of drug loaded carrier erythrocytes to the liver and spleen has been demonstrated.¹ By the use of intraperitoneal (IP) injection of carrier erythrocytes DeLoach et al.^{2,3} have demonstrated that carrier erythrocytes can not only be targeted to the lymphatic system but to normal circulation as well. In an attempt to determine the feasibility of targeting carrier erythrocytes to circulating murine T-cells we coupled a monoclonal antibody (Mab) (antimouse Thy1.2) to murine erythrocytes using chromic chloride as a coupling agent.⁴ Murine erythrocytes coupled with antimouse Thy1.2 have been shown to form rosettes with a cytotoxic T-lymphocyte line (CTL) *in vitro*.⁵

Mab-erythrocytes were shown to form rosettes with isolated murine lymphocytes *in vitro* (Fig. 1) and when mixed with mouse whole blood *in vitro*. No rosettes were observed when nonspecific Mab was coupled to murine erythrocytes. IP injection of [⁵²Cr]-labeled antimouse Thy1.2 Mab-erythrocytes resulted in mild targeting of cells to lymphnodes with no significant targeting to either the spleen, liver, or lung. Electron microscopic examination of cells from the peritoneum revealed significant numbers of Mab-erythrocytes engulfed by macrophages (Fig. 2) and some Mab-erythrocytes bound to lymphocytes (Fig. 3). When Mab-erythrocytes were injected intravenously (IV) significant targeting of radiolabeled Mab-erythrocytes to the liver was observed. When whole blood from these animals was examined using electron microscopy, rosettes were routinely observed (Fig. 4). Membrane fusion of erythrocytes with attached lymphocytes was not observed. Dense granules associated with erythrocytes seen in rosettes were confirmed as chromium using x ray elemental analysis. No circulating rosettes were observed when nonspecific Mab coupled erythrocytes were injected IV.

These results suggest that carrier erythrocytes coupled with antimouse Thy1.2 Mab can be directed to circulating lymphocytes *in vivo*. Since membrane fusion of erythrocytes with attached lymphocytes was not observed the use of this system would have to be limited to diffusible drugs.

References

1. E. Zocchi et al., Proc. Natl. Acad. Sci. USA. 86(1990)2040.
2. J. R. DeLoach et al., Comp. Biochem. Physiol. 84A(1986)447.
3. J. R. DeLoach et al., Biotechnol. Appl. Biochem. 10(1988)183.
4. E. R. Gold and H. H. Fundenberg, J. Immunol. 99(1967)859.
5. L. Chiarantini et al., Biotechnol. Appl. Biochem. (1992)In press.

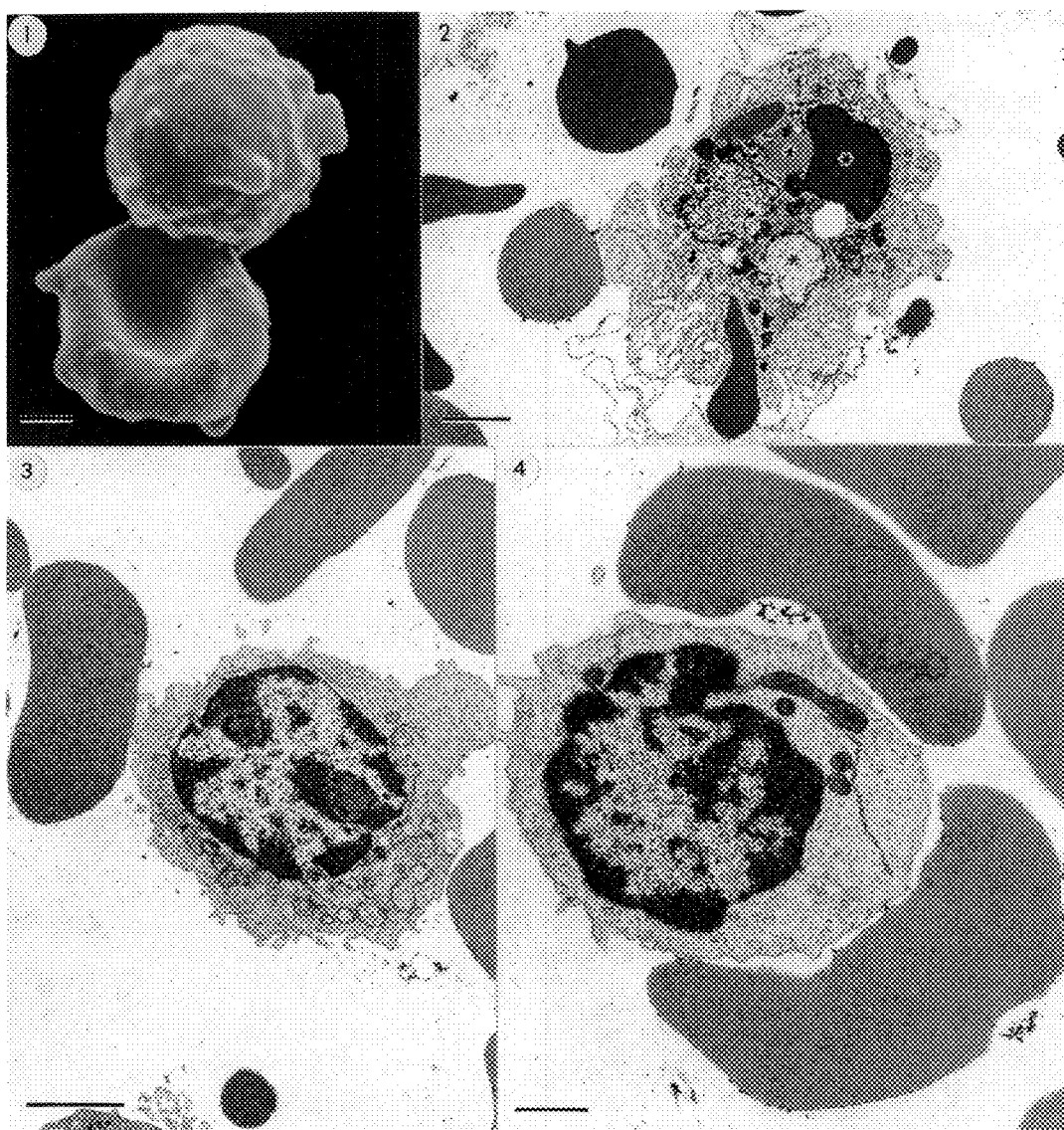


Fig. 1.--SEM of *in vitro* rosette resulting from incubation of isolated murine lymphocytes with Mab (anti Thy 1.2)-erythrocytes. Bar = $1\mu\text{m}$.

Fig. 2.--TEM of peritoneal macrophage containing numerous erythrocytes in various stages of disintegration (asterisks). Bar = $2\mu\text{m}$.

Fig. 3.--TEM of peritoneal lymphocyte with Mab (anti Thy 1.2)-erythrocyte attached. Bar = $2\mu\text{m}$.

Fig. 4.--TEM of lymphocyte-erythrocyte rosette recovered from circulation. Bar = $1\mu\text{m}$.

ELECTRON MICROSCOPIC AND ELECTRON PROBE X-RAY MICROANALYSIS (EPXMA) OF PROSTATIC INTRALUMINAL "CRYSTALLOIDS"

HX Bui,* A delRosario, M Abdulla, CE Sheehan, RJ Emerson, J Singh, JS Ross

Department of Pathology and Laboratory Medicine, Albany Medical College* and Stratton VA Medical Center, Albany, NY 12208

Prostatic intraluminal "crystalloids" are intensely eosinophilic, non-birefringent crystalline-like structures readily identified with light microscopy. Well documented to be associated with prostatic adenocarcinoma,¹⁻⁵ these rhomboidal, hexagonal, triangular, polyhedral, or needle-like structures are almost exclusively confined to well differentiated prostatic adenocarcinomas^{1,5} and may occasionally be seen in adjacent benign glands bordering the tumors.¹⁻⁵ Although of significant potential as a signal of nearby cancer in a limited biopsy of benign prostate, these "crystalloids" are poorly defined and their chemical composition has not been determined.^{2,4}

The study material consisted of ten radical prostatectomy specimens for adenocarcinoma which contained intraluminal "crystalloids" on light microscopy. Standard 5-micron paraffin sections of prostatic tissue were picked up onto a one inch spectrometrically pure carbon planchette. Deparaffinized sections were dried, coated with carbon in a JEOL vacuum evaporator and examined in a JEOL JSM 6100 scanning electron microscope (JEOL, Inc, Peabody, MA) equipped with a Kevex Quantum Delta Class energy dispersive x-ray spectrometer (Fisons Instruments, Inc, San Carlos, CA). EPXMA was performed at 15-20 kv at a working distance of 39 mm and spectra were collected over a 60-second time period.

Results and conclusions: 1) Prostatic intraluminal "crystalloids" identified on light microscopy can readily be demonstrated and highlighted by scanning electron microscopy. 2) "Crystalloids" consistently show a sulphur peak and a small sodium peak on EPXMA. General tissue background and control non-crystalloid prostatic corpora amylacea show no appreciable amounts of sulphur or other elements. 3) These findings indicate that the "crystalloids" are rich in elemental sulphur. 4) The clinical and biological significance of the sulphur-rich prostatic luminal "crystalloids" is currently unclear and is under further investigation.

References

1. Holmes EJ. Cancer 1977; 39:2073-2080.
2. Jensen PE, Gardner WA Jr, Piserchia PV. Prostate 1980; 1:25-31.
3. Bennett BD, Gardner WA Jr. JAMA 1988; 260(15):2287.
4. Ro JY et al. Prostate 1988; 13:233-239.
5. delRosario A et al. Lab Invest 1992; 66(1):A299.

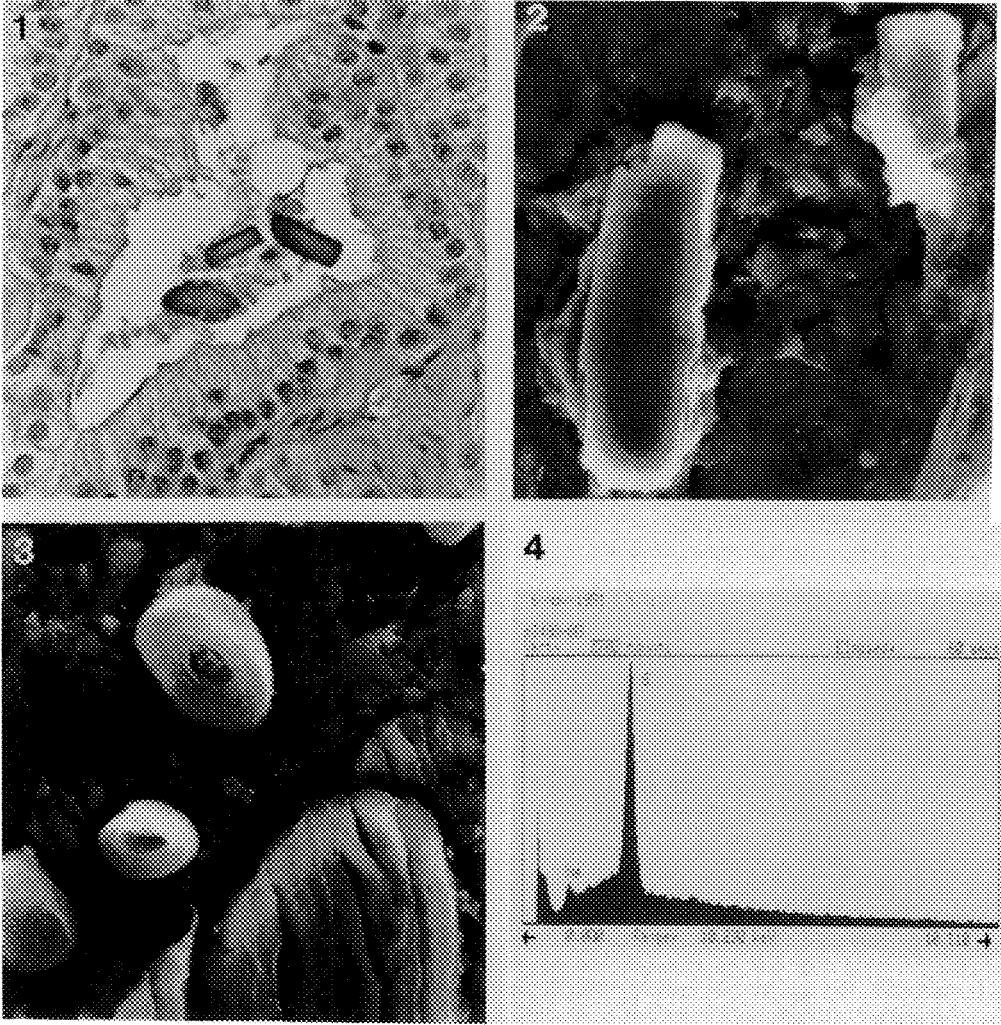


FIG. 1.-- Prostatic intraluminal "crystalloids" - intensely eosinophilic, non-birefringent crystalline-like structures, with various shapes may preferentially localize in or adjacent to low grade prostatic adenocarcinomas. (Hematoxylin and Eosin X 500).

FIG. 2.-- Scanning electron micrograph of prostatic intraluminal "crystalloids" (S.E.M. X 3450).

FIG. 3.-- Scanning electron micrograph of prostatic corpora amylacea (S.E.M. X 1520).

FIG. 4.-- Electron probe x-ray microanalytic (EPXMA) studies of prostatic intraluminal "crystalloids". A high sulphur peak and a lower sodium peak are consistently noted.

ULTRASTRUCTURAL CHARACTERIZATION OF MURINE Fc RI-BEARING CELLS IN IL-3 DEPENDENT BONE MARROW CULTURES WITH AND WITHOUT STEM CELL FACTOR

J. P. Goff¹, M. Rottem², J. P. Albert¹ and D. D. Metcalfe²

¹ Division of Molecular Virology and Immunology, Georgetown University Medical Center Rockville, MD 20852

² Mast Cell Physiology Section, NIAID NIH Bethesda MD 20892

It is known that mast cells arise from pluripotent hematopoietic progenitor cells and express their mature phenotypes in tissues (1,2). Information concerning the early development of mast cells and basophils is limited and the sequence of events involved in maturation is incompletely understood. Mast cells and basophils are unique in that they are the only cells known so far to express high-affinity receptors for IgE (Fc RI) on their surface (3). They are characterized in part, by both the presence of these receptors and metachromatic cytoplasmic granules that contain histamine. At early stages of development the distinction between mast cells and basophils by light microscopy is very difficult. Since mast cells and basophils express different biochemical and functional properties, accurate identification is essential for understanding the role these cells play in health and disease.

Hemopoietic stem cell factor (SCF) is the product of *Sf* locus in the mouse and the ligand for the proto-oncogene *c-kit* receptor. A number of studies have shown that SCF is involved in the growth and differentiation of mast cells. In vitro, in the presence of SCF in combination with other cytokines, rodent pluripotent progenitor cells give rise to all committed cell lineages, including mast cells (4).

To study early mast cells and basophils, cells from IL-3 dependent mouse bone marrow cultures were isolated on the basis of high affinity surface receptors for IgE using fluorescent activated cell sorting (FACS). Electron microscopy and morphometric analysis were used to identify and compare the morphological development of these cells when cultured in the presence of IL-3 or IL-3 and SCF for 3, 10, and 21 days. At each time point in culture, cells were prepared for TEM evaluation. Morphometric analysis was used to analyze changes in cell size, nuclear size, nucleus to cytoplasm ratio, granule size and granule number.

Fc RI-bearing cells could be identified in IL-3 dependent bone marrow cultures as early as 3 days. Mast cells express Fc RI before they can be identified as mast cells based on morphology (5).

Immature mouse mast cells and basophils differ from mature cells predominantly in the size, number and morphologic features of the granules (6). As the cells mature they accumulate increasing numbers of recognizable metachromatic granules. These granules appear to develop from large empty vacuoles in the active golgi region. Vacuoles fill progressively with small vesicles and then acquire a dense matrix. At 3 days mast cells show a few recognizable, but incompletely formed mast cell granules, with heterogeneous contents. The cell surface is unspecialized, with a few distinct short microvilli. As the cells mature (10 days) the cytoplasm contains increasing numbers of specific granules. These granules are still relatively immature, being only partially condensed and have vesicles beneath the granule membrane. In this intermediate stage of development the golgi is reduced and there is replacement of active golgi with endoplasmic reticulum and granules. The cell surface begins to show characteristic, regularly distributed cytoplasmic extensions. At 21 days, most of the mast cells that appeared in the cultures were mature. There was an increased number of granules over the cells at 10 days and most granules were completely condensed with homogeneous contents. The cell surface was typical of mature mast cells.

Cells cultured in the presence of IL-3 both with and without SCF showed characteristic changes as the cells mature (3 to 21 days). Cells from cultures supplemented with the combination of IL-3 and SCF showed evidence of earlier maturation and differentiation than with IL-3 alone.

References

1. KY Kitamura, et al. Blood 52:447, 1978.
2. K Stevens and KF Austen. Immunol Today 10:381, 1989.
3. HL Thompson, et al. J Clin Invest 85:1227, 1990.
4. NG Copeland, et al. Cell 63:175, 1990
5. M Rottem et al. (in press)
6. A Dvorak et al. Am Rev Respir Dis 128:s49-s52, 1983.

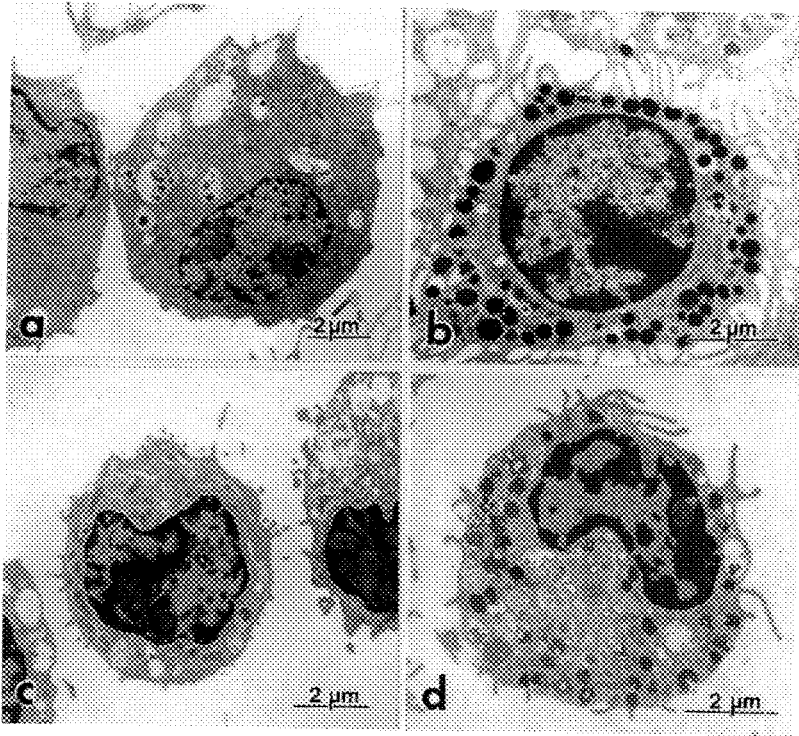


Figure 1. Mast cells from murine bone marrow-derived cultures supplemented with IL-3 or IL-3 in combination with SCF. (a) immature mast cell from cultures supplemented with IL-3. (b) mature mast cell from cultures supplemented with IL-3. (c) immature mast cell from cultures supplemented with IL-3 and SCF. (d) mature mast cell from cultures supplemented with IL-3 and SCF.

ULTRASTRUCTURAL AUTORADIOGRAPHY OF L6 SKELETAL-MUSCLE CELLS EXPOSED TO A TRITIATED MACROLIDE ANTIBIOTIC (LY237216) *IN VITRO*

S.L. White, C.B. Jensen, D.D. Giera, D.A. Laska, M.N. Novilla, and D.M. Hoover

Toxicology Research Laboratories, Lilly Research Laboratories, A Division of Eli Lilly and Company, Greenfield, IN 46140

In vitro exposure to LY237216 (9-Deoxy-11-deoxy-9,11-[imino[2-(2-methoxyethoxy)ethylidene]-oxy]-(9S)-erythromycin), a macrolide antibiotic, was found to induce cytoplasmic vacuolation in L6 skeletal muscle myoblast cultures (White, S.L., unpubl.). The present study was done to determine, by autoradiographic quantitative analysis, the subcellular distribution of ^3H -LY237216 in L6 cells.

L6 cells (ATCC, CRL 1458) were cultured to confluency on polycarbonate membrane filters (Millipore Corp., Bedford, MA) in M-199 medium (GIBCO® Labs) with 10% fetal bovine serum. The cells were exposed from the apical surface for 1-hour to unlabelled-compound (0 $\mu\text{Ci/ml}$) or 50 $\mu\text{Ci/ml}$ of ^3H -LY237216 at a compound concentration of 0.25 mg/ml. Following a rapid rinse in compound-free growth medium, the cells were slam-frozen against a liquid nitrogen cooled, polished copper block in a CF-100 cryofixation unit (LifeCell Corp., The Woodlands, TX). Specimens were dried in the MDD-C Molecular Distillation Drier (LifeCell Corp.), vapor osmicated and embedded in Spurr's low viscosity resin. Ultrathin sections collected on formvar coated stainless steel grids were counter-stained, then individually mounted on corks. A monolayer of Ilford L4 nuclear emulsion (Polysciences, Inc., Warrington, PA) was placed on the sections, utilizing a modified "loop method"¹. The emulsions were exposed for 7-weeks in a light-tight box at 4°C. Autoradiographs were developed in Microdol-X developer and examined on a Philips EM410LS transmission electron microscope. Quantitative analysis of compound localization employed the point and circle approach of Williams²; incorporating the probability circle method of Salpeter and McHenry³.

The distribution of silver grains over nucleus, mitochondria, cytoplasm, extracellular space and compound-induced cytoplasmic vacuoles was quantitatively determined. Six times as much radioactivity was observed over the compound-induced cytoplasmic vacuoles and vacuolar regions as was observed over the cytoplasm (figs. 1-2). Mitochondria had 2.5 times more radioactivity than the cytoplasm. Comparatively low levels of radioactivity were recorded over the nucleus and in the extracellular areas, being less than 1/5th and 1/2th that of the cytoplasm, respectively (Table 1).

The present study demonstrated accumulation of the tritium label in compound-induced cytoplasmic vacuoles. In previous work (unpublished), the prominence of the cytoplasmic vacuolization was found to be related to the length of exposure and concentration of LY237216. The significance of the slight increase of tritium label in mitochondria is unknown. The significant concentration of radiolabeled-LY237216 in compound-induced vacuoles suggests that LY237216, or a metabolite containing the radiolabel, is sequestered in the cytoplasmic vacuoles.

REFERENCES

1. J.R.J. Baker, *Autoradiography: A Comprehensive Overview*, New York: Oxford University Press (1989)
2. M.A. Williams, *Practical Method in Electron Microscopy*, Amsterdam: North-Holland (1977)
3. E.J. Salpeter, F.A. McHenry, *Advanced Techniques in Biological Electron Microscope Autoradiography*, New York: Springer (1973)

Table 1: Mean relative radioactivities of individual cellular sites in L6 cells

Source	Rel. Activity	Standard Error	Z
Vacuoles	6.326	0.0010	5326 ^a
Mitochondria	2.579	0.2234	7.066 ^a
Nucleus	0.233	0.0359	-21.36 ^a
Cytoplasm	0.996	0.0195	-0.205
Extracellular	0.443	0.1036	-5.375 ^a

^a Significantly different from 1 (random distribution), $p < 0.05$

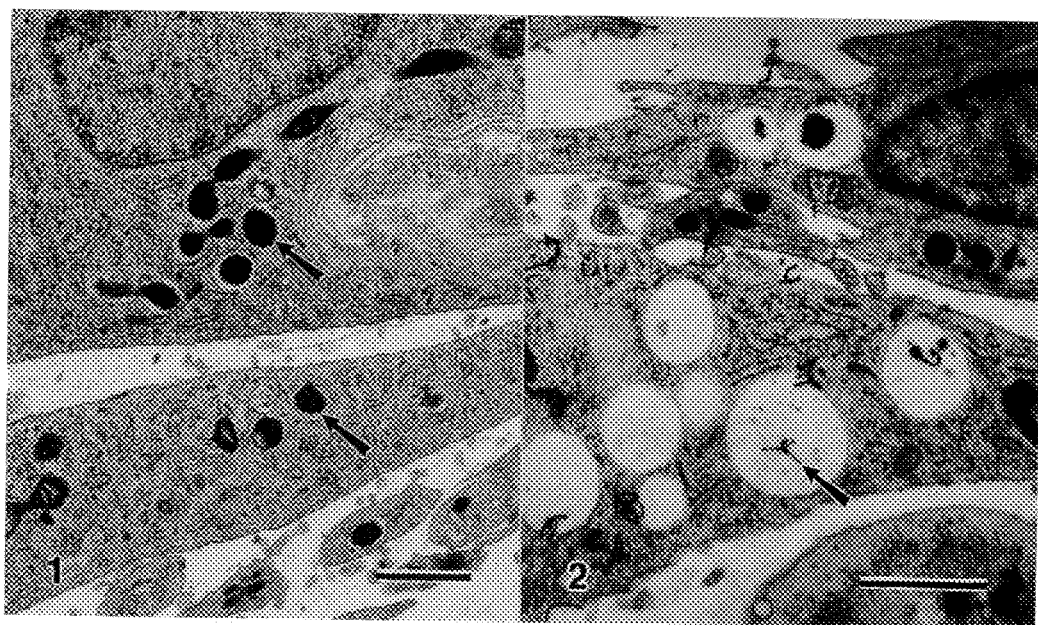


Fig. 1. Control cryo-preserved and freeze-dried L6 muscle cells. Ultrastructural detail visible include nucleus, mitochondria (arrows), Golgi apparatus, and rough endoplasmic reticulum. Note the absence of vacuoles. Bar = 1 μ m.

Fig. 2. Autoradiograph of L6 muscle cells after 1-hour exposure to 0.25 mg/kg ³H-LY237216 (50 μ Ci/ml). Silver grains are prominent over membrane-bound cytoplasmic vacuoles (arrow) and sparse over nuclear and extracellular areas. Bar = 1 μ m.

ULTRASTRUCTURAL STUDY OF EXPERIMENTAL DUODENAL ULCER IN A NEW ANIMAL MODEL

HX Bui,* A delRosario, M Abdulla, F Ballouk, V Bajakian, CY Lee, JS Ross

Department of Pathology and Laboratory Medicine, Albany Medical College* and
Stratton VA Medical Center, Albany, NY 12208

Various animal models have often been utilized as the basis of studies of the pathophysiology of peptic ulcer disease, however the ultrastructural changes in the evolution of duodenal ulcers produced in experimental animals have not been well elucidated.¹⁻² Utilizing a surgical method developed for the study of gastric ulcers^{3,4} we have established an experimental duodenal ulcer production technique in the rat which is highly reproducible and readily standardized.⁵ In the following time sequence study of experimental duodenal ulcers we present the ultrastructural features of ulcer induction and evolution.

Duodenal ulcers were produced in 150-200 gram male Sprague Dawley rats by application of 50% acetic acid for 30 seconds through a 3 mm polyethylene tube to the serosa 1.0-1.5 cm distal to the pyloric sphincter. Routine transmission and scanning electron microscopy were performed on duodenal specimens at specific time points subsequent to surgical ulcer generation. Thin sections were stained with uranyl acetate and lead citrate and examined with a Phillip's EM 300 transmission electron microscope. For SEM, specimens were post-fixed in 2% osmium for two days, coated with gold/palladium and examined with JEOL JSM-6100 scanning electron microscope (JEOL, Inc., Peabody, MA).

Results and conclusions.

- 1) At 15 minutes, the duodenal mucosa reveals early disintegration with readily identifiable splitting of the villi. Villus architecture has begun to collapse.
- 2) At 0.5-3 hrs, progressive disintegration of the mucosal villi continues with superficial epithelial necrosis and surface epithelial erosions. Ulcer crater formation becomes evident and gradually increases in size. The ulcer beds consist of necrotic debris and fibrinous deposits.
- 3) At 24-48 hours, discrete ulcers are well developed.
- 4) At three days, granulation tissue has formed lining the deeper layers of the ulcer.
- 5) We conclude that the duodenal ulcers generated in this new experimental animal model are ultrastructurally similar to naturally occurring human duodenal ulcers and that the experimental model may be useful to study the development and evolution of duodenal ulcer disease.

References

1. Szabo S. Laboratory Investigation 1984; 51(2):121-147.
2. Szabo S and Vattay P. Gastroenterology Clinics of North America 1990; 19(1):67-84.
3. Tarnawski A et al. Gastroenterology 1988; 94:A456.
4. Bui HX et al. Experimental and Molecular Pathology 1991; 55:261-268.
5. Bui HX et al. Lab Invest 1992; 66(1):A229.

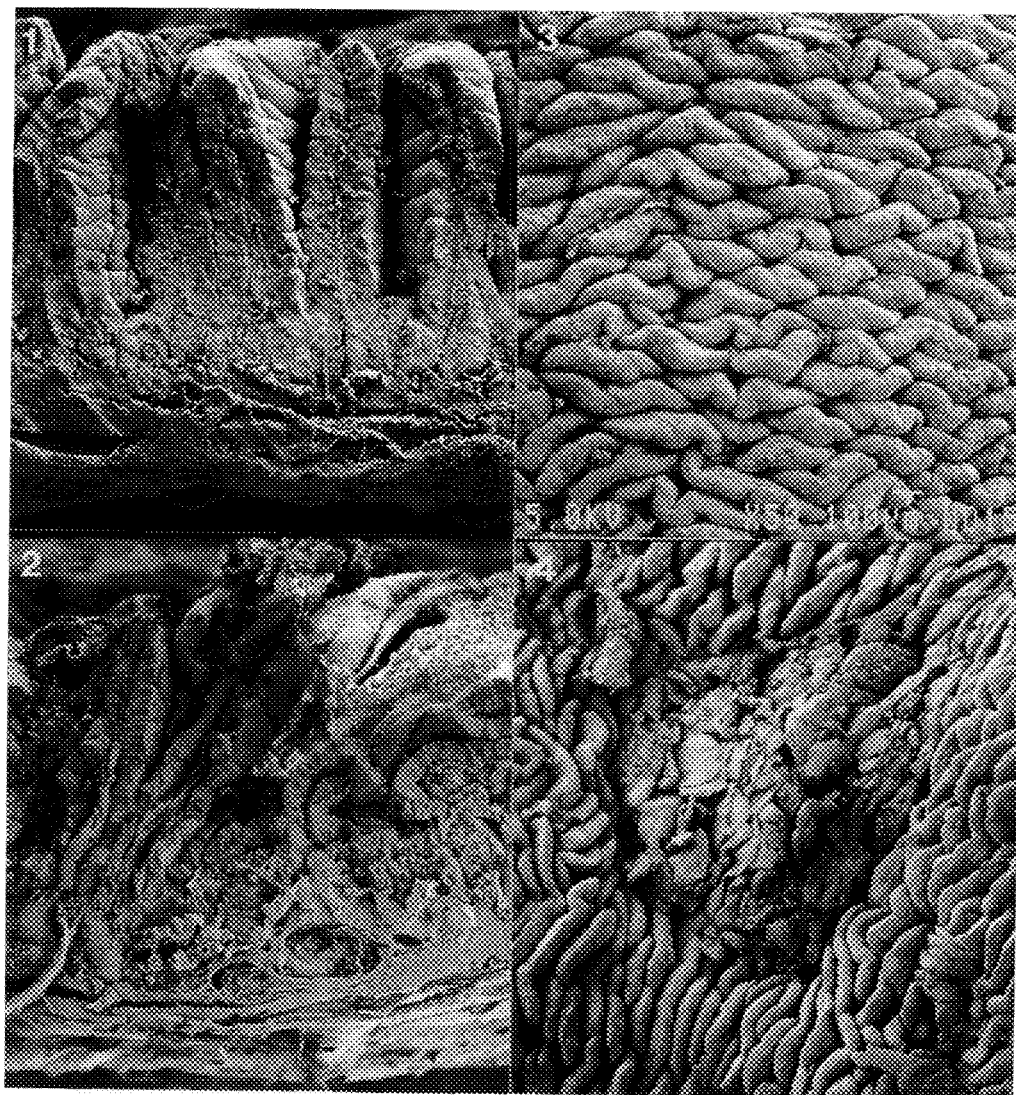


FIG. 1.-- Normal Control. Section of the wall of the rat duodenum showing regular arrangement of the villi (S.E.M. X 140).

FIG. 2.-- 15 minutes after acetic acid application. Section shows irregularity and disintegration of the villi (S.E.M. X 120).

FIG. 3.-- Normal control. Mucosal surface view showing regular packing of the villi (S.E.M. X 50).

FIG. 4.-- 3 hours after acetic acid application. Mucosal surface view showing ulcer formation with fragmentation of villi (S.E.M. X 35).

ROLE OF FREEZE-FRACTURE TECHNIQUE IN TUMOUR PATHOLOGY

Tapen M. Mukherjee and Jeffrey G. Swift

Electron Microscope Unit, Division of Tissue Pathology,
Institute of Medical & Veterinary Science, Frome Road, Adelaide, South Australia 5000

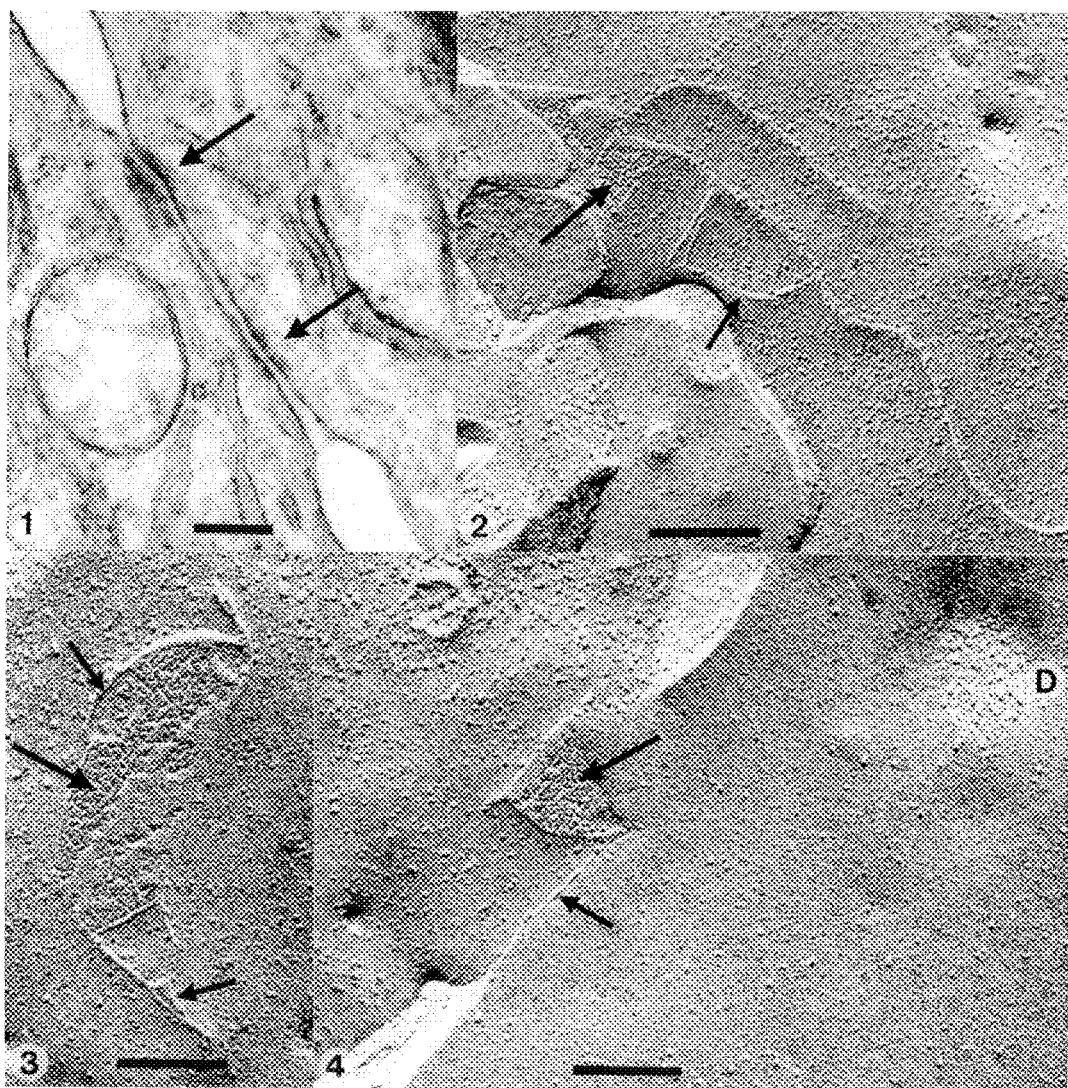
The freeze-fracture technique is unique in its ability to expose extensive face views of the interior of the cell membranes. This feature is particularly useful for studies of events occurring at the plasma membrane, such as exocytosis of secretory granules and of structural components within the membrane such as the intercellular junctions. We have used freeze-fracture preparations in conjunction with conventional thin sections to study the intercellular junctions in a variety of human tumours.¹

In well differentiated squamous cell carcinomas, desmosomes and tonofilament bundles are a prominent feature in thin sections. However in poorly differentiated squamous cell carcinomas the desmosomes are often not so well developed and may be seen at the "attachment sites" between the tumour cells only as "subplasmalemmal densities". These structures may represent poorly developed desmosomes or intermediate junctions (Fig.1).^{2,3} Freeze-fracture replicas of these tumours show the presence of gap junctions and focal tight junctions, in addition to the desmosomes (Figs. 2-4). The gap junctions can occur separately or together. Thus the application of the freeze-fracture technique, in addition to the usual thin section procedures, can enable a more comprehensive characterisation of the intercellular junctions that may be present in a tumour.

Both qualitative and quantitative abnormalities in intercellular junctions have been reported in a wide variety of human and animal tumours. However it is still not clear to what extent such changes in the junctional organization may be responsible for tumour invasion and metastasis.⁴ Vollmer et al.⁵ concluded from a study of a series of 52 cases of oat cell carcinoma of the lung, that those patients who demonstrated at the ultrastructural level intermediate junctions and especially desmosomes had a better prognosis of survival than those without any identifiable junctions. This observation alone emphasises the importance of studies of cell junctions in human tumours. It is here that the technique of freeze-fracture in association with the conventional thin section procedures can play a significant role to better characterise the morphology of cell junctions and thus assist in our understanding of the diagnostic and prognostic relationship of cell junctions and human tumours.

References

1. J.G. Swift et al., *J. Submicrosc. Cytol. Pathol.* (1989) 21, 239.
2. F.N. Ghadially, *Ultrastructural pathology of the cell and matrix*. 2 vols. 3rd Ed. Butterworths, London (1988)
3. D.W. Henderson et al., *Ultrastructural appearances of tumours: diagnosis and classification of human neoplasia by electron microscopy*. 2nd Ed. Churchill Livingstone, Edinburgh (1986)
4. R.S. Weinstein and B.U. Pauli, *Ciba-Found-Symp.* (1987) 125, 240.
5. R.T. Vollmer et al., *Hum. Pathol.* (1986) 18, 22.



Electron micrographs illustrating the range of junctions found in one case of squamous cell carcinoma of lung.

FIG. 1.-- Thin section appearance of "attachment site" between two tumour cells. Arrows indicate poorly developed desmosomes. Bar = $0.2\ \mu\text{m}$.

FIGS. 2-4.-- Freeze-fracture replicas of "attachment sites" showing combined gap junctions (large arrows) and tight junction strands (small arrows). D, desmosome. Bar = $0.2\ \mu\text{m}$.

ULTRASTRUCTURAL FEATURES OF PROGNOSTIC SIGNIFICANCE IN HUMAN ORAL CANCER

Karvita B. Ahluwalia and Nidhi Sharma

Department of Biophysics, Cell Biology and Electron Microscope Section, All India Institute of Medical Sciences, New Delhi 110029 INDIA

It is common knowledge that apparently similar tumors often show different responses to therapy. This experience has generated the idea that histologically similar tumors could have biologically distinct behaviour. The development of effective therapy therefore, has the explicit challenge of understanding biological behaviour of a tumor. The question is which parameters in a tumor could relate to its biological behaviour? It is now recognised that the development of malignancy requires an alteration in the program of terminal differentiation in addition to aberrant growth control. In this study therefore, ultrastructural markers that relate to defective terminal differentiation and possibly invasive potential of cells have been identified in human oral leukoplakias, erythroleukoplakias and squamous cell carcinomas of the tongue.

Fourteen samples were fixed in 2.5% glutaraldehyde in cacodylate buffer, postfixed in osmium and embedded in Durcupan. Thin sections were contrasted with uranyl acetate and lead citrate. For preserving cold-sensitive microtubules, some blocks were processed at 25°C to 30°C in addition to those processed at 4°C from the same sample. Acid hydrolases in acidic intracellular compartments were localized using cerium as capture agent for inorganic phosphate. Intracellular calcium was localized by the pyroantimonate method.

Tumors are generally graded for poor or good differentiation by observing a few light microscopic criteria. Biochemically, differentiation is assessed on the basis of a single marker, usually a secretory protein. We have been able to critically evaluate a number of ultrastructural parameters by electron microscopy and these are tabulated (Table to be shown). Subcellular details have been analyzed in context of their functional relationships for understanding cell behaviour and overall biology of the tumor. Detailed information has been obtained regarding endomembrane system and pathway of secretory proteins; expression of two distinct subpopulations of microtubules; distribution of calcium ions; keratin filament frequency, distribution patterns and configurations; dynamic instabilities at cell surface; lysosomal bodies and acidic compartments (Fig.1); presence or absence of adhesive protein in desmosomal junctions (Fig.2). Information obtained for several structural markers has been integrated to understand functional interrelationships between subcellular components. For tabulation of data semiquantitative scoring (+ to +++) has been

done, taking into account the degree of expression of each feature. Transient deviations due to local physiological conditions when present, are not recorded. From among the consistent, characteristic features a combination of markers is selected that indicate 1) the extent of differentiation of a lesion, 2) the degree of defective terminal differentiation, and 3) invasive potential of cells. These markers are assessed in correlation with histopathological findings and clinical parameters of prognostic significance such as lymph node involvement, recurrence and predisposing risk factors in individual patients. Each selected marker is thus a possible prognostic variable.

The study has revealed subtypes of tumors within a histological type. It demonstrates existence of a spectrum of differentiation between the two extremes of poor and good differentiation. It also shows the inadequacy of assessing tumor differentiation on the basis of a single marker. Such an electron microscopic study allows the crucial events of tumor progression, invasion and metastasis to come into focus at the subcellular level. On the basis of markers identified during this study, a protocol has been prepared for assessment of biological behaviour of the oral lesion. It could possibly provide a new direction for improved treatment to the clinician. There is perhaps no single technique outside electron microscopy that can throw light on several parameters related to overall biological behaviour of a tumor.

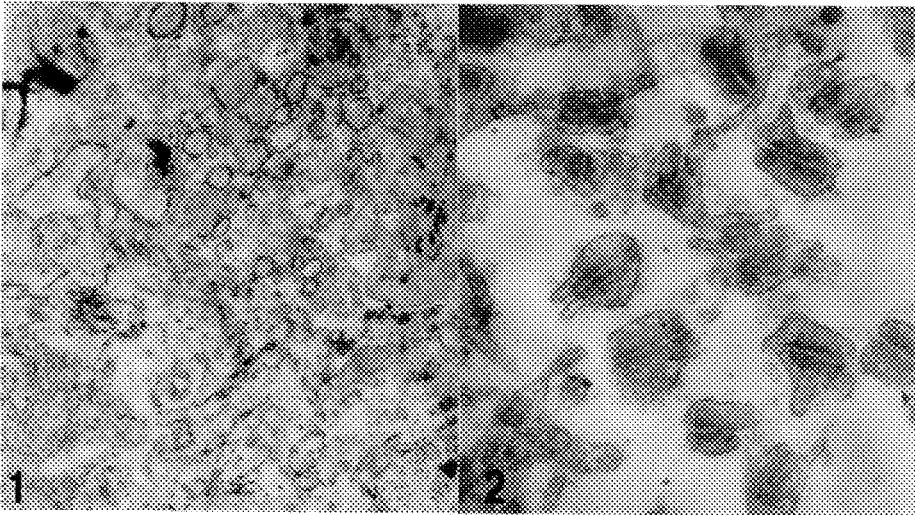


FIG. 1.--TEM of cell from carcinoma of tongue; acid hydrolases are present in lysosomes. x 12,560.

FIG. 2.--TEM of intercellular desmosomes in carcinoma of tongue; intermediate plaque of adhesive protein is absent. x 16,800.

IMMUNOTACTOID GLOMERULOPATHY: RECURRENCE OF DISEASE IN RENAL TRANSPLANT

George Price, Gregory Moses, Allen Holcomb, Lizardo Cerezo

Departments of Laboratory, Pathology, and Medicine, Orlando Regional Medical Center, 1414 Kuhl Ave., Orlando, FL 32806

Immunotactoid glomerulopathy (ITG) is a disease of the kidney, first described in 1980¹. It is characterized by the specific deposition of immunoglobulin in the renal glomeruli, producing diffuse mesangial expansion similar to that commonly noted in the sclerosing process of amyloidosis. However, these patients do not exhibit the clinical symptoms of patients with extra renal, or systemic disease, and therefore have a better prognosis. The demonstration by electron microscopy of fibrillar deposits that are thicker than that of amyloid is crucial to the diagnosis.

The association of this disease to an autoimmune response is demonstrated by the immunofluorescent staining of antihuman IgG and C3 to the affected glomeruli. Other immunoglobins may be implicated, but are not as common.

The differentiation of amyloidosis from ITG relies on two criteria. Amyloid has birefringent Congo red positivity by polarized light, whereas immunotactoid deposits are negative; and the fibrils of amyloid are smaller than those of immunotactoid (IT)². Immunotactoid fibrils have an average diameter of 18 nm, and appear thicker than the common 10 nm amyloid fibril.

ITG has been shown to occur in conjunction with other systemic diseases, but has not been directly associated with them. These diseases include vasculitis², and diabetes³.

A case report is presented of a 47 year old female with renal insufficiency. The clinical history included high blood pressure, proteinuria, and microscopic hematuria, and did not exhibit any symptoms of systemic amyloidosis. However, upon biopsy in 1983, the diagnosis of end stage kidney disease secondary to amyloidosis was made. The patient received a cadaveric transplant in 1987. The transplanted kidney was biopsied in 1990 to determine a differential diagnosis of rejection vs. recurrent disease.

By light microscopy, all the glomeruli have acellular eosinophilic nodular expansion of the mesangial areas, and were Congo red negative by polarized light. Further examination by electron microscopy revealed that the mesangium (Fig. 1) contained organized deposits of fibrils that were approximately 18 nm in diameter. (Fig. 2) Non-fibrillar electron dense deposits were not present.

These fibrillar deposits meet the two criteria set forth for the differentiation of immunotactoid glomerulopathy from systemic amyloidosis. This is the third reported case of ITG recurring in a renal transplant currently on record.

References:

- 1) Schwartz M, Lewis. The quarterly case: Nephrotic Syndrome in a middle aged man. Ultrastructural Path. 1980,575.
- 2) Orfila C, Meeus F, et al: Immunotactoid glomerulopathy and cutaneous vasculitis. Am J Nephrol. 1991,11:67-72.
- 3) Unpublished observations by these authors.

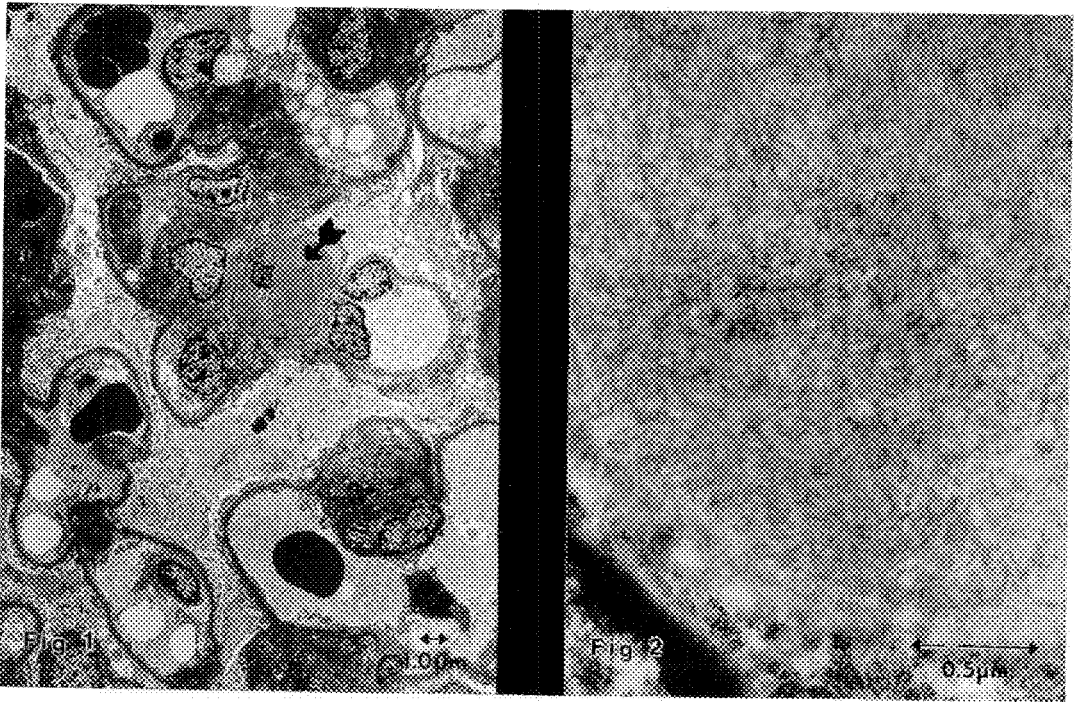


Figure 1.) Electron micrograph of abnormally expanded mesangial matrix in a glomerulus (arrow). 2,000 x

Figure 2.) Higher power micrograph of mesangial area from figure 1, revealing fibrils with an average diameter of 18nm. 40,000 x

ELECTRON MICROSCOPY OF HUMAN ATHEROSCLEROSIS: AORTIC FATTY STREAKS WITH TRANSITIONAL LESION FEATURES

K. Florian Klemp and J.R. Guyton

Department of Medicine, Baylor College of Medicine, Houston, TX 77030

The earliest distinctive lesions in human atherosclerosis are fatty streaks (FS), characterized initially by lipid-laden foam cell formation. Fibrous plaques (FP), the clinically significant lesions, differ from FS in several respects. In addition to foam cells, the FP also exhibit fibromuscular proliferation and a necrotic core region rich in extracellular lipid. The possible transition of FS into mature FP has long been debated, however. A subset of FS described by Katz et al. was intermediate in lipid composition between ordinary FS and FP.¹ We investigated this hypothesis by electron microscopic cytochemistry by employing a tissue processing technique previously described by our laboratory.² Osmium-tannic acid-paraphenylenediamine (OTAP) tissue preparation enabled ultrastructural analysis of lipid deposits to discern features characteristic of mature fibrous plaques.

Thirty-two unilateral FS from 24 autopsied aortas were selected, as were normal tissue blocks from contralateral sites. Blocks were fixed first in 3% glutaraldehyde in 0.1 M cacodylate buffer overnight at 4°C, then rinsed in cacodylate buffer 3 times for 5 minutes each at room temperature. Tissue was then post-fixed in cacodylate-buffered 1% OsO₄ for 2 hours. Three buffer rinses were followed by mordanting with 1% tannic acid in 0.05 M buffer for 30 min., a 5 min. rinse in the same buffer containing 1% NaSO₄, 70% ETOH 3x, 5 min. each, then treatment with 1% P-PDA in 70% ETOH for 30 min. A dehydration schedule of 70% ETOH, 3x 5 min., 95% ETOH, twice over 15 min., and absolute ETOH, 3x 5 min. was employed. Tissue was infiltrated with 1:1 ETOH:LX112 resin for 1 hour, then pure resin overnight, and 2 changes for 2 hours before embedding. Thin sections were cut on an LKB Ultratome 3 and examined on a JEOL 200CX electron microscope.

The OTAP cytochemical procedure provided excellent ultrastructural preservation of tissue components. It has been reported by several authors that initial extracellular lipid deposition may occur as a result of direct accumulation of lipid components from lipoproteins in the arterial wall, and is often intimately associated with tissue matrix proteins (Fig. 1).^{3,4} We have demonstrated biochemically and by EM that this phenomenon could be simulated in vitro.⁵ Occasionally low density lipoprotein-sized particles could be seen enmeshed in collagen fibers (Fig. 2). Lipid deposition was very intense at times and resembled the droplet and vesicle composition of mature fibrous plaques described ultrastructurally by our laboratory (Fig. 3).² While cholesterol ester in droplet form tended to be associated with elastin, vesicular lipid was more often interspersed with collagen fibrils. Cholesterol crystal clefts, a hallmark structure of mature fibrous plaques were found in 7 of 32 tissue blocks (Fig. 4). Necrosis of foam cells and subsequent deposition of their lipid contents are seldom in evidence. Our observations indicate that a substantial amount of extracellular lipid may accumulate directly without cellular intervention and that some fatty streaks have morphology similar to more advanced lesions and can be implicated as potentially transitional lesions.

REFERENCES

1. S.S. Katz et al., J. Clinical investigations, (1976) 58, 200.
2. J. Guyton and K. Klemp, J. Histochemistry and Cytochemistry, (1988) 10,1319.
3. C. Camejo, Adv. Lipid Research (1982) 19,1.
4. T.M.A. Bocan et al., Am. Journal of Pathology, (1986) 123,413.
5. J. Guyton et al., J. Lipid Research, (1991) 32,953.

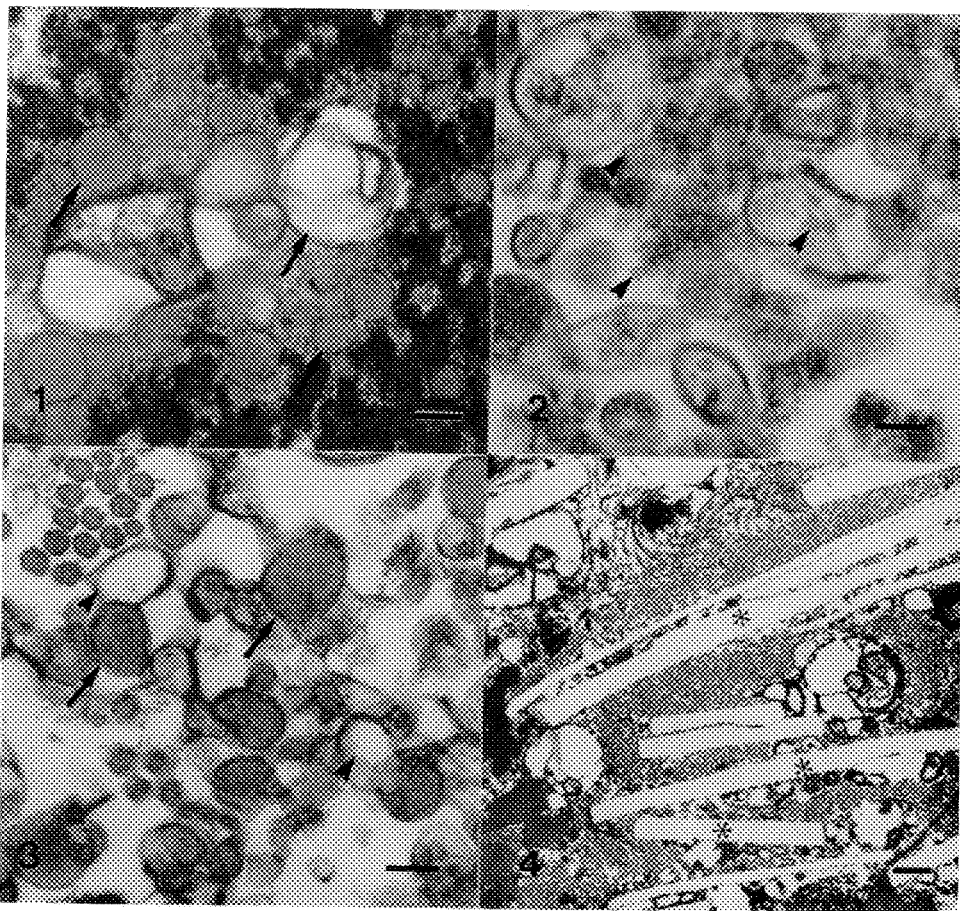


FIG. 1.--Extracellular lipid deposits (arrows) within elastic interstices. Bar = 100 nm.

FIG. 2.--Low density lipoprotein-sized (arrowheads) in the extracellular space. Bar = 80 nm.

FIG. 3.--Typical morphology of extracellular lipid deposits, including droplets (arrows) and vesicles (arrowheads). Bar = 100 nm.

FIG. 4.--Cholesterol crystal clefts (asterisks) amid collagen bundles in the extracellular space. Bar = 700 nm.

ELECTRON MICROSCOPY OF ASSOCIATED SPERMATOOZOA OF SQUIRREL
(*Funambulus pennanti*)

S.R.Bawa and H.K.Bains

Department of Biophysics, Panjab University, Chandigarh-160014, India

Associations amongst spermatozoa have been reported in a variety of vertebrate and invertebrate animals. Spermatozoa come together and are attached to each other only in the region of the head, their tails are free - required to steer the spermatozoa. We have studied sperm-sperm association in squirrel using electron microscopy.

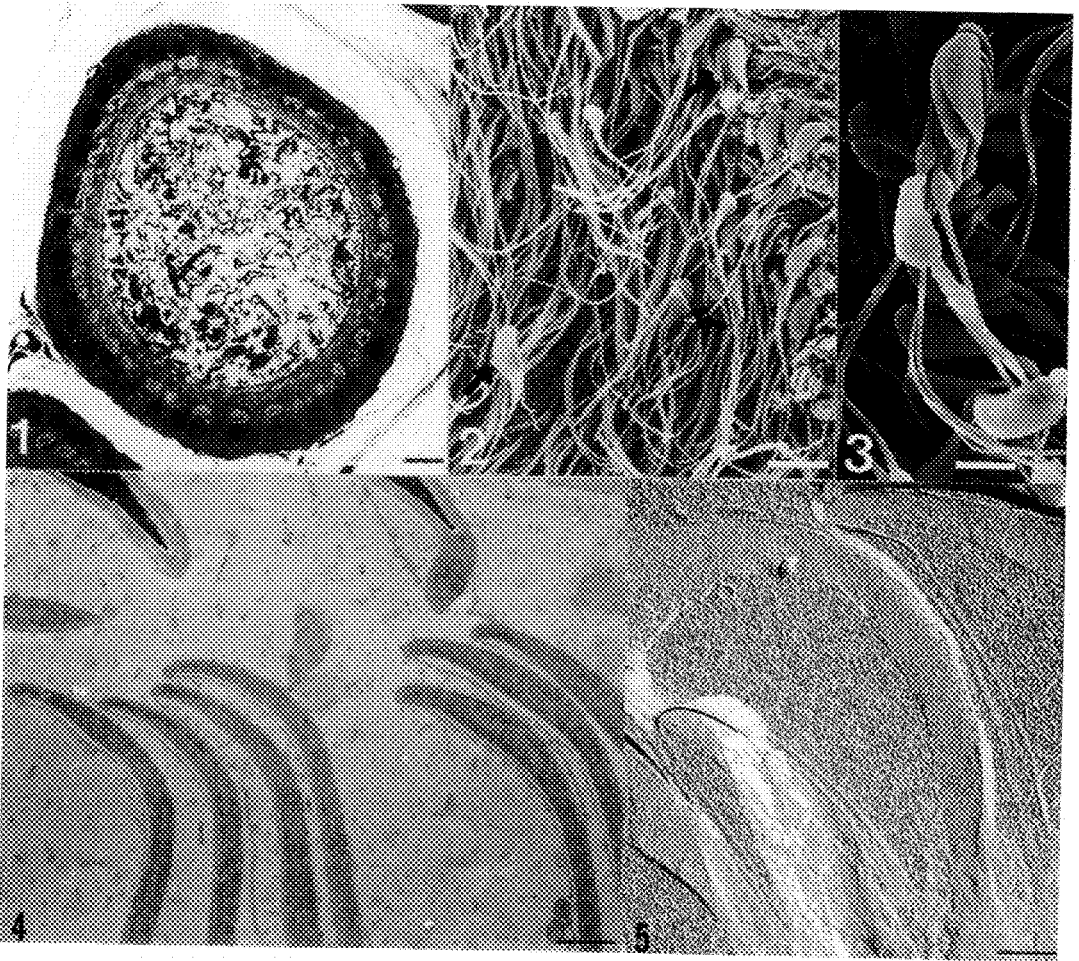
Small pieces of epididymides of adult squirrels (*Funambulus pennanti*) were fixed in cacodylate buffered glutaraldehyde and processed in a conventional manner for transmission and scanning electron microscopy. Ultrathin sections and freeze-fracture replicas were examined with JEOL 1200 EX electron microscope.

Stacks of associated spermatozoa are discernible in the lumen of the epididymal duct (Fig.1). In the scanning electron micrographs the spermatozoa in the epididymis line up in the form of rouleaux comprising of 5 or more spermatozoa (Fig.2). Sometimes the spermatozoa are organised in whirls (Fig.3). This sperm association resembles the characteristic rouleaux observed in guinea pig and Loris^{2,3}. Examination of ultrathin sections suggest that there is no cementing material holding these spermatozoa together except for the elaboration of the plasma membrane of the adhering spermatozoa (Fig.4). The plasma membrane especially on the concave side of the sperm head is found lifted away from the electron dense head and the lifted up plasma membrane is apposed to the convex surface of the neighbouring spermatozoon. The plasma membrane of the convex side of the sperm adheres intimately with its underlying electron dense sperm head. Such specialization of the plasma membrane is also apparent in the freeze-fracture replica (Fig.5). On the other hand, in mole (*Talpa* sp.) though the spermatozoa are stacked linearly there is no evidence of any kind of structural modifications of the plasma membrane⁴. Whereas in invertebrate spermatozoa^{5,6} associations involve adhesions or fusions or structural specializations of the adhering spermatozoon in the region of the head, the association is different in squirrel. Unlike the junctional specialization of the adhering plasma membrane in Loris spermatozoa, there is no fusion of plasma membranes of the associating spermatozoa in squirrel. Nevertheless such plasma membrane modifications effect the sperm-sperm association and presumably protect the acrosomal region of the spermatozoa from the onslaughts of the rigorous microenvironment these spermatozoa are subjected to later in the female tract^{3,7}.

References

1. D.S.Friend and D.W.Fawcett, J. Cell Biol (1973) 63, 641.
2. S.R.Bawa and G.Werner, in The Sperm Cell, The Hague: Martinus Nijhoff (1983) 245.
3. D.A.Phillips and J.M.Bedford, Gamete Res. (1987) 18, 17.
4. S.R.Bawa Unpublished.

5. R.Dallai and B.A.Afzelius, *Tissue Cell* (1985) 17, 561.
6. S.R.Bawa, *J. Cell Biol.* (1964) 23, 431.
7. This work was supported by the award of a Senior Research Fellowship by the University Grants Commission, Government of India to H.K.B. The award of Senior Fellowship by the Alexander Von Humboldt Foundation, Germany to S.R.B is gratefully acknowledged.



- Fig.1 LM of the epididymal duct of squirrel. Stacking of spermatozoa is visible. Bar= 1 μ m.
- Fig.2 SEM of associated spermatozoa in rouleaux (arrows). Bar= 10 μ m.
- Fig.3 Higher magnification SEM of sperm head in whirls. Bar= 5 μ m.
- Fig.4 TEM of sectioned epididymal spermatozoa. Concave and convex faces of the associated plasma membrane is seen. Bar= 05 μ m.
- Fig.5 Freeze-fracture replica depicting anterior portions of associated spermatozoa. Bar= 04 μ m.

ULTRASTRUCTURAL DIAGNOSIS OF RENAL ONCOCYTOMA

Shirley Siew, Mehboob Fatteh

Department of Pathology, Michigan State University, East Lansing, MI 48824, and Ingham Medical Center, Lansing, MI 48910

Renal oncocytoma is a comparatively rare tumor, having an incidence 1/20th that of renal cell carcinoma, from which it has to be differentiated. We report a case of a 61 year old man who was found to have albuminuria 100 mg/dL on a routine physical examination. A retrograde pyelogram showed splaying of the right upper pole infundibula. Two right renal tumors were shown on renal CT scan and there were multiple hypervascular masses on angiography. A right radical nephrectomy was performed. The kidney weighed 176 grams and measured 11 x 7.5 x 5 cm. There were several dark brown nodules in the upper pole, lower pole and midportion of the kidney. Some of the nodules protruded onto the cortical surface, stretching the overlying capsule, but, there was no evidence of capsular nor renal vein invasion. The largest nodule measured 4.5 x 4 x 4 cm. Histologic examination showed a distinct line of demarcation between the tumors and the normal kidney. Occasional thickened vessels were noted at the border. For the greater part, the tumor showed a tubular or acinar architecture, although the lumina of some of the tubules were narrow. The tubules were lined by large, polygonal eosinophilic cells with a granular cytoplasm. There was no evidence of nuclear atypicality nor mitotic activity. Thin walled blood vessels were present between the tubules. Transmission electron microscopy showed the presence of irregular tubules, surrounded by a well formed basement membrane. The tubules were separated by thin walled blood vessels (Fig. 1). The luminal surface of the cells lacked microvilli. Nuclei were comparatively small and irregular in shape. Lysosomes were concentrated towards the luminal surface. There were occasional lipid vacuoles. The cytoplasm contained large numbers of mitochondria with membranous cristae (Fig. 2). These ultrastructural characteristics are in keeping with those of a renal oncocytoma. Comment: The term oncocyte' is applied, at the light microscopic level, to large epithelial cells, which have a markedly eosinophilic and granular cytoplasm. Transmission electron microscopy shows the presence of an abundance of mitochondria filling the cytoplasm. Oncocytomas are tumors composed of a uniform population of such cells. Renal oncocytoma is considered to be a benign cortical adenoma. It has been postulated that it arises from proximal tubular epithelium. Features that distinguish renal oncocytoma from other adenomas are that they may reach a large size (7cm) and that they may be multicentric in the same kidney (reported in 5% of cases). The dark brown bulging nodules present in our case are typical of the gross appearance of renal oncocytoma. Various theories have been proposed to account for the marked increase of mitochondria, including that it is due to a neoplastic proliferation of them, at the expense of other subcellular organelles. The diagnosis of oncocytoma is established by the ultrastructural demonstration of the abnormal abundance of mitochondria.

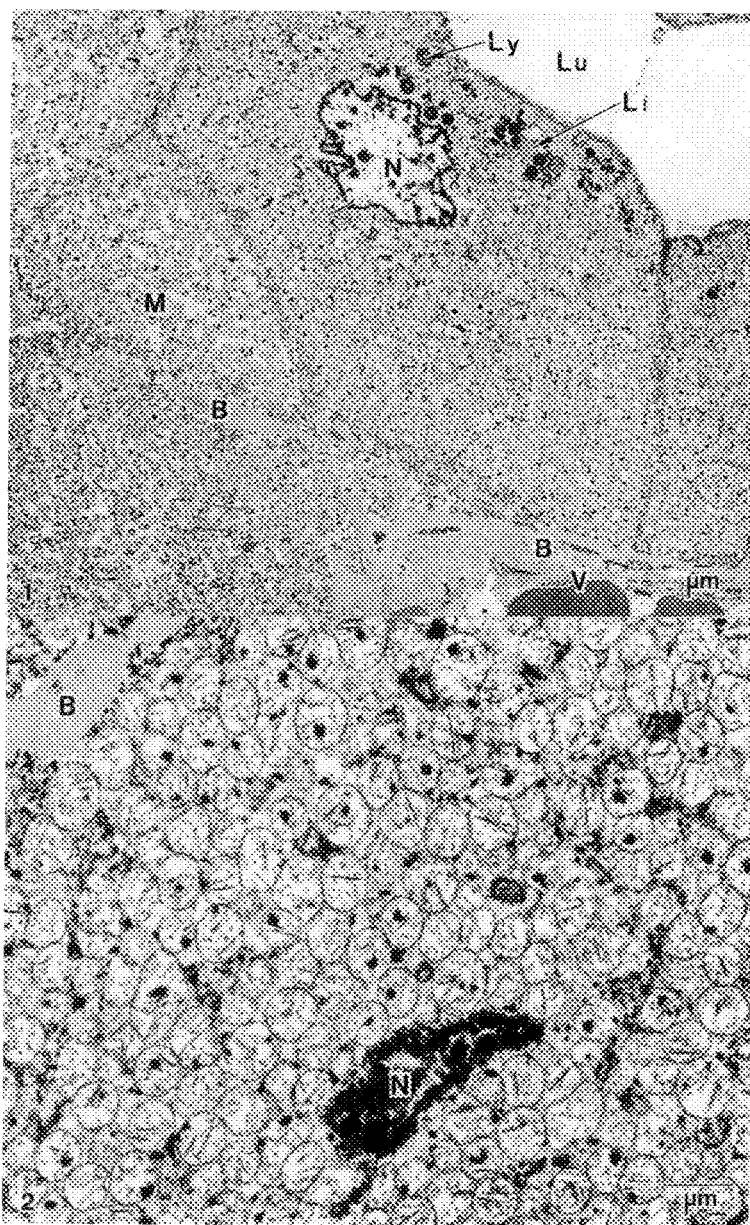


FIG. 1.--TEM Renal Oncocytoma. Closely packed tubules separated by blood vessels (V). Cells filled with mitochondria (M). B-basement membrane, N-Nucleus, Lu-lumen, Ly-Lysosomes, Li-Lipid vacuole.

FIG 2.--TEM Renal Oncocytoma. Cytoplasm packed with mitochondria with membranous cristae. N-nucleus, B-basement membrane.

ELECTRON MICROSCOPY AS AN IMPORTANT DIAGNOSTIC TOOL IN NEURONAL CEROID-LIPOFUSCINOSIS (N C L , Batten's Disease)

Wolfgang H. Muss⁺, Rudolf Puttinger⁺⁺, and Josef Thurner⁺

⁺Department of Pathological Anatomy, and ⁺⁺Department of Pediatrics, St. John's General County Hospital L K A, EM-Lab, Mueßner Hauptstrasse 48, A-5020 Salzburg AUSTRIA

Neuronal Ceroid-Lipofuscinoses (NCL) are a group of neurometabolic/neurodegenerative disorders characterized by an accumulation of metabolites (autofluorescent "lipopigments-Ceroid-Lipofuscin") in central and peripheral nerve system as well as in retina, skeletal muscle, fibroblasts, histiocytes and other body organs. Batten's Disease (syn: SPIELMEYER-VOGT Disease; juvenile onset NCL) presents with an autosomal recessive inheritance (1). Immunochemical studies (2) suggest that **subunit c of mitochondrial ATP-Synthase** is stored in the late infantile, juvenile and adult forms of NCL; chromosome studies indicate Batten's Disease maps to human chromosome 16 (3); erythrocyte and platelet **phospholipids** and **fatty acids** have been reported to be decreased (4), also concentrations of **phosphorylated dolichol** are reported to be 10 to 20-fold higher in brain from NCL than age-matched controls (5). Intracellular/lysosomal storage products histologically are PAS-positive, extractable and, ultrastructurally, the inclusions/accumulation products display characteristic recti- and curvilinear profiles as well as fingerprint bodies (for histological / ultrastructural classification criteria cf. (6)).

An eight-year-old girl with symptoms under suspicion of suffering from juvenile NCL underwent cutaneous and suction biopsy of rectal mucosa in order to confirm the clinical diagnosis and/or to exclude other metabolic storage diseases. Tissue pieces were immediately fixed after surgery either for histological processing in buffered formalin or, adhering to a routine/standardized fixation/processing procedure (cf. original paper, this volume 50th EMSA Proceedings, p... : MUSS W.: The Pro's for a Multiple Use and Safe Disposal with Recovery of Osmium Tetroxide Solution(s) in Routine Electron Microscopy). Also, a buffy coat from peripheral blood was prepared.

Histologic evaluation of skin, rectal mucosa as well as lymphocyte preparation revealed no obvious abnormalities, eg. PAS-positive suspicious substrata or striking vacuolization of lymphocytes. By LM of semithin sections at first glance no striking changes from normal could be observed. However, in some submucosal autonomic ganglia, striking vacuolization was observed, the vacuoles filled but only to some extent with stainable material. When looking at lymphocytes with LM-oil immersion objective x 100) about 10-15% of the lymphocytes turned out to contain single to multiple, more/less empty vacuoles. TEM of selected areas revealed the characteristic recti-, sometimes curvilinear profiles as well as fingerprint-inclusion bodies in cytoplasm of endothelial cells (skin, rectal mucosa), at places also with microtubular/(para-)crystalline structures, smooth muscle cells and Schwann cells (skin, rectum; not shown), as well as -most prominently- in sweat gland cells. On the other hand, vacuoles of the lymphocytes showed no prominent storage material (Figs. 1-4, insets).

Our morphological findings properly correlate with the biochemical data reported most recently (s. above) on suggested failure(s) of cellular metabolism. From our results it is concluded that careful LM and TEM evaluation of rectal mucosa and skin biopsies and buffy coat preparation are powerful tools in an early confirmation of clinical diagnosis of juvenile neuronal ceroid-lipofuscinosis.

References

1. K.J. Neumärker and C. Denk, pädiatr. prax. (1990/91) 41, 233
2. N.A. Hall et al., Biochem. J. (1991) 275, 269

3. M. Gardiner et al., *Genomics* (1990)8, 387
4. M.J. Bennett et al., *Neuropediatrics* (1990)21, 202
5. N.A. Hall et al., *Adv.Exp.Med.Biol.* (1989)266, 225
6. M.I. Filipe and B.D. Lake, Ed., *Histochemistry in Pathology*, Edinburgh, Churchill-Livingstone (1990) 117

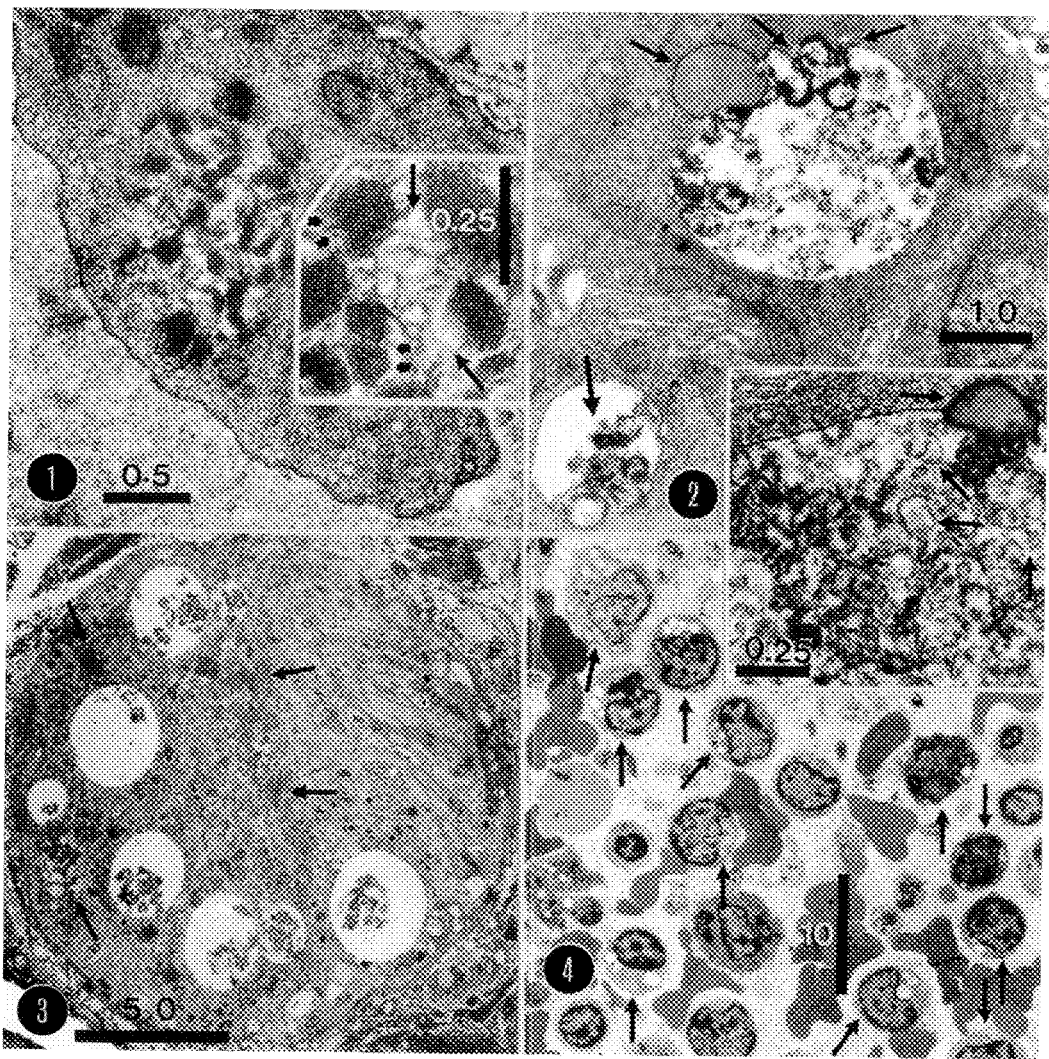


Fig. 1. Intracytoplasmic inclusions in endothelial cells; inset: detail of profiles and microtubular/(para-)crystalline structures. All bars equal μm.
 Fig. 2. Storage vacuoles in sweat gland cells; inset: detail of accumulated material (phospho?-lipid / curvi- and rectilinear profiles (sweat gland cell).
 Fig. 3. Vacuolized submucosal autonomic ganglion (rectum biopsy) with intracytoplasmic material accumulation and transferred to cytoplasmic vacuoles.
 Fig. 4. Low power EM micrograph from buffy coat preparation showing numerous lymphocytes with single to multiple vacuoles.

THE DISTRIBUTION OF "CAPSAICIN-SENSITIVE" NERVE FIBERS IN THE LYMPHATIC WALL
Fruschelli C., Guarna M., Pucci A.M., Alessandrini C., Crestini F.

Histology and General Embryology Institute - University of Siena - Italy

In a previous paper we have shown that guinea pig mesentery lymph collectors possess not only autonomic nerve fibers containing classical neurotransmitters but also peptidergic ones. These nerve fibers are sensitive to the depletory action of capsaicin, and are likely to be sensory in nature.

Therefore the aim of this study was to evaluate the effects of capsaicin of the nerve fibers of the lymphatic wall by ultrastructural methods and to study the distribution of the "capsaicin sensitive" nerve fibers in the lymphatic vessel wall.

The study was carried out on ten guinea pigs of both sexes, weighing between 180 and 350 gr. In order to examine the acute effects of capsaicin, one group of animals received a single subcutaneous injection of capsaicin (50 mg/Kg). Capsaicin was dissolved in a mixture of ethanol, Tween 80, saline (1:1:8, V/V/V). Control animals received the vehicle only. Treated and control animals were then killed by decapitation under ether anaesthesia 24h after the treatment. The mesenteries were rapidly removed, fixed and processed for conventional electron microscopy. Thin sections were cut with an Ultramicrotome Nova LKB, stained and examined under a Philips CM 10 Electron Microscope.

Ultrastructural changes were evident in unmyelinated nerve fibers located near the lymph capillary wall (Fig.1) and in the adventitia of the lymph collectors of the animals treated with capsaicin (Figures 1-2). The most frequent ultrastructural changes consisted of swelling axons containing clusters of organelles, including mitochondria, some granular vesicles, membranous sacs, and lysosome-like elements. Occasionally, axons in an advanced stage of degeneration were observed. The degenerating axons were represented by a pleomorphic osmiophilic material surrounded by or embedded in Schwann cell cytoplasm. These profiles represent degenerating axons phagocytosed by Schwann cell. However, in the mesenterial arteries and veins there were a greater number of unmyelinated nerve fibers containing degenerating axons, which were located at the junction of the media and adventitia and near the muscle cells of the media.

Our findings show that lymph vessels, as blood vessels, possess capsaicin sensitive nerve fibers also if in a smaller number than blood vessels. These nerve fibers are unmyelinated and are of a small diameter. Considering previous pharmacological data, these sensory unmyelinated nerve fibers could carry out a double function in the lymphatic wall: conveying sensory information to CNS which activate autonomic reflexes for the regulation of the lymph vessel contractility, and/or a local action through the release of multiple vasoactive peptides from their peripheral endings, which could be implicated in the regulation of lymph vessel permeability.

References

- 1) M. Guarna et al., *Lymphology* (1991) 24, 161.
- 2) P. Holzer, *Neuroscience* (1988) 24, 739.

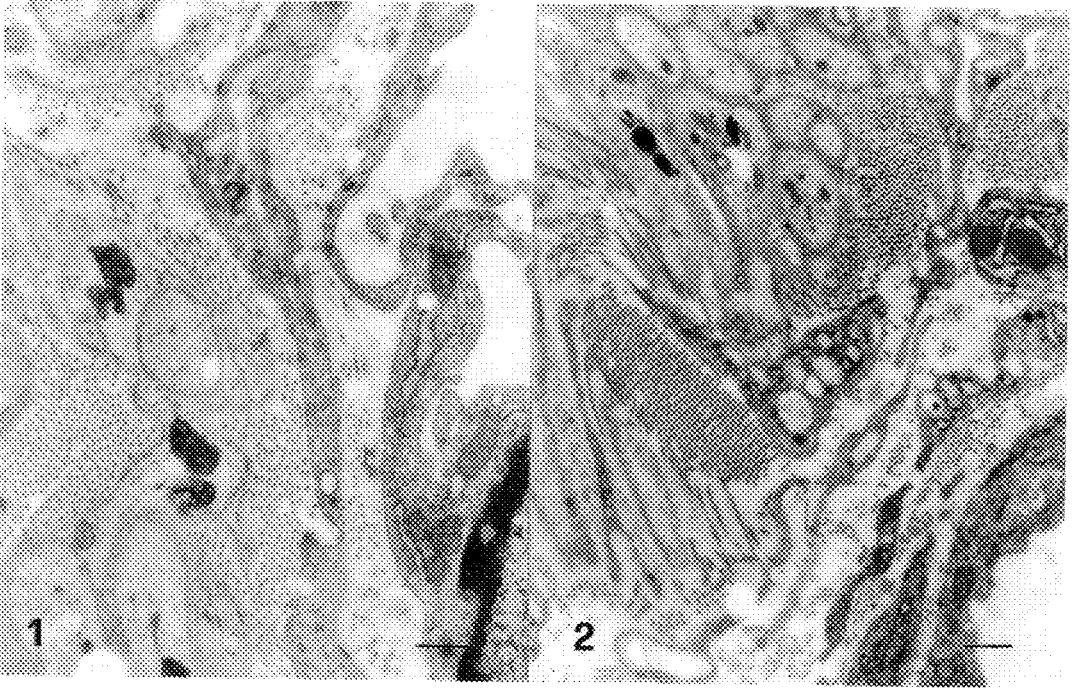


Fig.1- Unmyelinated nerve fiber containing some degenerating axons near the wall of the lymphatic capillary. Bar 0.39 μ m

Fig.2- Unmyelinated nerve fiber in the adventitia of the lymph collector, showing swelling axons containing electron-dense pleomorphic material. Bar 0.56 μ m

JANSKY-BIELSCHOWSKY SYNDROME, A LYSOSOMAL DISEASE FIRST DIAGNOSED CASE IN OMAN

Dr Line Buhl, Mr David Muirhead

Department of Electron Microscopy, Sultan Qaboos University,
PO Box 32485, Al Khod, Muscat, Oman

Introduction There are four lysosomal diseases of which the neuronal ceroid lipofuscinosis is the rarest. The clinical presentation and their characteristic abnormal ultrastructure subdivide them into four types. These are known as the Infantile form (Santavuori-Haltia), Late infantile form (Jansky-Bielschowsky), Juvenile form (Batten-Spielmeier-Voght) and the Adult form (Kuph's).

Case History: An 8 year old Omani girl presented with myoclonic jerks since the age of 4 years, with progressive encephalopathy, mental retardation, ataxia and loss of vision. An ophthalmoscopy was performed followed by rectal suction biopsies (fig. 1). A previous sibling had died of an undiagnosed neurological disorder with a similar clinical picture.

Method and Materials: Biopsies were divided between light microscopy, histochemistry and electron microscopy.

Tissue for light microscopy was fixed in 10% buffered formalin, processed according to conventional procedures to paraffin wax. 4 μ sections were cut and stained by Haematoxylin and eosin, PAS/diastase, Schmorl's, Luxol fast blue, Sudan black and long ZN.

The tissue for histochemistry was frozen in liquid nitrogen, sectioned and stained by the above methods. A section was fixed in formalin vapour for autofluorescence.

Tissue for electron microscopy was fixed in Karnowsky's fixative (2% Gluteraldehyde, 2.5% Paraformaldehyde in Cacodylate buffer), dehydrated in ethyl alcohol and embedded in Agar 100 resin. Ultrathin sections were stained by uranyl acetate/lead citrate, and examined on a Zeiss EM 900.

Results: The ophthalmoscopy showed characteristic optic atrophy and total aplasia of the vessels (Fig 2).

Light microscopy examination showed an oedematous rectal mucosal biopsy without diagnostic changes (Fig. 3). The special stains and histochemistry were inconclusive except for a weak focal autofluorescence.

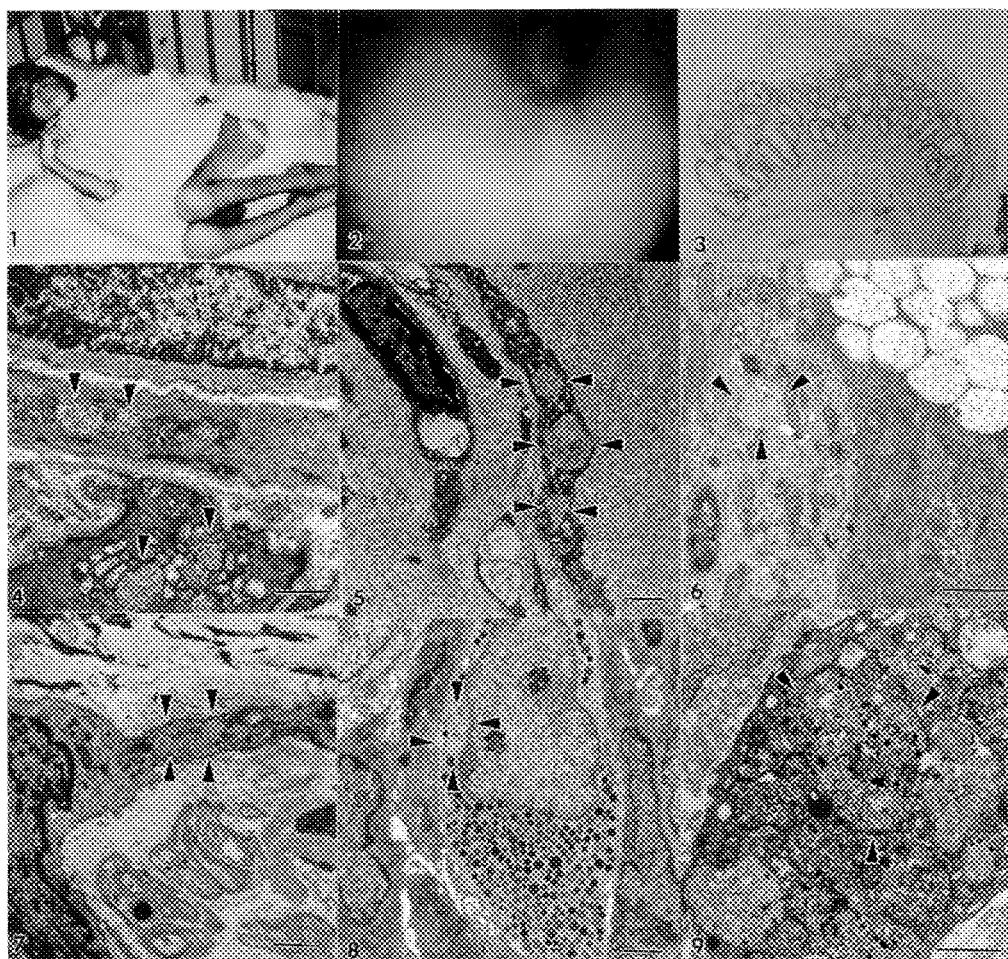
The electron microscopy showed curvilinear bodies within the lysosomes of smooth muscle, macrophages, endothelial cells, schwann cells, epithelial mucosal cells and mast cells (Fig.4 - 9)

Discussion The electron microscopic findings of curvilinear bodies confirmed a lysosomal storage disease, JANSKY-BIELSCHOWSKY SYNDROME. The finding of curvilinear bodies within the mast cells and epithelial cells have not previously been described.

This is an inherited metabolic disease with an autosomal recessive transmission with a risk factor of 25%. Future prenatal diagnosis can be made on uncultured amniotic cells processed for electron microscopy.

References

- 1) Benzeze, D., Textbook of the fundus of the eye, Chpt 21, p.435-464
- 2) Santavuori, P., Altia, M., Rapola, J., (1971) Developmental Medicine and Child Neurology Vol.16, No.5, Oct 1974 p.644-653
- 3) Ghadially, N. F., (1990) Ultrastructural Pathology of the Cell and Matrix Vol 2 pp 712-715.
- 4) Am. J. Med. Genet. 22(4):781-9 1985



- Fig. 1: 8 year old Omani Girl with severe physical disability.
- Fig. 2: Ophthalmoscopy showing fundus of the eye with optic atrophy and degeneration of the vessels.
- Fig. 3: Low power photomicrograph of rectal biopsy (H&E).
- Fig. 4: Electron micrograph of smooth muscle showing curvilinear bodies, arrow head (▶). Magnification $\times 17,500$ Bar= $5\text{ }\mu\text{m}$
- Fig. 5: Electron micrograph of endothelial cell showing curvilinear bodies arrow head (▶). Magnification $\times 13,200$ Bar= $5\text{ }\mu\text{m}$
- Fig. 6: Electron micrograph of epithelial mucosal cell exhibiting curvilinear bodies within the cytoplasm, arrow head (▶). Magnification $\times 21,000$ Bar= $5\text{ }\mu\text{m}$
- Fig. 7: Electron micrograph of a Schwann cell showing curvilinear bodies arrow heads (▶) Magnification $\times 15,000$ Bar= $5\text{ }\mu\text{m}$
- Fig. 8: Electron micrograph of mast cell showing curvilinear bodies within the cytoplasm, arrow heads (▶). Magnification $\times 13,200$ Bar= $5\text{ }\mu\text{m}$
- Fig. 9: Electron micrograph of the cytoplasm of a macrophage with curvilinear bodies in the lysosomes, arrow heads (▶). Magnification $\times 21,000$ Bar= $5\text{ }\mu\text{m}$

CYTOCHEMICAL METHODS FOR THE RAPID DEMONSTRATION OF INFECTION AT THE TISSUE-BIOMATERIAL INTERFACE

J. Hanker*, J.J. Dobbins**, P.E. Yates*, and B.L. Giammara**

*Dept. of Biomedical Engineering and Dental Research Center, University of North Carolina, Chapel Hill, NC 27599-7455

**Dept. of Biology, Bellarmine College, Louisville, KY 40205

***Analytical Electron Microscopy Laboratory, Graduate Programs and Research, University of Louisville, Louisville, KY 40292

Infection can be an extensive problem developing during implantation of an autogenous or prosthetic (biomaterial) device or graft.¹ Although culture techniques are invaluable in identifying the responsible microorganisms², the times required frequently emphasize the need for rapid staining methods which can reduce the classification times from days to hours. Studies in our laboratories³⁻⁷ over the past few years have resulted in microwave-accelerated stains and in methods developed by Giammara^{8,9}, which enable the rapid study of glass slides and coverslips by electron as well as light microscopy.

These methods have been utilized by us to show the absence of bacteria and fungi in hydroxylapatite/plaster craniofacial bone implants,¹⁰ hydroxylapatite-coated titanium hip implants,¹¹ and their presence in osseointegrated or oral endosteal titanium hollow cylinder implants and total artificial heart implant specimens^{2, 12-14}. Use of the ruthenium red-TCH-Os or ruthenium red-TCH-silver reactions enable evaluation of the implant specimens for mucinous, proteinaceous biofilms which promote the adherence of bacteria to the grafts. The Sigma HT100 Silver Stain modification³ of the Giammara PATS reaction⁴ enables staining of medically important fungi in these specimens unobstructed by the positive staining of the gram-negative bacteria clearly shown by the PATS reaction.⁵ These reactions employing the microwave-accelerated deposition of silver via silver methenamine enable the estimation of infection or colonization due to fungi or gram-negative bacteria rather than their mere presence. This is because by the use of the Olympus CUE-2 Microscopic Image Analysis System with these stained slides the sorting and counting of either the fungi⁶ or the gram-negative bacteria⁵ at the biomaterial-tissue interface could be accomplished. When a periimplantitis or site-specific infection arose at the interface of a failing osseointegrated endosteal titanium oral implant, the PATS reaction was able to show the presence of gram-negative anaerobic rods and fusobacteria as well as occasional spirochetes (Fig. 1). At the time of the autopsies, each ventricle from the artificial hearts was covered with a proteinaceous biofilm where Pseudomonas aeruginosa could be seen with the PATS reaction, Candida albicans with the Sigma HT100 Silver Stain, and Staphylococcus epidermidis with the Gram stain.

References

1. K.J. Geary et al. Differential effects of a gram-negative and a gram-positive infection on autogenous and prosthetic grafts. *J. Vasc Surg.* (1990)11, 339.

2. J.J. Dobbins et al. Demonstration of the bacterial-biomaterial interface in implant specimens. *Mater. Res. Soc. Symp. Proc.* (1989)110, 337.

3. Sigma Diagnostics Silver Stain HT100.

4. B. Giammara et al. Periodic acid-thiocarbohydrazide-silver methenamine(PATS) reaction. *Proc. 42nd Ann. Meet. Electr. Microsc. Soc. Amer.* (1984)264.

5. J. Hanker et al. Positive staining of outer membrane lipopolysaccharides of gram-negative bacteria: Microscopic image analysis to estimate the disease status of periodontal sites. *Microscopy Res. and Technique*, in press.

6. J. Hanker et al. Image analysis method to count silver-stained *Candida* in AIDS patients' subgingival plaques. *Mater. Res. Soc. Symp. Proc.* (1991)189, 371.

7. B. Giammara and J. Hanker. Ruthenium red-osmium bridging with TCH: new technique to stain biological specimens for light and TEM and to coat them for SEM. *Proc. 46th Ann. Meet. Electr. Microsc. Soc. Amer.* (1988)20.

8. B. Giammara et al. Hexamethyldisilazane drying for rapid detection of bacteria in implant specimens. *Proc. 45th Ann. Meet. Electr. Microsc. Soc. Amer.* (1987)878.

9. B.L. Giammara and J.S. Hanker. Xeroxographic-assisted location of areas or structures on clinical slides for electron microscopic examination. *Proc. 50th Ann. Meet. Electr. Microsc. Soc. Amer.* submitted.

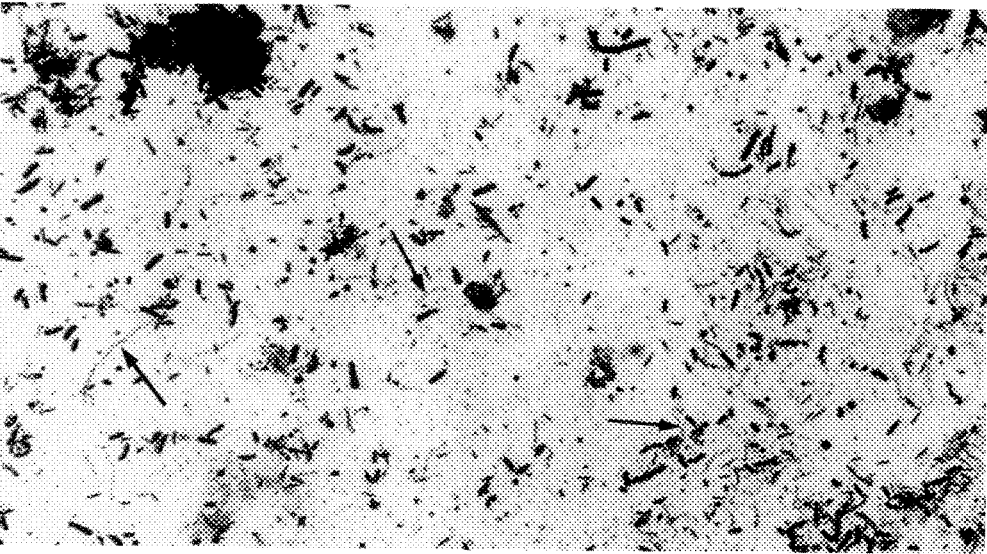
10. J.S. Hanker et al. *Mater. Res. Soc. Symp. Proc* (1986) 77.

11. P. Frayssinett et al. *Proc. 49th Ann. Meet. Electr. Microsc. Soc. Amer.* (1991)34.

12. A. Mombelli et al. *Oral Microbiol. Immunol.* (1987)2, 145.

13. M.G. Newman and T.F. Fleming. *J. Dent. Ed.* (1988) 52, 737.

14. J. Hanker et al. *Proc. 45th Ann. Meet. Electr. Microsc. Soc. Amer.* (1987)778.



1 →'s, Spirochetes

KEARNS-SAYRE SYNDROME, A MITOCHONDRIAL MYOPATHY FIRST DIAGNOSED CASE IN OMAN

Dr. Line Buhl*, David Muirhead*, Dr. David Doyle**

*Dept. of Electron Microscopy, Sultan Qaboos University PO Box 32485 AL khod Muscat, Oman

**Dept. of Neuropathology, Southern General Hospital, Glasgow, Scotland

Mitochondrial myopathy of the Kearns-Sayres Syndrome is described as a severe disorder which is progressive with CNS involvement, has metabolic acidotic crisis and is eventually fatal. The proportion of muscle fibres containing abnormal mitochondria maybe as low as 5-10% in cases presenting with severe clinical symptoms. There is no recognised treatment for this degenerative disease.

Case History: An 11 year old Omani girl well until the age of 5 years, showed increasing symptoms of external ophthalmoplegia, ptosis, tubular vision and retinitis pigmentosa. CT scan showed atrophy of the brain. Biochemistry revealed an elevated creatinine kinase. A muscle biopsy was performed at the age of 11 years. The patient had no known family history.

Method and Materials: The muscle biopsy was divided accordingly for light microscopy, histochemistry and electron microscopy.

Tissue for light microscopy was fixed in 10% buffered formalin, dehydrated in ethyl alcohol and embedded in paraffin wax. Sections were cut at 4 μ and stained by routine H&E, PTAH, PAS/diastase, Van Gieson and Gomori's Trichrome.

The tissue for histochemistry was frozen in liquid nitrogen, sectioned at 5 μ and stained by ATPase, NADH, acid phosphatase and succinate dehydrogenase.

The electron microscopy tissue was fixed in Karnowsky's fixative (2% glutaraldehyde, 2.5% paraformaldehyde in Cacodylate buffer) for 2 hours, post fixed in 1% osmium tetroxide, dehydrated in ethyl alcohol and embedded in Agar 100 resin. Semithin sections were examined, representative ultrathin sections were taken and examined in a Zeiss EM 900.

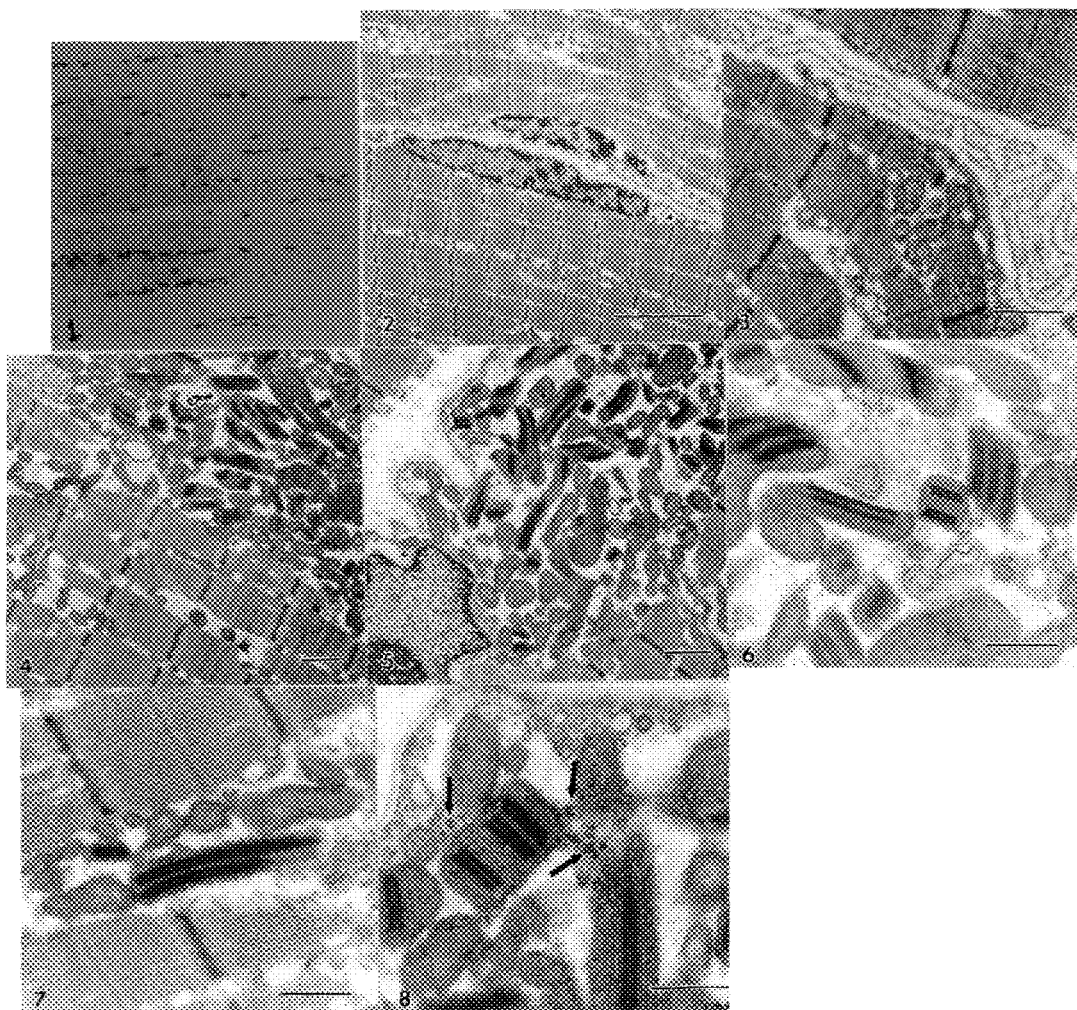
Results: Light microscopy and histochemistry showed no diagnostic changes (Fig. 1). There was no evidence of ragged red fibres with sub sarcolemma thickening.

The electron microscopy examination revealed muscle fibres showing some variation in fibre thickness (Fig. 2) with occasional duplication of the sarcolemma membrane (Fig. 3). Occasional muscle fibres showed an increase in the number of mitochondria with focal aggregation. The aggregated mitochondria were enlarged, and seen to have abnormal and elongated shape. They contained paracrystalline inclusions (Fig.4-8).

Discussion: The ultrastructural finding of atypical paracrystalline structures within the mitochondria in striated muscle along with the clinical picture gave the diagnosis of a KEARNS-SAYRES SYNDROME.

References:

- 1) Richard G. Dickersin, (1990) Diagnostic Electron Microscopy, A Text/Atlas
- 2) Feroze N. Ghadially, (1989) 3rd Edt. Ultrastructural Pathology of the Cell and Matrix



- Fig.1: Low power photomicrograph of left quadricep muscle without diagnostic changes.
- Fig.2: Electron micrograph of skeletal muscle showing variation in fibre size
Magnification x3,000 Bar= 5 μ m
- Fig.3: Micrograph showing duplication of sarcolemma membrane. Magnification
x12,000 Bar= 1 μ m
- Fig.4: Aggregation of mitochondria showing variation in size and shape
Magnification x7,000 Bar= 1 μ m
- Fig.5: Mitochondria with paracrystalline inclusions. Magnification x7000
Bar= 1 μ m
- Fig.6: Mitochondria with rectangular parallel inclusions, connected by transverse
projections. Magnification x20,000 Bar= 1 μ m
- Fig.7: Elongated mitochondria lying between muscle fibres showing paracrystalline
inclusions. Magnification x20,000 Bar= 1 μ m
- Fig.8: Abnormal mitochondria surrounded by glycogen granules arrow head (\blacktriangleright),
Magnification x30,000 Bar= 1 μ m

VANADIUM ACCUMULATION IN ALVEOLAR MACROPHAGES STUDIED WITH THE ZEISS CEM902

John J. Godleski, Rebecca C. Stearns, and Marshall Katler

Respiratory Biology Program, Harvard School of Public Health, 665 Huntington Avenue, Boston, MA 02115

Vanadium compounds are known to cause irritation of the respiratory system.^{1,2} Mechanisms of toxicity include actions at the cell membrane³ and mitochondria.⁴ However, the primary target of toxicity has not been delineated. Alveolar macrophages are the primary defensive cells of the lung and likely to interact with inhaled vanadium compounds. The purpose of this study was to identify sites of vanadium accumulation in alveolar macrophages. The Zeiss CEM902 with capabilities to detect vanadium within the ultrastructural context of the cell by Electron Spectroscopic Imaging (ESI) and by Electron Energy Loss Spectral (EELS) analysis was used for this investigation.

Lung macrophages of hamsters were obtained by bronchoalveolar lavage and cultured in Medium 199 with 5% fetal bovine serum at 1.4×10^6 cells/ml. One mM solutions of VCl_3 or $CoCl_2$ (as a control) were prepared in phosphate buffered saline (PBS) at pH 7.2. One hundred μ l of one of these solutions or PBS alone were added to each of the cultures to produce final concentrations of vanadium or cobalt solutions of 0.09mM. The macrophage suspensions were incubated at 37°C in 95% air + 5% CO_2 for 3 hours after which viability by trypan blue exclusion and the phagocytic functional capacity of the cells to ingest zymosan were determined. Ninety-five percent of the cultured cells in each tube were fixed in 2.5% glutaraldehyde in phosphate buffer with 0.01% $CaCl_2$ and post fixed with osmium tetroxide. The cells were embedded in araldite, sectioned at 30nm, and studied unstained with the Zeiss CEM902.

Cell viability was not affected by these incubations and was greater than 90% in controls and cells incubated with vanadium. Zymosan ingestion was slightly higher than PBS control in the cells exposed to the cobalt solution, but decreased to 44% of PBS control with vanadium. The cells incubated with vanadium had large irregularly shaped phagolysosomes which had accumulated and concentrated soluble vanadium. Figure 1 illustrates these structures. In Figure 2, a,b,c, the ESI of the distribution of vanadium in the macrophage is illustrated. Figure 3 is the EEL spectrum obtained from a phagolysosome. The lesser amounts of vanadium found in other cytoplasmic locations by ESI were also confirmed by spectral analysis. This study shows that accumulation of vanadium is primarily in the phagolysosome, but other sites including mitochondria also have detectable amounts in exposed cells.⁵

References

1. B.S. Levy, *et al.*, J. Occup. Med. (1984)26,8.
2. E.A. Knecht, *et al.*, Am. Rev. Respir. Dis. (1985)132:1181.
3. H.P. Bode. Biochem. Biophys. Acta. (1990)1022:163.
4. L. Zychlinski and J. Byczkowski, J. Arch. Environ. Contam. Toxicol. (1990)19:28.
5. This research was supported by NIH grants ES00002 and ES05947. Technical contributions of Cindy Hastings and Victoria Hatch are acknowledged.

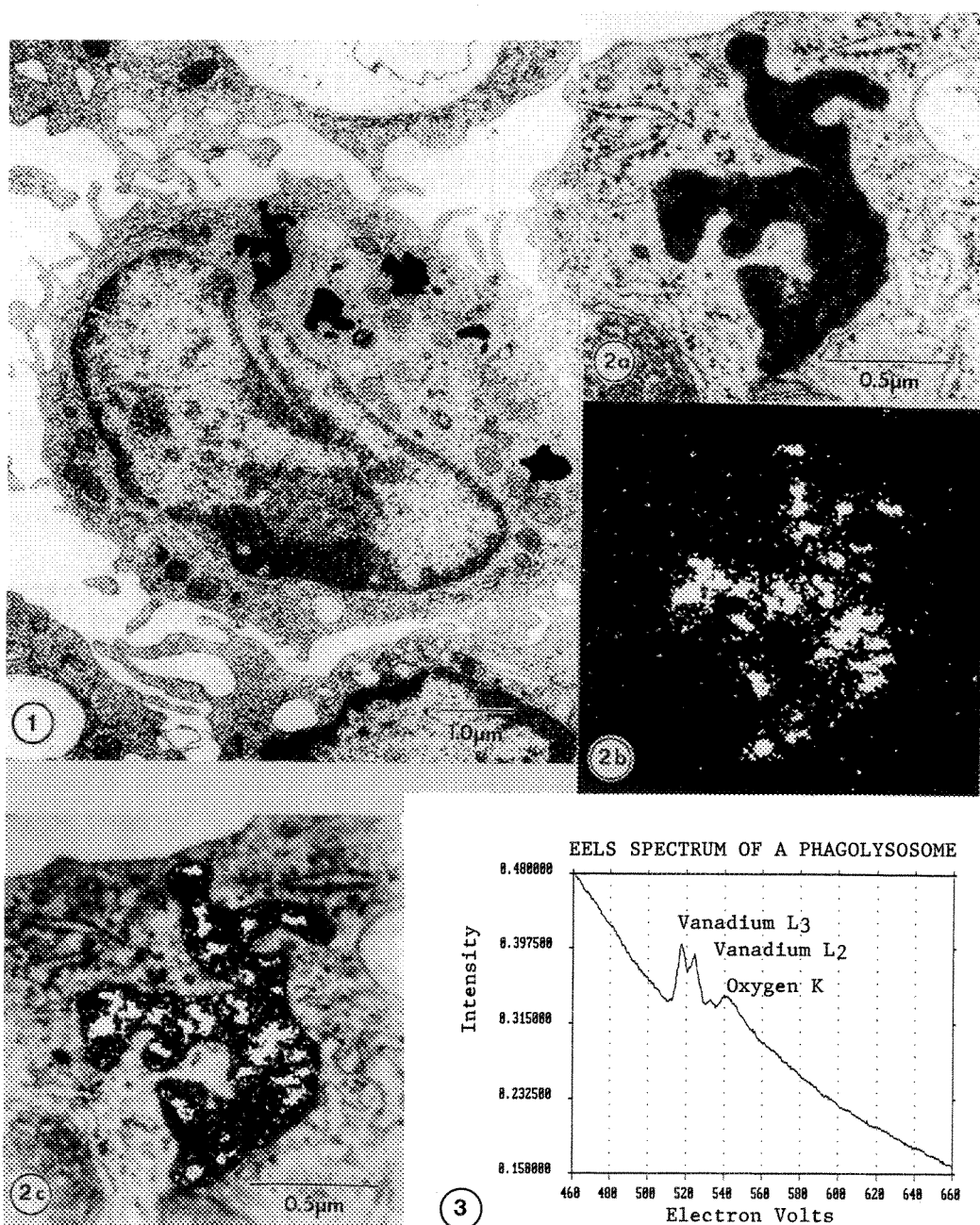


Fig. 1--Alveolar macrophage with numerous irregularly shaped phagolysosomes after vanadium exposure.

Fig. 2a--Higher magnification of a phagolysosome. 2b--The distribution of vanadium in the area of the cell shown in 2a. 2c--Overlay of the vanadium distribution on the ultrastructure of the cell.

Fig. 3--Serial EELS of a phagolysosome.

ULTRASTRUCTURE OF THE LESION INDUCED BY TOXIN T-514 ISOLATED FROM K. humboldtiana
IN THE ALVEOLAR REGION OF THE LUNG

Julio Sepúlveda-Saavedra*, Beatriz González-Corona*, Víctor A. Tamez Rodríguez**,
Ma. Victoria Bermúdez de Rocha**, Alfredo Pifeyro López**

*Department of Histology, **Department of Pharmacology-Toxicology. Facultad de
Medicina de la Universidad Autónoma de Nuevo León., Monterrey, N.L., México

It has been shown in previous studies that the toxin T-514 isolated from K. humboldtiana induces severe damage to the lung in treated rodents(1). Histopathological findings include edema, and alveolar hemorrhage. However, the ultrastructure of the lesion has not been investigated. In this study we used two species of rodents: Hamster and guinea pig, and a primate: Macaca fascicularis. Animals received different single dosis of the toxin via intraperitoneal. Control animals received only the vehicle (propylen glycol). Immediately after spontaneous death, lung samples were fixed in Karnovsky-Ito fixative, post fixed in osmium tetroxide and embedded in epon. Thin sections were prepared with an Ultratome V LKB, stained with uranyl acetate and lead citrate, and studied in an electron microscope Zeiss-EM109.

All treated animals showed the same ultrastructural findings, although the monkeys were less damaged. Main features are: Abundant Polymorphonuclear leukocytes (PMN) asociated to the endothelium of venules and capillary vessels of the interalveolar septum. PMN show abundant electrodense granules and characteristic nucleus, a well developed Golgi apparatus, vesicles and plasmalemmal folds and pseudopods, some of them show clear cytoplasmic areas probably due to intensive degranulation. All this changes have been reported to occur in association with PMN activation for cytolysis (2). Associated endothelial cells show abundant pinocytotic vesicles, intracellular edema and plasmalemmal destruction. In the neighboring basal membrane and alveolar epithelium, signs of lysis are identified. Alveolar cavities contain abundant granular material (fibrin), eritrocytes, macrophages and PMN.

This study shows evidence of the endothelial damage associated to the presence of PMN, that causes the damage to the basament membrane and alveolar epithelium leading to the hemorrhage observed with the light microscope. This images have been described for the "Adult respiratory distress syndrome" (3). In this experimental model of the syndrome, factors involved in it's development may be studied, such as activation of serum factors, and prostaglandins, that have been mentioned as mediators (4). This aspects are under current study in our laboratory.

REFERENCES

- 1.- M.V. Bermúdez de Rocha. Doctoral Thesis, Facultad de Medicina de la U.A.N.L., (1989).
- 2.- T.M. Valentine and T.D. Anderson. Proc. Ann., EMSA Meeting 47 (1989) 1078.
- 3.- C.G. Elliot, Amer. J. Med. Sci., (1985) 2, 70.
- 4.- Ph. Craddock, Amer. J. Emer. Med. (1985) 2, 78.

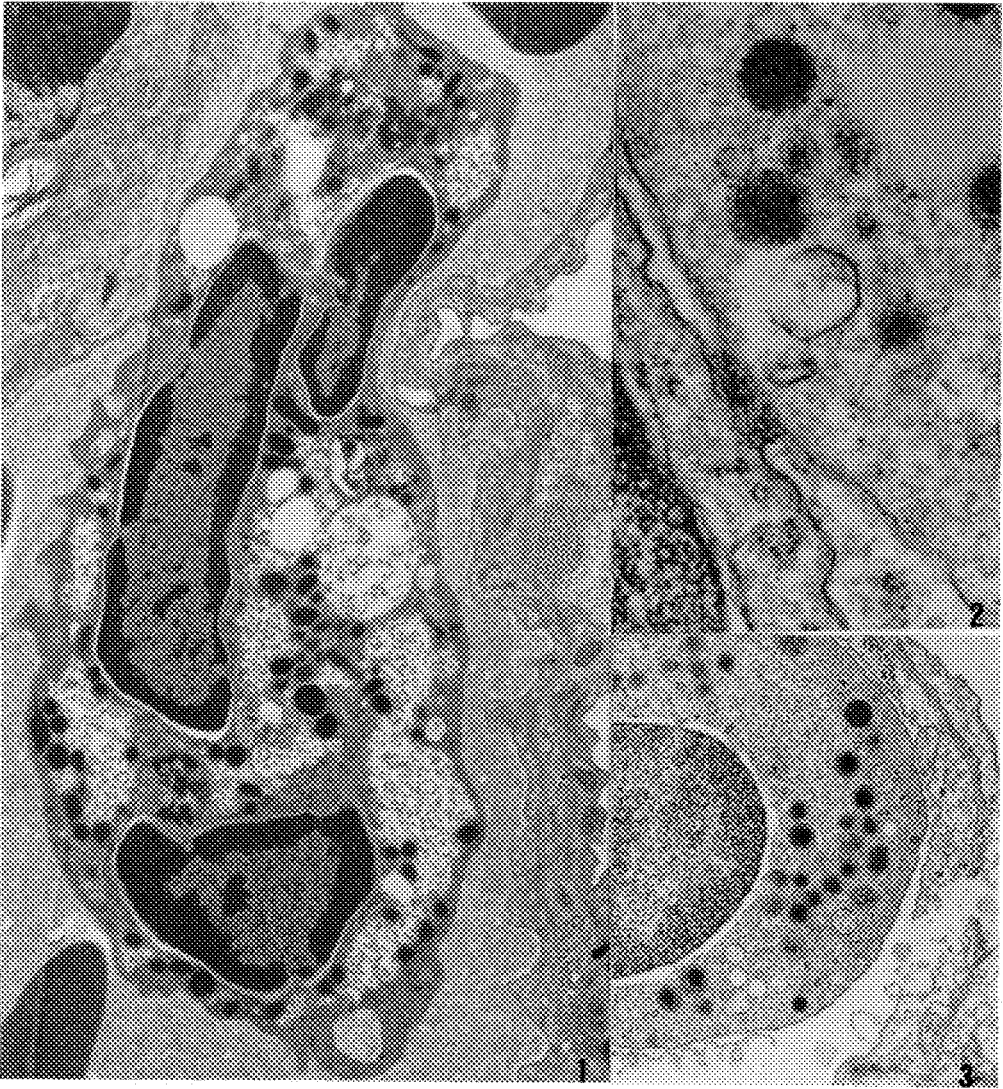


Fig. 1 PMN in alveolar vessel. Elongated cell with plasmalemmal processes, cytoplasm shows empty vesicles and areas of extracted cytoplasm, signs related to degranulation due to activity.

Fig. 2 Close contact between plasmalemma of PMN and endothelial cell.

Fig. 3 PMN in alveolar capillary, endothelial cell severely damaged. A rupture of the plasmalemma, basement membrane and alveolar epithelial cell can be seen.

ULTRASTRUCTURAL CHARACTERIZATION OF THE EFFECTS OF BETA-ALANYL-MELPHALAN IN MOUSE EHRlich ASCITES TUMOR CELLS AND MOUSE LIVER CELLS

Michael Adam, Bao-Ling Tsay Adam, and Lloyd Wolfinbarger, Jr.

Department of Biological Sciences, Old Dominion University, Norfolk, Virginia 23529

Beta-alanyl-melphalan (BAM) was demonstrated to have significant cancerocidal activity using both *in vitro* cultures and *in vivo* chemotherapy assays¹. Ultrastructural observations in the present study confirmed the antitumor activity of melphalan (MEL) and BAM. Results showed that the MEL affected the cellular elements causing marked cell damage both in mouse Ehrlich ascites tumor cells (MEATC) and mouse liver cells (MLC). BAM appeared to affect the cellular elements, with marked cell damage, only in MEATC, but not in the MLC. There were nuclear and cytoplasmic alterations in MEL and BAM treated MEATC, i.e. peripheral thickening of chromatin in nuclei, severe mitochondrial alterations, ribosome accumulation and autolysis phenomena which lead to the destruction of the subcellular structures.

Scanning (SEM), and transmission (TEM) electron microscopy were used for examination of the morphology of each cell line which were treated with anticancer drugs. Standard methods of fixation, dehydration, infiltration and embedding were employed². Fig. 1-3 demonstrate MEATC treated with saline, 0.1 mM MEL, and 0.1 mM BAM, for 24 hours, respectively. The surfaces of the saline treated cells contained short microvilli and (or) blebs. MEL treated cells showed a great variation in cell size and shape. Damaged cells appeared flattened and had lost significant portions of plasma membrane leaving behind a sponge-like mass. The appearance of damaged BAM treated cells exhibited an appearance similar to that of the melphalan-treated cells. Fig. 4-6 demonstrate MLC treated with saline, 0.1 mM MEL, and 0.1 mM BAM for 24 hours, respectively. Saline control cells revealed a dense monolayer of well attached cells with well defined surface morphology. MEL treated cells exhibited a marked decrease in cell density, a flattened appearance and shrinkage at the marginal regions. BAM treated cells demonstrated the typical dense monolayer of cells found in the control saline treated MLC. Fig. 7-9 show the ultrastructure of MEATC treated with saline, 0.1 mM MEL, and 0.1 mM BAM for 24 hours, respectively. In saline treated cells, the cytoplasmic organelles appeared typical. Morphologically damaged and non-damaged cells were seen in MEL treated cell populations. The majority of BAM treated cells showed great amounts of cell debris. Fig. 10-12 show the ultrastructure of MLC treated with saline, 0.1 mM MEL, and 0.1 mM BAM for 24 hours, respectively. Saline treated cells possessed well-defined features. Morphologically damaged and non-damaged cells were seen in MEL treated cell population. BAM treated cells appeared similar to the control saline treated MLC. These results indicated that MEL is toxic to MEATC and MLC and BAM is only toxic to MEATC but not toxic to the MLC.

REFERENCES

1. B.L. Tsay and L. Wolfinbarger, Jr., Cancer Chemotherapy and Pharmacology (1987)19,190.
2. M.A. Hayat, Principles and Techniques of Electron Microscopy (1989)

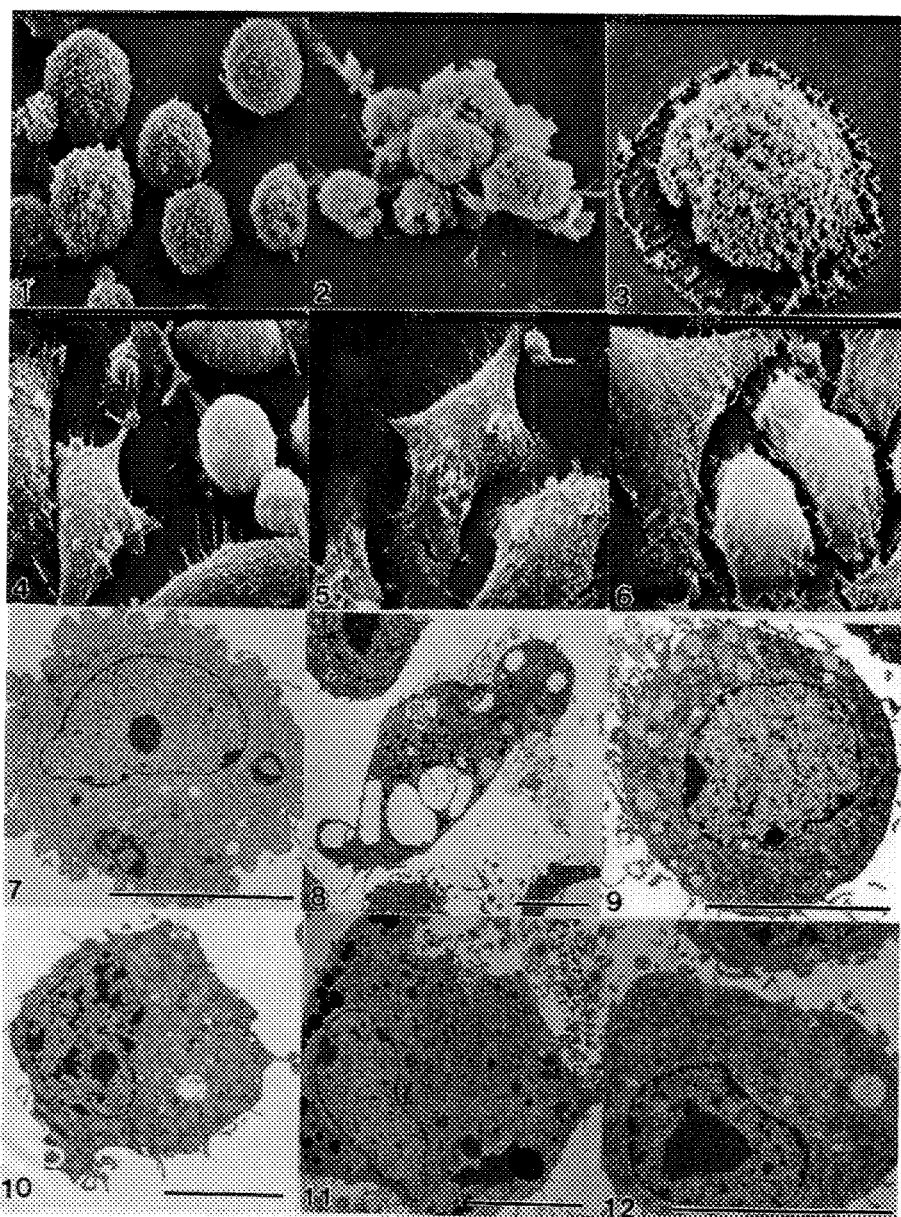


Fig. 1-3.--SEM of saline, 0.1 mM MEL, and 0.1 mM BAM treated MEATC. Bar = 20 μ m.
 Fig. 4-6.--SEM of saline, 0.1 mM MEL, and 0.1 mM BAM treated MLC. Bar = 20 μ m.
 Fig. 7-9.--TEM of saline, 0.1 mM MEL, and 0.1 mM BAM treated MEATC. Bar = 5 μ m.
 Fig. 10-12.--TEM of saline, 0.1 mM MEL, and 0.1 mM BAM treated MLC. Bar = 5 μ m.

ULTRASTRUCTURAL LOCALIZATION OF DNA TOPOISOMERASE II IN ORAL SQUAMOUS CELL CARCINOMA UTILIZING IMMUNOGOLD ELECTRON MICROSCOPY

M D'Andrea*, P Farber**, D Foglesong*

* Dept of Molecular and Cellular Biology, Rutgers Univ, Camden, NJ

** Dept of Pathology, Temple Univ Sch of Medicine, Philadelphia, PA

DNA topoisomerases are enzymes which insert transient breaks into duplex DNA and are important in DNA replication, transcription and recombination. There are two forms of the enzyme, Topoisomerase I which breaks and rejoins only one of the two strands of DNA and Topoisomerase II (Topo II) which breaks and rejoins both of the DNA duplex strands. The essential role of Topo II in cell proliferation is reflected in its abundance in dividing cells, including normal and neoplastic cells ¹.

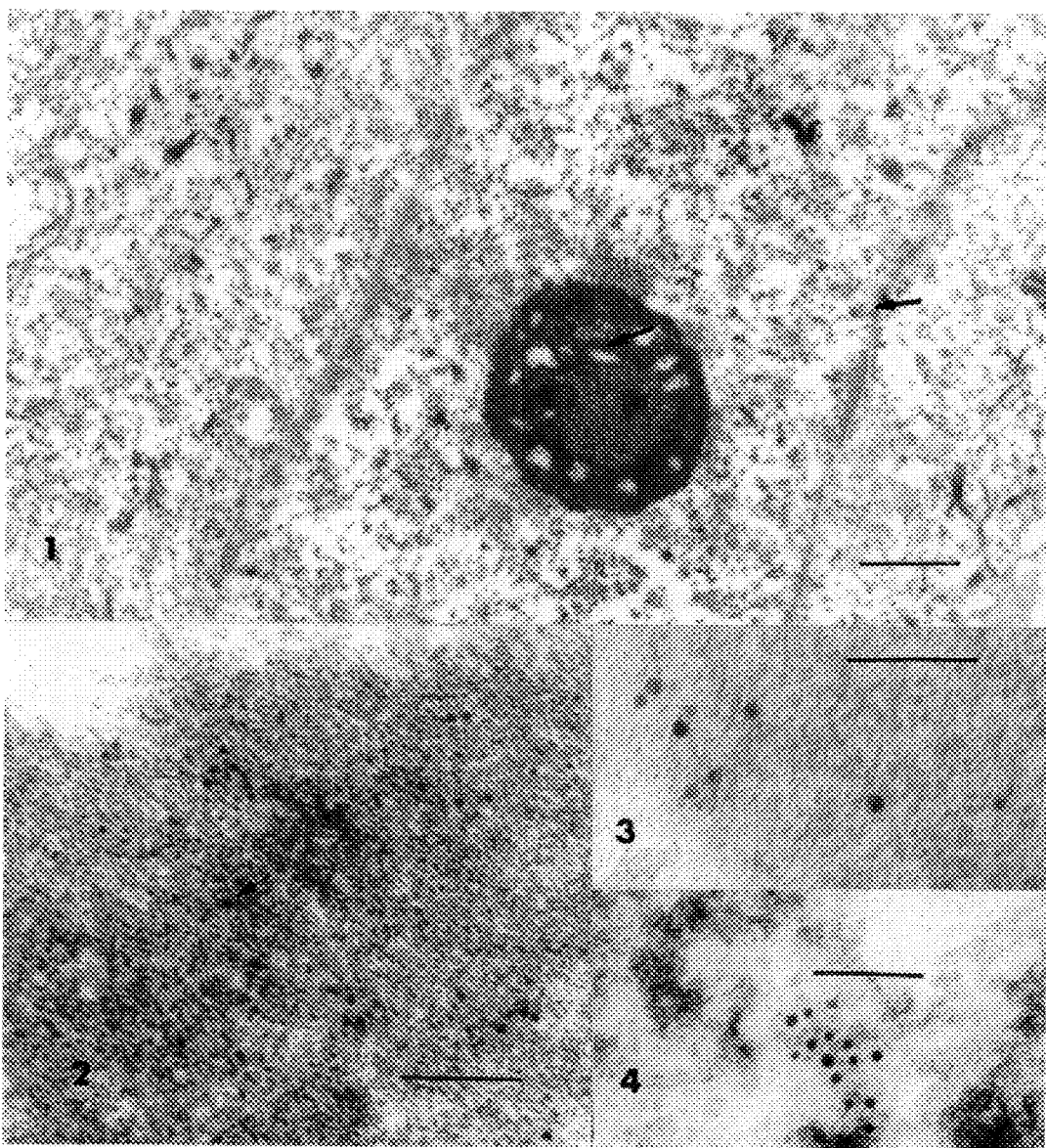
The technique of immunogold electron microscopy is a sensitive method for localizing tissue antigens at the ultrastructural level. We have utilized this technique to identify the intracellular sites of Topo II in oral squamous cell carcinoma.

Tumor tissue was fixed in 2% glutaraldehyde: 1% formalin for 3 hours at 4C. The tissue was then processed in LR White resin. The immunostaining procedure was performed according to an indirect immunogold procedure previously described ². Briefly, the grids were washed in 0.05M Tris buffer, pH 7.3, then placed in blocking serum for 1 hour at room temperature. The grids were then placed in primary antibody (anti-Topo II kindly provided by Dr Fred Drake) overnight. The grids were then washed in Tris buffer, and then incubated with Goat anti-rabbit serum labeled with colloidal gold (5nm) (Amersham) for 1 hour, stained with uranyl acetate and lead citrate and examined using a Phillips EM 300 microscope.

Previously, we have demonstrated increased expression of Topo II mRNA in human oral squamous cell carcinomas at the light microscope level using in situ hybridization techniques ³. Increased enzyme expression was noted in normal proliferating oral epithelial cells with highest levels observed in tumor cells. In the present study, carcinoma cells were identified by high nuclear-cytoplasm ratio, large nuclei with finely dispersed chromatin and large nucleoli. (figure 1) which are typical features of undifferentiated squamous cell carcinoma. Significant labeling, as evidenced by the presence of gold particles, was noted in the nucleoli, cytoplasm and heterochromatin (figures 2,3,4). Only scattered particles were observed in normal, non-neoplastic cells. These results confirm and extend our initial results which suggest that topoisomerase activity is elevated in neoplastic cells and could be valuable in identification and characterization of the neoplastic process.

References

1. Wang JC, Ann Rev Biochem (1985) 54,665.
2. D'Andrea et al. Proc Ann EMSA Meeting (1991) 25,312.
3. D'Andrea M, Farber P, Foglesong D Proc Ann AACR meeting 1992



- Fig 1: Low power of squamous cell carcinoma showing prominent nucleolus, tonofibrils and desmosomes. Arrows point to gold labeling in nucleolus and nucleus. (bar = 1 μ M)
- Fig 2: Higher power of nucleolus. Arrow points to anti-Topo II-gold particle. (bar = 0.1 μ M)
- Fig 3: Anti-Topoisomerase II labeling in nuclear heterochromatin. (bar = 0.05 μ M)
- Fig 4: Anti-topoisomerase II-gold labeling in cytoplasm (bar = 0.1 μ M)

INFLUENCES OF LOW AND HIGH DIETARY VITAMIN A ON RAT LIVER ULTRASTRUCTURE IN A TWO-STAGE HEPATOCARCINOGENESIS MODEL

A. J. Wasserman, L.W. Robertson*, J. R. McGill, I.M. Bahia and S.K. Durham

Department of Experimental Pathology and Electron Microscopy, Bristol-Myers Squibb
Pharmaceutical Research Institute, Princeton NJ 08543-4000. *Graduate Center for Toxicology,
University of Kentucky, Lexington, KY 40506

Polychlorinated biphenyls (PCBs) were used extensively in industrial processes and subsequently contaminated the ecosystem resulting in their accumulation in biological systems including man (Wassermann, 1979). Specific PCB congeners induce different microsomal enzymes. 3,3',4,4'-tetrachlorobiphenyl (TCB) is a 3-methylcholanthrene-like inducer, whereas 2,2',4,4',5,5'-hexachlorobiphenyl (HCB) is a phenobarbital-like inducer. A previous study documented that both PCBs are tumor promoters in DEN-initiated rats (Buchmann, 1986). High levels of vitamin A have been demonstrated to be protective against the development of chemically-induced injury and neoplasia (Sporn, 1976; Lotan, 1980). The effects of different concentrations of vitamin A on hepatocellular injury was examined in an established two-stage hepatocarcinogenesis model.

Adult female Sprague-Dawley rats were initiated by a single gavage administration of 150 mg/kg DEN. Rats were fed a normovitamin A diet for 2 weeks followed by a low (2,000 IU) vitamin A diet for 10 days. Rats were then fed diets either low (2,000 IU) or high (100,000 IU) in vitamin A. Two weeks after this dietary regimen, rats were given either corn oil (vehicle) or a PCB promotor. The PCBs were administered individually (300 µM/kg) or in combination (150 µM/kg each) bimonthly for 2 months. At necropsy, small cubes of liver were immersion fixed in 2% paraformaldehyde and 2.5% glutaraldehyde in 0.1 M phosphate buffer. Tissues were post-fixed in 1% OsO₄, dehydrated through a graded series of alcohols, and embedded in Epon epoxy resin. Centriobular and periportal areas were localized from one-micron thick sections, subsequently thin sectioned, and doubly stained in uranyl acetate and lead citrate.

No consistent morphologic change occurred in vehicle-treated rats on a low or high vitamin A diet (Fig 1). DEN predominantly affected fat-storing cells. Rats receiving PCBs, either individually or in combination, had ultrastructural lesions, regardless of DEN treatment status. The hepatocyte and associated biliary apparatus were the primary targets of PCB-induced injury. Hypertrophy and vesiculation of smooth endoplasmic reticulum, dilation of the rough endoplasmic reticulum and nuclear envelope, swelling of mitochondria, lipid droplet accumulation, peripheral margination of chromatin, and eccentric nucleoli were the major changes in hepatocytes (Figs 2-3). PCB-induced changes in the bile canaliculi included dilation and loss of microvilli (Fig 4). The order of severity of hepatic injury in PCB-treated rats on a low vitamin A diet was DEN/TCB = DEN/TCB + HCB > No DEN/TCB = No DEN/TCB + HCB >>> DEN/HCB = No DEN/HCB = DEN alone > corn oil.

Animals on either a high or low vitamin A diet had a similar spectrum of liver morphologic changes. However, animals receiving a high vitamin A diet had a reduction in the severity of PCB- or DEN-induced liver injury. The results of this study indicate that high doses of vitamin A provide prophylactic effects against DEN- or PCB-induced liver ultrastructural injury in a classic two-stage hepatocarcinogenesis experimental model.

References

1. M. Wassermann, et al., Ann NY Acad Sci. (1979) 320, 69.
2. A. Buchmann, Cancer Letters. (1986) 32, 243.
3. M. Sporn, Fed. Proc. (1976) 35, 1332.
4. R. Lotan, Biochim. Biophys. Acta. (1980) 605, 33.

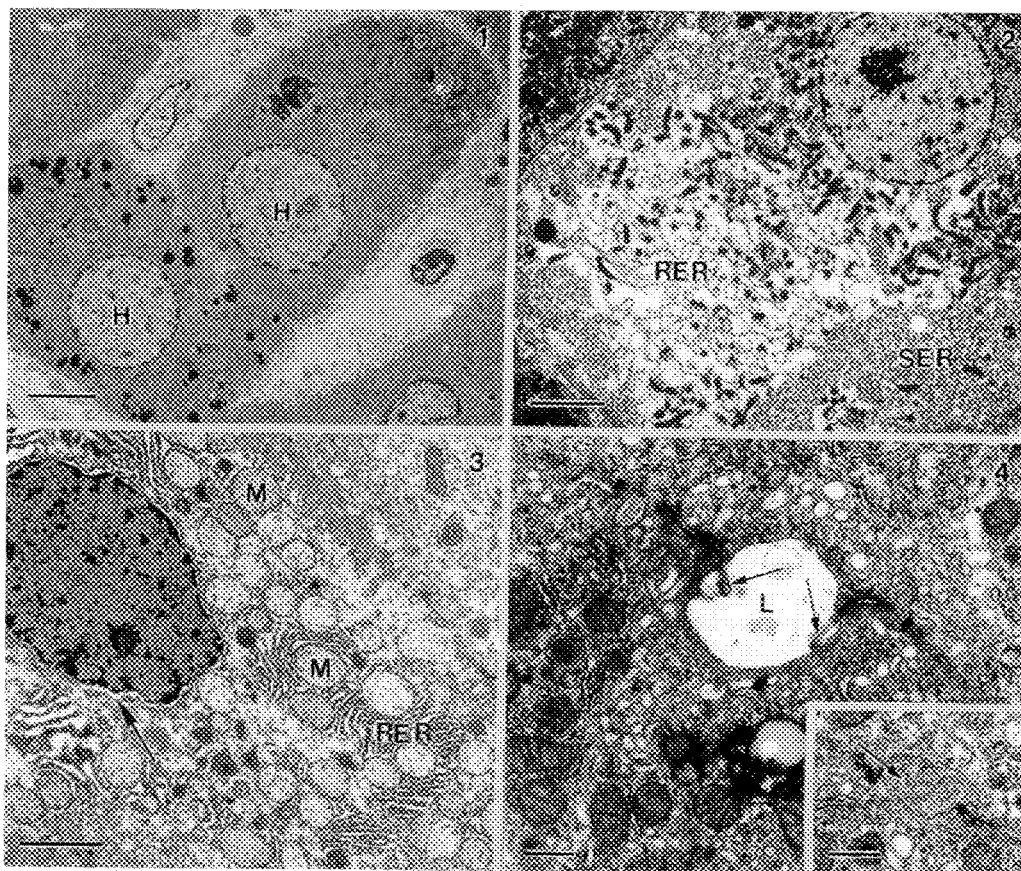


FIG. 1. Transmission electron micrograph (TEM) of the centrilobular region of the liver from a control animal. There are no consistent morphological changes. The hepatocytes (H) contain numerous mitochondria, modest profiles of rough endoplasmic reticulum and sparse profiles of smooth endoplasmic reticulum. Bar=5 μ .

FIG. 2. TEM of the liver of a rat on a low vitamin A diet and given DEN followed by TCB + HCB. The hepatocyte contains severe disorganization and dispersion of the rough endoplasmic reticulum (RER) accompanied by proliferation of the smooth endoplasmic reticulum (SER). Bar=5 μ .

FIG. 3. TEM of the liver of a rat on a low vitamin A diet and given DEN followed by TCB. There is dilation of the rough endoplasmic reticulum (RER) and nuclear envelope (arrow), and high volumetric swelling of mitochondria (M). Bar=2.5 μ .

FIG. 4. TEM of the liver of a rat on a low vitamin A diet and given DEN followed by TCB. The lumen (L) of the bile canaliculus is dilated and decreased numbers of microvilli (arrow) project into the lumen. Bar=0.5 μ . Inset: TEM of the liver of a rat on a high vitamin A diet. Note numerous microvilli (arrow) and smaller lumen diameter as compared with those of the low vitamin A rat. Bar=1 μ .

ULTRASTRUCTURAL EVALUATION OF METASTATIC TUMOURS IN BODY FLUID AND FINE NEEDLE ASPIRATION BIOPSIES

Marika Winnett

Department of Pathology, Women's College Hospital, Toronto,
Canada

Metastatic tumours present a diagnostic problem especially when the primary site is unknown. In many cases it is not possible to determine the primary site by light microscopic examination of the cytology material (1,2). Ultrastructural evaluation can demonstrate special cell characteristic features which may help in providing an accurate and specific diagnosis of these tumours.

A study was undertaken to evaluate the diagnostic usefulness of electron microscopy (EM), on a series of body cavity effusion and fine needle aspiration (FNA) specimens. A modified Kellenberger agarization method was used to process the centrifuged pellett specimens, followed by routine EM preparation (3). The study includes 82 malignant fluid and 53 FNA specimens. The ultrastructural morphology was evaluated to establish specific features that would characterize various tumour types which include adenocarcinomas, mesotheliomas, melanomas and lymphomas (4,5,6). In cases of adenocarcinoma specific ultrastructural features of different primary sites were recorded as shown in Figures 1-5. A conclusive diagnosis was obtained by electron microscopic examination in 91% of cases with malignant fluid effusion and 69% of the fine needle aspiration specimens. In contrast specific diagnosis was given by cytological examination in 36% of cases with fluid effusion and 39% of the FNA specimens.

Based on these findings the conclusion was made that electron microscopy has a very important place in the diagnosis of effusion and fine needle aspiration specimens and should be increasingly utilized on a selective basis for evaluation. We believe that EM is the best suited for recognizing cell types and histological patterns of growth in tumours. It seems that electron microscopy, if used appropriately, has a key role in the differential diagnosis of metastatic adeno carcinomas of unknown origin. Our experience indicates that it should be relied upon with greater frequency, enabling a more accurate diagnostic procedure.

References

1. Gondos B, Acta Cyto. 1978
2. Wuerker RB, Acta Cyto. 1983
3. Kellenberger E, J. Ultrastr. 1972
4. Hanna W, Acta Cyto. 1985
5. Mackay B, Ultrastr. Path. 1987
6. Herrera GA, Diag. Cytopath. 1985

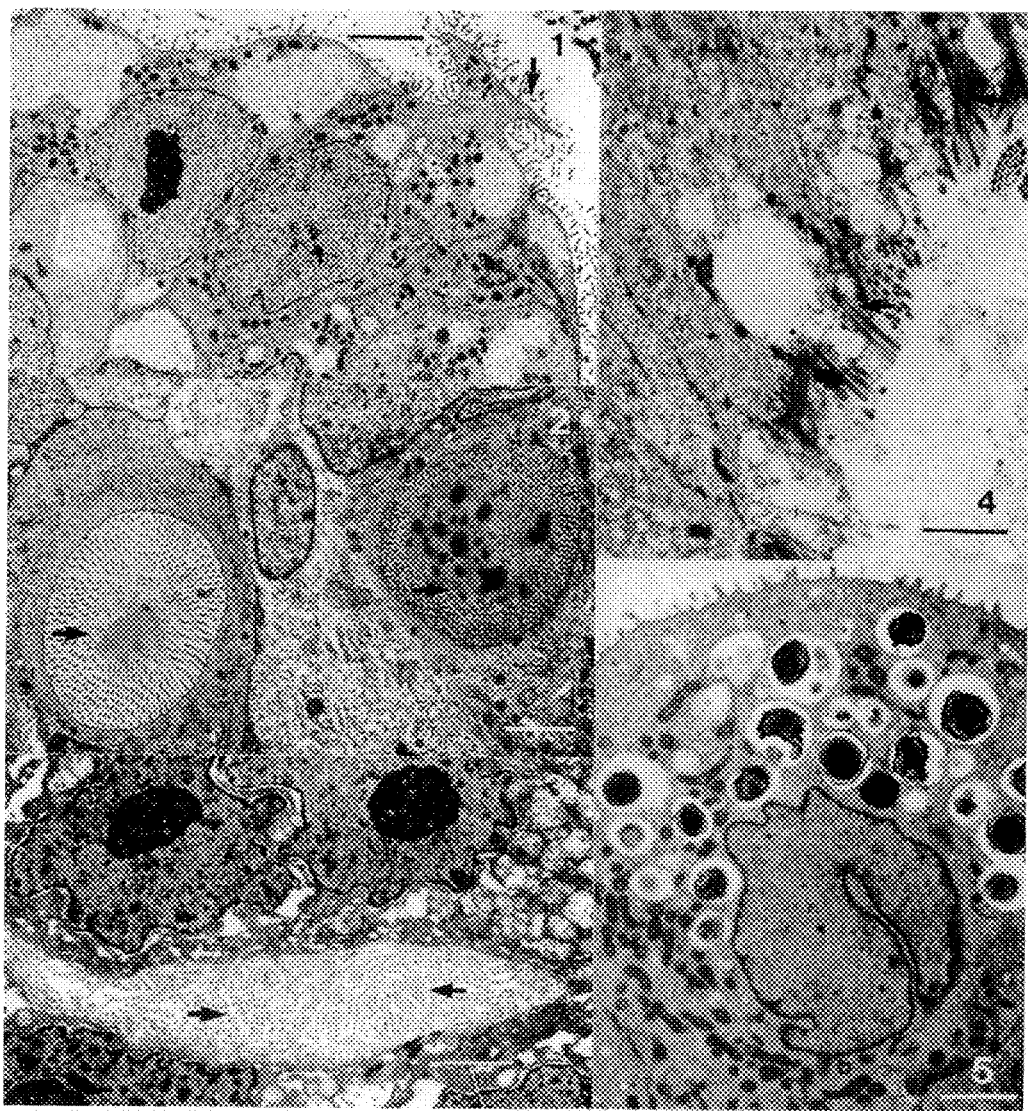


Fig.1 Metastatic ovarian adenocarcinoma of peritoneal fluid. Note the staghorn microvilli (arrows). Bar= 2 micron

Fig.2 Metastatic breast adenocarcinoma of pleural effusion showing multiple intra-cytoplasmic lumina (arrows). Bar= 2 micron

Fig.3 Metastatic mesothelioma of pleura fluid presents the characteristic bushy microvilli (arrows). Bar= 2 micron

Fig.4 Metastatic adenocarcinoma of the gastro-intestinal tract in liver aspiration. Note the rootlets (arrows). Bar= 2 micron

Fig.5 Metastatic bronchio alveolar carcinoma of pleura fluid with the characteristic inclusions. Bar= 2 micron

SILICONE GEL IN BIOLOGICAL SYSTEMS

William B. Greene¹, Lyle G. Walsh¹, Richard M. Silver², Joann Allen² and John C. Maize³

Departments of Pathology¹, Medicine² and Dermatology³, Medical University of South Carolina, Charleston, SC

Electron probe microanalysis of biopsies from two patients who had received silicone gel breast implants has revealed silicon (Si) in macrophages in an arthritic finger joint synovium (Fig. 1) and in a sclerodermatous skin lesion as well as in the fibrous capsule surrounding the implants in both patients (Fig. 2). The silastic envelope has been reported to be semipermeable with substances passing freely into and out of the implant.¹ The polymer usually contains silica filler with a particle size of 30µm to impart added firmness,² however, these sharp pointed crystals have not been fully characterized by Electron Microscopy. Silicone has been thought to be relatively inert, eliciting little or no tissue reaction. The substance has been injected or surgically placed into the human body as liquid, joints or in the form of breast augmentation prostheses. Recent reports have indicated that there is more than sufficient reason to change our thinking regarding this chemical and it's significance in biological reactions. There are 100,000 patients who undergo breast augmentation each year in the United States alone with over one million reported silicone implants. One clinical group reported that 4.4% of all new scleroderma patients had silicone breast implants.³ The patients reported in the study had implants from 2 to 21 years duration. The latency period may mean that scleroderma will increase parallel to the increase in breast augmentation over the last decade.

A common local reaction to implanted, silicone gel filled breast prostheses is the formation of a connective tissue capsule that surrounds the implant. Macrophages are attracted to the silastic envelope and are destroyed by the silicone, resulting in the elaboration of cytokine which stimulates the proliferation of fibroblasts. In some cases a collagen capsule is formed which may become hard and contract.^{4,5} The contraction has been suggested to be a cause for leakage of silicone from the containing envelope into the surrounding tissue.⁶

It is uncertain whether macrophage influx arises as a direct foreign body response to the implanted silastic (silicone polymer) envelope or as a response to silicone gel leaving the confines of the envelope. Silica has been shown to be selectively lethal to macrophages in cell culture.⁷ It is thought that the repeated killing of macrophages *in vivo* results in the mobilization of fibroblasts and the ensuing fibrogenesis that is characteristic of silicosis. Silicone particles are thought to be toxic because they are efficiently taken up by macrophages, internalized by phagosomes which then fuse with primary lysosomes. The secondary lysosomes formed by this union soon dissolve or become disrupted in some fashion and the silicone, along with the still potent lytic enzymes, escape into the cytoplasm where the enzymes destroy the macrophage. The resulting cellular debris contains silicone that may or may not have been altered by a passage through the previous macrophage. It is concluded from these observations that the silicone found in macrophages in the above remote tissues originated from the gel silicone polymer contained within the breast implants or from the surface of the silastic container bag.

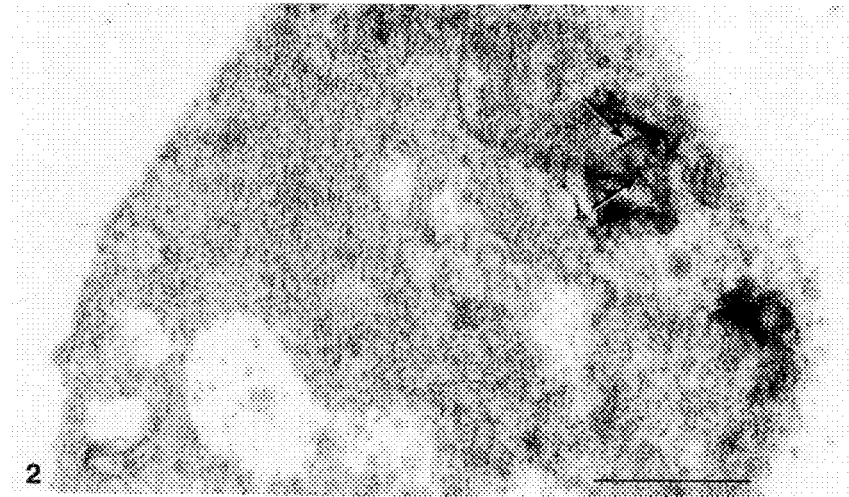
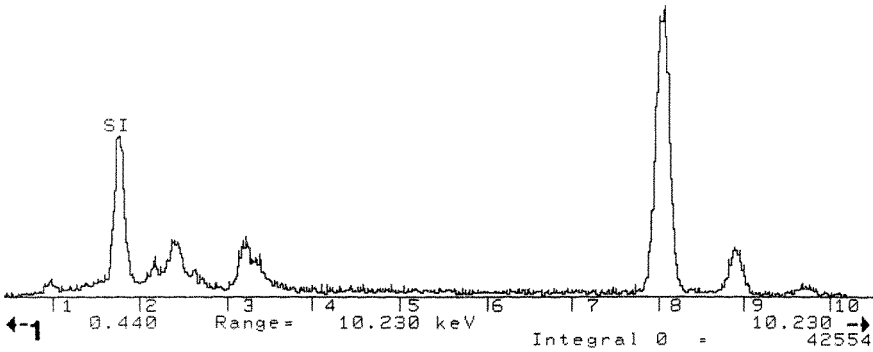


FIG. 1--EPMA of the finger joint synovium showing a moderate silica (Si) peak.
 FIG. 2--A cytoplasmic fragment of a macrophage showing dense spicule structures (arrows) within a proteinaceous matrix. Electron probe microanalysis (EPMA) confirmed that the densities were silica. Finger lesion from a paraffin block processed for TEM. X 82,500.

References

1. Fock K, Feng P, Tey B. *J Rheumatol* (1984)11,98.
2. Ben-Hur N, Neuman Z. *Plast Reconstr Surg* (1967)39,423.
3. Spiera H. *JAMA* (1988)260,236.
4. Gayou R, Rudolph R. *Ann Plast Surg* (1979)2,62.
5. Lugano EM et al. *Am Rev Respir Dis* (1984)129,767.
6. Dauber JH et al. *Am J Path* (1980)101,595.
7. Kagan E, Miller K. in HB Hersowitz ed. *Manual of Macrophage Methodology*, New York, Marcel Dekker (1981)137.

CISPLATIN-INDUCED CHANGES IN THE ADRENAL OF THE RAT

Casey M. Miller and Surinder K. Aggarwal

Department of Zoology, Michigan State University, East Lansing, MI 48824-1115

Cisplatin (CDDP) is one of the most valuable antineoplastic drugs available for the treatment of testicular, ovarian, lung, head and neck cancers¹. However, the drug has severe toxic side effects of which nephrotoxicity and gastrointestinal toxicity are the major dose limiting factors^{2,3}. CDDP causes hypocalcemia and hypomagnesemia. Hypocalcemia has been demonstrated to effect the parathyroid gland and the neurohypophysis secretions, which in turn control the stomach smooth muscle contractility and the kidney function. In rats it induces stomach bloating and ulceration. Injections (i.v) of calcium have been demonstrated to prevent stomach bloating, ulceration and preserve normal kidney function⁴. Present is an effort to study the effect of CDDP on adrenal gland as another endocrine gland.

Male swiss wistar rats [Cr1: (WI)BR] weighing 250 g were injected (i.p) with CDDP (7 mg/kg) in normal saline. Controls received saline injections only. Daily food and water intake and urine output were monitored by restricting the animals to metabolic cages. Animals were killed by decapitation on day 3 and day 5. Adrenal glands were removed and transferred to the fixative (2% glutaraldehyde in 0.05 M phosphate buffer at pH 7.4) for 2 h. Tissues were processed in routine manner for light and electron microscopy.

Cisplatin treatment causes significant telangiectasia both in the cortex and the medulla (Figs. 1A,B). There is a sharp decrease in the lipid contents of the zona fasciculata and zona reticularis with little change in the zona glomerulosa (Figs. 2A,B). CDDP causes coalescence of the fat droplets, swelling of the mitochondria and the outer nuclear membrane in the two layers of the cortex (Figs. 3A,B). Medullary region is usually atrophied with swollen epinephrine and norepinephrine granules (Figs. 4A,B). Biochemical quantitations are underway to determine the levels of catecholamines in the blood and urine using HPLC technique before and after CDDP treatment.

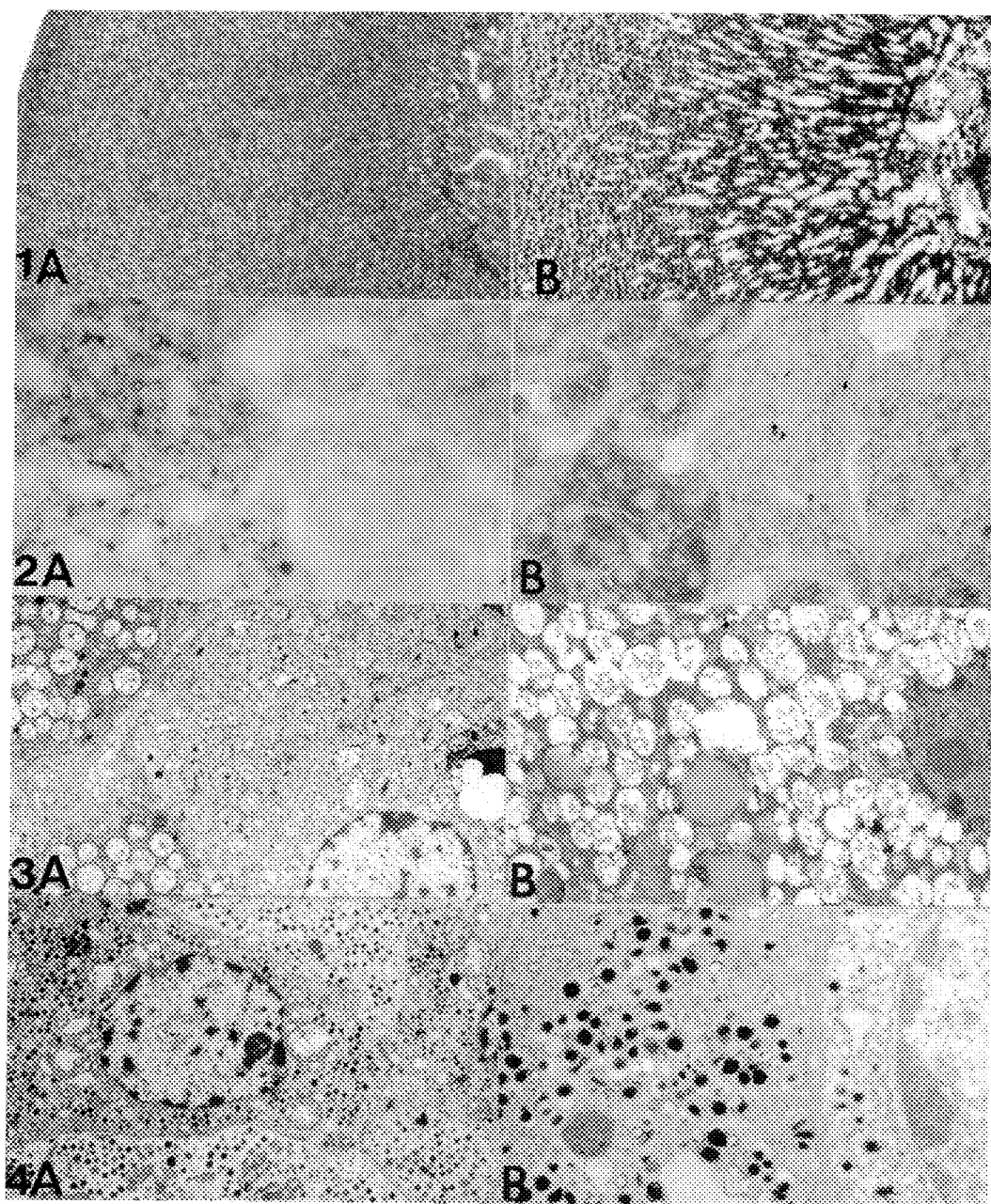
¹. Doll D, et al., 1991. Cancer Chemother Pharmacol 29: 71-74.

². Sartori S, Nielsen I, Maestri A, Beltrami D, Trevisani L, Pazzi P. 1991. Oncology 48: 356-361.

³. Jones MM, Basinger MA, Holscher, MA. 1991. Toxicology, 68:227-47.

⁴. Aggarwal SK and Fadool JM. 1987. Proc. Fifth Intl. Symp. Platinum metal Coordinat. Comp. Cancer Chemther pp 235-247, Martinus Nijhoff Pub. Boston, Mass.

Supported by Funds from the Office for Research Development, Michigan State University, East Lansing, Michigan.



Figs. 1A, Normal adrenal; B, CDDP-treated adrenal; 2A, Normal adrenal after Sudan staining; 2B, CDDP-treated Sudan stained; 3A, E.M. normal adrenal; 3B, CDDP treated adrenal; 4A, Normal medulla; 4B, CDDP treated medulla.

PIROXIMONE (MDL 19,205)-INDUCED ULTRASTRUCTURAL AND BIOCHEMICAL CHANGES IN EARLY ADRENAL MEDULLARY PROLIFERATIVE DISEASE IN RATS

J. Sprinkle-Cavallo, F.Y. Thompson, D.E. Loudy, M.W. Dudley, A.M. Ogden, and J.P. Gibson

Marion Merrell Dow Inc, 2110 Galbraith Rd, Cincinnati, Ohio, 45215

Piroximone is a cardiotonic agent (phosphodiesterase inhibitor) proposed for the treatment of congestive heart failure. The drug causes adrenal medullary proliferative disease (AMPD) in rats after 1 year or more of treatment. In this study we investigated the effects on adrenal chromaffin cells prior to the development of obvious hyperplasia. Male rats were administered 0, 300, or 600 mg/kg/day of piroximone in the diet for three months.

For morphometry studies, adrenals from 5 rats/group were fixed in 10% formalin and stained with hematoxylin and eosin (H&E). For differentiation of chromaffin cell types, left adrenals from 5 rats/group were fixed in 2% glutaraldehyde and 4% EM grade formaldehyde and stained with Gomori's methanamine silver and also (after pretreatment with 2.5% potassium dichromate in 1% sodium sulfate) with H&E as well as toluidine blue.¹ For electron microscopy studies, adrenal medulla from 5 rats/group was fixed in 5% glutaraldehyde with post-fixation in 4% paraformaldehyde.

The volume (mm^3) of adrenal medulla as estimated morphometrically² after 600 mg/kg/day (0.84 ± 0.05) did not differ significantly from that of control rats (0.94 ± 0.07). In addition, there was no evidence of diffuse hypertrophy or hyperplasia of adrenal medulla cells by H&E staining. Piroximone did, however, induce early AMPD changes in the form of multifocal hyperplasia of dark, basophilic chromaffin cells that were only discernible by light microscopy if the special fixative and histochemical procedures were used. Ultrastructurally these dark cells had dense cytoplasm and granules of either the norepinephrine (Fig. 1) or epinephrine (Fig. 2) type.

Typical norepinephrine- and epinephrine-producing cells were differentiated by both light and electron microscopy. By light microscopy, the number of epinephrine-producing cells was greater than that of norepinephrine-producing cells in both control and piroximone-treated rats. Ultrastructurally, in control rats, the norepinephrine-producing cells contained only norepinephrine-containing granules, while the epinephrine-producing cells contained both norepinephrine- and epinephrine-containing granules. Piroximone (300 and 600 mg/kg/day) decreased the number of norepinephrine-containing granules (Fig. 3) and, to a lesser extent, both the number and density of epinephrine-containing granules (Fig. 4). No differences were noted, however, in the number or size of small granule cells or in their granules by electron microscopy.

Piroximone decreased urinary excretion ($\mu\text{g}/24 \text{ hr}$) of norepinephrine (control: 2.15 ± 0.16 ; 600 mg/kg/day: 1.39 ± 0.20) and dopamine (control: 4.58 ± 0.36 ; 600 mg/kg/day: 2.54 ± 0.39). However, an increase in the urinary excretion (mg/24 hr) of calcium was observed (control: 15.2 ± 2.0 ; 600 mg/kg/day: 49.5 ± 13.3). Increased food consumption, observed in both piroximone-treated groups, has been associated with both increased urinary calcium levels and with AMPD in rats treated with sugar alcohols.³

These results indicate that the early AMPD observed in rats after piroximone treatment is associated with a decrease in catecholamine storage and secretion. Reduced catecholamine function may induce compensatory adrenal medullary proliferation leading to AMPD.

References

1. L.H. Honore, J. Histochem. and Cytochem. (1971)19, 483.
2. U.A. Boelsterli et al., Arch. Toxicol. (1984)56, 113.
3. A. Baer, J. Amer. College Toxicol. (1988)7, 71.

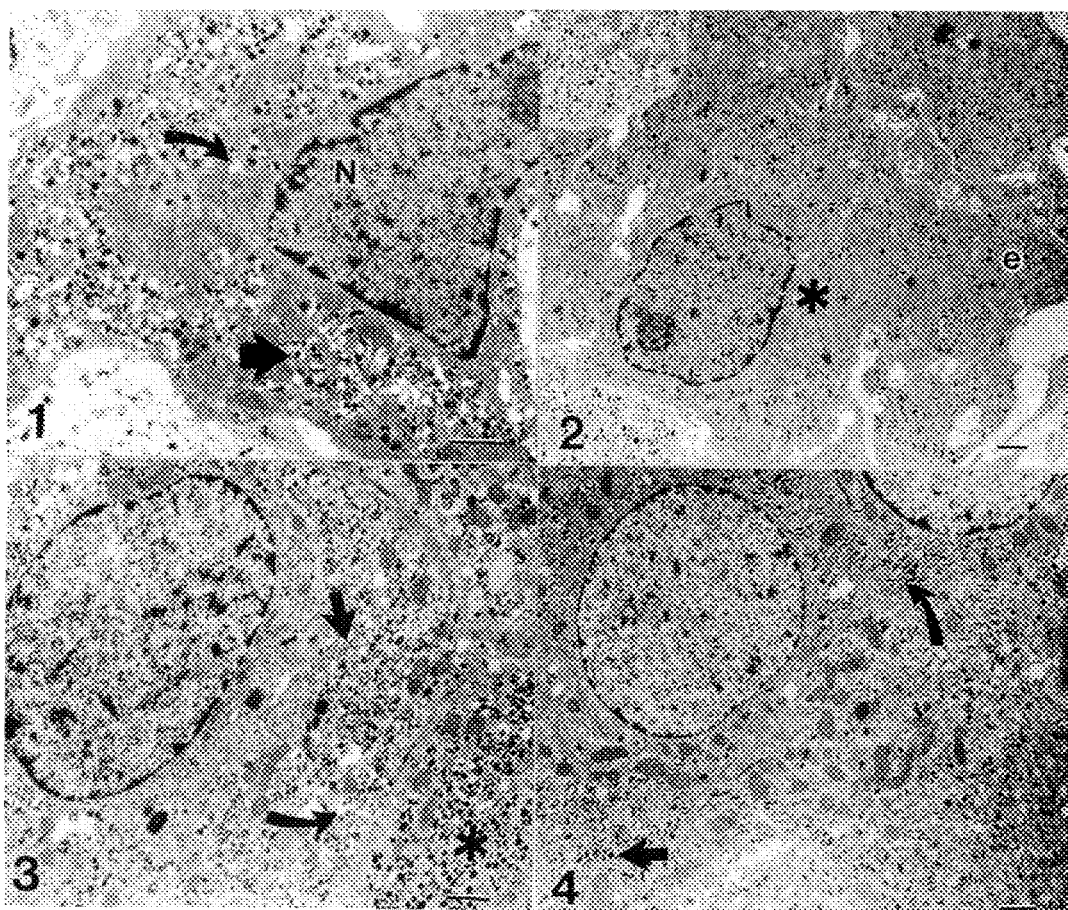


FIG. 1.--Dark norepinephrine cell from piroximone-treated (300 mg/kg/day) male rat appears polyhedral and shrunken with uneven nuclear (N) outline. Majority of norepinephrine granules have dense cores within clear vesicles (arrowhead). Note numerous empty vesicles (curved arrow). Bar = 1 μ m.

FIG. 2.--Cluster of dark, polyhedral epinephrine cells from piroximone-treated (300 mg/kg/day) male rat. Epinephrine granules are sparse near nucleus (*) but are more numerous at periphery (e). Very few norepinephrine granules present. Bar = 1 μ m.

FIG. 3.--Most norepinephrine granules in this norepinephrine cell from piroximone-treated (600 mg/kg/day) male rat have electron lucent core (arrow) or appear as partially empty vesicles (curved arrow). Adjoining cell contains more normal-appearing norepinephrine granules with dense cores (*). Bar = 1 μ m.

FIG. 4.--Epinephrine cells with decreased number of oval to elongated epinephrine granules (curved arrow) of low electron density. Very few norepinephrine granules (straight arrow) with dense cores are apparent. Bar = 1 μ m.

SUBSTRATUM MODIFICATION BY ENDOTHELIAL CELLS (EC) IN CULTURE

J.C. Lewis, I. Hermanns,* K.W. Grant, S. Evans, C. Gossen,* A. Dekker*, C.J. Kirkpatrick*

Department of Pathology, Bowman Gray School of Medicine, Winston-Salem, NC 27157; and

*Department of Pathology, Technical University of Aachen, D-5100 Aachen, Germany

Thrombosis resulting from blood interaction with prostheses is a concern following vascular grafting, and efforts have been made to endothelialize grafting materials and thereby reduce thrombogenicity. These efforts have focused upon altering polymer surfaces to enhance endothelial compatibility following surgery; however, using homologous EC attempts are being made to pre-seed grafting materials having defined surface characteristics. Such surfaces might be pre-absorbed with natural polymers as collagens, fibrin(ogen) or fibronectin. Irrespective of the starting character, these surfaces are rapidly altered following contact with tissues and body fluids, and as an extension by the EC themselves. To address this latter question, human umbilical vein endothelial cells (HUVEC) were seeded for whole-mount microscopy onto carbon-stabilized, formvar-coated surfaces to which either collagen Type IV or its CB3 fragment had been adsorbed.¹ Following culture for 3 or 24 hrs the cells were fixed *in situ* with glutaraldehyde, washed and processed for two-stage multiantigen immunogold microscopy.² The first stage was comprised of rabbit anti-human fibronectin and mouse antihuman collagen Type IV. These were followed by second stage probes including goat anti-rabbit IgG (5nM gold), goat anti-mouse IgG (15 nM gold) and goat anti-human IgG (10 nM gold) as a control. HUVEC readily attached to and spread upon collagen IV and the CB3 fragment; the degree of spreading was much more pronounced with CB3 at both 3 and 24 hrs. The primary difference between the culture times was in cell density, with more cells at 24 than 3 hrs (Fig. 1). This difference could be explained by the additional generation time. The interaction of cells with the substratum was complex. This included deposition of proteins on the surface and extension of delicate macromolecular bridges from the cell periphery. Through the use of immunogold microscopy, fibronectin, collagen and immunoglobulin could be detected in all samples, including those plated in the absence of serum. Initially, collagen (IV and CB3) was more dense on the substrate than on the cells, and this was consistent with surface coating prior to cell seeding (Fig. 3). Fibronectin and IgG, on the other hand, were derived either from the medium or secreted from the cells, and each was associated with the cells or the cell edge (Fig. 4,5). Notably, detection of all three peptides was reduced over time, and this may be interpreted as secondary conditioning of the surface by HUVEC secreted products.

¹Kirkpatrick et al. (1990) *Virch Arch B Cell Pathol* 58:207-213.

²Lewis J.C. et al. (1990) *Am J Pathol* 136:239-252.

FIG. 1.--Ultrastructural comparison of 3 hr (a) and 24 hr (b,c) cells. In all cases, the cells had a prominent nucleus (N) and an extensive hyalomere with mitochondrial networks (M), a cytoskeleton rich in microtubules (mt), actin stress fibers (sf) and lysosomes (L) in the perinuclear region. Weibel-Palade bodies (WP) and endocytic vesicles (V) characteristic to endothelial cells were commonly observed.

FIG. 2.--Immunogold cytochemistry showing the localization of fibronectin (fn, 5 nM) gold) collagen (col, 15 nM gold) and IgG (Ig, 10 nM gold) at the cell periphery (b) and on the unoccupied regions of the support film (c). The data in Figures 3-5 were obtained from three regions as indicated on 2a. Separate data were obtained for the formvar substrate (s), the cell edge characterized by microvilli (MV) and endocytic vesicles (EV), and the cellular cytoplasm (Cp). Note in 2b, the delicate network (arrowhead) which extends from the cell margin to the substrate. These "attachment plaques" are enriched in fibronectin as evidenced by the distribution of 5 nM gold.

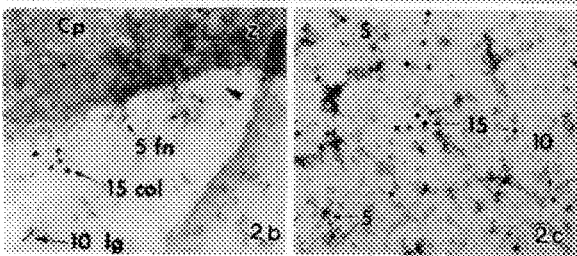
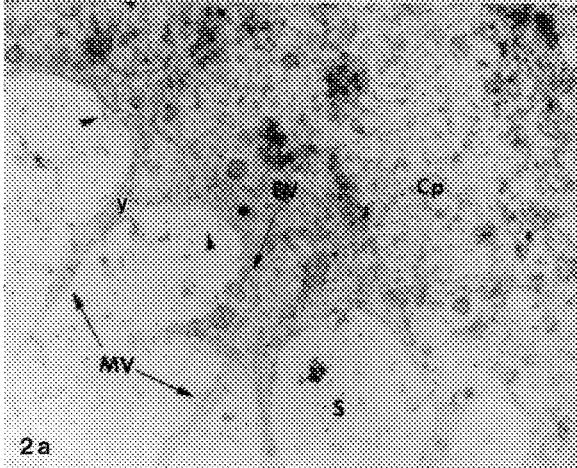
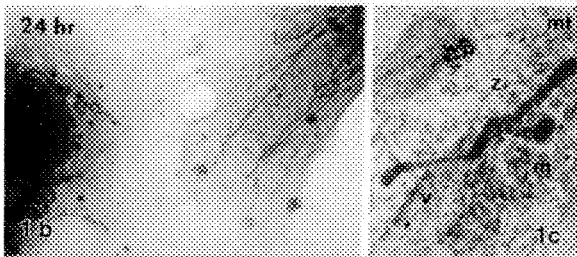
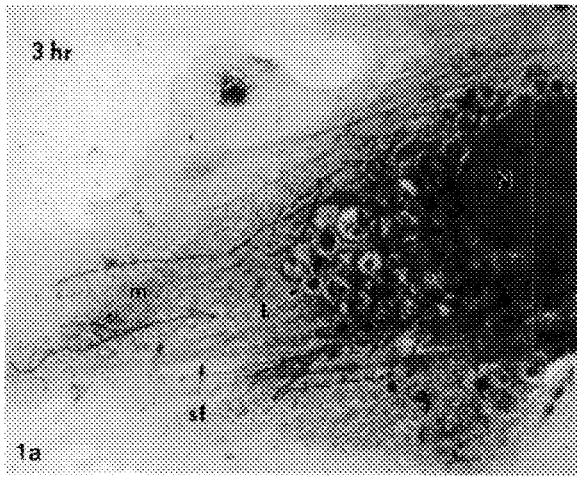


Figure 3

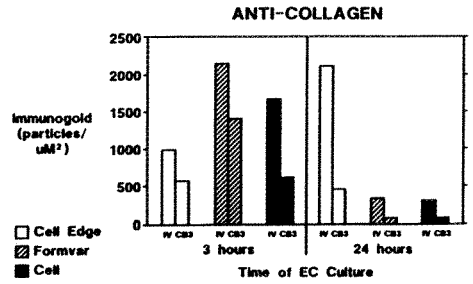


Figure 4

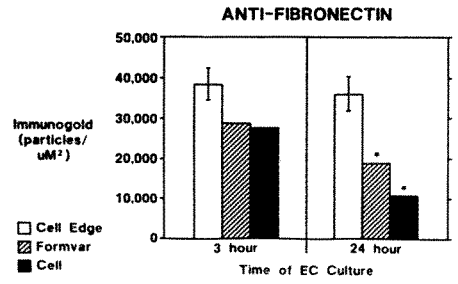
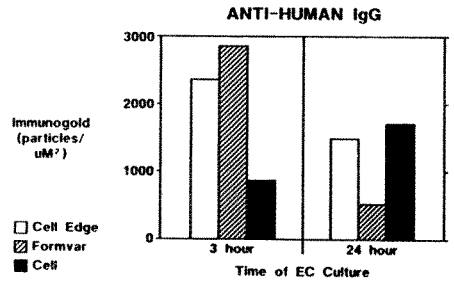


Figure 5



ANIMAL MODELS OF TRAUMATIC CRUSH INJURY TO SKELETAL MUSCLE

R. Coleman, I. Rubinstein, H. Ben-Ari, N. Ronen, M. Silbermann & O. S. Better

The Bruce Rappaport Faculty of Medicine and Rappaport Family Institute,
Technion - Israel Institute of Technology, P.O.Box 9649, Haifa 31096, Israel

One of the more serious conditions developing in humans buried or trapped under collapsed buildings is the development of Crush Syndrome, which frequently results in death (1,2). One of the effects of traumatic pressure damage to skeletal muscle is the development of myopathy and rhabdomyolysis resulting in severe life-threatening physiological disturbances. The aim of the present research was to develop animal models of traumatic pressure damage to limb muscles that mimic the effects of crush injury in humans, with the ultimate aim of improving strategies for the management of Crush Syndrome.

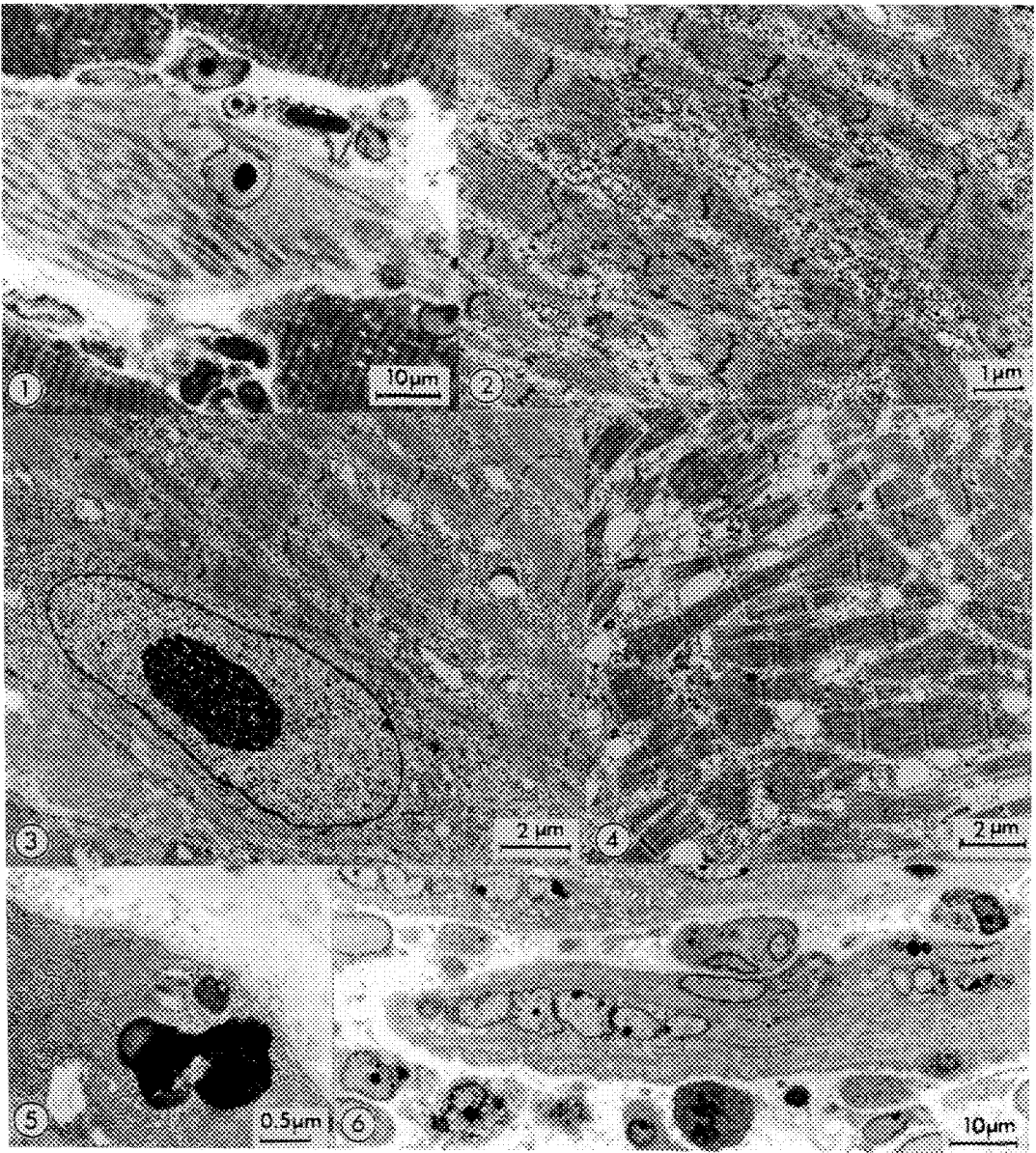
In this research a comparison was made between the effects of internal (compartmental) pressure induced in the anterior tibialis muscle of the hindlimbs of dogs and external local pressure in the same muscle in rats. In the dog model injection of autologous plasma to the anterior tibialis compartment causes a rise in internal pressure to 140 mm Hg vs 0+4 mm Hg in controls. This internal pressure was maintained for 4 hours and the muscle examined by histology and TEM after 7 days. In the rat model, Sprague-Dawley rats had their hindlimbs subjected to local external pressure (4.25 atmospheres) for 2 hours using a novel apparatus. The anterior tibialis was examined 4 days after the injury.

Results show that both internal and external pressure injuries lead to similar histological and ultrastructural responses. Myopathic damage includes swelling of myocytes, centralization of nuclei with enlarged nucleoli, disruption of sarcomeres and loss of myofilaments. The myocytes show many lipid inclusions and enlarged lysosome-like bodies, especially in peripheral regions. Many of the myocytes appear to be in the early stages of regeneration developing into myotube-like structures. The adjacent connective tissue contains large numbers of activated satellite cells and lipid-rich macrophages.

We are currently investigating the effects of post-injury treatment with hyperbaric oxygen or infusions of 20% mannitol to see if the processes of structural and functional repair in the muscle are improved.

References

1. O.S. Better et al., Mineral Electro. Metab. (1991) 16, 181.
2. E.G.L. Bywaters, Brit. Med. J. (1990) 301, 1412.
3. This research was supported in part by grants from the Israel Ministry of Defence (Technion 185-108), the Israel Ministry of Health and Technion VPR Fund (184-197).



Figs.1-6 Crush injury in anterior tibialis muscle of dogs (1,2,3,5) and rats (4,6)
 FIG 1. LM - Myocyte with myofibrillar damage. Note prominent nucleoli in nuclei of myocyte and in activated satellite cells.
 FIG 2. TEM - Myopathic changes in crush-damaged myocyte.
 FIG 3. TEM - Prominent nucleolus in nucleus of crush-damaged myocyte.
 FIG 4. TEM - Myopathic changes and disrupted sarcomeres.
 FIG 5. TEM - Large lysosome-like bodies are common near periphery of myocytes.
 FIG 6. LM - Myotube formation in regenerating myocytes. Note mitotic cell.

CORRELATIVE LIGHT AND TRANSMISSION ELECTRON MICROSCOPY OF TUBULAR AGGREGATES IN SKELETAL MUSCLE

Thomas G. Manfredi*, Wenjing Ding** and Roderick Bronson**

* The University of Rhode Island, Kingston, RI 02881

** USDA Human Nutrition Research Center on Aging at Tufts University, 711 Washington Street, Boston, MA 02111

Tubular aggregates (TAs) have been identified with a number of myopathies in humans. Periodic paralysis and muscle pain are frequently associated with TAs (1). Very little is known about the functional and anatomical significance of TAs in myopathic and aging human muscle. Recently, animal models for TAs have been identified which suggested that TAs are gender specific (2). However, recent studies suggest a need for more controls (3).

We examined the effects of diet and age on TAs in three strains of mice (DBA/2, B6D2F1, and B6C3F1). Approximately 300 fibers per animal were quantitatively examined using LM. Thin sections of the same fibers were examined with transmission electron microscopy. The tissue sections were fixed and dehydrated in ethanol using conventional procedures. Toluidine blue stain was applied to thick sections and TAs were identified as relatively homogenous dark blue masses (Fig.1). Skeletal muscle fibers from two age groups, 19 and 27 months old were examined for fiber and Z band damage, nucleated cell aggregations and TAs. Two main groups of mice were examined: ad libitum (AL) and 40% calorically restricted (RE).

LM examination showed no differences between groups in the occurrence of fiber and Z band damage or accumulation of nucleated cells. Seventy percent of muscle fibers in the AL fed mice had TAs and 18% of the fibers from RE mice showed evidence of TAs. EM examination of TAs (Fig. 2-4) showed no evidence of TA structural differences in young and old mice from both dietary groups. EM observation suggested that TAs show distinct orientations in myofibrils and may communicate with the sarcolemma. TAs were observed in two distinct regions, 1) close to the sarcolemma, 2) in the middle of the fiber. We believe that TAs are distinctive continuations of sarcoplasmic reticulum in skeletal muscle and that their appearance are diet and age related.

References

1. M.J. Danon, et al., Muscle & Nerve. (1989) 12, 265.
2. R.W. Kuncı, et al., Acta Neurophathol. (1989) 78, 615.
3. W.L. Rosenberg, et al., Arch. Neurol. (1985) 42.

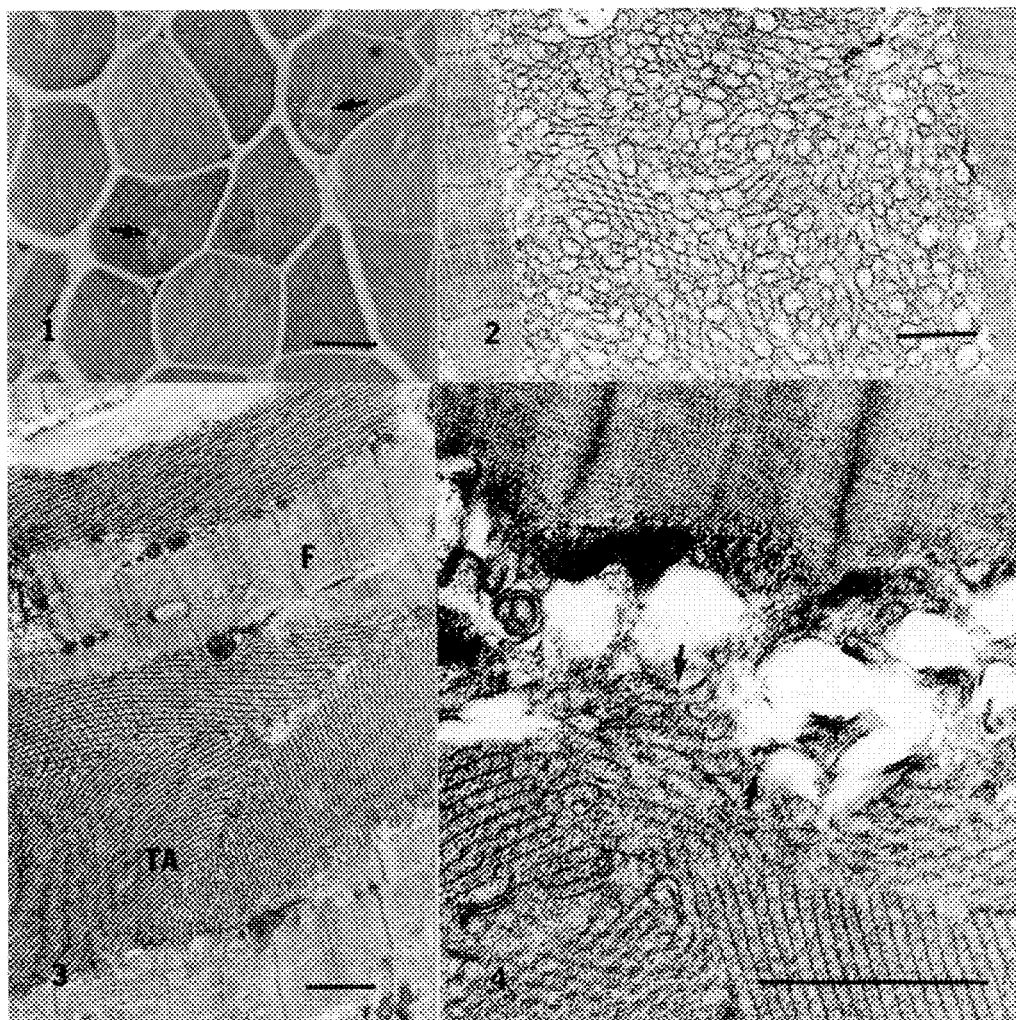


Fig. 1.-- LM of mouse skeletal muscle. Tubular aggregates (arrows) are identified. Bar=5um.

Fig. 2.-- TEM of mouse skeletal muscle. Fine structure of tubular aggregates. Bar=lum.

Fig. 3.-- TEM of mouse skeletal muscle. Tubular aggregates (TA) are located in the center and the edge of the fiber (F). Bar=lum.

Fig. 4.-- TEM of mouse skeletal muscle. There are communications between tubular aggregates and sarcoplasmic reticulum (arrows). Bar=lum.

EFFECTS OF RYANODINE AND CAFFEINE ON SUBCELLULAR ELEMENTAL DISTRIBUTIONS IN RELAXED AND TETANIZED RAT PAPILLARY MUSCLES

¹B.J. Hurley, ²M.E. Cantino and ¹D. E. Johnson

¹Center for Bioengineering, University of Washington, Seattle, WA 98195

²Dept. of Physiology and Neurobiology, University of Connecticut, Storrs, CT 06269

Regulation of intracellular free calcium is crucial to the process of contraction in cardiac muscle. Many inotropic agents are thought to exert their effects by way of changes in the levels of myoplasmic free Ca^{2+} . While the effects of caffeine and ryanodine on myocardial contractility share some similarities, their pharmacological properties appear to be quite different. Although both agents affect Ca sequestration by the sarcoplasmic reticulum, ryanodine appears to act specifically on the Ca release channels of the jSR¹, while caffeine may affect transsarcolemmal calcium transport and calcium sensitivity of the myofilaments as well.^{2,3} To date, several investigators have applied electron probe X-ray microanalysis (EPXMA) to study effects of one or the other of these agents on subcellular elemental distributions^{4,5}, however, none have compared them in the same system. We have used EPXMA to compare subcellular elemental concentrations in rat papillary muscle in the presence of caffeine and ryanodine, in relaxed and tetanized conditions.

Freeze-dried cryosections of right ventricular papillary muscles from adult male Sprague-Dawley rats were prepared and analyzed as described previously.⁶ In brief, papillary muscles were excised and mounted between a force transducer and a rotating post on a specially designed holder compatible with the cold metal block freezing device. Muscles were superfused with modified Tyrodes solution and stimulated at 0.2 Hz while recording the tension trace for at least 45 minutes prior to freezing to ensure viability. The length of the muscles were adjusted to produce maximal tension. Prior to freezing, the muscles were moved to a bath containing the extracellular marker NaCobaltic EDTA in a modified Tyrodes solution. In some cases the bath also contained either 10 mM caffeine or 10 μM ryanodine. Just prior to freezing, the sample holder was removed from the perfusion bath and attached to the freezing device plunger. The 0.2 Hz stimulation was terminated approximately 1 minute prior to freezing; no further stimulus was applied to relaxed muscles, whereas tetanized muscles were frozen after 4 seconds of stimulation at 10 Hz.

Freeze dried cryosections were analyzed at room temperature using a JEOL 1200EX STEM and a LINK AN10,000 analysis system. X-ray spectra were collected for 500 seconds live time in the STEM mode using a square raster approximately 50 nm on a side. Spectra were collected on mitochondria, A-band filament regions, and junctional SR (jSR) sites. The cobalt signal was used to help identify T-tubules, and by association, jSR. The cobalt signal was also used to correct for contamination of the jSR Ca signal by X-rays from the extracellular (T tubule) space.⁶ Corrections for extracellular calcium were similar in all experimental conditions, and amounted to about 25% of the total Ca counts in relaxed samples.

Addition of caffeine or ryanodine had little effect on concentrations of Mg, P, S, Cl or K, in either the relaxed or tetanized condition. Ca concentration was not detectably different in the mitochondrial and A band regions in any condition, but dropped significantly in the jSR with addition of caffeine or ryanodine, and remained low in tetanus. Sodium levels rose significantly with caffeine in all compartments measured, but showed little or no increase in the presence of ryanodine. These changes are illustrated in Figs. 1 and 2. Thus, while both caffeine and ryanodine at the applied concentrations produce reduction of jSR calcium, they have different effects on cytosolic Na levels.

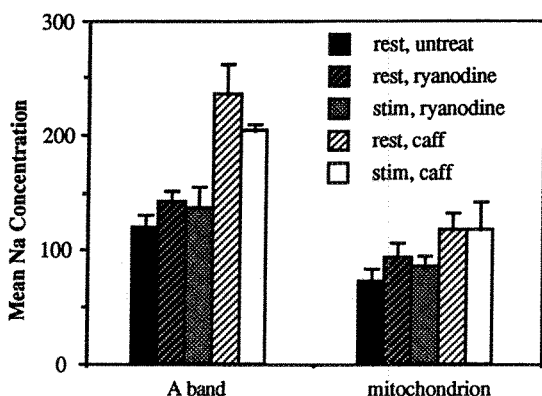


Fig. 1: Mean Na concentration, in mmols/kg dry wt. Error bars are standard errors of the mean. N = 3, 5, 2, 4, and 2 papillary muscles respectively for resting untreated, resting ryanodine, stimulated ryanodine, resting caffeine and stimulated caffeine treatments.

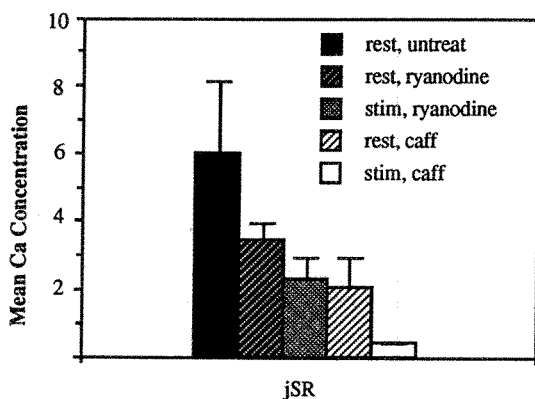


Fig. 2: Mean Ca concentration, in mmols/kg dry wt. Error bars are standard errors of the mean. N = 3, 3, 2, 3, and 1 papillary muscles respectively for resting untreated, resting ryanodine, stimulated ryanodine, resting caffeine and stimulated caffeine treatments.⁷

1. S. Fleischer et al. Proc Natl. Acad. Sci. (1985).82:7256.
2. J. R. Blinks et al. Circ. Res. (1972) 30:367.
3. G. B. McClelland and S. Winegrad. J. Gen. Physiol. (1980) 25:283.
4. M. F. Wendt-Gallitelli et al. Basic Res. Cardiol. (1980) 75: 66.
5. C. S. Moravec and M. Bond (1991) Am. J. Physiol. 260:H989-H997.
6. B. H. Hurley and M. E. Cantino Proc. XIIth Int. Cong. Elect. Microsc. (1990) San Francisco Press, San Francisco, p170.
7. This work was supported by NIH # K04 HL 02142 and an NIH predoctoral fellowship to BH. We are grateful for the expert technical assistance of Shellee Cunningham, Su Wan Chen and Linda Wilkinson.

EFFECTS OF AZITHROMYCIN IN TAPETAL AND ATAPETAL DOGS

A.B. Jakowski, J.H. Fortner, W.B. Milisen, P.M. Marsh, J.M. Carver and G.R. Lundeen

Drug Safety Evaluation, Pfizer Inc, Groton, Connecticut 06340

The tapetum lucidum is a reflective layer that lies beneath part of the retina in the eyes of many animals. It is believed to enhance night vision by reflecting light onto the sensory cells of the retina. Primates, including humans, do not have a tapetum. Routine safety studies have revealed that treatment of Beagle dogs with high doses of azithromycin, a novel macrolide antibiotic, causes changes in the color and reflectivity of the tapetal fundus. In order to determine whether the change is due to a direct effect on the tapetum as opposed to a change in transparency of the retina, a study was conducted that compared the effects of azithromycin treatment in normal versus congenitally atapetal dogs.

Animals were either treated with 100 mg/kg of azithromycin (treated) or methylcellulose vehicle only (control) for 35-36 days. This gave a total exposure of approximately 70X the recommended total human exposure. Ophthalmoscopic examinations revealed the typical color change and loss of reflectivity in the fundus of normal dogs, but no change was seen in atapetal animals.¹ Light and electron microscopic examination of the eyes of normal untreated animals showed the tapetum to be composed of closely packed, rectangular cells filled with parallel arrays of rodlets. Control atapetal dogs had rudimentary tapetal cells containing variably sized vacuoles and no rodlets. In treated, normal animals, the tapetal cells were markedly swollen and filled with vacuoles containing electron dense debris. In addition, the tapetum-choroid junction was not sharply defined, and swollen, vacuolated cells, both pigmented and nonpigmented, were seen scattered deep in the choroid. Rudimentary tapetal cells in the atapetal dogs showed similar changes. In agreement with previous safety studies, no signs of inflammation or necrosis were seen in either the tapetum or the overlying retina.

We conclude that the change in reflectivity and color of the tapetal fundus in normal dogs treated with azithromycin is due to swelling and vacuolation of the tapetal cells. The fact that a change in color was not seen in dogs lacking a tapetum argues that retinal transparency is not affected. Since the tapetal lesion reported here had no secondary effect on the retina, and humans do not possess a tapetum, the tapetal lesion produced by azithromycin is of no toxicologic significance to man.

References

1. J.H. Fortner, W.B. Milisen, G.R. Lundeen, A.B. Jakowski and P.M. Marsh Fundamental and Applied Toxicology (1992) to be published.

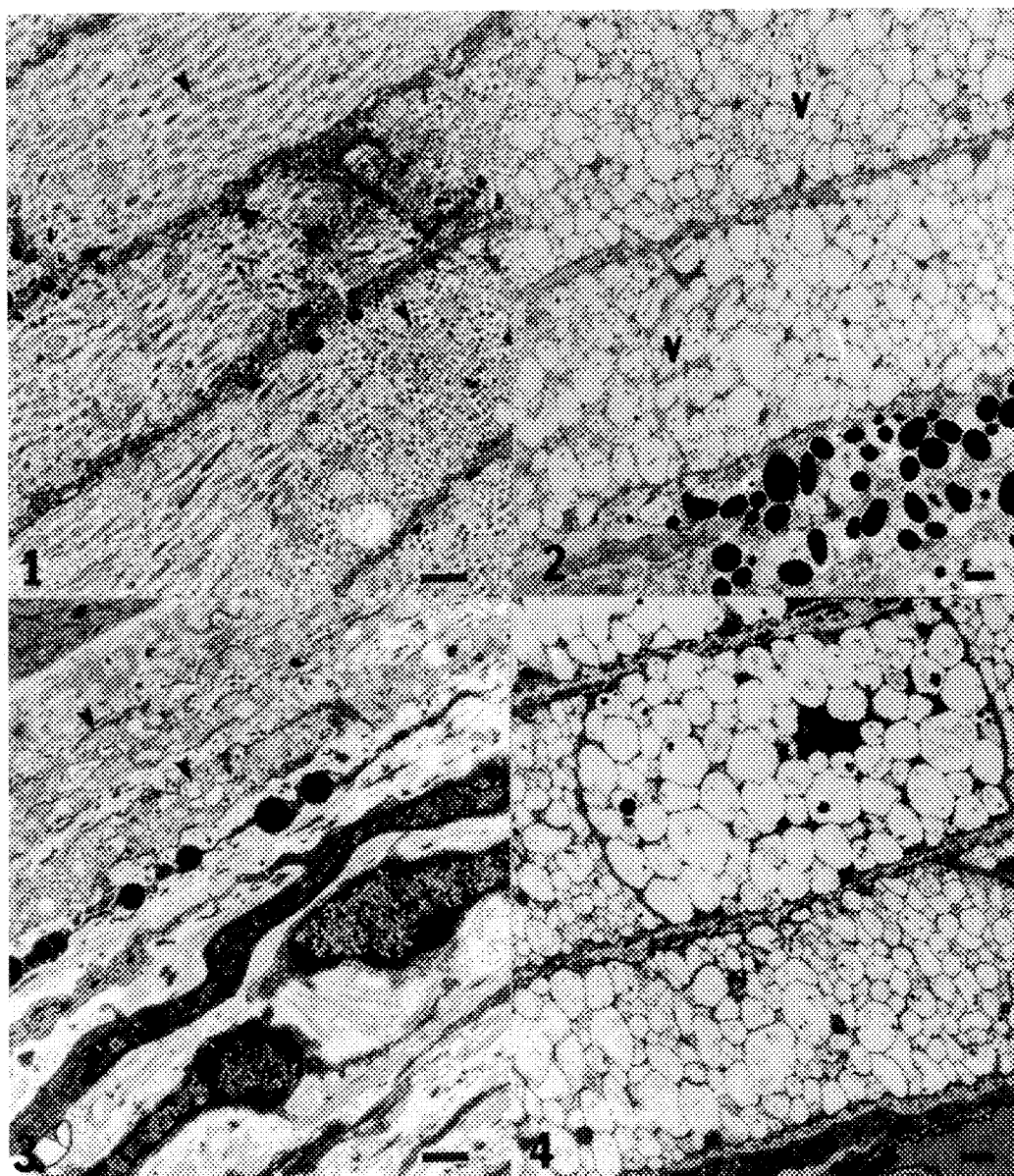


FIG.1. Control - normal tapetal cells showing parallel arrays of rodlets(arrows).
 FIG.2. Treated - tapetal cells filled with vacuoles (V) and lacking rodlets.
 FIG.3. Atapetal Control - rudimentary tapetal cells(arrows) containing variably sized vacuoles rather than normal arrays of rodlets.
 FIG.4. Atapetal Treated - rudimentary tapetal cells are markedly swollen and vacuolated. Response to treatment appears similar to normal tapetal cells.
 Bars = 1 μ m.

CHARACTERIZATION OF SPONTANEOUSLY OCCURRING CORNEAL CHANGES IN WISTAR RATS

K. W. Baker*, Z. Wojcinski*, I. Piscopo**, J. Rogers, B. Houston* and B. Gragtmans*
*Parke-Davis Research Institute, Mississauga, Ont., L5K 1B4, Canada
**Philips Electronic Instruments, Mahwah, N.J., 07430

Spontaneously-occurring changes in the cornea have been periodically observed during routine ophthalmologic examination of various strains of mice and rats^{1,2,3}. The clinical appearance of these changes has been variably described as corneal opacities, corneal dystrophy, or corneal roughness. The purpose of this study was to characterize corneal changes in Wistar rats by light and transmission electron microscopy (LM and TEM), and x-ray microanalysis.

A shipment of 43 male and 29 female 33 day old Charles River Wistar (CrI:(WI)BR) albino rats were examined clinically upon arrival and after 17 weeks. The right and left eyes were examined by ophthalmoscopy and selectively photographed using a Kowa RC-2 fundic camera. At necropsy eyes were removed and immersion fixed with gentle agitation for 24 hours in 2.5 % glutaraldehyde and 2.0% formaldehyde in a 0.1 M phosphate buffer. For LM, eyes were routinely processed for paraffin embedment, sectioned at 4 μ m, stained with hematoxylin and eosin (H/E) and assessed for the occurrence of corneal deposits. For x-ray microanalysis, tissues were preserved with aldehyde fixation only. Those tissues intended solely for ultrastructural characterization were secondarily fixed in 1% OsO₄ in a 0.1 M phosphate buffer for 2 hours at room temperature. All corneas were then sliced into four easily oriented strips and embedded in epon-araldite using flat embedding molds. Thin sections (approximately 1200 Å) were cut at right angles to the corneal surface. Sections of tissue intended for x-ray microanalysis were prepared on copper grids overlaid with carbon-coated formvar films. The x-ray microanalysis data was obtained from a Phillips CM 12 transmission electron microscope equipped with an EDAX analyzing system. Energy dispersive x-ray microanalysis conditions were 60 kV, a tilt angle of 10° and an emission current of 20 μ A. Analytical spot sizes and shapes were varied according to the area of interest. All data were reported by the "net counts" method⁴. In all cases the x-ray microanalysis data were collected from 0-20 Kev although, for clarity, the spectra may be displayed in a more limited range. Sections of OsO₄-fixed tissue were ultrastructurally characterized using a Phillips 300 electron microscope.

Varying degrees of corneal roughness were observed ophthalmologically in 40 of 43 males and 26 of 29 females. Lesions, described as multiple punctate or particulate opacities, were most often bilateral and located paracentrally (Fig 1).

Histologically, lesions were observed in only 21 of 40 males and in 15 of 26 females with clinically documented changes. These were comprised of basophilic particulate material, which occasionally formed linear plaques, lining the basement membrane of the anterior corneal epithelium (Fig 2).

An irregular distribution of electron dense deposits was observed ultrastructurally; sometimes displacing the basal epithelium yet always beneath the basal lamina (Fig 3). The largest of these presented a concentric laminar appearance with laminae varying in width and density and often including dense crystalline granules. Small deposits were also observed in corneas described as being clinically and histologically negative.

X-ray microanalysis data showed that these granules were predominately calcium and phosphorus with trace amounts of iron, zinc, sodium and aluminum. Hydroxyapatite crystals have been associated with soft tissue mineralization and may account for the large amounts of calcium and phosphorus present.

In summary, clinically-observed mineral deposits in the corneas of Wistar rats are similar in clinical, histological, and ultrastructural appearance and, in basic elemental constituents to those described in other strains and species^(1,2,3).

References:

1. T.J. Van Winkle and M.W. Balk, *Lab. An. Sci.* (1986)36:248-255.
2. R.W. Bellhorn, G.E. Korte and D. Abrutyn, *Lab. An. Sci.* (1988)38:46-50.
3. P.E. Losco and C.M. Troup, *Lab. An. Sci.* (1988)38:702-710.
4. F.V. Ungar, I. Piscopo, J. Letizia and E. Holtzman, *J. Cell Biol.* (1984)98:1645-55.

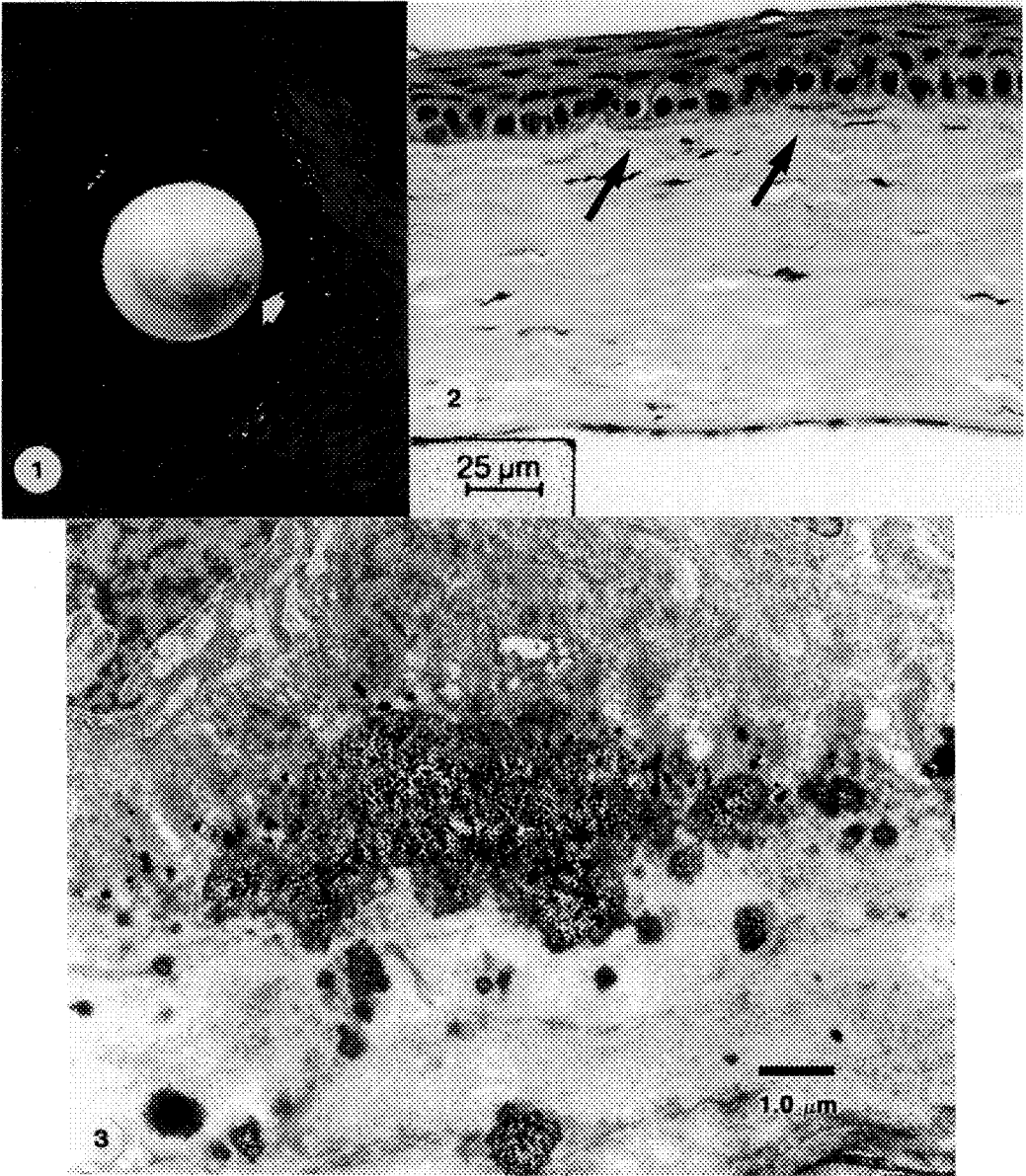


FIG. 1.--Ophthalmic photograph of rat eye opacities (arrow).
FIG. 2.--LM of rat cornea in cross-section with particulate opacities (arrows).
FIG. 3.--TEM of electron-dense deposits lining the basal lamina.

HEXACHLOROBENZENE TOXICITY IN THE RAT OVARY: II. ULTRASTRUCTURE INDUCED BY MEDIUM (10 mg/kg) DOSE EXPOSURE

Amreek Singh, Warren G. Foster*, Anna Dykeman, and David C. Villeneuve*

Atlantic Veterinary College, Charlottetown, PE. Canada. C1A 4P3; and *Environmental Health Directorate, Health Protection Branch, Tunney's Pasture, Ottawa, ON. Canada K1A 0L2

Hexachlorobenzene (HCB) is a known toxicant that is found in the environment as a by-product during manufacture of certain pesticides. This chlorinated chemical has been isolated from many tissues including ovary. When administered in high doses, HCB causes degeneration of primordial germ cells^{1,2} and ovary surface epithelium³ in sub-human primates. A purpose of this experiment was to determine a no-effect dose of the chemical on the rat ovary. The study is part of a comprehensive investigation on the effects of the compound on the biochemical, hematological, and morphological parameters in the monkey and rat.

Gelatin capsules containing HCB mixed with glucose were given to 12 Sprague-Dawley rats that weighed 250 g. The animals were housed in a carefully-controlled environment. A dose regimen of 0.0 or 10 mg/kg body weight (b.w.) daily for 90 days was followed. Six animals of the former group served as the control. At necropsy, one ovary from each animal was removed, and specimens from the organ were fixed in 2% phosphate-buffered glutaraldehyde, pH 7.3. The specimens were subsequently processed by conventional methods for transmission electron microscopy. Thin sections were examined and photographed in a Hitachi-7000 electron microscope.

Ultrastructure of the ovary from animals of the control group appeared normal. Primary follicles comprised a developing ovum, follicular or granulosa cells, and theca folliculi (Fig. 1). The ovum consisted of vesicular nucleus, and ooplasm that contained mitochondria distributed in characteristic clusters or aggregations (Fig.1). Ova were wrapped in follicular cells that were heterogeneous⁴, and occurred in small and large types. Theca folliculi, as illustrated in Figure 1, was composed of elongated cells. After exposure to HCB, developing ova showed signs of early degeneration where the mitochondria were scattered in the ooplasm (Fig.2). The cells in the theca folliculi seemed to be shortened and the nuclear shape was ovoid instead of long as depicted in Figure 2. We conclude that in the rat a 10.0 mg/kg b.w. HCB dose induces alterations in the ovary. Effects of these changes on the reproductive performance have not been established.⁵

References

1. M.J. Iatrapoulous et al., *Toxicol. Appl. Pharmacol.*, 37(1976)433.
2. A. Singh et al., *Proc. Ann. EMSA Meeting* 49(1991)130.
3. K.A. Babineau et al., *J. Submicrosc. Cytol. Pathol.*, 23(1991)457.
4. I.M. Rao et al., *Anat. Rec.*, 229(1991)177.
5. The work was immensely benefited from the technical aid given by Ms. Janny Arendez.

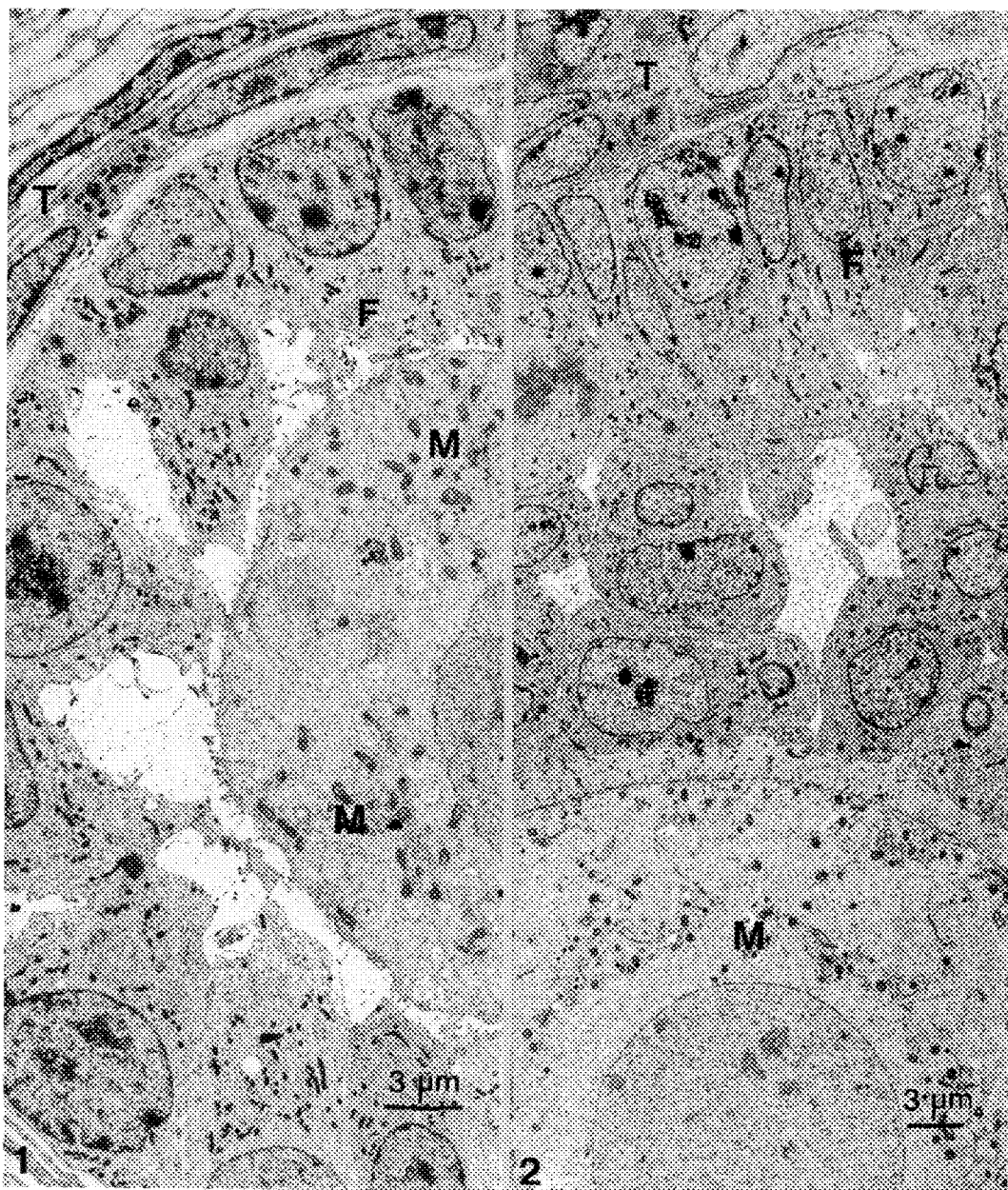


Fig. 1. Micrograph of portion of primary follicle from a rat of Control group. Note the typical clusters of mitochondria (M) in developing ovum. Theca folliculi (T) contains elongated cells. F = Follicular cell.

Fig. 2. Portion of altered growing follicle from a rat fed hexachlorobenzene. Follicle contains developing ovum at an early stage of degeneration that has mitochondria (M) scattered in cytoplasm. Theca cells (T) are oval. F = Follicular cell.

ULTRASTRUCTURAL ANOMALIES OF THE FLAGELLUM IN RELATION WITH ABNORMAL MOTILITY IN
HYBRID MICE (C57BL X CDI)F₁, TREATED WITH A MUTAGEN: ETHYL METHANE SULPHONATE
(EMS)

B.C. Ríos Cantú; M.G. Gallegos L. and E. Ramírez B.

School of Medicine, University of Nuevo Leon
Monterrey, México, A.P. 1563 C.P. 64000

In 1975, the effect of EMS on the dismorphic sperm fraction, was reported (1). Since then, the action of this drug at different levels on the seminiferous epithelium and over the spermatogenic process has been studied (2,3).

Modifications in relation to the finding of morphologically abnormal sperms have been described too (4). Likewise the lowering of the count and of the sperm motility have been used as evidence of genetic damage caused by drugs (5). Recently it has been described that EMS not only affects the morphology of sperm but also their concentration and their motility (6). The present study has been done to determine if the effect of EMS on sperm motility has a morphological cause. Hybrid mice were administered a dose of 200 mg/Kg. of EMS intraperitoneally, for five consecutive days. The epididymary and deferens ducts content was studied four weeks later. They were fixed in 2.5% glutaraldehyde and 1% osmium tetroxide; the material was included in epoxy-resin by the conventional method, sectioned and studied with a Zeiss EM 109 electron microscope.

Our observations included a range of changes that went from severe alterations that simultaneously affected the acrosome, the nucleus, and the flagellar elements (Figs. 1, 2 and 3) to minor modifications of flagellar structures. The later were changes in the number of microtubules and their arrangement (Figs. 4 and 5) or their complet absence (Figs. 2, 3, and 6). A partial absence of the outer dense fibers was also observed (Figs. 2, 3, 4, and 5).

Alterations in the flagellar ultrastructure observed in this study can be related to the altered sperm motility in mice treated with EMS. Microtubular alterations in disturbed spermiogenesis have been previously reported (4). The absence of nuclear ring caudal displacement and of nuclear indentations associated to an irregular distribution of the microtubules, may have the same genetic origin as the disarray or lack of axonemal microtubules.

REFERENCES.

- 1.- A.J. Wyrobeck et al. New York, Plenum Press (1978)
- 2.- M.G. Gallegos et al. An. Rec. (1987) 218, 47 A.
- 3.- L.E. Rodríguez et al. An. Rec. (1989) 223, 97 A
- 4.- M.G. Gallegos et al. EMSA PROC. (1991) pp 140
- 5.- G. Ficsor y L.C. Ginsberg. Mut. Res. (1980) 70: 383-387
- 6.- B.C. Ríos, Facultad de Medicina, U.A.N.L. Tesis, 1992

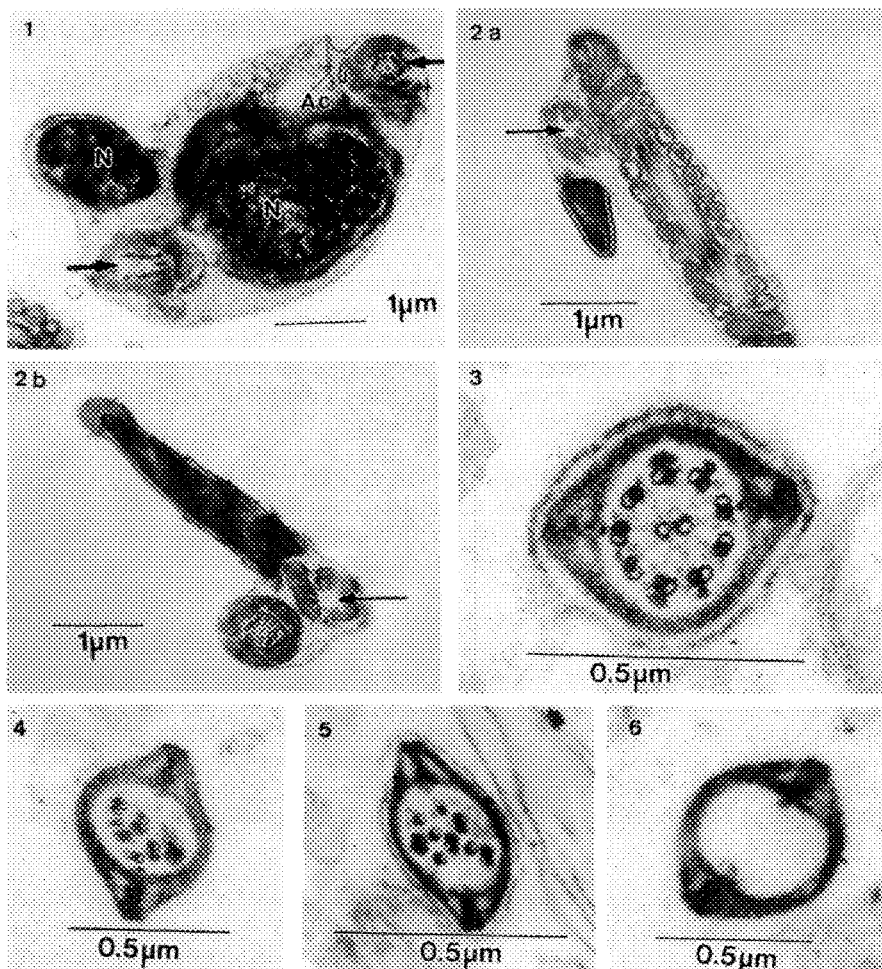


Fig. 1. Sperm with simultaneous nuclear (N) acrosomal (Ac) and flagellar (arrow) alterations.
 Fig. 2. The arrows show the microtubules absence in transverse sections of the flagellum. a) A little head sperm, b) Apparently biflagellated sperm.
 Fig. 3. Transverse section of the flagellar principal piece in which is observed the partial external dense fibers lack.
 Figs. 4 and 5.- Disorganization and partial absence of the flagellar elements.
 Fig. 6. A section in which was observed total absence of the axonemal microtubules and external dense fibers.

DEFECTIVE SPERM CELLS IN TWO CAPTIVE CHEETAHS: ANALYSIS BY TEM AND SEM

Lynn D. Gray, Robert Shane Simmons, Louisa Schmid Thedford*, David B. Holiday** and Cathey Marsh***

Departments of Cell Biology & Environmental Sciences, *The Vivarium and **Epidemiology & Biomathematics, The University of Texas Health Center at Tyler, P.O. Box 2003, Tyler, TX, 75710
***The Caldwell Zoo, P.O. Box 4280, Tyler, TX, 75712

Captive breeding of cheetahs (*Acinonyx jubatus*) is of great interest to zoological parks and preserves. Semen quality is a major factor in successful reproduction and ultrastructural assessment can be helpful in choosing suitable males. There is, however, relatively little ultrastructural data on cheetah spermatozoa as compared with other species. Studies using both light and electron microscopy have indicated a high percentage of defective spermatozoa in cheetahs¹ and have noted a number of specific defects including coiled tails, acrosomal malformations² and basal plate "pouches"³.

The present investigation was undertaken in cooperation with the Caldwell Zoo in Tyler, TX to assess the semen quality of two cheetahs utilized in their breeding program. One of the males (#1) has sired one cub, whereas the other male (#2) is unproven to date. Both SEM and TEM were used to qualitatively and quantitatively evaluate structural aspects of the sperm cells from these animals.

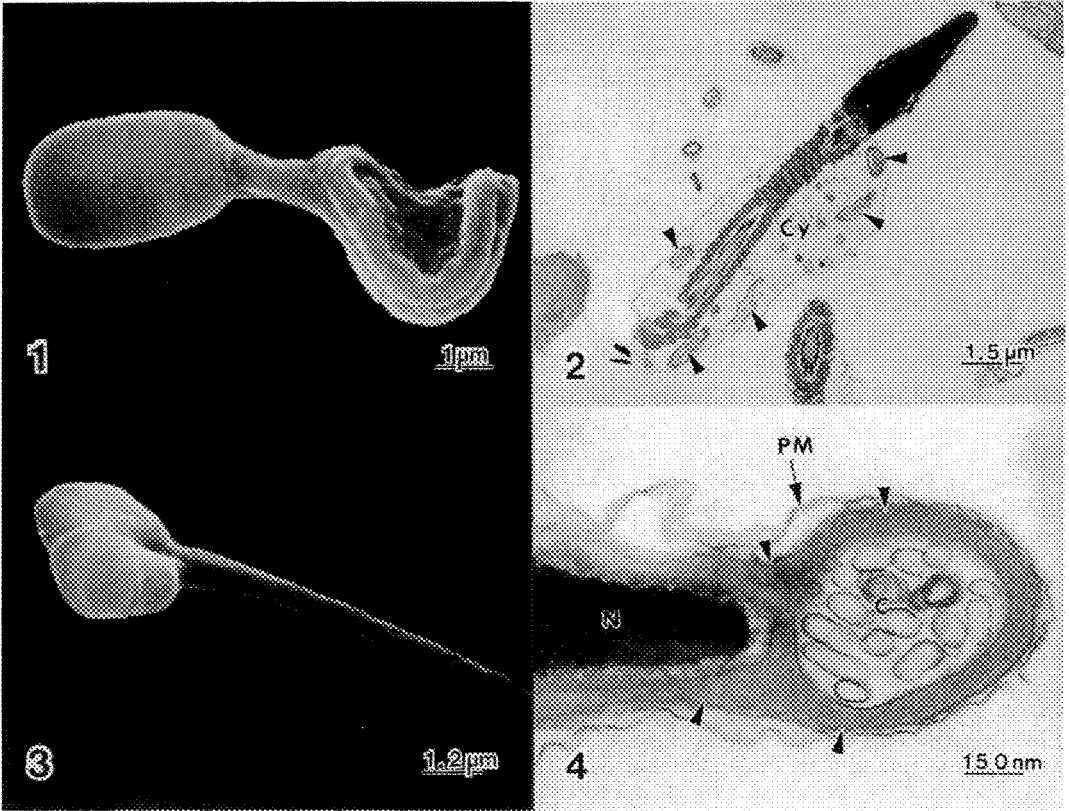
Semen was obtained from the tranquilized cheetahs by rectal probe electroejaculation. Fresh samples were evaluated for forward progression (F.P.) and percent motility. Concentration was not determined. The remainder of the semen was placed in room temperature, sodium cacodylate buffered, 3% glutaraldehyde and transported back to the lab for further processing. The samples were concentrated by centrifugation at 1000 X g, and processed through buffered OsO₄, *en bloc* stained in uranyl acetate and dehydrated in ethanol. Samples for SEM were removed, air dried on glass coverslips, and coated with Au/Pd. Samples for TEM were placed in acetone followed by infiltration and embedding in epoxy resin.⁴ Thin sections were cut with a diamond knife, collected on nickel reference grids and poststained in uranyl acetate and lead citrate.

For SEM, 100 sperm cells were evaluated by beginning at the top, left corner of the coverslip and scoring the first 50 cells moving left to right. The stage was then moved to the left, middle of the coverslip and the next 50 cells were scored accordingly. For TEM, coordinates were predetermined and evenly distributed over the grid to insure adequate sampling of the section. Profiles of the head and tail regions were examined in various planes of section until approximately 50 of each region had been scored. Primary emphasis was placed on defects likely to affect fertility.

Cheetah #1 showed 70% motility and 4-5 F.P. whereas cheetah #2 showed only 50% motility and a somewhat poorer F.P. of 3-4. The coiled or bent tail defects were the most common anomalies in either sample (#1: 48%, #2: 58% by SEM). Axonemal defects (#1: 38%, #2: 21% by TEM) were also common. These defects included disorganized microtubules (and other components) and deficient or supernumerary microtubules. Cytoplasmic droplets were common in both samples (#1: 48%, #2: 56% by SEM; #1: 40%, #2: 55% by TEM). Incidental defects included micro and macrocephaly, vacuolated nuclei and acrosomal blebs. Occasional double heads and double tails were observed. Both samples exhibited overall less defective sperm cells than the average 70% reported for cheetahs evaluated in a previous study.¹

References

1. D.E. Wildt et al., *Biol. Reprod.* (1983)29, 1019.
2. R.I. Coubrough et al., *Proc. Elect. Micros. Soc. Southern Africa* (1978)8, 57.
3. J.T. Soley and R.I. Coubrough, *Proc. Elect. Micros. Soc. Southern Africa* (1981)11, 121.
4. M.L. Davis, Doctoral Dissertation, Texas A&M University (1982), 111 pp.



- Fig. 1:** Coiled tail defect by SEM. Both cheetahs sampled had high numbers of bent and coiled tails.
- Fig. 2:** Coiled tail defect by TEM. Coiled tails were always contained within a cytoplasmic droplet (Cy). Axoneme profiles (arrowheads) were often more disorganized than those shown here.
- Fig. 3:** Bi-cephalic sperm cell by SEM. Double heads and tails were interesting but infrequent findings in both samples.
- Fig. 4:** Acrosomal bleb by TEM. The acrosome (arrowheads) is intact in this cell and appears to surround some cell cytoplasm (C) which contains membranous structures. This type of head defect was observed in both samples but its effect on fertility is speculative. Other features include the cell nucleus (N) and plasma membrane (PM).

FORMATION OF SPERMATOPHORE IN EJACULATORY DUCT OF YELLOW MEALWORM BEETLE, *Tenebrio molitor*: SEM STUDY

František Weyda*, George M. Happ**

*Institute of Entomology, Branisovská 31, 370 05 České Budějovice, CZECHOSLOVAKIA

** Department of Zoology, University of Vermont, Burlington, VT 05405

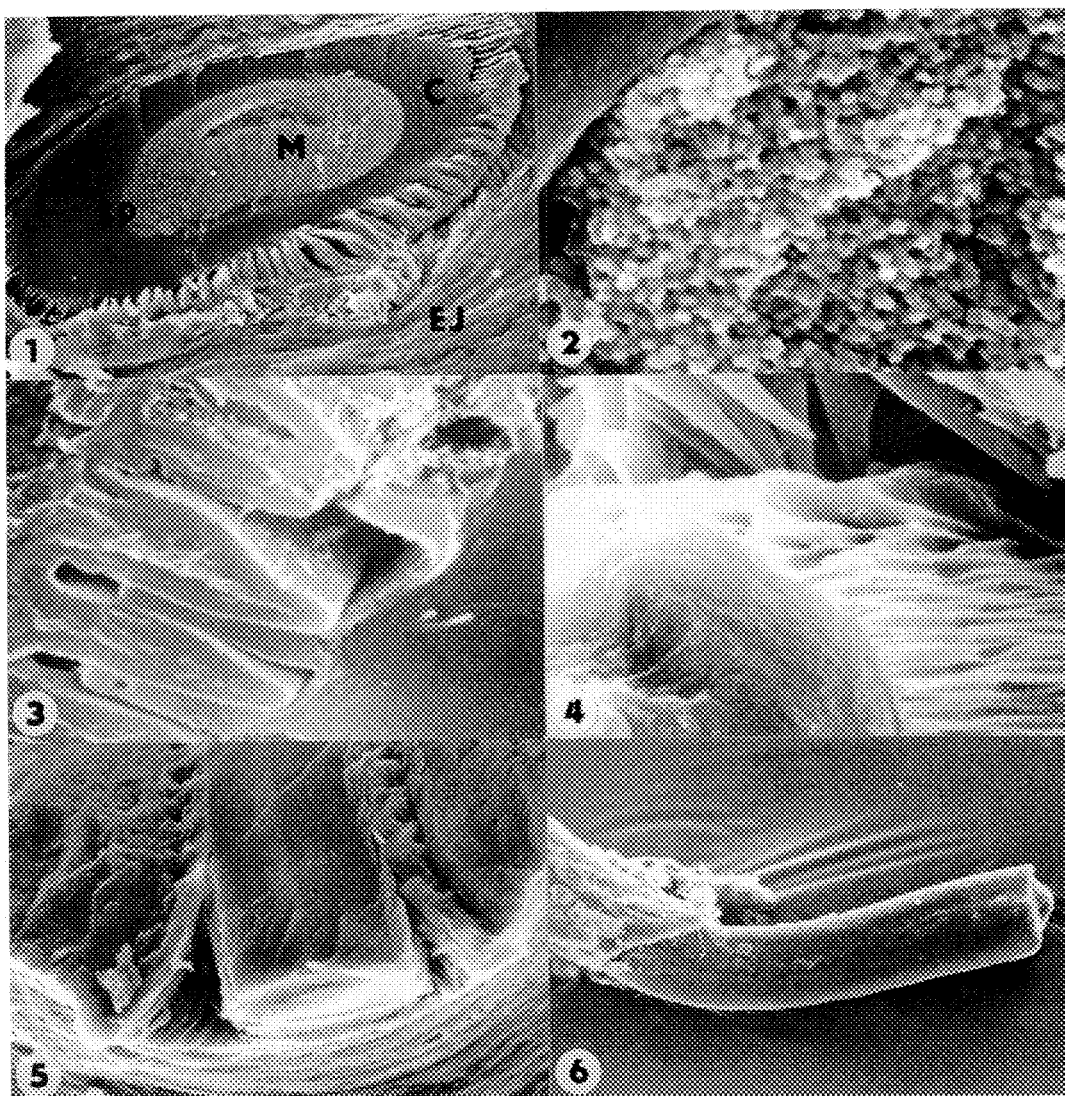
Main role of the accessory glands of *Tenebrio molitor* male is to facilitate transfer of sperm to the females. They produce heterogeneous secretions.^{1,2} Two anatomically distinct glands are present. While the tubular accessory glands (TAG) are composed of the secretory cells of one type only,³ the bean-shaped accessory glands (BAG) consist of eight cellular types.¹ Low viscosity secretion of the TAG mix with sperms forming seminal fluid while high viscosity secretions (spermatophorins) of the BAG are largely transformed into the insoluble wall and core of the spermatophore. The prespermatophoric mass is transferred to the ejaculatory duct (EJD) where solidify and forms the complex spermatophore. Immunocytochemical experiments with monoclonal antibodies based on the colloidal gold technique were used in order to understand exact composition of individual layers of the spermatophore.⁴ In the recent study we have used SEM to observe the whole process of the formation of spermatophore in the ejaculatory duct.

For the study of the ejaculatory duct and the spermatophore formed inside of it we have fixed dissected organs from adult male beetles (6-9 days old) in a mixture of 2.5% formaldehyde and 2.0% glutaraldehyde in cacodylate buffer for 1 hour. After washing in cacodylate buffer the ejaculatory ducts were postfixed in 2% osmium tetroxide for 1.5 hour. Then the organs were quickly frozen in liquid nitrogen and simply cut by precooled razor blade under control of binocular loupe in order to enable a study of their internal parts. Pieces of the tissue were then placed into ethanol and dried by critical point drying. They were observed in Jeol 100 CX and Tesla BS 300 scanning electron microscopes after sputter-coating by gold/palladium.

Formation of the spermatophore takes place in the lumen of the BAG, the grand junction and upper part of the ejaculatory duct. Whole process is very complex. The secretions from the BAG form individual layers of the spermatophore. We have found various situation here depending on the stage of the process of the spermatophore formation (Figures 1-6). The spermatophore located in the middle part of the EJD seems to be fully formed. Core (the main internal complex layer) and medulla (central layer) composed of the globular secretion are clearly visible (Figures 1-2). Also main outer layer of the spermatophore (wall) is formed as well as the layer containing seminal fluid and sperm cells. Surface of the spermatophore is rugged (Figure 4). It is caused by numerous longitudinal cuticular ribs on the surface of the cuticular lining of the middle part of the EJD (Figure 3). Numerous cuticular spines on the surface of the cuticular lining of the lower part of the EJD (Figure 4) enable movement of the fully formed spermatophore in proper direction. When reached the lower part of the EJD the spermatophore is fully formed (Figure 5). Surface of the spermatophore becomes smooth (Figure 6) due to glycoproteinaceous secretion on its surface.⁵

References

1. G. M. Happ, In: R. C. King and H. Akai (Eds), Insect Ultrastructure, Vol.2: Plenum Publishing Corp.(1984),365
2. G. M. Happ, Annu Rev. Entomol. (1992),303
3. N. M. Gadzama, C. M. Happ and G. M. Happ, J. exp. Zool. (1977),211
4. F. Weyda, unpublished data
5. This research was supported by competitive grants from the National Institute of Health (USA) and the Hasselblad Foundation (Sweden).



FIGURES- Ejaculatory duct and spermatophore of the yellow mealworm beetle (*Tenebrio molitor*) male.

FIG.1- Middle part of ejaculatory duct (EJ) with internal part of spermatophore (SP) consisting of core (C) and medulla (M). Magnification: x780.

FIG.2- Detail from Fig.1 showing structure of medulla. Magnification: x7300.

FIG.3- Cuticular ribs of the middle part of ejaculatory duct forming characteristic rugged shape of spermatophore. Magnification: x8750.

FIG.4- Lower part of ejaculatory duct with cuticular spines and rugged surface of spermatophore in the lumen. Magnification: x3700.

FIG.5- Fully-formed spermatophore in the lower part of ejaculatory duct. Magnification: x1250.

FIG.6- Part of the fully-formed spermatophore moved from the lower part of ejaculatory duct after cutting. Magnification: x380.

ULTRASTRUCTURE AND IMMUNOGOLD LABELING OF CYTOPLASMIC FIBROUS BUNDLES IN TOBACCO LEAF CELLS INFECTED WITH TOBACCO VEIN MOTTLING VIRUS

E. D. Ammar, D. W. Thornbury, and T. P. Pirone

Dept. of Plant Pathology, University of Kentucky, Lexington, Ky. 40546

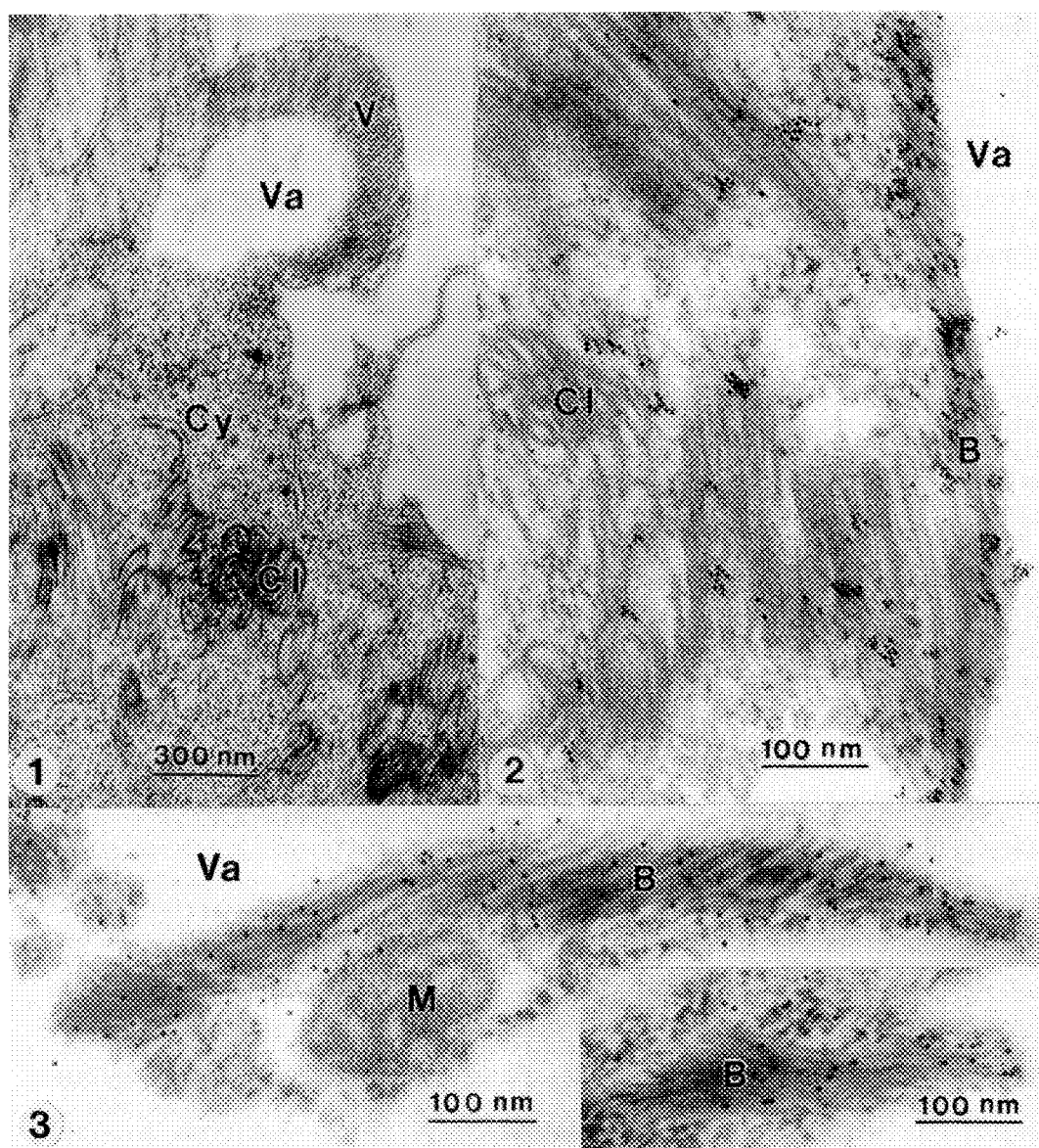
Tobacco vein mottling virus (TVMV) is a potyvirus, with flexuous filamentous particles ca. 765 nm long and 12-13 nm in diameter. TVMV is transmitted by sap inoculation and by aphid vectors.¹ Cylindrical inclusions characteristic of infections with potyviruses have been found in the cytoplasm of TVMV-infected tobacco leaves and protoplasts^{1,2}, and the presence of fibrous inclusions of unknown composition in the cytoplasm and nuclei of TVMV-infected tobacco has been reported.³ Here, we report the results of transmission electron microscopy (TEM) and immunogold labeling of cytoplasmic fibrous bundles found in TVMV-infected leaf cells, providing evidence that these bundles are composed of TVMV virions and/or coat protein.

Pieces of systemically infected tobacco leaves (cultivar Ky 14), from young plants inoculated with TVMV 2 weeks earlier, were prefixed in 2.5% glutaraldehyde, then fixed in 1% osmium tetroxide and embedded in Spurr's medium as described.⁴ However, for TEM-immunogold labeling, leaf samples were fixed only in 0.1% glutaraldehyde + 1% paraformaldehyde and embedded in L.R. White.⁵ Goat anti-rabbit serum conjugated to gold particles, 10 nm diameter, was used for post-embedding immunolabeling.

The most prevalent cytoplasmic inclusions in TVMV-infected leaf cells are the cylindrical inclusions (CIs). Fibrous bundles also were regularly found in the cytoplasm of these cells, usually appressed to the tonoplast membrane (Figs. 1-3). Fibrous bundles surrounded by this membrane frequently protruded into the cell vacuole, sometimes forming bridges along with mitochondria and ribosomes (Fig. 3). In some cases, filamentous virus-like particles similar in diameter to those of TVMV were discernible in the fibrous bundles (Fig. 1). In thin sections, following incubation with antibodies to TVMV virions, gold label was mainly attached to the fibrous bundles (Figs. 2,3) confirming that these bundles contained TVMV virions and/or virion coat protein. Some label was also attached to the CIs (Fig. 2), indicating that some TVMV virions or coat protein may be associated with the CIs. Association of virions with CIs has been reported with some other potyviruses.³

References

1. T.P. Pirone and J.G. Shaw, AAB Descriptions of Plant Viruses (1988)325.
2. J.F. Murphy et al., Phytopathology (1991)81, 371.
3. J.R. Edwardson and R.G. Christie, The Potyvirus Group, Univ. Florida Monograph 16 (1991)1-3.
4. E.D. Ammar et al., Phytopathology (1990)80, 303.
5. G.R. Newman, in M.A. Hayat, Ed., Colloidal Gold Principles, Methods, and Applications, New York: Academic Press (1989)2,47.



Figs. 1-3. Thin sections of cells from TVMV-infected tobacco leaves embedded in Spurr (Fig. 1) or L.R. White (Figs. 2,3) and viewed by TEM.

Fig. 1. Cylindrical inclusions (CI) in the cytoplasm (Cy), and bundles of filamentous virus-like particles (V) protruding into the vacuole (Va).

Fig. 2. Gold label attached to fibrous bundles (B), and to some cylindrical inclusions (CI).

Fig. 3. Gold-labeled fibrous bundles (B) protruding into the vacuole (inset), or forming a bridge along with mitochondria (M) and cytoplasmic ribosomes.

OPTIMIZATION OF DIAGNOSTIC ELECTRON MICROSCOPY FOR ENTERIC VIRUSES

C. D. Humphrey,* H.H. Huang,** and H. Tanaka***

*Division of Viral and Rickettsial Diseases, CDC, Atlanta GA 30333

**Nat'l. Taiwan Univ. Hospital, Taipei, Taiwan

***Instituto Adolfo Lutz, Sao Paulo, Brazil

Virus identification by negative stain electron microscopy (EM) is one of the most versatile and sensitive assays for rapid viral diagnosis. Electron microscopy is particularly important for the study of enteric viruses because they are difficult to cultivate and characterize. The gastroenteritis viruses most frequently identified include rotavirus (Fig. 1), enteric adenovirus (Fig. 2), enteric coronavirus (Fig. 3), calicivirus (Fig. 4), Norwalk agent, and astrovirus (Fig. 6). In addition, there are several unclassified viruses categorized as either small round structured viruses (Fig. 5) or small round viruses (Fig. 7).

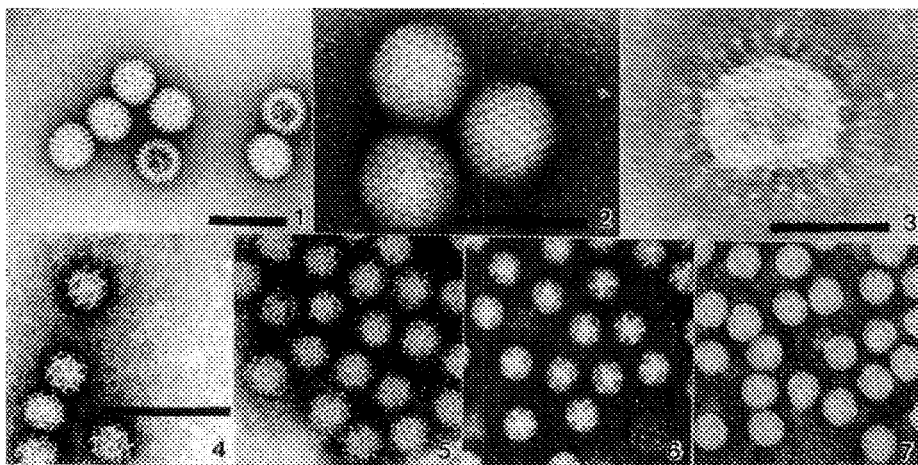
The great variety of methods and sample conditions suggested for negative stain EM may interfere with reproducibility of observations if different laboratories participating in a multicenter study are using different negative stain protocols. Furthermore, the numerous published methods may cause confusion for microscopists first attempting to choose a negative stain diagnostic method suitable for stool specimens.

Several methods, including direct EM (DEM) (1-3), agar diffusion procedures (4,5), and concentration techniques (6,7), were compared for their ability to adsorb and identify small viruses. Enterovirus 71 (EV-71) or astrovirus (ASV) grown in cell culture, and stool extracts containing ASV were used as test viruses. Glow discharge pretreatment of formvar-carbon-coated grids with a simple glow discharge device (8) was tested to determine its usefulness for increasing virus adsorption to grids. Glow discharge permitted a uniform distribution of virus and increased the number of virus particles adsorbed when either direct or immune EM approaches were tested. Agar diffusion methods, including pseudoreplica, did not significantly increase the numbers of particles adsorbed compared with those absorbed by using the simpler DEM methods, as long as optimal incubation times were allowed for the DEM methods. Results obtained from DEM methods were more reproducible than those obtained from agar diffusion methods. Agar diffusion also increased adsorption of extraneous debris. However, virus adsorbance reached maximum adsorbance more quickly with agar diffusion methods than with DEM. Concentration methods increased the numbers of particles trapped on grids proportionally to the amount of concentration when the methods worked optimally. However, the concentration methods were inconsistent in their performance, caused greater adsorption of extraneous substances, were relatively time consuming, and the 2-10 fold concentration increase only rarely improved the ability to find viruses in diagnostic preparations. Our observations support a conclusion that glow discharge pretreatment of grids and DEM methods for virus identification

by negative stain EM are more reliable, simpler to perform, and often require less sample per assay than agar diffusion or virus concentration methods.

REFERENCES

1. Hayat, M.A. and S. Miller, Negative Staining, New York: McGraw-Hill (1990).
2. Palmer, E.L., and M. Martin, Electron Microscopy in Viral Diagnosis, Boca Raton, Fla.: CRC Press (1988).
3. Doane, F.W. and N. Anderson, Electron Microscopy in Diagnostic Virology, Cambridge: Cambridge University Press (1987).
4. Anderson, N. and F. Doane, Appl. Microbiol. 24:495 (1972).
5. Boerner, C.F. et al., Opthamol. 88:1377 (1981).
6. Almeida, J.D., Yale J. Biol. Med. 53:5 (1980).
7. Hammond, G.W. et al., J. Clin. Microbiol. 14:210 (1981).
8. Aebi, U. and T. Pollard, J. Elec. Micros. Tech. 7:29 (1987).
9. We gratefully acknowledge Drs. Roger I. Glass and Mark Pallansch for reagent viruses, and support.



- FIG. 1 --Rotavirus. 0.5% uranyl acetate. Bar = 100 nm. (CDC/DVRD archives).
 FIG. 2 --Adenovirus. 0.5% uranyl acetate. Bar = 100 nm. (CDC/DVRD archives).
 FIG. 3 --Enteric Coronavirus. 2% phosphotungstic acid (pH 6.9) (PTA).
 Bar = 100 nm.
 FIG. 4 --Calicivirus. 2% PTA. Bar =100 nm. for Figs. 4-7.
 (CDC/DVRD archives).
 FIG. 5 --SRSV. 2% PTA.
 FIG. 6 --Astrovirus. 2% PTA.
 FIG. 7 --SRV. 2% PTA.

APPLICATION OF IMMUNOGOLD/QUANTITATIVE X-RAY MICROANALYSIS TO STUDY INFECTIOUS HEMATOPOIETIC NECROSIS VIRUS

Consetta M. Helmick¹, J. Franklin Bailey², Jeanene De Avila¹, and Sandra S. Ristow¹

¹ Department of Animal Sciences, Washington State University, Pullman, Washington, 99164

² Electron Microscopy Center, University of Idaho, Moscow, Idaho, 83843

Monoclonal antibody staining followed by immunogold labeling and energy dispersive x-ray microanalysis was utilized to detect the presence of the nucleoprotein (N) and glycoprotein (G) of infectious hematopoietic necrosis virus (IHNV) on the surface of cultured coho salmon embryo (CSE-119) and rainbow trout heart (RTH) cell lines. The objectives of this study were to first, demonstrate that anti-G and anti-N monoclonal antibodies labeled with streptavidin gold would identify virus bound to the surface of cultured fish cells. Secondly, we sought to demonstrate the quantities of colloidal gold particles associated with the surface region of IHNV infected cells at 1, 4, 6, 8, 14, 24, and 30 hours.

Cells and Infection. Rainbow trout heart cells and coho salmon embryo cells were grown to confluence in sterile 24 well tissue culture dishes containing 1% nitrocellulose/carbon coated nickel grids.¹ Each grid was infected with 10⁵ p.f.u. of the Hagerman virus (IHNV) or mocked infected for 1 hours at 20° C. After incubation with the virus, excess fluid was removed and fresh RPMI-1640 containing 5% glutaraldehyde in 0.1M PBS for 1 hours at 20° C. Grids were transferred to 5% BSA-PBS pH 7.4 containing 100mM glycine for 45 minutes. Excess fluid was removed and the appropriate dilution of antibody 1NDW14D (N) or 3GH135L (G) was added and incubated for 4 hours at 20° C. Other sets of identical grids were removed and fixed at 4, 6, 8, 14, 24, and 30 hours post infection. Grids were washed with 0.5M PBS pH 8.0. A biotinylated secondary antibody, goat anti-mouse IgG, at a 1:200 dilution was applied for 1 hour. After washing the grids, streptavidin gold (20nm), at a 1:200 dilution was applied and incubated for 1 hour. Grids were washed and postfixed in 2.5% glutaraldehyde in 0.1M PBS for 30 minutes. Then grids were rinsed with distilled water, air dried, and affixed to carbon specimen mounts and carbon coated.^{2,3,4}

SEM/X-Ray Analysis. Grids were examined in a scanning electron microscope equipped with an energy dispersive x-ray analyzer. The accelerating voltage of the primary beam was 15 kV, and the specimen tilt angle was set at 45 degrees. The x-rays were collected for 200 seconds from an 78.75 cm² area at a magnification of 1800 - 1900x.

An x-ray analysis of the gold was conducted to determine the levels of background elements and gold present in the label. Gold particles were not detected on the surface of uninfected RTH or CSE-119 cells, thus nonspecific binding or random trapping of gold particles did not occur. In the study presented, there is a notable disappearance and reappearance of the G and N proteins of the virus on the surface of the RTH cells during the 30 hours period (Fig. 1), possible corresponding to adsorption, internalization, uncoating, and reexpression events. In contrast, the virus binds continuously to the surface of the CSE-119 cells with a slight increase at 24 hours (Fig. 2). This condition might imply that the virus particles do not internalize or reexpress in the same manor as on RTH cells.

References

1. A.D. Hayat and et al., J. Micros. (1987)145,97.
2. J.L. Bartholomew and et al., J. Aquatic Animal Health (1990)2, 68.
3. J.E. Beesley, Colloidal Gold: A New Perspective for Cytochemical Marking. Oxford University Press p. 22.
4. S.A. Livesy and et al., SEM. (1989)3, 231.

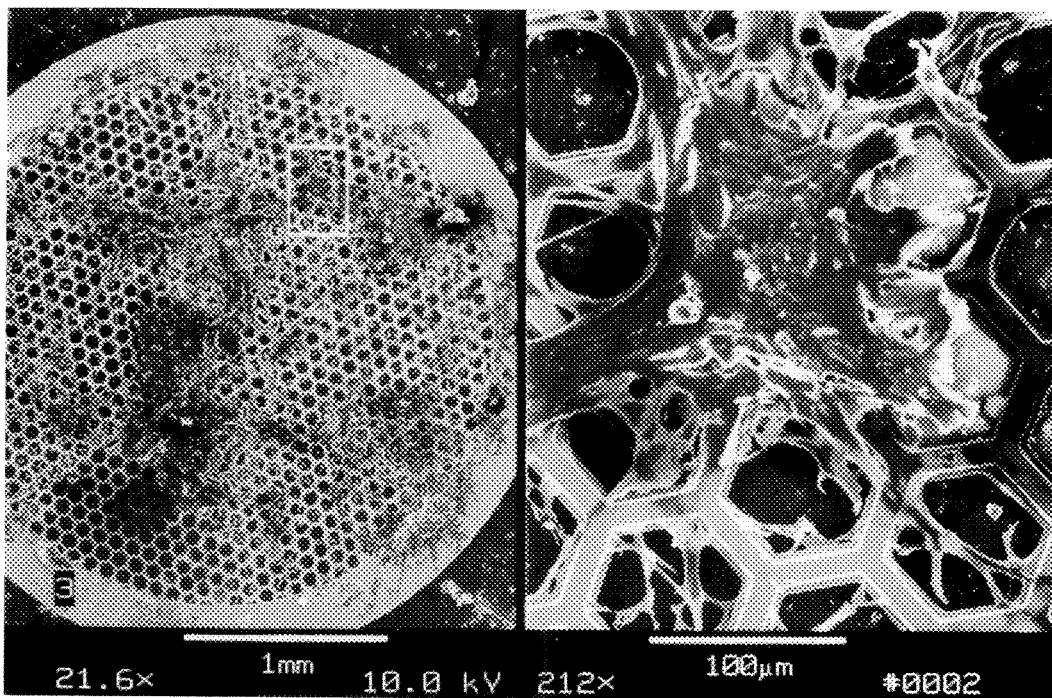
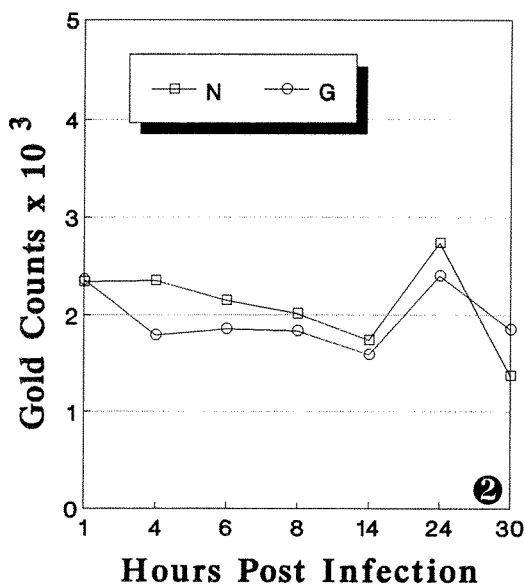
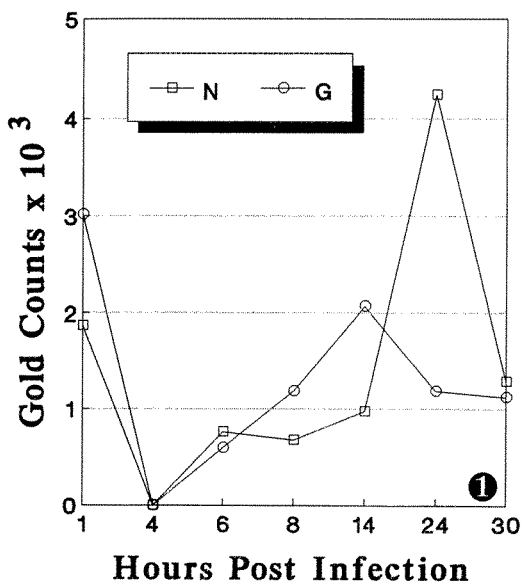


FIG. 1.--Rainbow trout heart (RTH) cells labeled with anti-N/gold and anti-G/gold antibodies.
 FIG. 2.--Coho salmon embryo (CSE-119) cells labeled with anti-N/gold and anti-G/gold antibodies.

FIG. 3.--Coho salmon embryo (CSE-119) cells.

ELECTRON AND IMMUNOELECTRON MICROSCOPY OF EXPERIMENTAL RESTON VIRUS INFECTION IN MONKEYS

Thomas W. Geisbert,* Peter B. Jahrling,* Nancy K. Jaax**

*Virology and **Pathology Divisions, United States Army Medical Research Institute of Infectious Diseases, Ft. Detrick, Frederick, MD 21702-5011

The tissues and fluids of five cynomolgus macaques (*Macaca fascicularis*) experimentally inoculated with Ebola-related Reston virus were examined by transmission electron microscopy (TEM) at various stages of disease to provide insight into the pathogenesis of this newly discovered; potential human pathogen. TEM information obtained from this investigation was compared with findings previously reported in monkeys naturally infected with Reston virus.^{1,2}

At necropsy, tissues were fixed in cacodylate-buffered 2% glutaraldehyde and processed according to conventional procedures for TEM, or were fixed in phosphate-buffered 2.5% paraformaldehyde + 0.1% glutaraldehyde and processed for post-embedment immunoelectron microscopy (post-IEM) as previously described.³ Serum, nasal exudate, and urine were also collected from sick and moribund animals and treated as described for suspected filoviruses in fluid specimens.⁴

Viral replication appeared most extensive in fixed tissue macrophages and interstitial fibroblasts (Fig. 1) in all five monkeys. Replication in hepatocytes, adrenal cortical cells, renal tubular epithelium, intestinal epithelium, sublingual salivary gland epithelium, and urinary bladder transitional epithelium was consistent. However, the number of parenchymal and epithelial cells replicating Reston virus varied among monkeys and appeared to increase as infection progressed. Monkey 57, sacrificed at the latest discernible stage of disease, showed a much higher incidence of parenchymal and epithelial cell infection (Figs. 2-4) than animals euthanized at earlier times. These observations corroborated results from a previous TEM study, employing naturally infected macaques, which suggested connective tissue was the first and preferred site of Reston virus replication.² Post-IEM of infected monkey tissues showed that Reston virus may be a separate filoviral species. Positive gold-sphere labeling of viral inclusions and virions (Fig. 5) was much more intense when thin sections of tissue were incubated with Reston virus guinea pig antisera than when incubated with prototype Ebola guinea pig antisera. No labeling was seen when tissue thin sections were incubated with Marburg guinea pig antisera or several Ebola murine monoclonal antibodies. Reston virions were easily demonstrated in sera (within 3 h of sampling) of all experimentally infected monkeys assayed after day 3 post inoculation (Fig. 6). This observation was later confirmed by viral infectivity titration, and demonstrated the usefulness of TEM to efficiently diagnose potential filoviral infections. The presence of Reston virions in urine and nasal exudate corroborated the visualization of viral replication in renal tubular epithelium, transitional epithelium of urinary bladder, and alveolar macrophages, and suggested that Reston virus might be transmitted by droplets or fomites.⁵

References

1. P.B. Jahrling et al., Lancet. (1990)335, 502-505.
2. T.W. Geisbert et al., J. Comp. Pathol. (1992)106, 137-152.
3. T.W. Geisbert and P.B. Jahrling, J. Clin. Pathol. (1990)43, 813-816.
4. T.W. Geisbert, J.B. Rhoderick, and P.B. Jahrling, J. Clin. Pathol. (1991)44, 521-522.
5. The views of the authors do not purport to reflect the positions of the Department of the Army or the Department of Defense (para. 4-3, AR 3670-5).

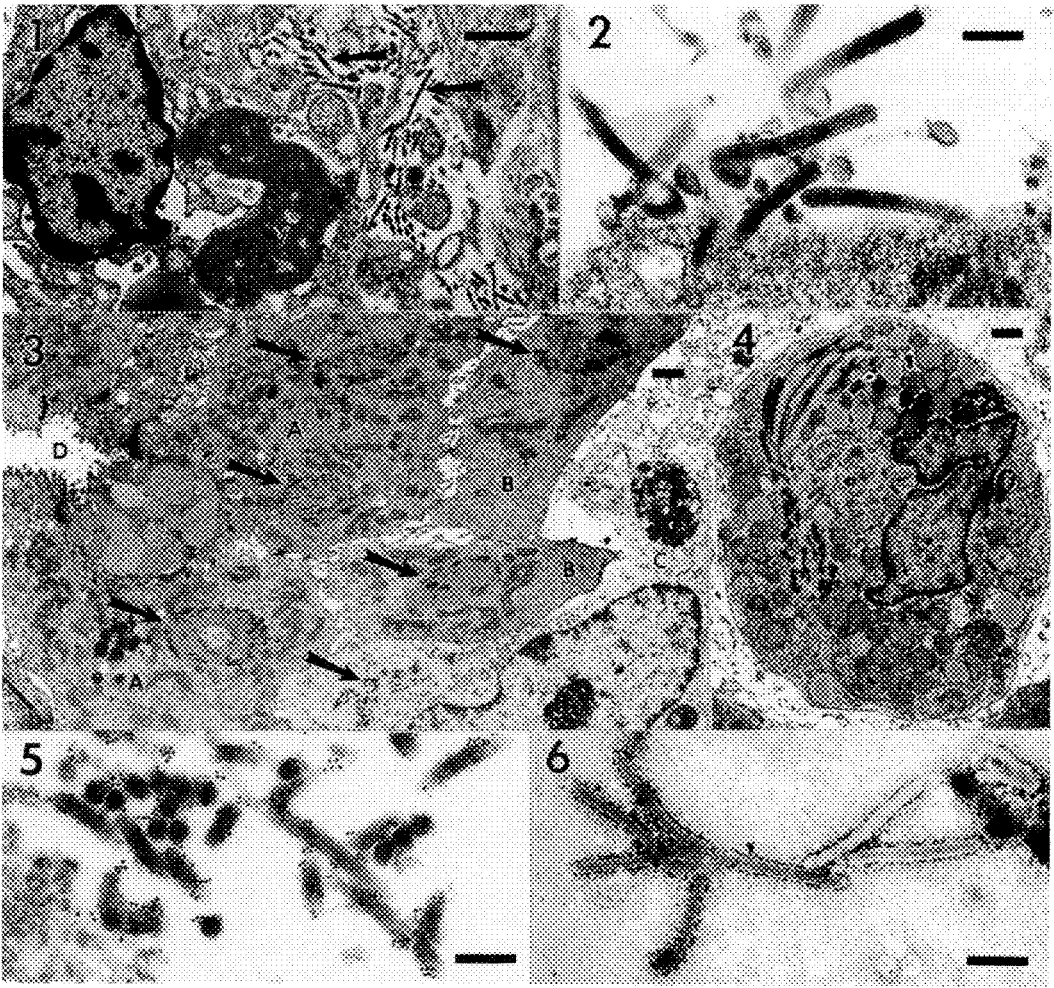


FIG. 1.--TEM shows Reston virus inclusion (V) in stromal fibroblast from monkey lung. Note presence of free virions (arrows) in interstitial space. Bar = 1 μ m.

FIG. 2.--High magnification TEM shows Reston virions budding from luminal surface of transitional epithelial cell from urinary bladder of moribund monkey. Bar = 0.2 μ m.

FIG. 3.--Low magnification TEM of cells surrounding duct (D) of monkey sublingual salivary gland. Note Reston virus inclusions (arrows) in cytoplasm of epithelial cells lining duct (A), epithelial cells removed from duct (B), and infiltrating macrophage (C). Bar = 1 μ m.

FIG. 4.--TEM of monkey adrenal cortical cell shows longitudinal, cross, and tangential sections of cytoplasmic Reston virus inclusion material. Bar = 1 μ m.

FIG. 5.--TEM of monkey liver shows positive gold-sphere labeling of Reston virions in space of Disse when incubated with guinea pig antisera raised against Reston virus. Bar = 0.2 μ m.

FIG. 6.--TEM shows Reston virions recovered from serum of infected monkey. Bar = 0.5 μ m.

THE USE OF SEM TO STUDY THE EFFECT OF BACTERIOSTATIC PROPERTIES OF SPONGES ON BACTERIAL ATTACHMENT AND GROWTH

Pontefract, R.D, and G. Bergeron

Microbiology Research Division, Health & Welfare Canada, Banting Research Ctr.,
Ross Avenue, Ottawa, Ont., Canada, K1A 0L2

Many bacteria possess the ability to adhere and grow on solid surfaces.¹ The existence of bacterial biofilms in food processing plants and in or on food processing equipment can have serious consequences, and various cleaning and sanitizing procedures are employed to deal with such contamination.^{2,3} Bacteriological monitoring methods are employed to test the efficiency of these cleaning procedures, and the most widely used technique is the swab rinse method whereby a moistened sterile swab is rubbed over the surface of the area to be sampled. One difficulty with this procedure is that the surface contact area of the swab is quite small, so that evenly swabbing a defined area can be difficult. To correct this problem, square sponges have been tried as substitutes to provide a much greater contact area. However, recent studies have shown that some sponges may contain bacteriostatic substances which can hinder test results.⁴ To determine whether some makes of sponges may contain bacteriostatic agents, SEM was used to examine samples which had been exposed to conditions to promote bacterial attachment and growth on their surface. The results of these observations were correlated with microbial tests to determine bacteriostatic activity of duplicate sponge samples.

For SEM, square (15mm/side) sponges were attached to stainless steel rectangles (to prevent floating) and were placed in a flow chamber where they were immersed in tryptic soy broth plus 0.6% yeast extract containing approximately 10^8 cells/ml L. innocua. The cell culture was circulated over the sponge squares at a flow rate of 200 ml/min. After 1.5h exposure for attachment, sterile TSBYE was circulated over the sponges for a further 2 h. The sponge squares were removed from the flow chamber, rinsed by agitating the squares in PBS pH7.3 for one min. and then fixed in 5% glutaraldehyde in cacodylate buffer pH7.4 for 0.5 h, rinsed again in dist. water and dehydrated in increasing concentrations of ETOH. The sponges were critical point dried, sputter-coated with platinum and examined at 15Kev in a Vickers LE2100 SEM.

To assess the bacteriostatic properties of the sponges TSYE agar Petri plates were prepared and seeded with an inoculum of L. innocua. Sterile sponge squares were placed in the centre of the plate which was incubated for 24 h. After incubation, clear zones were noted around the perimeter of the sponge squares denoting growth inhibition. The size of the clear zone around each sponge was measured.

SEM observations of different sponge samples indicated that there were differing degrees of bacterial attachment and growth. In some cases, there was very little bacterial attachment observed (Fig.1), whereas in another sample more bacteria were attached but no growth was visible (Fig.2). In some samples, considerable attachment and growth was noted (Fig.3). When these results were compared with the bacterial test results, it was found that the sponge samples with little or no bacterial attachment demonstrated the greatest area of bacterial inhibition (3-7mm) whereas the greater numbers of attached bacteria (with no growth) were observed in sponges that had a small but definite inhibition zone around them. However, the greatest degree of attachment and growth was observed in sponges

whose duplicate showed no inhibitory properties on the agar plates. The results of these tests indicate that some sponges possess a diffusible bacteriostatic agent that can affect the ability of bacteria to attach to their surface.

References:

1. Zobell, C.E., J. Bacteriol. (1943) 46, 39.
2. Dunsmore, D.G. and Thomson, M., J. Food Prot. (1981) 44, 21.
3. Zottola, E. A., J. Food Prot. (1986) 49, 856.
4. Llabres, C. M. and Rose, B. E., J. Food Prot. (1989) 52, 49.

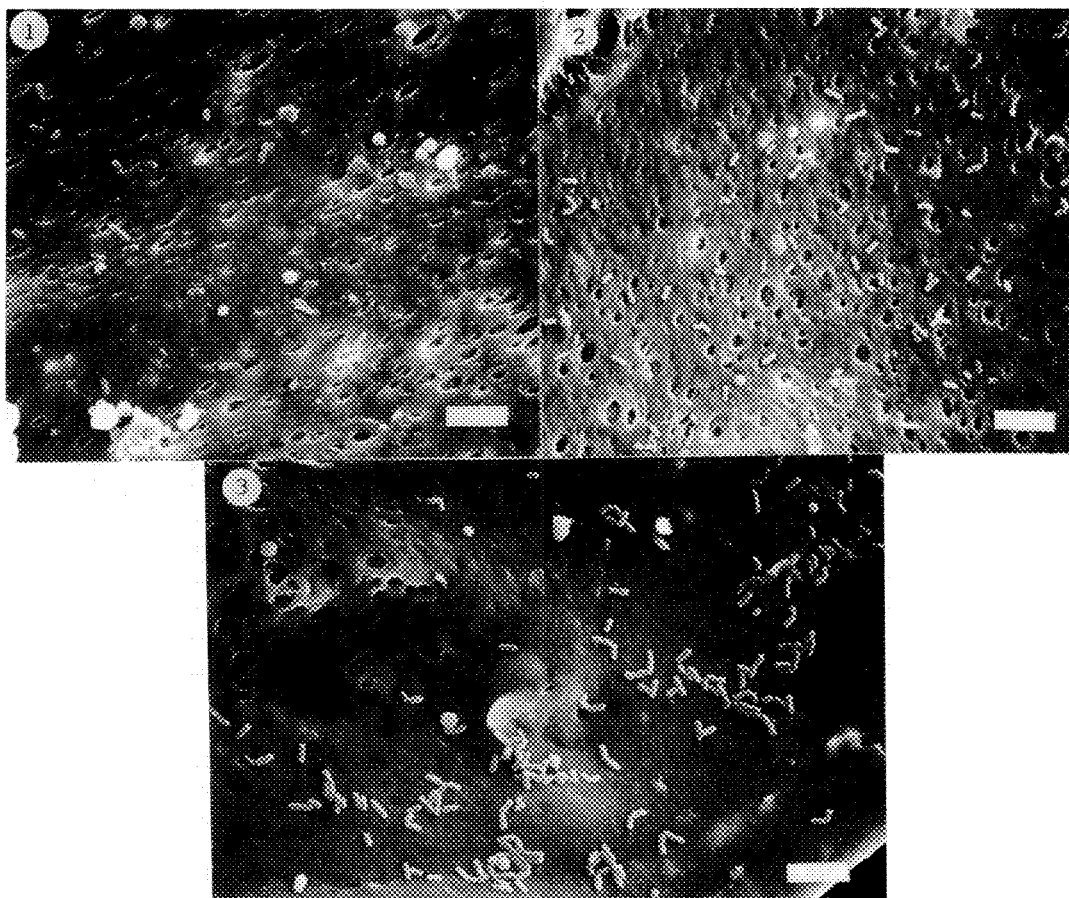


Fig.1. Few attached bacteria can be observed on surface of this sample and identical sample on agar plates showed greatest area of inhibition (3-7mm). Bar = 5.5 μ m.

Fig.2. More attached organisms can be observed on this sponge than was noted in previous figure. The zone of inhibition of duplicate sample on agar was very narrow (1-3mm). Bar = 5.7 μ m.

Fig.3. Large numbers of attached bacteria can be observed on this sample with considerable growth evident. No inhibition was noted with duplicate sponges on agar plates. Bar = 4.8 μ m.

RAPID DEMONSTRATION OF SEPTIC OR INFECTIOUS ARTHRITIS DUE TO GRAM-NEGATIVE BACTERIA

Jacob S. Hanker*, Paul R. Gross** and Beverly L. Giammara***

*Biomedical Engineering Dept., University of North Carolina, Chapel Hill, NC 27599-7455

**Dermatology Department, Pennsylvania Hospital, Philadelphia, PA 19107

***Analytical Electron Microscopy Labs., Graduate Programs & Research University of Louisville, Louisville, KY 40292

Blood cultures are positive in approximately only 50 per cent of the patients with nongonococcal bacterial infectious arthritis and about 20 per cent of those with gonococcal arthritis (1). But the concept that gram-negative bacteria could be involved even in chronic arthritis is well-supported (2). Gram stains are more definitive in staphylococcal arthritis caused by gram-positive bacteria than in bacterial arthritis due to gram-negative bacteria. In the latter situation where gram-negative bacilli are the problem, Gram stains are helpful for 50% of the patients; they are only helpful for 25% of the patients, however, where gram-negative gonococci are the problem. In arthritis due to gram-positive Staphylococci, Gram-stained smears are positive for 75% of the patients (1).

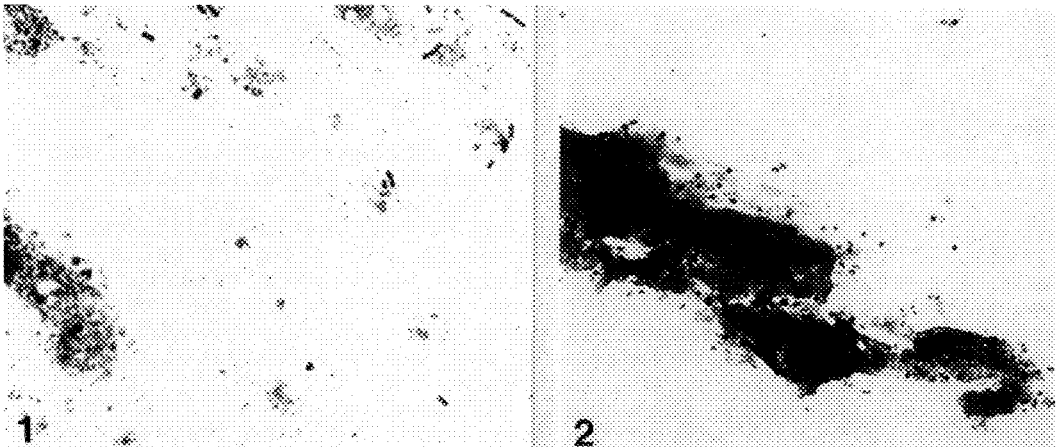
It appears, therefore, that due to the difficulty in discerning gram-negative bacteria with the Gram stain, or in culturing them, that other tests should be applied to classify bacteria that could be responsible for bone or joint pain in chronic or septic arthritis. The PATS reaction, developed by Giammara et al. (3) has been found useful by Giammara and Hanker (4,5) for the positive staining and differentiation of gram-negative bacteria. The silver deposited on gram-negative bacteria by this reaction can be examined on glass slides or coverslips by electron microscopy as well as light microscopy with techniques developed by Giammara et al. (6,7). This reaction has been useful in demonstrating gram-negative bacteria in aspirates or smears from infection sites such as those of periodontal disease (5) and burns (8). It was thought, therefore, that it might also be of value for examining samples obtained from secondarily infected sites of arthritis patients.

In two infections in an adult foot, Gram-stained smears showed nothing definitive with respect to gram-positive or gram-negative bacteria. With the PATS reaction, however, gram-negative coccobacilli (Figs. 1,2) were readily apparent in replicate smears. These could be due to Kingella kingae (Moraxella kingae) which is known to be important in the pathogenesis of bone and joint infections in children (9) and has more recently been implicated in adults (10,11). This could permit the initiation of therapy with antibiotics such as penicillin, to which Kingella are sensitive, prior to confirmation of the microscopic diagnosis by culture.

Although fungal infections are rare in arthritis (12), replicate smears should be stained by the Sigma Silver HT100 stain when arthritic infections could be caused by parasites such as fungi or protozoa.

References

1. D.L. Goldenberg and J.L. Leed. Bacterial arthritis. *New Eng. J. Med.* **312**, 764-771 (1985).
2. J.B. Winfield and W.N. Jarjour. Stress proteins, autoimmunity and autoimmune disease. *Curr. Top. Microbiol. Immunol.* **167**, 161-189 (1991).
3. B. Giammara et al. Periodic acid-thiocarbohydrazide-silver methenamine(PATS) reaction. *Proc. 42nd Ann. Meet. Electr. Microsc. Soc. Amer.* 264 (1984).
4. B. Giammara et al. Positive stain for light and electron microscopic demonstration of spirochetes in subgingival plaque and crevicular fluid samples from periodontal diseased sites. *Proc. 47th Ann. Meet. Electr. Microsc. Soc. Amer.* 1082 (1989).
5. J. Hanker et al. Positive staining of outer membrane lipopolysaccharides of gram-negative bacteria: microscopic image analysis to estimate the disease status of periodontal sites. *Microscopy Res. and Technique*, in press.
6. B. Giammara et al. Hexamethyldisilazane drying for rapid detection of bacteria in implant specimens. *Proc. 45th Ann. Meet. Electr. Microsc. Soc. Amer.* 878 (1987).
7. B.L. Giammara and J.S. Hanker. Xerographic-assisted location of areas or structures on clinical slides for electron microscopic examination. *Proc. 50th Ann. Meet. Electr. Microsc. Soc. Amer.*, submitted.
8. J.S. Hanker et al. The prompt demonstration without culturing of gram-negative bacteria in burn wound infections. *Proc. 49th Ann. Meet. Electr. Microsc. Soc. Amer.* 120 (1991).
9. Ronald de Groot et al. Bone and joint infections caused by *Kingella kingae*: six cases and review of the literature. *Revs. Infect. Dis.* **10**, 998-1004 (1988).
10. J. Rosenbaum et al. *Moraxella* infect. arthritis: first report in an adult. *Ann. Rheum. Dis.* **39**, 184-185 (1980).
11. A-M. Verbruggen et al. Infections caused by *Kingella kingae*: report of four cases and review. *J. Infect.* **13**, 133-142 (1986).
12. H.W. Murray et al. *Candida* arthritis. *Am. J. Med.* **60**, 587-595 (1976).



Figs. 1 and 2. Gram-negative coccobacilli, positively stained by the PATS reaction, are readily observed in smears from the foot of an arthritis patient. X800.

IMMUNOGOLD STUDY OF THE DIFFERENTIATION OF MALIGNANT HUMAN HEMATOPOIETIC CELLS

Etienne de Harven and Hilary Christensen

Department of Pathology, University of Toronto, Banting Institute, Toronto, Ontario, M5G 1L5, Canada

The sequential steps in the differentiation of hematopoietic cells may be characterized from several viewpoints, i.e. the appearance of specific ultrastructural features, of enzymes and/or of surface antigens. Megakaryocyte (MKC) progenitors develop alpha granules, surface protrusions and demarcation membranes (1) even before reaching the polyploid stage. They also express on their surfaces a platelet glycoprotein usually referred to as the 2b/3a complex. Monoclonal antibodies (mAbs) which recognize this glycoprotein are commercially available. Moreover, a monoclonal antibody against the 3a part of the complex (CD61) is, reportedly (2), expressed early in megakaryocytic differentiation.

It is difficult to collect megakaryocyte progenitor cells from normal bone marrow specimens. However, in cases of megakaryoblastic leukemia (M7, in the FAB classification) cells at various stages in MKC differentiation are present in the peripheral blood and can be readily concentrated by centrifugation on Ficoll-Hypaque gradients.

Pre-embedding labelling with 5 nm colloidal gold markers was used in a study of 6 cases of megakaryoblastic leukemia (M7). Peripheral blood leucocytes (PBLs) were primed with a murine mAb anti-CD61 (Y2/51, Dakopatts, Denmark), treated with goat antibodies against murine IgG₁ conjugated with 5 nm gold markers (GAM-G5, Janssen, Belgium) and then processed for TEM according to routine procedures (3). For relative quantification of the expression of the CD61 antigen, the number of gold markers was counted per 1 µm of cell contour, as originally recommended by Geoghegan (4). Counts were made on micrographs taken at 75,000X original magnification, selecting areas of the cell contour cut almost perpendicularly to cell surfaces. Since comparisons were made between cells observed in the same thin sections, errors resulting from variability in section thickness was presumably eliminated for comparative studies.

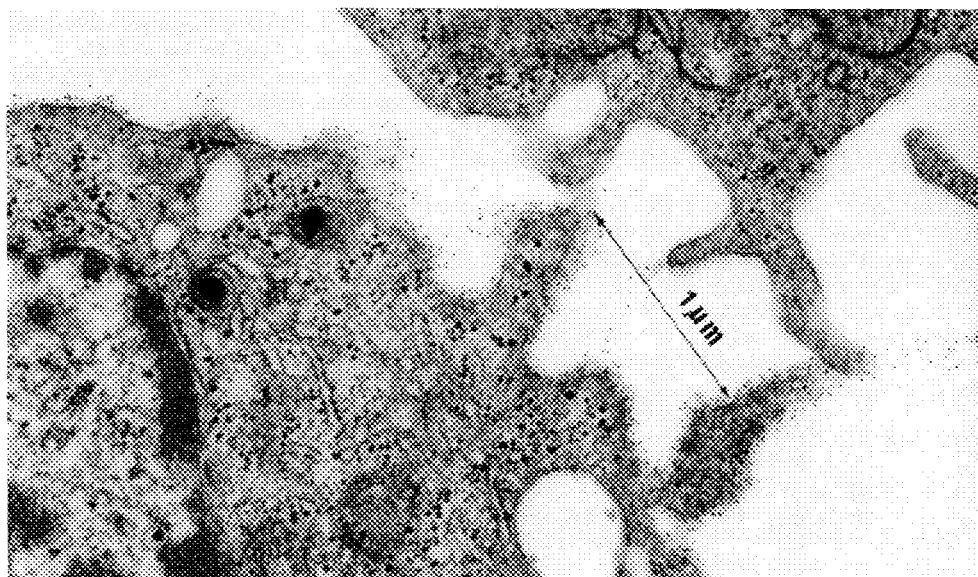
Leukemic cells were classified ultrastructurally in the following groups: 1) cells with no feature of differentiation, 2) cells with alpha granules, 3) cells with demarcation membranes, and 4) cells with broad surface protrusions. Considerable variations in levels of CD61 expression was observed in each group of cells. In addition, many primitive hematopoietic cells were clearly CD61 negative. Expressing the results as percentages of the labeling density observed on adjacent platelets was initially thought to be interesting. This mode of expression was, however, rejected for two reasons: a) there is no data indicating that the density of CD61 expression increases throughout differentiation (5), and b) platelets being much smaller than megakaryoblasts the frequency of oblique sectioning gives false impressions of high labeling density.

In conclusion, 1) labeling for CD61 permits the recognition of early megakaryoblasts which could not be identified by routine TEM, 2) the earliest blasts are probably CD61 negative, 3) the M7 leukemia cells do not appear to be blocked at one stage of megakaryoblastic differentiation, and 4) in M7 leukemia, the steps of megakaryoblastic differentiation cannot be correlated with levels of expression of CD61. Instead, differentiation of M7 cells appears extremely anarchic. Future studies will, hopefully, demonstrate whether or not this anarchic differentiation is restricted to malignant megakaryoblasts or whether it is also present in normal megakaryoblastic maturation. Study of umbilical cord primitive hematopoietic cells (5), with double labeling for CD61 and CD34, may prove informative in this respect.

References

1. Breton-Gorius, J., Reyes, F., Duhamel, G. et al.. Blood 51,45-60, 1978.
2. Koeller, O., Maas, W. D., Ludwig, J. et al. Proc. 82nd Am. Assoc. Cancer Res., vol.32, abs.1069, 1991.
3. de Harven, E. and Soligo, D. in Colloidal Gold, M. A. Hayat, ed., Academic Press, San Diego, 1989, Vol. 1, pp.230-249.
4. Geoghegan, W. D. and Ackerman, G. A. J. Histochem. & Cytochem.25:1187-1200, 1977.
5. Zucker-Franklin, D., Yang, JS., and Grusky, G. Blood 79:347-355, 1992.
6. The support of the Leukemia Research Research Fund, Toronto, Ontario, throughout these studies has been greatly appreciated.

Fig.1 Megakaryoblast with alpha granules, the surface of which is heavily labeled for CD61. Arrows indicate a 1 μ m stretch of cell contour used for counting purposes.



HEMOLYSIS OF ERYTHROCYTES BY THE HEMOLYTIC SYSTEM FROM THE BLOOD-FEEDING STABLE FLY, *STOMOXYS CALCITRANS*

H.J. Kirch,^a G. Spates,^a R. Droleskey,^a W.J. Kloft,^b and J.R. DeLoach^a

^aFood Animal Protection Research Laboratory, Agricultural Research Service, U.S. Department of Agriculture, Route 5, Box 810, College Station, TX 77845, U.S.A. and ^bInstitute for Applied Zoology, University of Bonn, An der Immenburg 1, D-5300 Bonn 1, Germany

Blood feeding insects have to rely on the protein content of mammalian blood to insure reproduction. A substantial quantity of protein is provided by hemoglobin present in erythrocytes. Access to hemoglobin is accomplished only via erythrocyte lysis. It has been shown that midgut homogenates from the blood feeding stable fly, *Stomoxys calcitrans*, contain free fatty acids and it was proposed that these detergent-like compounds play a major role as hemolysins in the digestive physiology of this species.¹ More recently sphingomyelinase activity was detected in midgut preparations of this fly, which would provide a potential tool for the enzymatic cleavage of the erythrocyte's membrane sphingomyelin.² The action of specific hemolytic factors should affect the erythrocyte's morphology. The shape of bovine erythrocytes undergoing *in vitro* hemolysis by crude midgut homogenates from the stable fly was examined by scanning and transmission electron microscopy.

The hemolysis of an erythrocyte solution by midgut homogenate from stable flies displayed a sigmoidal-like pattern. After a lag phase erythrocyte lysis increased dramatically at a rapid almost linear rate, before hemolysis finally stopped. Erythrocytes exposed to midgut homogenate immediately changed from normal biconcave discs (Fig. 1) into echinocytes (Fig. 2). This transformation was accompanied by the release of microvesicles from the erythrocyte's membrane. Before the erythrocyte population entered the phase of rapid cell lysis, the membrane spicules of echinocytes became blunt and membrane invaginations appeared (Fig. 3, arrow). With the beginning of cell lysis, smooth spherocytes were formed, which subsequently increased in number (Fig. 4). Some of these spherocytes had a single hole in their membrane. Transmission electron microscopy revealed that these holes were about 1 μ m in diameter (Fig. 5, arrows). Electrical cell sizing did not show any increase in cell volume during the transition from normal discocytes into spherocytes. Moreover, cell volume slightly decreased. However, by estimating the surface areas of discs and spheres, about 25-30% of membrane area is lost from the cells before lysis. The instantaneous change from discocytes to echinocytes could be suppressed if bovine serum albumin was added to the assay medium. In parallel the time required for completed hemolysis was delayed considerably in the presence of albumin.

The change from discocytes into echinocytes and the shape preserving effect of albumin strongly support the hypotheses of detergent-like material being involved in hemolysis. Many amphiphiles like fatty acids induce echinocytosis immediately³ which can be counteracted by the detergent-absorbing effect of albumin.⁴ The large membrane invaginations might be interpreted as a morphological marker for the participation of sphingomyelinase activity.⁵ However, we suggest that spherocytosis is caused by decreasing the cell surface area with respect to the cell volume. It is uncertain whether the loss of surface area can be completely attributed to the release microvesicles. Cell surface reduction would induce heavy mechanical stress inside the membrane which finally leads to membrane rupture.

References

1. G.E. Spates et al., Insect Biochem. 12(1982)707
2. G.E. Spates et al., Archs Insect Biochem. Physiol 14(1990)1
3. B. Deuticke, Biochim. Biophys. Acta 163(1968)494
4. H. Helenius and K. Simons, Biochim. Biophys. Acta 415(1975)29
5. H. Ikezawa et al, Arch. Biochem. Biophys. 199(1980)572

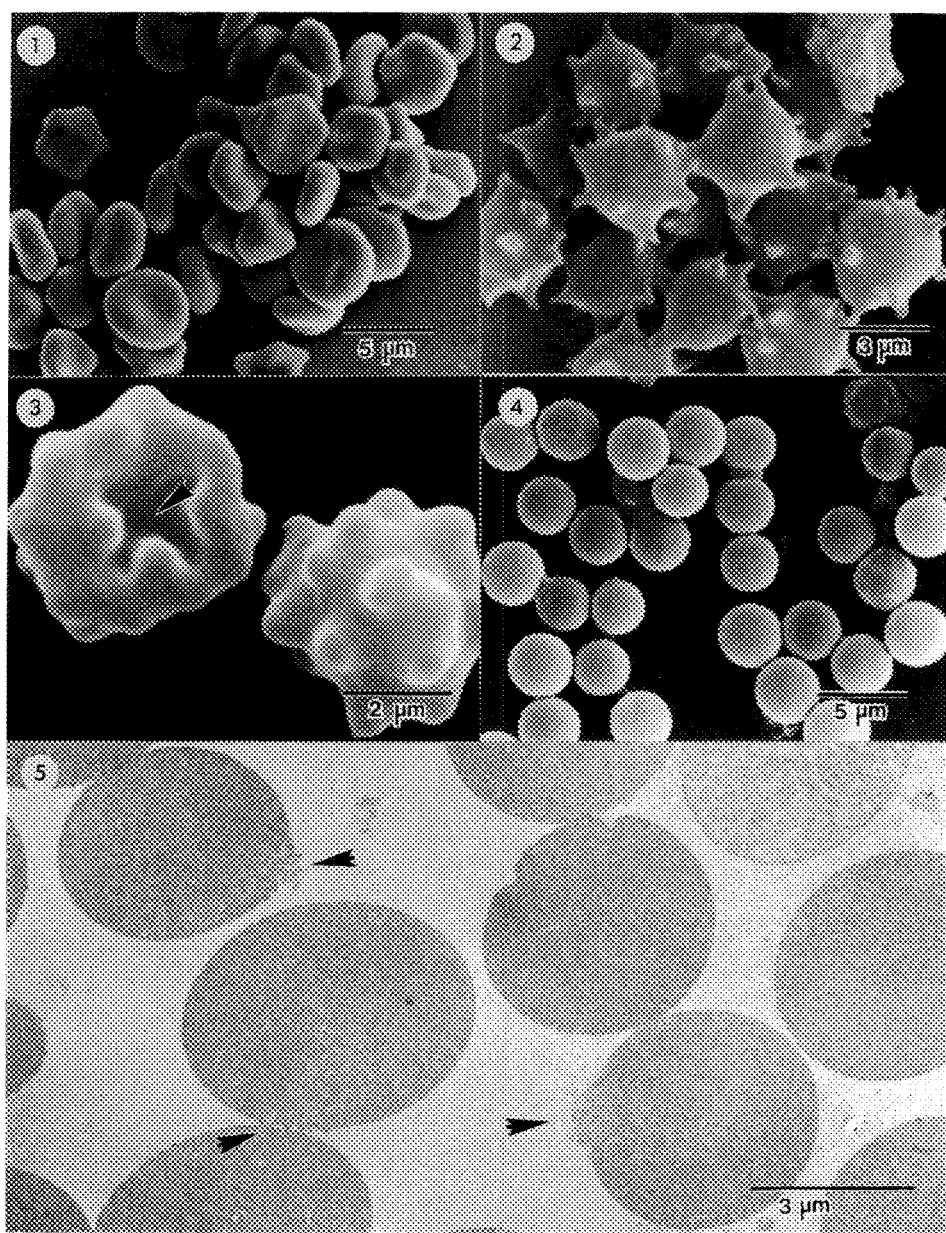


Fig. 1. Normal biconcave erythrocytes.

Fig. 2. Erythrocytes exposed to midgut homogenate change immediately into echinocytes.

Fig. 3. Erythrocytes before the onset of rapid cell lysis with membrane invaginations

Fig. 4. Erythrocytes during the period of rapid cell lysis are spherocytic.

Fig. 5. Thin section through erythrocyte spheres showing areas of damaged plasma membrane.

ENCAPSULATION BY HYPOTONIC DIALYSIS: THE ROLE OF ENDOCYTOSIS

Robert E. Droleskey,* Kathleen Andrews,* Laura Chiarantini,** and John R. DeLoach*

*USDA-ARS, Food Animal Protection Research Laboratory, Route 5, Box 810, College Station, TX 77845 and **Institute di Chimica Biologica, Università degli Studi, Via Saffi, 2, 61029 Urbino, Italy

Encapsulation of compounds by hypotonic dialysis is thought to occur via diffusion in which pores appear in the erythrocyte membrane when they are subjected to reduced osmotic pressure.¹ Under certain conditions encapsulation may also occur to some degree via endocytosis.²⁻⁵ It has recently been reported that the drug methotrexate may be entrapped primarily by endocytosis and secondarily by passive diffusion when erythrocytes were prepared via hypotonic dialysis.⁶ The objective of this study was to determine to what extent endocytic vesicles appear at specific stages of the hypotonic dialysis process.

Human and mouse erythrocytes, three replicates each, were subjected to slow hypotonic dialysis under the appropriate conditions for the production of carrier erythrocytes. Resealed, annealed, annealed cells after one wash in either hypotonic or isotonic buffer,⁷ and carrier cells from both of the washed annealed populations were fixed in 1% isoosmotic glutaraldehyde for examination using transmission electron microscopy. Sections were randomly photographed at the same magnification, 10/sample, negatives enlarged to the same final magnification and the percentage of cells in each field containing endocytic vesicles determined by a third party. Only those erythrocytes containing two or more vesicles were counted as having endocytic vesicles.

Vesicles did not appear to any significant degree until the annealed stage for human erythrocytes (Fig. 1), which was at maximum, while vesicles first appeared at the resealed stage of mouse erythrocytes. Mouse annealed cells (Fig. 2) contained almost 50% more cells with vesicles than did resealed cells (Table 1). Maximum endocytosis for mouse cells was found to occur after annealed cells were washed once in isotonic buffer. Human annealed cells washed once in hypotonic buffer had significantly lower percentage of cells containing vesicles than did annealed cells washed in isotonic buffer. At the carrier cell stage there was no significant difference in the percentage of cells containing vesicles for either species. The results of this study show that only approximately 10% of all carrier cells contain endocytic vesicles and that the process of endocytosis is a dynamic process which probably can not be controlled to reduce the formation of endocytic vesicles.

References

1. J. R. DeLoach, *Med. Res. Rev.* 6(1986)487.
2. S. L. Schrier, in R. Green and K. J. Widder, Eds., *Methods in Enzymology*, Orlando, Academic Press (1987).
3. I. Ben-Bassat et al., *J. Clin. Invest.* 51(1972)1833.
4. L. M. Matovcik et al., *Blood* 65(1985)1056.
5. J. T. Penniston and D. E. Green, *Arch. Biochem. Biophys.* 128(1968)339.
6. C. A. Kruse et al., *Biotechnol. Appl. Biochem.* 11(1989)571.
7. L. Chiarantini et al., *Blood Cells* 17(1991)607.

Table 1. Percentage of cells from specific stages of the encapsulation process with endocytic vesicles.

Cell encapsulation stage	% Cells with vesicles	
	HUMAN	MOUSE
Resealed	0.0 ^a	4.8 ± 5.0 ^a
Annealed	15.4 ± 4.2 ^b	9.0 ± 3.6 ^{b,c}
Hypotonic 1 st wash	7.7 ± 4.5 ^c	8.1 ± 3.7 ^c
Isotonic 1 st wash	12.1 ± 5.7 ^d	12.6 ± 6.3 ^b
Carrier, hypotonic	10.3 ± 4.4 ^d	8.4 ± 4.8 ^c
Isotonic carrier	11.1 ± 4.1 ^d	9.7 ± 3.9 ^{b,c}

Note. Data are $\bar{x} \pm SD$ (n = 30). Data in same column followed by a common letter superscript are not significantly different (P > 0.05).

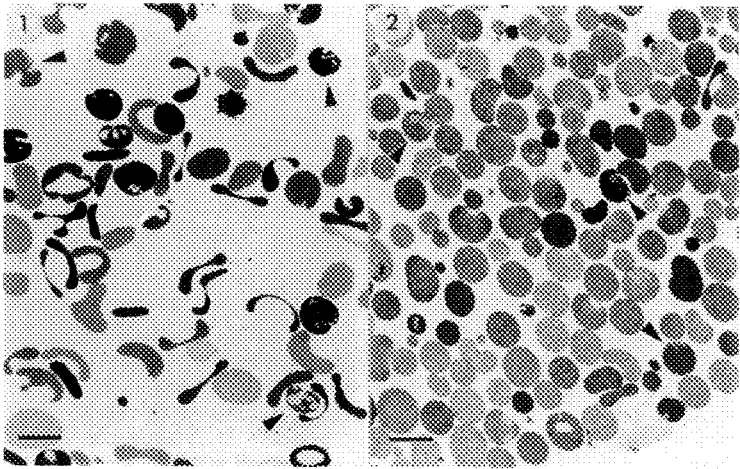


Fig. 1--Transmission electron micrograph of human resealed cells. Arrowheads indicate cells containing endocytic vesicles. Bar = 5 μ m.
Fig. 2--Transmission electron micrograph of mouse resealed cells. Arrowheads indicate cells containing endocytic vesicles. Bar = 5 μ m.

PHASE BEHAVIOR OF CATIONIC AND ANIONIC SURFACTANTS AT LOW CONCENTRATIONS

E. Naranjo

Department of Chemical and Nuclear Engineering, University of California, Santa Barbara, California 93106

Equilibrium vesicles, those which are the stable form of aggregation and form spontaneously on mixing surfactant with water, have never been demonstrated in single component bilayers and only rarely in lipid or surfactant mixtures¹. Designing a simple and general method for producing spontaneous and stable vesicles depends on a better understanding of the thermodynamics of aggregation, the interplay of intermolecular forces in surfactants, and an efficient way of doing structural characterization in dynamic systems.

Recently Kaler et al.¹ demonstrated the existence of spontaneous vesicles in aqueous mixtures of single-tailed cationic and anionic surfactants such as cetyltrimethylammonium tosylate (CTAT) and sodium dodecylbenzene sulfonate (SDBS). Vesicle formation is believed to result from the production of anion-cation surfactant pairs. Due to the strong electrostatic interactions between the oppositely charged headgroups present in cationic/anionic surfactant mixtures, the geometric packing ratio can be effectively tailored by varying the ratio of cationic to anionic surfactant².

An important unanswered question is the structural evolution of vesicles from the micellar species found along the water rich sides of the phase diagram. We have examined the phase behavior of CTAT and SDBS mixtures along a dilution path from the vesicle rich phase to the micellar phase³ with freeze-fracture transmission electron microscopy (TEM), dynamic light scattering, and differential scanning calorimetry. Surface tension measurements have determined a critical vesicle concentration CVC at a total surfactant concentration of 0.004 mM, independent of the CTAT/SDBS. The CMC of pure CTAT is 0.27 mM at 40°C and that of pure SDBS is 2.8 mM at 25°C^{1,3}. Samples are prepared by mixing CTAT and SDBS at CTAT/SDBS of 3/7 and 7/3 with deionized water to form total lipid concentrations of 1.2, 0.012, and 0.0012 mM. For freeze-fracture TEM, thin films of the sample liquid were trapped between copper planchettes and rapidly frozen from 25°C by plunging into liquid propane cooled by liquid nitrogen. The samples were fractured at -170°C and 10⁻⁷ Torr and replicated with platinum and carbon in a Balzers 400 freeze-etch device and cleaned by standard procedures⁴.

We find that the SDBS-rich solutions (CTAT/SDBS = 3/7) show a rather polydisperse population of vesicles 80 nm in diameter for 1.2 mM and 104 nm for 0.12 mM. In addition to vesicles, small spherical aggregates are also observed in the plane of the replica (fig. 1). Vesicles of similar size (60-80 nm) have also been observed at higher concentrations (~ 5 mM)³. In contrast, the CTAT-rich samples (CTAT/SDBS = 7/3) appear to be unstable with dilution as evidenced by a large increase in aggregate size. Figure 2 shows multilamellar vesicles with an average diameter of 1.4 μ m in the 1.2 mM solution. Larger (1.8 μ m) but more sparse MLV's are observed in the 0.012 mM sample. This increase in the hydrodynamic diameter of CTAT-rich solutions has also been observed in QLS measurements during 1 to 3 month periods. Vesicles in a 0.0012 mM solution, however, are smaller (270 nm) but are polydisperse and still much larger than observed at higher concentrations.

The strong interaction between CTAT and SDBS in aqueous solution manifests itself in a dramatic change in the formation of equilibrium vesicles over a range of compositions. The presence of an excess of either CTAT or SDBS has a significant effect on the stability of the spontaneous vesicles.

This interaction, we believe, should be investigated further. Equilibrium vesicle stability appears to be the result of an enhanced repulsive interaction between bilayers. Possible explanations range from enhanced undulation to hydration repulsion³. Further experimental characterization to discriminate between the effects of CTAT and SDBS could suggest new formulations for stable vesicles.

- 1) Kaler, E.W., Murthy, A.K., Rodriguez, B.E., & Zasadzinski, J.A.N. (1989) *Science* 245, 1371-1374.
- 2) Israelachvili, J.N., Mitchell, D.N., & Ninham, B.W. (1976) *J. Chem. Soc. Faraday Trans. II* 72, 1525-1568.
- 3) Kaler, E.W., Herrington, K.L., Murthy, A.K., Zasadzinski, J.A.N. (1991) *J. Phys. Chem.*, submitted.
- 4) Zasadzinski, J.A.N., & Bailey, S. (1989) *J. Electron Microscopy Technique* 13, 309-319.

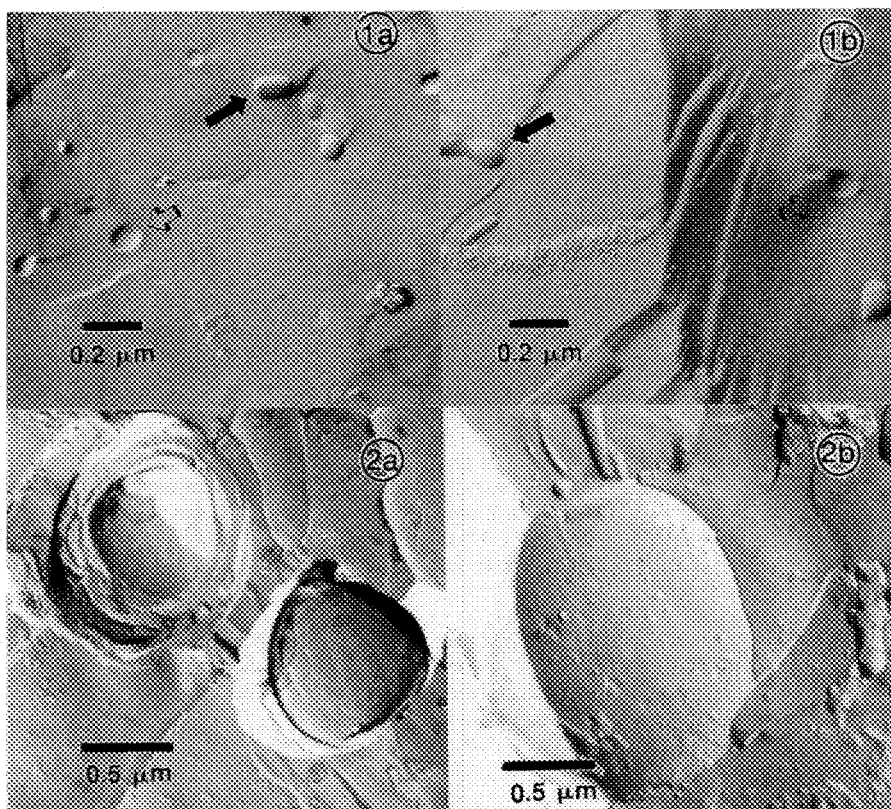


Figure 1. TEM images of freeze-fractured SDBS-rich vesicle fraction with (a) 1.2 mM and (b) 0.012 mM surfactant. Average vesicle diameter is 80 nm in (a) and 104 nm in (b). Open arrows show shadow pattern of vesicle plucked from the fracture surface, filled arrows shows shadow pattern of vesicle protruding from the surface.

Figure 2. TEM images of freeze-fractured CTAT-rich vesicles with (a) 1.2 mM and (b) 0.012 mM surfactant. Average vesicle diameter is 1.4 μm in (a) and 1.8 μm in (b).

DYNAMICS OF MEMBRANOUS ORGANELLES IN THE MITOTIC APPARATUS OF TWO CELL TYPES: A LIVE-CELL, LASER-SCANNING CONFOCAL STUDY

Clare M. Waterman-Storer, Jean M. Sanger and Joseph W. Sanger

Laboratory for Cell Motility Studies, Department of Anatomy and Pennsylvania Muscle Institute,
University of Pennsylvania, Philadelphia, PA 19104-6058

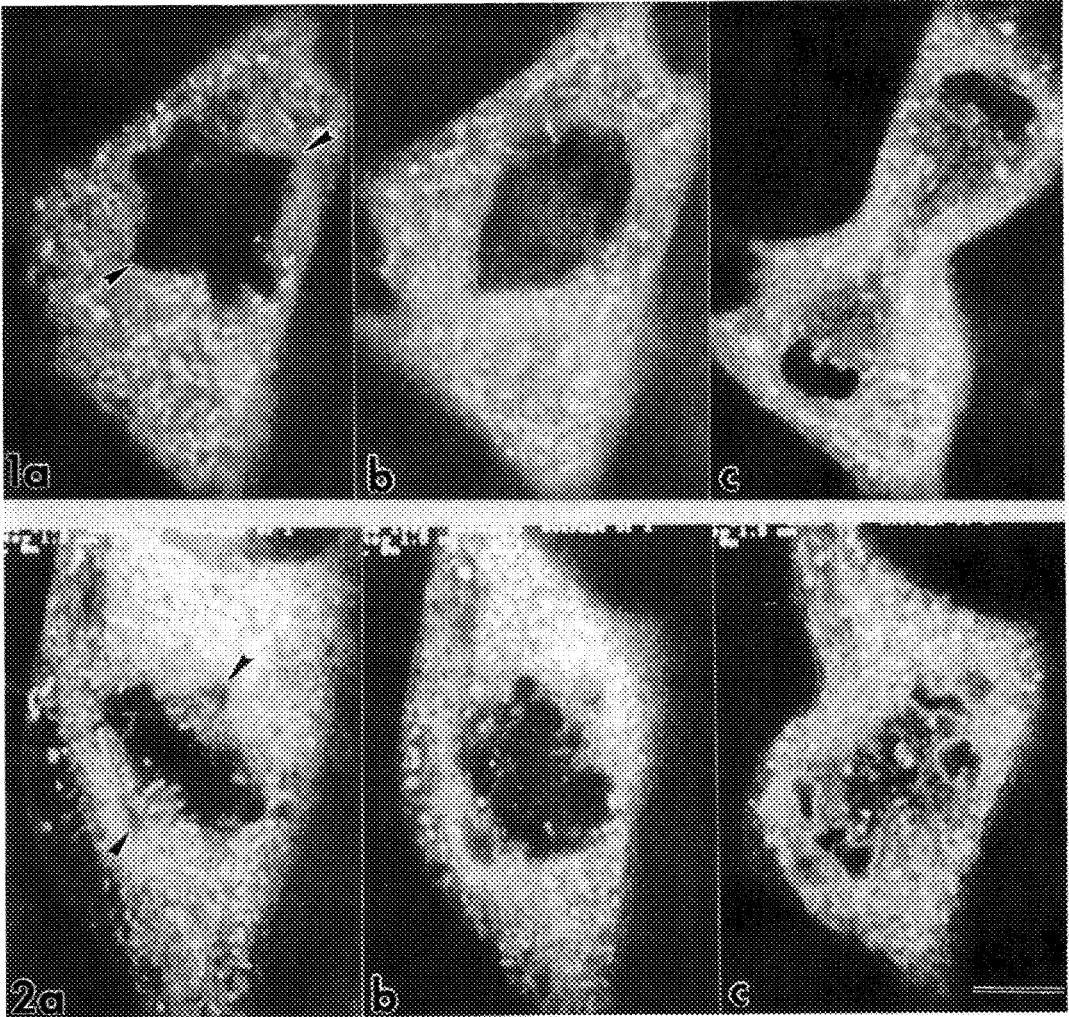
Membranous organelles comprise a large proportion of the living cell's cytoplasmic volume. In interphase, the endoplasmic reticulum (ER), mitochondria, and Golgi apparatus are characterized by a typical distribution in the cytoplasm. When cells enter M-phase, however, the cytoplasmic architecture undergoes dramatic rearrangements, as the nuclear envelope (NE) breaks down and the mitotic spindle assembles. During this process, the typical distribution of the membrane systems must be disrupted, so as to accommodate the cytoplasmic rearrangements. The role of membranous organelles within and around the mitotic apparatus has been a source of active investigation, as well as controversy. It is not known if membranes are an ubiquitous structural element of the spindle^{1,2}. Here, we present a laser-scanning confocal study of membrane dynamics in living mitotic cells, demonstrated by the fluorescent vital membrane dye 3,3'-dihexyloxacarbocyanine iodide (DiOC₆(3))³. By exploiting the thin focal planes achieved by the confocal microscope, the precise distribution of membranes within the spindle was attained in the two epithelial cell lines; PtK2 and LLC-PK. This study demonstrates that the distribution and quantity of cytoplasmic organelles within the spindle of living cells is cell-type specific.

Cultured cells (either PtK2 or LLC-PK) grown on coverslips were incubated for 5-15 minutes at 37°C in culture media containing 1.25 µg/ml DiOC₆(3). Excess dye was washed out, and the coverslips of cells were mounted on slides in culture media containing 0.3 units/ml Oxyrase® free radical scavenger. The cells were observed at 35-37°C on a Nikon Optiphot microscope equipped with the Bio-Rad MRC-500 confocal laser scanning head; illumination was provided by the 488 nm line of an argon ion laser. Z-series of single-scan optical sections of mitotic cells were taken every 1-2 minutes throughout cell division, with the pinhole aperture set as small as possible. Images were processed using the MRC-500 software; a 5x5 crispening convolution was applied to images prior to photographing them on a Polaroid Freeze-Frame video recorder. To compare membrane distribution within the mitotic spindles of the two cell types, the optical section that contained the centrioles (defined by a small circular region devoid of membranes at the spindle pole) was used as a reference, as that section necessarily would be through the central plane of the spindle.

Membrane distribution began to change from the onset of prophase in both cell types; as the cell rounded up, the lacy network of the cortical ER coalesced into vesicles which surrounded the nucleus. Following NE breakdown, as the mitotic spindle formed, fine reticululae lined up along kinetochore fibers. As cells achieved metaphase, differences in the two cell lines became apparent. PtK2 cells demonstrated a near absence of membrane staining within their well defined, diamond-shaped spindle; a few thin tubules penetrated the half-spindle from the centriolar region, running parallel to the spindle's long axis (fig 1a). Conversely, spindles of LLC-PK cells contained a plethora of tubular and small vesicular membranous structures, which extended from the centrioles to the chromosomes (fig 2a). As chromosome segregation proceeded, the interzone remained relatively devoid of membranes until the onset of anaphase B, whereupon membranous structures converged around the interzone (figs 1b&c, 2b&c). As cytokinesis commenced, organelles were excluded from the midbody by the contractile ring. Immunofluorescence staining with anti-tubulin suggests that membranes were associated with microtubules throughout mitosis. In addition, introduction of the microtubule-stabilizing drug, taxol, induced denser and more extensive arrays of membranous structures within the spindles of both cell types. Together these results suggest that the differences in membrane distribution between the two cell types examined may be determined by differences in the quantity of microtubules within the spindle.

References

1. J.M. Sanger et al., *Cell. Motil. Cytoskeleton* **13**(1989)301.
2. P.K. Hepler and S.M. Wolniak, *Int. Rev. Cytol.* **90**(1984)169.
3. M. Terasaki et al., *Cell* **38**(1984)101.
4. This research was sponsored by grants from the National Institutes of Health to J.W.S. and the National Science Foundation to J.M.S.



FIGS. 1-2.--Time-lapse, single scan confocal image of the membrane distribution within two dividing cells as demonstrated by the vital dye, DiOC₆(3). Chromosome position can be visualized as a non-staining negative image. The optical sections shown contain the central plane of the spindle, as indicated by the inclusion of the spindle poles (arrows). FIG. 1 shows three stages of mitosis in a PtK2 cell, metaphase (a), anaphase A (b) and telophase (c). Notice the near absence of fluorescent staining in the metaphase and anaphase spindles. FIG. 2 demonstrates the same phases of mitosis (a-c) in an LL-CPK cell. Membranes are much more abundant in the spindle of this cell type. Bar = 10 μ m.

CONFOCAL LASER SCANNING MICROSCOPICAL INVESTIGATION OF EPITHELIAL MEMBRANE POLARITY IN 3-DIMENSIONAL MDCK MULTICELLULAR CYSTS

Allan Z. Wang,¹ Jane C. Wang and Herbert S. Diamond

Medical Research Laboratory, Western Pennsylvania Hospital Foundation Research Institute, Pittsburgh, PA 15224

We have previously described the process of membrane polarity formation and reversal in MDCK epithelial cysts (Fig.1) using immunofluorescent staining on frozen sections. Apical surface of polarized epithelial cells faced the growth media and basal surface faced the cyst lumen by locating membrane domain-specific proteins (Fig.2).² Polarity reversal was demonstrated by showing that polarized distribution of membrane proteins were reversed after the suspension-cultured cysts were transferred into collagen I gel embedding (Fig.3). There was loss of endogeneous basal membrane protein and appearance of apical membrane protein at the luminal surface, indicating a novel mechanism for de novo formation of apical domain in the multicellular cysts.³

We now report the result of confocal laser scanning microscopy (CLSM). To study the 3-dimensional profile of membrane polarity formation and reversal in epithelial cells, cysts either formed by MDCK cells in suspension culture or transferred from suspension into collagen gel for 36 hours were stained with antibody against tight junction polypeptide ZO-1. The images were taken by a high resolution cooled CCD camera in a Zeiss CLSM for video-enhanced contrast or epi-fluorescent imaging, and processed with a Perceptics image processor and a Microvax computer front end. We scanned MDCK cysts with a Z-axis step size of 0.1 μm by Argon laser beam at 488 nm for FITC channel and at 514 nm for TRITC channel.

When scanning at the upper pole of suspension cultured MDCK cysts, linear staining of ZO-1 was shown between the adjacent cells (Fig.4). Linear distribution gradually disappeared, and was replaced by dotted staining between the adjacent cells close to the external surface of the cysts when scanned deeply at the median part of the cysts (Fig.5). Then linear staining gradually reappeared towards the bottom of the cysts (Fig. 6). When scanning started from either the top or the bottom of the cysts transferred into collagen gel, least fluorescent staining could be detected (Fig. 7,9). However, ZO-1 staining was seen at the center of the cysts with dotted staining between the adjacent cells near the lumen surface (Fig. 8). These results indicate that ZO-1 localizes between the adjacent cells close to the apical membrane domain of MDCK cysts grown in suspension culture. Relocalization of ZO-1 to the luminal side occurs when the cysts are transferred from suspension to gel embedded-culture. This confirms our previous reports derived from the 2-dimensional studies. The results also provide a 3-dimensional stereo images of ZO-1 in MDCK cysts, and this 3-D rendering provides additional information in respect to the process and mechanism of transport and fusion of multiple vesicles containing tight junction polypeptide into a polarity-reversed new lumen during a change of environment from suspension to gel-embedded culture.⁴

References:

1. Author for correspondence

2. A. Z. Wang et al., J. Cell Sci. 95(1990)137
3. A. Z. Wang et al., J. Cell Sci. 95(1990)153
4. This research was supported by grants from the Western Pennsylvania Hospital Foundation F-1011 and facilities in the NSF Science and Technology Center at Carnegie Mellon University DIR-8920118.

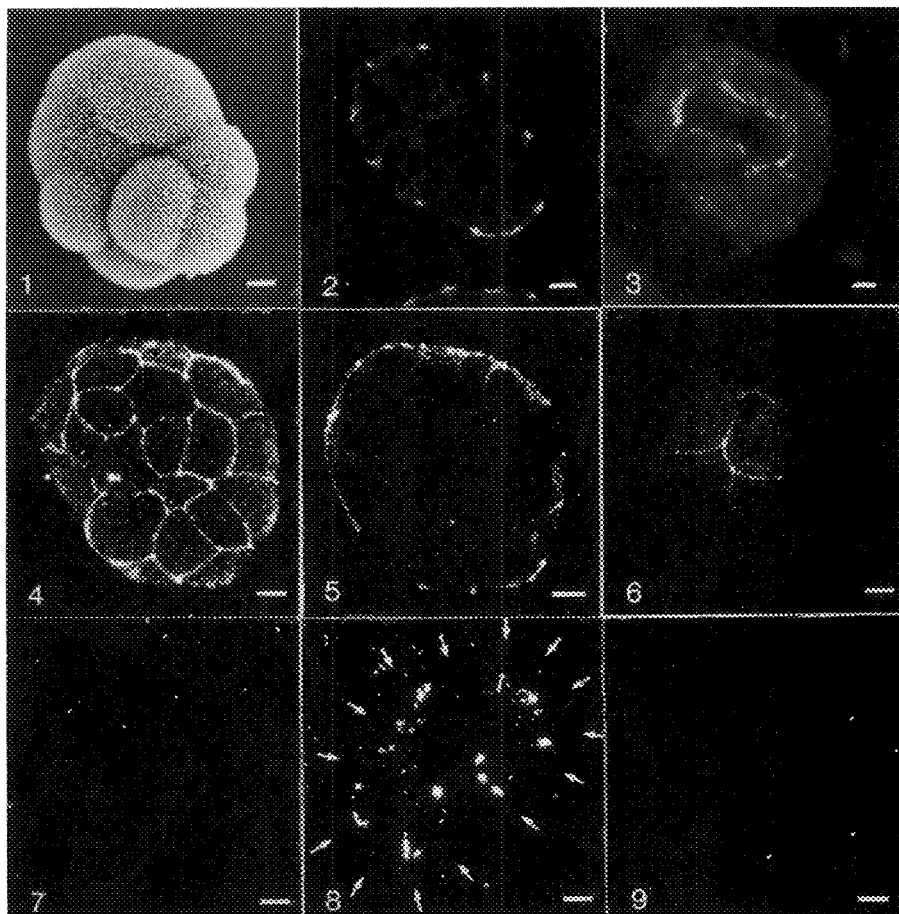


Fig. 1. -- SEM of MDCK cyst grown in suspension culture. Bar = 10 μ m
 Fig. 2. -- Immuno-staining of ZO-1 on MDCK cyst grown in suspension. Bar = 10 μ m
 Fig. 3. -- Immuno-staining of ZO-1 on MDCK cyst embedded in collagen type I gel for 24 h after transferred from suspension culture. Bar = 10 μ m
 Fig. 4-6. -- Confocal Laser Scanning Microscopy (CLSM) of ZO-1 images at upper pole (Fig.4), median part (Fig.5), and bottom pole (Fig.6) of MDCK cysts well-formed in suspension culture. Bar = 10 μ m.
 Fig. 7-9. -- CLSM of ZO-1 images at upper pole (Fig.7), median part (Fig.8) and bottom pole (Fig.9) of MDCK cysts embedded in collagen I gel for 36 h after transferred from suspension culture. Arrows indicate external surface of cyst. Bar = 10 μ m

ULTRASTRUCTURAL EVIDENCE OF SINK FUNCTION OF CENTRAL CANAL OF SPINAL CORD AS DEMONSTRATED BY CLEARANCE OF HORSERADISH PEROXIDASE

T.H. Milhorat, S. Nakamura, I. Heger, F. Nobandegani, S. Murray

Departments of Neurosurgery, State University of New York Health Science Center, Brooklyn 11203 USA, and Nihon University School of Medicine, Tokyo 179 JAPAN

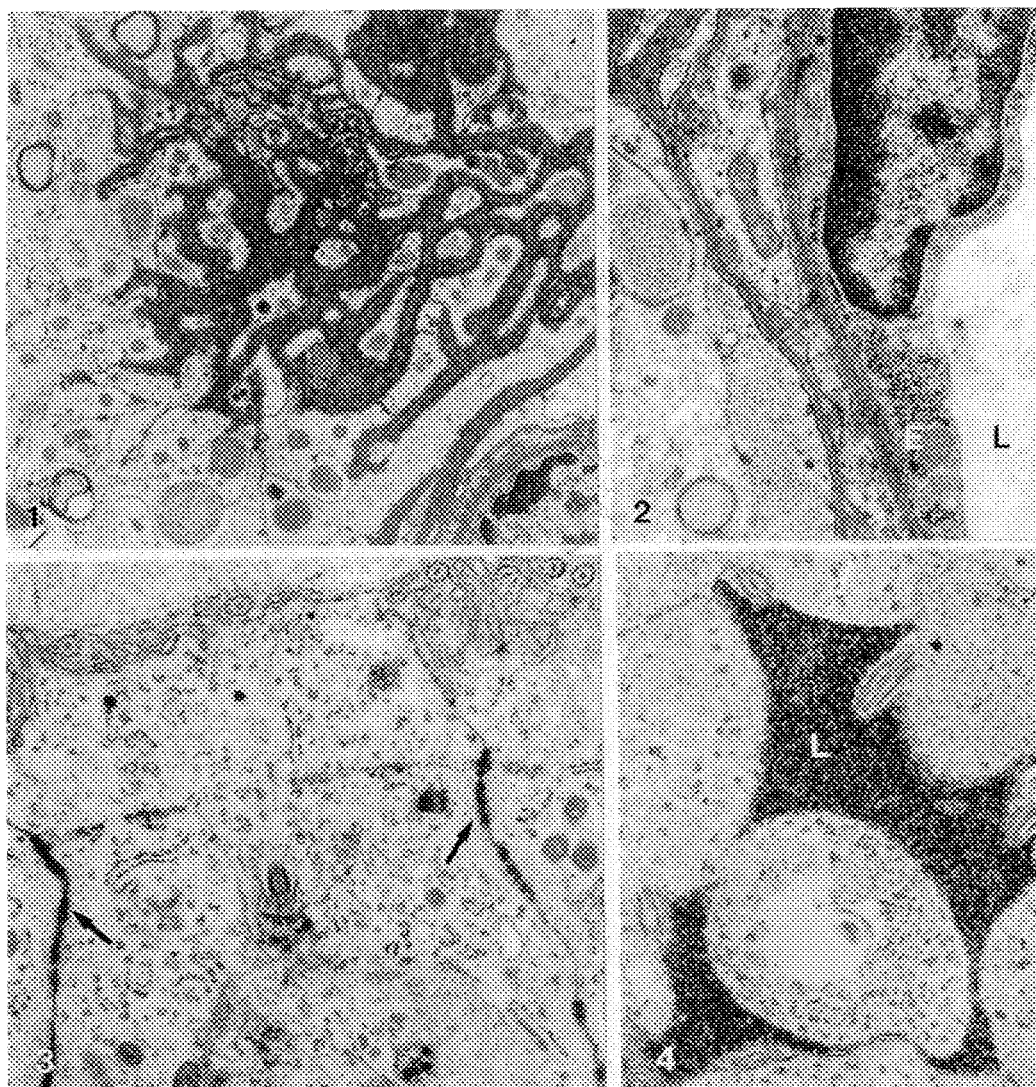
It has been recently reported that when Evan's blue dye is microinjected into the spinal cord, or when it is injected into blood following freeze lesioning of the spinal cord, the marker passes rapidly from the parenchyma into the central canal, and drains rostrally to the fourth ventricle (1). This pattern of clearance is similar to the clearance of blood and blood products in experimental hematomyelia (2), and suggests that the central canal functions as a sink for the extracellular compartment of the spinal cord.

In this study, 2ul of horseradish peroxidase (HRP) was microinjected into the dorsal columns of the thoracic spinal cord of rats using a previously described stereotactic technique (2). At intervals ranging from 10-60 minutes, the animals were perfused through the heart with 1% paraformaldehyde and 1% glutaraldehyde in 0.12M phosphate buffer. The spinal cords were removed *en bloc* and cut into 2cm axial sections which were immersed in fixative for a minimum of 7 days. Thereafter, the specimens were washed with a buffered solution of 0.1M Cacodylate (pH 7.2) and cut on a micro slicer (DTK-1000) to a thickness of 40um. The sections were incubated at room temperature in a saturated solution of 3,3' diaminobenzidine (free base) in 0.05 Tris-HCL buffer (pH 7.6) containing 0.001% H₂O₂, washed in distilled water, and post-fixed for 120 minutes in 2% OsO₄ in 0.4M phosphate buffer containing 5% glucose. The tissue was dehydrated in graded methanol and embedded in Epon 812. Thin sections were cut on an LKB Ultratome, stained with uranyl acetate and lead citrate, and examined under an electron microscope (JEM 1200 EX).

At the injection site, the reaction product of HRP was present within the extracellular clefts and lakes of the spinal cord parenchyma (Fig. 1), around the basement membrane of capillaries (Fig. 2), and within the intercellular clefts between adjacent ependymal cells (Fig. 3). The gap junctions joining ependymal cells appeared to provide no restraint to the movement of HRP. Within 60 minutes, the reaction product of HRP was visualized within the central canal 1 cm rostral to the injection site (Fig. 4). These findings demonstrate that the extracellular spaces of the spinal cord are anatomically continuous with the lumen of the central canal for molecules as large as HRP (molecular wt. 40,000 radius 25-30 Å), and provide an ultrastructural basis for clearance by sink action.

References

1. T.H. Milhorat et al., International Symposium on Hydrocephalus (1991), Tokyo, Springer Verlag, 199.
2. T.H. Milhorat et al., J. Neurosurg. (1991), 75, 911.



- Fig. 1. At 10 minutes, reaction product of HRP fills extracellular clefts and lakes in spinal cord parenchyma near injection site. x10,000.
- Fig. 2. Reaction product is present around basement membrane of endothelial cell (E). There is no reaction product present within capillary lumen (L). x24,000.
- Fig. 3. Reaction product fills intercellular clefts (arrows) between adjacent ependymal cells and extends to apical surface at 30 minutes. x20,000.
- Fig. 4. At 60 minutes, reaction product fills lumen (L) of central canal 1 cm rostral to injection site. x16,000.

ULTRASTRUCTURAL STUDY OF UPTAKE OF MONASTRAL BLUE BY THE PULMONARY INTRAVASCULAR MACROPHAGES OF SHEEP IN THE PRESENCE AND ABSENCE OF SURFACE COAT

B. Singh*, D. S. Jassal**, O. S. Atwal* and K. Minhas*

* Dept. Biomedical Sc., Univ. Guelph, Guelph, ON N1G 2W1, Canada, ** Neonatal Division, Dept. of Paediatrics, Hospital for Sick Children Research Institute, Toronto, ON M5G 1X8, Canada

Pulmonary intravascular macrophage (PIM) is an important mononuclear phagocyte of some animal species (1). In sheep these cells are actively involved in the clearance of microbes and endotoxins (2). By treating the tissue with tannic acid we have identified at the ultrastructural level a unique globular surface coat, arranged at a distance of 30-40 nm from the cell periphery. This coat is hypothesized to be lipoprotein in nature as tannic acid complexes with the globules to enhance their electron density. This surface coat is highly sensitive to in vitro lipolytic lipase digestion and in vivo heparin treatment (1).

We have examined the role of surface coat in the phagocytosis by comparing the uptake of a tracer dye, monastral blue (MB), by the PIMs in the presence and absence of surface coat. In one group (n=2), MB (3% suspension of copper phthalocyanine in 0.9% normal saline, Sigma Co.) was injected at a dose of 0.2 ml/kg IV and sheep were euthanized with an overdose of pentobarbital sodium after 30 minutes. Second group (n=2) was treated with heparin (50 IU/kg IV) to disrupt the surface coat, followed by an injection of MB (0.2 ml/kg IV) after half an hour and subsequently euthanized. Lungs were fixed for half an hour in situ by pouring the fixative (2% glutaraldehyde and 2.5% paraformaldehyde in 0.1M HCL-Sodium cacodylate buffer, pH 7.4) into the lungs by cannulating the trachea. The tissue samples collected from lung and liver were diced into 1mm³ pieces and immersion fixed for 90 minutes. Tissue was processed routinely for the TEM except for its treatment with tannic acid for 30 minutes before osmication. The ultrathin sections were stained with uranyl acetate and lead citrate.

In the control sheep PIM was seen lying against the capillary endothelium with a globular surface coat all around it. Some of the surface coat was seen in the endosomes. In MB treated sheep the dye complexed with the globules and altered their morphology. This complex was carried into the lysosomes. The MB was present in its native form inside the kupffer cells of liver. The ultrastructure of dye in the PIMs of heparin treated sheep was same as in kupffer cells in the liver. There was no change in the morphology of MB in the kupffer cells after heparin treatment. These results suggest that particulate material is internalized by the PIMs after it complexes with the surface coat material.

References

1. O.S. Atwal et al., Am. J. Anat. (1989) 186, 285-299.
2. A.E. Brain et al., AM. Rev. Resp. Dis. (1987) 136, 683-690.

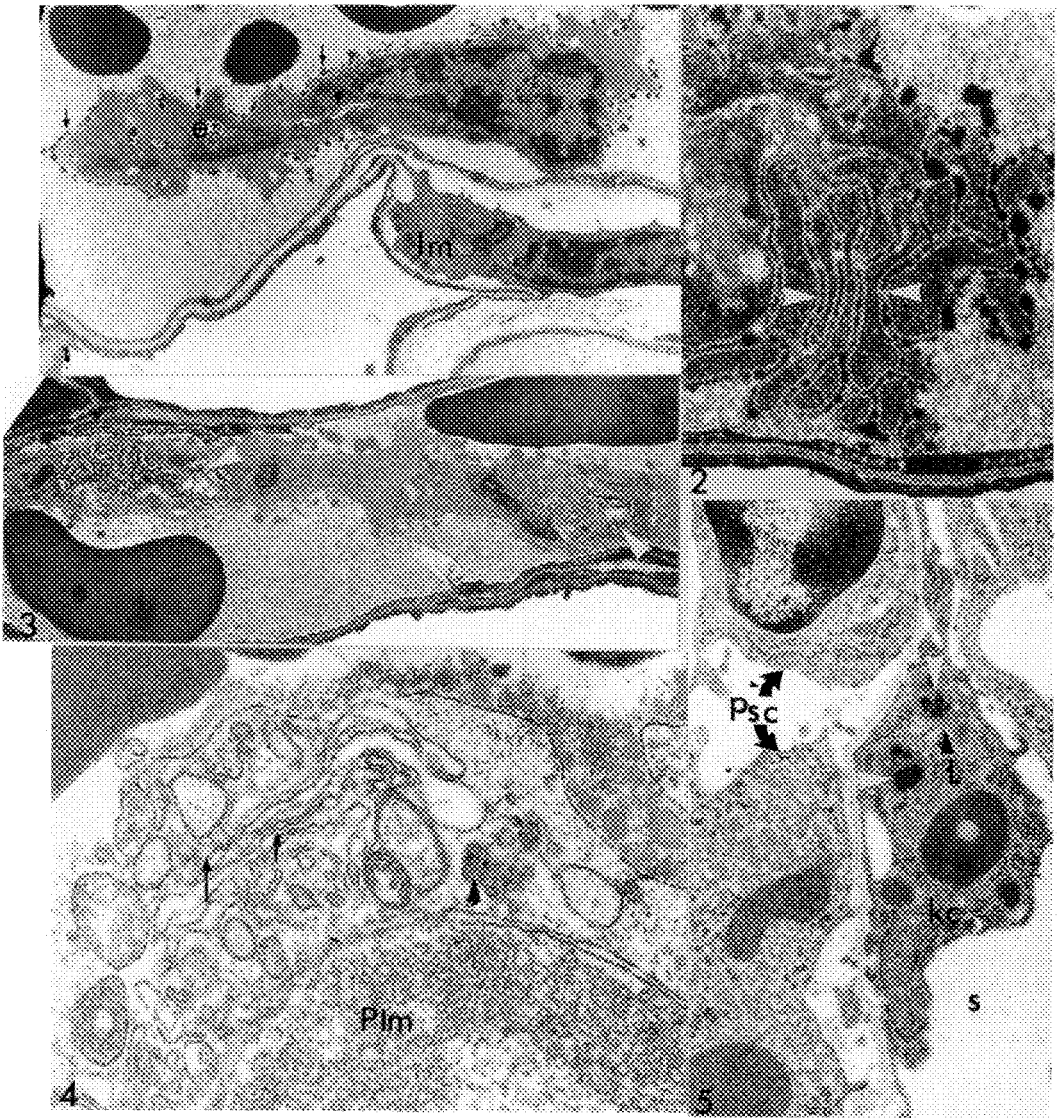


Fig. 1. TEM of a PIM from control sheep showing coat globules on the surface (arrows) and in the endosomes (e). Golgi cisternae (arrow head) are evident. Interstitial macrophage (Im) shows no surface coat. (X 7500)

Fig. 2. Electron micrograph of an edge of a PIM showing coat globules internalized through micropinocytosis vermiformis (arrow heads). (X 16000)

Fig. 3. Longitudinal view of a PIM demonstrating MB-surface coat complex inside the endosomes (arrowheads). (X 15000)

Fig. 4 Part of a PIM from a heparin treated sheep showing marked plasma membrane ruffling (arrows) and unmodified internalized dye particles (arrowhead). (X 35000)

Fig. 5. A kupffer cell (kc) having unaltered MB inside the lysosome (L-arrow). Perisinusoidal cell (psc) and sinusoidal space (s) are seen. (X 15000)

FISH KIDNEY CELL LINE IN RESPONSE TO HEAT SHOCK

Li-Chu Tung¹, Yung-Reui Chen², Shiu-Nan Chen³ and Guang-Hsiung Kuo³

1 Biology Department, National Taiwan Normal University, Taipei, Taiwan, ROC; 2 Botany Department and 3 Zoology Department, National Taiwan University, Taipei, Taiwan, ROC

In the present study, the ultrastructural changes of BPK cells, a fibroblast-like cell line, derived from the kidney of juvenile black porgy, *Acanthopagrus schlegelii*¹, under heat shock treatment are described.

The BPK cells were maintained in L-15 medium supplemented with 10% fetal calf serum and 0.15 M NaCl at 28°C. The heating was carried out in precalibrated water baths. Monolayers of cells, grown on coverslips in parafilm-sealed petri dishes were submerged under water for 30 min at 40°C treatments. Cells were fixed in 2.5% glutaraldehyde in 0.1 M cacodylate buffer supplemented with 6.6% sucrose, postfixed in 1% OsO₄ and flat embedded in Spurr's resin. Silver section were cut parallel to the substratum, stained with uranyl acetate and Reynold's lead citrate, and examined in a Hitachi H-600 electron microscope at 75 KV.

As shown in Figures 1 to 3, control cells shows well-developed profiles of membranes of endoplasmic reticulum (ER), prominent nucleus, elongated and convoluted mitochondria and other organelles. The central nucleus possesses a distinct and compact nucleolus with both the granular and fibrillar region. After the heat treatment, the deformities and irregularities in the fine structure of BPK cells were noted (Figs. 4,5,6). The cytoplasm revealed a more electron-transparent view and many vesicular structure with dilation and vesiculation apparently derived from ER were found. The mitochondrial vacuolation, fragmentation and degeneration with enlarged intracrestal spaces and swollen inner membrane were observed (Figs. 4,5). The changes of nucleus consists: more electron-transparent for nucleoplasm (Fig.4); swelling of the nuclear envelope; enlargement of the nuclear pore (Fig.4); segregation and degranulation of nucleoli (Fig.6).

Breakage of membranes and deformities of ER, nuclear envelope and mitochondria in heat-shock treated cells were well documented^{3,4}. Heat shock also demonstrate to be able to inhibit nucleolar function⁵. The change of nucleoli in heat-treated BPK cells might reflect a earlier stage of blockage for ribosome synthesis.

Reference

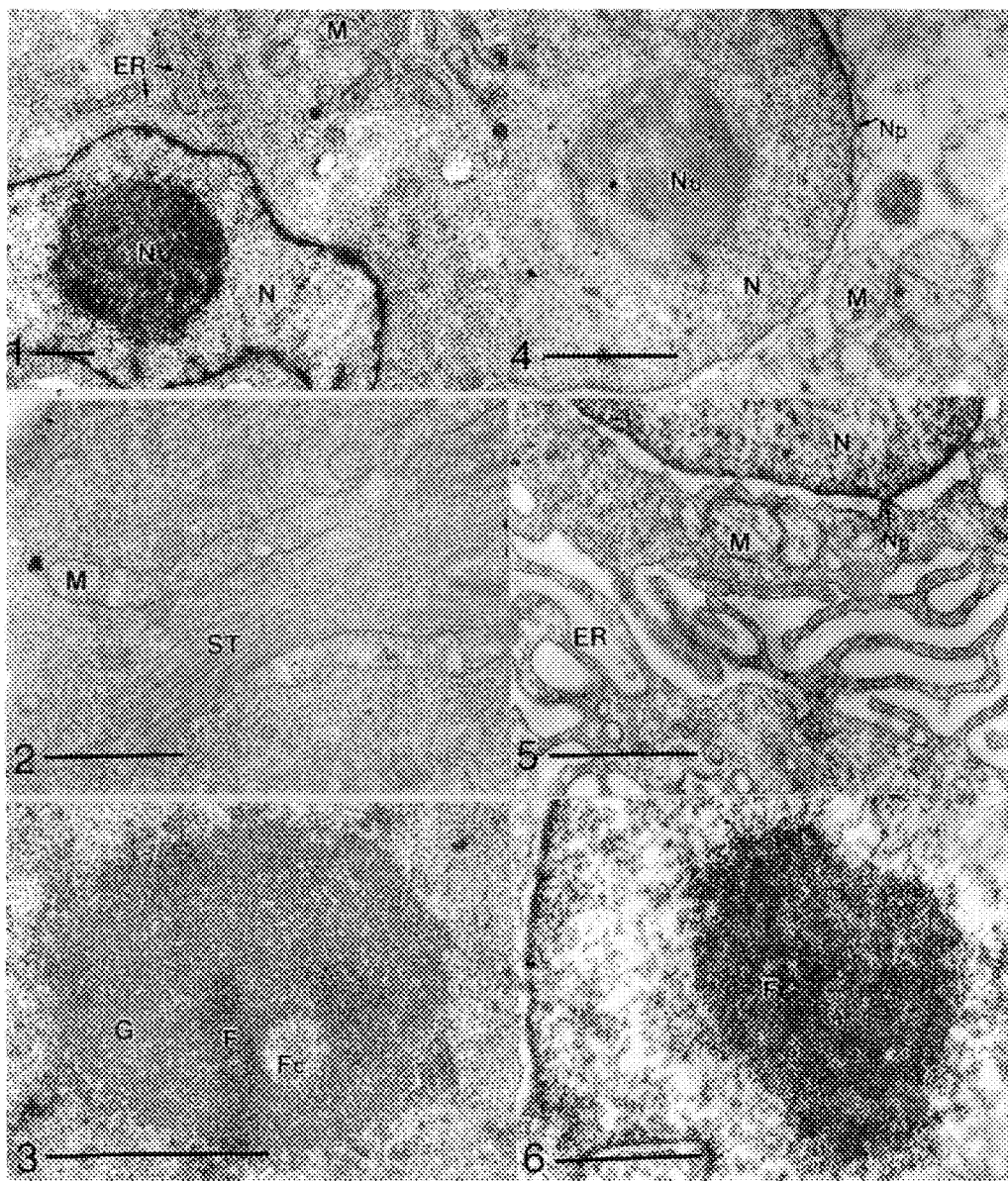
1. L. C. Tung et al., Fish Pathol. 26(1991)109.
2. L. C. Tung et al., Biol. Bull. NTNU 26(1992)42.
3. T. T. Shyy, et al., J. Cell Biol. 108(1988)997.
4. W. J. Welch, et al., J. Cell Biol. 101(1985)1198.
5. W. J. Welch, In "Heat shock proteins and immune response". S. H. E. Kaufmann (ed) Springer-Verlag Berlin (1991)31.

Figs. 1-3 Control BPK cells incubated at 28°C.

Figs. 4-6 BPK cells under heat treatment at 40°C for 30 min heat shock. Scales in 1 micrometer.

Abbreviations

F, Fibrillar region of nucleolus; Fc, Fibric center; G, Granular region of nucleolus; M, Mitochondrion; Mt, Microtubule; N, Nucleus; Np, Nuclear pore; Nu, Nucleolus; P, polysome; ST, Stress fiber.



GAP JUNCTIONS IN THE PROTHORACIC GLANDS OF THE TOBACCO HORNWORM, *MANDUCA SEXTA*

Ji-da Dai, M. Joseph Costello*, and Lawrence I. Gilbert

Departments of Biology and *Cell Biology & Anatomy, Univ. of North Carolina, Chapel Hill, NC 27599

Insect molting and metamorphosis are elicited by a class of polyhydroxylated steroids, ecdysteroids, that originate in the prothoracic glands (PGs). Prothoracicotrophic hormone stimulation of steroidogenesis by the PGs at the cellular level involves both calcium and cAMP (1). Cell-to-cell communication mediated by gap junctions may play a key role in regulating signal transduction by controlling the transmission of small molecules and ions between adjacent cells (2). This is the first report of gap junctions in the PGs, the evidence obtained by means of SEM, thin sections and freeze-fracture replicas.

The PG of *Manduca* is comprised of a homogeneous population of 200-250 very large cells (about 65 μm in diameter) which are interconnected and resemble a string of beads enclosed in a sheath, the basal lamina (Fig. 1). During development of the fifth instar larva, the cell size, shape and surface morphology of the PG undergo dramatic changes corresponding to steroidogenic activity of the glands (Siew, Rountree and Gilbert, unpublished data).

Conventional thin section analysis revealed that abundant cellular processes exist in the connecting area between cells and that they project deeply into the cytoplasm of the neighboring cell. Typical gap junctions are distributed in an organized manner, occurring on limited portions of the cell membrane, with preferential localization close to the distal end of these processes (Fig. 2). They are septilaminar structures with a central cleft 2-3 nm wide, similar in appearance to the 16-18 nm thick gap junctions found in other insect tissues (Fig. 3). The electron-dense strata of the septilaminar structures appear symmetric, i.e. each membrane is of the same thickness. There are cross-striations within this gap visible using *en bloc* uranyl acetate staining. Numerous multilamellar bodies are often seen in this area (Fig. 2). The size and frequency of both gap junctions and multilamellar bodies seem to be correlated with the animal's development stage or physiological state.

Freeze-fracture images of the region of contact between interdigitating processes reveals clusters of particles in the E face (Figs. 4 & 5). These clusters are most likely gap junctions based on their similarity to gap junction clusters reported for other insect organs (3). The clusters are often irregular in shape and the particles are always randomly arranged. Many of the particles are elongated, suggestive of dimers or bridging of adjacent particles, and these elongated particles are matched by a corresponding pattern of pits found in the P face (Fig. 5). Gap junctions, identified here using two morphological techniques, may promote the synchronization of secretory activity.

References

1. L.I. Gilbert et al., *BioEssays* (1988)8, 153.
2. P. Meda et al., *Mod. Cell Biol.* (1984)3, 131.
3. S. Caveney, in G.A. Kerkut and L.I. Gilbert, Eds., *Comprehensive Insect Physiology, Biochemistry and Pharmacology*, Vol. 2, New York: Pergamon Press (1985) 319.
4. This research was supported by grant DK-30118 from the National Institutes of Health.

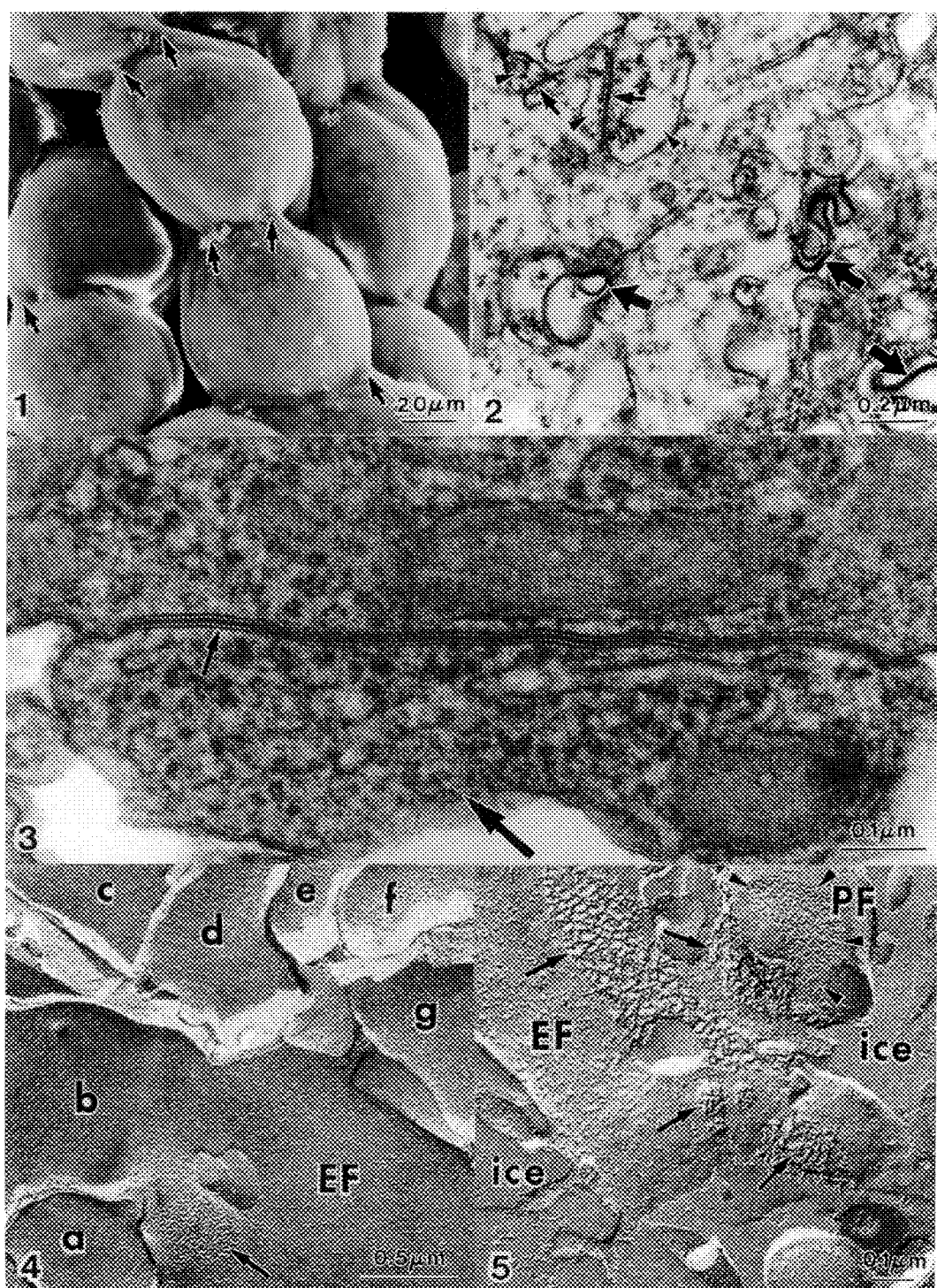
FIG. 1.--SEM of PG from a day 7 fifth instar larva, showing connecting area (arrows) between cells.

FIG. 2.--Thin section of the connecting area between cells of a day 3 fifth instar larva, showing the distal ends of cellular processes (arrowheads), gap junctions (sm. arrows) and multilamellar bodies (lg. arrows).

FIG. 3.--Thin section of the connecting area between cells of a day 7 fifth instar larva, showing a long gap junction (sm. arrow) and a projecting cellular process (lg. arrow).

FIG. 4.--Freeze-fracture image of several processes (a-g) all displaying E faces. A cluster of particles is indicated (arrow). Day 3 fifth instar larva. EF is E face fracture.

FIG. 5.--Freeze-fracture image of several clusters of particles on E faces (arrows) and one array of pits on a P face (arrowheads). Day 7 fifth instar larva. PF is P face fracture.



LOW-ANGLE SHADOWING AND COLLOIDAL GOLD-LABELING OF LIPOsome INTERACTION WITH THE EOSINOPHIL MAJOR BASIC PROTEIN

Margaret J. Hukee^{*,†}, Randa I. Abu-Ghazaleh,[†] and Franklyn G. Prendergast[†]

Electron Microscopy Core Facility^{*} and the Department of Biochemistry & Molecular Biology[†], Mayo Clinic & Foundation, Rochester, MN 55905

The eosinophil major basic protein (MBP) has been localized in the crystalloid core of the specific eosinophil granule.¹ High levels of MBP are present in sputa and at sites of epithelial damage in patients with bronchial asthma suggesting that MBP is released from the eosinophil. In vitro, the toxicity of MBP to mammalian cells, helminths, protozoa, and bacteria, has been demonstrated. MBP also induced the degranulation of platelets, basophils, and mast cells.¹ Since these events involve extracellular MBP and rupture of plasma membranes, the mechanism of toxicity may be due to a direct interaction between MBP and biological membranes. Fluorescence spectroscopy studies using synthetic lipid bilayers (liposomes) showed the ability of MBP to induce disorder, fusion and lysis of those membranes.² In this report, structural evidence is presented for liposome aggregation and possible lysis in the presence of MBP.

Using standard tip sonication techniques, liposomes were prepared from an equimolar mixture of 1 mM dimyristoylphosphatidylcholine (DMPC) and 1 mM dimyristoylphosphatidate (DMPA) in buffer containing 50 mM MOPS, 100 mM KCl at pH 7.4.² Native MBP (nMBP) or reduced and alkylated MBP (raMBP) were added to the liposomes to a final concentration of 10 μ M protein. Liposomes were adsorbed onto a carbon-coated grid, incubated with a rabbit antibody to MBP and labeled with goat anti-rabbit gold (15nm.) conjugate. This antibody has been used to localize MBP in eosinophil granules.³ After labeling, the liposomes were low-angle shadowed with platinum (80%) + palladium (20%), and examined by transmission electron microscopy. This method has been used successfully to label liposomes.⁴

When examining control liposomes in appropriate buffers (Figures 1 and 2), most were distributed singly but a few small aggregates were also found. Figure 3 shows the larger aggregates typical of those formed when nMBP and raMBP were each added to liposome preparations in the appropriate buffers. An interaction between nMBP and liposomes is shown in Figure 4. Some intact liposomes are present as well as liposomes that appear to be lysed. Figure 5 shows an aggregate induced by raMBP and labeled with antibody to MBP. Gold particles (arrows) were found on the surface of the aggregate and on smaller particles surrounding the aggregate that might represent free MBP. Liposomes without MBP were not labelled (Figure 6).

In conclusion, these findings support earlier data acquired with fluorescence spectroscopy,² and demonstrate that MBP can directly interact with acidic liposomes. These data support the theory that MBP released by eosinophils may target biological membranes when inducing cellular toxicity.

1. G. J. Gleich and C.R. Adolphson, *Adv. Immunol.* (1986) 39, 177.
2. R. I. Abu-Ghazaleh, G. J. Gleich, and F. G. Prendergast, *J. Memb. Biol.* (In Press).
3. M. S. Peters, M. Rodriguez, and G. J. Gleich, *Lab. Invest.* (1986) 54, 650.
4. J. Olive, O. Vallon, *JEMT* (1991) 18, 360.

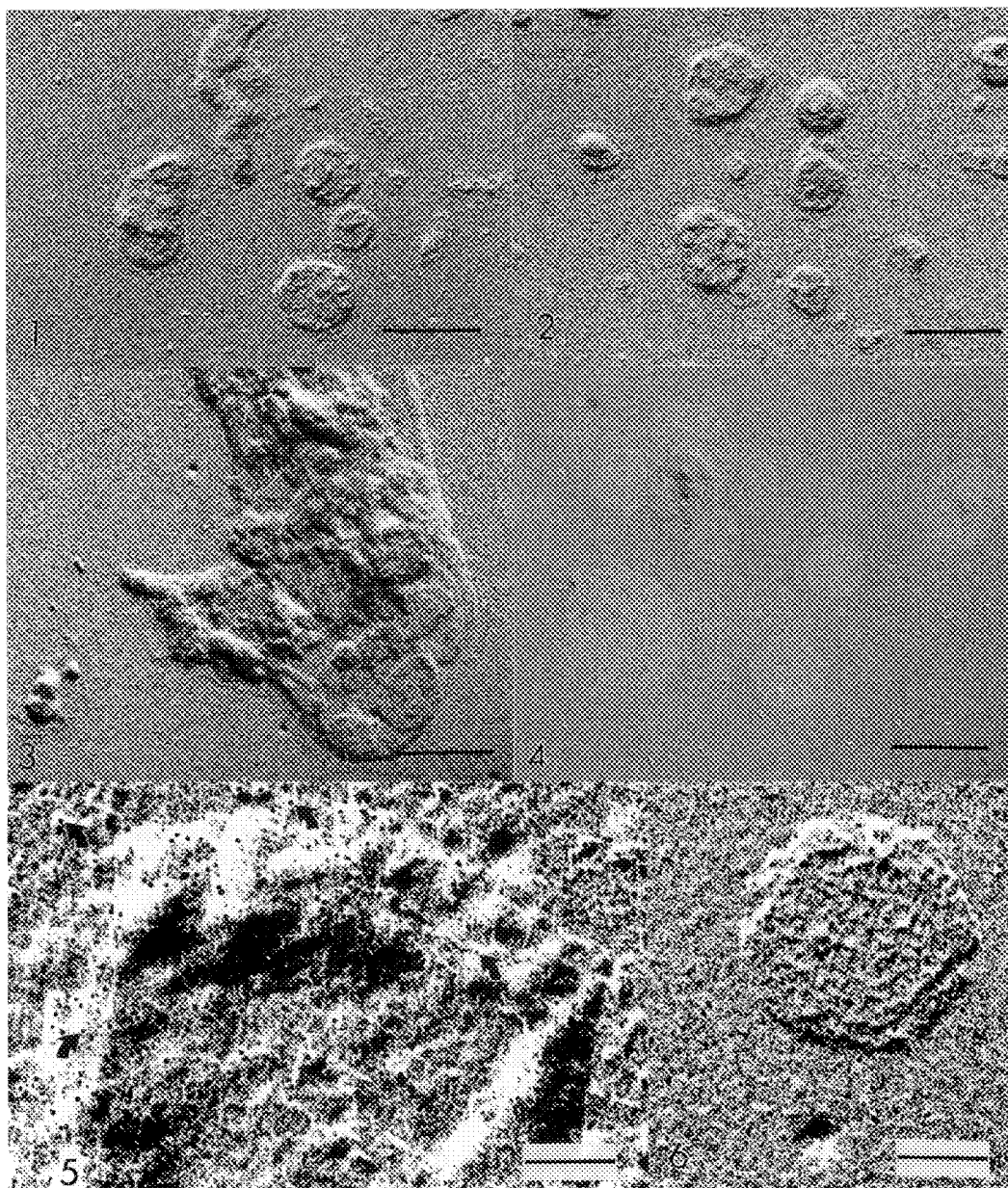


Figure 1: Control liposomes in buffer used for raMBP. Bar = 1 μ m.

Figure 2: Control liposomes in buffer used for nMBP. Bar = 1 μ m.

Figure 3: Liposomes + ra MBP showing aggregated liposomes. Bar = 1 μ m.

Figure 4: Liposomes + nMBP showing possible lysis of liposomes. Bar = 1 μ m.

Figure 5: Liposomes + raMBP and labeled with colloidal gold (arrows). Bar = 200 nm.

Figure 6: Liposomes with no protein and labeled with colloidal gold. Bar = 200 nm.

FREEZE-FRACTURE ELECTRON MICROSCOPY AND ENZYME ACTIVITY OF RECONSTITUTED CYTOCHROME OXIDASE

M. Tihova, B. Tattrie, & P. Nicholls

Department of Biological Sciences, Brock University, St. Catharines, Ont., L2S 3A1, Canada

Eukaryotic cytochrome oxidase (CO) is a multisubunit enzyme spanning the inner mitochondrial membrane. As the terminal component in the respiratory assembly it catalyzes the reduction of oxygen to water. The size, shape and other gross features of the 3-dimensional structure of this protein have been obtained only for its 2-dimensional crystal form.^{1, 2} The enzyme can be incorporated into liposomes of a defined lipid composition. Freeze-fracture electron microscopy of cytochrome oxidase vesicles (COV) has been combined with kinetic and spectroscopic measurements to study the phospholipid requirements for enzyme activity and protein orientation within the bilayers.

Cholate-dialyzed COV were prepared using beef heart enzyme with egg and synthetic phospholipids containing different hydrocarbon chains at two lipid to protein ratios. Fractionation on a positively charged (DEAE) column showed two main fractions: F-I, containing mainly empty vesicles, and F-II, containing mainly COV.

The enzyme orientation, its activity and its control by pH and potential gradients were used to determine the functional state of all the fractions. The mode of enzyme incorporation was characterized by size and shape distribution of the protein "bumps" on PVC replicas of freeze-fractured convex and concave surfaces. The areas of the individual protein particles as well as their contribution to the total vesicle area were determined using a Microcomputer Imaging Device (MCID) (Imaging Res. Inc.). An asymmetric height distribution of the protruding particles was well pronounced on the convex surfaces. COV have also been prepared with enzyme depleted of its third largest subunit (Subunit III). The size distribution of the III-depleted "bumps" indicated an average surface area half that of the undepleted system, suggesting the presence of a monomeric form of the enzyme which is normally dimeric in its undepleted state.

Tantalum-tungsten shadowing of the fractured samples is now being used to obtain images with higher resolution. These images may allow us to find out the arrangement of some of the subunits on the surfaces of the monomers and dimers.

Supported by NSERC(Canada) grant # A -0412 to Peter Nicholls.

References

1. R.A. Capaldi, S. Takamiya, Y. Zhang, D.G. Halphen & W. Yanamura, *Curr. Top. Bioenerg.* (1987) **15**, 91.
2. J. M. Valpuesta, R. Henderson and T. G. Frey, *J. Mol. Biol.* (1990) **214**, 237.

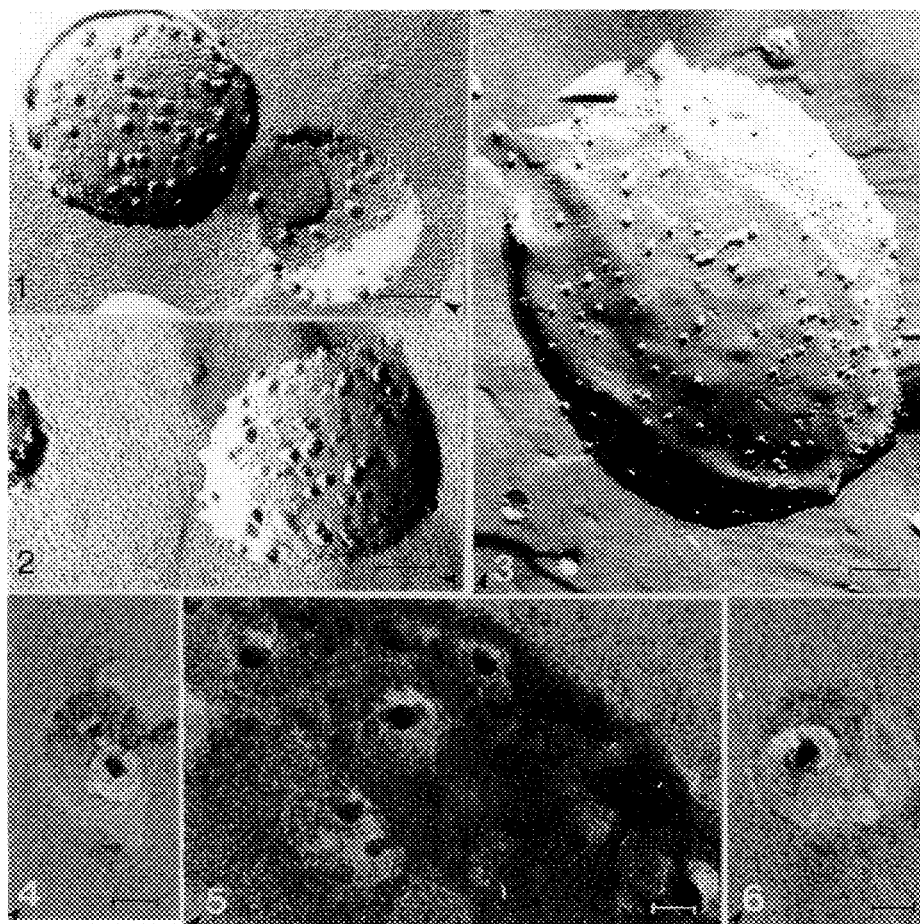


FIG. 1-3. Pt/C replicas from protein loaded liposomes of EPC/EPE(1:1,w:w). 1,2 - L:P=10; the protein covered area is 0.141. Bar=100 nm. 3 - L:P=25; the proportion of protein covered area is 0.087. Bar=100 nm.

FIG.4-6. Ta/W replicas of COV prepared from DOPC/DOPE (1:1,w:w) at L:P=10. Concave surfaces of proteoliposomes with different diameters. Micrographs have a higher resolution but a lower contrast. Some details on the surfaces of the monomers and dimers could be seen. Bar=10 nm.

INTERRELATIONSHIP OF THE CELLULAR DISTRIBUTION AND SECRETION OF REGULAR STRUCTURE (RS) PROTEIN IN BACILLUS LICHENIFORMIS NM 105

Xiaorong Zhu, Richard McVeigh and Bijan K. Ghosh

UMDNJ-Robert Wood Johnson Medical School, Dept. of Physiology and Biophysics, 675 Hoes Lane, Piscataway, N.J. 08854-5635

A mutant of Bacillus licheniformis 749/C, NM 105 exhibits some notable properties, e.g., arrest of alkaline phosphatase secretion and overexpression and hypersecretion of RS protein. Although RS is known to be widely distributed in many microbes, it is rarely found, with a few exceptions, in laboratory cultures of microorganisms. RS protein is a structural protein and has the unusual properties to form aggregate. This characteristic may have been responsible for the self assembly of RS into regular tetragonal structures. Another uncommon characteristic of RS is that enhanced synthesis and secretion which occurs when the cells cease to grow. Assembled RS protein with a tetragonal structure is not seen inside cells at any stage of cell growth including cells in the stationary phase of growth. Gel electrophoresis of the culture supernatant shows a very large amount of RS protein in the stationary culture of the B. licheniformis. It seems, Therefore, that the RS protein is cotranslationally secreted and self assembled on the envelope surface.

The RS mRNA content of cells grown for different periods of time, was compared by qualitative dot blot analysis using 1.8 kb of internal fragments of cloned RS gene. The RS mRNA was present in the early growth periods and declined significantly when the cells reached the stationary growth phase.

It was learned from our attempts to purify RS protein that it aggregates non-specifically with many cellular and noncellular material. Due to this aggregating tendency it was difficult to quantitatively analyze this protein by immunoassay. We performed semiquantitative analysis of RS protein by comparing the numbers of protein A labeled with colloidal gold (PAG) in the cryosections of cells grown for different time periods. Colloidal gold labeling for RS protein, in contrast to the amounts of mRNA, was very poor during early stages of growth, and very high when the cells were in the stationary phase of growth. It is also intriguing that cytoplasm was only sparsely labeled even when the envelope labeling was extremely high. Furthermore, the cryosections of cells at the stationary growth state showed the presence of many vesicles. These vesicles were very sparsely labeled with colloidal gold and thus indicated the presence of insignificant amount of RS protein in these vesicles. Preliminary studies of in situ hybridization showed that the mRNA of RS protein is primarily associated with the plasma membrane of B. licheniformis. This membrane associated mRNA is significantly high in the stationary phase cells. It is possible that membrane association significantly increases the half life of the of the mRNA which is possibly translated at the stationary phase of cell growth. Studies are in progress to test this and other possible hypotheses.

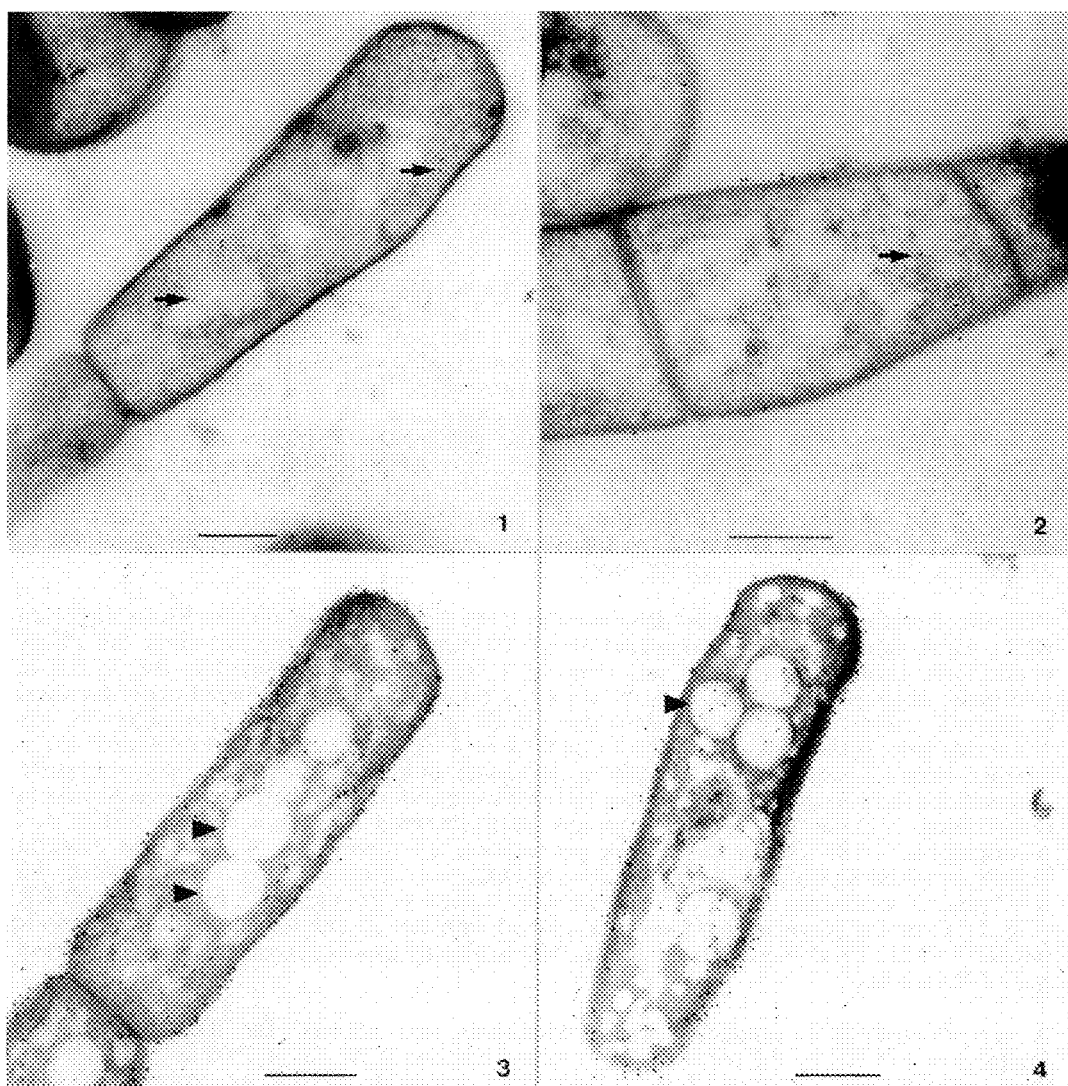


Fig. 1. Cryosections of *B. licheniformis* grown for 4 hr. and immunostained with protein A labelled (PAG) 15nm colloidal gold. There are only a few gold particles in the sections (arrows). This indicates that a very small amount of RS protein is present at this state of growth of cells. Bar in all micrographs = 0.5μ .

Fig. 2. Cryosections of *B. licheniformis* grown for 7 hr. and immunostained with 15nm PAG. Number of gold particles indicate no significant rise of the RS protein in the cells compared to 4 hr. growth.

Fig. 3 & 4. Cryosections of *B. licheniformis* grown for 10 and 12 hr. and immunostained with 15nm PAG. High number of envelop bound gold particles shows enhanced production of envelop associated RS protein. The sections also show the presence of significant number of vesicles (arrowheads).

ULTRASTRUCTURAL EVIDENCE FOR A PARASITOPHOUS DUCT IN HUMAN ERYTHROCYTES INFECTED WITH MALARIA PARASITES

Timothy Schneider, Bruno Pouvelle and Theodore F. Taraschi

Department of Pathology and Cell Biology, Jefferson Medical College, 1020 Locust St., Philadelphia, PA 19107

The human malaria parasite, *Plasmodium falciparum*, spends all but a few minutes of its 48 hour asexual life cycle in host erythrocytes (RBC). Models of the host-parasite complex, obtained by transmission and freeze-fracture electron microscopy, suggest that the intraerythrocytic parasite is contained in a continuous, sealed vacuole (PVM). The parasite has an obligate nutritional requirement for serum fatty acids, lipids and proteins. Since mature erythrocytes do not endocytose, a long standing enigma has been the mechanism by which intracellular parasites obtain access to these (macro)molecules. Using a variety of fluorescent labeled macromolecules and confocal fluorescence microscopy (CFIM), we demonstrated that macromolecules in serum did not cross the erythrocyte or PVM, but rather gained direct access to the aqueous space surrounding the parasite through a 'parasitophorous duct'.¹ Being limited by the resolution of the light microscope, we initiated TEM investigations to identify the duct at the ultrastructural level.

Parasitized erythrocytes (PE) were incubated with the electron dense marker, Ruthenium Red (RR), which labels only external membranes.² To insure that RR did not enter the PE by endocytosis, incubation with RR was done at 4 °C. PE were incubated in 0.2 % RR in phosphate buffered saline (PBS) at 4 °C for 4 h. Control cells were incubated under identical conditions except RR was not included. Both groups were fixed overnight in 3% glutaraldehyde, 0.1M sodium cacodylate, pH 7.4 at 4 °C. The cells were embedded in 2% agarose, rinsed 3 times with 0.1 M sodium cacodylate, dehydrated in graded steps of acetone and embedded in Araldite. Thin sections (60 nm) were collected on bare copper grids without poststaining. Multiple PE from both groups were observed in a Hitachi 7000 STEM and photographed at 80 kV. In the control preparation, all membranes were of low electron density as would be expected in the absence of OsO₄ and poststains (Fig. 1). By contrast, the RBC plasma membrane and PVM were densely stained in PE that were incubated with RR (Fig. 2). Only the plasma membrane was stained with RR in uninfected RBC. The densely labeled PVM in PE demonstrates that the PVM is directly exposed to the serum in support of our CFIM studies.¹

A second study was conducted under conditions that allowed for the active uptake (endocytosis) of RR by the parasite. PE were incubated in 0.2% RR in PBS at 37 °C for 3 h, fixed overnight in 3% glutaraldehyde, 0.1M sodium cacodylate, pH 7.4. As a control, PE were incubated under identical conditions without RR. Both groups were embedded in 2% agarose, postfixed in 1% OsO₄ for 1 h and dehydrated with acetone and embedded in Araldite. Thin sections (60nm) were collected on bare copper grids and poststained for 1 min. in 1% uranyl acetate and Sator's lead. The parasites in the PE incubated with RR were filled with electron dense stain (Fig. 3). Consistent with earlier observations², RR diffused through the duct into the vacuolar space and was endocytosed by the parasite. In contrast, membranes in the PE incubated without RR were barely visible and the parasite compartment was pale (Fig. 4).

References

1. B. Pouvelle et al, Nature (1991) 353, 73.
2. J. Luft, J. Cell Biol. (1964) 54A, 23.
3. This research was supported by USPHS grant AI 27247 and the UNDP/World Bank/WHO Special Program for Research and Training in Tropical Diseases.

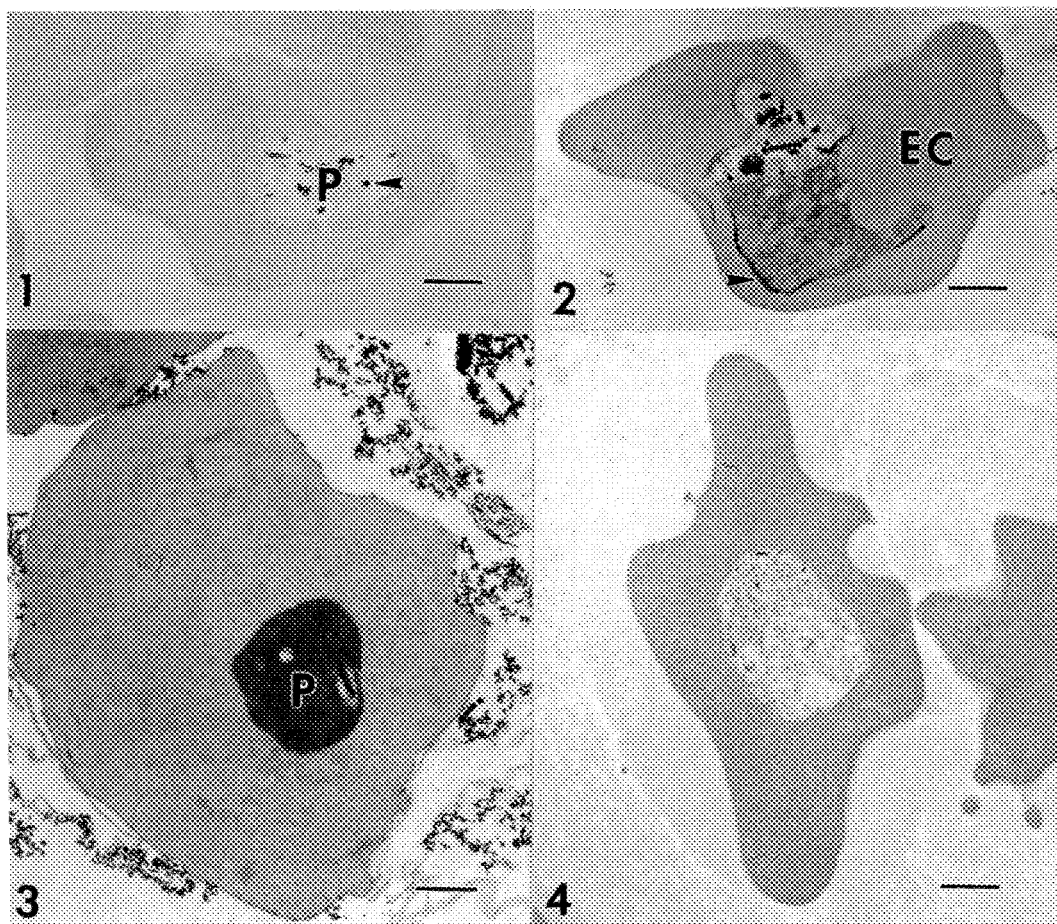


Fig. 1.--TEM of PE incubated with PBS for 4h at 4 °C and fixed in 3% glutaraldehyde, 0.1M sodium cacodylate, pH 7.4 at 4 °C. The membranes are only faintly electron dense. The electron dense structures in the parasite (P) are crystalline particles of hemazoin (arrow). Bar = 0.74 μ m.

Fig. 2.--TEM of PE incubated with PBS containing 0.2% ruthenium red at 4 °C for 4 h and fixed in 3% glutaraldehyde, 0.1M sodium cacodylate, pH 7.4. Electron dense labeling of the PVM is evident (arrow), consistent with diffusion of RR through the duct. No ruthenium red is observed in the erythrocyte cytoplasm (EC). Bar = 0.63 μ m.

Fig. 3.--TEM of PE incubated with 0.2 % ruthenium red in PBS at 37 °C for 3 h, fixed in 3% glutaraldehyde, 0.1M sodium cacodylate, pH 7.4, postfixed with OsO₄, and poststained with uranyl acetate and Sato's lead. Note the heavy concentration of RR in the parasite (P) but not in the erythrocyte. This is consistent with only the parasite being capable of endocytosis. Bar = 0.64 μ m.

Fig. 4.--TEM of PE incubated in PBS at 37 °C for 3 h, fixed in 3% glutaraldehyde, 0.1M sodium cacodylate, pH 7.4, postfixed with OsO₄, and poststained with uranyl acetate and Sato's lead. Note the lack of electron density in the parasite. Bar = 0.71 μ m.

REGIONAL DIFFERENTIATION OF THE MALPIGHIAN TUBULES OF *PIERIS CANIDIA* LARVA: AN ELECTRON MICROSCOPIC STUDY

W.W.K. Cheung and J.B. Wang

Biology Department, Chinese University of Hong Kong, Hong Kong

Malpighian tubules in insects arose primarily for the purpose of hydromineral regulation. In the small cabbage white *Pieris canidia* larva there are six tubules, with three on each side of the body. Together with the common cabbage white *Pieris brassicae* larva they are frequently encountered pests on cruciferous plants. Although physiological studies on the functions of *Pieris brassicae* larval malpighian tubules have been well documented, detailed ultrastructural studies on these tubules have not been thoroughly studied^{1,2}. For the sake of further understanding on how these malpighian tubules function an electron microscopic study of different regions of the malpighian tubules of *Pieris canidia* have been carried out.

Malpighian tubules of fourth instar *Pieris canidia* larvae were dissected out in buffered insect saline. Different regions of the tubules were fixed in 2.5% glutaraldehyde in 0.2M phosphate, pH 7.2, for 1 hr., and post-fixed in 1.0% osmium tetroxide in phosphate buffer. They were then dehydrated in alcohol/acetone series and then embedded in spurr resin. Sections were cut with a Reichart ultratome and sections were stained with uranyl acetate and lead citrate for observation under a Zeiss EM 9S-2 electron microscope.

Each malpighian tubule can be conveniently divided into four regions, namely rectal lead, iliac plexus, yellow region and white region. Their primary cells share some common features such as having microvilli containing mitochondria, an irregular outlined nucleus, numerous basal infoldings and a basement membrane of 0.3 μ in thickness (Figs. 1,2,3,4). However, the rectal lead has only scattered rough endoplasmic reticulum and basal infolds extending 1/2 distance to the apical border (Fig. 1). The iliac plexus has microvilli deeply invaginated in the apical cytoplasm to form canaliculi and the basal infolds extend to 4/5 distance to the apical border (Fig. 2). The yellow region has numerous mineral spherites found in the ground cytoplasm and the basal infolds only extend to 1/2 distance towards the luminal side (Fig. 3). The white region has scattered mitochondria and rough endoplasmic reticulum and there are scanty mineral spherites (Fig. 4). The above ultrastructural architecture of *Pieris canidia* larval malpighian tubules are in accord with the physiological functions performed by *Pieris brassicae* larva¹. Both the rectal lead and the iliac plexus probably function in secretion of a potassium rich urine to the tubule lumen. The yellow region might secrete minerals for storage and a sodium rich urine. The white region, however, might function primarily in sodium secretion and potassium reabsorption^{1,2}. These regional specialisations ensure that the secreted potassium could be recycled and excess mineral and other wastes could be ridded off³.

References

1. S.W. Nicholson, 1976, J. Insect Physiol. 22, 1623-1630.
2. J.A. Ramsay, 1976, Phil. Trans. Roy. Soc. B274, 203-226.
3. T.J. Bradley, 1984, Comp. Insect Physiol., Biochem. & Pharm. 4, 421-465.

FIG. 1--LS of rectal lead primary cell showing microvilli (mv) with mitochondria (m), nucleus (n) and basement membrane (bm). Bar=2 μ m.

FIG. 2--LS of iliac plexus primary cell showing microvilli (mv), canaliculi (c), mitochondria (m) and basement membrane (bm). Bar=2 μ m.

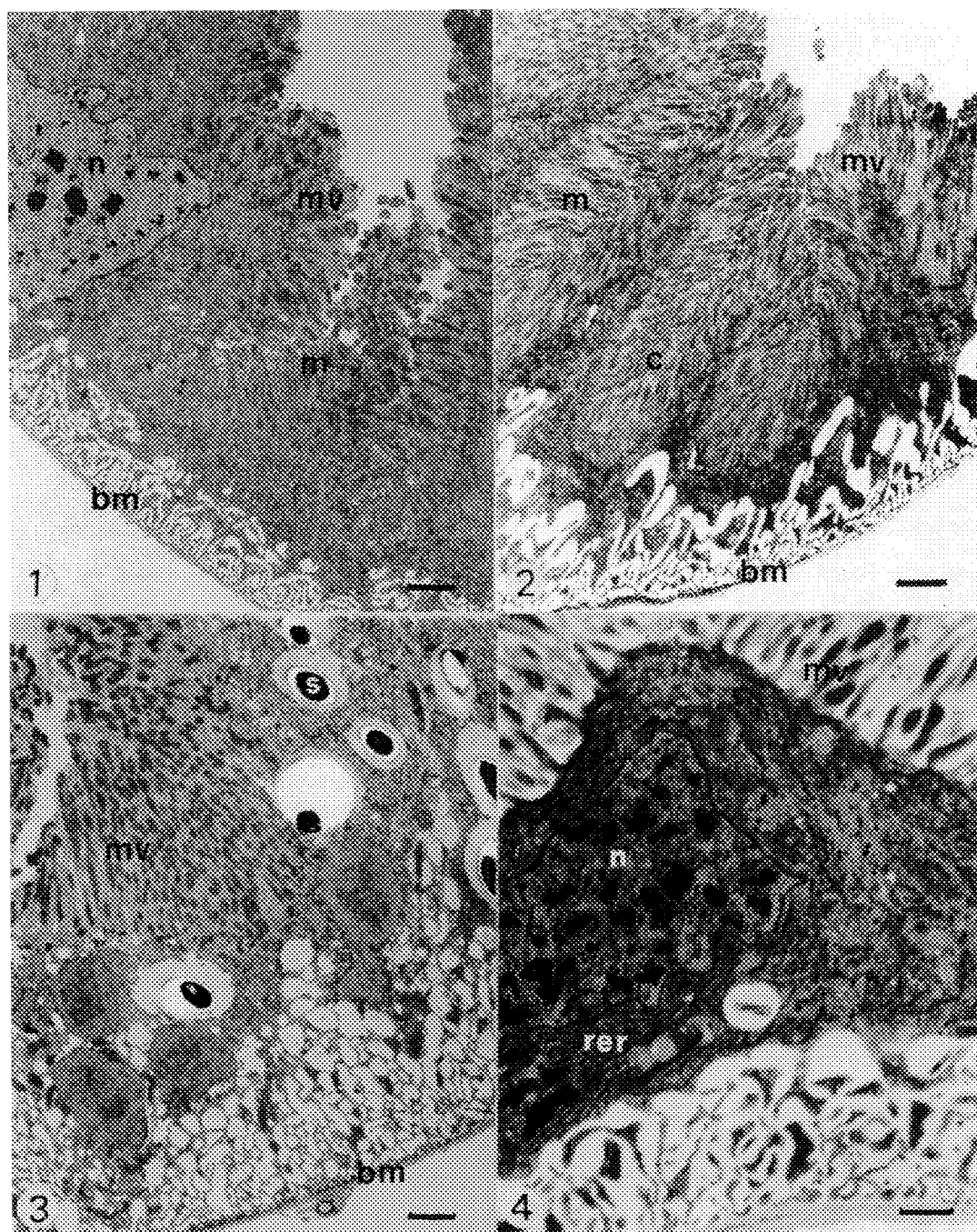


FIG. 3--LS of yellow region primary cell showing microvilli (mv), mineral spherite (s), and basement membrane (bm). Bar=2 μ m.

FIG. 4--LS of white region primary cell showing microvilli (mv), rough endoplasmic reticulum (rer) and nucleus (n). Bar=1 μ m.

ENDOCYTOSIS OF FOLATE LABELED PROTEINS: ULTRASTRUCTURAL LOCALIZATION IN KB CELLS

John J. Turek, Christopher P. Leamon, and Philip S. Low

Department of Veterinary Anatomy (JJT) and Department of Chemistry (CPL,PSL),
Purdue University, West Lafayette, Indiana, 47907

Recently, methods for the delivery of macromolecules into cells via covalent coupling to vitamins have been described for plant and animal cells^{1,2}. This method utilizing vitamin receptor endocytosis concentrates macromolecules inside the cell in an active form that is nondegradative. The purpose of this study was to determine the specific location of bovine serum albumin-folic acid-colloidal gold (BSA-F-CG) conjugates within KB cells. Bovine serum albumin was covalently coupled to folic acid (BSA-F) and used to stabilize 15 nm colloidal gold (CG) particles. KB cells were incubated with BSA-F-CG or BSA-CG at either 11°C for 2 hours or 37°C for 15 minutes to allow binding, and the cells washed to remove unbound material. Some cells were fixed immediately, and others were incubated for additional time periods. BSA-CG particles nonspecifically pinocytosed by control cells were only found in large dense endosomes after 6 hours incubation. In cells incubated with BSA-F-CG, CG particles decorated the plasma membrane, and were found in uncoated pits. At 30 minutes CG particles could be found in multivesicular bodies (MVB's), small vesicles, and dense endosomes. At 6 hours, CG particles were found in various dense endosomes, MVB's, dense endosomes associated with the Golgi apparatus, and free in the cytoplasm. Cells that were pulsed with BSA-F-CG for 15 minutes at 37°C had CG particles on the surface and uncoated pits, small vesicles and MVB's. After 60 and 360 minutes, BSA-F-CG was located in MVB's, clear and dense endosomes, and MVB's associated with the Golgi apparatus. Control cells incubated with BSA-CG had a few CG particles located in small clear endosomes at 15 minutes and large dense endosomes at 6 hours. For comparison, 5nm colloidal gold was stabilized with transferrin (TF) and incubated alone with KB cells or coincubated with 15 nm BSA-F-CG. The 5 nm TF-CG was localized in coated pits and on the rim of vesicular structures resembling CURL (Compartment of Uncoupling of Receptor and Ligand) at 15 minutes. There was no colocalization of TF-CG and BSA-F-CG at 15 minutes. TF-CG and BSA-F-CG were found separately and together in MVB's at 1 hour. At six hours TF-CG and BSA-F-CG frequently colocalized in large dense endosomes. Folate labeled proteins endocytosed in this study shared some common compartments with transferrin, but there were several points of divergence. Transferrin-CG is taken up via coated pits whereas BSA-F-CG enters the cell via uncoated pits. At 15 minutes, internalized TF-CG is associated primarily with vesicles resembling CURL, and BSA-F-CG is found in MVB's. At one hour, both TF-CG and BSA-F-CG may be found separately and together in MVB's, and at 6 hours both may be found separately and together in dense endosomes. The BSA-F-CG particles free in the cytoplasm may be released during transport of the ligand, possibly by MVB's that associate with the Golgi apparatus. The BSA-F-CG particles localized in this study may represent the normal location of endocytosed folate or their location could be an aberration of the normal pathway.

References

1. M.A. Horn et al., Plant Phys. (1990) 93, 1492.
2. C.P. Leamon et al., Proc. Natl. Acad. Sci. USA (1991) 88, 5572.

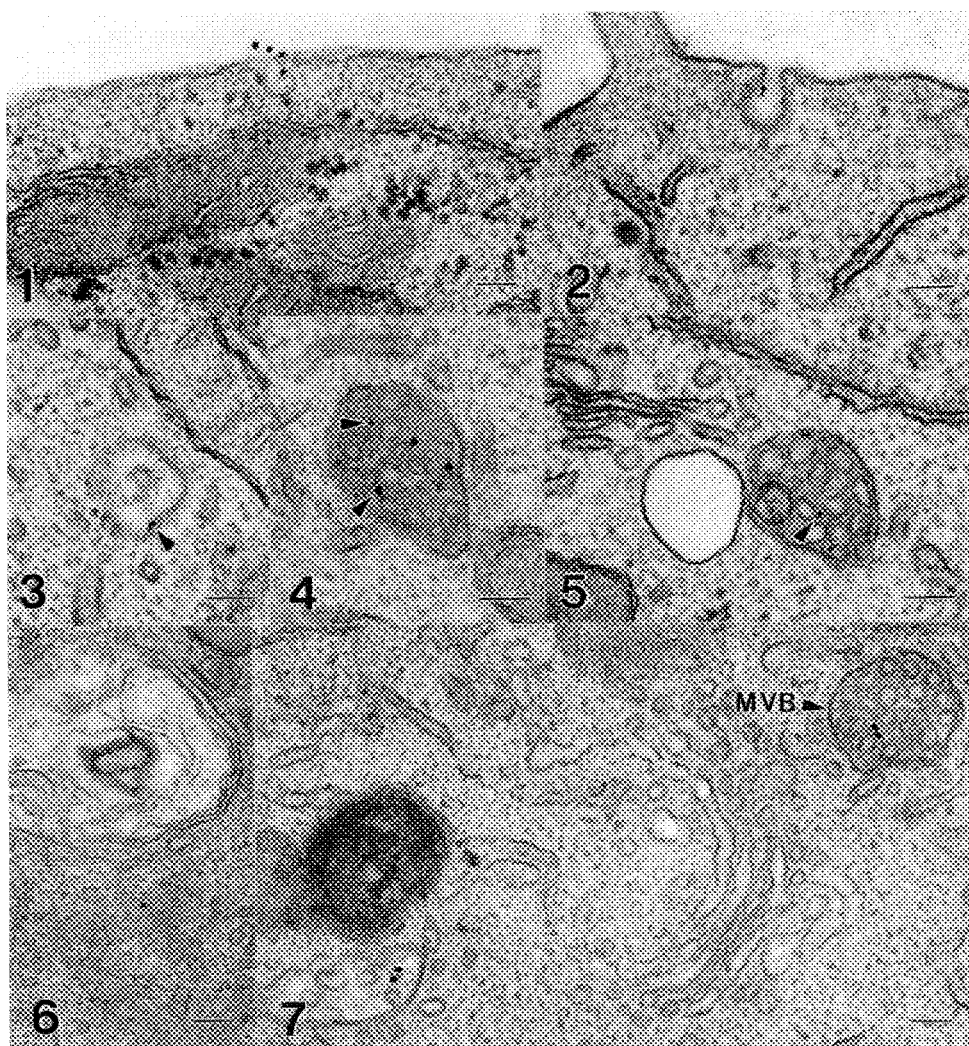


Figure 1.--BSA-F-CG particles being endocytosed by KB cell via an uncoated pit. Bar = 100 nm.

Figure 2.--TF-CG particles being endocytosed by KB cell via a coated pit. Bar = 100 nm.

Figure 3.--TF-CG particles on rim of vesicular structure resembling CURL. Bar = 100 nm.

Figure 4.--Colocalization of TF-CG and BSA-F-CG in multivesicular body. Bar = 100 nm.

Figure 5.--TF-CG in multivesicular body. Bar = 100 nm.

Figure 6.--BSA-F-CG particle that appears to be "free" in the cytoplasm of KB cell after 6 hours incubation. Bar = 100 nm.

Figure 7.--Two multivesicular bodies containing BSA-F-CG that appear in proximity to the Golgi apparatus. Bar = 100 nm.

COMPARISON OF QUANTIFIED COATED PIT PROFILES IN THIN SECTIONS AND FREEZE-FRACTURE REPLICAS OF GRANULAR EPITHELIAL CELLS OF THE TOAD URINARY BLADDER

Nancy L. Shinowara, Jenchang Yu* and Thomas A. Palaia

Division of Nephrology, Winthrop-University Hospital, Mineola, NY 11501; *Analytical Ultrastr. Ctr., Albert Einstein College of Medicine, Bronx, NY 10461

It is well known that stimulation of granular cells by arginine vasopressin (AVP) results in apical membrane changes, including an increased water permeability and an associated exocytotic delivery of aggregates of intramembrane particles. Endocytotic clathrin-coated pits appear in stimulated collecting duct principal cells, which transport water in mammalian kidneys.¹ Recently, presumptive coated pits (CPs), identified in replicas, were reported in apical membranes of stimulated granular cells.^{2,3,4} This study describes the comparison of structurally defined sectioned-CPs (s-CPs per unit membrane length with presumptive, replicated-CPs (r-CPs) per unit area in bladders when initial CP formation was expected.

Treatments for cannulated hemibladders (n = 4 toads/treatment) with no osmotic gradient were 0 or 5 min stimulation with 0.3 or 1.3 μM AVP (subthreshold doses for aggregates and water flow) or 50 μM AVP Ringer's solution before fixation in 2.5% glutaraldehyde with 1% tannic acid in 0.1 M sodium cacodylate buffer. Tissue samples from the distal third of bladders were prepared for freeze-fracture⁵ and thin sections (postfix: 1% OsO₄; 0.5% aqueous uranyl acetate en bloc; dehydrate: ethanol; embed: LADD LX112; section stain: LKB 2168 ultrostainer).

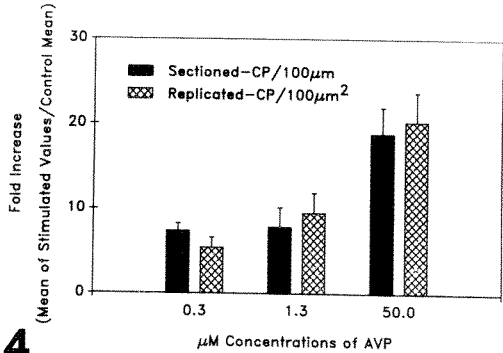
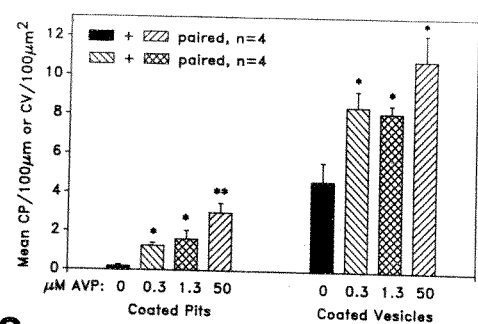
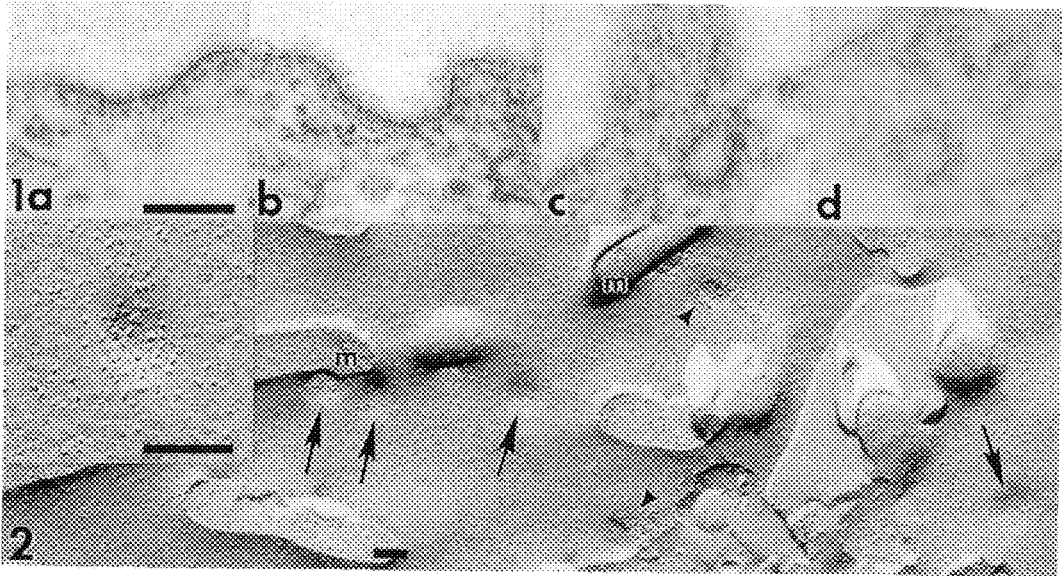
Morphometry: Cross-sectioned granular cells were sampled for s-CPs and coated vesicles (CVs). Sections mounted on 200 HS mesh copper grids were examined with a Zeiss 10 TEM. CPs/apical membrane length and CVs/area between the membrane and a 0.6-0.7 μm depth of cytoplasm were directly counted with a X25K magnification. Questionable CPs and CVs were photographed for further identification. CP and CV profiles were classified into 4 stages representative of endocytosis (Fig. 1). Apical membrane length per cell profile was measured using the displacement X and Y coordinates of the microscope. Perpendicular microvillar membrane was excluded. Total cell lengths of 1-1.7mm were scanned/bladder. A treatment sample had 307 \pm 26 cell profiles (range = 4-52 μm lengths/cell; mean lengths = 23 μm /35 control cells; 17 μm /56 cells stimulated by 50 μM AVP). Replicated-CPs (Fig. 2) were quantified from prints (x40-41K magnification) of p-face apical membranes of at least 10 randomly sampled cells. Minimum total membrane area/bladder was approximately 250 μm^2 . Data are presented as means \pm SEM with t-test analyses.

CPs, as revealed by section and replica methods, had similar profile shapes, sizes (Figs. 1,2 inset) and distributions. Stimulated cells had significant increases in total s-CPs (stages 1,2,3) and CVs compared to control values (Fig. 3). Only stages 1 and 2 of s-CPs/100 μm length were compared with r-CPs/100 μm^2 area. Stimulated cells had significant increases in frequencies for both s-CPs and r-CPs compared to their respective controls. The 50 μM AVP groups (2.64 \pm 0.42 s-CP/100 μm ; 29.59 \pm 4.03 r-CP/100 μm^2) had significantly (p<0.05) more CPs than lower dose groups. Both mean s-CP and r-CP values for CP formation after 5 min stimulation showed the same fold increases from control means for each AVP dose (Fig. 4).

It is concluded that granular cell s-CPs and r-CPs are the same structure. Analyses of quantifiable CP frequencies, as detected in sections and replicas, provide a manageable system for studying the functional morphology of CPs.

References

1. D. Brown et al., Eur. J. Cell Biol. (1988)46, 336.
2. N.L. Shinowara et al., Kidney Internat. (1990)37, 589a.
3. W.A. Kachadorian et al., Am. J. Physiol. (1990)258(Cell Physiol.27), C871.
4. N.L. Shinowara et al., J Cell Biol. (1991)115, 188a.
5. N.L. Shinowara et al., Biology of the Cell (1989)66, 65.



3

4

Fig. 1. Thin sections of apical membrane s-CPs (a-c) and CV (d) profiles were classified into 4 endocytotic stages: 1 (a), 2 (b), 3 (c) and 4 (d). Bar = 0.1 µm.
Fig. 2. Replica of p-face apical membrane of stimulated granular cell. Arrow, CP; arrowhead, aggregate; m, microvillus. Bar = 0.1 µm. INSET: CP with small intra-membrane particles in a flat, stage 1 depression. Bar = 0.1 µm.
Fig. 3. Frequencies of granular cell s-CPs and CVs significantly increased after 5 min stimulation with 3 different AVP doses: * significant from control means, $p < 0.05$; ** significant from 1.3 µM mean, $p < 0.05$. $n = 4$ toad bladders/treatment.
Fig. 4. Comparison of increases in mean frequencies of granular cell s-CPs and r-CPs from their respective control means after 5 min stimulation with 3 different doses of AVP. Both structures showed the same relative increases in frequencies.

IMMUNOGOLD LOCALIZATION OF INTRINSIC FACTOR IN RAT AND HUMAN STOMACH

Michael J. Becich, Dharendra N. Misra, Tamara Howard, and David H. Alpers*

Dept. of Pathology, Univ. of Pittsburgh School of Medicine, Pittsburgh, PA 15261; *Gastroenterology Division, Washington Univ. School of Medicine, St. Louis, MO 63110

There are several proteins that mediate uptake and transport of dietary cobalamin (vitamin B₁₂).¹ The gastric intrinsic factor (IF) is one of these which binds cobalamin in the gut lumen and allows for efficient intestinal absorption of the ingested vitamin. The IF has a rather novel and complicated secretory pathway and precise knowledge of the expression and cellular distribution will help us to understand the recognized defects in vitamin B₁₂ absorption and metabolism. Earlier studies using autoradiographic and immunocytochemical methods have identified different IF production sites for various animals: gastric chief cells in rodents; antropyloric cells in the hog; parietal cells in humans and most other species.²⁻⁴ In the present work, we have used immunogold electron microscopy for cellular and subcellular localization of IF.

Rat and human stomach tissues were fixed in Karnovsky's fixative and embedded in LR-gold. Silver/gold sections were reacted with rabbit anti-IF polyclonal antisera raised against human or rat recombinant antigen, washed with Tris buffer containing 0.25 M NaCl and 0.05% Nonidet P-40 (NP-40), and reacted with protein A-gold (15 nm). After further washing, the sections were vapour osmicated and stained with uranyl and lead. For control, the anti-IF antibodies were omitted or were preabsorbed with recombinant rat or human IF at varying concentrations.

The results (Table and Figs.) disclosed some new findings not discussed previously. Human IF was localized in highest concentrations in the parietal cells, but IF was absent from these cells in the rat. Subpopulations of chief cells showed labeling of exocrine granules in human as well as rat stomach. Occasional enteroendocrine cells also showed specific labeling with IF as did G-cells in human antrum. Also, an unexpected finding in human, in contrast to rat, was that the endothelial cell membranes in the lamina propria capillaries were labeled intensely.

Table 1. Reactivity of anti-IF antibody to different cell types

	Parietal	Chief	Endothelial	Endocrine
Rat	-	+++	-	+/-
Human	+++	++	+++	+

In parietal cells, IF was located on apical plasma membranes, tubulovesicle membranes and on noncoated vesicle membranes within the subplasmalemmal cytoplasm. In some chief cells, the secretory granules as well as apical membranes were heavily labeled. Endothelial cell staining was membrane and transport vesicle associated. This pattern suggests a redundant yet complex pattern of IF localization on the human stomach which is markedly different from that observed in the rat. Further studies modulating secretory activity will provide useful insight into the mechanisms of IF secretion.⁵

References

1. D. H. Alpers, Textbook of Gastroenterology and Nutrition in Infancy: Ed. E. Lebenthal, Raven Press, Ltd., New York (1989), pp.781-791.
2. J. S. Levine, P. K. Nakane and R. H. Allen, J. Cell Biol. (1981) 90, 644.
3. A. Smolka and R. M. Donaldson, Jr., Gastroenterology (1990) 98, 607.
4. C. Vaillant, N. U. Horadagoda and R. M. Batt, Cell Tissue Res. (1990) 260, 117.
5. Supported by NIDDK grant #DK-33487-06.

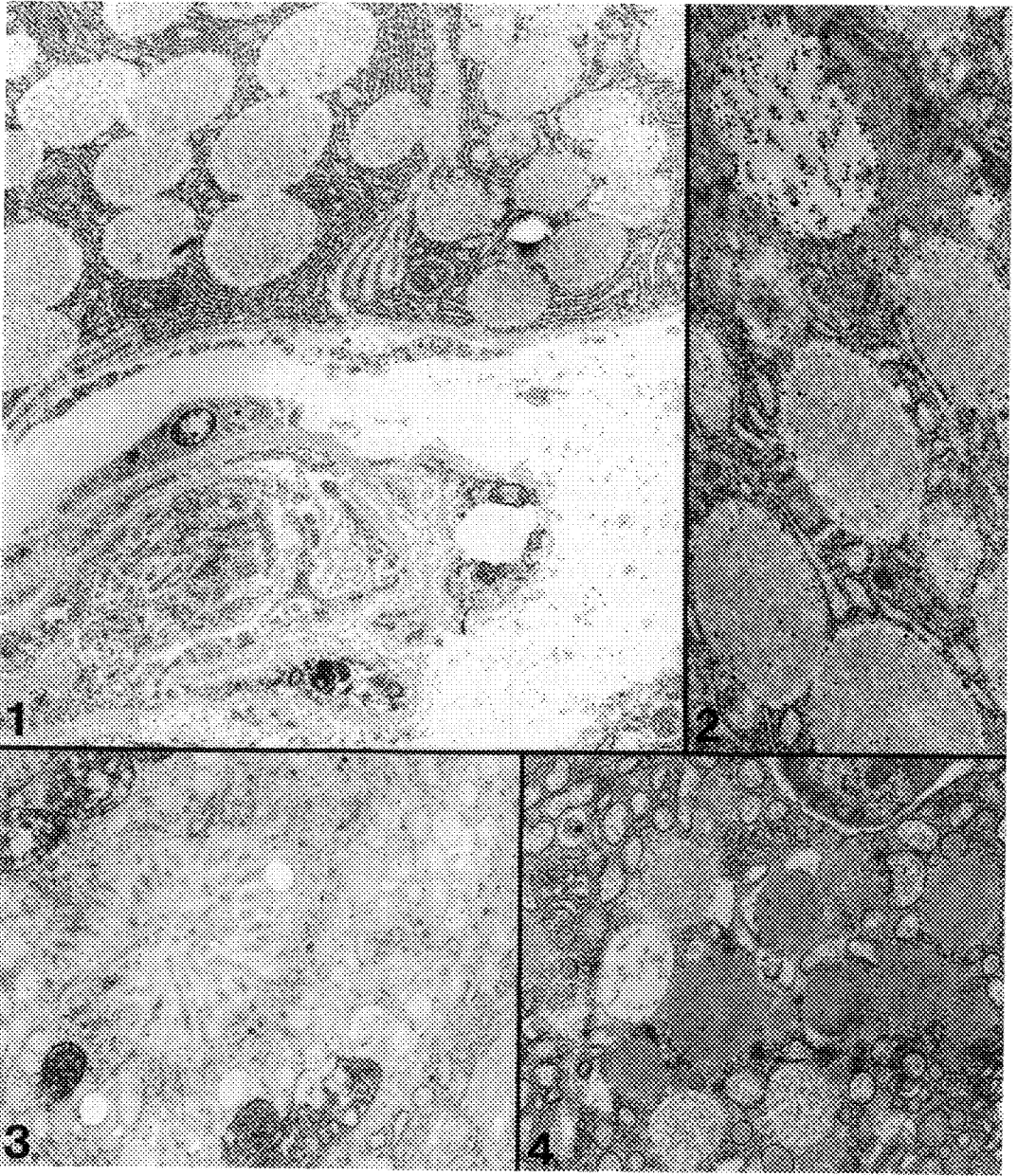


Fig. 1.-- Secretory granules in human chief cells show specific and more intense IF staining than those in neighboring cells (top). Note intense labeling of endothelium (bottom). X11,000.
 Fig. 2. -- Human chief cell shows staining of granules and apical membranes. X22,000.
 Fig. 3. -- Human parietal cell: staining of apical and tubulovesicle membranes. X11,000.
 Fig. 4. -- Rat chief cell: staining of secretory granules. X11,000.

MACROMOLECULAR SPECIALIZATIONS THAT MEDIATE LATERAL INTERACTIONS BETWEEN MICROFILAMENTS AND THE MEMBRANE AT FOCAL CONTACTS

Steven J. Samuelsson, Paul W. Luther, David W. Pumplin* and Robert J. Bloch

Departments of Physiology and Anatomy*, University of Maryland, School of Medicine, Baltimore, Maryland, 21201

Focal contacts are membrane specializations of cultured cells where stress fibers terminate and where the cell is most closely applied to the substrate¹. The organization of this cytoskeletal-membrane-extracellular matrix assembly has been well characterized.^{2,3} Immunofluorescence microscopy has shown that two focal contact-specific proteins, vinculin and talin, colocalize with microfilaments for several microns before the stress fiber terminates. This result raises the question of whether microfilament-membrane interactions are limited to the ends of microfilaments, or if lateral interactions also occur. We addressed this question by examining the cytoplasmic surface of isolated focal contacts in detail.

Xenopus cultures were sheared with a forceful stream of buffer then the samples were processed by quick-freeze, deep-etch, rotary-replication.^{4,5} This procedure exposes extensive areas of the ventral cell membrane, which can be examined from an *en face* aspect. As shown in Fig 1., the remaining stress fibers coursed close to the membrane and terminated upon discrete specialized areas. These areas contained a complex arrangement of both filamentous and globular structures. Similar specialized areas were seen at sites where stress fibers were removed by shearing (Fig 2-3). The specialized areas occurred intermittently as a linear array, extending several microns along the ends of stress fibers. When viewed in stereo, these specializations were seen to fill the space between the microfilaments and the membrane. At areas where the adjacent membrane was removed, the specializations were seen to be collinear with extracellular matrix filaments. The fact that the specialized areas were slightly elevated from the substrate suggests that this association occurs throughout the focal contact. The specialized areas are therefore positioned appropriately to participate in transmembrane interactions between stress fibers and the extracellular matrix. Indirect immunolabeling indicates that vinculin, talin and β_1 -integrin are located in the specialized areas (Figs 2-3).

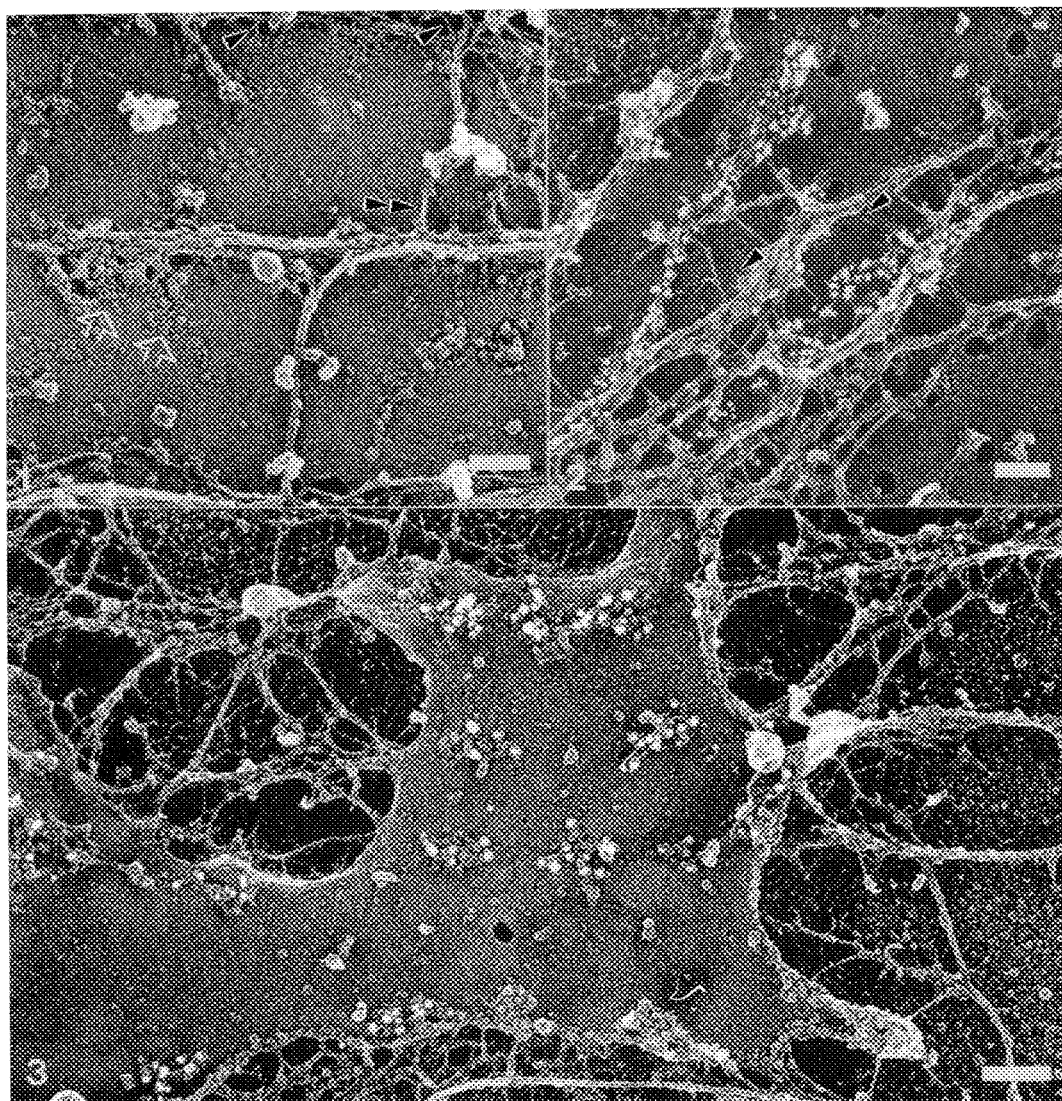
In addition to the filamentous-globular specializations, two types of filaments appeared to mediate microfilament-membrane interaction. One set has the diameter and platinum repeat of a microfilament; the second type is about half this diameter and is smooth. Both of these short filaments are roughly perpendicular with the microfilament bundle.

These studies produce clear evidence that microfilament bundles can interact laterally with the membrane at focal contacts, primarily via intermittent specialization that contain β_1 -integrin (Fig 3), vinculin (Fig 2) and talin (NS). In addition, two types of short filaments may also contribute to lateral interactions between microfilaments and the membrane.⁷

References

1. M. Abercrombie et al., *Exp. Cell Res.* 67(1971):359.
2. I. Singer, *Cell* 16(1979):675.
3. W-T Chen and S. J. Singer, *J. Cell Biol.* 95(1982):205.
4. Z. Avnur and B. Geiger, *J. Mol. Biol.* 153(1981):361.
5. D. W. Pumplin et al., *J. Elec. Microsc. Tech.* 14(1990):342.
6. P. W. Luther and R. J. Bloch, *J. Cytochem. Histochem.* 37(1989):75.

7. mAB 3-24 against vinculin was obtained from the Developmental Studies Hybridoma Bank (Dept of Biology, Univ of Iowa, Iowa City, IA). We thank Drs. K. Burridge, for the rabbit anti-chick talin antibody, and R. O. Hynes for the rabbit antibody against integrin.



Figs. 1-3: *Xenopus laevis* fibroblasts stabilized in 3 mM $ZnCl_2$, 60 mM NaCl, 0.67 mM KCl, 10 mM PIPES, pH 6.0, sheared with ice-cold 50 mM PIPES, 10 mM $MgCl_2$, pH 6.0 and fixed in either 2% glutaraldehyde/0.25% acrolein, 75 mM PIPES, pH 6.5 (Fig 1) or 0.5% paraformaldehyde/75 mM cyclohexylamine, 10 mM $MgCl_2$, 10 mM PIPES, pH 6.5 (Figs 2-3).⁶ Bars = 0.1 μm . Fig 1: Microfilaments approach the membrane. Membrane-associated aggregates (open arrows). ~8 nm, short filaments (double arrowhead); ~4 nm filaments (arrowheads). Fig 2: Ventral membrane sheared clear of microfilaments. Membrane aggregates linearly situated over ECM fibers labeled for β_1 -integrin. Fig 3: Similar fibroblast membrane labeled with an antibody against vinculin.

USE OF LANTHANUM AS A CONDUCTIVE MATERIAL IN SECONDARY ELECTRON IMAGING

P.D. Gupta and Shashi B. Relia

Centre for Cellular & Molecular Biology, Hyderabad 500 007, India

The use of colloidal lanthanum (La) as a conductive material in preparatory procedures for scanning electron microscopy of dehydrated non-conductive biological specimens has been explored for the present study. The ability of La to bind certain moieties of the plasma membrane has been successfully employed to impart conductivity to a wide variety of biological material.^{1,2} LaNO₃ solution (2%) in 0.1M cacodylate buffer (CB) was treated with 0.01N NaOH with vigorous shaking. At pH 7.5 - 7.8 faint flocculent material appeared which indicated the formation of colloidal La. This solution was used for incubation of fresh and/or fixed biological specimen as described. Specimens were incubated in 1% La solution (final concentration) for 3h and 6h followed by fixation in 2.5% glutaraldehyde (glu) for 15 min or specimens were incubated and fixed simultaneously in 1% La and 2.5 glu (final concentration) in 0.1M CB for 3h. Then washed and post fixed in 1% OsO₄ in 0.1M CB for 30 min. Tissues were dehydrated in ascending grades of acetone and dried by the CPD technique. After mounting on metallic stubs, the specimens were examined in JEOL 100 CX electron microscope with scanning attachment in the voltage range 20-40 kV and beam current of 50 μ A and also in SEM Hitachi S 520 in the voltage range of 1-30 kV and beam current 10-100 μ A. It has been shown that La generates enough secondary electrons to form an optimal image having a good contrast. The resolution achieved in this preparation is as good as that obtained in metal-coated samples (Figs.1,2). In contrast to metal-coated samples, masking of topographical features is not observed in La incubated samples. The later samples are transparent (Fig.2). The technique is applicable to a variety of specimens such as lipid vesicles (Fig.3), algae (Fig.4), ciliates, single cell suspensions (Fig.2), various tissues of rat (Fig.5) and radical of germinating beans (Fig.6). La was also used for the preparation of biological material for back-scattered imaging mode. To study the process of phagocytosis, yeast cells were coated with La and incubated with cultures of macrophage tumor AK-5 cells. The engulfed yeast cells could be detected inside the cell as dark bodies (Figs.7,8).

The various combinations with and without osmium suggested that La alone can be used to impart conductivity to different types of biological specimens. Applicability of this method is very wide and gives flawless images of a wide variety of samples. These specimens could be examined in the voltage range of 1-40 kV, higher kV definitely gives better images. The samples were observed upto 15,000 magnification without loss of details and without charging effect. La incubated samples could be observed for a sufficient duration of time, whereas in some of the conductive staining methods observation time becomes a limiting factor.³ Present studies reveal that La deposited on the plasma membrane is sufficient to generate enough secondary electrons to form an image which is quite stable and has enough contrast.

References

1. P.D.Gupta and S.K.Malhotra, Cytobios (1971)4, 21.
2. P.D.Gupta and N.M.Pattnaik, Cytobios (1986)46, 17.
3. J.A.Murphy, SEM (1980)I, 209.

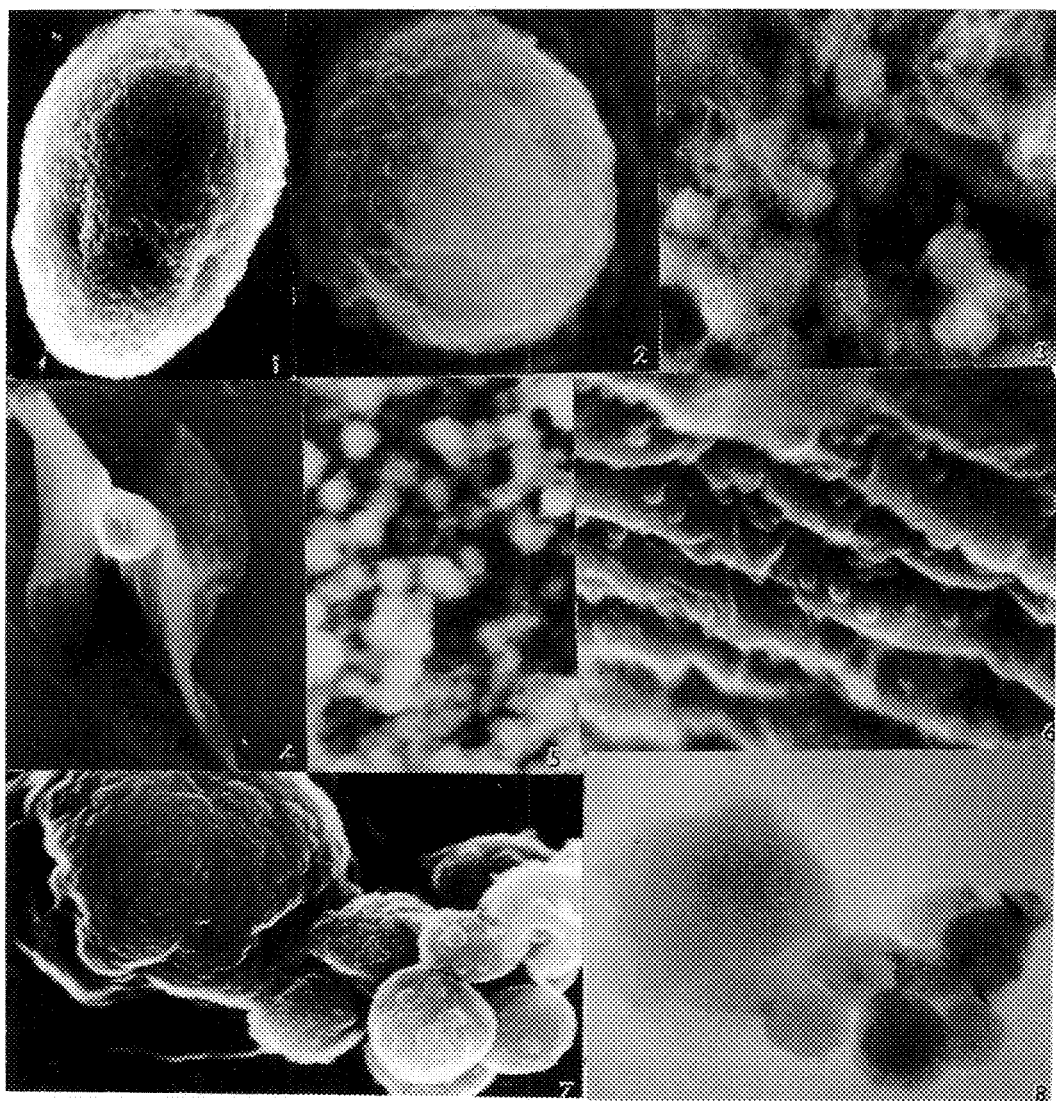


Fig.1. Gold coated ZAH cell x 8,400. Fig.2. Lanthanum treated ZAH cell x 8,400. Fig.3. Lanthanum treated phospholipid vesicles x 16,800. Fig.4. Lanthanum treated phytoflagellate x 1,800. Fig.5. Endometrium of rat uterus, lanthanum treated x 4,200. Fig.6. Lanthanum treated root tip x 2,200. Fig.7. Lanthanum treated yeast with AK-5 cell x 16,800. Fig.8. Same as in Fig.7 Back-scattered image x 16,800.

UNIQUE METHOD OF TISSUE CULTURE PREPARATION FOR ELECTRON MICROSCOPY

Fen Wang, Lindsay B. Ledford, Jonathan F. Head, Robert L. Elliott

Mastology Research Institute, Baton Rouge, LA 70816

A simplified technique of growing monolayer cells for electron microscopic examination has been developed. Our procedure has eliminated many difficult steps and therefore is easier than those reported by others^(1,2).

Regular Beem capsules for routine embedding for electron microscopy were used (Fig. 1). Prior to tissue inoculation capsules were washed with 5% HCl and gas sterilized. A 0.5 ml cell suspension of MCF-7 cells (10,000/ml) was placed in the capsules and cells settled in the pyramid portion (Fig. 2). Culture medium was alpha-MEM with 10% FCS. Capsules were incubated at 37°C for 3 days. They were then fixed in 70% ethanol for 20 minutes and stained with crystal violet. The pyramid portion of the capsule was cut off and monolayer cell growth was confirmed by examination under a microscope (Fig. 3).

After proof of cell growth duplicate capsules were gently rinsed in 0.1 M cacodylate buffer for three times and fixed in 3% glutaraldehyde for 30 minutes. Capsules were then rinsed twice in 0.1 M cacodylate buffer and left in buffer for 12 hours. The capsules were fixed in 2% osmium tetroxide buffer for 30 minutes and then dehydrated in increasing concentrations of ethanol, infiltrated with propylene oxide, embedded in epoxy resin and placed in the oven for 3 days. Tissue blocks were removed from the capsules and placed in the ultramicrotome. The presence of a cell monolayer in the tip of the resin was confirmed by inspection with the ultramicrotome binocular microscope. Blocks were then trimmed and thin sections cut on a diamond knife. Sections were placed on copper grids, stained and examined in an electron microscope.

Ultrastructural evaluation showed excellent monolayer cell growth (Fig. 4). Membrane and intracellular organelles were well preserved (Fig. 5). The method eliminated the need for trypsin digestion in tissue culture preparations for electron microscopy. This better preserved the surface glycoproteins and receptors on the plasma membrane (Fig. 6). This is very important in performing electron immunocytochemistry. Our method is very useful for studying the ultrastructural effects of drug toxicity on cells and widens the horizons for more knowledge of cell biology.

References

1. E. Asafo-Adjei et al., J. Electr. Microsc. Tech. (1987) 5:367-372.
2. R.M. Pinto et al., Stain Tech. (1990) 65:51-53.

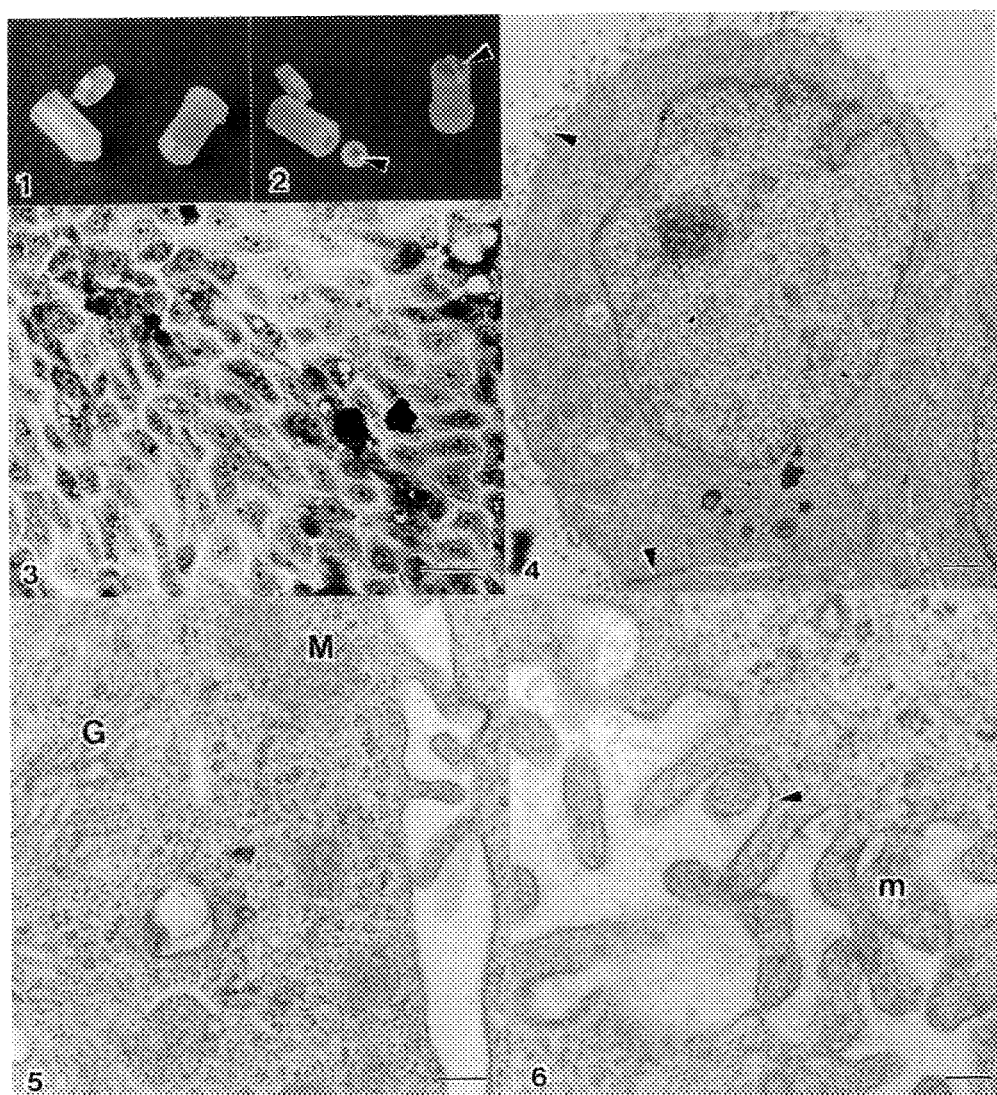


Fig. 1.--Regular Beem capsules.

Fig. 2.--Shows monolayer cells stained with crystal violet in pyramid portion of capsule (arrows).

Fig. 3.--Photomicrograph showing monolayer cell growth.
Bar = 0.17 mm

Fig. 4.--Electron micrograph of monolayer cells. Microvilli on surface and tight junction intact (arrows). Bar = 1 um

Fig. 5.--High power electron micrograph of epithelial cell showing good preservation of intracellular organelles - Golgi(G) and Mitochondrial(M). Bar = 0.25 um

Fig. 6.--Ultrastructure of cell surface showing great preservation of plasma membrane (arrow) and microvilli (m). Thus keeping surface antigens intact. Bar = 0.1 um

ELEMENTAL DISTRIBUTION IN TRACE METAL-TREATED *PISOLITHUS TINCTORIUS* PREPARED BY PROPANE JET AND HIGH PRESSURE FREEZING METHODS

C.J. McQuattie*, K.L. Klomparens**, J.I. Wood**, J.W. Heckman, Jr. **

* USDA Forest Service Research Laboratory, Delaware, OH 43015

** Center for Electron Optics, Michigan State University, East Lansing, MI 48824

Localization of trace metals on or within mycorrhizal (M) fungi may serve a protective function for roots of forest trees growing in soils containing high concentrations of metals such as Pb and Al. The presence of both Pb and Al have been demonstrated in the M fungus *Pisolithus tinctorius* after preparation by propane jet (PJ) freezing and freeze substitution.^{1,2} High pressure freezing (HPF) is an alternative method of cryopreparation that has demonstrated excellent ultrastructural preservation in studies of developing ascospores.³ The purpose of this study was to compare ultrastructural preservation and trace metal localization in *P. tinctorius* using PJ freezing and HPF methods.

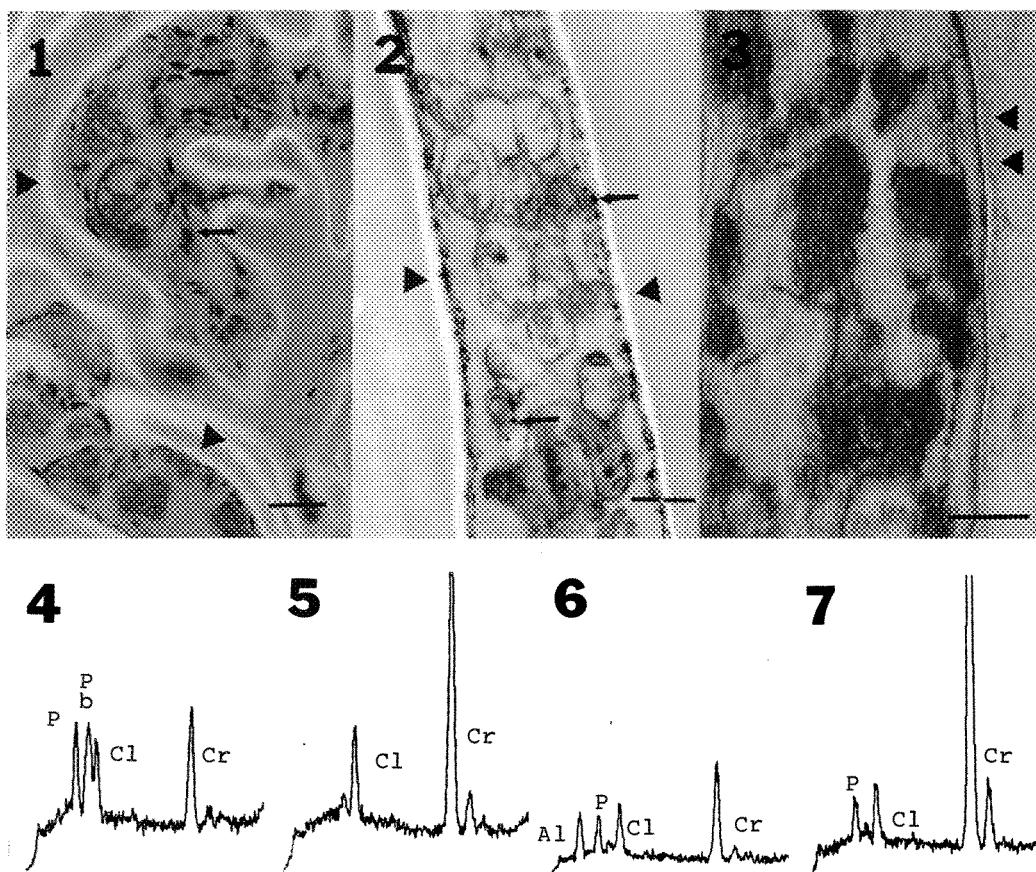
Hyphae of *P. tinctorius* were grown in nutrient broth at pH 4.0 in still culture and room T° unamended or amended with 50 ppm Pb (as PbCl₂) or 50 ppm Al (as AlCl₃). After 10 days, hyphal tips were frozen by PJ or by HPF. Hyphae were freeze-substituted in either 1% OsO₄ (to compare morphology) or 1% chromium trioxide⁴ (to allow for microanalysis without P peak overlap) in acetone and embedded in Spurr's epoxy resin. Sections were collected on copper grids, carbon-coated and examined in a JEOL 100 CX II TEM/SCAN and energy dispersive X-ray microanalysis (EDS) performed with a Link Systems AN 10000. Post staining was not done on any sections. Electron energy loss was used to compare section thickness.

Morphology was similar for fungal hyphae prepared by either PJ freezing or HPF (Figs. 1,2). Electron-dense granules were observed in hyphae grown in nutrient broth + Pb when prepared by either freezing method. More contrast was noted in hyphal walls prepared with Cr (Fig. 3) than with Os.

The EDS spectra from electron-dense granules of hyphae grown in nutrient broth + Pb showed peaks of P and Pb after PJ freezing (Fig. 4) but not after HPF (Fig. 5). Similarly, EDS spectra of fungal hyphae grown in nutrient broth + Al showed the presence of Al and P after PJ freezing (Fig. 6) but Al was not seen after HPF (Fig. 7). The Cl peaks from resin were similar in all spectra. Zierold et al.⁵ found similar morphology and, in contrast to this study, similar elemental composition in HPF and impact-frozen erythrocytes. In this study, HPF resulted in acceptable morphological preservation of metal-treated fungal tissue samples. Our results suggest that, under our described experimental conditions, HPF should be used with caution for elemental analysis and distribution studies.

References

1. C.J. McQuattie et al., Intern. Conf. on Heavy Metals in the Environ. (1991) Vol. 2, 314.
2. C.J. McQuattie and K.L. Klomparens, Proc. EMSA (1991), p. 282.
3. R.E. Edelmann et al., Proc. EMSA (1991), p. 70.
4. Zimmerman, A. Botanical Microtechnique, Henry Holt and Co., New York. (1893) p. 177.
5. K. Zierold et al., J. Microsc. (1991) 161 (2), RPI.
6. We acknowledge C. Bricker and L. Sadowski for assistance with the Balzers High Pressure Freezer at Miami University, Oxford, OH, (NSF grant #88-20387 to M. Powell and A. Allenspach).



FIGS. 1-3 -- Hyphae of *P. tinctorius* grown in nutrient broth + Pb. Bars = $0.5\mu\text{m}$.

FIG. 1. -- Os-prepared fungal hyphae, HPF. Dense granules (arrows), wall layer (arrowheads).

FIG. 2. -- Os-prepared fungal hyphae, PJ. Dense granules (arrows), wall layer (arrowheads).

FIG. 3. -- Cr-prepared fungal hyphae, HPF. Wall layer (arrowheads).

FIGS. 4-7--All spectra drawn to same scale.

FIG. 4. -- EDS spectrum from PJ, Cr-prepared, Pb-treated hypha.

FIG. 5. -- EDS spectrum from HPF, Cr-prepared, Pb-treated hypha.

FIG. 6. -- EDS spectrum from PJ, Cr-prepared, Al-treated hypha.

FIG. 7. -- EDS spectrum from HPF, Cr-prepared, Al-treated hypha.

MORPHOMETRIC ESTIMATION OF VIRAL BURDEN IN CELL CULTURE MATERIAL BY TRANSMISSION ELECTRON MICROSCOPY (TEM)

S.T. Bierley*, T.M. Monticello*, E.M. Morgan**, and J.R. Leininger*

*Pathology Associates, Inc., Durham, NC 27713, and **Microbiological Associates, Inc., Rockville, MD 20850

A major concern in the manufacture of cell culture-derived biotechnology products is the contamination of the cultures by potentially pathogenic agents such as retroviruses. Cell lines may have retroviral particles visible by TEM even when viral burden can not be demonstrated by infectivity assays or reverse transcriptase activity¹. The supernatant of the post-production cell cultures, therefore, must be evaluated by TEM for viral burden. An important question, however, is how to establish a quantitative viral load estimate for the evaluation of a purification process. The FDA recommends that a purification process for viral contaminants remove or inactivate 3-5 logs over the estimated viral burden.

Conventionally, negative staining has been utilized for TEM evaluation of retroviral particle load. Recently, an alternative method which utilizes plastic embedding with thin sectioning and TEM, has been demonstrated to be a superior technique to negative staining². In order to further validate the plastic embedding with thin sectioning method, we evaluated cell culture supernatant (pellets) for retroviral burden at various dilutions, from two cell lines. Morphometric determinations were made as to the number of viral particles present per unit volume and compared to results obtained by infectivity assay. Since the morphometric calculation for viral density assumes even distribution of viral particles, we also evaluated and calculated viral counts on multiple thin sections taken throughout selected pellets.

Each viral culture fluid sample was concentrated twice by centrifugation. The remaining supernatant was then centrifuged to obtain a viral culture 'pellet' which was fixed in glutaraldehyde-formaldehyde and measured (μm^3). The pellets were processed and embedded in Spurr's epoxy resin. Thin sections ($0.08\mu\text{m}$) were cut, mounted on 200 mesh copper grids (grid space = $85\mu\text{m}^2$), and routinely stained. Viral-like particles were quantified from 10 grid squares; a total volume of $5780\mu\text{m}^3$. The total number of viral particles in the entire pellet are calculated as follows:
 $(\text{number of viral particles}/5780\mu\text{m}^3)(\text{total volume of pellet})$.

Retroviral particles were easily recognized and quantified (Figure 1). Viral particle counts for each pellet at each dilution are presented in Table 1. A direct correlation of viral density existed between the infectivity assay and the TEM quantitative results. Furthermore, even distribution of viral particles in the pellet was demonstrated evidenced by equal viral counts from each representative section of the pellet. An even distribution of viral particles throughout the pellet supports the morphometric methodology for determination of viral load. Results from the present studies demonstrate that plastic embedding with thin sectioning and TEM morphometric quantification is a valid method for determining retroviral burden in cell culture supernatant.

References

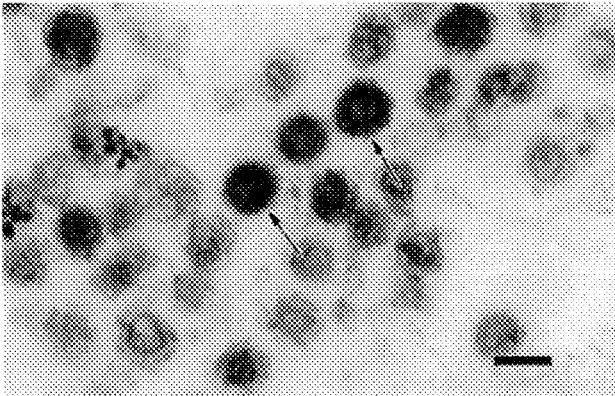
1. Bergmann, D.G. and Wolff, D.A. Intervirology 16:61-70 (1981).
2. Bierley, S.T., Monticello, T.M., Watkins, L.G., Bond, S.E., Poiley, J.A., et al., Proceedings, Southeastern Electron Microscopy Society, Vol. 15, (1992).

TABLE 1

Viral Conc. (particles/ μ l)	Pellet Vol. (μ m ³)	TEM Viral Density (particles/ μ m ³)	Total Viral Count/Pellet		
			Section 1	Section 2	Section 3
Sample A					
1.8×10^4	1×10^9	15730	2.7×10^9	ND*	ND
1.8×10^3	1×10^9	871	1.5×10^8	ND	ND
1.8×10^2	2×10^9	136	4.7×10^7	4.6×10^7	4.8×10^7
Sample B					
1.2×10^4	1×10^9	4994	8.6×10^8	ND	ND
1.2×10^3	3×10^9	153	7.9×10^7	ND	ND
1.2×10^2	2×10^9	25	8.6×10^6	11×10^6	11×10^6

*Not determined

FIGURE 1. Pellet of a cell culture supernatant demonstrating retrovirus-like particles (arrows). Bar=0.1 μ m.



HUMAN GALLSTONES: SPECIMEN PREPARATION AND LIGHT MICROSCOPY

Ronald Sinicki* and Christopher Viney†

*Department of Materials Science and Engineering FB-10 and the †Molecular Bioengineering Program, Center for Bioengineering WD-12, University of Washington, Seattle, WA 98195

Several methods for removing gallstones from the human body are in use or under investigation. They range from noninvasive techniques (dissolving; ultrasound lithotripsy), through minor surgery (use of wire basket lithotripter; laser lithotripsy), to major surgery. The choice of procedure seeks to accomplish removal of stones while minimizing the cutting of patient tissue, the post-treatment rehabilitation time, and the overall cost. The effectiveness of a given procedure will vary, depending on the size and number of stones present, and especially on their composition and microstructure. Attempts have therefore been made to correlate gallstone structure (from computerized tomography studies or magnetic resonance imaging¹ with the least severe procedure needed to break up and remove the stone. Such empirical correlations can be facilitated by additional *in vitro* microstructural characterization of stones, which attempt to relate the *in vivo* observations to likely fracture paths and mechanisms. It is convenient to distinguish between three broad categories of gallstone.² Cholesterol gallstones are associated with cholesterol supersaturation, when the level of cholesterol in bile exceeds the amount that the bile salts can keep in solution; they contain more than 25 wt% cholesterol and are relatively rare. Pigment gallstones contain less than 25 wt% cholesterol, and result from the precipitation and agglomeration of bilirubin and other inorganic salts. Mixed stones are the most common, and form the subject of our present investigations. Viewed in cross-section, they contain radiating crystals of cholesterol, together with concentric layers of apparently amorphous pigment. There are few literature references to the study of gallstone structure by light microscopy. We found only one reference to the microscopy of thin sections;³ others described low resolution reflected light studies of surfaces generated by dividing stones with a sudden impact delivered to a sharp knife. The drought of high resolution light micrographs even extends to pathology atlases.

Our own experiments were performed on mixed gallstones provided in normal saline; they were initially divided into quarters with a sharp knife (Fig. 1), so that the effects of more than one specimen preparation procedure could be compared on the same stone. Preparation of thin sections for transmitted light microscopy is made difficult by the extreme hardness of the inorganic constituents, and the friability of the stones when dehydrated. We initially contemplated embedding stone fragments in paraffin, plastic resin or gelatin. Because the embedding medium should ideally match the hardest constituent of the sample, we immediately excluded the possibility of using a paraffin medium.

Use of a plastic resin requires that the sample first be dehydrated, so that the medium can wet and penetrate the specimen microstructure while it sets, and so that later evaporation of water does not destroy adhesion at the interface between the sample and the medium. To achieve specimen dehydration, we tried two approaches: combinations of heat and vacuum, and alcohol dehydration. The single literature reference to thin specimen preparation suggests that heating mixed gallstones to 40°C for 6-48 hours is effective at dehydration.³ Our own attempts at treating mixed gallstones in this way converted them into a useless mass of powder. Intact specimens were obtained by drying in vacuum alone. Alcohol dehydrations were performed on quartered stones by successively immersing them for one hour in baths having alcohol concentrations by volume of 30%, 60%, 80%, 90%, 100% and 100%. However, we expect that alcohol dehydration will give less representative microstructures than vacuum drying, because alcohol is a solvent for cholesterol. A residue is left if the alcohol is subsequently allowed to evaporate from the baths, and the dehydrated stones are quite friable. Because the embedding medium (Estratil AL-100 Reposo-ESPANA) described in ref.3 was unavailable locally, the following common media were used in attempts to embed dehydrated gallstone quarters:

- BioRad A2032 LR white hard grade embedding medium;
- a typical bone sectioning medium, consisting of 85 ml methyl methacrylate, 10 ml glycol methacrylate, and 5 ml dibutyl phthalate mixed with 5 grams PEG distearate, catalyzed with 7 ml benzoyl peroxide for every liter of solution;
- JB-4⁺ from PolySciences.

In all cases, the gallstones dissolved in the embedding medium at room temperature (Fig.2). The dissolution proceeds less rapidly at lower temperatures, but, as polymerization rates also decrease at lower temperature, the colder samples have more time in which to dissolve.

Specimen embedding in a saline gelatin medium was more successful. Saline solution was prepared by adding 8.5 g Morton rock salt to 1 liter of de-ionized water. Knox unflavored gelatin (one packet, approx. 7 grams) was added in various concentrations to this solution (2/3 cup, 1 cup or 2 cups). After specimens were embedded, the gelatin was frozen. A new razor blade was used to pare thin slivers by hand from embedded material. Observation of the thinnest slivers between crossed polars at low magnification (Fig.3) revealed radially oriented cholesterol crystals (birefringent), and concentric rings of pigment, in agreement with the microstructures observed in reflected light (Fig.1). Viewed at higher magnification, material from approximately midway between the center and the edge of a mixed gallstone (Fig.4) reveals a microstructure consisting of an unoriented composite of cholesterol and inorganic matter. This type of fine-grained, composite, spheroidal microstructure is consistent with a high degree of mechanical toughness and resistance to lithotripsy.

References

1. R.L. Baron *et al.*, American Journal of Roentgenology 151 (1988) 1123.
2. A.J. Harding Rains, Gallstones, Springfield IL: Charles C. Thomas (1964).
3. A. Garcia Ontiveros *et al.*, Klinische Wochenschrift 68 (1990) 496.
4. The authors are grateful to Dr John Halsey for providing gallstones, and to Dr Sum P. Lee and Paulette Brunner for useful discussions. Support was provided by the Washington Technology Center.

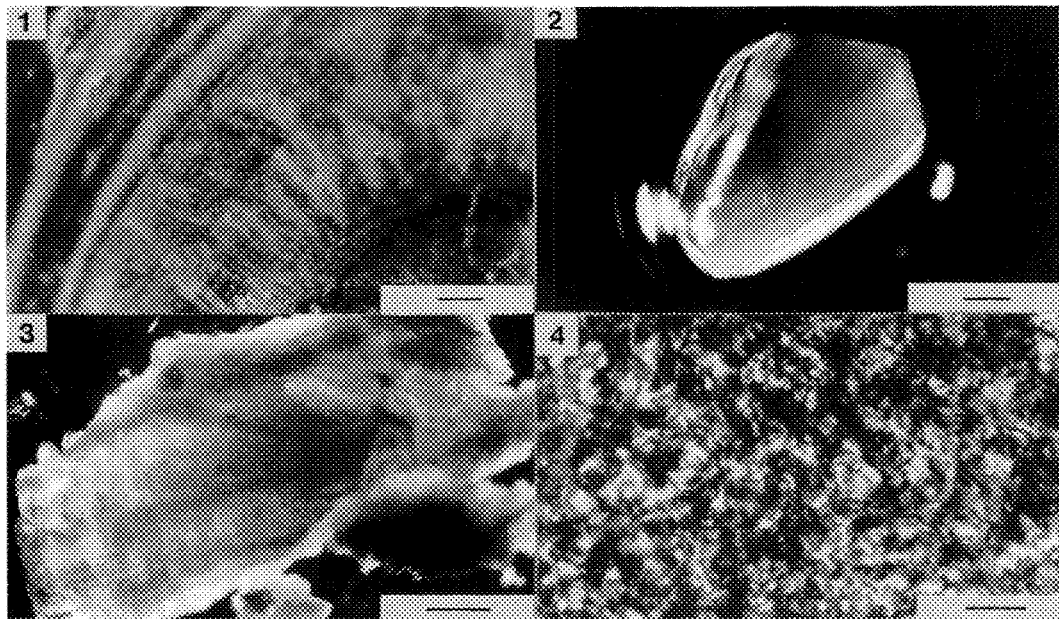


FIG. 1.--Cross-section of quartered mixed gallstone, after drying in vacuum for 1 hour. Reflected light. Bar = 100 μ m.
FIG. 2.--Mixed gallstone quarter dissolving in BioRad A2032 LR white hard grade embedding medium at room temperature; fragment previously dried in vacuum for 1 hour. Reflected light. Bar = 100 μ m.
FIG. 3.--Thin sliver pared from mixed gallstone quarter mounted in frozen saline gelatin solution. Transmitted light; crossed polars. Bar = 100 μ m.
FIG. 4.--High-magnification view of sliver pared from mixed gallstone quarter mounted in frozen saline gelatin solution. Transmitted light; crossed polars. Bar = 20 μ m.

IMPROVED PRESERVATION OF FREEZE-DRIED BIOLOGICAL SPECIMENS

Martha N. Simon, Beth Y. Lin, and Joseph S. Wall

Biology Dept., Brookhaven National Laboratory, Upton, NY 11973

Specimens prepared by the wet-film technique¹ (injecting unstained biological specimens into a drop of buffer on a thin carbon substrate which has never seen air, washing extensively, blotting to a thin layer of liquid, plunging the grid into nitrogen slush, and freeze-drying overnight) then visualized in the scanning transmission electron microscope (STEM) usually have reasonably well-preserved structures. However, there is a certain variability from day to day and sometimes even from one area to another on a given grid. This can occur for different reasons which may be inextricably related. The thin carbon film can be non-uniform at the molecular level with hot spots for strong attachment of some specimens, a part of a biological specimen may attach strongly while the rest of it thrashes about in Brownian motion ruining any perceivable structure, and the final thickness of liquid before freeze-drying may vary slightly which may affect the preservation of the structure.

By including other solvents such as ethanol(EtOH), glycerol(Glyc), and ethylene glycol(EG) in the usual wash buffer of 20mM NH₄Ac, the interaction of the specimen with the carbon film could be different as could the freeze-drying. As trial specimens, tobacco mosaic virus (TMV), apoferritin, and a yeast LA virus capsid² were used. Solutions of 5%, 10%, 20% and 50% solvents were used as wash buffers. Little effect was seen on TMV alone, either in the background or the mass, but it is a rather robust specimen normally. Consequently, TMV was included with the other specimens as the usual internal standard. The apoferritin appeared best using only 20mM NH₄Ac as the wash buffer; it was not improved by EtOH, and was somewhat fuzzier when treated with Glyc or EG (data not shown). However, interesting results were obtained with the yeast virus capsid.

Many different viral capsids, hollow spheres with interesting morphologies, are very sensitive to deposition on carbon film and freeze-drying. Sometimes they can be beautifully preserved, but unfortunately they often look like "pac-men" (which could be expected if part of a sphere attaches, collapses and cracks before being deposited). Mass measurements indicate that these forms can be equal to or lower in mass than intact looking capsids. This phenomenon has been seen with capsids of bacteriophage T7, herpes simplex virus, B. subtilis ϕ 29, and the yeast virus described below.

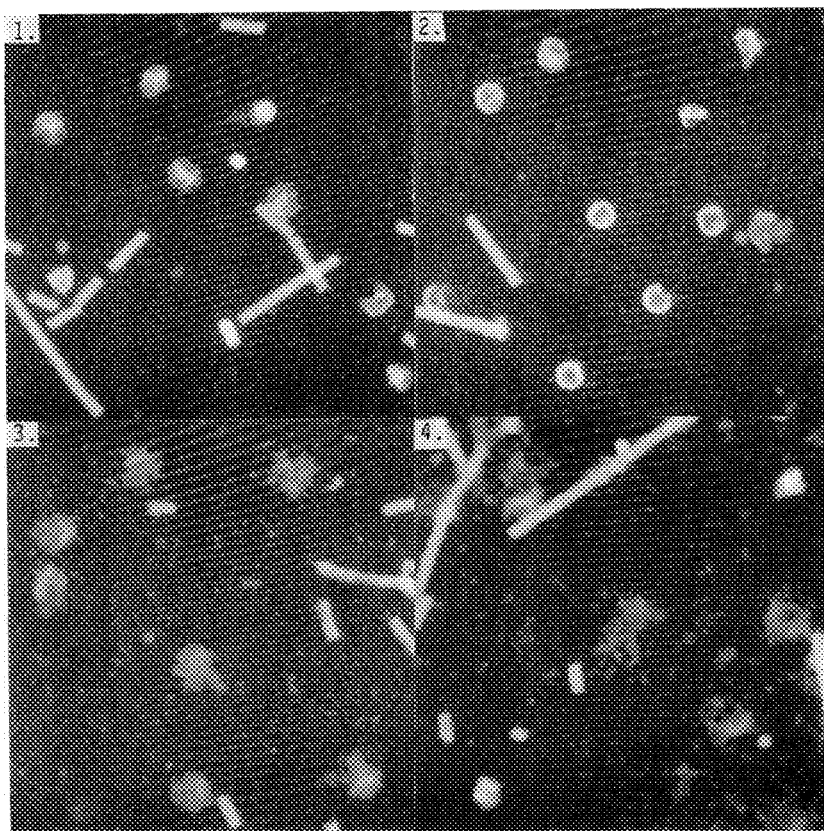
The yeast capsids did not appear well-preserved using only 20mM NH₄Ac as the wash buffer. However, including 20% EtOH gave a much higher proportion of reasonably well-preserved capsids. Interestingly, both Glyc and to a lesser extent EG seemed

References

1. J.S. Wall, J.F. Hainfeld and M.N. Simon, EMSA Bull. (1991) 21:2,81-86.
2. R. Wickner, in Yeast RNA Virology: The Killer Systems, CSH Press (1991) 1, 263-295.
3. Supported by DOE/OHER and NIH Grant RR01777.

to melt out the structures. This can be seen in Figs. 1-4. A series of EtOH washes of different concentrations showed that 5% was little different from the control, 10% gave a somewhat higher proportion of well-preserved capsids, and 50% gave highly condensed (squashed) structures (data not shown).

While these results appear promising, the problems about variability have not been completely solved. In all cases, even under the worst conditions, an occasional well-preserved capsid could be found. Similarly, with the best condition of 20% EtOH, occasional ruined capsids could be found. However, the proportion of well-preserved structures can clearly be influenced rationally.



Figs. 1-4 are dark field STEM micrographs of yeast virus capsids treated with different injection and wash buffers. The full-scale of each is 0.512 microns.

- FIG. 1. Washed with only 20mM NH_4Ac .
- FIG. 2. Washed with 20mM NH_4Ac plus 20% EtOH.
- FIG. 3. Washed with 20mM NH_4Ac plus 20% EG.
- FIG. 4. Washed with 20mM NH_4Ac plus 20% Glyc.

SOME QUANTITATIVE APPLICATIONS OF VASCULAR CORROSION CASTING

Fred E. Hossler

Department of Anatomy, J.H. Quillen College of Medicine, East Tennessee State University, Johnson City, Tennessee 37601

Preparation of replicas of the complex arrangement of blood vessels in various organs and tissues has been accomplished by infusing low viscosity resins into the vasculature. Subsequent removal of the surrounding tissue by maceration leaves a model of the intricate three-dimensional anatomy of the blood vessels of the tissue not obtainable by any other procedure.¹ When applied with care, the vascular corrosion casting technique can reveal fine details of the microvasculature including endothelial nuclear orientation and distribution (Fig. 1), locations of arteriolar sphincters (Fig. 2), venous valve anatomy³ (Fig. 3), and vessel size, density, and branching patterns.¹ Because casts faithfully replicate tissue vasculature, they can be used for quantitative measurements of that vasculature. The purpose of this report is to summarize and highlight some quantitative applications of vascular corrosion casting. In each example, casts were prepared by infusing Mercor, a methyl-methacrylate resin, and macerating the tissue with 20% KOH.² Casts were either mounted for conventional scanning electron microscopy, or sliced for viewing with a confocal laser microscope.

By observing endothelial nuclear imprints on casts, the number, size, and orientation of endothelial cells per unit area can be determined (Fig. 4). If infusion and transmural pressures are monitored, casts can also be used to measure vessel diameters. By weighing casted tissue before and after maceration, the vascular volume of a tissue can be calculated from tissue and resin densities.^{2,4} Figures 5 and 6, show casts of rat heart and hamster lung, respectively, for which vascular volumes of 10%, and 12% were calculated. In the heart sample the capillary density was about 2700/mm². Changes in the alveolar vasculature of lung in emphysema can be estimated from casts using a computer driven confocal laser microscope.⁴ Stored images of normal (Fig. 6) and emphysemic (Fig. 7) hamster lung casts are made bimodal (Figs. 8A and 8B), the area of each mode is measured by the computer software, and the volume of the alveolar vasculature of the tissue sample is calculated mathematically. In this case, emphysema decrease the volume of the alveolar vasculature by about 40%. The confocal laser microscope has the advantages of a narrow depth of field, and thus its image is not affected by the usually uneven surfaces of the sectioned casts. In summary, the application of vascular corrosion casting for quantitative determinations merits further investigation.

References

1. A. Lametschwandtner et al., Scan. Electr. Micros. (1984)II, 663.
2. F.E. Hossler et al., Scan. Elect. Micros. (1986)IV, 1469.
3. F.E. Hossler and R.F. West, Am. J. Anat. (1988)181, 425.
4. F.E. Hossler et al., J. Electron Micros. Tech. (1991)19, 406.

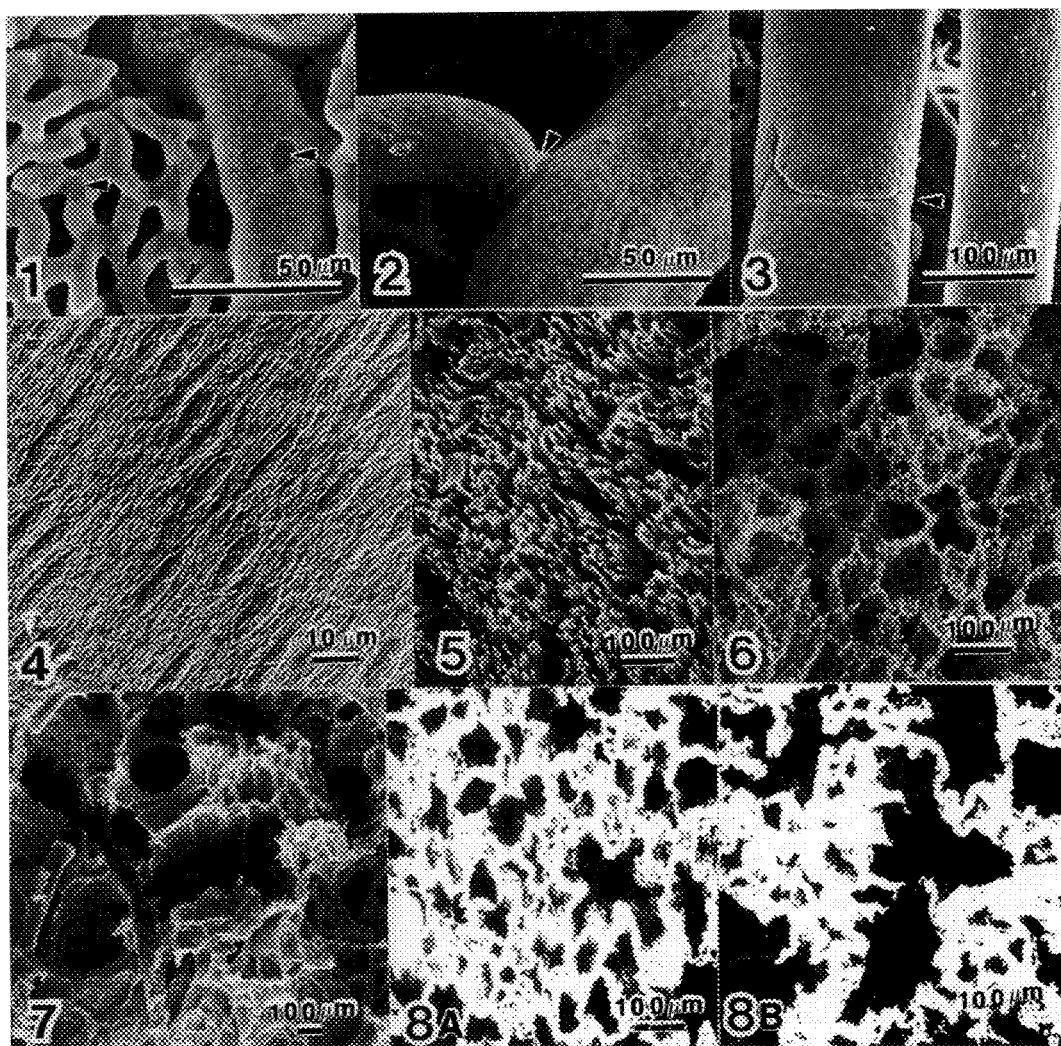


FIG. 1. -- Cast of vasculature of bronchus of hamster lung. Arrows: endothelial nuclear imprints on vein and capillary.

FIG. 2. -- Cast of arteriole of duckling eye. Arrow: Site of sphincter.

FIG. 3. -- Cast of artery and vein of duckling eye. Arrow: valve.

FIG. 4. -- Surface of cast of artery (duckling eye). The endothelial nuclear imprints occurred at a density of $3700/\text{mm}^2$.

FIG. 5. -- Cross section of cast of rat myocardial microvasculature.

FIG. 6. -- Cast of normal hamster lung microvasculature.

FIG. 7. -- Cast of ephysemic hamster lung microvasculature.

FIG. 8. -- Bimodal images of hamster lung microvasculature prepared with a confocal laser microscope. A: normal; B: emphysemic.

IN SITU CRYOFIXATION OF LUNG TISSUE USING THE PS1000, A HAND-HELD METAL MIRROR CRYOFIXATION DEVICE

John J. Godleski, Rebecca C. Stearns, Marshall Katler, Robyn Rufner, Theresa D. Sweeney and Fred G. Lightfoot†

Respiratory Biology Program, Harvard School of Public Health, 665 Huntington Ave., Boston, MA 02115 and †Department of Anatomy, George Washington University, 2300 I Street, N.W., Washington, D.C. 20037

We have previously reported methods to cryofix the extracellular lining layers of the large airways and trachea.¹ We seek to study the extracellular lining layers of both airways and alveoli *in situ* because it is the interaction of these lining materials with inhaled particles that determines the subsequent responses of phagocytic cells to the particles.^{2,3} Cryopreservation of the lining fluids of lung parenchyma is difficult because of the complexity of distal lung structure, and the need to fix the lung in its natural state, i.e., filled with air. Any method used must be able to obtain the frozen specimen from the inflated lung. This requirement precludes the possibility of having a cryogen come into primary contact with the internal surface of an alveolus. However, if optimal fixation through the pleura could be attained, then the lining layers of subjacent alveoli could be studied. In this report, we describe a new method to cryopreserve distal lung tissue for optimal study of the extracellular lining layers of the alveolus. Alveolar tissue is sufficiently preserved in the inflated state to maintain its *in vivo* characteristics.

Rats were sacrificed with an overdose of pentobarbital. The trachea was cannulated, and the chest opened to expose both lungs. The lungs were then inflated with 5 ml of air. Lobes were tied off with thread at their bronchi and the thread used to hold the lobe out of the chest. The distal most portion of the lobe was then slam frozen with the PS1000 (Delaware Diamond Knives Inc., Wilmington, DE). This instrument has a pneumatically activated hammer and a polished copper mirror (anvil) which was precooled in liquid nitrogen. For cryofixation, the tissue was slammed against the mirror by the hammer. After *in situ* fixation, the tissue and PS1000 were returned immediately to liquid nitrogen. The specimens were then freeze-dried, embedded in spurr or araldite resin, and sectioned at 1 μ m for light microscopy, and at 60 nm for ultrastructural examination. At least three, and in most cases, five biopsies were obtained from each animal. Figure 1 illustrates the light microscopic appearance of the tip of a lobe fixed with the PS1000. The top of the illustrated specimen was cryofixed at the anvil, the bottom was compressed by the hammer. Note the well preserved alveoli immediately subjacent to the pleura at the top. A thin fluid layer is visible on the pleural surface; the cellular components and the collagen and elastin of the pleura are also seen clearly. The underlying alveolus is visible, and also well preserved. The deeper tissue has both compression and ice crystal damage. The structure and fluid layer of the pleura at the bottom are less well seen as would be expected from this tissue farthest away from the metal mirror. In Figure 2a and b the ultrastructure of the pleura and subjacent alveoli are illustrated. The preservation of pleural and alveolar structure of an area closest to the metal mirror is illustrated, and the extracellular lining layer of the alveolus can be seen. This new instrument provides a unique and important way to preserve tissues that has not been available to date.⁴

References

1. J.J. Godleski, *et al.* Proc. of EMSA. (1991)49, 72.
2. L. Kobzik, *et al.* J. Immunol. (1990)144, 4312.

3. L. Kobzik, *et al.* FASEB J. (1992), in press.
4. This research was supported by NIH Research Grants HL-31021 and ES-00002 and EPA Research Grant 818130.

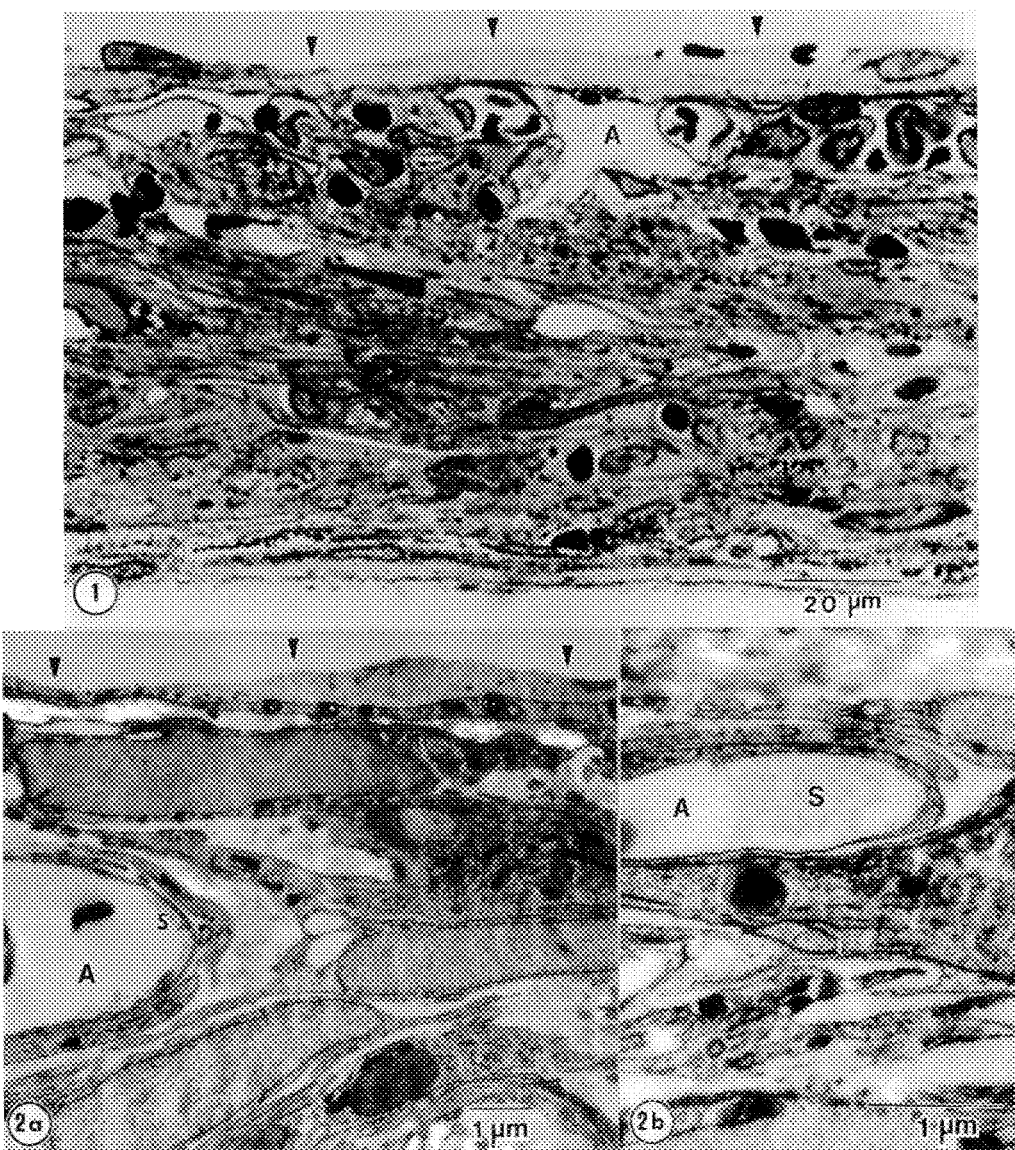


Fig. 1--Rat lung tissue cryofixed with the PS1000 and freeze dried. Arrowheads point to the slam-frozen pleural surface with a layer of fluid. A = alveoli.
Fig. 2a and b.--Ultrastructure of cryofixed rat lung tissue. Labels as in in Fig. 1. S = Extracellular alveolar lining material.

IN SITU METAL MIRROR CRYOFIXATION OF RAT KIDNEY FOR ELECTRON PROBE X-RAY MICROANALYSIS

Craig C. Freudenrich*, Daniel Hockett*, Kerri Winter*, Peter Ingram⁺, and Ann LeFurgey*

* Division of Physiology, Department of Cell Biology, Box 3709, Duke University Medical Center, Durham, NC 27710; ⁺ Research Triangle Institute, Research Triangle Park, NC 27709

Many studies of proximal tubule function require information about the elemental composition in subcellular compartments that can be obtained by electron probe x-ray microanalysis (EPXMA). While experiments of this type have been performed on isolated proximal tubule preparations,¹ it is also necessary to conduct parallel experiments on intact tissue to verify those results obtained with isolated tubules. One limitation in conducting EPXMA analysis on whole tissue is obtaining adequately cryopreserved tissue. Metal mirror cryofixation techniques have yielded excellent preservation in dissected tissues or cell cultures.² Therefore, experiments were performed to assess the efficacy of *in situ* metal mirror fixation of the intact rat kidney.

Male rats were anesthetized with sodium pentobarbital (50 mg/kg). The left kidney was exposed, elevated, separated from the surrounding viscera by a thin sheet of Parafilm (American Can Co., Greenwich, CT), and kept moist with 0.9% NaCl solution. The kidney was then briefly blotted to remove excess fluid, cryopreserved *in situ* with a portable metal mirror cryofixation device (PS1000, Delaware Diamond Knives, Wilmington, DE), and transferred to storage vials in liquid N₂. The frozen tissue was cryosectioned according to previous methods,¹ except that an ion spray device (Diatome, Fort Washington, PA) was used to reduce static electricity inside the cryochamber. The cryosections were then freeze-dried, carbon-coated, and analyzed by EPXMA imaging (128 x 128 x 4 s dwell time) to determine the elemental distribution in cytoplasmic, mitochondrial, and nuclear compartments.^{3,4} In addition, some portions of the frozen tissue were freeze-substituted and prepared for light microscopy to assess the overall preservation of tubule structures.¹

The metal mirror method of *in situ* freezing preserved gross tubule morphology as indicated by the presence of proximal tubules with intact brush borders and open lumens (Figure 1). Furthermore, these methods yielded large, flat cryosections of entire tubules, in which mitochondria, nuclei, and basolateral membranes of individual proximal tubule cells could be easily observed (Figure 2) and elemental information from these compartments could be obtained by EPXMA (Figure 3, Table 1). Analysis of the EPXMA images (Table 1) revealed that the cells were undamaged by the freezing process because: (1) cytoplasmic Na was low and cytoplasmic K was high, i.e. the K/Na ratio was 4.7 which is similar to that observed in whole rat kidney cryopreserved by plunge-freezing;^{5,6,7} (2) Cl levels in all compartments were low; (3) low levels of mitochondrial Ca were observed. In summary, these results demonstrate the feasibility of the metal mirror method of *in situ* cryopreservation of the kidney for EPXMA and form the basis for future studies of proximal tubule function under normal physiological and pathophysiological conditions (e.g. ischemia, diabetes).

1. A. LeFurgey et al., J. Am. Soc. Nephrol. 1 (1991) 1305.
2. R. Nassar et al., Scanning Electron Microscopy I (1986) 309.
3. A. J. Spencer et al., J. Am. Soc. Nephrol. 1 (1991) 1321.
4. A. LeFurgey et al., J. Microscopy 165 (1992) 191.
5. F. Beck et al., Kidney Int. 17 (1980) 756.
6. F. Beck et al., Kidney Int. 22 (1982) 250.
7. A. J. Saubermann et al., Kidney Int. 29 (1986) 682.
8. This work was supported by the American Diabetes Association and NSF DIR9106607. The authors gratefully acknowledge Fred Lightfoot (George Washington University), Joe Tabeling and Norm Woodside (Delaware Diamond Knives), and Stacie Kirsch (Diatome) for their technical support.

TABLE 1. Subcellular element content in proximal tubule cells of *in situ* cryopreserved rat kidney.

Element	Cytoplasm	Mitochondria	Nucleus
Na	57 ± 4 (80)	44 ± 3 (76)	40 ± 7 (6)
K	270 ± 6 (80)	272 ± 3 (76)	338 ± 14 (6)
P	247 ± 7 (80)	301 ± 4 (76)	336 ± 23 (6)
Cl	76 ± 3 (80)	68 ± 3 (76)	58 ± 5 (6)
Ca	7.9 ± 1.0 (80)	2.6 ± 0.6 (76)	3.8 ± 0.2 (6)

Element content unit = nmol/mg dry weight; Data are means ± SE (number of 6 pixel sample areas for cytoplasm or number of sampled organelles for mitochondria and nucleus) of 8 cells from 3 rats.

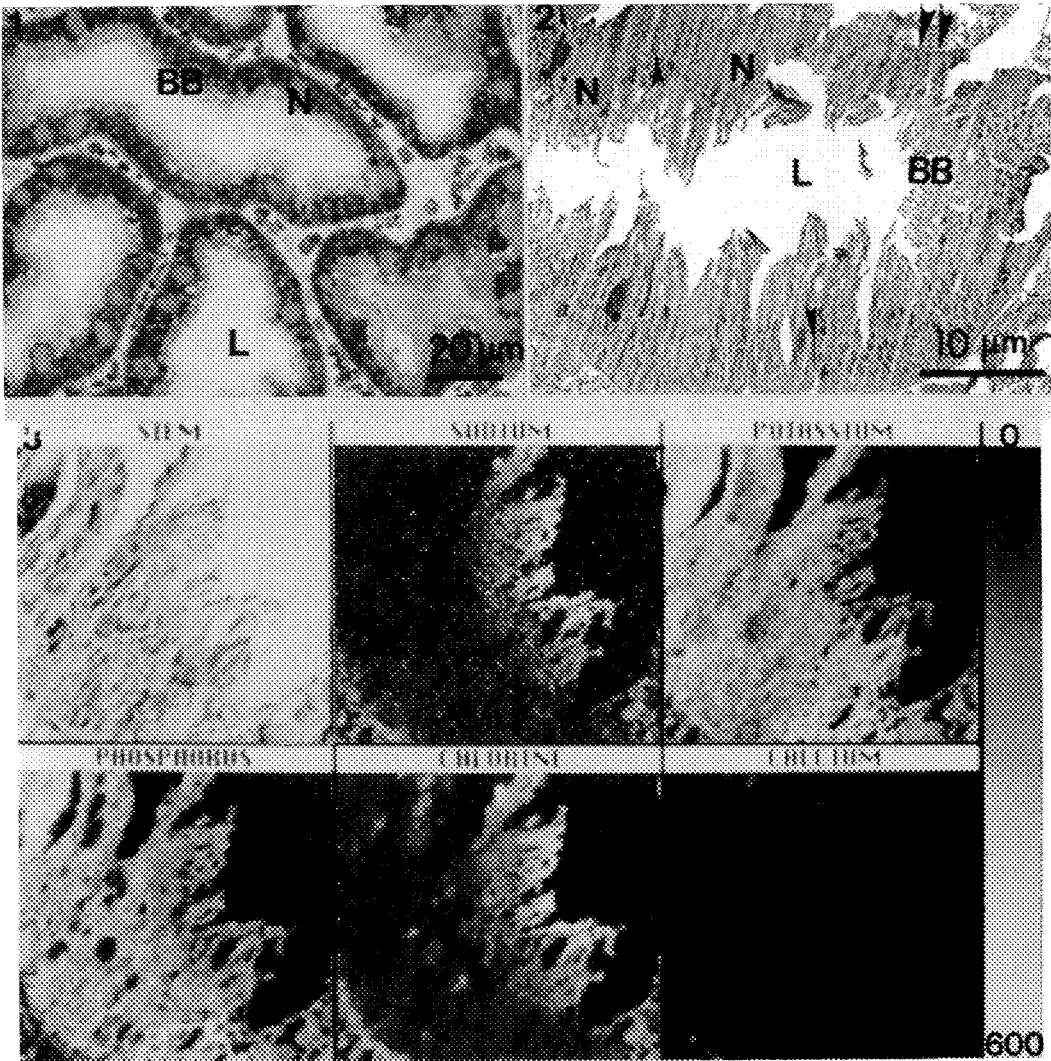


Fig. 1. Light micrograph of freeze-substituted section. Symbols: L, lumen; N, nucleus; BB, brush border; Bar, 20 μm.

Fig. 2. Transmission electron micrograph of unstained freeze-dried cryosection. Symbols: L, lumen; N, nucleus single arrow, mitochondria; BB, brush border; double arrow, basolateral membrane; Bar, 10 μm.

Fig. 3. Quantitative EPXMA images of a segment of the freeze-dried cryosection in Fig. 2. Image ~ 12, 400x.

SEM ANALYSIS OF FISH SCALE CROSS SECTIONS : A TECHNIQUE STUDY

M.E. Lee*, A. Moller*, P.S.O. Fouche**, I.G Gaigher**

*Electron Microscope Unit, University of the North, Sovenga, 0727, South Africa

**Zoology Department, University of Venda, Sibasa, South Africa

Scanning electron microscopy of fish scales has facilitated the application of micro-structures to systematics.¹ Electron microscopy studies have added more information on the structure of the scale and the associated cells, many problems still remain unsolved, because of our incomplete knowledge of the process of calcification. One of the main purposes of these studies has been to study the histology, histochemistry, and ultrastructure of both calcified and decalcified scales, and associated cells, and to obtain more information on the mechanism of calcification in the scales. The study of a calcified scale with the electron microscope is complicated by the difficulty in sectioning this material because of the close association of very hard tissue with very soft tissues. Sections often shatter and blemishes are difficult to avoid.² Therefore the aim of this study is firstly to develop techniques for the preparation of cross sections of fish scales for scanning electron microscopy and secondly the application of these techniques for the determination of the structures and calcification of fish scales.

In this study cross-sectioned scales of *Labeo umbratus*, were prepared using four methods. Firstly fresh scales were frozen in isopentane and either fractured or cut using a surgical scissor. Secondly the cut cross-sections were air dried and some of the samples were etched in 1% HCl to delineate the layers in the fibrillary plate. Thirdly frozen cross sections were fixed in 2,5% glutaraldehyde in a phosphate buffer, dehydrated in a series of ethanol solutions, followed by critical point drying (CPD). Fourthly the scales were embedded in resin, mechanically cut and finally polished using a 0,25µm diamond slurry. Cross-sections were studied in a scanning electron microscope using the secondary (SE) mode and x-ray mode.

The preparation of cross-sections of the scale by cryo-fracturing (Fig. 1) is unsatisfactory due to irregular shattering of the fibrillary plate. The fibrous nature of this plate is clearly evident but does not provide any useful information. The application of cryo-cutting produces vertical cutting marks, however, the layered structure in the fibrillary plate are clearly seen (Fig.2). The two distinct layers in the osseous layer correspond to the "limiting layer" as previously described.³ Cross-sections produced by CPD preparation are also unsatisfactory as the individual layers are separated (Fig. 3). The texturing and layering in the fibrillary plate as revealed by HCl etching are shown in detail in Figure 4. The cross-section produced by embedding and mechanical polishing (Fig. 5) appears to partially dislodge the osseous layer and to distort the layered structure in the fibrillary plate. X-ray analysis (Fig. 6) shows the Ca distribution to predominate in the osseous layer. Although some authors^{1,2} stated that the fibrillary plate showed no signs of calcification, X-ray analysis has shown that the Ca distribution predominates in the osseous layer, and some calcification was found in the fibrillary plate. The latter two techniques are complimentary and both provide information on the layering and texturing of the fibrillary plate by SEM which to date has not been described in the literature.

1. J.-Y. Sire, J. Fish Biol. (1986)28, 713.

2. M.M. Fouda, J. Fish Biol. (1979)15, 173.

3. O. Wallin, Rep. Inst. Freshwat. Res. (Drottningholm). (1957)38, 385.

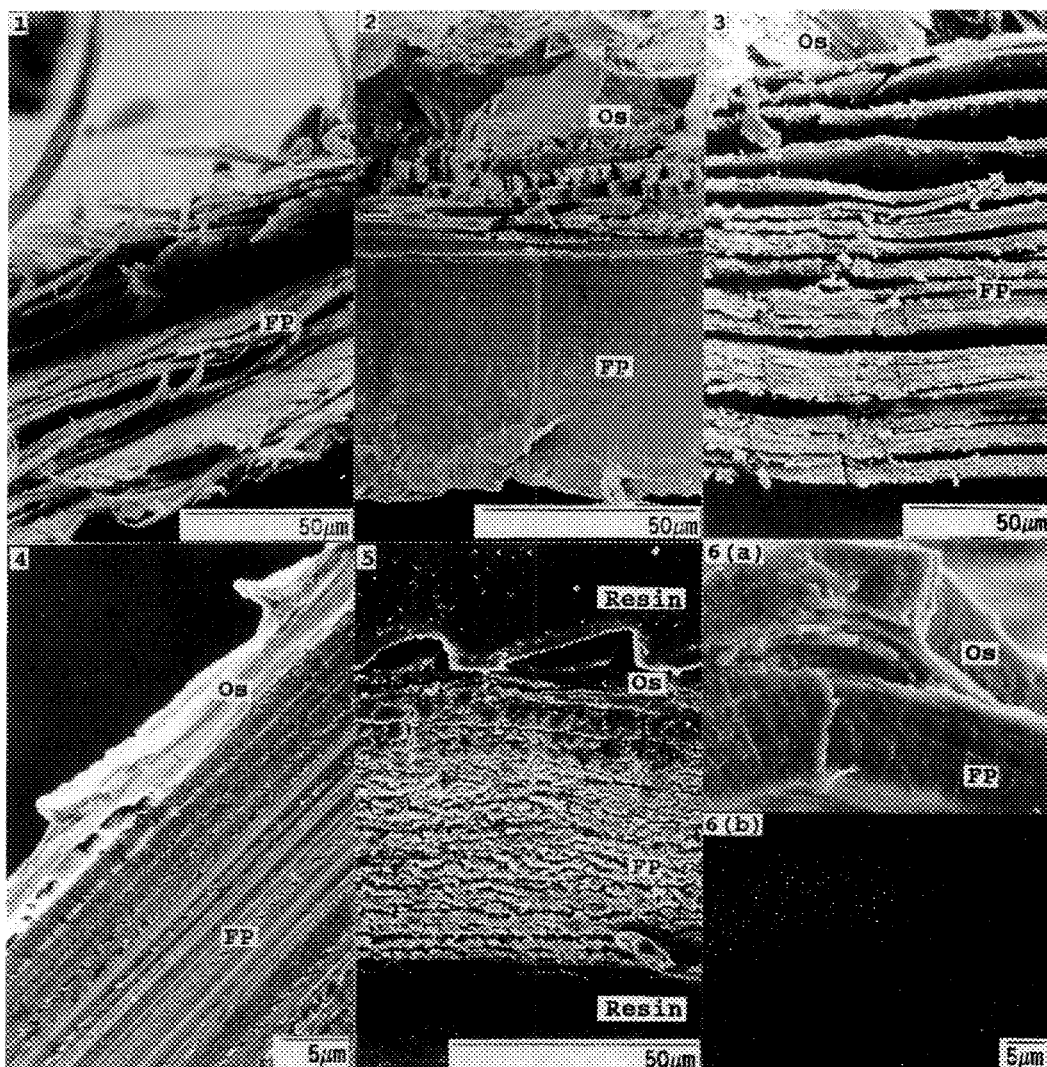


Fig. 1--SEM micrograph showing effects of scale preparation by freezing and fracturing. The fibrous nature of fibrillary plate (FP) is well illustrated.

Fig. 2--SEM micrograph showing effects of scale preparation by freezing and cutting. Note the layering in the osseous layer (Os).

Fig. 3--SEM micrograph showing effects of scale preparation by freezing, cutting, fixing and CPD.

Fig. 4--SEM micrograph showing effects of scale preparation by freezing, cutting and etching. Texturing and delineation is clearly defined.

Fig. 5--SEM micrograph showing distortion of the layers caused by the process of embedding and polishing.

Fig. 6--(a) S.E. micrograph and (b) X-ray map indicating Ca distribution which predominates in the osseous layer.

ALTERNATIVES TO TRADITIONAL EPOXY EMBEDDING "KITS": NOVEL CHOICES

J.A. Mascorro and G.S. Kirby

Department of Anatomy, Tulane Medical School, New Orleans, LA 70112

Epoxy resin embedding "kits" invariably are offered as one epoxy resin coupled with the hardeners dodecynyl succinic anhydride (DDSA), nadic methyl anhydride (NMA) and the amine catalyst 2,4,6-Tri(dimethylaminomethyl)phenol (DMP-30). This well-known mixture has been used widely for many years¹, perhaps in part because it is offered in the form of a convenient kit. Microscopists should be aware that packaged kits, even though they produce successful results, possess a never-changing high viscous character that could compromise optimum infiltration or damage delicate specimens. Past studies^{2,3,4} have shown clearly that the kit components DDSA and DMP-30 are particularly viscous compounds. Replacing DDSA with the less viscous nonenyl succinic anhydride (NSA), and substituting either dimethylaminoethanol (DMAE) or benzyldimethylamine (BDMA) as the catalyst of choice in place of DMP-30 will significantly reduce the viscosity of the overall mixture while producing easily manageable media that maintain fluidity longer, insure optimum infiltration, and ultimately produce results equal to those obtained with traditional kits.

Embedding media utilizing original Epon 812 or a similar high viscosity resin, Eponate 12, were prepared in usual kit form with DDSA, NMA and DMP-30. A vertically oriented viscometer was filled by aspiration with 9ml of either embedding media. The media then was allowed to flow out under the effect of free gravity, and the Flow Rate (time necessary for media to empty) and Volume Flow Rate (amount of media flowing in time) were determined. Viscosity (cp) then was calculated by using the Hagen-Poiseville relation for laminar flow (ie., fluids that flow fast are low viscosity; fluids that flow slowly are high viscosity). Epon 812 and Eponate 12 next were mixed in novel combination with NSA/NMA/BDMA (NSA and BDMA are less viscous⁴) and similar testing conducted. Testing for Flow Rate (FR) and Volume Flow Rate (VFR) was performed at 5, 30, and 60 minute intervals from initial mixing, in order to determine the effect of time on the hardening character of embedding media. Various soft biological tissues were perfusion fixed and dehydrated routinely, infiltrated for 6 hrs, polymerized for 24 hrs @68°C, sectioned, and double-stained with lead citrate and uranyl acetate.

Epon 812 and Eponate 12 embedding media, when combined with the usual and highly viscous kit components displayed a very slow FR and VFR at all time intervals, and the cp of both embedding media was higher, particularly 60 minutes after mixing (Tables I, III). The FR for the traditional Epon 812 mixture nearly quadrupled from 5 to 60 min after initial mixing, and the concurrent VFR distinctly slowed from 0.0232 ml/sec @5 min to 0.0064 ml/sec @60 min (Table I). The ultimate cp shown by this mixture also became very elevated as a function of time (Table I). This general trend, ie., slower FR accompanied by reduced VFR and increased cp also was evident with Eponate 12 media prepared in the traditional manner (Table III). On the other hand, clear changes were evident when the anhydride DDSA and the catalyst DMP-30 were removed from the traditional kit and replaced with the less viscous NMA and BDMA. Both Epon 812 and Eponate 12, in novel mix with NSA/NMA/BDMA, showed a significantly faster FR as well as a higher VFR and subsequently a lower overall cp (Tables II, IV). Similar testing has shown that the epoxy resins LX 112 and Embed 812 yield embedding media showing more desirable and lower viscosity characteristics when prepared in novel combination with NSA/NMA and either DMAE or BDMA^{3,4}.

All embedding media, regardless of viscosity, performed satisfactorily in terms of infiltrating capability, polymerization, cutting qualities, stainability, and produced sections with strength and stability within the vacuum and heat of the microscope column. It is important to note that microscopists have wide choices when considering the viscosity of an embedding medium. This parameter can be manipulated easily by matching alternative catalysts and anhydrides with an epoxy resin of choice, thus producing specific media for specific embeddings. This could be important when dealing with tissues susceptible to infiltration wave damage, or while infiltrating hard biological or plant tissues.

TABLE I - TRADITIONAL MIXTURE
EPON 812/DDSA/NMA/DMP-30

<u>Time From Initial Mixing</u>	<u>Flow Rate</u>	<u>Volume Flow Rate</u>	<u>Viscosity (Centipoise)</u>
5 min	6:27.84 min	0.0232 ml/sec	106.3 cp
30 "	17:39.36 "	0.0085 "	290.7 "
60 "	23:29.13 "	0.0064 "	386.6 "

TABLE II - NOVEL MIXTURE
EPON 812/NSA/NMA/BDMA

<u>Time From Initial Mixing</u>	<u>Flow Rate</u>	<u>Volume Flow Rate</u>	<u>Viscosity (Centipoise)</u>
5 min	3:05.13 min	0.0486 ml/sec	42.6 cp
30 "	7:47.59 "	0.0192 "	107.6 "
60 "	12:05.67 "	0.0124 "	167.0 "

TABLE III - TRADITIONAL MIXTURE
EPONATE 12/DDSA/NMA/DMP-30

<u>Time From Initial Mixing</u>	<u>Flow Rate</u>	<u>Volume Flow Rate</u>	<u>Viscosity (Centipoise)</u>
5 min	1:21.33 min	0.1107 ml/sec	25.2 cp
30 "	4:45.97 "	0.3906 "	88.7 "
60 "	7:26.91 "	0.2014 "	138.6 "

TABLE IV - NOVEL MIXTURE
EPONATE 12/NSA/NMA/BDMA

<u>Time From Initial Mixing</u>	<u>Flow Rate</u>	<u>Volume Flow Rate</u>	<u>Viscosity (Centipoise)</u>
5 min	1:17.11 min	0.1167 ml/sec	18.9 cp
30 "	2:42.74 "	0.0553 "	39.8 "
60 "	3:58.68 "	0.0377 "	58.4 "

References

1. J.H. Luft, J. Biophysic. Biochem, Cytol., 9:409-413, 1961.
2. J.A. Mascorro and G.S. Kirby, EMSA Proceedings, 44:222-223, 1986.
3. J.A. Mascorro and G.S. Kirby, Proceedings, XIth International Congress for Electron Microscopy, 138-139, 1990.
4. J.A. Mascorro and G.S. Kirby, EMSA Proceedings, 49:292-293, 1991.

HIGH-PRESSURE FREEZING AND FREEZE SUBSTITUTION OF PLANT TISSUE

William P. Sharp and Robert W. Roberson

Department of Botany, Arizona State University, Tempe, AZ 85287-1601

The aim of ultrastructural investigation is to analyze cell architecture and relate a functional role(s) to cell components. It is known that aqueous chemical fixation requires seconds to minutes to penetrate and stabilize cell structure which may result in structural artifacts.¹ The use of ultralow temperatures to fix and prepare specimens, however, leads to a much improved preservation of the cell's living state.^{2,3,4} A critical limitation of conventional cryofixation methods (i.e., propane-jet freezing, cold-metal slamming, plunge-freezing) is that only a 10 to 40 μm thick surface layer of cells can be frozen without distorting ice crystal formation.⁴ This problem can be allayed by freezing samples under about 2100 bar of hydrostatic pressure which suppresses the formation of ice nuclei and their rate of growth. Thus, 0.6 mm thick samples with a total volume of 1 mm³ can be frozen without ice crystal damage.² The purpose of this study is to describe the cellular details and identify potential artifacts in root tissue of barley (*Hordeum vulgare* L.) and leaf tissue of brome grass (*Bromus mollis* L.) fixed and prepared by high-pressure freezing (HPF) and freeze substitution (FS) techniques.

Tissue samples (1-2 mm³) were suspended for 5 min in a 15.0% (w/v) aqueous dextran solution (38,800 MW) and then placed in specimen holders that had previously been coated with a freshly prepared vegetable lecithin solution. Samples were immediately frozen in a Balzers HPM 010 High-Pressure Freezing Machine and prepared for transmission electron microscopy by FS.^{2,4}

This work has shown that good ultrastructural preservation of cytoplasmic components of both leaf (Figs. 1,4) and root tissues (Figs. 2,3,) can be achieved with HPF in the presence of dextran. Signs of gross freeze damage were not observed and only few samples exhibited minor freeze damage. The cell wall consisted of a finely granular matrix that was intensely and uniformly stained with uranium and lead salts (Figs. 1-3). Breaks in the cell wall, believed to be the result of HPF, were occasionally observed in both samples (Figs. 1,3). Nuclei were spherical with a well preserved nucleoplasm (Figs. 1-3). The plasma membrane was well stained and evenly appressed to the smooth inner surface of the cell wall. Membranes of the Golgi bodies, endoplasmic reticulum and the nuclear envelope were often not well contrasted (Fig. 3). Golgi vesicles had an electron opaque content (Fig. 3). Electron transparent gaps between the cytoplasm and the inner surface of the cell wall (Figs. 1,3) and "blebbing" the chloroplast outer membrane (Fig. 4) are thought to be additional artifacts of HPF. Microtubules were well preserved (Fig. 5) yet not abundant throughout the cytoplasm.⁵

References

1. M.A. Hayat, *Micron Microscopica Acta* (1986)17, 115.
2. S. Craig and L.A. Staehelin, *Eur. J. Cell Biol.* (1988)46, 80.
3. J.Z. Kiss *et al.*, *Protoplasma* (1990)157, 64.
4. R.W. Roberson and M.S. Fuller. *Protoplasma* (1988)146, 143.
5. This work was supported by a CLAS MINI-GRANT, No. MG-89-007.

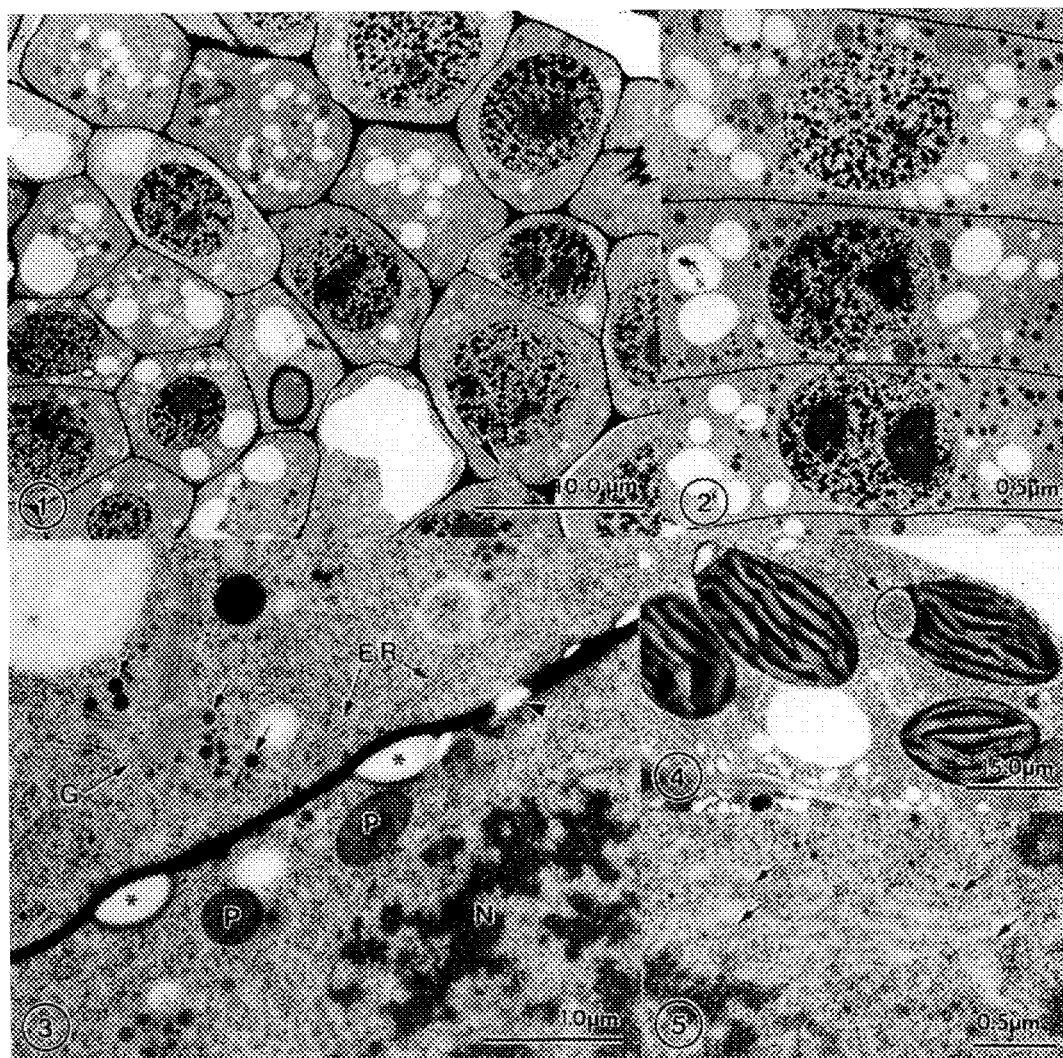


FIG. 1.--Leaf tissue of *B. mollis*. Note well preserved cytoplasm and break in cell wall (arrow).

FIG. 2.--Cells of stele from center of *H. vulgari* root.

FIG. 3.--Central root cells of *H. vulgari*. Note endoplasmic reticulum (ER), Golgi body (G), Golgi vesicles (arrows), plastids (P), cytoplasm-cell wall separations (asterisk), break in the cell wall (arrowhead), and nucleus (N).

FIG. 4.--Mesophyll cell of leaf of *B. mollis*. Blebbing of chloroplast membrane is noted (arrow).

FIG. 5.--Central root cell of *H. vulgari* showing microtubules (arrows).

ENZYMATIC DIGESTION OF SEEDS AS A PREPARATION TECHNIQUE FOR SCANNING ELECTRON MICROSCOPY

Randy Scott* and W. R. Ocumpaugh**

* E. M. Center, TAMU, College Station Texas

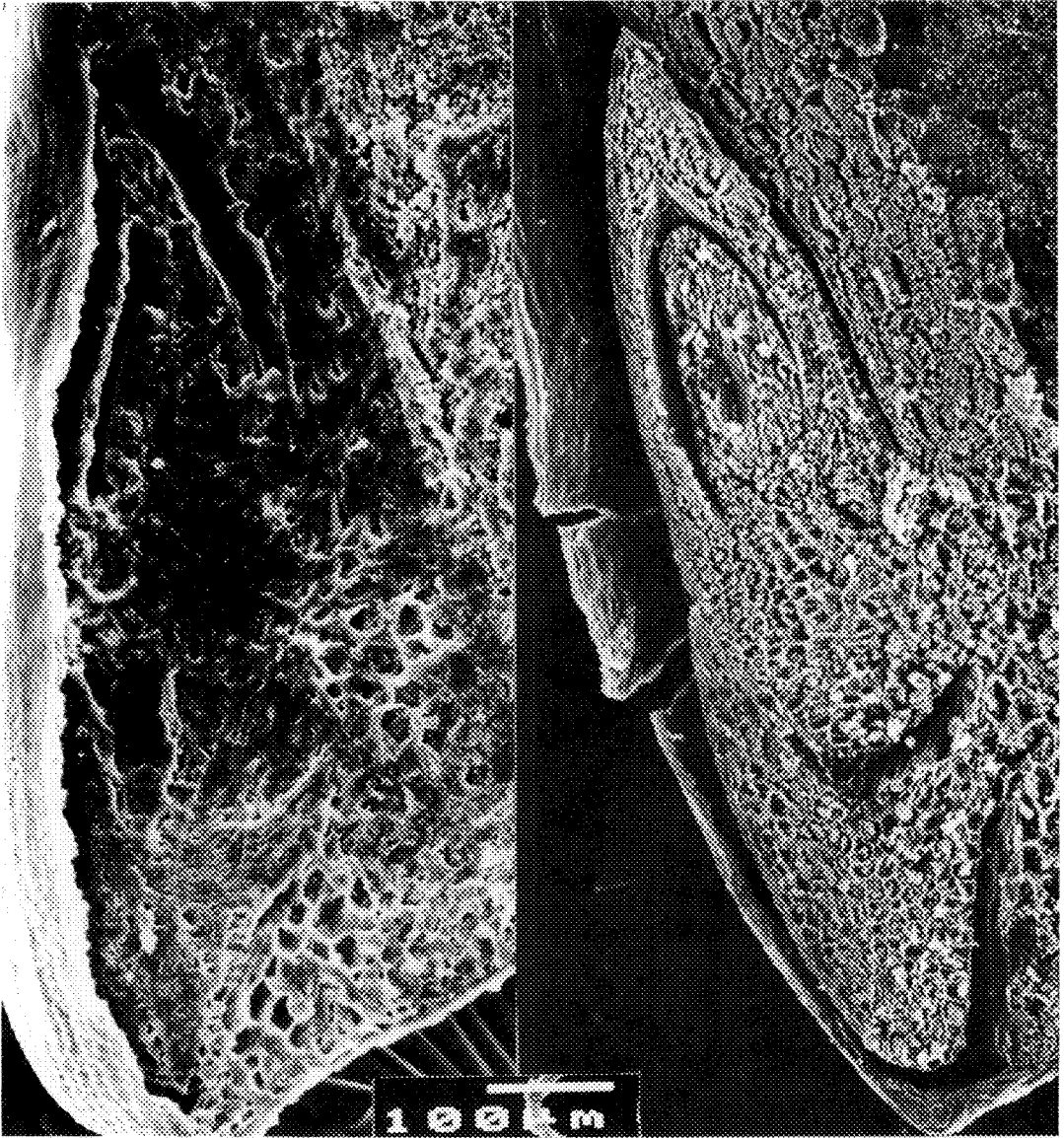
**Texas Agricultural Experiment Station, Beeville, Texas

The study of the microstructure of seed is an area of interest. Work in progress was confused by the difficulty in determining what part of the monocot seed was embryo and what part was endosperm. Routine histological facilities were not available and the imaging of the scanning electron microscope was desired.

The image seen on the left was prepared by simply cutting, mounting and coating the seed. This micrograph presents a puzzle to those of us who are not very familiar with the structure of seeds. Note, some organization is in evidence in the long section down the middle of a grass seed. With imagination, it might be thought that the embryonic leaflets can be seen. The rootlet and other structure presents a confusing display.

Seeds cut in long section were subjected to room temperature digestion in a physiological mixture of amylase and maltase of a period of ten minutes. Fixation with FAA at 20 degrees centigrade was followed by ethanol dehydration and critical point drying. Dry samples were mounted and sputter coated for presentation to the SEM.

The image on the right is an example of the results of the above procedure. Note that on the upper left the leaflet structure is clearly defined. At the lower left the developing root structure is seen, and between the root and leaflet the hypocotyl or stem appears. The extreme upper right of this image also shows the storage grains in the endosperm.



NON TREATED SEED

ENZYME TREATED SEED

CRYOFIXATION OF VARIOUS BIOLOGICAL SAMPLES BY HIGH PRESSURE FREEZING

LUCY RU-SIU YIN

MICROSCOPY CENTER, UNIVERSITY OF MASSACHUSETTS, AMHERST, MA 01003

The ultimate aim of ultrastructural fixation of biological specimen is to preserve all the compartments in their native state. Cryofixation is a superior method than conventional chemical fixation in reaching this goal. However, ice crystal formation during cryofixation often damages the structures. High pressure (2100 bar) freezing provides a way to alter freezing properties while cool down the specimen at a relatively high rate, minimizing the ice crystal formation.^{1,2} Nearly vitrified samples (up to 500 μ m) have been obtained with this method.³ Samples in suspension tend to get lost during high pressure freezing. The low percentage (~30%) of successfully cryofixed specimens can be improved if the sample completely fills the cavity of the metal specimen carriers in which the specimen is frozen. Various methods to overcome sample loss are reported in this study.

Using The Balzers High Pressure Freezing Unit (HPM 010), the samples tested were: root tips of mung bean *Phaseolus aureus* (Fig. 1) developing embryos of *Drosophila melanogaster* (Fig. 2) mature sperm of honey bee *Apis mellifera* (Fig. 3) and baker's yeast *Saccharomyces cerevisiae* (Fig. 4 and 5). Samples were prepared by mixing or covering with one of the following solutions immediately prior to freezing: 1-hexadecane; 1-octadecanol; 1% agar in 10% sucrose or 30% sucrose. Higher percentages (>50%) of specimens using the first three treatments survived high pressure freezing. All of the frozen samples were transferred to a suitable freeze substitution medium. A temperature controller was used to cool an in-house designed apparatus with LN₂. Freeze substitution proceeded below 193K for two days and 233K for one day before the samples were slowly warmed up to 277K. The substitution medium was then replaced by anhydrous acetone and samples were embedded in Spurr's resin. Thin sections from various treatments were evaluated. These freezing techniques proved to be useful for high quality preservation and freeze substitution of the sample tested.

References

1. H. Moor, in Steinbrech RA, Rierold K (eds) Cryotechniques in biological electron microscopy. Berlin, Springer, (1987) 175-191.
2. R. Dahl and L.A. Stachelm, J. Electr. Microsc. Tech. 13 (1989) 165-174.
3. D. Studer et al., Microsc. Intern. Suppl. 3(1989) 253-269.

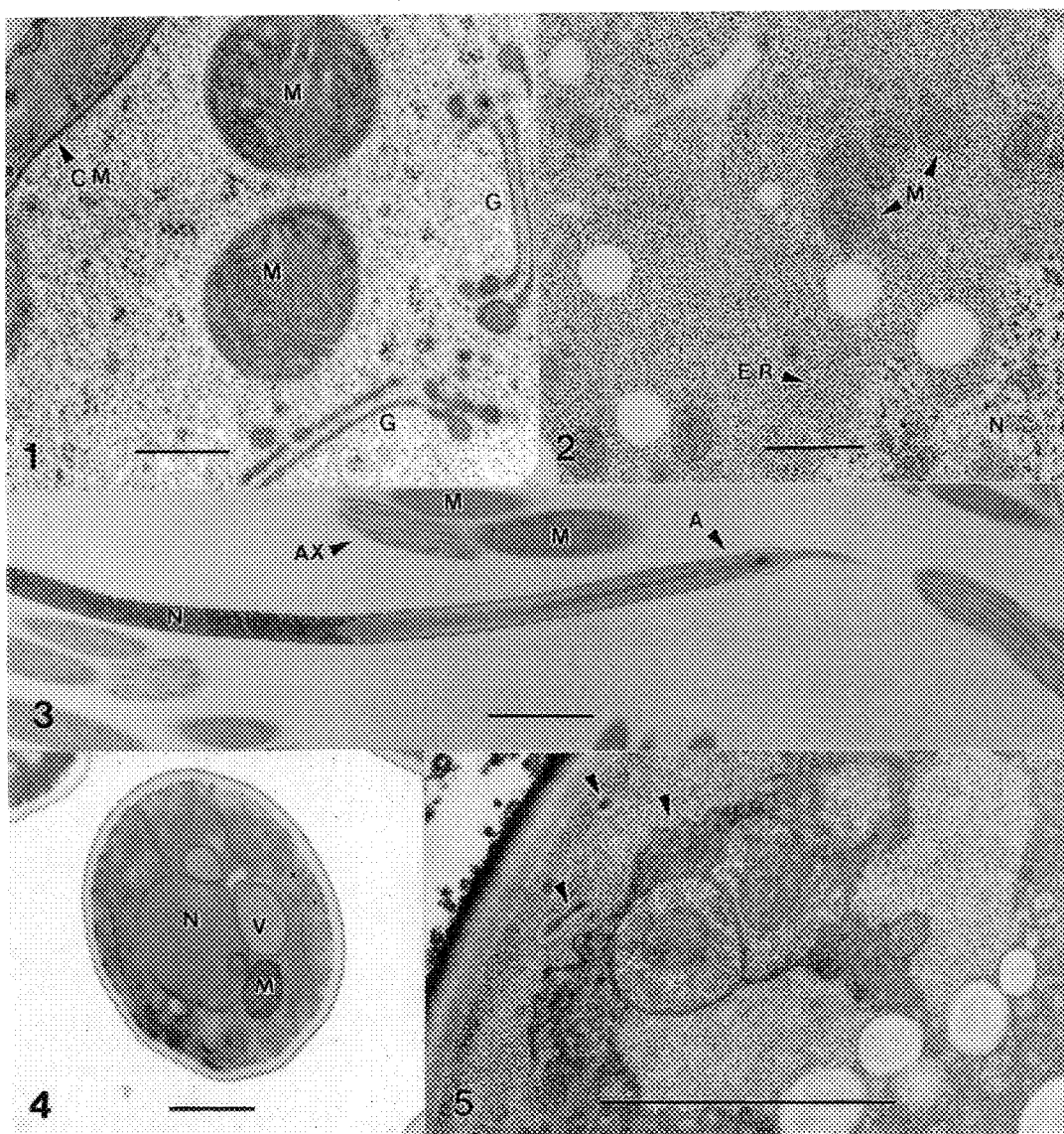


FIG. 1. Mung bean *Phaseolus aureus* root tip cell showing well fixed cell membrane (CM), mitochondria (M), and Golgi (G). Bar=0.2 μ m.

FIG. 2. Cells near the center of fruit fly *Drosophila melanogaster* embryo showing nucleus (N), mitochondria (M), and endoplasmic reticulum (ER). Bar=0.1 μ m.

FIG. 3. Sperm of honey bee *Apis mellifera* showing acrosome (A), nucleus (N) and the oblique view of the tail which contains two mitochondria (M) and one axoneme (AX). Bar=1 μ m.

FIG. 4. Baker's yeast *Saccharomyces cerevisiae* showing nucleus (N), mitochondria (M), and vesicles (V). Bar=1 μ m.

FIG. 5. Portion of a yeast showing elaborated cell membrane (Arrows). Bar=1 μ m.

PRO's FOR A MULTIPLE/REPEATED USE AND SAFE DISPOSAL WITH RECOVERY OF OSMIUMTETROXIDE SOLUTION(S) IN ROUTINE ELECTRON MICROSCOPY

Wolfgang H. Muss

Department of Pathological Anatomy, EM-Laboratory, St. John's General Hospital
 L K A, Muelöner Hauptstrasse 48, A-5020 Salzburg AUSTRIA

Double fixation with an/aldehyde(s) and osmiumtetroxide is most commonly employed to process tissues for electron microscopy. The metal Os is precious and recycling would keep a toxic substance out of the environment and conserves a non-renewable resource. Since the pure substance is expensive, the handling of crystals & solutions is critical if not hazardous, disposal of used working solutions seems to be problematic (waste or recovery?; How to do it properly/safely according to new regulations concerning disposal of harmful and toxic lab-chemicals?..) one looks out for solutions. Searching for a routine and standard method which works satisfyingly concerning preservation of ultrastructure in human tissue, a method which is reliable and reproducible, low in cost as well as simple in handling, disposal and recovery of OsO_2 precipitate over a period of now 4 years - a schedule sufficient also for higher demands was developed: after a fixation routine (PRE: 0.5% formaldehyde + 1.5% glutaraldehyde=GA in 0.1M phosphate buffer; MASTER: 4% GA in 0.1M phosphate buffer; fix.at room temperature (RT) 10 min and up to 3 hours, respectively; rinsing) followed by POSTFIXATION (1-1.5 hrs, at RT) with the solution according to (1) modified as:

- i) STOCK SOLUTION Os : 50 ml of 2% aqueous OsO_4 are prepared (4 x 12.5 ml, see below). After complete dissolution freeze & store at -20/-25°C until use.
- ii) STOCK SOLUTION A : 4.52% (w/v) $NaH_2PO_4 \cdot H_2O$ (= 0.328 M) in a.bidest.
- iii) STOCK SOLUTION B : 5.04% (w/v) NaOH (= 1.260 N) in a.bidest.
- iv) STOCK SOLUTION C : 10.80% (w/v) D-Glucose in a.bidest. (25 ml are sufficient for preparing 20 times the working solution). Freeze and store at -25°C until use.

WORKING SOLUTION: is essentially the same as in (1); stock solutions are allowed to warm up to RT. Then mix up with clean pipets and glassware:

- 11.25 ml of a mixture of 10.5 ml stock soln A and 2.2 ml of stock soln B
- + 1.25 ml of stock solution C
- + 12.50 ml of stock solution Os : that gives 25 ml of 1% OsO_4 in isotonic, 0.13 M MILLONIG phosphate buffer, pH 7.3; 340 ± 5 mosmol/kg.

Fill into a clear, screw-capped glassbottle and use solution repeatedly. Use until color turns markedly to violet/brownish black. Slightly darkened or yellowish solutions work well. After each osmication procedure the solution-aliquots from specimens are pipetted back to the clear glass storage bottle and frozen again until further use. As a **potent indicator** for successful **osmication** the staining quality of the azure II-methyleneblue-basic fuchsin sequence (2) in semithin sections was taken as a measure.

A very simple but effective inactivation of used or working solutions to be discarded is the precipitation of OsO_4 by absolute ethanol. Precipitates can be filtered and stored for pooling in order to recover unused OsO_2/OsO_4 by the method of (3).

Concluding from the results obtained over 4 years of experience thus it is possible to lower the consumption of pure OsO_4 to about 1.5 to 2 g a year (based on an average osmication requirement of about 1500 TEM-specimen blocks) and to lower with that also the costs most efficiently as it was possible in our EM-Lab from 1989-1991. Actual consumption (7/1992; about 750 specimen blocks) is 0.75 g of pure OsO_4 cryst. Figs. 1-6 demonstrate the quality obtainable from muscle tissue fixed only with buffered formalin in the operating theater and -later on- fixed with the routine protocol given in brief (see above). Which quality is achievable with an OsO_4 solution

used a 3rd time after having osmicated 290 specimens previously is demonstrated in (4) this volume.⁵

References

1. G. Millonig, J. appl. Physics (Proc.EMSA 1961)32, 1637 (Abstr.)
2. C.D. Humphrey and F.E. Pittman, Stain Technol.(1974)49, 9
3. J.A. Kiernan, J. Micr. (1978)113, 77
4. W.H. Muss, Proc.Ann.Meet.EMSA(1992)50,..... (this volume)
5. Parts of this paper have been presented as a poster (in German) at the 25th Ann. Meetg.German Soc.for EM at DARMSTADT/FRG, 1-7 Sept.1991. Manuscript for a full length paper to be submitted in Ultrastructural Pathology or J.El.Micr.Techn. in preparation.

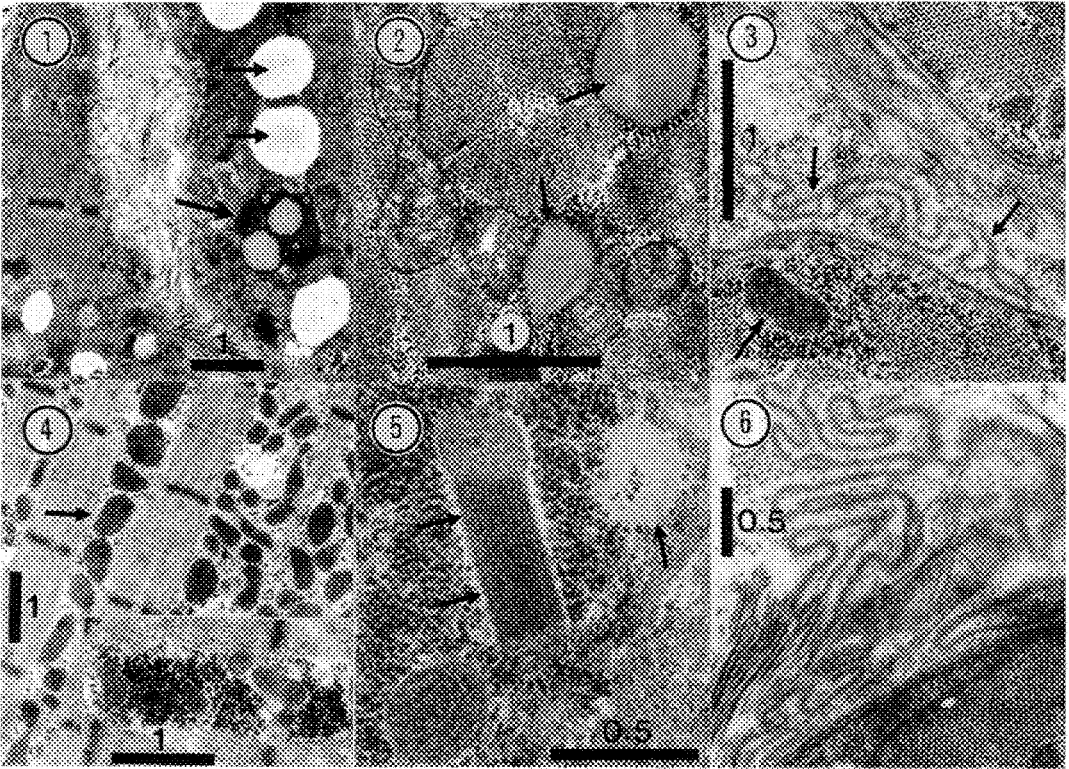


Fig. 1. "Control"= OsO₄ solution freshly prepared (Øx). Note preservation of lipofuscin bodies but loss of lipids due to dehydration agents (EtOH, acetonitrile).
 Fig. 2. "Control", same biopsy as before (Ø x) but lipid content retained by treating specimens with p-phenylenediamine in lower ethanols.
 Fig. 3. Atrophic fibers discernible by foldings of their basal lamina; note preservation (5x OsO₄= used for the fifth time after having osmicated 220 specimens).
 Fig. 4. Quality of ultrastructural preservation: mitochondria in a patient with mitochondrial myopathy. Inset: glycogen preservation (5x, used after 220 specimens).
 Fig. 5. Another preparation; mitochondrial myopathy (6x, used after 200 specimens).
 Fig. 6. Ultrastructural preservation "hors concours"(7x, used after 280 specimens). Compare with Fig.3 above. All figures show human skeletal muscle. Bars equal 1μm.

JET FREEZING IN ENZYME AND COSMETIC RESEARCH

T. Müller+, S. Moser+, M. Vogt+, B.E. Brooker" and N. Terren*

+ Balzers Union AG / BAL-TEC, FL-9496 Balzers, P. of Liechtenstein

" AFRC Institute of Food Research, Reading Laboratory, RG2 9AT UK

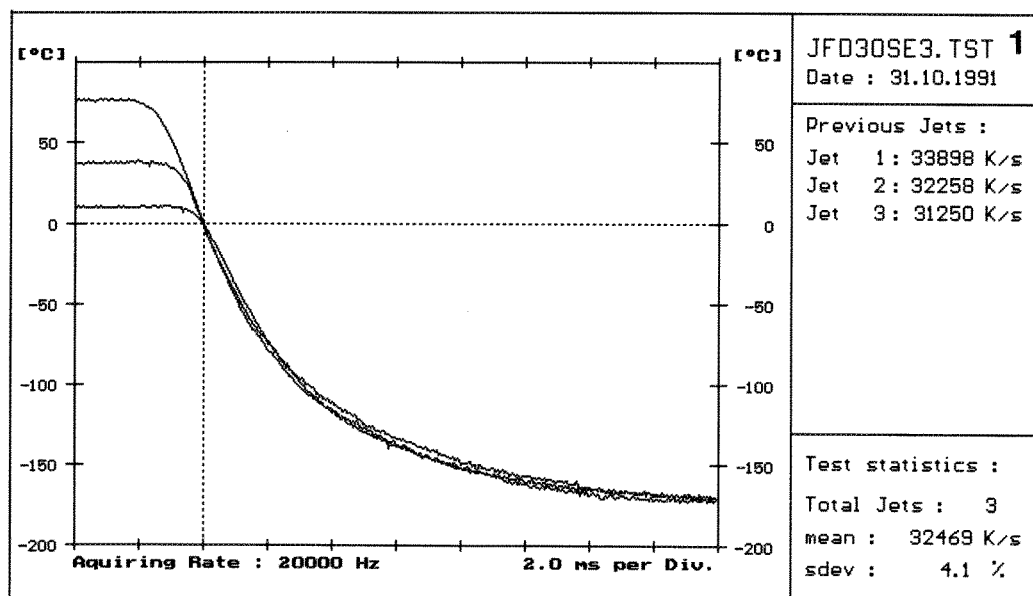
* L'Oréal, Rech. Appl. et Dével. F-94152 Rungis Cedex, France

Freezing has turned out to be the only method capable of immobilizing biological material in its natural state. Freeze-fracturing and replication complete this preparation protocol of specimens for transmission electron microscopy (TEM) which is based on purely physical methods [1,2]. With a propane-jet, specimens of a thickness up to 20 μm can be frozen without detectable ice crystal formation [3]. Cell and macromolecule suspensions, emulsions, liquids and polymers in a solvent [4] can be "sandwiched" between two copper foils and kept in place while a coolant is moved very rapidly against the opposite surfaces. In the present jet freezing device (JFD 030) the temperature of the specimen, while residing in a thermostatically controlled chamber, can be monitored between 10 and 90°C immediately prior to freezing. Thus physiologically interesting situations can be immobilized and any precooling of the specimen is avoided. A special device enables the absolutely simultaneous exposure of the specimen to the double-sided jet of the coolant. High cooling rates with an exceptional reproducibility are achieved routinely (Fig.1).

Enzymes in a non-aqueous solvent, such as alcohols, have been found to have significant advantages over conventional aqueous systems including change in enzyme specificity, high operational stability, ease of product recovery and synthesis of specific optical isomers [5]. In addition to enzyme and substrate, these systems often require small amounts of water for activation. To investigate the relationship between particle size, energy input, catalytic activity, and the nature of the solvent, TEM has been used in conjunction with this rapid freezing technique which immobilizes the system without disrupting or otherwise changing it. For this purpose, protease type VII (subtilisin from *Bacillus licheniformis*) was dispersed in reagent grade hexanol containing 1% water, using high energy sonication (MSE Soniprep 150). Although crystals of hexanol were produced by this freezing method, they were small relative to the size of enzyme particles (Fig.2).

From a cosmetic industry specimen - a dispersion of oil droplets in water, stabilized by liposomes without any additional surfactant (system patented by L'Oréal BF 2 485 921 and 2 490 504) - all components could be visualized and interpreted by their individual appearance (Fig.3).

References: [1] H. Moor (1971) Phil. Trans. Roy. Soc. Lond. B. 261:121-131. [2] R.L. Steere (1971) Proc. 29th Ann. Meeting EMSA :242-243 [3] M. Müller, N. Meister and H. Moor (1980) Mikroskopie Wien 36:129-140. [4] T. Müller, H. Hakert and Th. Eckert (1989) Colloid & Polymer Science 267:230-236. [5] J.S. Deez and J.D. Rozzell (1988) TIBTECH., 6:15-19.



T(start) 1: 37°C/ 2: 75°C/ 3: 10°C; pN2: 6 bar; cryogen: Propane

Cooling rate measurement (0 to -100°C) was carried out by a 20 μ m thick copper/constantan thermocouple, placed between two standard copper supports. The signal, after amplification, was digitized and recorded by a personal computer (Compaq 80286) equipped with an A/D converter (dash 8, Keithley). The data were recorded and processed by our own software written in TURBO PASCAL 5.0.

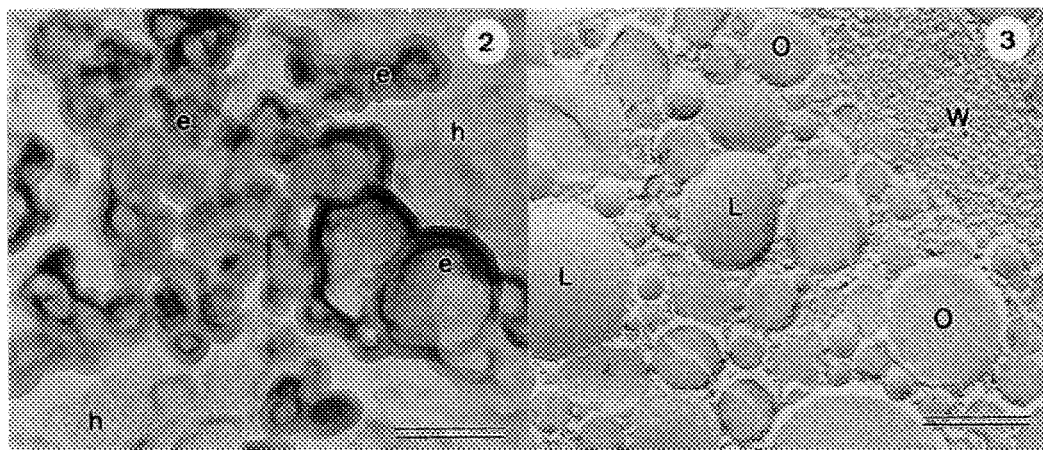


Fig.2: Freeze-fracture replica of an enzyme dispersion, aggregating in hexanol after sonication: e=enzymes, h=hexanol. Fracturing and rotary shadowing at 30° elevation with Pt-C at -100°C. Bar = 200 nm
Fig.3: Freeze-fracture replica of an oil droplet (O) dispersion in water (W) stabilized with liposomes (L). Fracturing, sublimation, shadow casting at 45° elevation with Pt-C at -105 °C. Bar = 200 nm

DISCERNING WATER CONTAMINATION DURING FREEZE-FRACTURING ON STEARIC ACID CRYSTAL SHEETS

Theo Müller and Heinz Gross*

Balzers Union AG / BAL-TEC, Balzers, Principality of Liechtenstein
*Institut für Zellbiologie, ETH-Hönggerberg, Zürich, Switzerland

In high vacuum (HV) systems, as well as in ultra high vacuum (UHV) systems that have not been sufficiently baked out, the main component of the residual gas atmosphere is water. Adsorbed water is present on all surfaces of the vacuum chamber. Whether or not ice introduced into such a vacuum system sublimates depends on its saturation pressure (at the surface, as a function of the specimen temperature) and on the surrounding partial pressure of water (p_{H_2O}) [1]. These facts must be considered when fracturing frozen biological material [2,3] in vacuum systems. Thus the critical condensation temperature (162, 144.5, 130 K for 10^{-6} , 10^{-8} , 10^{-10} mbar, respectively) is an important factor in discussions of specimen fracture face contamination. Possibilities to reduce the rate of water condensation include the use of UHV ($p < 10^{-9}$ mbar) and/or surrounding the specimen with a cold, optically dense shroud system. When such a shroud is used, water molecules originating outside the shroud can only reach the specimen surface if they condense on and reevaporate from the shroud surface at least once (probability at $T < 123$ K is less than 10^{-4}).

Freeze-fractured stearic acid crystal sheets exhibit bimolecular steps with hydrophilic head groups and large terraces with hydrophobic tails. Ice crystals specifically decorate the hydrophilic sites [4]. Stearic acid can be used as a water-free membrane system model providing a defined and easy to interpret fracture surface for the investigation of water contamination.

In order to investigate all possible sources of water contamination, we carried out freeze-fracturing experiments in a UHV system [5] (prototype of BAF 500K, Balzers) equipped with an optically dense shroud. We recorded the total pressure as well as the p_{H_2O} with a quadrupole mass spectrometer (QMG 112, Balzers). When stearic acid crystals sandwiched between two copper supports were fractured, no increase of the p_{H_2O} took place. In contrast, fracturing yeast (*Saccharomyces cerevisiae*) or liposome suspensions always provoked a total pressure increase from 8×10^{-10} mbar to approximately 8×10^{-9} mbar (Fig.1). Contamination-free stearic acid crystals show the typical "stair-like" fractures (Fig.2). Using a specially designed inlet [6], water was condensed on freeze-fractured stearic acid at 123 K (Fig.3). The ice crystals clearly decorate the hydrophilic steps. In a key experiment (inside the closed shroud at 123 K) we placed a stearic acid sandwich between two yeast sandwiches and fractured them all simultaneously. The pressure rise during the fracturing process, detected from outside the shroud, proved that water vapor was released from the water-containing yeast specimen. As there was no other water source, the water for the ice crystals on the stearic acid (Fig.4) originated from the neighbouring yeast specimens. Thus even under optimal vacuum conditions, water-

containing biological specimens can contaminate themselves and neighbouring specimens: At $T < 130\text{K}$, the specimens act as highly efficient cryo pumps.

References:

- 1 Honig RE and Hook HO (1960). RCA review: 360-368
- 2 Moor H (1966). Int. Rev. of Experim. Pathol. 5: 170-216
- 3 Steere RL (1971). Proc. 29th Ann. Meeting EMSA, 242-243
- 4 Walzthöny D, Moor H, and Gross H (1981). Ultramicrosc. 6: 259-266
- 5 Gross H, Müller T, Wildhaber I, and Winkler H (1985) Ultramicrosc. 16: 287-304
- 6 Gross H, Kuebler O, Bas E, and Moor H (1978) J. Cell Biology 79: 646-656

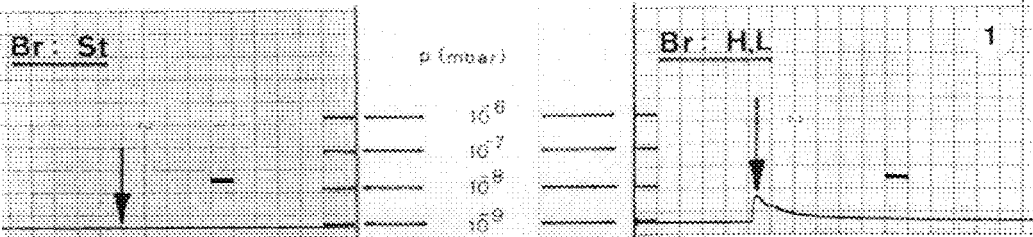


Fig.1: Total pressure, outside the shroud, during fracturing stearic acid (St) or water-containing specimens (H,L). Bars = 1 s

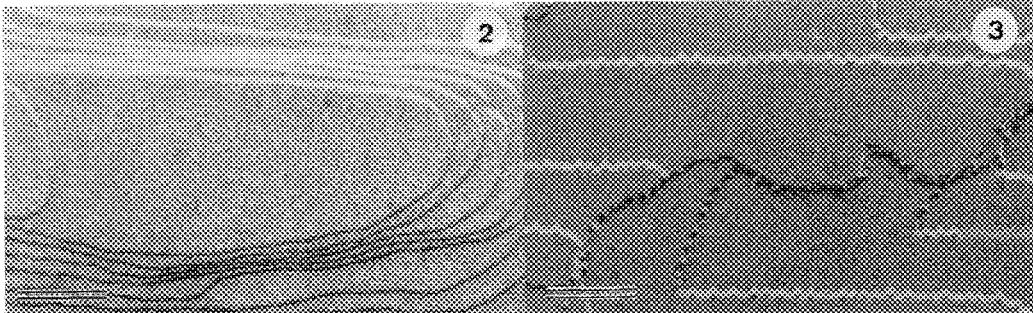


Fig.2: Uncontaminated stearic acid crystal

Fig.3: Ice crystals decorate the hydrophilic steps

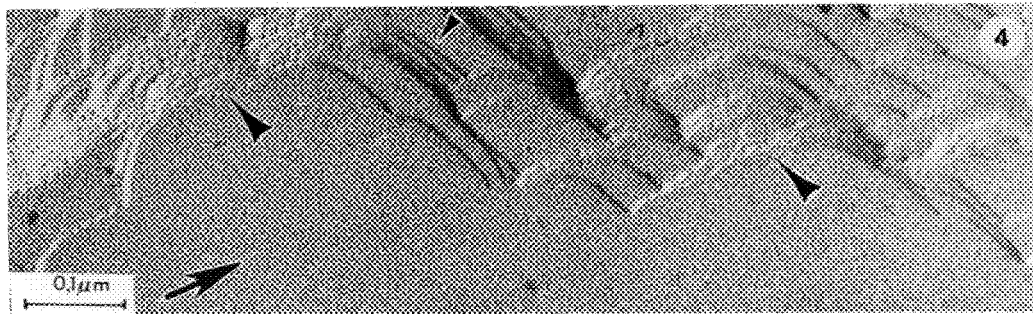


Fig.4: Water vapor contamination on stearic acid steps (large arrow heads). Bars in Figs. 2-4 = 100 nm

SIMPLE DESICCATION METHOD FOR SCANNING ELECTRON MICROSCOPY USING DIMETHOXYPROPANE

František Weйда

Institute of Entomology, Branisovská 31, 370 05 České Budějovice, CZECHOSLOVAKIA

A number of techniques such as critical point drying (the most commonly used method of drying cells and tissues), freeze-drying or freeze-substitution are available to process various tissues preparations for scanning electron microscopy (SEM). Those techniques are more or less complicated (depending also on expensive equipments) and time consuming. While more simple air-drying from aqueous suspension or organic solvents can be used for some rigid biological specimen, it is generally not satisfactory for most tissues and biological objects.^{1,2} On the opposite, rapid and simple procedure using hexamethyldisilazane (HMDS) and air drying has been successfully applied to insect and mite tissues without observable artifacts.³ We have developed similar simple and rapid method using dimethoxypropane (DMP) and air drying. DMP has previously been used for chemical dehydration of tissues.^{4,5}

Unfixed (stored in ethanol) or fixed (by the conventional way) specimens are placed in diluted DMP (mixture of 1 part of DMP with 3 parts 100% ethanol) for 30 minutes (DMP is acidified with 5 ul of concentrated HCl per 100 ml of DMP). Also living animals may be fixed by this way.⁵ DMP dehydrates specimens; dilution it with ethanol make the whole process slower and thus less dangerous for tissues. The specimens were then placed in pure DMP (not acidified) for 15 minutes. Then specimens are removed and leaved to desiccate in air in a clean place (for example partly covered Petri dish). Prepared specimens are mounted, coated with metal and observed in scanning electron microscope.

We have compared several species and tissues from various animals: entomoparasitic nematodes, eggs and adults of spider mites (*Tetranychus urticae*), oribatids, pauropods (*Allopaupopus sp.*), symphylans, chilopods (*Geophilomorpha*), collembolans (*Onychiurus sp.*, *Tomocerus sp.*), diplurans (*Campodea sp.*), ants, larvae and hemocytes of lepidopterans (*Galleria mellonella*), gills of trout (*Trutta trutta*), cancer and blood cells of mice as well as some plant material (leaves). We have also compared our method with similar method using HMDS. Results obtained with DMP are comparable with those obtained with HMDS. Most of our results is shown in Figures 1-16. Sometimes, HMDS revealed better preservation of the shape. Both methods using air drying from organic solvents were not always suitable for whole bodies (Figures 2 and 3) but they are suitable for bodies divided into several parts by cutting (Figure 4). Small species are usually better preserved than bigger ones. It is difficult to generalize which animal species will be sufficiently preserved when using DMP. So, it is necessary to try it and evaluate, if results fit our requirements. If the results are insufficient, then it is necessary to select other method of preparation of specimens for SEM. Air drying from DMP is not so universal like critical point drying. But it represents quick and inexpensive method (like method using HMDS) with mostly adequate preservation of surface in various species especially in those with rigid cuticular surface like arthropods.⁶

References

1. R. M. Albrecht et al., J. Microsc. (1976)108, 21
2. P. B. Bell, Scanning Electron Microscopy (1984), 52
3. J. L. Nation, Stain Technol. (1983)58, 347
4. L. L. Muller and T. J. Jacks, J. Histochem. Cytochem. (1975)23, 107
5. J. M. Bjerke, T. P. Freeman and A. W. Anderson, Stain Technol. (1979)54, 29
6. This research was supported by a grant from the Hasselblad Foundation, Sweden.

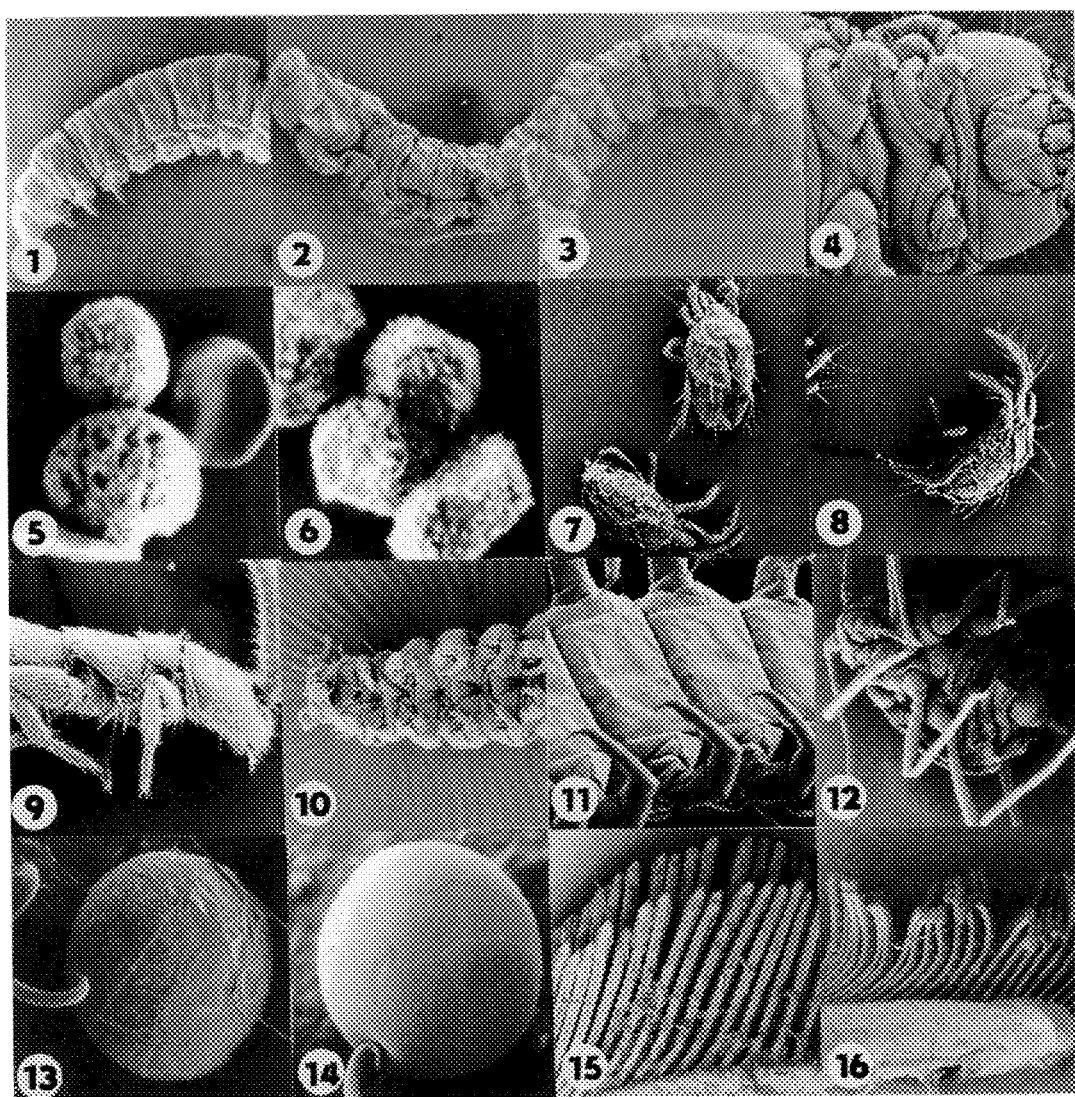


FIG.1- Larva of *Galleria mellonella* dried by CPD. Magn. = x8. FIG.2- Larva of *G. mellonella* dried on air from HMDS. Magn. = x8. FIG.3- Larva of *G. mellonella* dried on air from DMP. Magn. = x8. FIG.4- Larva of *G. mellonella* (cut body) dried on air from DMP. Magn. = x25. FIG.5- Mouse Gardner lymphosarcoma cells and red blood cells dried on air from HMDS. Magn. = x500. FIG.6- Mouse Gardner lymphosarcoma cells dried on air from DMP. Magn. = x500. FIG.7- Female of *Tetranychus urticae* dried on air from HMDS. Magn. = x45. FIG.8- Female of *T. urticae* dried on air from DMP. Magn. = x45. FIG.9- *Campodea* sp. dried on air from HMDS. Magn. = x50. FIG.10- *Allopauiropus* sp. dried on air from DMP. Magn. = x250. FIG.11- Chilopod (*Geophilomorpha*) dried on air from DMP. Magn. = x90. FIG.12- *Acyrtosiphon pisum* dried on air from DMP. Magn. = x30. FIG.13- Egg of *T. urticae* dried by CPD. Magn. = x300. FIG.14- Egg of *T. urticae* dried on air from DMP. Magn. = x300. FIG.15- Gills of trout dried by CPD. Magn. = x10. FIG.16- Gill of trout dried on air from DMP. Magn. = x10.

SNAPSHOT BLOTTING: THE TRANSFER OF NUCLEIC ACIDS AND NUCLEOPROTEIN COMPLEXES FROM ELECTROPHORESIS GELS TO EM GRIDS

Stephen D. Jett

Department of Cell Biology and the Cancer Center, University of New Mexico School of Medicine,
Albuquerque, NM 87131

The electrophoresis gel mobility shift assay is a popular method for the study of protein-nucleic acid interactions. The binding of proteins to DNA is characterized by a reduction in the electrophoretic mobility of the nucleic acid. Binding affinity, stoichiometry, and kinetics can be obtained from such assays;¹ however, it is often desirable to image the various species in the gel bands using TEM. Present methods for isolation of nucleoproteins from gel bands are inefficient and often destroy the native structure of the complexes. We have developed a technique, called "snapshot blotting," by which nucleic acids and nucleoprotein complexes in electrophoresis gels can be electrophoretically transferred directly onto carbon-coated grids for TEM imaging.

The technique is an adaptation of a previous DNA spreading method that employs glow discharge and spermidine to make the grid surface hydrophilic.² Carbon films are stably attached to the grids using an adhesive to permit the film to withstand the physical stresses of the procedure. Prior to separation by agarose gel electrophoresis, samples are fixed with glutaraldehyde.³ Glow-discharged grids are soaked in a spermidine solution, and inserted into the gel bands that have been located by ethidium bromide staining. Gel electrophoresis is resumed for 30 seconds, and the grids are removed from the gel, rinsed with water, dehydrated with ethanol, and shadowed with tungsten prior to imaging. Care is taken to keep the grids moist during the transfers to minimize surface-tension forces that can destroy complexes as the samples cross an air-liquid interface.

We have used this technique to study the assembly of transcription complexes. Figure 1a shows an agarose gel in which nucleoprotein complexes have been assembled using a 458 base pair DNA restriction fragment containing an *Eco*R1 restriction enzyme binding site and an *E. coli* RNA polymerase promoter (phage lambda P_L). The location of the binding sites had been previously determined by DNA sequence analysis.⁴ *E. coli* RNA polymerase ($M_r=450,000$) and/or a cleavage-defective mutant⁵ *Eco*R1(Q111) protein dimer ($M_r=62,000$) were fixed with the DNA in a HEPES-MgCl₂ buffer containing ATP, GTP and the dinucleotide ApU. The samples were processed as described above, and the grids were shadowed with 20 Angstroms of tungsten and imaged in a TEM at 50 kV. Figures 1b-1e show images of the complexes obtained from selected gel bands. The location of the proteins bound to the DNA correspond to sites predicted from sequence analysis. The sizes of the proteins correspond to their relative molecular weights. The "snapshot blot" procedure should be of great utility in the structural characterization of a wide variety of biologically important protein-nucleic acid complexes that are difficult to isolate by other procedures.

References

1. M. G. Fried, *Electrophoresis* 10 (1989) 366.
2. J. Griffith and T. Formosa, *J. Biol. Chem.* 260 (1985) 4484
3. J. Sogo et al., in J. Sommerville and U. Scheer Eds., *Electron Microscopy in Molecular*

Biology: a Practical Approach, Oxford:IRL Press (1987) 61.

4. P.A. Pavco and D.A. Steege, J. Biol. Chem. 265 (1990) 9960.

5. K. King et al., J. Biol. Chem. 265 (1989) 11807.

6. This work was carried out in the laboratory of Dr. David G. Bear, and was supported by grants from the National Science Foundation and the National Institutes of Health Minority Biomedical Research Support program.

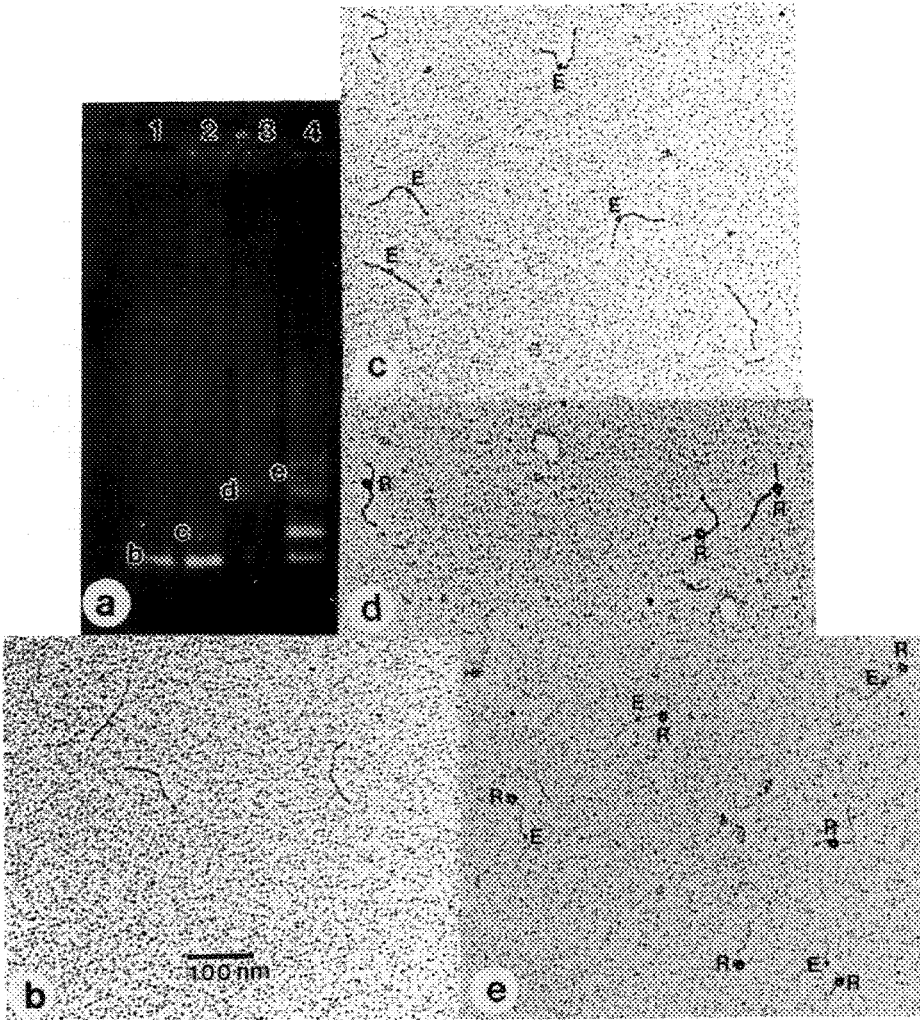


Figure 1. (a) Separation of DNA-protein complexes by an agarose (1%) electrophoresis gel. Lane 1, 0.2 μ g of 458 bp DNA restriction fragment described in text; Lane 2, DNA + 0.4 μ g EcoR1(Q111); Lane 3, DNA + 0.6 μ g RNA polymerase; Lane 4, DNA + EcoR1(Q111) + RNA polymerase. (b)-(e) Electron micrographs of the grids inserted into the corresponding bands of gel shown in (a). "R" denotes *E. coli* RNA polymerase and "E" denotes the cleavage-defective EcoR1(Q111) mutant enzyme. See text for experimental details.

A CRYOGENIC TECHNIQUE FOR THE ENVIRONMENTAL SCANNING ELECTRON MICROSCOPY

Robert Baron, Lynne C. Garone

Polaroid Corporation, Waltham, MA 02254

Understanding the distribution of fluid in a self-contained multi-layer film developing system can yield insights into the mechanistic process and impact the design of the product i.e. hardener levels, timing layers, hydrophobicity of layers. One of the challenges to the microscopist presented with this problem is the difficulty associated with imaging a wet photographic system at sufficient resolution to study any structural changes of the layers. Many indirect methods such as water uptake measurements as a function of time¹ or model structures have been used. None have the ability to look at the individual layers as a function of developing time in it's true "wet state".

A cryogenic method has been developed using the Environmental Scanning Electron Microscope (ESEM), which permits the observation of individual layers in the developing photographic system. The ESEM's lack of stringent vacuum requirements allows this imaging². The photographic system is developed in the normal way. The developing process is stopped at various times by submerging the entire photographic system in liquid nitrogen. In many cases, the samples can be fractured in the liquid nitrogen and observed under the ESEM, however, we have found that the detail in the individual layers (often as thin as 1 μm) can best be studied if the sample is faced off in a cryogenic microtome operated at about -20C. The sample is then transferred cold to a specially designed holder on an Oxford cold stage at -70C on the ESEM and is imaged with air at 2.1 Torr at 20 KV.

These studies have contributed to a further understanding of the photographic process and the swelling performance of various photographic coatings. (Figures 1-4)

References

1. R. J. Cox, Ed., Photographic Gelatin, London and New York: Academic Press (1972)29.
2. N. Baumgarten, Nature (1989)341,81.

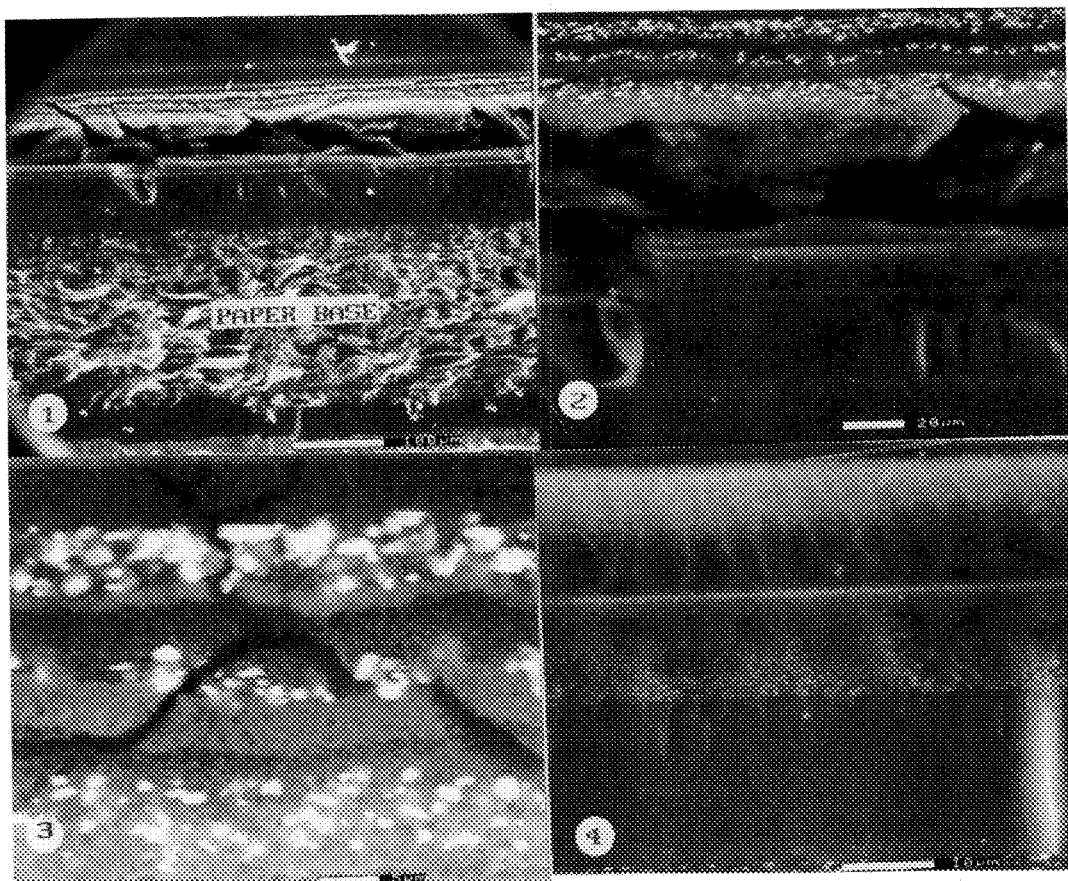


FIG. 1.--ESEM of processed photographic system showing all the system components: negative with film base, developer layer, positive with paper base.

FIG. 2.--Higher magnification ESEM of FIG. 1.

FIG. 3.--ESEM of negative. Note multi-layer structure with silver halide emulsions.

FIG. 4.--ESEM of positive.

TECHNIQUES FOR PREPARING THE *LOLIUM PERENNE* COLEORHIZA FOR SCANNING ELECTRON MICROSCOPE EVALUATION

Susan B. G. Debaene, John S. Gardner*, and Phil S. Allen

Dept. of Agronomy and Horticulture, 275 WIDB, Brigham Young University, Provo, Utah 84602; *Electron Optics Laboratory, 128 WIDB, Brigham Young University, Provo, Utah 84602

The coleorhiza is a nonvascular sheath that encloses the embryonic radicle in Poaceae, and is generally the first tissue to emerge during germination. Delicate hairlike extensions develop from some coleorhiza cells prior to radicle emergence. Similar to root hairs, coleorhiza hairs are extremely sensitive to desiccation and are damaged by exposure to negative water potentials. The coleorhiza of *Lolium perenne* is somewhat spherical when first visible, after which a knob forms at a right angle to the caryopsis due to inner pressure from the elongating radicle. This knob increases in length until the radicle finally punctures the coleorhiza. Standard fixation procedures cause severe desiccation of coleorhiza cells and hairs, making morphological study of the coleorhiza difficult^{2,3}. This study was conducted to determine a more successful process for coleorhiza preservation.

Lolium perenne caryopses were imbibed for 40 hr, at which point approximately 80% had visible coleorhizae. Caryopses were divided into two stages of coleorhiza development: spherical (early development) and knobbed (advanced development). Four preparation procedures were tested: a) glutaraldehyde-acrolein fixation followed by standard processing to 100% ethanol¹ and critical point drying (GA/CPD). The three remaining procedures all began by freezing whole caryopses in liquid freon and then liquid nitrogen, followed by: b) freeze substitution in dry acetone with 1% OsO₄ at -80° C for 7 days and critical point drying (FS/CPD), c) freeze substitution (as above) followed by freeze drying (FS/FD) and d) direct freeze drying of specimens under high vacuum (FD).

Undesired changes in coleorhizae occurred during GA/CPD fixation. Severe deflation caused wrinkling of coleorhiza cells. Spherical coleorhizae retracted into the caryopsis (Fig. 1). Some knobbed coleorhizae were punctured by elongating radicles during GA/CPD fixation (Fig. 2).

FS/CPD circumvented complete retraction of spherical coleorhizae, but large areas of cells developed appreciable damage (Fig. 3). Many coleorhiza hairs broke during FS/CPD, possibly due to excessive handling required by this procedure.

Preservation of the spherical coleorhiza shape was achieved by FS/FD (Fig. 4). However, this process did not preserve the turgid appearance of cells and hairs. Large cracks formed in the coleorhiza. Breakage of hairs was also common.

In contrast, FD preserved coleorhizae, eliminating cell damage and tissue retraction and extension observed with other preparation techniques (Fig. 5,6).

References

1. W. M. Hess. Stain Tech. (1966), 41, 27.
2. F. J. Marousky and S. H. West. J. Amer. Soc. Hort. Sci. (1988). 113, 845.
3. S. H. West and F. Marousky. Crop Sci. (1989). 29, 787.

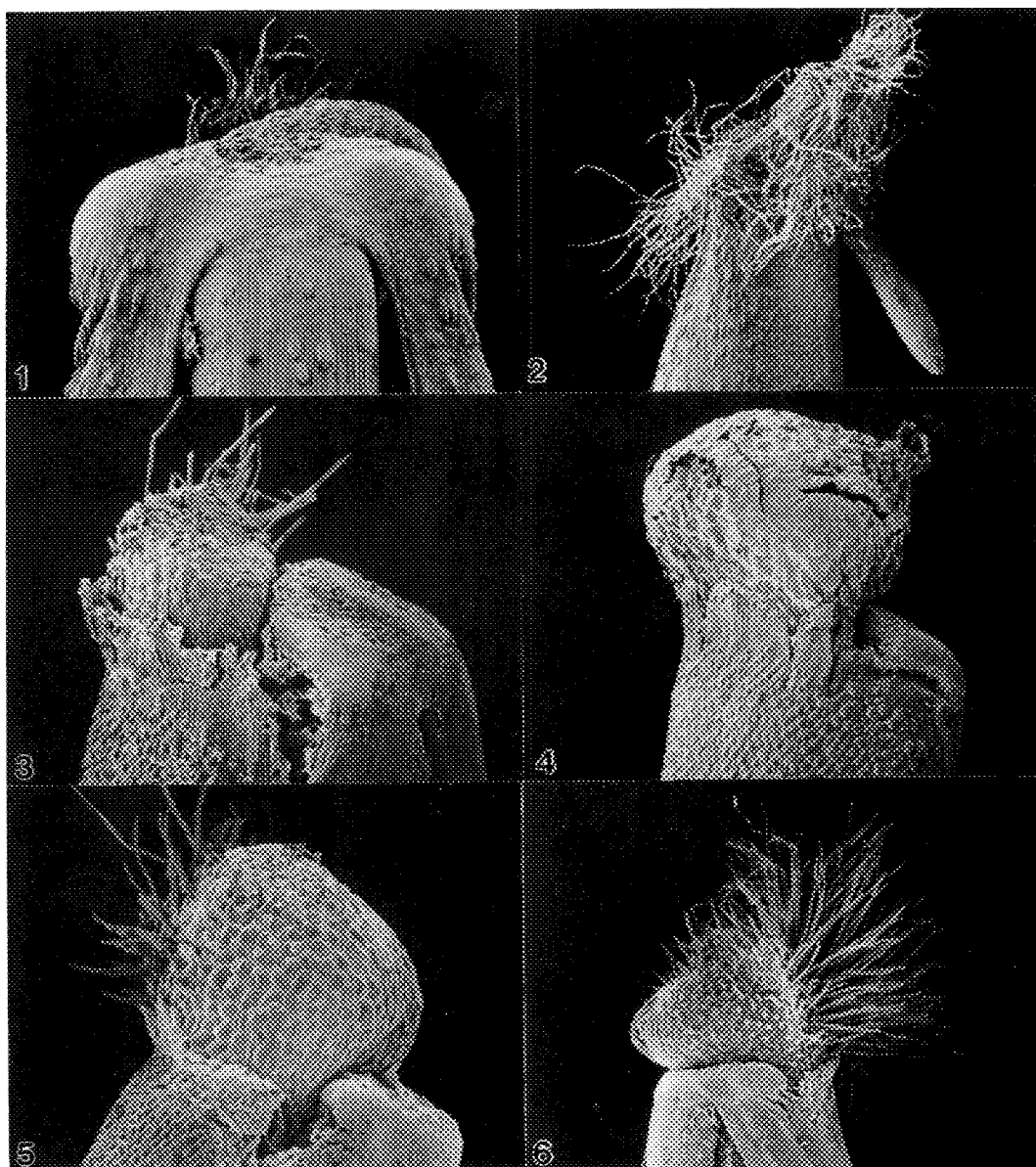


Fig. 1-6. SEM images of *Lolium perenne* coleorhizae. Fig. 1. Coleorhiza retracted into caryopsis during fixation. Mag. = 90X. Fig. 2. Emerging radicle elongated through coleorhiza during fixation. Mag. = 35X. Fig. 3. Coleorhiza incurred cell damage although retraction did not occur during freeze substitution and critical point drying. Mag. = 95X. Fig. 4. Coleorhiza retained shape but developed cracks and holes during freeze substitution and freeze drying. Mag. = 85X. Fig. 5. Coleorhiza preserved during freeze drying. Mag. = 90X. Fig. 6. Emerging radicle did not elongate through coleorhiza during freeze drying. Mag. = 40X.

USE OF THE TANNIC ACID/PARA-PHENYLENEDIAMINE LIPID CYTOCHEMICAL TECHNIQUE FOR SCANNING ELECTRON MICROSCOPY OF ATHEROSCLEROTIC ENDOTHELIUM

K.A. Robinson and R.P. Apkarian

Divison of Cardiology, Emory University and Yerkes Research Center, Atlanta, GA 30033

A cytochemical technique for the preservation and visualization of neutral lipid in atherosclerotic tissue was developed by Guyton and Klemp¹. This tannic acid/para-phenylenediamine (TA-PDA) procedure prevented the extraction of extracellular lipid by dehydrating solvent, which permitted it to be imaged in the aortic subendothelium by TEM². We applied the technique to enable documentation by SEM of lipid particles associated with the luminal surface of aortic endothelium during experimental atherogenesis. Preliminary results in a porcine model had suggested that a lipid exocytic, or retro-endocytic, process might occur in chronic hyperlipidemia³.

New Zealand White rabbits were fed a diet containing 1% cholesterol for 2 wk. Under deep anesthesia they were perfusion fixed with 2.5% glutaraldehyde in 0.1 M cacodylate, pH 7.4, at 100 mm Hg pressure and 37°C for 15 min. One cm² segments of arch and thoracic aorta were excised and immersed in the same fixative for 24-48 h at 4°C, rinsed in cacodylate buffer, opened longitudinally, and sutured to cardboard templates with the luminal surfaces exposed. All samples were postfixated in 1% OsO₄ for 1 hour; some were immediately dehydrated (routine preparation) while others were treated by the TA-PDA procedure as follows: mordanted with 1% tannic acid in 0.05 M cacodylate for 30 min, rinsed with 1% NaSO₄ in 0.05 M cacodylate for 5 min, rinsed briefly with 70% ethanol, and stained with 1% para-phenylenediamine in 70% ethanol for 30 min. They were then dehydrated according to the same schedule as conventionally prepared samples (70, 80, 90, 100% over 50 min), and critical point dried from liquid CO₂ in a Polaron 3000 using thermoregulation and flow monitoring. After attachment to aluminum supports and sputter coating with 15 nm Au/Pd, the specimens were imaged in the conventional SE mode of an ISI DS-130 equipped with a LaB₆ emitter.

Conventionally prepared specimens displayed the usual atherosclerotic changes including foam cell lesions with occasional endothelial micro-ulcerations, as well as endothelial cell (EC) lipid inclusions (Fig. 1). Such features were also observed in TA-PDA treated samples; however, these further displayed abundant luminal surface-associated spheroidal structures up to 1.9 μ m in size (Fig. 2). Occasionally these appeared to have arisen from EC lipid inclusions by an exocytic/retro-endocytic process (Fig. 3). Additionally, a population of smaller particles in the size range of blood lipoproteins were observed adherent to the EC (Fig. 4).

These results suggest that conventional specimen preparation procedures largely remove EC luminal surface-associated lipid particles, presumably by extraction during ethanol dehydration. Conversely, the TA-PDA treatment preserves these structures allowing them to be studied by SEM. Whether the particles are an artifact of the initial chemical fixation, however, remains a question to be addressed by alternate procedures such as cryofixation.

References

1. J.R. Guyton and K.F. Klemp, *J. Histo. and Cyto.*, (1988) 36, 1320.
2. K.F. Klemp and J.R. Guyton, *Proc. 49th Mtg. EMSA*, (1991), 92.
3. K.A. Robinson and R.P. Apkarian, *Scanning Microsc.*, (1991) 5(2), 533.
4. This research was supported in part by NIH Grant RR-00165 from the National Center for Research Resources to the Yerkes Primate Center.

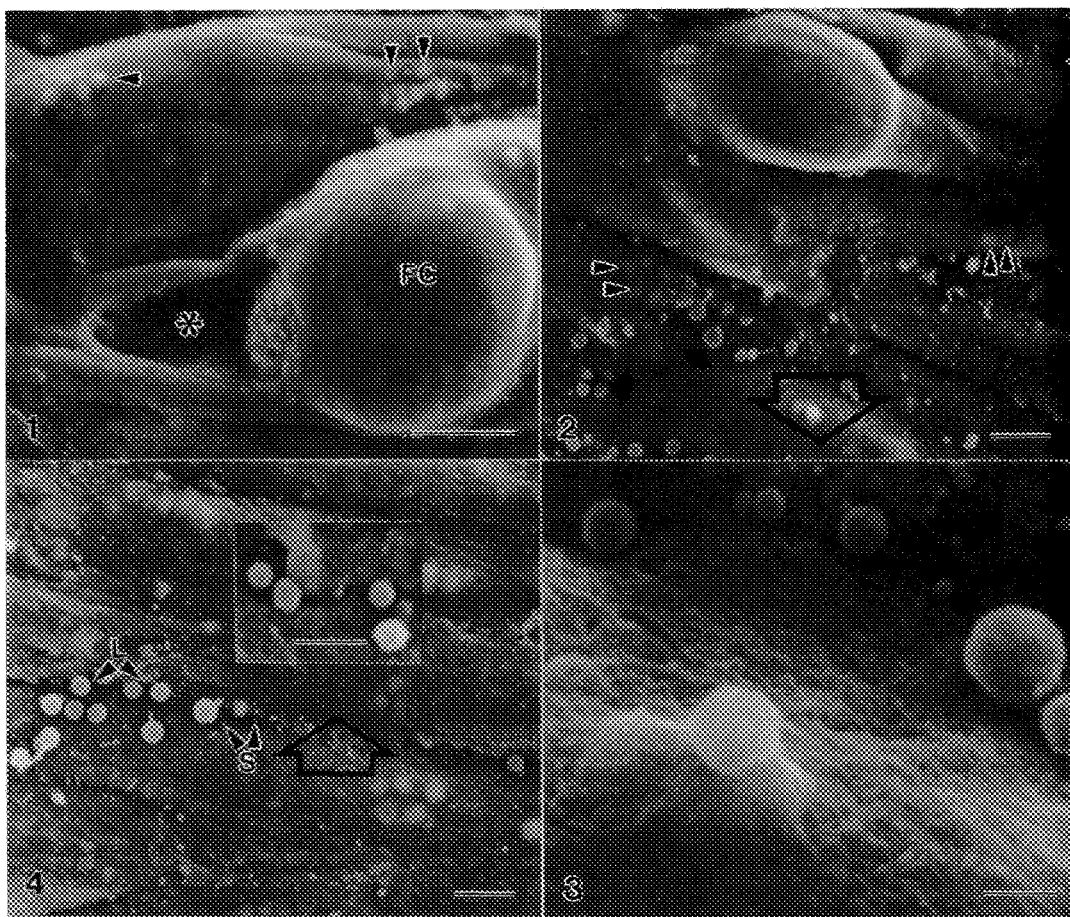


FIG. 1.--Foam cell lesion (FC), EC microulceration (*), lipid inclusions (arrowheads). Routine preparation. Bar=5 μ m.

FIG. 2.--Foam cell lesion (FC), lipid inclusions (arrowheads), surface-associated spheroids (arrows). TA-PDA treatment. Bar=5 μ m.

FIG. 3.--Area from box in Fig. 2 at 25° tilt. Bar=1 μ m.

FIG. 4.--Large (L) and small (S) spheroids. Inset from area in box. TA-PDA treatment. Bar=5 μ m; inset bar=1 μ m.

XEROXOGRAPHIC-ASSISTED LOCATION OF AREAS OR STRUCTURES ON CLINICAL SLIDES FOR ELECTRON MICROSCOPIC EXAMINATION

Beverly L. Giammara* and Jacob S. Hanker**

*Analytical Electron Microscopy Laboratory, Graduate Programs and Research, University of Louisville, Louisville, KY 40292

**Dept. of Biomedical Engineering, School of Medicine, University of North Carolina, Chapel Hill, NC 27599-7455

Recent studies in our laboratories have resulted in the development of microwave-accelerated silver stains for the demonstration of basement membranes and fungi (1-3), gram-negative bacteria (4,5), type III collagen, endoneurium, perineurium (6-8), DNA (9), and DAB or PPD-PC cytochemical or immunocytochemical reaction products (10). We have also found that the very structure in a specimen that raised a question by light microscopy can be mapped with a Micro-Locator Slide and then located and examined by the SEI and BEI modes of SEM by the techniques collated in this summary.

First the silver stained clinical slide is examined by light microscopy and areas and structures of interest mapped with the Micro-Locator Slide.* After these areas and structures are photographed, the Microlocator-Slide (Fig. 1a) is placed on top of the clinical slide which is Fig.1b and a copy of them (Fig. 2a) is made with an office copy machine (Xerox) enlarging them 140%. The numbers where the micrographs were taken are clearly marked on the copy showing the Micro-Locator Slide superimposed on the stained tissues or cells. This copy may be further enlarged as in Fig. 2b. After removal of the coverslip by soaking in xylene, the glass piece with the tissue or cells is HMDS-dried as a substitute for critical point drying (11). After air-drying in a dessicator, the specimen is mounted on SEM stubs with tissue side up and carbon-coated or sputtercoated with 200 nm gold. If the tissue design clearly allows the area of interest to be selected, carbon paint can be used to cover areas not of interest, if desired. Identifying areas by low mag polaroids or hand drawings can also aid in locating them in the SEM. Using the backscattered-electron detector in the reversed polarity mode, the silver stained structures stand out very black against a light background and can be clearly seen. With the landmarks of the tissue design it is not too difficult to find the exact same areas; and very often the very same cells or structures photographed in the LM can be correlated with higher magnification SEI and BEI images.

Acknowledgement: David J. Birch for technical assistance.

References:

1. B. Giammara et al. Proc. 42nd Ann. Meet. Electr. Microsc. Soc. Amer. 264 (1984).
2. J. Hanker et al. Proc. XIIth Int. Cong. Electr. Microsc. 616 (1990).
3. Sigma Diagnostics Silver HT100.
4. B. Giammara et al. Proc. 47th Ann. Meet. Electr. Microsc. Soc. Amer. 1082 (1989).
5. J. Hanker et al. Microsc. Res. and Technique, in press.
6. B. Giammara et al. Proc. 47th Ann. Meet. Electr. Microsc. Soc. Amer. 952 (1989).

*LAB-AIDS, 33 Sewall Ave., Winthrop, MA 02152

7. B. Giammara et al. Proc. XIIth Int. Cong. Electr. Microsc. 158 (1990).
8. B. Giammara et al. Microscopy Res. and Technique, submitted.
9. J. Hanker and B. Giammara. Proc. 42nd Ann. Meet. Electr. Microsc. Soc. Amer. 262 (1984).
10. J. Hanker et al. Proc. 43rd Ann. Meet. Electr. Microsc. Soc. Amer. 704 (1985).
11. B. Giammara et al. Proc. 45th Ann. Meet. Electr. Microsc. Soc. Amer. 878 (1987).

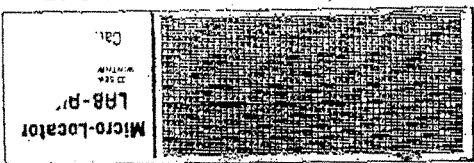


Fig. 1a - Micro-Locator Slide



Fig. 1b - Clinical Slide

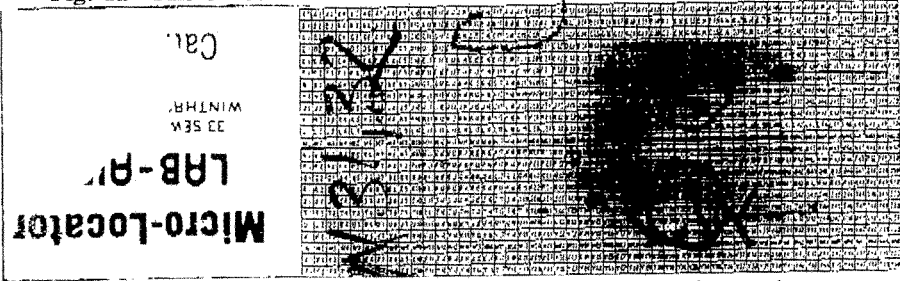


Fig. 2a - Enlarged Xerox copy of both slides, superimposed.

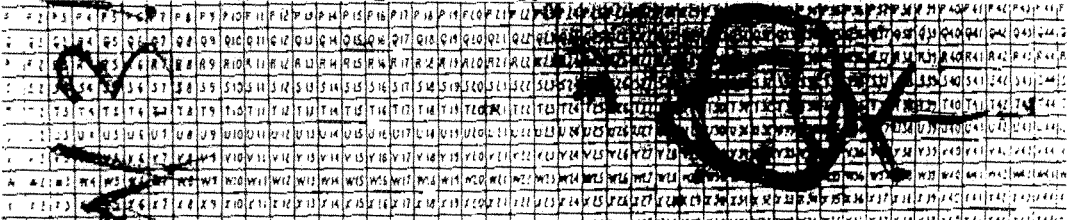
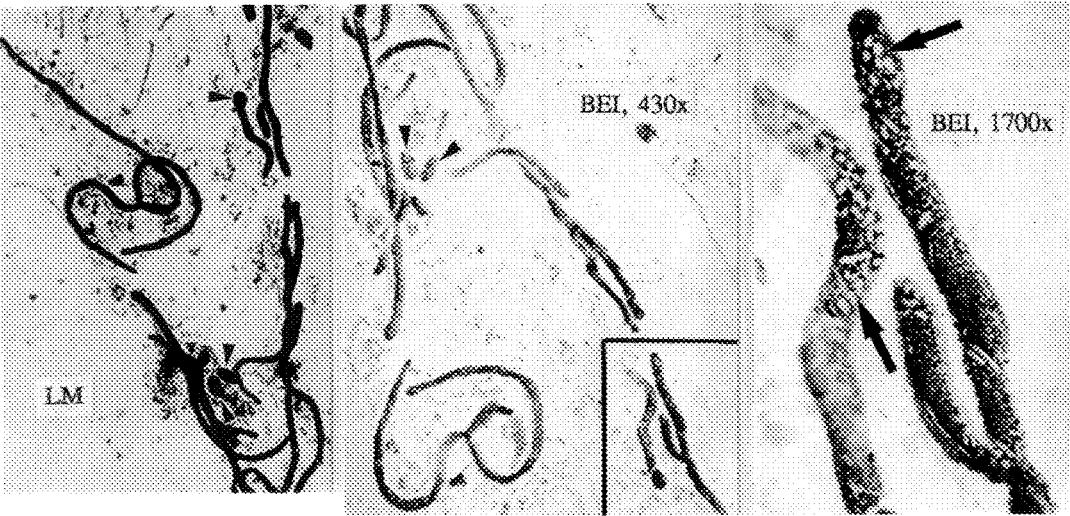


Fig. 2b - Larger Xerox copy shows numbered area identified by LM to be viewed by SEM.



An improved method of detection Auer rods in acute myelogenous leukemia by LM & TEM

K. Chien, M. Ngan and S. Lee

Pathology & Laboratory Medicine, Cedars-Sinai Medical Center,
Los Angeles, California 90048

Auer rods are large, elongated, eosinophilic granules that contain peroxidase, lysosomal enzymes and crystalline inclusions. They are specific for acute myelogenous leukemia (AML) and are present in leukemic blasts and promyelocytes. Their incidence is about 10-20 percent and varies between different subtypes of AML. We present here an improved method of detecting Auer rods by the use of epon-embedded plastic sections.

By knowing the exact cell counts, optimum amount of peripheral blood of AML patients is placed in a modified 1ml T.B. syringe which acts as a small centrifuge tube. For example, if the patient's white cell count is 5 times higher than normal, we use 1/5ml of blood so that it will produce a optimum thickness of the buffy coat. After centrifugation at 3,000 rpm for 10 minutes, the serum above the buffy coat is pipetted off and 3% buffered gluteraldehyde is gently added¹. The buffy coat is fixed from 30 min to overnight. After fixation, by pushing the rubber plunger with a straightened paper clip, the solidified buffy coat can be easily removed from the syringe and trimmed so that each piece contains platelet, WBC and RBC cell layers. Specimens are processed and embedded in epoxy resin in the routine manner. One micrometer sections are stained with a modified MBAF Stain for LM². Areas of interest are subsequently thin-sectioned for TEM examination.

By light microscopy, the large Auer rods or cluster of small auer rods are stained deeply eosinophilic by this modified MBAF Stain, in contrast to the pinkish color with Giemsa stain. Furthermore, these cells are concentrated at the bottom of the buffy coat and just above the red blood cell zone (fig.1), in contrast to the random distribution in the smear, thereby minimizing the time required to screen the slide. Finally, if the Auer rods cannot be identified with certainty, this cell layer can be ultra-thin sectioned and precisely identified by TEM (fig.2,3).

The presence of Auer rods is useful in distinguishing acute myelogenous leukemia from acute lymphoblastic leukemia and leukemoid reactions in which they do not occur. Although there are other methods of diagnosing AML such as histochemical stains and flow cytometry, the method we described is fast, convenient and can be performed in most laboratories.

REFERENCES

1. R. D. Anderson, J. Ultrastruct. Research, 13(1965)263.
2. K. Chien et. al., Proc. Ann. ENSA Meeting 45(1987)631.

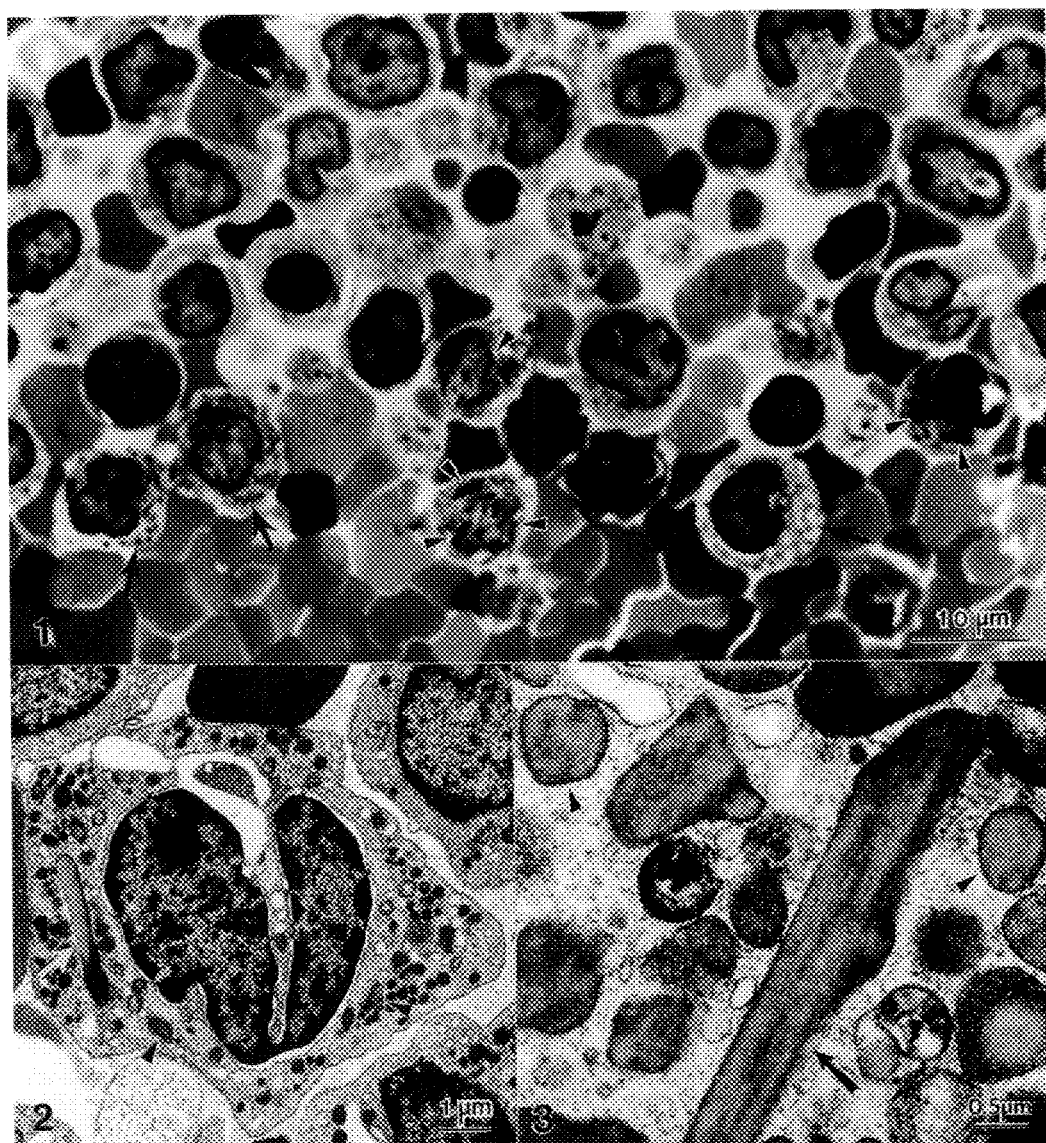


FIG. 1--LM of buffy coat from AML patient. Large Auer rods (arrowheads) or clusters of small Auer rods (arrows) in cells are stained deeply eosinophilic by modified MBAF Stain. These cells are concentrated at bottom of buffy coat and just above the RBC zone. FIG. 2--TEM of AML cell containing Auer rods in longitudinal (arrow) and transverse (arrowheads) planes of section. FIG. 3--TEM of Auer rods. Both longitudinal (arrow) and transverse (arrowheads) views show typical crystalline structure.

A LANGENDORF PREPARATION FOR QUICK-FREEZING SMALL HEARTS

Joachim Sommer*, Teresa High*, Peter Ingram**, Rashid Nassar*, and Neal Shepherd*

*Div. of Physiology, Dept. of Cell Biology and Dept. of Pathology, Duke Univ. and VA Med. Ctrs., Durham, N.C., 27710

**Research Triangle Institut, Research Triangle Park, NC 27709

The validity of studies of cell structures at high spatial and temporal resolution depends on the fidelity with which tissue preparation maintains *in vivo* conditions. Optimal preservation of structural substrates of precisely timed physiological intracellular events is offered by cryopreservation followed by freeze-fracture and freeze-substitution; we have established criteria for gauging that quality of cryopreservation in skeletal and cardiac muscle.^{1,2,3} Cryopreservation is indispensable for electron probe x-ray microanalysis (EPXMA) of freeze-dried cryosections. We have developed a Langendorf preparation for small hearts (Figs.1,2) suitable for use in our quick-freeze device ("Cryopress"; Med-Vac, Inc., St. Louis, MO 63117) to a) investigate the spatial distribution of physiologically important elements (e.g. calcium) during excitation-contraction coupling (ECC), especially in intact avian hearts and, b) assess damage to cardiac ultrastructure that is caused by pathological conditions (e.g. ischemia), rather than by artifacts due to chemical fixation (e.g. membrane damage by glutaraldehyde). In our Langendorf preparation, the tips of hearts can be quick-frozen at optimal freezing conditions,³ and comparative studies of the hearts of different animal species performed.

METHODS: Under pentobarbital anesthesia and after i.p. injection of a small amount of heparin, hearts from small animals (frog, mouse, finch) are quickly removed under a dissecting microscope. The left pectoral trunc is cannulated and connected to a perfusion apparatus. The heart is put into a special holder (Figs.1,2) in which it is perfused and electrically stimulated. The specimen holder is made of Delrin with a conical bore (Fig.2) into which the heart is gently pulled by the metal cannula and tubing that connects it with the perfusion apparatus (Figs. 1,2). The heart is electrically stimulated using curled, springy Pt-Ir wires on opposite sides of the cone. The wires are held in place by set-screws. The tip of the heart is allowed to extend a few mm below the lower rim of the Delrin holder. The specimen with the holder, still connected to a Langendorf set-up, is then moved to the quick-freezing device. A few seconds before dropping, the perfusion is disconnected and excess fluid is sucked off the tip of the beating heart. The heart is stimulated at a preset interval before being quickfrozen by impact on a liquid-He-cooled polished copper block. The frozen heart is separated from the Delrin holder under liquid nitrogen with a dental drill and faced to fit the chuck of a Reichert cryoultramicrotome for cryosectioning.

RESULTS: Figs. 3,5 show unstained freeze-dried cryosections of intact bird heart. Fig.4 shows a stained thin section following freeze-substitution and plastic embedding (Figs. 4,5 are from the same bird heart). Fig. 3 clearly reveals SR substructures (arrows) critical for ECC (free SR, EJSR). Preliminary EPXMA of cryosection of Fig. 5 indicated elemental distributions typical of healthy, viable cells (e.g. K:Na ratio 16:1, low [Ca] in cytoplasm [<10 mmol/kg dry wt] and mitochondria [<5 mmol/kg]). The preparation is useful for studying spatial displacements of physiologically important elements during ECC in cardiac muscle, and structural alterations following experimental interventions over time in the absence of fixatives and cryoprotectants.

REFERENCES:

1. R. Nassar et al., Scanning. Electron. Micros. (1986)I, 309
2. H. Dalen et al., J. Micros. (1992), in press
3. J. R. Sommer et al., J. Cell. Mol. Cardiol. (1988),20, 285
4. This research was supported by NIH grant RO1HL-12486 and the VA Research Service.

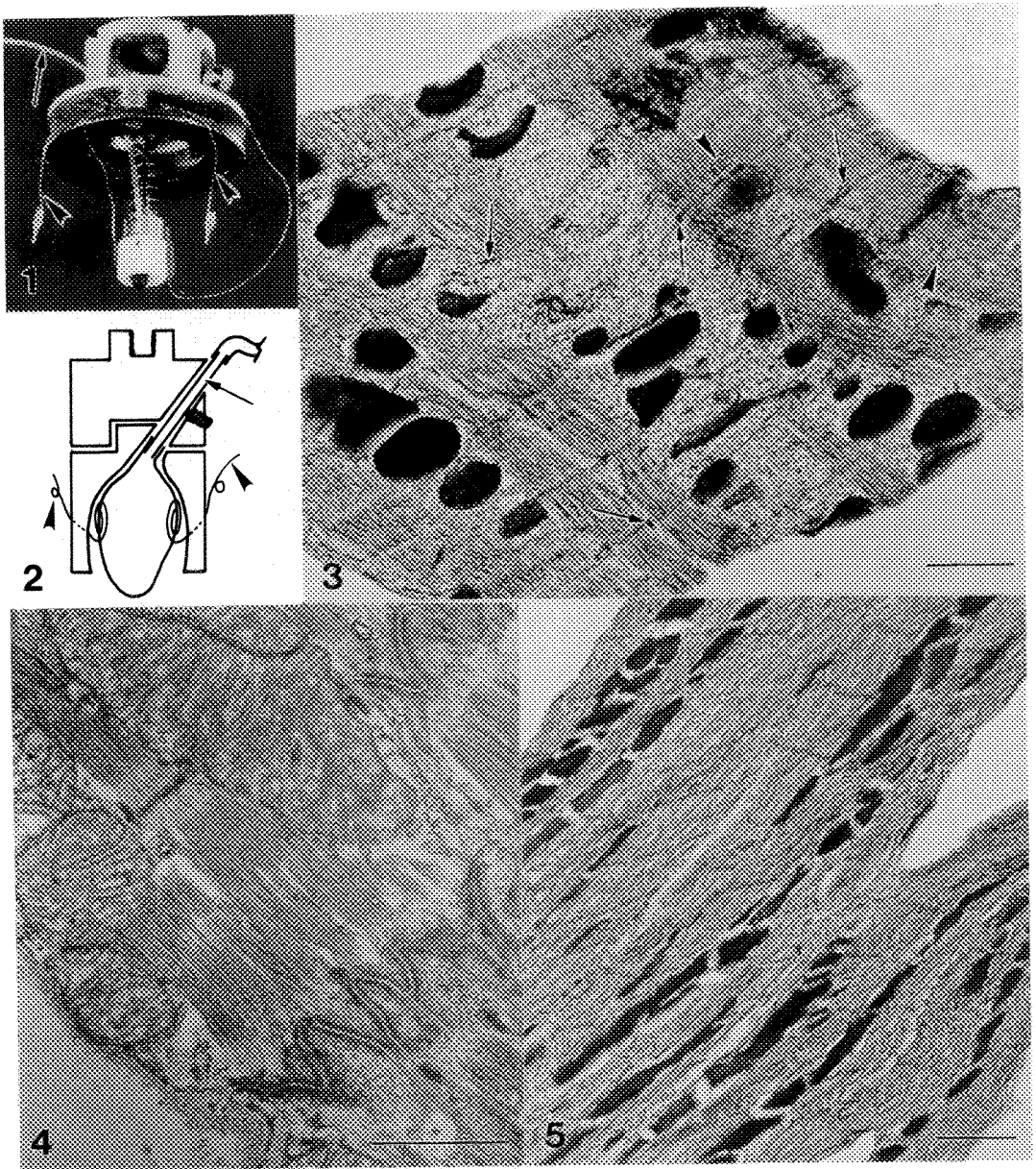


Fig. 1.--The specimen holder attached to the dropping head of the quick-freeze device, with stimulation wires (arrowheads) and tubing (arrow) for Langendorff perfusion.
 Fig. 2.--Schematic drawing of specimen holder containing a small heart and showing stimulation wires (arrowheads), cannula tied into left pectoral trunc (arrow), and tubing.
 Fig. 3.--Cryosection of quick-frozen finch heart. Free SR (arrowheads) and EJSR (arrows).
 Fig. 4.--Thin stained section of plastic embedded finch cardiac tissue adjacent to Fig. 3 following quick-freezing and freeze-substitution. All bars: 1 μ m.
 Fig. 5.--Cryosection of finch heart quick-frozen in holder of Fig. 1. Quantitative mapping revealed a high K:Na ratio and low cytoplasmic and mitochondrial [Ca] (see text).

HOW TO SAMPLE THE ENTIRE LENGTH OF A SINGLE MUSCLE FIBER QUICK-FROZEN AFTER ELECTRICAL POINT STIMULATION FOR HIGH RESOLUTION EM

Joachim R. Sommer, Teresa High, Betty Scherer, Isaiah Taylor, and Rashid Nassar

Div. of Physiology in Dept. of Cell Biology, and Dept. of Pathology, Duke Univ. and VA Med. Ctrs., Durham, N.C., 27710

We have developed a model that allows the quick-freezing at known time intervals following electrical field stimulation of a single, intact frog skeletal muscle fiber isolated by sharp dissection. The preparation is used for studying high resolution morphology by freeze-substitution and freeze-fracture^{1,2}, and for electron probe x-ray microanalysis of sudden calcium displacement from intracellular stores in freeze-dried cryosections,^{3,4} all in the same fiber. We now show the feasibility and instrumentation of new methodology for stimulating a single, intact skeletal muscle fiber at a point resulting in the propagation of an action potential, followed by quick-freezing with sub-millisecond temporal resolution after electrical stimulation, followed by multiple sampling of the frozen muscle fiber for freeze-substitution, freeze-fracture (not shown) and cryosectioning. This model, at once serving as its own control and obviating consideration of variances between different fibers, frogs etc., is useful to investigate structural and topochemical alterations occurring in the wake of an action potential.

METHODS: Single, intact skeletal frog muscle fibers (*m. semitendinosus*, *R. temporaria*) were isolated by sharp dissection with a hand-held diamond knife (L.A.B. Instruments, Carson City, NE 89701) (Fig.1) and processed as previously described¹, except for the wiring: short ends of silver wires (with their tips free of insulation) were bent to oppose each other across one end of a single muscle fiber (Fig.2). The propagation (as opposed to field stimulation) of action potentials down the fiber under these conditions was verified and measured with intracellular electrodes. Our design of the diamond knife for the cryosections (Diatome-US, Fort Washington, PA 19035) leaves both corners of the cutting edge free (Fig.3). For cutting, the frozen specimen is positioned such that the diamond cuts at an angle so that adjacent tissue escapes damage and can be used for additional sampling (Figs.4,5) by cryosectioning, freeze-substitution or freeze-fracture. The cryosections are freeze-dried in a Balzers FDU 010 freeze-dry unit evacuated with a turbomolecular pump on a schedule controlled by a heating ramp over about 24 hrs, and carbon coated. The carbon-coated sections, after breaking the vacuum, are transferred to a desiccator and kept under vacuum for storage.

RESULTS: 1. Propagating action potentials (velocity 2.0 ± 0.2 m/s, mean \pm S.E., $n=5$, at 21°C) can be produced with our experimental design. 2. Multiple samples of cryosections with excellent cryopreservation can be obtained along the entire length of a single muscle fiber (Figs.7-9). There is little tissue damage where the free corners of the knife strike (Fig.5), allowing immediately adjacent tissue to be recut, or processed for freeze-substitution (Fig.6) and freeze-fracture. 3. A diamond knife with free corners is *conditio sine qua non*. 4. Hand-held diamond knives, now available in different angles and widths, facilitate fiber dissection immensely. 5. The methodology may be useful for studying analogous problems in other cells.

REFERENCES:

1. R. Nassar et al., Scann. El. Microsc. (1986)I, 309
2. H. Dalen et al., J. Microsc. (1992), in press
3. P. Ingram et al., in Zierold & Hagler, eds., Electron Probe Microanalysis, Berlin Heidelberg: (Springer-Verlag 1989)/252
4. A. LeFurgey et al. J. Microsc. (1992), in press
5. This research was supported by NIH grant RO1HL-12486 and the VA Research Service.

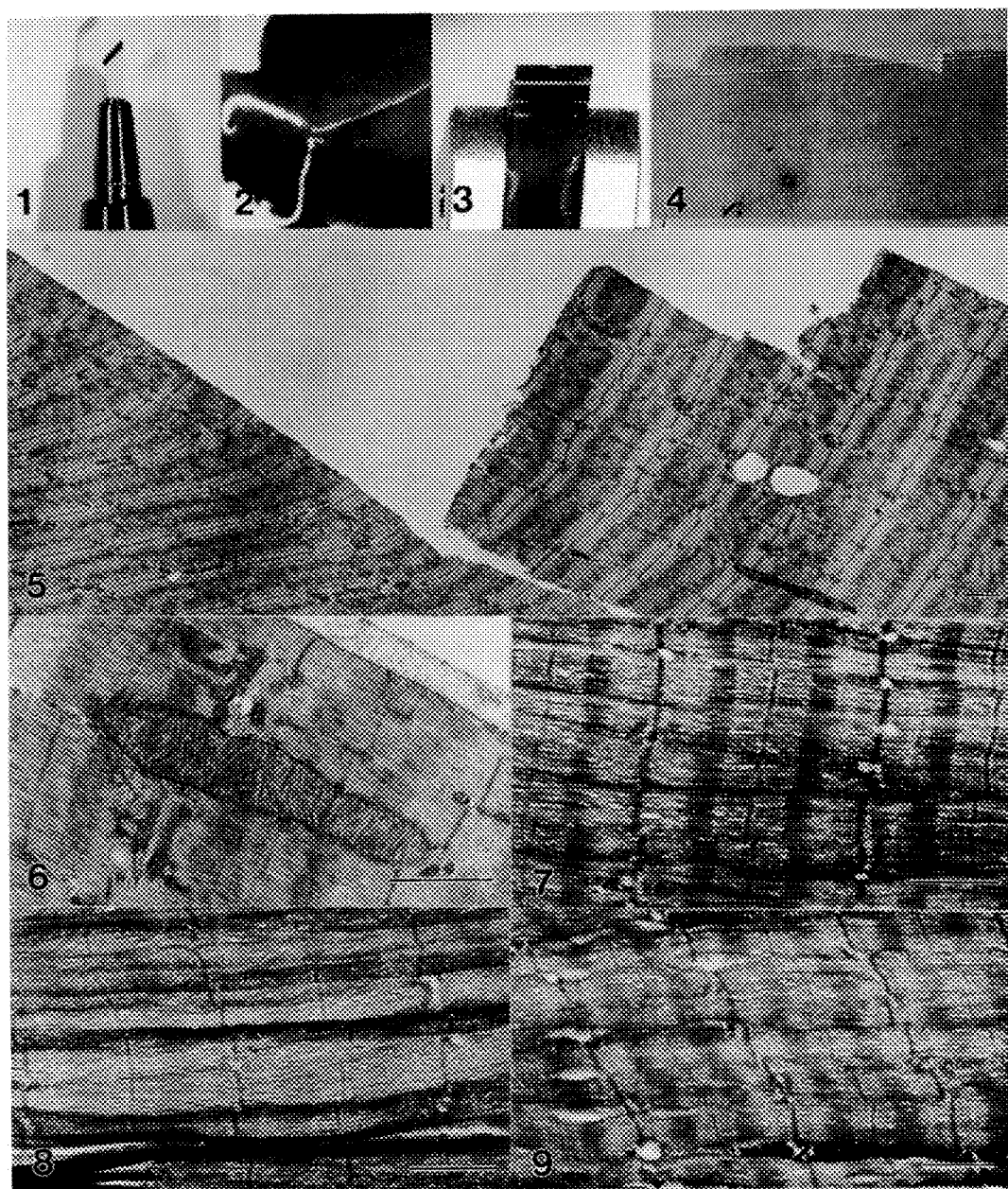


Fig. 1.--Hand-held diamond. Note smooth sides for easy dissection between adjacent fibers.
 Fig. 2.--The ends of two silver wires are bent toward the muscle fiber on a cushion of gelatin.
 Fig. 3.--Corners of the diamond knife are free, causing little harm to adjacent tissue (Fig.5).
 Fig. 4.--Two adjacent sampling points of a single fiber at very low power EM.
 Fig. 5.--Higher power EM of point of sampling showing integrity of cell structure at cut edges.
 Fig. 6.--Freeze-substitution from same fiber as in Figs. 7 through 9 below. All bars = 1 μ m.
 Fig. 7.--through 9. Cryosections, Fig.7 closest to the point of stimulation (see Fig.2).

IN SITU MICROTOMY AND SERIAL BLOCK FACE IMAGING BY SEM

Alan M. Kuzirian* and Stephen B. Leighton**

*Marine Biological Laboratory, Woods Hole, MA 02543

**Biomed. Engineering & Instrument. Program, NCRR, National Institutes of Health, Bethesda, MD 20892

The ability to view objects, including subcellular structures, in three-dimensions is crucial to understanding their form and function. For example, the three-dimensional (3-D) structure of the brain and its neurons has been the central focus of neuroanatomists for well over 100 years. Yet, what role a nerve cell's three dimensional structure plays in controlling the flow of information within the nervous system remains a mystery. Part of the problem has been the difficulty in obtaining an accurate 3-D picture of a nerve cell's shape as well as documenting its synaptic interconnections. Although many neurobiologists have turned to biochemical studies in recent years, it is becoming clear that precise structure and network diagrams will be necessary to relate the work of cell biologists with that of computational neuroscientists.

To increase the ability to gather this kind of information, a new method, called Serial Block Face Imaging (SBFI), was developed to obtain serial images of epoxy embedded tissue without much of the tedium, distortion, and possible loss of sections associated with traditional serial sectioning for large-scale 3-D reconstructions. A miniature microtome was built which operates inside the specimen chamber of a scanning electron microscope (SEM).¹ As sections are cut, they are discarded and the remaining block face is sequentially: etched with an oxygen plasma, coated by a gold sputtering device, and imaged—all within the SEM. Because the block face is imaged while fixed with respect to the electron optics, problems of orientation, and alignment are avoided. The plasma etching differentially etches the epoxy faster than the tissue, thus providing relief to the block face and improving image quality.^{2,3}

SBFI has the following additional advantages: 1. with epoxy embedded specimens, specific areas of interest can be investigated further with conventional ultramicrotomy and TEM, thus establishing direct morphologic correlations between many resolution levels from the same sample; 2. depth of etching and section thickness can be tailored to the tissue and desired results (theoretical section thickness <50nm) to maximize time and effort per sample; 3. the system can be automated to a high degree using new digital SEM's, micro-computer control of the microtomy/etching-sublimation process, and digital image acquisition, processing and storage.

We have demonstrated a reasonable resolution level (<20nm) with epoxy embedding and oxygen plasma etching. To improve this resolution for more detailed subcellular or molecular studies, we are now investigating and propose the possibility of ultra-cryomicrotomy with serial freeze etching of fixed or unfixed tissues utilizing differential low vacuum/accelerating voltages within the SEM. Thus, freezing would replace embedding, freeze etching would replace plasma etching, and low voltages would eliminate the need for metal coatings. Again, direct high resolution correlations on the same tissue is possible by conventional TEM of freeze-dried/substituted and embedded samples, or metallic replicas.⁴

We anticipate that the SBFI technique will significantly aid in producing 3-D reconstructions which will help to better understand the structure and function of a broad range of biological materials. The SBFI technique uses to its full advantage the large depth of field and magnification range of an SEM to sample large surface areas rapidly, thus bridging the gap between serial section reconstructions at the light and transmission electron microscopic levels.⁵

References

1. S.B. Leighton, Scan. Elect. Microsc. (1981)1981,73.
2. A.M. Kuzirian and S.B. Leighton, Scan. Elect. Microsc. (1983)1983,1877.
3. S.B. Leighton and A.M. Kuzirian, Biol. Bull. (1987)173, 444.
4. W.P. Wergin and E.G. Erbe, Scanning, (1992)14, 17.
5. We acknowledge Drs. D.L. Alkon, NINDS, and S.R. Goldstein, BEIP, NIH, and JEOL, Inc., Peabody, MA.

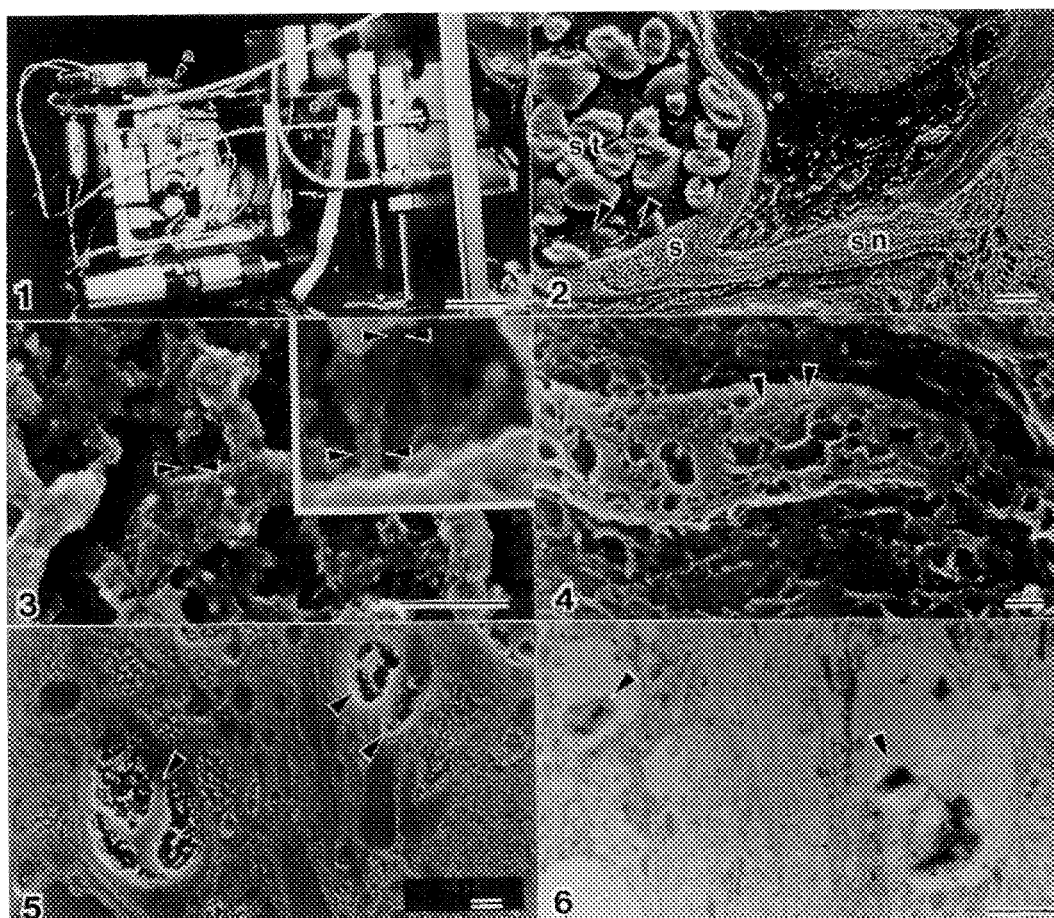


FIG. 1.--Photograph of mini-microtome and its major components: a, RF antenna; b, sputter coater; c, position motor for RF antenna and sputter coater; d, back of microtome and threaded shaft for specimen advance (arrowhead); e, motorized micrometers for X-Y stage movement; f, gas (oxygen and argon) inlet tube. Scale = 30mm.

FIG. 2.--Etched epoxy preparation of molluscan (*Hermisenda*) vestibular organ illustrating sensory hair cells (s) with kinocilia (arrowheads), calcareous stones (st) with which they interact, and efferent static nerve (sn). Scale = 10 μ m.

FIG. 3.--SBFI of nuclear heterochromatin of epoxy embedded, oxygen etched neuron at intermediate (x20,000) and high magnifications (x75,000; inset) to illustrate high resolution, ultrastructural capabilities of technique (arrowheads in both photos indicate same 60nm fiber; arrows in inset demarcate 18nm fiber). Scale = 1 μ m.

FIG. 4.--SBFI image of ethanol embedded, ultra-cryosectioned nervous system of *Hermisenda* illustrating longitudinally cut axon with putative neuronal (synaptic) vesicles (arrowheads). Scale = 1 μ m.

FIG. 5.--SBFI illustrating HRP/DAB reaction product (arrowheads) in small and larger neurites of iontophoretically injected neuron used for tracing neural networks. Scale = 4 μ m.

FIG. 6.--TEM of serially adjacent field illustrating HRP/DAB product (arrowheads) in same neurites as FIG 5; conventional thin section prepared just prior to mounting, etching, and imaging in SBFI System. Scale = 2 μ m.

MICROSCOPIC EVALUATION OF STRUCTURAL CHANGES IN BRITTLE, HYDRATED, GELATIN CAPSULES

J. Robson*, G. Snow*, J.Y. Park*, R.C. Moretz*, H.-O. Krenkel** and A. Angel*

*Boehringer Ingelheim Pharmaceuticals Inc., P.O. Box 368, Ridgefield, CT 06877

**Dr. Karl Thomae GmbH, Postsach 1755, D7950 Biberach an der Riss 1, Germany

Gelatin capsules are a commonly used dosage form for prescription medications. Storage conditions as well as drug formulation can directly affect capsule integrity over time. Often, capsule brittleness following storage can be related to water loss. (1) In this report an encapsulated drug formulation containing 77% anhydrous citric acid became brittle following two years of storage at 25° C/60% RH. However, Thermogravimetric data showed that capsule brittleness did not result from changes in water content. Both normal(without drug formulation) and brittle capsules contained 12% water. Microscopy was then applied to examine capsule walls to determine if the change in physical integrity could be related to a structural change.

LM of normal capsules showed both the interior and exterior walls to be smooth, without indentations. SEM examination of the interior wall of the normal capsules revealed fairly smooth walls (Fig. 1). Sections of normal capsules examined with the TEM revealed intact walls with little variation between sections or capsules (Fig. 2). Examination of capsules stored for one year revealed interior surfaces stippled with particulate identified as active ingredient(AI) and citric acid. The particulate was not fused to the interior wall and no morphological changes were observed for the AI or citric acid when compared to known active/excipient morphology. (2) In contrast, the interior wall of capsules stored for two years showed striking morphological changes. LM presented an eroded interior wall indicating a loss or redistribution of gelatin. TEM further illustrated that the structure of the capsule had been altered; subsurface pockets were seen throughout the section of the capsule (Fig. 3). TiO₂ particles, a whitener used in the capsules, were redistributed in the areas where degradation was apparent. SEM presented irregular interior surfaces with abundant particulate fused to the capsule wall (Fig. 4). The fused particulate presented structure which contrasted with the known morphology of the citric acid and AI starting materials indicating that dissolution and recrystallization had taken place. Comparable crystal structure was determined when AI and citric acid were dissolved in water and allowed to recrystallize at room temperature.

In conclusion, microscopic examination of the gelatin capsules demonstrated that storage conditions permitted excipient (citric acid)/AI dissolution/recrystallization. This resulted in an erosion of the interior wall leading to capsule brittleness.

References

1. Kontny, M.J. and Mulski, C.A., *Int. J. Pharm.*, (1989), 54, 79-85.
2. APhA and PhSGB (publishers), *Handbook of Pharmaceutical Excipients*, (1986), 78-79.

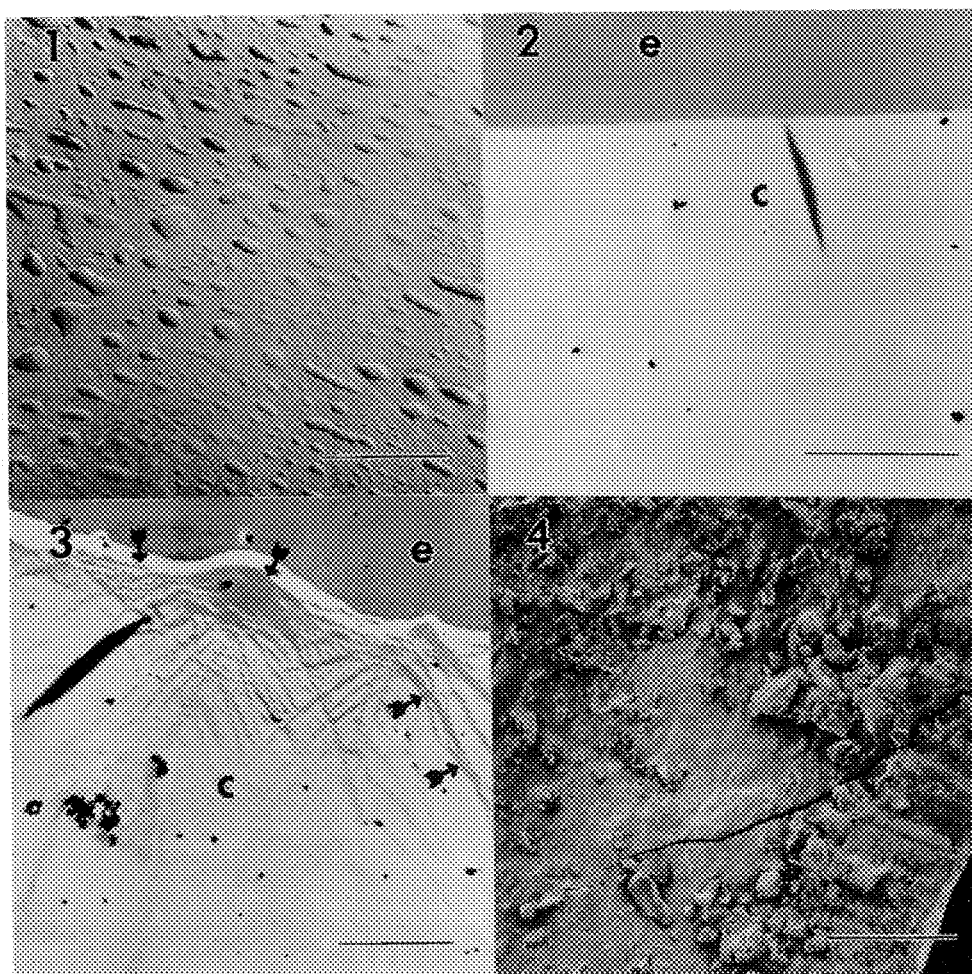


Fig. 1 SEM image showing normal capsule interior wall. Bar=100 μ m

Fig. 2 TEM section of normal capsule. c=capsule wall, e=epon Bar= 5 μ m

Fig. 3 TEM section of brittle capsule showing loss or redistribution of gelatin(arrows). Bar=5 μ m

Fig.4 SEM image of irregular internal surface of brittle capsule. Note fused particulate associated with wall. Bar=100 μ m

ERRORS AND DISTORTION INDUCED UNDER SOME OPERATING CONDITIONS IN A CONFOCAL LASER SCANNING MICROSCOPE (CLSM)

Harry Leung and Gwendolyn Jeun

Zoology Department, University of Western Ontario, London, Ontario, Canada. N6A 5B7

Fluorescent beads have been recommended and used frequently as calibration standards for fluorescent microscopy.^{1,2} However, during our work with a CLSM we observed that images of these beads varied in diameter with changes in illumination level, detector aperture diameter, and signal amplification (gain). In addition, XZ images showed distortion in proportion to such changes.

Images from 9 μm fluorescent beads (Excitation Max. @ 458 nm) were collected with a BIORAD MRC600 CLSM attached to a Nikon Diaphot-TMD inverted microscope. A Nikon Planapo 60x (NA=1.4) oil immersion objective was used in all experiments. The beads were embedded in 5 % gelatin to prevent drifting. Using an illuminating wavelength of 488 nm, the beads were optically sectioned at their equators under varying conditions of laser illumination, detector aperture diameter and gain. To eliminate image variations due to size differences among the beads, all images in Fig 1 were collected from the same bead. Those in Fig 2 were from another similar sized bead.

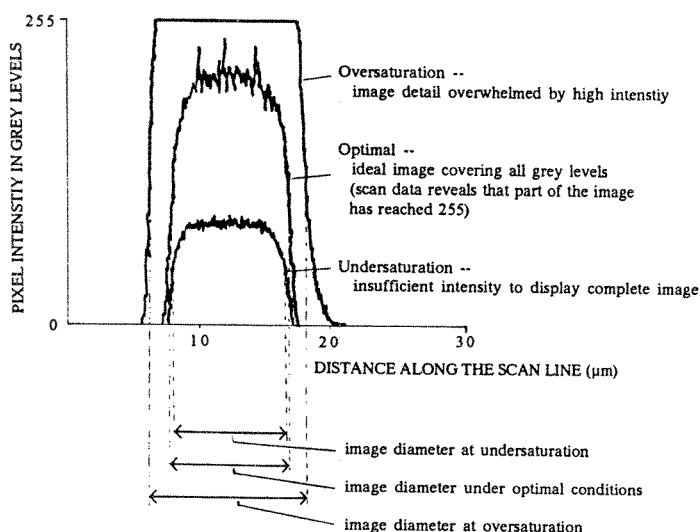
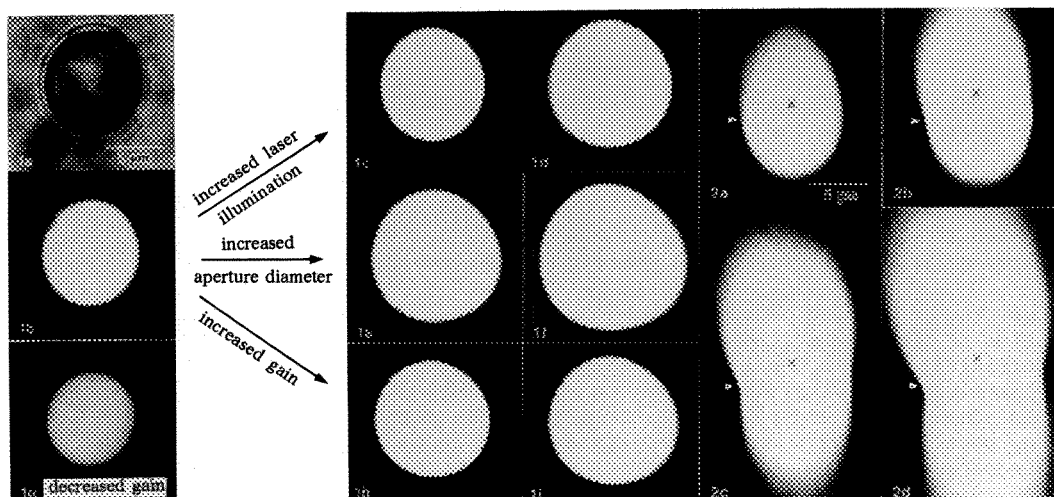
Conventional bright field imaging (non-confocal) showed the fluorescent bead used in the experiments to be a sphere 9 μm in diameter (Fig 1a). Its phase contrast image (not shown) also measured 9 μm . These images did not vary in size with changes in illumination, detector aperture diameter and gain. At minimal laser illumination, with the smallest aperture diameter and the gain set to a point where peak white (grey level 255 on a scale of 256) was just displayed, the confocal image matched the bright field image in diameter (Fig 1b). These conditions were considered optimal. Increasing any of the three variables resulted in oversaturation and a larger bead image. (Fig 1 c to f, h and i). Setting the gain too low, resulted in undersaturation and a smaller bead image (Fig 1 g). Intensity profiles, along the bead's equator, show that the image diameter is indeed larger at oversaturation and smaller at undersaturation (Fig 3).

In addition to size variations, all XZ images were distorted. The least distorted image, collected under the optimal conditions described above, was egg shaped rather than the expected spherical shape (Fig 2a). With increased illumination, a larger detector aperture, or with a higher gain, the image was elliptical (Fig 2 b). Further increase in laser illumination or gain made the image larger but did not induce further change in the shape. However, a larger detector aperture produced a halo on either end of the ellipse which expanded in both directions as the aperture diameter was increased (Fig 2 c and d). From these distorted images, it was not possible to determine the bead's center. Fig 2 shows the center of an XZ image (marked by an 'x') as half the total image length measured from top to bottom. However, this differs from the position of the bead's equator (marked by an arrowhead) as calculated from the XZ scan data.

The errors and distortion described may be related to the the following factors: lensing effect and excessive light scattering on the convex bead surface; density differences between the sample and the mounting medium; thickness of the cover glass; refractive index of the immersion oil; numerical aperture of the objective lens, spherical and chromatic aberrations. We recommend the use of minimum laser illumination with the smallest possible detector aperture, (ie. just enough to obtain satisfactory results) to minimize these errors. Fluorescent beads should be used with caution as size standards for CLSMs.³

REFERENCES:

1. Lansing Taylor, D., and Salmon, E.D. (1989) *Methods in Cell Biol.* 29: 207-237
2. Sisken, J.E. (1989) *Methods in Cell Biol.* 30: 113-126
3. We thank Dr. Michael Locke for critical review of the manuscript. This work was supported by NSERC of Canada grant #A6607.



3

Fig 1 The image of a fluorescent bead appears to vary in size with changes in laser illumination, detector aperture diameter and signal gain. (a)conventional bright field; (b)optimal confocal conditions, ie. 1% laser illumination , 1 mm aperture diameter and gain just to 255 (66%); (c and d) laser illumination at 3%(c) and 10 %(d); (e and f) aperture diameter of 4 mm(e) and 7 mm(f); (g to i) gain at 55 %(g), 85%(h) and 100%(i).

Fig 2 Distortion in XZ images in relation to detector aperture diameter. (a)1mm; (b)1.6 mm; (c)3 mm; (d) 5 mm. Laser illuminated from beneath; minimum illumination; gain at 53%.

Fig 3 Intensity profiles, along the bead's equator at oversaturation, optimum and undersaturation. Optimal conditions are those described in Fig 1b; oversaturation, is that of Fig 1i; undersaturation, is that of Fig 1g.

SEM STUDY OF CYTOSKELETON OF OSTEOBLASTS IMMOBILIZED ON HA-CERAMIC DURING BIOCOMPATIBILITY TESTING

P. FRAYSSINET*, C. DELGA*, P. CONTE*, N. ROUQUET*, M. NADAL**

*BIOLAND Inc., 132 Route d'Espagne, 31100 Toulouse, FRANCE

**Labo. d'Histologie, Faculté de Médecine de Rangueil, Toulouse, FRANCE

Some standards for biocompatibility testing of biomaterials requires the determination of the cytoskeleton aspect of differentiated cells in contact with the material (1). It is usually determined by indirect immunofluorescence staining of cytoskeleton proteins and examination with a light microscope.

This examination is difficult on non transparent material and the resolution is very poor. In order to study the interaction of osteoblast cytoskeleton with HA-macroporous ceramics, we grew chicken embryo osteoblasts on the material then we extracted cell membranes to expose the cytoskeleton proteins. They were then examined in SEM.

Chicken embryo osteoblasts are grown on HA-macroporous ceramic in a DMEM medium supplemented with 10 % foetal calf serum in a 5 % CO₂ and 98 % humidity atmosphere (2). Before a confluent monolayer is formed, membranes are detergent extracted in a solution of Triton X 100 (1 % in PBS) during 6 mn. Specimens are then fixed for 15 mn in a Karnovsky's solution and fixed in PBS. Thereafter they are immersed again in a Triton X 100 solution (1 % in PBS) for 15 mn and refixed for 30 mn. Specimens are then dehydrated in ethanol according to the conventional procedures, immersed in acetone and critical point dried. They are coated by gold-palladium and examined on a Jeol at 25 Kv.

Cells are immobilized on the ceramic and form multilayers (Fig. 1. and 2) containing an extracellular matrix. Isolated cells spread over the ceramic and are attached to the ceramic at some contact points. After membrane extraction, an actin and associated proteins network is shown (Fig. 3). Points of contact are observed (Fig. 4 and 5) on both the smooth face of grains or in the grain junction zones. Membrane bound actin nucleating sites seems to be well preserved. Proteins mediating the attachment of the cytoskeleton to the ceramic cannot be seen. No material particles can be found inside the actin network and the ceramic under the network does not seem to be altered.

This method makes it possible to observe the connection of some of the cytoskeleton proteins with the material and to determine a disturbance in their arrangement. Furthermore, cytoskeleton proteins can be labelled with colloidal gold in order to identify the proteins observed.

References.

1. Naji, A., Harmand, MF., J. Biomed, Mat. Res. 1990, 24: 861-871
2. Frayssinet, P., Bonneville, P., Autefage, A., Bonel, G., in : limb salvage-major reconstructions in oncologic and non tumoral conditions. Langlais, Tomeno (eds). Springer Verlag. 1991.

Legend.

Fig. 1 : SEM microphotograph of chicken embryo osteoblasts immobilized on HA macroporous ceramic. bar 100µm

Fig. 2 : Higher magnification showing a multilayered culture on the ceramic. bar :10µm

Fig. 3 : Isolated cells grown on the ceramic with the membrane extracted showing the cytoskeleton. bar :10µm

Fig. 4 : Point of contact between the cytoskeleton and the ceramic. bar :1µm

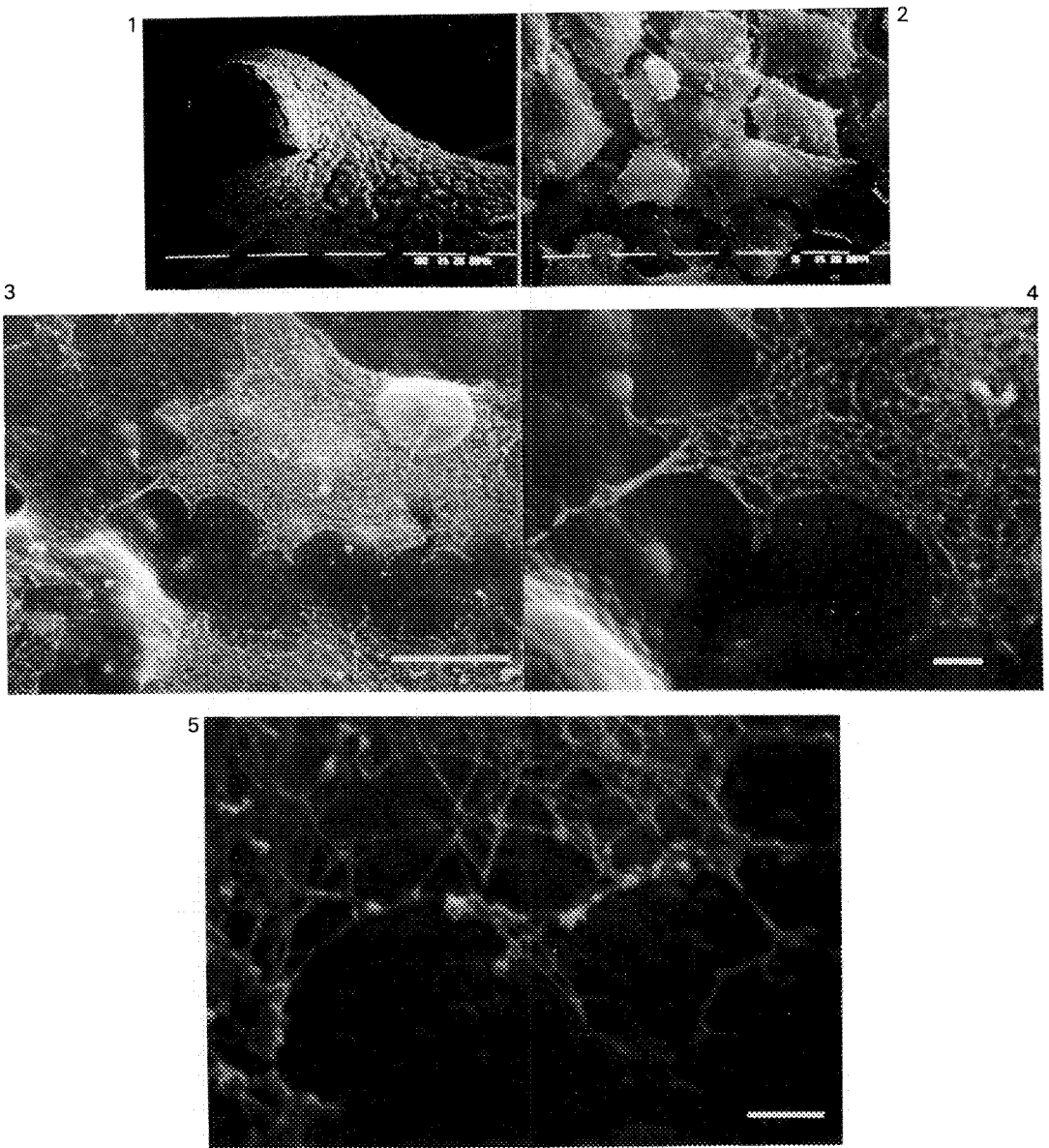


Fig. 5 : Cytoskeleton proteins attached to the ceramic in the grain junction zone. bar : 1 μ m

STRUCTURE OF EMULSIFIED AND UNEMULSIFIED LIPID-PROTEIN FOOD SYSTEMS REVEALED BY SCANNING ELECTRON MICROSCOPY AND LASER SCANNING CONFOCAL MICROSCOPY

François Lamarche and Diane Montpetit

Food Research and Development Centre, Agriculture Canada, 3600 Casavant Blvd. W, St-Hyacinthe (QC), CANADA, J2S 8E3

Lipids and proteins are major constituents of numerous food systems where they contribute significantly to the kinesthetic and organoleptic properties. Physical (creaming, coalescence, flocculation) and chemical deterioration (lipolysis, fat oxydation, fat soluble vitamins) are also prevented by lipid-protein interactions. Scanning electron microscopy (SEM) and confocal scanning laser microscopy (CSLM) were used to visualise emulsified and unemulsified lipid-protein model systems.

Model lipid-protein systems were prepared by an extraction procedure described by Melnychyn¹. Grain or grain mixtures were mixed with cheese whey in a Rietz disintegrator. The slurry obtained from this process was fed in a Sharples solid bowl separator to isolate an aqueous extract of solubles and a fraction containing insoluble residues. These two fractions, respectively referred to as soluble (s) and insoluble (i) fraction were spray-dried in a Niro atomiser. Six samples (3 soluble and 3 insoluble) were obtained by processing three different grain mixtures: soybean extracted with whey (WS), soybean/canola mixture extracted with whey (WCS) and canola/wheat extracted with whey (WCW). The fat contents and the degree of emulsification of the samples were:

Sample	WSs	WSi	WCWs	WCWi	WCSs	WCSi
Total fat(%)	12.0	13.9	15.4	11.8	15.4	18.9
Fraction of bound fat (% total)	91.7	24.5	94.8	44.9	96.3	19.0

As shown in Figs. 1 and 2, the structure of soluble and insoluble fractions were very similar and characteristic of spray-dried aqueous material. The microscopic appearance of soluble samples extracted with hexane was unchanged (Fig. 1). Hexane extraction of insoluble samples resulted in the creation of surface cavities that were once occupied by fat globules (Fig. 3). Because the dye (Nile blue A 0.1%) could not reach lipid structures embedded in the protein matrix, little detail was seen in soluble fractions under CSLM (Fig. 4). However, large lipid inclusions, observed in insoluble fractions (Fig. 5), were removed by the extraction step (Fig. 6). The later information revealed that the solvent extraction procedure was efficient. SEM and CSLM can be used to observe the fat structure in unemulsified lipid-protein systems, but CSLM is more convenient. The emulsified fats cannot be detected by either techniques since they are embedded in a protein matrix.

¹Melnichyn, P., U.S. Patent 4,869,918, September 26, 1989.

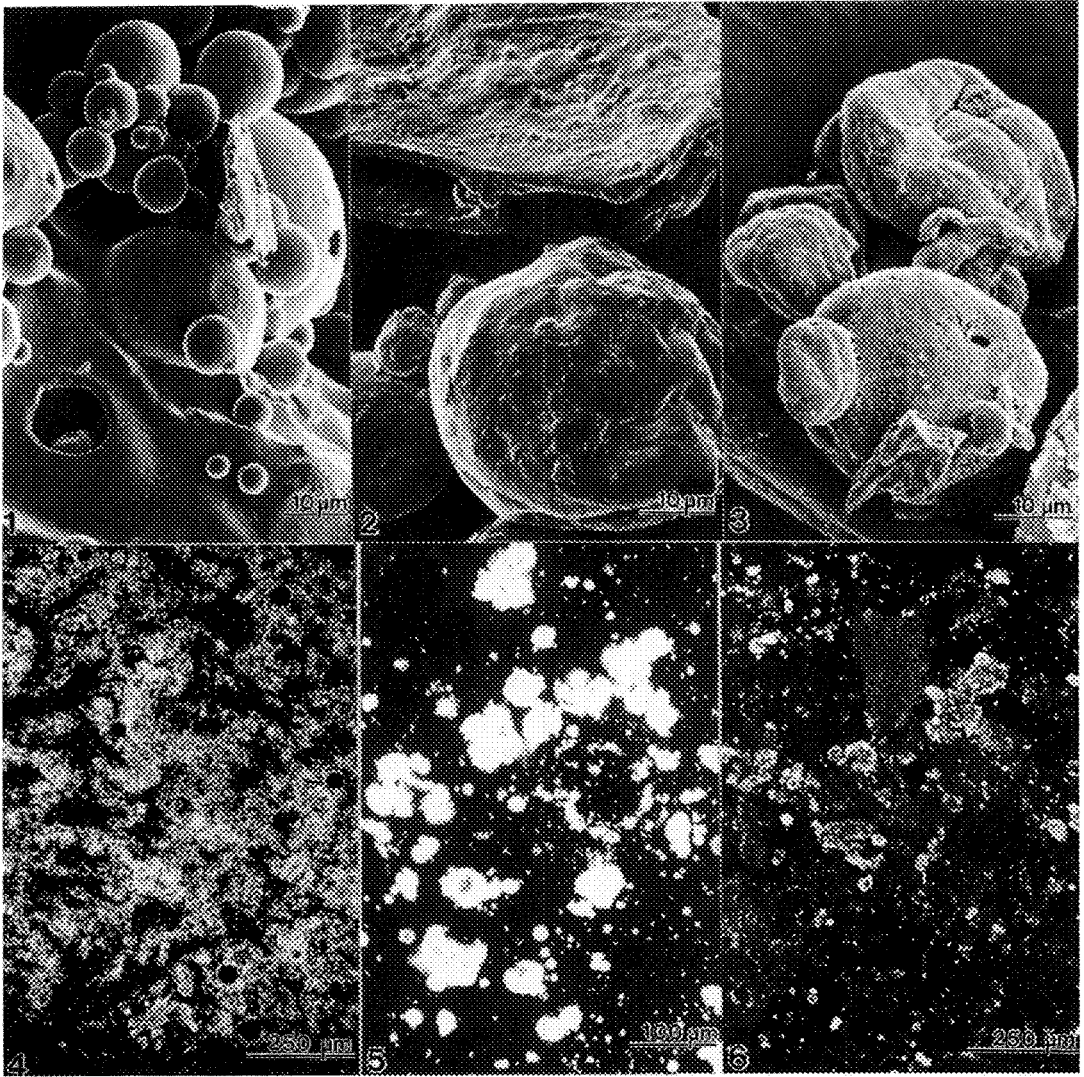


Fig. 1. -SEM of soluble whey-soybean fraction (WSs). The structure is typical of spray-dried liquid solutions. Bar=10 μ m.

Fig. 2. -SEM of insoluble whey-canola-wheat fraction (WCWi) obtained by spray drying. Bar=10 μ m.

Fig. 3. -SEM of insoluble whey-canola-wheat fraction (WCWi) extracted three times with hexane. Note the presence of holes indicating that surface fat have been removed by solvent. Bar= 10 μ m.

Fig. 4. -CSLM of soluble whey-canola-soybean fraction (WCSs) dispersed in a 0.1% Nile blue A solution. Bar= 250 μ m.

Fig. 5. -CSLM of insoluble whey-canola-soybean fraction (WCSi), dispersed in a 0.1% solution of Nile blue A. Bright spots indicate the presence of lipids. Bar= 100 μ m.

Fig. 6. -CSLM of insoluble whey-canola-soybean fraction (WCSi), extracted with hexane, dispersed in a 0.1% solution of Nile Blue A. Bar= 250 μ m.

ENHANCED INFORMATION FROM BIOLOGICAL MATERIALS THROUGH TECHNOLOGICAL IMPROVEMENTS IN CRYO-ELECTRON MICROSCOPY

Marc J.C. de Jong, Wim M. Busing and Max T. Otten

Philips Electron Optics, Building AAE, 5600 MD Eindhoven, The Netherlands

Biological materials damage rapidly in the electron beam, limiting the amount of information that can be obtained in the transmission electron microscope. The discovery that observation at cryo temperatures strongly reduces beam damage (in addition to making it unnecessary to use chemical fixatives, dehydration agents and stains, which introduce artefacts) has given an important step forward to preserving the 'live' situation and makes it possible to study the relation between function, chemical composition and morphology.

Among the many cryo-applications, the most challenging is perhaps the determination of the atomic structure. Henderson and co-workers were able to determine the structure of the purple membrane by electron crystallography, providing an understanding of the membrane's working as a proton pump. As far as understood at present, the main stumbling block in achieving high resolution appears to be a random movement of atoms or molecules in the specimen within a fraction of a second after exposure to the electron beam, which destroys the highest-resolution detail sought.

Electron crystallography is therefore performed under well-defined conditions, aimed at minimising beam damage:

- the specimen is held at cryo temperatures;
- large-surface cryo blades above and below the specimen reduce ice condensation and shield against the warm objective-lens pole pieces, reducing specimen-stage drift;
- searching for suitable areas takes place under low-dose conditions, while focussing is done on adjacent areas, aided by established and optimised low-dose procedures;
- the exposure is made at relatively low magnifications (30 000 to 50 000x), in some instances by a spot-scan exposure;
- the focus is set as accurately as possible.

Some remaining obstacles in electron crystallography were the limited resolution of the TEMs used to date (due to the 'low' voltage around 120 kV); the loss of contrast because of the restricted coherence of LaB₆ instruments; the low currents in small spots and thus long spot-scan exposure times with LaB₆ instruments; and the difficulty of accurate focussing at the low magnifications used for recording. These obstacles are reduced or removed altogether by some recent technological improvements in electron microscopy.

Higher resolution (Fig. 1) and at the same time less beam damage are obtained by using higher accelerating voltages. The use of a Field Emission Gun (FEG), such as the one on the Philips CM20 FEG, strongly improves the coherence and enhances the contrast for small high-resolution detail (Fig. 2). The FEG also provides high currents in small, fully coherent spots, allowing spot-scan exposure with exposure times per spot down to milliseconds, reducing initial beam-induced specimen movement as well as the total exposure time. Accurate focussing at low magnifications is now possible with a special lens for the CM microscopes, which provides a further magnification of up to 15x, raising the magnification on the TV monitor to about 12 million times for a recording magnification of 50 000x. With the new lens, the true focus can be determined under low-dose conditions with an accuracy better than 20 nm.

These technological improvements add significantly to the ability to investigate biological materials at cryo temperatures and provide another step forwards in obtaining high-resolution information from beam-sensitive specimens.

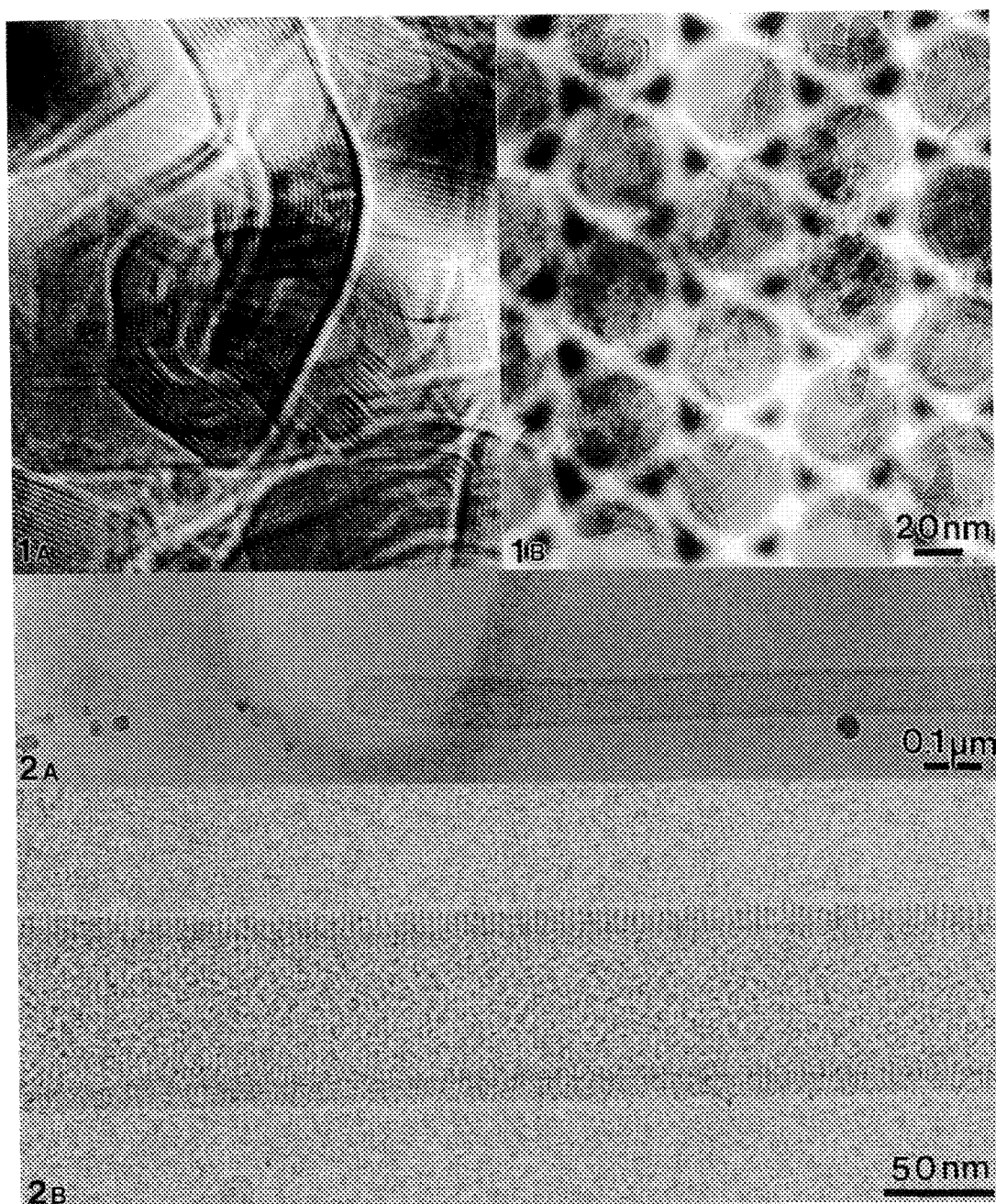


Fig. 1. Detail (A) and overview (B) from a spot scan image from graphitised carbon, showing full retention of the coherence even in small probes.

Fig. 2. OverView (A) and detail (B) of acetylcholine receptor channels in a tubular vesicle from the postsynaptic membrane of a torpedo ray, photographed at cryo-temperature using low dose facilities on a Philips CM20 FEG. (Image courtesy of Dr. Nigel Unwin, Cambridge, UK).

DETECTION OF CYCLOSPORIN A AND ITS CYTOSOLIC BINDING PROTEIN, CYCLOPHILIN, IN CYC A HIGH-PRODUCING STRAIN of *Tolypocladium terricola*

Vladimír Matha*, Alexander Jegorov*, František Weyda**

* Galena Co., Research Unit, Branisovská 31, 370 05 České Budějovice, Czechoslovakia

**Institute of Entomology, Branisovská 31, 370 05 České Budějovice, Czechoslovakia

Cyclosporin A (Cyc A), a cyclic fungal undecapeptide produced by various deuteromycetes^{1,2} is a potent immunosuppressant widely used in human medicine to prevent rejection of transplanted organs such as a kidney, liver, heart and bone marrow.³ Although originally isolated as an anti-fungal compound, practically no attention was devoted to its effect on the physiology of its high-producing organisms. In vertebrate cells, the cytosolic Cyc-A binding protein, cyclophilin, is expected to be a primary target involved in the regulation of Cyc A immunosuppressive effect. Similarly, the direct cyclophilin-mediated effect (toxicity) confirming the key role of this Cyc A receptor in Cyc A function, was determined even in *Neurospora crassa* and *Saccharomyces cerevisiae*. Induction of Cyc A resistance in both microorganisms was characterized by either of the complete lost of cyclophilin or by the lost of its ability to bind Cyc A.⁴

We demonstrate here that in Cyc A high-producing strain of *Tolypocladium terricola*, the resistance to the metabolite is not cyclophilin-dependent. Both Cyc A and its binding protein were shown to be present in the hyphae of high-producing strain by using of colloidal gold immuno TEM, however, the concentration of cyclophilin was significantly reduced and represented approx. 10% of the other cytosolic cis-trans isomerase (macrophilin). Cyc A (as well as cyclophilin and macrophilin) was determined by using of both polyclonal and monoclonal antibodies which confirmed not only the presence of the metabolite but also the presence of free epitope which is responsible for the specific interaction between Cyc A and its receptor. Fungi were fixed in formaldehyde (EM grade) and embedded into LR White resin. Ultrathin sections were incubated in antibodies for 3 hours (in refrigerator at 10° C), washed in PBS/BSA (phosphate buffered saline/bovine serum albumine) and TRIS/BSA and incubated with protein A/protein G mixture diluted with TRIS/BSA 1:20 for 1 hour. Sections were stained in lead citrate. For double immunostaining we have used double face method. Results are shown on Figure 1-6.

The using of binding assay we have identified the presence of another Cyc A-binding protein(s) in the lysate of the high producing strain. This compound which seems to be immunologically quite different from cyclophilin (no cross-reactivity between the new binding protein and anti-cyclophilin polyclonal antibody was determined) and could represent a new group of Cyc A binding protein(s) responsible for adaptation of high-producing organisms to the metabolite.

In addition to the binding protein, morphological and physiological adaptations of the high-producing strain characterized by the induction of KCN insensitive respiration, reduction of size and inner membrane morphology of mitochondria and production of high amount of lactate into the cultivation medium.

References

1. M. Tropschug, I. B. Barthelmess and W. Neupert, Nature (1989)342, 953
2. A. Jegorov, V. Matha and J. Weiser, Microbios Letters (1990)45: 65
3. M. M. Dreyfuss, Sydowia (1986)39, 22
4. A. Warburg and R. Traber, Progress Med. Chem.: Elsevier Science Publishers (1988), 133

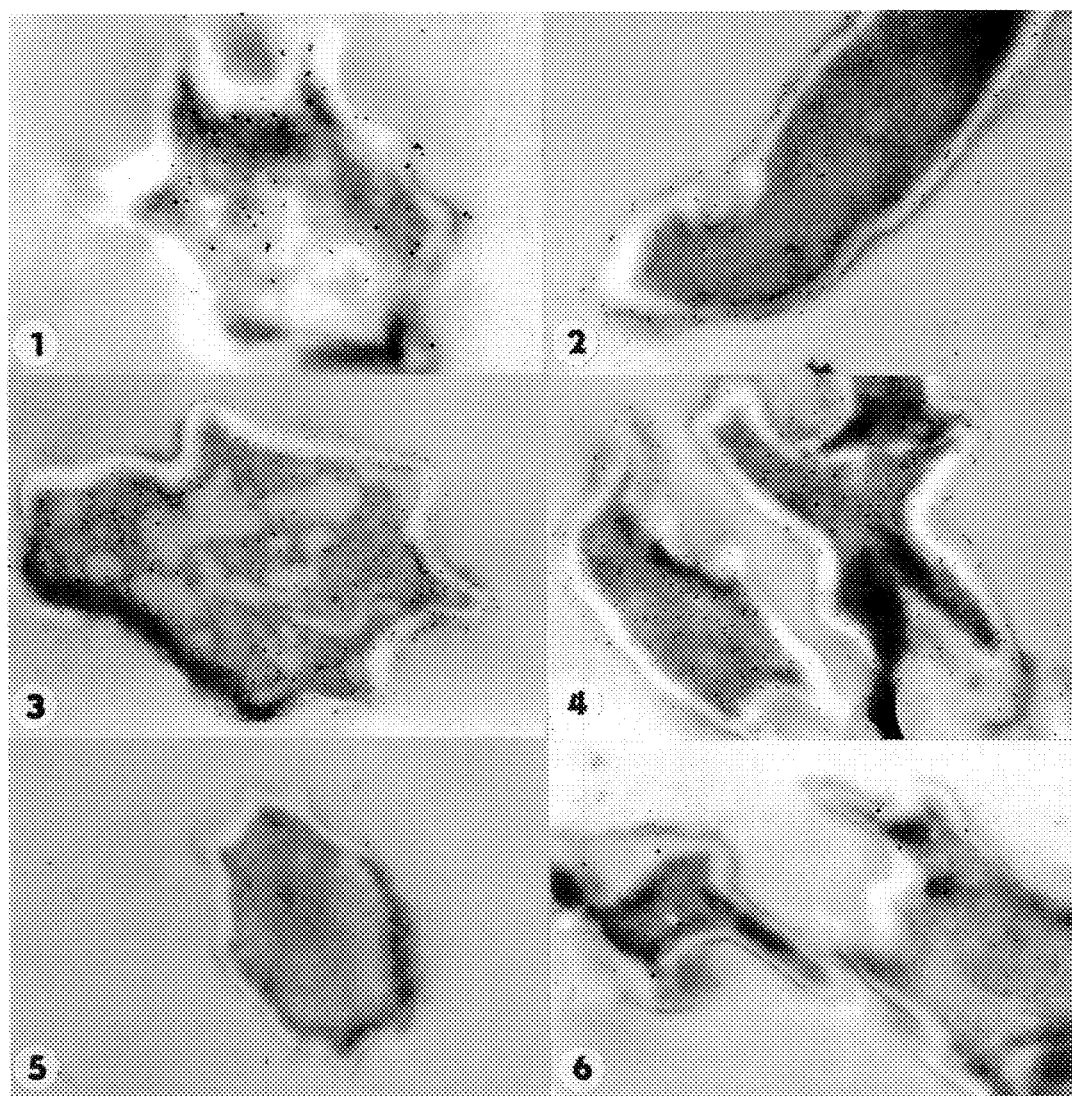


FIG.1- Localization of cyclosporin A in *Tolypocladium terricola*. Magnification = x57500.
 FIG.2- Localization of cyclophilin in *Tolypocladium terricola*. Magnification = x40700.
 FIG.3- Localization of macrophilin in *Tolypocladium terricola*. Magnification = x29000.
 FIG.4- Localization of macrophilin in *Tolypocladium terricola*. Magnification = x22500.
 FIG.5- Control reaction to localization on Figures 1-4. Magnification = x46300.
 FIG.6- Double staining: Cyclosporin (10 nm gold particles) and cyclophilin (20 nm gold particles) in *Tolypocladium terricola*. Magnification = 33800.

IMMUNOCYTOCHEMICAL DETECTION OF HEPATIC CARBOHYDRATE METABOLIC ENZYMES: IMPROVED RESOLUTION WITH POLYETHYLENE GLYCOL EMBEDDING AND VISIO-BOND SEMITHIN SECTIONS

Kuixiong Gao, Randal E. Morris, Bruce F. Giffin and Robert R. Cardell

Department of Anatomy and Cell Biology, University of Cincinnati College of Medicine, Cincinnati, OH 45267

Several enzymes are involved in the regulation of anabolic and catabolic pathways of carbohydrate metabolism in liver parenchymal cells. The lobular distribution of glycogen synthase (GS), phosphoenolpyruvate carboxykinase (PEPCK) and glycogen phosphorylase (GP) was studied by immunocytochemistry using cryosections of normal fed and fasted rat liver.¹ Since sections of tissue embedded in polyethylene glycol (PEG) show good morphological preservation and increased detectability for immunocytochemical localization of antigenic sites,^{2,3} and semithin sections of Visio-Bond (VB) embedded tissue provide higher resolution of cellular structure,⁴ we applied these techniques and immunogold-silver stain (IGSS) for a more accurate localization of hepatic carbohydrate metabolic enzymes.

For this study, slices (2 mm) of paraformaldehyde perfused liver from normal or diabetic rats were infiltrated with 90% PEG-1540 plus 5% glycerol and 5% water at 55°C and embedded in PEG-1540. Sections (5 μ m) were transferred onto Digene silanated slides with the aid of agarose blocks.³ Incubation with the primary antibody (rabbit antiserum against each enzyme) was followed by IGSS. After ethanolic dehydration, sections were mounted with VB and visualized in a Nikon FXA microscope. For semithin sections, IGSS-processed 5 μ m PEG sections or 10 μ m cryosections were counterstained with 0.3% pyronine Y, dehydrated with alcohol and embedded in a thin layer (0.3 mm) of VB. Periportal and centrilobular regions were cut from the large sections and embedded in VB again. Sections (0.30-0.65 μ m) were cut on an ultramicrotome, transferred onto glass slides, dried on a 55°C plate, and directly mounted in VB for light microscope examination with brightfield, epipolarization, or dark field illumination.

At low magnification, sections of PEG embedded liver gave lobular patterns of enzyme distribution similar to those in cryosections (Fig. 1), however, at higher magnification, they provided better resolution of the cytoplasmic localization of these enzymes (Figs. 2-4). Resolution of subcellular structures and antigenic sites were improved even further by use of VB semithin sections (Figs. 5 and 6). The gold-silver particles were discernable as individual dots and concentrated in certain compartments of the cytosome; they never appeared in nuclei. The dark antigenic signal is distinguished easily from pyronin-staining in the hepatocytes. These new methods provide excellent morphology and antigen localization and may be useful for other immunocytochemical studies.

References

1. B.F. Giffin, *et al.*, J. Cell Biol. 115 (1991) 3, pt 2, 2619.
2. J.B. Bard and A.S. Ross, J. Histochem. Cytochem. 34 (1986) 1237.
3. K.X. Gao and J.D. Godkin, J. Histochem. Cytochem. 39 (1991) 537.
4. K.X. Gao and H.B. Peng, J. Cell Biol. 105 (1987) 4, pt 2, 1278.

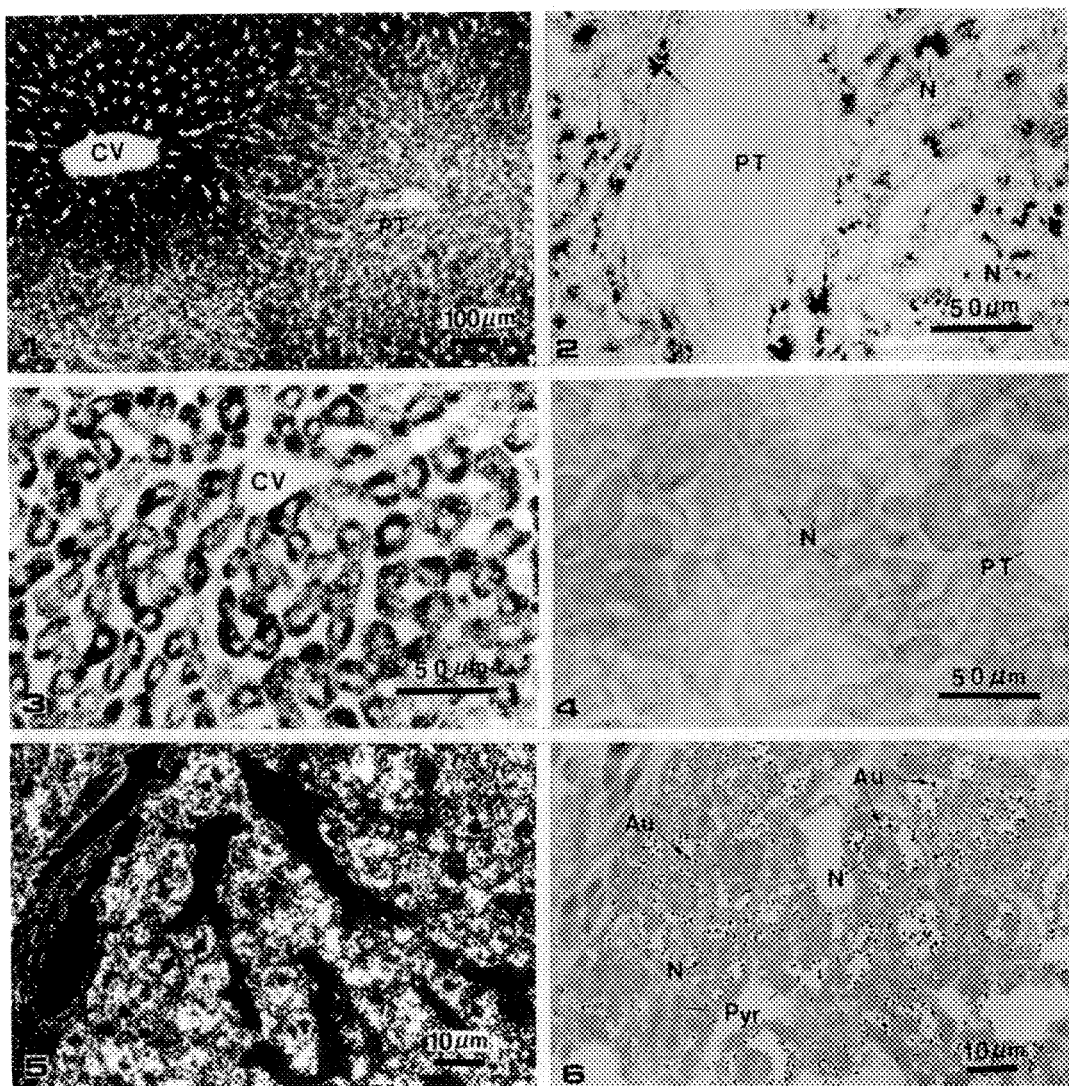


Fig. 1. Lobular distribution pattern of GS in normal rat liver. 10 μ m cryosection with IGSS. CV, central vein; PT, portal tract. [Bar=100 μ m]

Fig. 2. Subcellular distribution of GS in periportal hepatocytes of diabetic rat liver. Note large IGSS aggregates of GS (arrow) in cytosome around nuclei (N). 5 μ m PEG section with IGSS.

Fig. 3. GS is more diffuse in cells near central vein (CV). Fig. 4. Control experiment using normal rabbit serum instead of primary antibody. No immunostain was found. N, nuclei; PT, portal tract. [Bar=50 μ m in Figs. 2-4]

Fig. 5. Darkfield image of VB (0.65 μ m) semithin section of 10 μ m immunostained cryosection showing PEPCK (white spots) distribution. Fig. 6. Same preparation as in Fig. 5 viewed with normal transmitted light. Au with arrow, PEPCK; Pry, pyronin-philic particles. [Bar=10 μ m in Figs. 5 and 6.]

TRANSMISSION ELECTRON MICROSCOPY OF THE CATALYTIC ACTIVITY OF ADENOSINE MONOPHOSPHATE DEAMINASE IN MURINE LUNG

K. Bielat* and G. Tritsch**

*Department of Pathology, Roswell Park Cancer Institute, Buffalo, NY 14263

**Department of Experimental Biology, Roswell Park Cancer Institute, Buffalo, NY 14263

AMP deaminase was visualized in a manner analogous to our previous approach with adenosine deaminase (1). The chloro-analog of AMP, i.e., 6 Chloropurine riboside 5' monophosphate (CPRMP) (from Sigma) was shown to be a substrate of this enzyme which liberates Cl^- which is precipitated with added Ag^+ , and, after exposure to light electron dense Ag^0 grains are deposited at loci of enzyme activity. The substrate at a concentration of 1.1 mM in 50 mM HEPES buffer, pH 7.2, in the presence of 150 mM K^+ (as the acetate), 3mM ATP and 10 μM pentostatin (deoxycoformycin) was incubated with freshly excised tissue from a female C-57 BL/6 mouse. The substrate concentration is 1.4 times K_m for rabbit muscle enzyme (Sigma), and K^+ and ATP are allosteric activators of this enzyme. Because many cells have ecto 5'-nucleotidase activity, pentostatin was added to prevent manifestation of adenosine deaminase activity of dechlorination of any nucleoside that might be formed.

The mice were killed by cervical dislocation and the gastrocnemius muscle was dissected from the animal. Tissue blocks of 0.5mm³ or less were incubated in the assay mixture for 10 minutes at 37°C with agitation. The control medium lacked the substrate. The incubation medium was replaced with 2.5% glutaraldehyde in 0.1 M HEPES containing silver nitrate at a final concentration of 2mM and the blocks were allowed to fix for 1 hour at room temperature. The fixative was removed and the blocks were washed 3X with 0.2M HEPES buffer, pH 7.4, for 5 minutes each. Osmication was achieved with 2% osmium tetroxide in 0.15M cacodylate buffer, pH 7.4 for 3 hours at room temperature. The fixative was removed and the blocks were washed 3X for 5 minutes each in 0.2M cacodylate buffer. Dehydration was performed with a graded series of ethanol 30%, 50%, 70%, 90% for 5 minutes each and 2X in 100%. Infiltration was conducted with 100% ethanol-Spurr epoxy resin 1:1 for 2 hours at room temperature followed with pure Spurr resin for an additional 3 hours also at room temperature. Embedding was done in #00 gelatin capsules filled with pure Spurr resin and polymerized at 70°C for 24 hours. The tissue blocks were trimmed with razor blades to a trapezoid shaped face and thin sections were cut with glass knives on a Porter-Blum MT-2 ultramicrotome and collected on uncoated 200 mesh copper grids and examined unstained in a Siemens 1A transmission electron microscope operating at a potential of 80kv.

Figure 1 is a transmission electron micrograph of an unstained section of murine lung allowed to react with CPRMP in the presence of deoxycoformycin and Ag^+ . Erythrocytes show uniform distribution of electron dense silver grains of relatively uniform size in the cytoplasm with no concentration at the cell membrane as was found for adenosine deaminase (1). Several loci of high activity were found at the alveolar surface. The localization of silver grains represents discrete microloci of catalytically active AMP deaminase.

This communication visualizes loci of enzyme activity and is therefore different from the use of antibodies against enzyme protein, which need not necessarily represent catalytically active entities. The relative uniformity in size of the silver grains indicates that the enzyme activity at the various locations is uniform and that we

are not seeing regions with markedly different levels of activity. It is also evident from the micrograph, that our reagents were able to diffuse to all parts of the tissue under our experimental conditions. This technique is an improvement of the original developed by Nakatsu (2) for light microscopy, the advantage being increased resolution of the localization of the catalytic activity.

1. K.L. Bielat and G. Tritsch, *Molecular and Cellular Biochemistry* (1989) 86:135-142.
2. K. Nakatsu, *Journal of Histochemistry and Cytochemistry* (1975) 23:194-199.

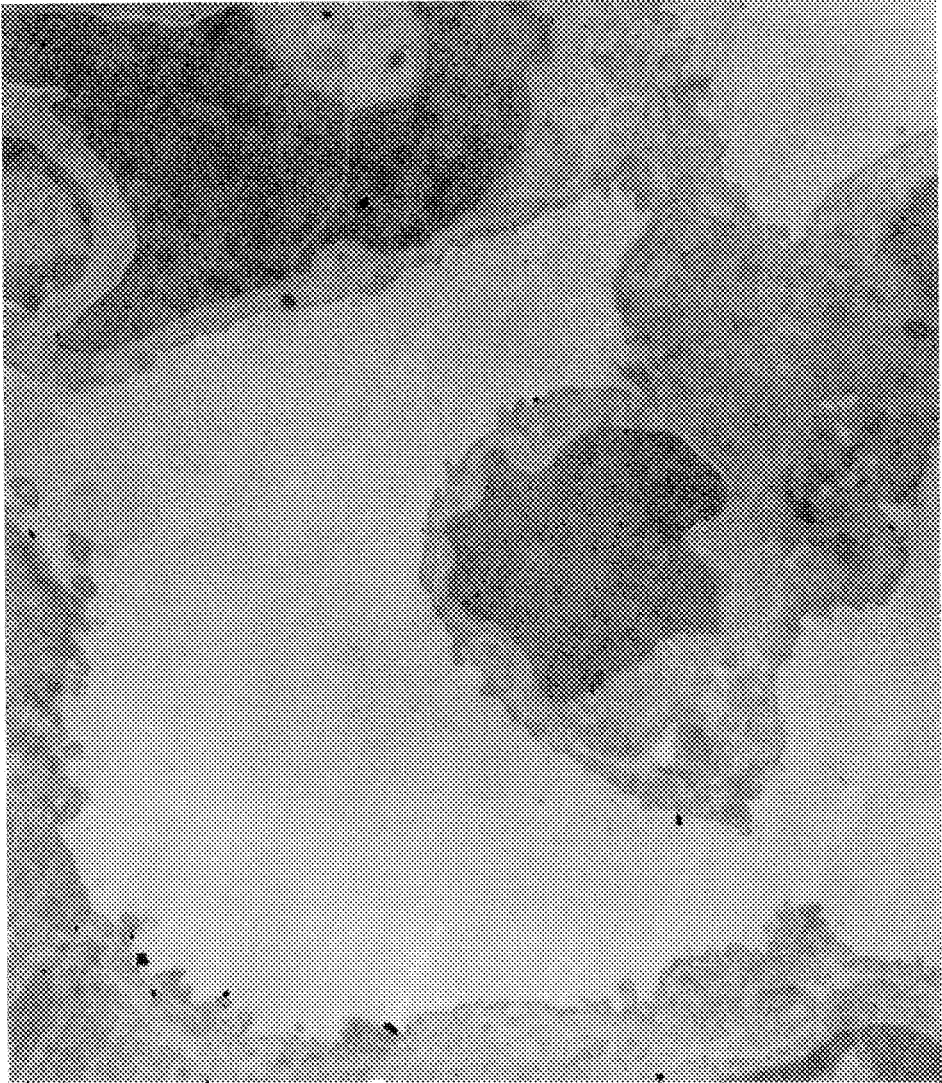


Figure 1: An unstained section of murine lung with electron dense silver grains of relatively uniform size visible within the cytoplasm of the erythrocytes. Several loci of high enzymatic activity are seen at the alveolar surface. Original magnification - 6000X.

ROLE OF PKC ISOZYME III (α) IN WATER TRANSPORT IN AMPHIBIAN URINARY BLADDER

A.J. Mia^{*}, L.X. Oakford^{**}, P.D. Thompson^{*}, Z.H. Ning^{*}, and T. Yorio^{**}

^{*}Division of Science and Mathematics, Jarvis Christian College, Hawkins, TX 75765

^{**}Departments of Anatomy and Pharmacology, TX Col. of Osteop. Med., Ft. Worth, TX 76107-2690

Vasopressin stimulated water flow across renal epithelia is thought to occur through a V₂ receptor coupled to adenylyclase. The increase in water flow occurs as a result of a fusion of water channels with the apical membrane and is indicative of an increase in membrane capacitance following hormone addition.

What controls the cycling of water channels and their insertion into the membrane is uncertain. Our laboratory has demonstrated that renal epithelia as well as amphibian urinary bladder membranes, contain a vasopressin V₁ receptor which upon activation results in the breakdown of phosphoinositide and the formation of inositol triphosphate and diacylglycerol, the latter an activator of protein kinase C (PKC). The initiation of transepithelial water flow also appears to involve V₁ receptors and possibly activation of PKC. To test this hypothesis, we have been using activators of PKC, such as phorbol esters and mezerein, as pharmacological tools to determine if PKC activation results in similar physiological responses as the hormone (1). Several PKC isozymes, upon activation, are known to be translocated to the apical membrane as visualized by FITC immunofluorescence (2,3). Previously, we reported co-localization of PKC subtypes I (γ) and II (β) in toad urinary bladders using monoclonal antibodies and protein A-gold probes (4). This report includes the localization of PKC subtype III (α) and its distribution pattern using immunogold labeling.

Toad urinary bladders excised from doubly pithed toads, *Bufo marinus*, were set up as sacs. An osmotic gradient was established and ADH 10mU/ml was added to the serosal side of the sacs while mezerein 10^{-6} M was added to the mucosal side. Tissues incubated for 60 min, received fixation in 2% glutaraldehyde in PIPES buffer (0.02M) for 1 hr and processed according to procedures described previously (4,5). Immunogold labeling was carried out using monoclonal antibodies for the PKC subtype III similar to procedures described previously (4,5). Air dried grids were stained with uranyl acetate and lead citrate prior to TEM studies.

Figure 1 illustrates the distribution pattern of PKC isozyme III in the cytosol of the granular epithelial cells following stimulation with mezerein for 60 min. Protein A-gold particles were found to be distributed singularly and in dense isolated clusters. Tissues challenged with ADH for 60 min under identical experimental conditions, show a similar distribution of clustered gold particles over these isolated dense bodies (Fig. 2) as well as on the apical membrane domain (Fig.3) and may appear exterior to the apical plasma membrane possibly due to exocytosis (Fig. 4). Many of these dense bodies labeled with the gold particles were observed to be in direct contact with the microfilaments (Fig.1, arrows). However, control tissues also show localization of clustered gold particles over isolated dense bodies (Fig. 5). These observations suggest that perhaps PKC type III is localized in the cytosol prior to its translocation to the apical membrane. Control tissues, lacking antibodies, but exposed to 0.1% BSA and monodispersed protein G-gold probes, showed no binding of gold particles (Fig. 6). Expression of the protein A-gold particles over the cytosol as well as over the membrane domains indicated possible translocation of PKC type III to the apical membrane following hormone activation.

References

1. T. Yorio and N. Satumtira, Biol. Cell (1989) 66, 7-12.
2. T. Ito et al., J. Cell Biol. (1988) 107, 929-937.
3. D. Mochly-Rosen et al., Cell Regulation (1990) 1, 693-706.
4. A. J. Mia et al., Proc. EMSA (1991) 302-303.
5. A. J. Mia et al., Tissue and Cell (1991) 23, 161-171.
6. This work was supported by NHLBI and DAMD 17-91-C-1096 grants (AJM/TY).

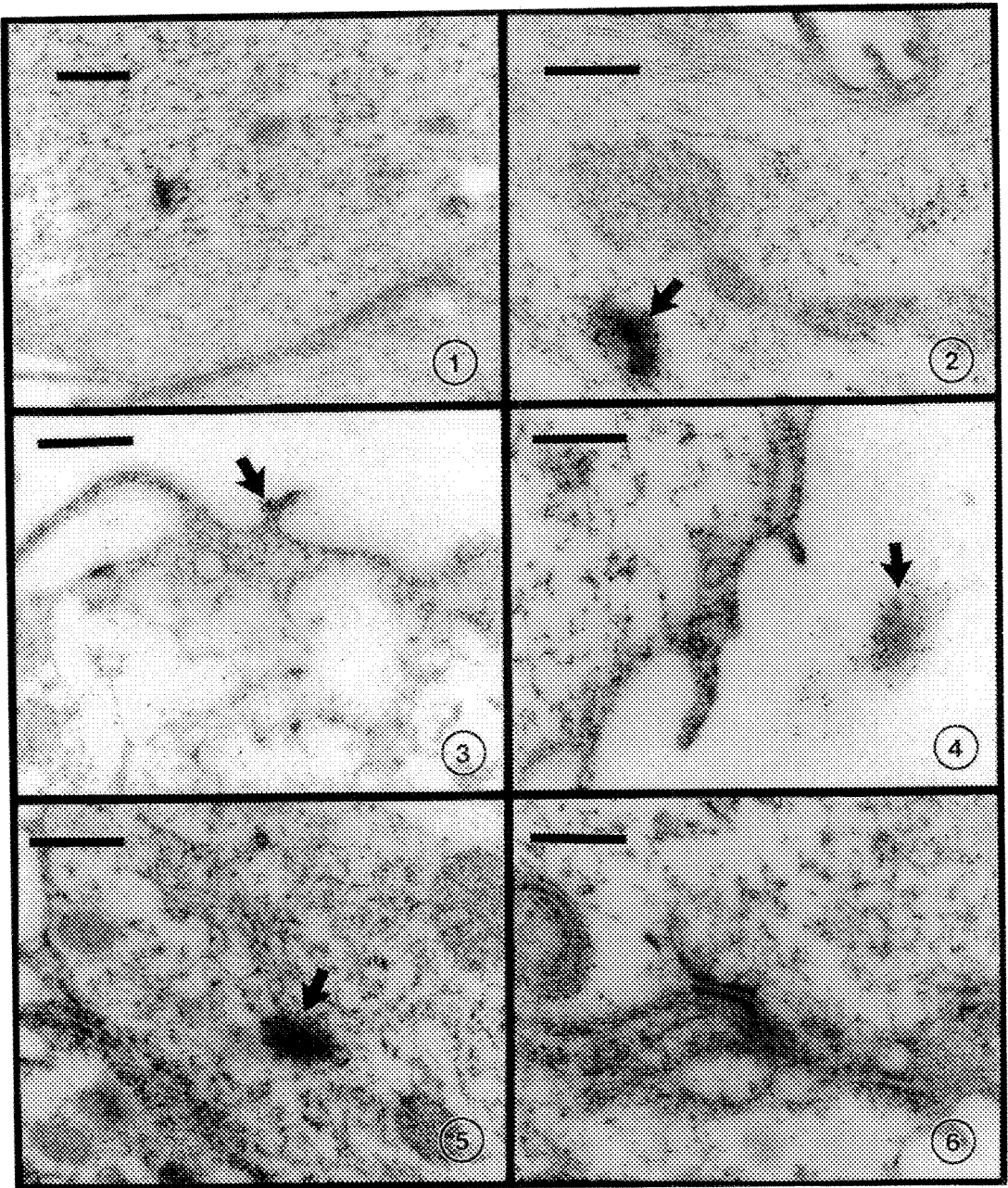


Fig.1. Localization of PKC subtype III in MZ-treated tissue showing distribution of protein A-gold particles (10nm) in the cytoplasm and on a discrete cytoplasmic dense body. Bar = 1000nm.

Fig.2. Localization of PKC subtype III in a diffused cytoplasmic body in ADH-stimulated tissue (arrow). Bar = 500nm.

Fig.3. Localization of PKC subtype III in the microvilli of MZ-stimulated tissue (arrow). Bar = 500nm.

Fig.4. Localization of PKC isozyme III in the diffused body exterior to the apical plasma membrane (arrow). Bar = 500nm.

Fig.5. Localization of PKC isozyme III in control tissue (arrow). Bar = 500nm.

Fig.6. Control tissue exposed to 0.1% BSA and protein A-gold probes showing no gold localization. Bar = 500nm.

IMMUNOHISTOCHEMICAL LOCALIZATION OF GENE EXPRESSION IN *ONCHOCERCA VOLVULUS* USING LATEX SPHERES AS AN SEM MARKER

David Kreitzer*, Rocky S. Tuan* **,Kenneth J. Shipley*

* Department of Orthopaedic Surgery, **Biochemistry and Molecular Biology, Thomas Jefferson University, Philadelphia, Pa.

Onchocerca volvulus, the filarial parasite responsible for river blindness, is being studied for identification of sera reactive antigens. In an attempt to localize these reactive antigens, scanning electron microscopy is being utilized as a correlative technique with light microscopic observations.

Worm material is obtained by nodulectomy. The nodules were fixed in a modified Carnoy's fixative, dehydrated through graded ethanol and embedded in paraplast. Sections were cut at 8µm, mounted onto glass slides and baked to dryness. Prior to immunohistochemical treatment, sections were deparaffinized with histoclear and xylene, and rehydrated through graded ethanols to water.¹

Rehydrated sections were rinsed with PBS and then reacted with primary antibodies derived from antisera raised against a recombinant fusion protein derived from a cloned antigen of *O. volvulus*. The plasmid source of this antigen was derived from genomic screening of the *O. volvulus* cDNA library with antisera derived from onchocerciasis patients or from infected, nonpermissive hosts. Protein A with attached 1µm diameter latex spheres was then reacted with the tissue. Sections with no primary antibodies were utilized as controls.¹ Following immunohistochemical treatment, slides were dehydrated through graded ethanols and critical point dried. Tissue sections were mounted onto aluminum stubs, sputter coated with gold, and viewed in a JOEL 35-C utilizing the SEI mode.

Figure 1 shows a low power view of a nodule, where profiles of male and female worms are seen. Figure 2 shows a higher power of a female worm with a five times enlargement of an area of nodule tissue showing microfilariae which have been released from the adult female worm. Figure 3 is a control showing a portion of adult female worm containing microfilariae with few beads. Figures 4-6 show views of female worm body walls and microfilariae labeled with beads.²

References

1. R. Tuan et al., Molecular and Biochemical Parasitology. (1991) 49, 191.
2. This work is supported in part by research grants from the Edna McConnell Clark Foundation and the National Institutes of Health (HD 15822 and HD 21355).

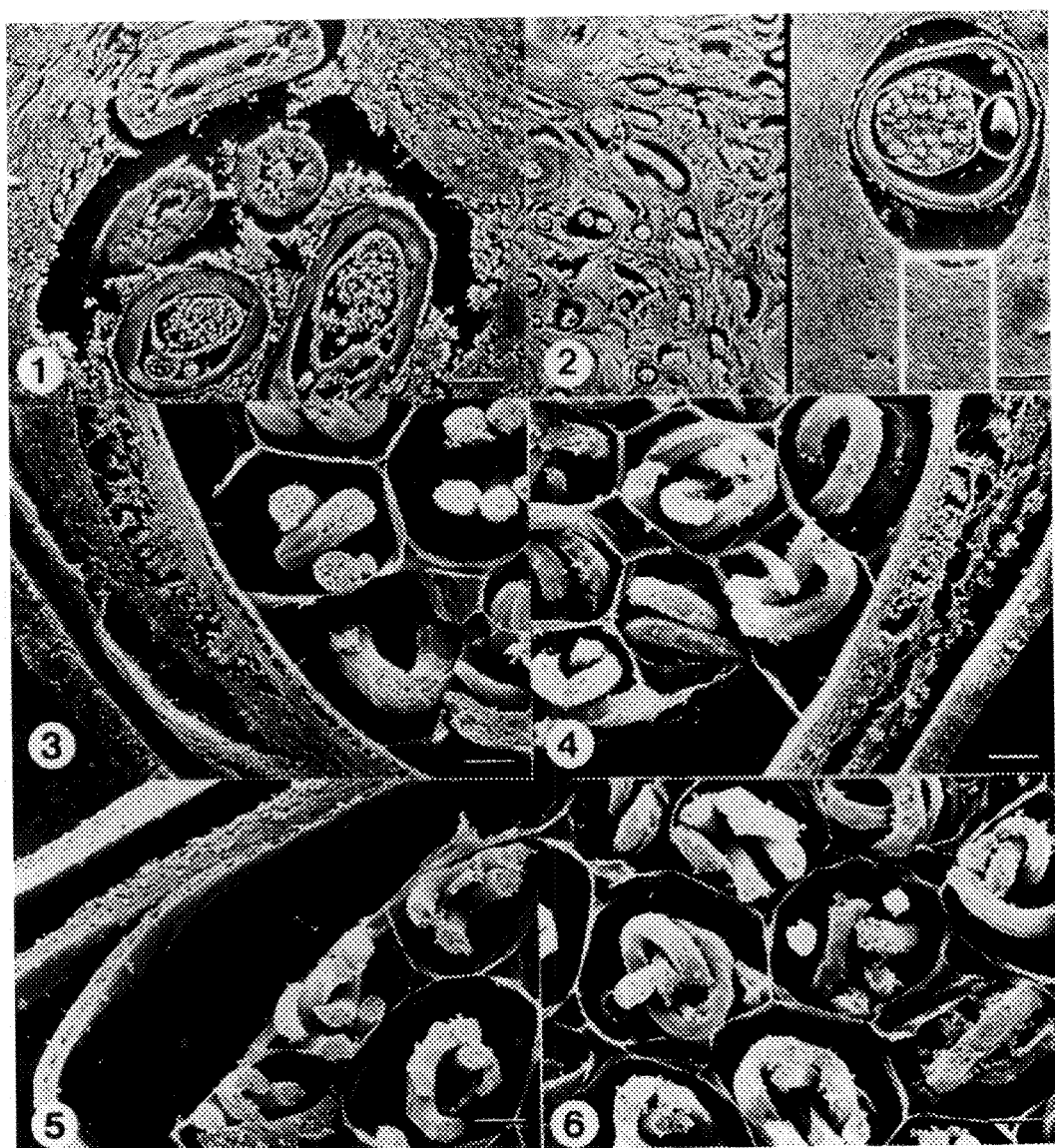


FIG. 1.--Low power view of nodule, showing cross sections of male (open arrows) and female (closed arrows) worms. Bar = 100um.
 FIG. 2.--Cross section of female worm and surrounding nodule tissue, showing microfilariae in nodule. Bar = 100um with 5X enlargement of insert.
 FIG. 3.--Immunohistochemical control section, showing body wall of female worm and microfilariae devoid of beads. Bar = 10um.
 FIGS. 4,5,6.--Views of bead labeled antigens of female worms and microfilariae from immunohistochemical positive sections. Bar = 10um.

CYTOCHEMICAL DETECTION OF GENE EXPRESSION: LIGHT AND ELECTRON MICROSCOPE EVALUATION OF BACTERIAL β -GALACTOSIDASE REACTION PRODUCT

Hsiao-Sheng Liu*; Emma Lou Cardell**; Peter Stambrook**; and Robert R. Cardell**

*National Cheng Kung University, Tainan Taiwan; and **University of Cincinnati, Cincinnati, OH 45267

Recombinant DNA technology allows the introduction of genes into the genome of cells *in vitro* and *in vivo*. "Reporter" genes cotransfected with other genes of interest indicate successful transfection because cellular expression can be detected by histochemistry, autoradiography, or *in situ* hybridization histochemistry (1,4,5). The *Escherichia coli* gene, *lacZ*, is a frequently used reporter gene because it does not affect the usual functions or activities of the cell; the gene is present and expressed in successive generations; and bacterial β -galactosidase (β -gal), the enzyme produced as a result of expression of the gene, can be detected cytochemically (1,4,5). Studies that evaluate transfected cells among mixed cell populations *in vivo*, e.g. gene therapy and cell lineage studies, can benefit from the detectability of the cytochemical reaction product at the light and electron microscope levels (2). After incubation at pH 7.4 in X-gal (5-bromo-4-chloro-3-indolyl- β -D-galactoside), a commercially available indigogenic substrate, a blue-green reaction product results in cells that have synthesized functional bacterial β -galactosidase enzyme. This reaction product is visible in intact cells, and is retained during processing and embedment for thin section analysis in the transmission electron microscope. This report demonstrates the value of *lacZ* as a reporter gene using a clone of transfected HTD114 cells of human fibrosarcoma origin, selected for their high *lacZ* expression. Figure 1 is a dark field image of reaction product in 1 μ m thick epon sections of cells that were incubated in X-gal, fixed, pelleted, osmicated, dehydrated, and embedded by routine methods (3). Figure 2 shows the appearance of the reaction product at the ultrastructural level. At both LM and EM levels, the reaction product varies in quantity among cells; appears focally concentrated in some cells, diffuse in others; and is confined to the cytosome with a noticeable ring-like distribution around the nucleus in yet other cells. Dark field analysis of sections is especially helpful for detecting relatively low quantities of reaction product. The distinctive ultrastructural appearance of the reaction product allows the unequivocal identification of cells expressing *lacZ* as well as the ultrastructural features of the cells. Ultrastructural characterization of the cell is often important for precise identification of cell type, especially in tissues such as lung in which there are many different cell types.

References

1. Z. Lojda, *Histochemie* 23 (1970), 266.
2. T. Mikawa, A. Borisov, A.M.C. Brown and D.A. Fishman, *Dev. Dynamics* 193 (1992), 11.
3. J.L. Parkes, E.L. Cardell, G. Grieninger and R.R. Cardell, *Anat. Rec.* 227 (1990), 321.
4. B. Pearson, P.L. Wolf and J. Vasquez, *Lab. Invest.* 12 (1963), 1249.
5. J.R. Sanes, J.L.R. Rubenstein and J.F. Nicolas, *EMBO J.* 5(12) (1986) 3133.
6. This work was supported by Grant DK 27097 from NIH.

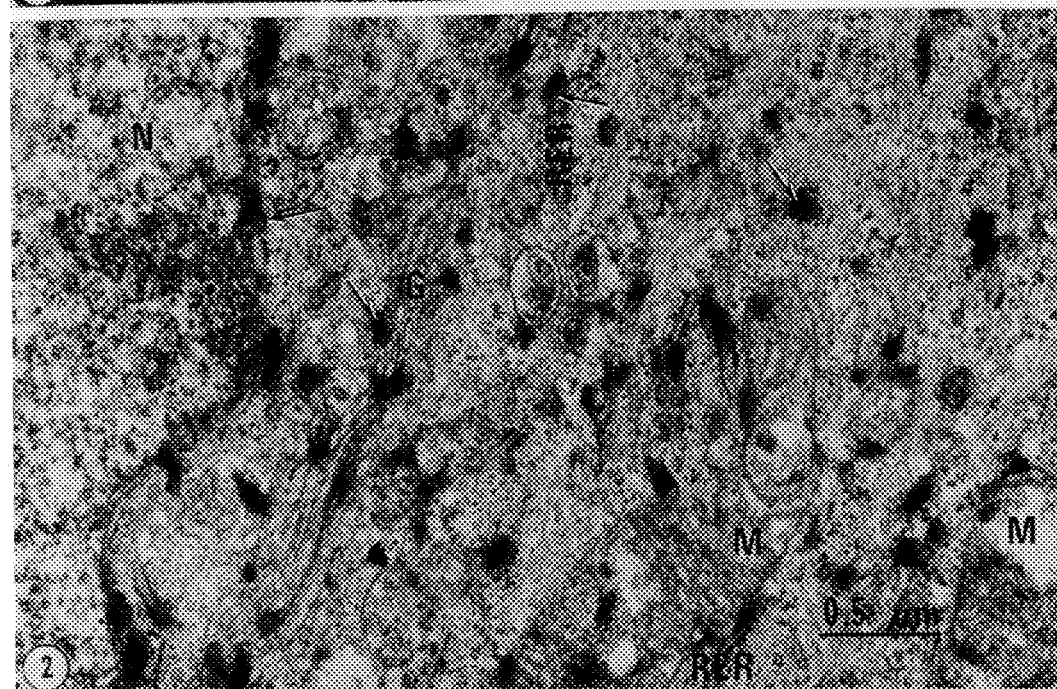
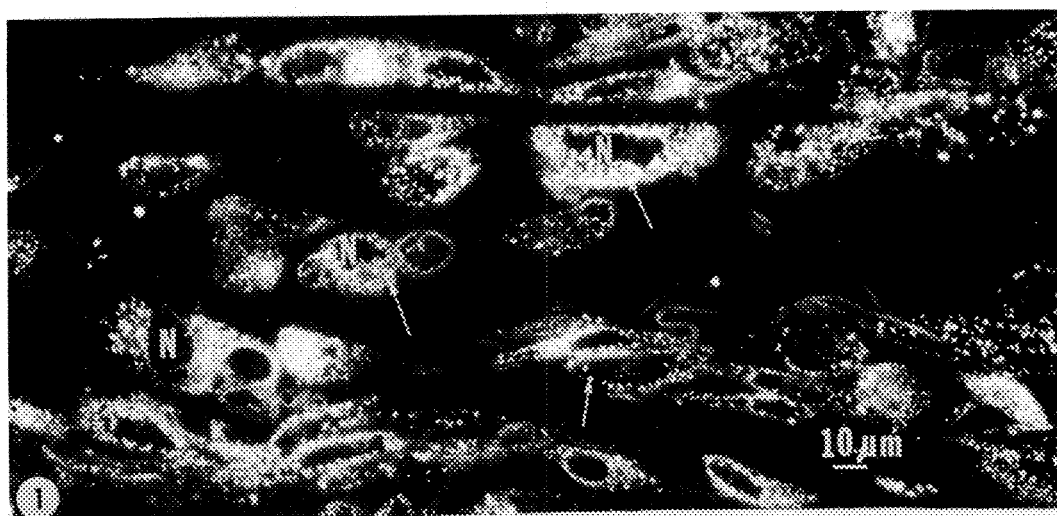


Figure 1. Dark field image of β -galactosidase reaction product in cultured cells. Note variation in content of reaction product among cells. Reaction product not present in nucleus. (Nucleus, N; Reaction Product, arrow)

Figure 2. Electron micrograph showing typical electron dense reaction product in cytosome of cell. No reaction product is in the nucleus, but frequently is associated with membranes in cytosome. (Nucleus, N; Reaction Product, arrows; Mitochondrion, M; Golgi Apparatus, G; Rough Endoplasmic Reticulum, RER)

IN SITU HYBRIDIZATION DETECTION OF GENE EXPRESSION FOR HEPATIC METABOLIC ENZYMES

Robert R. Cardell, Betty B. Davis, and Richard L. Drake

Dept of Anatomy & Cell Biology, Univ of Cincinnati College of Medicine, Cincinnati, OH 45267

Key enzymes involved in gluconeogenesis and glycolysis are uniquely distributed within the liver lobule as shown, for example, by periportal hepatocytes having higher activities and quantities of the former and pericentral cells having higher activities and quantities of the latter enzymes. In this report we describe changes in the patterns of mRNA for a key gluconeogenic enzyme, phosphoenolpyruvate carboxykinase (PEPCK), in normal rats and diabetic rats with/without insulin treatment.

A 1.0 kb cDNA for rat PEPCK was subcloned into pGEM-3Z. ³²P-labeled antisense and sense (control) RNA probes were produced and used for Northern blot analysis which showed that the antisense probe recognized a 2.8 kb mRNA in rat liver which corresponds to the PEPCK mRNA.¹ The sense probe showed no affinity for mRNA from rat liver, lung or colon. ³⁵S-labeled antisense and sense RNA probes were prepared for *in situ* hybridization.² These were degraded to an average length of 100-200 bases by alkaline hydrolysis. Six to 10 μ m paraffin and frozen sections of rat liver were mounted on Tespa treated slides and were post-fixed in 4% paraformaldehyde in PBS for 20 min, treated with 20 μ g/ml proteinase K, and further fixed in 4% paraformaldehyde. The sections were treated with acetic anhydride, dehydrated and air dried prior to hybridization. The ³⁵S-UTP labeled RNA probes were dissolved at a final concentration of 1.0×10^5 cpm/ μ l in a hybridization solution with 50% formamide and used to hybridize each section at 55°C overnight under glass coverslips. The slides were washed at a high stringency and treated with RNase A. After rinsing, the slides were dehydrated and air dried before autoradiography using Ilford K5 nuclear track emulsion.³ Some sections were stained in 0.02% toluidine blue and others were mounted unstained for image analysis.

PEPCK mRNA in normal rats is greatest in the periportal region of the hepatic lobule and decreases across the lobule to a lower amount in the pericentral region (Fig. 1). Specific grain counts indicated higher numbers of silver grains per 1000 μ m² of cytoplasm in periportal and midlobular hepatocytes than in cells concentric to a central vein especially those in the first cell layer. Few silver grains are found over sections hybridized to the sense (control probe). Diabetes causes a substantial increase in the density of silver grains over all regions of the liver lobule, thus a periportal to pericentral gradient is still apparent (Fig. 2). In addition, specific grain counts indicate the amount of PEPCK mRNA in the pericentral region of the liver lobule in diabetic rats has increased substantially and is now at a level similar to the amount of message localized in the periportal region of the liver lobule in normal rats. Insulin treatment of diabetic animals causes the lobular distribution of PEPCK mRNA to resemble the normal periportal pattern. These results clearly demonstrate that lobular gene expression is a dynamic process which changes in response to the physiological status of the animal.

References

1. H. Yoo-Warren, *et al.*, Proc. Natl. Acad. Sci. 80 (1983) 3656.
2. D. Melton, *et al.*, Nucl. Acids Res. 12 (1984) 7035.
3. D.G. Wilkinson, *et al.*, Cell 50 (1987) 79.
4. Supported in part by NIH Grant DK-27097.

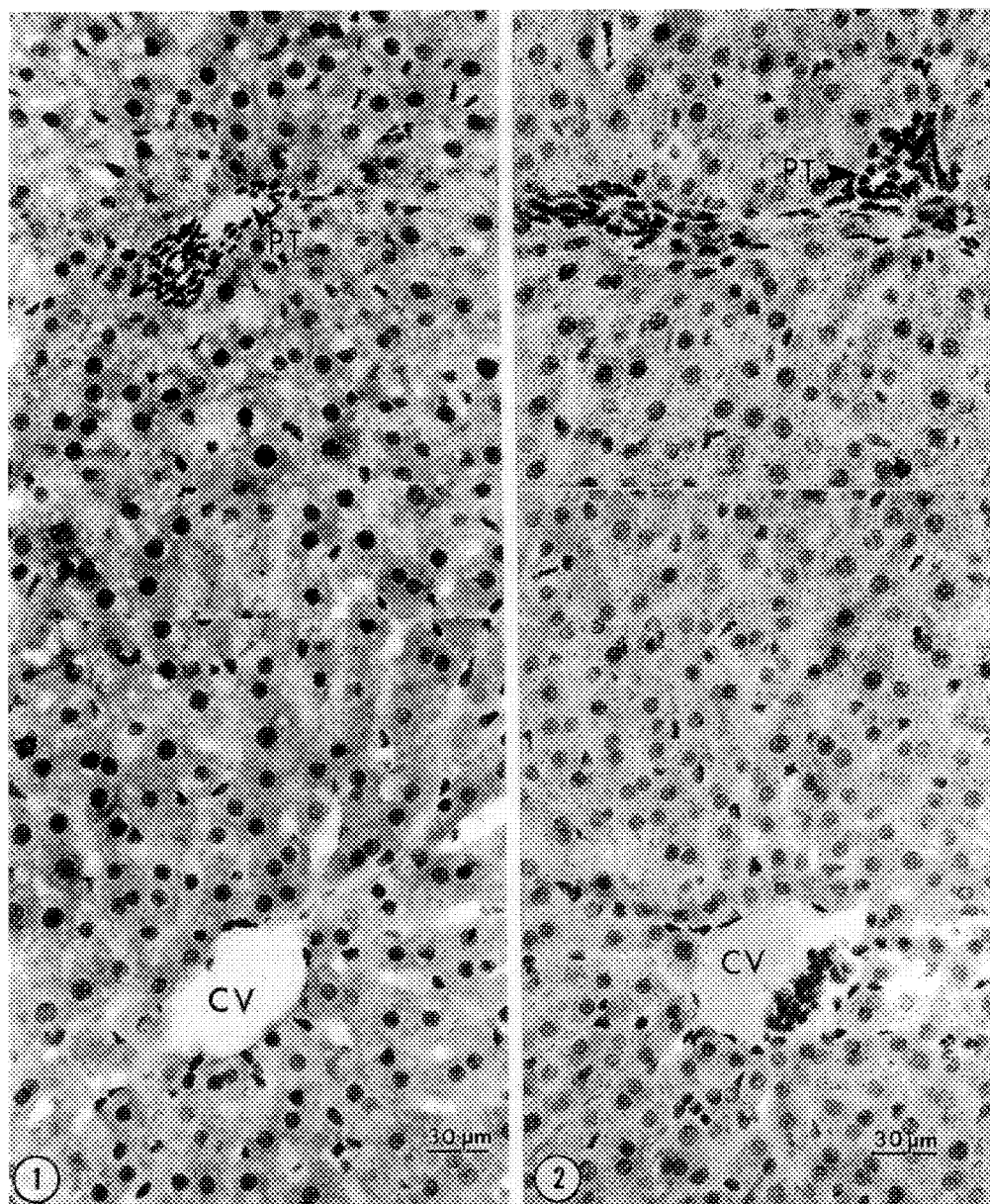


Figure 1. PCK antisense RNA probe hybridization to PEPCK mRNA in a frozen section of normal rat liver. Silver grain density indicates the level of mRNA is higher around the portal tract (PT) than the central vein (CV) with intermediate levels in the midlobular region.

Figure 2. PCK antisense RNA probe hybridized to PEPCK mRNA in a frozen section of diabetic rat liver. Silver grain density indicates the elevated concentration of PEPCK mRNA in all regions of the liver lobule with a gradient similar to normal tissue, more mRNA around the portal tract (PT) than the central vein (CV).

CYTOCHEMICAL LOCALIZATION OF GLYCOGEN SYNTHASE ACTIVITY IN RAT LIVER

John E. Michaels and Robert R. Cardell

Dept. of Anatomy and Cell Biology, Univ. of Cincinnati College of Medicine, Cincinnati, OH 45267-0521

Glycogen synthase (GS) is the rate limiting enzyme for liver glycogen synthesis and its activity varies with the phosphorylation state of the enzyme.^{1,2} The current study focused on changes in the intralobular patterns of distribution of cytochemically localized GS activity during glycogen synthesis.

Normal and adrenalectomized (ADX) rats were fasted overnight to reduce liver glycogen to minimal levels. Fasted ADX rats received 2 mg dexamethasone (DEX) 0-8 h prior to sacrifice to stimulate glycogen synthesis. Liver was removed, rapidly frozen in isopentane cooled in liquid nitrogen, then cryostat sectioned. GS activity was localized histochemically by 3 h incubation in medium containing both UDP-glucose and glucose 6-phosphate. Glycogen was formed as reaction product.^{3,4} Control incubations omitted the substrate. Two stains were used to identify glycogen: 1) iodine staining of the incubated sections was rather specific for the newly formed glycogen (Figs. 1-6), whereas 2) periodic acid-Schiff (PAS) stained both native and nascent glycogen.

GS activity was slight and variable in fasted normal rats (Fig. 1). In contrast the sections from fasted ADX rats (Fig. 2) showed discrete localization of GS activity as large aggregates of glycogen in random cells. After 2 h DEX treatment GS activity increased slightly ranging from highly concentrated to dispersed in some hepatocytes, whereas others showed none.

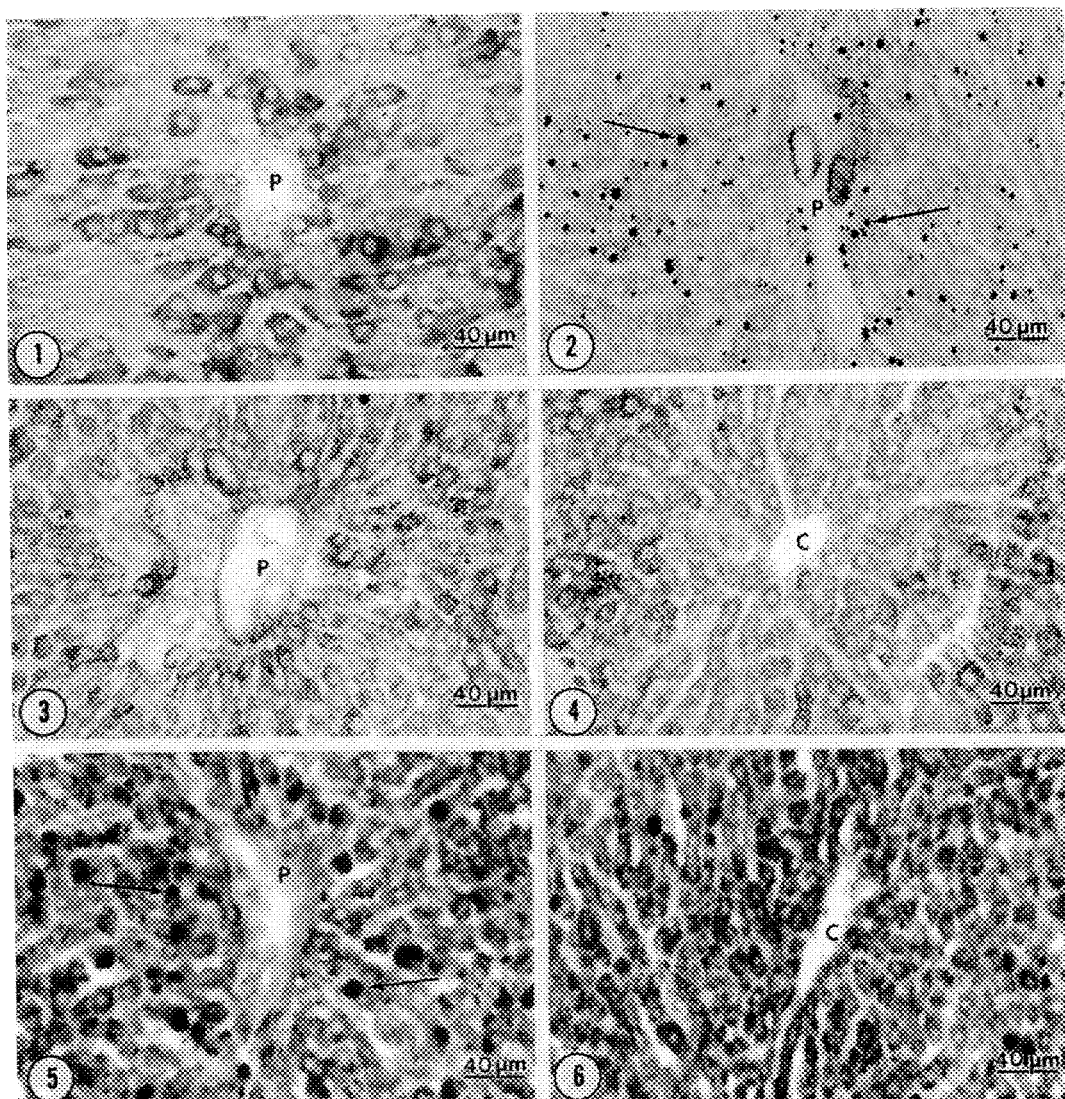
After 4 h DEX treatment (Figs. 3 and 4), incubated sections stained with iodine showed GS activity noticeably concentrated in periportal hepatocytes (Fig. 3). However, activity in individual hepatocytes was variable throughout the lobule. Some hepatocytes displayed abundant reaction product and adjacent cells contained little or no activity.

After 8 h DEX treatment (Figs. 5 and 6) GS activity was more evident throughout the lobules. Most, if not all, hepatocytes demonstrated substantial GS activity, but with wide variation between adjacent cells. Concentration of reaction product in periportal and centrilobular regions was similar, but reaction product tended to be more aggregated periportally (Fig. 5) and dispersed in the centrilobular region (Fig. 6).

The results illustrate that during stimulation of glycogen synthesis GS activity does not occur uniformly in hepatocytes throughout the liver lobule. Initially, activity was restricted to a few random hepatocytes. Hepatocytes demonstrating GS activity increased with time of DEX treatment. Although activity became concentrated periportally at 4 h DEX treatment, the random distribution of cells showing activity persisted with cells showing no activity adjacent to cells with high activity. The variation in GS activity in adjacent hepatocytes suggests that these cells may be in a different physiological state and less responsive to the conditions of incubation. The distribution of GS activity during stimulation of glycogen synthesis was similar to observations made employing the same model, but observing the distribution of silver grains in radioautographs of liver sections from rats injected with tritiated glycogen precursors.^{5,6}

References

1. D.L. Friedman and J. Larner, *Biochemistry* 2 (1963) 669.
2. F.Q. Nuttall *et al.*, *Amer. J. Med (suppl.)* 85 (1988) 77.
3. J.-P. Denizot, *Histochem.* 55 (1978) 117.
4. A.A. Smith, *J. Histochem. Cytochem.* 18 (1970) 756.
5. J.E. Michaels *et al.*, *Amer. J. Anat.* 170 (1984) 23.
6. Supported by NIH Grant #DK27097.



All figures from cryostat sections incubated 3 h, iodine stained to show GS activity (new glycogen) and except for Fig. 1 counterstained with light green.

Fig. 1. Periportal (P) region from fasted normal rat shows little GS activity.

Fig. 2. Periportal (P) region from fasted ADX rats shows GS activity as aggregated glycogen (arrows).

Figs. 3 and 4. Periportal (P) and centrilobular (C) regions from fasted ADX rat after 4 h DEX. GS activity appears more concentrated periportal, wide range of activities is evident.

Figs. 5 and 6. Periportal (P) and centrilobular (C) regions from fasted ADX rat after 8 h DEX. Most cells show GS activity that is more clumped (arrows) periportal and more dispersed near central vein.

ACETYLCHOLINESTERASE (AChE) DEMONSTRATED BY A VASCULAR PERFUSION INCUBATION TECHNIQUE

Zhongrong Luo, Ernest F. Whitter, Panya S. Manoonkitiwongsa, and Robert L. Schultz

Department of Anatomy, School of Medicine, Loma Linda University, California 92350

For the cytochemical demonstration of enzymes, the commonly employed procedures involve using chopped small cubes or sections of tissue incubated in a proper medium. With the chopped tissue, penetration of substrate and capturing agents is very slow. When using frozen sections artifacts are difficult to avoid. Also proper vibratome sections are hard to achieve with small organs such as the pineal gland. In order to overcome these disadvantages, we have developed a vascular perfusion incubation technique for the demonstration of AChE.

With this technique, a simple gravity flow apparatus for vascular perfusion with two glass containers for fixative and Tyrode solution was used. A needle (19g) with a 32 cm long vinyl tube was connected to the apparatus by a three-way valve. Adult Djungarian hamsters were anesthetized with 1.5 g/kg urethane. The needle was inserted into the ascending aorta through the left ventricle. The following solutions were then perfused for the times indicated: Tyrode, 1 min; fixative (1% purified glutaraldehyde and 2% formaldehyde, 0.05 M cacodylate buffer, pH 7.2), 5 min; Tyrode, 10 min; substrate-free incubation medium, 10 min; complete incubation medium, 20 min; pause for 10 min; repeat of the last two steps four times; isotonic sodium sulphate, 10 min; buffered sulphide, 30 min; isotonic sodium sulphate, 10 min; fixative (3% glutaraldehyde and 2% formaldehyde, 0.05 M cacodylate buffer), 5 min. The entire pineal gland and pieces of the tongue were taken. After osmium postfixation standard electron microscopic procedures were used.

The simplified copper-thiocholine method¹ was used and two modifications were made to prepare the incubation medium for AChE. First, instead of 75 mg acetylthiocholine iodide in 20 ml of medium, 15 mg was used in this technique. Second, in order to increase the permeability of cell and organelle membranes, 0.3% Triton X-100 was added in the pre- and complete incubation media.

As shown in figure 1, AChE activity was localized in the perinuclear cistern and cisternae of the ER. These findings are similar to those observed in guinea pig pineal gland², which was incubated by conventional methods. The AChE activity was also found in motor end plates, and axolemma of myelinated nerve fibers (Fig. 2). An important advantage of this technique is the even distribution of reaction product that is achieved. Also, one may survey the AChE activity in the entire animal.

References: 1. P.R. Lewis and D.P. Knight, North-Holland Publishing Company, Amsterdam. New York. Oxford (1977), 209

2. Z. Luo, R. L. Schultz, and E. F. Whitter, Anat. Rec. (1990),226:481-488

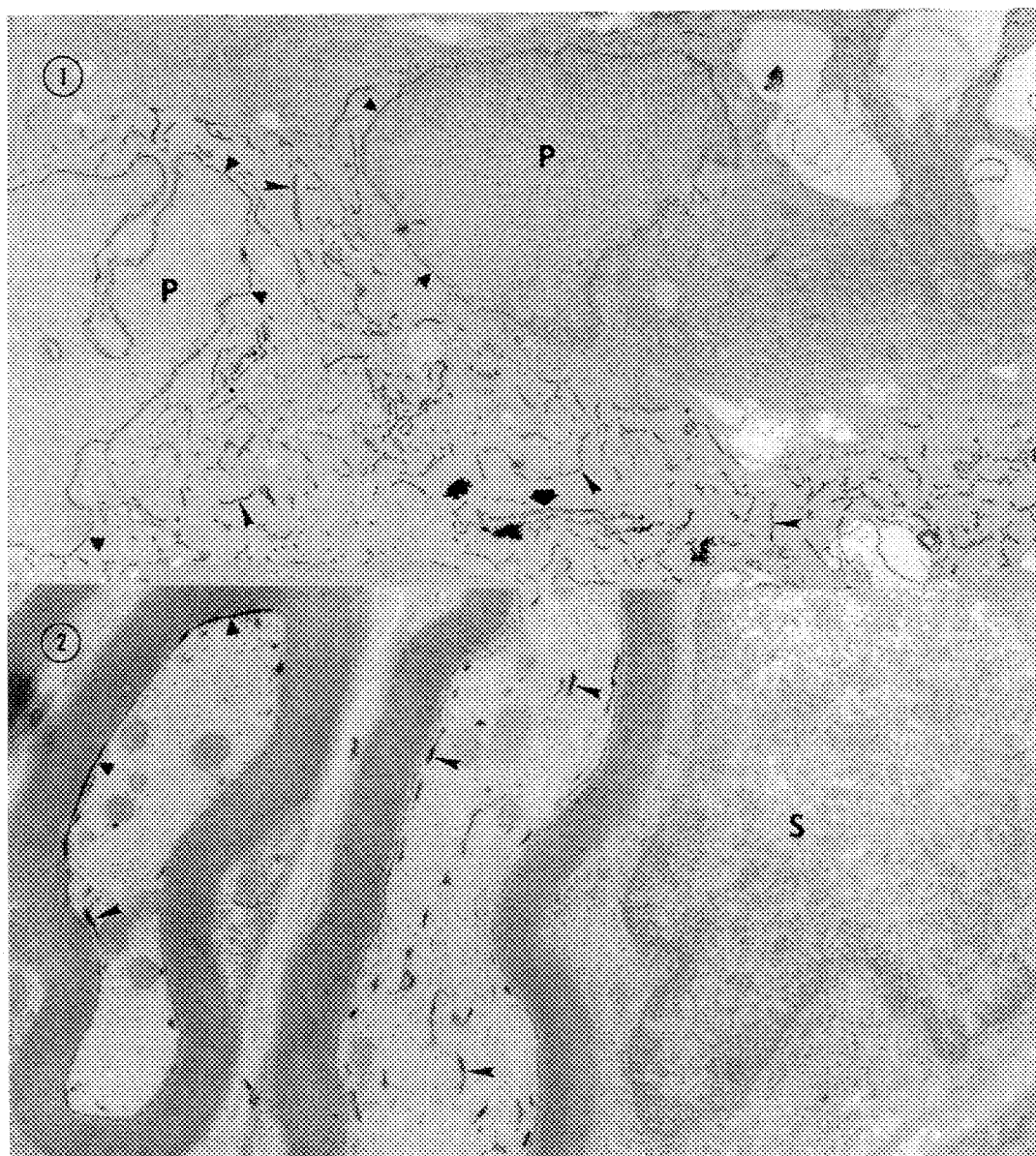


Fig. 1. This micrograph shows AChE positive pinealocytes (P) in a hamster pineal gland. The reaction product is seen in the perinuclear cistern (triangles), the cisternae of ER (arrowheads), and in a saccule of Golgi apparatus (arrows). X13,000.

Fig. 2. The AChE activity is shown in the axolemma (triangles) and the cisternae of smooth ER (arrowheads) in myelinated nerve fibers in hamster tongue. A part of a Schwann cell (S) can be seen at the right of the nerve fibers. X25,000.

LOCALIZATION OF HYDROGEN PEROXIDE AND SERUM ALBUMIN IN EXPERIMENTAL OPTIC NEURITIS: COMBINED CYTOCHEMISTRY AND IMMUNOCYTOCHEMISTRY

E. Ann Ellis and John R. Guy

Department of Ophthalmology, College of Medicine, University of Florida, Gainesville, FL 32610

The oxidant, hydrogen peroxide (H_2O_2), is discharged by inflammatory cells that infiltrate the central nervous system and has been shown to play a role in disruption of the blood-brain barrier (BBB) and demyelination in the optic neuritis of experimental allergic encephalomyelitis (EAE)¹, an animal model for multiple sclerosis (MS). Alterations in the BBB and vascular permeability in EAE have been studied with exogenous, injected tracers; but there have been no studies of native, endogenous proteins. In order to study the role of oxidants in vascular permeability in EAE, we localized H_2O_2 at the ultrastructural level followed by immunocytochemical localization of endogenous serum albumin in the optic nerves of guinea pigs sensitized to EAE.

Strain 13 guinea pigs, sensitized to EAE, were euthanized with sodium pentobarbital; the eyes and attached optic nerves were dissected out, fixed, reacted for H_2O_2 by a modified cerium-NADH oxidase method¹, and embedded in epoxy resin. Sections on nickel grids were oxidized for 30 min with 1% periodic acid followed by 5 X 5 min washes in deionized water. Grids were floated 2 X 5 min on 0.02 M phosphate buffered saline (PBS), pH 7.2, 0.1 M NaCl, 2% teleost gelatin, 2% nonfat dry milk, 0.05% Tween 20 and then reacted with rabbit anti-guinea pig serum albumin antibodies in the same buffer plus additives for 2 h at room temperature. After 2 X 5 min washes in PBS, 0.5 M NaCl plus additives, followed by 2 X 5 min washes in 0.02 M Tris-HCl buffered saline (TBS), 0.5 M NaCl, 2% teleost gelatin, 0.05% Tween 20, grids were reacted with 10 nm gold labeled goat anti-rabbit IgG antibodies for 1 h at room temperature. After 2 X 5 min washes in TBS plus additives, grids were washed 5 X 5 min in deionized water, then examined and photographed without poststaining at 75 kV. Control grids were incubated with PBS followed by the gold labeled antibody or with albumin antibody absorbed with guinea pig serum albumin.

Albumin localized within the lumen of vessels, in the basement membrane and into the extracellular matrix (Fig. 1). Albumin co-localized with H_2O_2 in and around some vessels in the meninges (Figs. 2, 3) and in perivascular and intercellular spaces in the optic nerve head (Figs. 4, 5). This combination of cytochemical localization followed by immunocytochemistry provides a method to study, simultaneously, the role of oxidants and endogenous proteins such as albumin or enzyme antioxidants in the pathogenesis of EAE.

References

1. J. Guy, E. A. Ellis, N. A. Rao, Arch Ophthalmol (1990) 108, 1614.
2. This research was supported by NIH Grant 5R01EY07982-02 and a departmental grant from Research to Prevent Blindness, New York, NY.

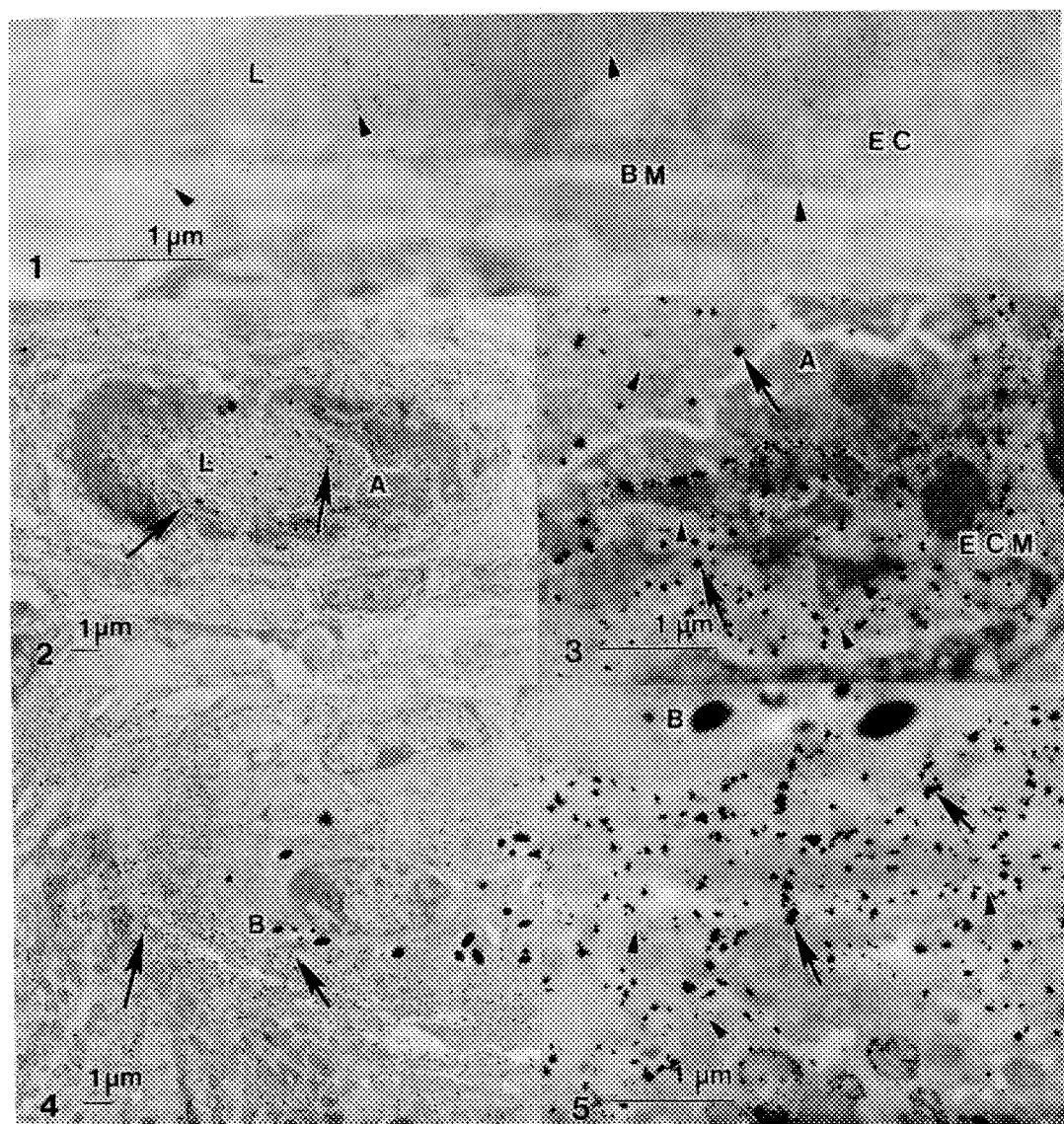


FIG. 1.--Gold labeled albumin (arrow heads) in a vessel in the myelinated retrobulbar optic nerve. Lumen (L); Basement Membrane (BM); Endothelial Cell (EC).

FIG. 2.-- H_2O_2 (arrows) in and around a vessel in the meninges. Note reference point (A) for Fig. 3.

FIG. 3.--Higher magnification of Fig. 2. Gold labeled albumin (arrow heads) and H_2O_2 (arrows) in lumen and extracellular matrix (ECM).

FIG. 4.-- H_2O_2 (arrows) in the optic nerve head. Note reference point (B) for Fig. 5.

FIG. 5.--Higher magnification of Fig. 4. H_2O_2 (arrows) and albumin (arrowheads) in intercellular spaces.

PLASMINOGEN ACTIVATOR INHIBITOR 1 (PAI-1): IMMUNOGOLD LOCALIZATION WITHIN PLATELET-FIBRIN THROMBI

J.C. Lewis, R.R. Hantgan, W.G. Jerome, K.G. Grant, *A. Dekker, *S. Handt, *C.J. Kirkpatrick

Depts. of Pathology and Biochemistry, Bowman Gray School of Medicine, Winston-Salem, NC 27157; and *Dept. of Pathology, Technical University of Aachen, D-5100 Aachen, Germany

Thrombosis, the major clinical sequelae to atherosclerosis, is complex and encompasses a multiplicity of interactions among plasma proteins, platelets and other blood cells, and vascular endothelial cells. Thrombolysis, in a fashion paralleling thrombus progression, is also influenced by a multiplicity of interactions, and recent evidence has suggested that both platelets and endothelial cells play a role in prolonging the lytic process. This prolongation is detrimental to prognosis following vascular occlusion. We have previously reported that thrombin-stimulated platelets will prolong clot lysis when included in an in-vitro assay comprised of tissue-type plasminogen activator, plasminogen, and fibrin(ogen).¹ This observation has been expanded in the present study to include TNF stimulated human umbilical vein endothelial cells, and our data document the association of platelet and EC derived PAI-1 with the fibrin network. HUVEC grown on carbon-stabilized, formvar-coated gold grids for whole mount IVEM were stimulated with tumor necrosis factor, prior to clot initiation and subsequent lysis, by addition to the cultures of fibrinogen, t-PA, plasminogen and thrombin-stimulated platelets. At selected times of lysis following polymerization, based upon laser light scattering kinetic studies, the samples were fixed and processed for PAI-1 localization using the immunogold technique.² When observed by SEM, the partially lysed thrombi consisted of an anastomosing fibrin network that extended from endothelial cell surfaces (Figure 1). Within the thrombus, the delicate, branching fibrin strands often were focused at points containing the activated platelets. The interaction of fibrin with endothelial cells was evidenced by IVEM as a delicate extracellular array extending between and among adjacent cells (Figure 2 a,b). Immunogold probes, documenting PAI-1, were distributed in clusters along the fibrin (Figures 1b,c). PAI-1, although cellular in origin, was not associated with the surfaces of either platelets or endothelial cells. The specificity of PAI-1 localization was verified through inclusion of a non-related immunogold probe which bound in substantially lower concentration and without site selectivity (Figure 2c). We conclude that HUVEC and platelets modulate thrombolysis through the release of PAI-1 which binds to fibrin and retards plasminogen activation.³

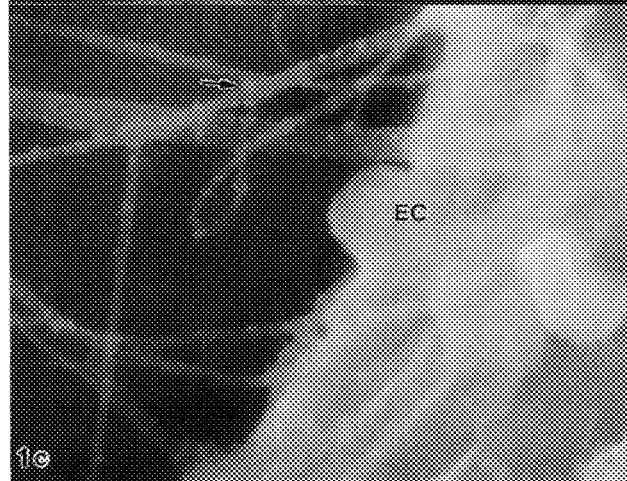
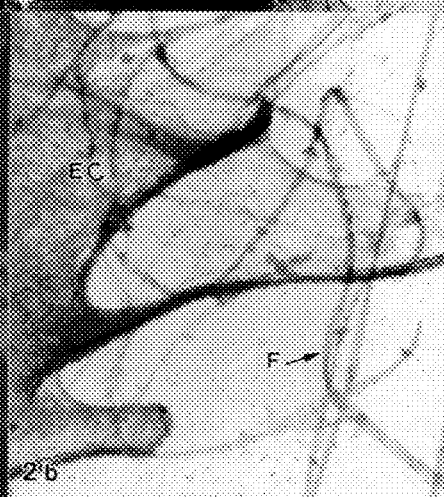
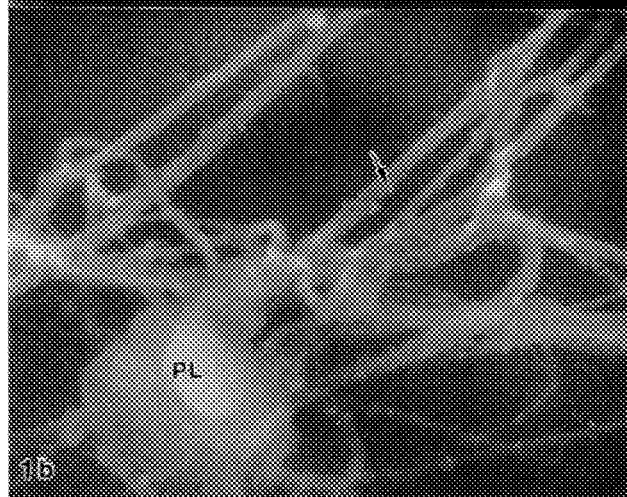
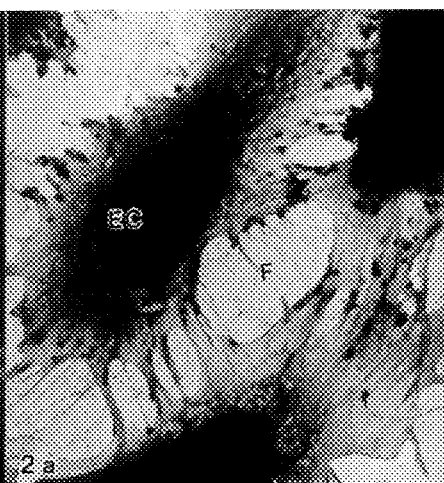
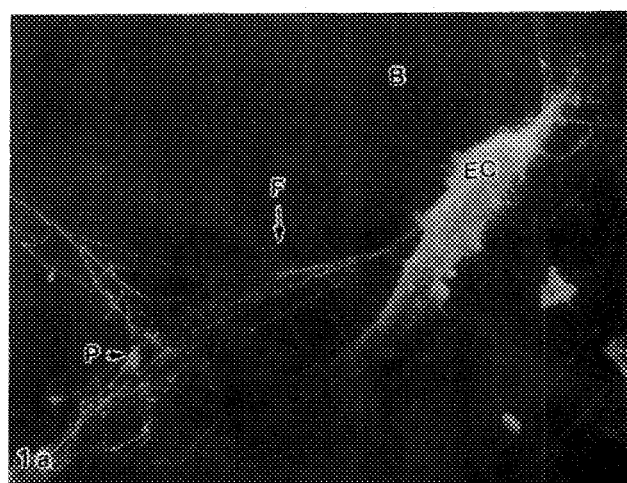
1. Hantgan, R.R. et al. (1991) *Thromb. Haemost.* 65:718.

2. Lewis, J.C. et al. (1990) *Am J Pathol* 136:239-252.

3. Supported by grants: NIH RR-02722, CA-12197; NCBST 90-IN-5; American Heart 900709.

FIG. 1.-- Scanning electron micrographs illustrating the distribution of PAI-1 within thrombi. 1a) Overview of thrombus showing an endothelial cell (EC) and fibrin network (F) containing a platelet (P). 1b,1c) PAI-1, within the thrombus was associated with fibrin strands (F) but was absent from either platelet (PL in b) or endothelial cell (EC in c) surfaces.

FIG 2.-- IVEM electron micrographs illustrating anti-PAI-1 localization. 2a) An overview showing portions of three endothelial cells (EC) and the delicate extracellular fibrin network (F). 2b). The immunogold probe was localized to the fibrin network and was absent from the adjacent endothelial cell surface (EC). 2c) When observed at higher magnification, the specific anti-PAI-1 immunogold (5 nM) was in high density along the fibrin fibers, whereas the 15 nM nonspecific probe was sparse and randomly located.



IMMUNOCYTOCHEMICAL LOCALIZATION OF NITROGEN OXIDE SYNTHASE, NADPH DIAPHORASE AND SOLUBLE GUANYLYL CYCLASE IN NEURONAL AND NON-NEURONAL TISSUES OF THE RAT

Gerard D. Gagne*, Harald H.H.W. Schmidt** and Mahlon F. Miller*

Department of Cellular and Microscopic Research* and Signal Transduction Group**,
Abbott Laboratories, Abbott Park, IL 60064

Nitric signal transduction involves two protein components, NO synthase (NOS) types I-III, which form nitrogen oxides (NO) from L-arginine and soluble guanylyl cyclase (GC-S), which is activated by NO and catalyzes the conversion of GTP to cyclic GMP.¹ A polyclonal antiserum (6761-8) to rat cerebellar type I NOS and a monoclonal antibody to rat lung GC-S (B4) were generated in order to localize both signal transduction proteins in various rat tissues. NOS was also visualized by its NADPH-diaphorase (NADPH-d) properties through NADPH-dependent nitroblue tetrazolium (NBT) formazan formation.

Tissues were excised from adult Wistar rats, frozen in hexane/dry ice and 8 μ m sections were cut with a cryomicrotome. The sections were thaw-mounted onto microscope slides and fixed by immersion in cold acetone. NOS-I and GC-S were visualized by indirect immunoperoxidase using antibodies 6761-8 and B4, respectively. The sections were incubated with the antisera (diluted in PBS containing 1% BSA) for 30 minutes at 37°C followed by peroxidase-conjugated antibody to rabbit IgG or mouse IgG. The peroxidase label was rendered visible using DAB and 0.005% H₂O₂ (pH 7.6). For histochemical staining of NADPH-d slides were immersed for 20-30 minutes at 37°C in 50 mM TBS (pH 8.0) containing 1mM NADPH, 0.5mM NBT and 0.2% Triton X-100.

In the CNS of the rat the majority of NOS-I immunoreactivity was located in the cerebellar cortex (Fig. 1 A,C), particularly in basket and granular cells which make contact with Purkinje cells. The Purkinje cells were not labeled by antibody to NOS-I but were stained positively for GC-S (Fig. 1 B,D). In the hippocampus NOS-I immunoreactivity was observed in pyramidal cells of Ammons Horn and in the granular cells of the dentate gyrus (Fig 2A). GC-S immunoreactivity was also located in the pyramidal cells (Fig. 2B). The distribution of NADPH-d activity paralleled the staining pattern for NOS-I in most regions of the brain. Strong NOS-I and NADPH-d activity was observed in individual nerve fibers, nerve bundles and ganglia of the peripheral nervous system (Fig. 3). Non-neuronal cells which stained positively for NOS-I and NADPH-d included epithelial cells of the bronchi, the gastric mucosa of the forestomach, and the macula densa cells of the kidney (Fig. 4). Strong NADPH-d activity, but no NOS-I staining, was observed in the growing tips of long bones (Fig. 4A).

The findings in brain suggest that NO functions as an intercellular messenger generated in specialized neurons (granular cells) regulating GC-S activity in specific target cells (e.g Purkinje cells). The localization of NOS-I in non-neuronal tissues suggests that it may have important para-neuronal functions such as mediating renal tubulo-glomerular feedback and bronchodilation. Our findings may be the first histological evidence for the presence of an NOS-like substance in bone tissue where osteoclastic inhibition by NO has been shown.²

REFERENCES

1. W.P. Arnold *et al.*, Proc Natl Acad Sci USA (1977)74, 3203.
2. I. MacIntyre *et al.*, Proc Natl Acad Sci USA (1991)88, 2936.

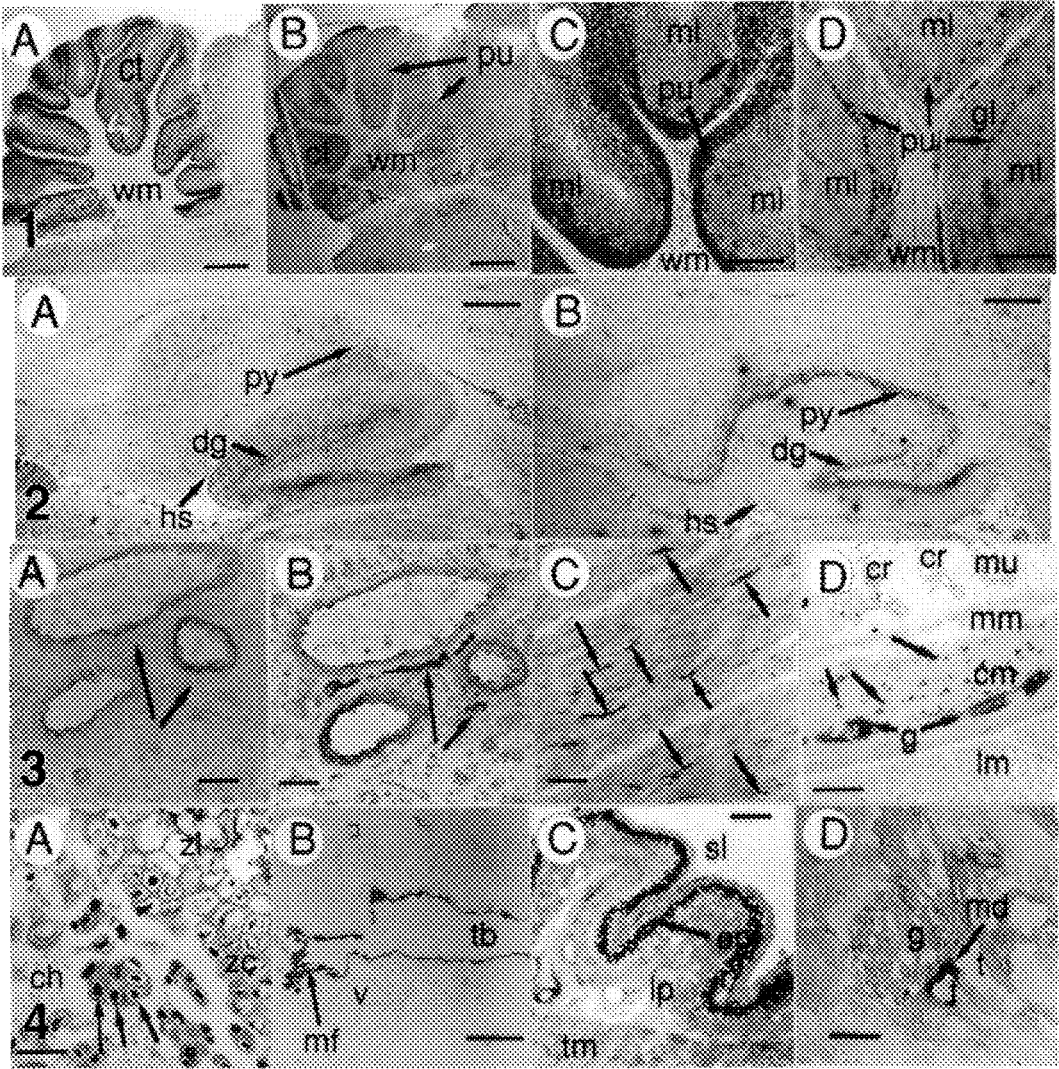


FIG. 1.--Localization of NOS-1 (A, C) and GC-S (B,D) in cerebellum. ct-cerebellar cortex, wm-white matter, pu-Purkinje cells, ba-basket cells, gl-granular and ml-molecular layers. Bars= 1 mm (A,B), 0.2 mm (C,D).

FIG. 2.--Localization of NOS-I (A) and GC-S (B) in hippocampus. dg-dentate gyrus, py-pyramidal cells, hs-hippocampal sulcus. Bars= 0.5 mm.

FIG. 3.--Labeling of peripheral nitrinergic nerves for NOS-I. Adjacent sections of neurovascular bundles from rat pancreas were treated with anti-NOS-I (B) and pre-immune serum (A). NOS positive nerve fibers and ganglia are also demonstrated in circular muscle of forestomach (C) and duodenum (D). cm-circular muscle, cr-intestinal crypts, mm-muscularis mucosa, lm-longitudinal muscle. Bars=25µm.

FIG. 4.--Non-neuronal tissue stained for NADPH-d (A) or NOS-I (B). Label is seen in bone growth tip (A), lung epithelium (B), forestomach (C), and kidney (D). ch-chondrocytes, zl-zone of lacunar enlargement, v-vein, tb-terminal bronchiole, mf-mucosal folds, tm-tunica media, lp-lamina propria, ep-epithelium, sl-lumen, gl-glomerulus, md-macula densa, t-tubule. Bars= 50 µm (A,D), 0.5 mm (B), 0.1 mm (C).

AN IMMUNOELECTRON MICROSCOPY INVESTIGATION OF SIMIAN IMMUNODEFICIENCY
VIRUS (SIV) INFECTED AA2 CELLS

W.N. Norton, C.R. Brown*, M.K. Rippey*, M. Lewis**, P.M. Zack*

Biology Department, Southeastern La. Univ., Hammond, LA 70402

*USAMRIID, Fort Detrick, Frederick, MD 21702-5011

**Henry M. Jackson Foundation, 1500 E. Gude Dr., Rockville, MD 20850

Human immunodeficiency virus (HIV), the causative agent of AIDS, and simian immunodeficiency virus (SIV) are both retroviruses and members of the lentivirus family. The initial step leading to infection for HIV and SIV involves the binding of a viral envelope protein, GP120, to a specific surface determinate, CD4, which serves as a receptor site.¹ The clinical manifestations of SIV infection in the Asian macaque, an important primate host of the virus, are similar to those detected in humans diagnosed with AIDS. Consequently, SIV and its host represent a potentially valuable system in which drugs and vaccines focused against HIV can be subjected to testing.

The primary objectives of this investigation were to establish a reproducible immunoelectron microscopy related procedure for the analysis of specific SIV antigenic sites and to determine the ultrastructural effects of SIV induced cytopathogenicity and syncytium formation in cultured AA2 cells, a representation of transformed human B lymphocytes. The cells were infected with either the PBj or EllS strain of SIV. Observations were conducted by scanning electron microscopy (SEM) and transmission electron microscopy (TEM) at 2, 4 and 7 days post infection. AA2 cells demonstrated a greater sensitivity to the PBj strain as expressed by ultrastructural changes at equivalent time points. The most pronounced cellular alteration revealed by SEM was a progressive loss of microvilli (Figs. 1,2). The number of infected cells per sample and the relative quantity of viral particles present per cell appeared to increase at each successive time point. Aggregates of fused cells, ranging in number from 2 to 21, were a common feature of all representative samples examined. The cellular complexes, termed syncytia, were distinguished by substantial quantities of viral particles along the cellular surface. The immunoelectron microscopy phase of this experiment was designed to employ a mixture of primary antibodies generated against several SIV proteins, including GP120, GP32, P28 and P16 which represent a surface coat glycoprotein, a transmembrane glycoprotein and nucleocapsid proteins, respectively. Thin-sectioned viruses displayed consistent and extensive labeling of the nucleocapsid and viral envelope by 10nm colloidal gold particles (Fig. 3). The majority of discernible 30nm colloidal gold particles detected by SEM along the surface of infected AA2 cells appeared to associate with viruses and did not constitute meaningless background (Fig. 4). The protocol developed for this experiment should prove beneficial in future immunoelectron microscopy related investigations of SIV.

References

1. S. Putney and R. Montelaro, in A. Neurath, Ed., *Immunochemistry of Viruses*, II. The Basis For Serodiagnosis And Vaccines, New York: Elsevier (1990)307.
2. This research was supported by the U.S. Army Research Office of Scientific Services Program.

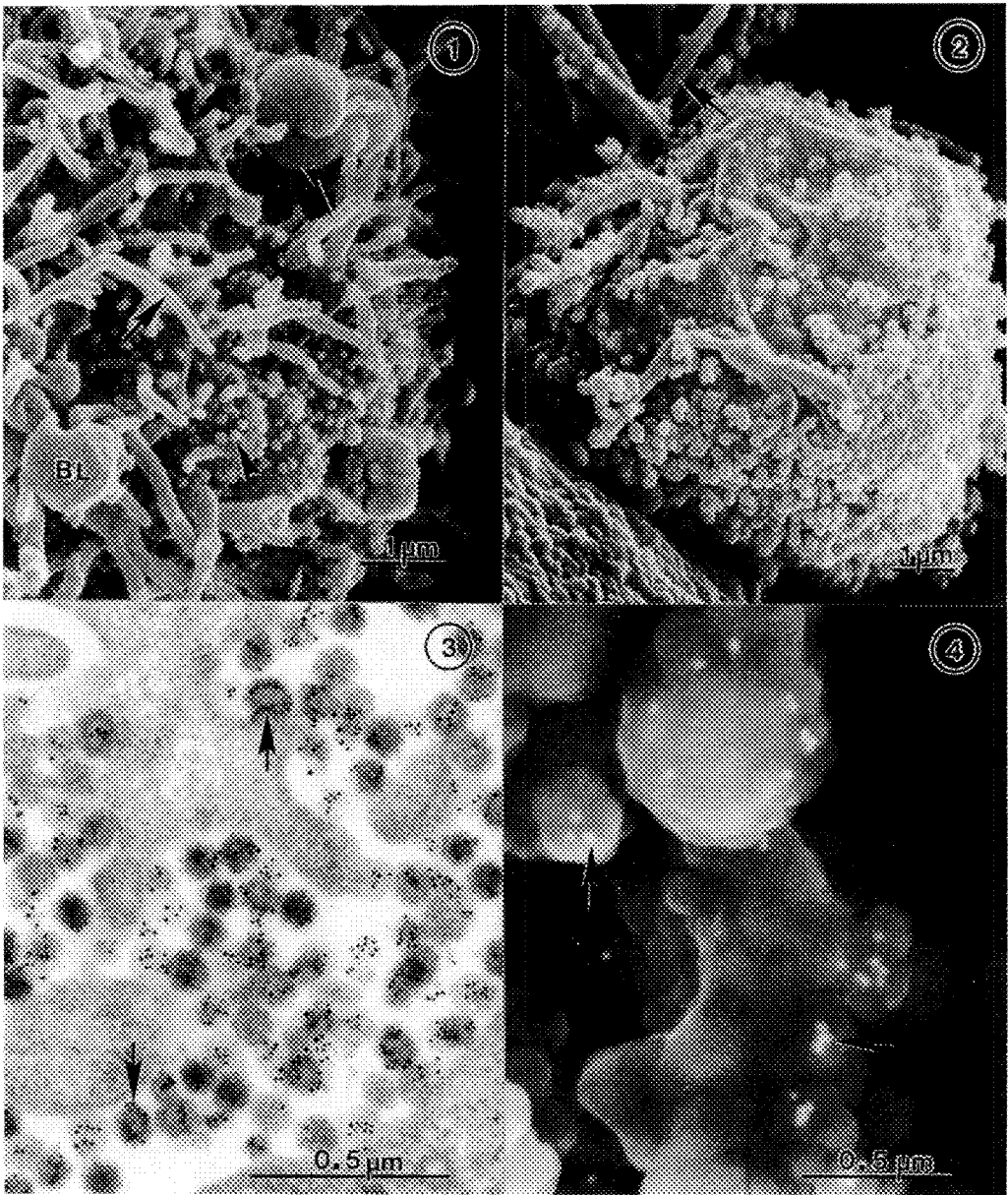


Fig. 1 Surface of AA2 cell is characterized by presence of viruses (arrowhead), microvilli (arrows) and membranous blebs (BL). Ellis strain: 2 days post-infection.
 Fig. 2 Substantial quantity of viruses is evident along surface of infected cell that possesses relatively few microvilli (arrow). PBj strain: 7 days post-infection.
 Fig. 3 Ten nanometer colloidal gold particles are distributed, preferentially, over viruses (arrows) associated with AA2 cell. PBj strain: 4 days post-infection.
 Fig. 4 SEM illustrates localization of 30nm colloidal gold particles on surface of discernible viruses (arrows). PBj strain: 4 days post-infection.

EM LOCALIZATION OF CHROMAFFIN CELL ATPase

V. Kriho and G. D. Pappas

Department of Anatomy and Cell Biology, University of Illinois at Chicago, Chicago, IL 60612

During exocytosis of the chromaffin granules, ATP is released. ATP can then be hydrolyzed by the ecto-ATPases of the plasma membrane to provide adenosine for reuptake or for activation of P_1 purinoceptors.¹ Chromaffin granule membranes also possess ATPase activity. This activity is linked to the uptake of catecholamines from the cytoplasm into the membrane-bound granule compartment.^{2,3,4}

In this report we combine EM cytochemistry and immunogold labelling to provide further evidence for the presence of ATPase on both the plasma membrane and granule membranes of bovine chromaffin cells in culture.

Figures 1a and b demonstrate the results of EM cytochemistry. Figure 1a shows part of an intact chromaffin cell incubated for 1 hr at 37° in a cytochemical medium containing Ca^{++} , Mg^{++} , Ce^{+++} (Ce^{+++} is the precipitating ion) and ATP. Ecto-ATPase activity manifests itself as a dense $CePO_4$ precipitate on the external face of the plasma membrane. Figure 1b shows an area where the cell has ruptured, allowing penetration of the precipitating medium into the cell. Under these circumstances, chromaffin granules also exhibit intense ATPase activity.

The distribution of chromaffin cell ATPase activity was further investigated using immunogold labelling. The primary antibody used in this study is an affinity purified, polyclonal antibody generated against a vacuolar H^+ ATPase from bovine kidney medulla and cortex.⁵ A pre-embedding immunogold labelling procedure was used on the cell seen in Figure 2a to demonstrate ATPase immunoreactivity of the plasma membrane. Figures 2b and 2c show ATPase labelling of the chromaffin granule as the result of post-embedding immunogold labelling of sections of LR White (b) and polyethylene glycol (c). Immunogold labelling results closely parallel the cytochemical demonstration of ATPase activity, i. e., antigenic sites are located on both the chromaffin cell granule and plasma membrane.

The antibody used in this study is composed of 3 major immunoreactive subunits. Western Blot analysis shows cross reactivity with only one of the major subunits, the 31kD. The 31kD immunoreactive subunit is present in whole cell extract, in granules and membranes.

In summary, our cytochemical results show the presence of Ca/Mg ATPase activity on the external surfaces of the plasma membrane of bovine chromaffin cells. ATPase activity is also detected on the external face of the chromaffin granule. The immunogold labelling pattern closely follows the cytochemical localization of ATPase activity. Western blot analysis suggests that the ATPases of the chromaffin cell plasma membrane and chromaffin granule may be immunologically related to the proton pumping ATPase of the kidney medulla and cortex, since they apparently share the 31kD protein.^{6,7}

References

1. M. Torres et al., Archives Biochem. & Biophys. 279(1990), 37.
2. P. Banks, Biochem. J. 95(1965), 95
3. D. Njus and G. K. Radda, Biochim. Biophys. Acta 463(1978), 219.
4. D. K. Apps and G. Schatz, Eur. J. Biochem. 100(1979), 411.
5. S. Gluck and J. Caldwell, J. Biol. Chem. 262(1987), 15780.
6. The ATPase antibody was the generous gift of Dr. S. Gluck.
7. This work was supported in part by NIH grant NS 28931.

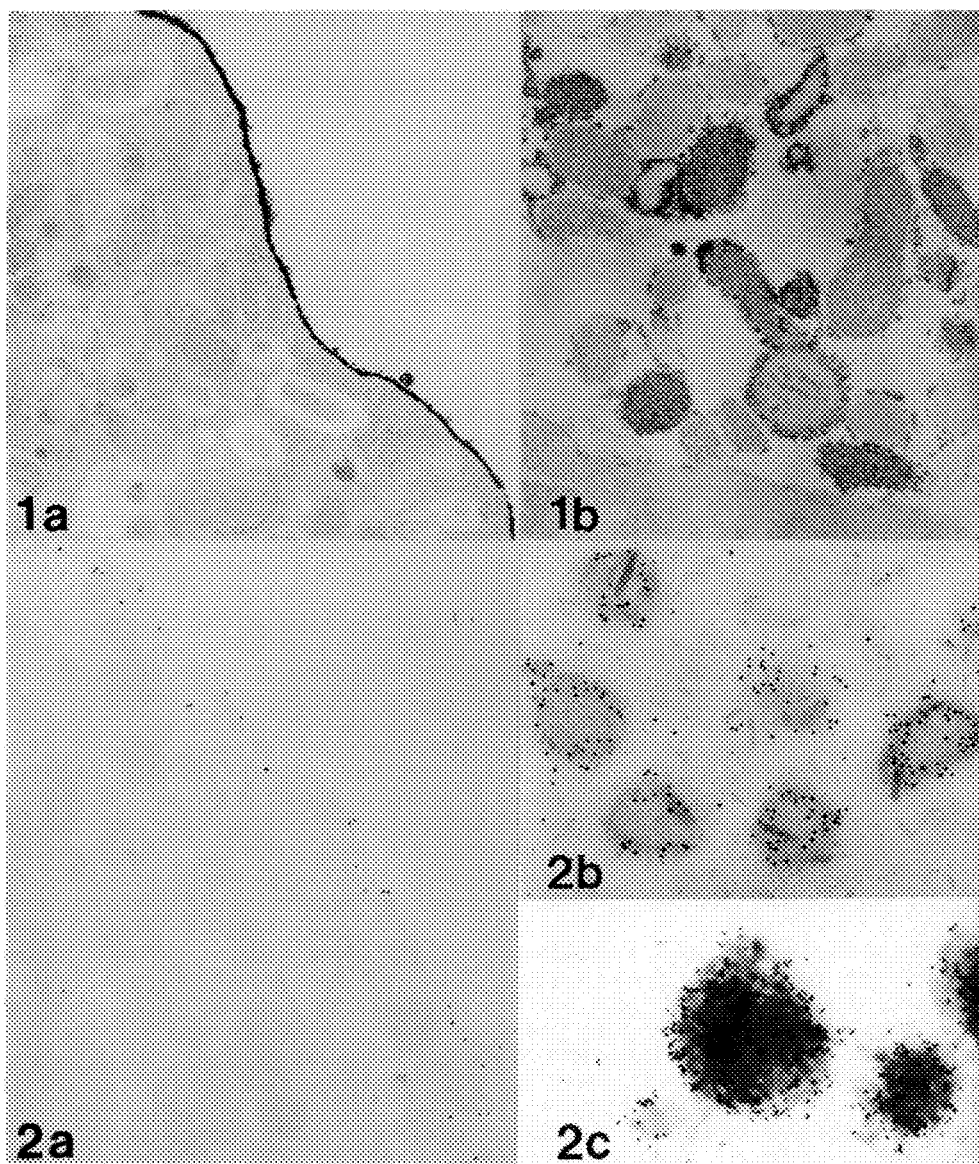


FIG. 1. Dense cytochemical reaction product indicates ATPase activity. ATPase activity is present (a) on the external face of the plasma membrane of a bovine chromaffin cell and (b) on chromaffin granules. CG = chromaffin granule, M=mitochondria. Mag. (a) = X 30,000; (b) = X 45,000.

FIG. 2. Immunogold labelling of chromaffin cells using an ATPase antibody and colloidal gold. (a) Pre-embedding labelling confirms the presence of ATPase sites on the plasma membrane. Post-embedding immunogold labelling of an LR White section (b) and a polyethylene glycol section (c) demonstrates ATPase antigenic sites on chromaffin granules. Mag.= (a) = X 30,000; (b) = X 60,000; (c) = X 75,000.

CA⁺⁺-ATPASE ACTIVITY IN THE HINDGUT EPITHELIAL CELLS OF ONISCUS ASELLUS

G.M. Vernon*, A. Jean Pierre* and R. Witkus**

*Division of Science and Math., The College at Lincoln Center,
Fordham University, New York, N.Y. 10023

**Department of Biological Sciences, Fordham University,
Bronx, N.Y. 10458

Specialized junctional complexes and the ultrastructural morphology of the hindgut epithelial cells indicate that the terrestrial isopod hindgut epithelium functions in transport.¹ The hindgut is divided into an anterior hindgut (typhlosole region), a posterior hindgut (papillate region) and a rectum. Using mitochondrial morphometry as an indicator of cell transport activity, Coruzzi et al.¹ demonstrated that the posterior hindgut of Armadillidium vulgare is active in osmoregulation to a greater degree than O. asellus. A study was undertaken to determine if this difference is reflected in the CA⁺⁺-ATPase activity of the hindgut epithelial cells of O. asellus.

The technique used was that described by Berridge and Gupta.² The hindgut was dissected and fixed for thirty minutes in a 2.5% solution of glutaraldehyde, 0.1M Na cacodylate (pH 7.2) and 0.15M sucrose. The tissue was washed in several changes of 0.05M Na cacodylate (pH 7.2) at 4 °C and transferred to 0.09M Tris maleate for 1 hr. The tissue was incubated in a medium consisting of 2 mM Tris-ATP, 80 mM Tris-maleate, 5 mM CaCl₂ and 3.6 mM Pb (NO₃)₂ and kept for two hrs. After incubation the tissue was washed in 0.08M Tris-maleate, postfixed in 1% OsO₄, dehydrated in a graded series of acetone and embedded in Araldite/DDSA. Controls were run in which the calcium was omitted or ouabain added. Sections were prepared and examined on an Hitachi HU 11B transmission electron microscope.

CA⁺⁺-ATPase activity was localized in the deep apical infoldings of cells in the papillate region (Fig. 1). No activity was evident in the basal infoldings (Fig. 2) in this region. In the anterior hindgut cells no activity was present in the apical region (Fig. 3). Only slight activity was detected in the basal region. In the rectum CA⁺⁺-ATPase activity was localized only in the highly convoluted lateral membranes (Fig. 4). No activity was associated with either the apical or basal infoldings. The regions of localization of CA⁺⁺-ATPase in O. asellus differed from that described by Zung³ for Armadillidium vulgare. This may reflect differences in osmoregulatory capability.

References:

1. L. Coruzzi, E.R. Witkus and G.M. Vernon, Exp. Cell Biology (1982) 50, 229.
2. M.J. Berridge and B.L. Gupta, J. Cell Science (1968) 3, 17.
3. J. Zung. (1986) Fordham University Ph.D. Thesis.
4. This research was supported by an Ambrose grant.

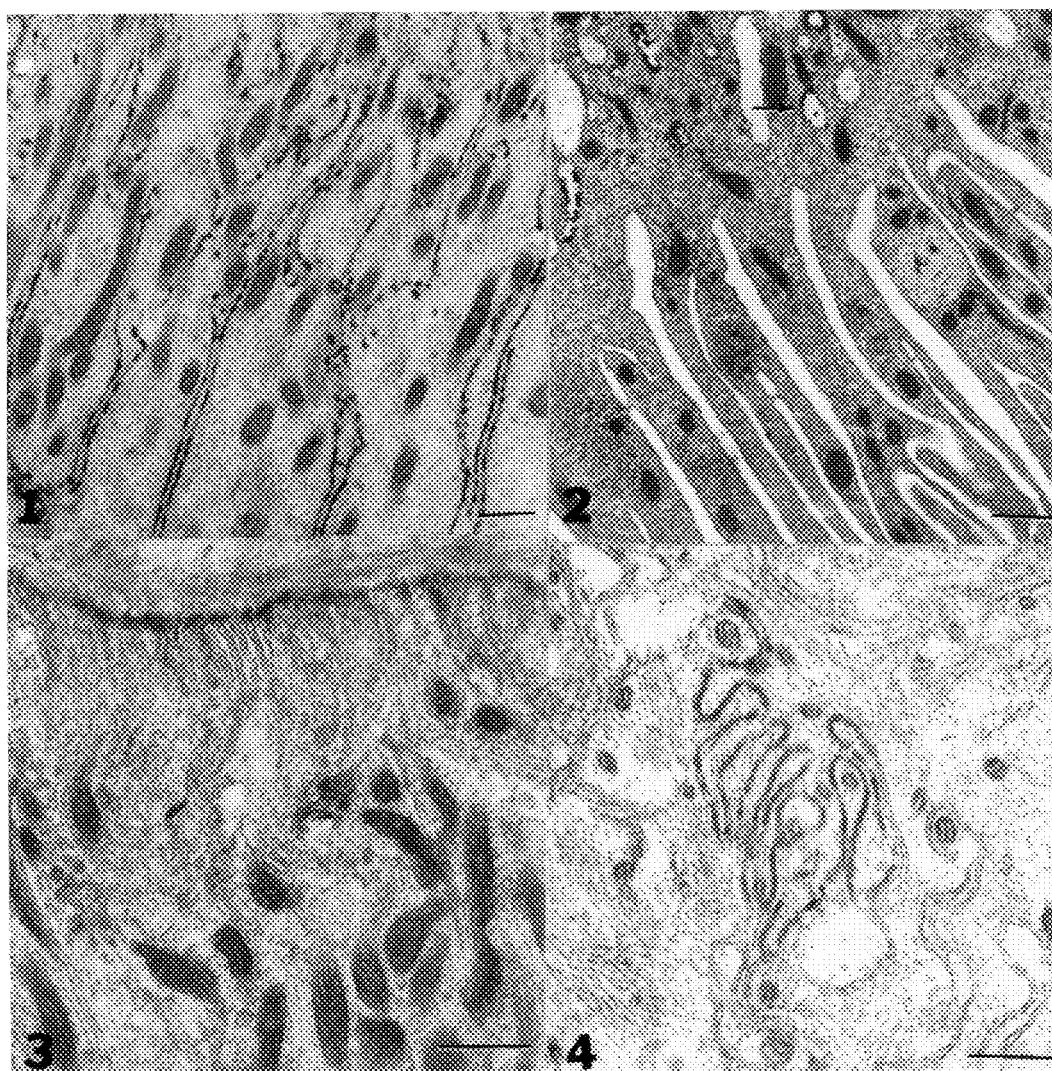


FIG. 1.-- TEM of apical infoldings of papillate cell showing Ca^{++} -ATPase activity. Bar = 0.5 μm .

FIG. 2.-- TEM of basal infoldings of papillate cell. Note reaction product (arrow) in deep apical infoldings. Bar = 0.5 μm .

FIG. 3.-- TEM of apical region of anterior hindgut cells. Bar = 0.5 μm .

FIG. 4.-- TEM of lateral plasma membrane of rectum cells showing Ca^{++} -ATPase activity. Bar = 0.5 μm .

Ca⁺⁺-ATPASE ACTIVITY IN THE HEPATOPANCREAS CELLS OF ONISCUS ASELLUS

G.M. Vernon*, A. Surace and R. Witkus**

*Division of Science and Math., The College at Lincoln Center,
Fordham University, New York, N.Y. 10023

**Department of Biological Sciences, Fordham University,
Bronx, N.Y. 10458

The hepatopancreas consists of a pair of bilobed tubules comprised of two epithelial cell types.¹ S cells are absorptive and accumulate metals such as copper and zinc.² Ca⁺⁺ concentrations vary between the S and B cells² and during the molt cycle.³ Roer and Dillaman⁴ implicated Ca⁺⁺-ATPase in calcium transport during molting in Carcinus maenas. This study was undertaken to compare the localization of Ca⁺⁺-ATPase activity in the S and B cells during intermolt.

The technique used was that described by Berridge and Gupta.⁵ The hepatopancreas was dissected and fixed for thirty minutes in 2.5% glutaraldehyde, 0.1M Na cacodylate (pH 7.2) and 0.15M sucrose. The tissue was rinsed with 0.05M Na cacodylate (pH 7.2) at 4 °C and transferred to 0.09M Tris maleate for 1 hr. The tissue was incubated for 2 h in a medium consisting of 2 mM Tris-ATP, 80 mM Tris-maleate, 5 mM CaCl₂ and 3.6 mM Pb (NO₃)₂. The tissue was rinsed in several changes of 0.08M Tris-maleate, postfixed in 1% OsO₄, dehydrated in a graded series of acetone and embedded in Araldite/DDSA. Controls were run in which the calcium was omitted or ouabain added. Sections were prepared and examined on an Hitachi HU 11B transmission electron microscope.

Ca⁺⁺-ATPase activity was not evident on the microvillar surface anywhere along the length of the gland (Fig. 1). There was no Ca⁺⁺-ATPase localization along the lateral plasma membranes of the distal hepatopancreas cells (Fig. 2). However, localization was evident along the lateral membranes between S and B cells and between B and B cells in the mid and mature glandular regions (Fig. 3). Reaction product was observed from a point just basal of the tight junction to just above the basal membrane. There was no evident localization along the basal membrane infoldings of either the mid or mature glandular regions (Fig. 4). These results indicate that both S and B cells in the mid and mature glandular regions are involved in active transport of calcium.

References:

1. J. Frenzel, Mitt. Zool. Sts. Neapel (1884) 5, 50.
2. W. Wieser, Am. Zool. (1968) 8, 395.
3. Z. Szyfter, Bulletin de la Societe des Amis des Sciences et des Lettres de Poznan, 95.
4. R. Roer and R. Dillaman, Am. Zool. (1984) 24, 893.
5. M.J. Berridge and B.L. Gupta, J. Cell Science (1968) 3, 17.
6. This research was supported by a Faculty Challenge Grant.

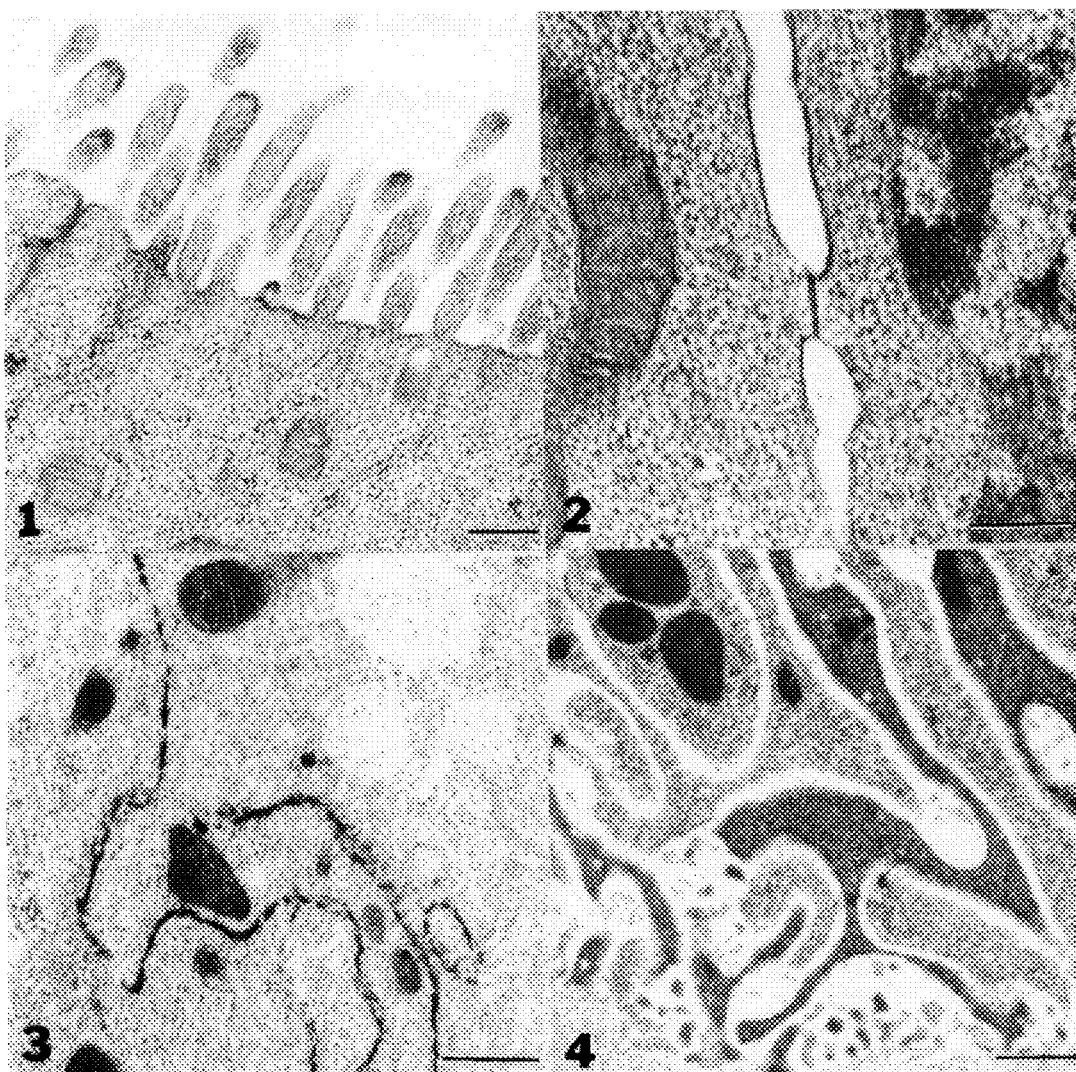


FIG. 1.-- TEM of microvilli of distal hepatopancreas cell. Bar = 0.25 μm .

FIG. 2.-- TEM of lateral plasma membranes of distal hepatopancreas cells. Bar = 0.2 μm .

FIG. 3.-- TEM of lateral plasma membranes of mid glandular hepatopancreas showing $\text{Ca}^{++}\text{ATPase}$ localization. Bar = 0.5 μm .

FIG. 4.-- TEM of basal membrane infolding in mid glandular region. Bar = 0.5 μm .

IMMUNOELECTRON MICROSCOPIC DETECTION OF MANNAN-ANTIGEN ON YEAST CELLS OF CANDIDA ALBICANS

Mercedes Edwards, Robert Trimble and William Samsonoff

Wadsworth Center for Laboratories and Research, New York State Department of Health, Empire State Plaza, P.O. Box 509, Albany, New York 12201-0509

Candida albicans (Ca) is an opportunistic fungal pathogen of worldwide distribution. In recent years, infections by this fungus have received increased attention due to their prevalence in immunocompromised hosts (e.g. AIDS patients). However, Ca infection mechanisms are still to be ascertained. Investigations on the antigenicity of this organism have found that mannan, a component of its cell wall, is a major circulating antigen in systemic candidiasis.^{1,2} A few previous reports using electron microscopy,^{3,4} have indicated that mannan is located at the cell wall, but the resolution of the published micrographs did not afford a conclusive determination of the antigen distribution.

Here we present results from a TEM immunogold study of Ca thin sections using rabbit antibodies raised against purified cell wall mannan.⁵

Yeast cells were fixed with 0.2-0.5% glutaraldehyde and 2% formaldehyde in cacodylate buffer (pH 7.2), with agitation for 4 h at room temperature and at 4°C overnight; for some samples the buffer contained 0.5% saponin. After three buffer washings (with or without saponin) the samples were dehydrated and embedded in epoxy resins, or LR White, according to standard protocols. A few samples were osmicated prior to dehydration. Thin sections were incubated with rabbit anti-mannan IgG and treated with goat anti-rabbit IgG-gold. Gold particles were counted on numerous micrographs, in measured cell areas of cell wall or cytoplasm, as well as on the section background. Results were evaluated statistically.

Sites of mannan-antibody reactions labeled by the gold particles are shown in Figures 1-3. No significant differences existed between young (budding) and old (mother) cells (Fig. 1). In all cases, antigenic sites were found predominantly at the cell envelope (cell wall and plasma membrane; Figs. 2 and 3). Gold particles were negligible or absent on section background and on control cells (incubated with normal rabbit immunoglobulin; not shown). Mannan antigen(s) of Ca cell envelope, as demonstrated here, is(are) well preserved using standard TEM fixation and embedding methods.

References

1. R. A. Calderone and P. C. Braun, Microbiol. Rev. (1991)55, 1.
2. R. D. Nelson et al., Clin. Microbiol. Rev. (1991)4, 1.
3. M. Horisberger and M. Vonlanthan, Arch. Microbiol. (1977)115, 1-7.
4. D. Poulain et al., in E. Drouchet, G. T. Cole, L. de Repentigny, J. P. Latagé and B. Dupont (ed). Plenum Press, NY, pp. 149-150.
5. We are grateful to Dr. J. Domer (Tulane University, New Orleans, LA) for her gift of the purified mannan.

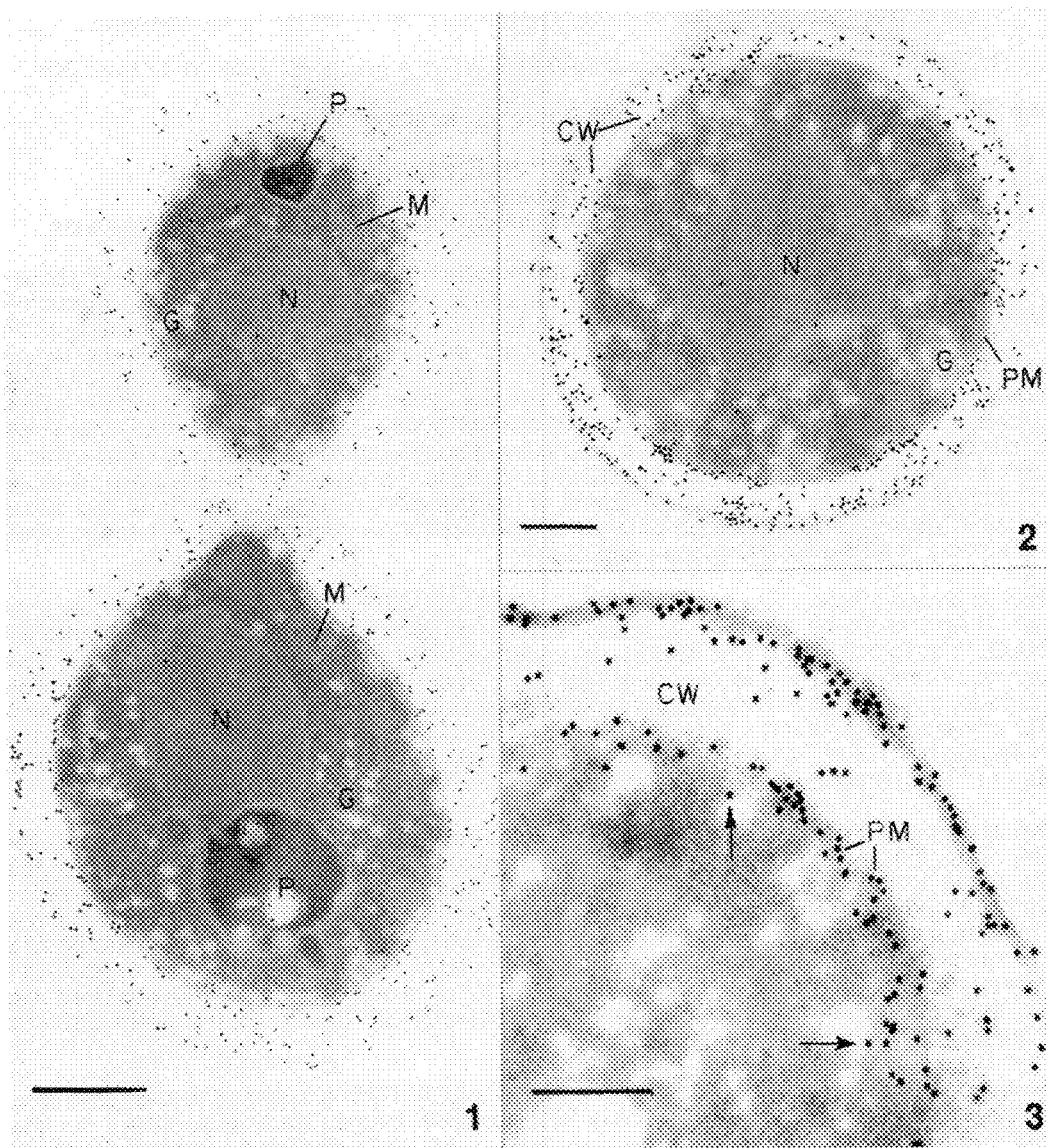


FIG. 1.--Visualization of gold labels on mother (lower) and daughter (bud, upper) cells. Nucleus (N), peroxisome (P), mitochondrion (M), glycogen (G). Note gold particles at the bridge area between the two cells. Bar = 0.5 μ m.
 FIGS. 2 and 3.--Distribution of gold particles predominantly at the cell envelope (cell wall, CW and plasma membrane, PM). Antigen sites are distributed within the entire cell envelope. Note particles at PM invaginations (arrow). Bars = 0.25 μ m.

DETECTION OF 1-nm IMMUNOGOLD LABELS WITH A FIELD-EMISSION TEM/STEM

Max T. Otten¹, York-Dieter Stierhof², and Bruno M. Humbel³

¹ Philips Electron Optics, Building AAE, 5600 MD Eindhoven, The Netherlands

² Max-Planck-Institut für Biologie, D-7400 Tübingen, Germany

³ Institute of Molecular Biology, University of Utrecht, 3584 CH Utrecht, The Netherlands

The size of the gold labels is known to be an important factor affecting immunogold labelling efficiency. In many cases it has been found that the smaller the label, the better the efficiency. Ultra-small gold colloids were therefore introduced to increase the sensitivity of the immuno-gold labelling technique. Such ultra-small labels are difficult to detect in the regular TEM image and for efficient detection silver enhancement is needed to enlarge the gold labels. Unfortunately, the reliability of the various silver-enhancement methods is poorly known. Possible problems are the lack of control over reproducibility, homogeneity and efficiency of the enhancement and the possibility of spontaneous nucleation of silver particles without a gold precursor (non-specific silver precipitation) and merging of several gold labels into a single silver particle. An assessment of these factors requires a technique that allows visualisation of the unenhanced ultra-small gold labels as well as silver-enhanced ones, preferably in relation to the tissue morphology.

Backscattered-electron imaging on a Field Emission Gun (FEG) SEM has been shown to be able to resolve the ultra-small gold labels. Another possibility, High-Angle Annular Dark-Field (HAADF) imaging using a FEG STEM instrument was investigated in this study. HAADF¹ is a technique that employs the electrons that have been Rutherford scattered in the forward direction, giving a signal similar to that of backscattered-electron imaging but at least a factor 100 higher than the latter at the high voltages of the STEM (200 kV). Previously HAADF on a Philips CM12/STEM instrument equipped with a LaB₆ emitter was shown to be able to detect larger (15 nm) immunogold labels with high efficiency².

The specimens used in this study were unstained resin sections of *E. coli* bacteria, labelled with an OmpA-specific rabbit anti-serum and nominally 1 nm gold colloids coupled to goat anti-rabbit IgG. The microscope used was a Philips CM20 FEG/STEM, equipped with a Schottky field emitter³. The instrument was operated at 200 kV with a spot size of 1.5 nm at a probe current of ~500 pA. The detector used for HAADF imaging was the standard annular dark-field detector, mounted in the so-called near-axis position (3 cm off the optical axis, thereby leaving room for mounting a PEELS or TV on axis). The camera length used was 100 mm, giving HAADF acceptance angles between 2° (given by the inner detector diameter) and 6° (outer detector diameter).

It was found that HAADF imaging on the CM20 FEG/STEM is superior to backscattered-electron imaging with the FEG SEM. The STEM HAADF image clearly shows the 1 nm gold labels even at primary magnifications as low as 50 000x (thereby allowing whole-cell overviews) (Fig. 1), whereas on the FEG SEM magnifications of 200 000x are needed to visualise the gold labels. In addition, the HAADF STEM image provides the best contrast for the gold labels, while ultrastructural detail from the cells is well visible (Fig. 2).

References

- 1) M.T. Otten (1991) *J. Electron Microscopy Technique* 17, 221-230.
- 2) M.T. Otten, D. Stenzel, D. Cousens (1990) *Australian EM Newsletter* 27, 10-16.
- 3) P.M. Mul, B.J.H. Bormans, M.T. Otten (1991) *Philips Electron Optics Bulletin* 131, 53-62.

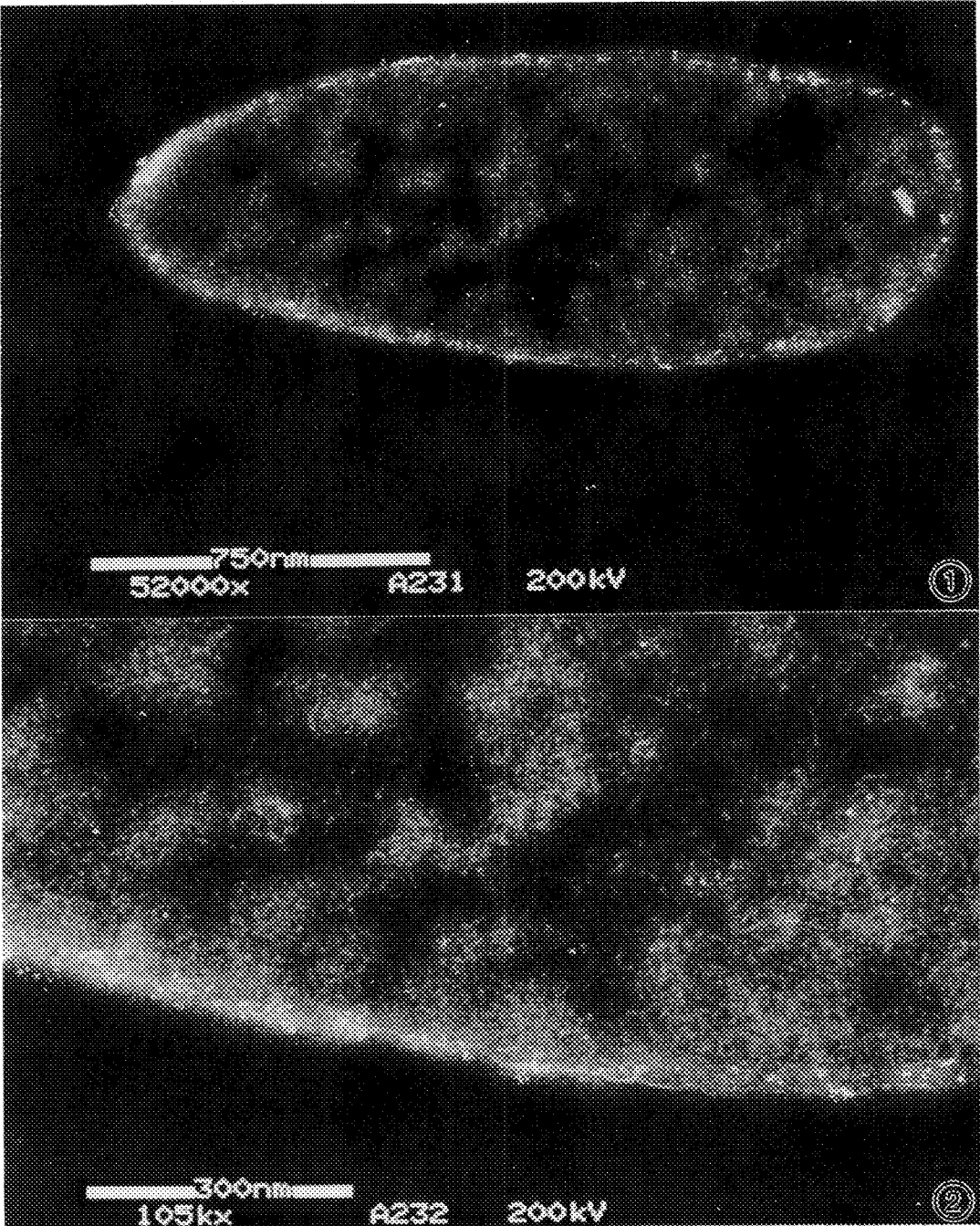


Fig. 1. HAADF STEM image of a whole *E. coli* bacterium with unenhanced ultra-small gold labels.
Fig. 2. HAADF STEM image of a detail of the same *E. coli* bacterium as in Figure 1, showing unenhanced ultra-small gold labels and ultrastructural cell detail.

ULTRASTRUCTURAL PATHOLOGY AND IMMUNOHISTOCHEMISTRY OF MUSTARD GAS LESION

J.P. Petrali, S.B. Oglesby, T.A. Hamilton and K.R. Mills

Comparative Pathology, USAMRICD, Aberdeen Proving Ground, Maryland 21010-5425

The ultrastructural pathology of sulfur mustard gas (HD) skin toxicity has been documented for several model systems.^{1,2} In animal models, development of skin basal cell nuclear pathology was followed by progressive cytoplasmic changes leading to cell death. These cellular changes along with a disabling of hemidesmosomes at the lamina lucida were persistent features leading to the formation of characteristic microblisters at the dermal-epidermal junction.¹ In this paper we correlate an ultrastructural pathologic study of HD exposed hairless guinea pig skin with a companion immunohistochemical study describing HD effects on extra-cellular structural proteins of the dermal-epidermal junction. The structural proteins summarized for this report are bullous pemphigoid antigen and laminin.

Skin sites of hairless guinea pigs were exposed to 10ul HD vapor for 8 minutes and harvested at selected post exposure time periods up to 24 hours.³ Control sites were taken from semiadja-cent non-exposed skin. Control and HD-exposed samples for ultrastructural study were immersion fixed for 24 hours in a cacodylate-buffered combined fixative of 1.6% formaldehyde and 2.5% glutaraldehyde. Following three washes in 0.1M cacodylate buffer (pH 7.4 and mOsm 190), samples were postfixed in 1% osmium tetroxide for 1 hour, dehydrated in graded ethanol and embedded in epoxy resins. Ultrathin sections were counterstained with uranyl acetate and lead citrate for study by transmission electron microscopy. Samples selected for immunohistochemistry were immediately plunge-frozen in liquid freon. Cryosections, 12um thick, were collected onto gelatin coated glass slides and air dried. Following a 5 minute wash in PBS (pH 7.6, mOsm 300), sections were then immunohistochemically incubated with working dilutions of specific antibody to bullous pemphigoid antigen (BPA) and laminin according to the following antibody sequence: 3% normal goat serum (20 minutes), specific primary antisera (BPA or laminin 1 hour), peroxidase conjugated goat bridging antibody (30 min), and DAB. Cryosections not treated with specific primary antibody were used as method controls.

Ultrastructural analysis revealed the typical progression of basal cell pathology and formation of characteristic microblisters at the basement membrane zone (Fig.1). Companion immunohistochemical localizations demonstrated that control sections were consistently reactive for BPA at the lamina lucida in that area most proximal to basal cell plasma membranes. Following exposure to HD, BPA reactivity was diminished at early times and subsequently lost to specific antisera at later time periods (Fig 2). Laminin was localized throughout the entire lamina lucida in control sections. However, at later time periods after HD exposure, immunolocalization was scanty and conformed to the structurally altered lamina lucida at microblister lesion sites (Fig.3). The results of this combined ultrastructural and immunohistochemical study indicate that proteins of extracellular matrices of the basement membrane zone are affected during the development of HD-induced skin pathology.

References

1. J.P. Petrali et al., J. Toxicol. Cut. & Ocular Toxicol., (1990) 9, 193
2. J.P. Petrali et al., J. Toxicol. Cut. & Ocular Toxicol., (1991) 10, 315
3. M.M. Mershon et al., Fundam. Appl. Toxicol., (1990) 15, 622

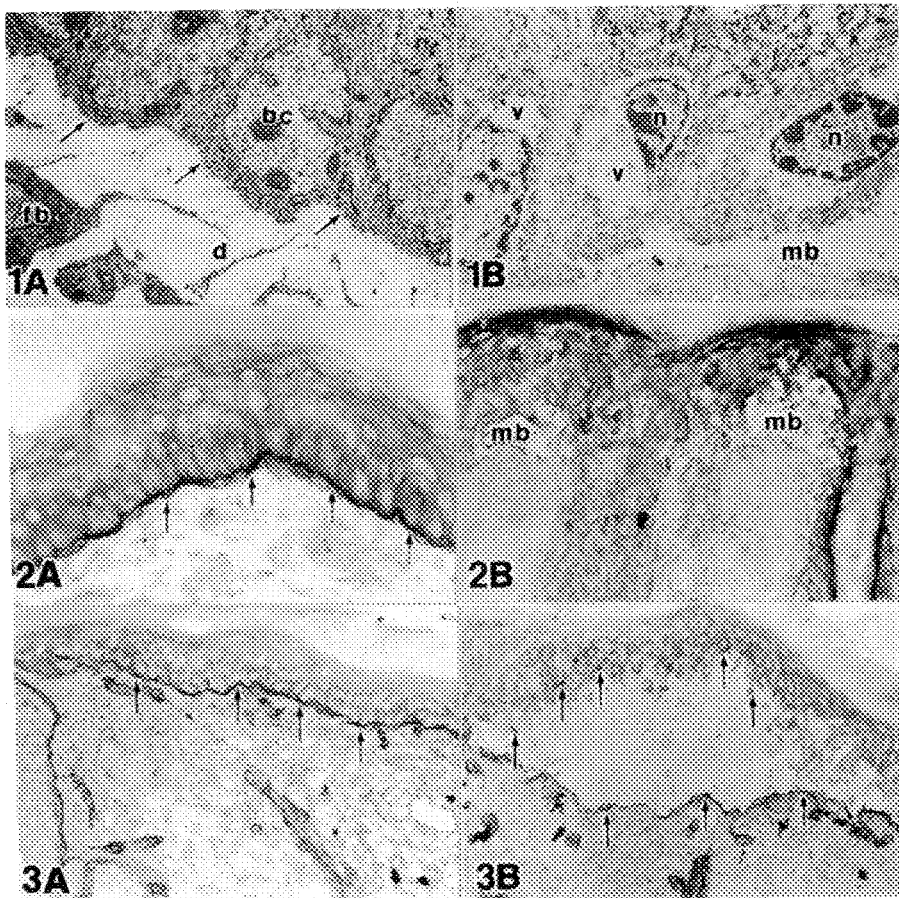


Figure 1. Electron micrographs of basement membrane zone of hairless guinea pig skin. A. Non-exposed control skin with epidermal basal cell (bc), basement membrane (arrows) composed of the lamina lucida and basal lamina. Dermis (d) with fibroblasts (fb). B. HD-exposed skin with pyknotic nuclei (n) of basal cell, vacuolated cytoplasm (v) and microblister formation (mb) at the dermal-epidermal junction. Magnifications 4800X.

Figure 2. Light micrographs of immunohistochemically localized BPA in hairless guinea pig skin. A. Non-exposed control skin with BPA (arrows) localized to the lamina lucida. Magnification 330X. B. HD-exposed skin with microblister formation (mb) and the complete absence of immunoreactivity for BPA. Magnification 200X.

Figure 3. Light micrographs of immunohistochemically localized laminin. A. Non-exposed control skin with laminin (arrows) localized throughout the lamina lucida. B. At a microblister of HD-exposed skin showing scanty localization of laminin (arrows). Magnifications 165X.

LOBULAR PATTERNS OF THE IMMUNOCYTOCHEMICAL LOCALIZATION OF ENZYMES INVOLVED IN HEPATIC CARBOHYDRATE METABOLISM

Bruce F. Giffin, Randal E. Morris, Richard L. Drake and Robert R. Cardell

Dept of Anatomy and Cell Biology, Univ of Cincinnati College of Medicine, Cincinnati, OH

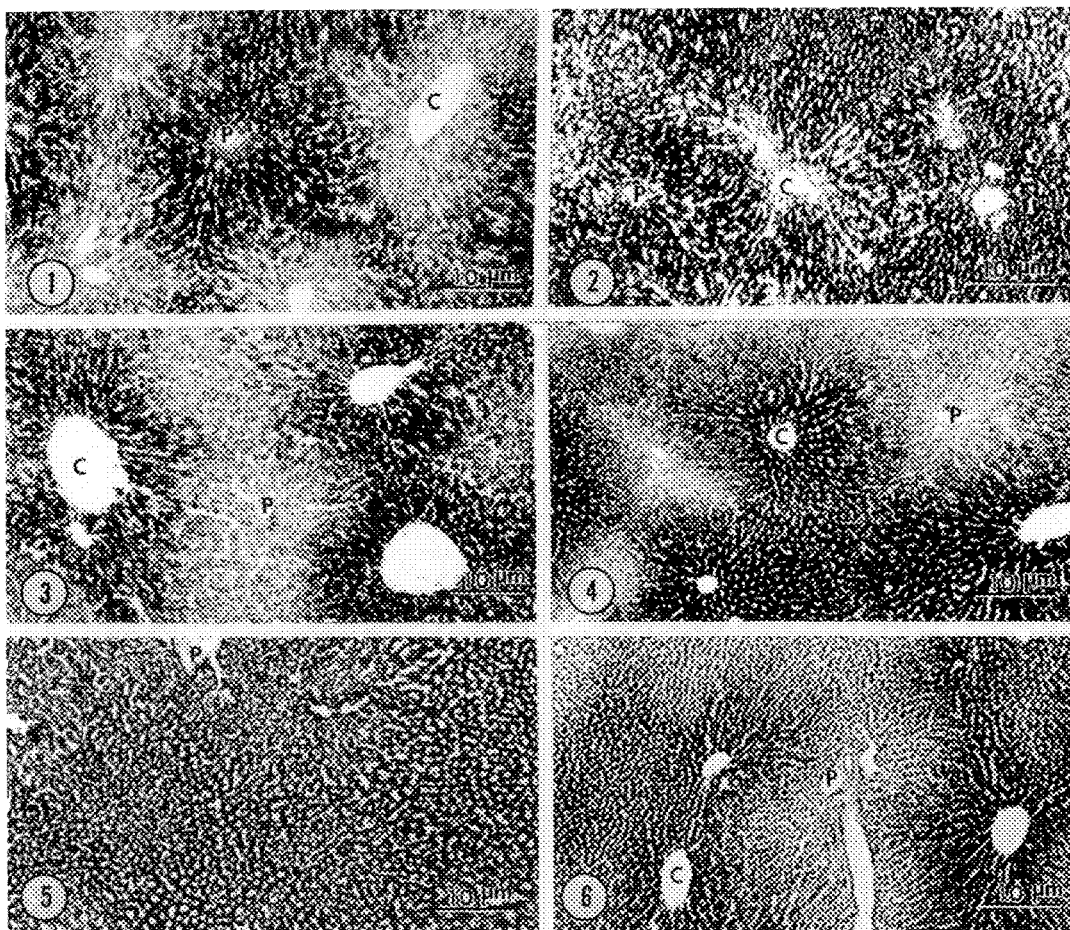
A heterogeneous distribution of many of the enzymes involved in carbohydrate metabolism has been demonstrated within the lobules of the liver.¹ Biochemical studies have demonstrated that hepatocytes in the periportal zone exhibit higher activities of gluconeogenic enzymes, whereas higher activities of glycolytic enzymes are found in cells surrounding the central vein (pericentral).² These studies were undertaken to determine the lobular distribution of phosphoenolpyruvate carboxykinase (PEPCK), glycogen synthase (GS) and glycogen phosphorylase (GP) in fed and fasted rats with an immunocytochemical technique using a gold conjugated secondary antibody.

Livers of fed and 24 h fasted adult male Sprague-Dawley rats were fixed by transcardial perfusion with 4% (w/v) paraformaldehyde in phosphate-buffered saline (PBS) for 20 minutes. Following cryoprotection of liver in 30% sucrose overnight, 10 μ m sections were cut and incubated in polyethylene slide boxes with blocking buffer (PBS, 0.5% (w/v) Triton X-100, 5% normal rabbit serum (for PEPCK and GS) or normal goat serum (for GS), 2% bovine serum albumin, 0.95 fish gelatin, pH 7.5) overnight at 4°C. Antibodies against PEPCK (1:10,000), GS (1:2000) and GP (1:2000) were diluted in blocking buffer and tissue sections incubated for 3 hours at room temperature. After extensive washing (6 x 5 min with PBS containing 0.5% (w/v) Triton-X 100), tissue sections were incubated with the appropriate 5 nm gold conjugated secondary antibody diluted 1:5 in blocking buffer overnight at 4°C. A photochemical silver enhancement technique (Sigma Chemical, St. Louis, MO) was used to visualize the lobular distribution of the gold conjugated secondary antibodies by light microscopy. Serial sections were stained with hematoxylin to evaluate morphology and the PAS reaction for the determination of hepatic glycogen. Fresh liver samples from fed and fasted animals were used in Western blot analysis of PEPCK, GS and GP.³

Fed animals demonstrated a heterogeneous distribution of both PEPCK (Fig. 1) and GS (Fig. 3). A decreasing periportal to pericentral gradient was detectable for PEPCK while GS was more intensely localized in the hepatocytes surrounding the central vein. Fasting for 24 h induced the expression of PEPCK by midlobular hepatocytes and increased the intensity of staining in the periportal region (Fig. 2). This increase was confirmed by Western analysis. In contrast, although Western analysis showed a slight decrease in the content of GS in the fasted rat, there was no change in the pericentral localization of this enzyme (Fig. 4). GP was homogeneously distributed throughout the liver lobule in the fed animal (Fig. 5) and Western analysis showed no change in the content of the enzyme. However, there appears to be a redistribution represented by a slight decrease in the periportal region after fasting (Fig. 6). Data from this study on the lobular distribution of these enzymes of hepatic carbohydrate metabolism is consistent with our functional understanding of the periportal and pericentral hepatocytes.

References

1. K. Jungerman and N. Katz, *Hepatology* 2 (1982), 385.
2. K. Jungerman and N. Katz, *Physiol. Rev.* 69 (1989), 708.
3. S.D. Hsu, *et al.*, *Arch. Biochem. Biophys.* 281 (1990), 152.
4. This work was supported by Grant DK 27097 from NIH.



All figures are 10 μ m frozen sections of rat liver processed for immunocytochemistry as described in text. C: central vein; P: portal tract.

Figure 1. Liver from fed rat stained for PEPCK shows a periportal localization of the enzyme.

Figure 2. After fasting for 24 hours PEPCK expression is induced in midlobular region resulting in a steepened periportal to pericentral gradient.

Figure 3. Liver from fed rat stained for GS shows a predominant pericentral localization of the enzyme.

Figure 4. After fasting for 24 hours there is no change in the pericentral distribution of GS.

Figure 5. Liver from fed rat stained for GP shows a homogeneous distribution of the enzyme throughout the liver lobule.

Figure 6. After fasting for 24 hours GP is more localized in the region of the central vein.

MICROSCOPIC EXAMINATIONS OF TOXIC MARINE MICROALGAE

David O'Neil, Cynthia Leggiadro, Gwang Hoon Kim, Lawrence Fritz

Institute for Marine Biosciences, National Research Council of Canada, Halifax,
Nova Scotia, Canada

A number of microalgae have been implicated in toxicity episodes in cultured shellfish in Eastern Canada^{1,2}. *Nitzschia pungens* f. *multiseries* and *Prorocentrum lima* are two organisms that have been shown to produce the toxins associated with poisonous shellfish. The present study examines these organisms by light microscopy (DIC and fluorescence), and SEM.

The pennate marine diatom, *N. pungens* (fig. 2), has been shown to produce a potent neurotoxin, domoic acid, in pure culture³. The distinctive features of this pennate diatom are illustrated in Fig. 1. The silica covering (frustule) consists of parallel rows of costa with multiple rows of minute pores (poroids). *P. lima* (fig. 5) is a dinoflagellate that has been found to produce a toxin known as okadaic acid⁴. This toxin has been associated with ciguatera, a fish poison, and was implicated in a recent toxic shellfish event in Eastern Canada. The cellulosic thecal plates are adorned with regular, distinctive pattern of pores (fig. 4).

Recently we have begun an investigation of cell surface components in these cells by various cellular labels. One group of cell surface labels are lectins, which are a group of plant proteins with specific binding affinities for particular sugar residues⁵, usually associated with a protein. Twelve lectins conjugated with fluorescein isothiocyanate (FITC) were tested for their abilities to label these algae. *Triticum vulgaris* (wheat germ agglutinin) showed specificity for the surface of *N. pungens* (Fig. 3) indicating the presence of a glycoconjugate of N-acetylglucosamine. *P. lima* (fig. 6) showed binding affinity for Con canavalin A, indicating the presence of α -D-glucose residues.

By the use of such cell surface labels, we hope to develop cellular markers to differentiate toxic from non-toxic species and strains of marine microalgae.

References

1. S. Bates, et al, Can. J. Fish. Aquat. Sci. 46, (1989) 1203, 1215.
2. A. Jackson, et al, Proc. 5th Int. Conf. on Toxic Marine Phytoplankton, (1991)
3. D. Douglas and S. Bates, Can. J. Fish. Aquat. Sci., vol. 49, (1992) 97, 102.
4. Y. Murakami, et al, Bull. Jpn. Soc. Sci. Fish. 48, (1982) 69, 72.
5. P. v. Sengbusch, et al, Protoplasma 111 (1982) 38, 52.

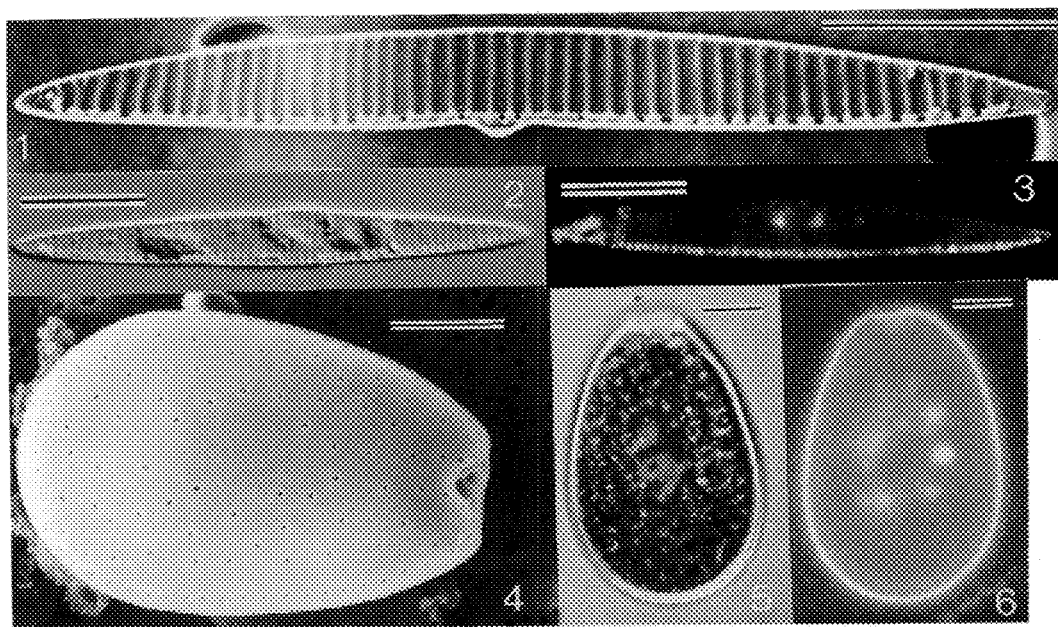


Fig. 1. SEM micrograph of *N. pungens* silicious frustule after acid removal of organic material.

Fig. 2. Differential Interference Contrast (DIC) image of *N. pungens*.

Fig. 3. Fluorescence image of *N. pungens* labelled with WGA lectin/FITC.

Fig. 4. SEM micrograph of *P. lima* after freeze-drying.

Fig. 5. DIC image of *P. lima*.

Fig. 6. Fluorescence image of *P. lima* labelled with Con A lectin/FITC.

NOTE: all scale bar markers are 10μm.

SEM OBSERVATIONS OF BLOOM-FORMING TOXIC DIATOMS FROM MONTEREY BAY, CALIFORNIA

E. A. Hale *, J. M. Krupp **, D. L. Garrison *

* Institute of Marine Science, University of California, Santa Cruz, CA 95064

** Electron Microscope Facility, University of California, Santa Cruz, CA 95064

In the late summer of 1991, large numbers of seabirds in northern Monterey Bay, California died after showing unusual neurological symptoms. The first suspects were dinoflagellates, planktonic algae known to produce the toxins responsible for paralytic shellfish poisoning (PSP). Although toxic dinoflagellates were found, no evidence for PSP was present. Subsequent chemical analysis of tissue and stomach contents from affected birds and from locally collected northern anchovy showed high concentrations of domoic acid. During the seabird kill in Monterey Bay, the plankton was dominated by *Pseudonitzschia australis* (= *Nitzschia pseudoseriata*) a diatom not previously known to produce domoic acid.

Domoic acid is a naturally occurring amino acid that acts as a potent neurotoxin. The first widely recognized incident of domoic acid poisoning in humans occurred in 1987 when over 100 persons from Prince Edward Island, Canada were stricken and 4 later died after consuming cultured mussels. The affliction has been termed amnesic shellfish poisoning (ASP) because of the neurological symptoms manifested and to distinguish it from the better known PSP caused by dinoflagellates. The source of domoic acid was attributed to a bloom of the diatom *Nitzschia pungens* f. *multiseries*.

Since the original Canadian episode of ASP and subsequent annual blooms there, other instances of domoic acid poisonings have been reported. In southern Washington several people showed symptoms of domoic acid toxicity after consuming razor clams. Domoic acid was found in Dungeness Crabs resulting in a brief closure of the northern California coastal crab fishery. Domoic acid and blooms of diatoms were implicated in the seabird kills around Monterey Bay. Since the discovery of toxic concentrations of domoic acid in the Pacific coastal food web, efforts have been launched to monitor the presence of toxin producing diatoms in a manner similar to the established monitoring of dinoflagellate blooms responsible for PSP/Red Tide alerts.

Establishing an effective ASP monitoring program is complicated by two important factors. First, several diatom species, toxic and non-toxic, overlap in size and gross frustule morphology when observed with the light microscope. Within the assemblage of 18 species sharing similar morphology, (i.e., the *Pseudonitzschia* complex which includes *P. australis* and *N. pungens* f. *multiseries*) three have now been reported to be toxic. At the present time, the most reliable way to identify diatoms implicated in domoic acid poisoning is with the scanning electron microscope. The features used for identification are the distribution and arrangement of the smallest pores in the cell walls. The number of these poroids/micrometer and the number of rows of poroids grouped together are regarded as reliable characteristics for identification

Second, experimental work has suggested that domoic acid is produced by diatoms when growth is limited by factors other than nitrogen availability. Environmental conditions must be favorable for toxin production. Therefore, not all species of diatoms capable of producing domoic acid will manifest this trait at all times. Further, toxin producing forms must be present at some minimum concentration to present a health hazard. Under some conditions the presence of certain species can be serious, even life threatening. At other times, the same species may be benign. The economic and health consequences of correctly, or incorrectly, identifying toxic conditions are significant. Additional studies are now in progress to differentiate between the toxic and non-toxic forms using characteristics seen with the SEM and to establish an effective and accurate monitoring program.

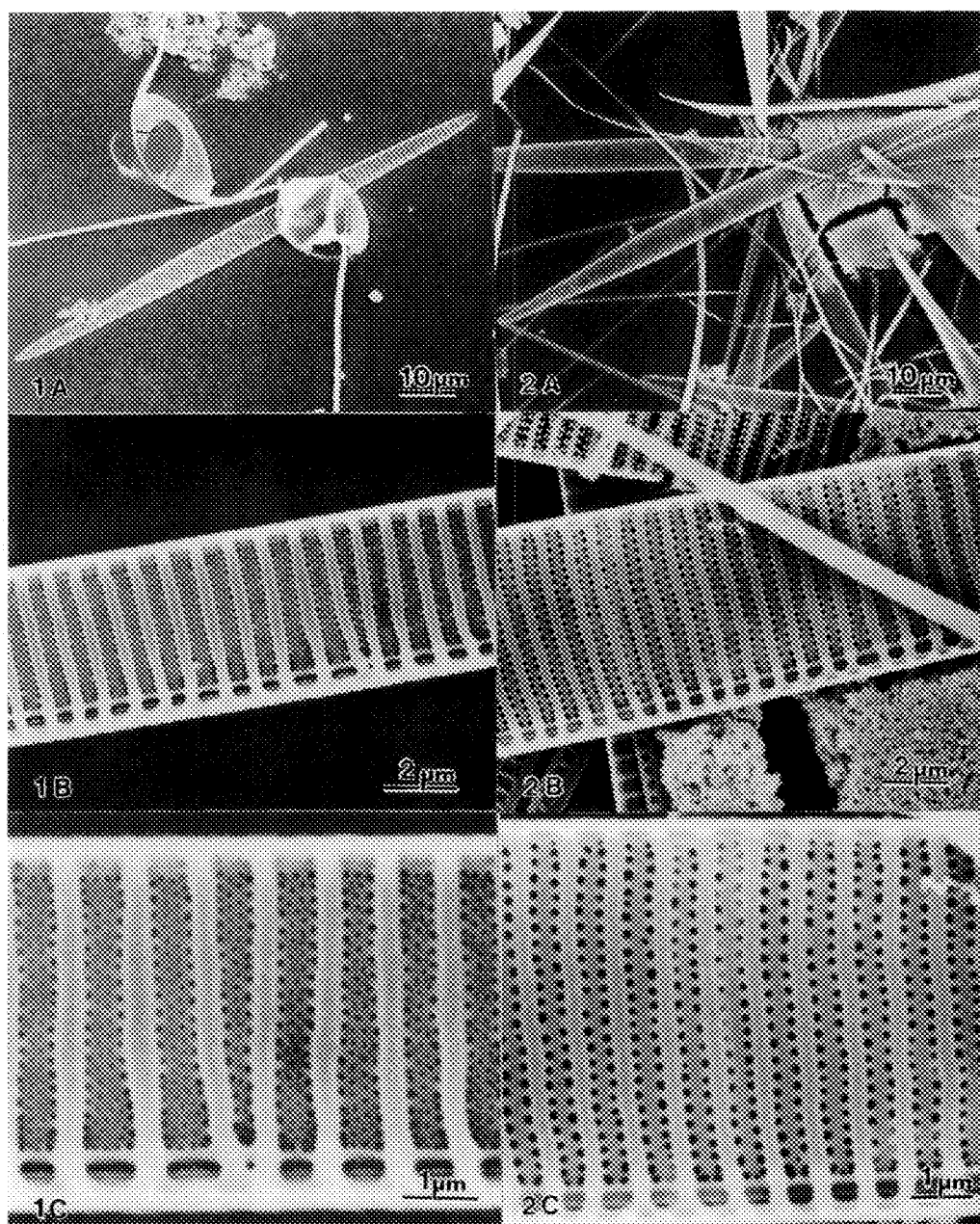


FIG. 1A - C.-- *Nitzschia pungens* f. *multiseries* collected from Monterey Bay, California.

FIG. 2A - C.-- *Pseudonitzschia australis* (= *Nitzschia pseudoseriata*) collected from Monterey Bay, California.

THE APPLICATION OF ENVIRONMENTAL SCANNING ELECTRON MICROSCOPY TO MARINE BIOLOGY

Richard Ray

Naval Research Laboratory
Stennis Space Center, MS 39529-5004

Preparation of marine biological material for standard scanning electron microscopy (SEM) requires extensive manipulation, including fixation, removal of salts, dehydration, and either air drying or critical-point drying because the SEM operates at high vacuum. Non-conducting samples including biological material must be coated with a conductive film of metal before the specimen can be imaged.

The Electroscan Corporation (Wilmington, MA) recently introduced a new development in SEM technology—the environmental scanning electron microscope (ESEM). This instrument uses a unique secondary electron detector capable of forming high resolution images at pressures in the range of 0.1 to 20 torr. If water vapor is used as the specimen environment, wet samples including wet biofilms can be observed directly. This paper illustrates the use of the ESEM to view bacteria, dinoflagellates, and diatoms on surfaces.

Biofilms on metal surfaces were fixed in 4% glutaraldehyde in filtered seawater, rinsed with distilled water to remove salts, and examined in the ESEM. Dinoflagellates and diatoms were fixed in the same manner and then stored in 70% alcohol. Organisms were collected with a pipette and imaged directly in a countersunk sample mount of the Peltier cooling device maintained at 4°C and imaged in an environment of water vapor at 2 to 6 torr to maintain samples in a hydrated state. Bacteria and other microorganisms were viewed directly with minimal sample preparation (Figures 1–6).

Acknowledgments

This work was supported by the Office of Naval Research, Program Element 61153N, through the NOARL Defense Research Sciences Program. NOARL Contribution Number PR92:067:333.

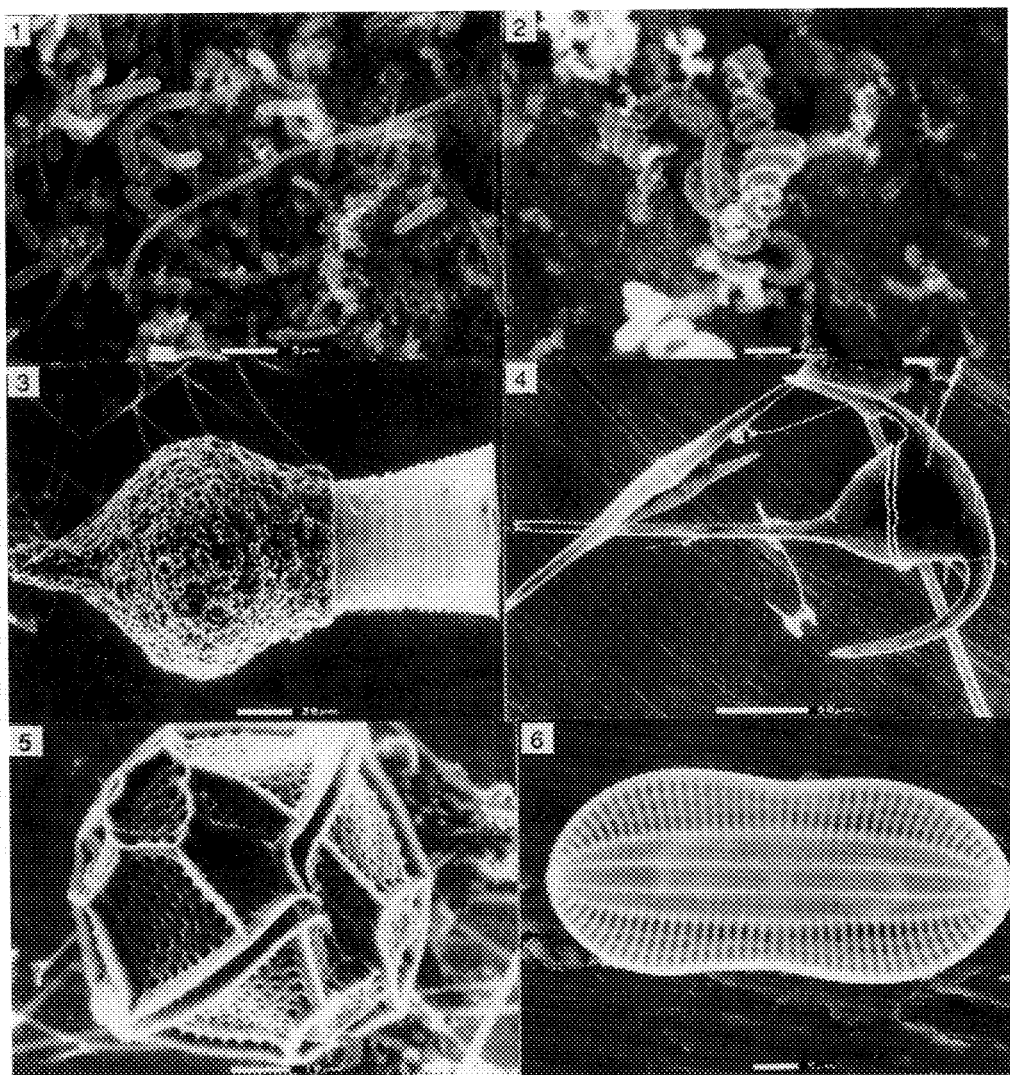


FIG. 1. — Bacteria on metal surface.
 FIG. 2. — Bacteria on metal surface.
 FIG. 3. — Tintinid from drop of seawater.
 FIG. 4. — Dinoflagellate from drop of seawater.
 FIG. 5. — Dinoflagellate from drop of seawater.
 FIG. 6. — Diatom from drop of seawater.

TIME-LAPSE X RAY MICROSCOPE MOVIE OF THE GERMINATING GARDEN PEA SEED

Sterling Newberry, J. A. Vozzo,* and Michael Marko**

CBI Labs, 11 S. Westcott Road, Schenectady NY 12306-9405

*USDA, Forestry Sciences Laboratory, P.O. Box 906, Starkville, MS 39759

**Biological Microscopy and Image Reconstruction Facility, Wadsworth Laboratories, New York State Dept. of Health, Empire State Plaza, Albany, NY 12201-0509

The plant embryo is relatively insensitive to x-rays.¹ One should like to take advantage of this property to follow the early processes of seed germination by time-lapse x-ray microscopy. Preliminary work has shown that radiation exposure can be reduced by two orders of magnitude if a minimum number of frames are exposed and the movie then generated by slowly dissolving one frame into the next.² Image processing also helps the problem of low contrast in the living image. Present work has been directed against the problem that geotropism makes the embryo grow out of the plane of the picture (the instrument does not operate horizontally). The approach taken should also simplify the problems of maintaining a suitable environment for the seed and make the instrument available between exposures when working with seeds which have long germination times. The garden pea was chosen as a test material because of its environmental tolerance, short maturation cycle, and similarity to pine seeds in size and radiation tolerance.

The removable, fixed position specimen stage is shown in Fig. 1. The seed is glued to a bar of silicon wafer using instant gel cement. It is then immersed in water for a presoak and rigidly located on the stage under a binocular microscope. Three legs, one spring loaded, are used to center the stage above the x-ray source. An alignment collar on the half frame camera back has notches which align the film with the stage. The unit is then rotated to align with the microscope camera housing. The camera is shown in place on the x-ray microscope in fig. 2. Between exposures the specimen was stored with the specimen plane vertical in a saturated water vapor chamber consisting of a covered glass dish with a layer of water on the bottom. With a presoak of 24 hrs. and 21°C ambient, it was not necessary to heat or stir the water to maintain growth. The environmental chamber is illustrated in fig. 3.

A total of 39 exposures were taken starting at 1 hr. intervals and ending with 15 min. intervals during a 24 hour period starting 4 hrs. after presoak. Subsequently the seed and its unirradiated control were potted in normal soil. The two plants are shown on their 24th day in fig. 4. Representative frames are shown in fig. 5. Time-lapse movies will be shown at the meeting.

Discussion of results:

Removing the seed between exposures is a practical solution to the enumerated problems. The simple alignment procedure is adequate for whole specimen field of view, i.e. low magnification. To attempt to show cell structure the specimen should be moved closer to the source thus giving higher magnification but correspondingly smaller field of view, perhaps only a growing root tip or root hairs encountering soil particles. Suitable artificial soils need to be developed. Perhaps carbon granules with thin layers of nutrients will suffice.

References

1. J. A. Vozzo, Materials Evaluation (1988)46, 1450.
2. S. P. Newberry, X-Ray Microscopy III, A. Michette Ed., Springer, in press.
3. This work has been supported in part by Biotechnology Resources grant RR 01219 to the Biological Microscopy and Image Reconstruction Facility.

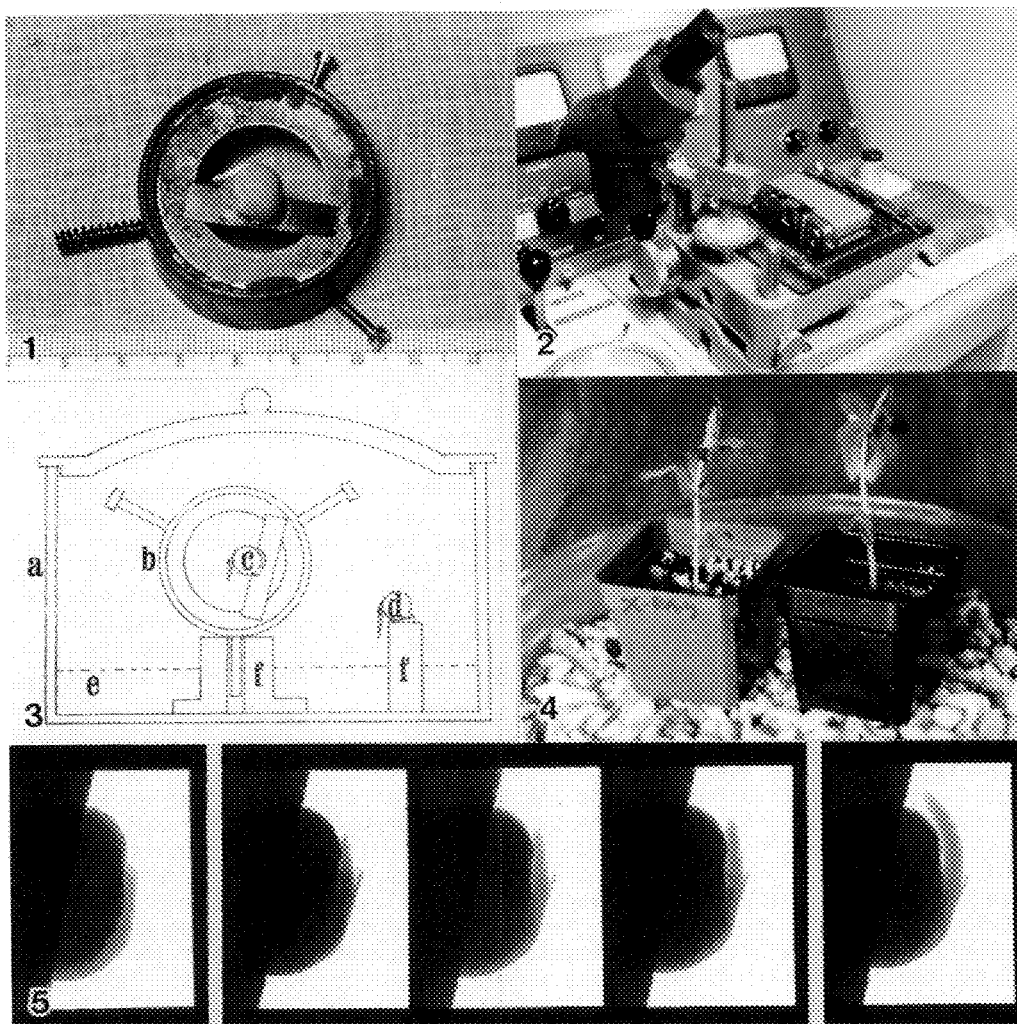


FIG. 1.--Specimen holder with germinating seed of garden pea. Note three legs for centering with x-ray target.

FIG. 2.--Camera in place on X-Ray Microscope. Lead cover removed to show camera. Specimen holder is hidden inside camera. Stereo Microscope for optical inspection of sample and checking field of view.

FIG. 3.--Sketch illustrating the mounting of sample holder in the environmental chamber for storage between exposures. Covered dish, a; spec. stage, b; sample, c; control, d; water, e; and stainless supports, f. Also note the specimen is above water level.

FIG. 4.--Growing plants from tested seeds at day 24, irradiated on left, unirradiated on right.

FIG. 5.--Samples from the time-lapse series. First frame, 3 consecutive frames, and last frame.

CUTICULAR PENETRATION OF *SESBANIA EXALTATA* STEM TISSUE BY PENETRATION PEGS FROM APPRESSORIA OF THE PLANT PATHOGENIC FUNGUS: *COLLETOTRICHUM TRUNCATUM*

R. N. Paul and G. H. Egley

U.S.D.A./A.R.S., Southern Weed Science Laboratory, Stoneville, MS 38776

Colletotrichum truncatum is a potentially useful pathogen for the biocontrol of the weed *Sesbania exaltata* [(Raf.) Cory]. Information on the infection process is important in optimizing the use of this pathogen as a mycoherbicide. Successful infection of a host species depends upon the fungus' ability to penetrate the plant's defenses. Some fungi bypass the host plant cuticle by invading through stomates or other openings on the epithelial surface. *Colletotrichum* is capable of breaching the cuticle by means of a penetration peg¹ produced from an appressorium. We investigated this process by examining *S. exaltata* stem tissue 24h after inoculation.

Young *S. exaltata* plants were inoculated by hand with an aqueous suspension (4×10^6 /ml) of conidia. After 24 h, infected regions, as marked on the stem, were fixed in 4% (v/v) glutaraldehyde and post-fixed in 1% (w/v) OsO₄. Following the 70% (v/v) stage in a graded acetone dehydration series, the tissues were incubated in 1% (w/v) p-phenylenediamine (PPD) in 70% acetone, to provide enhanced lipid retention^{2,3}. After sectioning, the Spurr-embedded tissues were observed both stained and unstained in a TEM. Some samples, quench-frozen in liquid nitrogen, were observed and photographed on a cold stage in an SEM.

Germ tubes of *Colletotrichum* often grew only a few microns before forming appressoria over the junction between two epithelial cells (Fig.1). A cross section of an appressorium early in the process of cuticle penetration is shown in Fig. 2. An insipient penetration peg (PP) is seen closely appressed to the host cuticle. Vesicles seen in close association with the peg appear to be continuous with an extensive smooth ER (SER) which may have a transport function in the cuticular attack apparatus. No collar, as described in⁴, is obvious. At higher magnification, this same section, and a section about 0.3µm distant, show evidence of enzymatic attack on the cuticle in the form of osmiophilic striations preceeding a dome of osmiophilic material. This may be a lipidic cuticle breakdown product preserved by PPD. An apparently later stage in penetration is seen in Fig.5. Dense material (arrows) is still seen in close proximity to the severed cuticle edges (Cu). An SER is visible. The hypha, projecting through the cuticular opening, appears to be attacking the middle lamella.

1. C.G. Van Dyke and C.W. Mims. Can J. Bot. 69(1991) 2455.
2. J.M. Ledingham and F.O. Simpson. Stain Technol. 47(1972) 239.
3. R.N. Paul and C.G. McWhorter. Proc. EMSA(1990) 676.
4. G.E. Brown. Phytopathology. 67(1977) 315.

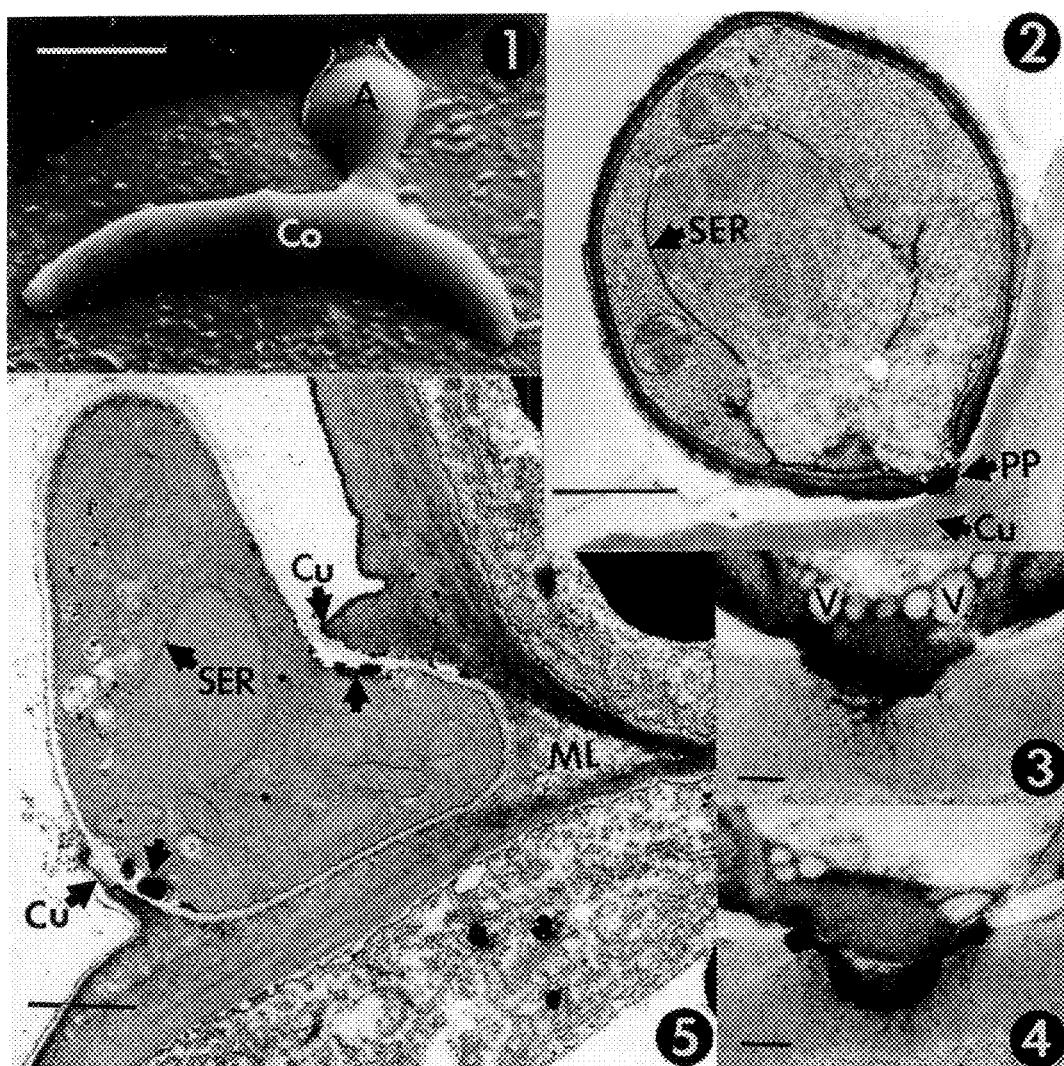


FIG. 1.--Cryo-SEM of conidium (Co) with appressorium (A). Bar = $5\mu\text{m}$.

FIG. 2.--TEM of appressorium showing early stage of cuticular penetration. An SER, separating two distinct cytoplasmic regions, appears continuous with vesicles associated with the penetration peg (PP). Cu = cuticle. Bar = $1\mu\text{m}$.

FIG. 3.--Higher magnification of peg from Fig. 2. Note the large vesicles (V) at the top of the structure, and the dense osmiophilic mass at the point of cuticular penetration. Dense osmiophilic checkering of the cuticle may be evidence of cutinase activity. Bar = $0.1\mu\text{m}$.

FIG. 4.--TEM of peg in section about $0.3\mu\text{m}$ from that observed in Fig. 3. This appears to be the center of the peg. Note the dome of osmiophilic material. The host cuticle is half penetrated. Bar = $0.1\mu\text{m}$.

FIG. 5.--TEM of appressorium with beginning hyphal growth. Cuticular penetration is complete. Osmiophilic masses within the appressorial cell wall (arrows), may be the product of cutinase activity. Bar = $1\mu\text{m}$.

EFFECT OF ACID DEPOSITION ON TRICHOME MORPHOLOGY AND DOGWOOD ANTHRACNOSE BIOLOGY

Kyle T. Thornham, R. Jay Stipes and Randolph L. Grayson

Department of Plant Pathology, Physiology and Weed Science, and
College of Agriculture and Life Sciences EM Facility,
Virginia Tech (VPI&SU), Blacksburg, VA 24061-0331

Dogwood anthracnose, caused by *Discula destructiva* (1), is another new catastrophic tree disease that has ravaged natural populations of the flowering dogwood (*Cornus florida*) in the Appalachians over the past 15 years, and the epidemic is prognosticated to continue (2). An estimated 9.5 million acres have been affected, primarily in the Appalachian Mountains, from VA southwards, alone, and an estimated 50% of all dogwoods in PA have been killed. Since acid deposition has been linked experimentally with disease induction, and since the disease incidence and severity are more pronounced at higher elevations where lower pH precipitation events occur, we investigated the effect of acidic foliar sprays on morphologic changes in the foliar cuticle and trichomes (3), the initial sites of infection and foci of *Discula* sporulation.

Individual 3-mo-old greenhouse-grown plants were sprayed daily with HCl-acidified distilled water at pHs of 1-7 for 7 days. Cork borer disk samples were harvested prior to treatment, and daily thereafter for 7 days. Samples were fixed in 4% glutaraldehyde, then in OsO₄, dehydrated in an ethanol series, critical point dried, sputter coated with Au/Pd and viewed with a Phillips 505 SEM. Micrographs were processed from Polaroid Type 55 film.

Samples from leaves treated with highly acidic solutions (pH 1-4) displayed desiccated trichomes from their tips to their bases (Figs. 2,4), whereas samples treated at pH 5 caused some trichomes to deteriorate and become similar to trichomes given low pH treatments. In essence, treatments at pH 5 show cumulative effects and appear to represent a transitional interface for acidic environments. Exposures at pHs 6 and 7 produced no observable abnormal effects (Figs. 1,3). This trichome shrinkage and accompanying tissue damage (Fig. 4) might facilitate nutrient metabolite leakage and a site for entry of germinating fungal spores. In summary the injury site represents an infection court for *Discula*.

References

1. S. C. Redlin, Mycologia 83:633-642, 1991.
2. C. R. Hibben & M. L. Daughtrey, Plant Disease 72:199-203, 1988.
3. S. C. Redlin, Phytopathology 80:1066, 1990.
4. Special thanks are expressed to Ms. Jean L. Ratliff for assistance.

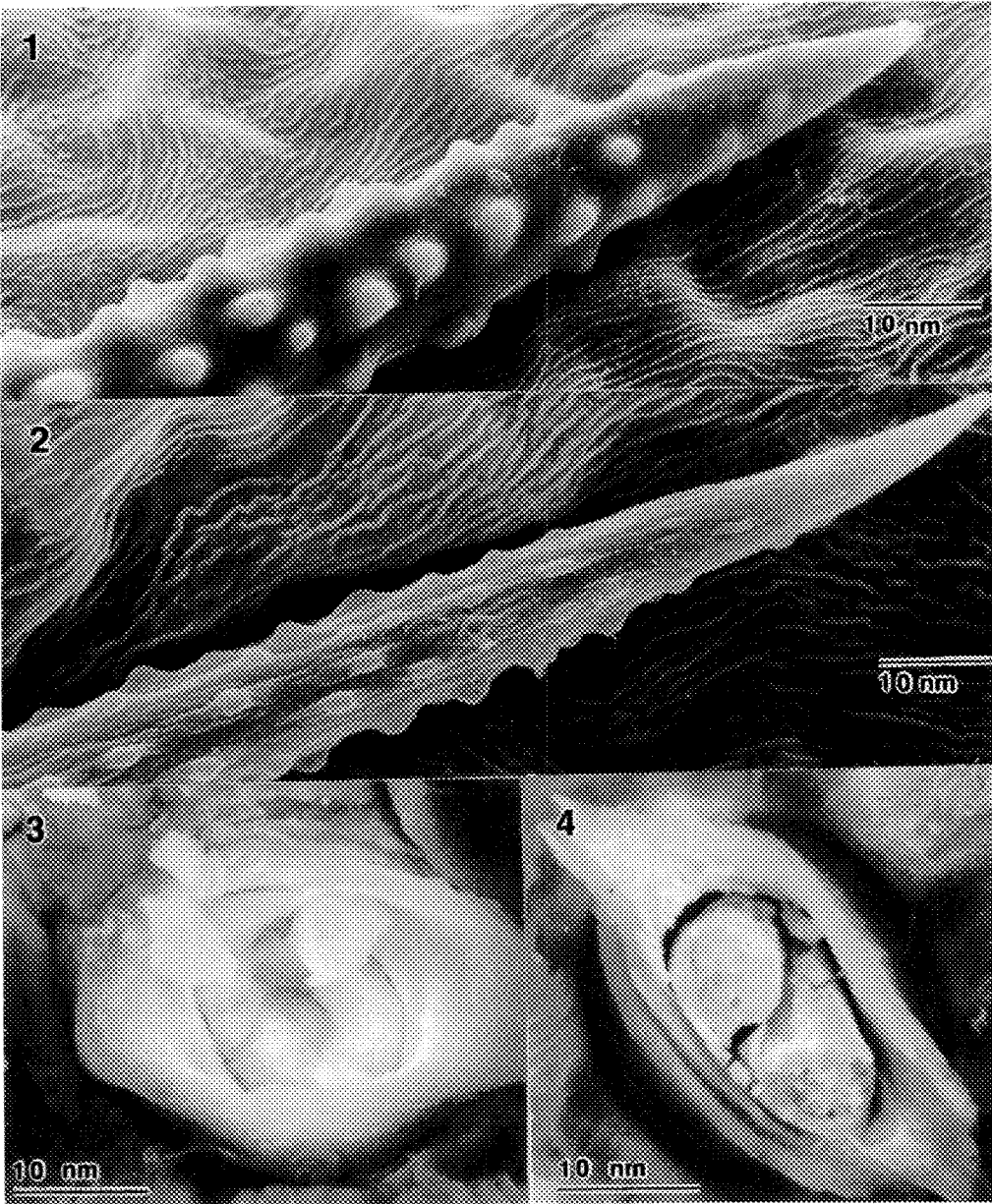


Fig. 1. Trichome, pH 7, exposure day 5.
Fig. 2. Trichome, pH 3, exposure day 2.
Fig. 3. Trichome base, pH 7, exposure day 5.
Fig. 4. Trichome base, pH 2, exposure day 2.

AN INVESTIGATION INTO THE ULTRASTRUCTURE AND HISTOCHEMISTRY OF GLANDULAR TRICHOMES OF JOHNSONGRASS [*Sorghum halepense* (L.) Pers.] LEAVES

R. N. Paul, C. G. McWhorter, and J. C. Ouzts

USDA/ARS P.O. Box 350, Stoneville, MS 38776

Secretory trichomes have been described on johnsongrass leaves previously, but there is little knowledge of their ultrastructure or the nature of their secretion. Since johnsongrass is a pernicious weed, there is much interest in the nature of compounds found on its foliar surface, and the possible effect of these extrusions on herbicide efficiency. This report describes the results of an investigation into the ultrastructure of the secretory apparatus, and into the nature of the secretion.

Tissue was collected from growth chamber grown johnsongrass, ranging in height from 30-60 cm, with 5-10 true leaves. Leaf samples were taken from along the apex of fully expanded 5th - 8th true leaves. SEM and TEM were performed as described previously¹. Unsectioned leaf segments were stained using several standard histochemical techniques, fastened to glass slides using two-way stick tape and observed and photographed with a Nikon Labophot-2 light microscope using an epi-Nomarski attachment.

A CryoSEM of a secretory trichome from a young leaf is shown in Fig. 1. The amount of secretion varies with leaf age, humidity, etc. but appears to be consistent among trichomes along the same row on the leaf surface. Sections observed by TEM reveal the basal cell (Figs. 2,3, BC) to be thick-walled with dense cytoplasm, presumably as the result of its secretory function. The cap cell (CC), even in very young (rolled) leaves, appears to be little more than an extension of the basal cell cuticle. Cytoplasmic debris, including membranes and organelles, is sometimes seen inside the cap cell (Figs. 3,4). The wall common to both the basal cell and cap cell contains numerous large plasmodesmata (Fig. 3. arrows, inset). A dense plug at the tip of the cap cell (Fig. 4), was often found to have different staining characteristics than the secretion. This plug is absent in the trichome in Fig. 2.

Results of LM (Figs. 5-10) showed overall trichome staining from both adaxial and abaxial leaf surfaces to be consistent. The two cell types within a trichome (basal and cap), did possess different staining characteristics. The basal cell usually did not stain at all, probably because of poor stain penetration. Cap cells stained positively for lipid (Figs. 6,7), protein (Figs. 8,9), and polysaccharide (Fig. 10), and negatively for pectin, polyphenols, steroids and alkaloids. The secretion itself only stained positively for callose and carbohydrate. This is contrary the results obtained by² in investigating the secretions of representatives of several subfamilies, including other members of the johnsongrass subfamily (Panicoideae). They found that all trichomes secrete protein and pectin but not callose. It is possible that secretion was removed during some of the more drastic staining procedures leading to false negative results.

References

1. R. N. Paul and C. G. McWhorter. Proc EMSA (1990) 676.
2. V. Amarasinghe. Protoplasma (1990) 156, 45.

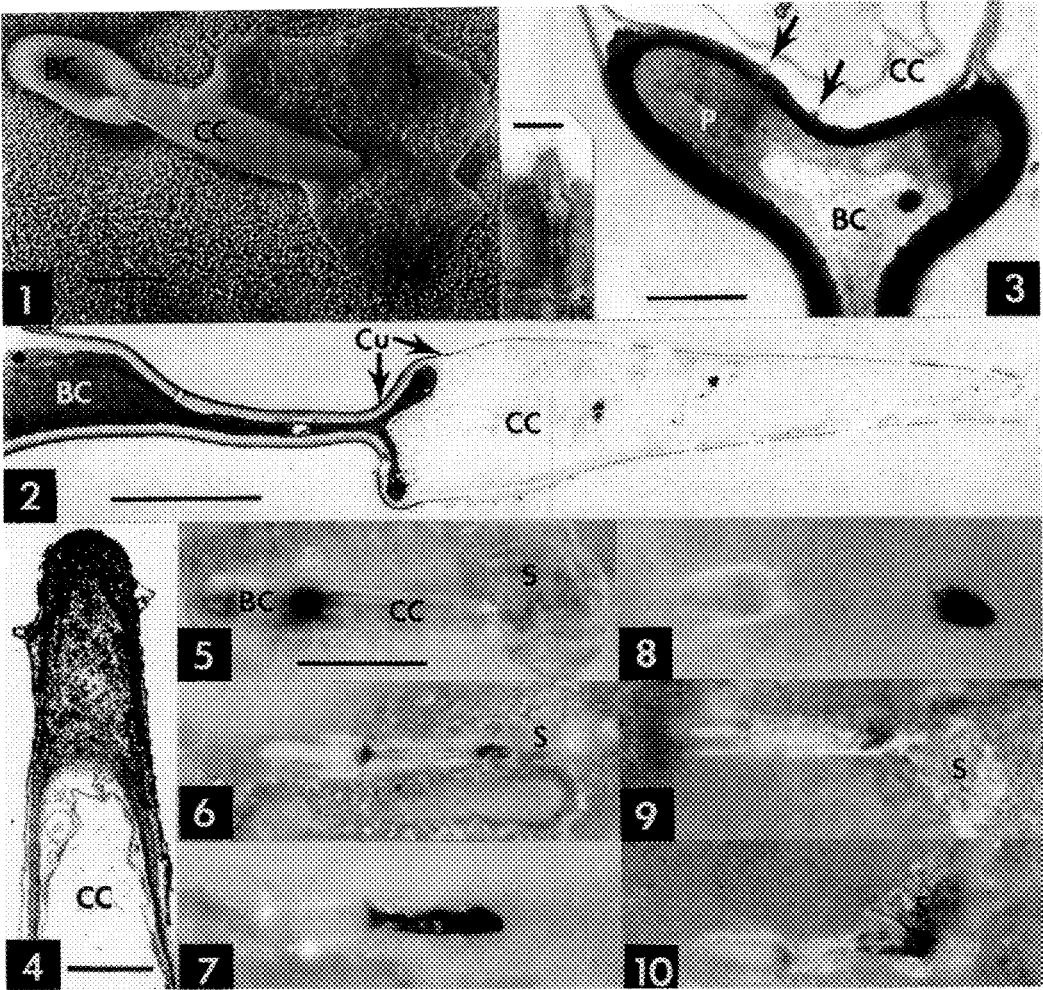


FIG. 1--- CryoSEM of secretory trichome. BC = basal cell; CC = cap cell; S = secretory product. Bar = 10 μ m.

FIG. 2--- TEM of entire glandular trichome. Cu = cuticle. Bar = 5 μ m.

FIG. 3--- TEM of junction of basal cell and cap cell. Arrows denote positions of plasmodesmata. P = plastid. Bar = 1 μ m. INSET: High magnification of plasmodesmata. Bar = 0.1 μ m.

FIG. 4--- TEM of dense plug in tip of some trichomes. Bar = 1 μ m.

FIG. 5--- LM of trichome stained with toluidine blue. An unstained secretion is resolved. Bar = 25 μ m for Figs. 5 - 10.

FIG. 6--- LM of Sudan IV for lipids.

FIG. 7--- LM of Nile blue for lipids.

FIG. 8--- LM of mercuric bromophenol blue for proteins.

FIG. 9--- LM of Coomassie brilliant blue for protein.

FIG. 10---LM of PAS stain for polysaccharides.

ULTRASTRUCTURE AND SENESCENCE IN AN ACHLOROPLASTIC MUTANT OF *Hordeum vulgare* L. cv. Dyan

R.H.M. Cross*, C.E.J. Botha**, A.K. Cowan**, and B.J. Hartley**

Electron Microscopy Unit* and Department of Botany** Rhodes University, Grahamstown, South Africa

Senescence is an ordered degenerative process leading to death of individual cells, organs and organisms. The detection of a conditional lethal mutant (achloroplastic) of *Hordeum vulgare*¹ has enabled us to investigate ultrastructural changes occurring in leaf tissue during foliar senescence.

Examination of the tonoplast structure in six and 14 day-old mutant tissue revealed a progressive degeneration and disappearance of the membrane, apparently starting by day six in the vicinity of the mitochondria associated with the degenerating proplastid (Fig. 1.) where neither of the plastid membrane leaflets is evident (arrows, Fig. 1.). At this stage there was evidence that the mitochondrial membranes were undergoing retrogressive changes, coupled with disorganization of cristae (Fig. 2.). Proplastids (P) lack definitive prolamellar bodies. The cytoplasmic matrix is largely agranular, with few endoplasmic reticulum (ER) cisternae or polyribosomal aggregates. Interestingly, large numbers of actively-budding dictyosomes, associated with pinocytotic vesicles, were observed in close proximity to the plasmalemma of mesophyll cells (Fig. 3.). By day 14 however, mesophyll cells showed almost complete breakdown of subcellular organelle structure (Fig. 4.), and further evidence for the breakdown of the tonoplast. The final stage of senescence is characterized by the solubilization of the cell wall due to expression and activity of polygalacturonase and/or cellulose.² The presence of dictyosomes with associated pinocytotic vesicles formed from the mature face, in close proximity to both the plasmalemma and the cell wall, would appear to support the model proposed by Christopherson for the secretion of cellulase. This pathway of synthesis is typical for secretory glycoproteins.

The results presented therefore indicate an ordered sequence of events leading to gross degeneration of cellular integrity. These events appear to commence with loss of tonoplast structural integrity, followed by degeneration of plastids and associated mitochondria, and culminate in the breakdown of the plasmalemma and solubilization of the cell wall.

References

1. C.E.J. Botha, A.K. Cowan, R.H.M. Cross and B.J. Hartley. Proc. E.M. Soc. SA (1991) 21: 75-76.
2. R.E. Christopherson *Plant Senescence: It's Biochemistry And Physiology*. eds. W.W. Thomson, E.A. Nothnagel and R.C. Huffaker (1987) ASP, 89.

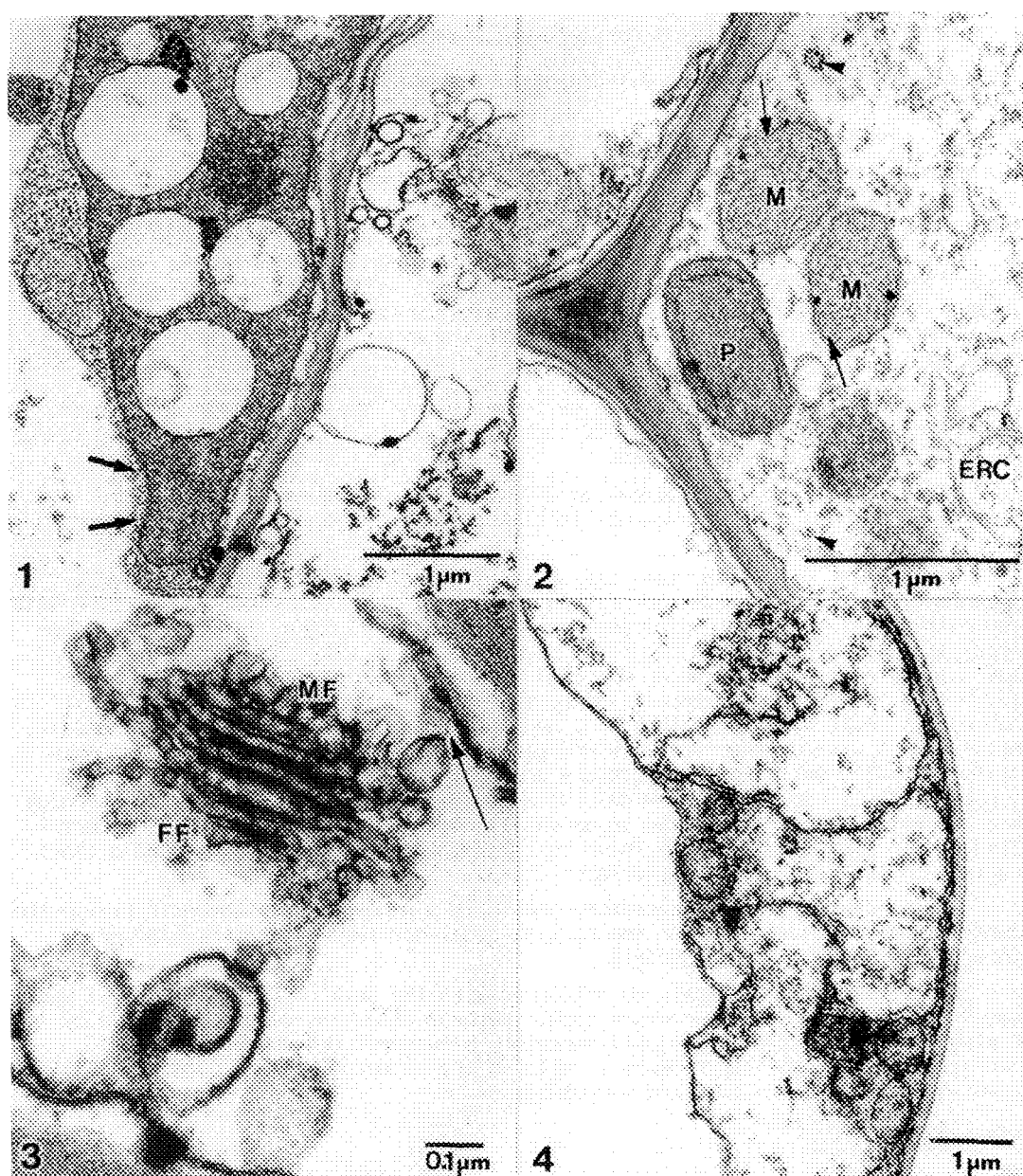


Fig. 1. A highly vesiculate, osmiophilic-globule- containing degenerating plastid, of six-day mutant mesophyll cell.
 Fig. 2. Detail from 6 day-old mutant cell showing mitochondria (M), with disorganised, imperfect membranes (unlabelled arrows). Proplastid (P), agranular cytoplasmic matrix, with few ER cisternae, (ERC) and polyribosome aggregates (arrowheads).
 Fig. 3. Detail of 6 day-old mutant mesophyll cell. Dictyosome has clearly-defined forming face (FF) and mature face (MF). Note pinocytotic fusion of vesicles with plasmalemma (arrow).
 Fig. 4. Detail from 14 day-old mutant mesophyll cell, showing almost complete breakdown of cytoplasmic material.

THE LEAF MESOPHYLL OF COYOTILLO (*Karwinskia humboldtiana* Zucc.) MORPHOLOGICAL CHARACTERIZATION

J. Ruiz Ordóñez*, T.E. Torres Cepeda**, A. Piñeyro López*

Histology Department, Farmacology-Toxicology Department, Facultad de Medicina*, U.A.N.L., Monterrey, N.L., México 68000. Facultad de Ciencias Biológicas**, U.A.N.L. Monterrey, N.L., México, 68000

Karwinskia humboldtiana, a semi arid shrub of México known by the common names coyotillo or tullidora produces several toxins (1) with high toxicity against humans (2) and ruminants (3). These toxins are present in different organs of the plant (4,5). In relation to morphology, with the exception of the histological study of Lux and Earl (6), we have little information applicable in defining what kind of tissue, internal secretory structures or cells are involved in the production, storing or distribution of these toxins. The aim of this work is to offer some structural description of coyotillo mesophyll especially the features of the internal secretory structures,

Fresh leaves in physiological mature stage were obtained from the field, and processed by routine techniques of light microscopy and transmission and scanning electron microscopy.

Under light microscopy the leaf in longitudinal section displays palisade parenchyme formed by single row of long, pyramidal cells and spongy parenchyme with roundish cells. The most conspicuous structure in this area is a secretory nodule occupying almost the entire height of mesophyll. This nodule is formed by basophyllic cells and amorphous material surrounded by a double-flattened cell layer (fig.1). Ultrastructural examination shows the palisade and spongy parenchyme cells with a small central nucleus, abundant vacuoles and mitochondria, chloroplasts with grains of starch and plastoglobuli, generally aligned along a thin cell wall, while in the secretory nodule the flattened cells show large vacuoles, small nucleus and few chloroplasts. Here the basophyllic cells have high electrodensity and are immersed in an until now, unidentifiable amorphous material (fig.2). In high magnification these cells show abundant mitochondria and a small nucleus inside a very dense cytoplasm (fig.3).

At third dimension the secretory nodule is a wide cavity with cells lining the duct (fig.4). The mid vein, on the abaxial side, has three different kind of internal secretory structures (fig.5)

Our findings have certain coincidences with the work of Lux and Earl (6) who named this structure the secretory canal, perhaps after the description made by Curtis and Lersten (7) in the oily secretory structures present in *Hypericum perforatum*. The high electrodensity cells in the secretory nodule have not been reported previously in electron microscopy.

REFERENCES:

- 1.- Dreyer, D. et al., J. Am. Chem. Soc., 97 (1975) 4986.
- 2.- Padron Payou, F., Gaceta Médica de México 81 (1951) 299.
- 3.- Charlton, et al., Am. J. Vet. Res. 31 (1971) 1381.
- 4.- Clavijero, F.J., Ed. Porrúa México (1982) 31-32.
- 5.- Domínguez X. et al., Rev. Latinoamer. Quim. 7 (1976) 46.
- 6.- Lux, A., Earl, P.R., Pub. Biol. U.A.N.L., México 3 (1989) 83.
- 7.- Curtis, J.D., Lersten, N.R., New Phytol. 114 (1990) 579.

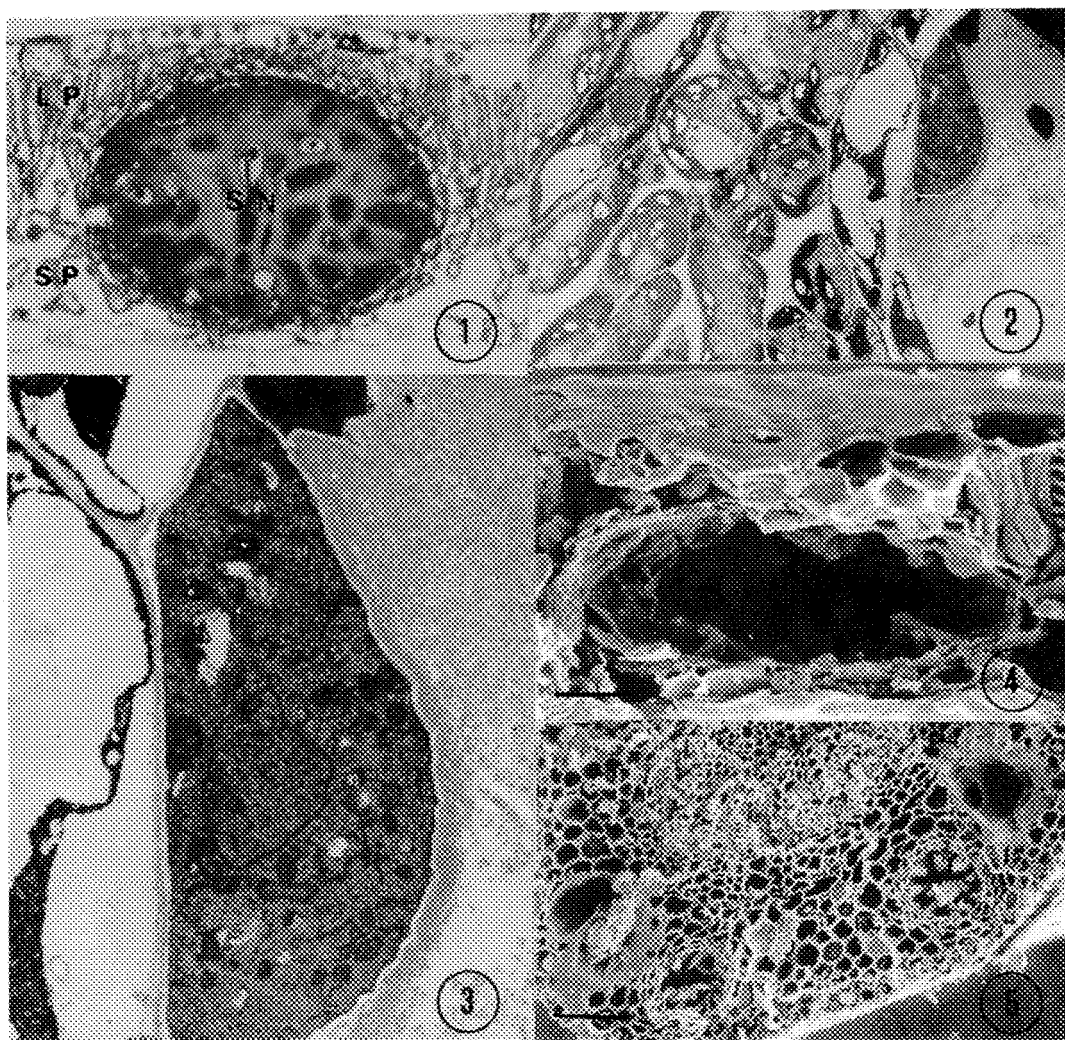


Fig. 1 Light microscopy image of leaf mesophyll and secretory nodule. Long palisade cells (LP), Spongy parenchyme (SP), Secretory nodule (SN). 120X

Fig. 2 Transmission electron micrograph showing the palisade cells, spongy cells and secretory nodule. 2,700X

Fig. 3 Higher magnification image of high electrodensity cell. 8,800X

Fig. 4 Scanning electron micrograph of secretory nodule. Bar=20 μ m

Fig. 5 Scanning electron micrograph of mid vein secretory nodules. Bar=50 μ m

GENERATIVE CELL MITOSIS IN POLLEN TUBES OF *NICOTIANA TABACUM*: ULTRASTRUCTURE AND THREE-DIMENSIONAL RECONSTRUCTION

Hong-Shi Yu and S. D. Russell

Department of Botany and Microbiology, University of Oklahoma, Norman, OK 73019

In bicellular pollen, the two sperm cells are formed by mitotic division of the generative cell (GC) in the pollen tube. This division is characterized by several unique features, including: lack of a pre-prophase band (PPB), absence of a metaphase plate, absence of normal spindle formation, and irregular patterns of cytokinesis.¹ Purportedly, this is the result of spatial constraints within the pollen tube,^{2,3} which *in vivo* may be as narrow as 3 μm (as in *Nicotiana*) and slightly wider *in vitro*. Immunofluorescence studies of GC mitosis have been published in the last five years²⁻⁷, but only one incomplete ultrastructural report on GC division *in vitro* is available.⁸ This study is the first using three-dimensional (3-D) techniques to reconstruct the mitotic apparatus of the GC *in vivo*.

Tobacco flowers (*Nicotiana tabacum* L.) were hand pollinated. Eight to 9.5 h later, 1 mm long stylar segments were collected and fixed using 3% glutaraldehyde in a 0.1 M cacodylate 0.1 M sucrose buffer (5 h at RT), followed by 1% buffered OsO_4 overnight at 4°C. After routine processing, serial longitudinal sections about 100 nm thick were cut and collected on Formvar-coated slot grids. Twenty GCs and pairs of sperm cells at different stages of division were reconstructed using an IBM AT computer with the Colorado HVEM "3-D Reconstruction Software".

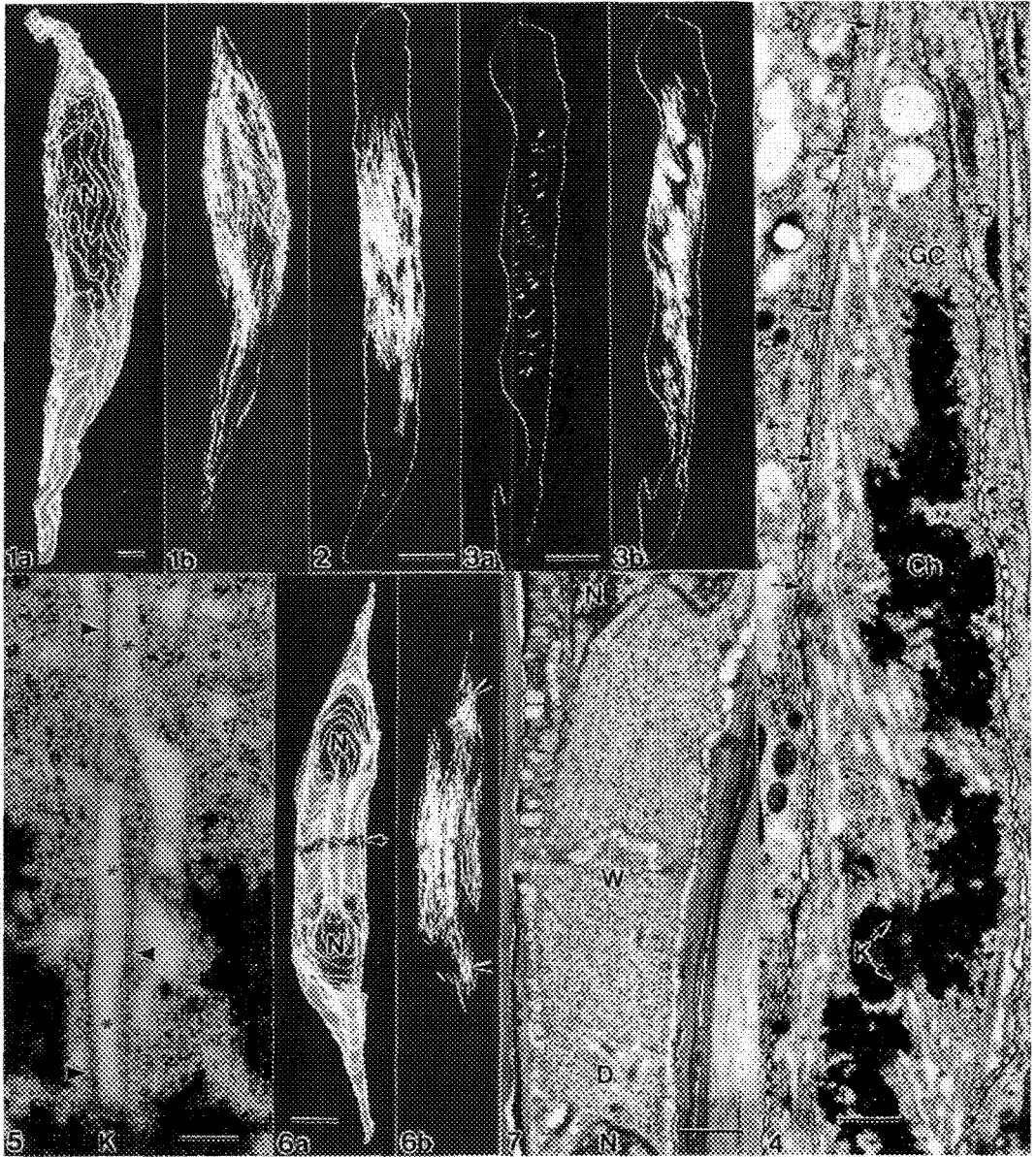
The GC at interphase is elongated and contains a basket-shaped system of microtubules (MTs), consisting of bundles and single MTs (Fig. 1). As the GC enters prophase, cortical MTs decrease and the mitotic apparatus begins to form in the nuclear region. By late prophase, kinetochores become linked with dense bundles of MTs in the region occupied by the former nucleus (Fig. 2). No PPB of MTs forms prior to prophase, unlike most higher plant cells.

In tobacco, the 21 pairs of kinetochores are distributed unevenly at intervals along the long axis of the GC (Fig. 3a). No traditional metaphase plate is organized. The unique metaphase spindle consists of two superbundles of opposite polarities from which kinetochore bundles branch (Figs. 3b, 4). Both kinetochore and non-kinetochore fibers are intimately and extensively associated with tubular ER in the mitotic apparatus (Figs. 4, 5), presumably providing anchorage and a calcium environment crucial for MT dynamics⁹. The mitotic poles are indistinct. During anaphase, kinetochore fibers shorten and superbundles separate, moving the two sets of chromosomes apart.

During early telophase, a dramatic increase in MTs occurs between the two resulting nuclei, suggesting *de novo* polymerization of interzonal fibers forming the phragmoplast (Fig. 6). Cytokinesis is completed by typical cell plate formation (Fig. 7).¹⁰

References

1. B. A. Palevitz and A. Tiezzi, Int. Rev. Cytol. (in press).
2. B. A. Palevitz and M. Cresti, Protoplasma 150(1989)54.
3. O. Terasaka and T. Niitsu, Bot. Mag. (Tokyo) 102(1989)143.
4. M. Raudaskowski et al., Biol. Cell 61(1987)177.
5. P. Taylor et al., Sex. Plant Reprod. 2(1989)254.
6. B. A. Palevitz, Protoplasma 157(1990)120.
7. B. Liu and B. A. Palevitz, J. Cell Sci. 98(1991)475.
8. J. Burgess, Planta 95(1970)72.
9. D. A. Callaham and P. K. Hepler, in G. McCormack and P. H. Cobbald, Eds., Cellular Calcium: a Practical Approach, Oxford: Oxford University Press (1991)383.
10. This research was supported by USDA NRICGP grant 91-37304-6471.



Abbr.: *Ch* chromosome; *D* dictyosome; *GC* generative cell; *K* kinetochore; *N* nucleus; *W* cell wall.
 FIG. 1--3-D reconstructions of GC in *N. tabacum* at interphase. a. GC; b. MT system. Bar = 2 μm .
 FIG. 2--3-D reconstruction of kinetochore bundle formation during late prophase. Bar = 5 μm .
 FIG. 3--3-D reconstructions of metaphase GC. a. Kinetochores; b. Metaphase spindle. Bar = 5 μm .
 FIG. 4--TEM micrograph illustrating one GC superbundle (arrows) at metaphase. Bar = 1 μm .
 FIG. 5--TEM micrograph of MTs (arrowheads) and associated ER (asterisks). Bar = 0.3 μm .
 FIG. 6--3-D reconstructions of early telophase. a. Nascent sperm cells with crosswall (arrow). b. Interzonal MT fibers form phragmoplast; spindle remnants at pole (arrowheads). Bar = 5 μm .
 FIG. 7--TEM micrograph showing crosswall separating two sperm nuclei at telophase. Bar = 1 μm .

CORRELATIVE SEM, FREEZE-FRACTURE, AND LASER SCANNING MICROSCOPY OF *TILLETIA CONTROVERSA* TELIOSPORE SHEATH MORPHOLOGY

Kimberly A. Rowe, John S. Gardner, and W. M. Hess

Department of Botany and Range Science, 401 WIDB, Brigham Young University, Provo, UT 84602

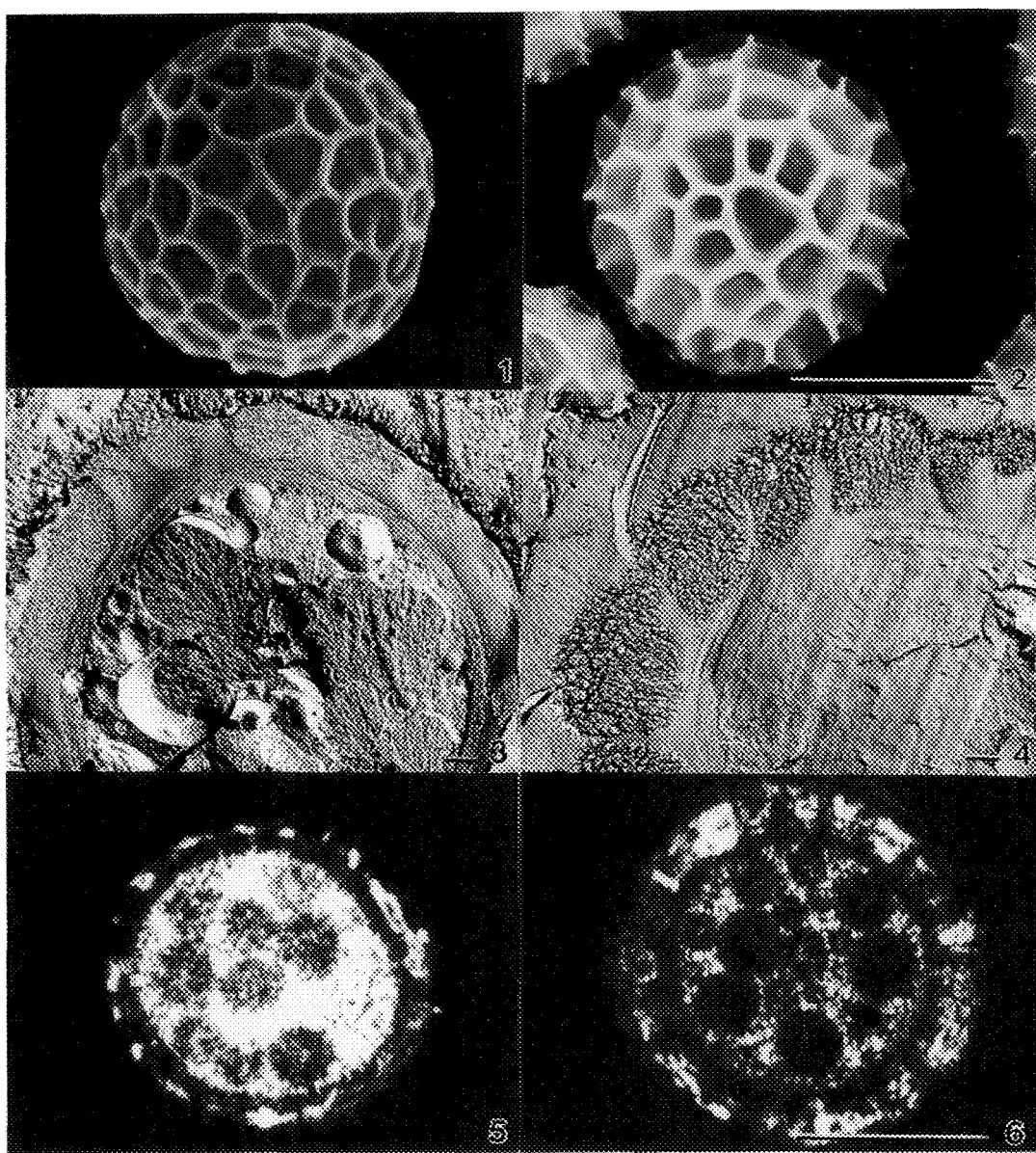
The bunts of wheat are infected by *Tilletia* which have teliospores with complex multilayered walls¹. The outer layer or sheath of *Tilletia controversa* teliospores is difficult to characterize unless it is hydrated². The morphology of the sheath has been characterized with freeze-fracture¹, thin sectioning^{1,3} and SEM⁴ studies. By using specialized, time-consuming thin-sectioning specimen preparation procedures the sheath can be a factor in distinguishing *T. caries* and *T. controversa* teliospores⁴. Distinguishing the species is important for marketing wheat⁵. The purpose of these investigations was to develop better methods to characterize the sheath which will help to distinguish teliospores of these two species and races of *Tilletia* much more easily and quickly.

For SEM studies teliospore samples were hydrated in either distilled water or 2% potassium hydroxide (KOH) for 8 hrs. Spores were then frozen in liquid nitrogen or and freeze-dried under high vacuum. The spores were coated with 15 nm of gold before examination. For freeze-fracture studies teliospores were hydrated either in distilled water or 2% KOH for 8 hrs. Spores were then frozen in liquid freon for processing. Freeze-fracture replicas were examined with TEM. For laser scanning microscopy (LSM) studies teliospores were processed as described above for SEM except that after freeze-drying they were placed in immersion oil on microscope slides before examination with LSM with an argon laser at 488 nm. At 20 kV sheaths were penetrated by electrons from the SEM so only the underlying pattern of the exospore wall was visualized (Fig. 1). When spores were treated with KOH the sheaths were more easily visualized because the sheaths were expanded (Fig. 2). The differences were even more evident with freeze-fracture (Figs. 3-4). With LSM the differences were also evident (Figs. 5-6).

These observations demonstrate that KOH treatment of *T. controversa* teliospores caused the sheaths to expand more than with standard hydration⁶. With critical point drying the differences were not evident as sheaths collapsed during processing. Therefore, it is necessary to freeze-dry specimens to visualize these differences. The use of KOH for teliospore sheath expansion will make it possible to characterize morphological races of *Tilletia* teliospores more quickly.

References

1. W. M. Hess, Perspectives in Plant Pathology, Today & Tomorrow's Printers and Publishers, New Delhi, (1989), 467.
2. J. S. Gardner, J. V. Allen, and W. M. Hess, Mycologia (1983), 75, 333.
3. W. M. Hess and E. J. Trione, Plant Disease (1986), 70, 458.
4. J. S. Gardner and W. M. Hess, Proc. XIth Int. Cong. Elect. Mic. (1990), 706.
5. E. J. Trione and M. J. Hall, Agron. J. (1986), 78, 148.
6. S.O. Graham, Mycologia (1959), 51, 477.



Figs. 1-2. Scanning electron micrograph of *T. controversa* teliospores. Fig. 1. Hydrated with distilled water, frozen in liquid nitrogen, and freeze-dried. Fig. 2. KOH treated, frozen in liquid nitrogen, and freeze-dried. Bar = 10 μ m.

Figs. 3-4. Transmission electron micrographs of freeze-fracture replicas of *T. controversa* teliospores. Fig. 3. Hydrated with distilled water, frozen in liquid freon then fractured. Fig. 4. KOH treated, frozen in liquid freon then fractured. Bars = 1 μ m.

Figs. 5-6. Laser scanning micrographs of *T. controversa* teliospores. Fig. 5. Hydrated with distilled water, freeze-dried, mounted in immersion oil. Fig. 6. KOH treated, freeze dried, mounted in immersion oil. Bar = 10 μ m.

PLANTS IN RESPONSE TO COPPER TOXICITY

Ching-Chiann Tsay, Yu-Fen Huang, Li-Wen Wang and Yung-Reui Chen

Department of Botany, National Taiwan Univ., Taipei, Taiwan, ROC

Plant response to heavy metal in soil varies with plant species, their developmental stages and the ways of pollution^{1,2}. Plants seedlings studied by morphological and biochemical markers through hydroponic culture can provide a way for screening Cu-tolerant plants which are potential plants for removing copper from Cu-polluted soil.

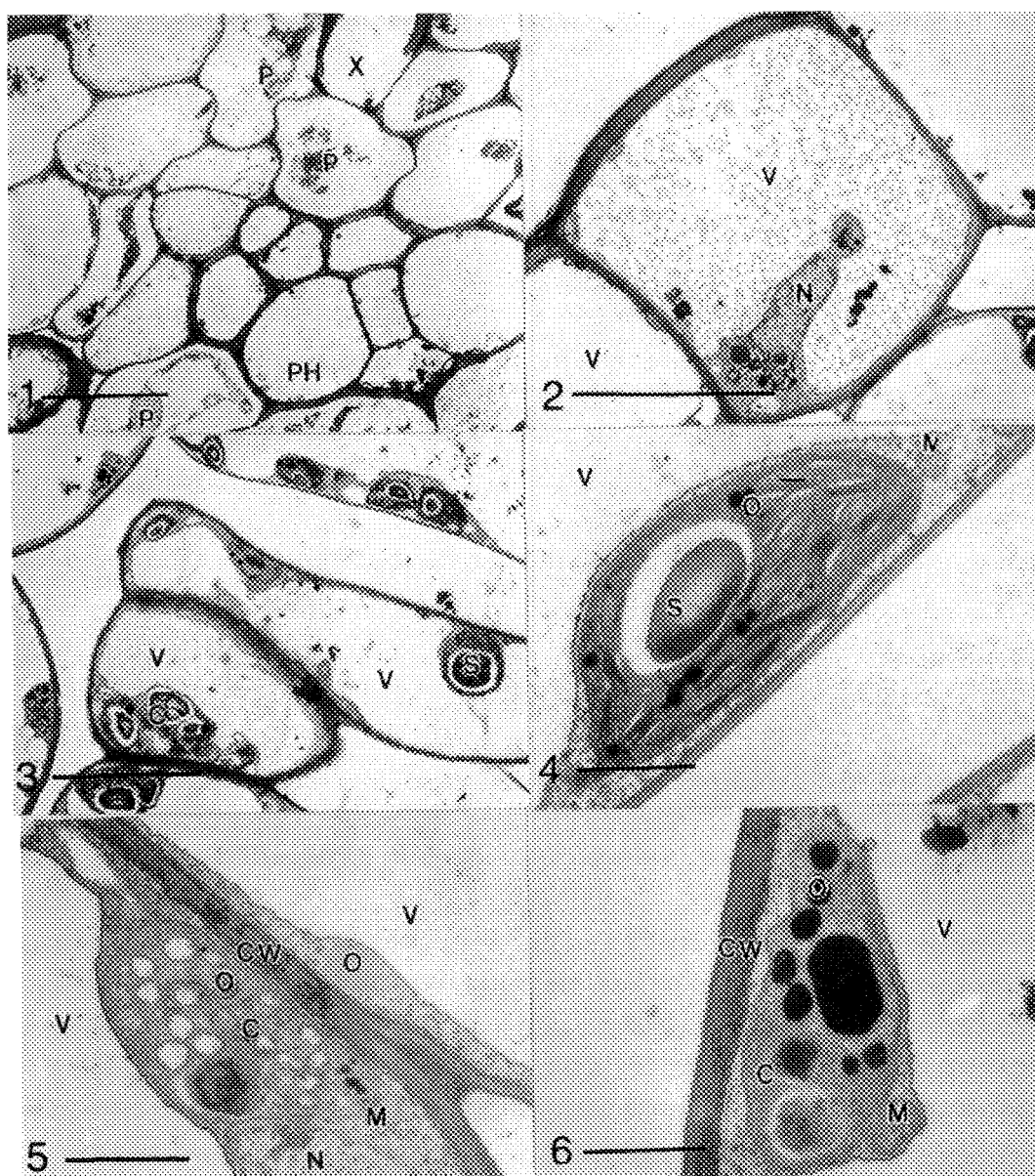
Seeds of tested plants obtained from both commercial sources and open field of Cu-polluted regions were germinated in petri dishes. Ten-day-old seedlings were transferred to a Hoagland's solution containing different concentrations of copper. Tested plants with symptoms of copper toxicity were collected as the materials for microscopic observations with OM and TEM, and for isozyme analysis with PAGE electrophoresis.

Among eighteen tested plants, only *Miscanthus floridulus* and *Dianthus barbatus* were more tolerant to excess copper. Most infected plants showed growth retardation in root and shoot, and sometimes leaf chlorosis. Root elongation of primary root and development of lateral roots were greatly inhibited by excess copper. The major infections on leaves were small leaf with thick blade, the closing of stomata and change structure of mesophyll cells. Ultrastructural studies on infected plants showed following events: easily deplasmolyzed protoplasm in cells of vascular tissues (Fig. 1); dense deposits in vacuole and cell wall of leaf epidermal cells (Fig. 2) and mesophyll cells (Fig. 3), and cells in vascular tissues (Fig. 1): aggregation of several chloroplasts in group (Fig. 3); disorganization of thylakoid membranes of chloroplast (Figs. 4-6); a markedly increasing size of oil drops in chloroplast (Fig. 6). Acid phosphatase, peroxidase and superoxide dismutase are potential enzyme markers for testing plant response to copper stress.

Cu-induced peroxidation of membrane lipid resulting in the extensive degradation of intracellular membrane has been suggested³. The disintegration of membrane system is associated with the accumulation of oil drop in cytoplasm and chloroplast⁴. The deposits in vacuole or cell wall related the accumulation of copper has been reported⁵. The changes of isozyme patterns did not reflect the tolerance of plant to excess copper.

References

1. D. A. Wilkind, New Phytol. 80(1978)623.
2. H. W. Woolhouse, Encloped. Plant Physiol. 12(part c)(1983)245.
3. A. K. Mattoo et al., J. Plant Physiol. 123(1986)193.
4. Y. R. Chen, et al., Proc. Natl. Sci. Council. ROC 12(1988)62.
5. J. C. Fernandes and F. S. Henriques, Bot. Rev. 57(1991)246.
6. This study was supported by a grant from National Science Council, ROC, No. NSC-80-0211-B002-20.



Figs. 1-6. Cells in different tissues of *Celosia argentea* in response to excess copper. Fig. 1, Plasmolyzed cells in vascular tissues of root. Fig. 2, Dense deposits leaf epidermal cell. Fig. 3, Dense deposits and aggregated chloroplasts in mesophyll cells. Figs. 4-6, Oil drops in degrading chloroplasts. Bars in Figs. 1-3 are 1 μ m and Fig. 4-6 are 1 μ m.

Abbreviation: CW, Cell wall; C, Chloroplast; M, Mitochondrion; N, Nucleus; M, Mitochondrion; O, Oil drop; P, Parenchyma; PH, Phloem; S, Starch grain; V, Vacuole; X, Xylem.

SAMPLE PREPARATION FOR IMMUNOCYTOCHEMICAL LOCALIZATION OF SMALL SOLUBLE ORGANIC MOLECULES IN PLANT CELLS

Patrick Echlin*, Paul Monaghan** and David Robertson**

* Department of Plant Sciences, University of Cambridge, Cambridge, CB2 3EA, UK

** Institute of Cancer Research, Haddow Laboratories, Sutton, Surrey, SM2 5NG, UK

Highly soluble organic molecules, such as alkaloids, sugars, amino acids, plant growth substances and secondary metabolites, play an important role in the growth and development of plants. Although a great deal is known about the metabolism of these chemicals, there is only fragmentary evidence as to where precisely in the plant body many of these materials are synthesized, how they are transported and where they are either utilized or stored. Recent developments in histochemical and immunocytochemical procedures coupled with both invasive and non-invasive imaging methods offer techniques which can be used to establish the spatial location of these substances, provided they remain in their natural place in the cells and tissue during the processes of sample preparation. This paper considers the current state in the development of such procedures with particular reference to the alkaloid nicotine.

Nicotine, (molecular weight 162) is the principle alkaloid of the tobacco plant *Nicotiana tabacum* which in wild plants varies between 0.003 to 3.0% of the dry weight and in cultivated tobacco can reach as high as 8% DW. It is not an inert end product of metabolism, but is in a dynamic state fluctuating both in local concentration and rate of turnover. It is believed to be synthesized in root apical meristems, transported in the xylem to the leaves either as the free base or as the dissolved salt where it is stored either in the cells of the photosynthetic tissues as citrate or maleate or as free nicotine in specialized glandular trichomes. It is highly soluble in most polar and non-polar liquids.

The local concentration of nicotine in tobacco plant tissue may be measured by first extracting the alkaloid in a 10% ethanol in water solution and then measuring the nicotine concentration either by UV absorption spectrometry or high performance liquid chromatography. The cellular localization of the alkaloid is achieved by means of immunocytochemical procedures using polyclonal antisera against nicotine coupled either to the fluorochrome, fluorescein isothiocyanate (FITC) for fluorescent and confocal microscopy, or to colloidal gold for transmission electron microscopy. The immunocytochemical procedures used in association with this work were carried out on thick (2 µm) and thin (100 nm) sections of fixed and embedded tobacco root tip and leaf material.

A large number of preparative protocols have been devised and at each stage in the preparative procedure, ie fixation, dehydration and embedding, measurements were made to see how much nicotine remained in the tobacco tissue. Immunocytochemical staining was subsequently carried out only on tissue samples which were shown to retain a substantial amount of nicotine.

Earlier studies (1) had shown that conventional fixation using organic aldehydes, with and without post-fixation in osmium tetroxide, followed by polar liquid dehydration and resin embedding, gave excellent structural preservation but retained little or no nicotine. More success was achieved with vapour fixation. Fresh leaf samples were first suspended in controlled humidity chambers at between 24 and 98% RH for several days, and exposed to the vapour of an aqueous formaldehyde solution maintained over a molecular sieve. The presence of the molecular sieve had the effect of lowering the partial vapour pressure of water which enabled the formaldehyde vapour to have its effect on partially dried leaf tissue. The partially dehydrated and vapour fixed tissues were directly slowly infiltrated at room temperatures with either of the two hydrophilic acrylic resins (LR gold/LR white) which can tolerate up to 30% water in the tissue. The partially dry, formaldehyde fixed tissues were not dehydrated in polar liquids prior to infiltration with the resin. The resin mixtures were polymerized at room temperatures with white light. Exposure to controlled humidity (drying) and vapour fixation with formaldehyde, resulted in a virtual 100% retention of nicotine in the tissue. The subsequent resin infiltration reduced these values to between 50-80%. However, these tissues

were difficult to section, and gave poor structural integrity in which only the main tissue types could be identified. The use of an aldehyde, albeit in the vapour phase, confirmed the earlier studies by Coetzee and van der Merwe (2) who showed that a 2.5% solution of glutaraldehyde in phosphate buffer caused only 5-10% losses of reducing sugars and amino acids from leaf tissue.

In a third set of experiments, samples of leaf and root tissue were fixed overnight at 293 K in a dilute formaldehyde-glutaraldehyde fixative, rapidly dehydrated to 90% methanol while lowering the temperature from 273 to 233 K and then infiltrated with LR gold at 248 K and polymerized at the same temperature using white light. This procedure gave good structural preservation at both the light and EM level and retained 50% of the nicotine after fixation and 48% after fixation and dehydration. In a final set of experiments, the process of progressive lowering of temperature dehydration was coupled with low temperature embedding in Lowicryl. Tobacco root and leaf tissue were fixed for one hour at 293 K in a dilute glutaraldehyde-formaldehyde fixative in phosphate buffer, dehydrated to 100% ethanol while progressively lowering the temperature to 223 K, then infiltrating the sample with Lowicryl HM20 at the same temperature and polymerizing the resin at 223 K using UV. This procedure gave excellent structural preservation and retained 64% of the nicotine after fixation and 61% after fixation and dehydration. There were only minimal losses of nicotine during the embedding and polymerization procedures.

The use of fresh unfixed frozen sections has not proved successful. Although sections may be cut and frozen dried, the wet chemical procedures associated with the immunocytochemical processes cause the nicotine to be relocated or lost. Further work is anticipated in which the tissues are first briefly fixed in formaldehyde vapour followed by quench cooling, cryosectioning and freeze drying. Freeze substitution methods have not been tried as it is believed that the polar liquids would cause the unfixed samples to lose nicotine even at the low temperatures associated with this procedure.

Our preliminary studies show that organic aldehydes interact with nicotine in such a way as to make them less soluble in the polar and hydrophilic chemicals used in specimen preparation. This interaction does not appear to affect the immunogenicity of the nicotine molecule. The loss of nicotine is further diminished by carrying out the dehydration and embedding at low temperatures. It is suggested that these same procedures can form the basis of the immuno-localization of other small organic molecules in plant tissue.

1. Echlin P et al. Proc 4th International Botanical Microscopy Meeting. Durham University (1991) Paper C5
2. Coetzee J and van der Merwe CF. Microscopy **135** 147 1984

The authors acknowledge the assistance of Brian Chapman and Rachel Holmes (Cambridge) and to the Philip Morris Research Centre, Richmond, VA, for the nicotine antisera.

LOCALIZATION OF SILICA IN *EQUISETUM ARVENSE* (HORSETAIL)

Barbara A. Reine

Botany Dept. KB-15, University of Washington, Seattle, WA 98195

Silica is deposited as amorphous silica gel in the shoots (as well as in leaves, roots and reproductive structures) of many vascular plants such as grasses and cereals (notably rice and oat), hemp, pea, nettle, palms, sedges, and horsetails. Of this group, the horsetails, grasses and sedges, exhibit an especially pronounced capacity to take up large amounts of silicon as silicic acid from the soil and polymerize it as hydrated silica in various tissue locations and sometimes specialized cells (3). The application of this naturally produced silica and other minerals to technology, has stimulated a renewed and refocused interest in biomineralization (2). Historically, the silica-impregnated shoots of horsetails (*Equisetum*) were used by pioneer settlers for scouring dirty dishes and as a substitute for sandpaper. Today, rice hulls, whose silica content can exceed 20 wt.%, are pyrolyzed commercially to produce silicon carbide whiskers and platelets for use in composites. Rice hulls are also used as fuel in co-generation plants in rice-growing regions of the country but if combustion takes place in certain oxygen concentration and temperature regimes, crystalline "free silica" forms to a substantial extent and, if discharged as respirable dust, may present a significant public health risk.

There is also considerable interest with relevance to efforts to develop advanced materials in learning how to mimic nature's methods of producing self-assembling structures. One of the vascular plants that exhibits extensive silicification is *Equisetum arvense* whose silica content can be as high as 20 % dry weight (1). Information about the specific form and location of the silica at various points in the plant and as affected by the seasonal growth cycle and soil nutrients, is of relevance to gaining further insight into the process of silicification itself.

Mature (ie dead) specimens of *Equisetum arvense* were gathered during the autumn and very young samples in late winter from disturbed sites along pathways on the campus of the Univ. of Washington. Both leaves and stem (internode) segments were prepared for optical and scanning electron microscopy (using a JEOL 840A SEM) and EDS analysis (using a Tracor Northern 5400 Series II) by a number of methods. Results show that silica is distributed widely in the leaf and stem epidermis; occurring in the stomatal cells, epidermal papillae and epidermal cell surfaces (Figs. 2 and 4). Silica concentrations are much greater on the outside, tangential surface of the epidermal cells than on the radial and inside surfaces. Analysing stems in cross section, revealed silica to be present in the cortex cell walls as well, though in much lower concentrations than in the outer surface of the epidermis. This observation was supported by the fact that incineration (to remove organic material) of cross sections of stems left a prominent epidermal shell containing lace-like cortex cell walls. It may be that the nature as well as the concentration of silica in the epidermis is different from that inside the stem.

REFERENCES

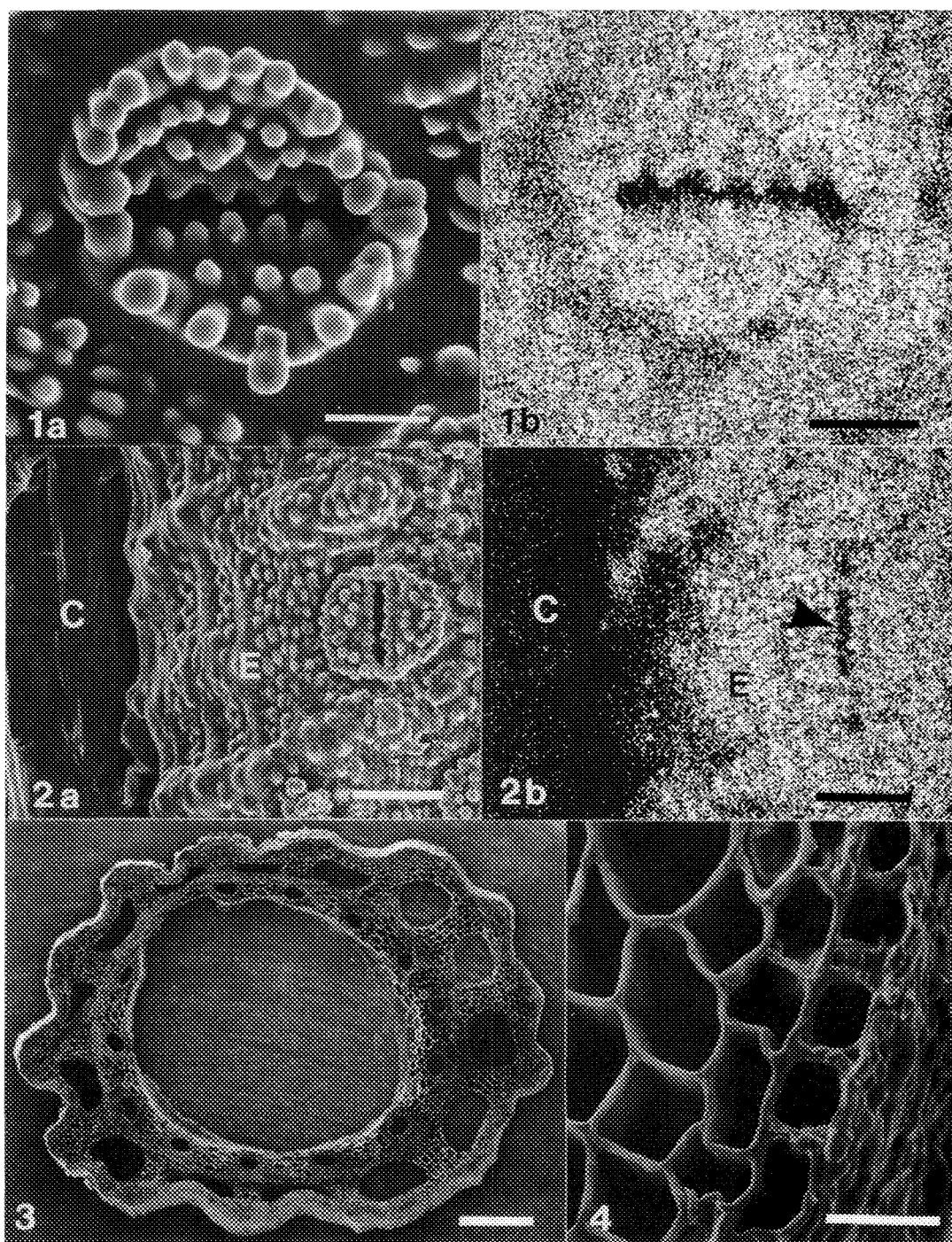
1. J. C. Lewin and B. E. F. Reimann, *Ann. Rev. Pl. Physiol.* 20(1969)289.
2. K. Simkiss and K. M. Wilbur, *Biomineralization*, New York: Academic Press (1989)6.
3. T. L. Simpson and B. E. Volcani, ED., *Silicon and Siliceous Structures in Biological Systems*, New York: Springer-Verlag (1981)383.

Fig. 1a and b. SEM view and silicon X-ray map of stoma from stem of young plant. Bar = 10 μ m.

Fig. 2a and b. SEM view and silicon X-ray map of stem surface showing split in epidermis (E) revealing underlying cortex (C). (arrow indicates open stoma). Bar = 25 μ m.

Fig. 3. Stem cross section mounted directly on aluminum stub. Bar = 500 μ m.

Fig. 4. Stem cross section showing epidermis and underlying cortex cells. Bar = 25 μ m.



SECONDARY-WALL DEVELOPMENT IN THE COTTON FIBER

W. R. Goynes, B. F. Ingber, AND B. A. Triplett

USDA, ARS, Southern Regional Research Center, P.O. Box 19687, New Orleans, LA 70179

Secondary wall thickness is considered to be a function of maturity in cotton fibers. Normal fibers are formed from a single epidermal cell of a fertilized ovule. Development of these cells into fibers occurs in two, possibly overlapping, stages. Fibers begin to elongate at anthesis, and elongation continues for approximately 20 days postanthesis (DPA). As this elongation period ends, deposition of secondary wall begins, and continues for 25-30 days until the boll "matures" and opens. The exact period of elongation and secondary thickening is dependent on factors such as variety, growing temperature, and light level. Between six and nine weeks, wall thickening terminates as bolls begin to open.

Changes in wall thickness as a function of maturation time of several cotton varieties, including Pima SJ5, Stoneville 215, and Texas Marker 1, have been examined using transmission and scanning electron microscopy. Field-grown fibers were used in the study, but in some cases fibers from plants grown in growth chambers under controlled conditions were compared. Harvested, undried fibers were chemically fixed and critical point dried. These fibers were studied whole, and were embedded and sectioned for examination of internal structures.

Figure 1 is a TEM of a 15 DPA fiber section showing the oval-shaped primary wall with no secondary cellulose layers. As secondary layer development begins, this wall becomes thicker. All fibers on a seed do not develop concurrently. In the SEM in figure 2, sections from three fibers show two to have developed thick walls, while the wall of the third is thin, or immature.

The effect of growing season on rate of fiber maturity was shown by comparing fibers harvested in August, during the normal growing season, to those harvested in November from the same plants but from seed that had developed during the autumn. Figure 3 shows cross sections of Pima SJ5 fibers, 56 DPA, from a summer growing season, all exhibiting mature wall thickness. Figure 4 illustrates the difference in wall development for Pima SJ5 fibers grown for 56 days during autumn. The thin cell wall indicates a very slow rate of secondary cellulose development as compared to fibers from these same plants grown during the summer growing season.

This microscopical study of the developing cotton fiber wall illustrated that initiation of wall thickness is not uniform among fibers from a single boll, that fibers from different varieties may show differences in wall thickening rates, that fibers grown early in the growing season have a dramatically different maturity rate than do fibers grown late in the growing season, and that even at boll opening (maturity) many fibers have not reached a wall thickness that would classify them as mature.

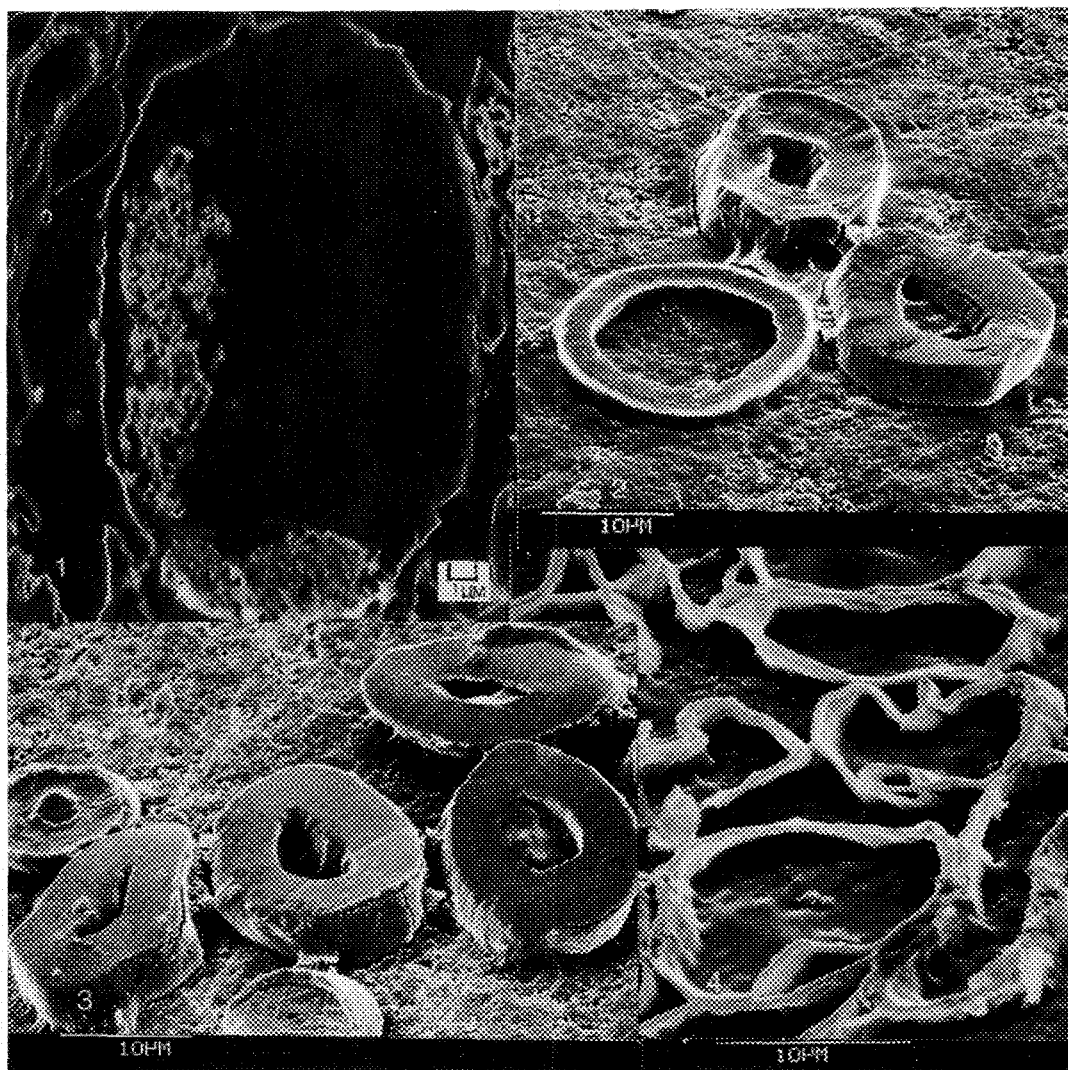


FIG. 1.--Fiber cross section (15 DPA) showing thin primary-wall. (TEM)
 FIG. 2.--Thick sections from 49 DPA Pima SJ5 showing one thin- and two thick-walled fibers. (SEM)
 FIG. 3.--Sections of mature-walled 56 DPA Pima SJ5 fibers from a summer growing season. (SEM)
 FIG. 4.--Sections of thin-walled 56 DPA Pima SJ5 fibers from an autumn growing season. (SEM)

SPACE-EXPOSED SEED EXPERIMENT DEVELOPED FOR STUDENTS

DONNA LEEPER, KELVIN BRIDGERS, AND ERNEST C. HAMMOND

**DEPARTMENT OF PHYSICS, MORGAN STATE UNIVERSITY
HILLEN ROAD & COLD SPRING LANE, BALTIMORE, MD 21239**

The SEEDS project was flown in orbit aboard the Long Duration Exposure (LDEF) for nearly six years. During this time in space, the tomato seeds received an enormously abundant supply of cosmic radiation. Upon the return of the LDEF to earth, the SEEDS project was distributed throughout the United States and 30 foreign countries for analysis. The purpose of the experiment was to determine the long term effects of cosmic rays on living tissue. At Morgan, the analysis performed varied from germination and growth rates to electron microscopy and x ray analysis.

In analyzing the seeds under the electron microscope, usual observations were performed on the nutritional and epidermic layers of the seed. These layers appeared to be more porous in the space-exposed seeds than in the Earth-based control seeds. This unusual characteristic may explain the increase in the space seeds' growth pattern. (Several test results show that the space-exposed seeds germinate sooner than the Earth-based seeds. Also, the space exposed seeds are growing at a faster rate.) The porous nutritional region may allow the the seeds to receive necessary nutrients and liquids more readily. Thus, enabling the plant to grow at a much faster rate.

Roots, leaves, and stems were cut into small sections and mounted. After sputter coating the specimens with Argon gas, they were ready to be viewed under the electron microscope. While the specimens were under the electron microscope, several photographs were taken. The x ray analysis displayed possible identifications of calcium, potassium, chlorine, copper, aluminum, silicon, phosphate, carbon, and sometimes sulfur and iron. The highest concentrations were shown in potassium and calcium. The space exposed specimens displayed high concentrations of potassium, calcium, and chloride. Whereas the Earth-based specimens displayed high concentrations of potassium, copper, and chloride. Therefore, there is a distinct difference in the concentration of copper and calcium in the two specimens. There were significantly high concentrations of copper in the earth-based specimens, whereas there was no copper in the space exposed specimens. Also, there were high concentrations of calcium in the space exposed specimens, whereas the calcium concentrations were much lower in the earth-based specimens.

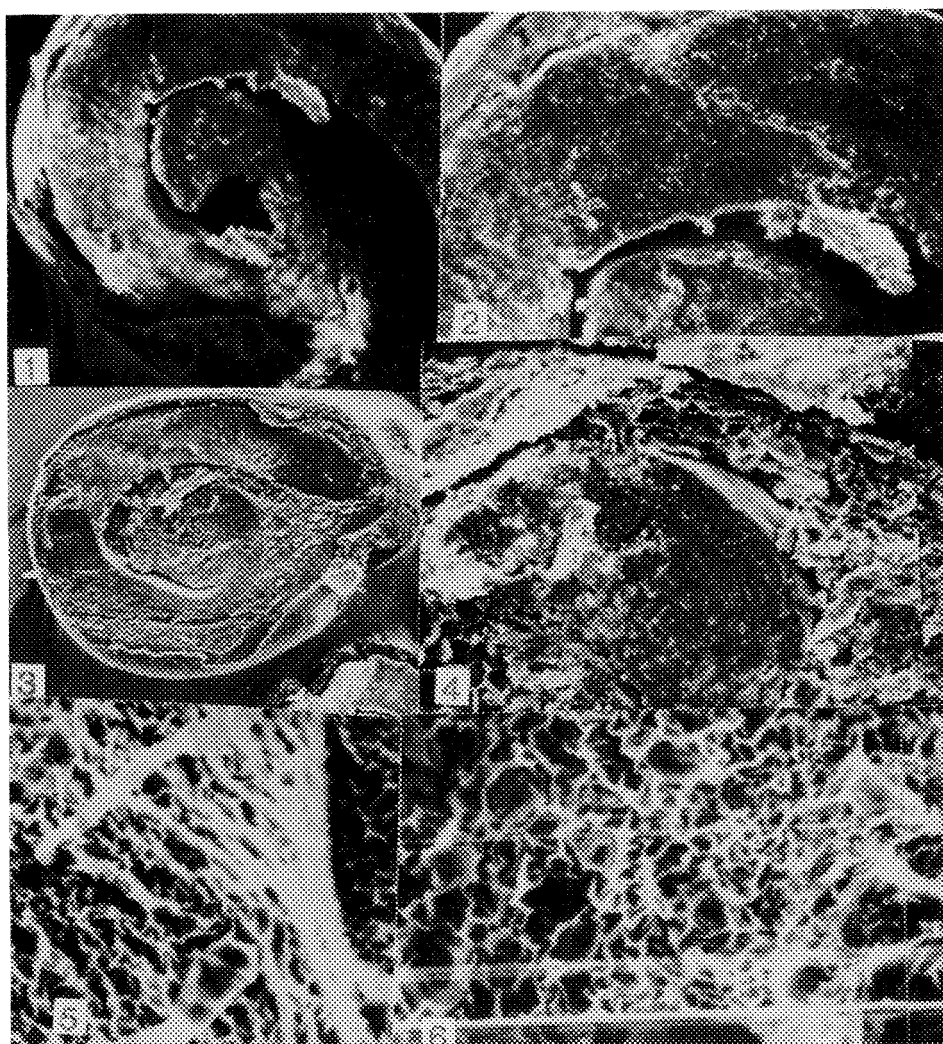


Fig. 1. - -Longitudinal section of a control or earth - based tomato seed at 0.037 KX magnification

Fig. 2. - -Higher magnification of Fig. 1. showing it's healthy nutritional layers

Fig. 3. - -Longitudinal section of a space at 0.022 KX magnification.

Fig. 4. - -Higher magnification of Fig. 3. showing the "flaky" or "porous" nutritional layer.

Fig. 5. - - The leaf of a space exposed tomato plant at 0.30 KX magnification.

Fig. 6. - - The leaf of an earth based tomato plant at 0.48 KX magnification.

ULTRASTRUCTURAL AND CHLOROPHYLL CONTENT CHANGES OF LEAVES IN PEANUT PLANT CAUSED BY IRON DEFICIENCY

Yang-Zenq Tsai, Kwan-Long Lai and Chau-Yunn Lee

Department of Agronomy, National Taiwan University, Taipei, Taiwan,
R. O. C.

Yield of peanut is significantly low at Hua-lien area where is Fe-deficiency because of high pH value in soil. In order to understand the effect of iron ion on the growth and development in peanut plant, a series of experiments were conducted. First, two peanut cultivars namely Tainan Sel. 9 and Tainan 11 were used as excised root and embryo culture *in vitro* with Fe-proficiency or Fe-deficiency treatment. The result showed that the growth of excised root or embryo was significantly inhibited and the symptom of chlorosis appeared on the leaves caused by Fe-deficiency.¹

Those peanut plants which were grown in the conditions of Fe-proficiency and higher pH showed much more in plant height, node number, the first branch length, primary or secondary roots and dry weight than Fe-deficiency one. And content of microelements Fe, Mn, Cu, Zn or relative mobility ratio was also higher significantly in Fe-proficiency treatment than that in Fe-deficiency one. Particularly, Fe/Mn molar ratio may regard as an evaluate index for Fe-deficiency or Fe-proficiency.²

The object of the third study is chiefly to elucidate the effect of iron and different pH values on the chlorophyll content of peanut plant in hydroponics and observe the ultrastructural change of chloroplast to be caused by iron-deficiency. Two Virginia cultivars (Penghu 2 and Chiba bunch) and two Spanish cultivars (Tainan Sel. 9 and Tainan 11) were selected as materials. The peanut leaves in culture solution contained iron ion presented green in color, and the well development in chloroplast and the grana stacks in close parallel arrangement. However, the leaves in no iron treatments showed chlorosis and were rather low in total chlorophyll content and chlorophyll a and b and presented the reduction in the number of grana as well as the stratum in loose form and the increment in accumulation of starch grains. From this result, it suggested that iron is an utmost important element in peanut yield.³

References

1. C. Y. Lee et al., Mem. Coll. Agric. Natl. Taiwan Univ. (1990) 30 (2), 6.
2. C. Y. Lee, et al., Chinese Agron. J. (1991) 1, 69.
3. The research was supported by a grant from the Council of Agriculture, Executive Yuan, R. O. C.

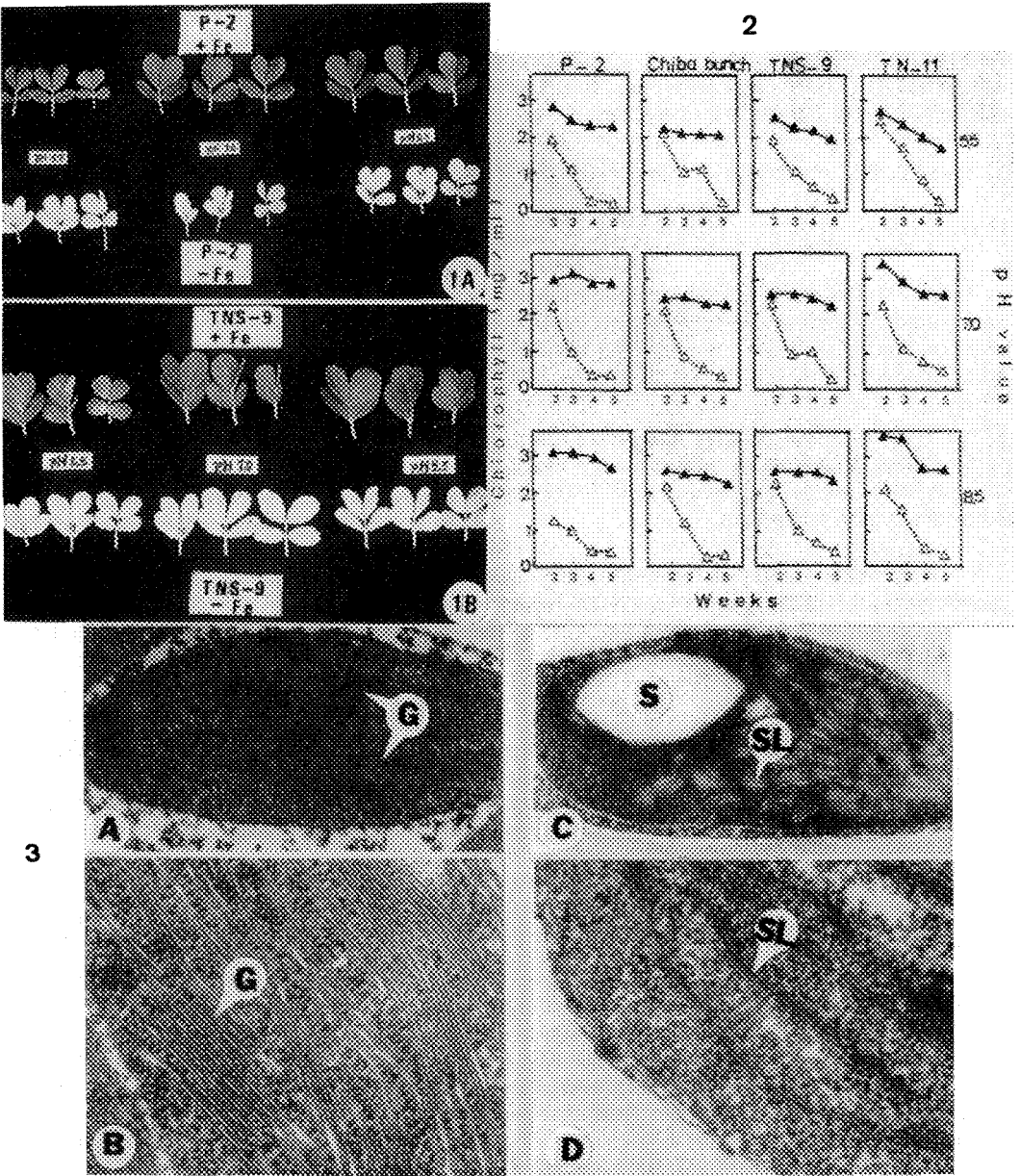


Fig . 1. The effects of the iron and pH value on the peanut leaves of Penghu 2 (A) and Tainan Sel. 9 (B).
 Fig . 2. The effect of the iron and pH value on the chlorophyll content of peanut plant. Culture solution contained 5.5 ppm EDTA-Fe (▲) and no EDTA-Fe (△) , respectively.
 Fig . 3. Effect of iron on the ultrastructure of chloroplast of peanut Tainan sel. 9.
 A. Culture solution contained EDTA-Fe(X 27,000) C. Culture solution contained no EDTA-Fe(X 27,000)
 B. Culture solution contained EDTA-Fe(X 50,000) D. Culture solution contained no EDTA-Fe(X 50,000)
 G : granum S : starch grain SL : stroma lamellae

UV ABSORPTION MICROSPPECTROPHOTOMETRY OF PLANT CELL WALLS IN RELATION TO BIODEGRADATION

D.E. Akin, L.L. Rigsby, W.S. Borneman, and R.D. Hartley

Russell Research Center, ARS-USDA, Athens, Georgia 30613

A major limitation to the biodegradation of plant cell walls is the presence of phenolic compounds, which covalently link to carbohydrates and render these potentially digestible components unavailable for microbial utilization. A more detailed understanding of phenolic compounds and their association within specific cell types is required for development of strategies to enhance biodegradation of plant fiber for efficient utilization of foods and feeds. UV absorption microspectrophotometry was employed to characterize the phenolics within cell walls of a series of plants with different biodegradabilities. Scanning electron microscopy was used to assess the degradation of specific cell types incubated with fiber-digesting microorganisms from the rumen ecosystem.

UV absorption microspectrophotometry was undertaken on a software-controlled, monochromator system (Zeiss UMSP-80) using a 75 W xenon lamp for scanning a region from 230 to 350 nm in 2-nm intervals. Phenolic acid-arabinoxylan esters, which were isolated from bermudagrass cell walls, were used as standards. For evaluation of plants, leaves of two temperate (orchardgrass and Ky-31 tall fescue) and one subtropical grass (bermudagrass) and leaflets of a legume (alfalfa) were embedded in JB 4 Plus and sectioned 4 μm thick. Walls of plant cells having different biodegradabilities were selected, and an aperture 1.56 μm in diameter was positioned over the wall and, where possible, over a designated layer of a cell wall. Spectra were compared with those of condensed phenolic compounds (i.e., lignins) and phenolic acid-arabinoxylan esters from the literature and with standards assessed by microspectrophotometry.

The more refractory cell types (e.g., mestome sheath) (Figs. 1, 2) showed spectral patterns with strong absorption maxima at 280 nm (Fig. 4). In all grasses but not alfalfa, a shoulder or maximum occurred at ca 320 nm, which is indicative of phenolic-arabinoxylan esters; absorption at ca 320 was more prominent in temperate grasses than in bermudagrass. Biodegradation of epidermis was variable based on plant type (Figs. 1, 2, 3). In the more recalcitrant epidermal cells of bermudagrass, strong maxima occurred at ca 276 nm and shoulders at ca 320 nm (Fig. 4). In contrast, the completely degraded epidermis of orchardgrass had no UV absorption maxima. In some tissues such as parenchyma bundle sheath of bermudagrass, UV absorption spectra indicative of phenolic acid-arabinoxylans occurred (Fig. 4) and were associated with limited biodegradation of these cell types (Fig. 1).

UV absorption microspectrophotometry can characterize and differentiate phenolic compounds within plant cell types and provide information on the limitations to biodegradability.

References

He and Terashima, *Holzforschung* (1991) 45, 191.

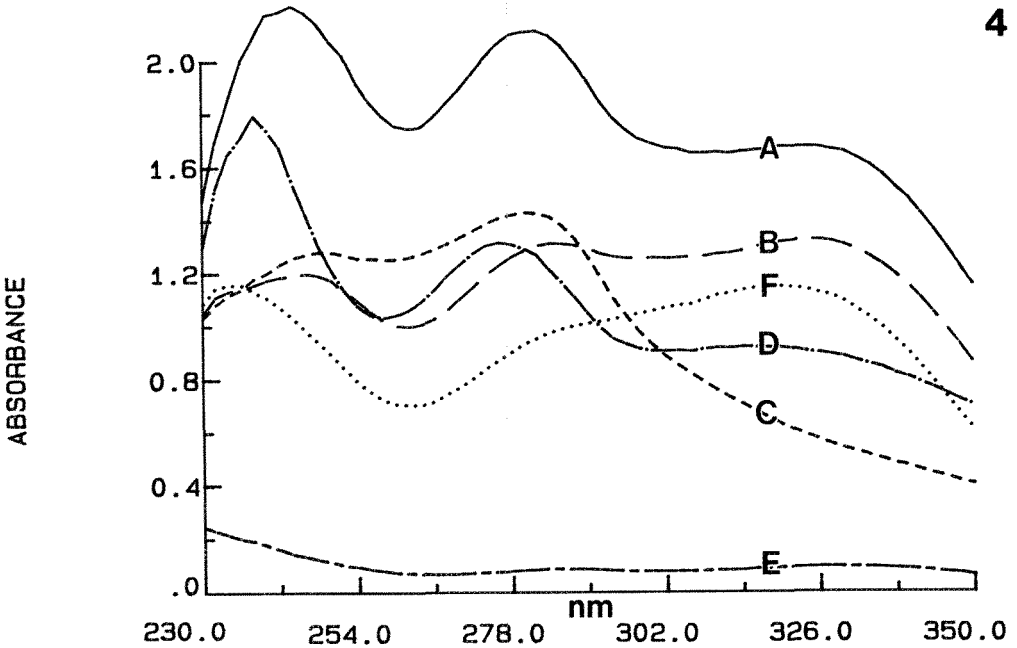
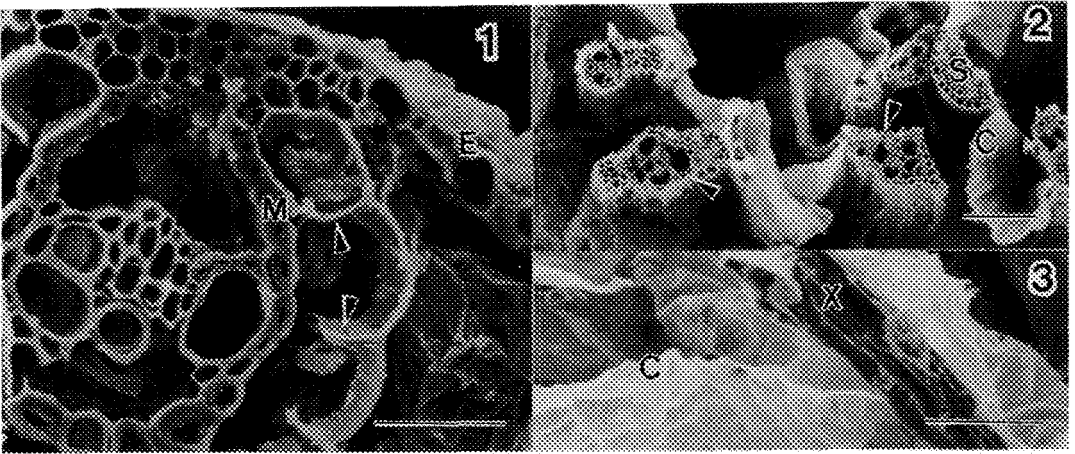


FIG. 1. -- SEM of bermudagrass leaf blade degraded by rumen microorganisms for 7 d showing resistance to digestion of mestome sheath (M) and upper layer of epidermal wall (E) and partial digestion of parenchyma bundle sheath (arrows). Bar = 30 μ m.

FIG. 2. -- SEM of orchardgrass leaf blade degraded by rumen microorganisms for 7 d showing loss of all but mestome sheath (arrows), sclerenchyma (S), and cuticle (C); all epidermis is degraded. Bar = 100 μ m.

FIG. 3. -- SEM of alfalfa leaflet degraded by rumen microorganisms for 7 d showing resistance of xylem (X) and cuticle (C). Bar = 50 μ m.

FIG. 4. -- UV absorption spectra of cell types with various degradabilities: mestome sheath of bermudagrass (A) and orchardgrass (B), xylem of alfalfa (C), epidermis of bermudagrass (D) and orchardgrass (E), and parenchyma bundle sheath of bermudagrass (F).

INTRAMEMBRANE PARTICLES DISTRIBUTION IN THE NATURALLY SYNCHRONOUS STAGE OF *PHYSARUM POLYCEPHALUM*

Randolph Taylor and Henrie Turner

Department of Biology, Electron Microscopy Section, Morris Brown College, Atlanta, Georgia 30314

Comparative ultrastructural investigations of the *Physarum polycephalum* intramembrane particles in the plasma membrane at different stages of the cycle has provided valuable information in relation to possible changes that occur in the plasma membrane of higher organisms.⁴ In addition, it gives insight on how plasma membrane changes correlate with gene expression and gene regulation in eukaryotes.^{1,2,4,5} In this report Freeze-fracture-etched techniques were utilized to study the arrangements of intramembrane particles (IMP) distribution and density at eight hours of the naturally synchronous plasmodial stage.

Axenically maintained microplasmodia of *Physarum polycephalum* (M₃C) were harvested in mid-exponential growth phase by centrifugation at 1000 rpm for 2 min in a clinical centrifuge. The pelleted microplasmodia were suspended in Yeast tryptone broth medium. Aliquots of the suspended microplasmodia were spread in 3 cm circles with a wide mouth pipette onto sterile filter paper which was supported with a wire screen contained in a petri dish. The cells were then starved for 2 hours at 24 C. Following starvation, the cells were fed semidefined medium supplemented with hemin and incubated at 24 C. Samples of the microplasmodia were collected randomly from the petri plates, place in plancettes and frozen with a propane-nitrogen jet freezer. Frozen specimens were placed immediately in liquid nitrogen, fractured, etched and shadow-coated with platinum and carbon using the Blazars BAF 360. Following the cleaning of the replicas with sulfuric acid, and acetone, the replicas were washed several times in distilled water. The replicas were mounted on uncoated grids and examined with a Hitachi 300 transmission electron microscope.

Scanning electron microscopy to verify absence of encystment revealed surface convolutions and veins commonly present at this stage.^{3,6} A representative freeze-fracture-etched profile of synchronously replicated plasmodia (Fig.1) illustrates the protoplasmic half (P face) and small areas of the extracellular half (E face) of the plasma membrane. Small clusters of intramembrane particles on the protoplasmic half of the plasma membrane can be seen (Fig. 1). In addition, numerous depressions can be seen in the fractured face (Fig. 1A). These depressions were more pronounced at high magnifications (Fig. 1B). Cytoplasmic components were also prevalent, showing the typical structures when deep fractured replicas of eight hours post-fusion were examined.

The findings in this study showed the presence of aggregation of IMP at eight hours. Following vegetative growth, it appears that intramembrane particles aggregation become more pronounced with higher relative density of particles, indicating a possible relationship to biochemical events.² The marked changes in density and distribution of IMPs over the time course of this study, suggests that IMP can serve as indicators of increased plasma membrane component activity in cell communication with the environment. Subsequently, the results suggest that it is possible to correlate IMP arrangement, distribution and density with morphogenesis.

Further the results may make it possible to investigate events unique to early - S, late - S and G₂ of the Physarum cell cycle by probing the IMP structure and arrangements.

1. Affolter, H.U., Behreno, K. Seebeck, T. and Brown, R. (1970). FEBS Letters Vol. 107, No. 2.
2. Cotes, N.P., Neelin, J.M., Pallotta, D. (1982). J. of Biochem. 60 (3): 263-71.
3. Goodman, E.M. (1972). J Bact. 111. 242-247.
4. Shraideh, Z. et al. (1982). Cell Biology International Reports, Vol. 6. 851.
5. Turner, H., Hogan, T.C. (1982). J. Protozool. 29 (3), pp 341-347.
6. Turner, H.M. and Johnson (1975). cytobios (12) 95-107.

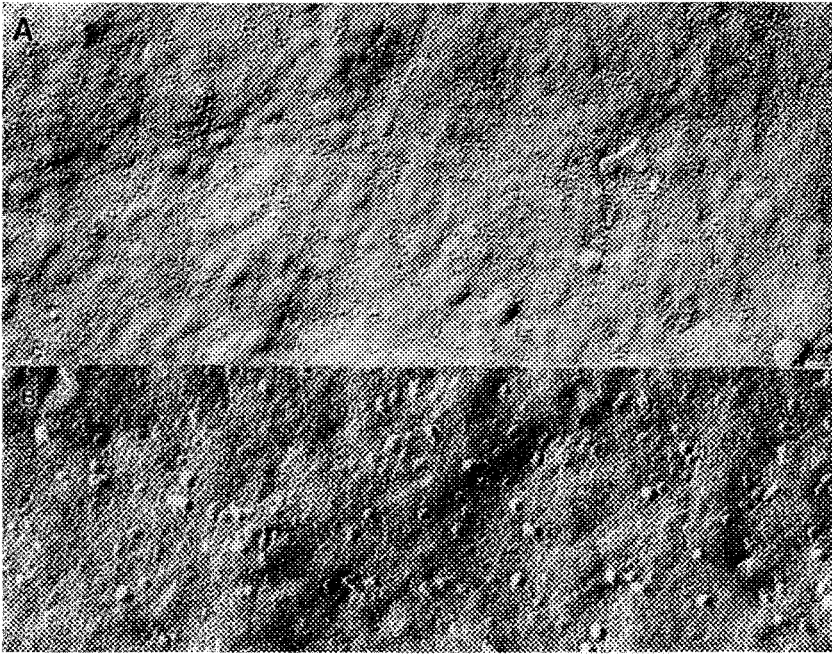


Fig. 1A. Electron micrograph of a synchronously replicating plasmodia depicting intramembrane particles and depressions throughout the fracture plane. X80,000. Fig. 1B. High magnification of the replicating plasmodia. The depression and the IMP are more visible. X180,000.

BACTERIAL ENVELOPE PROFILES REVEALED BY FREEZE-SUBSTITUTION

L.L. Graham and T.J. Beveridge

Department of Microbiology, University of Guelph, Guelph, Ontario, Canada, N1G 2W1

Traditional methods of processing bacteria for thin section electron microscopy rely on chemical fixation and dehydration under conditions which maximize specimen deterioration. Cryotechniques, however, use physical fixation (rapid freezing) and are slowly being recognized as a superior alternative to the more conventional methods. Freeze-substitution is a cryotechnique which combines cryofixation with a gentle chemical fixation and dehydration regimen, yielding specimens amenable to standard embedment procedures and ultramicrotomy. Previous study has shown that freeze-substitution retains the molecular composition of eubacteria better than conventional methods of processing.³ In this study we extend our observations and show that a simple freeze-substitution protocol reliably preserves the ultrastructure of a diverse range of microorganisms including archaeobacteria and anaerobic eubacteria.

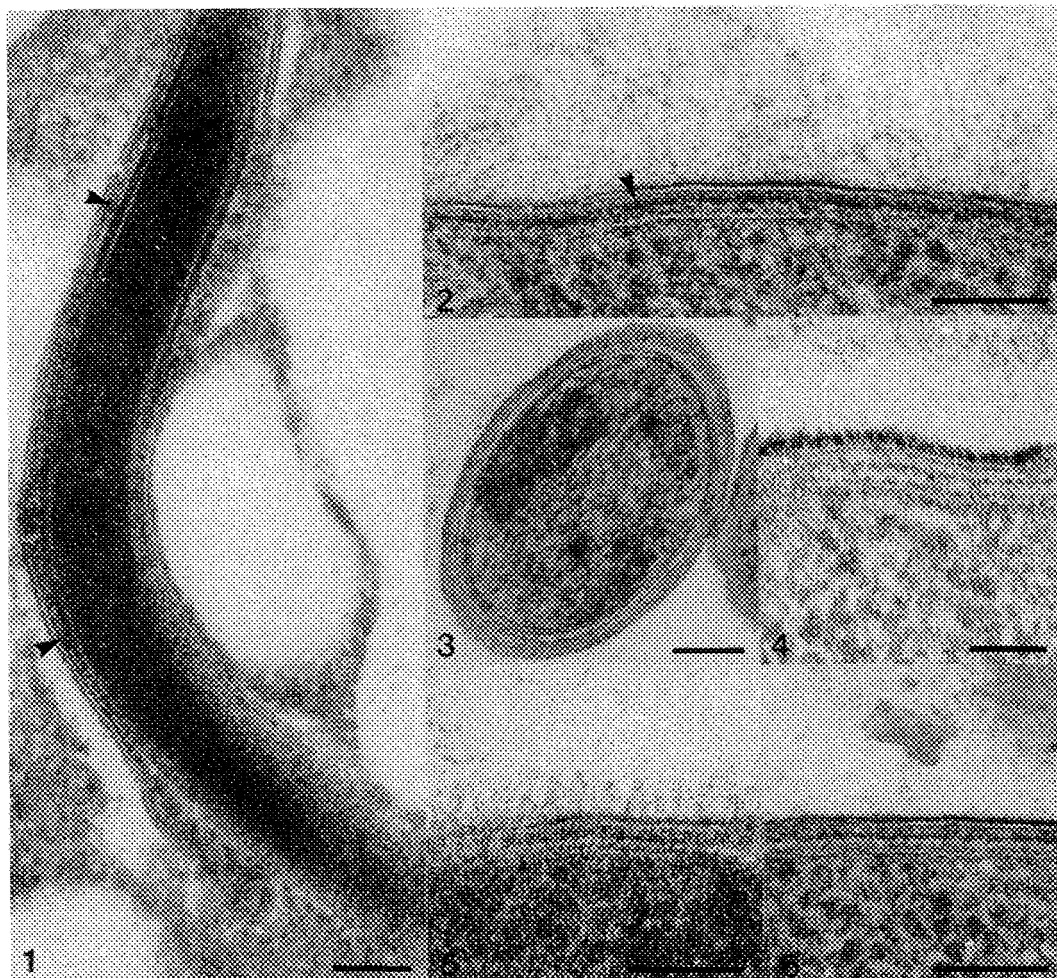
All cells were harvested from broth cultures in mid-exponential growth phase. Cells were not washed or treated with cryoprotectants prior to processing. Cells were collected by gentle centrifugation and to the cell pellet was added an equal volume of molten Noble agar (1%, 60°C), the mixture stirred and rapidly spread as a thin layer (approx. 20 µm) on cellulose ester membranes. Portions of these membranes were plunge frozen in liquid propane (-196°C) and immediately transferred to vials containing substitution medium (also at -196°C) which routinely consisted of 2% uranyl acetate and 2% OsO₄ in anhydrous acetone in the presence of molecular sieve. Substitution was performed over 72 h at -80°C, after which time vials were warmed to room temperature, washed with 6 changes of fresh anhydrous acetone and infiltrated overnight with a 1:1 mixture of acetone:Epon 812. Samples were embedded in fresh Epon 812 and polymerized at 60°C. Sections were cut with a Reichert-Jung Ultracut E ultramicrotome, post-stained and examined in a Philips EM 300.^{3,4}

Figures 1-6 show the ultrastructural detail retained by the freeze-substitution technique. In all instances cell membranes were well preserved. The periplasmic gel⁵, characteristic of most gram negative organisms, was observed in a spirochaete (Fig.1). Fragile structures such as the exopolysaccharide polymers of *E. coli* (Fig. 2) and the S layer of *Campylobacter fetus* (Fig.3 and 4) were retained and for the first time, the O antigen of *Pseudomonas aeruginosa* PAO1 lipopolysaccharide was visualized (Fig.5 and 6). Freeze-substitution reliably preserves bacterial ultrastructure and accurately retains spatial relationships between the various components of cell envelopes, confirming biochemical studies. It is clearly an improvement over conventional methods of chemical fixation and is applicable to a wide range of organisms.⁶

References

1. T.J. Beveridge and L.L. Graham, Microbiol. Rev. (1991) 55, 684.
2. L.L. Graham, Electron Microsoc. Rev. (1992) 5, 77.
3. L.L. Graham and T.J. Beveridge, J. Bacteriol. (1990) 172, 2141.
4. L.L. Graham *et al*, J. Bacteriol. (1991) 173, 1623.

5. J.A. Hobot *et al*, J. Bacteriol. (1984) 160, 143.
6. This research was supported by grants from the Medical Research Council and the Natural Sciences and Engineering Research Council, Canada.



- All figures are TEM's of thin sectioned, post-stained, freeze-substituted specimens.
- Fig. 1. *Treponema denticola* ATCC 33520. Note the dense periplasm (arrow). Bar=100 nm.
- Fig. 2. *Escherichia coli* HIS 1. Periplasmic gel (arrow) and fibrous exopolysaccharide capsule are evident. Bar=100 nm.
- Fig. 3. *Campylobacter fetus* subsp. *venerealis* UA809. Note the S layer external to the outer membrane. Bar=100 nm.
- Fig. 4. S layer of *C. fetus*. Note its close association with the outer membrane. Bar=50 nm.
- Fig. 5. *Pseudomonas aeruginosa* PAO1. The fringe external to the outer membrane is the lipopolysaccharide O antigen. Bar=100 nm.
- Fig. 6. An isogenic mutant of *P. aeruginosa* PAO1, lacking the O antigen. No fringe is visible. Bar=100 nm.

ELECTRON CRYO-MICROSCOPY OF NUCLEOCAPSIDS OF SENDAI VIRUSES

P. M. Charest, J. Jakana, M. F. Schmid, S. Vidal*, D. Kolakofsky*, and W. Chiu

Verna and Marrs McLean Dept. of Biochemistry and W. M. Keck Center for Computational Biology, Baylor College of Medicine, One Baylor Plaza, Houston, TX, 77030; *Département de Microbiologie, Centre Médical Universitaire, Genève, Switzerland

The Sendai virus is a member of the parainfluenza viruses. It is pathogenic in infants and children causing severe respiratory tract infection. The virion contains five structural proteins and two non-structural proteins encoded by the negative-strand RNA genome included in the nucleocapsid (NC). The physical nature of the NC helix may appear different under various ionic strength conditions or according the protocols used to isolate and process them for electron microscopy¹⁻³. In the present work, electron cryo-microscopy has been applied to visualize the nucleocapsids of the Sendai virus in different salt conditions. Chemical treatments were avoided to eliminate possible artifactual conformations of the nucleocapsids and to facilitate direct and more reliable structural interpretations. We have used both 100 and 400 kV electrons to image the intact virions as well as the NC. The primary effect of electron energies on the images is a higher contrast seen at lower voltage.

In low salt, the predominant features from the purified NC are helical filaments with chevron shapes and isolated assemblies with C or ring shapes (Fig. 1). The average and dominant helical pitch of the NC is 71 Å and the filament has a diameter of ≈200 Å. Few NC exhibited a 58 Å pitch while others showed a larger pitch (110 Å) or even a combination of these values on the same filament. However, the 71 Å pitch was the dominant feature among nucleocapsids. Other features have also been observed in the low salt condition, such as ribbon-like structures (Fig. 2). The diameter of the ribbon is ≈180 Å with a length ranging from 0.6 to 1.5 μm. In some micrographs, the ring shape structure appeared attached to the end of a ribbon, which itself appeared connected to a helical filament. In the high salt condition, the helical pitch of the NC appeared more homogeneous, e.g. being either of 58 Å or of 71 Å. The nucleocapsids appeared less curvy and no C shape structure has been observed in such higher ionic strength. The diameter of the filaments is of ≈200 Å (identical as in low salt condition) (Fig. 3). Entire virions in low and high salt conditions were also investigated. At small defocus setting, a membranous feature of 40-50 Å is resolved. When a higher defocus value was used, the lipid separation was not resolved whereas the external spikes and internal nucleocapsids become more visible (Fig. 4). Though the complete virions are of variable diameters, all of them, in low ionic strength, look spherical and do not have pleomorphic shapes. When the virions are suspended in the high salt buffer, they appeared distorted and many of them have been broken. Nevertheless, the helical pitch of the liberated NC is similar to that of the purified NC.

Electron cryo-microscopy has been used to define the structural diversity of the NC under different chemical and purification conditions. In addition to the previously observed helical filaments, the C or ring shape assemblies have been discovered from the frozen, hydrated specimens. These observations suggest new avenues for examining the mechanism of assembly and disassembly of the NC which is essential in the understanding of the packaging process of the mature Sendai virion.⁴

References

1. E. H. Egelman et al. J. Virol. (1989) 63, 2233.
2. M. H. Heggeness et al. Proc. Natl. Acad. Sci. (1980) 77, 2631.
3. M. H. Heggeness et al. Virol. (1981) 114, 555.
4. This research was supported by the National Institute of Health grants (NS 25877 and RR 02250) and the W. M. Keck Foundation.

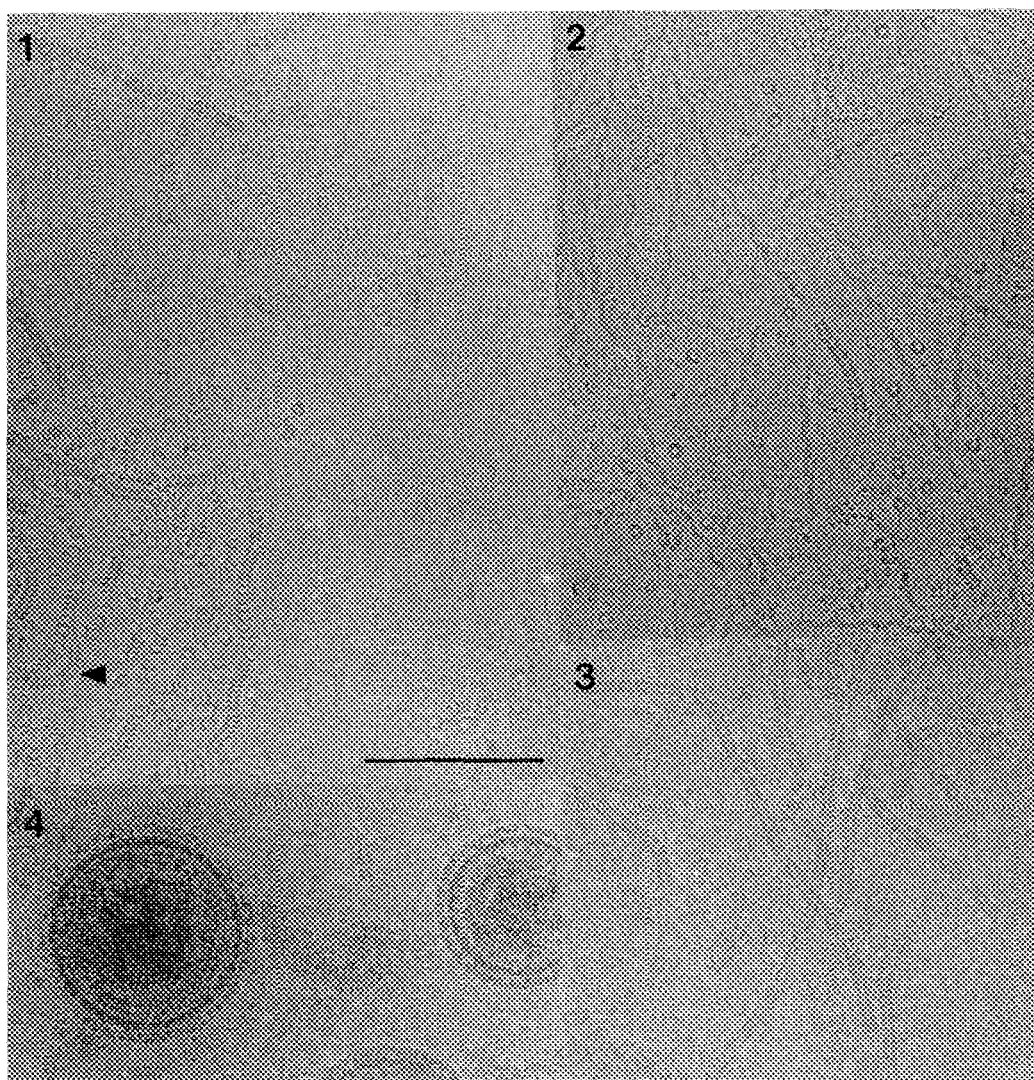


Fig. 1. Nucleocapsids (NC) in low salt buffer (10 mM Tris, pH 7.5, 1 mM EDTA). The helical filaments appear sometimes curvy or bent (arrow). Note the presence of C and Ring shape structures.

Fig. 2. Ribbon-like structures observed with purified NCs suspended in low salt buffer.

Fig. 3. NCs in high salt buffer (1.5 M NaCl, 10 mM Tris, pH 7.5, 1 mM EDTA). The helical filaments are predominantly straight and helical turns are more compact. No C or Ring shape structure were observed.

Fig. 4. Sendai virion in low salt buffer. Spikes and internal NCs are visible in defocus image.

Scale Bar = 200 nm

ELECTRON MICROSCOPY AND LASER SCANNING MICROSCOPY OF HIGH-PRESSURE FROZEN FREEZE-SUBSTITUTED SAMPLES OF *SORDARIA HUMANA*

Kirk J. Czymmek

Department of Botany and Plant Pathology and Center for Electron Optics, B-5
Pesticide Research Center, Michigan State University, East Lansing, MI 48824

The process of spore formation (ascosporogenesis) has not been clearly defined in ascomycete fungi. Many conflicting reports exist concerning details of ascospore initial development¹. The relatively slow fixation (up to several minutes) of conventional chemical techniques does not adequately preserve many structures for which ultrarapid freezing techniques (within milliseconds) are particularly suited². High-pressure frozen freeze-substituted samples of the ascomycete *Sordaria humana* were thick-sectioned for laser scanning microscopy (LSM) and thin-sectioned for transmission electron microscopy (TEM). Perithecia were too large (up to 500 μ m in diameter) to freeze adequately using plunge or propane-jet freezing techniques. The LSM was used to examine portions of the perithecia which were too large for viewing by TEM without taking numerous low magnification micrographs.

High-pressure freezing allowed excellent preservation of membranes (Figs. 1, 2), microtubules and associated structures (Fig. 2), and many details within developing ascospore initials (Figs. 3, 4). Segments of a smooth-contoured double-membraned cylinder enveloped individual nuclei with accompanying cytoplasm, lipid bodies and organelles to form ascospore initials (Fig. 1). Envelopment of each ascospore initial appeared to be facilitated by a modified nuclear associated organelle with numerous microtubules emanating along its axis (Fig. 2). Details observed within developing ascospore initials (Figs. 3, 4) included the presence and behavior of nuclei, microbodies, multi-vesicular bodies, and cisternae. LSM of the coencytic zone (Fig. 5) showed a large region filled with numerous vacuoles. Results regarding nuclear behavior, microtubule organization and ascospore initial wall development will be presented.

References

1. A. Beckett, in G. Turian and H.R. Hohl, Ed., The Fungal Spore, London: Academic Press (1981)107.
2. J.C. Gilkey and L.A. Staehelin, J. Electr. Microsc. Tech. (1986)3, 177.
3. We thank C. Bricker and L. Sadowski at Miami University, Oxford, Ohio for use of the high-pressure freezer (NSF grant # 88-20387 to M. Powell and A. Allenspach).

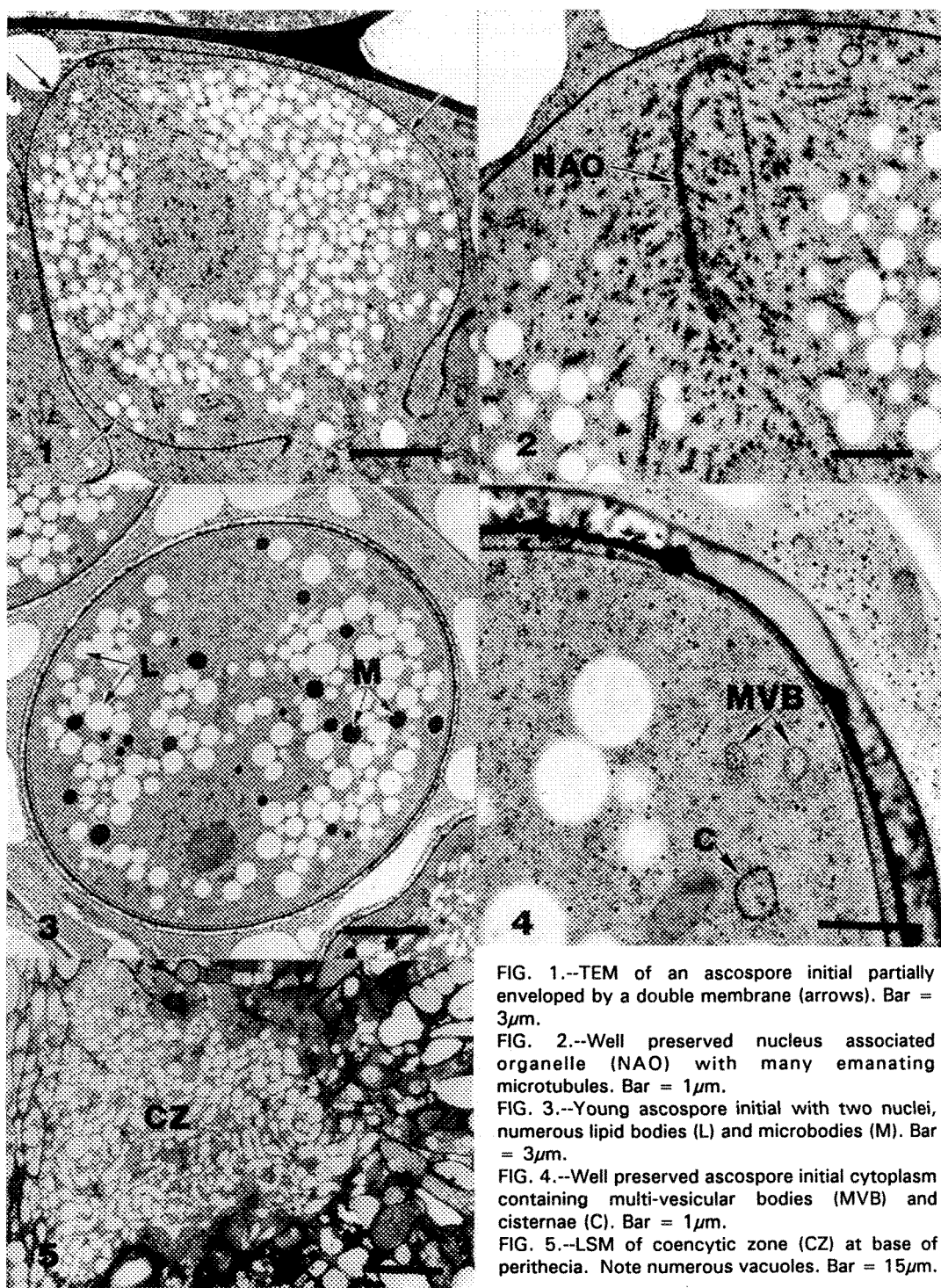


FIG. 1.--TEM of an ascospore initial partially enveloped by a double membrane (arrows). Bar = $3\mu\text{m}$.

FIG. 2.--Well preserved nucleus associated organelle (NAO) with many emanating microtubules. Bar = $1\mu\text{m}$.

FIG. 3.--Young ascospore initial with two nuclei, numerous lipid bodies (L) and microbodies (M). Bar = $3\mu\text{m}$.

FIG. 4.--Well preserved ascospore initial cytoplasm containing multi-vesicular bodies (MVB) and cisternae (C). Bar = $1\mu\text{m}$.

FIG. 5.--LSM of coenocytic zone (CZ) at base of perithecia. Note numerous vacuoles. Bar = $15\mu\text{m}$.

TEM ANALYSIS OF BASIDIOSPOROGENESIS IN *PANELLUS STYPTICUS*

Wilma L. Lingle, Ronald P. Clay and David Porter

Department of Botany, University of Georgia, Athens, GA 30602

Panellus stypticus is a white-rot basidiomycete of world-wide distribution^{1,2,3}. The 0.5 cm to 2.5 cm diameter gilled basidiocarps are evident from late summer through winter, usually on dead hardwood limbs. Basidiocarps can revive from desiccation when moistened, often generating more basidiospores. Basidiospores are thin-walled, hyaline and amyloid (i.e., they stain with Melzer's iodine solution)³. In the present study the ultrastructure of events in basidiosporogenesis in *P. stypticus* was investigated using transmission electron microscopy (TEM). Conventional fixation (CF), using aqueous-based fixatives, and plunge freezing followed by freeze substitution (FS) fixation procedures were employed. Gold-tagged wheat germ agglutinin (WGA), *Ricinus communis* agglutinin (RcA) and α -amylase were used to investigate the composition of cytoplasmic and extra-cytoplasmic polysaccharides and cell walls, and to localize polysaccharides which may be involved in the ability to revive from desiccation.

FS was superior to CF in preserving cytological features and retaining cell wall and extracellular materials. Basidiosporogenesis in *P. stypticus* was continuous and asynchronous. Young dikaryotic basidia, presumably prior to karyogamy, were observed among remnants of wall material from basidia which had already released basidiospores (Fig.1). Synapsis, all stages of meiosis I and prophase of meiosis II were observed. The nuclear envelope breaks down during meiosis I, temporarily re-forms during interphase I (Fig.2), and is at least partially broken down during meiosis II. Many events in spore development, including sterigma initiation (Fig. 3) and elongation, organelle translocation and nuclear migration (Fig. 4), were observed. Spindle pole bodies (SPBs) with microtubule arrays were seen associated with nuclear migration into developing spores (Fig. 4). All cell walls observed were positive for WGA, indicating the presence of chitin (Figs. 5,7). Septa delimiting basidiospores from sterigmata labeled heavily with WGA (Fig. 5). Basidiospores had an α -amylase-positive outer cell wall layer (Fig. 6). Only after basidiospore release were surfaces of sterigmata and basidia similarly labeled. This amyloid layer may provide protection against desiccation and thus allow continued production of basidiospores after rewetting. This is the first investigation of basidiosporogenesis in a homobasidiomycete preserved for TEM by FS.

References

1. R. Blaich and K. Esser, Archives of Microbiology (1975)103, 271.
2. H. H. Burdsall, Jr. and O. K. Miller, Jr., Nova Hedwigia (1975)51,79.
3. O. K. Miller, Jr., 1970. Michigan Botanist (1970)9,17.

FIG. 1.--Young, presumably dikaryotic, basidia have not elongated to extend past remnants of old basidia. Basidial apices are devoid of major organelles. Nuclei (N), mitochondria and vacuoles (V) are located in mid- and basal regions of basidia. Bar = 1 μ m.

FIG. 2.--Nuclear envelope (arrows) in telophase I is re-formed around daughter nuclei (N). Spindle MTs extend between daughter nuclei through fenestrae (arrowheads) in nuclear envelopes. Astral MTs radiate from SPBs. Bar = 0.5 μ m.

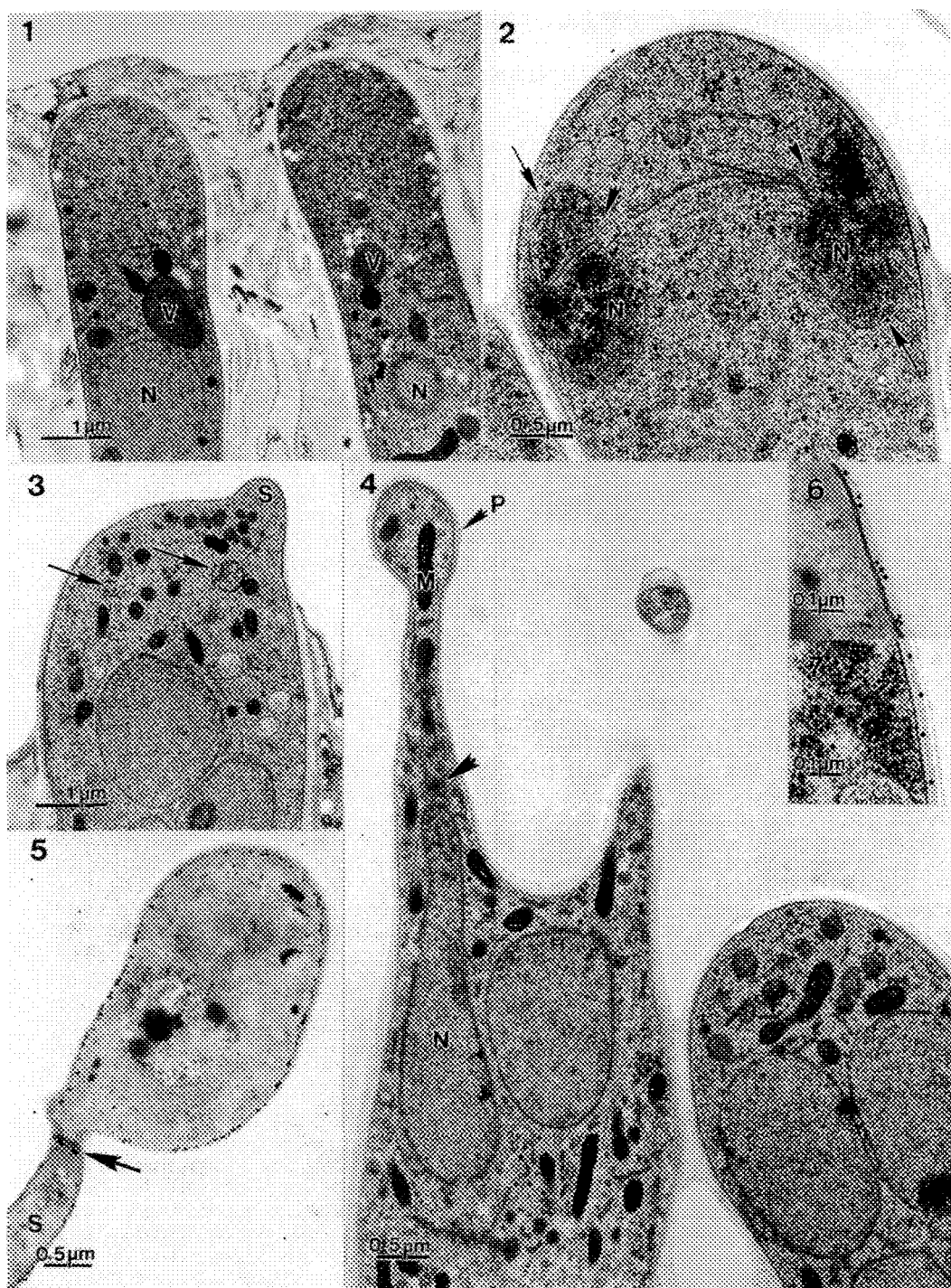
FIG. 3.--Thin wall of young sterigma (S) is continuous with inner wall layer of basidium. Elaborate Golgi equivalents (arrows) which produce coated vesicles are present. Bar = 1 μ m.

FIG. 4.--Sterigma tip is expanded to form basidiospore initial which ultimately will become the basidiospore. Pellicle (P) covers the expanding tip. Mitochondrial profile (M) is in basidiospore initial. Elongate nucleus (N) is situated at base of sterigma, with SPB (arrowhead) at tapered apex of nucleus. Numerous MTs extend from the SPB toward the basidiospore initial, while other MTs radiate out from the SPB to encase the nucleus. Bar = 0.5 μ m.

FIG. 5.--CF, WGA-labeled, nearly mature basidiospore is separated from sterigma (S) by WGA-labeled septum (arrow). Inner spore wall and sterigma wall also are labeled with WGA. Bar = 0.5 μ m.

FIG. 6.--Detail of CF basidiospore wall shows only outer layer labeled with α -amylase. Bar = 0.1 μ m.

FIG. 7.--Detail of FS basidiospore wall shows the inner layer labeled with WGA. Bar = 0.1 μ m.



CALCIUM UPTAKE AND CHANGES IN MEMBRANE MORPHOLOGY OF CL.SPOROGENES BACTERIAL SPORES

B.J.Panessa-Warren, G.T.Tortora* and J.B.Warren**

Dept. of Allied Health Resources, Health Sciences Ctr., SUNY Stony Brook, N.Y. 11794; *Dept. of Medical Technology, Health Sciences Ctr., and Clinical Microbiology, University Hospital, SUNY Stony Brook, N.Y. 11794; **Instrumentation Division, Brookhaven National Laboratory, Upton, N.Y. 11973

The bacteria comprising the genus, Clostridium, cause many severe infections in humans (tetanus, gas gangrene, botulism), and are particularly virulent and difficult to kill. Like the other spore forming bacteria, Clostridial endospores have a high calcium content (1-15% by wt), which is believed to play a role in the resistivity of this spore to sporocides. This paper presents a series of experiments which compare normal clostridial spore morphology and ultrastructure, to the morphology of identical spores treated to reveal sites of calcium deposition; study the effects of calcium depletion; and determine by TEM and SEM if the spores have the capability to alter their shape or respond to their environment to facilitate infection.

Clostridium sporogenes (ATCC 3584) was grown in cooked meat media and subsequently washed and filtered in deionized water. The spores were harvested in distilled water, heated to 80 C for 20 min to kill any remaining vegetative cells, washed 3 times in sterile distilled water, and stored at 2-8 C until needed. For routine TEM, spores were placed in warm 2% agar and fixed for 2 hrs in 3% glutaraldehyde in 0.1M cacodylate buffer (pH 7.2), followed by 2 rinses in buffer, 1 rinse in distilled water and post fixation in 1% aqueous osmium tetroxide for 1 hr. For SEM a droplet of spores was placed on a cleaned SEM stub to which an equal volume of 3% glutaraldehyde was added. After 1 hr the stub was placed in a vial filled with fresh 3 % glutaraldehyde. The SEM stubs with the attached spores were rinsed 2 times in buffer and once in distilled water. All microscopy samples were dehydrated in acetone. Spores were also fixed in glutaraldehyde containing either 1% or 2% calcium chloride, 2% barium chloride or 1% lanthanum chloride. To identify sites of high calcium (Ca) concentration by acid crystallization, spores were treated with 20 % oxalic acid or 10 % sulfuric acid to form in situ crystals of either calcium oxalate or calcium sulphate.

To determine whether tubulin or actin are involved in spore architecture, attachment or movement, spores were incubated with colchicine or cytochalasin B prior to fixation. Because the cytochalasin B had to be dissolved using DMSO, the effect of DMSO alone on the spores was also studied. All SEM specimens were washed in buffer, dehydrated in acetone, critical point dried, and coated with AuPd. SEM samples were viewed in an AMRay 1000A SEM (15 KV), and thin sections were imaged in a Philips 300 (80 KV).

Unstained thin sections of spores fixed in calcium chloride revealed extensive electron dense deposits within the protoplast, spore coat and exosporium. Spores treated with barium (Ba) showed an electron dense staining at the outer spore coat only, and those treated with lanthanum (La) showed uptake at the spore coat and protoplast. Although both La and Ba were modestly incorporated and stored at the spore coat and to a lesser extent in the protoplast, the spores exhibited a selective, profound preference for Ca uptake and storage throughout the spore. By SEM those spores fixed in the presence of either Ca or Ba appeared lozenge-shaped. Some spores clearly had a pointed apical region and a distal or tail region. The exosporium was covered with 50-90nm membranous projections (Fig.1). Some spores appeared to be more round with less distinct distal regions, and no membranous projections. To insure that these morphological differences were not representative of spore contamination, the spore suspension was incubated anaerobically and aerobically on agar plates. No contamination was found.

When spores were incubated in EDTA (which chelates Ca), all of the spores revealed apex and tail regions as well as projections on their exosporial membranes. Spores treated with colchicine produced SEM images identical to the normal control spore populations. All cytochalasin treated spores had low exosporial projections, small regions of smooth membrane, and clear polarity.

In summary, C.sporogenes endospores seem to preferentially incorporate and store Ca. When Ca is not available to the spore, either by Ba substitution or Ca chelation with EDTA, all of the spores exhibit exosporial projections and a prominent tail region. The lack of response to colchicine, suggests that tubulin does not play a role in the spore architecture, nor in the appearance of the membrane projections. When treated with cytochalasin B, or EDTA, all of the spores have low exosporial membrane projections, exhibit a distinct "tail" region and often show attachments to the SEM substrate, suggesting that Ca as well as perhaps actin, may play a role in the morphological transformation of the spore and attachment.

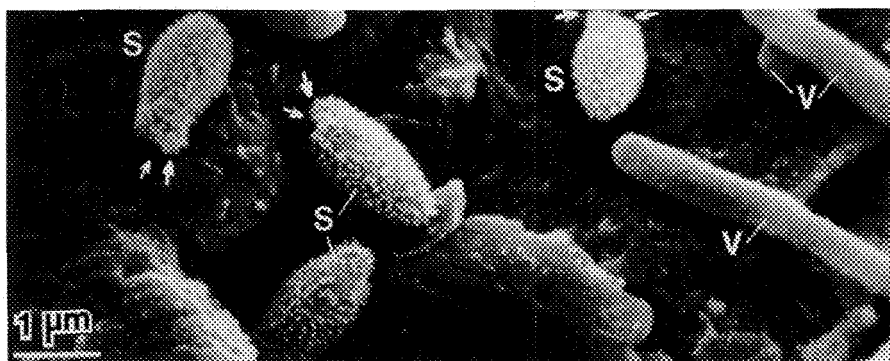


Fig.1. Cl. sporogenes endospores (S) with exosporial membrane projections and tail regions (arrows). Vegetative cells (V).

MULTIPLE MINERAL PRECIPITATIONS INSIDE MAGNETOTACTIC MICROORGANISMS

M. Farina (1), U. Lins, H.G.P. Lins de Barros and R. Broderick (2)

1- Instituto de Biofísica Carlos Chagas Filho, UFRJ, Cidade Universitária, Rio de Janeiro, 21949 Brasil

2- Department of Pharmacology and Experimental Therapeutics, University of Maryland, Scholl of Medicine, Maryland 21201

Magnetotactic microorganisms have been described mainly as swimming magnetic bacteria (MB) from natural waters which produce magnetite crystals (1) or as the magnetotactic multicellular aggregate (MMA) producing the iron sulphides greigite, pyrite (2) and possibly pyrrhotite (3). Also regions containing iron and oxygen were described in MMA but with no complete analytical information (3). We present here, some new aspects on mineral precipitations inside both MB and MMAs.

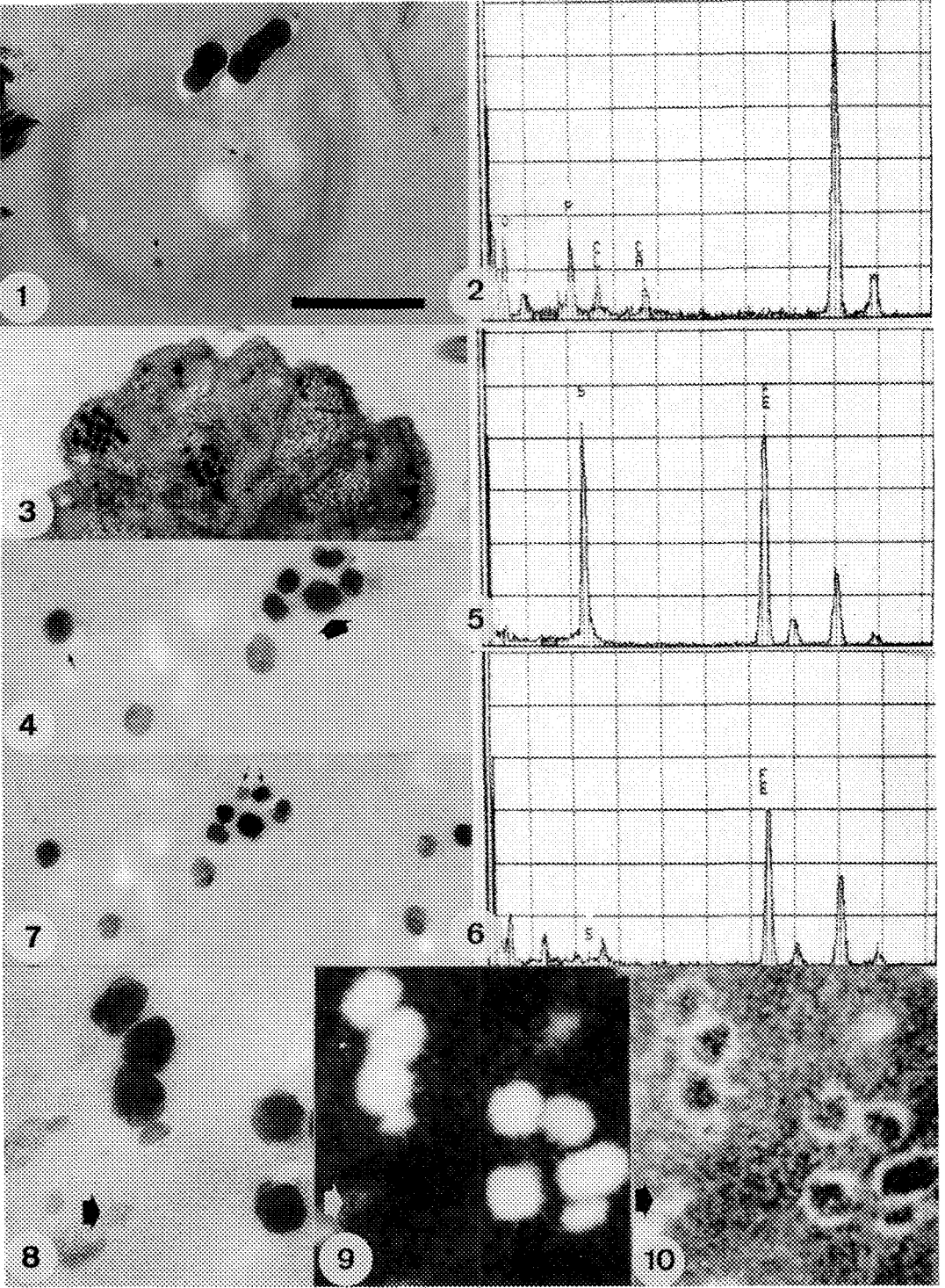
Figure 1 shows a magnetic bacterium obtained from non saline waters under the transmission electron microscope, with typical magnetite crystals (dark regions). Small electron dense regions (arrows) containing oxygen, phosphorus and calcium are depicted here for the first time by electron probe microanalysis (EPMA) (Fig. 2). Since no phosphorus in buffer solutions was present, we discard any artifactual effect from sample preparation. Because in all MB observed earlier only the mineral magnetite was found, we concluded that in the present case the mineralization paths are independent from each other.

Inside each MMA cell component, chains of electron dense regions are present (Fig.3). In figure 4 the large arrow indicates a typical crystal identified as greigite (Fe_3S_4) (spectrum in Fig.5). The less dense regions in figure 4 like the one indicated by the small arrow contain iron and small amounts of oxygen. No sulphur is present inside this region (spectrum in Fig.6). The sample was tilted before each analysis to guarantee that the electron beam was pointed to individual crystals. Figure 7 (arrows) shows two crystals not initially seen in figure 4.

Figures 8, 9 and 10 represent respectively bright field, iron electron distribution image (EDI) and oxygen EDI of ultra thin sectioned unstained MMA under the ZEISS CEM902 electron microscope. Oxygen surrounds the iron sulphide crystals (white rings in Fig.10) as well as it is present in entire regions (arrows). The presence of oxygen may not represent simply an inorganic oxidation, as it would be difficult to comprehend further oxidation of iron sulphides without the presence of sulphur (arrows in figures 4, 8, 9 and 10). So, we conclude that these iron oxygen containing regions may be thought as iron storage precursors for crystal precipitation. EPMAs were performed in a JEOL 1200 EX microscope with LaB6 filament operating in the scanning transmission mode with Tracor Northern analytical system. Bar represents $0.5\mu\text{m}$ in Fig.1 and 4, $1.0\mu\text{m}$ in Fig.3, $0.2\mu\text{m}$ in Fig.8.

References

- 1- R.P. Blakemore, in R.B. Frankel and R.P. Blakemore, Eds., Iron Biominerals, New York: Plenum (1991) 51.
- 2- S. Mann et al., Nature (1990) 343, 258.
- 3- M. Farina et al., Nature (1990) 343, 256.
- 4- This research was supported by a grant from CNPq and FINEP agencies from Brasil and University of Maryland at Baltimore - DRIF/SRIS Fund.



SCANNING ELECTRON MICROSCOPY OF ERYTHROPHAGOCYTOSIS BY *Entamoeba histolytica* TROPHOZOITES

Victor Tsutsumi,* Adolfo Martinez-Palomo* and Kyuichi Tanikawa**

* Department of Experimental Pathology, Center for Research and Advanced Studies, I.P.N. Mexico City, Mexico 07360

** Department of Internal Medicine, Kurume University School of Medicine. Kurume, Japan

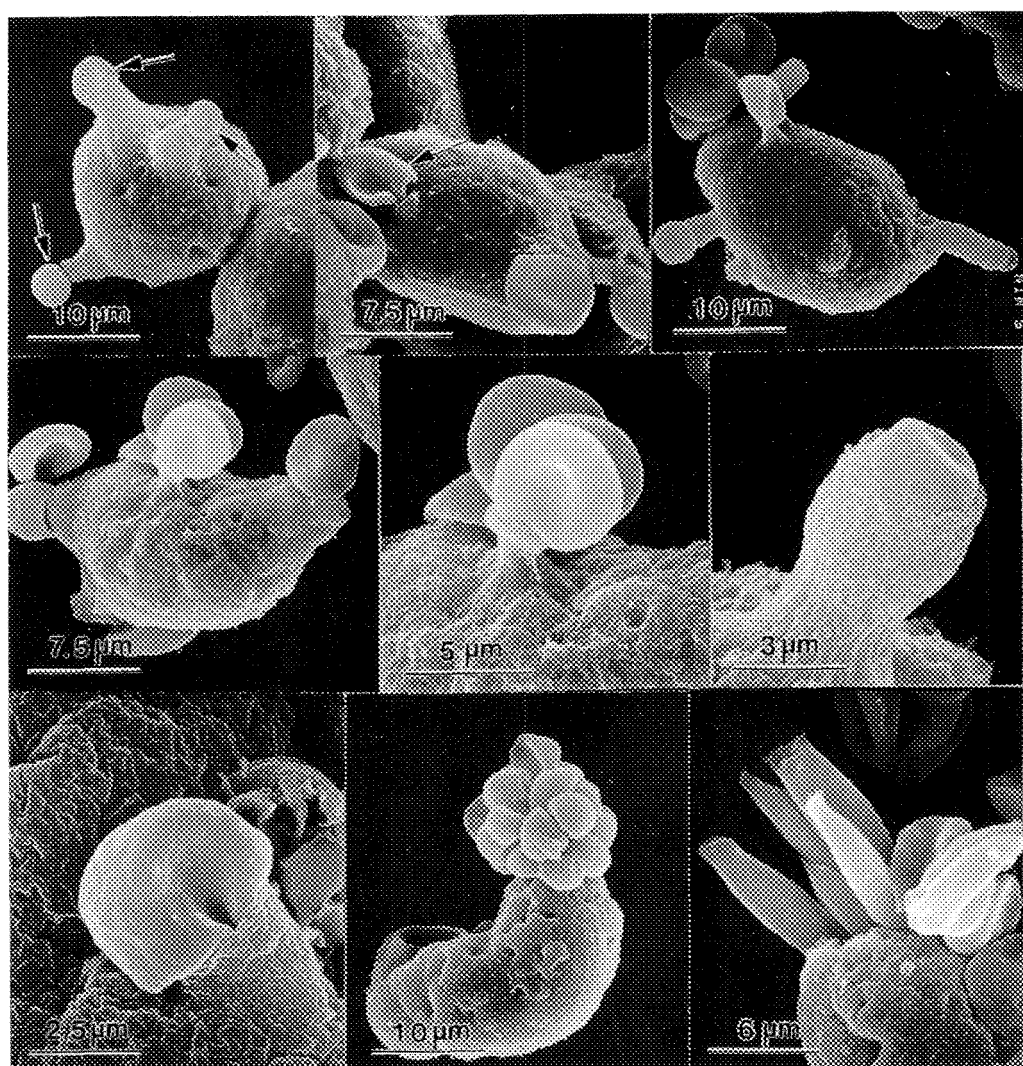
The protozoan parasite *Entamoeba histolytica* is the causative agent of amebiasis in man. The trophozoite or motile form is a highly dynamic and pleomorphic cell with a great capacity to destroy tissues. Moreover, the parasite has the singular ability to phagocytize a variety of different live or death cells. Phagocytosis of red blood cells by *E. histolytica* trophozoites is a complex phenomenon related with amebic pathogenicity and nutrition.¹

We analyzed by scanning electron microscopy (SEM) the time-lapse sequence of erythrocyte ingestion by a virulent strain of *E. histolytica* trophozoites. Axenic cultures of amebas were placed in chamber plastic slides with 4 rectangular wells (Lab-tec, Nunc, Inc. Naperville, IL). Trophozoites were firstly left to self attach to the plastic surface of wells by incubating for 30 min at 37°C. Human red blood cells (group 0, Rh⁺) were added to the wells in a ratio of 1/100, ameba/erythrocytes.² After an interaction of 3, 5, 10, 15 and 30 min, cells were fixed with 2.5% glutaraldehyde and processed for SEM. At early interactions (3-5 min) the trophozoites were surrounded by intact erythrocytes. Endocytosis of these erythrocytes were observed at any site of the ameba surface by extending a long or short cytoplasmic processes (Figs. 1,2). The top of these ameba extensions presented one (Fig. 1,2,3) or various erythrocytes (Fig. 5) apparently being suctioned (Fig. 6), producing deformations of the normal cell shape (Fig. 7). Late cell interactions (10-30 min) were characterized by a polarization of the process of red blood cells endocytosis. Most of the erythrocytes were localized at one pole of the trophozoites giving an aspect of a bouquet of flowers in a vase (Fig. 8). Elongated and partially disrupted erythrocyte ghosts were also observed at the polarized site (Fig. 9).

Erythrophagocytosis by *E. histolytica* is a distinct process of endocytosis characterized by suction of cells randomly at early stages and a polarization of the phagocytic event at one end of the parasite.³

References

1. A. Martinez-Palomo, Ed., The Biology of *Entamoeba Histolytica*, Chichester: Research Studies Press (1982)96.
2. V. Tsutsumi et al., Trans. R. Soc. Trop. Med. & Hyg. (1992) (in press).
3. This work was supported in part by grants from CONACYT (Mexico) and Rockefeller and MacArthur foundations (USA).



FIGS. 1,2. Three minutes interaction between trophozoites and erythrocytes. The tops of long (1) or short (2) ameba cytoplasmic extensions show the ingestion of erythrocytes (arrows).

FIGS. 3,4,5. Five minutes interaction. Erythrocytes are still localized randomly on the surface of trophozoites. Multiple cell ingestion is seen (4,5).

FIGS. 6,7. Ten minutes interaction. Partially deformed erythrocytes are observed at the top of cytoplasmic extensions.

FIGS. 8. Fifteen minutes interaction. The process of red blood cells phagocytosis has been polarized to one end of the trophozoite.

FIG.9. Thirty minutes interaction. The polarized process of endocytosis shows also disrupted erythrocyte ghosts.

BACTERIAL BIOFILM BEHAVIOR IN WATER-SUPPLY LINES OF DENTAL UNITS

B. D. Tall,* K. S. George,** R. T. Gray,* and H. N. Williams**

*Divisions of Microbiology and Pathology, Center for Food Safety and Applied Nutrition, Food and Drug Administration, Washington, DC 20204 and **Department of Microbiology, University of Maryland Dental School, Baltimore, MD 21201

Studies of bacterial behavior in many environments have shown that most organisms attach to surfaces, forming communities of microcolonies called biofilms. In contaminated medical devices, biofilms may serve both as reservoirs and as inocula for the initiation of infections.¹ Recently, there has been much concern about the potential of dental units to transmit infections.² Because the mechanisms of biofilm formation are ill-defined, we investigated the behavior and formation of a biofilm associated with tubing leading to the water syringe of a dental unit over a period of 1 month.

After new tubing was installed on the syringe, the unit was used in the usual manner. At 8 h, daily (day 2 to day 8), every third day (day 9 to day 27), and on day 30, a 5 cm tubing sample (TS) was removed. The residual water from the TS was drained into a sterile tube. Viable plate counts were performed on biofilm samples removed from luminal tubing surfaces (LTS) and on the residual water by using dilute peptone medium. Another part of the TS was fixed in 3% glutaraldehyde in 0.2 M sodium cacodylate buffer, pH 7.2, and prepared for evaluation by scanning electron microscopy (SEM).

Culture results revealed an approximate 1.5 log increase over the first 6 days for both the planktonic and biofilm populations (Fig. 1), with *Pseudomonas* species the predominant bacteria recovered. SEM revealed an absence of bacteria on LTS at 8 h (data not shown) and day 3 after new tubing was installed (Fig. 2). However, further SEM evaluation of LTS, specifically those of samples taken at day 7, showed bacteria present as single cells or in doublets (Fig. 3). In contrast, complex microcolonies were observed at day 30 (Figs. 4 and 5). These results suggest that the predominant colonization of the LTS occurred between day 3 and day 7, with biofilms of greatest complexity forming between day 7 and day 30. It is noteworthy that in the day 7 samples, bacteria were found adhering to the sides of parallel ridges observed in the LTS, suggesting that colonization occurred first within these protected areas. In contrast, at day 30 the ridges were not observed. Apparently the conditioning of the LTS, the established microcolonies, and the complexity of the biofilm were sufficient to obscure the ridges. Changes in bacterial flora colonizing the LTS were observed by both SEM and the culture method. At day 7 the predominant bacteria observed by SEM were rod-shaped, whereas at day 30 the predominant bacteria were spiral-shaped. The spiral-shaped bacteria were not recovered by the culture technique. These results demonstrate the dynamics of biofilm formation, corroborating the results of other studies; they also describe a bacterial biofilm that may serve as a reservoir for bacterial contamination of water delivered by dental units and may present a health risk for immunocompromised dental patients.¹

1. J. W. Costerton and H. M. Lappin-Scott, ASM News. (1989)55, 650.

2. M. V. Martin, Br. Dent. J. (1987)163, 152.

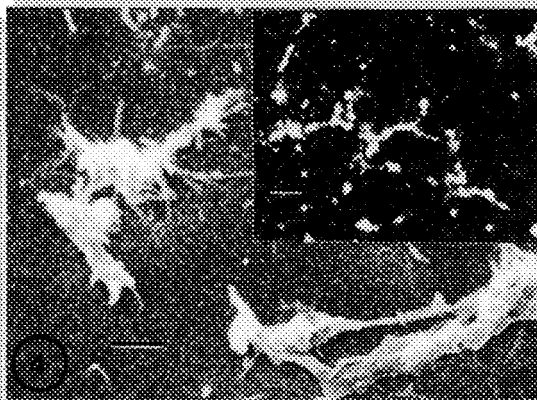
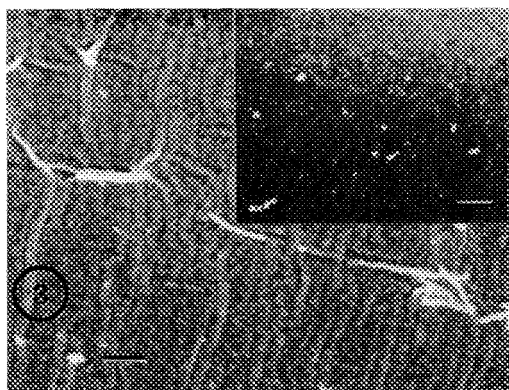
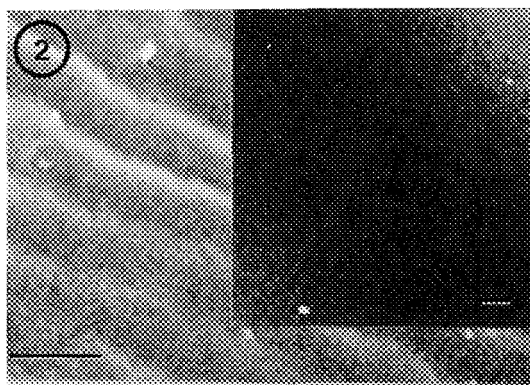
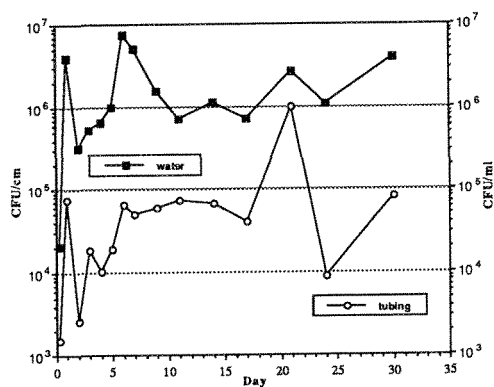


Fig. 1. Bacterial viable counts from residual water and biofilm samples.

Fig. 2. SEM of LTS at day 3 after new tubing was installed. Bar marker for figure and inset = 5 and 20 μm , respectively.

Fig. 3. SEM of LTS at day 7 after new tubing was installed. Bar marker for figure and inset = 5 and 10 μm , respectively.

Fig. 4. SEM of LTS at day 30 after new tubing was installed. Bar marker for figure and inset = 5 and 10 μm , respectively.

Fig. 5. SEM of microcolony on LTS at day 30 after new tubing was installed. Bar marker = 1 μm .



**ELECTRON MICROSCOPY OF MALACOSOMA DISSTRIA (LEPIDOPTERA: LASIOCAMPIDAE)
NUCLEAR POLYHEDROSIS VIRUS IN HEMOCYTE CULTURES**

A.J. Brownwright, J.A. MacDonald, and S.S. Sohi

Forest Pest Management Institute, Forestry Canada, P.O. Box 490, Sault Sainte Marie, Ontario P6A 5M7, Canada

The forest tent caterpillar, *Malacosoma disstria*, is a significant pest of hardwoods in Canada and the United States. Periodic heavy outbreaks of this insect cause appreciable losses in tree growth and fiber production in aspen stands and reductions in the yield of maple syrup and syrup products. Furthermore, large numbers of migrating larvae can have adverse effect on tourism and recreation. The Forest Pest Management Institute is trying to develop biorational control agents for this pest. A nuclear polyhedrosis virus (NPV) of this insect has shown promise as an insecticide, and has been successfully used in field trials. At present the virus can be produced only in the host larvae. However, continuous cell lines, IPRI-MD-66 and IPRI-MD-108, have been established from the hemocytes of this insect to develop an alternative method of virus production.^{2,3}

This paper presents a light microscope (LM) and transmission electron microscope (TEM) study of the replication of this NPV in IPRI-MD-66 cells.² Healthy and NPV-infected cells were processed according to a modification of the previously published technique.^{4,5} Briefly, cells were fixed in 2.5% glutaraldehyde in 0.05 M cacodylate buffer, pH 7.3, for 4 h at 4 °C, washed in 10% sucrose cacodylate buffer, post fixed in OsO₄ and encapsulated in 1% agar after rinsing in water. After en bloc staining in 2.5% aqueous uranyl acetate, the cells were dehydrated in an ethanol series and embedded in Araldite 6005 or L R White.

Healthy untreated cells had typical hemocyte characteristics as shown in Figure 1. In early stages of NPV infection nuclei became hypertrophied, virogenic stroma appeared, and the normal pattern of chromatin was disrupted (Fig. 2). As infection progressed, free nucleocapsids and subsequently multicapsid virions were observed. On day 6 post infection (p.i.), most cells showed evidence of infection ranging from early stages (Fig. 2) to cells with nuclei filled with well developed polyhedral inclusion bodies (PIBs), incorporating multicapsid virions (Fig. 3 & 4). Both nuclei and cytoplasm contained p10 protein. Although some aberrant forms of PIBs and virions occurred, the majority of infected cells produced large numbers of PIBs containing multicapsid virions ultrastructurally indistinguishable from the virus produced in vivo.

References

1. W.G.H. Ives and J.A. Muldrew, Fish. Environ. Can., Canadian Forestry Service, North. Forest Res. Centre Inf. Rep. (1978)NOR-X-204, 10.
2. S.S. Sohi, Can. J. Zool. (1971)49, 1355.
3. S.S. Sohi, Proc. Internat. Colloq. Invertebr. Tissue Culture (1973)3, 27.
4. S.S. Sohi et al., Can. J. Microbiol. (1981)27, 1133.
5. S.S. Sohi et al., Intervirology. (1984)21, 50.
6. We express sincere appreciation to Mrs. B.J. Cook for her excellent technical assistance.

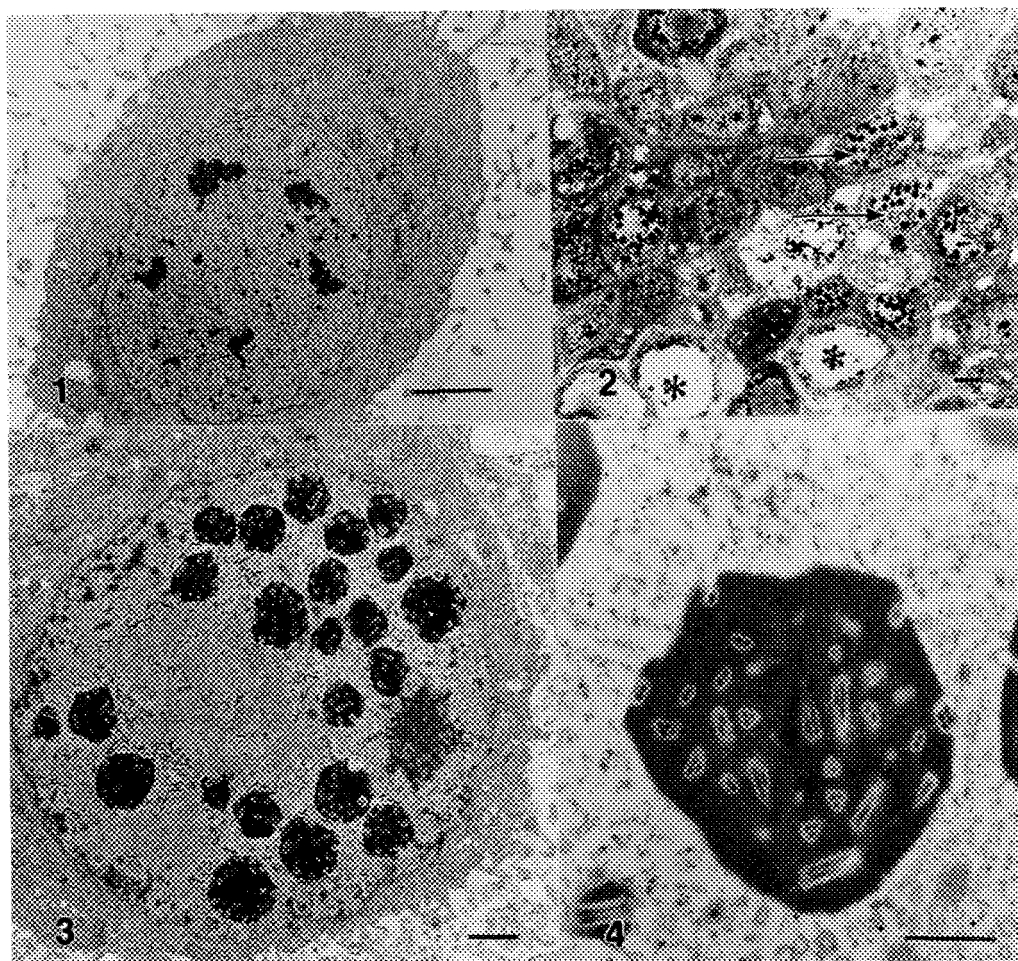


FIG. 1.-- TEM of healthy untreated IPRI-MD-66 cell. Bar = 3 μ m.
 FIG. 2.-- LM of infected cells 6 days post infection (p.i.). Note hypertrophied nuclei containing polyhedral inclusion bodies (PIBs) and virogenic stroma (arrow), and infected cells which have disintegrated, (asterisks). Bar = 20 μ m.
 FIG. 3.-- TEM of hypertrophied nucleus of infected cell 6 days p.i. showing PIBs with occluded and nonoccluded multicapsid virions. Bar = 1 μ m.
 FIG. 4.-- Close up of TEM of PIB showing occluded virions. Bar = 0.5 μ m.

HUMAN-HAIR ANALYSIS

BRENDA E. LAMBERT AND ERNEST C. HAMMOND

**DEPARTMENT OF PHYSICS, MORGAN STATE UNIVERSITY HILLEN
ROAD & COLD SPRING LANE, BALTIMORE, MD 21239**

The purpose of this study was to examine the external structure of four human hair shaft samples with the scanning Electron Microscope (SEM) and to obtain information regarding the chemical composition of hair by using the attached x ray microanalysis unit.

The hair samples were obtained from two female subjects. Sample A was taken from a black female and had not undergone any type of chemical processing. Sample B, C, D were taken from a white female, and were natural, processed, and unpigmented, i.e. "gray", respectively. Sample C had been bleached, tinted, and chemically altered using a permanent wave technique.

The SEM images revealed characteristics of the external cuticular layer for all samples. The edges of the scales along a single shaft were oriented in the same direction. The scale edges were smooth and close to the overlapping scales in both sample A and D. In sample B the edges were not as smooth while in sample C the edges were nonuniformly loose and jagged indicating some damage as a result of chemical processing. The distance between overlapping scales was less for sample A than for sample B. This could indicate a relationship between scale length and hair curliness.

The qualitative element analysis using the x ray unit displayed the expected presence of sulfur (as a result of disulfide cross-links inherent in hair chemistry.) Another element common to all samples was copper. The element potassium was present in sample B and C. Neither potassium nor calcium were present in sample D. The rarely found element, rhenium, was present in sample C and D.

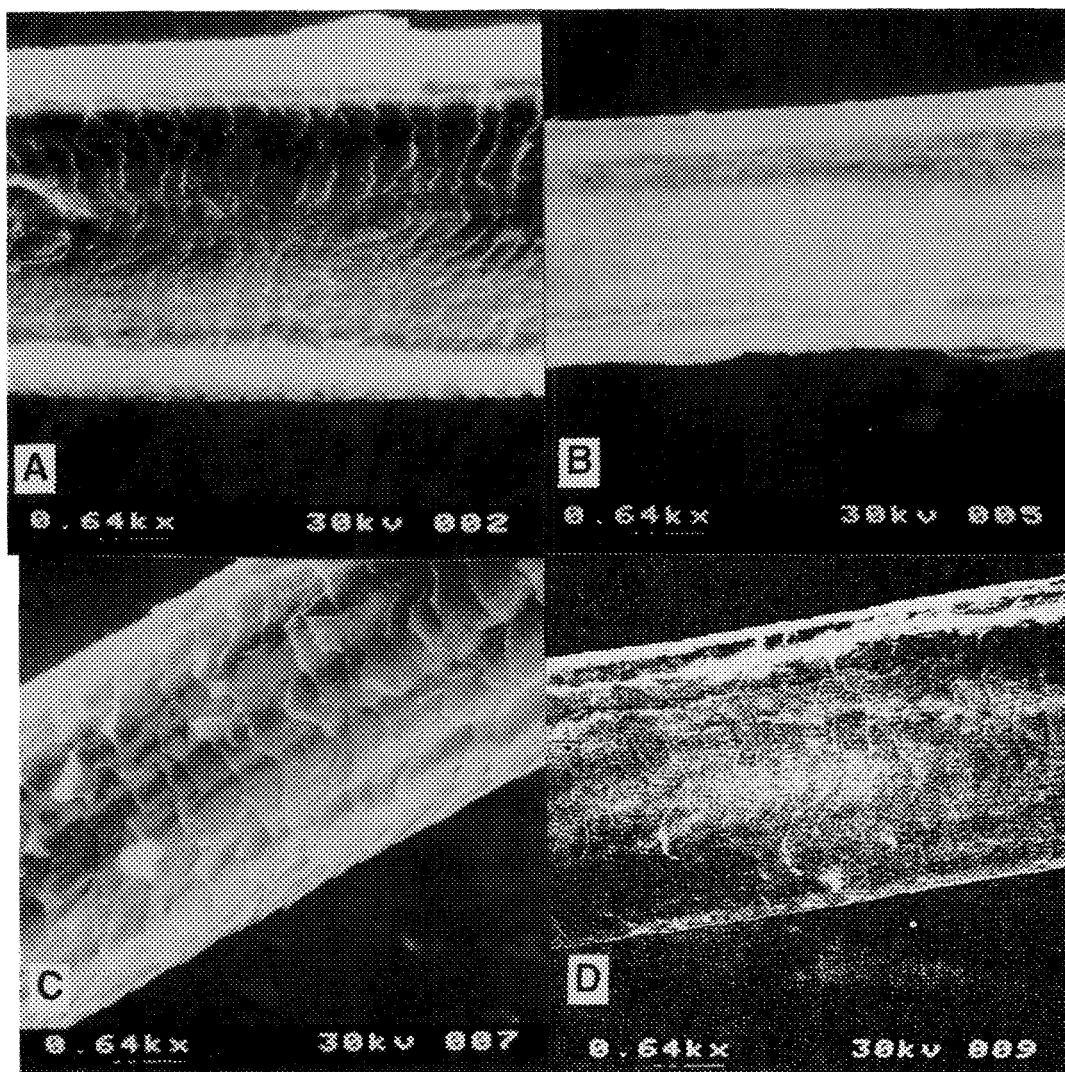


Fig. A.-- Sample A. Micrograph of a human hair form a black female. The hair is unprocessed with natural pigmentation.

Fig. B.-- Sample B. Micrograph of a human hair from a white female. Hair is unprocessed with natural pigmentation.

Fig. C.-- Sample C. Micrograph of a human hair from a white female. The hair has undergone chemical processing.

Fig. D.-- Sample D. Micrograph of a human hair from a white female. The hair is unprocessed and nonpigmented.

ULTRASTRUCTURE OF THE GILL OF PALAEMONETES PUGIO AS COMPARED TO THE STRUCTURE OF UROPOD SETAE THROUGHOUT THE MOLT CYCLE

Nancy L. Andon and Richard M. Dillaman

Center for Marine Science Research, University of North Carolina at Wilmington, Wilmington, North Carolina 28403

In order to grow, crustaceans must shed their old cuticle (molt) and replace it with a new, larger one. To achieve this, it is necessary to form a new, preexuvial, cuticle under the old cuticle prior to molting. In most of the integument this does not present a problem; however, in the gill, the addition of the preexuvial layer might create an extended barrier to ion and gas exchange. In order to determine whether gills have devised a strategy to deal with this potential problem, the ultrastructure of the gills from the grass shrimp *Palaemonetes pugio* were examined throughout the molt cycle. The timing of the sequential steps of the molt in the cuticle other than the gills was determined by examining the light microscopic appearance of the setae at the margin of the uropods. Stevenson¹ described the cuticle of the dorsal carapace throughout the molt cycle and correlated those events with setae formation. Consequently, separation and subsequent retraction of the hypodermis from the old cuticle and deposition of the new cuticle have been widely used as a convenient, non-invasive means of determining molt stage in crustaceans.

Anterior gills examined at intermolt (stage C₁) had a hypodermis that was tightly apposed to the cuticle (Fig. 1a). The cuticle had several distinct layers, the most obvious being the outermost, electron dense, lipid-containing, epicuticle. Setae from the same animal (Fig. 1b) showed no separation of the underlying hypodermis. By early premolt (Stage D₁) there was no detectable change in the ultrastructure of the gills (Fig. 2a), but the setae showed clear evidence of hypodermal retraction (Fig. 2b). By late premolt (Stage D₂) preexuvial cuticle formation was extensive (Fig. 3a) as evidenced by a new epicuticle beneath the old cuticle. Setae from the same D₂ animal likewise showed extensive new cuticle formation. By early in post-molt (Stage A₁) cuticle deposition appeared complete in the gill (Fig. 4a) while in the setae the cuticle had not yet reached its maximum thickness (Fig. 4b). In summary, the gills of *P. pugio* appear to delay the onset of the molt cycle and then abbreviate the events of new cuticle deposition. The probable net effect of this strategy is that the interruption of gill function is minimized.

References

1. J.R. Stevenson, Amer. Zool. (1972)12, 373.

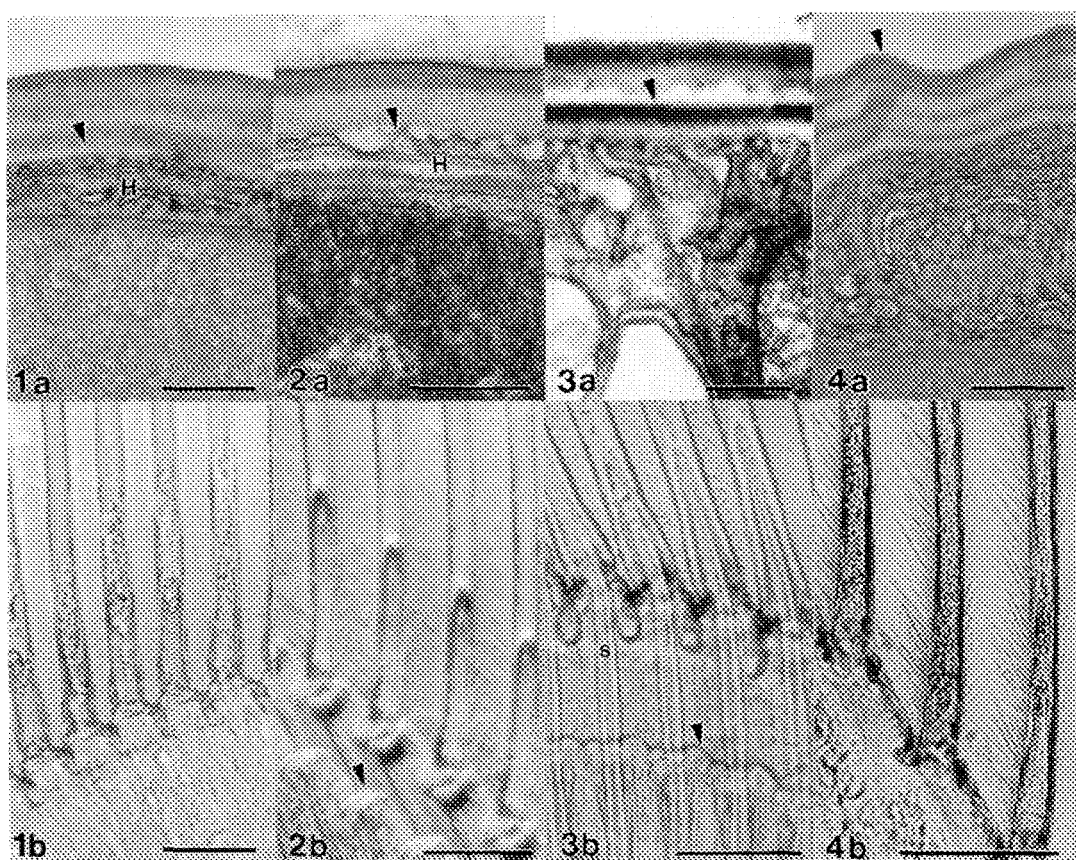


FIG. 1a. Gill of stage C_4 (intermolt) shrimp. Note cuticle (arrow) apposed to underlying hypodermis (H). Bar = $1.0\mu\text{m}$.

FIG. 1b. Light micrograph of uropod from same C_4 shrimp showing setae. Bar = $100\mu\text{m}$.

FIG. 2a. Gill of stage D_2 (early premolt) shrimp with hypodermis (h) still apposed to cuticle (arrow). Bar = $1.0\mu\text{m}$.

FIG. 2b. Light micrograph of uropod from same D_2 shrimp. Note moderate hypodermal retraction from the setae (arrow). Bar = $100\mu\text{m}$.

FIG. 3a. Gill of stage D_3 (late premolt) shrimp. Note separation of the overlying old cuticle and deposition of an extensive new cuticle (arrow). Bar = $1.0\mu\text{m}$.

FIG. 3b. Uropod from same D_3 shrimp. Note extensive new setae formation (s) and retraction of the hypodermis from the old setal platforms (arrow). Bar = $100\mu\text{m}$.

FIG. 4a. Gill of stage A_2 (early postmolt) shrimp showing essentially complete cuticle deposition (arrow). Bar = $1.0\mu\text{m}$.

FIG. 4b. Uropod from the above A_2 shrimp showing setae with slightly thinner cuticle than in 1b. Bar = $100\mu\text{m}$.

ULTRASTRUCTURAL ANALYSIS OF UNIQUE GLYCOCONJUGATES IN THE RAT OLFACTORY SYSTEM

James E. Crandall*, Linda C. Hassinger and Gerald A. Schwarting*

E.K. Shriver Center, Waltham, MA 02254 and *Program in Neuroscience, Harvard Medical School, Boston, MA 02115

Cell surface glycoconjugates are considered to play important roles in cell-cell interactions in the developing central nervous system. We have previously described a group of monoclonal antibodies that recognize defined carbohydrate epitopes and reveal unique temporal and spatial patterns of immunoreactivity in the developing main and accessory olfactory systems in rats.¹ Antibody CC2 reacts with complex α -galactosyl and α -fucosyl glycoproteins and glycolipids. Antibody CC1 reacts with terminal N-acetyl galactosamine residues of globoside-like glycolipids. Antibody 1B2 reacts with β -galactosyl glycolipids and glycoproteins. Our light microscopic data suggest that these antigens may be located on the surfaces of axons of the vomeronasal and olfactory nerves as well as on some of their target neurons in the main and accessory olfactory bulbs.

We have begun studies to more precisely localize these glycoconjugate antigens at the ultrastructural level by using EM immunocytochemical techniques. Our first objective was to determine whether the antigenicity of the molecules could be preserved with aldehyde fixatives that would allow preservation of ultrastructural features. Since our prior data were obtained with frozen sections that would be inappropriate for electron microscopy, our second objective was to see whether adequate immunoreactivity could be obtained in tissue sections cut with a Vibratome without the use of detergents that might impair the quality of membrane preservation. Immunoreactivity for all three glycoconjugates is preserved with a fixation procedure that uses a combination of aldehydes. Adult rats are perfused intracardially with physiological saline followed with 2% paraformaldehyde/0.5% glutaraldehyde in 0.12M phosphate buffer, pH 7.2. After storage in the same fixative overnight at 4°C, the brains are removed and 50 μ m sections cut with a Vibratome. Sections are incubated with hybridoma supernatant overnight and then immunoreacted with peroxidase-conjugated anti-mouse IgM antibody. Reaction product is visualized with 0.001% hydrogen peroxide and 0.03% 3,3' diaminobenzidine. Sections are subsequently osmicated, dehydrated and embedded in Epon wafers between siliconized slides. Stained regions are trimmed and attached to blanks for thin sectioning.

The distribution of CC2, CC1, and 1B2 immunoreactivity in the accessory olfactory bulb in Vibratome-cut sections processed through to plastic embedding is virtually identical to that obtained in frozen sections. CC2 immunoreactivity is present in the nerve, glomerular and external plexiform layers throughout the rostrocaudal extent of the AOB (Figure 1). CC1 immunoreactivity is present in the nerve and glomerular layers of only the rostral half of the AOB (Figure 2). Ultrastructurally, CC2 immunoreactivity can be detected on or between adjacent axon membranes in the olfactory nerve layer. CC2 and CC1 immunoreactivity can also be seen related to selective groups of dendrites in the glomerular layer (Figures 3&4). CC2 immunoreactivity is present in extracellular spaces immediately adjacent to these dendrites (Figure 3). Some CC2 antigens also appear to be localized intracellularly. Although this requires further investigation, globosides have been previously demonstrated intracellularly in endothelial cells.² It may be that other globo-series glycolipids (e.g., CC2) can also be expressed intracellularly in the olfactory system.³

References

1. Schwarting G.A. & Crandall J.E. *Brain Res.* (1991) 547:239-248.
2. Gillard B.K., et al. *Exp. Cell Res.* (1991) 192:433-444.
3. This study was supported by NIH grant DC-00953, MR Core Grant HD-04147, and the Dept. of Mental Retardation of the Commonwealth of Massachusetts (Contract:1000-10003-SC).

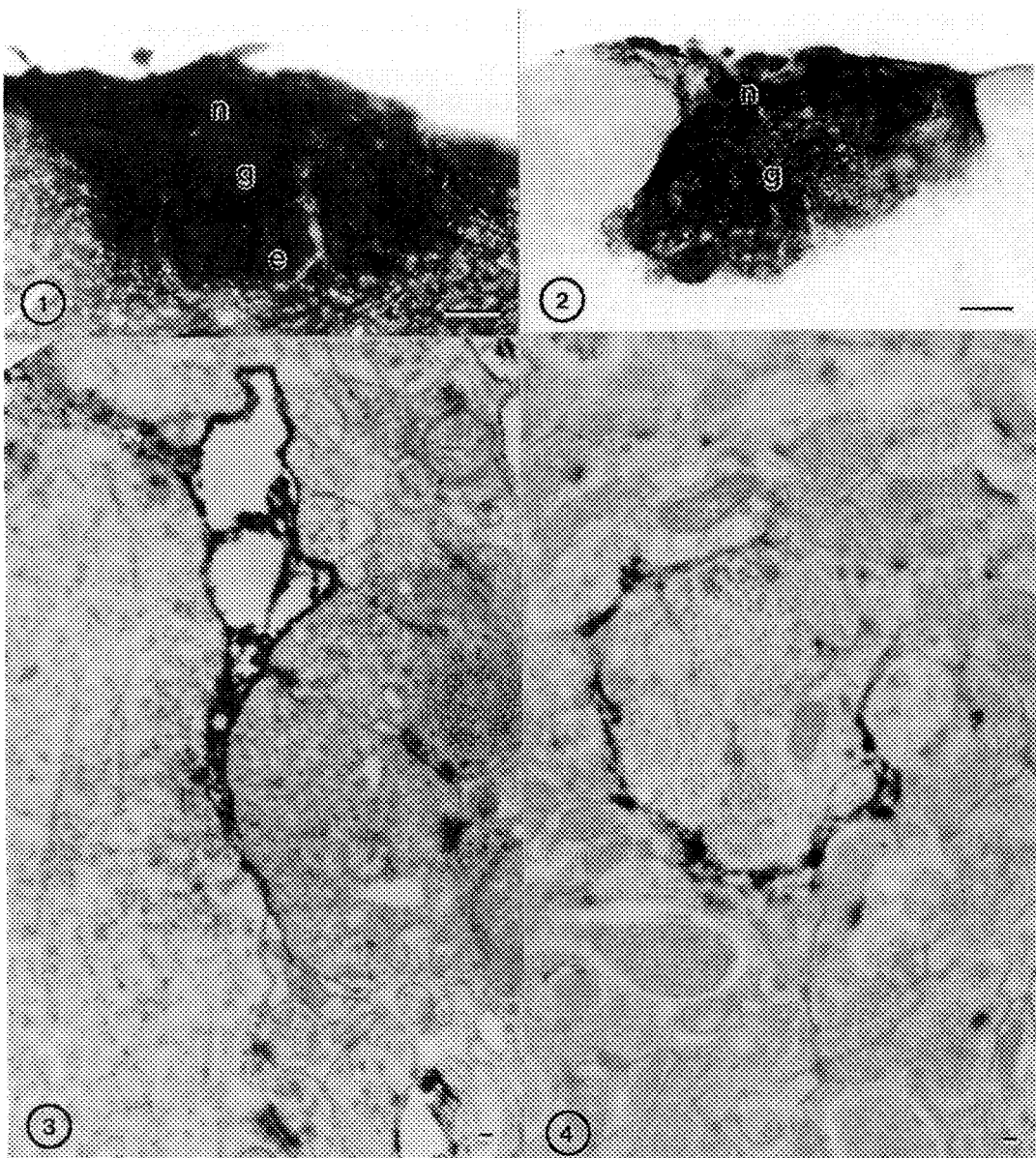


FIG. 1. -- LM of CC2 immunoreactivity in nerve (n), glomerular (g) and external plexiform layers (e) of accessory olfactory bulb. Bar = 100 μ m.

FIG. 2. -- LM of CC1 immunoreactivity in the nerve (n) and glomerular (g) layers of accessory olfactory bulb. Bar = 100 μ m.

FIG. 3. -- EM of CC2 immunoreactivity associated with dendrites and extracellular spaces. Bar = 100 nm.

FIG. 4. -- EM of CC1 immunoreactivity associated with dendritic surfaces. Bar = 100 nm.

BANDED AGGREGATES CONTAINING FIBRILLIN ARE PRESENT IN THE CARTILAGE MATRIX ADJACENT TO CHONDROCYTES IN INDIVIDUALS AFFECTED WITH SCOLIOSIS

Douglas R. Keene, Magaret Fairhurst, Catherine C. Ridgway, and Lynn Y. Sakai

Shriners Hospital for Crippled Children, Research Unit, Portland, Oregon 97201

Matrix microfibrils are present in the connective tissue matrices of all tissues. Following standard TEM processing, they appear in cross section as cylindrical fibrils 8-10 nm in diameter, often associated with amorphous elastin. They are also seen in the absence of amorphous elastin, for example in the shallow papillary layer of skin, and also in cartilage matrix (Figure 1). Negative stain and rotary shadowing studies⁽¹⁾ suggest that microfibrils are composed of laterally associated globular structures connected by fine filamentous strands ("beaded strings"), and that they are extendable. Immunoelectron microscopy has demonstrated that fibrillin, a 350 Kd glycoprotein, is distributed along all microfibrils with a relaxed periodicity of about 54 nm⁽²⁾. The gene coding for fibrillin has recently been identified and is defective in the Marfan syndrome^(3,4).

Herein we describe another structure containing fibrillin with features distinct from microfibrils. At lower magnification, these structures might be mistaken for collagen fibrils, particularly since they have the same overall periodicity (Figures 2 and 3). A difference in banding can be recognized at high magnification. Within each major period, well stained collagen fibrils are seen to have many minor bands, whereas the banded fibrillin aggregates usually have only one broad band (compare Figures 5 and 6). In this respect, these aggregates also appear very similar to broad-banded aggregates of type VI collagen, except that the periodicity of the type VI containing aggregate is larger and it does not label with antibodies specific for fibrillin⁽⁵⁾. Additionally, the circumference of a banded fibrillin aggregate is usually less uniform along its length. Gold particulate deposition directed by a monoclonal antibody which has been demonstrated to recognize fibrillin⁽¹⁾ displays labeling of these structures in register with their periodicity (Figures 4 and 7).

In our experience, these banded aggregates are present only rarely in the matrix of normal human cartilage. However, we have observed their presence quite frequently in the vicinity of chondrocytes in all cartilage sampled from individuals affected with severe scoliosis. We are currently uncertain about the significance of these unusual aggregates, but suggest that their presence in cartilage might be helpful in the diagnosis of scoliosis⁽⁶⁾.

References

1. D.R. Keene et al., *J. Histochem. Cytochem.* 39(1991):441.
2. L.Y. Sakai, D.R. Keene and E. Engvall, *J. Cell Biol.* 103(1986):2499.
3. C.L. Maslen et al., *Nature* 352(1991):334.
4. H.L. Dietz et al., *Nature* 352(1991):337.
5. D.R. Keene, E. Engvall, R.W. Glanville, *J. Cell Biol.* 107(1988):1995.
6. This work was supported by the Shriners Hospital for Crippled Children; Electron Microscopy Facilities were provided in part by the Fred Meyer Charitable Trust and in part by the R. Blaine Bramble Medical Research Foundation.

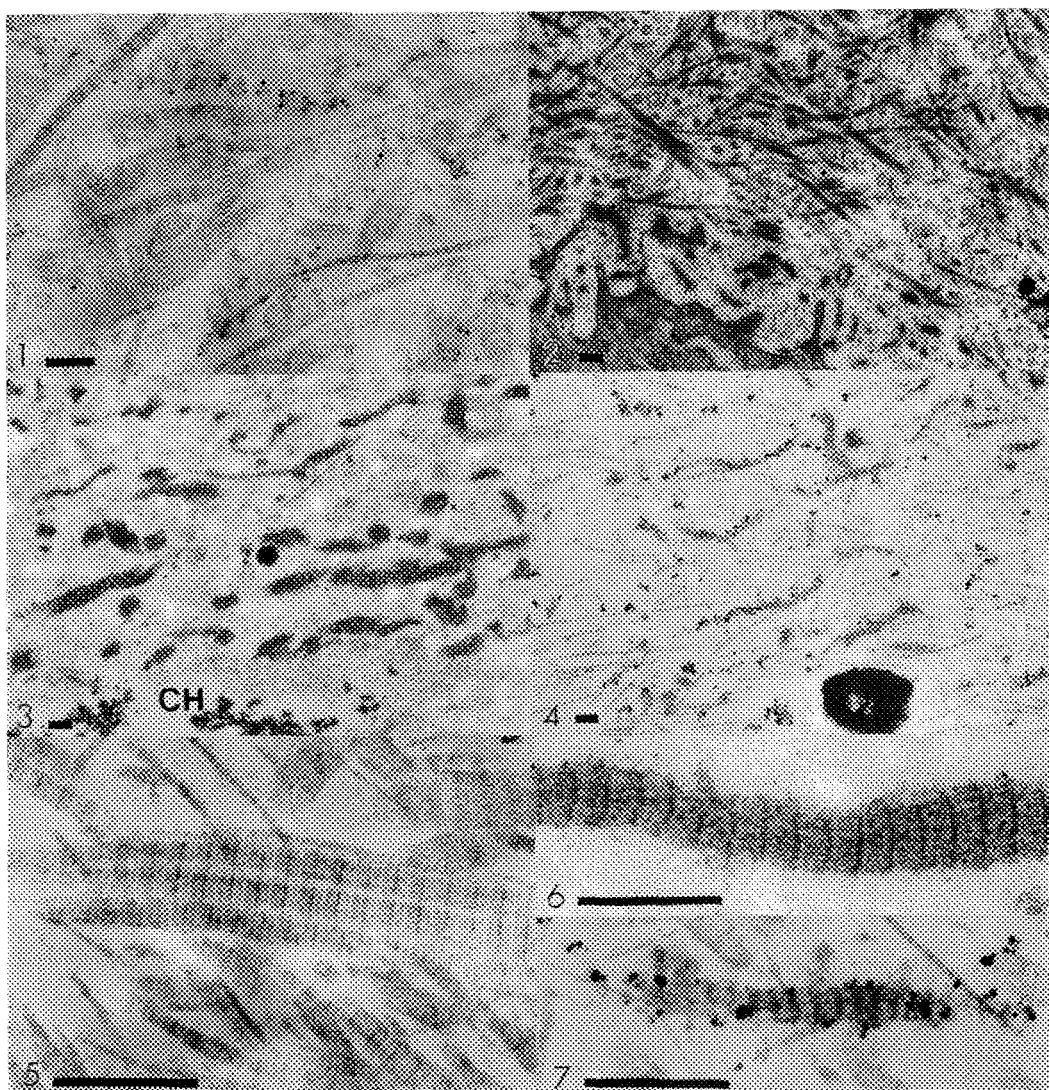


Figure 1. Microfibrils, present in normal human cartilage, decorated with 5 nm gold particles directed by a monoclonal antibody specific for fibrillin.

Figure 2. The typical appearance of normal human cartilage matrix adjacent to a chondrocyte, demonstrating a lack of fibrillin aggregates.

Figure 3. Banded fibrillin aggregates adjacent to a chondrocyte (CH) in scoliotic cartilage appear similar to collagen fibrils in their overall banding periodicity.

Figure 4. Fibrillin specific immuno-gold labeling of scoliotic cartilage demonstrates labeling of the broad banded aggregates.

Figure 5. Well stained collagen fibrils in human cartilage demonstrate many bands within a single period.

Figure 6. A single, broad band per period is easily recognized in the fibrillin aggregates.

Figure 7. Fibrillin antibody directs gold label in a pattern which matches the periodicity of the aggregate.

ALL SCALE BARS = 200 nm

NEUTROPHIL MIGRATION THROUGH IN VITRO INTERSTITIAL MATRIX

E.J.Roemer and S.R.Simon

Departments of Pathology and Biochemistry & Cell Biology,
SUNY at Stony Brook, Stony Brook, NY 11794

We are developing an in vitro interstitial extracellular matrix (ECM) system for study of inflammatory cell migration. Falcon brand Cyclopore membrane inserts of various pore sizes are used as a support substrate for production of ECM by R22 rat aortic smooth muscle cells. Under specific culture conditions these cells produce a highly insoluble matrix consisting of typical interstitial ECM components, i.e.: types I and III collagen, elastin, proteoglycans and fibronectin.

R22 cells are plated on inserts, grown to confluence and maintained in culture for 8-10 days in the presence of ascorbic acid. Matrix with selectively labeled components can be produced by growing the R22 cells in medium containing radiolabeled precursors. After removal of the R22 cells, the ECM coated membranes are ready for use with inflammatory cells. Neutrophils (PMN) are isolated from human blood and placed in the upper portion of the ECM-membrane insert and chemoattractant agents are added to the medium in the underlying well. Inserts are examined at various time points to assess PMN response to chemotatic stimulus. Samples are fixed in 3.7% formaldehyde and 0.1% glutaraldehyde in cacodylate buffer, rinsed, dehydrated and embedded in LR White plastic. For light microscopy sections are cut, stained with toluidine blue and examined on a Zeiss microscope. Ultrathin sections cut on a diamond knife are stained with uranyl acetate and lead citrate and examined on a JEM 1200 EX. Scanning EM samples are fixed as above, dehydrated, critical point dried, coated with gold palladium and examined on a JSM 5300. PMN migration and matrix degradation can be correlated by measuring the soluble counts released from radiolabeled ECM by activated cells.

ECM coated porous membranes provide a means for the examination of cell migration. The system described here, composed of multiple components, is remarkable in its ultrastructural and chemical similarity to interstitial matrix. It provides us with a unique tool for studying the role of inflammatory cell-interstitium interactions in disease processes.

1. Supported by NIH, HL-14262; NYS Office of Science and Technology, SUSB Biotechnology Center; and Cortech Inc. The aid of the SUSB Microscopy Imaging Center and Dr.R.Cameron are gratefully acknowledged.

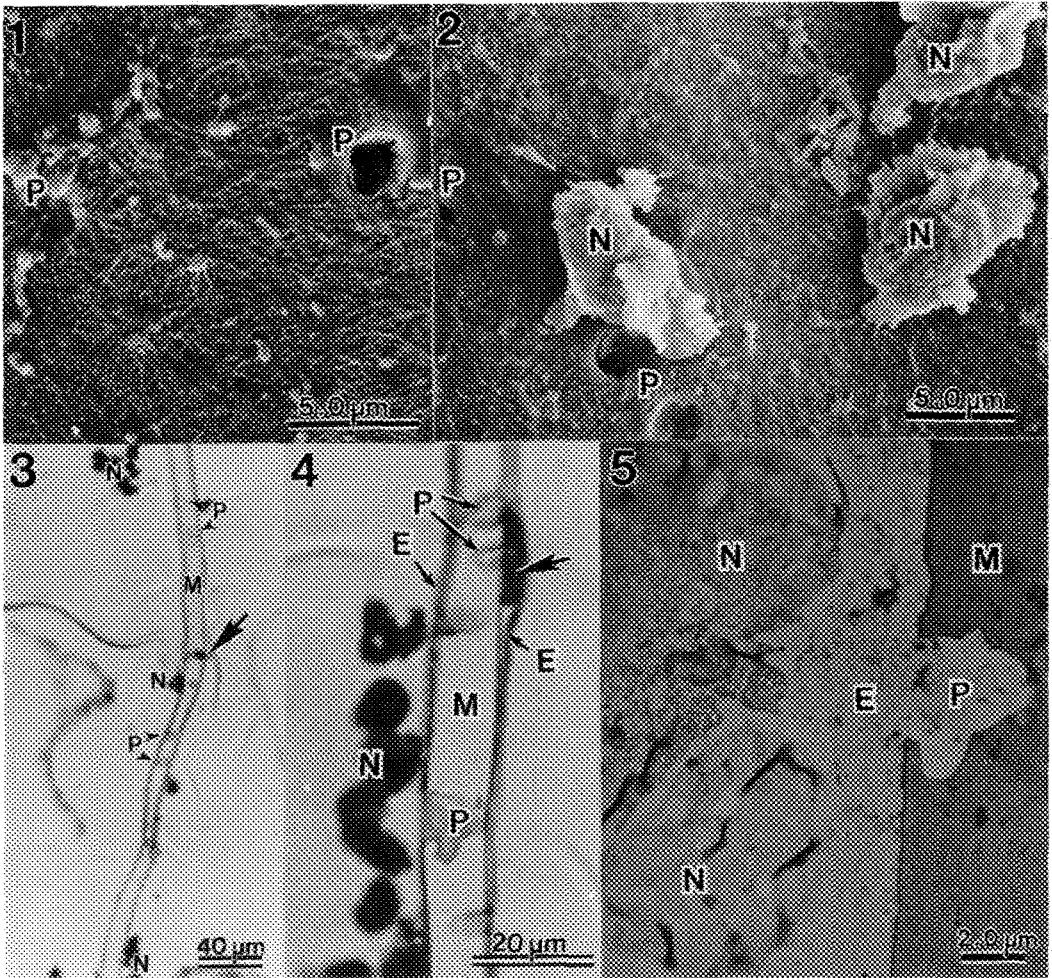


Fig.1: SEM image of ECM on 3.0µm pore membrane. P = pore. (cracking is due to beam damage at unsupported pore locations). Bar = 5.0 µm

Fig.2: SEM image of activated PMNs on ECM-membrane insert. P = pore, N = PMN. Bar = 5.0 µm.

Fig.3 & 4: Light micrographs of activated PMNs on ECM-membranes. M = membrane, P = pore, N = PMN, E = ECM. In fig.3: arrow = PMN in pore. Bar = 40µm. In fig.4: arrow = PMN exiting pore between membrane and ECM. Bar = 20µm.

Fig.5: TEM image of activated PMNs adjacent to pore on ECM-membrane insert. M = membrane, E = ECM, N = PMN, P = pore. Bar = 2.0µm.

DESMOSOMAL DISTRIBUTION IN THE EPIDERMIS OF A NON-CONTRACTING HUMAN SKIN EQUIVALENT

L.X. Oakford*, S.D. Dimitrijevic** and R. Gracy**

*E.M. Core Facility, Department of Anatomy & Cell Biology. **Tissue Repair Unit, Department of Biochemistry & Molec. Biol., Texas College of Osteopathic Medicine/University of North Texas, 3500 Camp Bowie Blvd., Ft. Worth, TX 76107-2699

In intact skin the epidermal layer is a dynamic tissue component which is maintained by a basal layer of mitotically active cells. The protective upper epidermis, the *stratum corneum*, is generated by differentiation of the suprabasal keratinocytes which eventually desquamate as anuclear corneocytes. A similar sequence of events is observed *in vitro* in the non-contracting human skin equivalent (HSE) which was developed in this lab (1). As a part of the definition process for this model of living skin we are examining its ultrastructural features. Since desmosomes are important in maintaining cell-cell interactions in stratified epithelia their distribution in HSE was examined.

Skin equivalents were produced according to Hevelone *et al.* (2). Mature equivalents were immersion fixed for 1h at room temperature in 2% glutaraldehyde and 1% tannic acid (low molecular weight, Polysciences Inc., PA) which was buffered in 0.125M PIPES, pH 7.4. A secondary fixation with 1% osmium tetroxide in PIPES was carried out for 45min. *En bloc* staining was then done for 1h with aqueous 1% uranyl acetate followed by dehydration through a graded ethanol series (10,30,50,70,95,100% x3). After substitution into propylene oxide the samples were infiltrated overnight in Polybed 812 (Polysciences Inc., PA) then polymerized at 70°C. Thin sections were cut with diamond knives on a Sorvall MT2-B ultramicrotome, collected on 150 mesh Ni grids, and stained with saturated ethanolic uranyl acetate and Sato's calcined lead citrate (3). The stained sections were examined on a Hitachi H-600 and micrographs recorded to Kodak SO-163 electron image film.

In HSE a desmosome free zone of cells, about 2 layers thick, was found sandwiched between two layers of cells connected by a substantial number of desmosomes. This desmosome-free zone may be seen in the micrograph shown in Figure 1. From this figure it may also be seen that all the cells contain the characteristic keratin fibers associated with epidermal keratinocytes. The zone appears to be located about half way through the epidermis. Note that the outer surfaces of the zonal keratinocytes do occasionally contain a desmosome but that the interface between these two layers is desmosome-free.

The appearance of this zone may be a signal for the beginning of the *stratum corneum*. Such a weak bilayer would certainly facilitate and easy desquamation. Current studies are directed towards establishing whether this zone is produced cyclically or continuously.

REFERENCES

1. Dimitrijevic *et al.* 1992 (Publication in preparation)
2. Hevelone, J. C., Dimitrijevic, S. D. and Gracy, R.W. 1991. *In Vitro Cell & Dev. Biol.* 27A:387-396.
3. Sato *et al.* 1986. *J. Electron Microsc.* 35(3) 304-306.
4. This work was supported by a grant from the N.I.H. (AG01274) and a grant from Johnson & Johnson's Consumer Products Division..

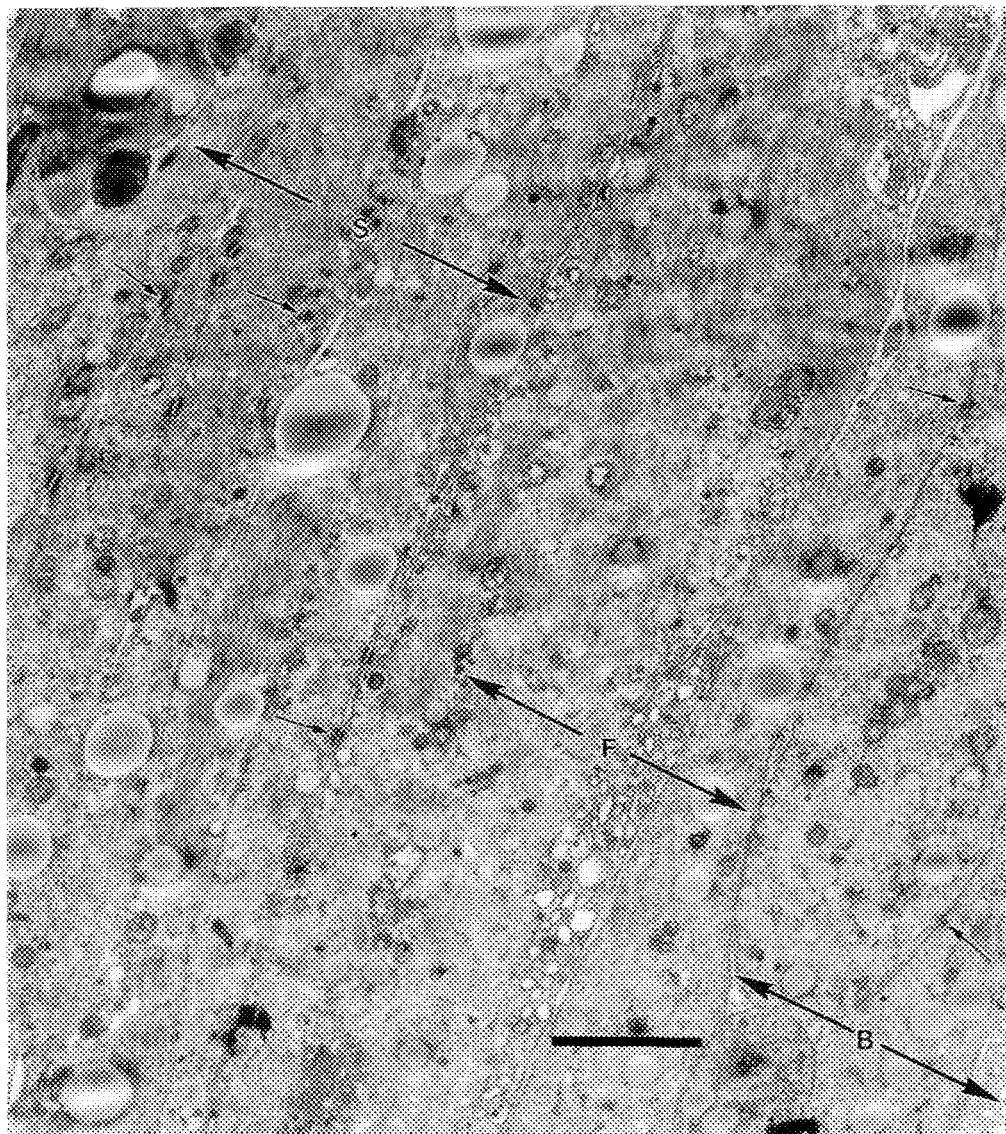


Figure 1. Formation of a desmosome-free zone (F) between two layers of keratinocytes in a non-contracting human skin equivalent. Note the desmosomes (arrows) in the basal (B) and suprabasal (S) keratinocytes. Bar = 2 μ m.

THE INNERVATION OF TOAD LYMPH HEARTS: AN ULTRASTRUCTURAL STUDY

Pucci A.M., Fruschelli C., Rebuffat A., Guarna M., Alessandrini C., Fruschelli M.

Histology and General Embryology Institute, University of Siena - Italy

Amphibians have paired muscular pump organs, called "lymph heart", which rhythmically pump back the lymph from the large subcutaneous lymph sacs into the veins. The structure and ultrastructure of these organs is well known¹ but to date there is a lack of information about the innervation of lymph hearts². Therefore has been carried out an ultrastructural study in order to study the distribution of the nerve fibers, and the morphology of the neuromuscular junctions in the lymph heart wall.

Adult toads (*Bufo bufo*) were used for the study. The animals were anaesthetized with ether, the lymph hearts were rapidly removed, immersion fixed in Karnovsky's fixative and then processed for conventional electron microscopy. Serial ultrathin sections were cut with an Ultramicrotome Nova LKB, stained and observed under a Philips CM 10 transmission electron microscope.

Few myelinated nerve fibers and numerous axon bundles, consisting of unmyelinated axons of small diameter, surrounded by Schwann cell are present in the adventitia and in the media of the lymph heart wall. Axon bundles containing typical axonal varicosities, partially covered by the Schwann cell, are frequently observed close to the striated muscle cell of the lymph hearts (Figure 1). They are separated from muscle cell sarcolemma only by basal lamina. The majority of these varicosities lay between 30 and 50 nm from the outer surface of the striated muscle cell (Figures 2-3). These varicosities contain numerous clear vesicles and few large dense-core vesicles (100nm diameter). On the other hand numerous unmyelinated nervous fibers constituted of axons, partially covered by Schwann cell, and containing dense-core vesicles, are localized near endothelial cells, at a distance of not less than 2µm (Figure 4).

These ultrastructural data suggest that lymph hearts possess a complex innervation pattern of nerve fibers containing classical neurotransmitters and neuropeptides. The dense innervation observed in these organs and the high frequency of typical neuromuscular junctions suggest that the innervation might have a functional role in the generation and/or modulation of the rhythmic contractile activity of these organs.

References

- 1) R. Schipp and R. Flindt, (1968) Zeitsch. Anat. Entwickl. 127, 232.
- 2) K. Greber and R. Schipp, Verh Dtsch Zool Ges (1986), 79, 276.

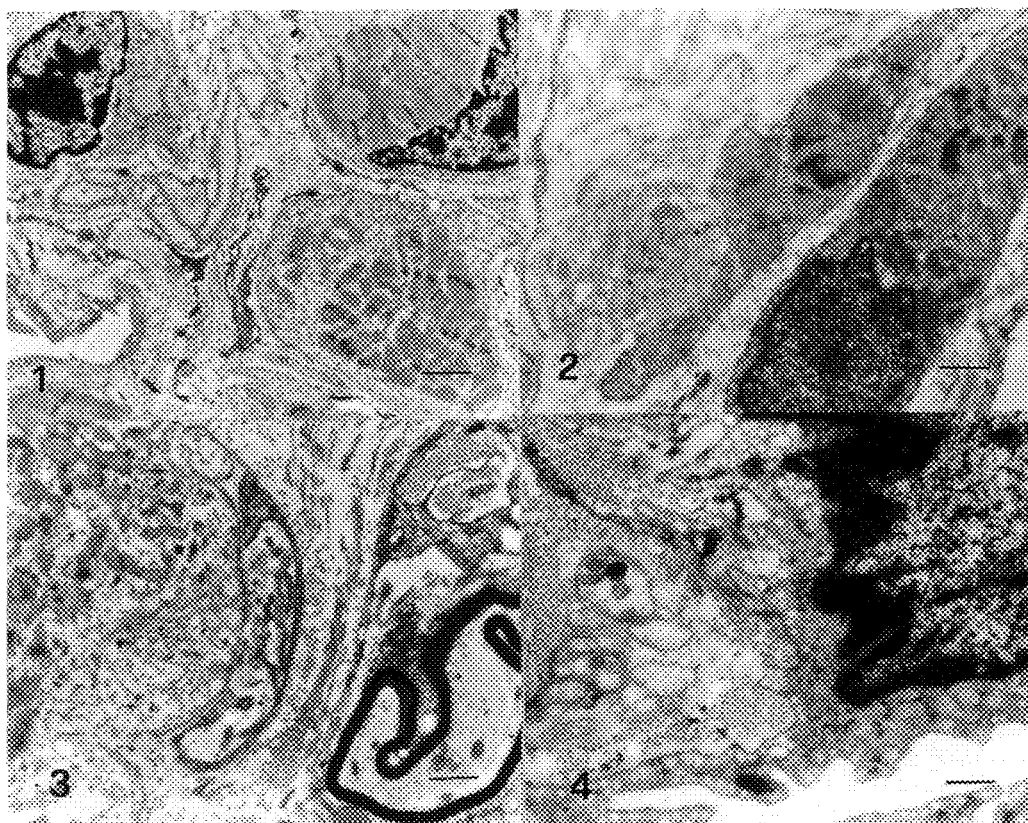


Fig. 1- Lymph heart wall. Unmyelinated nerve fiber is visible between the endothelial cells and the striated muscle cells. Bar 1.4 μ m

Fig. 2- Axon varicosity contains numerous clear vesicles and some large dense core ones, placed in a depression of the striated muscle cell surface. Bar 0.7 μ m

Fig. 3- Axon varicosity contains numerous mitochondria and heterogeneous vesicles close to a striated muscle cell apophysis. Bar 1 μ m

Fig. 4- Axon varicosities partially ensheathed by Schwann cell near endothelial cell. Bar 0.45 μ m

ULTRASTRUCTURAL CHARACTERIZATION OF AN EXTRACELLULAR MATRIX PRODUCED BY LEISHMANIA MEXICANA PIFANOI

Carlos Argüello

Department of Experimental Pathology, Center for Research and Advanced Studies, National Polytechnical Institute, 07000 Mexico, D.F. Mexico

In a previous study¹ it was shown that *Leishmania braziliensis* promastigotes secreted metabolic products to the culture media. These metabolites called "excreted factors"² were chemically characterized as polysaccharides and glycoproteins that reacted with antileishmania sera. These observations together with the recent characterization of lipophosphoglycans³ and phosphoglycan⁴ lead us to investigate by ultrastructural procedures if leishmania is able to produce an extracellular matrix, in axenic culture conditions. In this study, *Leishmania mexicana* were cultured in minimum essential medium, supplemented with 10% fetal calf serum, at 22°C. Under these conditions, the parasites tend to associate forming small aggregates, called "rosettes" in which the flagellum is oriented inwards and the cell body outwards (Fig.1). In order to retain their association I supposed the existence of an adhesive substance that kept the parasites together. To test this possibility, rosettes were fixed with glutaraldehyde in cacodylate buffer 0.1 M, or with glutaraldehyde containing 1 mg of ruthenium red, that binds to glycoproteins or polyanionic polysaccharides of extracellular matrices. The rosettes were absorbed on the surface of a millipore filter with a pore of 0.45 µm, fixed as mentioned above and prepared for scanning and transmission electron microscopy. Only those samples that included ruthenium red during fixation of the parasites revealed the existence of an extracellular matrix. The matrix is formed by a complex network of a fibrillar and granular material in which the rosettes of parasites were embedded (Fig. 2). The fibrillar network is constituted by two types of filaments. There are large thick filaments of more than 500 nm of length and 80 nm of diameter, that tend to orient in a parallel array and short thin filaments of 130 nm length and 52 nm thick. These filaments established direct associations with the cell surface through any part of the parasite. (Figs. 2,3). There are also long and linear filaments (50 nm thick) decorated by small granules (70 nm) that resemble proteoglycans (Fig 3). Samples prepared without ruthenium red did not preserve the matrix and facilitate the observation of parasites into the rosettes (Fig. 4).

These findings demonstrated that unicellular organisms such as *Leishmania mexicana* are able to synthesize an extracellular matrix that associated the parasites together. The functional role of the matrix is unknown, but it may be related to the growth and differentiation of the parasites.⁵

References

1. A. G. Hernández et al., The Biochemistry of Parasites. Pergamon Press Oxford. (1991) 47.
2. G. M. Slutsky et al., Infect. Immun. (1979) 26, 916.
3. S. J. Turco. Parasitol. Today. (1988) 4, 255.
4. M. J. McConville. Cell Biol. Internat. Rep. (1991) 9, 779.
5. This investigation received financial support from the UNDP/World Bank/WHO Special Programme for Research and Training in Tropical Diseases.

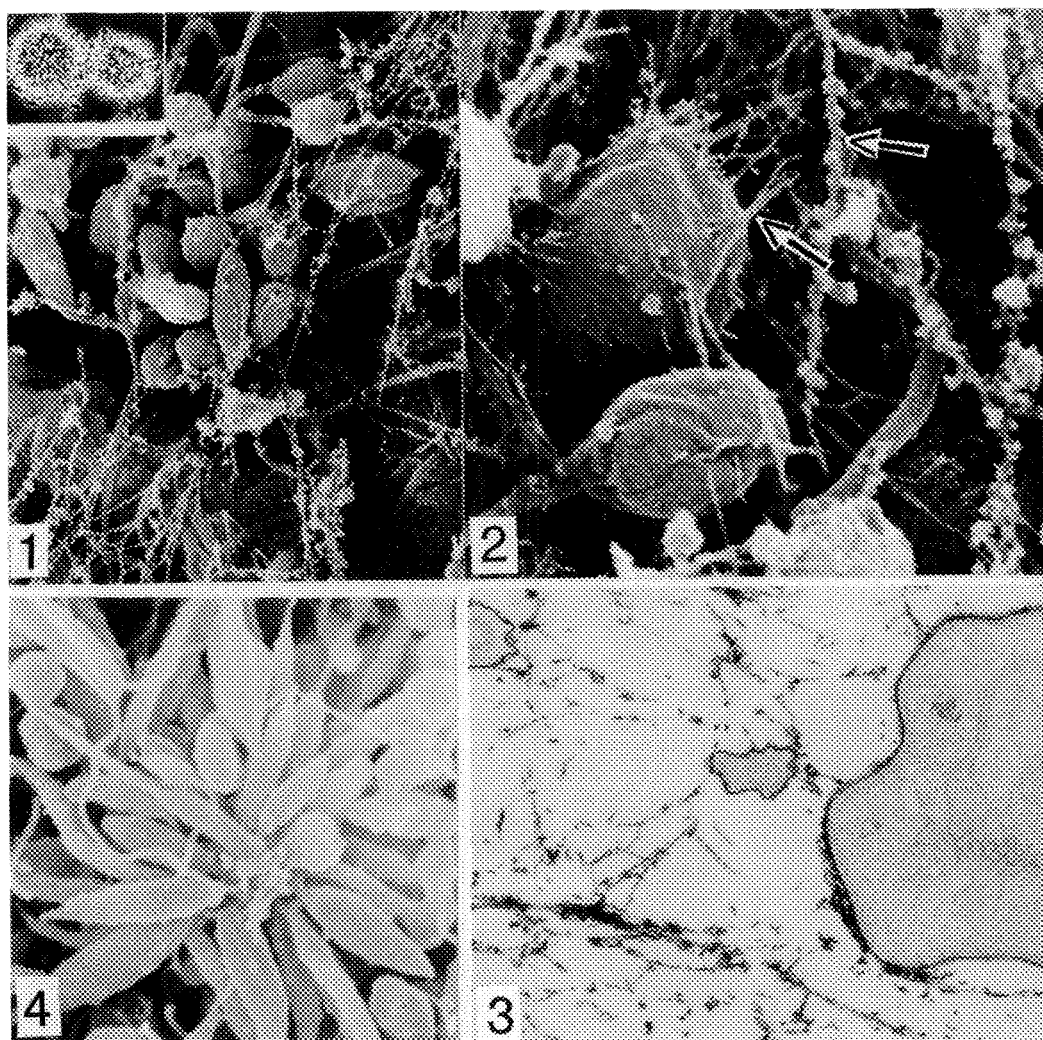


FIG. 1. -- INSET. LM of two rosettes formed by the association of parasites with the flagellum oriented inwards. 200 X. ---SEM of a rosette absorbed on a millipore filter and fixed with glutaraldehyde containing ruthenium red. Note the complex network of a fibrilar extracellular matrix. 2000 X.

Fig. 2.-- SEM of the matrix showin that it is formed by fibrilar and granular material that stablish direct contact with the cell surface (arrows). 6000 X.

Fig. 3.-- TEM of the fibrilar matrix that binds to the cell membrane of the parasite. 6000 X.

Fig. 4.-- SEM of a rosette fixed with glutaraldehyde without ruthenium red. Notice the absence of the extracellular matrix. 2000 X.

THREE - DIMENSIONAL ANALYSIS OF SPINDLE STRUCTURE IN THE YEAST,
SCHIZOSACCHAROMYCES POMBE (*S. POMBE*)

Rubai Ding

HVEM Laboratory, Dept. MCD Biology, Univ. of Colorado, Boulder, CO
80309-0347

Mitosis in yeast is currently the subject of many genetic and molecular biological studies, but structural work on yeast mitosis has been comparatively limited due in part to the difficulty of obtaining well preserved samples. A structural study of yeast spindles is important because yeast are unicellular, eukaryotic organisms that may provide a simple model of mitosis. *S. pombe* was chosen because much is known about its molecular biology, and there are several mutants that affect its mitosis. Here we describe a method for obtaining well preserved samples of *S. pombe* during mitosis using high pressure freezing. This method has been used together with EM of serial sections and computer facilitated reconstruction to build three dimensional (3-D) models of spindle structures.

S. pombe were collected at mid-log phase and frozen with a high-pressure freezer. These samples were freeze substituted at -90°C in 2% OsO₄ and 0.05% uranyl acetate in acetone. After at least 48 hours at -90°C , cells were warmed to room temperature, rinsed with acetone and gradually infiltrated with Epon-Araldite. Serial thin sections were picked up on formvar-coated slot grids and stained with uranyl acetate and lead citrate. The samples were imaged in a JEM-100 electron microscope at 16,000X. Serial negatives were digitized by video into a MicroVax computer hosting a Parallax graphics device. Microtubules (MTs) in cross sectional profile were tracked by hand, and spindle MT distributions were analyzed by computer.

Our fixation of *S. pombe* results in elegant preservation of cellular ultrastructure (Fig.1). Spindle MTs are well contrasted and embedded in a dense nuclear matrix (Fig.2). 3-D models show that the spindle consists of MTs originating at opposite spindle pole bodies and interdigitizing near the center of the spindle (Fig.3). At the zone of overlap, MTs have a square packing, particularly during the later stage of mitosis. Bridges are often seen between adjacent MTs, and a neighbor analysis of these MTs shows a preferred spacing of 40 nm and a preferred angular separation of 90° when near neighbors are anti-parallel (Fig.4a,b). These results suggest that MT-MT interactions are important in spindle elongation and stability. This method will soon be applied to different mutants to correlate their phenotype with their genotype and elucidate the mechanism of mitosis.

References

1. Tanaka, K. and T. Kanbe (1986) J. Cell Sci. 80, 253-268
2. McDonald, K. et al. (1991) EMSA Bull. 21: 47-53
3. This work was supported by NIH grant RR00592-20

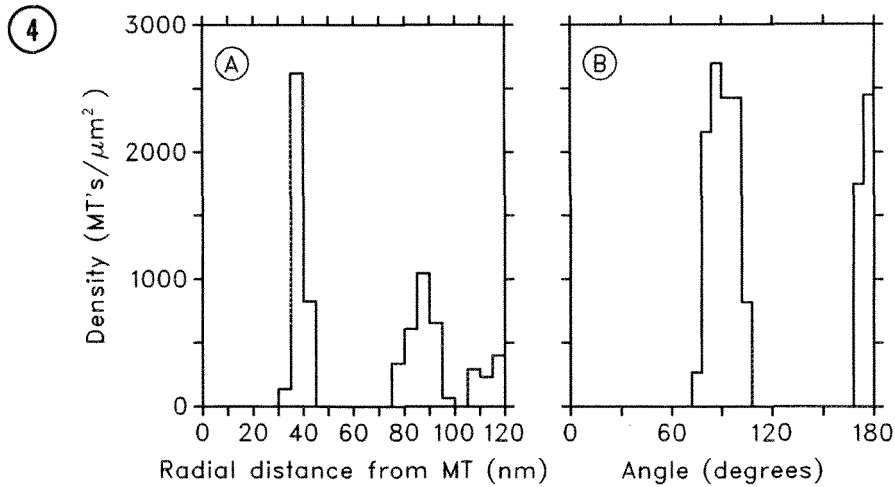
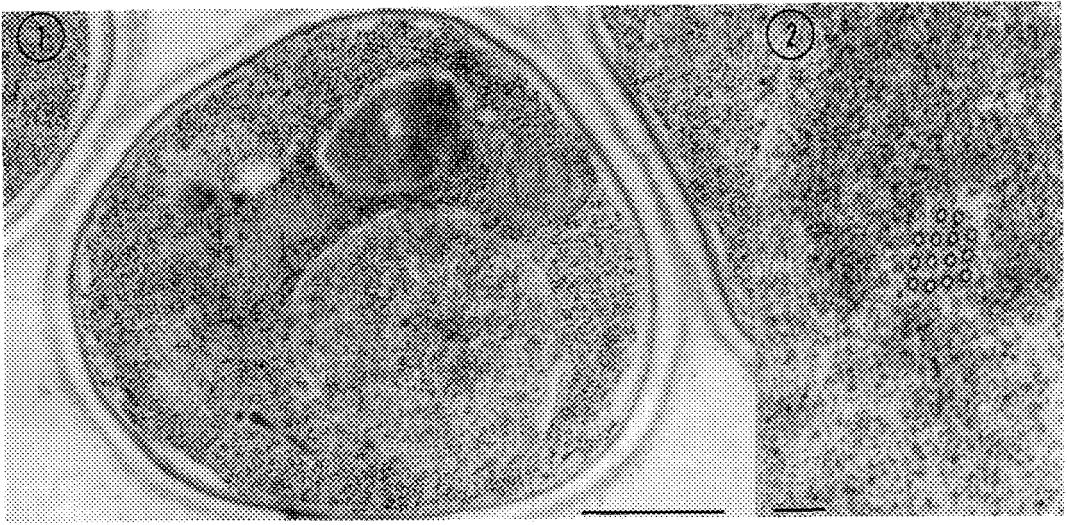


Figure 1. Low magnification view of *S. Pombe* after high pressure freezing and freeze substitution. Bar = 1 μm

Figure 2. Cross section through a mitotic spindle of *S. pombe* illustrating a square packing of MTs. Bar = 0.1 μm

Figure 3. 3-D computer reconstruction of a mitotic spindle. The spindle consists of MTs originating from opposite pole bodies and overlapping in the center of the spindle.

Figure 4. Neighbor density analysis of MT distributions in the overlap region from Fig. 3. MTs from opposite poles have a preferred spacing of 40 nm (4a) and an angular separation of 90° (4b).

THREE-DIMENSIONAL RECONSTRUCTION OF LARGE SUBCELLULAR STRUCTURES: A METHOD FOR COMBINING AXIAL TILT TOMOGRAPHY WITH SERIAL RECONSTRUCTION OF THICK SECTIONS

Gabriel E. Soto, Maryann E. Martone, Stephan Lamont, Bridget O. Carragher, Thomas J. Deerinck, Stephen J. Young and Mark H. Ellisman

San Diego Microscopy and Imaging Resource, University of California San Diego, La Jolla, CA 92093-0608

The study of subcellular structures requires the resolution afforded by the electron microscope. However, cellular organelle systems can extend for tens of microns and therefore cannot be encompassed in a single thin section required for conventional electron microscopic observation. Even with the use of high voltage electron microscopy, section thickness is limited to no more than a few microns. Visualization of 3-dimensional cellular structure in large volumes of tissue can be achieved by using 3-dimensional reconstructions based on serial sections. This approach is often tedious, requiring an extremely large series of thin sections in order to encompass the structure of interest. This method also suffers from technical difficulties in obtaining, processing and maintaining adequate registration over large numbers of sections. We have been exploring a method in which the number of sections is reduced by employing a series of thick sections in which the structures of interest are selectively stained. Three-dimensional information is extracted from each section using axial tilt tomography. The resulting serial volumes are then aligned and linked to form a single volume which is displayed using volume rendering techniques.

Figure 1 shows a reconstruction produced by linking four serial tomograms of the Golgi apparatus in a spinal ganglion neuron. Tissue was obtained from Epon-Araldite embedded bullfrog spinal root ganglia in which the cis-face of the Golgi apparatus was selectively stained by osmium impregnation¹. Four serial sections through a spinal ganglion were cut at a thickness of 2 microns, collected on formvar-coated slot grids and examined at 400 KeV on a JEOL 4000EX intermediate high voltage electron microscope. A single axis tilt series through +60 to -60 degrees in 2 degree increments was taken for the same centrally located neuron in each section at a magnification of 4000x. The negatives for each tilt series were then digitized and stored on disk using a 14 bit cooled CCD camera under the control of a Sun/4 330 computer. The digitized tilt series was normalized and aligned and the volume reconstructed by r-weighted back projection using the software package Suprim². Alignment of the serial volumes was accomplished by slicing each volume into individual planes along the z dimension and registering the last slice of one volume to the first slice of the next volume with the aid of fiducial marks. The aligned slices of each of the 4 volumes were then merged and restacked into a single large volume. The resulting volume was rendered and manipulated using the program ANALYZE³.

This method appears promising for characterizing the 3-dimensional organization of subcellular structures over many microns while maintaining resolution sufficient to discern ultramicroscopic detail. The use of linked serial tomograms allows us to view the structure of the cis-face of the Golgi apparatus extending over an 8 micron thick volume of tissue using only 4 serial sections. In comparison, a reconstruction of a similar volume of tissue from conventional thin sections would require over 80 serial sections. While the alignment of the serial volumes appears accurate, we are in the process of validating this technique by using a specimen of known 3-dimensional geometry. In addition, we are streamlining the procedure by acquiring digital images of the sample directly from a CCD camera attached to the microscope. We are also currently exploring the use of this technique to investigate the continuity of components of the neuronal endomembrane system in the bullfrog spinal ganglion and in the dendrites of cerebellar Purkinje neurons.

Footnotes and References

¹ J. D. Lindsey and M. H. Ellisman, *J. Neurosci.* (1985) 12(5), 3111.

² J. K. Stoops et al. *J. Structural Biol.* (1991) 106, 172. Obtained from J. P. Schroeter and J. - P. Bretaudiere, University of Texas, Houston

³ R. A. Robb and C. Barillot, *IEEE Trans. Med. Image* (1989) MI-8, 217. Obtained from the Biological Imaging Resource, Mayo Foundation.

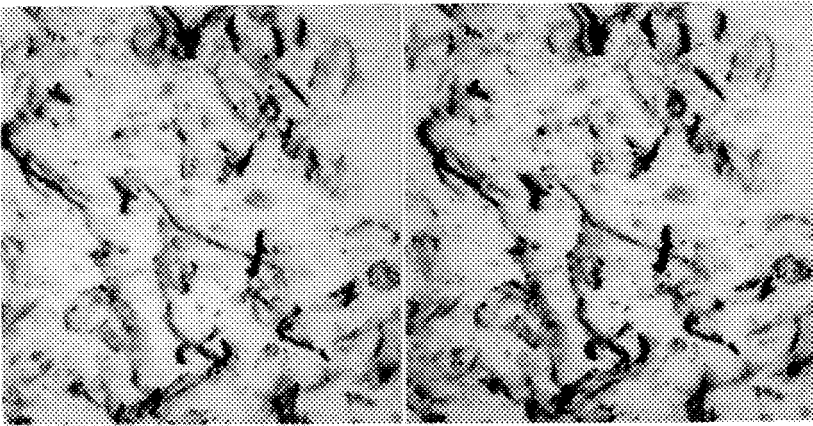


Fig. 1 Stereo-pair of a three dimensional volume of selectively stained cis-face saccules of the Golgi apparatus in a frog spinal ganglion neuron created by linking serial tomograms derived from 4 serial 2mm-thick sections. Magnification=4000X.

PREPLATE NEURONS IN EMBRYONIC MOUSE CORTEX: ULTRASTRUCTURAL OBSERVATIONS USING PHOTOCONVERSION OF THE FLUORESCENT LIPOPHILIC DYE DiI

Linda C. Hassinger and James E. Crandall*

E.K. Shriver Center, Waltham, MA 02254 and *Program in Neuroscience, Harvard Medical School, Boston, MA 02115

We have begun to look directly at small numbers of afferent axons to early generated neurons that form the preplate in the developing mouse cortex. The carbocyanine dye DiI (1',1'-dioctadecyl-3,3,3',3'-tetramethyl-indocarbocyanine) has proved especially useful for this goal.¹ DiI labels axons and their terminals with greater sensitivity and without some of the disadvantages of axon filling with HRP. The increased sensitivity provided by labeling embryonic axons with DiI has given us new insights into the development of cortical afferents. For instance, we reported originally that afferents from the thalamus were present below the cortex as early as embryonic day 15 (E15) based on HRP injections into mouse embryos.² By using DiI placements into the thalamus in aldehyde-fixed brains, we now know that thalamic fibers reach the cortex 24 hrs earlier.

Embryos from timed-pregnant B6C3 mice are perfused intracardially with a rinse of physiological saline followed by 2% paraformaldehyde/0.5% glutaraldehyde in 0.1M phosphate buffer (PB) (pH 7.2). Brains are removed into 2% paraformaldehyde overnight at 4°C. Crystals of DiI on the plugged tips (30-80 µm diameter) of glass micropipettes are placed into one of three sources of cortical afferents: brainstem, thalamus and cortex. Brains are stored in 0.1M PB with 0.02% sodium azide at 37°C for 1-3 weeks. Sections 50-100 µm in thickness are cut with a Vibratome into cold phosphate-buffered saline.

Another important advantage to using DiI to label axons is the ability to photoconvert the fluorescent dye into an electron dense reaction product.³ Labeled axons and preplate neurons are photoconverted for further ultrastructural analysis. An ultraviolet light source is projected through a fluorescein filter set and a 16X Neofluor microscope objective onto the fluorescent cells and fibers of interest while the tissue is flooded with ice-cold 0.03% 3,3' diaminobenzidine (DAB) in 0.1M Tris buffer (pH 8.2). The DAB solution is replaced every 10 minutes. Conversion into brown DAB reaction product is monitored visually with light microscopic optics and usually takes 30-40 minutes, dependent on the intensity of the fluorescently labeled cells. After photographic documentation, sections are subsequently osmicated, dehydrated, and embedded in Epon between siliconized slides. Thin sections with and without heavy metal staining are examined with the electron microscope. Labeling in this example occurred after placement of a small crystal of DiI in the intermediate zone of the E13 cerebral wall (Figs. 1&2). Subsequently, fluorescently labeled cells and fibers are photoconverted to an electron dense DAB reaction product. Ultrastructure of one of several labeled preplate neurons and their processes presents good membrane preservation (Figs. 3&4). Photoconversion of DiI labeled cells and processes allows ultrastructural characterization of different target cells in the embryonic cortex contacted by different sources of afferent axons, depending on the placement of the dye.⁴

References

1. Godement, P., et al. *Development* (1987) 101:697-713.
2. Crandall, J.E. & Caviness, V.S., Jr. *Develop. Brain Res.* (1984) 14:185-195.
3. Sandell, J.H. & Masland, R.H. *J. Histochem Cytochem.* (1988) 36:555-559.
4. This study was supported by NIH grant NS-24386, MR Core Grant HD-04147 and by the Dept. of Mental Retardation of the Commonwealth of Massachusetts (Contract: 1000-10003-SC).

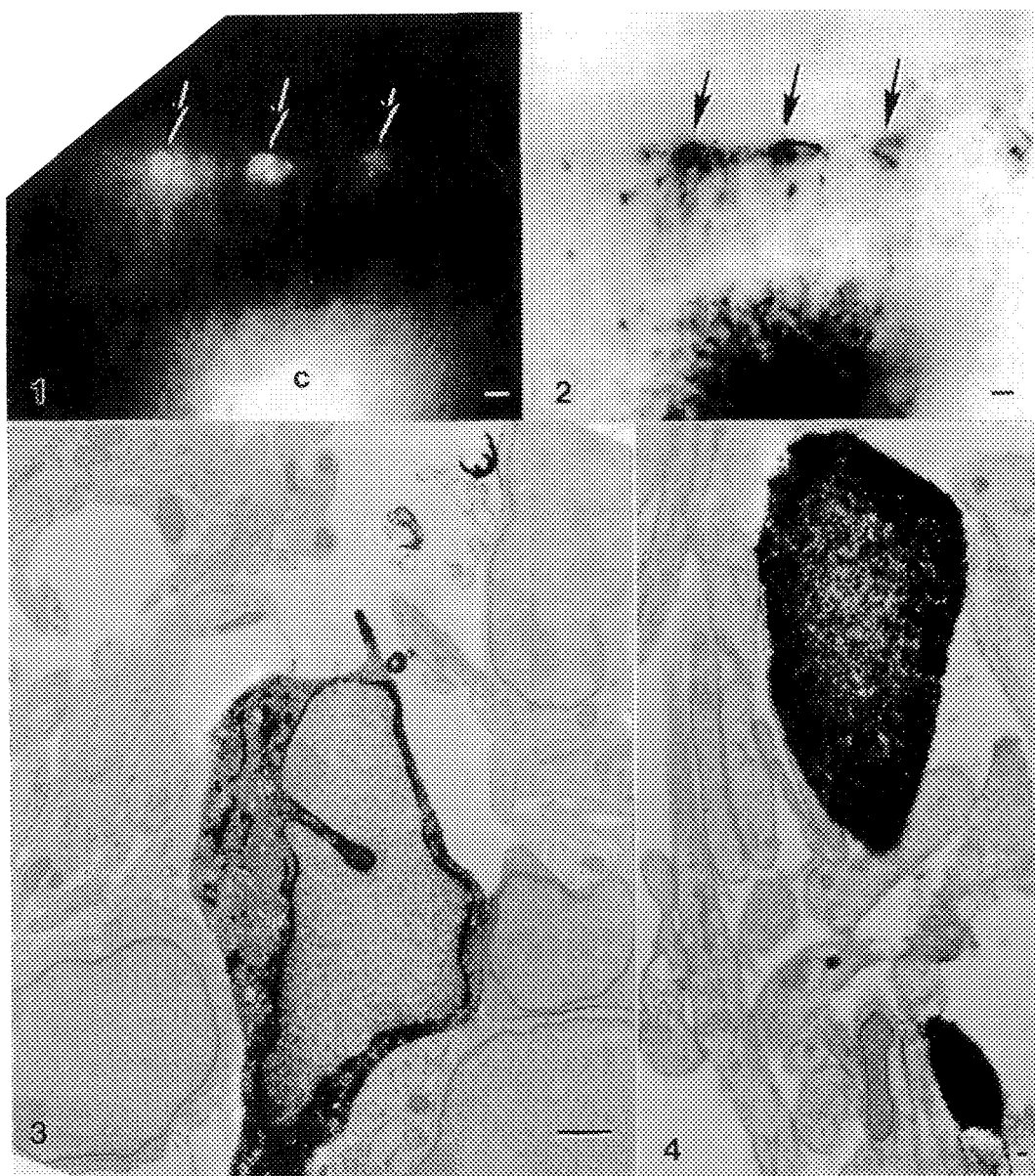


FIG. 1. -- Three fluorescent preplate neurons (arrows) in E13 cortex after placement of DiI in the cerebral wall (c) and three weeks of incubation. Bar = 10 μ m.

FIG. 2. -- Neurons (arrows) and dye placement after photoconversion to electron-dense DAB reaction product. Bar = 10 μ m.

FIG. 3. -- Cell soma in preplate contains DAB reaction product in cytoplasm surrounding the nucleus. Bar = 1 μ m.

FIG. 4. -- Labeled processes amidst the preplate neuropil. Bar = 0.1 μ m.

USE OF LOW-TEMPERATURE SEM TO OBSERVE SEASONAL VARIATION IN WAX DEPOSITION AND STOMATAL APERTURES IN THREE COMMON TREE SPECIES

William P. Wergin^{*}, Thomas W. Brakke^{**} and Eric F. Erbe^{*}

^{*}Electron Microscopy Laboratory; ARS-BARC; Beltsville, MD 20705

and ^{**}Biospheric Sciences Branch; NASA/GSFC; Greenbelt, MD 20771

The waxy covering or cuticle that covers the outer epidermal cells of leaves protects most plants from desiccation, pollution and many types of pathogens. This covering is generally interrupted only by the guard cells which form a stoma or pore that allows for the necessary gas exchange that occurs between the inner tissues of the leaf and the surrounding environment. The SEM has frequently been used to study the ultrastructure of the cuticle and the stomates because of their importance in the taxonomy, pathology and physiology of plants.¹ However, the results have been contradictory because chemical fixatives, dehydrating agents and critical point drying, procedures that are used to prepare specimens for conventional SEM studies, probably alter the waxy cuticle and the status or turgor of the guard cells.^{2,3} To avoid these problems we have utilized a technique for biological specimens that allows us to quickly freeze tissue in liquid nitrogen and to coat and observe the frozen samples.³ To accomplish this a Hitachi S-570 SEM was equipped with an EMscope SP2000A Sputter Cryo System. Leaf samples were collected from the field, mounted on stubs, quenched in liquid nitrogen slush, sputter coated with gold and transferred to the cryostage for low temperature SEM observation.

Results indicate that wax deposition on the lower epidermal cells continues throughout the growing season (Figures 1-6). During this period the morphology of the wax platelets also changes (Figures 3-6) and the guard cells and stomates can become encumbered or occluded with wax accumulations (Figures 4 & 6).

We conclude that the seasonal variation which occurs in the structure of the cuticle appears to greatly reduce the possibility of using the structure of wax platelets as a criterion in taxonomic studies. Furthermore, the results raise a more serious consideration; namely, how is transpiration affected by the accumulating and occluding of waxy deposits in and around the stomates.

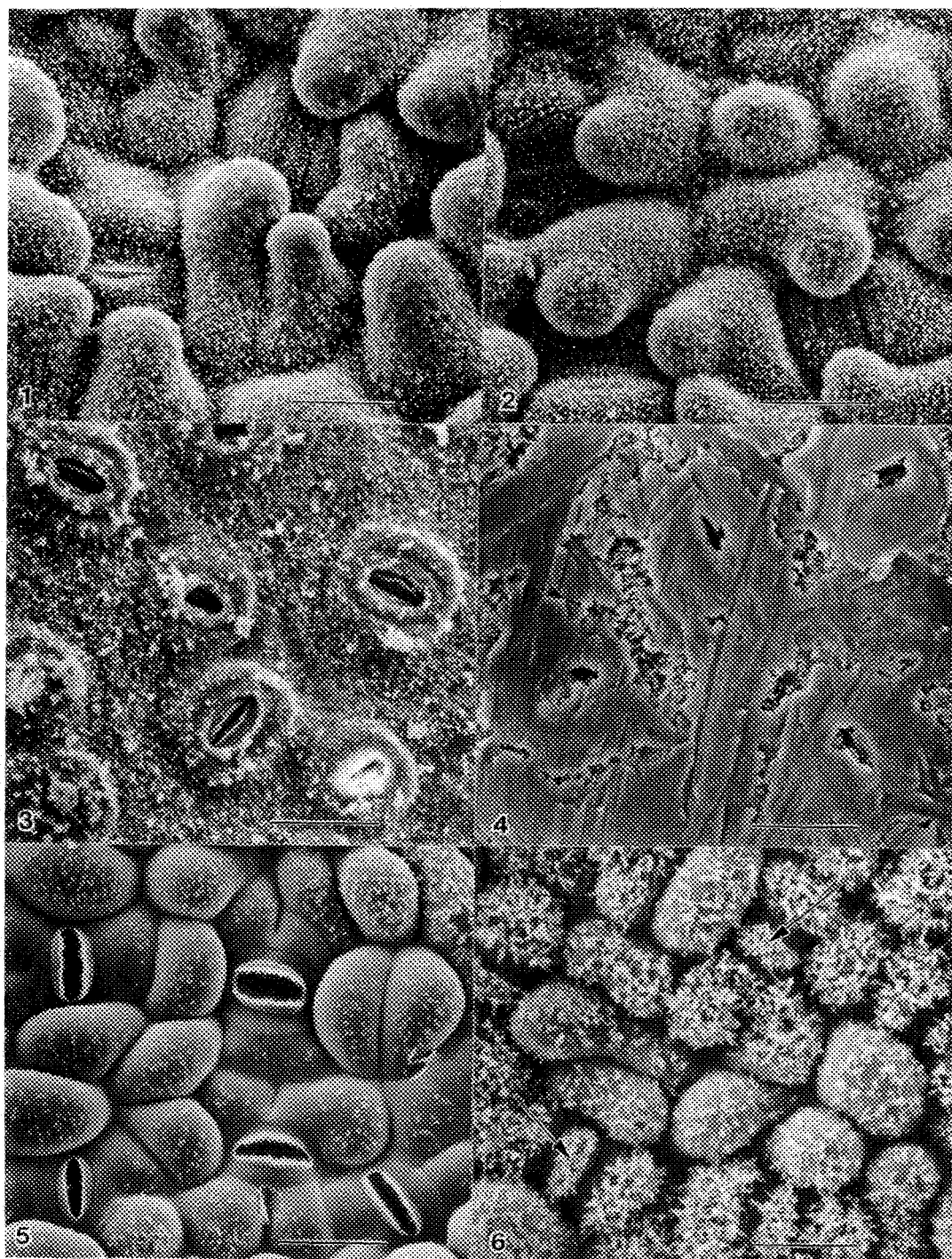
References:

1. H. P. Wilkinson, *Anatomy of the Dicotyledons*, Oxford: Clarendon Press (1979)97.
2. D. W. Eveling, *New Phytol.*, 96(1984)229.
3. W. P. Wergin and E. F. Erbe, *Scanning*, 12(1990)69.

Figures 1 & 2. Lower surface of leaves from yellow poplar, *Liriodendron tulipifera* L., trees that were sampled on 5/3/90 (Fig. 1) and 10/22/90 (Fig. 2). The waxy cuticle present at the time of the May sampling appears to thicken during the summer months. Bar = 20 µm.

Figures 3 & 4. Lower surface of leaves from red oak, *Quercus rubra* L., trees that were sampled on 5/10/90 (Fig. 3) and 9/25/90 (Fig. 4). Although the stoma can be observed in the latter sampling (Fig. 4), the guard cells appear heavily coated with cuticular waxes. Bar = 20 µm.

Figures 5 & 6. Lower surface of leaves from red maple, *Acer rubrum* L., that were sampled on 5/3/90 (Fig. 5) and 8/28/90 (Fig. 6). Stomates on leaves from the August sampling, Fig. 6 (arrows), appear to be occluded with flocculent wax platelets. Bar = 20 µm.



ELABORATE HULL CUPULES OF CHITON EGGS FOCUS THE SPERM: A SCANNING ELECTRON MICROSCOPE STUDY

John Buckland-Nicks

Department of Biology, St. Francis Xavier University, Antigonish,
Nova Scotia, Canada B2G 1C0

The outer hull of most chiton (Mollusca: Polyplacophora) eggs is elaborated into complex spines or cupules that project from the surface effectively increasing egg diameter. Cupules are either open or closed in free-spawning species but are reduced to flat plates in brooding forms¹. In open cupule species such as Mopalia ciliata (Fig. 1) invariably sperm swim inside the cupules and become segregated into one of seven internal channels. This was first demonstrated by rolling eggs on sticky tape to remove cupules prior to sputter coating (Fig. 2). Sperm penetrate the thin hull at the base of each cupule during the first stage of fertilization (Figs. 3, 4). One can slice the egg in half using a Keisei microknife (Japan) and examine sperm penetration at the cut surface (Fig. 3).

The sperm are positively attracted to the cupules as few sperm attempt to penetrate the hull between cupules (Figs. 2 & 4). This morphological data corroborates findings by Miller² that some chiton eggs release sperm chemoattractants.

The area of egg surface beneath the cupules has been shown in two studies to be rich in microvilli^{3,4}, and it is with individual microvilli that the needle-like sperm must fuse⁵.

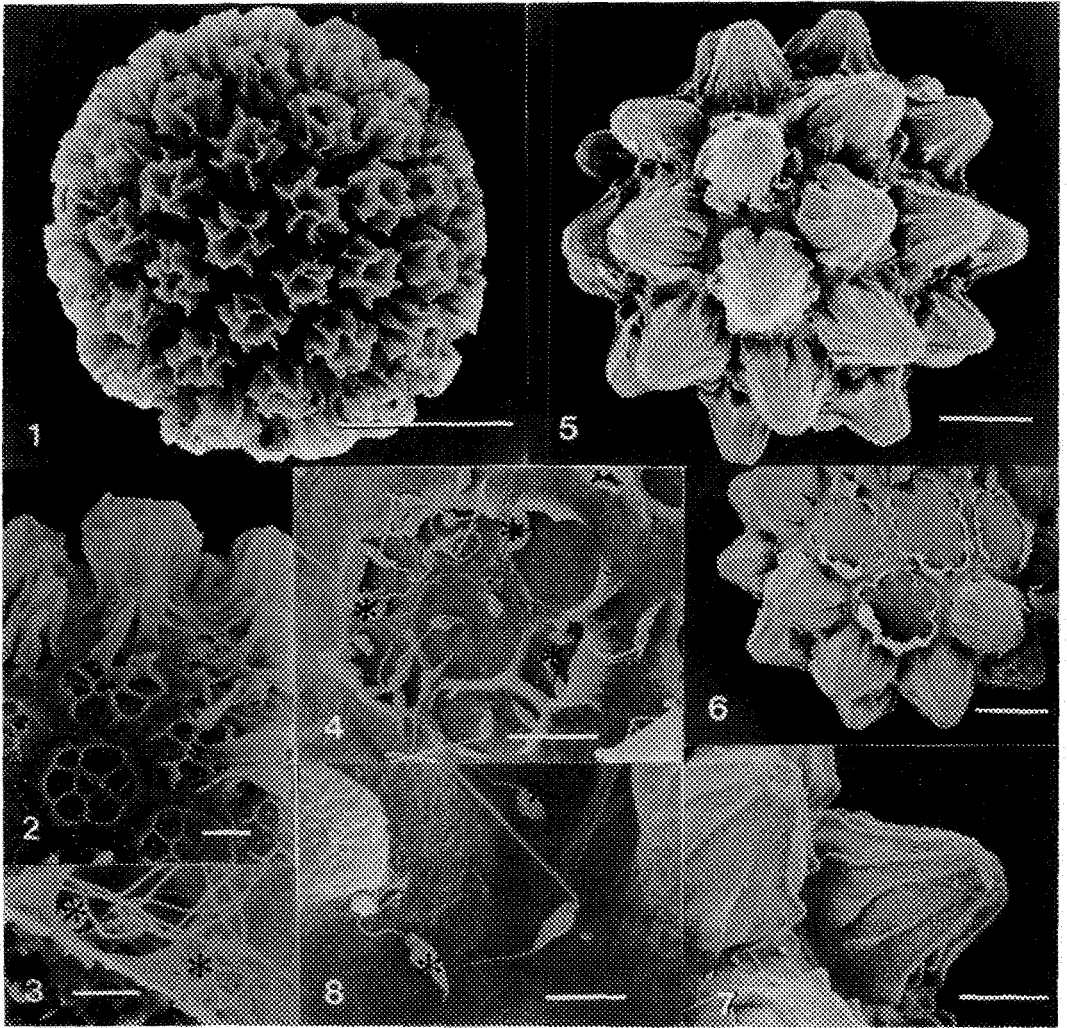
In closed cupule species, such as Lepidochitona dentiensi (Fig. 5), the majority of the egg surface is banned to the sperm. Sperm can only penetrate the hull in the region between the cupules (Figs. 6, 7). In this region there are numerous micropores in the hull which permit penetrating sperm (Fig. 8) ready access to the vitelline layer beneath.

In brooding species such as Lepidochitona fernaldi and L. caverna, the hull cupules are reduced to flattened plates. Nevertheless the plates block sperm access to the area of the egg surface beneath them and sperm must penetrate the hull between the plates in the region of micropores.

Thus, in open cupule species sperm can gain easier access to the egg membrane by swimming inside the cupules, whereas in closed cupule species, cupules block sperm to the region between cupules. In both cases the regions to which the sperm are focused represent specialized areas of the egg surface.

References

1. D.J. Eernisse, Biol. Bull. (1988) 174, 287.
2. R. Miller, J. Exp. Zool. (1977) 202, 203.
3. H.-P. Richter, Helgol. Wiss. Meeresunters (1976) 28, 250.
4. L. Selwood (née Bedford) Z. Zellforsch. (1970) 104, 178.
5. J. Buckland-Nicks et al., Gamete Res. (1988) 21, 199.
6. This research was supported by an NSERC of Canada grant.



FIGS.1-4. Scanning electron micrographs of fertilized eggs of Mopalia ciliata:

FIG. 1. Mature egg of M. ciliata: open cupule species. Bar = 100 μ m

FIG. 2. Egg of rolled on sticky tape to remove hull cupules. Bar = 20 μ m

FIG. 3. Sperm (*) from concentrate penetrating egg inside cupule (removed). Bar = 10 μ m

FIG. 4. Bisected egg: sperm (*) penetration visible at cut surface inside cupules. Bar = 4 μ m

FIGS.5-8. Scanning electron micrographs of fertilized eggs of Lepidochitona dentiens:

FIG. 5. Mature egg of L. dentiens: closed cupule species. Bar = 40 μ m

FIG. 6. Egg hull cupules removed: no sperm inside cupules. Bar = 40 μ m

FIG. 7. Sperm visible between intact hull cupules. Bar = 20 μ m

FIG. 8. Sperm penetration (*) visible in region of micropores between cupules. Bar = 4 μ m

MICROSCOPIC STUDY OF THE ROOM TEMPERATURE DEFORMATION MECHANISMS IN $\beta + \gamma$ - (70 at.% Ni -30 at.% Al) *in situ* COMPOSITE

A. Misra and R. Gibala

Department of Materials Science and Engineering, The University of Michigan,
 Ann Arbor, MI 48109-2136

Ductile phase reinforcement is an attractive approach for enhancing the room temperature ductility and toughness of brittle intermetallics such as β -NiAl. For example, a directionally solidified alloy of nominal composition 70 at.% Ni -30 at.% Al, having a two-phase β (brittle matrix) and γ (ductile second phase) microstructure, exhibits up to 9% tensile ductility at room temperature [1]. In the present investigation, a microscopic study has been made to understand the mechanisms involved in the ductility enhancement of the $\beta + \gamma$ composite.

Slow directional solidification results in an aligned rod-like γ microstructure in a single crystal β -NiAl matrix (63.1 at.% Ni) which has an approximate $\langle 001 \rangle$ growth direction. The γ rods are not perfect single crystals and some low angle boundaries are seen (Fig. 1). A part of the β -NiAl matrix is present as the 3R martensite (L1₀ structure) which is heavily twinned and when tilted to end-on orientation shows the typical spot-splitting across the twinning plane, $\{110\}$, in the zone axis diffraction pattern (Fig. 2). However, the stress-induced martensite in β -NiAl (63.1 at.% Ni) is known to have the 7R structure with a high density of $\{111\}$ stacking faults [2]. Hence, the ductility enhancement is not a result of a stress-induced martensitic transformation.

Surface observations of the deformed specimens reveal slip traces in the β phase emanating from the points where the slip traces of the γ phase intersect the interface, suggesting a slip transfer mechanism (Fig. 3). The typical dislocation substructures observed in the deformed specimens are shown in Fig. 4. In the γ phase, the dislocations are predominantly of the $a\langle \bar{1}01 \rangle$ screw type. In Fig. 4a, the dislocations labelled 'a' have Burgers vector $\underline{b} = a[0\bar{1}1]$, and the dislocations labelled 'b' have $\underline{b} = a[\bar{1}01]$. Further, in Fig. 4a the directions $[0\bar{1}1]$ and $[\bar{1}01]$ point towards the interface and hence, the dislocations in the γ phase appear to move towards the interface and finally get absorbed in it. In the β phase, $\underline{b} = a[0\bar{1}0]$ dislocations are seen to generate at the interface ahead of the point where the γ phase dislocations pileup (Fig. 4b). The character of the dislocations in the β phase was confirmed by image simulation to be $a\langle 010 \rangle$ since the conventional $\mathbf{g} \cdot \mathbf{b}$ analysis may be inconclusive for elastically anisotropic materials (Fig. 5). The transfer of slip from the ductile γ phase to the brittle β matrix resulting in the generation of mobile $a\langle 010 \rangle$ dislocations explains the ductility enhancement observed in the $\beta + \gamma$ composite.

References

1. R. D. Noebe, A. Misra and R. Gibala, ISIJ International, 31 (1991) 1172.
2. V. V. Martynov, K. Enami, L. G. Khandros, S. Nenno and A. V. Tkachenko, Phys. Met. Metall., 55 (1983) 136.
3. This research was funded by NSF Grant No. DMR-9102414.
4. The materials used in this investigation and the mechanical tests results were provided by R. D. Noebe, NASA Lewis Research Center, Cleveland, Ohio.

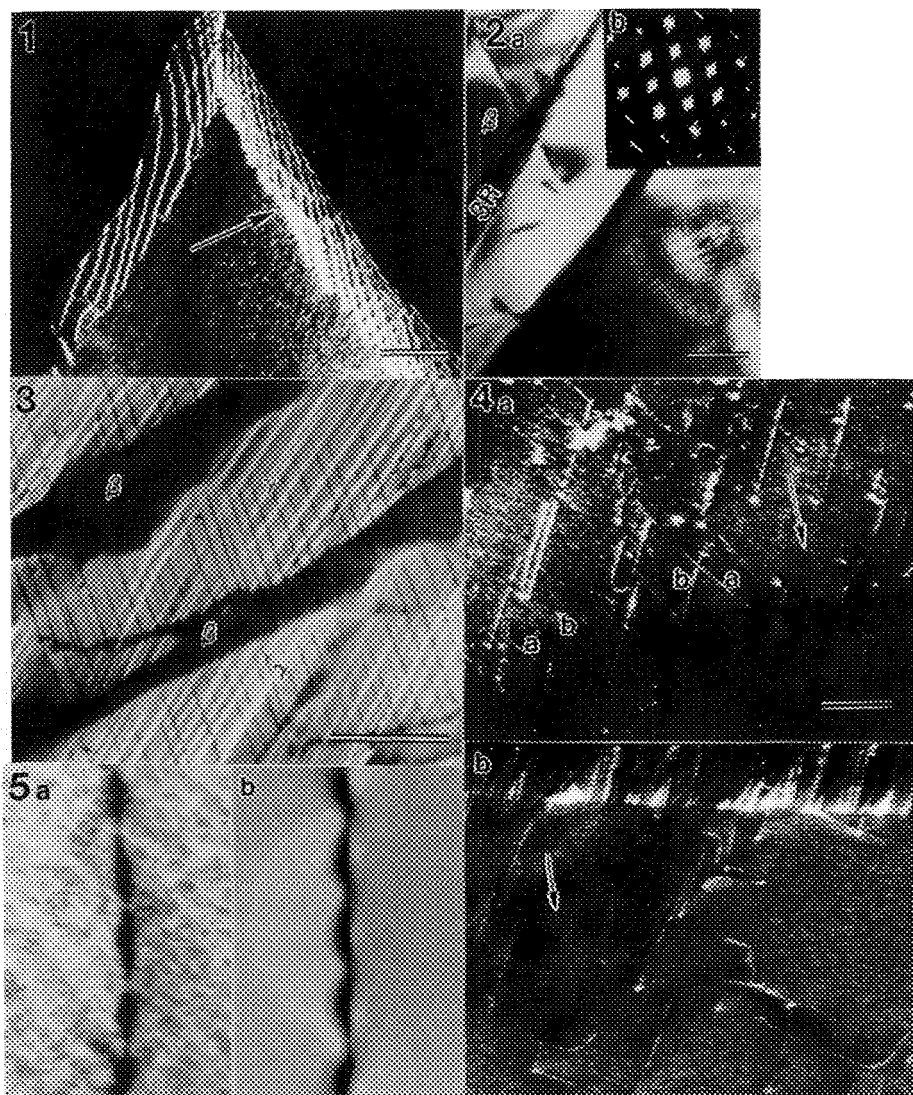


Fig. 1 WB TEM micrograph of low angle boundaries in γ' phase. $\mathbf{B} = [101]$. $\mathbf{g} = \bar{1}11$. Bar = 200 nm.

Fig. 2 (a) BF TEM micrograph of 3R martensite in the β phase and (b) corresponding $[001]$ diffraction pattern showing $\{110\}$ spot-splitting. Bar = 200 nm.

Fig. 3 Nomarski interference optical micrograph of the surface of a deformed specimen showing slip traces in both phases. Bar = 20 μm .

Fig. 4 WB TEM micrographs showing the slip transfer across γ'/β interphase boundary. (a) $a\langle 101 \rangle$ screw dislocations of the γ' phase getting absorbed in the interface. $\mathbf{B} = [101]$. $\mathbf{g} = 1\bar{1}\bar{1}$. (b) $a\langle 010 \rangle$ dislocations getting emitted into the β phase from the interface. $\mathbf{B} = [001]$. $\mathbf{g} = \bar{0}20$. Bar = 200 nm in both (a) and (b).

Fig. 5 (a) BF TEM micrograph showing a $\mathbf{b} = a[010]$ dislocation of the β phase. (b) Computer simulated image of the same dislocation.

THREE-DIMENSIONAL EXAMINATION OF THE CYTOSKELETAL SHEETS OF MAMMALIAN EGGS

Carolyn A. Larabell*, David G. Capco**, G. Ian Gallicano**, Robert W. McGaughey**, Karsten Dierksen***, and Kenneth H. Downing*

*West Coast Facility for IVEM, Lawrence Berkeley Lab., Univ. of California, Berkeley, CA 94720

**Molecular and Cellular Biology, Dept. of Zoology, Arizona State University, Tempe, AZ 85287

***Max-Planck-Institut für Biochemie, Martinsried, West Germany

Mammalian eggs and embryos contain an elaborate cytoskeletal network of "sheets" which are distributed throughout the entire cell cytoplasm.¹ Cytoskeletal sheets are long, planar structures unlike the cytoskeletal networks typical of somatic cells (actin filaments, microtubules, and intermediate filaments), which are filamentous. These sheets are not found in mammalian somatic cells nor are they found in nonmammalian eggs or embryos. Evidence that they are, indeed, cytoskeletal in nature is derived from studies demonstrating that 1) the sheets are retained in the detergent-resistant cytoskeleton fraction²; 2) there are no associated membranes (determined by freeze-fracture)²; and 3) the sheets dissociate into filaments at the blastocyst stage of embryogenesis¹. Embedment-free sections of hamster eggs viewed at 60 kV show sheets running across the egg cytoplasm (Fig. 1). Although this approach provides excellent global views of the sheets and their reorganization during development, the mechanism of image formation for embedment-free sections does not permit evaluation of the sheets at high resolution. In order to characterize their substructural organization, therefore, thicker resin-embedded sections (0.4 - 1.0 μm) of both detergent-extracted (Fig. 2) and intact (Fig. 3) cells were analyzed at 400 kV on a JEOL 4000 EX microscope. The planar nature of these structures is demonstrated by analysis of a cross-sectional view of several sheets (Fig. 3), in which each sheet appears to be composed of two individual filaments approximately 10-11 nm in diameter, and an *en face* view through a single sheet (Fig. 4), which suggests it is composed of a meshwork of fibers. Visual analysis of numerous stereo pairs at tilt angles between -60° and $+60^\circ$ enabled us to propose a model of the substructural organization of these unique cytoskeletal elements. As the specimen is tilted, it becomes clear that the sheet spans the entire thickness of the section (even those that are 1.0 μm thick) and is actually composed of two closely apposed arrays of fibers. The fibers within each of these arrays are held in register with neighboring fibers by regularly placed lateral crossbridges, producing a structure resembling a square lattice. Finally, the two parallel fiber arrays comprising each sheet are interconnected by short (20 nm long) crossbridges at regular intervals. Optical diffraction patterns are compatible with a structure composed of two closely apposed square lattices. This filamentous skeleton, which is seen in detergent-extracted specimens, is decorated with a tightly packed layer of particulate material in intact cells (best viewed in quick-freeze, deep-etch, rotary-shadowed specimens). A three-dimensional reconstruction of this structure using tomographic techniques is in progress. Tilt series of images covering the range from -60° to $+60^\circ$ were recorded with a slow scan CCD-camera on a Philips 200FEG microscope. The setting of the tilt angle and the recentering of the specimen were controlled automatically by an external computer. Rapidly cycling through these images greatly facilitates an accurate perception of this highly organized, three-dimensional structure as it moves from the cross-sectional to *en face* view.

1. D.G. Capco and R.W. McGaughey, *Develop. Biol.* (1986)115, 446.
2. R.W. McGaughey and D.G. Capco, *Cell Motil. & the Cytoskel.* (1989)13, 104.

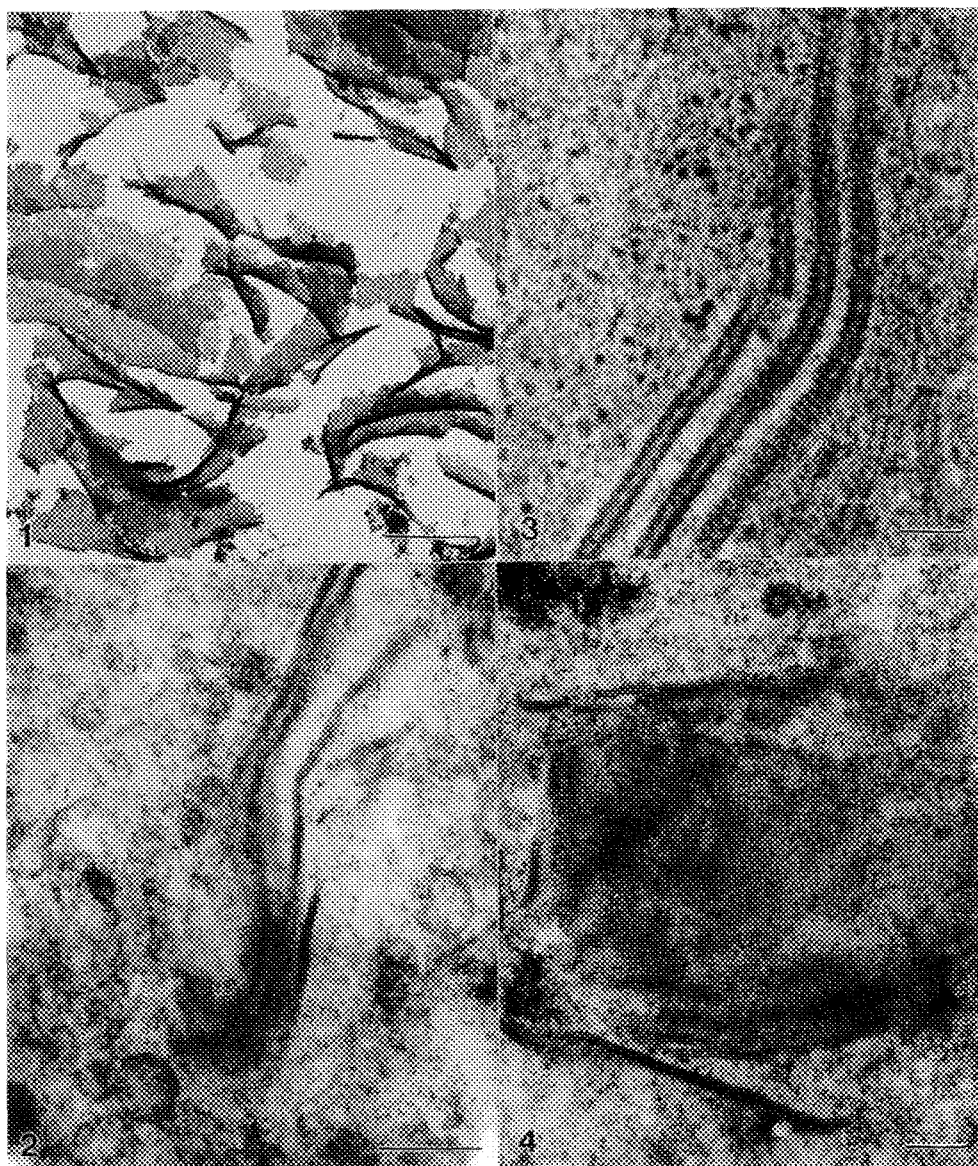


Fig. 1. Embedment-free section of detergent-extracted hamster egg showing cytoskeletal sheets in cross-sectional and *en face* views (viewed at 80 kV). Bar = 0.5 μ m.

Fig. 2. Resin-embedded section (0.5 μ m thick) of detergent-extracted egg showing cross-sectional and *en face* views of the sheets (viewed at 400 kV). Bar = 0.5 μ m.

Fig. 3. Cross-section of an intact egg showing three sheets, each of which appears to be composed of two parallel fibers (viewed at 400 kV). Bar = 0.1 μ m.

Fig. 4. *En face* view of sheet, which suggests it is composed of a meshwork of fibers (viewed at 400 kV). Bar = 1.0 μ m.

NUCLEAR CHANGE DURING DIFFERENTIATION OF
ENTAMOEBA INVADENS

M. Morales-Vallarta*, B. Mata-Cárdenas**, E. Ramírez-Bon***

*Facultad de Ciencias Biológicas, UANL, Ap. Postal 119 San Nicolás de los Garza, N. L., México

**Unidad de Investigaciones Biomédicas del I.M.S.S., Monterrey, N. L., México

***Facultad de Medicina, UANL, Monterrey, N. L., México

The cyst of *Entamoeba histolytica* is the infective phase of this parasite, but much of its differentiation process remains unknown since it is not possible its *in vitro* encystation. However, differentiation of *E. invadens*, an ameba that parasites reptiles is used as an experimental model for amebiasis — research, specially in differentiation aspects, since *E. invadens* can be induced to *in vitro* encystation.

The nuclear division during encystation of *E. invadens* has been described by some authors^{1,2}, but this work, has described this process through light microscopy. In the present work we report the morphologic nuclear change and the chromatin organization observed by electron microscopy.

Trophozoites of *E. invadens* IP-1 were grown in TP-S-1 medium³, and encysted in Rengpien and Bailey medium (AEM)⁴. During encystation several samples were analysed for different times. The cysts of trophozoites were washed with phosphate buffer saline, postfixed in 1% osmium tetroxide in 0.2 M phosphate — buffer pH 7.2 dehydrated in ethyl alcohol and embedded in epoxi resin. Thin sections were stained with uranyl acetate and lead citrate and observed in a Zeiss EM 109 electron microscope.

The largest percentage of mitotic figures was reached between 28 and 32 h in AEM with a percentage of — synchrony of approximately 50%. Through the analysis of many mitotic figures at several observed — times, we could conclude the sequence of nuclear changes that occur during mitosis. The figure 1 shows the interphase nucleus with the heterochromatin typically associated to the nuclear envelop. The first manifestation of mitosis was the observation of chromosome-like structures around the center of the nucleus (Fig. 2). After this, the chromosome-like structures lost its organization and acquire a distribution approximately equatorial (Fig. 3). Then, the nucleus begins its elongation (Fig. 4) and, at this stage bundles of microtubules appear parallelly arranged into the nucleus (Fig. 5). Simultaneously, — the chromosome-like structures begin a non-synchronous motion toward the poles producing a stage of — early telophase (Fig. 6). Centrioles were not observed. Figure 7 shows the nuclear structure of the — cyst stage ameba and, if the figure 7 is compared to figure 1, differences of the organization of chromatin among both, cyst and trophozoite nuclear stages are evident; in the trophozoite the chromatin is peripherically associated to internal surface of nuclear envelop, but in the cyst large condensations — of chromatin are associated to internal nuclear surface, however some regions of this internal nuclear surface are free of chromatin. During all mitotic process the nuclear envelop remains intact.

The current results show that the mitotic process in *E. invadens* presents stages that are resembling, — but not equal to the four phases of a typical mitosis: prophase (Fig. 2), metaphase (Fig. 3), anaphase (Fig. 4), and telophase (Fig. 5). The large chromatine-condensation structures in the cyst nuclei present probably a high order condensation of the chromatin, producing the inhibition of the genetic — expression, but we don't know the significance of the condensations of chromatin that remain associated to the internal nuclear membrane through the encystation.

References:

1. C.C. Narasimhamurti: Parasitology 54(1964)95-103.
2. M. Morales-Vallarta. et al. Arch. Invest. Méd. (Méx.). 13(Supl. 3) (1982): 211-216.
3. L.S. Diamond, J. Parasitol. 54(1968):1047-1056
4. S, Rengpien and G.B. Bailey. J. Parasitol. 61(1975):24-30

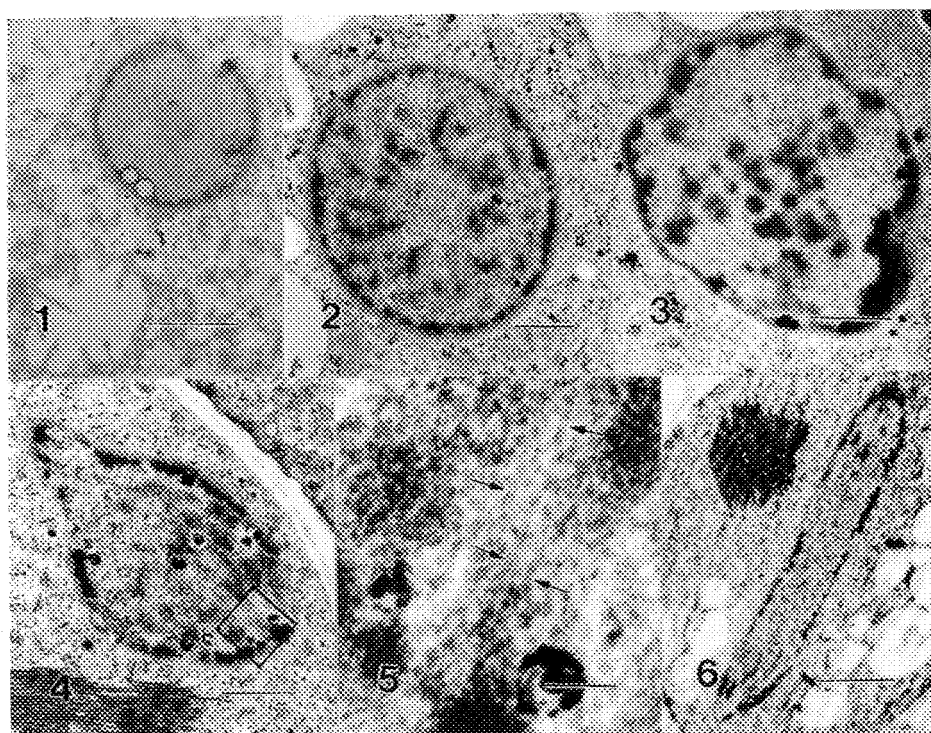


Fig. 1. Nucleus in interphase of *Entamoeba invadens* trophozoite. The heterochromatin is peripherally associated to internal surface of nuclear envelope. Bar = 5 μ m.

Fig. 2. Prophase stage. Chromosome-like structures -- appeared around the center of the nucleus. Bar = 1 μ m.

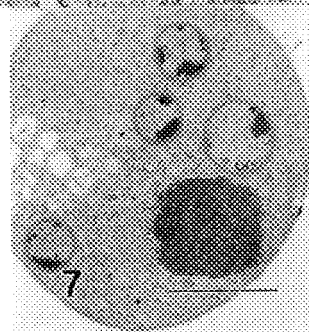
Fig. 3. Metaphase stage. The chromosome-like structures adopt an approximately equatorial distribution. Bar = 1.5 μ m.

Fig. 4. The nucleus begin to elongate by the formation of a intranuclear spindle and the chromosome-like structures start the migration toward the poles. Chromatin condensations remain associated to nuclear membrane. Bar = 2 μ m.

Fig. 5. Amplification of the insert square in fig. 4. Spindle microtubules are seen clearly parallelly arranged (arrows). Bar = 0.5 μ m.

Fig. 6. The chromosomes-like structures have almost arrived to the poles, but chromatine condensations remain associated to nuclear membrane. Bar = 5 μ m.

Fig. 7. Mature cyst of *E. invadens*. The four nuclei show very large condensation of chromatin always associated to nuclear envelope. Bar = 5 μ m.



THE BONE-DENTAL IMPLANT INTERFACE: HVEM AND TEM OBSERVATIONS

D.E. Steflik*, D.J. Berkery**, G.R. Parr*, A.L. Sisk*, P.J. Hanes*,
F.T. Lake*, B.B. Singh* and P. Brewer*

*School of Dentistry, Medical College of Georgia, Augusta GA 30912

** Wadsworth Center for Laboratories and Research, New York State
Department of Health, Albany, NY 12201-0509

Previous studies^{1,2} have suggested the prerequisite of bone interfacing successful endosteal dental implants. This is the concept of osseointegration of dental implants within the jaw. However, the morphology of the actual bone interface on the ultrastructural level is lacking. This current study attempts to elucidate, with correlative high voltage electron microscopy (HVEM) and conventional electron microscopy (TEM), the morphology of the bone-dental implant interface.

Two months after extraction of all premolars, 120 root form and blade-type implants were placed into the mandibles of 30 adult dogs. This report will be restricted to 12 implants retrieved from animals euthanized after 5 mo of unloaded healing (control); and 12 implants loaded for 6 mo from animals euthanized 11 months after implantation. Following vascular perfusion with glutaraldehyde the implants were block resected with their encasement of mandibular tissues, fixed by immersion for 24 hr in glutaraldehyde and post-fixed with 1% OsO₄ for 2 hr. After embedding in EMBED 812, the samples were cut into 1mm sections and implants were cryofractured³ from the oral tissues. The retrieved tissue samples were reembedded and sectioned (undecalcified). Sections were viewed with a JEOL 100 CX or an AEI EM7 1.2 MV HVEM.

Mineralized bone was shown to closely appose significant regions of the implants, often separated from the implant by only a 20-50 nm electron dense deposit (fig 1). Especially in control samples osteoblasts (Os) were observed adjacent to the implant penetrating into the mineralized matrix (MM). In the loaded samples, Os were often observed associated with a connective tissue stroma (CTS) adjacent to existent mineralized bone (fig 2). HVEM showed the interaction of the Os with the collagen fibers (fig 3) which were aligned parallel to the implant surface. Other regions showed the MM to be separated from the implant by a wider electron dense deposit which sometimes contained fibrillar elements. These observations demonstrate the healthy interaction of mandibular bone to the implants. Data suggests that bone supporting implants may be laid down in two ways. Perhaps from the implant surface via Os backing off at early time periods; and toward the implant via Os and a CTS at later time periods. By using the 3-D capabilities of HVEM in conjunction with routine TEM, exciting opportunities exist to examine oral tissue interfaces to implants⁴.

References

1. T. Albrektsson et al., Acta. Orthop. Scand. (1981)52, 155.
2. D.E. Steflik et al., J. Biomed. Mat. Res. (1989)23, 895.
3. D.E. Steflik et al., Ann. NY Acad Sci. (1988)523, 4.
4. Study supported by NIDR Grant DE08586 and NIH Grant PHS RR01219

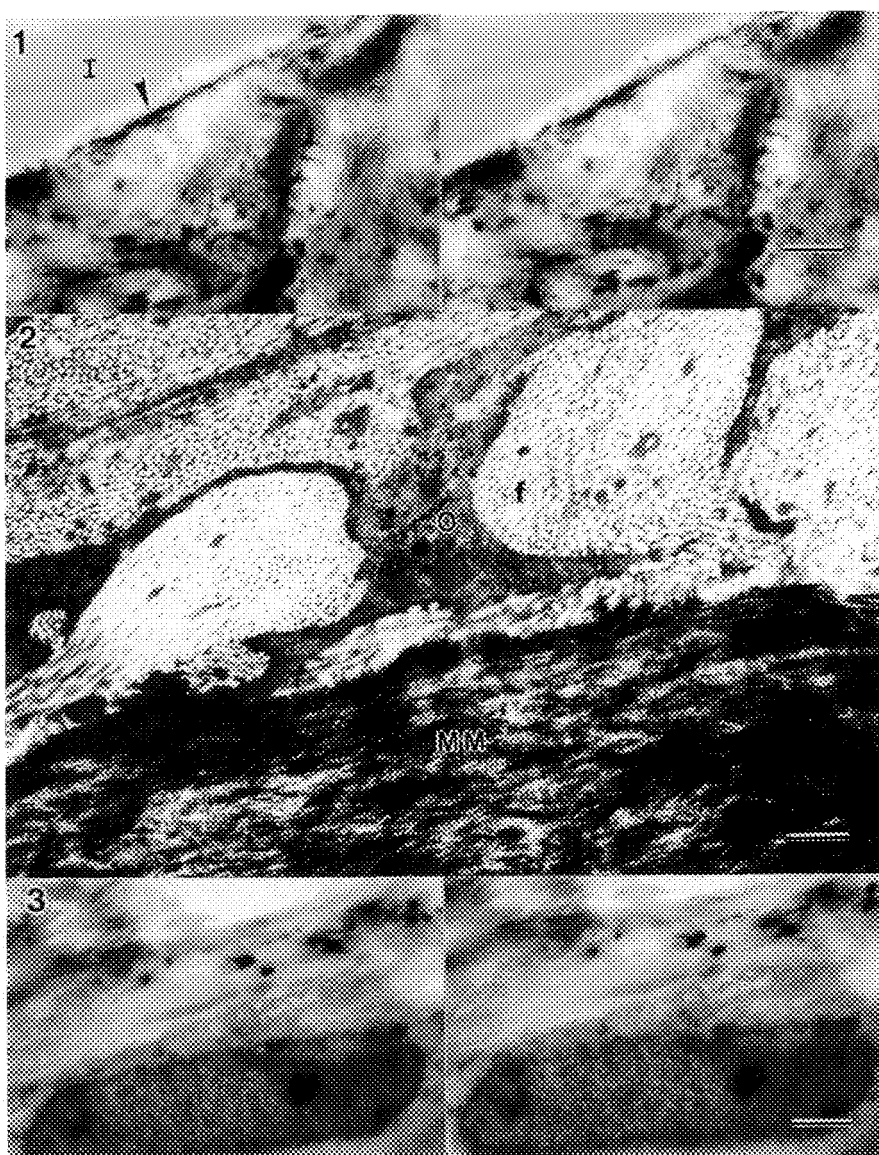


FIG. 1.--HVEM stereo-pair demonstrating dense mineralized bone closely apposed to the space previously occupied by a titanium root form implant (I). An electron dense deposit (arrowhead) is interposed between the bone and the implant. 0.5 μm section. Uranyl and lead stain. Tilt \pm 20 degrees. Bar = 1.0 μm . [Mag = 10,000]

FIG. 2.--TEM of an osteoblast process (O) interacting with unmineralized collagen fibers (f) and with the mineralized collagen fibers of the mineralized bone matrix (MM). Bar = 1.0 μm . [Mag = 10,000]

FIG. 3.--HVEM stereo-pair demonstrating a portion of an osteoblast interacting with unmineralized collagen fibers which were observed upon the mineralized matrix. Tilt = \pm 20 degrees. Bar = 1.0 μm . [Mag = 8000]

INNERVATION OF ENDONEURIAL MICROVESSELS IN HUMAN SURAL NERVE

John L. Beggs, Peter C. Johnson, Astrid G. Olafsen, C. Jane Watkins

Division of Neuropathology, Barrow Neurological Institute, Phoenix, Arizona 85013

The blood supply (vasa nervorum) to peripheral nerves is composed of an interconnected dual circulation. The endoneurium of nerve fascicles is maintained by the intrinsic circulation which is composed of microvessels primarily of capillary caliber. Transperineurial arterioles link the intrinsic circulation with the extrinsic arterial supply located in the epineurium. Blood flow in the vasa nervorum is neurogenically influenced (1,2). Although a recent hypothesis proposes that endoneurial blood flow is controlled by the action of autonomic nerve fibers associated with epineurial arterioles (2), our recent studies (3) show that in addition to epineurial arterioles other segments of the vasa nervorum are also innervated. In this study, we examine blood vessels of the endoneurium for possible innervation.

Transverse segments of normal human sural nerve were processed for electron microscopy. Segments were also embedded in paraffin for an immuno-method of localizing axons using an antibody directed at a neuronal protein (PGP 9.5).

Thirty-two % of the blood vessels residing in the subperineurial space and connective tissue septa exhibited perivascular PGP 9.5 positivity. Perivascular nerve fibers were generally much smaller ($\approx 0.3 \mu\text{m}$) in diameter compared to the unmyelinated fibers in the endoneurium proper (mean diameter of $\approx 1.2 \mu\text{m}$). Generally, several axons were associated with a Schwann cell subunit (Fig 1). Perivascular axon varicosities contained dense cored vesicles ($\approx 100 \text{ nm}$) and a variety of agranular vesicles (Fig 1). Most of the microvessels in the endoneurium which exhibited perivascular nerve fibers did not have a continuous smooth muscle layer and were considered to be post-arteriolar capillaries or small venules.

This study combined with previous studies (3) shows that innervation of the vasa nervorum is not confined to epineurial and transperineurial arterioles but is extended to a population of endoneurial microvessels. Innervation of small vessels may play a role in the regulation of blood flow in the endoneurium and possibly influence their permeability characteristics (4).

References

1. P. A. Low et al., *Int. Rev. Neurobiol.* (1989)31, 355.
2. M. Kihara and P. A. Low, *J. Physiol.* (1990)422, 145.
3. J. Beggs et al., *J. Neuropath. Exp. Neurol.* (1991)50, 704.
4. This research was supported by NIH grant 1-RO-1 DK38163

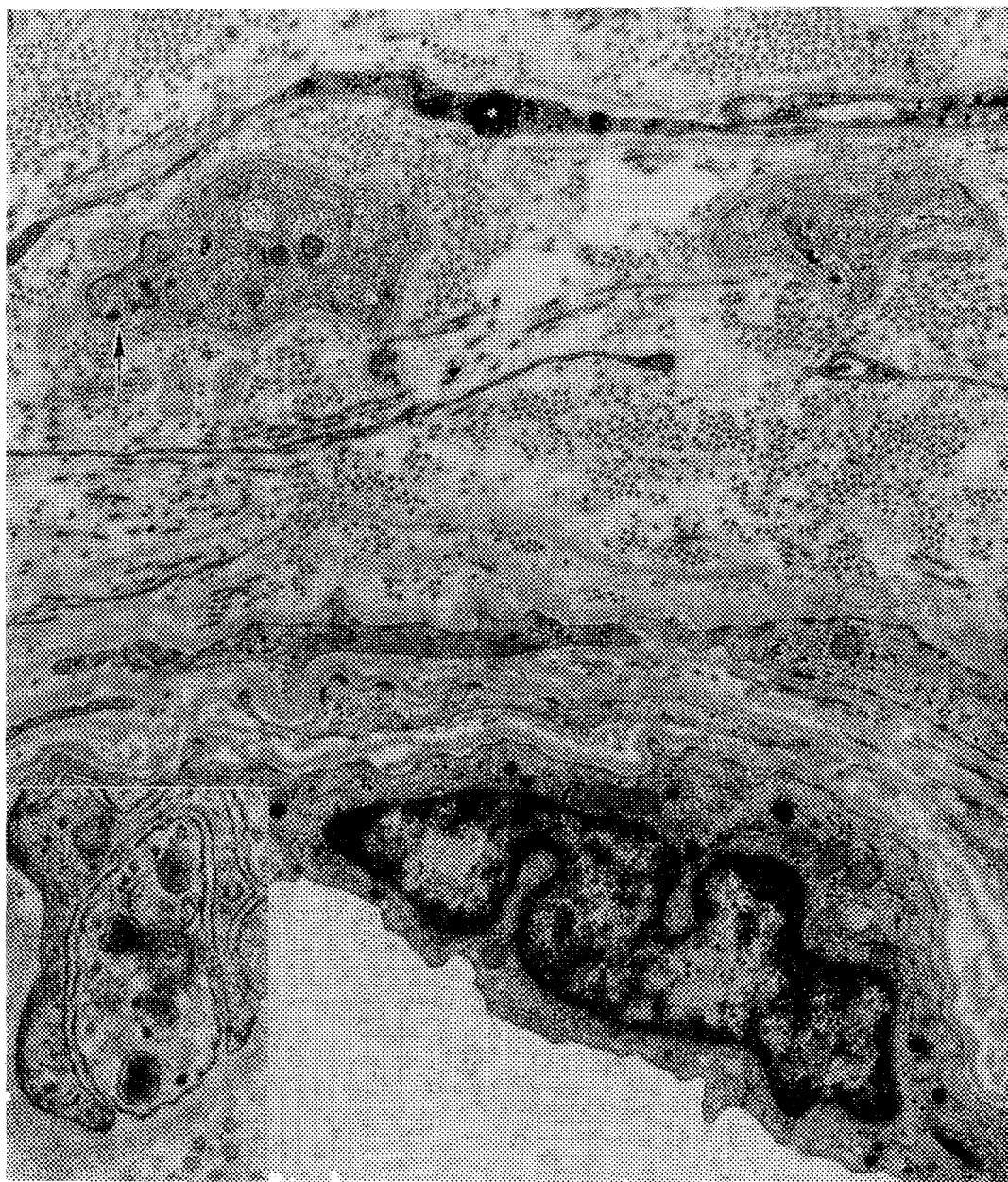


FIG. 1.--Endoneurial microvessel exhibits two perivascular Schwann cell subunits containing several axons. An axon varicosity (arrow) is shown in inset. Large dense cored vesicles and agranular vesicles are evident.

ULTRASTRUCTURE OF GYPSY MOTH (*LYMANTRIA DISPAR*) NEPHROCYTES

Kathleen S. Shields

USDA Forest Service, Northeastern Forest Experiment Station, Center for Biological Control of Northeastern Forest Insects & Diseases, Hamden, Connecticut 06514

Nephrocytes are endocytotic cells that exist in distinct groups at fixed sites within the body cavity of arthropods.¹ They can be identified by their uptake of the vital dye, Trypan blue. The only types of nephrocyte that have been described in the insect order Lepidoptera are the pericardial cells, which have been described in many species¹, and the cells of the unusual "organe rameux" of *Bombyx mori*.²

Gypsy moth, *Lymantria dispar*, larvae were injected with either a 1% solution of Trypan blue in saline, or with saline alone. They were dissected at intervals from the fourth larval instar until pupation, and nephrocytes were identified, removed, and prepared for examination by SEM and TEM using conventional histological methods.

Gypsy moth larvae have a discrete group of nephrocytes, approximately 17-26 in number, located in the ventral part of the body cavity. The cells are tightly attached to the ventral surface of a layer of fat body that encircles the gut at the junction of the foregut with the midgut (FIG. 1). The cells somewhat overlap each other, and are arranged in an irregular row that extends across the fat body. Nephrocytes are connected to each other and to the fat body by ligament-like fibers and by tracheolar attachments. They are large, smooth-surfaced cells, with single, branching nuclei.

The other group of nephrocytes in *L. dispar* is the pericardial cells (FIG. 2, 3), which lie along both sides of the dorsal vessel and are restricted to the abdomen. They are attached to the heart, and to the alary muscles and underlying fat body by connective fibers. The cells are generally spindle-shaped, although occasionally irregular in contour, and have smooth surfaces.

The two types of nephrocytes have similar ultrastructure. They are surrounded by a basement membrane, and the peripheral cytoplasm is characterized by infoldings of the plasma membrane, forming an extensive network of labyrinthine channels (FIG. 4). The channel openings are guarded by single or multiple diaphragm-like structures, which are 30-50 nm wide (FIG. 5). Many invaginations of the membrane lining the channels occur, resulting in numerous coated pits and vesicles (FIG. 6).

The ventral nephrocytes described here in *L. dispar* may be typical of nephrocytes in many other Lepidoptera, and perhaps Trichoptera. Similar groups of cells were observed in the same ventral location in larvae of *Galleria mellonella*, *Manduca sexta*, *Malacosoma disstria*, and *Rhyacophila* sp.

References

1. A.C. Crossley, in G.A. Kerkut and L.I. Gilbert, Eds., Comprehensive Insect Physiology, Biochemistry and Pharmacology, Oxford: Pergamon (1985) 3, 487.
2. L. Lavenseau et al., Int. J. Insect Morphol. & Embryol. (1981) 3, 235.

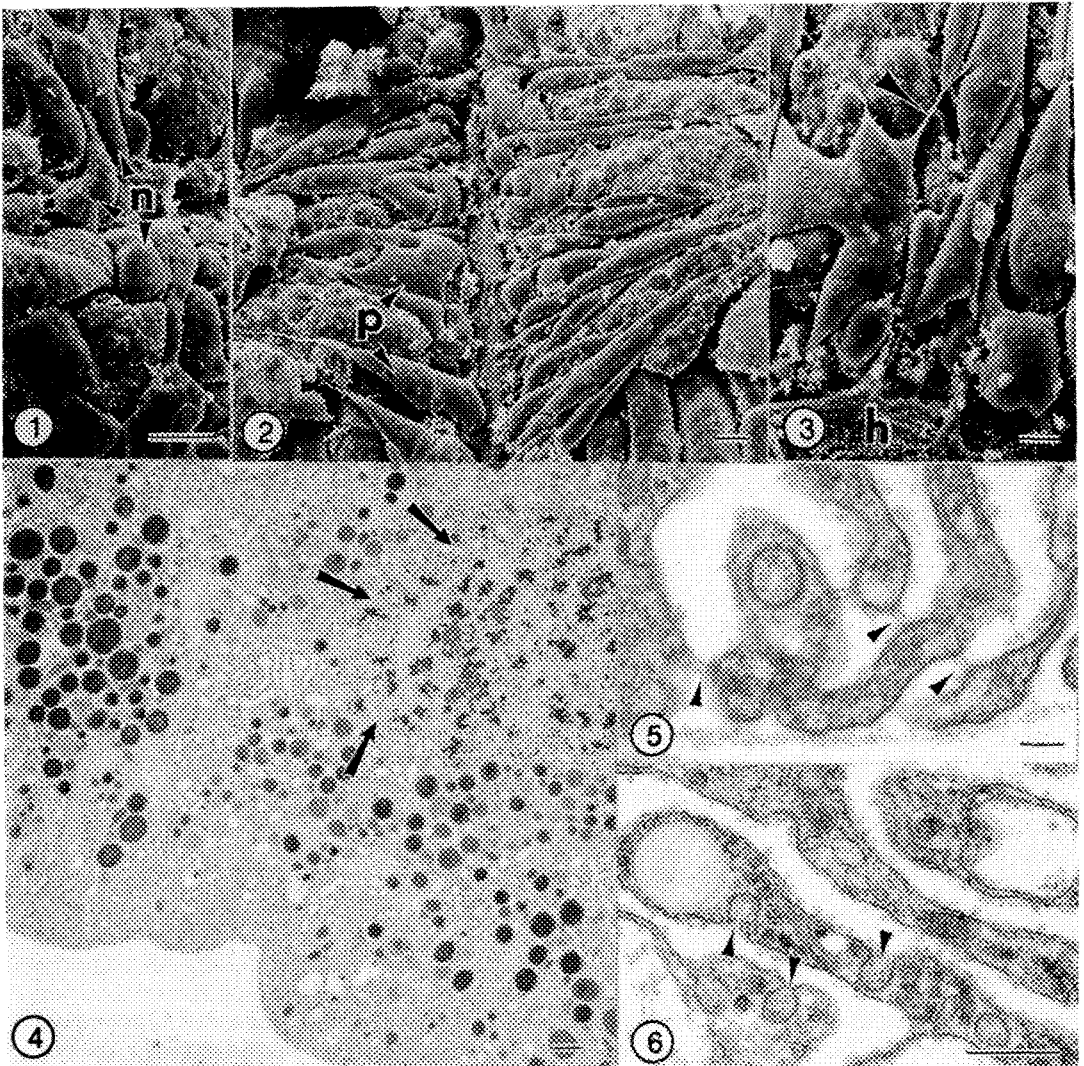


FIG. 1.--SEM of ventral nephrocytes (n) attached to circumesophageal fat body. Bar = 100 μ m.
 FIG. 2.--SEM of pericardial cells (p) lying along both sides of gypsy moth heart. Bar = 100 μ m.
 FIG. 3.--Higher magnification SEM of pericardial cells and connective fibers (arrow) which attach cells to heart (h), alary muscles and underlying fat body. Bar = 100 μ m.
 FIG. 4.--TEM of ventral nephrocyte. Note ruffled nucleus (arrows), lucent and dense vacuoles, and network of channels at cell periphery. Bar = 1 μ m.
 FIG. 5.--TEM of cell periphery showing basement membrane and channel openings guarded by diaphragm-like slits. Bar = 0.1 μ m.
 FIG. 6.--TEM of labyrinthine channel. Invaginations of membrane lining the channel result in numerous coated pits and vesicles. Bar = 0.5 μ m.

3-D ANALYSIS OF CELLULAR LIPID METABOLISM: RECONSTRUCTION OF THE TUBULAR NETWORK

W.G. Jerome^{*}, B.F. McEwen^{**}, L.K. Minor^{***}, G.H. Rothblat^{****}, J.M. Glick^{****}

^{*}Dept Pathology, Bowman Gray Sch of Med, Winston-Salem NC 27157, ^{**}Wadsworth Cntr for Labs and Res, Albany NY 12201, ^{***}Ortho Pharmaceutical Corp, Raritan NJ 08869, ^{****}Dept Physiol and Biochem, Medical College of Pennsylvania, Philadelphia PA 19129

A predominant feature of early atherosclerotic lesions is the presence of macrophages and smooth muscle cells in which large quantities of lipid have accumulated. This lipid occurs within both small, cytoplasmic, cholesterol ester droplets and large, lipid-swollen secondary lysosomes. Time resolved studies suggest lysosomal engorgement promotes the disease progression. Using cultured cells we have shown that lysosomal engorgement in smooth muscle cells is accompanied by the elaboration of an extensive network of tubules¹. The tubules are rich in acid hydrolases and appear to be an extension of the trans Golgi network. As part of our effort to understand the causes and significance of lysosomal lipid accumulation we have undertaken to characterize the extent and development of the tubular network. The tortuous nature of the network makes it difficult to visualize by conventional thin section electron microscopy. Thus, intermediate voltage electron microscopy of thick (1-3 μ m) sections in which the tubules have been contrasted using acid phosphatase cytochemistry² has been essential to these studies. Cultured rabbit smooth muscle cells were incubated with sonicated lipid droplets composed of 72% cholesteryl oleate, 25% triolein, and 3% phospholipid. Prior to incubation, cells had no visible lipid stores and 92% of cells showed no acid phosphatase-containing tubules. In cells with tubules, the tubules occupied less than 0.1% of the cell volume. In contrast, after 4 h of exposure to droplets 81% of cells showed lysosomal lipid accumulation with 67% exhibiting extensive, interconnecting, acid phosphatase positive tubular networks. Although stereo-pair images provided much information about the extent of the network (figure 1), the exact relationship of the network to lipid-engorged lysosomes was somewhat ambiguous due to superposition of objects. In order to clarify the relationship of network to lysosome, a tomographic reconstruction was computed from an IVEM tilt series encompassing $\pm 60^\circ$ in 2° increments. Images were digitized using a DAGE model 81 video camera. Rotational alignment using fiduciary markers was accomplished using the algorithm described by Lawrence³. Translational alignment and weighted back-projection reconstruction were carried out as described by McEwen⁴. Volumes were rendered using a PIXAR computer graphics workstation. The reconstruction (figure 2) revealed that extensions of the network made contact with the lipid-swollen lysosomes suggesting that the network might transfer hydrolases directly to secondary lysosomes⁵.

1. Jerome, W. G., Minor, L. K., Glick, J. M., Rothblat, G. H. & Lewis, J. C. (1991) *Exp Molec Pathol* 54, 144-158.
2. Gomori, G. (1952) *Microscopic histochemistry: principles and practice*, (University of Chicago Press, Chicago).
3. Lawrence, M. C. (1992) in *Electron Tomography*, ed. Frank, J. (Plenum Press, Inc, New York) pp. In press.
4. McEwen, B. F., Radermacher, M., Rieder, C. L. & Frank, J. (1986) *Proc Natl Acad Sci (USA)* 83, 9040-9044.
5. Work supported by American Heart Association Grant 900709, NIH Program Project HL-22633, NIH Training Grant HL-07443, and NIH Biotechnology Resource grants RR-02722 (MICROMED) and RR-01219 (BMIRR).

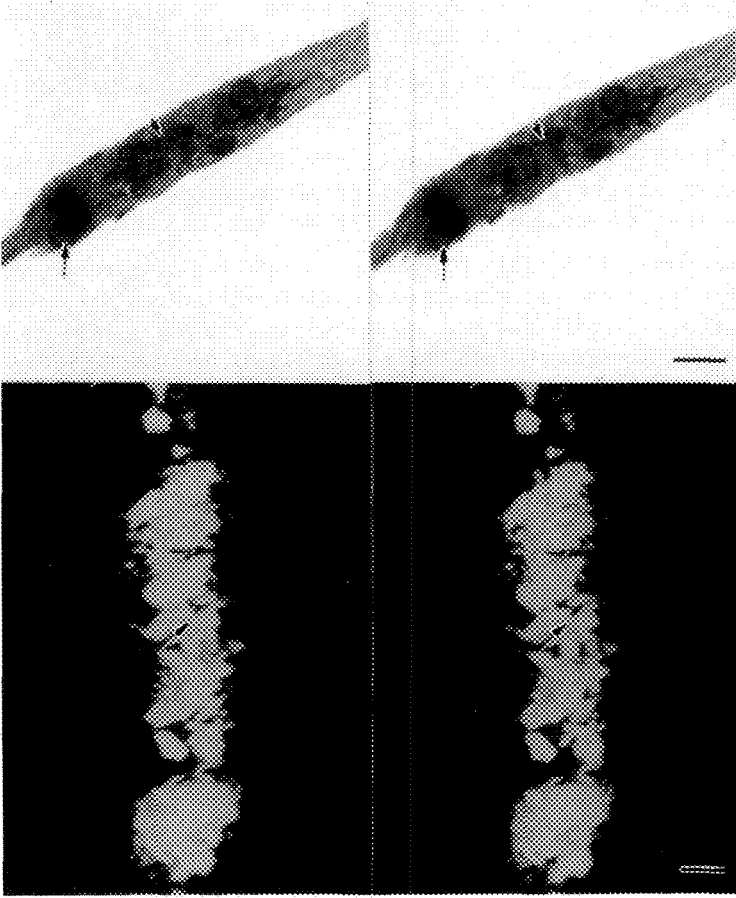


FIG 1. Stereo-pair IVEM of smooth muscle cell. Lipid-engorged lysosomes appear as spherical structures (arrows) outlined by dense acid phosphatase reaction product. Reaction product also accentuates the contrast of the network which appears to make contact with at least one of the secondary lysosomes (arrowhead). Bar = 1 μ m.

FIG 2. Stereo-pair of tomographic reconstruction of acid phosphatase containing compartments from the same cell shown in FIG 1. Density thresholds for the renderings were set such that cellular details other than acid phosphatase compartments are not visualized. These settings also removed some of the less dense acid phosphatase containing areas. However, even at these stringent settings, a connection (arrowhead) between the tubular network (to the right of the arrowhead) and a lipid-filled lysosome (to the left of the arrowhead) is clearly evident. Bar = 0.5 μ m.

KINETIC STUDY OF MITOCHONDRIA IN ERYTHROPOIESIS OF ANEMIZED AMPHIBIANS, APPLYING RHODAMINE 123, FLOW CYTOMETRY AND IN SITU DETECTION OF OXIDATION-REDUCTION ENZYMES

Aurora Marques Cianciarullo, Álvaro Luiz Bertho*, and Maria de Nazareth Leal de Meirelles**

Laboratório de Biologia Celular, Instituto Butantan, São Paulo 05504;
 *Depto. de Protozoologia and **Depto. de Ultraestrutura e Biologia Celu
 lar, Instituto Oswaldo Cruz-FIOCRUZ, Rio de Janeiro 21040, BRASIL

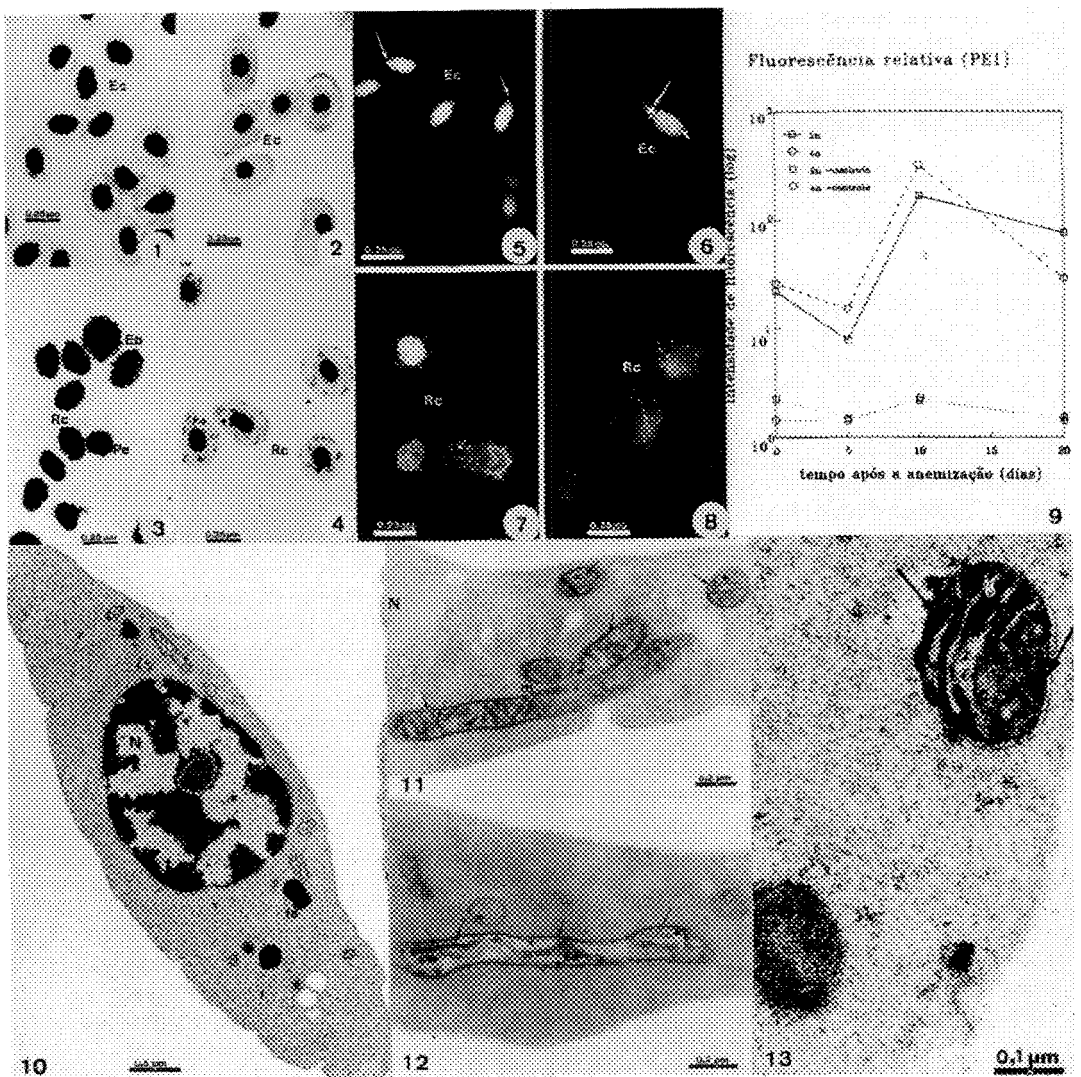
Amphibians erythropoiesis is similar to that of vertebrates in general, comprising: (1) an erythropoietin hormonal stimulation, for differentiation, (2) a lineage of precursor maturing cells, (3) alfa and beta globin chains synthesis, (4) an adequate iron supply for heme synthesis, followed by (5) the final hemoglobin (Hb) biosynthesis. Several studies try to establish a correlation between mitochondria and heme synthesis¹, and the final Hb biosynthesis^{2,3,4}.

In toads *Bufo ictericus* 2n and frogs *Odontophrynus americanus* 4n we verified the occurrence of a similar behaviour, in response to the anemia. Within the times studied, the 10th day after the hemolytic anemia, induced by phenylhydrazine, revealed to have the maximum cellular activity, after the applied methodologies. In order to select mitochondrial population in living cells, we used Rhodamine 123 (Rh 123) fluorescent dye⁵, and examined in a Zeiss Photomicroscope. This study was followed by a quantitative analysis in a flow cytometer EPICS-751 (Coulter Electronics). The intensity of incorporated Rh 123 by the mitochondria, the granularity and cells size were detected through the laser detour signals⁶. With the purpose to follow the possible functional changes that occur, related to the mitochondrial morphologic modifications, we localized three electron transport chain enzymes: cytochrome-oxidase, isocitrate and succinate dehydrogenase, through ultrastructural cytochemistry methods⁷.

Our aftermath point to that the 10th day coincides with the reticulocyte stage, showing to have the maximum activity, in accord with citations in the literature. It also suggests that mitochondria could be in a high active functional state. These facts could be also related with the synthesis of crista membranes, in the course of a progressive mitochondrial lamellation⁸, as a function of changes in mitochondrial activity, directed to heme and the final Hb biosynthesis.⁹

References:

1. Rose and Olson (1983) J Biol Chem, 258(7):4298
2. Brunner et al. (1972) Experientia, 28:569
3. Brunner et al. (1992) Comp Biochem Physiol, in press
4. Cianciarullo et al. (1989) Comp Biochem Physiol, 94A(3):525
5. Johnson et al. (1980) Proc Natl Acad Sci USA, 77:990
6. Shapiro (1985) Alan R Liss, Inc., New York, pp 1-158
7. Meirelles and De Souza (1982) Exper Parasitol, 53:341
8. Brunner et al. (1991) Comp Biochem Physiol, 98B(2/3):227
9. This research was supported by FINEP, CNPq, Instituto Butantan and FIOCRUZ.



Figs.1-4. Kinetic of erythroid cells after anemia induction: (1)normal, (2)5th, (3)10th and (4)20th days, stained by new methylene blue and Rosenfeld. Ec-Erythrocyte; Eb-Erythroblast; Rc-Reticulocyte; Pe-Proerythroblast.

Figs.5-8. The same kinetic, stained by Rhodamine 123.

Fig.9. Relative fluorescence (PEI) by flow cytometry: intensity of incorporated Rh 123 x time after anemization (days).

Fig.10. Reticulocyte of *Bufo ictericus* 2n, at the 10th day, processed by routine protocol of electron microscopy. N-nucleus; nu-nucleolus; fe-iron inclusion; arrow head-polysomes.

Figs.11,12. "In situ" detection of cytochrome-oxidase in both mitochondria and modified mitochondria. m-mitochondria; arrows-inner membrane and cristae.

Fig.13. Isocitrate dehydrogenase detection at the 10th day after anemization. Arrow-intercristae space.

ULTRASTRUCTURE OF THE BASAL BODY APPARATUS IN EPIDERMAL CELLS OF A SPONGE LARVA (*APLYSILLA* SP: DEMOSPONGIAE)

R.L. Pinto and R.M. Woollacott

Department of Organismic and Evolutionary Biology, Harvard University, Cambridge, MA 02138

The basal body and its associated rootlet are the organelles responsible for anchoring the flagellum or cilium in the cytoplasm. Structurally, the common denominators of the basal apparatus are the basal body, a basal foot from which microtubules or microfilaments emanate, and a striated rootlet. A study of the basal apparatus from cells of the epidermis of a sponge larva was initiated to provide a comparison with similar data on adult sponges.

Sexually mature colonies of *Aplysilla* sp were collected from Keehi Lagoon Marina, Honolulu, Hawaii. Larvae were fixed in 2.5% glutaraldehyde and 0.14 M NaCl in 0.2 M Millonig's phosphate buffer (pH 7.4). Specimens were postfixed in 1% OsO₄ in 1.25% sodium bicarbonate (pH 7.2) and embedded in epoxy resin. The larva of *Aplysilla* sp was previously described (as *Dendrilla cactus*) based on live observations and SEM by Woollacott and Hadfield.¹

Lateral portions of the epidermis of this larva are composed of a monociliated pseudostratified columnar epithelium. At the surface the cells are approximately 3.0 µm in diameter, but extend approximately 25 µm in length into the interior. The single cilium, basal body, and rootlet are situated close to the posterior side of the cell body and provide a site from which microtubules and electron dense-arms emanate (Figs. 1, 2, 3). Some of the microtubules anchor the basal body to the posterior side of the cell membrane. Others, along with the electron-dense arms, radiate around the basal apparatus and appear to converge at a small vesicle in the cytoplasm (Fig. 3) and not at the anterior side of the membrane as occurs in some metazoans. Microtubules radiating from the basal foot to the lateral cell membrane are thought to provide stability at the point of anchorage for the cilium.² Although some microtubules in the sponge epidermal cell connect to the posterior side of the cell membrane, the function of others attaching to vesicles within the cytoplasm is uncertain. A centriole oriented perpendicular to the basal body is adjacent to the distal end and posterior side of the rootlet. The rootlet is unstriated and descends deeply into the basal cytoplasm (Fig. 1). The absence of striations in the basal foot and in the rootlet of this sponge larva depart from the general pattern observed in many different multicellular animals³, but is known to occur in choanocytes of other sponges.⁴ Evidence exists that striations in rootlets are the result of lateral interactions between the longitudinal filaments and that extracted foot filaments separate where striations are broken.⁵ The rootlet filaments in this sponge appear tightly cohesive. How the absence of striations in these cells may affect the contractile ability of the rootlet and, therefore, the movement of the cilium is unknown. Observations of living larvae indicate that the cilia of the lateral portions of the epidermis beat actively and establish a metachronal wave. Finally, a Golgi complex is found closely appressed to the rootlet (Fig. 1). The consistent presence of a Golgi complex with the rootlet we observed in this sponge larva is paralleled by a similar association in choanocytes of other adult sponges.⁶ While not general features of metazoans, the association of Golgi with the basal apparatus and the presence of nonstriated rootlets are now documented in at least two distinct cell lines of nonhexactinellid sponges.

1. R.M. Woollacott and M.G. Hadfield, Trans. Amer. Micr. Soc. 108(1989)410.
2. M.A. Sleight and N.R. Silvester, J. Submicrosc. Cytol. 15(1983)101.
3. D.R. Pitelka, In M.A. Sleight, Ed., Cilia and Flagella, New York: Academic Press (1974)437.
4. R.D. Barnes and F.W. Harrison, In F.W. Harrison and J.A. Westfall, Eds., Microscopic Anatomy of the Invertebrates. Vol 2, New York: Wiley-Liss (1991)2.
5. G.E. Olson and J.B. Rattner, J. Ultrastruc. Res. 51(1975)409.
6. F.W. Harrison and L. De Vos, in F.W. Harrison and J.A. Westfall, Eds, Microscopic Anatomy of the Invertebrates. Vol. 2, New York: Wiley-Liss (1991)29.

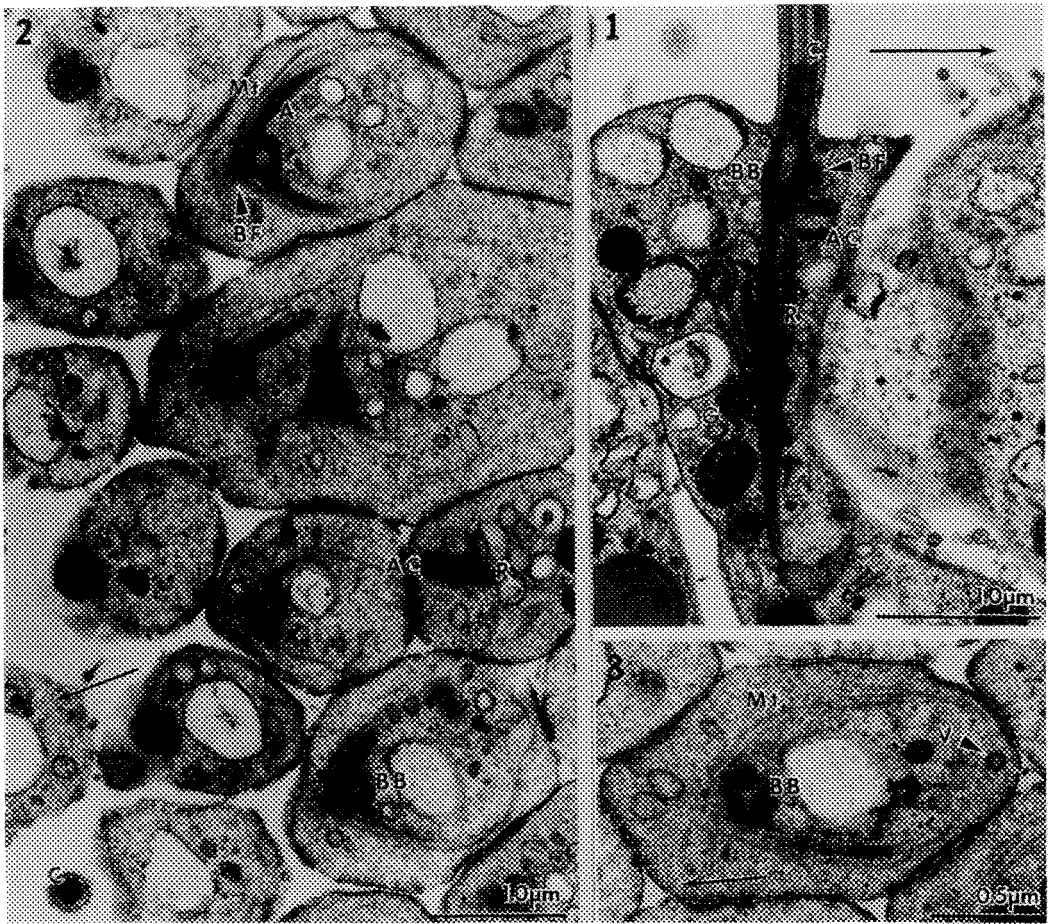


FIG. 1.--Longitudinal section of epidermal cell showing cilium (C), basal body (BB) and unstriated rootlet (R). Note spherical basal foot (BF) and accessory centriole (AC) on posterior side of cell (arrow) and Golgi (G) appressed to rootlet.

FIG. 2.--Slightly oblique, transverse section illustrating basal body and foot with radiating microtubules (Mt) and electron-dense arms (A), rootlet and accessory centriole.

FIG. 3.--Transverse section of basal body with microtubules that converge at small vacuole (V).

TEMPORAL AND SPATIAL INTERRELATIONSHIPS OF CONFRONTING CISTERNAE TO NUCLEAR ENVELOPE

John R. Palisano

Department of Biology, Emory & Henry College, Emory, VA 24327

Although confronting cisternae (CC) have been observed in a variety of tumor cells^{1,2} and normal fetal rat, mouse, and human epithelial tissues,^{3,4} little is known about their origin or role in mitotic cells. While several investigators have suggested that CC arise from nuclear envelope (NE) folding back on itself during prophase,⁵ others have suggested that CC arise when fragments of NE pair with endoplasmic reticulum.⁶ An electron microscopic investigation of 0.25 μ m thick serial sections was undertaken to examine the origin of CC in HeLa cells.

HeLa cells, obtained from American Type Culture Collection (CCL 2), were cultured in minimum essential medium containing 10% calf serum in a mixture of 5% CO₂ in air. Cells were harvested by mitotic shake-off 3 or 4 days after passage while they were in exponential growth phase. The mitotic cells were fixed for 1 hr in 0.5% glutaraldehyde in 0.1 M Na cacodylate buffer pH 7.2 and rinsed 3 times in 5 min changes of the same buffer. Cells were placed in 1% tannic acid buffered in 0.1 M Na cacodylate pH 7.2 and rinsed 3 times in 5 min changes of the same buffer. Cells were post-fixed in 1% OsO₄ buffered in 0.1 M Na cacodylate buffer, pH 7.2, for 1 hr and rinsed 3 times in the same buffer. The cells are embedded in 2% agarose, dehydrated in 25% ethanol and stained in bloc in 25% ethanol saturated with uranyl acetate for 30 min. The cells were then dehydrated in a graded ethanol series and 100% propylene oxide and embedded in epon.

Electron micrographs from mitotic HeLa cells indicate that CC are most prevalent during prophase, and as the cells progress through the phases of mitosis, the number of CC profiles rapidly diminishes. The longest segments of CC are observed during prophase (Fig. 1). The fact that the CC during prophase frequently delineate the former nucleus and that the number and length of CC profiles drop dramatically before metaphase (Fig. 2) suggests that the CC probably represent NE folding back on itself. Shorter profiles of CC are infrequently observed in late telophase or early interphase in daughter cells (Fig. 3).

Three-dimensional reconstruction of electron micrographs of serially-sectioned HeLa cells supports the hypothesis that CC arise from NE fragments folding back on themselves. While it is impossible to rule out any association between NE and ER in the formation of CC, no evidence of such an association has been seen in three-dimensional reconstructions of several serially-sectioned HeLa cells in prophase. Furthermore, none of the reconstructions of cells in telophase or interphase indicate any association of persistent CC profiles with the reassembling NE or ER in the daughter cells.

While caution must be exercised in interpreting dynamic events, such as mitosis from electron microscopy investigations which necessitate fixing cells in time, three-dimensional reconstruction of thick sections from mitotic HeLa cells does reveal organelle interrelationships in ways never possible from random sections of cells. The absence of any relationship of CC to either newly assembled NE or ER in daughter cells suggests that CC profiles are simply remnants of NE which eventually will be recycled to the membrane subunit pool. No evidence was found to support the idea that short fragments of NE remain attached to chromosomes⁷ during any phase of mitosis and serve as the site at which newly assembled NE will occur. Three-dimensional reconstructions of electron micrographs suggest that CC arise from NE fragments which fold back on themselves and not pairing of NE with ER as several investigators have suggested. The micrographs also suggest that persistent CC do not serve as a preformed source of NE or ER in daughter cells, and that most profiles of CC separate into single cisternae which join the vesicular membrane pool as do all other cells' NE.⁸

References

1. E. C. Chew, Cell Biol. Internat'l. Reports (1986) 10, 683.
2. J. F. M. Nunes et al., J. Submicrosc. Cytol. (1986) 18, 441.

3. J. McDougall, *J. Cell Sci.* (1976) 22, 67.
4. J. R. Palisano, *Cell Biol. Internat'l. Reports* (1990) 14, 1025.
5. I. Nakanishi et al., *Acta Pathol. Jpn.* (1986) 36, 261.
6. B. R. Brinkley et al., *J. Ultrastruct. Res.* (1967) 19, 1.
7. F. Lampert, *Humangenetik* (1971) 13, 285.
8. This research was supported in part by Jeffress Research Grant (J-211). Portions of work done at Micromed Facility, The Bowman Gray School of Medicine, Wake Forest University, Winston-Salem, NC.

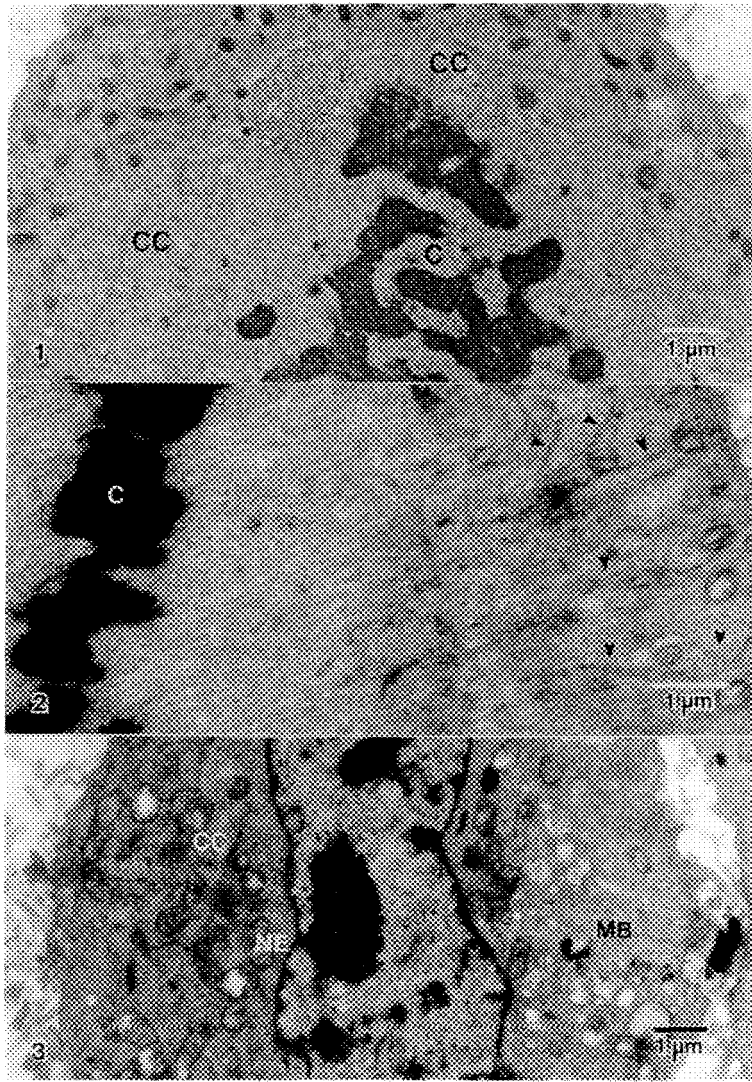


FIG. 1. – Cell in prophase. Long segments of CC in close association with chromosomes (C). Bar = 1 µm.
 FIG. 2. – Typical metaphase section. Cell is devoid of CC but contains numerous ER (arrowheads). Bar = 1 µm.
 FIG. 3. – Section of cell in telophase. Short segment of CC seen in close proximity to nuclear envelope (NE) which has reformed. Midbody (MB) is present. Bar = 1 µm.

INTERNAL COMPARTMENTATION OF THE MITOCHONDRION: AN HVEM TOMOGRAPHIC STUDY

Michael Marko, Ardean Leith, Bruce McEwen, Joachim Frank*, Carmen Mannella*

Wadsworth Center for Laboratories and Research, New York State Department of Health, Empire State Plaza, Albany, NY 12201-0509; and *Department of Biomedical Sciences, State University of New York at Albany

Much of what is known about the internal organization of the mitochondrion has been inferred from thin-section electron microscopy. This work has shown this organelle to have two membranes (outer and inner) and a matrix (the area bounded by the inner membrane), but there is considerable uncertainty about the 3D shape of the cristae (the infoldings of the inner membrane) and the nature of the contacts between the inner and outer membranes. Attempts to reconstruct the mitochondrion's interior by serial sectioning have failed because the required resolution (5-10 nm) cannot be practically achieved in the z-direction. The only 3D views provided until now have come from high-resolution SEM of freeze-cleaved and metal-shadowed mitochondria.¹

We have reconstructed an isolated rat-liver mitochondrion in a pellet that was glutaraldehyde-fixed, osmicated, and embedded in Epon. Sections 0.4 μm -thick were cut and stained with uranyl-lead. A single-axis tilt series consisting of 64 images at 2° intervals from -58° to +68° was recorded at 20,000x using the Albany HVEM at 1.0 MeV. Image fields were digitized using a modified Dage model 81 video camera. The mitochondrion to be reconstructed (1.65 μm cross-section diam, see Fig. 1) was contained in 360x325 windows, which were rotationally aligned using colloidal gold fiducial markers and a least-squares-based algorithm.² Translational alignment (by cross-correlation after cosine stretching), R* weighting, and back-projection were done as in previous work³ using SPIDER.⁴ Volume rendering was done on a Pixar II image computer.

The reconstruction (presented in stereo in Fig. 2) includes approximately one-half of a mitochondrion whose conformation is close to "orthodox", i.e. like that seen in tissue. The cristae, which are white against the darkly stained matrix, exhibit extremely complex shapes. There are numerous empty, randomly oriented, plate-like "cisternae" (marked P) and other, more expanded intracristal compartments containing granular material (G). The inner membrane also has numerous, long, flat folds along its periphery (F) and a few narrow, tube-like invaginations (T). Determination of the continuity between these internal compartments is underway. Improved resolution will be needed to resolve the outer and inner membranes (and any zones of contact) on the periphery of the organelle.⁵

References:

1. J.L. Winslow, et al., J. Electron Microsc. Tech. 18(1991)241.
2. M.C. Lawrence, in J. Frank, Ed., Electron Tomography, New York:Plenum (1992)197.
3. B.F. McEwen et al., Proc. Natl. Acad. Sci. USA 83(1986)9040.
4. J. Frank et al., Ultramicroscopy 6(1981)343.
5. Supported by NIH grants RR01219, R01-GM40165 and NSF grant 89-16315.

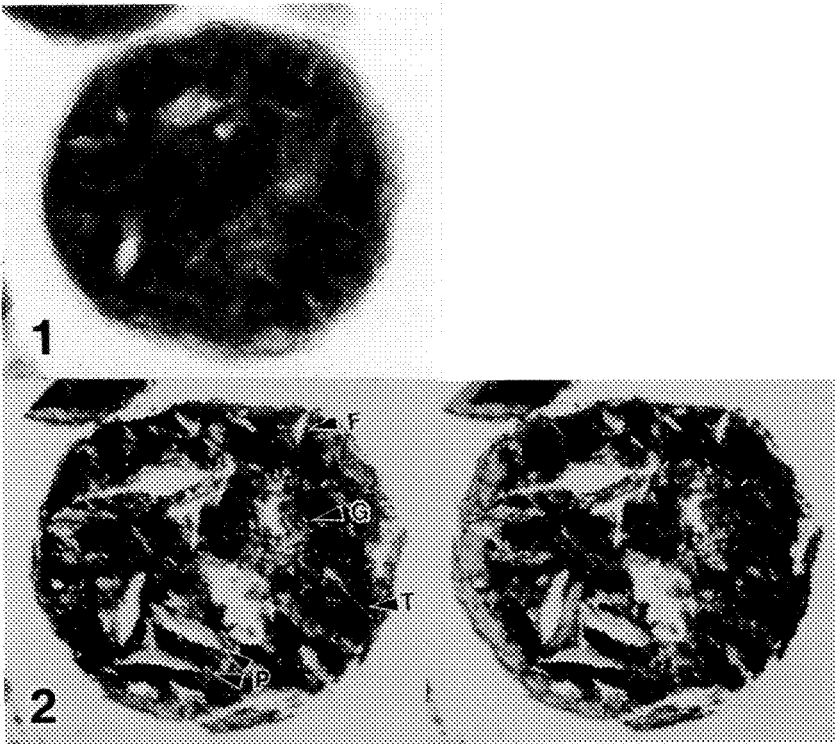


Fig. 1 HVEM micrograph of untilted section containing the rat-liver mitochondrion reconstructed by tomography.

Fig. 2 Stereo view of mitochondrial reconstruction, with internal compartments labelled as described in text.

AN ULTRASTRUCTURAL ANALYSIS OF THE SYMPATHETIC INNERVATION OF THE RABBIT EAR ARTERY AND MIDDLE CEREBRAL ARTERY AND THEIR BRANCHES

John T. Dodge and John A. Bevan

Department of Pharmacology, University of Vermont, Given Bldg., Burlington, VT 05405

Unlike many peripheral vascular beds, the sympathetic nervous system exerts little control on cerebral blood flow.¹ The contractile response of isolated rabbit middle cerebral artery (MCA) segments to electrical field stimulation of its intramural nerves is less than in a similar-sized artery from the ear.² This study was undertaken to characterize and compare the perivascular neuromuscular relationships and innervation density of similar-sized arteries varying in diameter from these two different regional arterial beds to see if there were structural correlates for these functional differences.

New Zealand White rabbits were anesthetized and perfusion-fixed with 2.5% glutaraldehyde and 2% paraformaldehyde in 0.1M phosphate buffer, pH 7.4 at 80mm Hg and at 37°C. Tissues were dissected out, post-fixed in 2% osmium tetroxide, dehydrated in a graded ethanol series, and embedded in Durcupan ACM (Fluka). Three arteries from the ear and four cerebral arteries were investigated. The vessels ranged in size from 400 μm i.d. to 105 μm i.d. Transverse sections of each artery were cut with a diamond knife, stained in uranyl and lead stains, and examined in a JEOL 100 CXII electron microscope at 60kV. Quantitative measurements were done using the Sigma-Scan™ Measurement System with a digitizing tablet linked to a computer. The chromaffin reaction procedure modified by Gibbins³ was used to identify catecholamine-containing vesicles.

Results for the neuromuscular cleft width measurements show that in the ear arteries collectively the average cleft width for all varicosities is significantly closer (1.5 μm) in ear arteries than in cerebral arteries (4.6 μm). When arteries of similar size are compared: the main side branch (400 μm i.d.) of the central ear artery has an average cleft width for "bare" varicosities (devoid of Schwann cell processes) of $1.43 \pm .11$ μm , and the middle cerebral artery (380 μm i.d.) is $5.03 \pm .41$ μm , a significant difference. The differences become greater when smaller comparable sized arteries are examined. The terminal branch ear artery (TB) at 235 μm i.d. has an average cleft distance of $0.82 \pm .06$ μm , the narrowest cleft width of all vessels studied, while the first-order branch (M1) of the MCA at 200 μm i.d. has a cleft distance of $5.17 \pm .49$ μm .

The distribution of the neuromuscular cleft width expressed as a percentage of the total shows that varicosities in the ear arteries are more closely grouped within the inner adventitial layer of the artery, while cerebral arteries have varicosities spread throughout the adventitia. In ear arteries about 84% of all "bare" varicosities are within 2 μm of the nearest smooth muscle cell and only 19% for the cerebral vessels.

When determining the nerve density (the number of "bare" varicosities per 100 μm circumference of the outer medial wall), there is little difference in the densities of innervation for comparable sized arteries in the two vascular beds. For example, 5.1 varicosities per 100 μm in the TB artery and 4.9 varicosities in M1 of the cerebral arteries. However, particularly in the cerebral vessels and in ear vessels, as the size (i.d.) of the artery decreases the density of innervation is reduced. MCA has an average of 6.3 "bare" varicosities per 100 μm whereas M3 the smallest branch (105 μm i.d.) has only 1.5 varicosities per 100 μm .

Using the chromaffin reaction technique, all varicosities observed in the ear arteries contain only small (40-50nm diameter) and some large (90-120nm) dense-cored vesicles (noradrenergic). In cerebral

arteries about 86% of the varicosities show mainly small and some large dense-cored vesicles (noradrenergic) and 14% of the varicosities had small (40-50nm) clear vesicles (cholinergic).

The structural results showing a greater neuromuscular cleft width and a wider distribution of nerve profiles in the cerebral circulation provide a correlation with functional results that demonstrate the influence of the sympathetic perivascular innervation in this bed is less than that in the ear circulation.⁴

References

1. J.A. Bevan and D. Van Riper, In: *Neurotransmission and Cerebrovascular Function*, Volume II, (eds. J. Seylay and R. Sercombe), Amsterdam/New York, (1989) 65.
2. D. Van Riper and J.A. Bevan, *Circ. Res.* (1991) 68, 568.
3. I.L. Gibbins, In: *Monoaminergic Neurons: Light Microscopy and Ultrastructure*, (ed. H. Steinbusch), New York, John Wiley Inc. (1987) 179.
4. This research was supported by USPHS Grants HL-32383 and HL-32985 and by the Totman Medical Research Trust.

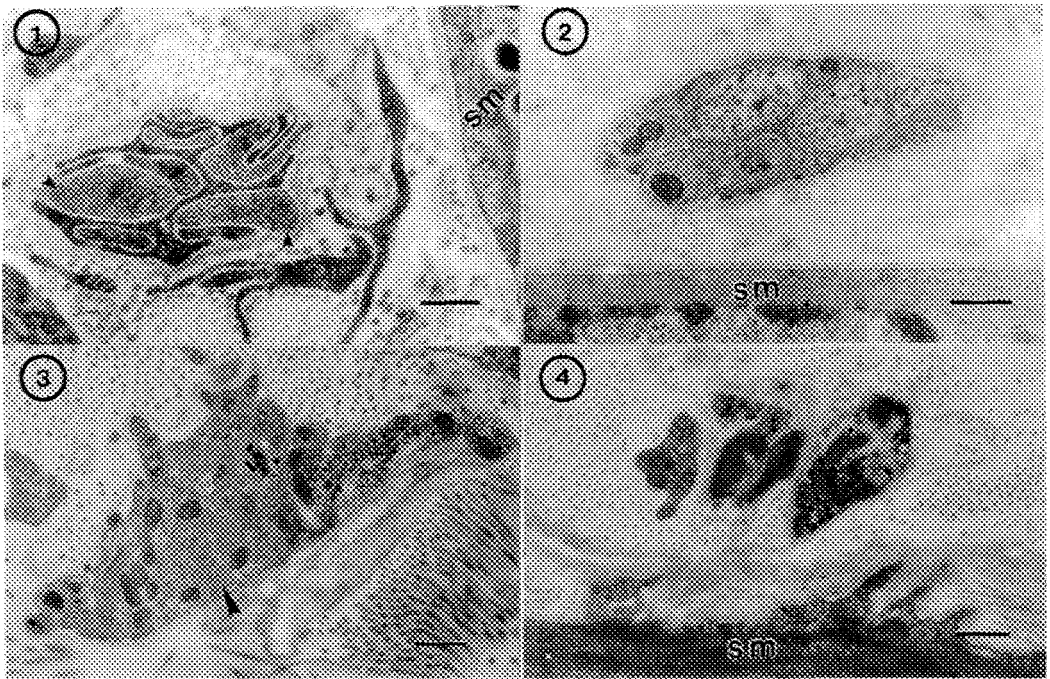


FIG. 1.--TEM of a rabbit middle cerebral artery showing a nerve bundle with varicosities (arrowheads). Smooth muscle (SM). Bar = 0.5 μ m.

FIG. 2.--TEM of a rabbit terminal branch of the central ear artery showing a close neuromuscular relationship. Smooth muscle (SM). Bar = 0.5 μ m.

FIG. 3.--TEM of a rabbit MCA prepared by the chromaffin reaction technique showing varicosities with small and large dense-cored vesicles and a large varicosity with clear vesicles (arrowhead). Bar = 0.5 μ m.

FIG. 4.--TEM of a rabbit main side branch of the central ear artery, chromaffin reaction, showing a large "bare" varicosity with small and large dense-cored vesicles. Smooth muscle (SM). Bar = 0.5 μ m.

AUTHOR INDEX*

A

Abdulla, M., 608, 614
 Abu-Ghazaleh, R. I., 708
 Ackerley, C. A., 1562
 Adam, M., 642
 Adamian, M., 482
 Adams, F., 1766
 Adams, W. W., 266
 Adar, F., 1506
 Advani, A. H., 42, 260, 1216, 1332
 Aebi, U., 490
 Agard, D. A., 498, 588, 1044
 Ager, J. W., III, 1516
 Aggarwal, S. K., 652
 Ahluwalia, K. B., 618
 Ahn, C. C., 1196
 Aita, S., 382
 Akin, D., 494
 Akin, D. E., 864
 Aksay, I. A., 154, 304, 1020, 1024
 Al-Jassim, M. M., 1384
 Alani, R., 394
 Albert, J. P., 604, 610
 Alessandrini, C., 630, 898
 Alexander, K. B., 150, 1210
 Ali, S. Y., 1592
 Allard, L. F., 944
 Allem, R., 316
 Allen, J., 650
 Allen, N. S., 574
 Allen, P. S., 766
 Allen, S., 496
 Allen, S. M., 180
 Allen, T. D., 492
 Allietta, M., 1138
 Allison, J. E., 22
 Alpers, D. H., 722
 Altounian, Z., 56
 Amali, A., 1226
 Amankwah, K. S., 562
 Ammann, N., 1588, 1666
 Ammar, E. D., 676
 Amos, W. B., 1158
 An, B-R., 398
 Anderson, I. M., 1240
 Anderson, J. R., 1488
 Anderson, K. L., 546
 Anderson, R., 1390
 Andon, N. L., 888

Andrews, K., 692
 Andrews, R. A., 1696
 Andrews, S. B., 1566, 1574
 Angel, A., 780, 1328
 Annis, E. K., 1032
 Aoki, Y., 962
 Apkarian, R. P., 768, 1292
 Apt, S., 402
 Arena, J., 582
 Argenta, L. C., 1104
 Argüello, C., 900
 Armstrong, J. T., 1656, 1744
 Artaxo, P., 1482
 Ashraf, A., 384, 1028
 Ashton, F. T., 960
 Atwal, O. S., 702
 Audier, M., 26

B

Baayen, R. P., 1588
 Backus, M., 1586
 Baden, S., 1102
 Baek, S. S., 188
 Bagnall, K. E., 70
 Bahia, I. M., 646
 Bahnck, D., 1338
 Bailey, J. F., 680
 Bains, H. K., 624
 Bajakian, V., 614
 Baker, K. W., 666
 Baker, T. S., 454, 524, 998
 Baldwin, J., 1536
 Balkin, D., 400
 Balladore, J. L., 1268
 Ballouk, F., 614
 Bancel, P. A., 118
 Ba-Omar, T. A., 548
 Baradet, T., 1056
 Barbee, T. W., Jr., 1732
 Barbillat, J., 1498, 1500, 1514
 Barish, L., 410
 Barkan, S., 1736
 Barmak, K., 1356
 Baron, R., 764
 Barrett, R., 1720
 Bartelt, N. C., 332
 Bartick, E. G., 1528
 Bashir, R., 1396
 Bassell, G., 552
 Bastin, G. F., 1622, 1632, 1648
 Batchelder, D. N., 1512
 Bates, J. K., 352
 Batson, P. E., 1340
 Batstone, J. L., 1346, 1352, 1372
 Bauer, E., 332
 Baumann, F. H., 1474
 Bawa, S. R., 624
 Bazett-Jones, D. P., 450, 504, 1564
 Bazylinski, D. A., 1022
 Bean, J. C., 248
 Bean, J. C., 1338
 Becher, P. F., 150
 Becich, M. J., 722
 Bednar, J., 590
 Beeching, M. J., 128
 Beggs, J. L., 920
 Behal, S. K., 288, 1778
 Behrens, S.-E., 460
 Bellotto, D., 1582
 Belnap, D. M., 998
 Ben-Ari, H., 658
 Beniac, D., 466
 Bennett, J. C., 58
 Benninghoven, A., 1550, 1552
 Bentley, J., 336, 346, 1230, 1238
 Bergeron, G., 684
 Bergmann, A., 496
 Berkery, D. J., 918
 Bermúdez de Rocha, M. V., 640
 Bernatowicz, T. J., 1714
 Berta, Y., 62, 156, 362
 Bertero, G. A., 200
 Bertho, A. L., 926
 Betlach, M. C., 436
 Better, O. S., 658
 Bevan, J. A., 934
 Bevol, A. J., 1780
 Beveridge, T. J., 868
 Beyer, A., 554
 Beyerlein, R. A., 322
 Bielat, K., 794
 Bierley, S. T., 732
 Bird, D., 1182
 Bitler, W. R., 32, 36
 Blackburn, D. H., 1540
 Blauner, P., 1388
 Bleay, S. M., 1776
 Bleeker, A. J., 292
 Bloch, R. J., 724
 Block, S. M., 424
 Boeckstein, A., 1588

*Page numbers in italics refer to Part II.

AUTHOR INDEX*

Boisset, N., 1064
 Boivin, R., 48
 Bolsover, S. R., 1160
 Bonardi, M., 1750
 Bonavita, J. C., 1698
 Bonnell, D. A., 1480
 Booy, F. P., 452, 522, 532
 Borneman, W. S., 864
 Boswell, F. W., 58
 Botha, C. E. J., 844
 Botros, K. Z., 1458
 Botton, G., 1202
 Boublik, M., 462
 Bouchet, S., 1542
 Bovard, K. K., 592
 Bovin, J.-O., 296
 Bow, 252, 1380
 Bowden, M., 1510
 Bowman, D., 500
 Bowser, S. S., 572
 Boyd, J. D., 46, 204
 Boyes, E. D., 98, 1630
 Bradley, J. P., 1722, 1724
 Brakke, T. W., 908
 Braue, W., 344
 Braunfeld, M. B., 1044
 Bravman, J. C., 240
 Brekke, D. W., 408
 Brennenstuhl, A. M., 316
 Bretaudiere, J. P., 542
 Brewer, P., 918
 Briant, C. L., 1204
 Bridgers, K., 860
 Bright, D. S., 1610, 1786
 Brink, J., 1054
 Brock, J. M., 942
 Broderick, R., 878
 Bronson, R., 660
 Brooker, B. E., 756
 Brown, C. R., 814
 Brown, J. C., 452, 522, 532
 Brown, M. L., 450
 Brownlee, D. E., 1722, 1724
 Brownwright, A. J., 884
 Brundage, R., 422
 Bryant, F. R., 1392
 Brydson, R., 1258
 Buchanan, R. A., 1566, 1574
 Buchanan, R., 978
 Buckland-Nicks, J., 910
 Buckley, D. E., 1330
 Buckley, M. J., 1096

Buettner, H., 1004
 Buhl, L., 632, 636
 Bui, H. X., 608, 614
 Buljan, S. T., 152
 Bulter, I. S., 1536
 Bungay, P. M., 420
 Burke, M. G., 60, 174, 1218
 Burns, D. L., 528
 Burnside, B., 480
 Busch, J., 30
 Buseck, P. R., 312, 1488
 Busing, W. M., 788, 980
 Butwell, N. B., 1582

C

Cai, Z. X., 90
 Calarco, P. G., 600
 Calderone, M. A., 1494
 Callahan, D. L., 1210
 Callahan, R., 1142
 Callstrom, M. R., 300
 Cambell, C. E., 22
 Cameron, M., 378
 Camp, R. E., 946
 Campbell, A., 1364
 Campbell, S. M., 1300
 Camus, P. P., 1616
 Cantino, M. E., 662
 Cao, B., 1418
 Cao, W., 374
 Capco, D. G., 914
 Carbone, K., 526
 Carcia, P. F., 140
 Cardamone, L., 570
 Cardell, E. L., 800
 Cardell, R. R., 792, 800, 802, 804, 828
 Carim, A. H., 32
 Carl, R. T., 1524
 Caron, M., 316
 Carpenter, D. A., 1758
 Carpenter, D. O., 564
 Carpenter, G. J. C., 396, 1444
 Carpenter, R. W., 212, 252, 344, 1380
 Carr, M. J., 86, 1310
 Carragher, B. O., 904
 Carrejo, J., 1418
 Carrington, W., 500
 Carter, C. B., 76, 112, 120, 214, 236
 Carter, K. C., 500, 558, 560
 Carver, J. M., 664

Caspar, D. L. D., 518
 Cassella, J. P., 1592
 Catalano, M., 184
 Catterall, A. C., 1592
 Cedillo, C. M., 260, 1216
 Cerezo, A., 1478
 Cerezo, L., 620
 Chabala, J. M., 1772
 Chakel, J., 1710
 Chamberlain, S. C., 488
 Chandra, S., 1604
 Chang, W. Z., 1732, 1734
 Chang, Y. C., 190
 Chapman, A. R., 1776
 Charest, P. M., 870
 Charlesworth, J., 974
 Chatton, J.-Y., 420
 Chen, H., 1728
 Chen, R. T., 1142
 Chen, S. J., 340
 Chen, S.-N., 704
 Chen, X., 56
 Chen, Y., 1280
 Chen, Y.-R., 704, 852
 Cheng, C., 1512
 Cheng, L., 602
 Cheng, M., 270
 Cheng, P. C., 1608
 Cheng, R. H., 454, 996
 Cheng, S. C., 1248, 1454
 Cheng, Y., 122, 258
 Chern, C. S., 242
 Chemock, R. S., 1052
 Cheung, W. W. K., 716
 Chiang, Y.-M., 1212
 Chiarantini, L., 606, 692
 Chien, K., 772
 Chiou, W. A., 50
 Chisholm, M. F., 1470
 Chittipeddi, S., 1362
 Chiu, W., 512, 870, 1054
 Cho, K., 126
 Choi-Feng, C., 322
 Christensen, A. K., 1080
 Christensen, H., 688
 Christensen, M., 496
 Chrysoulis, S., 1652
 Chu, S. S., 1384
 Chu, T. L., 1384
 Chu, X., 318
 Chuang, S.-F., 1370
 Chun, C. H., 188

AUTHOR INDEX*

Cianciarullo, A. M., 926
 Ciardelli, T. L., 540
 Cinelli, A., 476
 Citron, R., 1106
 Clark, W. A. T., 250
 Clausing, R. E., 336
 Clay, R. P., 874
 Clerkx, A. C. M., 1588
 Cliff, G., 1228, 1464
 Cochran, W. T., 1362
 Cockayne, D., 1190
 Cockayne, E., 118
 Coene, W. M. J., 100, 136, 138, 986
 Cole, M. W., 1398
 Coleman, J. R., 558
 Coleman, R., 658
 Colling, J. A., 968
 Collins, R. T., 1372
 Colpitts, T. S., 1374
 Conley, R. R., 470
 Conte, P., 784
 Conway, J. F., 532
 Cooke, C. A., 556
 Cooper, M. S., 12
 Corbett, J. M., 58
 Corcoran, S. F., 1682
 Cosandey, F., 226, 242
 Cossement, D., 1436
 Costello, M. J., 706
 Cowan, A. K., 844
 Cowan, S., 438
 Cowley, J. M., 102, 142, 330,
 348, 370, 982, 1224,
 1460, 1462
 Cox, D. M., 1778
 Crandall, J. E., 890, 906
 Crowley, K. D., 378
 Crestini, F., 630
 Cross, B., 1752
 Cross, R. H. M., 844
 Crowley, K. D., 378
 Crozier, P. A., 302, 1418
 Cuomo, J. J., 108
 Czymmek, K. J., 872
 Czyzewski, Z., 954

D

Dahmen, U., 20, 114
 Dai, J.-D., 706
 Daigne, B., 1546
 Dalton, M. S., 598
 Damsky, C. H., 600

D'Andrea, M., 644
 Danilatos, G. D., 1298, 1302
 Dao, L. H., 372
 Das Chowdhury, K., 344
 DasGupta, B. R., 530
 Dash, J., 34
 Da Silva, E., 1520
 Davis, B. B., 802
 Davis, R. F., 252
 Dean, S. J., 1428
 De Avila, J., 680
 Debaene, S. B. G., 766
 De Boni, U., 562
 Decker, D., 564
 DeCosta, P., 126
 Deerinck, T. J., 904
 DeHaven, P. W., 1760
 de Harven, E., 688
 de Jong, A. F., 100, 136
 de Jong, M. J. C., 788, 942, 980
 De Keyzer, R., 1612
 Dekker, A., 656, 810
 Delga, C., 784
 Delhay, M., 1498, 1514
 Dellby, N., 1192
 DeLoach, J. R., 606, 690, 692
 delRosario, A., 608, 614
 de Nazareth, M., 926
 de Neijis, E. O., 1010, 1422
 Denker, M., 1132
 Denton, L. R., 1762
 Denton, R. A., 1082
 de Rijk, M., 470
 DeRosier, D. J., 514, 516, 518, 538
 de Ruijter, W. J., 988
 DeSimone, D. W., 598
 Dhamelincourt, P., 1498, 1514
 Diamond, H. S., 698
 Diaz, R., 518
 Dierksen, K., 914
 Dijkstra, J. M., 1632, 1648
 Dillaman, R. M., 888
 Dimitrijevič, S. D., 896
 Ding, D.-K., 274
 Ding, R., 578, 902
 Ding, W., 660
 DiOri, J. P., 1090
 Disko, M. M., 288, 1778
 DiVincenzo, D. P., 118
 Dixit, G. A., 1392
 Dobbins, J. J., 634
 Dodelet, J. P., 1436

Dodge, J. T., 934
 Dogan, B., 46
 Dogan, F., 304
 Doi, T., 1774
 Donlon, W. T., 22
 Donohue, P., 140
 Donovan, J. J., 1646
 Doorn, S. S., 1706
 Doremus, R. H., 1114
 Dorset, D. L., 430, 1166, 1168,
 1440, 1442, 1446
 Dowling, W. E., 22
 Downing, K. H., 130, 914
 Downing, R. G., 1728
 Doyle, D., 636
 Drake, R. L., 802, 828
 Dravid, V. P., 74, 1186, 1694
 Drewien, C. A., 66
 Droleskey, R. E., 606, 690, 692
 Drouin, D., 1644
 Duan, J. Z., 1368, 1420
 Dubochet, J., 590
 Dudley, M. W., 654
 Duff, R. H., 412
 Dufner, D. C., 52
 Duncumb, P., 1674
 Dunlap, J. R., 1642
 Dunn, D. N., 1434
 Dunn, S. M., 126, 1004
 Durham, S. K., 646
 Dyar, M. D., 1742
 Dykeman, A., 668
 Dyson, P. W., 1176

E

Eades, J. A., 84, 1184, 1242
 Eaglesham, D. J., 230
 Earnest, T. N., 434
 Earnshaw, W. C., 556
 Easterbrook, D., 1318
 Echer, C. J., 20
 Echlin, P., 854, 1148
 Eckart, D. W., 1398
 Eckert, J., 1196
 Edmiston, C. E., Jr., 1088
 Edwards, M., 822
 Edwards, R. J., 544
 Egelman, E. H., 448
 Egerton, R. F., 1248, 1264
 Egley, G. H., 838
 El-Ghor, M., 1400
 Elliot, D., 560

AUTHOR INDEX*

Elliott, R. L., 728
 Ellis, E. A., 808
 Ellis, G., 1318
 Ellisman, M. H., 904, 946,
 1040, 1060

Elser, V., 118
 Emerson, R. J., 608, 948
 Endoh, H., 962
 Engel, A., 438
 Erbe, E. F., 908, 1074, 1314
 Erlandsen, S. L., 1320
 Eshita, T., 1378
 Etoh, T., 962
 Etz, E. S., 1540
 Evans, B., 1560
 Evans, N. D., 42, 1256, 1344
 Evans, S., 656
 Everist, S. C., 1688
 Ewing, R. C., 352, 378

F

Fagan, P. J., 110
 Fagerberg, W. R., 1668
 Fairhurst, M., 892
 Fan, G. Y., 96
 Fang, J., 172
 Farber, P., 644
 Farina, M., 878
 Farnworth, M. A., 15650
 Farrow, N. A., 1058
 Farthing, I., 1658
 Fatemi, M., 1376
 Fatteh, M., 626
 Fay, F. S., 422, 500, 560
 Fejes, P., 1408, 1410
 Fejöl, M., 564
 Feldherr, C. M., 494
 Fendler, J. H., 1014
 Feng, J., 388
 Fertiitta, A., 496
 Fey, E. G., 508
 Fialin, M., 1624, 1626
 File, D. M., 1762
 Fine, A., 468
 Fiori, C. E., 1636, 1770
 Fishell, G., 474
 Fisher, A. T., 1244
 Fisher, K. A., 18
 Fisher, R. M., 584, 1076, 1368
 Fisher, W. W., 260, 1216
 Fister, T., 1710
 Flamion, B., 420

Fletcher, R., 1708
 Flicker, P. F., 530
 Flynn, C. P., 146
 Fogarty, K., 500, 560
 Foglesong, D., 644
 Follstaedt, D. M., 334
 Fonda, R. W., 254
 Fortner, J. H., 664
 Foster, W. G., 668
 Fouche, P. S. O., 744
 Fountain, G. G., 1350
 Fox, A. G., 1174
 Fragu, P., 1602
 Francis, L. F., 338
 Francis, N. R., 514
 Francis, S. M. N., 470
 Frank, J., 464, 580, 932,
 1062, 1064
 Frankel, R. B., 1022
 Frayssinet, P., 784
 Frear, D. R., 1684
 Freudenrich, C. C., 742, 1584
 Friel, J. J., 1654
 Fritz, L., 830
 Fruschelli, C., 630, 898
 Fruschelli, M., 898
 Fultz, B., 1196
 Fung, S. C., 288
 Furcinitti, P. S., 1002
 Furrer, P., 590
 Furuya, F. R., 526
 Furuya, K., 1712

G

Gagne, G. D., 812
 Gai, P. L., 80, 98
 Gaigher, I. G., 744
 Gajdardziska-Josifovska, M.,
 134, 244, 284, 326
 Gallego, R., 144
 Gallegos L., M. G., 670
 Gallicano, G. I., 914
 Gallois, B., 242
 Gao, K., 792
 Gao, Y., 234
 Gardiner, D. J., 1510
 Gardner, J. S., 766, 850
 Garone, L. C., 764
 Garratt-Reed, A. J., 350, 1022,
 1206, 1212, 1274
 Garrison, D. L., 832
 Gauvin, R., 1266, 1644

Geballe, T. H., 240
 Gehring, K., 434
 Geisbert, T. W., 682
 Geller, J. D., 1316, 1662
 Gelles, J., 426
 George, K. S., 882
 Gérard, P., 1268
 Gerdes, M., 558
 Germani, M. S., 1486
 Gerrard, D. L., 1502
 Ghiradella, H., 1006
 Ghosh, B. K., 712
 Ghoshroy, S., 1668
 Giammara, B. L., 634, 686, 770,
 1094
 Giannuzzi, L. A., 32, 36
 Gibala, R., 912
 Gibson, C. C., 420
 Gibson, J. M., 292, 324
 Gibson, J. P., 654
 Gibson, W. M., 1726
 Giera, D. D., 612
 Giffin, B. F., 792, 828
 Gijbels, R., 1612
 Gilbert, L. I., 706
 Gilbert, S. H., 422
 Gilles, C., 1626, 1652
 Gilson, D. F. R., 1536
 Girard, F., 1546
 Giraud-Guille, M.-M., 1008
 Gjønnnes, J., 1164, 1456
 Gjønnnes, K., 1456
 Glaeser, R. M., 520
 Glick, J. M., 924
 Godfrey, T. J., 1478
 Godleski, J. J., 638, 740
 Goehner, R. P., 1310
 Goff, J. P., 604, 610
 Gogol, E. P., 446
 Goheen, M. P., 1088
 Goldberg, M. W., 492
 Goldstein, J. I., 1660
 Goldstein, M. A., 542, 544
 Golijanin, D., 1686
 Gong, S., 1412
 Gonzalez, F., 316
 González-Corona, B., 640
 Gooding, F. W., 1630
 Goss, R., 970
 Gossen, C., 656
 Gould-Kostka, J. L., 528
 Goyal, A., 72

AUTHOR INDEX*

- Goynes, W. R., 858
 Grabel, L., 602
 Gracy, R., 896
 Gragtmans, B., 666
 Graham, L. L., 868
 Grant, K. G., 810
 Grant, K. W., 656
 Gray, K. H., 1136
 Gray, L. D., 672
 Gray, R. T., 882
 Grayson, R. L., 840
 Greene, W. B., 650, 1594
 Greulich, F. A., 86
 Greve, J. M., 524
 Grieves, J. R., 42
 Griffin, B. J., 1232, 1306, 1324
 Griffin, R. D., 1696
 Griffiths, D. P., 386
 Griffith, J. E., 1124
 Grigorieva, I. V., 70
 Grochulski, W. D., 998
 Gronskey, R., 256, 1420
 Gross, H., 758
 Gross, P. R., 686
 Grovenor, C. R. M., 1478
 Grundke-Iqbal, I., 540
 Guarna, M., 630, 898
 Gubbens, A. J., 1192, 1570
 Guelton, N., 1436
 Guerfi, A., 372
 Gunderson, R. H., 1094
 Gunnison, K. E., 1024
 Guo, X. W., 440
 Gupta, P. D., 726
 Gurevitch, A. C., 42
 Guy, J. R., 808
 Guyton, J. R., 622
 Gwydir, S., 1004
- ### H
- Hageman, G., 486
 Hagler, H. K., 1582
 Hainfeld, J. F., 526
 Hale, E. A., 832
 Hall, E. L., 164
 Hall, J. B., 322
 Hamilton, T. A., 826
 Hammond, E. C., 860, 886, 1098, 1100
 Hance, R., 1364
 Handt, S., 810
 Hanes, P. J., 918
 Hangas, J., 1184
 Hanker, J. S., 634, 686, 770, 1094
 Hanna, L., 98, 1630
 Hansen, P. L., 1258
 Hantgan, R. R., 810
 Happ, G. M., 674
 Harada, Y., 940, 962
 Harauz, G., 466
 Hard, R., 570
 Harmer, M. P., 1772
 Harper, R. G., 394
 Harrach, H. S. von, 968
 Harris, P. J., 420
 Hartford, E. H., Jr., 76
 Harthcock, M. A., 1522
 Hartley, B. J., 844
 Hartley, R. D., 864
 Hartmann, I. R., 1630
 Harvey, J. F., 1398
 Haselgrove, C., 1056
 Haselgrove, J. C., 1056
 Hashimoto, H., 310, 1194
 Hashimoto, M., 962
 Hashimoto, T., 944, 1208
 Hassinger, L. C., 890, 906
 Hasoon, F., 1384
 Hattangady, S. V., 1350
 Hatten, M. E., 474
 Hawi, A., 1326
 Hayes, A., 482
 Hayworth, M. S., 1576
 Hayzelden, C., 1352
 Head, J. F., 728
 Headley, T. J., 86
 Heath, J. P., 428, 576
 Heatherly, L., 336
 Heckman, J. W., Jr., 730
 Hefter, J., 64, 1700
 Heger, I., 700
 Hegerl, R., 1000
 Heijligers, H. J. M., 1622, 1632, 1648
 Heinrich, K. F. J., 1638
 Heitlinger, E., 490
 Hejna, J., 958
 Helfand, M. A., 196
 Hellman, E. S., 76
 Helmick, C. M., 680
 Hembree, G. G., 308, 1476
 Henderson, P. L., 1762
 Heng, Y. M., 1578
 Henn, C., 438
 Hens, M. D., 598
 Hermanns, I., 656
 Herring, J., 956
 Herring, R. A., 990
 Herrington, C. R., 1662
 Herrmann, K.-H., 92
 Hess, W. M., 850
 Hessler, D., 1060
 Heuer, A. H., 146, 228, 1102
 Heyman, R. V., 1618
 Heywood, B. R., 1026
 High, T., 774, 776
 Hill, B., 598
 Hills, C. R., 1310
 Hillyard, S., 1222
 Hippel, P. H. von, 446
 Hiraga, K., 1188
 Hiraoka, Y., 588
 Hiroi, H., 1712
 Ho, J. T., 270
 Ho, R., 1568
 Hobbs, L. W., 38, 350, 994, 1274
 Hockett, D., 742, 1584, 1586
 Hodges, R. L., 1392
 Hoeff, S., 1708
 Hoffman, D. W., 1702
 Holcomb, A., 620
 Holiday, D. B., 672
 Holifield, B. F., 428
 Holm, J., 970
 Holynska, B., 1754
 Holzman, L. M., 306, 1616
 Homma, Y., 1286
 Honeycutt, J. W., 1354
 Hong, L., 1196
 Hönger, A., 438
 Hooper, J., 1318
 Hoover, D. M., 612
 Hopke, P. K., 1484
 Horita, Z., 54
 Horn, E., 960
 Horowitz, R. A., 498
 Horton, J. A., 168
 Horton, L. L., 336, 346
 Hossler, F. E., 738
 Housley, R. M., 1774
 Houston, B., 666
 Hovington, P., 1234
 Howard, D. J., 1344
 Howard, T., 722
 Howell, P. R., 32, 36

AUTHOR INDEX*

Howie, A., 1150
 Howitt, D. G., 1312
 Hren, J. J., 1140
 Hsia, S. L., 1366
 Huang, H. H., 678
 Huang, S., 502
 Huang, S. C., 166
 Huang, Y., 330, 1460
 Huang, Y.-F., 852
 Huckabee, M. L., 152
 Huffman, D. R., 298
 Huggins, B. J., 322
 Hui, S. W., 270, 1016
 Hukee, M. J., 708
 Hull, R., 248, 1338
 Humbel, B. M., 824
 Humphrey, C. D., 678
 Humphreys, T. P., 1350
 Hunt, J. A., 1200, 1566
 Huong, P. V., 1542
 Hurley, B. J., 662
 Hurley, J. P., 408
 Huston, M. E., 300
 Hwang, J., 1694

I

Ichihashi, M., 936
 Ihn, K. J., 278
 Iijima, S., 1188
 Ikeda, J. A. S., 1212
 Ikeo, N., 1334
 Ikuhara, Y. (Nogoya), 78
 Ikuhara, Y. (CWR), 146
 Ikuhara, Y. H., 78
 Ingber, B. F., 858
 Ingram, P., 742, 774, 1116,
 1118, 1584, 1586
 Inoué, S., 416
 Inoue, T., 1378
 Iqbal, K., 540
 Irwin, R. B., 1362
 Ishida, H., 1538
 Ishitani, A., 1538
 Iwatuki, M., 1144

J

Jäger, J., 432
 Jaax, N. K., 682
 Jackman, J. A., 396
 Jacob, W., 1612
 Jahrling, P. B., 682
 Jakana, J., 512, 870

Jakes, K. A., 1534
 Jakowski, A. B., 664
 Jamieson, M. G., 1142
 Janowski, G. M., 1696
 Janssens, K., 1766
 Jap, B. K., 434
 Jarnik, M., 490
 Jassal, D. S., 702
 Jayaram, R., 176, 1220
 Jegorov, A., 790
 Jennings, D. A., 1104
 Jensen, C. B., 612
 Jeon, H., 1354
 Jerome, W. G., 810, 924
 Jesson, D. E., 1470
 Jeulin, D., 994
 Jett, S. D., 762
 Jeun, G., 782
 Jiang, R., 602
 Jiao, J., 298
 Jie, Y., 356
 Johnson, A. E., 1560
 Johnson, A. W. S., 1176, 1232
 Johnson, C. V., 558
 Johnson, D., 30
 Johnson, D. E., 662
 Johnson, J. E., 454
 Johnson, J. E., Jr., 540
 Johnson, P. C., 920
 Johnson, R. H., 584
 Johnson, W. L., 1196
 Jones, C., 1100
 Jones, D. W., 1112
 Jones, K. M., 1384
 Jones, K. W., 1766
 Jones, N. L., 574
 Jones, R., 1364
 Jonker, B. T., 1382
 Josephs, R., 510, 1036
 Joy, D., 1278
 Joy, D. C., 944, 954, 1208,
 1284, 1642, 1672, 1678
 Jun, H., 126

K

Kabaya, A., 82
 Kakibayashi, H., 936
 Kanazawa, T., 1334
 Kaneyama, T., 232, 1180
 Kang, S., 64
 Kannan, V. C., 1362
 Karduck, P., 1666, 1768

Karr, T. L., 596
 Kaser, S. A., 352
 Kastner, B., 460
 Katagiri, G., 1538
 Katler, M., 638, 740
 Katon, J. E., 1534
 Katrinak, K. A., 312, 408
 Kauer, J. S., 476
 Kaufman, H. S., 1322
 Kaufmann, R., 1558, 1598
 Kaushik, V., 1364
 Kawai, N. T., 1504
 Kear, B., 242
 Kedersha, N. L., 458
 Keene, D. R., 892
 Keller, J. C., 1108
 Keller, L. P., 1724
 Kelly, T. F., 1616
 Kenik, E. A., 60, 1210, 1214,
 1218, 1230
 Kenway, P. B., 1228
 Kersker, M., 382, 1040, 1188
 Kessel, M., 528
 Kessler, S. W., 604
 Khiznichenko, V., 348
 Kihlborg, L., 104
 Kikuchi, T., 1712
 Kikuchi, Y., 1378
 Kim, G. H., 154, 188, 830
 Kim, H. S., 1448
 Kim, J., 956
 Kim, J. S., 188
 Kim, K.-H., 398
 Kim, K.-S., 144
 Kim, M. J., 184, 212, 252
 Kim, Y., 1474
 Kim, Y. J., 354
 Kimura, T., 978
 King, A. H., 220, 1438
 King, C. A., 1338
 Kirby, G. S., 746
 Kirch, H. J., 690
 Kirgios, C., 1004
 Kirk, R. G., 1590
 Kirkpatrick, C. J., 656, 810
 Kirshenbaum, A. S., 604
 Kisielowski, C., 1474
 Kitamura, S., 1144
 Kleinz, J., 1000
 Klemp, K. F., 622
 Klepeis, S., 1390
 Klöck, W., 1718

AUTHOR INDEX*

Kloft, W. J., 690
 Klomparens, K. L., 730
 Knecht, D. A., 594
 Kobayashi, K., 280
 Koenig, J. L., 1496
 Kohls, C. L., 1300
 Kolakofsky, D., 870
 Kolatkar, P. R., 524
 Kolosov, V. Yu., 1348
 Komem, Y., 1356
 Kömüves, L. G., 576
 Korte, G. E., 486
 Kortright, J. B., 256
 Koster, A. J., 136, 1044
 Kotera, M., 1670
 Krakow, W., 108, 118
 Krause, H. B., 1452
 Krause, K. R., 318
 Krause, S. J., 1400, 1402, 1416
 Kreitzer, D., 798
 Krenkel, H.-O., 780
 Kriho, V., 816
 Krishnan, K. M., 1260
 Krishnamurthy, S., 158
 Krivanek, O. L., 96, 974, 1192,
 1262, 1308, 1570
 Kriven, W. M., 354
 Krizan, K. E., 1096
 Kroeger, D. M., 72
 Krupp, J. M., 832
 Kuan, T. S., 1370
 Kubo, Y., 78
 Kudoh, J., 382
 Kulik, J., 1272
 Kulkarni, V. S., 530
 Kumakhov, M. A., 1726
 Kundmann, M. K., 1262
 Kuo, G.-H., 704
 Kuzirian, A. M., 778
 Kuzuo, R., 940
 Kvam, E. P., 400, 1396

L

Lábár, J. L., 1636
 Laffoon, J. E., 1096, 1108
 Lai, K.-L., 862
 Lairson, B. M., 240
 Lake, F. T., 918
 Lakis, R. E., 1660
 Lalande, G., 1436
 Lam, A. C., 1394
 Lam, W. W., 364, 366, 368

Lamarche, F., 786
 Lamb, L. D., 298
 Lambert, B. E., 886
 Lamm, S., 1038
 Lamont, S., 904, 1060
 Landers, S. C., 574
 Landis, W. J., 582
 Langmore, J. P., 536
 Lankosz, M., 1754
 Larabell, C. A., 914
 Lark, G., 502
 Larson, D. J., 1616
 Laska, D. A., 612
 Latta, H., 1072
 Launay, J.-C., 1544
 Lawrence, J. B., 10, 500, 558
 Lawrence, J., 560
 Leamon, C. P., 718
 Leapman, R. D., 1250, 1566,
 1572, 1574
 Leasure, R. M., 1136
 Ledford, L. B., 728
 Lee, C.-K., 362
 Lee, C. S., 184
 Lee, C. Y., 614
 Lee, C.-Y., 862
 Lee, J. L., 222
 Lee, J.-D., 1402
 Lee, M. E., 744, 1010, 1422, 1424
 Lee, Ping, 1590
 Lee, Psyche, 478
 Lee, R. J., 356
 Lee, S., 772
 Leeper, D., 860
 LeFurgey, A., 742, 1584, 1586
 Leggiadro, C., 830
 LeGoues, F. K., 1340, 1342
 Lehman, J. L., 1042
 Lehner, C., 1504
 Leigh, S. D., 1706
 Leighton, S. B., 778
 Leininger, J. R., 732
 Leith, A., 932, 1320
 Lempert, G. D., 1272
 Lenain, B., 1520
 Lenburg, M., 602
 Leonard, K. R., 534
 Leong, D. B., 196
 Le Page, Y., 1178, 1444
 L'Espérance, G., 162, 316,
 1202, 1234, 1266
 Letsoalo, A. M., 1422

Leung, H., 782
 Levin, I. W., 1532
 Levine, L. E., 1356
 Levi-Setti, R., 1694, 1772
 Levy, H. A., 504
 Lewis, E. N., 1532
 Lewis, J. C., 574, 656, 810
 Lewis, M., 814
 Lewis, M. R., 1036
 Li, L. S., 272
 Li, Y. Q., 242
 Li, Z., 1046
 Li, Z. G., 110, 140
 Liang, H.-B., 1410
 Liao, L. X., 56
 Libera, M., 24
 Lichte, H., 100
 Lieberman, M., 1584, 1586
 Lifshitz, L., 560
 Lifshitz, Y., 1272
 Lightfoot, F. G., 740
 Likharev, S. K., 1692
 Liliental-Weber, Z., 232
 Lillemoe, K. D., 1322
 Lilly, N. A., 1576
 Lin, B. Y., 736
 Lin, C.-H., 1242
 Lin, C. S., 50
 Lin, H. T., 150
 Lin, K., 1370
 Lin, P. S. D., 950
 Lin, S. H., 212
 Lin, Z., 1034
 Lingle, W. L., 874
 Lins de Barros, H. G. P., 878
 Lins, U., 878
 Linton, R. W., 1132, 1136,
 1552, 1614, 1710
 Liou, F. T., 1392
 Liu, D. R., 1270, 1702
 Liu, H.-S., 800
 Liu, J. (ASU), 122, 258, 308,
 1140, 1224, 1288, 1462
 Liu, J. (U. Wash), 304, 1024
 Liu, J. B., 1420
 Liu, W., 1064
 Liu, Y., 180
 Livingston, J. D., 180
 Lloyd, D. J., 162
 Lloyd, J. R., 1386
 Lo, W. K., 1126
 Loane, R. F., 1222

AUTHOR INDEX*

- Long, J. C., 972
 López, A. Piñero, 640, 846
 Loretto, M. H., 148
 Lorimer, G. W., 1464
 Loudy, D. E., 654
 Lours, P., 114
 Love, G., 1658, 1776
 Low, P. S., 718
 Lu, P., 226, 242
 Lu, Y., 1678
 Lücken, U., 432
 Lührmann, R., 460
 Lundeen, G. R., 664
 Luo, S., 1642
 Luo, Z., 806
 Luther, P. W., 724
 Lutz, J., 1518
 Lux, R. A., 1398
 Luzzi, D. E., 28, 210, 254
 Ly, T. D., 1312
 Lyman, C. E., 1660
 Lynch, R., 560
 Lyon, M. K., 1002, 1146
- ### M
- Ma, H., 212
 Ma, Y., 1164
 McAfee, G. H., 1428
 McCaffrey, J., 396
 McCarthy, J. J., 1616
 McCartney, M. R., 54, 106, 134, 244, 284, 326, 988
 McComb, D. W., 1150, 1258
 McConville, R. L., 196
 McCormick, M. A., 204
 MacDonald, J. A., 884
 McDonald, K., 578
 McEwen, B. F., 580, 582, 924, 932, 1062
 McGaughey, R. W., 914
 McGinn, P., 400
 McGough, A. M., 510
 McGuire, A. V., 1742
 McGuire, G. E., 1366
 McHargue, C. J., 346
 McHenry, J., 288
 McIntosh, J. R., 578
 McKay, G. A., 1748
 McKee, D. W., 166
 McKelvy, M. L., 1522
 McKenzie, D., 1190
 Mackenzie, J. M., Jr., 1048
 McKernan, S., 112, 120, 214
 McKinley, B. J., 1518
 McKinnon, A. W., 1156
 McMahon, C. J., Jr., 210
 McNeil, J. A., 500
 McQuattie, C. J., 730
 McVeigh, R., 712
 McWhorter, C. G., 842
 Maize, J. C., 650
 Makita, Y., 1194
 Maldonado, J. G., 260, 1216
 Malecki, M., 566
 Malis, T. F., 46, 194, 390
 Malloy, C. R., 1582
 Malta, D. P., 1350, 1374
 Mancuso, J. F., 946
 Manfait, M., 1520
 Manfredi, T. G., 660
 Maniar, P., 1364
 Mankos, M., 102, 982
 Mannella, C. A., 440, 932
 Manoonkitiwongsa, P. S., 806
 Mansfield, J., 1182
 Maracas, G. N., 1380
 Marchesse-Rugona, S., 1046
 Marcus, J. N., 592
 Marinenko, R. B., 1634
 Marko, M., 486, 836, 932, 1320
 Marks, L. D., 74, 282, 290, 320, 984, 1434
 Markunas, R. J., 1350, 1374
 Marr, K. M., 1002, 1146
 Marsh, C., 672
 Marsh, P. M., 664
 Martin, W. H., 1276
 Martinez, J. P., 1268
 Martinez-Palomo, A., 880
 Martini, J. A., 1114
 Martoglio, P. A., 1534
 Marton, D., 1272
 Martone, M. E., 904, 1060
 Mascorro, J. A., 746
 Masliah, E., 1060
 Mason, T. O., 1694
 Massa, H., 496
 Massover, W. H., 1012
 Masters, B. R., 586, 1120
 Mastovich, J. M., 948, 1322
 Mastronarde, D., 578
 Mata-Cárdenas, B., 916
 Matha, V., 790
 Matlock, D. J., 260, 1216
 Matsuda, M., 1090
 Matsuda, T., 68
 Matsudaira, P., 512
 Maurette, M., 1716
 Mawn, M. P., 1552
 Maxwell, W. B., 946
 Mayer, J., 1042, 1198
 McGill, J. R., 646
 Meier, R. J., 1508
 Meizner, G. D., 288
 Melanson, L., 516
 Mercer, F. W., 196
 Merkle, K. L., 234
 Meirelles, M. L., 926
 Meshii, M., 50
 Metcalfe, D. D., 604, 610
 Metzger, G. J., 960
 Meyer, C. E., 1192
 Meyer, T. J., 1136
 Mia, A. J., 796
 Michael, J. R., 86, 1122, 1310, 1684
 Michaels, J. E., 804
 Michishita, K., 78
 Midgley, P. A., 70
 Miercke, L. J. W., 436
 Mikula, R. J., 364, 366, 368
 Milankov, K., 562
 Milanovich, F. P., 1518
 Milburn, D., 1098
 Mildner, D. F. R., 1728
 Milhorat, T. H., 700
 Milisen, W. B., 664
 Miller, C. M., 652
 Miller, D. J., 1242
 Miller, M. F., 812
 Miller, M. K., 174, 176, 1220
 Miller, N. C., 1784
 Miller, R. L., 260, 1216
 Mills, K. R., 826
 Minhas, K., 702
 Minor, L. K., 924
 Miracle, D. B., 158
 Mishra, R. K., 198
 Misra, A., 912
 Misra, D. N., 722
 Misra, M., 456
 Mitchell, T. E., 170, 342
 Mitra, A. K., 436
 Moberly, W. J., 30, 158, 402, 1432
 Mogab, C. J., 1364
 Moh, J. R., 1584
 Mohraz, M., 444

AUTHOR INDEX*

Mollenhauer, H. H., 1070
 Moller, A., 744
 Monaghan, P., 854
 Monson, G., 1490
 Monticello, T. M., 732
 Montpetit, D., 786
 Moodenbaugh, A. R., 88
 Mooney, C. B., 1128, 1130
 Mooney, P. E., 974
 Moore, E. D. W., 560
 Moore, S., 1184
 Moore, T. M., 966
 Morales-Vallarta, M., 916
 Morar, J. F., 1340
 Moretz, R. C., 780, 1328
 Morgan, D. G., 516
 Morgan, E. M., 732
 Morgan, P. E. D., 1774
 Morris, R. E., 792, 828
 Morykwas, M. J., 1104
 Moser, S., 756
 Moses, G., 620
 Moses, M., 1098
 Mosesson, M. W., 1090
 Mosley, W. C., 192
 Müller, T., 756, 758
 Muchnick, T. L., 1328
 Muirhead, D., 632, 636
 Mukherjee, T. M., 616
 Munoz, V. A., 364, 366, 368
 Murakoshi, H., 936
 Murr, L. E., 42, 260, 1216, 1332
 Murray, S., 700
 Muss, W. H., 628, 754
 Musselman, I. H., 1136
 Myers, S. M., 334
 Myklebust, R. L., 1636, 1640

N

Nadal, M., 784
 Nagaoka, N., 1194
 Nakamura, S., 700
 Nakatsuka, H., 978
 Naranjo, E., 694
 Narayanaswamy, D., 320
 Nassar, R., 774, 776
 Nelson, A. C., 584
 Nelson, C., 20
 Nemanich, R. J., 1354
 Nemoto, M., 54
 Neudeck, G. W., 1396
 Newberry, S., 4, 836

Newbury, D. E., 1250, 1294
 Newcomb, W. W., 452, 522, 532
 Ngan, M., 772
 Nguyen, C., 268
 Nguyen, H. T., 268
 Nguyen, T. D., 256
 Nicholls, P., 710
 Nichols, B. L., 576
 Nielsen, C., 82, 1144
 Ning, Z. H., 796
 Niou, C.-S., 42, 1332
 Nishiyama, Y., 280
 Nishioka, H., 1334
 Nkansah, F. D., 1362
 Nobandegani, F., 700
 Nolan, T. A., 944
 Norris, P., 242
 Norton, M. G., 76, 236
 Norton, W. N., 814
 Novilla, M. N., 612

O

Oakford, L. X., 796, 896
 Ochs, R. L., 506
 O'Connell, M. F., 1574
 Ocumpaugh, W. R., 750
 Odom, R. W., 1556, 1710
 Ogden, A. M., 654
 Oglesby, S. B., 826
 Ogura, K., 1334
 Ohishi, T., 1188
 Oho, E., 1276
 Ohring, M., 1432
 Ohyama, J., 940
 Oikawa, T., 382, 1188
 O'Keefe, M. A., 20, 116, 144
 Okumura, T., 82
 Olafsen, A. G., 920
 Olins, A. L., 504
 Olins, D. E., 504
 Oliveira, M. A., 524
 Olmsted, S. B., 1320
 Olowolafe, J., 1364
 Olsen, K. H., 406
 Olson, N. H., 454, 524, 998
 O'Neil, D., 830
 O'Nions, R. K., 1154
 Opas, M., 484
 op de Beeck, 100
 Orokos, D., 568
 Ortiz, M., 144
 O'Shea, S., 1156

Osheim, Y., 554
 Ostreicher, K. J., 152, 404
 O'Toole, E., 578
 Otten, M. T., 138, 788, 824, 942, 980
 Ottensmeyer, F. P., 1058, 1578
 Ouabbou, A., 1268
 Ourmazd, A., 1474
 Ouyang, F., 1308
 Ouzts, J. C., 842
 Owen, C., 516
 Ozaki, Y., 1530

P

Packwood, R. H., 1652
 Paddy, M. R., 588
 Paine, D. C., 1344
 Palaia, T. A., 720
 Palisano, J. R., 930
 Pan, M., 302, 1406, 1412
 Pan, Y., 34
 Panessa-Warren, B. J., 876
 Panté, N., 490
 Pappas, G. D., 816, 1066
 Park, C., 156
 Park, J.-C., 1400
 Park, J. S., 1702
 Park, J. Y., 780
 Park, K., 992, 1382
 Park, M., 1416
 Park, P. C., 562
 Park, S.-H., 398
 Parker, D. L., 1746
 Parr, G. R., 918
 Pasquinelli, G., 1292
 Patel, R. B., 1328
 Paul, R. N., 838, 842
 Pawley, J. B., 950, 1278
 Payette, C., 364, 366, 368
 Payne, R. S., 1258
 Peachey, L. D., 960, 1056
 Pegler, P., 1406
 Peischl, R., 1326
 Pell, R. J., 1522
 Pella, P. A., 1754
 Pennycook, S. J., 1470
 Perdigao, J., 1092, 1110
 Peretti, F. J., 470
 Perkes, P. R., 312
 Perovic, A., 206
 Perovic, D. D., 1336
 Perovic, V., 206

AUTHOR INDEX*

Perreau, M., 1716
 Perry, D., 400
 Perry, K., 422
 Peters, K.-R., 1276, 1296, 1304
 Peterson, P. A., 386
 Peticolas, L. J., 1338
 Petrali, J. P., 826
 Petrovic, J. J., 342
 Pfullmann, T., 1184
 Phaneuf, R. J., 332
 Phelps, J. M., 1706
 Phillips, M. J., 1562
 Philpott, D. E., 1078
 Pichoir, F., 1650
 Pickering, H. W., 36
 Pierre, A. J., 818
 Piñeyro López, A., 640, 846
 Pindak, R., 270, 278
 Pinto, R. L., 928
 Pirone, T. P., 676
 Pirouz, P., 146, 228
 Piscopo, I., 666
 Pitt, H. A., 1322
 Piwnica-Worms, D., 1586
 Plass, R., 984
 Pocard, N. L., 300
 Pontefract, R. D., 684
 Porter, D., 874
 Porter, J. R., 160, 1774
 Porter, K. R., 8, 546, 1056
 Posthill, J. B., 1350, 1374
 Pouchou, J.-L., 1650
 Pouvelle, B., 714
 Prendergast, F. G., 708
 Prentis, P. F., 548
 Price, G., 620
 Price, J., 1040
 Price, M. W., 1696
 Probst, W., 1042
 Prodan, A., 58
 Pucci, A. M., 630, 898
 Pumpin, D. W., 724
 Purdy, G. R., 206
 Puttinger, R., 628

Q

Qian, W., 938
 Qian, Y., 1452
 Qin, L. C., 350, 1274
 Qiu, N., 44, 202
 Quinones, S., 1332

R

Rabalais, J. W., 1272
 Radermacher, M., 440
 Radicati di Brozolo, F., 1710
 Radmilovic, V., 116
 Radzimski, Z. J., 386, 1680
 Ramani, A. S., 32, 36
 Ramirez B., E., 670
 Ramirez-Bon, E., 916
 Ramos, C., 260, 1216
 Ramos, J. W., 598
 Ranck, J.-L., 518
 Ransom, D. G., 598
 Ratnaparkhi, P. L., 218
 Ray, D. A., 974, 1308
 Ray, M., 1132
 Ray, R., 834
 Rebuffat, A., 898
 Reedy, M. K., 1138
 Reffner, J. A., 1526, 1528
 Reffner, J. R., 1032
 Rehbach, W. P., 1768
 Reine, B. A., 856
 Relia, S. B., 726
 Rémond, G., 1624, 1626, 1652
 Rempfer, G. F., 6
 Rez, P., 312, 1226, 1430
 Rick, R., 1580
 Ridgway, C. C., 892
 Rieder, C. L., 14, 572
 Rigsby, L. L., 864
 Rios Cantú, B. C., 670
 Rippy, M. K., 814
 Ristow, S. S., 680
 Ritchie, S., 58
 Rivas, J. M., 1332
 Rivera, N. M., 108
 Rivers, M. L., 1766
 Roberson, R. W., 748
 Roberts, R. C., 470
 Robertson, D., 854
 Robertson, J. D., 478
 Robertson, L. W., 646
 Robinson, J. P., 530
 Robinson, K. A., 768
 Robson, J., 780, 1328
 Rodriguez, V. A. Tames, 640
 Roemer, E. J., 894
 Rogers, J., 666
 Roggli, V. L., 1116
 Roitman, P., 1402

Romana, L. J., 346
 Rome, L. H., 458
 Romero, R. J., 260, 1216
 Romig, A. D., Jr., 1122, 1684
 Ron, A. E., 1288
 Ronen, N., 658
 Roof, D. J., 482
 Rosbash, M., 560
 Rose, H., 94
 Rose, J. H., 1386
 Rosenberg, G. D., 1746
 Rosenblatt, G. M., 1516
 Rosenbusch, J. P., 438
 Ross, F. M., 248, 324, 1338
 Ross, J. S., 608, 614, 948
 Rossmann, M. G., 524
 Rossoni, P. G., 1700
 Rotermund, H. H., 286
 Roth, K. E., 572
 Rothbard, D. R., 412
 Rothblat, G. H., 924
 Rottem, M., 610
 Rouquet, N., 784
 Roussel, B., 1500
 Rowe, K. A., 850
 Rowlands, N., 1040
 Roy, R. A., 108
 Rozgonyi, G. A., 1354
 Ruben, G. C., 276, 540
 Rubinstein, I., 658
 Rudder, R. A., 1350
 Rudenberg, F. H., 1086
 Rudenberg, H. G., 1084, 1086
 Rueckert, R. R., 524
 Rufner, R., 740
 Rugar, D., 952
 Ruiz Ordóñez, J., 846
 Ruiz, T., 518
 Rupp, G., 568, 570
 Russ, J. C., 1050, 1620
 Russell, P. E., 386, 1128, 1130, 1680
 Russell, S. D., 848

S

Sabatini, R. L., 88
 Sachs, R., 496
 Sadhukhan, P., 392
 Sagalowicz, L., 250
 Sagen, J., 1066
 Saint-Jacques, R. G., 48, 372, 1436
 Sakai, L. Y., 892

AUTHOR INDEX*

- Salamanca-Riba, L., 992, 1382
 Salmon, E. D., 414
 Samsonoff, W., 822
 Samuelsson, S. J., 724
 Sanger, J. M., 696
 Sanger, J. W., 696
 Sankey, O. F., 212
 Sano, T., 54
 Sarikaya, M., 154, 304, 1020, 1024
 Sartore, R., 1690
 Sasaki, K., 70
 Sasaki, T., 1378
 Sass, R. L., 542
 Sass, S. L., 222
 Sathe, S., 444
 Sato, H., 280
 Sato, M., 956
 Saubermann, A. J., 1618
 Saunders, M., 1182
 Sawatski, J., 1504
 Sawyer, L. C., 1030
 Scala, C., 1292
 Schabes-Retchkiman, P. S., 338
 Schaper, J. A., 1290
 Scherer, B., 776
 Schippert, M., 950
 Schmid, M. F., 512, 870, 1054
 Schmidt, H. H. H. W., 812
 Schmidt, L. D., 318, 338
 Schmidt, T. J., 454
 Schneider, T., 714
 Schoessow, K. A., 406
 Schroeter, J. P., 542, 544
 Schulson, E. M., 172
 Schultz, R. L., 806
 Schwander, P., 1474
 Schwarcz, D., 1432
 Schwark, D. W., 1032
 Schwarting, G. A., 890
 Schwartz, J. M., 318, 338
 Schwartz, R. W., 1688
 Schwartzman, A. F., 144
 Schwarz, R. B., 170
 Schwoeble, A. J., 356
 Scott, R., 750
 Scott, V. D., 1658, 1776
 Secco, F., 1404
 Sedat, J. W., 588, 1044
 Seo, Y., 82
 Sepúlveda-Saavedra, J., 640
 Seraphin, S., 298
 Serwer, P., 452
 Setna, R. P., 1478
 Seuntjens, J. M., 86
 Shaapur, F., 1426
 Shah, M. B., 504
 Shand, R. F., 436
 Shao, Z., 1138, 1472, 1568
 Sharma, N., 618
 Sharma, R., 1360, 1404
 Sharov, V. A., 1728
 Sharp, W. P., 748
 Sharps, P. R., 1374
 Shattuck, T. W., 1488
 Sheehan, C. E., 608, 948
 Sheehan, J. G., 1282
 Sheem, S., 1518
 Sheinin, S. S., 1448, 1454, 1458
 Shelburne, J. D., 1116
 Shemlon, S., 126
 Shepherd, N., 774
 Sherman, W. M., 412
 Sherwood, R. D., 1778
 Shields, K. S., 922
 Shimizu, R., 962, 1664, 1676
 Shin, H.-H., 62, 156
 Shin, K., 178
 Shin, K. S., 184
 Shindo, D., 382, 1188
 Shinowara, N. L., 720
 Shipley, K. J., 798
 Shoemaker, G. L., 412
 Shull, J. L., 354
 Siebenlist, K. R., 1090
 Siew, S., 624
 Sigaud, G., 268
 Silbermann, M., 658
 Silcox, J., 1222, 1358
 Silver, R. M., 650
 Simko, S. J., 1782
 Simmons, R. S., 672
 Simon, G. T., 1578
 Simon, M. N., 736
 Simon, S. R., 894
 Simons, D. S., 1548
 Sinfelt, J. H., 288
 Singer, R. H., 552
 Singh, A., 220, 668, 1438
 Singh, A. K., 1362
 Singh, B., 702
 Singh, B. B., 918
 Singh, J. K., 608, 948
 Sinicki, R., 734
 Sinkler, W., 28
 Sisk, A. L., 918
 Stółko, W., 964
 Slodzian, G., 1546, 1600
 Small, J. A., 1494
 Small, M., 1388
 Smith, B. J. E., 1512
 Smith, D., 1388
 Smith, D. A., 1356
 Smith, D. J., 54, 244, 284, 326, 388, 988
 Smith, D. L., 1630
 Smith, G. D. W., 1478
 Smith, K. L., 472, 564
 Smith, M. F., 536
 Smith, P. L., 1366
 Smith, P. R., 440, 444
 Smith, S. D., 384, 1028
 Smith, T. J., 524
 Snow, G., 780
 Soejima, T., 1054
 Sohi, S. S., 884
 Sokola, D., 1630
 Solorzano, I. G., 26
 Somlyo, A. P., 16, 1472, 1568
 Somlyo, A. V., 16, 1138, 1472, 1568
 Sommer, J. R., 774, 776
 Song, C., 84
 Song, M. J., 582
 Soni, K. K., 1694, 1772
 Sosinsky, G. E., 442, 514
 Soto, G. E., 904, 1060
 Spargo, A. E. C., 128, 1176
 Spates, G., 690
 Spector, D. L., 502
 Spellman, L. M., 252
 Spence, J. C. H., 938, 1126, 1172
 Spengler, B., 1558, 1598
 Speyer, R. F., 62, 156, 362
 Spinnler, G. E., 308, 1288
 Spontak, R. J., 300, 384, 1028
 Spring, K. R., 420
 Sprinkle-Cavallo, J., 654
 Sreeram, A. N., 1274
 Srinivasan, S. R., 170
 Staley, J. T., 1020
 Staman, J. W., 1392
 Stambrook, P., 800
 Stamp, T. C. B., 1592
 Stanis, C., 1388
 Stark, T. J., 386
 Stasiak, A., 590

AUTHOR INDEX*

Stearns, D. G., 122
 Stearns, M. B., 122, 258
 Stearns, R. C., 638, 740
 Steeds, J. W., 70, 1152, 1162
 Steel, E. B., 1706
 Steere, R. L., 1074
 Stefflik, D. E., 918
 Stein, H. J., 334
 Steven, A. C., 452, 456, 522, 532
 Stevenson, J. S., 1094
 Stierhof, Y.-D., 824
 Stine, K. J., 1018
 Stipes, R. J., 840
 Stobbs, W. M., 216
 Stockmayer, W. H., 276
 Stoffyn, P., 1330
 Streiffer, S. K., 240
 Ström-Olsen, J. O., 56
 Stroud, R. M., 436
 Strutt, A. J., 1252
 Stubbs, G., 530
 Stupp, S. I., 262, 272
 Subramanian, M. A., 80
 Subramanian, R., 40, 358
 Suematsu, H., 342
 Suenaga, M., 88, 90, 238
 Sueyoshi, T., 1144
 Suga, H., 1670
 Sukedai, E., 310, 962
 Sukow, C. A., 1354
 Suliman, A.-H., 1110
 Sun, S., 1572
 Sundaram, S., 1408
 Sundaesan, R., 1392
 Sundberg, M., 104
 Sung, C. M., 152, 404
 Surace, A., 820
 Sutherland, A. E., 600
 Sutliff, J. A., 166
 Suzuki, S., 1040
 Suzuki, T., 78
 Svensson, G., 104
 Swann, J. W., 472, 564
 Swann, P. R., 394
 Swartzlander, A. B., 1384
 Swedlow, J. R., 588
 Sweeney, T. D., 740
 Swiech, W., 332
 Swift, E., Jr., 1110
 Swift, J. G., 616
 Swyt, C. R., 1770
 Szarowski, D. H., 472, 564

T

Tabbernor, M. A., 1174
 Tadayon, B., 1376
 Tafoya, B. C., 1688
 Takahashi, H., 82
 Takahashi, K., 78
 Takaya, K., 1596
 Takeo, M., 34
 Takeyasu, K., 1138
 Talbot, H., 994
 Tall, B. D., 882
 Tallant, D. R., 1688
 Tam, M. W., 132
 Tamm, L. K., 1138
 Tan, T. Y., 1366
 Tanaka, H., 678
 Tanaka, M., 232, 940, 1180
 Tanaka, Y., 280
 Tanikawa, K., 880
 Tanji, T., 990
 Taraschi, T. F., 714
 Tarin, P. M., 260, 1216
 Tattree, B., 710
 Taylor, D. L., 418
 Taylor, I., 776
 Taylor, M. A., 1758
 Taylor, R., 866
 Terauchi, M., 232, 940, 1180
 Terreault, B., 48
 Terren, N., 756
 Terris, B. D., 268, 952
 Tersoff, J., 1340
 Terukina, S., 1090
 Teshima, J., 1334
 Thangaraj, N., 114
 Thedford, L. S., 672
 Theodore, N. D., 1404, 1406,
 1408, 1410, 1412, 1418
 Thomas, D., 514
 Thomas, E. L., 266, 274, 380, 1032
 Thomas, G., 208, 374
 Thomas, K. L., 1724
 Thompson, A. M., 1772
 Thompson, F. Y., 654
 Thompson, M. N., 976
 Thompson, P. D., 796
 Thornbury, D. W., 676
 Thornham, K. T., 840
 Thurner, J., 628
 Tichelaar, W., 534
 Tietz, H., 100

Tihova, M., 710
 Tillack, T. W., 1138
 Timmons, M. L., 1374
 Tindale, N. W., 1488
 Tischler, M. A., 1372
 Tivol, W. F., 1168, 1446
 Tonomura, A., 68, 990
 Torres Cepeda, T. E., 846
 Tortora, G. T., 876
 Totoda, S. D., 314
 Trachtenberg, S., 534, 536
 Trask, B., 496
 Travis, J. L., 568
 Treado, P. J., 1532
 Trimble, R., 822
 Triplett, B. A., 858
 Tritsch, G., 794
 Tromp, R. M., 294
 Trus, B. L., 452, 456, 522, 532
 Tsai, F., 348, 360, 370
 Tsai, K.-H., 144
 Tsai, Y.-Z., 862
 Tsay Adam, B.-L., 642
 Tsay, C.-C., 852
 Tsugoshi, T., 1712
 Tsukada, N., 1562
 Tsuno, K., 940
 Tsutsumi, V., 880
 Tuan, R. S., 798
 Tulloch, P. A., 1176
 Tunberg, B., 1106
 Tung, L.-C., 704
 Turek, J. J., 718
 Turner, H., 866
 Turner, J. H., 20
 Turner, J. N., 472, 564, 1168, 1446
 Turner, S., 1706
 Tuttle, B. A., 1688
 Twisten, R. D., 324
 Twieg, R. J., 268
 Twigg, M. E., 1376
 Tyerman, J., 368
 Typke, D., 1000

U

Ueda, T., 978
 Umezawa, T., 240
 Urdanetta, E. C., 210
 Uyeno, D., 1088

V

Van Daele, A., 1612

AUTHOR INDEX*

van den Engh, G., 496
 Vander Voort, G. F., 1606
 Vanderwalker, D. M., 186
 Vander Wood, T. B., 1492
 Van Dyck, D., 100
 Van Grieken, R., 1482
 Van't Hof, J., 1038
 Vecchio, K. S., 40, 358
 Veilleux, G., 372
 Venables, J. A., 308
 Venkatesan, S., 1396
 Verbeeck, A., 1612
 Verkerke, R., 1588
 Vernon, G. M., 818, 820
 Vezie, D. L., 266, 1032
 Vidal, S., 870
 Viehland, D., 992
 Villeneuve, D. C., 668
 Vincent, R., 1162
 Viney, C., 264, 734
 Vitarelli, J., 1680
 Vogel, M. W., 470
 Vogt, M., 756
 Vozzo, J. A., 836

W

Wagstaff, J. H., 1748
 Waldo, R. A., 1782
 Walian, P., 434
 Walker, C. T., 1658
 Wall, J. S., 462, 736
 Wall, Jennifer, 1132
 Wall, Joseph, 1390
 Walsh, L. G., 650, 1594
 Walther, P., 1280
 Wampler, W. R., 334
 Wang, A. Z., 698
 Wang, F., 728
 Wang, G. J., 454
 Wang, J. B., 716
 Wang, J. C., 698
 Wang, L., 1462
 Wang, L. M., 352, 378
 Wang, L.-W., 852
 Wang, S.-Y., 102, 142, 982
 Wang, X., 1642, 1672
 Wang, Y.-L., 550
 Wang, Y. Y., 1568
 Wang, Z. L., 72, 336, 1170,
 1244, 1256
 Ware, N. G., 1740
 Warner, R. R., 1576

Warren, J. B., 876
 Wasserman, A. J., 646
 Watanabe, M., 54
 Waterman-Storer, C. M., 696
 Watkins, C. J., 920
 Watson, J. H. L., 2, 1068
 Waytena, G., 1254, 1430
 Weatherly, G. C., 206, 224
 Webster, S., 1512
 Weesner, F. J., 1524
 Wei, C. C., 1392
 Weisel, J., 1056
 Weiss, J. K., 102, 134, 142, 244,
 988, 1430
 Welch, D. O., 90
 Welkie, D. G., 1554
 Welland, M. E., 1156
 Wellis, D., 476
 Wells, C. L., 1320
 Wells, O. C., 1608
 Welnhofer, E. P., 568
 Wen, S., 84, 388
 Werber, G., 64
 Wergin, W. P., 908, 1314
 West, P. E., 1046
 Westmacott, K. H., 20
 Weyda, F., 674, 760, 790
 Wheeler, R., 1242
 White, J., 476
 White, S. L., 612
 Whittaker, C. A., 598
 Whitter, E. F., 806
 Wight, S., 1704
 Williams, D. B., 182, 1200, 1236,
 1252, 1772
 Williams, E. D., 332
 Williams, H. N., 882
 Williams, S., 1038
 Willich, P., 1628
 Wilson, S. R., 1416
 Windsor, E. S., 1706
 Wingfield, P., 456
 Winnett, M., 648
 Winter, K., 742
 Wisniewski, H., 540
 Witcomb, M. J., 20
 Withiam-Leitch, M. L., 570
 Witkus, R., 818, 820
 Wittig, J. E., 44
 Wittry, D. B., 1730, 1732, 1734
 Wojcinski, Z., 666
 Wolfenbarger, L., Jr., 642

Wong, K., 1358
 Wong, T. M. H., 1156
 Wood, J. I., 730
 Woodcock, C. L., 498
 Woodward, J. T., 1134
 Woollacott, R. M., 928
 Wu, S., 1612
 Wunderlich, B., 1032
 Wuttig, M., 992

X

Xhoffer, C., 1482
 Xiao, S. Q., 228, 1102
 Ximen, J., 950
 Xing, Y., 558
 Xu, P., 282, 1434

Y

Yadavalli, S., 146
 Yagi, K., 280
 Yamada, A., 1106
 Yamamoto, K., 1670
 Yamazumi, K., 1090
 Yang, J., 1014, 1138
 Yang, S. V., 1748
 Yao, N., 288, 1778
 Yates, P. E., 634, 1094
 Yen, H., 1396
 Yin, L. R.-S., 752
 Yokota, Y., 962
 Yorio, T., 796
 York, B. R., 1764
 Yoshida, M., 1378
 Yoshida, T., 68
 Yoshikawa, H., 1664, 1676
 Young, M. C., 446
 Young, S. J., 904, 1040, 1060
 Yu, H., 1016
 Yu, H.-S., 848
 Yu, J., 720
 Yu, X., 448
 Yuasa, T., 1774

Z

Zack, P. M., 814
 Zaharias, R., 1108
 Zaitz, M. A., 1756
 Zaluska, A., 56
 Zaluzec, N. J., 1466
 Zandbergen, H. W., 106
 Zanota, A., 400
 Zasadzinski, J. A. N., 278, 1134

AUTHOR INDEX*

Zeissler, C. J., 1788
Zemyan, S. M., 1236
Zernow, L., 42
Zhang, H., 74
Zhang, J., 406
Zhang, J. P., 74, 124
Zhang, W., 380
Zhang, X., 246, 1038
Zhao, J., 242
Zhao, X. K., 1014
Zheng, P., 48
Zhong, Q., 1480
Zhou, C., 38
Zhou, D., 298
Zhou, L., 1128, 1130
Zhu, X., 712
Zhu, Y., 88, 90, 238
Zielinski, E. M., 240
Zolensky, M., 1720
Zreiba, N. A., 1616
Zuo, H. J., 1696
Zuo, J. M., 1172, 1450

Notes

Notes